FIRE SUPPRESSION SYSTEM PERFORMANCE OF ALTERNATIVE AGENTS IN AIRCRAFT ENGINE AND DRY BAY LABORATORY SIMULATIONS

SP 890: VOL. II

RICHARD G. GANN, EDITOR

NIST

United States Department of Commerce

Technology Administration

National Institute of Standards and Technology

November 1995

FIRE SUPPRESSION SYSTEM PERFORMANCE OF ALTERNATIVE AGENTS IN AIRCRAFT ENGINE AND DRY BAY LABORATORY SIMULATIONS

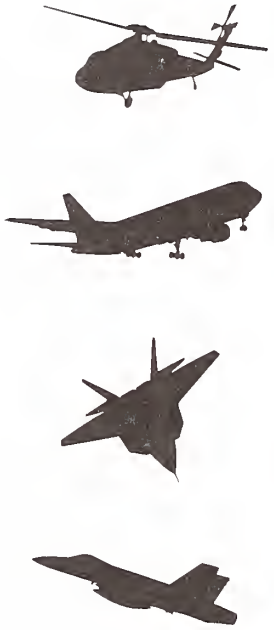

SP 890: Vol. II

RICHARD G. GANN, EDITOR

NIST

Certain commercial products are identified in this report in order to specify adequately the equipment used. Such identification does not imply recommendation by the National Institute of Standards and Technology, nor does it imply that this equipment is the best available for the purpose.

Building and Fire Research Laboratory
National Institute of Standards
and Technology
Gaithersburg, MD 20899

U.S. Department of Commerce
Ronald H. Brown, Secretary
Technology Administration
Mary L. Good,
Under Secretary for Technology

National Institute of Standards
and Technology
Arati Prabhakar, Director

November 1995

National Institute of Standards
and Technology
Special Publication 890, Vol. II
Natl. Inst. Stand. Technol.
Spec. Publ. 890, Vol. II
634 pages (Nov. 1995)
CODEN: NSPUE2

U.S. Government Printing Office
Washington: 1995

For sale by the Superintendent
of Documents
U.S. Government Printing Office
Washington, DC 20402

EXECUTIVE SUMMARY

Richard G. Gann
Building and Fire Research Laboratory

Halon 1301 (CF_3Br), one of the chemicals identified as detrimental to stratospheric ozone, had become the choice for suppressing in-flight fires in nearly all types of aircraft. Production of new halon 1301 was stopped on January 1, 1994, and efforts are underway to identify near-term replacements for critical applications, focussing on available or currently emerging chemicals and technologies. In particular, the three military services and the Federal Aviation Administration (FAA) have pooled resources to provide solutions for two applications: engine nacelles and dry (avionics) bays, while realizing that there are other aircraft areas also in need of protection. This project was managed at Wright Patterson Air Force Base (WPAFB), with oversight provided by a Technology Transition Team of the four sponsors.

The first major objective of the program was to identify the optimal available alternative fluid(s) for use in suppressing fires in aircraft engine nacelles and dry (avionics) bays. In October, 1993, based on extensive laboratory research and real-scale testing at WPAFB, the sponsors decided on a reduced list of candidates for each application; for engine nacelles: C_2HF_5 (HFC-125), C_3HF_7 (HFC-227ea), and CF_3I; for dry bays: C_2HF_5, C_3F_8 (FC-218), and CF_3I. Much of the laboratory-scale research leading to that decision has been described in NIST Special Publication 861, *Evaluation of Alternative In-Flight Fire Suppressants for Full-Scale Testing in Simulated Aircraft Engine Nacelles and Dry Bays*. That report documents the comprehensive experimental program to screen the performance of possible suppressant chemicals as a means to identify the best candidates for subsequent full-scale aircraft fire extinguishment evaluation at Wright Laboratory, and addresses the compatibility of these agents with flight systems, people, and the environment. In particular, apparatus and measurement methods suited to aircraft applications are carefully described, and extensive performance data are provided and analyzed. The reader is referred to that report as a prerequisite and companion to the current document.

The subsequent research described in this report falls into two broad categories:

Part 1: Knowledge to help differentiate among chemicals, leading to selection of the optimal currently available option(s) for in-flight fire suppression

Fire Suppression Efficiency. Most of the laboratory-scale information was reported in SP 861. In new studies in a deflagration/detonation tube, simulating fire suppression in a dry bay, FC-218 provided the best overall performance; HFC-125 was comparable under many conditions. CF_3I had the greatest positive impact at low addition levels, but showed non-monotonic behavior of flame speed and shock pressure at higher levels. In fire suppression efficiency measurements in a turbulent spray burner simulating engine nacelle fires, CF_3I was found to be more efficient than either HFC-125 or HFC-227ea. However, at an elevated temperature of 150 °C, the three chemicals performed equally on a mass basis.

Stability During Storage. There should be no problems with designing long-term storage capability for any of the four agents. The agents were tested for chemical stability in the presence of likely storage materials for over a year under typical in-use pressures and temperatures. The stability of HFC-125, HFC-227ea, and FC-218 was excellent. Samples of CF_3I were observed to be stable at 23 °C; however, during exposure at 100 °C and especially at 150 °C, small amounts of CO_2 and an unknown chemical appeared whose concentration increased with exposure time. Each of the four chemicals is compatible with a choice of materials for the storage containers: gasket materials, lubricants, and metals. Each agent caused only minor swelling in at least three of the elastomers and at most moderate swelling in the greases. The long-term deformation of the seven elastomers showed that at least two elastomers are compatible with each of the agents. The long-term stability of the seven elastomers, evaluated using compression set measurements, showed that at least two elastomers were not subject to excessive permanent deformation in each of the four agents. Long-term immersion of coupons of container metals at storage temperatures and pressure in each of the four candidate agents or halon 1301 produced little mass change or visual corrosion, although CF_3I showed some small interaction with three of the metals at high temperature. Slow strain rate tests of the metals in four of the agents at 20 °C and 150 °C and 5.86 MPa showed no difference from metal samples immersed in inert argon. CF_3I was not compatible with a titanium alloy at elevated temperature.

Safety Following Discharge. Predictions of the production of HF during fire suppression indicate that fires in dry bays are suppressed sufficiently quickly that only small amounts will be formed. For engine nacelle fires, the model developed here predicts that HFC-227ea, HFC-125 and FC-218 would produce similar amounts, while the more efficient CF_3I would produce far less. Exposure to surfaces heated by the fire would produce more HF from CF_3I than from an equal amount of the other three chemicals. Samples of aircraft materials that might be located near or downstream of an engine nacelle fire were immersed in 1 % or 10 % aqueous HF and then stored at 100 % relative humidity for 30 days at 22 °C. No significant degradation was seen. While accidentally-discharged CF_3I will decompose under both normal outdoor and indoor lighting, laboratory measurements and dispersion modeling show that the concentrations of potentially toxic photolysis products (HF, COF_2) are not likely to be sufficient to hinder prompt escape.

Discharge Performance. All four of the chemicals can be expected to discharge and disperse well from their storage and distribution systems at temperatures near 20 °C. At the lower temperatures experienced during high altitude flight or cold weather operation, CF_3I and HFC-227ea, with their higher boiling points, would not disperse as well as the other two chemicals.

Optimal Currently Available Option. Based on the results available in October, 1994, we recommended the selection of HFC-125 as the optimal candidate for Phase III examination for both engine nacelle and dry bay fire suppression. FC-218 possesses an extremely long environmental lifetime. While CF_3I was the most efficient suppressant, being virtually a drop-in replacement for halon 1301 in some tests, it had three drawbacks: its inhalation toxicity in cardiac sensitization testing, inconclusive stability and materials compatibility data, and a relatively high boiling point. HFC-227ea has a similar boiling point, and thus would also perform less well at low temperatures. The knowledge that has accrued in the final year of the project has not changed our perspective on this recommendation. During the fall 1994 meetings of the Technology Transition Team, these data and the results of an extensive and carefully constructed series of real-scale live-fire tests at Wright Patterson Air Force Base led the Team to recommend HFC-125 as the candidate for Phase III evaluation for both applications.

Part 2: Knowledge to assist in the development of engineering design criteria and suppressant system certification

Agent Discharge Behavior. The rate at which a suppressant will emerge from its storage container depends on the thermodynamic properties of the stored fluid and any pressurizing gas as well as the initial conditions in the container. Effective design of the suppression hardware requires quantitative performance measures for these chemicals. The NIST computer code PROFISSY accurately calculates binary vapor-liquid equilibria within the storage bottle, data needed by storage system designers. Laboratory data show that the nitrogen dissolved in the stored liquid agent significantly affects the agent discharge whether in a direct release system for dry bays or a piping system for engine nacelles. A NIST-developed storage bottle discharge model, which incorporates nitrogen degassing, generally predicts agent discharge times to within a factor of two, but occasionally a factor of four. The only required inputs for the model are the initial conditions in the vessel. For plumbed engine nacelle systems, a new, validated model can be used to facilitate calculations of transient, two-phase pipe flow. We have developed a flow chart to organize the use of these tools into a coherent process for optimal design of a new discharge system.

Engine Nacelle Fire Suppression Guidance. The selection of the mass of agent to be stored on an aircraft should be based on the amount needed to quench the worst realistic fire. For engine nacelles with ribs and other obstructions, this is a baffle-stabilized pool fire. Heating the air stream and, to a lesser extent, increasing the pressure, increases the mass of agent needed for flame extinction, while the fuel flow had no significant effect. A step-by-step procedure has been developed that gives guidance in determining fire suppressant concentrations and discharge times for flame extinguishment. It shows the relative importance of agent injection duration, air flow and velocity, agent/air mixing mode, and fire scenario. A reasonable target concentration for an agent in the fire zone is that needed to quench the most flammable fuel/air mixture, both ensuring flame suppression and preventing re-ignition during the period of injection.

Real-Time Concentration Measurement. Determination of the dispersion of the suppressant following discharge requires measurements of its concentration that are well-resolved in both time and space. We examined two instruments (based on thermal conductivity and infrared absorption) in order to assess their ability to perform *in situ* measurements with the ~1 ms time resolution needed for dry bay applications. Neither performed well. Both were improved extensively and showed potential. However, both need further work to be useful in practical systems. A review of the sensing literature shows a number of alternative approaches, but none that could be accurately adapted to this application without a significant development and testing effort. The most promising are time-resolved mass spectrometry and mid- and near-infrared absorption combined with fiber optics to provide easy access and the needed spatial resolution.

Certification Guidance. HFC-125 closely replicates the physical and dispersion properties of halon 1301. Thus it is an excellent simulant for hardware development and can be used to certify those engine nacelle fire suppression systems that still rely on halon 1301. The mixing time for agent entrainment behind an obstacle is different under non-fire conditions than for fire conditions. A method for using the non-fire data to approximate the fire suppression concentration has been developed.

Interaction with Metal Fires. In laboratory experiments, none of the four alternative chemicals nor halon 1301 showed exacerbation of burning of magnesium or titanium rods. It is not explicitly known

why the flare-ups observed during the introduction of halon 1301 to real metal fires were not observed here. However, it may be useful to know that in the circumstances replicated in the laboratory tests, the alternative agents did not worsen the combustion relative to that with halon 1301 present.

TABLE OF CONTENTS

Page

PART 2 (continued from Volume I)

9. SUPPRESSION OF ENGINE NACELLE FIRES

Anthony Hamins, Thomas Cleary, Paul Borthwick, Nickolai Gorchkov,
Kevin McGrattan, Glenn Forney, and William Grosshandler
Building and Fire Research Laboratory

Cary Presser, Chemical Sciences and Technology Laboratory

Lynn Melton, Department of Chemistry, University of Texas, Dallas, Texas

Contents

9.1 Overview

The engine nacelle encases the jet engine compressor, combustors, and turbine. A nacelle fire is typically a turbulent diffusion flame stabilized behind an obstruction in a moderately high speed air flow. The fuel source for a fire in the nacelle are leaking pipes carrying jet fuel or hydraulic fluid, that can feed the fire either as a spray or in the form of a puddle or pool. Extinguishment occurs when a critical amount of agent is transported to the fire. After suppression of the fire, re-ignition can occur as fuel vapor makes contact with a hot metal surface or an electrical spark due to shorted wires.

Because of its many positive attributes, halon 1301, or trifluorobromomethane (CF_3Br), has been used as a fire extinguishing agent for protecting aircraft engine nacelles. Fortunately, in-flight fires are not frequent. In commercial U.S. aircraft during the 18 year period from 1956 to 1974, a total of 56 nacelle fires occurred. In U.S. military aircraft, 80 to 90 noncombat fires occurred annually during that period (Altman *et al.*, 1983). In general, halon systems have been very effective in suppressing nacelle fires (Tedeschi and Leach, 1995). As halon 1301 is replaced with possibly less effective suppressant, continued effective aircraft protection becomes a challenge. For this reason, organized guidance in the determination of the amount of replacement agent required for protection of engine nacelles over a range of operating conditions is needed. In this study, a series of experimental measurements were conducted and simple models were developed in an effort to provide an improved understanding of the influence of various parameters on the processes controlling flame stability in engine nacelles. The knowledge gained is compiled into usable tools which may assist suppression system designers determine the mass and rate of agent injection required for engine nacelle fire suppression.

This section is broken into several subsections. In Section 9.2, a brief description of the range of parameters which characterize the temperature and flow field in engine nacelles is provided in an effort to understand possible fire conditions. The historical development of current halon 1301 fire protection systems in engine nacelles is described and current specifications for design and certification are summarized. In Section 9.3, the results of four distinct experiments are discussed. First, the suppression effectiveness of candidate replacement agents are tested on a turbulent jet spray flame. Second, suppression of a baffle stabilized pool fire is described. Third, the impact of the replacement agents on ignition temperature of fuel/air/agent mixtures flowing over a hot metal surface is discussed. Finally, experiments determining the flammability limits of propane/air/HFC-125 mixtures are discussed. A detailed description of the experimental methods and results are included for each configuration. The experimental studies are summarized in a discussion that emphasizes the importance of agent entrainment into the recirculation/combustion zone of obstacle stabilized flames. In Section 9.4, computational modeling of gaseous agent injection into a mock engine nacelle is described. The calculations are compared to measurements conducted in a wind tunnel in an effort to validate the model. In Section 9.5, a simple model is developed to give guidance on agent concentration requirements for flame suppression in generic nacelle configurations. A step-by-step procedure is proposed as a guideline for fire protection system design and certification. Key findings and recommendations are compiled in Section 9.6, acknowledgments are cited in Section 9.7, and references are listed in Section 9.8.

9.2 Review of Nacelle Geometry and Fire Protection Systems

There is no such thing as a typical engine nacelle. Each aircraft type has a nacelle with a distinct geometry and with varying amounts of clutter in the form of tubes, boxes, and so on. It is possible,

Table 1. Engine nacelle characteristics

Aircraft	Free Volume (m^3)	Max Air Flow (kg/s)	Max T_{air} (°C)	Max T_{wall} (°C)	System
YF-16	1.5[b]	1.1[b]	150[b]	230[b]	1301[b]
F-15/F-100	2.4[b]	0.9[b]	≈320[b]	≈300[b]	1301[b]
F-111/TF-30	a	1.2[b]	110[b]	140[b]	1202[b]
S-3A/TF-34	0.60[b]	1[b]	210[b] @sea level	77[b] @sea level	none[b]
F-22	2.8[c]	0.2[c]	a	a	a
727/JT-8D	a	0[b]	a	a	1301[b]
F/A-18	1.1[d]	0.9[d]	330[d]	390[d]	1301[d]
F-104/J-79	a	12[b]	180[b]	660[b]	none[b]

a data not available.
b McClure *et al.*, (1974)
c Kolleck (1993)
d Picard *et al.*, (1993)

however, to idealize a nacelle through characterization of key parameters. An idealization facilitates estimation of the minimum amount of agent required for fire protection.

Current fire protection systems for engine nacelles consist of one or more bottles and pipes leading to the nacelle. The piping that carries the agent into the nacelle is a simple tube. Nozzles are not typically used. In some cases, a tee is used to enhance agent dispersion throughout the nacelle. The diameter of the tube carrying the agent is a means to control the rate of agent injection. For halon 1301, the agent enters the nacelle as a two phase flow which rapidly flash vaporizes. Agent is typically introduced into the nacelle at a single location, although some aircraft such as the B2 have as many as 12 agent injection locations. Unfortunately, very few public documents are available which describe aircraft engine nacelle geometries in detail.

The range of conditions which exist in engine nacelles are of interest, because this information facilitates proper design of fire protection systems. For example, the air temperature in the nacelle impacts flame stability and the ease of extinguishment. The maximum wall surface temperature poses a hazard as it may promote the ignition of a leaking jet fuel or hydraulic fluid line. Maximum wall temperatures in current aircraft nacelles can be as high as 650 °C. Bleed air from the engine, flowing through the nacelle, can also act as an ignition source and can be as high as 600 °C according to Altman *et al.*, (1983), although no specific aircraft types are mentioned. Advanced aircraft may even have higher surface and air temperatures (Altman *et al.*, 1983). Table 1 lists values of the free volume, air flow, and maximum values of the air and wall temperatures in nacelles for a number of different aircraft under typical operating conditions. Table 1 also presents the agent type currently used for aircraft fire protection, which includes halon 1301 (CF_3Br) and halon 1202 (CF_2Br_2). Unfortunately, much of the available information is anecdotal, such as the response to a written survey presented in the Booz-Allen-Hamilton report (Kolleck, 1993). Comprehensive, detailed information on

these parameters is reported by McClure *et al.*, (1974) for the F-111 aircraft. That report is an excellent model of determination of key engine nacelle parameters.

Actual values of the maximum nacelle wall temperature, the air flow, and the maximum air temperature in the nacelle vary as a function of aircraft velocity, ambient temperature, and specific location within the nacelle as well as many other parameters. Minimum air temperature in the nacelle can reach values as low as -60 °C, depending on ambient conditions. The pressure inside the nacelle varies with altitude. For a F-111 aircraft, pressures can be sub or super-ambient, varying from 13 to 124 kPa (2 to 18 psia) (McClure *et al.*, 1974). Typical average free stream air velocities in nacelles cover a wide range of values, with maximum velocities as high as 100 m/s in some aircraft (Altman *et al.*, 1983).

9.2.1 Development of Agent Requirements. The history of halon 1301 engine nacelle suppression system requirements provides insight to fire prevention strategies currently employed for engine nacelle fire extinguishment. The following chronology is not meant to be a comprehensive history, but details the development of the technical basis for the current Military Specification and its potential deficiencies, either in terms of under- or over-design. Understanding the current guidelines for halon 1301 systems should assist in the development of new guidelines for alternative agents.

Suppression systems for protected aircraft engine nacelles have primarily relied on halon 1202 and, predominately, halon 1301 since the late 1950s. At present, most U.S. military and civilian aircraft use halon 1301 (McClure, 1974; Kolleck, 1993). In the 1950s, halon 1301 proved to be a most effective fire extinguishing agent in engine nacelle applications given the premiums placed on weight and storage volume inherent in aircraft. A knowledge base of halon systems was built upon the experience and experimental programs of the Civil Aeronautics Administration (CAA) and the military. A large fraction of that knowledge base was utilized in MIL-E 22285, the Military Specification written in 1959, specific to halon 1301 systems for (military) aircraft. Commercial aircraft have similar requirements.

Some aircraft with single engines (F-15) or pylon mounted engines (KC-135) do not have active fire protection for the engine nacelle(s) (McClure, 1974). An engine nacelle fire usually renders the engine inoperable or it is purposely shut-down, thus, in the case of single engine planes there is little reason to suppress a fire since the aircraft would be without power. In the case of pylon-mounted, multi-engine aircraft, an engine fire can continue to burn and not pose a threat to the rest of the aircraft; damage is limited to the engine.

The initial research performed by the CAA (the predecessor to the Federal Aviation Administration) dealing with in-flight aircraft engine fires took place between 1940 and 1943 (Grieme, 1941; Hansberry, 1948). Aircraft engines at that time were all of the piston/propeller type. Interestingly, that work was performed on the grounds of the National Bureau of Standards in Washington, DC prior to CAA's establishment of the Technical Development and Evaluation Center in Indianapolis. Full-scale engine/wing assemblies were tested in front of a wind tunnel to simulate flight conditions. Tests were performed with the engine running and fuel fires initiated in the nacelle to closely match in-flight fire scenarios. Data concerning relative agent efficiencies, required amounts, and design of distribution systems were gathered (Grieme, 1941). With the introduction of jet engine propulsion, more research and development on nacelle fire protection followed. Klein (1950a) reported the results of the Jet Engine Fire Protection Program of the U.S. Air Force. The effect on fire suppression of a number of agents, distribution systems (consisting of perforated piping), and agent injection rates were investigated. The CAA performed a number of tests on the XB-45 aircraft, evaluating methyl bromide and halon 1202 (Hughes, 1953). Perforated piping distribution rings were used to disperse the agent in the annular cross-section of the nacelle.

In the early 1950's, a simpler and more efficient design termed the high-rate-discharge (HRD) system was developed at the CAA (Hughes, 1953; Middlesworth, 1954; Hansberry, 1954; 1956). No distribution rings were employed; agent was injected through an open tube at a rate much higher than previous systems employing perforated piping and/or nozzles. In the high-rate-discharge system, agent dispersion occurs primarily by the turbulent mixing of the agent jet and the nacelle air. It was found that less agent was required to suppress nacelle fires with this technique and the less complicated design saved weight. This technique is described in MIL-E 22285. Hansberry (1956) reported on design features which were empirically found to increase effectiveness of the HRD technique. He reported that agent outlets should be as far forward as possible in zones with high air flow, and the outlets should be positioned to produce a helical spray pattern. Also, discharges parallel or perpendicular to the nacelle centerline were "not effective" (less effective). Agent discharge durations varied between 0.5 and 0.9 s for the initial HRD tests. This was translated into a design discharge duration of less than 1 s. Equations giving the weight of extinguishing agents as required for HRD systems as a function of air flow and net volume of the nacelle, for a "smooth" and "rough" zone in low air flows and for "smooth" zones in high air flow were reported.

The selection of the most suitable agent for nacelle applications was an ongoing task through the 1940's and 1950's and prior to halon 1301, other extinguishing agents were used or considered, most notably carbon tetrachloride, carbon dioxide, methyl bromide, chlorobromomethane, and D-L (a mixture of chlorobromomethane and carbon dioxide developed in Germany). The German Air Ministry sponsored the research leading to chlorobromomethane and D-L systems for aircraft (NFPA Quarterly, 1948; Klein, 1950b). Both full-scale engine fires and small-scale testing were performed in the U.S to evaluate suppression efficiency of various agents. Chlorobromomethane, methyl bromide, carbon dioxide, Freon 12, Freon 22, methyl iodide, and a patented mixture of methyl bromide, ethyl bromide and ethylenechlorobromide were considered by the Air Force for jet engine fire protection (Klein, 1950a). The CAA studied methyl bromide, CO_2, bromochloromethane and halon 1301 (Hansberry, 1956). In the late 1940s, the Air Force Air Material Command began an agent development program for a superior fire extinguishing agent (Klein, 1950b). A superior agent was defined as providing better extinguishing properties than bromochloromethane (BC) over a temperature range from -65 to 160 °F, would be less toxic and less corrosive than BC, suitable for class A,B, and C fires, and have a higher specific gravity than BC.

A comprehensive screening of candidate fire suppression agents was performed by the Purdue Research Foundation (Malcolm, 1950). The bench-scale apparatus used for that study was the Bureau of Mines flammability apparatus (Coward and Jones, 1939) which was found to give repeatable results. The apparatus was used to determine if a mixture of combustible vapor, air and agent could be ignited by an inductive spark generated across a electrode gap. A map of the fuel/air and agent ratios that could be ignited starting from the flammability limits of the fuel in air alone represented the flammable range of the mixture. Peak agent concentrations required to inert n-heptane/air/agent mixtures at room temperature were obtained. The peak value was considered a measure of the relative agent effectiveness. HFC-125 and HFC-227 were not included in that study, but halon 1301 and CF_3I were included. A driving force in the agent selection for HRD systems also included physical characteristics such as agent volatility.

It was recognized that the ability to make temporal concentration measurements would provide a means to evaluate a suppression system without resorting to actual aircraft engine fire testing or merely relying on calculations, visual observations, and discharge duration estimates (New and Middlesworth, 1953). A suitable measurement technique was developed such that concentration measurements could be made during simulated flight conditions or actual aircraft flight (Demaree and Dierdorf, 1959). The suppression system evaluation was based on concentration measurements at various locations in the nacelle to confirm that the desired design concentration was achieved and

maintained during flight or under simulated flight conditions. The design concentration was obtained by measuring concentrations during a number of tests of various aircraft extinguishing systems that were deemed adequate for extinguishing full-scale fires. It was concluded that a concentration of 6 % by volume of halon 1301 over a duration of not less than 0.5 s at all sampling locations in the nacelle was sufficient to extinguish all test fires (Demaree and Dierdorf, 1959). It was not stated what the minimum duration in any single location should be, implying a lower limit of 0.5 s. It turns out that the inerting concentration from the Bureau of Mines flammability apparatus for a n-heptane/air/halon 1301 mixture at ambient temperature and near atmospheric pressure is also approximately the same value, 6.1 % (Malcolm, 1950). This small-scale result, though known at the time of the concentration apparatus development, was not apparently considered during the design concentration identification process. The Military Specification was published in 1959, and except for an addendum in 1960, remained unchanged. The Military Specification calls for a 6 % volumetric concentration and 0.5 s minimum duration for all locations in the protected area. Suppression research after the implementation of the Military Specification (MIL-E 22285) in 1959 continued because of concerns related to the significant changes in the nacelle environment for advanced (supersonic) aircraft.

Concerns relating to nacelle fire protection, as well as other fire safety issues were raised during the early phase of supersonic aircraft development. Supersonic flight presents unique aircraft environments not encountered in subsonic flight. Gerstein and Allen (1964) detail some of the aircraft environmental factors associated with fire hazards during supersonic flight. Those factors directly related to nacelle fires include:

1. Temperature: elevated skin surface temperatures, high stagnation air temperatures and low ambient air temperatures.

2. Pressure: typically low ambient pressure.

3. Air Flow: high air flow.

McClure *et al.*, (1974) reported extensively on the operating environment in the F-111 nacelle, a supersonic aircraft. They listed high temperatures, both surface and ram-air temperatures and high air flow conditions. Recently, (Picard *et al.*, 1993) the U.S. Navy's F/A-18 aircraft was put through extensive testing to examine the possible causes of a high incidence of engine nacelle fires. A large amount of in-flight nacelle temperature (surface and air) and air flow data were gathered.

Studies with the Aircraft Engine Nacelle Fire Test Simulator showed that for many nacelle conditions, the amount of halon 1301 required for suppression was much less than current guidelines, provided that very rapid injection took place, and hot surface re-ignition did not occur (Johnson and Grenich, 1986). In some cases, a factor of ten decrease was observed. In addition, peak agent concentrations lower than the design concentration were found to extinguish nacelle fires. Johnson and Grenich (1986) also reported the effects of simulated battle damage to a particular nacelle configuration. Depending on the exact details of the damage, agent requirements changed and current guidelines were not sufficient.

No changes in the concentration and duration requirements in the Military Specification were promulgated due to changes in nacelle conditions associated with supersonic flight. The performance history of aircraft engine nacelle suppression systems confirms the reliable nature of those systems designed to meet the Military Specification (Botteri *et al.*, 1972; Tedeschi and Leach, 1995) which suggests a conservative design philosophy.

9.2.2 Specifications for Aircraft Fire Protection. Typically, there is air flow through the nacelle to provide cooling of hot surfaces and to sweep out combustible vapors. While serving these important functions, the air flow also dilutes the extinguishing agent after a discharge, and carries it out of the nacelle rapidly. The number of air exchanges per unit time (volumetric air flow/ net volume) depends on the aircraft design and reaches highs of about one per second (Kolleck, 1993). No lower limit can be placed on the number of air exchanges because a ground fire scenario is possible where, for most aircraft, no nacelle air flow is provided. Clearly, the amount of agent required to achieve a specified concentration in the nacelle depends on the air flow and the nacelle volume. Those two variables along with a description of the nacelle geometry are the parameters in the design guidelines of the Military Specification.

Section 3.8.1 of the Navy Specification MIL-E 22285, and Section 3.2.2.3.9b of the Air Force Specification MIL-F-87168, both entitled "Quantity of Agent," detail design guidelines for the minimum quantity of halon 1301 to be discharged into a nacelle. The two Military Specifications are very similar. The design guidelines are given below, presented in English and SI units. The actual specifications are broken into two major categories. The first category includes rough nacelles with low air flows and smooth nacelles. For these cases, the Military Specification calls for the larger value of either of the following two formulas:

$$W(lbs) = 0.05\,V(ft^3)\ , \quad W(kg) = 0.80\,V(m^3) \tag{1}$$

$$\begin{aligned} W(lbs) &= 0.02\,V(ft^3) + 0.25\,\dot{W}_{air}(lbs/s)\ , \\ W(kg) &= 0.32\,V(m^3) + 0.25\dot{W}_{air}(kg/s) \end{aligned} \tag{2}$$

For a rough nacelle interior with a high air flow:

$$\begin{aligned} W(lbs) &= 3\,[\,0.02\,V(ft^3) + 0.25\,\dot{W}_{air}(lbs/s)\,]\ , \\ W(kg) &= 3\,[\,0.32\,V(m^3) + 0.25\,\dot{W}_{air}(kg/s)\,] \end{aligned} \tag{3}$$

For a deep frame nacelle interior with a high air flow:

$$\begin{aligned} W(lbs) &= 0.16\,V(ft^3) + 0.56\,\dot{W}_{air}(lbs/s)\ , \\ W(kg) &= 2.57\,V(m^3) + 0.56\,\dot{W}_{air}(kg/s) \end{aligned} \tag{4}$$

where W is the mass of agent, $\dot{W}_{air}$ is the mass flow of air passing through the zone at normal cruising conditions, and V is the "free" volume of the zone. The nacelle free volume is defined as the total nacelle volume minus the volume due to clutter. Low air flow is defined as less than 0.45 kg/s (1 lb/s) at cruise and high air flow is defined as greater than 0.45 kg/s (1 lb/s) at typical cruise conditions.

By definition, a smooth nacelle has no circumferential ribs protruding into the nacelle; a rough nacelle has circumferential ribs protruding less than 15 cm (6 in.) into the nacelle; a deep frame nacelle has circumferential ribs greater than 15 cm (6 in.) protruding into the nacelle, or a configuration with cavities 15 cm (6 in.) or more in depth (measured transversely). A smooth nacelle may contain clutter such as electronic housings, hydraulic and fuel lines, transducers, and clamps which may create flow disturbances. The ribs are added to a nacelle to provide structural integrity.

Section 3.9 of the Military Specification specifies that the discharge duration of the agent must be less than 1 s, measured from the time the agent exits the delivery tube and begins to enter the nacelle. Section 3.8 of the Military Specification, entitled "Concentration of Agent," details the performance criteria of the extinguishing system. "Actuation of the extinguishing system shall produce a concentration of agent at least 6 % by volume (22 % by weight) in all parts of the affected zone. This condition shall persist in each part of the zone for at least 0.5 s at normal cruising condition."

The Military Specification does not provide references or any discussion pertaining to the design guidelines or performance criteria. It is recommended that the rationale for any revision of the Military Specifications be fully documented. Available documentation, however, points out obvious connections between experimental studies and the Military Specification. Hansberry (1956) reported the agent requirements for smooth nacelles (Equations (1) and (2)). Many reports resort to speculation regarding the derivation of the Military Specifications (Altman *et al.*, 1983; McClure and Springer, 1974; Gerstein and Allen, 1964). Hansberry (1956) did not derive the smooth nacelle equation, but only states that it was empirically derived. Although the air flows investigated ranged from 0 to at least 16 lb/s, the range of nacelle volumes was not reported.

Examination of Equation (2) shows that it is not dimensionally consistent. Without documentation regarding its rationale, several authors have speculated on its derivation. Gerstein and Allen (1964) and McClure *et al.*, (1974) suggested the following:

$$W = X_c \rho_{agent} V + \frac{\rho_{agent} t X_c}{\rho_{air} (1 - X_c)} \dot{W}_{air} \tag{5}$$

This equation gives the mass of agent (W) required to provide the volume (V) and the incoming air flow ($\dot{W}_{air}$) with the design concentration (X_c) over the discharge time (t). The agent and air densities (ρ_{agent} and ρ_{air}) are evaluated at ambient conditions in the nacelle. Assuming a one second discharge time for the agent and isothermal mixing of air and gaseous agent at 21 °C and atmospheric pressure, the equation reduces to:

$$W(lbs) = 0.023\, V(ft^3) + 0.34\, \dot{W}_{air}(lbs/s) \tag{6}$$

The coefficients in Equation (6) are consistent with those in Equation (2). This type of analysis (Equations (5) and (6)) began with the early CO_2 systems (Mapes, 1954). The analysis assumed an idealized partition of the agent between the volume and the incoming air flow and lacks any physical basis related to spatial and temporal mixing of agent in the nacelle volume. It is only speculation that the design guidelines for smooth nacelles evolved from such a theoretical basis and were confirmed with full-scale testing. The design equations for rough nacelles and deep-framed nacelles cannot be derived from such a simple argument and probably evolved from testing. For example, the effects of transverse ribs (a rough nacelle design) were reported by the CAA (Hughes, 1953). The fact that the design guidelines for rough nacelles with a high air flow (Equation (3)) are the same as the guidelines

for smooth nacelles (or rough nacelles) with a low air flow (Equation (2)) multiplied by a factor of three, also suggests an empirical foundation.

Interestingly, parameters which may be important in flame stability such as the air temperature, the pressure and hot metal surface temperatures are not explicitly addressed in the design guidelines (Equations (1)-(4)). In addition, the actual dimensions and spacing of the ribs in rough nacelles are not considered, except for the case of very deep nacelles, which are treated separately.

The suppression guidelines will be reconsidered in Section 9.5 in terms of a simple model which endeavors to give guidance on agent mass delivery rate and concentration requirements for flame suppression in a generic nacelle using the replacement agents.

9.3 Measurements Characterizing the Stability Limits of Engine Nacelle Fires

9.3.1 Background. The search for a replacement for halon 1301 has led to testing of alternative agents in the Wright Patterson full-scale Aircraft Engine Nacelle Test Facility as well as in bench scale experiments (Grosshandler *et al.*, 1994). There are, however, many nacelle geometries and operating conditions for which a new suppressant is needed. Because testing cannot be performed for all possible aircraft and conditions, knowledge is needed which will provide guidance in the extension of the full-scale data to untested systems and conditions. For these reasons, experiments are conducted in several experimental configurations, over a range of conditions which are thought to resemble fires which may occur in a nacelle.

The key parameters that affect flame stability and thereby control flame extinction and the prevention of re-ignition are agent effectiveness and flow field dynamics. Flow field dynamics govern the rate of agent entrainment and the concentration of agent in a fire zone. Pitts *et al.*, (1990) outlined current understanding of fire suppression, incorporating a comprehensive review of the relevant literature, in addition to a discussion of agent effectiveness, test methods, and the role of different suppression mechanisms. A large number of studies have been conducted on fire suppression and a great deal is known about the relative efficiencies of various species in laminar flames (Grosshandler *et al.*, 1994). A large number of laminar flame studies have investigated the structure of inhibited flames to learn about mechanisms of flame inhibition (Pitts *et al.*, 1990; Grosshandler *et al.*, 1994). Global measures of the effectiveness of an agent has been quantified through heat capacity considerations (Tucker *et al.*, 1981; Sheinson *et al.*, 1989).

It has been shown that a criterion for reactant ignition and flame extinction involves the Damköhler Number (D) which is the ratio of a characteristic flow time to a characteristic chemical reaction time, *i.e.*, $D \equiv t_{flow}/t_{chem}$. For laminar nonpremixed flames, Liñan (1974) showed that as D decreases, the maximum flame temperature and the fuel burning rate decrease until a critical value of the Damköhler number is obtained, D_e, such that the flame abruptly extinguishes. Liñan (1974) also showed that as the maximum reactant temperature increases, a critical value of the Damköhler number is obtained, D_i, such that the reactants abruptly ignite. The Damköhler number criteria for ignition and extinction suggest a number of strategies for extinguishing fires and preventing re-ignition. These strategies include increasing the flow field strain rate or flame stretch (to decrease t_{flow}), cooling the reactants, reactant removal, or chemical inhibition which increases t_{chem} (Williams, 1974).

Engine nacelle fires can occur either in the form of a spray or a puddle. In either type of fire, flame stability is enhanced by flow field obstacles, which act as flame holders. There is a rich literature base regarding the stability of baffle stabilized flames. If a flame is established behind a flow obstacle or bluff body, a recirculation zone will form. The presence of the recirculation zone enhances

flame stability. In this situation, the obstacle acts as a flame holder. Flame blow-off occurs when air flows past the obstacle at sufficiently high velocities (Zukowski and Marble, 1955; Lefebvre, 1983). A large number of engineering studies have focussed on the stability of baffle stabilized premixed flames with application to turbine engine design. A comprehensive summary of the results is given by Lefebvre (1983). Some investigators indicate the importance of the structure of the recirculation zone in stabilizing flames, and in particular the characteristic time for mass exchange between the free stream and the recirculation zone (Longwell *et al.*, 1953; Bovina, 1958; Winterfeld, 1965). Mestre (1955) found that flame blow-off was related to the characteristic time for entrainment into the recirculation zone. The relative size of the enclosure surrounding the flame holder has also been found to effect flame stability by changing the character of the recirculation zone (Lefebvre, 1983; Winterfeld, 1965). In general, the blow-off velocity increases and flame stability is enhanced by a number of factors including a reduction in velocity, increase in inlet temperature, increase in gas pressure, reduction in turbulence intensity, change in the equivalence ratio towards the flammability peak, increase in the flameholder size, increase in the flameholder drag coefficient (through changes in the shape of the flameholder), reduction in geometric blockage and for liquid fuels increase in fuel volatility, and finer atomization for liquid sprays (*i.e.*, reduction of mean drop size). Several models describing blow-off of baffle stabilized premixed flames have been developed. Beér and Chigier (1983) suggested that

$$\frac{V_{bo}}{p^{n-1} \cdot d} = constant \tag{7}$$

where V_{bo} is the free stream velocity at blow-off, d is the baffle diameter, p is the pressure, and n is the reaction order which characterizes the global combustion processes. For kerosene, which is nearly identical to JP-8 jet fuel, Lefebvre and Halls (1959) recommended that n=2.0. Equation (7) states that an increased velocity or decreased values of d or p, leads to diminished flame stability until a critical value is obtained when flame blow-off occurs.

Flame suppression of baffle stabilized flames by an agent is analogous to the flame blow-off studies by Lefebvre and coworkers. The time required for an agent to entrain into the recirculation zone is a key parameter in understanding suppression of baffle stabilized flames by a suppressant. This characteristic mixing time or residence time is extremely important in developing fire protection strategies, since it influences the free stream agent concentration and duration required to obtain extinction. Agent entrainment into a baffle stabilized combustion zone is influenced by the free stream flow, the baffle size, and the free stream agent concentration/duration. These ideas, related to agent mixing into a baffle stabilized combustion zone, will form the basis of the simple suppression model developed in Section 9.5.

Few studies have investigated the effectiveness of an agent in suppressing bluff body stabilized flames. Hirst and Sutton (1961) measured enhanced stability in obstacle stabilized pool flames. Flame stability was characterized by the air velocity required to blow-off a flame. Flame stability was measured to be a function of the obstacle size. The blow-off velocity increased, obtained a maximum, and then decreased, as the height of the obstacle above the fuel surface increased. In a series of papers, Hirst, Dyer, and coworkers reported interesting results regarding the suppression of obstacle stabilized flames (Hirst *et al.*, 1976; 1977; Dyer *et al.*, 1977a; 1977b). An obstacle stabilized pool fire may occur when liquid jet fuel or hydraulic fluid forms a puddle behind a rib in the nacelle. Interpretation of their results in terms of a simple mixing model, described in detail in Section 9.3.2.3.4, suggests two key points. First, a characteristic mixing time (τ) for the agent to

entrain into the recirculation zone behind a flame holder or obstacle is a principal parameter governing flame suppression. The characteristic entrainment or mixing time is equal to the characteristic residence time in the recirculation zone. This result suggests that the Damköhler number flow time, t_{flow}, is related to the mixing time, τ, in the case of baffle stabilized flames. Second, the minimum agent concentration required to achieve extinction in baffle stabilized pool fires are consistent with the peak flammability limits of a reactive system. The agent concentrations required for suppression of baffle stabilized fires can be a factor of two larger than agent concentrations required to extinguish cup burner flames burning the same fuel. The flammability limits define conditions under which self-sustaining combustion can or cannot exist. Although peak flammability limits have been measured for a large number of halogenated molecules, there are no data available in the literature for HFC-125 (C_2HF_5), the agent selected by the Halon Transition Team for halon replacement (Malcolm, 1950). Section 9.3.5 describes measurements of the flammability limits for HFC-125 in propane/air mixtures.

9.3.2 Suppression of a Baffle Stabilized Spray Flame. Grosshandler and coworkers (1994) developed a baffle stabilized coaxial turbulent spray burner for testing the effectiveness of gaseous fire suppressants. Experiments were performed using jet fuel and hydraulic fluids with the air at ambient and elevated temperatures. The agents tested were nitrogen, four perfluorinated compounds, C_2F_6, C_3F_8, C_4F_{10}, and cyclo-C_4F_8; four hydrogen/fluorine compounds, CF_3CHFCF_3, $CF_3CH_2CF_3$, C_2HF_5, and CFH_2CF_3; the mixture 60 % CH_2F_2/40 % C_2HF_5; the chlorinated agents CHF_2Cl and $CHFClCF_3$; CF_3Br, and CF_3I. In addition, sodium bicarbonate powder ($NaHCO_3$) was tested. The measurements rated the relative suppression behavior of the different agents. The research described here extends that study to a broader range of conditions, typical of in-flight engine nacelle environments, and focuses on the performance of the three down-selected agents, namely HFC-125 (C_2HF_5), HFC-227 (C_3HF_7), and CF_3I.

A fuel spray represents a unique combustion situation. A ruptured high pressure fuel, lubricant or hydraulic fluid line can supply a steady flow of fuel for a fire stabilized behind obstacles in the engine nacelle. Small droplets quickly evaporate and the momentum from the spray efficiently entrains the air necessary for combustion. Extinguishment of the burning spray will occur when a critical amount of agent entrains into the combustion zone.

Flame stability is also influenced by parameters other than the rate of agent entrainment. These include the air flow and temperature, the fuel type, the pressure, and the agent type (CF_3I, HFC-125, or HFC-227). The key objective of the studies reported in this subsection was to compare the effectiveness of the candidate agents in suppressing obstacle stabilized spray flames under a variety of conditions typical of nacelle fires. The effectiveness of the agents in suppressing other types of combustion phenomena will be addressed in Sections 9.3.3-9.3.5 where obstacle stabilized pool fires, ignition over a heated plate, and flammability limits will be considered, respectively.

9.3.2.1 Experimental Method and Apparatus. No standard laboratory apparatus exists for evaluating the effectiveness of an agent in extinguishing an in-flight nacelle spray fire. One apparatus used for spray flame suppression measurements is mentioned in the literature, but details of its operation or experimental results are not reported (Hirst, 1963). The experimental facility used here was based upon the earlier NIST study which has been described in detail (Grosshandler *et al.*, 1993; 1994; 1995; Vazquez *et al.*, 1994).

Figure 1 shows a cross-sectional view through the burner. The apparatus incorporated an air delivery system, a fuel delivery system, an agent injection system, and a combustion zone. Air at atmospheric pressure co-flowed around a 1.9 cm diameter fuel tube within a 0.5 m long, 7.3 cm inner diameter stainless steel tube. The fuel was injected along the centerline through a pressure-jet nozzle

(Delevan model 0.5-45-B)[1] that formed a 45° solid-cone spray, typical of a simple oil furnace or gas turbine combustor. The exit of the nozzle extended 0.2 cm beyond the open end of the stainless steel pipe. The flame was stabilized by a steel disk (nominally 3.5 cm diameter and 0.2 cm thick) attached to the body of the nozzle. A pyrex tube with an 8.6 cm inner diameter, supported on a brass ring, contained the flame 6.3 cm beyond the outer steel casing. A black and white photograph of the turbulent jet spray burner was presented in an earlier report (Grosshandler *et al.*, 1994). Figure 2 shows a schematic drawing of the nozzle, the stabilization disk, and the fuel spray. A torroidal vortex of length L was created as the air/agent mixture flowed past the stabilization disk.

A number of modifications to the original burner design (Grosshandler *et al.*, 1994) were introduced to improve performance and experimental control. The diameter was increased from 5.0 to 7.3 cm to diminish fuel spray impingement on the burner walls and thereby minimize the formation of a fuel puddle on the bottom of the pyrex tube. A water jacket surrounding the fuel line was added to prevent heating of the fuel for experiments where the air temperature was increased. Earlier results showed that a heated fuel supply could impact flame stability (Grosshandler *et al.*, 1994).

Measurements showed that the orientation of the nozzle relative to the tube axis affected flame stability. To insure that the cantilevered fuel line-nozzle system was properly aligned, a tri-spoke (each 1 mm diameter) alignment guide was attached to the fuel line approximately 10 cm upstream of the nozzle exit.

The air was supplied through a sonic orifice by a high capacity compressor at 900 kPa. The pressure was monitored upstream of the sonic orifice allowing determination of the air flow. Average velocities across the burner cross-section could obtain values as high as 50 m/s. Temperatures from ambient to approximately 350 °C, measured with a type-K thermocouple positioned 1 m upstream of the combustion zone, were obtained using a 60 kW electric air heater.

JP-8 aviation fuel was stored in an 18 liter tank and delivered to the burner with an electric pump at pressures controllable to 1.1 MPa. The fuel pressure was fixed at 900 ± 10 kPa and the flow was controlled by a needle valve and monitored using a rotameter. The flow was calibrated at the operating temperatures and pressure. An analysis of the JP-8 fuel shows that it contains many components. The measured heat of combustion for JP-8 was 46.52 kJ/g and the elemental (mole based) composition was 34.1 % carbon and 65.9 % hydrogen (Grosshandler *et al.*, 1994). This is consistent with the $C_{12}H_{22}$ molecular structure for JP-8 used by Johnson *et al.*, (1988) with a corresponding molecular weight of 166 g/mole. The measured liquid density at room temperature was 0.81 g/ml. The same JP-8 batch was used for all of the experiments described in this section.

A series of super-ambient pressure experiments were conducted by replacing the pyrex tube shown in Figure 1 by a 40 cm long brass tube fitted with a butterfly valve at the tube end, facilitating control of the pressure which was varied from ambient to 135 kPa (5 psig). Figure 3 shows a schematic drawing of this confined spray apparatus, which allowed steady control of the system pressure. A pyrex observation window and three ports allowed access for ignition, a pressure gage, and an automatic fuel shutoff which was triggered by flame extinction.

The independent parameters which were controlled in the spray burner facility were the air flow, the agent delivery interval or injection duration, the air temperature, the system pressure, the fuel flow, and the agent temperature. Table 2 lists the range of the independent parameters which were investigated. Extinction measurements were performed with three gaseous agents for all conditions. They

---

[1] Certain trade names and company products are mentioned in the text or identified in an illustration in order to specify adequately the experimental procedure and equipment used. In no case does such identification imply recommendation or endorsement by the National Institute of Standards and Technology, nor does it imply that the products are necessarily the best available for the purpose.

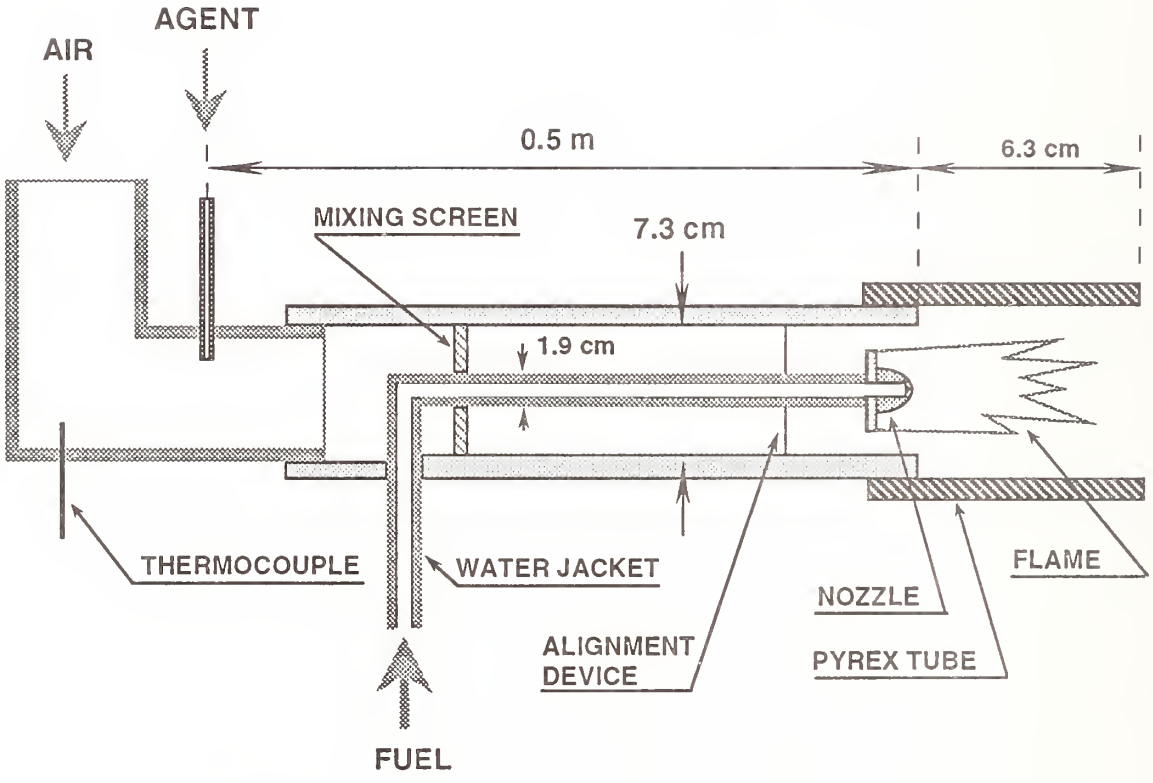

Figure 1. Schematic drawing of the turbulent jet spray burner.

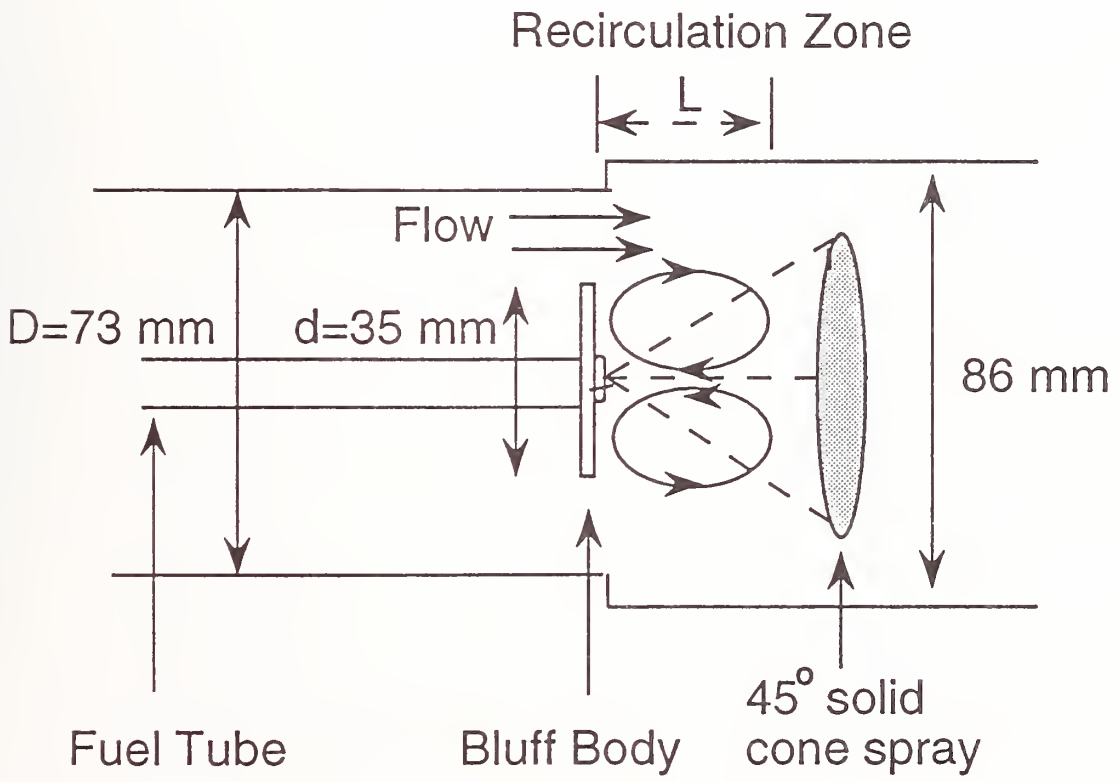

Figure 2. Schematic diagram of the recirculation zone behind the stabilization disk.

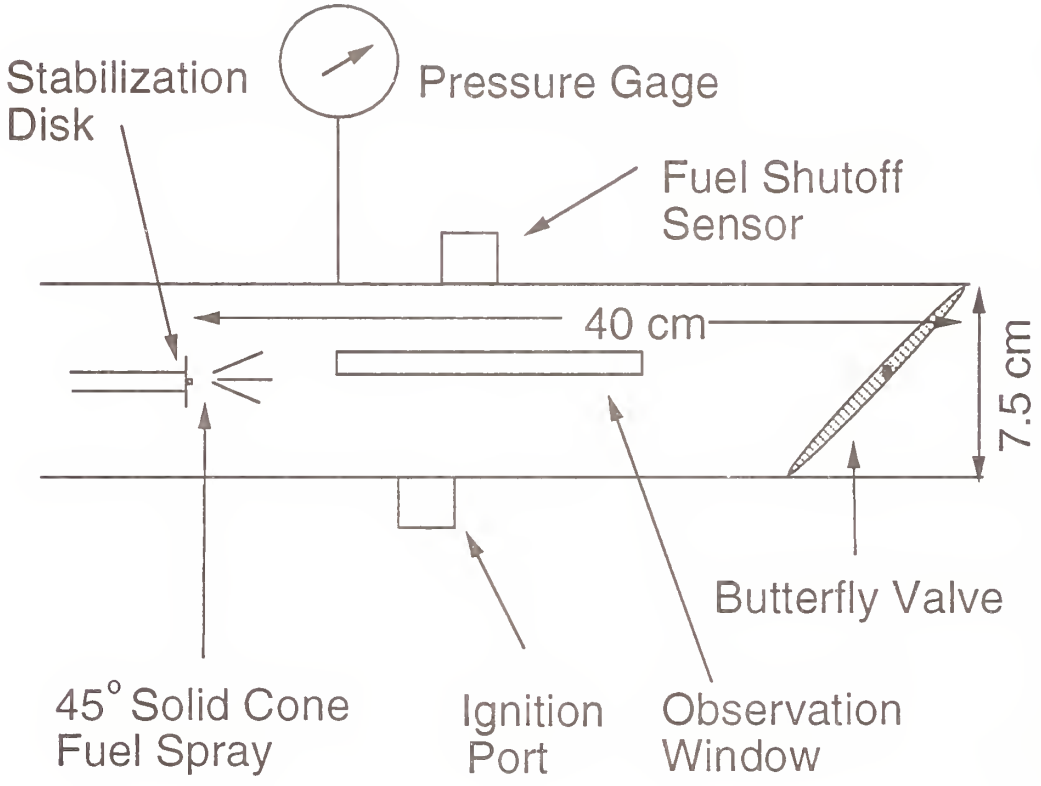

Figure 3. Schematic diagram of the confined spray burner.

Table 2. Operating parameters in the spray burner

Parameter	Range
air velocity	2 - 33 m/s
agent delivery interval	50 - 800 ms
air temperature	20 - 350 °C
system pressure	101-135 kPa (0-5 psig)
fuel flow 1. air flow constant 2. global ϕ constant	14 - 28 ml/min
agent temperature	20 - 150 °C

were CF_3I, C_2HF_5 (HFC-125), and C_3HF_7 (HFC-227). Extinction measurements were also performed using CF_3Br to establish a performance reference. In some experiments gaseous N_2 was also tested. The primary dependent experimental parameters were the agent mass and the rate of injection required for suppression.

9.3.2.2 Agent Injection. The injection mechanism, shown in Figure 4, consisted of the agent supply connected to a stainless steel storage vessel through a metering valve, and to the burner through a computer controlled solenoid valve. The storage volume, including a 1.0 or 2.25 liter pressure vessel and associated plumbing, was 1040 or 2290 ± 10 ml, respectively. The agent pressure was adjustable up to 687 kPa. The agent temperature and pressure in the storage vessel were measured with a type-K thermocouple and a pressure transducer located upstream of the solenoid valve. Uniform dispersion across the air stream was enhanced by injecting the gas in a radial direction into a reduced diameter (25 mm) section of the air pipe through two 6 mm diameter tubes. Screens with 50 % open area were placed 40 mm and 80 mm downstream of the injection point to ensure complete mixing between the air and agent prior to encountering the flame zone. For some experiments, the agent was heated to 150 °C by wrapping heating tape over the agent storage vessel. The amount of injected agent was controlled by varying the initial pressure and the time that the solenoid valve was open.

The agent injection system under idealized conditions (incompressible flow, massless valves, no pressure losses) was designed to deliver a square-wave pulse of agent to the burner for the amount of time programmed by the computer controller. The actual flow deviated somewhat from an ideal square wave pulse. Examples of this are seen in Figure 40 of Section 11, where the measured transient agent concentration between the outer wall and the fuel line just upstream of the stabilization disk is shown. The character of the agent pulse varied from a perfect square wave to an upward sloping or a downward sloping concentration trace. A portion of this character was attributed to the mechanics of the solenoid actuation mechanism. The agent concentration was calculated as the average concentration over the injection interval. Measurements showed that small deviations from a square wave pulse had only minimal effect on the agent mass required to obtain flame extinction.

There was a delay between the time when the solenoid was triggered and the time when the flow of agent actually began. When the valve opened, pressure waves were created which reverberated in the injection system at the acoustic velocity, causing the flow rate to modulate. In order to avoid flow

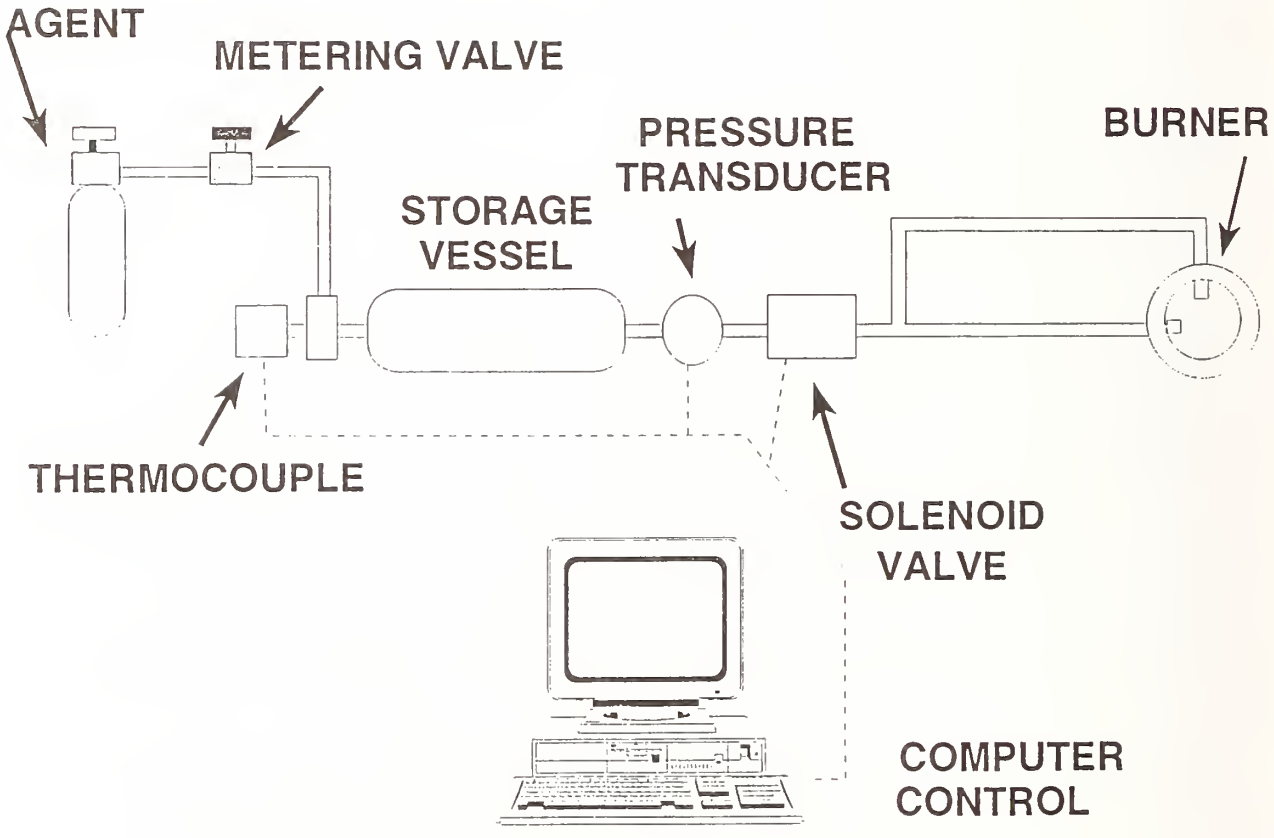

Figure 4. Schematic diagram of the agent injection mechanism.

restrictions, a large solenoid valve was required. Unfortunately, the valve opened and closed at different rates, depending on the agent vessel pressure. The minimum achievable delivery time was approximately 60 ms. Control of the solenoid opening time was limited to ± 16 ms, which was related to the 60 Hz electro-servo control.

The mass of agent delivered to the air stream was determined by measuring the mass loss, m, in the vessel of volume V, at pressure P, and temperature T, using the Redlich-Kwong equation of state:

$$m = \frac{PVM}{RT}\left[\frac{1}{1-bm/V} - \frac{am/(VRT^{3/2})}{1+bm/V}\right]^{-1} \tag{8}$$

where M is the molecular weight of the gaseous agent, R is the gas constant, and a and b are constants dependent upon the critical properties of the agent (Van Wylen and Sonntag, 1978). The initial temperature was measured, and the final temperature was determined by assuming that the expansion occurred isentropically following the relation:

$$\frac{T_f}{T_i} = \left(\frac{P_f}{P_i}\right)^{\frac{\gamma-1}{\gamma}} \tag{9}$$

where γ is the ratio of the specific heats of the gas and the subscripts i and f refer to initial and final conditions. By measuring the change in pressure, Equation (8) was used in an iterative fashion to determine the total mass injected into the burner. Equation (9) assumes that the gas was ideal. From Equation (8), the deviation from ideal gas behavior was found to be a maximum of 7 % for the gaseous agents. The pressure data were collected at a rate of 1000 Hz, with the initial and final conditions found from the average of at least 500 points measured one-half second prior to the release of the agent and one-half second after the solenoid valve closed. A mass-time curve has been described in detail (Grosshandler *et al.*, 1994).

The mass of agent added to the flame was determined from Equation (8), and the actual time interval of agent injection into the burner was estimated from the linear portion of the slope in the mass-time curve. The mass flow of agent was determined from the ratio of the mass injected to the time of injection over a linear portion of the slope in the mass-time curve.

The agent mass fraction is denoted as ß, which is defined as the ratio of the mass flow of agent, $\dot{m}_i$, to the total mass flow of agent and air, $\dot{m}_{Air}$:

$$\beta \equiv \frac{\dot{m}_i}{\dot{m}_i + \dot{m}_{Air}} \tag{10}$$

Discussion of the suppression measurements in terms of the agent mass fraction facilitates comparison of the experimental results with similar measurements under other flame conditions or in different combustion configurations. An effective agent is characterized by a small value of ß.

9.3.2.3 Experimental Results and Discussion. The protocol used in the experiments was to ignite the fuel spray with a propane torch and to set the air flow to the desired level. The flame was

allowed to burn for ≈20 s to ensure steady operation. If a smaller "pre-burn" or warm-up time was used, the flame was less stable. Experiments were conducted for a single agent over a range of conditions. When the agent was changed, the storage vessel was evacuated and flushed several times with new agent to purge contaminating gases from the system. The pressure in the vessel was adjusted with the solenoid valve closed using the inlet metering valve. Initially, a pressure was chosen which was expected to be insufficient to extinguish the flame. Data acquisition was initiated and the response of the flame to the injection process was observed. If the flame was not extinguished, the pressure in the agent vessel was increased and the experiment repeated immediately. Eventually a pressure was found which was sufficient to suppress the flame. This procedure was repeated at least twice for each condition. Each extinction data point, therefore, represents many experiments. It is estimated that a total of over 1000 suppression experiments were conducted. Uncertainty in the mass of agent required to extinguish the spray flame was estimated as 15 %, based on repeat measurements and a propagation of error analysis.

9.3.2.3.1 Characterization of Facility. A series of experiments were carried out to determine reasonable baseline conditions for the fuel and air flows, the diameter of the stabilization disk, the location of the pyrex tube, and the impact on flame stability of a layer of soot deposited on the stabilization disk.

The air and fuel flows were varied to ascertain how the flame was affected by the operating conditions. Figures 5 and 6 show the average observed flame length as a function of the fuel and air flows respectively. As the air flow increased, the visible flame length decreased, until at very high air flows the flame extinguished. At high air flows, the flame appeared like a rapidly swirling luminous ball. Some amount of blue emission was visible in photographs, but not by visual observation. Little flame luminosity was observed beyond 10 cm downstream of the nozzle. For air velocities less than 2 m/s, the flame appeared as an ignited spray cone, nearly blue for the first 2 cm downstream from the nozzle and then yellow. Under these conditions, a luminous recirculation zone was not observed to exist, and apparently, the inertia associated with the fuel droplets was much greater than the momentum associated with the torroidal vortex behind the stabilization disk. Low air velocity flames were achievable only after ignition at moderate air velocities and careful, slow decrease of the air flow. As the fuel flow increased, the flame length increased and the flame appeared more luminous.

The trajectory of fuel droplets was observed to change with air flow. Under non-combusting conditions with a low air flow, the droplets traveled on near-linear trajectories in the downstream direction, at approximately 45° from the axis. As the air flow increased, a critical value was obtained which caused the droplets to alter their trajectories. Further increases in the air flow, caused the droplets to turn nearly 180°, causing them to be entrained into the torroidal vortex behind the stabilization disk. Apparently the momentum associated with the droplets was overwhelmed by the momentum associated with the torroidal vortex of the recirculation zone. For a fuel flow of 21 ml/min (0.28 g/s), the critical air velocity causing a change in droplet trajectory was approximately 17 m/s. Under combusting conditions, observation of the fuel droplet trajectories was not possible, due to obscuration by flame luminosity as well as a decreasing droplet diameter associated with fuel evaporation. These observations suggest that the flame structure and stability may be influenced by complex droplet dynamics occurring in the flame. In addition, the droplet size distribution is expected to change with fuel flow through the nozzle.

An operating condition of 21 ml/min was selected for the JP-8 flow. An air velocity of 7.5 m/s at ambient temperature and pressure was selected as a reasonable baseline operating condition. These conditions produced a 13 kW flame with an overall equivalence ratio of about 0.1. Under these conditions, a layer of soot formed on the nozzle and stabilization disk surface in a matter of minutes.

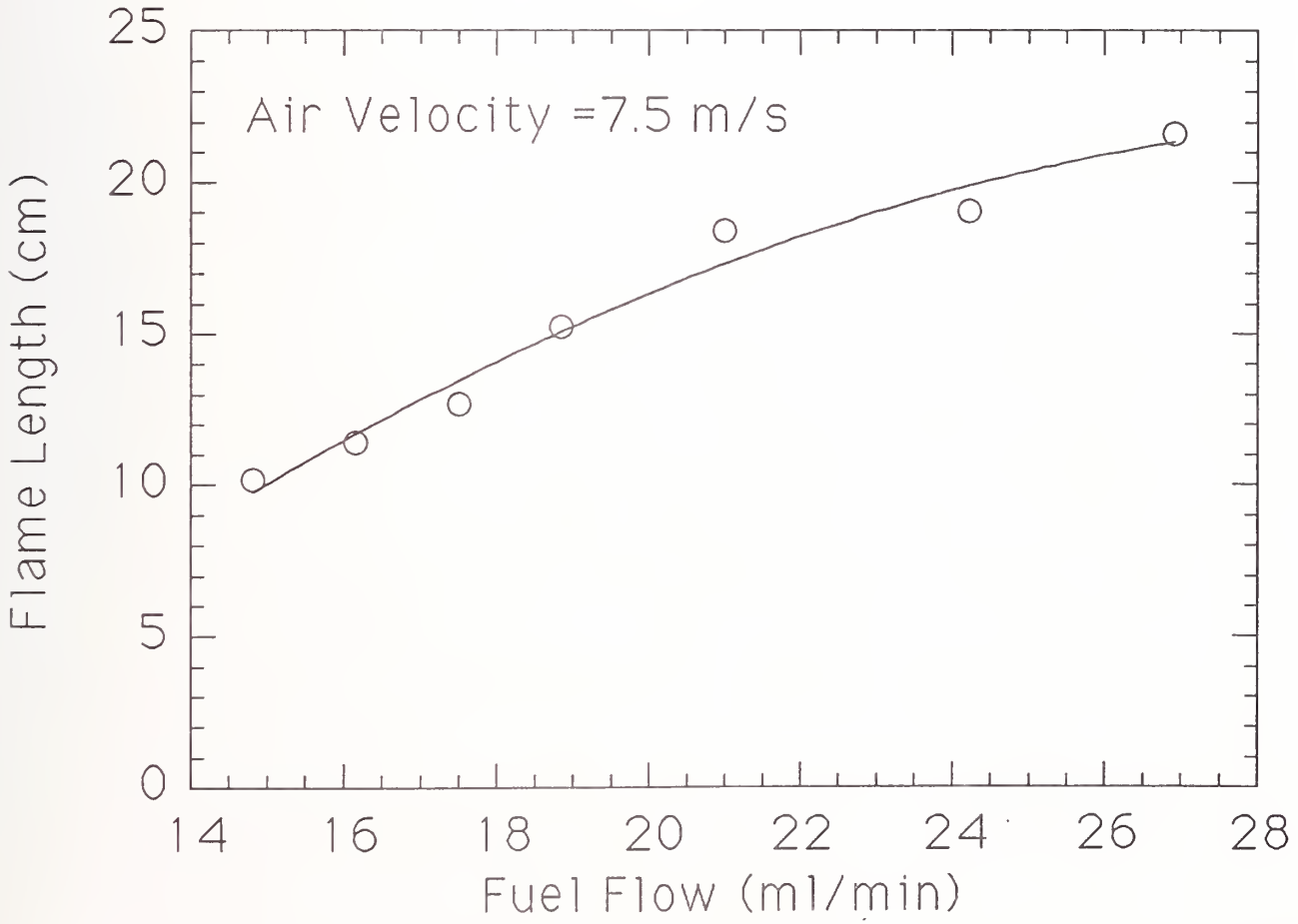

Figure 5. Measured spray flame length as a function of fuel flow.

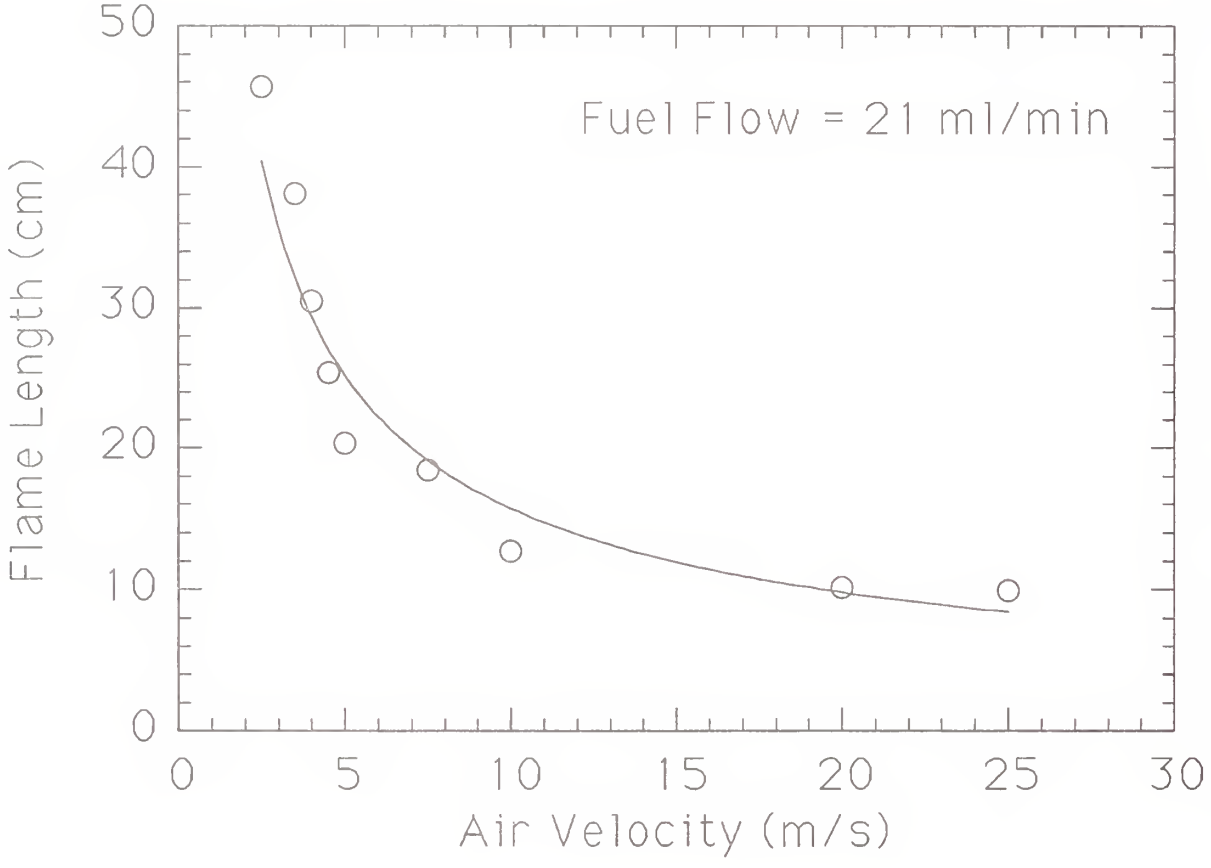

Figure 6. Measured spray flame length as a function of air flow.

Accumulation of a large amount of soot was found to increase flame stability. A possible explanation for this is that the soot acted like a thermal insulator, reducing heat losses to the stabilization disk/flame holder. Thus, the soot was cleaned periodically (every ≈3 min). Cleaning necessitated closing the fuel flow and extinguishing the flame.

Measurements showed that the location of the pyrex tube had little impact on the critical agent concentration at extinction for distances greater than 6.3 cm downstream of the nozzle. For shorter distances, the flame was easier to extinguish. Therefore, the pyrex tube was maintained 6.3 cm downstream of the nozzle for all flame extinction experiments.

Experiments were conducted to compare flame extinction measurements in the original burner (Grosshandler *et al.*, 1994) to measurements in the new burner. Figure 7 shows the critical HFC-227 mass fraction (β) required to extinguish JP-8 spray flames as a function of air velocity for short agent injection intervals (65 ms). The critical agent concentrations are similar in the two burners, with the original burner slightly more stable. This is not surprising considering the blow-off results described in Section 9.3.2.3.2 below.

An annular shaped steel disk (4 cm O.D., 1.5 cm I.D.) was placed on axis, downstream of the spray nozzle, to test the impact of a (secondary) flow field obstacle on flame stability. Using the standard configuration, with the primary (3.5 cm diameter) obstacle in place upstream of the nozzle and with fuel flowing, a propane pilot flame was used to ignite the fuel. If the obstacle was more than approximately 6 cm downstream of the nozzle, then it was not possible to stabilize a flame behind the secondary obstacle. The flame would blow-off as soon as the pilot flame was removed. Both a metal and a ceramic stabilizer were tested, yielding the same results. If the obstacle was moved to within approximately 6 cm of the nozzle, the flame jumped back and attached itself to the primary obstacle. Thus, it was not possible to stabilize the (45° solid cone) spray flame unless ignition occurred within the recirculation zone. The recirculation zone downstream of the secondary obstacle apparently did not provide conditions suitable for flame stabilization.

Experiments conducted with air as the extinguishing agent demonstrated that the flame could not be suppressed simply by blowing it out (Grosshandler *et al.*, 1994). When air was injected into the burner, the flame was observed to fluctuate momentarily, but was never extinguished. The flame also fluctuated when agent was injected into the burner. This was probably associated with a rapid change in the overall free stream velocity, which has an effect on the character of the recirculation zone.

In baffle stabilized flames such as the spray burner, the agent concentration in the recirculation zone is the key to flame suppression. Because isothermal flow dynamics upstream of the fire source play an important role in the rate of agent entrainment into the recirculation zone, quantitative measurements of the transient agent concentration were conducted as a function of spatial location under non-combusting conditions. This was accomplished using the aspirated hot film probe described in detail in Section 11 of this report. CF_3Br was injected (250 ms duration) into a moderate air flow (velocity = 5 m/s). Measurements were made 2 cm upstream of the stabilization disk (see Figure 1). The results, which are shown in Figure 8, indicate that agent mixing was fairly uniform across the tube diameter. The agent injection rate and duration were also investigated and are described in detail in Section 11.

9.3.2.3.2 Flame Blow-off. Flame stability in the original (5.3 cm) and the redesigned (7.3 cm) burners was directly compared by measuring the air velocity required to blow-off the JP-8 spray flames. A series of stabilization disks were tested with diameters of 2.22 cm, 2.86 cm, 3.49 cm, and 4.13 cm, all 4 mm thick, and all made from the same steel stock. A 3.49 mm diameter, 2 mm thick disk from a different steel stock was also tested. Figure 9 shows the air blow-off velocity (V_{bo}) as a function of the diameter of the stabilization disk. The same type of nozzle and fuel flow was used in all tests (21 ml/min). Changing the stabilizer diameter had a small effect on flame stability, with the

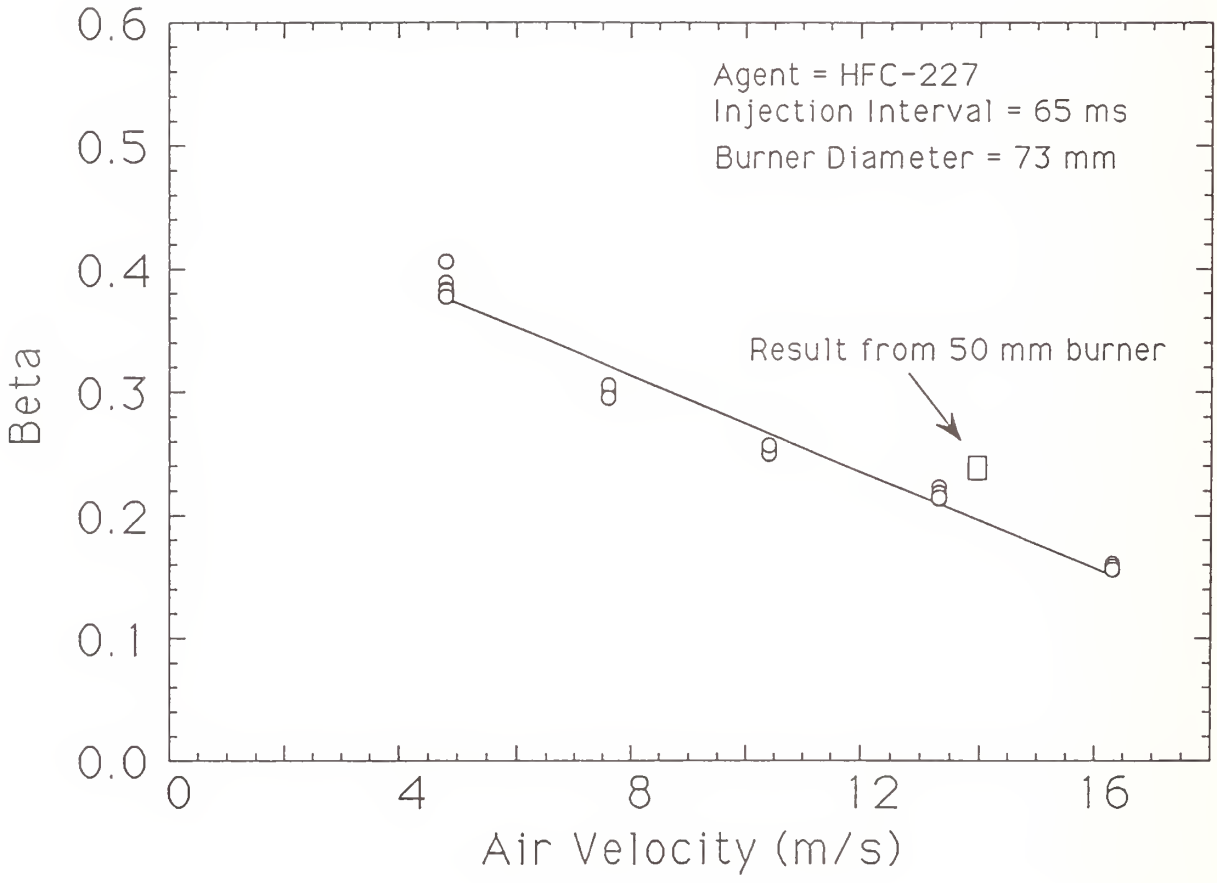

Figure 7. The critical mass fraction of HFC-227 at extinction for the JP-8 spray flame as a function of air velocity for a 65 ms injection interval.

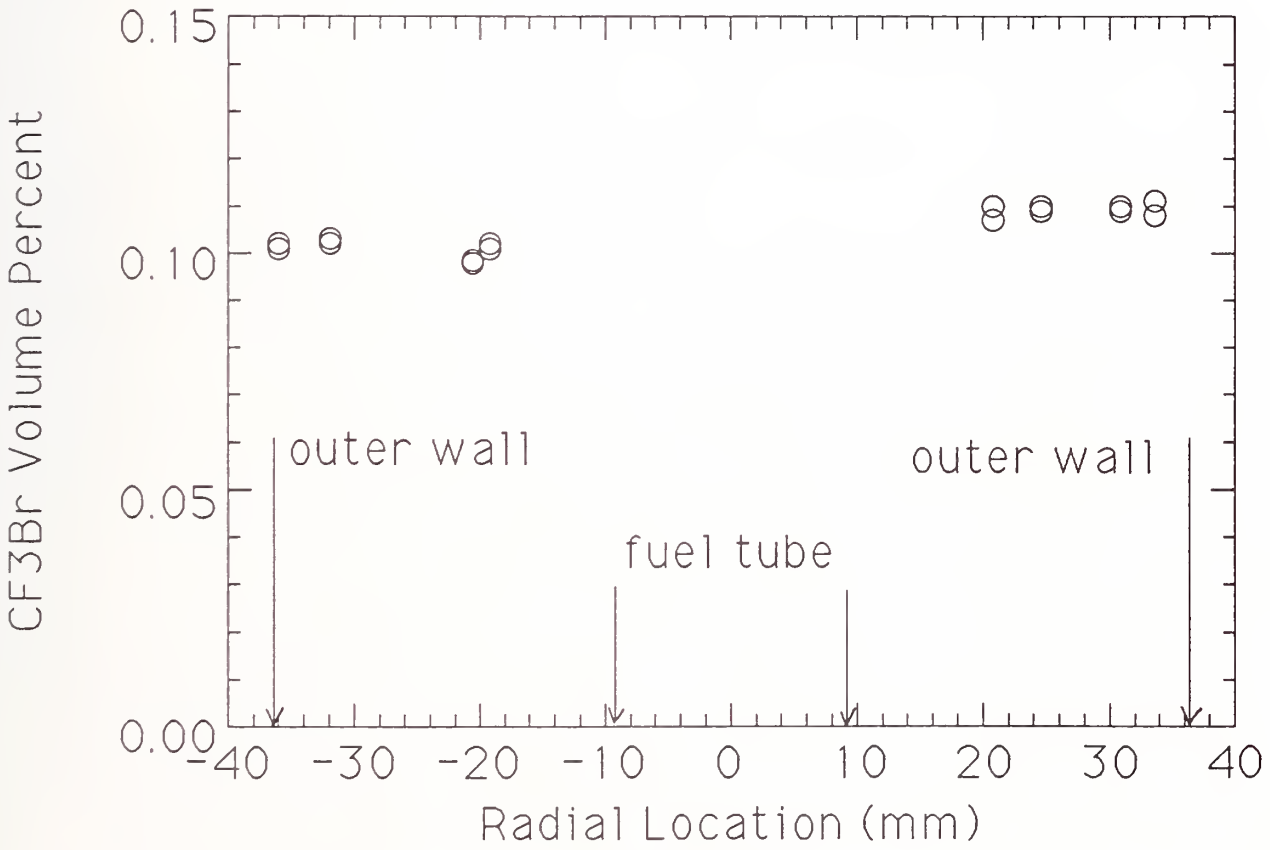

Figure 8. CF_3Br concentration as a function of location in the spray burner.

3.5 cm diameter disks (2 mm and 4 mm thick) yielding the most stable flames in both burners. A stable flame was sustainable until the air velocity across the duct was approximately 33 m/s in the 7.3 cm burner. Flames could not be stabilized with the 2.2 cm disk in either burner, nor with the 4.1 cm disk in the original (5.3 cm) burner. Blow-off velocities in the original burner were approximately 25 % higher than in the modified burner (7.3 cm) for the same disk diameter. This difference was attributed to the stabilizing effect of geometric blockage. The blockage (B) can be quantified as the ratio of the open (or non-blocked) area to the total area:

$$B = \frac{D^2 - d^2}{D^2} = 1 - (d/D)^2 \qquad (11)$$

where D is the burner diameter and d is the baffle diameter. The effect of blockage on flame stability has been investigated by Winterfeld (1965) and discussed by Lefebvre (1983). Winterfeld's results will be described in detail in Section 9.3.2.3.4.

9.3.2.3.3 Effect of Air Velocity. A fixed injection time of 700 ms was chosen to test the performance of the three alternative agents in extinguishing the spray flame. The selection of this injection interval facilitates comparison of the results with suppression results from other configurations. Figure 10 shows the critical mass of CF_3Br and the three alternative agents at extinction as a function of air velocity. For conditions below the data points, the flames were not extinguished, whereas for conditions above the data points, the flames were extinguished. A single data point may represent as many as three to ten experiments. The measurements showed that halon 1301 (CF_3Br) required the least amount of mass to extinguish the flames, followed by CF_3I, and the other two agents, HFC-125 (C_2HF_5) and HFC-227 (C_3HF_7), which were measured to have nearly identical effectiveness. CF_3Br required as much as a factor of three less mass than HFC-125 or HFC-227 to extinguish the spray flames. As the air velocity (V) increased, the agent mass required to achieve flame extinction increased, obtained a maximum, and then decreased. At high air velocities, the flames were less stable and easier to extinguish, *i.e.*, less agent was required to extinguish them. At V=33 m/s, air with no agent addition caused flame extinction.

Figure 11 shows the critical mass delivery rate of agent at extinction as a function of air velocity for the same data as shown in Figure 10. The rate is determined from the ratio of the mass delivered to the injection period. The injection period is related to the solenoid opening time and is estimated by measuring the depletion of agent from the reservoir. As the air velocity increased, the mass delivery rate increased, obtained a maximum, and then decreased, similar to Figure 10. The data are consistent with Figure 10. CF_3Br required the smallest delivery rate to extinguish the flames, followed by CF_3I, and the other two agents, HFC-125 and HFC-227, which were measured to have nearly identical effectiveness.

Figure 12 shows the critical mass fraction of agent at extinction (ß, as defined in Equation (10)) as a function of air velocity for the same data as shown in Figures 10 and 11. As the air velocity increased from 3 m/s, ß decreased. For very low air velocities (2 m/s), ß decreased or remained nearly the same as the results for V= 3 m/s. For all agents, the values of ß for the low air velocity spray flame results were very similar to agent extinction concentrations measured in cup burner flames and in opposed flow diffusion flames (OFDF) at low (25 s^{-1}) strain rates (Grosshandler *et al.*, 1994). Table 3 documents the correspondence between the flame extinction measurements in the three burners. All tests were conducted with JP-8 fuel. The correspondence between the cup burner results and the low strain rate OFDF results have been previously documented (Grosshandler *et al.*, 1994).

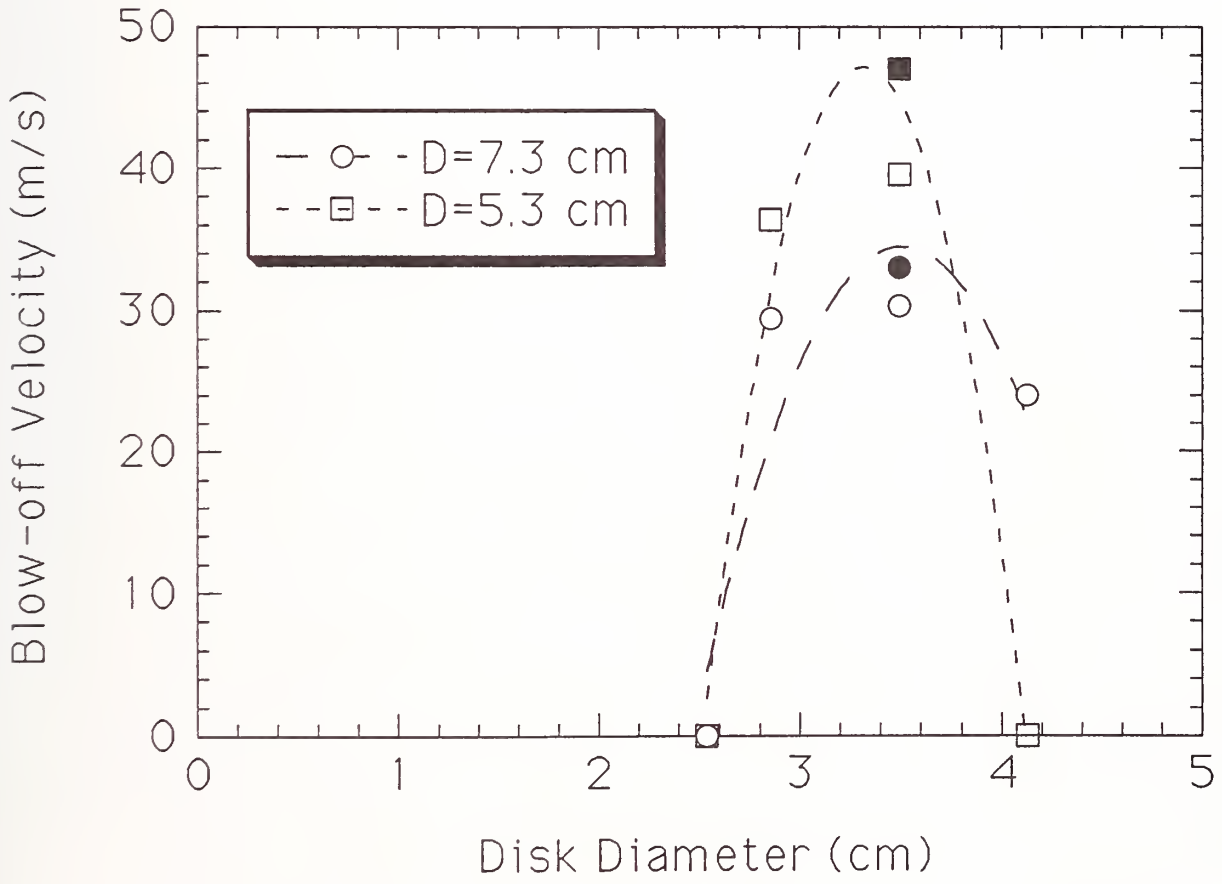

Figure 9. Air blow-off velocity as a function of the diameter of the stabilization disk. The filled and open symbols represent disks with thicknesses of 4 mm and 2 mm, respectively.

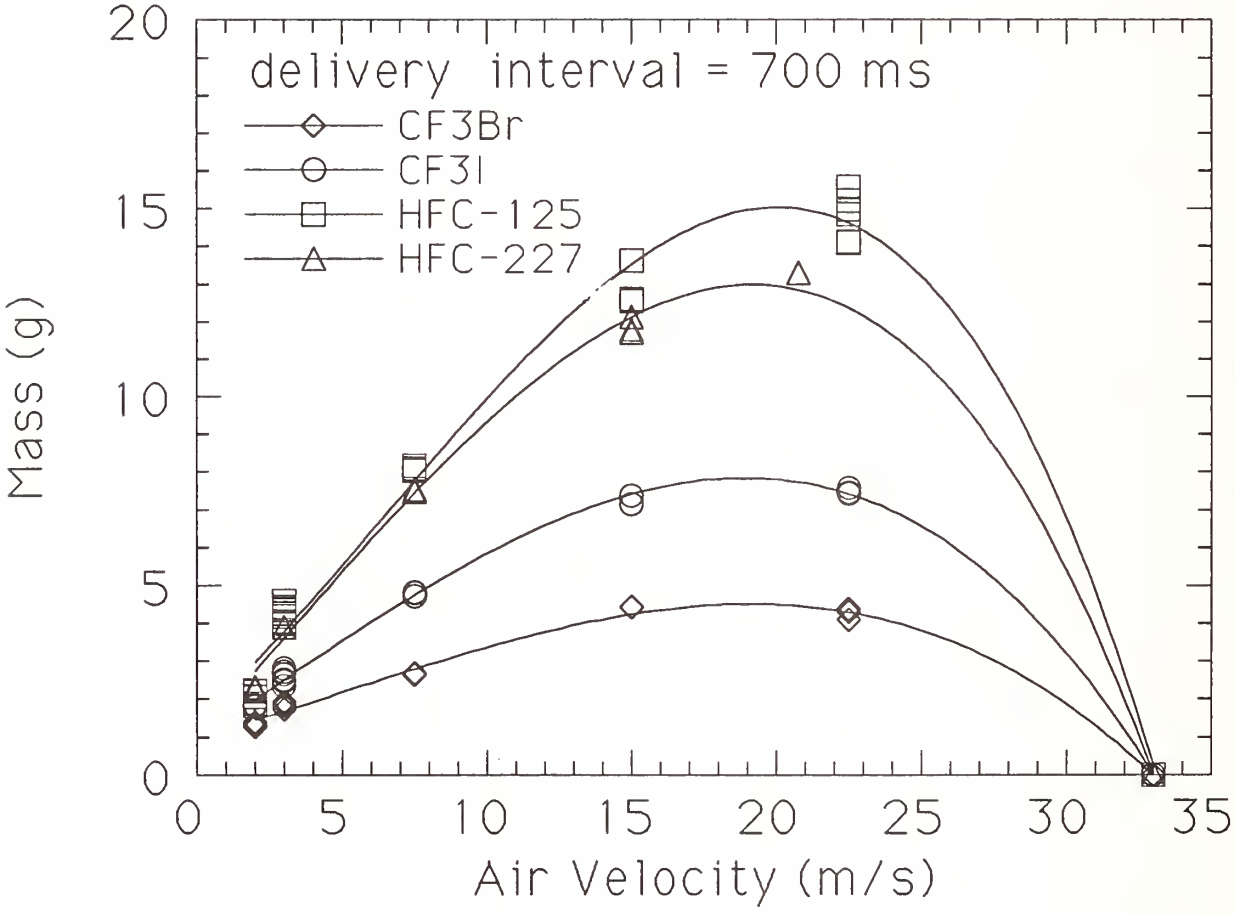

Figure 10. The critical mass of agent at extinction as a function of air velocity.

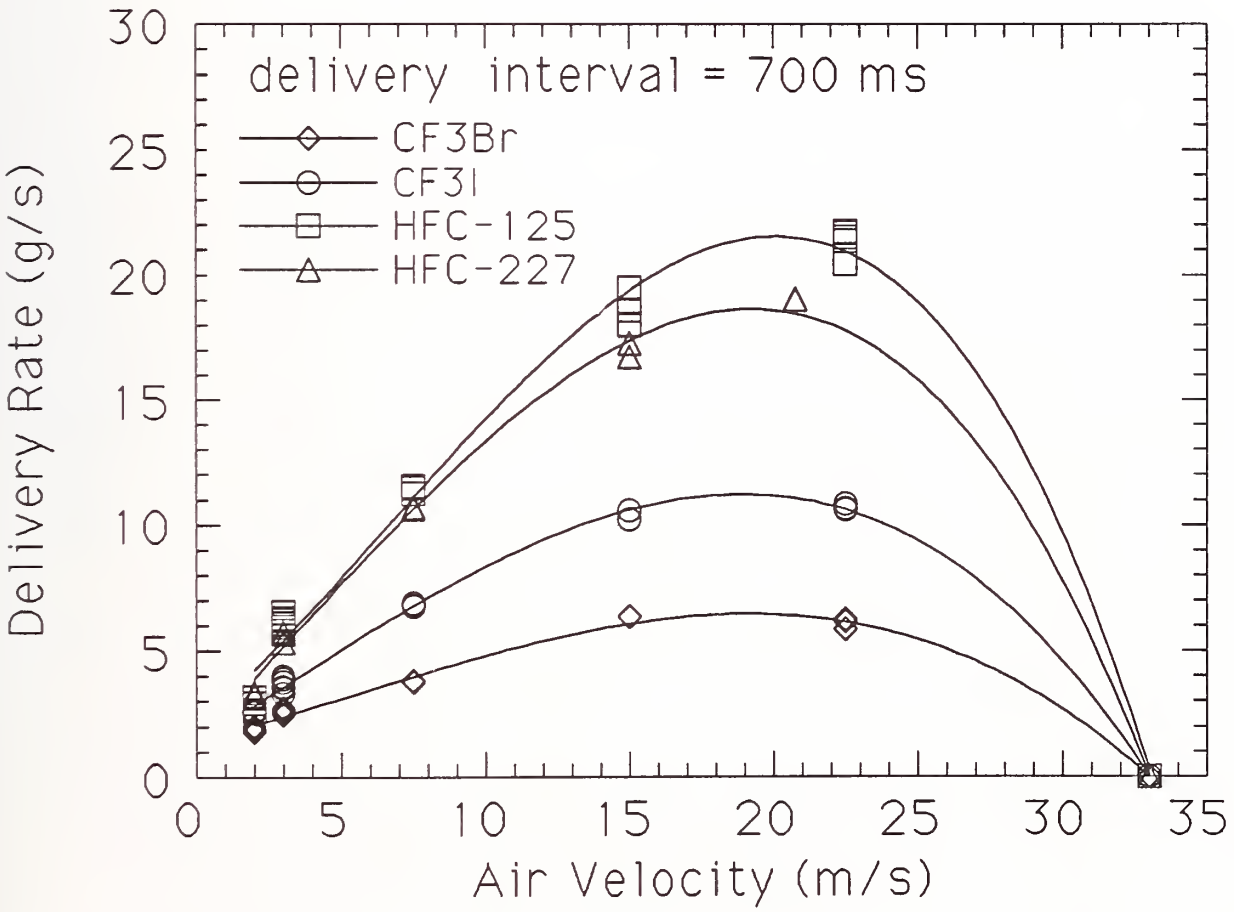

Figure 11. The critical mass delivery rate of agent at extinction as a function of air velocity.

Table 3. Comparison of the critical agent mass fraction at extinction measured in different burners

Agent	Cup Burner	Air Velocity (m/s) in Spray Burner			Strain Rate (s^{-1}) in OFDF burner		
		3.0	15	22	25	80	175
CF_3Br	0.14	0.16	0.085	0.05	0.13	0.080	0.050
CF_3I	0.18[b]	0.21	0.13	0.09	a	a	a
HFC-125	0.28	0.30	0.21	0.17	0.28	0.22	0.16
HFC-227	0.27	0.28	0.20	0.15	0.26	0.20	0.14

a Not measured

b Measured with heptane as fuel. The agent concentration required to extinguish heptane and JP-8 cup burner flames has been measured to be within 4 % of each other for many agents (Grosshandler *et al.*, 1994).

Table 3 shows that a correspondence also exists between the critical agent mass fractions for moderate (80 s^{-1}) strain rates in the OFDF burner (Hamins *et al.*, 1994) and moderate air velocities (15 m/s) in the spray burner. The same correspondence holds for high (22.5 m/s) air velocities in the spray burner and high (175 s^{-1}) strain rates in the OFDF burner.

It should be noted that extinction measurements in the OFDF and cup burner were quasi-steady experiments. Agent concentration was slowly increased until the flame extinguished. The spray experiments involved transient agent injection. Yet, for long injection intervals, the spray experiments were similar to the quasi-steady agent addition methodology and a direct comparison of the results in the three very different configurations is not unreasonable. A plausible explanation of the phenomena follows. As the air flow increased in the spray flame, the characteristic Damköhler number flow time in the recirculation zone decreased and the flow field strain rate increased, facilitating flame extinction with less agent. At high enough air flows, no agent at all was necessary to achieve extinction and flame blow-off was observed. This is analogous to the OFDF results (Hamins *et al.*, 1994). This suggests that the same processes that control flame extinction in simple diffusion flames govern flame extinction in the baffle stabilized spray flame. The correspondence is surprising because a baffle stabilized turbulent spray flame is very different in character from the laminar diffusion flames stabilized in the OFDF and cup burners. Quantitative modeling of the correspondence would require a detailed understanding of the interaction between the chemistry and fluid dynamics/droplet interaction in the recirculation zone of the turbulent jet spray flame. The practical implication of the results shown in Table 3 is that it is not necessary to test the suppression effectiveness of agents in every possible configuration. The results can be scaled from one burner to another.

An interesting model for flame blow-off was reported by Ballal and Lefebvre (1981), who correlated blow-off data for premixed gaseous turbulent flames from many investigators over a large range of velocities and flame holder diameters and shapes. Their model suggests that blow-off is proportional to the product of the square of the laminar flame speed (S_L) and the flame holder diameter (d):

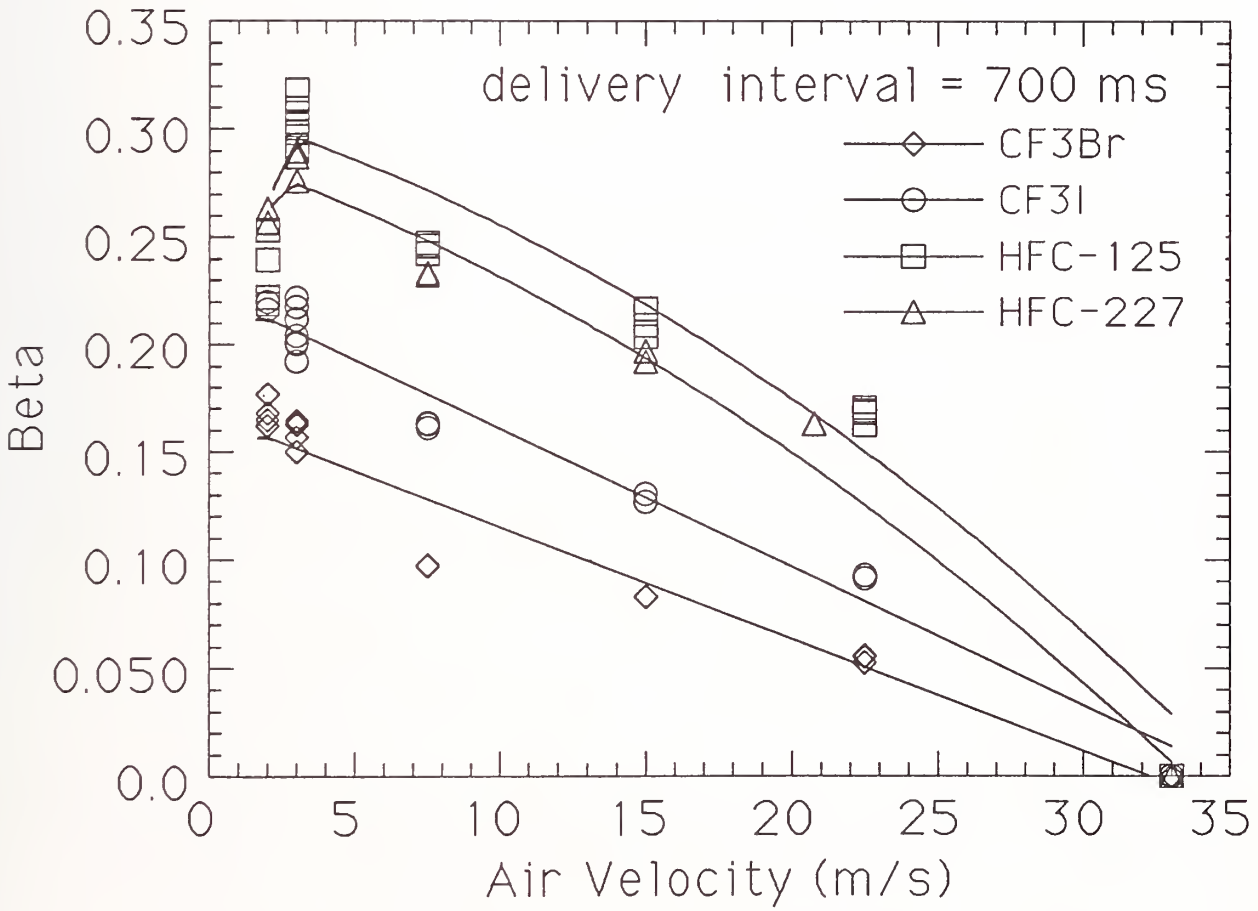

Figure 12. The critical mass fraction of agent at extinction as a function of air velocity.

$$V_{bo} = \frac{d \cdot C_s \cdot S_L^2}{\alpha_o} \tag{12}$$

where C_s is a coefficient which takes into account the drag associated with the geometry of the flame holder and α_o is the thermal diffusivity of the gases. Application of this approach to flames suppressed by agent addition necessitates flame speed information as a function of suppressant concentration. For a particular mixture flow, flame extinction would be predicted to occur for combinations of flame speeds and baffle diameters below a critical threshold. Figure 13 shows the flame speed as a function of CF_3I, C_2HF_5, and CF_3Br concentration for stoichiometric methane/air flames (Babushok *et al.*, 1995a; Babushok, 1995). Figure 13 shows that flame speeds of 10 cm/s are obtained when agent concentrations obtain values of 1.8 %, 2.1 %, and 3.9 % (by volume), respectively, for CF_3Br, CF_3I, and C_2HF_5. It is possible to compare these results to the spray flame results in Table 3 for an air velocity of 15 m/s, where concentrations correspond to 1.8 %, 2.2 %, and 6.0 % (by volume) for the same agents, respectively. Thus, the premixed flame results and the results in the spray flame burner follow similar trends when interpreted in terms of Equation (12). Application of Equation (12) to the extinction of baffle stabilized flames merits further investigation. Successful application of this equation would imply that information from premixed flame studies would be an adequate predictor of suppression behavior.

9.3.2.3.4 Effect of Agent Injection Interval. Figure 14 shows the critical mass of CF_3Br and the three alternative agents at extinction as a function of the delivery interval or injection duration for a constant air velocity equal to 7.5 m/s. For conditions below the data points, the flames were stable, whereas for conditions above the data points, the flames were extinguished. As the delivery interval increased, the agent mass required to achieve flame extinction increased in a near linear fashion. CF_3Br required the least amount of mass to extinguish the flames, followed by CF_3I, and the other two agents, C_2HF_5 and C_3HF_7. These two agents were measured to have nearly identical effectiveness. The relative effectiveness of the various agents is consistent with the results shown in Figure 10-12.

Figure 15 shows the critical rate of mass injection required to achieve flame extinction as a function of delivery interval for the same data as shown in Figure 14. As the delivery interval increased, the critical rate of mass injection decreased and approached an asymptote for long delivery intervals. The relative effectiveness of the various agents is consistent with the results shown in Figure 14.

Figure 16 shows the critical mass fraction (ß) as a function of delivery interval for the same data as shown in Figures 14 and 15. The curves are similar to those in Figure 15. As the delivery interval increased, the critical ß decreased, and approached an asymptote for long delivery intervals. The curves for all of the agents in Figure 16 were nearly identical in shape, but were displaced along the y-axis.

These data can be explained in terms of a phenomenological model first developed by Longwell *et al.*, (1953) to explain blow-off of premixed flames by treating the recirculation zone as a well-stirred reactor. The key parameter in this model is the characteristic mixing time of reactants to entrain from the free stream into the recirculation zone. Support for this model also comes from Mestre (1955), who found that the blow-off velocity was related to the characteristic time for entrainment into the recirculation zone. Here, the model is extended to treat agent entrainment into the recirculation zone and subsequent extinction of combustion occurring in that zone. The assumptions used to develop the model are as follows. The flame is stabilized in the eddy or recirculation zone

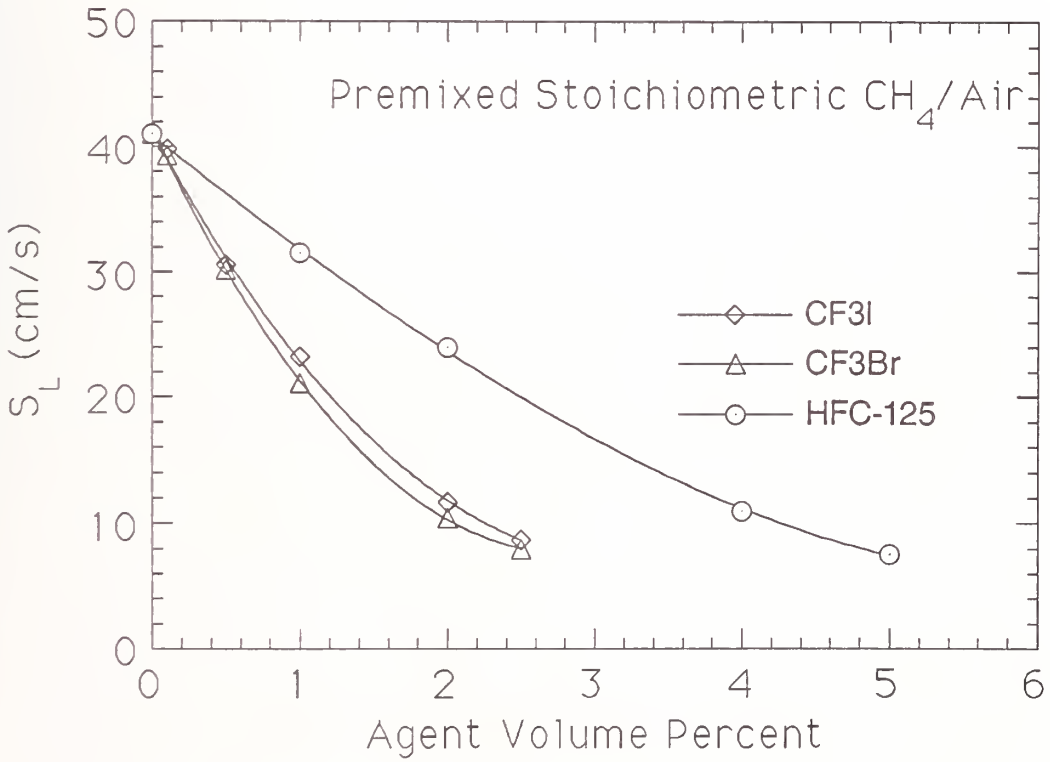

Figure 13. The flame speed as a function of inhibitor concentration in stoichiometric methane/air premixed flames. Results from Babushok (1995) and Babushok et al. (1995a).

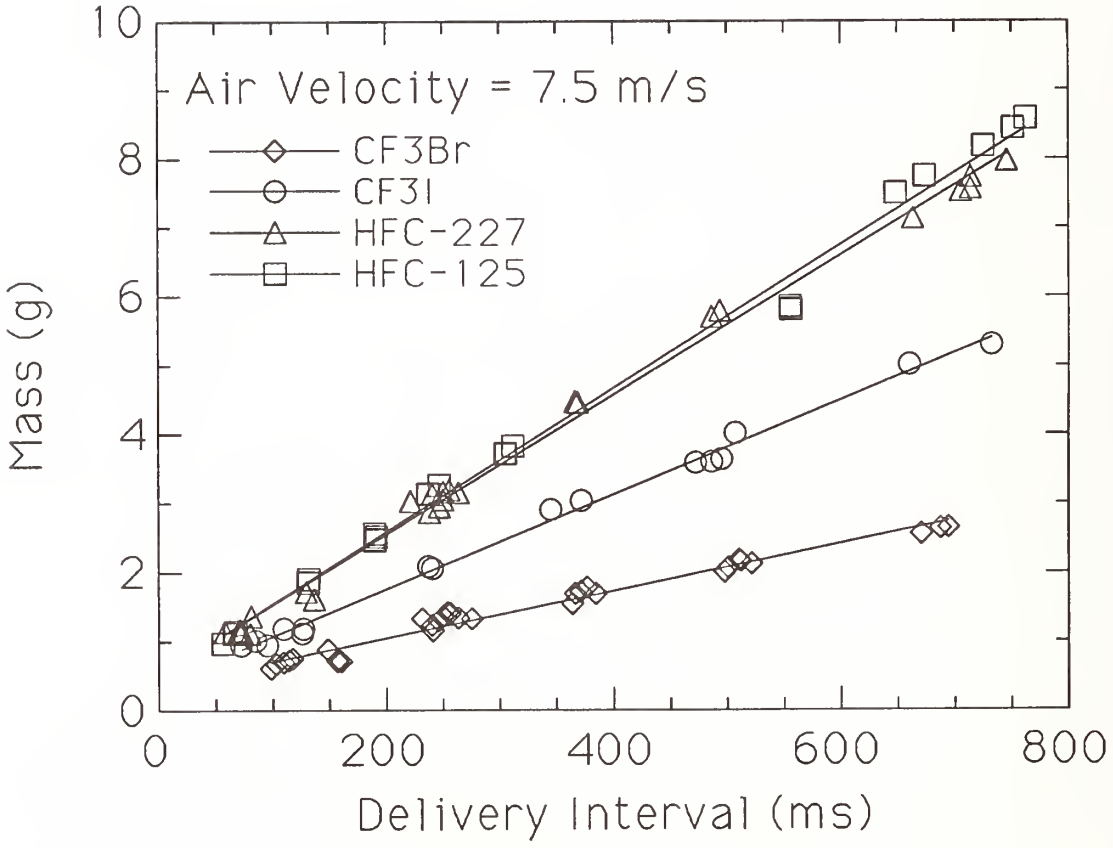

Figure 14. The critical mass of agent at extinction as a function of the agent delivery interval.

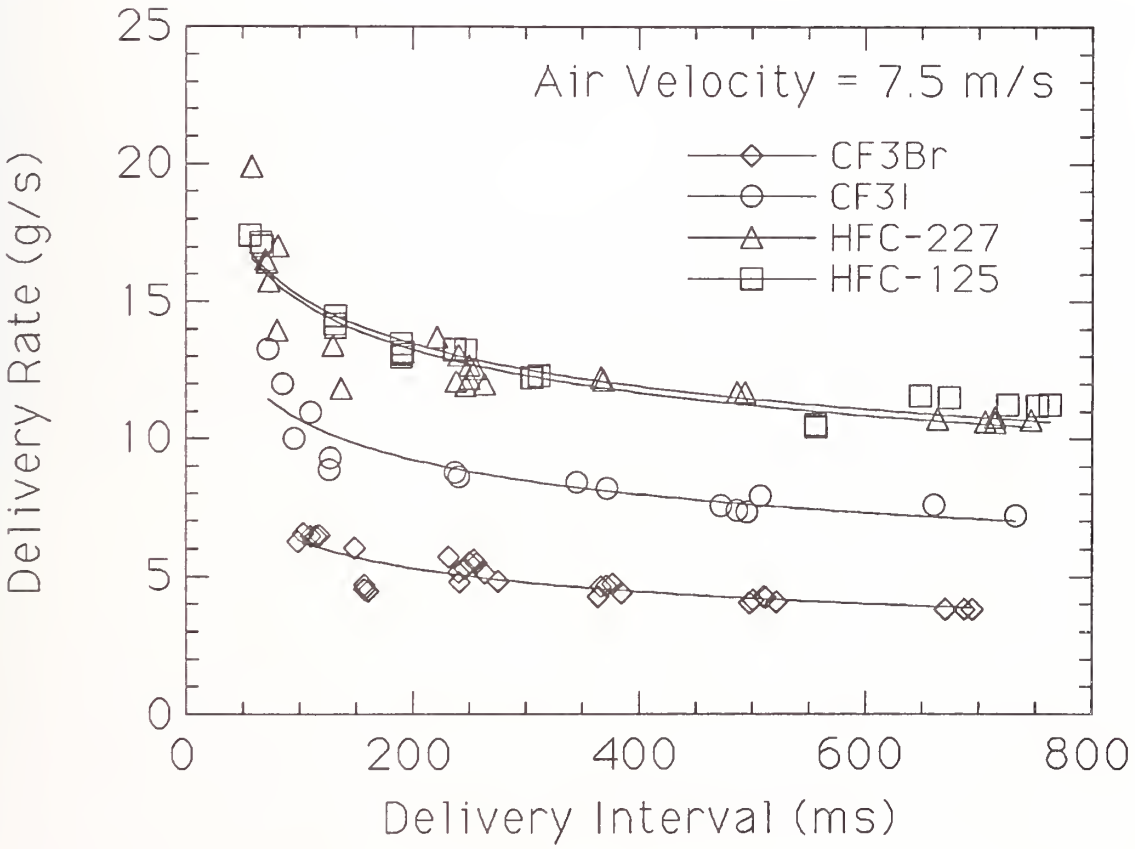

Figure 15. The critical rate of mass injection of agent at extinction as a function of agent delivery interval.

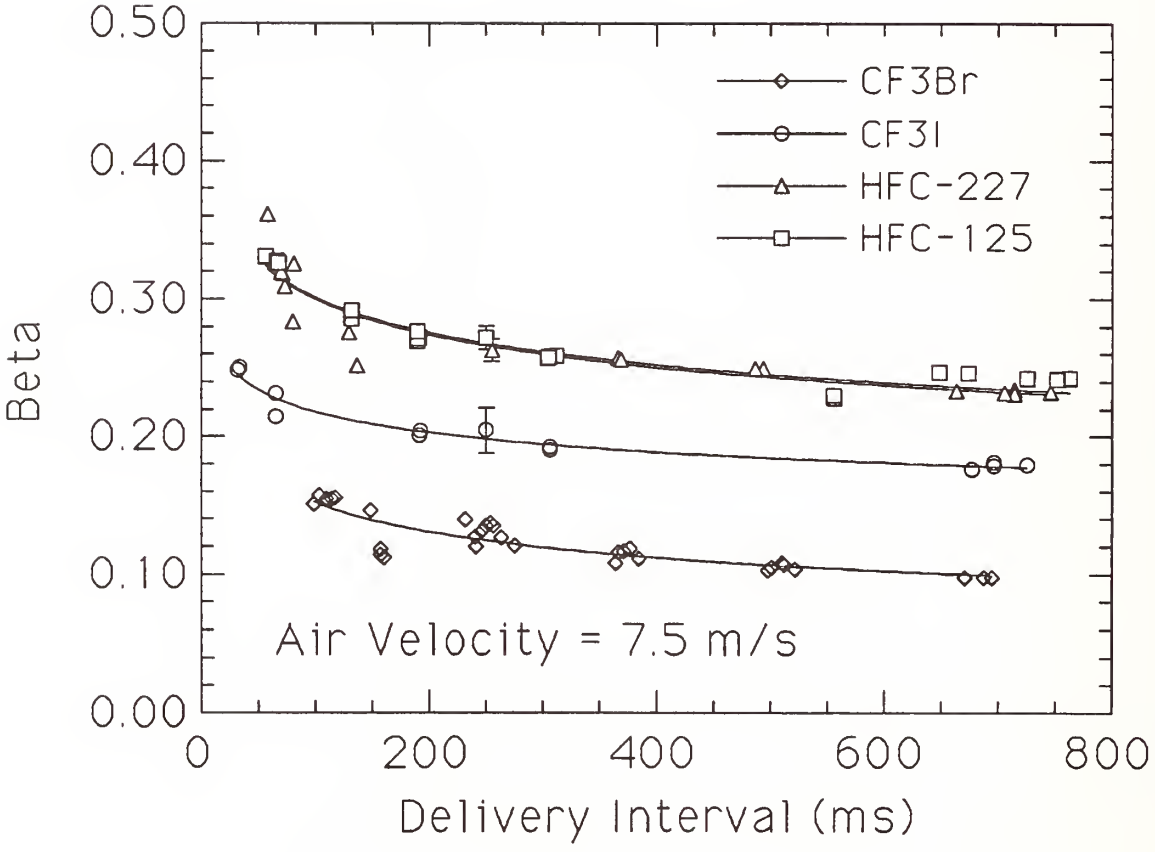

Figure 16. The critical agent mass fraction at extinction as a function of agent delivery interval.

behind the obstacle. To extinguish the flame, the agent (volume based) concentration (X) must obtain a critical value. This concentration depends on the agent type and the free stream air velocity as shown in Figures 10-12. The recirculation zone is homogeneous and mixing of the agent in the zone is instantaneous. Spray characteristics such as the droplet size distribution and momentum are considered unimportant. Applying these assumptions, it is possible to develop a simple model to predict the critical agent concentration at extinction as a function of the injection duration (Δt) and the concentration of agent for long injection times.

Applying this model, the baffle stabilized flame extinction experiments can be interpreted as follows. A pulse of agent is injected into the air stream. The agent/air mixture passes the obstacle and a portion of the agent is entrained into the recirculation zone behind the obstacle. Initially, the agent mole concentration (X) in the recirculation zone is zero. As the agent is entrained into the recirculation zone, the concentration there is given by:

$$X = X_f \left[1 - e^{(-t/\tau)}\right] \tag{13}$$

where X_f is the free stream agent mole concentration, t is the time from initial agent entrainment into the recirculation zone, and τ is the characteristic mixing time for entrainment into the recirculation zone. For very long injection times ($\Delta t >> \tau$), the concentration in the recirculation zone will approach the free stream agent concentration, X_f. Experiments reported by Bovina (1958) confirm the form of Equation (13).

Our well stirred reactor model requires that at flame extinction, the agent concentration in the recirculation zone obtains the same critical value, regardless of agent injection duration. Thus, the model suggests that the critical agent concentration in the free stream required to achieve extinction, $X_c(\Delta t)$, for a finite injection interval (Δt) is related to the critical agent concentration in the free stream, $X_\infty(\Delta t >> \tau)$, for long injection intervals ($\Delta t >> \tau$) and an exponential term associated with the extent of mixing:

$$X_c(\Delta t) = \frac{X_\infty(\Delta t >> \tau)}{1 - e^{(-\Delta t/\tau)}} \tag{14}$$

Interpretation of the spray flame extinction experiments by Equation (14) shows that the critical extinction concentration is determined by the ratio ($\Delta t/\tau$). This relationship is shown in Figure 17 where the term (X_c/X_∞) is plotted as a function of ($\Delta t/\tau$). For long injection durations, the denominator in Equation (14) becomes 1.0 and X_c is equal to X_∞. For short injection intervals, very high agent concentrations are required to obtain extinction. For example, when ($\Delta t/\tau$) = 1, the critical agent concentration (X_c) is approximately a factor of 1.5 times X_∞. When ($\Delta t/\tau$) = 0.5, the critical agent concentration (X_c) is approximately a factor of 2.4 times X_∞. In addition, X_c is constrained such that $X_c \leq 1$. Equation (14), therefore, implies that there exists a critical injection duration (Δt_c) such that no matter how large the agent concentration, the flame cannot be extinguished. The value of the critical injection duration is:

$$\Delta t_c = -\tau \ln\left(1 - \frac{X_\infty}{X_c}\right) \tag{15}$$

For τ equal to 100 ms, representative of conditions in the spray burner for an air velocity of 3 m/s (discussed below), and X_∞ equal to 0.1, Equation (15) yields a value of Δt_c equal to 11 ms. Unfortunately, the minimum solenoid opening time was much larger than this value, so the veracity of Equation (15) was not empirically tested in the spray burner.

Bovina (1958) found that the time constant (τ) in Equations (13)-(15) is related to the baffle diameter (d) and the upstream velocity (V):

$$\tau \cong \frac{d}{V} \tag{16}$$

Bovina (1958) also found that the upstream turbulence level was an important factor in the mixing time. Winterfeld (1965) verified that τ was inversely proportional to the upstream velocity for both combusting and non-combusting cases over a range of Reynolds numbers extending from $\approx 1.5 \cdot 10^4$ to $2.2 \cdot 10^5$. Winterfeld (1965) found that in addition to d and V, the time constant was also a function of the blockage ratio and the geometry of the flame holder. Figure 18 shows Winterfeld's results, where the non-dimensional characteristic mixing time is plotted as a function of the square of the ratio of the baffle diameter (d) to the enclosure diameter (D). Increased blockage (increasing values of d/D) increased the value of τ. Figure 18 shows that τ was approximately a factor of two larger for a combustion situation as compared to an isothermal case, over the entire range of Reynolds numbers tested. Both the isothermal and combusting results were well fit by the form:

$$\tau = \frac{d}{V} \cdot [\, a + b \cdot \log(\frac{d}{D})^2] \tag{17}$$

Equation (17) is nearly identical to Equation (16), but includes a correction term for the effect of geometric blockage.

The velocity in Equations (16) and (17) refer to the velocity of the air/agent mixture. For cases where the agent composes a small percentage of the mixture, the free stream air velocity is a good approximation of the total velocity (V). Winterfeld's model suggested that mixing actually occurs over the surface which bounds the recirculation zone from the free stream. His measurements showed that the length of the recirculation zone increased significantly with increased free stream velocity. Measurements by others have led to the opposite conclusion (Lefebvre, 1983).

A two parameter fit to the extinction data shown in Figure 16 (after conversion to mole fraction from mass fraction) using Equation (14), allows determination of the parameters X_∞ and τ. By definition, the agent mole fraction (X) is related to the mass fraction (ß) by the expression:

$$X = \frac{(\beta/M)}{[(\beta/M) + (1-\beta)/M_a]} \tag{18}$$

where M_a and M are the molecular weight of air (=28.96 g/mole) and the agent, respectively.

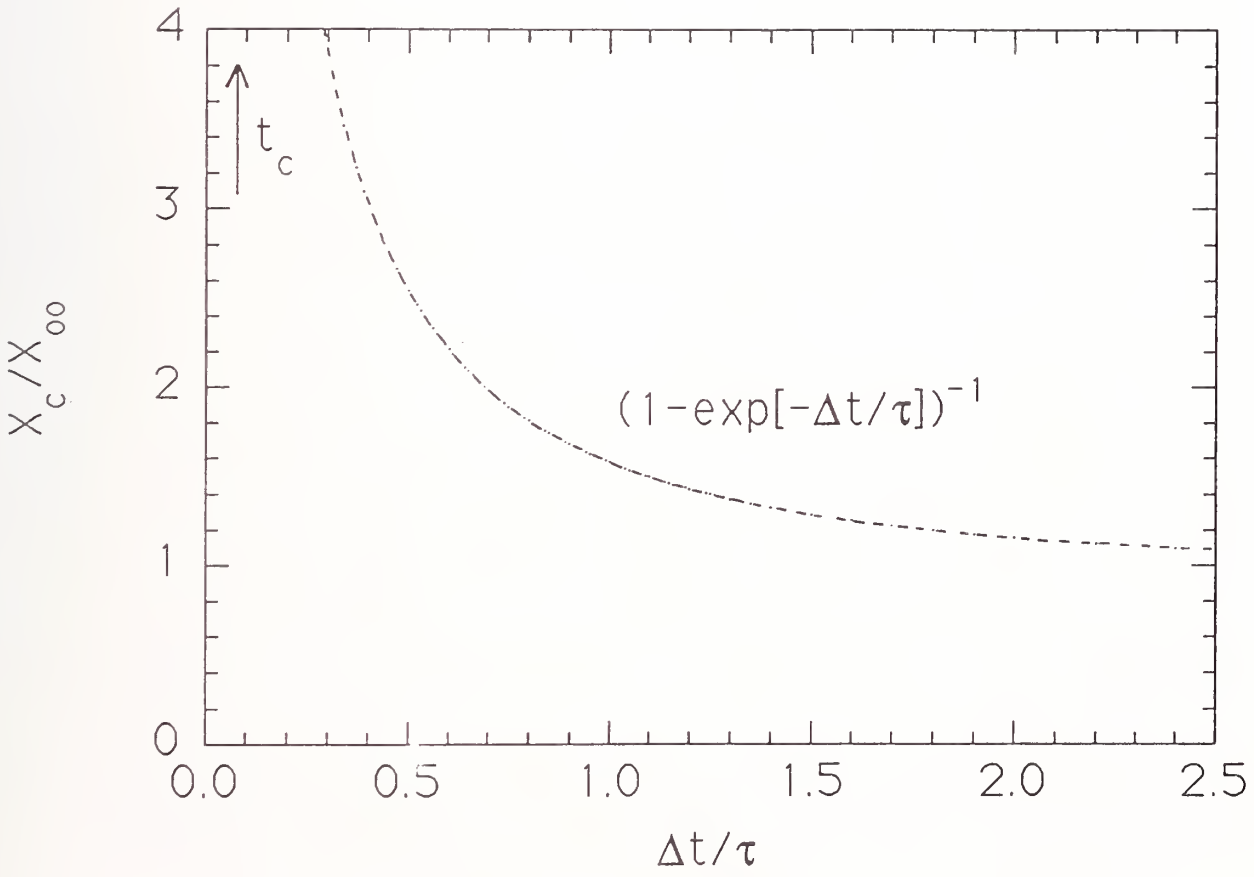

Figure 17. The term (X_c/X_∞) in Equation 14 plotted as a function of $(\Delta t/\tau)$.

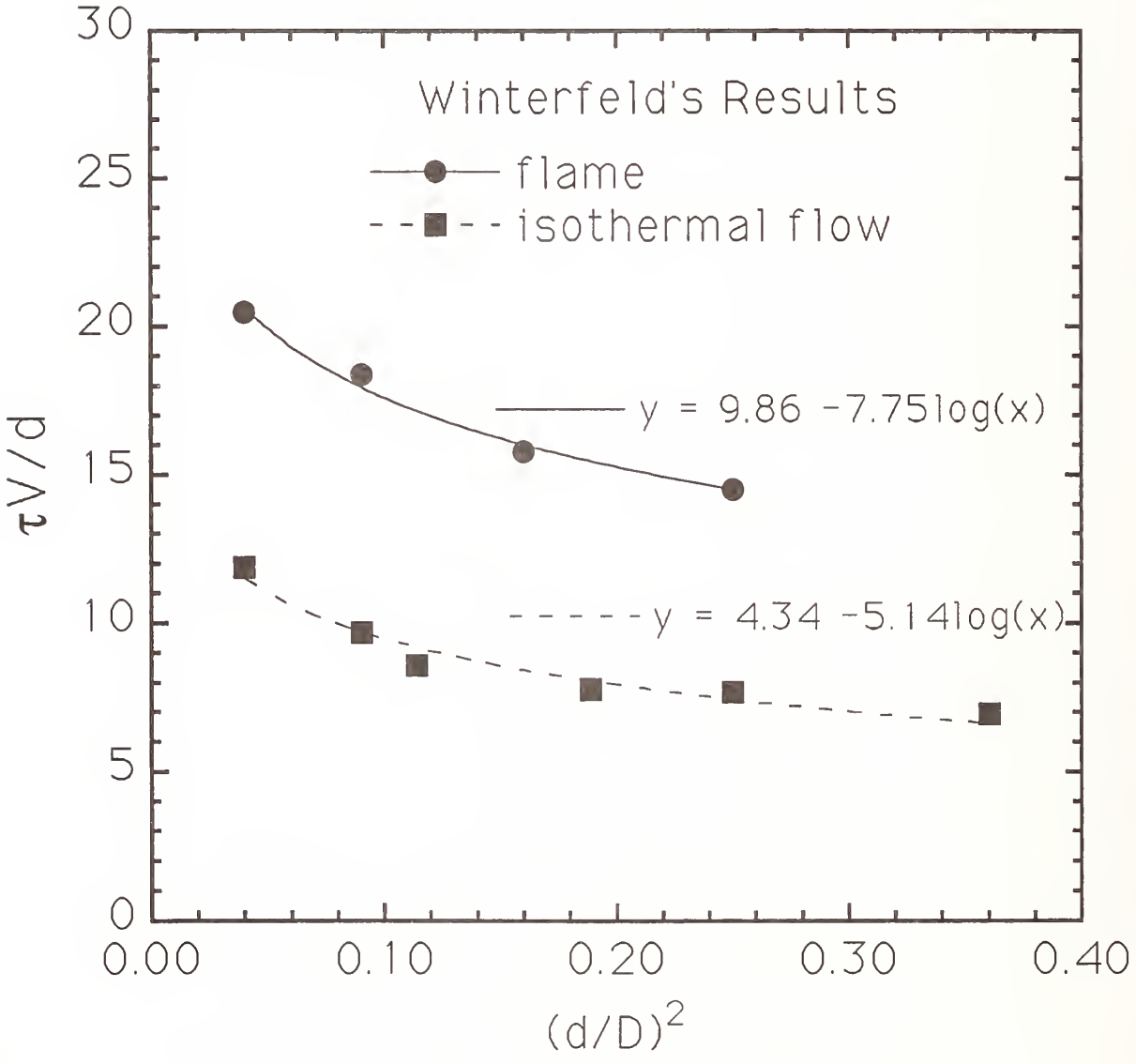

Figure 18. The non-dimensional characteristic mixing time as a function of $(d/D)^2$, as reported by Winterfeld (1965) for baffle stabilized premixed flames in an enclosure.

The critical mole fraction of HFC-125 at extinction for air velocities of 3.0 and 7.5 m/s is shown in Figure 19. The same data presented in Figure 16 for HFC-125 is shown in Figure 19 in terms of the critical mole fraction at extinction. Interpreting the curves in terms of Equation (14) shows that a best two parameter fit for the V=3.0 m/s data yields τ= 99 ms and X_∞=0.10. Because Equation (16) suggests that $\tau \propto (1/V)$, the 7.5 m/s data should be well represented by τ=40 ms (=99 ms/2.5). A plot using 40 ms for τ leads to a reasonable fit of the V=7.5 m/s data using Equation (14) as shown in Figure 19. The fit yields a value of 0.078 for X_∞.

The correspondence between extinction concentrations in the spray burner, cup burner, and OFDF implies that X_∞ is related to a universal criterion for flame extinction, referred to as the critical Damköhler number. As such, X_∞ is controlled by the interaction between the chemistry associated with combustion of the fuel/air/agent mixture and the fluid mechanical flow field. Once X_∞ is known, X_c is controlled by τ, the rate of agent entrainment into the recirculation zone.

Equation (14) and the results in Table 3, suggest that the Damköhler number flow time for flame extinction must be related to the characteristic residence or mixing time, τ, in the recirculation zone of a baffle stabilized flame. For a flame stabilized by an object or a bluff body, this time is related to the free stream air flow, the size of the obstacle, and geometric blockage.

Figure 20 shows measurements of the critical agent mole fraction at extinction as a function of injection interval for two different bluff body disks. The flames behind the 4.13 cm disk were more stable than the flames behind the 2.86 cm disk. The blockage factor, B, (see Equation (11)) for the 2.86 cm and 4.13 cm diameter (4 mm thick) disks were 0.85 and 0.68 respectively. Equation (16) predicts a 30 % increase in the characteristic mixing time based on the increased disk diameter (from 2.86 cm to 4.13 cm). Fitting the 4.13 cm disk extinction concentration data with a two parameter fit for τ and X_∞, yields τ = 93 ms.

Winterfeld (1965) studied the combined effect of disk diameter and blockage on the characteristic mixing time for premixed flames over a wide range of blockage ratios. Winterfeld's (1965) results (Equation (17)) predict that the combination of increased disk diameter and increased blockage should lead to a 14 % and not a 30 % increase in τ, yielding a value of 81 ms rather than 65 ms. A plot using τ=81 ms leads to a reasonable prediction of the extinction results for the 2.86 cm disk (4 mm thick) as shown in Figure 20. No direct comparison was made with the results using the reference disk (3.5 cm diameter, 2 mm thick), because disk thickness and material differences influence the measured agent extinction concentrations, presumably through differences in the detailed structure of the recirculation zone. Figure 21 is an example of application of Winterfeld's results for combusting flows (shown in Figure 18), to determine mixing times for various flow velocities in an enclosure of diameter D (=7.3 cm). The mixing time is plotted as a function of the square of the ratio of the baffle diameter (d) to the enclosure diameter (D). Relatively large changes in the mixing time occurred for small changes in $(d/D)^2$. The mixing times, determined by fits to the extinction data, for the spray burner were ≈99 and 40 ms for air velocities equal to 3.0 and 7.5 m/s respectively (see Figure 19). Winterfeld's results predict mixing times equal to ≈170 and 65 ms for V=3.0 and 7.5 m/s. The ratio of values determined from Winterfeld's data to our measurements in the spray burner are a factor of 1.7 and 1.6, respectively, for the same air velocities. It was encouraging, however, that the relative difference in the two configurations were nearly the same. These difference are not surprising considering that Winterfeld's results are for premixed flames. In addition, the flows that Winterfeld studied were for relatively high Reynolds numbers and the baffle thickness was not reported nor its material composition.

As expressed through Equation (14), the simple well-stirred reactor/spray flame model has no explicit dependence on pressure, air temperature, or fuel droplet characteristics. These parameters are not thought to impact agent mixing. Molecular diffusion is not expected to play a role either and therefore agent type should not effect the characteristic agent mixing time.

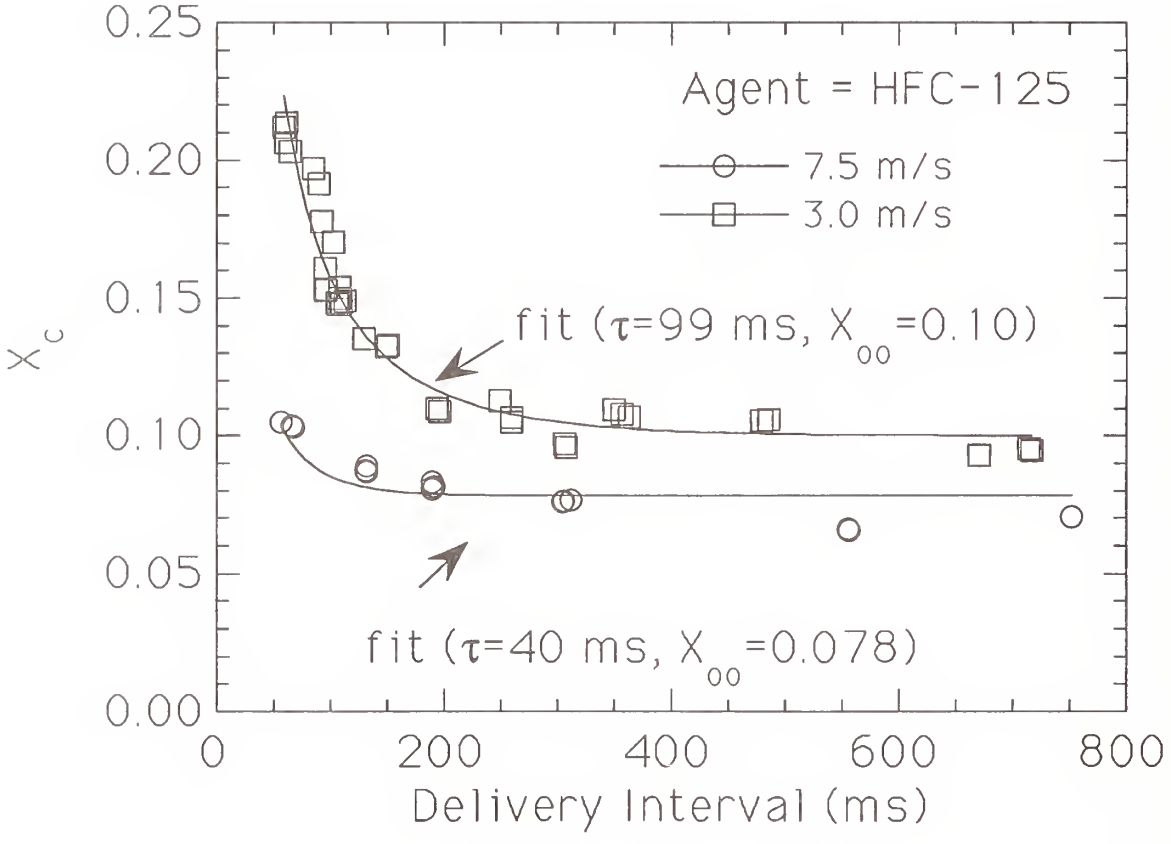

Figure 19. The critical mole fraction of HFC-125 at extinction for air velocities of 3.0 m/s and 7.5 m/s.

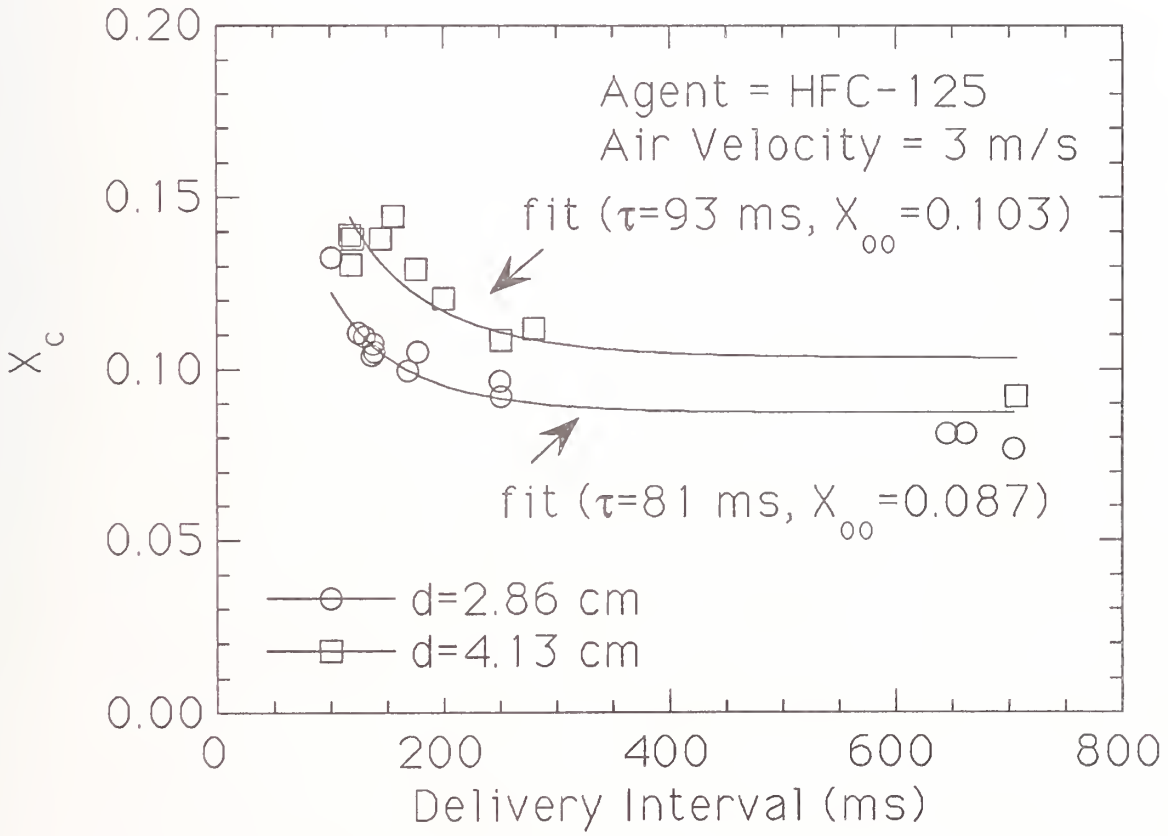

Figure 20. The critical mole fraction of HFC-125 at extinction as a function of injection interval for two different bluff body diameters with the air velocity equal to 3 m/s.

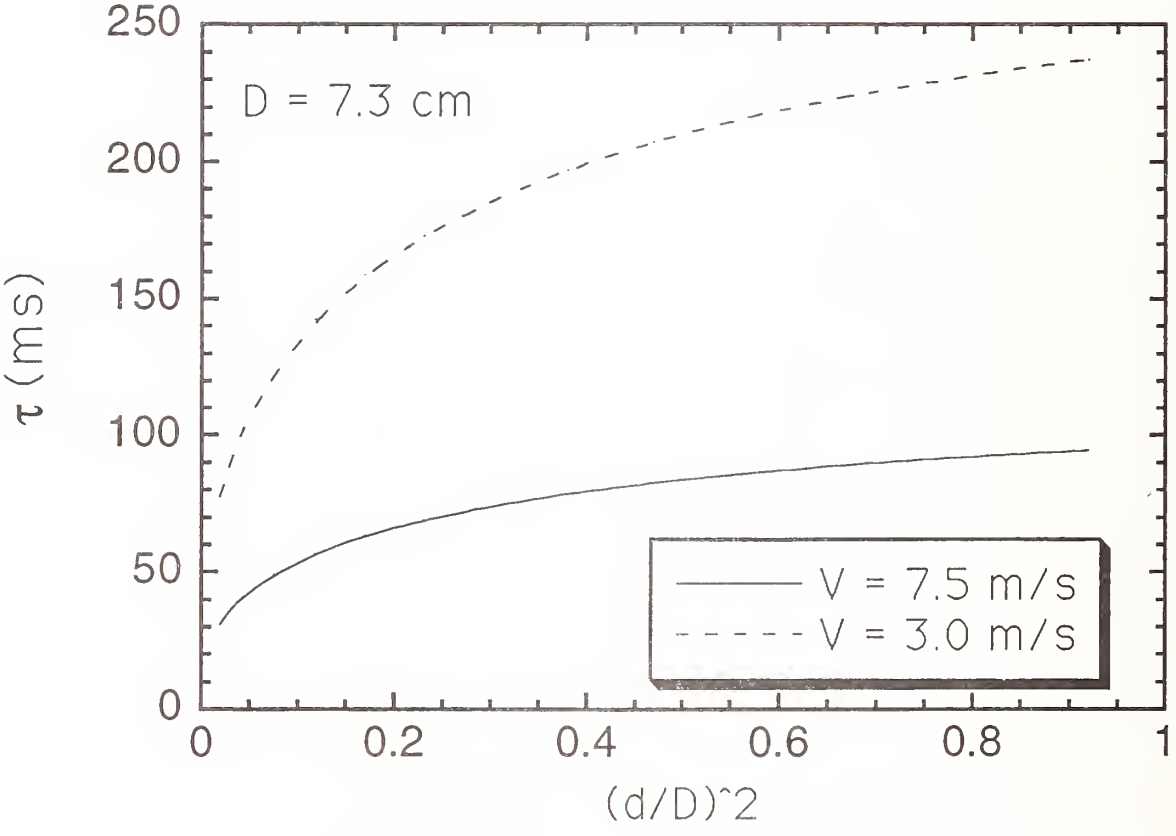

Figure 21. Application of Winterfeld's results to determine the characteristic mixing times as a function of air velocity for a fixed enclosure diameter (D).

The spray flame testing described in this and subsequent sub-sections was conducted with the 3.5 cm diameter disk (2 mm thick) and with air velocities of 7.5 m/s, yielding a mixing time constant equal to approximately 40 ms. In subsequent experiments described below, the agent delivery interval was held constant at 250 ms, yielding a value for the ratio ($\Delta t/\tau$) as approximately equal to 6, indicating that $X_c \approx X_\infty$. Thus, the value of τ is not expected to play a role in the extinction results discussed in this and subsequent sub-sections.

9.3.2.3.5 Effect of Air Temperature. The air was preheated and extinction measurements were conducted with the average air temperature in the burner varying from ambient to 350 °C under conditions of a constant air velocity of 7.5 m/s and for an agent delivery interval of 250 ms. The increase in temperature affected flame stability in several ways. First, since the air velocity at the bluff body was held fixed, the mass flow of air decreased as much as 50 % because of the drop in density. Heating of the JP-8 in the fuel line was minimized because the coaxial water jacket cooled the fuel line. As seen in Figure 22, the agent mass fraction (ß) required to suppress the JP-8 spray flame increased as the air temperature increased. This was expected; increased air temperature enhances flame stability through enthalpy addition and the results were also consistent with measurements of the effect of reactant temperature on the stability of baffle stabilized flames as characterized by flame blow-off (Lefebvre, 1983). Surprising, however, was the reduction in the relative effectiveness of CF_3I as compared to the HFCs for moderate temperatures. The relative effectiveness of CF_3I was still better than HFC-125 and HFC-227 for temperatures lower than approximately 100 °C, as noted previously, but was only as effective as those agent for temperature greater than 100 °C. CF_3Br remained the most effective agent over the temperature range studied. In relative terms, CF_3I and CF_3Br required larger relative changes in agent concentration to achieve extinction as the air temperature increased, as compared to HFC-125 or HFC-227. These results were consistent with earlier measurements of the critical agent concentration requirements at extinction for heated air flows in spray flames (Vazquez *et al.*, 1994) and counterflow diffusion flames (Grosshandler *et al.*, 1995), and may be due to diminished chemical effectiveness of these agents (CF_3Br and CF_3I) as the agent concentration increases.

For some aircraft applications, cold temperatures can be expected. For sub-ambient air temperatures, the stability of the spray flame can be expected to decrease and suppression can be expected to require less agent. All measurements reported here, however, utilized gaseous agent. For a two-phase agent delivered under cold temperature conditions, the rate of evaporation and flashing may detrimentally impact the amount of agent required for flame suppression.

9.3.2.3.6 Effect of Agent Temperature. Figure 23 shows the critical ß as a function of agent temperature for the three alternative agents under conditions of a constant air velocity of 7.5 m/s and for agent delivery intervals of 250 ms. Extinction measurements were conducted with the three alternative agents heated to temperatures as high as 150 °C (300 °F). The results showed that the gas phase agent temperature had no effect on flame stability. Because the majority of the air/agent mixture was air, the agent was diluted and the final mixture temperature approached the air stream temperature. In addition, the tubing walls were not insulated and the agent pulse was relatively short (less than 1 s), promoting equilibration of the gas mixture to ambient temperatures. These results do not imply that heating or cooling of the agent will not affect the rate of agent dispersion or evaporation. In these tests, the agent was introduced in the gas phase. In the nacelle, the agent will be delivered as a two-phase fluid which raises issues associated with the rate of agent evaporation, etc.

9.3.2.3.7 Effect of Pressure. Figure 24 shows the critical agent mass as a function of system pressure for the three alternative agents under conditions of a constant air velocity equal to 7.5 m/s

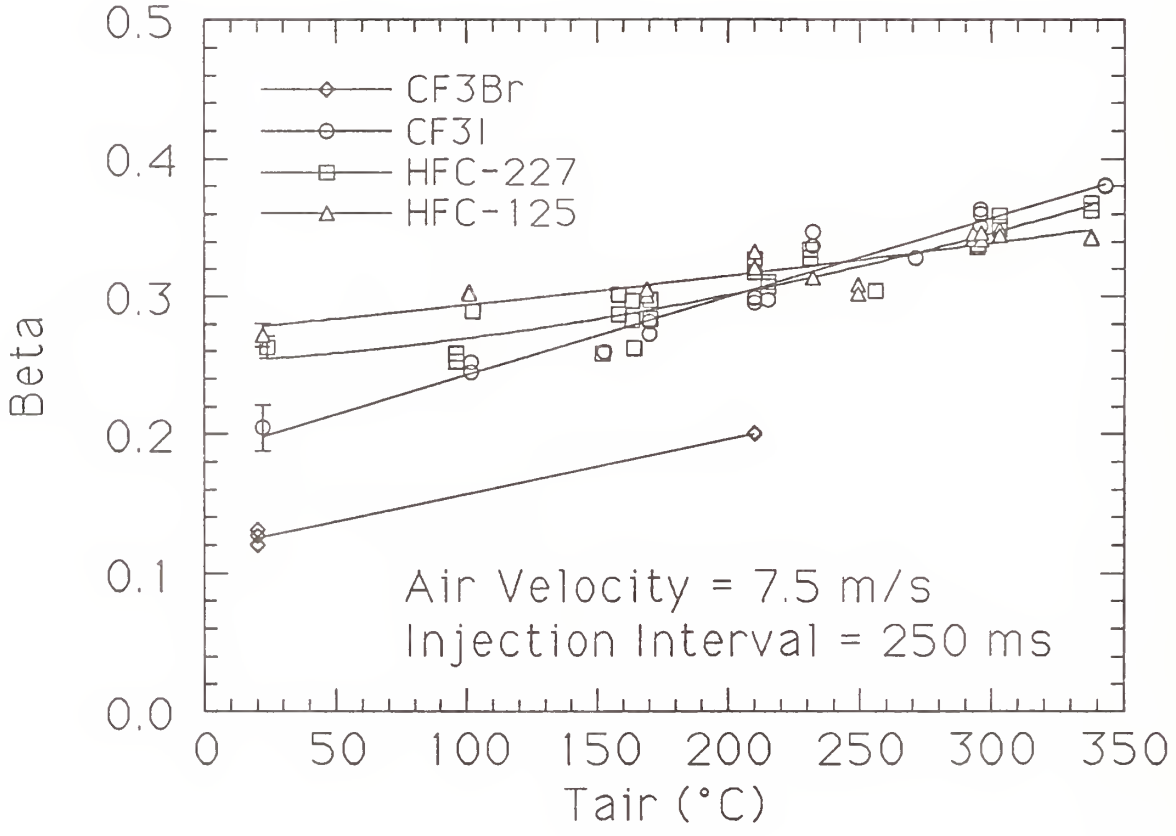

Figure 22. The critical agent mass fraction at extinction as a function of the air temperature.

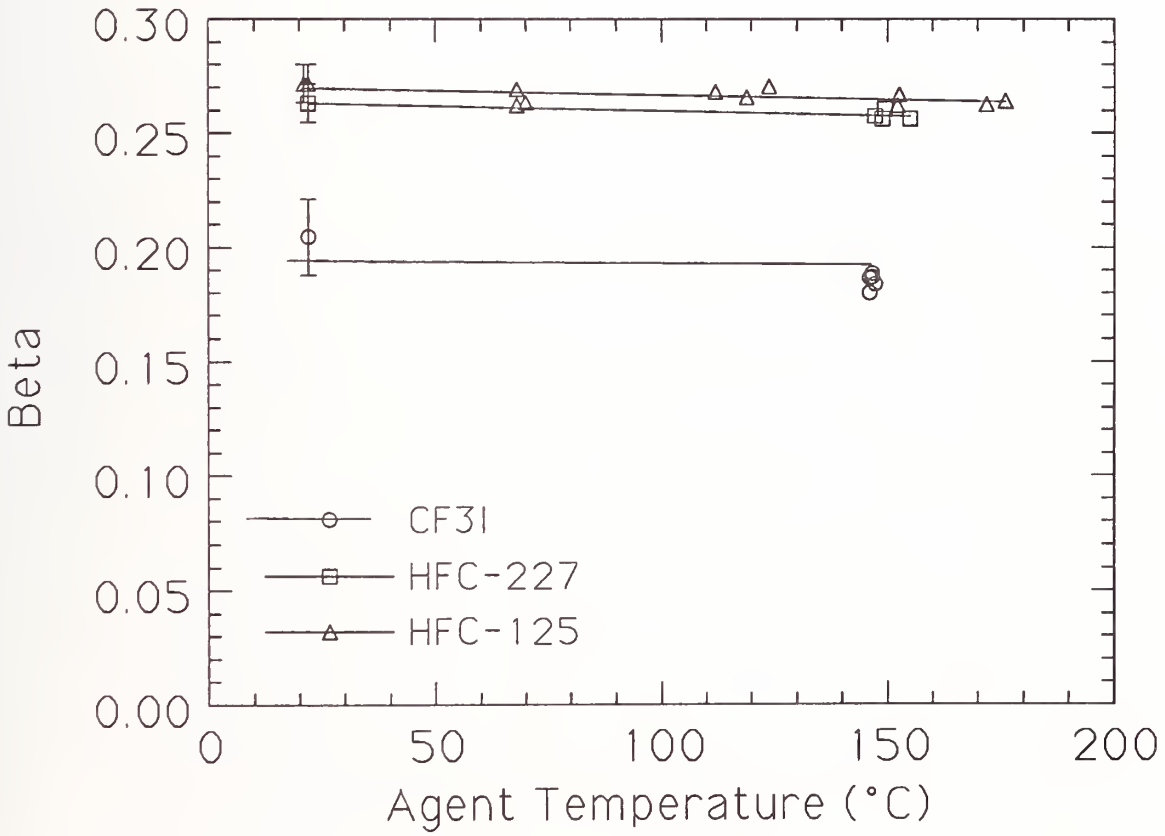

Figure 23. The critical agent mass fraction at extinction as a function of agent temperature.

and for an agent injection interval of 250 ms. As the pressure increased, more agent mass, in a near-linear fashion, was required to extinguish the spray flames. In addition to the super-ambient data in Figure 24, the data representing the ambient case (0 psig or 101 kPa) were also determined utilizing the confined spray apparatus. Those results were similar to the results determined using the standard burner configuration.

Figure 25 shows the critical agent mass fraction at extinction (ß) as a function of system pressure for the three alternative agents under conditions of a constant air velocity equal to 7.5 m/s and for an agent injection interval of 250 ms. As the pressure increased, the critical ß remained constant for all three agents. Thus, the mass flow of agent required to extinguish the spray flames increased linearly with the mass flow of air. The results imply that the key chemical processes that control flame extinction were not sensitive over the rather narrow pressure variation studied. It should be noted that a small pressure dependence may result for high air velocities. Equation (7) and the results of Hirst and Sutton (1961), who studied the effect of reduced pressure on the air blow-off requirements of baffle stabilized pool fires, predict increased air blow-off velocities (V_{bo}) as the pressure increases. Thus, increases in V_{bo} due to enhanced pressure would alter the profile of the critical agent mass fraction at extinction (ß) as a function of the air velocity. For the velocity range of interest (<10 m/s), however, it appears that the pressure dependence is negligible.

In aircraft applications, pressure decreases with altitude. The experimental results suggest that the mass flow of air through the nacelle is the parameter of interest, and that flame suppression will require less mass flow of agent if the mass flow of air decreases with pressure.

9.3.2.3.8 Effect of Fuel Flow. Figure 26 shows the critical agent mass fraction at extinction (ß) as a function of fuel flow for the three alternative agents under conditions of a constant air velocity of 7.5 m/s and for an agent injection interval of 250 ms. As the fuel flow increased, ß remained approximately constant. As the fuel flow increased, the global equivalence ratio increased, where the global equivalence ratio was defined as the molar fuel/air ratio divided by the stoichiometric fuel/air ratio. It is not clear, however, how changes in the global equivalence ratio impact the combustion processes in the spray burner. A higher fuel flow does not necessarily imply that the fuel concentration in the recirculation zone obtains a higher value. The fuel droplet size distribution may shift to larger sizes as the fuel flow increases. This would actually lead to diminished fuel evaporation rates and decreased flame stability (Lefebvre, 1983). Yet, the results in Figure 26 indicate that the stability of the spray flame is relatively insensitive to the fuel flow over the range of values tested.

Figure 27 shows the critical mass fraction (ß) as a function of fuel flow for the three alternative agents under conditions of a constant global equivalence ratio (0.11), for agent injection intervals of 250 ms. As the fuel flow increased, the air flow increased by the same factor. Figure 27 shows that the critical agent mass fraction required to achieve extinction decreased as the fuel and air flows increased. This series of experiments was undertaken to study the effect of fuel flow while eliminating the impact of the global equivalence ratio. Interpretation of the results is difficult, however, because the air flow has a large impact on flame stability as noted in Figures 10-12.

9.3.2.4 Summary of Spray Flame Results. The following equation summarizes the agent mass fraction requirements for flame suppression in the turbulent jet spray burner as a function of operating conditions:

$$\beta = \beta_o f_1(P) f_2(Q_{fuel}) f_3(T_{agent}) f_4(T_{air}) f_5(V_{air}) f_6(\Delta t/\tau) \quad (19)$$

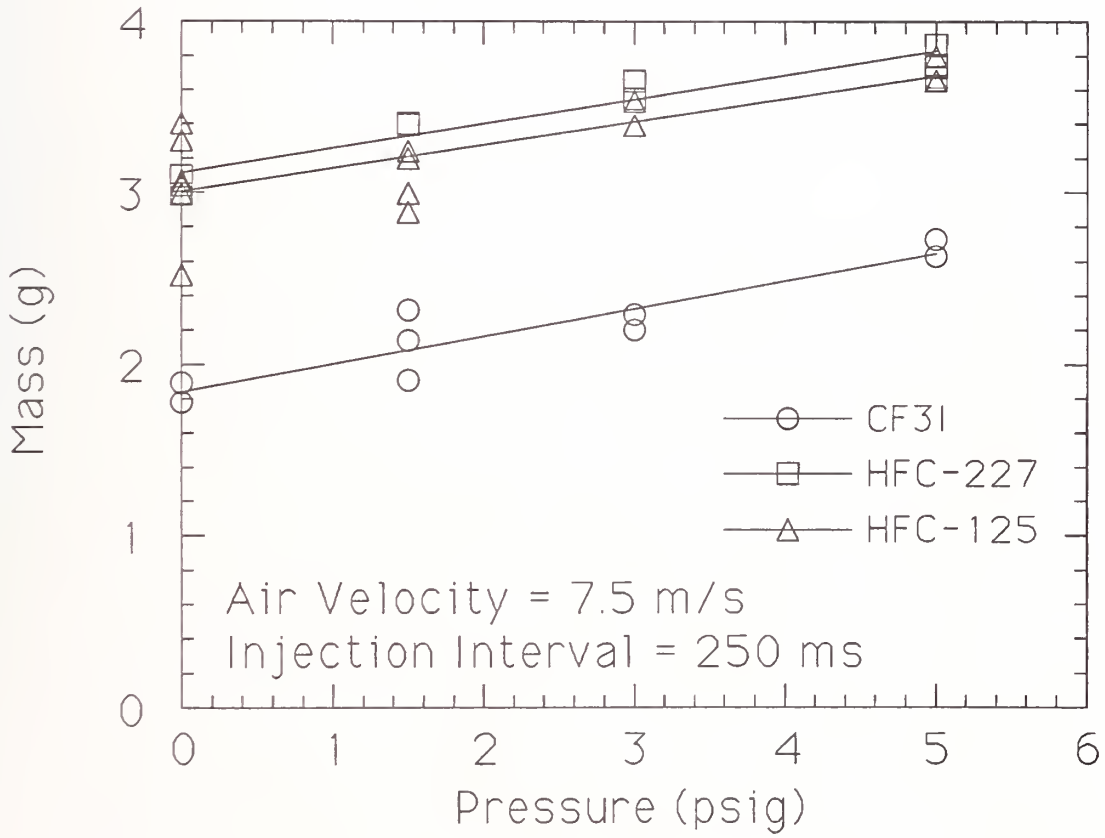

Figure 24. The critical agent mass at extinction as a function of system pressure.

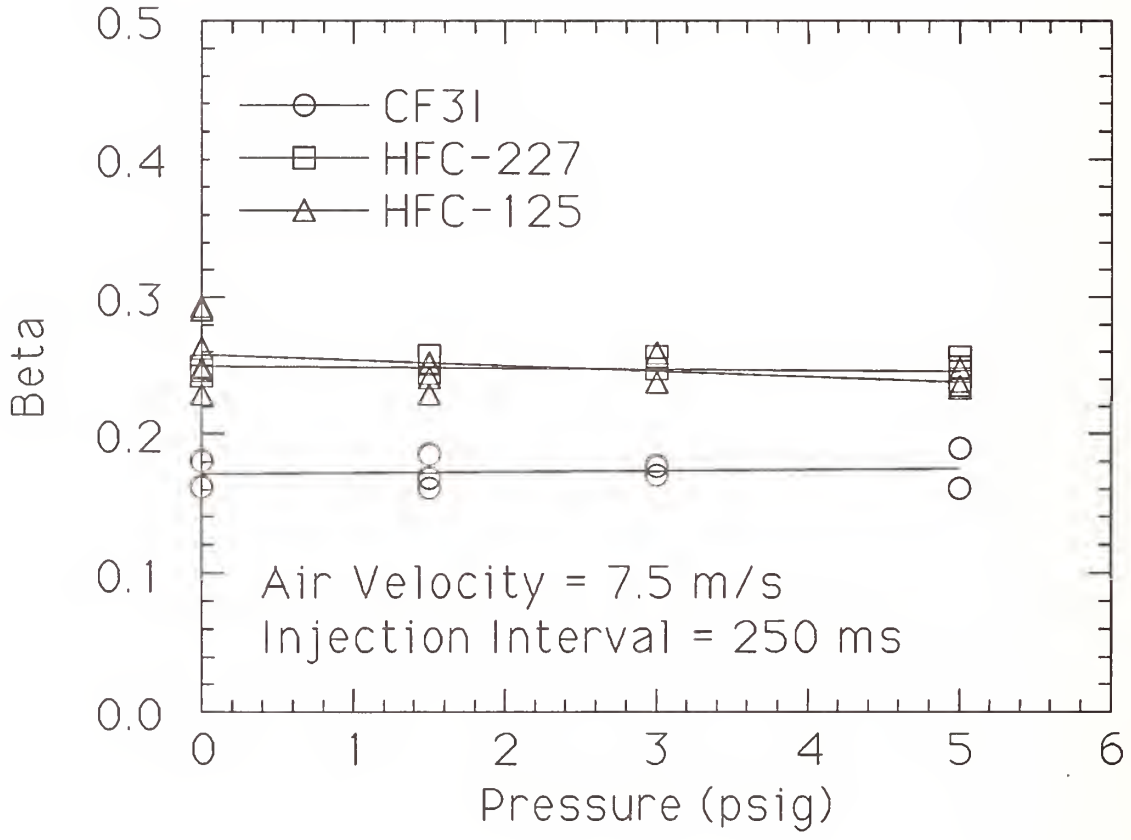

Figure 25. The critical agent mass fraction at extinction as a function of system pressure.

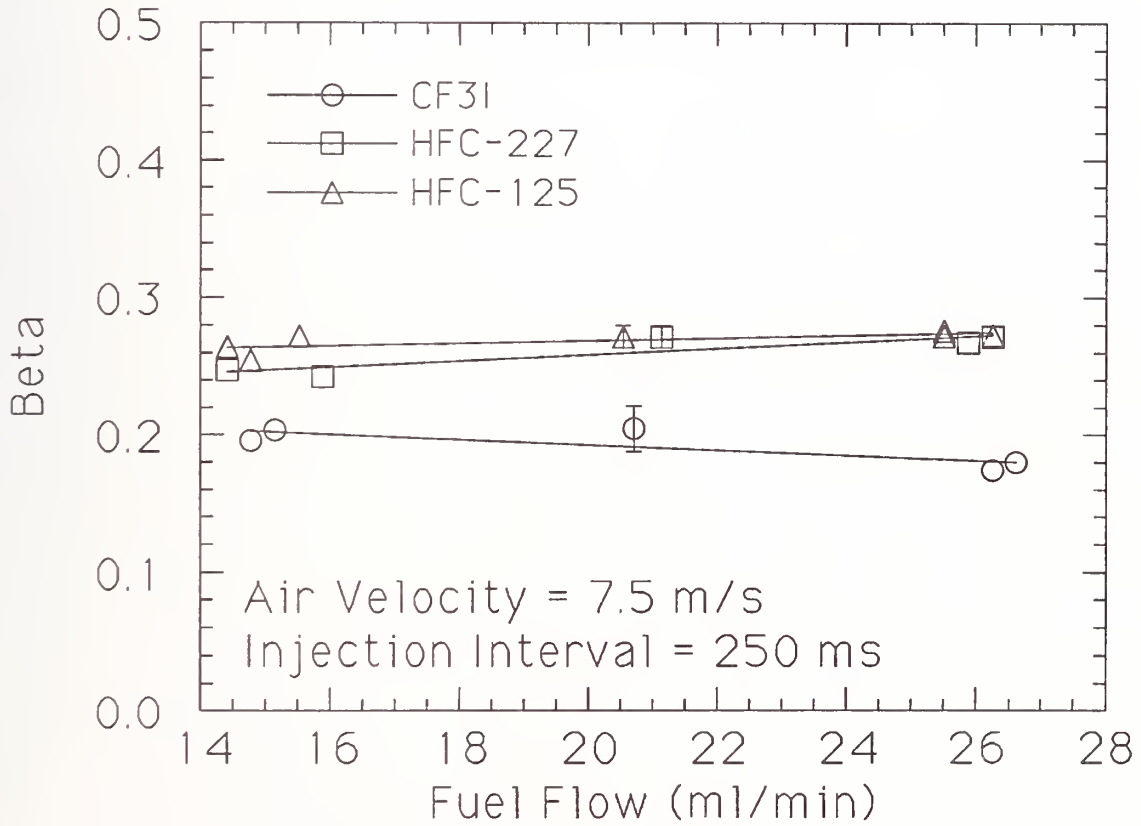

Figure 26. The critical agent mass fraction at extinction as a function of fuel flow under conditions of a constant air velocity (=7.5 m/s).

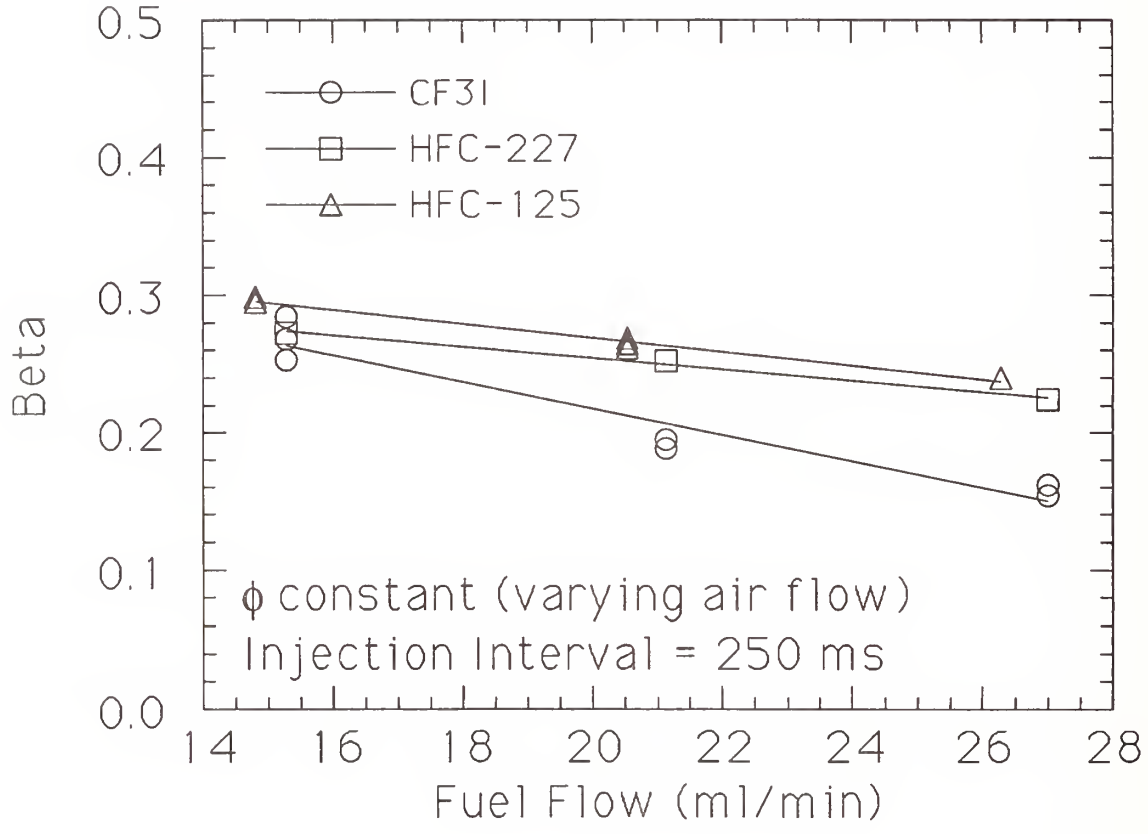

Figure 27. The critical agent mass fraction at extinction as a function of fuel flow under conditions of a constant global equivalence ratio (=0.11).

Table 4 defines the symbols, range of conditions, and reference conditions used in Equation (19), where β is defined as the mass fraction of agent at extinction as conditions vary and β_o is the mass fraction of agent at extinction at reference conditions.

The correction terms to Equation (19) as the operating conditions change are listed in Table 5. Table 6 gives the values of agent molecular weight, β_o, and the values of the polynomial coefficients for use in the functions $f_4(T_{air})$ and $f_5(V)$, the correction terms for non-baseline conditions in Equation (19). To determine f_6, a series of algebraic calculations must be completed as outlined in note "bb" of Table 5. First, X must be determined. This requires input of X_∞ and τ, which can be calculated from the values of d, D, and V, and knowledge of M and β_o which are listed in Table 6.

9.3.3 Suppression of a Baffle Stabilized Pool Fire. A pool fire resulting from a puddle of jet fuel or hydraulic fluid can pose a serious fire threat under certain conditions in a nacelle. In an air flow, the stability of a pool fire can be greatly enhanced if an obstacle at the leading edge of the pool is present. In some nacelle configurations, obstacles in the form of structural ribs or other bluff bodies are present at locations where combustible liquids could form a puddle. Middlesworth (1952; 1954) reported that the agent extinguishing requirements greatly increased with the presence of transverse structural ribs situated in the lower part of FR-4 and XB-45 nacelles. This was attributed to difficulties in extinguishing pool fires between structural ribs.

The literature on the stability of baffle stabilized pool fires is limited, but many important findings have been reported. Hirst and Sutton (1961) reported the effects of reduced pressure (below 1 atm) and air flow on kerosene pool fires. The pool fire was located on an airfoil in a wind tunnel and the ambient pressure was independently controlled for different air flows. The airfoil provided a smooth transition to the leading edge of the pool (the fuel tray was recessed in the airfoil and was horizontal to the surface). The dimensions of the liquid pool burner were 0.13 x 0.13 and 0.022 m deep. At low air flows, the flame was held near the leading edge of the pool and was blown across the pool surface. At higher air flows (depending on the ambient pressure) the flame was blown off and the fire was extinguished. As the ambient pressure decreased, the air velocity required for blow-off (V_{bo}) decreased. Obstructions in the form of vertical metal plates extending the width of the fuel tray were placed directly in front of the tray. Plate heights varied from 3.2 mm to 51 mm. It was shown that these obstructions had a dramatic impact on V_{bo}. An intermediate obstruction height (16 m) yielded the highest critical air velocity. Thus, the stabilizing effect of a baffle in front of a pool fire can be very significant.

Hirst *et al.*, (1976) examined kerosene pool fire suppression with methyl bromide (CH_3Br) in a wind tunnel facility similar to the one used by Hirst and Sutton (1961). Minimum agent concentrations required to extinguish pool fires stabilized behind baffles ranging from 10 mm to 64 mm were measured. The baffle height producing the most stable flame (requiring the highest methyl bromide concentration to extinguish) was determined to be 25 mm. The effect of air velocity on the minimum agent concentration required for extinction was examined for the 25 mm baffle. At the lowest air velocity examined, 4.5 m/s, the methyl bromide concentration was the highest (~6 % by volume). The minimum extinction concentration decreased to 4.2 % as the air velocity increased to 15 m/s. Dyer *et al.*, (1977a) examined kerosene pool fire suppression in the same apparatus at lower air velocities, testing methyl bromide, halon 1301, halon 1211 and nitrogen as agents. The minimum extinction concentration for methyl bromide increased to a maximum of 7.5 % (by volume) at an air velocity of 1 m/s. The results for halon 1211 and halon 1301 showed similar trends with the same minimum extinction concentration as methyl bromide, but the air velocity at the peak concentration was from 2.5 m/s to 3.0 m/s. The time to extinguish the baffle stabilized pool fires at low air velocities as a function of concentration was reported for methyl bromide and nitrogen. Figures 28

Table 4. Guidelines for suppression of spray flames

Parameter	Symbol	Parameter Range	Reference Value
system pressure	P	101 - 135 kPa	101 kPa
fuel flow	Q_{fuel}	16 - 28 ml/min	21 ml/min
agent temperature	T_{agent}	20 - 150 °C	20 °C
air temperature	T_{air}	20 - 350 °C	20 °C
free stream air velocity	V	3 - 33 m/s	7.5 m/s
injection interval	Δt	50 - 750 ms	700 ms

Table 5. Correction terms to Equation (19)

Correction term	Value of correction term
$f_1(P)$	1 [aa]
$f_2(Q_{fuel})$	1
$f_3(T_{agent})$	1
$f_4(T_{air})$	$a+ b\cdot T + c\cdot T_2$
$f_5(V)$	$e + f\cdot V + g\cdot V^2$
$f_6(\Delta t)$	$X\cdot M/[X\cdot M+(1-X)\cdot M_{air}]/\beta_o$ [bb]

aa some small pressure dependence is anticipated for high air velocities, see text.

bb where $X = X_\infty/[1-e^{(-\Delta t/\tau)}]$

$\tau = 1.44\cdot(d/V)\cdot(9.86-7.75\log[d/D]^2)$

$X_\infty = (\beta_o/M)/[(\beta_o/M)+(1-\beta_o)/M_{air}]$

M = the Molecular weight of the agent; see Table 6.

M_{air} = Molecular weight of air (=28.96 g/mole).

Table 6. Values of β_o and polynomial coefficients for $f_4(T_{air})$ and $f_5(V)$ of Equation (19)

Agent	M (g/mole)	β_o	a	b (1/°C)	c $(1/°C)^2$	e	f $(m/s)^{-1}$	g $(m/s)^{-2}$
CF_3I	196	0.16	1.1	$3.5\cdot10^{-3}$	0	1.4	$-4.0\cdot10^{-2}$	0
HFC-125	120	0.24	1.1	$8.2\cdot10^{-4}$	0	1.3	$-1.7\cdot10^{-2}$	$-5.7\cdot10^{-4}$
HFC-227	170	0.23	1.1	$9.0\cdot10^{-5}$	$3.8\cdot10^{-6}$	1.3	$-2.0\cdot10^{-2}$	$-5.3\cdot10^{-4}$

and 29 show the reported data, fit to Equation (14). The transport time was subtracted before the data were fit. A best two parameter fit to the data yielded τ= 6 s and X_∞=6 % for methyl bromide and τ= 5 s and X_∞=38 % for nitrogen. These values are significantly greater than the spray burner results reported in the previous section.

Since the baffle stabilized pool fire appears to be dramatically more stable than the spray fire, a short series of combustion and non-combustion experiments were conducted in this configuration. For expediency, the apparatus at Walter Kidde Aerospace (WKA) of Wilson, North Carolina was utilized. Tests similar to those reported by Hirst *et al.*, (1976) and Dyer *et al.*, (1977a) were performed at WKA under direction from NIST as part of this project. WKA delivered the test data to NIST for further analysis. These results should be considered preliminary, because the number of experiments and parameters tested were limited due to time restrictions and resource availability.

The main objective of the measurements was to confirm the experimental results of Dyer *et al.*, (1977a), which indicated that the mixing time was very large in baffle stabilized pool fires, that the minimum agent concentration required to achieve flame extinction was significantly larger than the concentration require to suppress cup burner flames under certain conditions, and that the maximum agent concentration approximately corresponds to the peak flammability limit of the agent.

9.3.3.1 Experimental Method and Apparatus. The experimental apparatus was based on the design described by Hirst *et al.*, (1977a). Figure 30 is a side view of the apparatus which consisted of a wind tunnel with a square cross-section (0.30 m x 0.30 m x 3.6 m long) suitable for combustion experiments and a 0.10 m x 0.20 m rectangular liquid pool burner. A cross-sectional view is shown in Figure 31. The burner had a cooling system and fuel level control. The liquid level was maintained 13 mm below the burner rim by replenishing the burned fuel with a gravity feed device (Bajpai, 1974). This prevented fuel spillage at high air flows. An airfoil and an adjustable height baffle were located upstream of the pool fire. Air was supplied by a rotary-vane blower which could produce steady air velocities in the range from 1 m/s to 10 m/s (± 2 %) in the test section. The air velocity was monitored by a vane anemometer. A viewing window provided optical access to the fire location. Each test was videotaped, showing the fire, an event lamp which indicated the agent injection pulse timing, and the vane anemometer readout. Timing sequences were obtained by frame-by-frame analysis of each video record. JP-8 was the fuel tested.

Liquid agent was expelled from a storage container placed on a load cell with a 0.01 kg resolution. The recorded mass loss of agent divided by the injection duration yielded the mean mass flow. To ensure that the mass flow was nearly constant over the injection duration for some of the longer (up to 20 s) injections, the storage bottle was super-pressurized with nitrogen to a final pressure of 2.75 MPa, with make-up nitrogen continuously added from a pressure regulated source during agent injection. The storage bottle was not disturbed during the process, so insignificant amounts of nitrogen would dissolve in the liquid phase. Short and long injection durations yielded the same measured mean mass flows with this configuration for the same needle valve setting.

Agent was introduced through a nozzle in the center of a large plenum connected to a fixed 0.10 m x 0.10 m cross-section of the wind tunnel. After leaving the nozzle, the agent spray hit a deflecting disk which dispersed it radially. A coarse screen was located downstream to improve the agent dispersion by grid induced turbulent mixing. A solenoid valve controlled the agent flow time, while a needle valve just before the nozzle provided a flow rate adjustment.

A series of non-combusting experiments were performed to validate the uniformity of the agent concentration in the tunnel for typical discharges at three separate initial air flows (1 m/s, 2 m/s, and 5 m/s mean velocities in the duct) and four baffle heights (0 mm, 13 mm, 25 mm, and 50 mm). A Statham analyzer was used to measure the HFC-125 concentration as a function of time at various

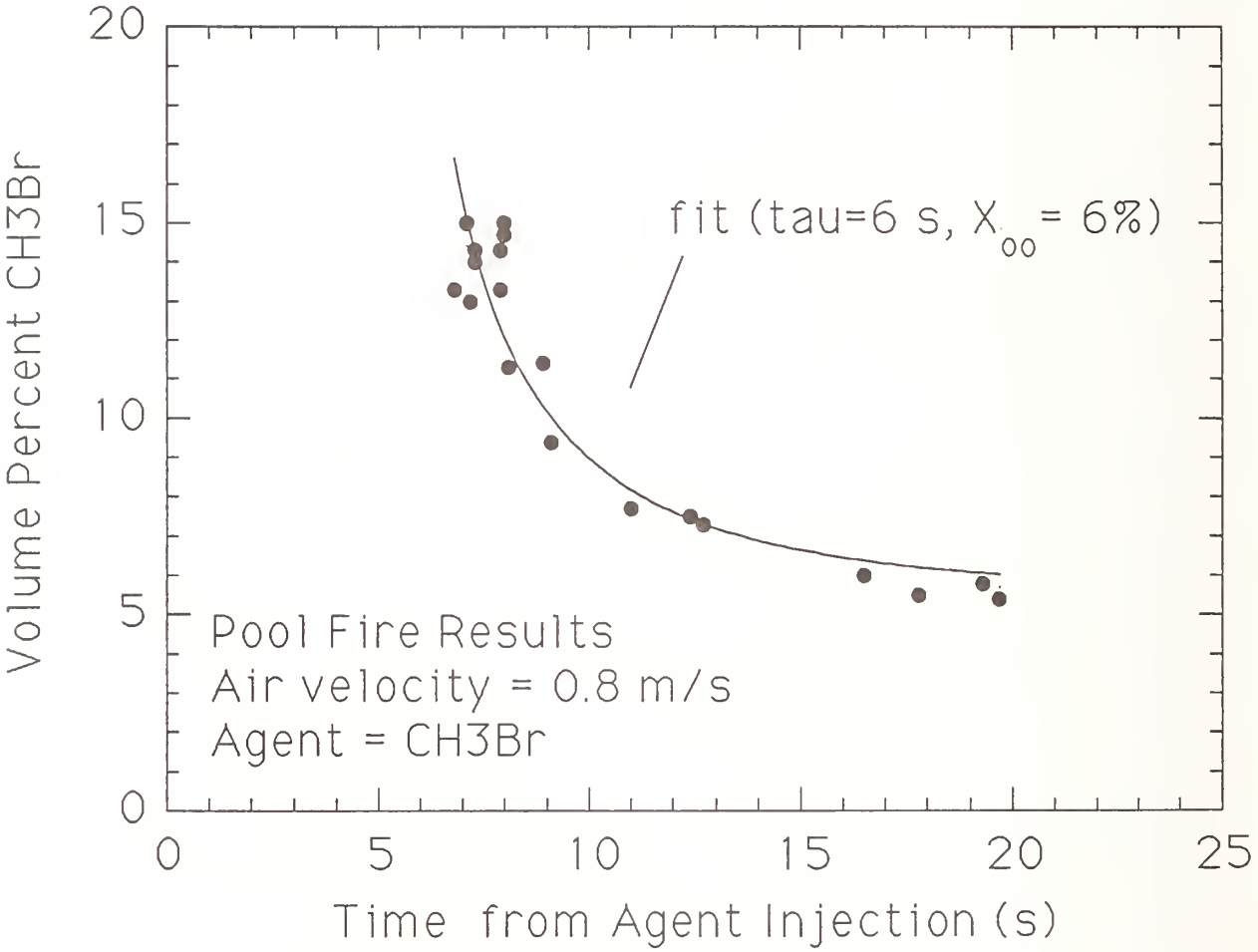

Figure 28. The volume percent of CH_3Br in the oxidizer at extinction as a function of time from agent injection for kerosene pool fires. Data taken from Dyer et al. (1977a).

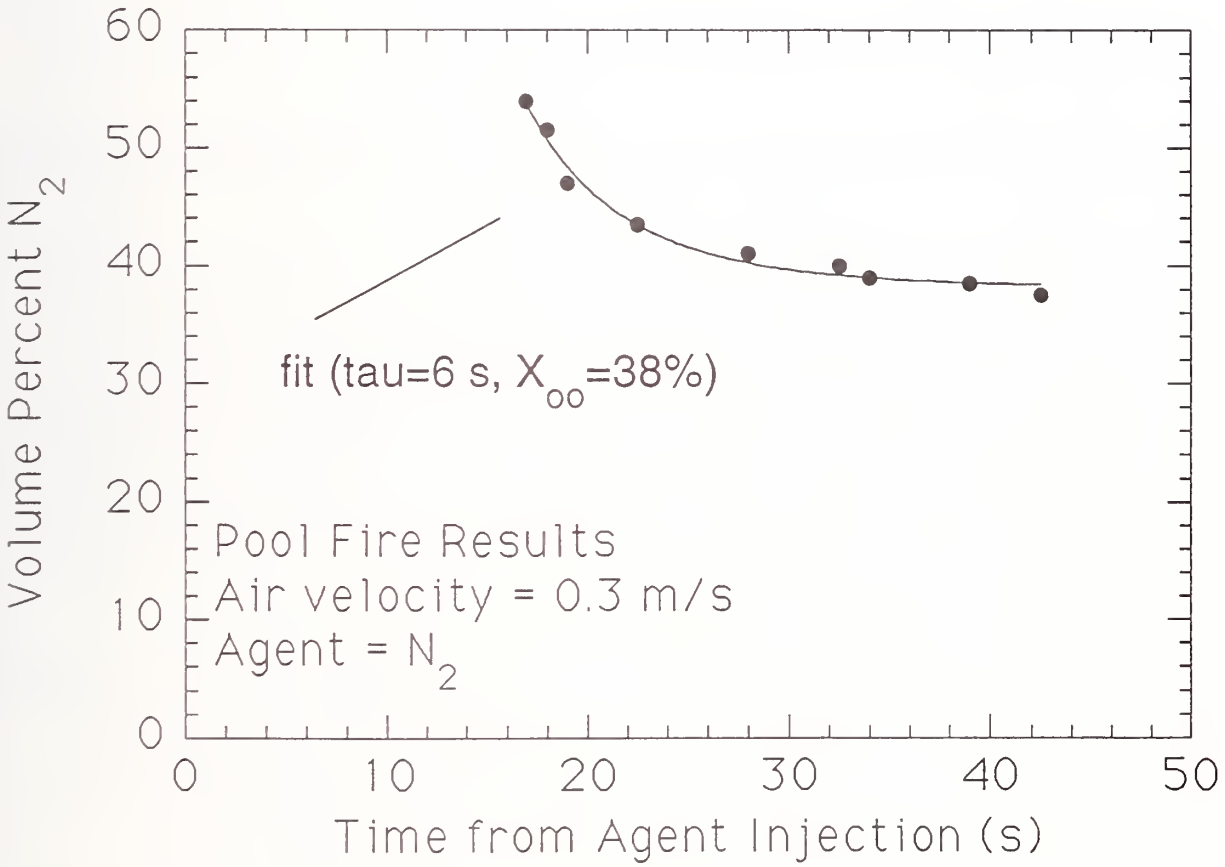

Figure 29. The volume percent of N_2 in the oxidizer at extinction as a function of time from agent injection for kerosene pool fires. Data taken from Dyer et al. (1977a)

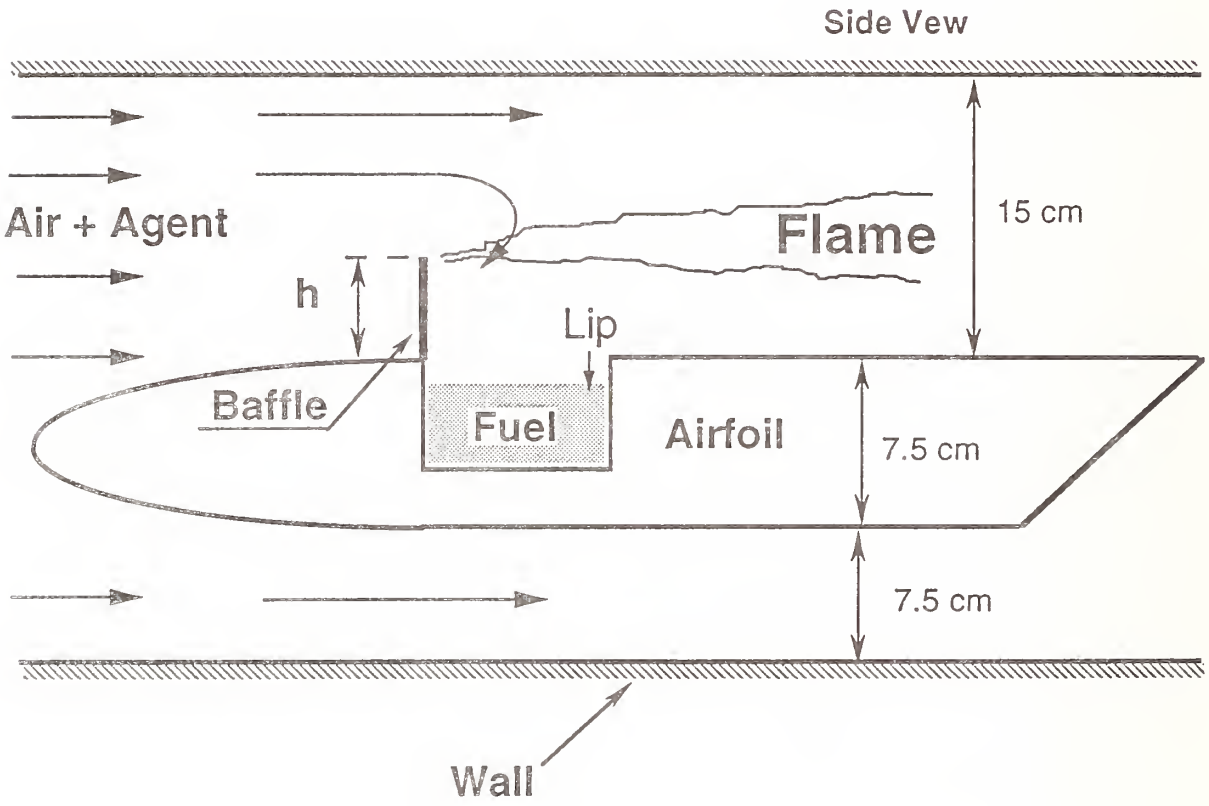

Figure 30. Side view of the wind tunnel/pool fire apparatus.

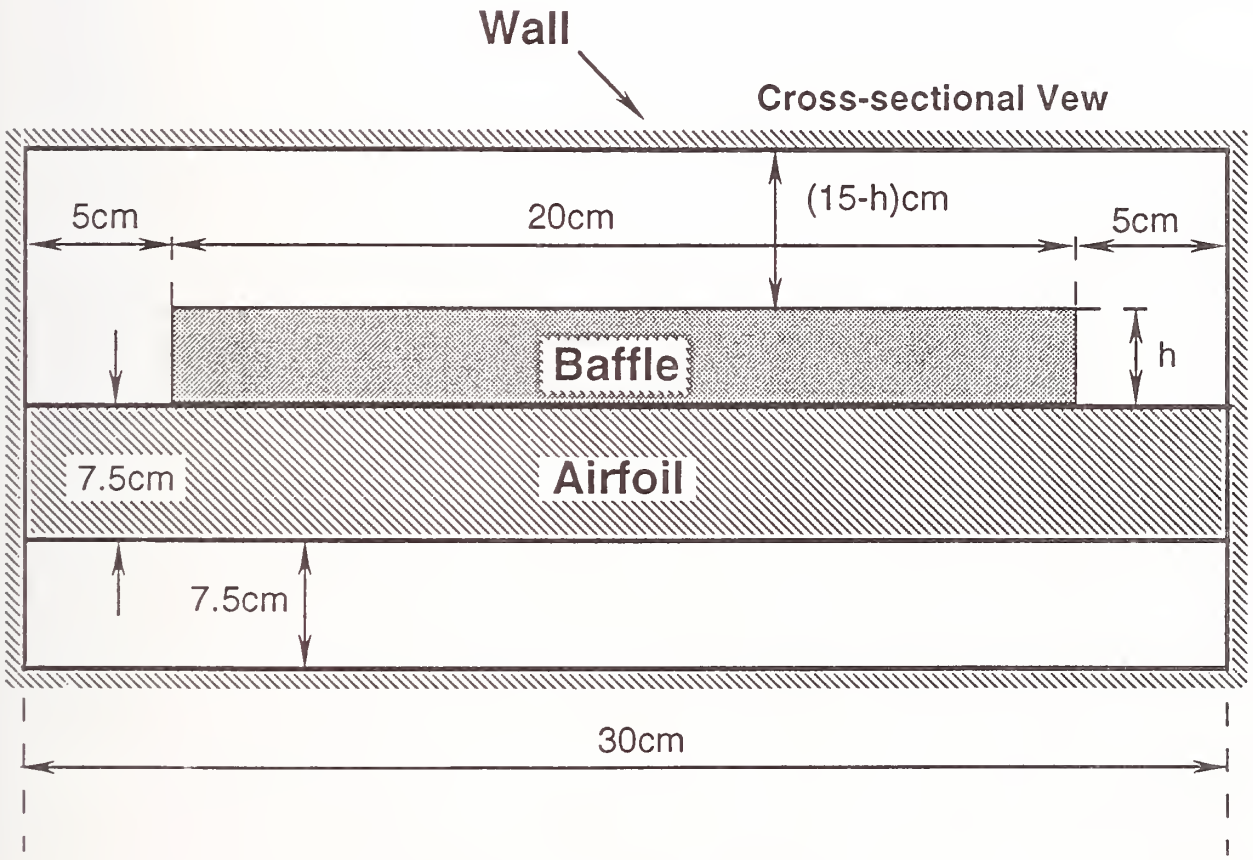

Figure 31. Cross-sectional view of the wind tunnel/pool fire apparatus.

locations upstream from the test section, and at various locations behind the baffle. That instrument was calibrated for HFC-125 and had a relatively fast response time (< 50 ms).

Pool fire extinction tests were conducted in the following manner. The agent mass flow was preset by adjustment of the needle valve, then checked with an automatic valve opening and closing sequence yielding a 1.0 s flow duration pulse. The blower fan was set to give the desired air velocity. Video recording was started, then the pool fire was lit. The agent was injected when the temperature on the top outer wall of the burner pan reached 150 °C. The preheat time changed depending on the baffle height, varying from 300 s to 600 s. A manual button controlled the opening and closing of the agent solenoid valve. The valve remained open until the pool fire was extinguished and was then immediately closed to conserve agent. The mass of agent dispensed and the duration of the valve opening sequence were recorded. If the pool fire was not extinguished after 15 s of agent flow, then the test was terminated and the fire extinguished with a back-up CO_2 extinguishing system. The video record provided an accurate means of determining the extinction time.

9.3.3.2 Experimental Results. The non-combusting experiments confirmed the transport delay time of the agent as it traveled from the injection location to the pool fire location. The concentration profile was confirmed to be sufficiently uniform in time and space for the purposes of these tests. The spatial variation was ± 10 % for the air flows examined in the combusting experiments. It took approximately 0.5 s for the agent to obtain its final concentration from the moment of agent detection by the analyzer.

The pool fire tests were limited in terms of air flows, although five different baffle heights were examined. Tests at an initial air velocity of 2 m/s were conducted with HFC-125, while tests at an initial air velocity of 1 m/s were conducted primarily with HFC-227. An attempt was made to blow-off a pool fire stabilized behind the 6 mm baffle by increasing the air flow. At air velocities of 11 m/s (the limit of the blower) the flame was not blown-off. Tests were conducted well below this value.

Initial calculations of the agent volumetric concentrations (agent volumetric flow/ total volumetric flow) suggested a critical extinction concentration higher than expected for HFC-125. One complicating factor was identified during the analysis of the data. During the agent injections the vane anemometer reading changed from its steady setting. The relative change in the anemometer reading depended on the agent injection rate. It was not surprising that the anemometer reading changed during the agent injection because the anemometer was calibrated for air flows at ambient pressure and temperature. But additionally, the structure of the flame was observed to change almost immediately after agent injection. The flames tended to elongate and appeared more turbulent which is consistent with a higher flow velocity. In light of these observations, along with the higher than expected estimated critical concentrations, an examination of the anemometer discrepancy was performed.

The equation that gives the relationship between the indicated vane anemometer velocity of a fluid at a density different from the calibrated fluid density is $V_1=V_o(\rho_0/\rho_1)^{0.5}$ (Perry *et al.*, 1984), where V_1 and V_0 are the true and recorded velocities, and ρ_1 and ρ_0 are the fluid density of the flow being measured and the density of air at ambient conditions, respectively. The mixture density of the agent and air flow was estimated by assuming both adiabatic and isothermal mixing at 5 °C. The corrected velocity was ≈15 % less using the adiabatic mixture density as compared to the isothermal mixture density. Gas phase temperature measurements at locations just before the airfoil indicated temperatures on the order of 0-15 °C (ambient air temperatures reached 30 °C during the testing). For the analysis, a mixture temperature of 5 °C was used.

Figure 32 shows the corrected anemometer velocity for a long discharge test. This corrected velocity is significantly different from the initial velocity of 2 m/s. This implies that the volumetric flow changed dramatically due to agent discharge. An explanation is that the air flow from the blower

is sensitive to the pressure in the duct, since the air flow is not choked. Due to the orientation of the agent nozzle, agent injection induces an ejector-type flow response that pulls more flow from the blower during the injection. The phenomenon was observed during nitrogen injections in the NIST mock nacelle (see Section 9.4).

The digital output from the anemometer was updated at a rate of 0.5 Hz. In addition, it is evident that the instrument electronically averages over the update cycle. Some agent injection events were over before the maximum velocity change was recorded. Therefore, even if the change in air flow due to agent injection was assumed to occur instantaneously, the corrected flow must be estimated for some tests.

The corrected air velocity measurements are listed in Tables 7 and 8, along with the initial air velocity, the mean agent mass flow, the agent concentration and the extinction time or total agent flow time for non-extinguished (N.E.) fires, for the HFC-125 and HFC-227 experiments, respectively. The reported extinction time represents the interval between when agent first reached the baffle, which was evident in the video record as an approaching vapor cloud and the rapid disappearance of flames. Agent transport times were comparable to the transport times inferred from the concentration measurements.

9.3.3.3 Discussion of Experimental Results. Figures 33 and 34 show the agent concentrations as a function of the time required to obtain flame extinction for HFC-125 at an initial air velocity of 2 m/s and for HFC-227 at an initial air velocity of 1 m/s, respectively. The data were consistent with the form of Equation (14), the simple extinction mixing model described for the spray burner. The data were analyzed assuming that the agent concentration pulse was like a step change and that the velocity was constant during the suppression event. Although the results for the different baffle heights showed some variation, the trends did not appear to be significant for the rapid extinction results, and could not be fully characterized from the limited data. Therefore, the solid lines represent a fit to all of the extinction data using the functional form of Equation (14). The values of $X_{\infty}(\Delta t>>\tau)$ (see Equation (14)) for extinction by HFC-125 and HFC-227 were measured as approximately 12 % and 11 % (by volume) respectively. These values were greater than the extinction concentrations measured in the cup burner, as expected from the results of Dyer *et al.*, (1977a) for suppression of baffle stabilized pool fires with low air flows. The characteristic mixing times from the data fits were 0.5 s for HFC-125 (with the air velocity approximately equal to 3 m/s) and 0.7 s HFC-227 (with the air velocity approximately equal to 1.5 m/s). Since the characteristic mixing time is independent of agent type, the results display the expected trends. As the velocity increased, the mixing time decreased, but not inversely proportional to the velocity as predicted by Equations (16) and (17). Nor are the values of the mixing times consistent with the results of Dyer *et al.*, (1977a).

The characteristic mixing time inferred from the data of Dyer *et al.*, (1977a) for methyl bromide were much longer than the values reported here. The results for methyl bromide injections were for air velocities of 0.76 m/s. The results of Dyer *et al.*, (1977a) may be partly due to velocity effects (see Equations (16) and (17)), or to a slow increase in the agent concentration, instead of the assumed step function. In any case, the results show that under similar air flow and baffle height conditions, a baffle stabilized pool fire is **much more difficult** to extinguish than a baffle stabilized spray flame (where the baffle is in the middle of the flow field).

9.3.4 Suppression of Re-ignition. After suppression of a nacelle fire, hot fuel vapor may exist at levels which are flammable, leading to the possibility of re-ignition. A puddle of hydraulic fluid or jet fuel from a leaking fuel line will vaporize as heat is transferred from a nearby hot metal surface. Under normal engine operating conditions, hot metal surfaces which could cause ignition exist along the interior wall of the nacelle which separates the jet engine combustor from the nacelle. In addition,

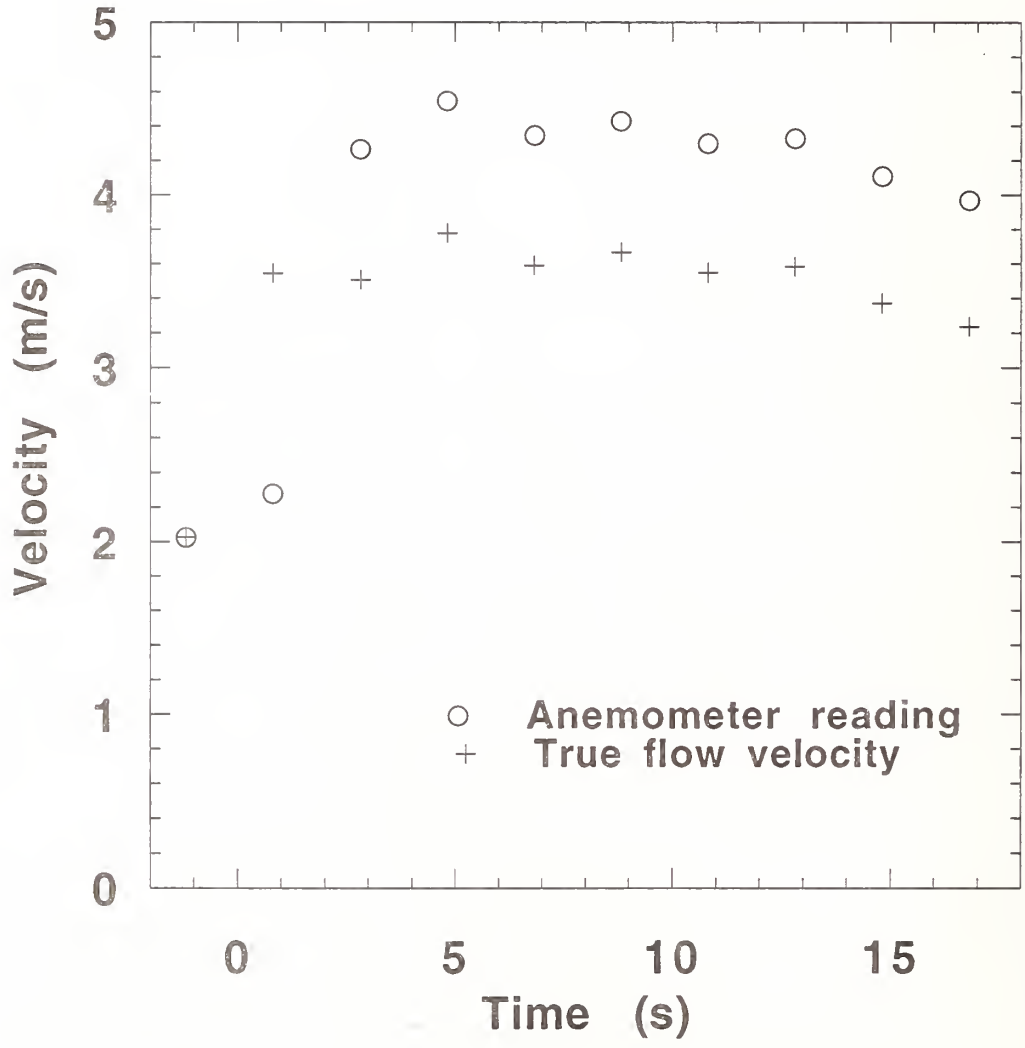

Figure 32. The corrected anemometer velocity as a function of time during agent discharge.

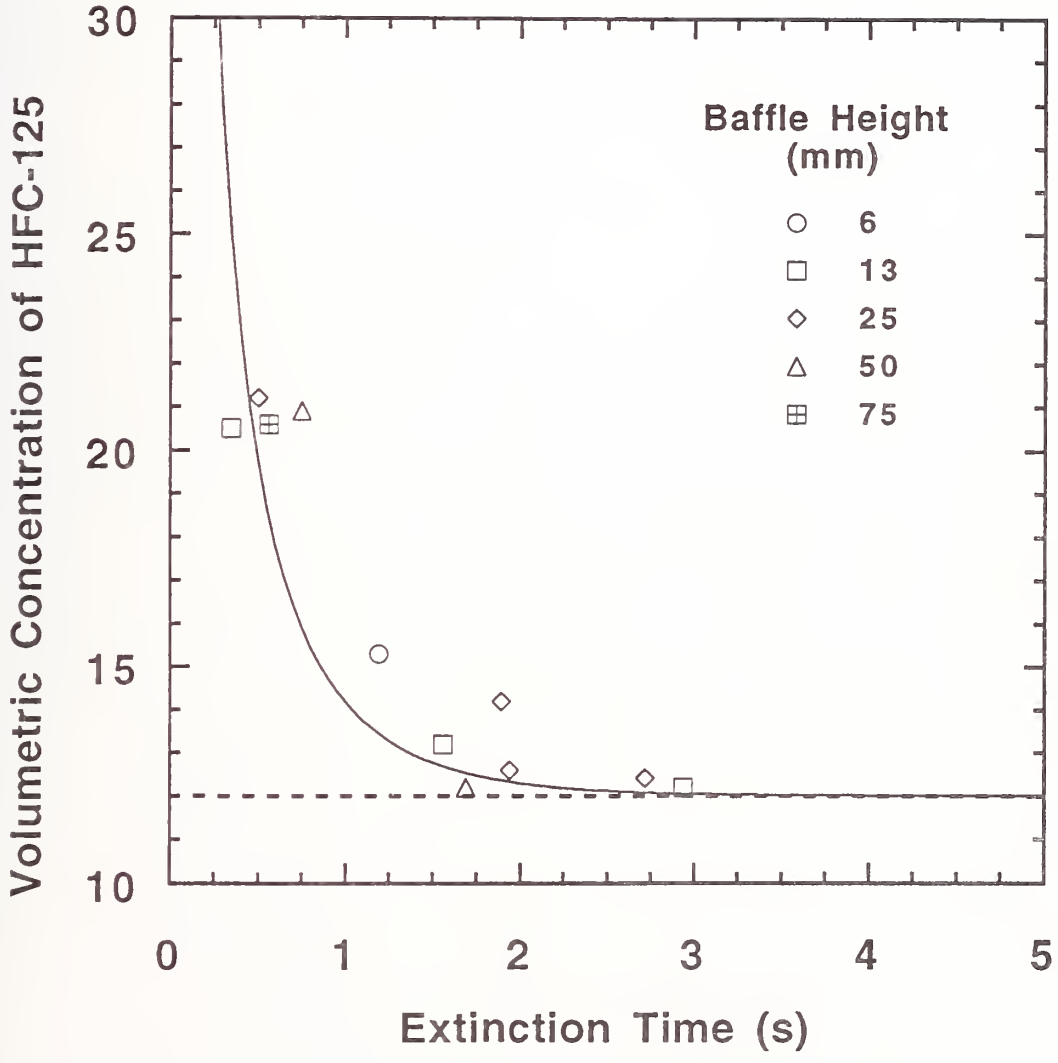

Figure 33. The critical volume percent of HFC-125 in the oxidizer as a function of time to extinguish the flame.

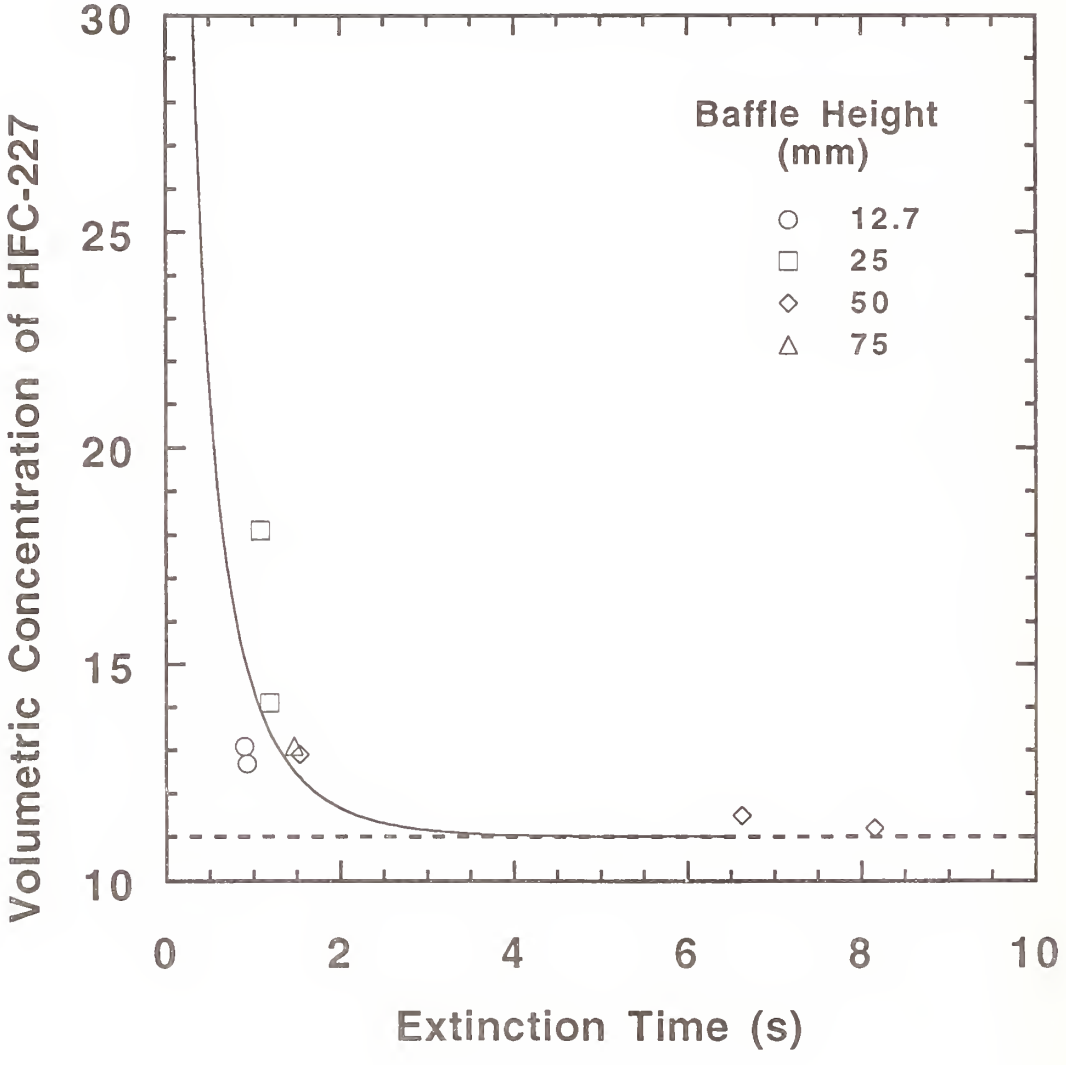

Figure 34. The critical volume percent of HFC-227 in the oxidizer as a function of time to extinguish the flame.

Table 7. Experimental data on the suppression of pool fires using HFC-125

Baffle height (mm)	Initial air velocity (m/s)	velocity during agent flow (m/s)	Mean agent mass flow (kg/s)	Agent Concentration (Vol. %)	Extinction time (s)
6.3	1.90	3.38	0.255	15.3	1.19
13	2.04	3.31	0.175	10.7	24, N.E.
13	1.98	3.45	0.203	11.9	14, N.E
13	2.03	3.94	0.237	12.2	2.94
13	2.01	3.69	0.241	13.2	1.56
13	1.98	4.23	0.430	20.5	0.34
25	1.96	2.56	0.095	7.5	19, N.E.
25	1.96	2.91	0.143	10.0	19, N.E.
25	2.03	3.59	0.192	10.8	15.5
25	1.92	3.85	0.236	12.4	2.72
25	1.98	3.67	0.228	12.6	1.94
25	1.96	3.44	0.242	14.2	1.89
25	1.95	4.27	0.448	21.2	0.50
50	1.98	3.24	0.142	8.9	17, N.E.
50	1.98	3.64	0.214	11.9	9, N.E.
50	1.85	3.93	0.246	12.2	1.69
50	1.99	4.26	0.441	20.9	0.75
75	2.03	3.67	0.231	12.7	9.97
75	1.96	4.24	0.432	20.6	0.56
25	1.06	2.07	0.105	10.3	15, N.E.
25	1.01	1.90	0.105	11.2	19, N.E.
25	1.06	3.09	0.194	12.7	3.25
25	1.01	2.94	0.202	13.9	1.56

Table 8. Experimental data on the suppression of pool fires using HFC-227

Baffle height (mm)	Initial air velocity (m/s)	velocity during agent flow (m/s)	Mean agent mass flow (kg/s)	Agent Concentration (Vol. %)	Extinction time (s)
13	1.05	1.93	0.145	10.9	11, N.E.
13	1.01	2.47	0.222	13.1	0.90
25	1.05	2.39	0.165	10.1	6.25
25	1.03	2.50	0.243	14.1	1.19
25	0.95	2.09	0.261	18.1	1.09
50	1.00	2.08	0.129	9.0	15, N.E.
50	1.00	2.22	0.172	11.2	8.15
75	0.94	1.69	0.10	8.6	10, N.E.
75	0.94	1.14	0.08	10.4	19, N.E.

hot metal surfaces may occur due to heating by the fire itself. Re-ignition may then arise from contact of the reactive fuel/air mixture with the hot metal surface. Conditions which lead to re-ignition are controlled by the time temperature history of the reactive mixture and to a lesser extent, by the type of metal surface and the chemical composition of the fuel. Recent experiments in the Wright Patterson Aircraft Engine Simulator show that when a hot (700 °C) metal surface was present, flame extinction required almost an order of magnitude more agent than if the hot surface were not present, presumably due to re-ignition (Bennett and Caggianelli, 1995).

Re-ignition is kinetically and phenomenologically distinct from flame extinction and should be independently considered. Historically, the re-ignition problem was a concern long before the search for halon 1301 alternatives. In this sense, the re-ignition problem can be considered as independent from the flame suppression problem, perhaps requiring a separate solution.

A standard test method for determination of auto-ignition temperatures of liquid chemicals is ASTM-E 659-78 (1978), which utilizes a heated 0.5 L borosilicate glass round-bottom, short-necked test flask. The auto-ignition temperature of a fluid is defined as the temperature at which its vapors will ignite in air at atmospheric pressure without an external ignition source. In the auto-ignition test, the ignition delay time varies for each experiment. The fuel/air ratio can also play a role. Because of the long ignition delay times, decomposition of the original fuel molecule into a variety of intermediates may occur. The ASTM-E 659-78 test vessel is not appropriate for use with halogenated compounds, because the decomposition products are known to react with borosilicate glass.

For aircraft applications, the minimum hot surface ignition temperature of a reactive mixture flowing over a hot metal surface may be a more appropriate test. This is because actual nacelle conditions are very different than in the ASTM-E 659-78 test. Surface material, system pressure, air temperature, surface size, air flow, and even the geometry and location of a baffle can all be factors (Johnson *et al.*, 1988; Laurendeau, 1982).

A large number of studies have investigated the ignition of fuel vapor on hot metal surfaces (Smyth and Bryner, 1990; Clodfelter, 1990; Johnson *et al.*, 1988; Kuchta, 1975; Altman *et al.*, 1983; Klueg and Demaree, 1969; Sommers, 1970; Strasser *et al.*, 1971; Cutler, 1974; Detz, 1976; Goodall

and Engle, 1966; Kumagai and Kimura, 1956; Snee and Griffiths, 1989). The purpose of many of these studies was to determine the lowest temperature at which ignition occurs. Residence time was found to be a key factor in the measured ignition temperature. Such measurements also serve as a basis for comparison of the hazard of different fuels. For example, the surface temperature at ignition of alkanes generally decreases with chain length (Smyth and Bryner, 1990). Some testing has focussed on jet fuels and hydraulic fluids used specifically in aircraft applications (Kuchta, 1975; Johnson *et al.*, 1988; Clodfelter, 1990).

Minimum hot metal surface ignition temperatures for JP-8 (or kerosene) for ambient temperatures and pressures and low air flows have been found to vary from 360 °C to 650 °C, depending on test conditions (Parts, 1980; Beardsley, 1967). The minimum hot metal surface ignition temperature was found to increase with increasing ventilation velocity, and decrease with increased ventilation temperatures (Johnson *et al.*, 1988; Strasser *et al.*, 1971). The hot metal surface results can be compared to the measured JP-8 and kerosene auto-ignition temperatures of 224 ° and 229 °C, with associated time delays of 174 and 210 s, respectively (Johnson *et al.*, 1988, Zabetakis *et al.*, 1954).

Few experiments, however, have been conducted to study the effectiveness of halogenated agents in suppressing ignition. Finnerty (1975) studied the effect of halon 1301 on the auto-ignition of propane in a static sub-atmospheric system. Lemon *et al.*, (1980) tested halogenated solid/liquid/binder mixtures which adhere to hot metal surfaces in an attempt to prevent re-ignition. Mulholland *et al.*, (1992) conducted inhibition experiments using chlorinated compounds in well stirred reactors and compared these results to detailed kinetic models. Both ignition and extinction conditions were modeled. Others have modeled ignition using detailed kinetics. Griffiths *et al.*, (1990) compared calculated and measured auto-ignition temperatures for alkanes in a closed vessel. Kumar (1989) and Vlachos *et al.* (1994) modeled stagnation point flow, coupled with detailed kinetics to predict the minimum surface temperature at ignition for H_2/O_2/dilutent and CH_4/air mixtures respectively, in the vicinity of a hot surface. Sano and Yamashita (1994) developed a 2-D laminar flow model to investigate the ignition of methane-air mixtures flowing over a hot surface. Their results show that ignition over a hot plate is controlled by the diffusion of heat and mass as well as chemical reactions. They found that the equivalence ratio and the free stream velocity of reactants had little effect on the ignition delay. The ignition delay time decreased exponentially with increases in the area of the hot surface. Sano and Yamashita's investigation was limited to C1 chemistry due to the computationally intensive nature of their model. Others have considered the detailed kinetics associated with inhibition by halogenated compounds on the ignition of fuel/air mixtures in well stirred and plug flow reactors (Barat *et al.*, 1990; Mulholland *et al.*, 1992; Babushok *et al.*, 1995b; 1995c).

The objective of the studies described here was to test the relative effectiveness of halogenated agents in suppressing the ignition of flammable reactants flowing over a hot metal surface under well-controlled conditions.

9.3.4.1 Experimental Method and Apparatus. Two experimental devices were used. Experiments were first conducted to determine the amount of agent needed to suppress the ignition of a JP-8 fuel spray. There were difficulties, however, in obtaining repeatable results. Thus, a gaseous flow of propane replaced the liquid spray. Use of a gaseous fuel represents a most dangerous case, *i.e.*, when a liquid fuel has completely vaporized.

A schematic diagram of the first apparatus is shown in Figure 35. Propane (99 % purity) flowed through a 3 mm (outer diameter) tube in a stagnation point flow towards a heated metal disk located approximately 5 mm away. The disk was 14 mm in diameter, made of a wound ribbon composed primarily of nickel. The metal surface was heated by a regulated power supply which provided up to 200 W. An optical pyrometer was used to measure the surface temperature of the heated disk. With

power applied to the metal disk, a fairly uniform temperature (± 30 °C) was measured in an annular section of the disk, from approximately 2 mm to 6 mm from the disk center. With use, the metal surface oxidized, and the temperature became less uniform requiring replacement of the metal disk. A coflowing mixture of air and gaseous agent flowed through a 86 mm (inner diameter) pyrex tube about the fuel flow. With the fuel and oxidizer flowing, flame ignition occurred in a repeatable fashion by increasing the power through the metal disk. Various amounts of agent were added to the air flow and the temperature of the heated metal disk was measured at flame ignition using an optical pyrometer. The effectiveness of N_2, HFC-125, HFC-227 and CF_3I were compared in suppressing ignition.

The second test apparatus was based on a device described previously (Smyth and Bryner, 1990). The main difference between this experiment and the first was that the fuel and air were premixed in this apparatus, but were not in the first apparatus. A reactant mixture containing agent, fuel, and air flowed over a heated foil. The temperature of the foil was slowly increased until ignition was observed. Figure 36 is a schematic diagram of this apparatus which included two dc power supplies, a foil holder, rolled thin (13 μm) foil strips, sub-miniature ungrounded type-K thermocouples with a 250 μm stainless steel sheath, fuel gas cylinders (methane, ethene, and propane with purities of 99.97 %, 99.5 %, and 99.0 % respectively), rotameters for fuel, air and agent flow control, the burner assembly and quartz chimney (1.1 cm diameter), and a data acquisition system. The thermocouple was used to measure the temperature of the foil which was held in a unique, spring loaded support (Smyth and Bryner, 1990). Testing with different types of metal foils was attempted and a number of different fuels were tested including methane, ethene, and propane. The distance from the chimney exit to the hot metal surface was maintained at 6 mm for all tests. The flow of reactants was 912 ml/min (16 cm/s), except in one series of experiments using stoichiometric ethene/air mixtures, when the flow was varied to determine its effect on the measured ignition temperature. The angle of the flow impinging on the hot metal surface was maintained at 45°, except in one series of experiments using stoichiometric ethene/air mixtures, when the angle was varied to determine its effect on the measured ignition temperature. In the standard configuration, the reactant mixture flowed near the heated metal surface for approximately 90 ms (Smyth and Bryner, 1990). Reproducibility of the measurements (± 10 °C on average) was similar to that reported by Smyth and Bryner (1990).

9.3.4.2 Experimental Results and Discussion. For small propane fuel flows (<10 ml/min) in the first apparatus, the critical temperature of the hot metal disk at ignition was measured to occur at approximately 1025 °C (± 25), not unlike auto-ignition temperatures reported previously for stoichiometric propane-air mixtures over a heated nickel surface (Smyth and Bryner, 1990). The flame could then be extinguished by decreasing the applied power through the metal disk. Figure 37 shows that the critical ignition temperature increased with increasing fuel flow. This is interpreted as being related to the residence time of the reactive mixture on the hot metal surface. As the residence time decreased, key chemical reactions involving chain initiation and branching have less time to proceed and higher temperatures were necessary to initiate flame ignition. This is consistent with the Damköhler number criteria for flame ignition (Liñan, 1974). Measurements showed that increased or decreased (by 50 %) air flow had a negligible effect on the critical ignition temperature for the reactants flowing over the hot metal surface.

Figure 38 shows the critical ignition temperature of the heated metal disk as a function of agent concentration in the oxidizer stream for a propane flow of 8 ml/min. For small CF_3I concentrations, flame ignition required substantially higher surface temperatures than for the other agents. Thus, CF_3I was significantly more effective than HFC-125 and HFC-227, which were more effective than N_2, in suppressing ignition.

A second series of experiments were undertaken where agent effectiveness was measured under premixed conditions in the same device used by Smyth and Bryner (1990). A complete description of

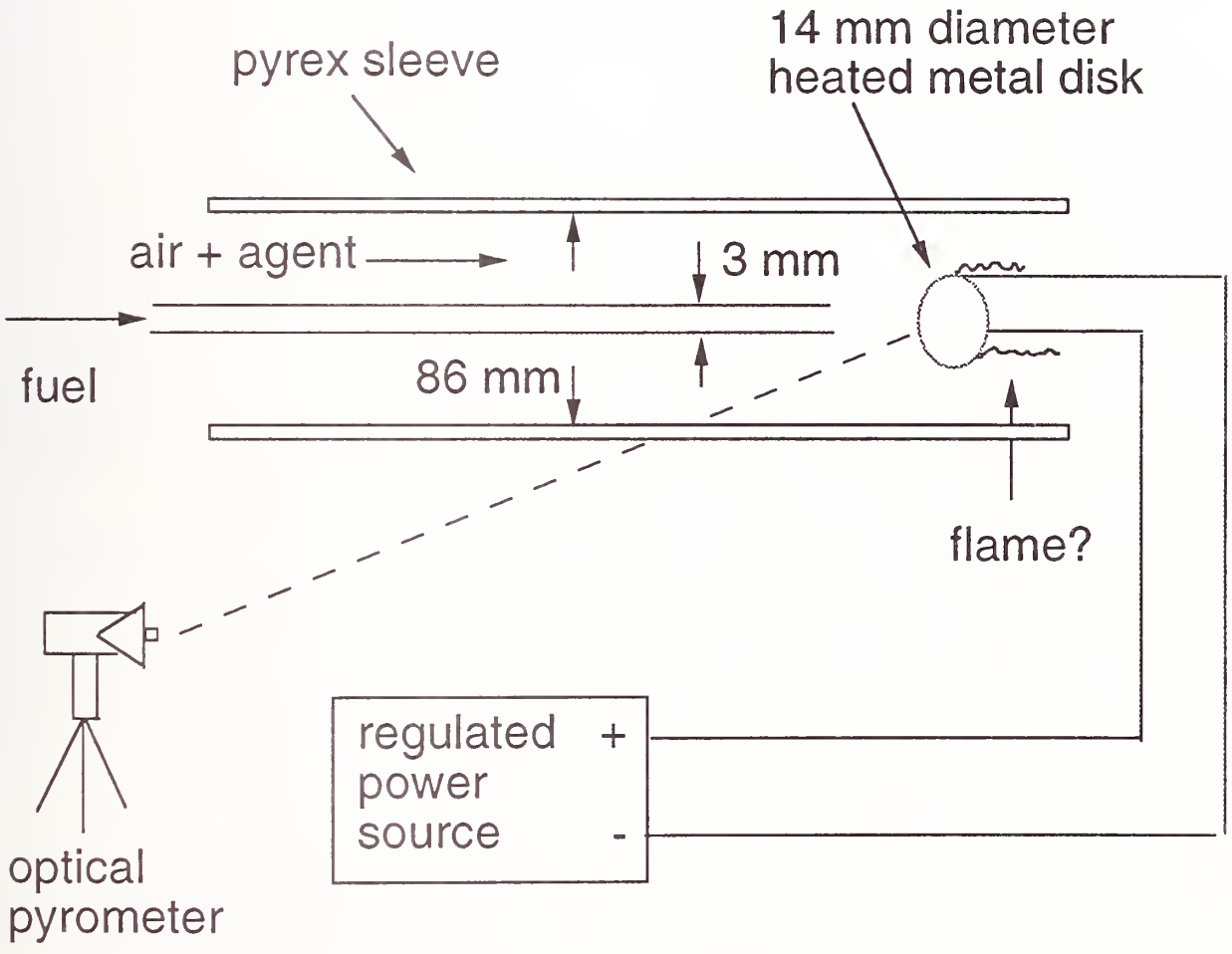

Figure 35. Schematic diagram of the first short residence time hot surface ignition apparatus.

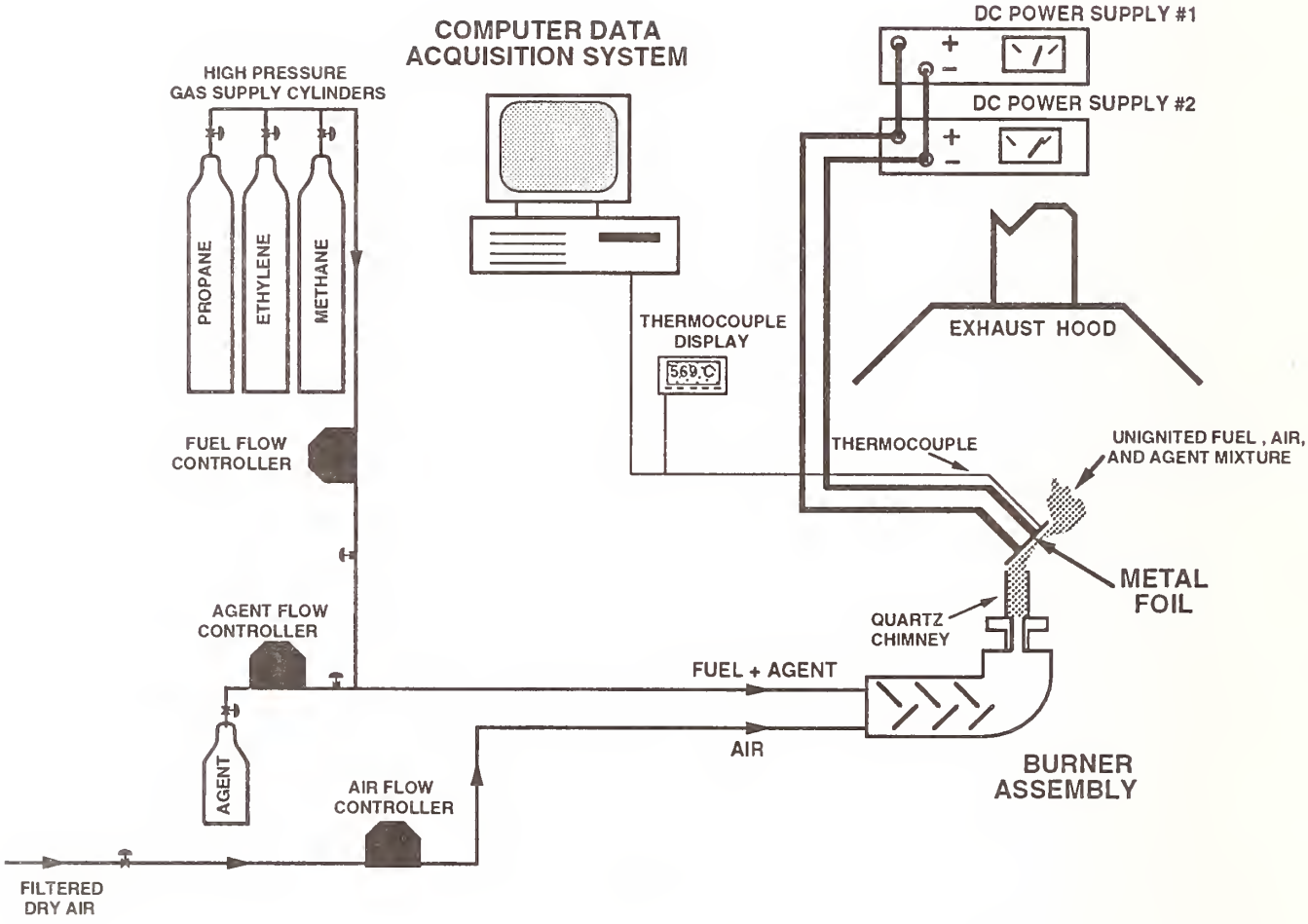

Figure 36. Schematic diagram of the second short residence time hot surface ignition apparatus.

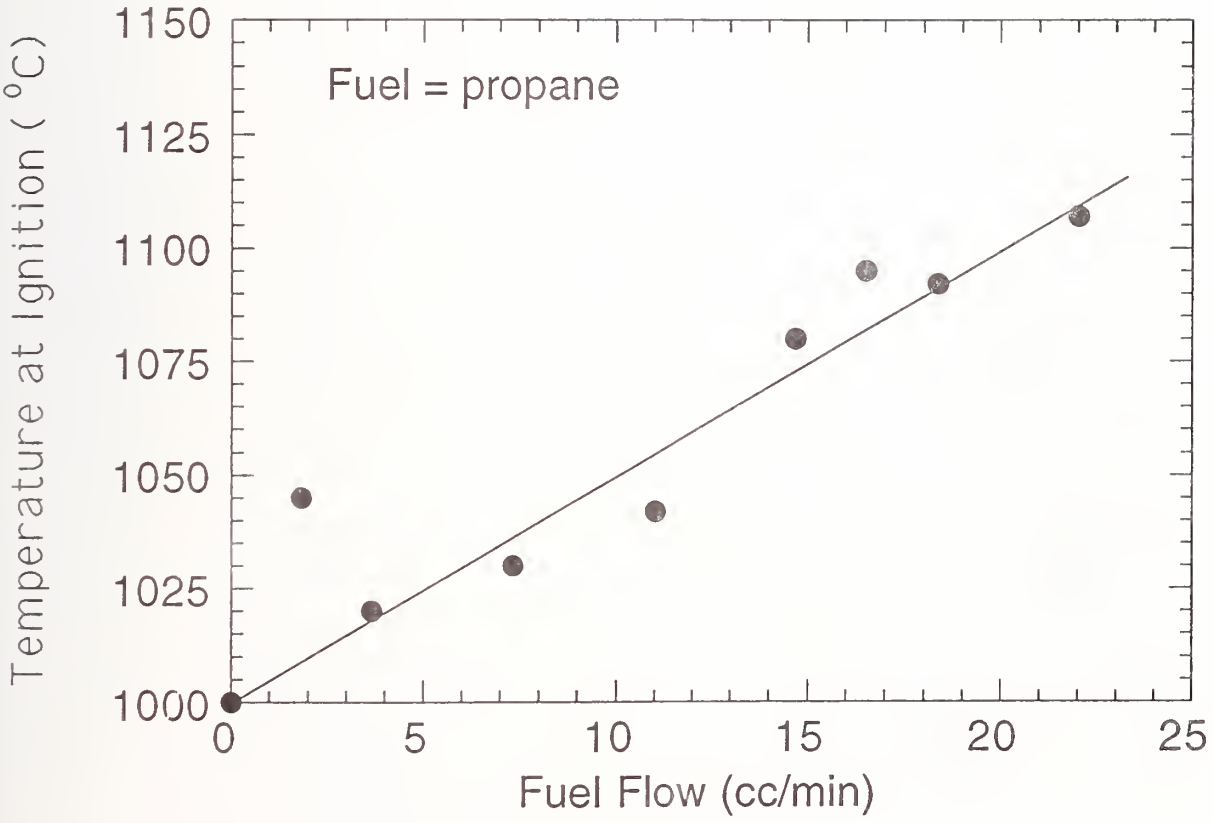

Figure 37. The critical ignition temperature as a function of increasing fuel flow.

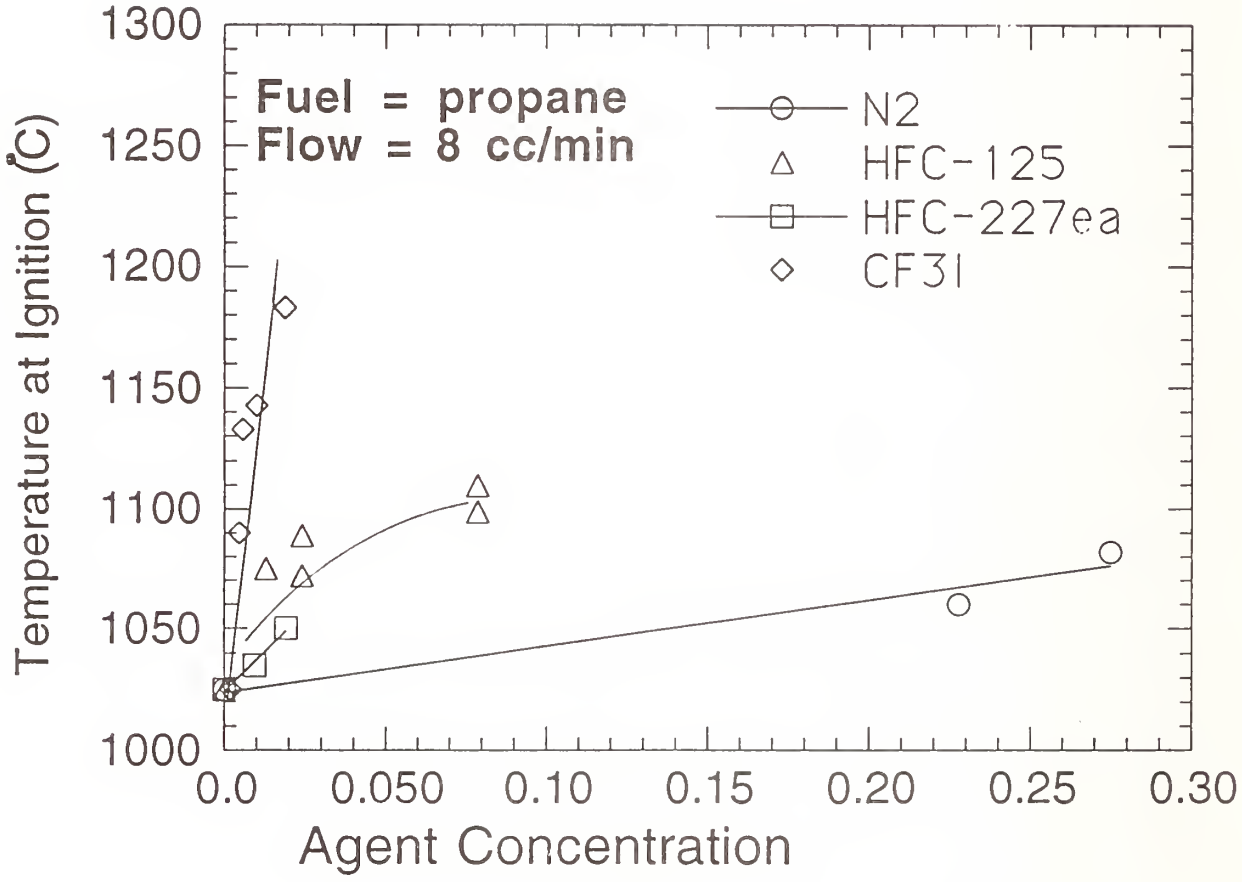

Figure 38. The critical ignition temperature as a function of agent concentration in the oxidizer stream.

the experimental apparatus and procedures is given by Smyth and Bryner (1990). In these experiments, a premixed blend of fuel, air, and agent flowed over a heated nickel surface. Both titanium and stainless steel failed in the presence of even small agent concentrations for temperatures below the ignition temperature, precluding any testing with these metals. The effectiveness of N_2, HFC-125, HFC-227, CF_3Br, CF_3I were compared in suppressing ignition for stoichiometric mixtures of methane/air, ethene/air, and propane/air.

The angle of the flow impinging on the hot metal surface was varied from 25° to 90° in stoichiometric ethene/air mixtures to determine its effect on the measured ignition temperature. The reactant velocity exiting the chimney was 16 cm/s. The results showed essentially no change in the measured ignition temperature with the reactant approach angle relative to the metal surface until the reactant stream was flowing at an angle equal to 90°, stagnation point flow. Under those conditions, the ignition temperature was measured as nearly 80 °C less than for the other cases. This result is consistent with the notion that increased residence time leads to a decreased ignition temperature.

Previous results (Smyth and Bryner, 1990) have shown that small changes in the flow rate of reactants over the hot metal surface had little influence on the ignition temperature. Measurements in a stoichiometric ethene/air mixture confirmed the results of Smyth and Bryner (1990), showing that changes in reactant flow had negligible impact on the measured ignition temperature for velocities from 8 cm/s to 24 cm/s. Decreased ignition temperatures were expected from these measurements, because decreased velocities imply increased residence time for the reactants near the heated metal surface. Also contrary to expectations, the measured ignition temperature increased somewhat (≈30 °C) for decreased velocities (at 4 cm/s and 5 cm/s). Although unlikely, a possible explanation of these results was that air was entrained into the mixture as the velocity decreased, altering the mixture from stoichiometric to lean, requiring higher temperatures to achieve ignition. All other tests were conducted for the same reactant velocity, equal to 16 cm/s.

Figures 39 and 40 show the nickel surface temperature required to obtain ignition in stoichiometric methane/air and ethene/air mixtures, respectively, as a function of agent concentration in the mixture. The results demonstrate a close correspondence between the measured temperature increase required to obtain ignition in this apparatus and those measured in the first set of experiments described above. The measured ignition temperatures in the absence of agent were approximately 970 °C and 760 °C for the methane/air and ethene/air mixtures respectively, which is consistent with the results of Smyth and Bryner (1990) and Laurendeau (1982). In general, the presence of agent impacted the measured ignition temperature. Figures 39 and 40 show that CF_3Br and CF_3I are consistently effective suppressants of ignition. Of key interest, the results show that HFC-125 slightly promotes ignition in stoichiometric CH_4/air mixtures. Experiments in C_3H_8/air mixtures also show a promotion effect. In the C_2H_4 mixture, however, the presence of HFC-125 has very little impact on ignition. HFC-227 was also measured to promote ignition in the CH_4/air mixtures. The methane results were generally consistent with those for ethene. CF_3I and CF_3Br are highly effective ignition suppressants, whereas HFC-227 and HFC-125 were very poor ignition suppressants and were found to slightly promote methane/air ignition in some instances.

The residence time in these experiments was estimated as 90 ms. This is smaller than residence times that may occur in the nacelle when a fuel puddle sits on top of a hot metal surface and boils. In that case, the residence time may be on the order of seconds. Results in the auto-ignition experiments have shown that as the residence time increases, the ignition temperature will decrease (Zabetakis *et al.*, 1954). Auto-ignition temperatures have been reported with associated ignition delay times that are hundreds of seconds in duration (Zabetakis *et al.*, 1954). Thus, the experiments described here are useful for comparing the relative suppression effectiveness of different agents, but are not useful in a determination of worst case conditions.

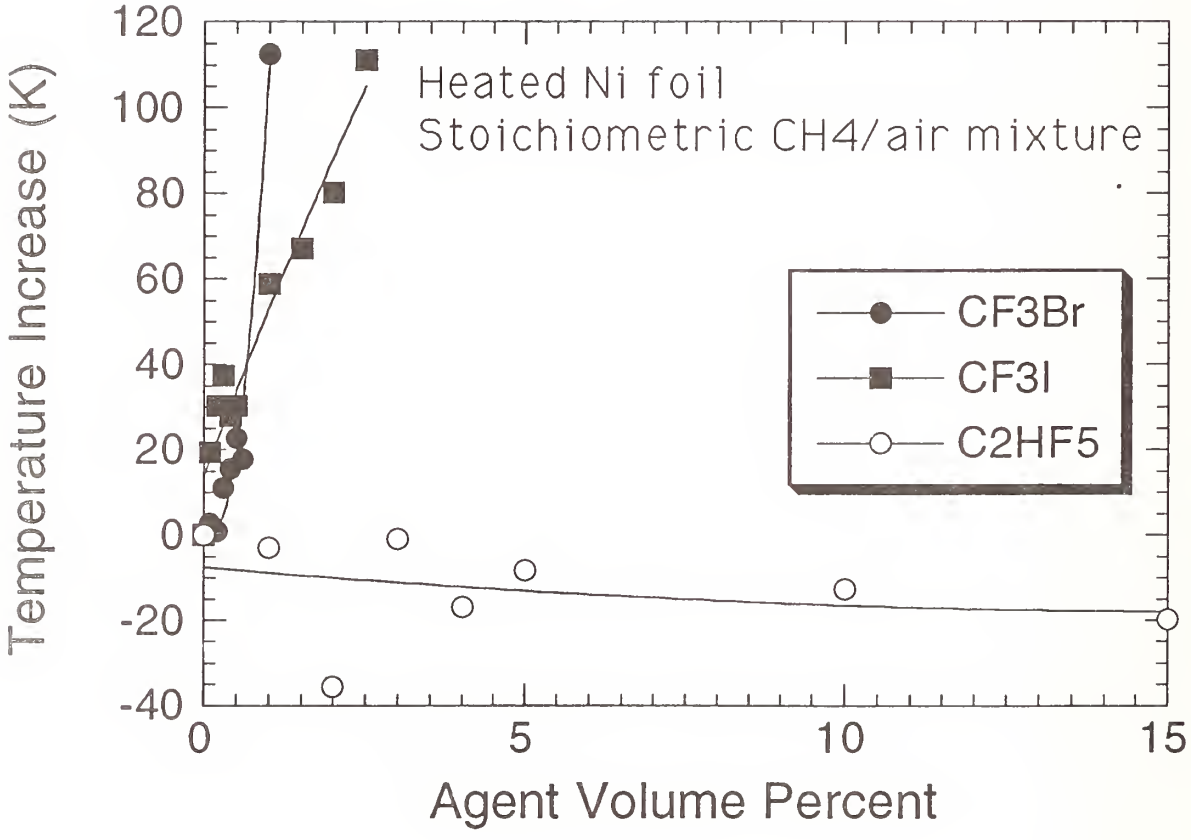

Figure 39. Change in the critical ignition temperature as a function of agent volume percent in mixtures of agent in stoichiometric methane/air.

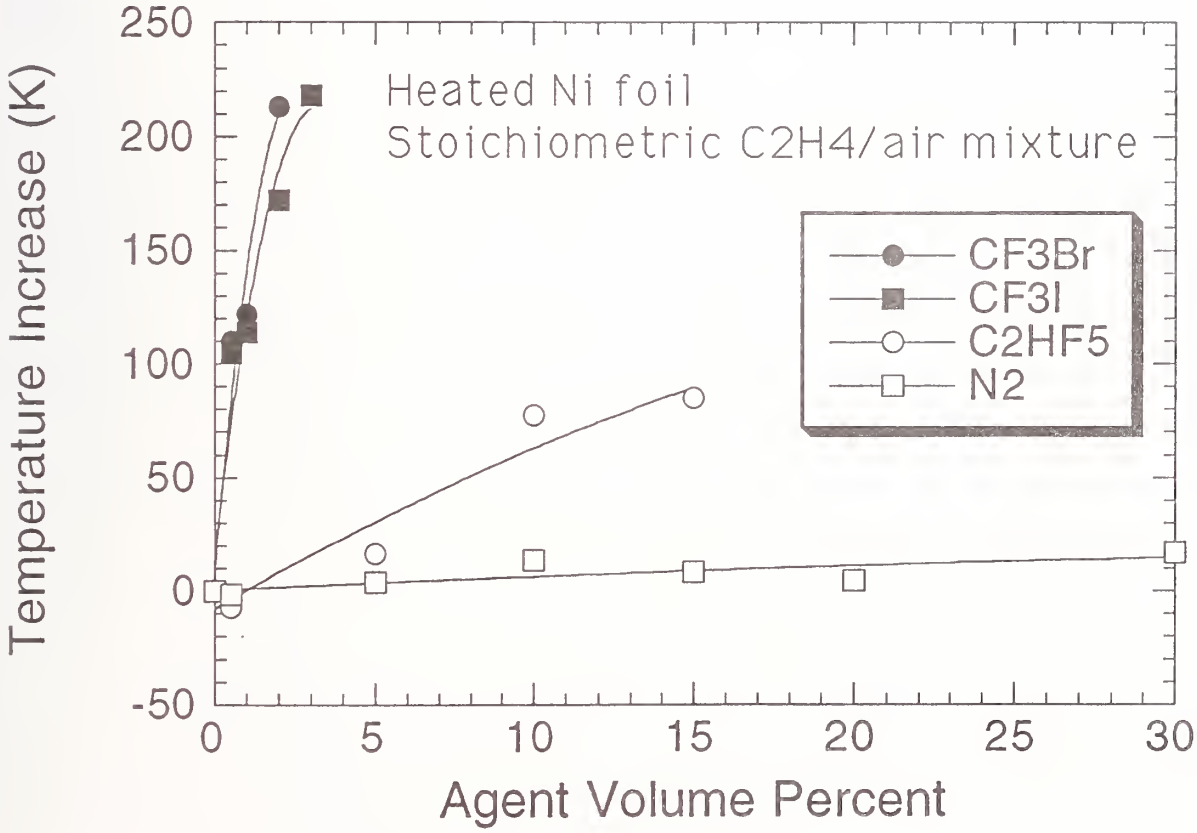

Figure 40. Change in the critical ignition temperature as a function of agent volume percent in mixtures of agent in stoichiometric ethene/air.

Selection of an agent for nacelle applications should carefully consider possible hazards associated with reactant re-ignition. The results determined here indicate that the re-ignition problem in the engine nacelle may be more severe with use of HFC-125 as compared to CF_3Br. At best, HFC-125 has little impact on the suppression of ignition. A possible approach to the re-ignition problem, is to consider using the peak flammability limit as a target concentration for the agent in the fire zone. This insures both flame suppression and the prevention of re-ignition for a period of time on the order of the agent injection duration. After this period, however, it is likely that re-ignition may still be possible and therefore other prevention strategies should be considered.

In future efforts, detailed models of ignition suppression with halogenated compounds would be helpful in predicting ignition phenomena in engine nacelles. Such models will require consideration of detailed inhibition chemistry.

9.3.5 Flammability Limits

9.3.5.1 Background. A large number of experimental arrangements have been used to measure flammability limits. Typical flammability curves take on a "D" like shape when the fuel concentration is plotted as a function of the critical or limiting agent concentration. The fat part of the "D", also called the flammability peak, can be considered the most hazardous condition, because these conditions require the highest agent concentration to inert the mixture. A standard test apparatus is a vessel filled with gaseous reactants equipped with an ignition device as described in ASTM-E 681-94 (1994). Flammability limits have also been determined using one dimensional premixed laminar flames (Lewis and von Elbe, 1961; Strehlow, 1984) and have been related to the extinction of symmetric counterflow twin premixed flames extrapolated to zero stretch rates (Yamaoka and Tsuji, 1978).

Flammability limits for hydrocarbon/air mixtures have been extensively studied (Coward and Jones, 1939). Although flammability limits have been measured for many halogen containing molecules in heptane/air mixtures, no data is available for C_2HF_5 (Malcolm, 1950; Landesman and Basinski, 1964). Fuel type and initial temperature have been shown to impact the halocarbon concentration required to inert a reactant mixture (Malcolm, 1950; Landesman and Basinski, 1964). Thus, care must be taken in interpreting flammability limit data as the peak flammability limits vary with initial temperature, pressure, and reactant type.

The goal of this work was to determine the inerting concentration of HFC-125 for peak flammability conditions in propane/air mixtures.

9.3.5.2 Experimental Method and Apparatus. A detailed description of the experimental apparatus is given by Womeldorf *et al.*, (1995). Two streams of premixed reactants (agent/propane/air) flowed towards each other in a stagnation point flow such that two premixed flames were established between the ducts of an axisymmetric counterflow burner. A nitrogen flow around the reactants was used to reduce ambient disturbances. Flame extinction was determined for several values of reactant flows. The I.D. of the ducts was 25 mm. Stainless steel (40 mesh/cm) screens were used to insure a flat velocity profile of reactants exiting the ducts. The flow of reactants was controlled with rotameters that were calibrated with a bubble flowmeter or a dry test meter. The reactants used were breathing quality air and C.P. grade (99 %) propane. Propane was selected as the fuel because the chemistry associated with its breakdown is not unlike other large alkanes and the experiment required use of gaseous reactants. The agent tested was HFC-125. CF_3Br was also tested to validate the methodology with previous work. The entire apparatus was placed in a negatively pressurized enclosure which was vented to prevent combustion byproducts from entering the laboratory. The distance between the top and bottom ducts was maintained at 16 mm. The composi-

tion and flow of reactants from the top and bottom ducts were kept equal, yielding symmetric twin flames.

The fundamental flammability limit was defined as the critical agent concentration, for a particular fuel/air mixture, at a global flow field strain rate equal to zero analogous to Yamaoka and Tsuji (1978). The global strain rate was defined as the gradient of the mean velocity of reactants exiting the ducts. Because it is not possible to produce a zero strain rate flame, measurements were made at very low strain rates and the results were then extrapolated to zero.

9.3.5.3 Experimental Results and Discussion. Figure 41 shows the measured flammability limits for CF_3Br and C_2HF_5 where the percentage of propane in the reactant mixture is plotted as a function of the limiting percentage of agent in the mixture. Conditions to the left of each curve, represent flammable conditions. Measurements presented in Figure 41 were for low strain rates (15 to 35 s^{-1}). The results appear to be approximately independent of strain rate. Figure 42 shows the limiting C_2HF_5 percentage as a function of strain rate. A linear fit yields a near zero slope line. The low strain rate results shown in Figure 41 can be interpreted as flammability limits with the peak at 12 (± 3) volume percent for C_2HF_5.

Previous results for the peak flammability limits for CF_3Br in heptane/air mixtures were reported as 6.1 % (Malcolm, 1950). Although, these measurements were conducted with propane, previous results with N_2/air/fuel mixtures have shown that the peak inerting concentrations are highly similar (within 5 %) for many alkanes, with only a small shift occurring in the value of the fuel percentage at the peak agent inerting concentration (Macek, 1979). Our results for the peak flammability limits of CF_3Br (shown in Figure 41) in propane/air mixtures are consistent with the results reported previously for heptane/air/CF_3Br mixtures (Malcolm, 1950).

9.3.6 Discussion and Summary of Combustion Experiments. The key to suppression of a baffle stabilized flame is the characteristic mixing time and the required critical agent concentration. The mixing times are dependent on the interaction of the baffle geometry and the upstream flow conditions, primarily the air velocity. Differences in the flow field associated with the spray flame and the pool fire reported here are likely to have a large impact on the relative ease of fire suppression in these two configurations. Although both flames were baffle stabilized, the flow fields were very different. The baffle in the pool fire was adjacent to a wall, whereas in the spray burner, the baffle was located in the middle of the flow field. In addition, the combustion scenario was distinct in the two configurations.

9.3.6.1 Suppression of Baffle Stabilized Flames. The spray flame represents a two-phase combustion situation where a portion of the fuel droplets were entrained into the recirculation zone, vaporized, and reacted with the oxidizer. In the pool fire, the top of the baffle acts as a flame holder. The appearance of the fire depends on the baffle height and the air flow. For low air flows and small baffle heights, the flame appeared to be laminar. For moderate air flows and baffle heights, the pool fire looked like a ball of flame stabilized behind the baffle. Heat from the flame feeds back to vaporize the liquid fuel. If the baffle was too high the flame was less stable due probably to diminished heat feedback. If the baffle was too low, the flame was less stable, due probably to the relatively large flow field strain rate associated with a small recirculation zone. This idea is consistent with the measurements reported by Hirst and Sutton (1964) who measured peak flame stability for intermediate sized baffle heights. In the spray burner, flame stability also peaked at an intermediate baffle length and it was not possible to stabilize flames for very small or very large baffles as discussed in Section 9.3.2.3.2.

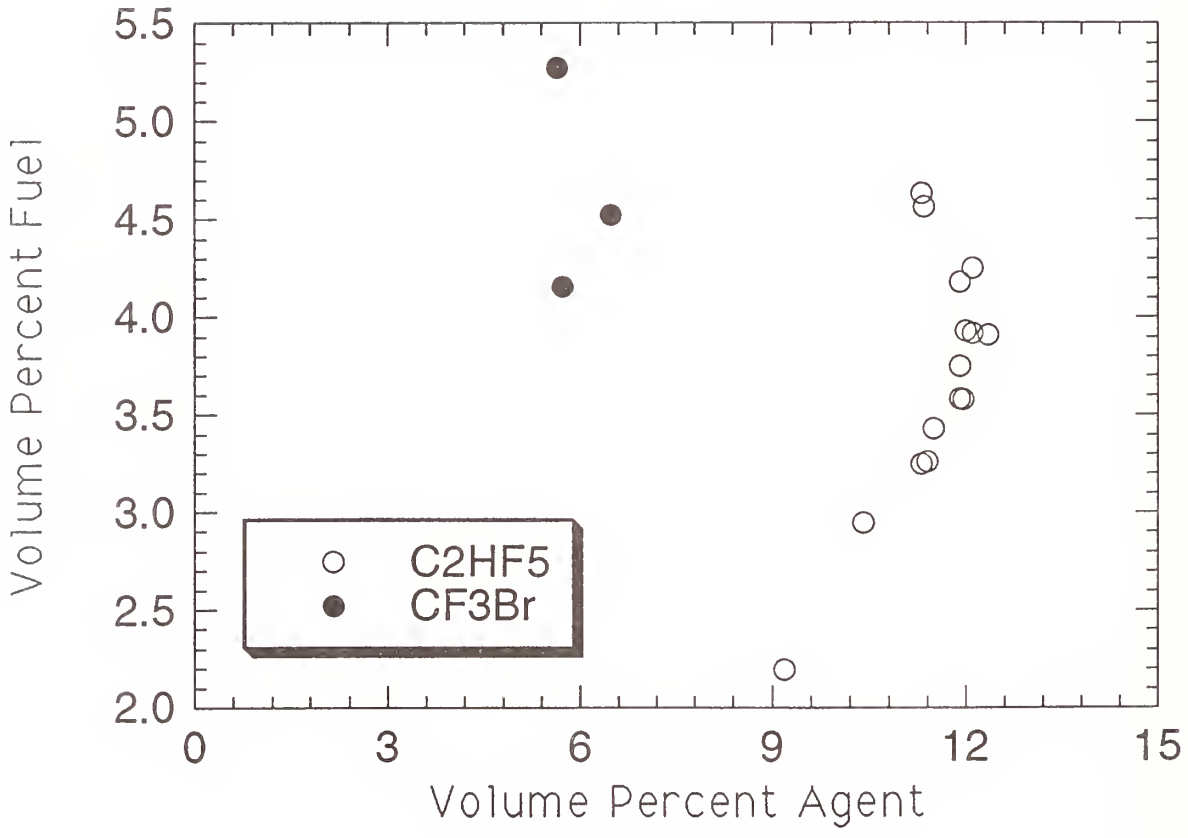

Figure 41. The flammability limits for CF_3Br and C_2HF_5 plotted as the percentage of propane in reactive mixtures of agent/propane/air as a function of the limiting percentage of agent in the mixture.

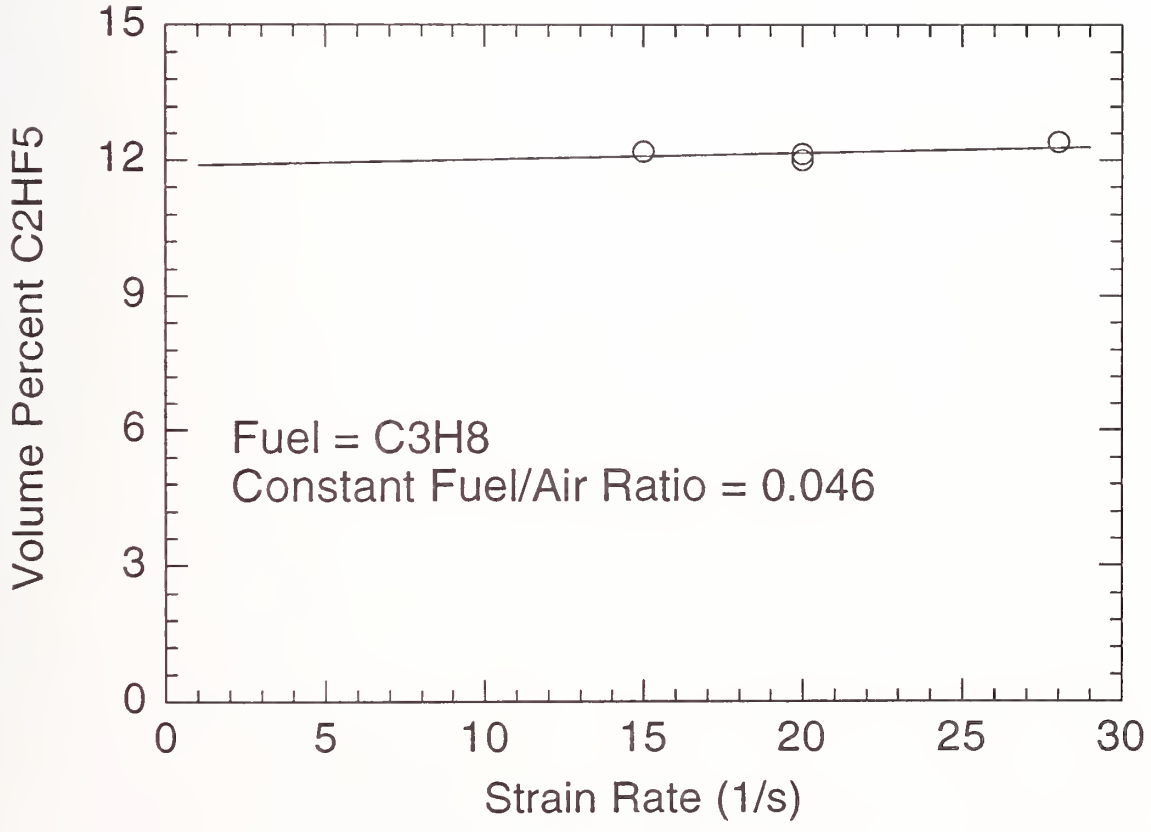

Figure 42. The concentration of C_2HF_5 at extinction as a function of the global flow field strain rate.

Combustion in a recirculation zone is modeled here as a well-stirred reactor (see Section 9.3.2.3.4). For very low air flows, the pool fire extinction measurements (discussed in Section 9.3.3) yield values that are consistent with the inerting of rich premixed combustion, indicating that the flow field could be effectively modeled as a well-stirred reactor. For low air flows in the spray burner, combustion was not observed to occur in the recirculation zone (see description in Section 9.3.2). The flame was a luminous 45° cone of combusting liquid droplets, with a structure not unlike a diffusion flame. The dynamic structures of the recirculation zones were not characterized in either of the configurations. Little is known about even such basic parameters as the size of the recirculation zone or its global equivalence ratio. In the spray flame, for example, only a portion of the fuel droplets may be entrained into the recirculation zone, depending on the relative momentum of the droplets and the torroidal vortex associated with the recirculation zone. Inherent differences in the structure of the combustion zones in each of the configurations could yield differences in agent suppression effectiveness.

The volume fractions of HFC-125 required to suppress the turbulent spray flames and the stabilized pool fires were measured as 9 % and 12 % (by volume) respectively for similar baffle sizes and air flows. This is in comparison to a value of 9 % measured in the cup burner and a 12 % peak flammability limit measured for HFC-125 and discussed in Section 9.3.5. The same type of fuel (JP-8) was used in the spray, pool, and cup burner experiments. The flammability limit study was conducted with propane. yet, it is possible that use of a different fuel can yield a different peak flammability limit. Previous studies, however, using a number of different alkanes showed that the peak flammability limits were highly similar from fuel to fuel for inert agents (Macek, 1983). In general, the spray flame measurements corresponded closely to the cup burner results (as discussed in Section 9.3.2.3.3) and the pool fire measurements corresponded closely to the measured peak flammability limits. The pool fire results of Dyer *et al.*, (1977a) also support the correspondence between agent suppression concentrations in baffle stabilized pool fires and peak flammability limits. Their results for N_2 and CH_3Br were discussed in Section 9.3.3 and are shown in Figures 28 and 29. A fit of their data using Equation (14) yields values of X_∞ equal to 6 % and 38 % for CH_3Br and N_2, respectively. These results correspond closely to the peak flammability limits for these agents in hydrocarbon fuels (Macek, 1979; Malcolm, 1950). It should also be noted, although perhaps only a coincidence, that the current Military Specification of a 6 % nacelle concentration requirement for halon 1301 corresponds to the peak flammability limit for halon 1301 in a heptane/air mixture (Malcolm, 1950). In terms of the re-ignition problem, using the flammability limits as an agent target concentration insures both flame suppression and the prevention of re-ignition.

The limitations of treating the recirculation zone as a continuously stirred tank reactor (CSTR) were tested by using available numerical combustion models (Glarborg *et al.*, 1986) which examine the key parameters that control flame stability such as temperature, pressure, characteristic mixing (or residence time), and equivalence ratio, in addition to detailed inhibition chemistry. Attempts to model the extinction results using detailed kinetics in a CSTR code for stoichiometric methane/air mixtures plus inhibitor (1 % to 6 % agent by volume) yielded calculated residence times at extinction that were approximately two orders of magnitude smaller than the residence times (τ) measured in the spray burner at extinction (Babushok *et al.*, 1995b). This indicated, as expected, that transport effects in the recirculation zone of the spray burner must be considered in detail.

9.3.6.2 Mixing in a Baffle Stabilized Flow Field. Few studies have examined the rate of entrainment into a recirculation zone behind obstacles (Lefebvre, 1983). Winterfeld (1965) found that the mixing time in baffle stabilized premixed flames was approximately a factor of two larger than mixing times for the non-combusting case. Increased blockage ratio was found to increase the characteristic mixing time in an identical manner for both combusting and non-combusting situations

(Winterfeld, 1965). The difference between combusting and non-combusting flows can be partly attributed to increased viscosity in the combusting case, which leads to decreased Reynolds numbers. Unfortunately, Winterfeld's investigation was for Reynolds numbers larger than those utilized in the spray burner or encountered in a typical nacelle. Bovina (1965) also studied entrainment in baffle stabilized flames, but effects due to blockage were not addressed.

Hirst and Sutton (1961) showed that the stability of pool fires was dependent on the size of a baffle upstream of the pool. Pool flames with baffles several centimeters in length were very difficult to extinguish, representing very hazardous conditions. We have shown that the characteristic mixing time for an agent entraining into a baffle stabilized flame is much larger for a baffle against the wall, as in the pool fire configuration, than for a baffle in the middle of the flow field as studied in our spray burner. This confirms the conclusions made by Hirst and Sutton (1961). It should be noted that no experiments were made with the fuel spray stabilized by a baffle against a wall and it is not clear if such a configuration would be more or less hazardous than a baffle stabilized pool fire. In such a case, the recirculation zone may not be very different than the baffle stabilized pool fire. Certainly such a configuration could occur in a nacelle.

To compare mixing in the two flow situations, detailed numerical simulations of the fluid dynamics associated with entrainment of an agent into the recirculation zone behind an obstacle were undertaken. Isothermal flow calculations were performed in an effort to quantify the rate of agent entrainment as a function of Reynolds number and flow field geometry. The Reynolds number (Re) is defined as:

$$Re = \frac{Vd}{\nu} \tag{20}$$

where V is the average upstream velocity, d is a characteristic length scale, and ν is the kinematic viscosity of the agent/air mixture. The characteristic length scale, d, in the Reynolds number was taken as the baffle height in the pool configuration and the diameter in the spray configuration.

The flow field was calculated based on the two dimensional (2D) Navier-Stokes equations describing transient convection in an enclosure. No turbulence model or other empirical parameters were introduced. The details of the methodology are described in McGrattan *et al.*, (1994).

Injection of agent was simulated by slightly altering the density of the fluid in the form of a long square wave pulse. The average density of fluid in the control volume directly behind the obstacle and one baffle diameter downstream was monitored as a function of time. It was also possible to include variation of thermophysical properties of the air/agent mixture.

The concentration of agent (normalized to the free stream) in a region behind the baffle, located adjacent to the wall and in the middle of the duct was calculated as a function of time using the two-dimensional model for flows characterized by Reynolds numbers from 500 to 4000. The blockage factor B was held constant at 0.8. The agent mixes into the recirculation zone and obtains its free stream concentration in 25 to 40 nondimensional time units. A fit to the data using Equation (13) allowed determination of the characteristic nondimensional mixing time constant ($\tau \cdot V/d$) for each corresponding Reynolds number. Thus, a dimensional characteristic mixing time, τ, in units of seconds, could be calculated for combinations of V and d. The dimensional characteristic mixing time determined from this type of calculation is shown in Figure 43 for obstacles 3.5 cm in diameter, located in the center of the flow field and against a wall as a function of time. The mixing times for the obstacle in the center of the flow field is significantly less than the mixing time for the obstacle against the wall. The mixing times decreased as the velocity increased, although the rate of decrease was larger than expected from Equation (16).

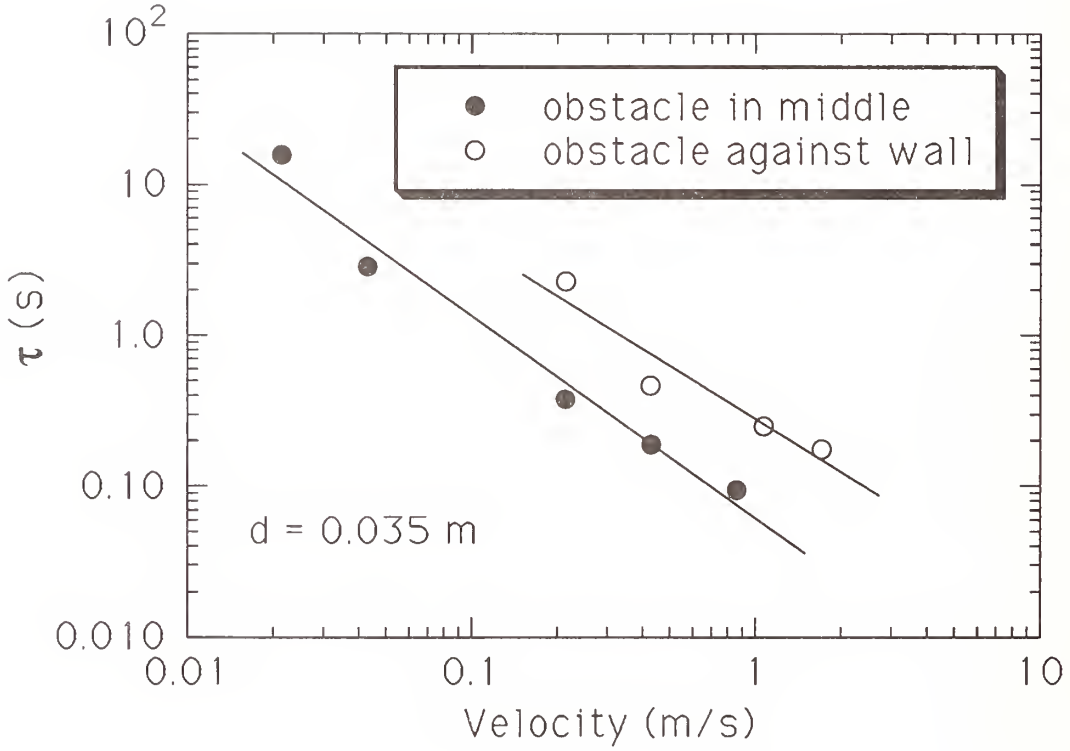

Figure 43. The characteristic mixing time as a function of air velocity for 3.5 cm obstacles against a wall and in the middle of the flow field calculated using the 2D flow model.

These results are consistent with the trends found for the mixing times measured in the spray and pool burners. In those combusting cases, the mixing times in the pool fire (with a baffle against the wall) and in the spray flame burner (obstacle in the middle of the flow field) was measured as approximately 0.7 s and 0.1 s respectively for 3 m/s air velocities and similar baffle diameters. Thus, the difference in mixing times for the two geometries was approximately a factor of 7. It is not surprising that the ratio of mixing times for the simulations and the experiments were not equal. First, the simulations were conducted for an isothermal situation. The detailed structure of the recirculation zones undoubtedly plays a role in the turbulent exchange processes which govern the characteristic mixing time and the structure of the combusting zones are certainly very different from isothermal zones. Second, the detailed geometric configuration used in the pool fire experiments was not as simple as a baffle abutting a wall. The air/agent mixture flowed around the finite sides of the baffle. In addition, a lip was present on the downstream end of the burner to prevent fuel spillage (see Figure 30). Third, the calculations were based on a 2D model. The 3D effects almost certainly play a role. The simulations do, however, confirm the trends in the measurements, which suggest that the baffle stabilized pool configuration is a more dangerous fire scenario in terms of forcing agent into the fire.

Various agents have different thermophysical properties such as viscosity and molecular diffusion coefficients. For example, the molecular diffusion coefficient of HFC-125 is approximately a factor of two less than N_2 under ambient conditions. A calculation was performed to test the effect of molecular diffusion on the characteristic mixing time. This was accomplished by varying the Schmidt number for the agent. The Schmidt number (Sc) is defined as:

$$Sc = \nu/D_m \tag{21}$$

where D_m is the molecular diffusion coefficient. The calculation was conducted for a Reynolds number equal to 500 and with an obstacle in the middle of the flow field. The results showed that changes in the Schmidt number had negligible effect on the characteristic mixing time. These results suggest that agent type will not effect the rate of agent entrainment into a baffle stabilized fire zone for a well dispersed slug of gaseous agent. Other thermophysical properties may play a role however, most notably, the Jakob number which governs the rate of flashing and is indicative of agent dispersion (Grosshandler *et al.*, 1994).

9.3.6.3 System Design Considerations. Safe design of fire protection systems requires an understanding of plausible worst case situations.

- The most dangerous combustion situations, evaluated in terms of Equation (14), are characterized by large values of the parameters τ and X_∞. For the conditions studied in this report, the most dangerous situations were associated with pool fires rather than spray flames. For the same air velocities and baffle lengths, the values of τ and X_∞ were both larger for the baffle stabilized pool fire than for the spray flame. Furthermore, a comparison between the results shown in Figure 9 and those of Hirst and Sutton (1961), suggest that the blow-off velocity, for baffles with similar diameters, was much higher in the pool fire configuration.

- Besides the fire configuration, other parameters can be considered to add to fire hazard, as discussed above in terms of the spray fire. These include the flow velocity, air temperature, system pressure, fuel flow and other parameters not studied in this report such as fuel volatility, and the droplet diameter distribution of the liquid fuel. In this regard, the results from the

extinction measurements in the spray burner were used to develop simple equations as guidelines for design of suppression systems (see Section 9.3.2.4). However, the spray burner guidelines are applicable to full-scale under certain conditions only. This is because geometric factors, material properties, operating conditions and fire scenario may impact flame stability. For example, the agent concentration at extinction and the blow-off velocity are both affected by the blockage ratio. These are specific not only to each nacelle geometry, but also to each particular fire scenario. The function $f_6(V)$ (see Tables 4-6), related to the free stream air velocity as discussed in Section 9.3.2.4, is another example. As presented in Figure 12, the agent mass fraction at extinction decreased for high air flows. Similar behavior was observed in full-scale testing (Bennett and Caggianelli, 1995; Johnson and Grenich, 1986). Discerning application of $f_6(V)$ would allow a reduced agent weight penalty for high air flows. Yet, for an arbitrary fire in an arbitrary or geometrically uncharacterized nacelle, it is not possible to predict the free stream air velocity at the fire location which is a local parameter. Nor is it possible to predict the total air flow where the required agent mass obtains a maxima, as seen in Figure 10. This is because the nacelle geometry is not a series of simple baffles in a free stream. Fluid flow in a cluttered nacelle environment will cause interaction between the recirculation zones. This may impact the values of the local characteristic mixing times. Furthermore, it is not clear that the blow-out velocity is related only to the baffle length and fuel type. Fire size and fuel puddle dimensions may also be a factor. In addition, only scant data are available for suppression of pool fires at higher air velocities.

- For all of these reasons, agent concentrations in full-scale applications should be at levels such that the maximum agent concentration required for extinction is available for all possible air velocities, unless a full-scale testing program investigating a number of different fire scenarios can prove otherwise.

- Preliminary design guidelines for an alternative agent might consider an agent target concentration in the fire zone equal to the peak agent flammability limit. This would ensure flame extinction and suppression of re-ignition (for a time period on the order of the agent injection duration for typical nacelle conditions). A methodology to achieve such a guideline is suggested in Section 9.5 where agent mixing in the nacelle is viewed as a series of idealized transient processes, amenable to algebraic modeling. The mixing details are not modeled, nor are they known for generic nacelle geometries, but limiting cases are studied which suggest the values of the minimum agent mass delivery rates. The model is based on idealized global mixing models describing agent dispersion and dilution for the bulk temporal concentration, and a local mixing model for flame extinction or concentration build-up at specified locations. The input data for the model were inferred from the results of the small-scale spray and pool experiments described above. It should be noted that the flammability limits are pressure, temperature and probably fuel sensitive as well.

9.4 Flow Field Modeling and Validation in a Mock Nacelle

The agent concentration in the flow field is the key to extinguishing a fire and preventing re-ignition. The character of agent delivery and mixing in the flow field is then a key aspect of a fire suppression system. Because of its low boiling point and other thermophysical properties, use of CF_3Br has ensured rapid evaporation and dispersion of the agent into a target volume. Upon use of one of the candidate replacement agents, it is possible that the evaporation and dispersion characteristics may be diminished. In order to enhance dispersion, the location, number, placement, and orientation, and even

shape of agent injection nozzles may need to be carefully optimized. Computational fluid dynamics (CFD) is a tool that allows three-dimensional modeling of transient problems in non-simple geometries. CFD is a completely accepted methodology in the aircraft industry and is depended upon for aircraft design. The purpose of this subsection is to demonstrate the viability of CFD in treating the problem of agent mixing in an engine nacelle. CFD has apparently been used in the design of the fire protection system for the B2 aircraft (Kinsey, 1994). The B2 has a highly unusual nacelle geometry and standard protection system design was not appropriate. A detailed analysis of agent flow inside of the nacelle under non-combusting conditions was developed. Through use of CFD, a design using multiple agent injection locations was generated to improve agent dispersion (Kinsey, 1994). Unfortunately, no report is available concerning this work.

Since there are many nacelle types, a single representative geometry was considered. The geometric configuration was an idealized reduced-scale version of the Wright Patterson full-scale nacelle test facility. Combusting flow conditions were not considered in the simulations, because the isothermal flow dynamics upstream of the fire source are thought to control agent/air mixing and because agent certification is performed at ambient temperatures. The purpose of this portion of the investigation was to model agent concentration as a function of location, rate, and orientation of agent injection.

Because temperatures as high as 350 °C (650 °F) are not uncommon in engine nacelles and because the candidate agents have relatively low boiling points, evaporation of the liquid-phase agents will be rapid. Under realistic conditions, it is unclear to what extent liquid phase flow phenomena will impact suppression effectiveness through differences in agent dispersion. Because problems associated with modeling an evaporating two-phase flow are much more difficult, only gas-phase phenomena were considered. Information regarding criticality of the number, placement, and orientation of agent injection nozzles as well as the rate of gaseous agent injection were considered.

To insure that the computational results were reliable, a flow tunnel with agent injection was developed and measurements were compared to the computations.

9.4.1 Description of the CFD Model

9.4.1.1 Introduction. Three scenarios were examined. First, agent was injected through a tee so that the initial agent flow was perpendicular to the air flow, and parallel to the plane defined by a cross section of the nacelle. Second, a baffle attached to the inner wall of the nacelle was examined. Third, cases involving agent inlets oriented 15° towards the far end of the nacelle were examined. The geometry of these configurations will be described in detail below. Sensitivity of the agent concentration to various parameters was examined. It was observed that changes to the agent and air inlet velocities caused the most change in downstream agent concentration.

9.4.1.2 Modeling Assumptions. CFDS-FLOW3D (Harwell Laboratories, 1992) was used to perform the numerical simulations described here. This model solves equations for the conservation of mass, momentum and energy. The fully compressible form of these equations was used due to the high velocities at the agent inlet (up to 50 m/s) encountered in these simulations. The conservation of energy equation was neglected since we assume that all flows are isothermal. The standard k-ε model of Launder and Spalding (1974) was used to model turbulence. Various turbulence levels were input at the boundaries without significant changes in the results of the simulations.

The agent, nitrogen, was modeled using the "additional scalar" option of the field model. The field model simulates flow of additional fluids using the species mass conservation equation:

$$\partial\frac{\rho S}{\partial t}+\nabla\cdot(\rho US)-\nabla\cdot((\frac{\mu_T}{\sigma_S}+\rho D)\nabla S) = 0 \quad (22)$$

where ρ is the density of the carrier fluid (air in this case), t is time, U is the fluid velocity, μ_T is the turbulent viscosity, D is a diffusion coefficient, σ_s is the turbulent Prandtl number for the scalar, and S is the mass fraction of the additional scalar. Convection and diffusion control the rate at which the agent moves from one portion of the nacelle to another. It was found that the convection was the dominant mechanism for transporting the agent. Computer simulations were run to steady state and took approximately 7 hours of central processing time on a Silicon Graphics Indigo II workstation.

9.4.1.3 The Computational Grid. The grid used to simulate the cases discussed in this report is illustrated in Figure 44. It consisted of 64,000 grid cells. Simulations with twice the number of grid cells were performed with little change in results. It was therefore felt that 64,000 was a sufficient number of grid cells to resolve the flow. All cases simulated were symmetric about a plane passing through the axis of the nacelle and an agent inlet. Therefore, only one half of the nacelle was simulated with the field model. The control volume sizes ranged from 2 mm on a side near the agent inlet to 4 cm near the far boundary where air/agent mixtures exited the nacelle. Air flowed through the annular region between cylindrical tubes which was modeled as having a 30.4 cm O.D. of the inner tube and a 45.0 cm I.D. of the outer tube. The cross sectional area of the annular region was 0.087 m^2. Boundary conditions were specified at each inlet, outlet, and walls. The air inlet velocity was taken from the experimental measurements described in Section 9.4.2 below. The velocity was approximately 3 m/s for most cases. The agent inlet velocity was such that the volume flow rate was either 0.012 or 0.025 m^3/s. The outlet at the far end of the nacelle was modeled as an open or pressure boundary condition. A no-slip boundary condition was used at the walls.

The experimental configuration was used as a basis for the computer simulations. Agent was discharged through a nozzle into the annular test section. Two nozzle types were used. Most experiments used a tee shaped nozzle which injected two round jets perpendicular to the axis of the test section and parallel to a tangent defining the annular region. Some calculations considered a straight round tube (1.5 cm inner diameter) flush to the inner wall of the outer cylinder which defined the test section, with the jet discharging nearly perpendicular to the air flow. A summary of the cases which were studied is presented in Table 9. The agent volume percent varied from 3.4 % to 8.6 % as the agent flow varied from 0.012 m^3/s to 0.25 m^3/s. Geometric details of the air and agent inlets and flow baffles which were attached to the inner nacelle wall are described below.

9.4.2 Experimental Facility. Measurements of the inlet velocity profile dictated the boundary conditions used in the calculations. Figure 45 is a schematic diagram of the flow tunnel which consisted of an air blower, a wood plenum and converging section, and a clear plastic test section.The fan speed was adjustable, providing air velocities in the test section from 1 m/s to 10 m/s. Screens were attached to the end of the converging section to provide a flat velocity profile of air at the test section inlet. The test section consisted of two coaxially arranged plastic tubes, each 2 m long. The inner tube was fitted with an aerodynamic nose section to prevent flow separation.

Two nozzle types were used. Most experiments used a tee shaped nozzle which injected two round jets perpendicular to the axis of the test section and parallel to a tangent defining the annular region. A schematic drawing of the injection tee is shown in Figure 46. The inner diameter of each of the agent flows was 1.56 cm. Some experiments were conducted with a straight round tube (1.5 cm inner diameter) flush to the outer surface of the test section with the jet discharging perpendicular to the crossflow. Mixing was worse in this case, so measurements were focussed on use of the tee.

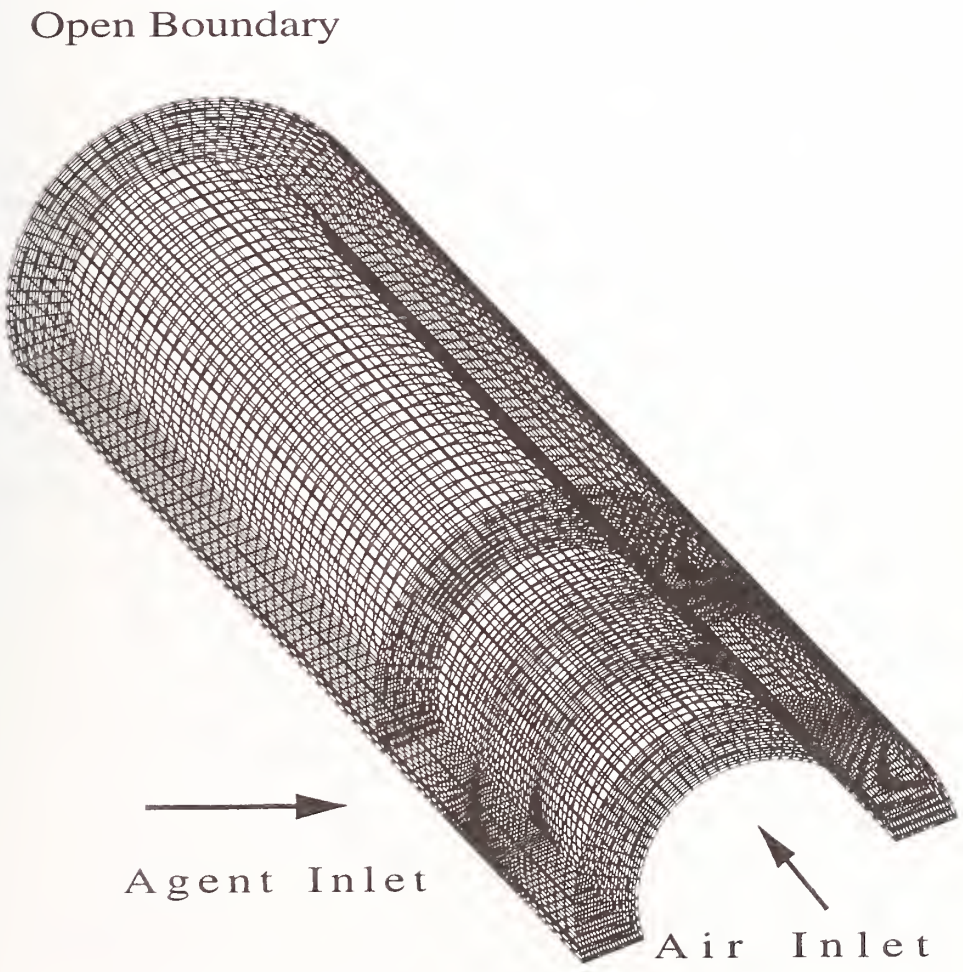

Figure 44. Schematic diagram of the computational grid used in the CFD simulations.

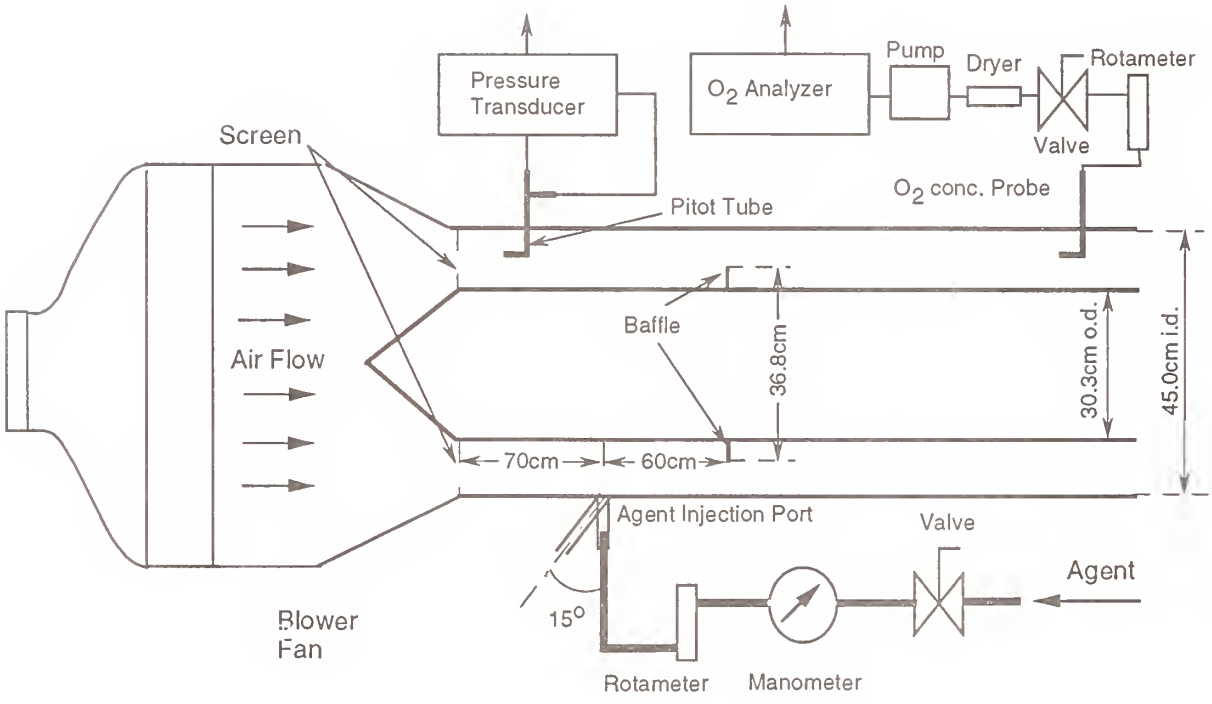

Figure 45. Schematic diagram of the flow tunnel.

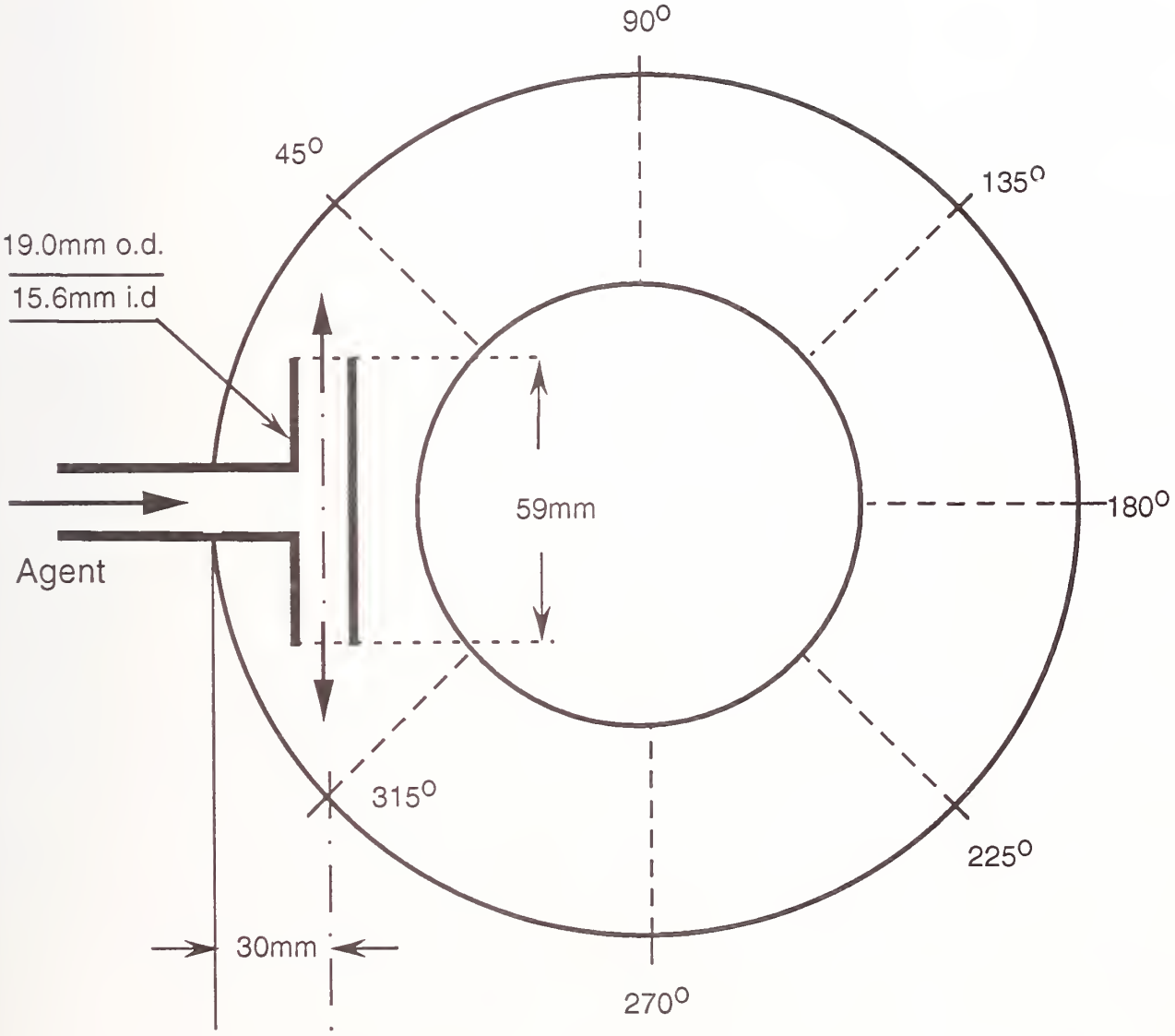

Figure 46. Schematic diagram of the agent injection tee.

Table 9. Description of numerical computations

Case	Injection Locations	Type of Injection	Air Velocity (m/s)	Agent Volume Percent	Agent Flow (m^3/s)
1	1	tee	3.0	4.5	0.012
2	2	tee	3.0	4.5	0.012
3	4	tee	3.0	4.5	0.012
4	1	tee	3.0	8.6	0.025
5	2	tee	3.0	8.6	0.025
6	4	tee	3.0	8.6	0.025
7	1	tee	3.0	4.5	0.012 baffle on interior wall
8	1	15 degree	3.0	4.5	0.012
9	2	15 degree	3.0	4.5	0.012
10	4	15 degree	3.0	4.5	0.012
11	1	15 degree	3.0	8.6	0.025
12	2	15 degree	3.0	8.6	0.025
13	4	15 degree	3.0	8.6	0.025
14	1	tee	3.3	4.2	0.012
15	1	tee	3.5	3.9	0.012
16	1	tee	4.0	3.4	0.012

Gaseous agent was discharged through a nozzle into the test section at a location 70 cm downstream of the test section inlet. Measurements were made after a steady state flow had been achieved. Gaseous nitrogen was chosen as the agent. N_2 flowed from six cylinders connected in series to the test section through a 2.5 cm pipe. The flow passed through a regulating valve, a manometer, and a rotameter, allowing control and determination of the agent flow. The rotameter readings were corrected for back pressure. Uncertainty in the N_2 flow was estimated as 13 %.

In some experiments, baffles or ribs were placed in the flow field in order to mimic the flow field typically encountered in nacelles. Ribs were installed 60 cm downstream from the point of injection. The ribs were attached to either the inner or outer walls of the annular region with extending from 30.3 cm to 36.7 cm in the radial direction on the inner wall and from 45.0 cm to 39.5 cm on the outer wall.

9.4.2.1 Agent Concentration Determination. The agent concentration was determined by measuring the depletion of oxygen at selected locations within the test section using the following equation:

$$[Agent] = \frac{([O]_o - [O])}{[O]_o} \tag{23}$$

where $[O]_0$ and [O] are the oxygen (volume based) concentrations in the air flow, before and during injection respectively, and [Agent] is the agent volume fraction in the air flow. The local oxygen concentration was measured by a paramagnetic oxygen analyzer in conjunction with gas sampling. The analyzer had a 1 s response time. Gas samples were collected through a stainless-steel cylindrical tube with a 1.4 mm inner and 3.2 mm outer diameter. The probe had a right angle bend 8 cm from the sampling orifice. The probe was inserted into the stream through a hole in the wall of the test section with the orifice facing the flow (see Figure 45). Measurements were made 96 cm and 184 cm downstream from the point of agent injection for many angles and several radial locations. All measurements were time averaged over a period of 10 s. Uncertainty in the agent concentration measurements are estimated as 18 % based on repeat measurements and a propagation of error analysis.

9.4.2.2 Air Flow Measurements. A pitot tube was used to measure the air speed as a function of location in the test section, both upstream and downstream of the agent injection location. Measurements were conducted with a 3 mm diameter stainless steel pitot tube and a differential pressure transducer. All measurements were time averaged for a 10 s period. The pitot tube was mounted facing the incoming flow. Uncertainty in the velocity measurements was estimated as 8 % based on repeat measurements and a propagation of error analysis.

9.4.2.3 Characterization of the Flow Tunnel Without Agent Injection. Figure 47 shows measurements of the inlet air velocity as a function of radial location across the annular region, 65 cm upstream and 90° from the agent injection location. In the absence of agent injection, the air velocity profile is almost flat as a function of radial location. In this case, the average air speed was approximately 3.3 m/s. From measurements taken 35 mm from the inner wall of the test section, Figure 48 shows that the air velocity was uniform as a function of angle around the annulus, except at 0°, where the flow was disturbed by the agent injection tee, causing a 10 % velocity decrement. When the straight tube was used for agent injection, no velocity decrement was observed. The Reynolds number for this flow was equal to $7.5 \cdot 10^4$, where the characteristic spatial dimension (d) was taken as the distance between the inner and outer tubes forming the annular region. Fully developed flow in the tube was expected 2.6 m downstream from the test inlet, which is just beyond the end of the test section (Blevins, 1984).

A hot wire probe was used to characterize the turbulence intensity at the test section inlet. Measurements were obtained at a sampling rate of 2 kHz at several locations across the annular region. The turbulence intensity (TI) was characterized as:

$$TI = \frac{\sqrt{u'^2}}{\langle u \rangle} \tag{24}$$

where u'^2 is the square of the average velocity fluctuations in the axial direction. The average velocity fluctuation is defined as the difference between the time varying (*e.g.*, u) and the time-averaged (<u>) velocity:

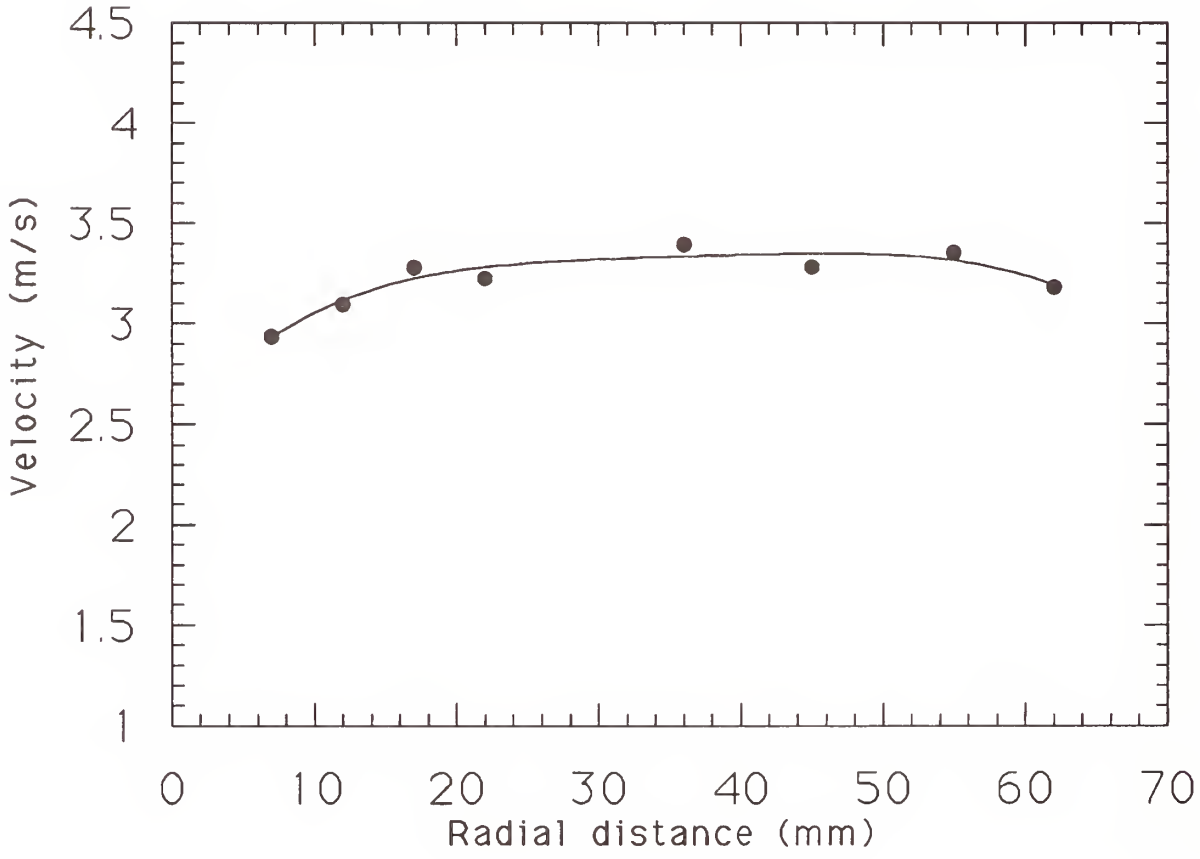

Figure 47. The velocity as a function of radial location, at locations 65 cm upstream and 90° from the agent injection.

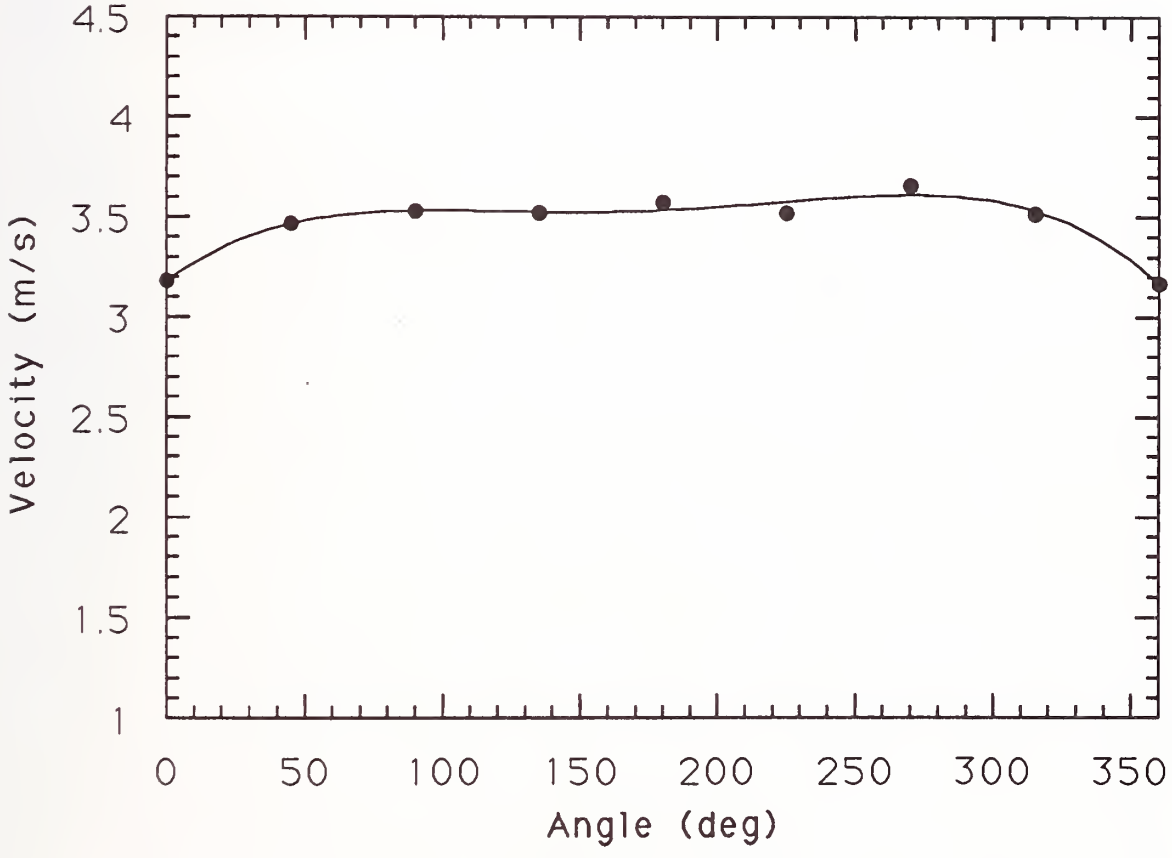

Figure 48. The air velocity as a function of angle around the annular test section at a location 65 cm upstream from the agent injection.

$$u' = \langle u \rangle - u \tag{25}$$

For inlet velocities of ≈5 m/s, the turbulence intensity 8 cm downstream of the test section inlet was measured to be ≈0.0065 indicating a nearly laminar flow. Because of the Reynolds number, TI increased downstream, obtaining values close to 0.03 on average. Flow visualization using smoke confirmed that the air flow was essentially laminar. The upstream velocity was measured for Cases 1, 4, 7, and 11 (see Table 9), and used as a boundary condition in the corresponding calculations.

9.4.3 Comparison of Calculations with Experimental Measurements. Experimental measurements were performed in an effort to validate the numerical simulations. Measurements were conducted for conditions corresponding to Cases 1, 7, and 14 listed in Table 9. The other cases represent numerical simulations where the effect of varying the location and number of agent injection nozzles on agent dispersion was tested.

Figure 49 compares the experimentally measured agent volume percent to the calculations (for Case 1) as a function of angular location in the nacelle, for positions equidistant from the inner and outer nacelle walls, 96 cm downstream from the agent injection location. Figure 50 shows a similar comparison for locations 184 cm downstream from the point of agent injection. The experimental uncertainty of 18 %, estimated from repeat measurements and a propagation of error analysis, is indicated by the error bars in the figure. In many instances, the calculations fall outside of the error bars. Uncertainty of the input to the model calculation, namely the air and N_2 flows, resulted in an uncertainty in the calculated agent concentration distribution. The magnitude of the uncertainty varies as a function of location in the nacelle and is steepest for locations of large concentration gradients. For example, the uncertainty in the location of the calculated agent concentration maxima in Figure 49 was equal to approximately 40°. A higher air flow or a lower N_2 flow shifted the calculated maxima from 140° to 100°, in better agreement with the measured agent concentration maxima. In general, the computed profiles were characterized by steep gradients and narrow peak half-widths, whereas the measured profiles were relatively broad.

Figure 51 compares the experimentally measured agent volume percent to the calculations for Case 7 with a baffle on the inner wall of the flow field as a function of angular location in the nacelle, for positions equidistant from the inner and outer nacelle walls, 96 cm downstream from the agent injection location. Figure 52 shows a similar comparison for locations 184 cm downstream of the agent injection. The calculations generally follow the trends experimentally measured. Little difference was experimentally measured between the cases with and without the baffle as seen by comparing Figures 49 and 51, or Figures 50 and 52. The agent concentration 96 cm downstream from the agent injection location shown in Figure 51 were asymmetric, whereas 184 cm downstream, they were symmetric. This indicates some asymmetry in the experimental configuration. The measurements were repeated after carefully checking the placement of the tee in the flow field. Measurements yielded nearly the same results. Thus, the reasons for the asymmetry are not clear.

Figure 53 compares the experimentally measured agent volume percent to the calculation for Case 8 as a function of angular location in the nacelle, for positions equidistant from the inner and outer nacelle walls, 96 cm downstream from the agent injection location. Figure 54 shows a similar comparison for locations 184 cm downstream from the point of agent injection. The computations predict agent concentration peaks ± 90° from the injection location, whereas the measurements show peaks along the angle of injection.

The key difference between the numerical and laboratory experiments which remains unresolved is that agent concentration gradients in the laboratory measurements are smoother and less steep than

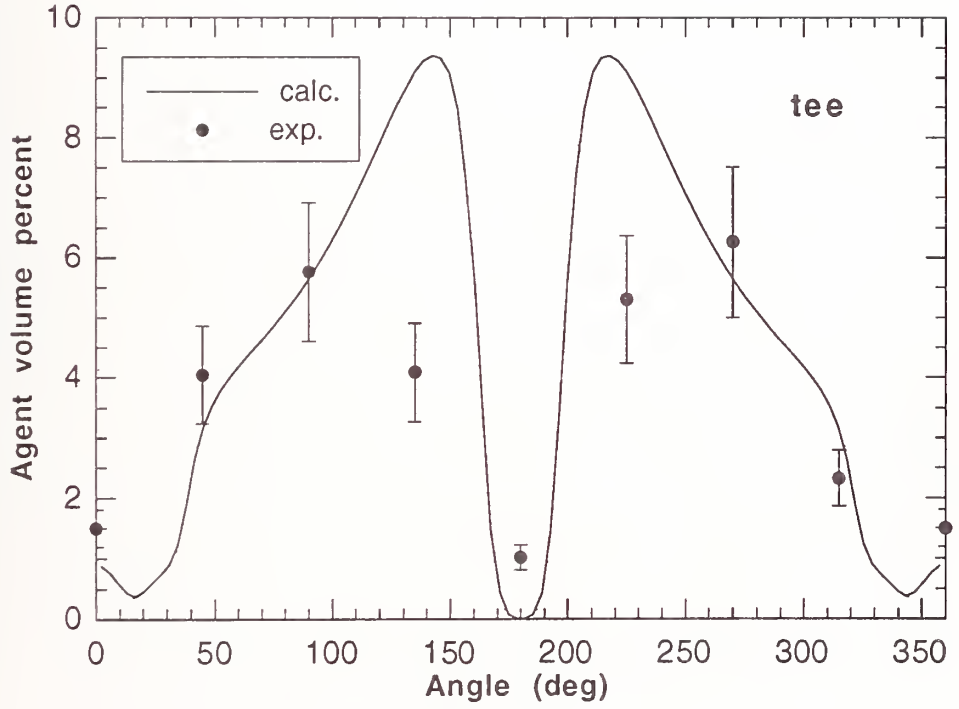

Figure 49. A comparison of the measured and calculated agent volume percent distribution 96 cm downstream from the agent injection tee. The average air velocity was 3.0 m/s and the agent flow was 0.012 m^3/s (Case 1).

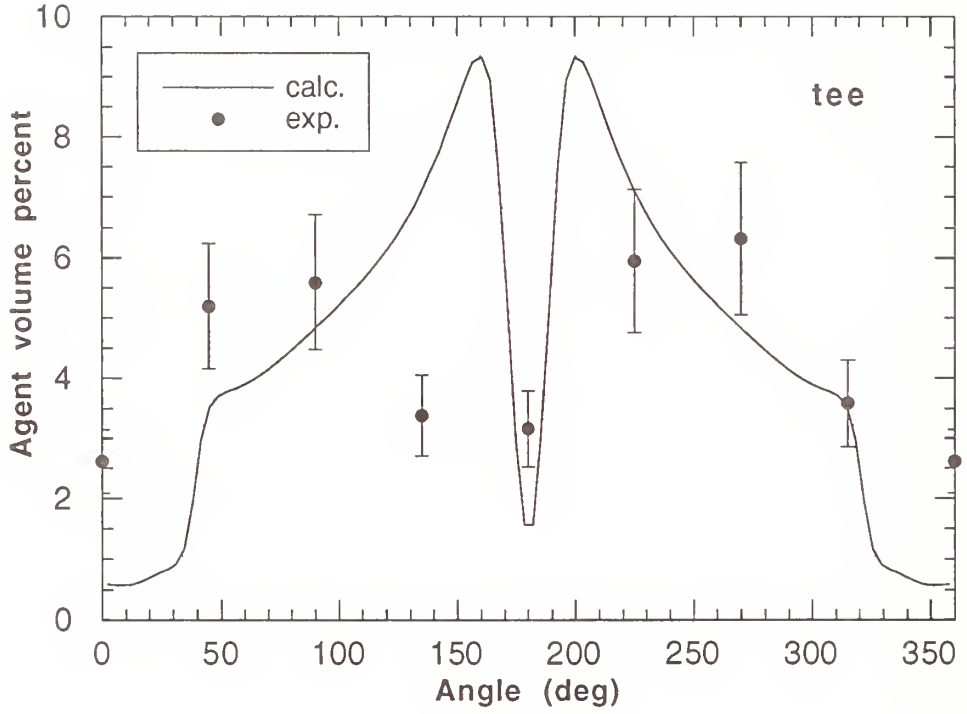

Figure 50. A comparison of the measured and calculated agent volume percent distribution 184 cm downstream from the agent injection tee. The average air velocity was 3.0 m/s and the agent flow was 0.012 m^3/s (Case 1).

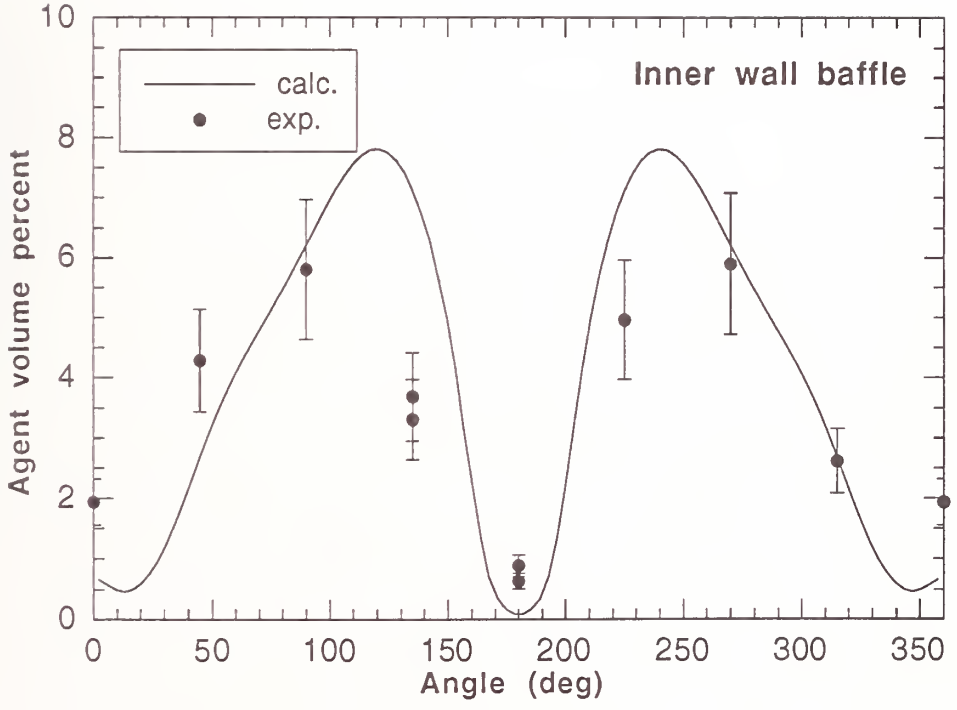

Figure 51. A comparison of the measured and calculated agent volume percent distribution, 96 cm downstream from the agent injection tee for Case 7, a baffle on the inner wall.

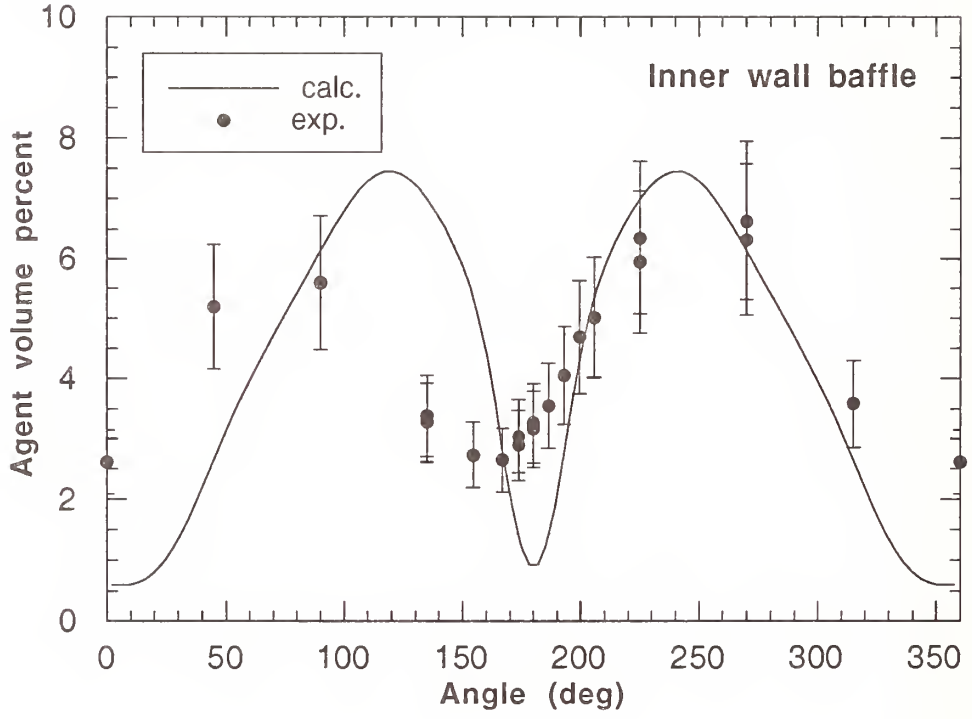

Figure 52. A comparison of the measured and calculated agent volume percent distribution, 184 cm downstream from the agent injection tee for Case 7, a baffle on the inner wall.

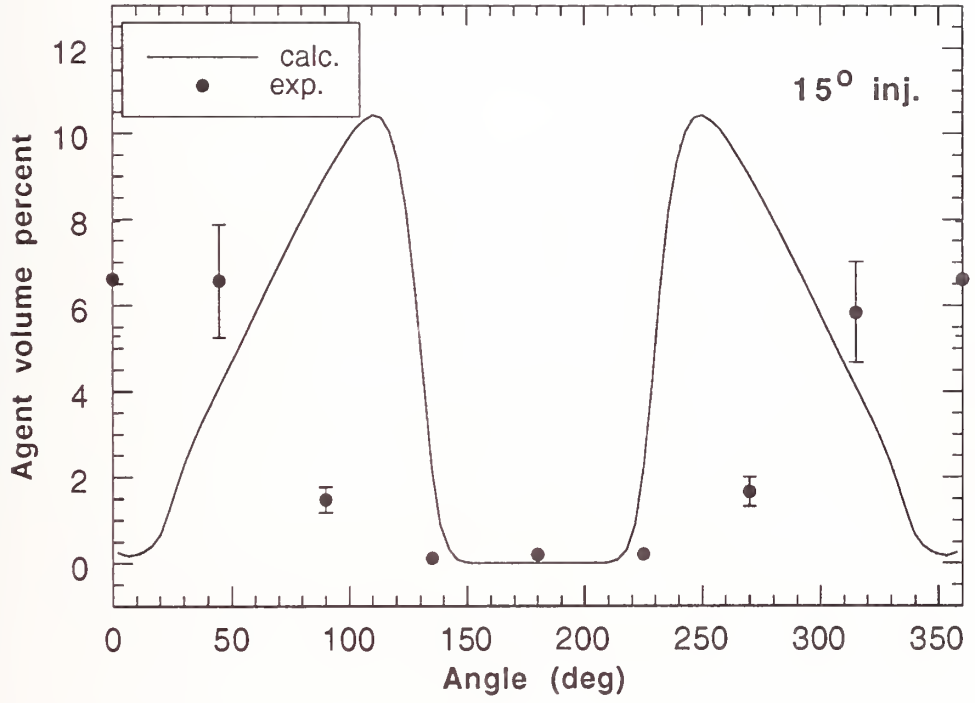

Figure 53. A comparison of measured and calculated agent volume percent distribution 96 cm downstream from the (15°) injection tube. The air velocity was 3.0 m/s and the agent flow was 0.012 m^3/s (Case 8).

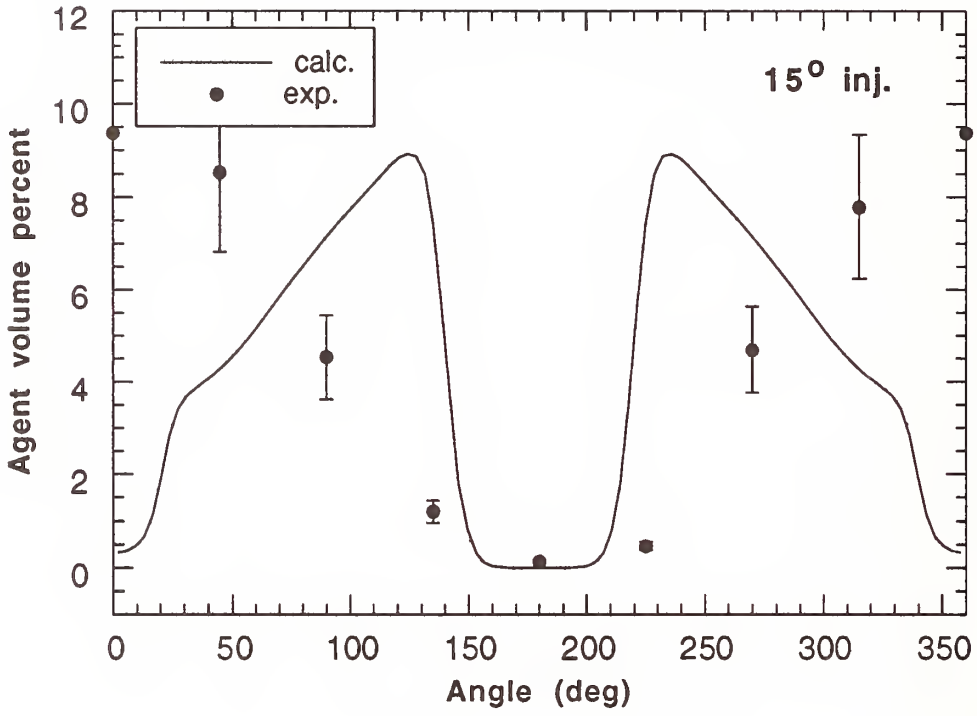

Figure 54. A comparison of measured and calculated agent volume percent distribution 184 cm downstream from the (15°) injection tube. The air velocity was 3.0 m/s and the agent flow was 0.012 m^3/s (Case 8).

in the numerical calculations. The numerical computations predict localized regions of high concentrations which are not observed in the experiments.

There are several possibilities that may explain these differences. Most involve the use of correct boundary conditions for the air and agent flows. Another possibility explored was the variation in the spread angle of the agent jet. Several angles from 0° to 5° were examined with little change in agent concentrations. If the actual spread angle was much greater than 5°, then the calculated agent concentration distribution downstream would be more diffuse, more closely matching the experimental measurements.

Another possible explanation for the difference between computations and experiments was that the agent flow exiting the tee was not properly modeled. The assumption that the agent velocity exiting the tee was uniform over the entire opening was tested and the agent flow characteristics inside and near the exit of the tee were examined as illustrated in Figure 55. The grid near the tee exit was resolved into 20 x 20 grid cells instead of the 2 x 4 grid cells used in Cases 1 to 13. The fluid velocity is indicated by the length and direction of the vectors. The agent concentration is indicated by the gray scale. Note that the velocities (as indicated by arrow length) are much higher near the top of the tee than the bottom due to the presence of the recirculation zone near the bend in the tee. The agent velocity then was approximately twice the average velocity in the top half and zero in the bottom half. This detailed flow pattern was used as a boundary condition at the tee in a case similar to Case 1 with the result that downstream agent concentrations did not change appreciably.

Another possibility explanation for the modeling/experimental differences is associated with the error introduced through the k-ε turbulence model. Empirical parameters were used to calibrate the k-ε model. Though the k-ε parameters used here were calibrated for applications involving air flow, they may be incorrect for this particular application. Another possibility involves the interaction of the agent jet with the side walls of the nacelle tube. It is important to resolve the boundary layer at the wall properly in order to account for the aerodynamic drag of the bulk flow. It was thought that the grid resolution near the wall was sufficient. This was checked by refining the grid, which resulted in little change in the calculated agent concentration.

Because of the discrepancy between measurements and computations, many model parameters were varied in order to examine the sensitivity of results to changes or uncertainty in input parameters. The model parameters that were investigated were the average agent inlet velocity, the spread angle of the agent leaving the nozzle, the velocity distribution of the agent across the nozzle, the average air velocity, the distribution of the air velocity across the air inlet, and the turbulent intensity boundary conditions for both the air and agent flows. To summarize, the model is most sensitive to the ratio of the agent inlet velocity to the air inlet velocity. The other parameters noted above did not have a significant effect on the simulated distribution of agent in the mock nacelle. Figure 56 shows results from Cases 1 and 14-16. These cases were the same except that the air inlet velocity varied from 3.0 m/s for Case 1, to 4.0 m/s for Case 16. Note that the region of high concentration for Case 1 (3.0 m/s) was located approximately three-quarters (135°) of the way around the tube from the inlet tee (whereas the region of high agent concentration in the 4.0 m/s case was located from one-quarter (45°) to one-half (90°) of the way around the nacelle. Similar results were found when varying the agent inlet velocity (or equivalently the inlet mass flow). Small increases in agent inlet velocity enabled the agent to traverse farther around the nacelle. The model is not sensitive to the velocity profiles of the agent and air (as long as the average velocity across the inlet remained constant), turbulence levels, or the spread angle of agent exiting the injector.

9.4.4 Numerical Simulations. Shaded contours of volume concentration are presented in the plane of injection and at 96 cm and 184 cm downstream from the injection plane in Figures 56-61 for all of the cases listed in Table 9.

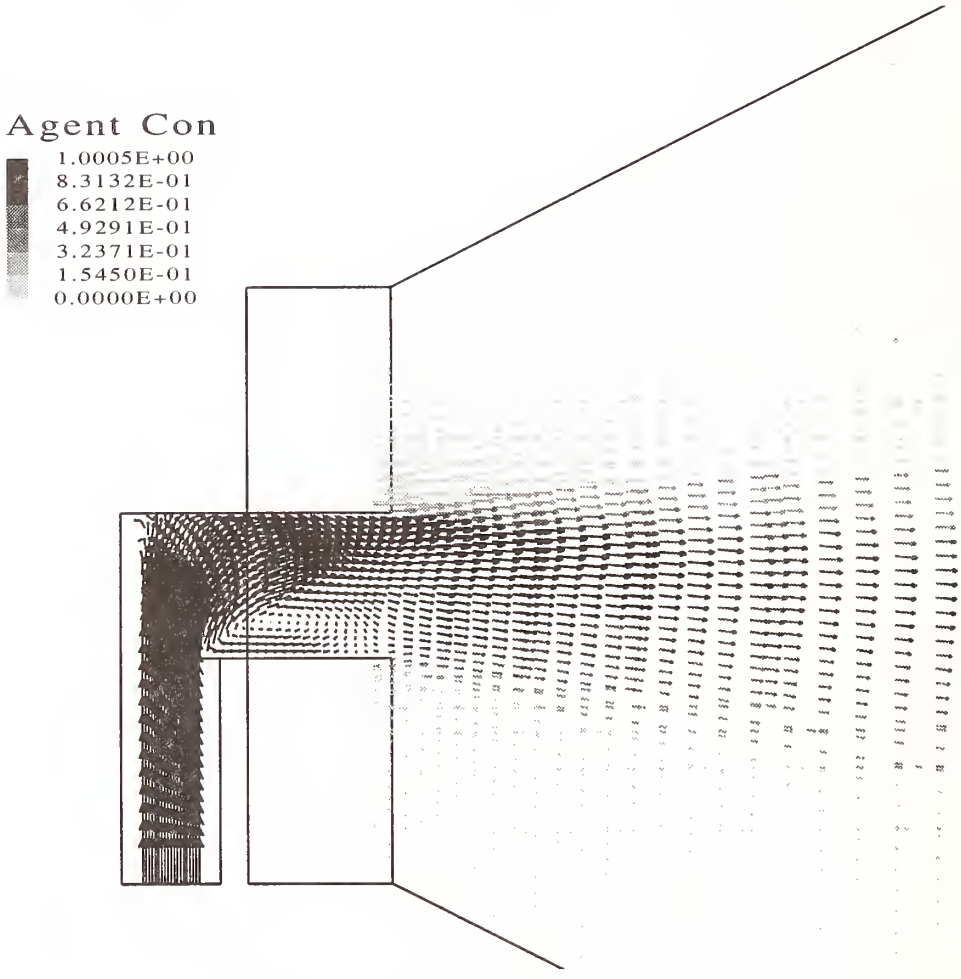

Figure 55. The character of the agent flow inside and near the exit of an injection tee. The fluid velocity is indicated by the length and direction of the arrows.

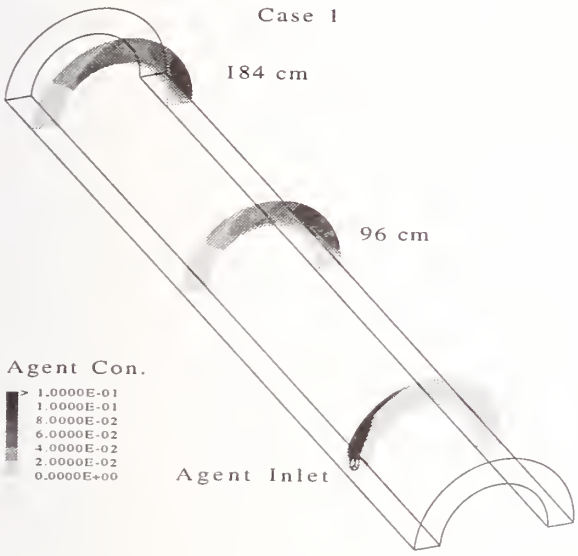

(a) 3.0 m/s

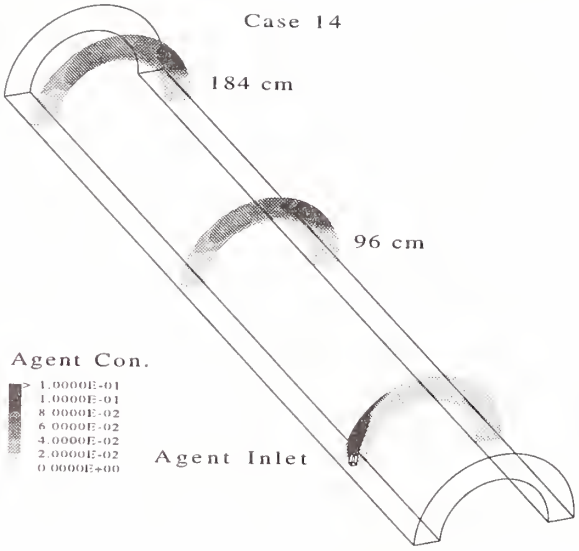

(b) 3.25 m/s

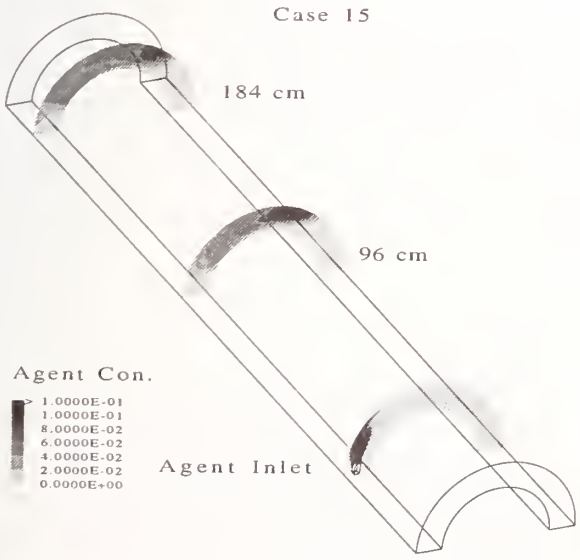

(c) 3.5 m/s

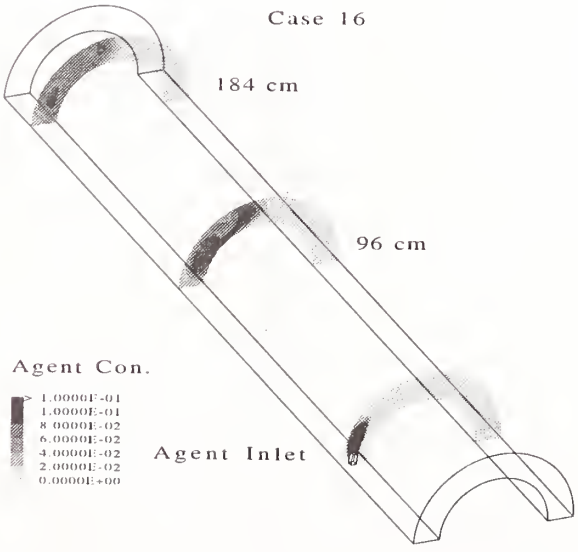

(d) 4.0 m/s

Figure 56. The calculated agent concentration in three vertical planes for Cases 1, and 14-16, for agent injected through a single tee for air velocities vaarying from 3.0 m/s to 4.0 m/s. The agent flow was 0.012 m^3/s.

Figure 57 presents results from Cases 1-3 (see Table 9). The total mass flow rate was 0.012 m^3/s. The agent inlet velocity for the two tee case was 50 % of the one tee case and the inlet velocity for the four tee case was 25 % the velocity of the one tee case, such that the total agent flow into the nacelle was constant. The agent volume fraction in the figure is indicated by the gray scale. Its value varied from near zero to greater than 10 %. The simulations predict that injecting agent at several locations around the nacelle results in a more even distribution of agent down stream.

Figure 58 presents results from Cases 4-6. The conditions were the same as those in Cases 2-4 except that the total agent flow rate was doubled to 0.025 m^3/s. Again, with more agent inlets, the agent distribution was more even downstream.

Figure 59 shows the computed results for Case 7, where the fluid flows past a baffle on the interior wall of the nacelle. The results for Case 1, with identical conditions except no baffle present, are also shown. The baffle does not significantly influence the agent concentration distribution.

Figure 60 compares Cases 8-10 with the agent introduced through tubes inclined 15° downstream rather than through a tee (see Figure 45). The total agent flow was 0.012 m^3/s, the same as that used in Cases 1-3. Compared to Figure 58, the agent distribution was marginally better when it was introduced by the tees. Again, the agent distribution was more even downstream when agent was introduced at multiple locations around the nacelle.

Figure 61 compares Cases 11-13 with agent introduced through a tube inclined 15° from the perpendicular to the axis in the downstream direction. The total agent flow was 0.025 m^3/s, twice that used in Cases 8-10.

9.4.5 Conclusions. The use of flow field modeling can facilitate design optimization of an agent delivery system. The capability of computational fluid dynamics to model gaseous agent concentration in a generic engine nacelle should not, however, be fully accepted until it has been experimentally validated for representative flow conditions. In general, the CFD model has shown that an injector in the shape of a tee (with the tee oriented perpendicular to the flow direction) enhanced agent dispersion as compared to a single agent inlet (oriented 15° downstream). In addition, the simulations showed that increasing the number of agent injection nozzles increased agent dispersion. A baffle had little impact on the downstream agent dispersion for agent injected from a tee. Research remains to properly model two-phase agent flow and rapid evaporation in a nacelle environment (see Section 8 of this report for a discussion of two-phase flow modeling).

9.5 A Simple Model for Agent Delivery Requirements

A simple model describing the agent delivery requirements for engine nacelle fire suppression was developed as a complement to full-scale nacelle fire testing. Preliminary design guidelines for estimating agent mass requirements and the specific system performance criteria, agent concentration and duration, were proposed for each alternative agent using the model results. It must be pointed out that the proposed guidelines must be related to actual fire suppression system performance and appropriate safety factors applied to the mass requirements.

9.5.1 Simple Mixing Models Applied to Engine Nacelle Fire Suppression. The development of Military Specification (Mil E 22285) described in Section 9 suggests a conservative approach in terms of system performance. The sections of that Military Specification of interest here are the guidelines for agent amount, discharge time, and specific performance criteria (agent concentration and duration) of a suppression system. The guidelines for agent amount are meant to aid system designers in

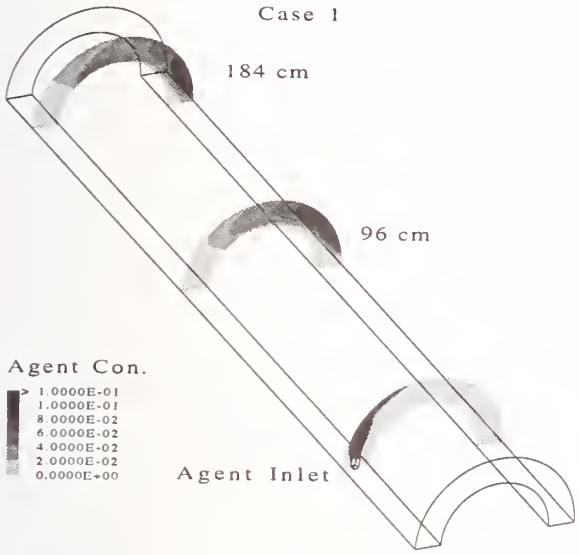

(a) One tee

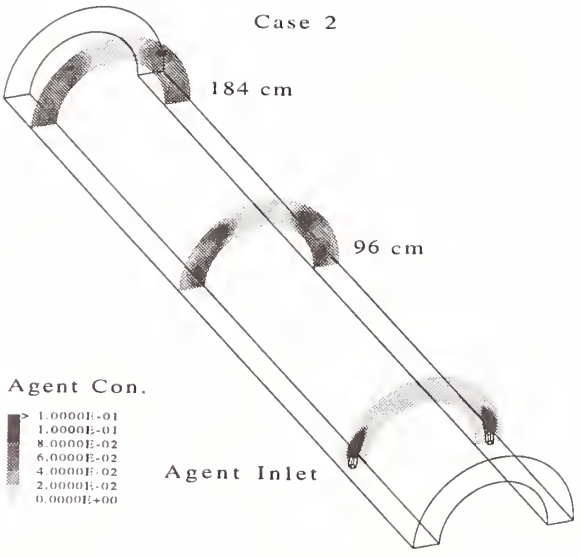

(b) Two tee's

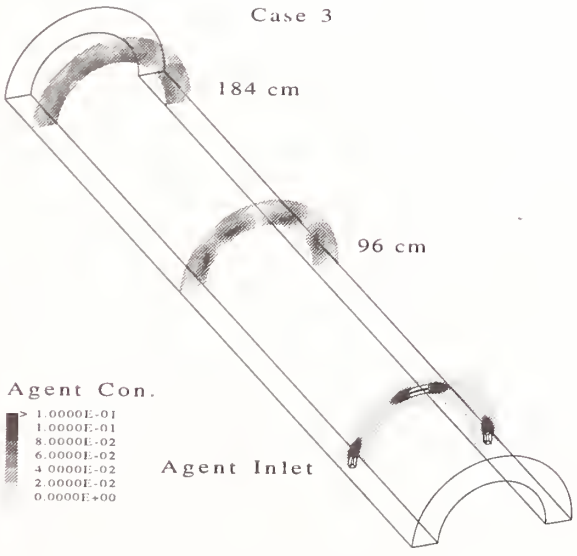

(c) Four tee's

Figure 57. The calculated agent concentration in three vertical planes for Cases 1-3, for agent injected through one, two, and four tees. The bulk air velocity was 3.0 m/s. The agent flow was 0.012 m^3/s.

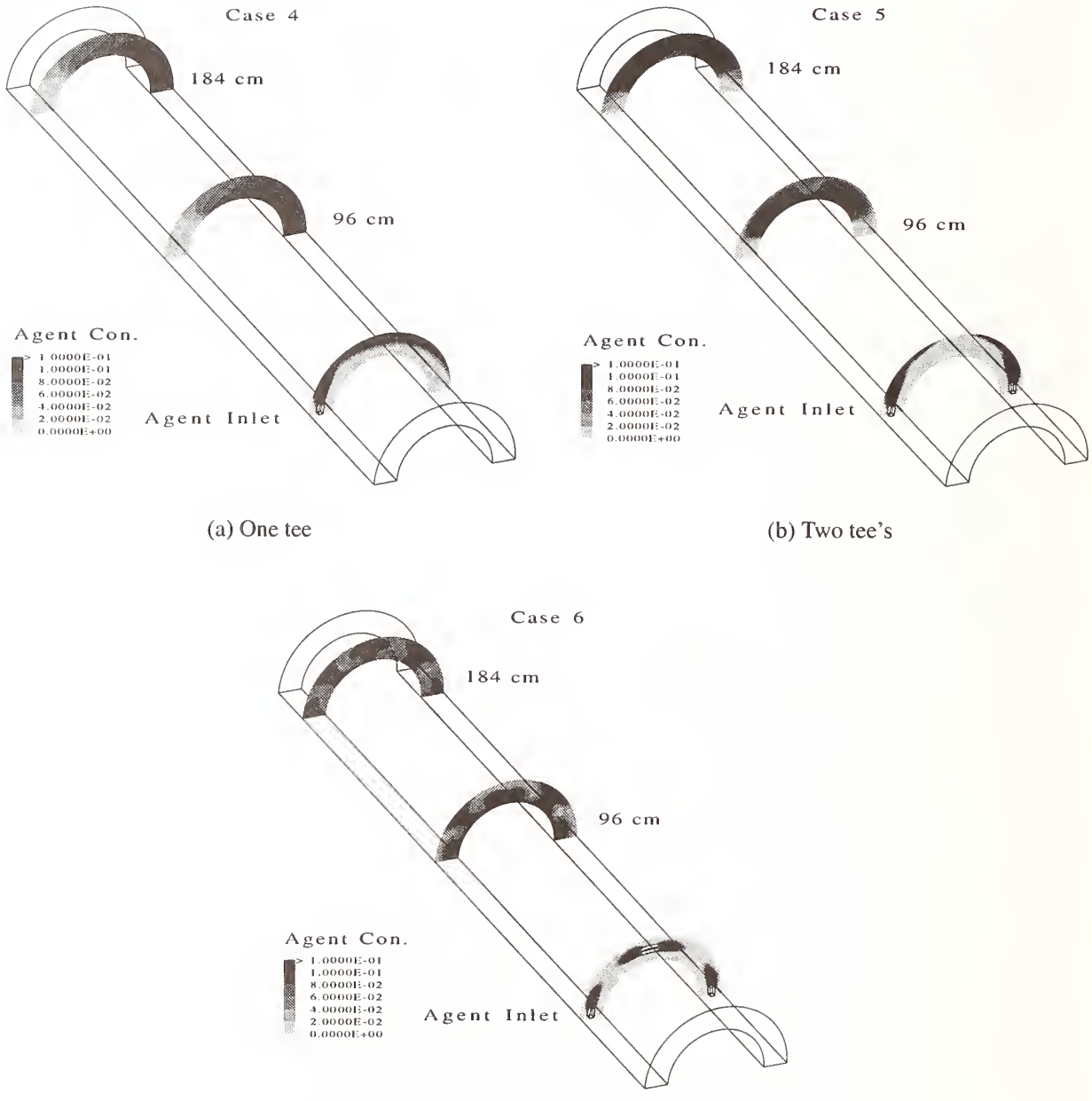

(a) One tee

(b) Two tee's

(c) Four tee's

Figure 58. The calculated agent concentration in three vertical planes for Cases 4-6, for agent injected through one, two, and four tees. The bulk air velocity was 3.0 m/s. The agent flow was 0.025 m^3/s.

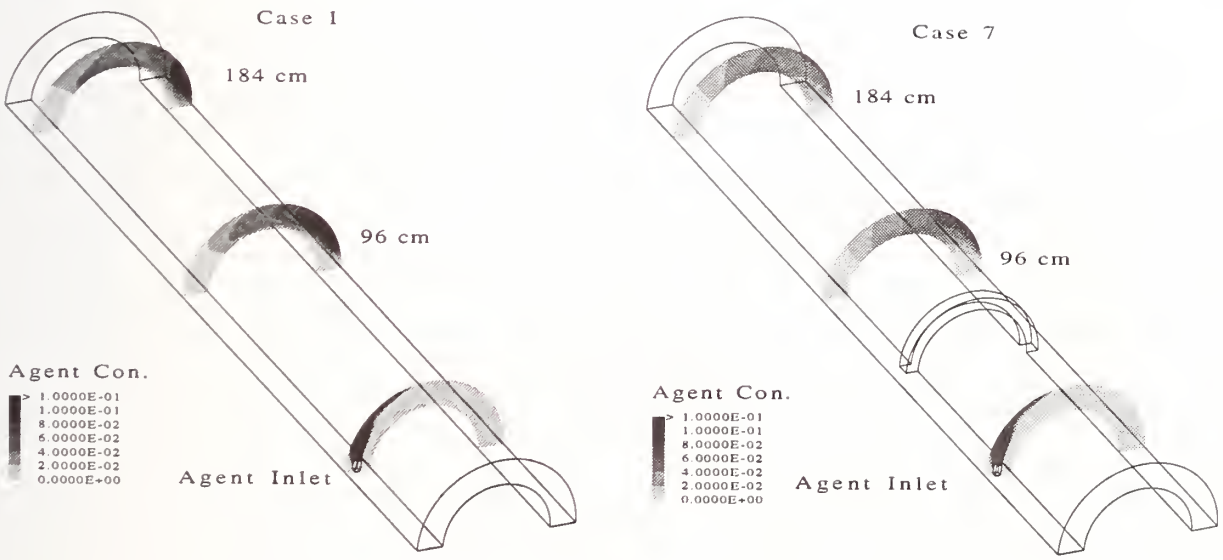

(a) No baffle

(b) baffle

Figure 59. The calculated agent concentration in three vertical planes for Case 7, for flow past a baffle on the inner wall, as compared to no baffle (Case 1). The bulk air velocity was 3.0 m/s. The agent flow was 0.012 m^3/s.

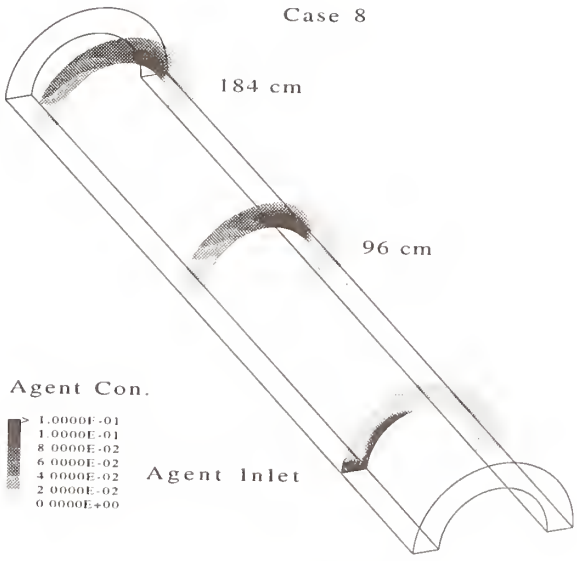

(a) One inlet

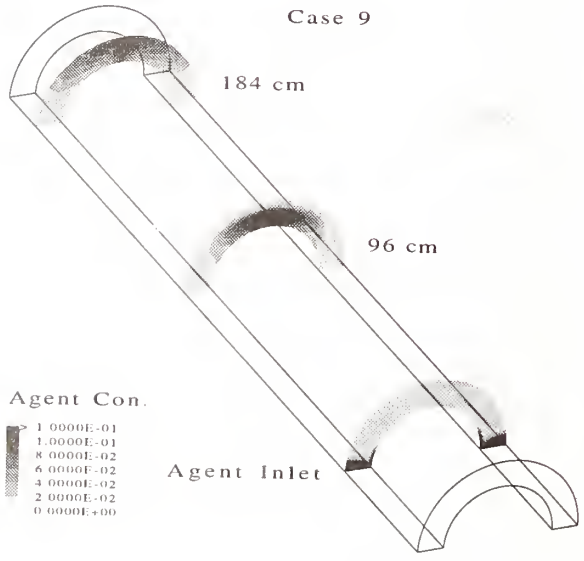

(b) Two inlet's

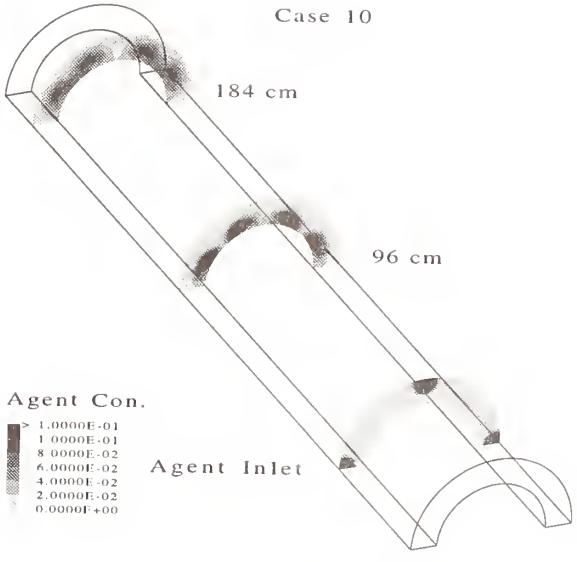

(c) Four inlet's

Figure 60. The calculated agent concentration in three vertical planes for Cases 8-10, for agent injected through one, two, and four inclined tubes. The bulk air velocity was 3.0 m/s. The agent flow was 0.012 m^3/s.

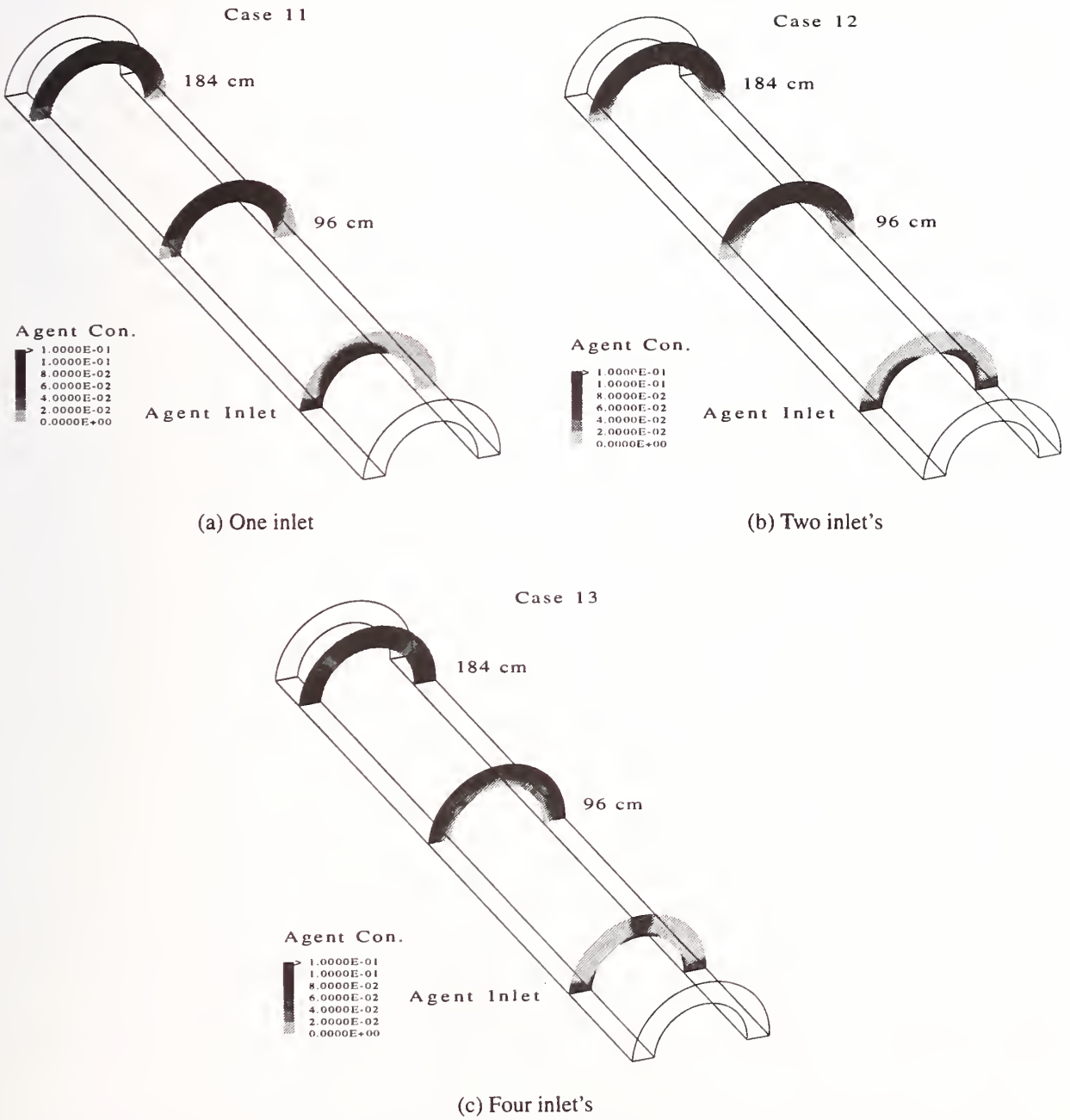

(a) One inlet

(b) Two inlet's

(c) Four inlet's

Figure 61. The calculated agent concentration in three vertical planes for Cases 11-13, for agent injected through one, two, and four inclined tubes. The bulk air velocity was 3.0 m/s. The agent flow was 0.025 m^3/s.

meeting the performance criteria set forth in the Military Specification. An alternative agent will have different suppression characteristics, which will preclude the use of the Military Specification as it stands. Guidelines for designers and performance criteria for alternatives to halon 1301 are required for safe and efficient system design.

Keeping in mind that the likely halon 1301 replacement may require a much higher volumetric concentration to be effective in extinguishing nacelle fires, a logical question is: "what are the implications of a higher agent target concentration relating to design guidelines and performance criteria?" A direct method to explore the impact of design parameters and system variables is to perform a series of full-scale fire tests, varying design parameters (agent, injection rate) and system variables (air flow, volume, nacelle geometry, fire scenario, etc.) to determine how those variables impact the minimum agent mass required to suppress the fires. Tests with and without fires would also be needed to relate certification test results to the worst case fire scenario suppression requirements. Clearly, the number of full-scale tests would be very large, essentially repeating the early CAA research for each alternative agent. The full-scale testing performed at Wright-Patterson AFB for the Halon Replacement Program for Aviation was limited in terms of air flows, configurations, and fire scenarios, although a number of other variables were examined.

A complementary method to full-scale testing proposed here is a model that describes the agent delivery requirements for generic nacelle geometries. The model was used to explore the impact of air flow, mixing modes, nacelle volume, agent injection duration, and fire scenario on the agent requirements for suppression. All of the details of mixing are not simulated, nor are they known for a generic nacelle geometry, but limiting cases were covered which suggest the values of the minimum agent mass delivery rates to achieve flame suppression. Allowances for un-modeled phenomena such as imperfect mixing, inadequate description of the fire scenario and additional safety factors need to be considered for a conservative design methodology.

The model is based on idealized global mixing models describing agent dispersion and dilution for the bulk temporal concentration, and a local mixing model for flame extinction or concentration build-up at specified locations. The local mixing phenomena were inferred from small-scale experiments previously described in Section 9.3. In principle, computational fluid dynamics (CFD) could provide the answers pertaining to dispersion and the concentration profiles for every single configuration, but at this point, it is impractical to do such calculations because current CFD capability cannot provide a comprehensive description of fire suppression phenomena. Although CFD can provide answers pertaining to agent dispersion and mixing in specific nacelle-like configurations, it is not yet possible to do such calculations with consideration of two-phase flow for both agent and fuel and the detailed inhibition chemistry associated with the replacement agents. Nor is it possible to model all in-flight nacelle conditions, each with its own very different time-varying temperature and flow boundary conditions. Although CFD may prove to be a useful tool in specific applications and future designs, the focus here was to provide simple guidelines on alternative agent delivery rates for engine nacelle fire protection system designers. It is highly likely that discharge testing with concentration measurements for certification will remain relevant to document system performance when an alternative agent is used. Therefore, the relationship between certification criteria and flame suppression requirements needs to be explored for the alternative agents.

The mixing models presented here for the bulk flow are well known, and have been used for decades to describe industrial mixing in blending operations and concentration profiles in chemical reactors. The mixing extremes that are covered are the plug flow "segregated" case and the perfectly stirred "homogenous" case. The plug flow model assumes either no mixing of the components (the extreme) or mixing with the incoming air flow only. The perfectly stirred scenario implies intense, chaotic motion leading to a spatially homogenous system. A definition of a perfectly stirred system is that any given particle after being introduced into the volume has an equal probability of being

anywhere in the mixing volume, and as a consequence, the concentration is uniform throughout the mixing volume. Such a model was successfully employed in Section 9.3 to treat flame extinction in a recirculation zone. In chemical reactors, plug flow is typically assumed for tubular reactors, where the mean velocity profile is unidirectional. An example of a system that approaches perfectly stirred behavior is a liquid-filled tank with an impeller operating at high speed. Deviations from true plug flow occur with turbulent backmixing or molecular diffusion leading to axial dispersion. Deviations from the perfectly stirred case occur from quiescent "dead" spaces in the volume, concentration boundary layers, and by-passing of incoming fluid. In many cases the phenomena giving rise to the deviations from the ideal cases can be modeled or quantified by experiments if sufficient effort is expended.

In the bulk flow models, deviations from the idealized cases were not considered. The description of a particular nacelle is given by any number of perfectly stirred or plug flow regions in series and/or parallel. The transfer of agent from one region to another was taken into account by solving the transient mass balance equations for each region. The agent is assumed to be introduced as a gas, which then mixes isothermally with air.

The agent concentration for any given location as a function of time is required to assess the suppression system performance. One extreme case is to assume that the agent flows as a plug and does not mix with the air stream. Thus, the bulk "free stream" concentration is 100 % for the volume occupied by the plug, and its duration at any location in the nacelle is equal to the nacelle volume (V) divided by the total (air and agent) volumetric flow ($\dot{Q}_{total}$). The next case is where the agent mixes perfectly with the incoming air stream, and flows downstream as a plug. A good approximation would be agent dispersed from many locations in a cross section with flow in one direction. The bulk "free stream" concentration is equal to the agent volumetric flow ($\dot{Q}_{agent}$) divided by the total (agent and air) volumetric flow ($\dot{Q}_{total}$). The duration at any location is equal to the nacelle volume divided by the volumetric flow ($V/\dot{Q}_{total}$).

For a perfectly stirred region (PSR), the steady-state (long agent injection duration) bulk concentration is equal to the agent volumetric flow divided by the total flow of agent and air ($\dot{Q}_{agent}/\dot{Q}_{total}$). The mixing volume and total volumetric flow determines the dynamics of the concentration build-up. Assuming isothermal, constant volume conditions, the solution to the mass balance equation for a step change in agent flow entering the nacelle is:

$$X(t) = X_f + (X_0 - X_f)(e^{-t/\tau_1}) \tag{26}$$

where X(t) is the volumetric concentration in the nacelle, X_f is the volumetric agent concentration entering the nacelle ($\dot{Q}_{agent}/\dot{Q}_{total}$), X_0 is the initial concentration, and τ_1 is the characteristic mixing time given by the mixing volume divided by the total volumetric flow ($V/\dot{Q}_{total}$). A step change from a fixed volumetric flow of agent, to zero agent flow gives

$$X(t) = X_p(e^{-t/\tau_2}) \tag{27}$$

where X_p is the concentration in the PSR when the agent flow is stopped (at time t=0) and τ_2 is the characteristic time given by the total volume divided by the air flow ($V/\dot{Q}_{air}$).

The solutions above for step changes in the incoming stream concentration and flow are indicative of cases where the initial agent injection takes place in a perfectly stirred region, or a constant concentration plug flow feeds a perfectly stirred region. Analytical solutions are obtainable for other cases where the concentration of the incoming flow is a known function of time. A relevant case is

when one perfectly stirred region provides the feed to another perfectly stirred region (PSRs in series). This situation is a reasonable model for certain nacelles (see Section 9.5.2). The solution to the concentration in the second PSR is given by one of the following equations below. If the feed concentration is given by Equation (26), the solution to the concentration in the second PSR is:

$$X(t) = X_p e^{-t/\tau_3} + K(1 + \frac{\tau_1}{\tau_1 - \tau_3}(e^{-t/\tau_3} - e^{-t/\tau_1}) - e^{-t/\tau_3}) \tag{28}$$

if $\tau_1 \neq \tau_3$ and

$$X(t) = X_0 e^{-t/\tau_3} + K(1 - e^{-t/\tau_3}) - \frac{K}{\tau_3} t e^{-t/\tau_3} \tag{29}$$

if $\tau_1 = \tau_3$, where K is the constant feed concentration into the first PSR multiplied by the fraction of the total flow entering the second PSR and τ_3 is the volume of the second PSR divided by the volumetric flow rate into that PSR. If the feed concentration is given by Equation (27), the solution for the concentration in the second PSR becomes

$$X(t) = (X_0 - K_p \frac{\tau_2}{\tau_2 - \tau_3}) e^{-t/\tau_3} + K_p \frac{\tau_2}{\tau_2 - \tau_3} e^{-t/\tau_2} \tag{30}$$

if $\tau_2 \neq \tau_3$ and

$$X(t) = (\frac{K_p}{\tau_3} t + X_0) e^{-t/\tau_3} \tag{31}$$

if $\tau_2 = \tau_3$, where K_p is the peak concentration achieved in the first PSR multiplied by the fraction of total flow entering the second PSR and X_0 is the initial concentration in the second PSR. Likewise, solutions for more PSRs in series begin with the solution to the previous PSR.

So far the bulk or "free stream" concentration has been described. A description of agent mixing from the free stream into eddies behind bluff bodies in the case of certification concentration and into fire locations is needed in order to relate certification concentration and duration to agent requirements sufficient to extinguish various types of fires. This local mixing phenomena is described in terms of a characteristic mixing time, analogous to the characteristic mixing time described for the PSR bulk mixing. The location of a certification probe may likely be in an eddy behind a bluff body (rib, etc). In that case the characteristic mixing time depends on the flow velocity, viscosity and characteristic dimension of the bluff body as shown in Section 9.3.6. For the flows considered here, the diffusive term can be ignored since the mixing is convection dominated.

Mixing from the free stream into a fire stabilized behind a bluff body is much slower than mixing into the same location without any fire due to the expanding hot gases increasing the fluid viscosity which affects the flow field and the rate of agent entrainment or mixing. Two different baffle

stabilized fire scenarios were explored; a spray fire, and a pool fire. Extinction times for both scenarios were fit to the same first order equation, Equation (14):

$$X_\infty = X_c (1 - e^{-\Delta t/\tau_f})$$

where X_∞ is the critical free stream agent concentration at extinction for long injection durations ($\Delta t > 3\tau_f$), X_c is the critical free stream agent concentration for short agent injection intervals, and τ_f is the characteristic mixing time associated with the given fire scenario as discussed in Section 9.3.

Considering the characteristic mixing times for combusting and non-combusting cases, it is obvious that local mixing behind baffles is very different. This observation necessitates that relationship between the certification test and real fire scenarios must be explored so that certification criteria specify safe conditions for the worst case fire scenario considered.

9.5.2 Agent Requirements for Generic Nacelles. Two generic nacelle models are described below which represent the extremes in the bulk mixing phenomena.

Model No. 1 — It is assumed that the bulk flow of agent is a plug flow and the fire zone or certification locations are located downstream from the injection plane. Perfect mixing of agent and air occurs at the injection plane.

Model No. 2 — The entire nacelle volume is treated as a perfectly stirred region. The bulk flow feeds the fire zone or certification locations.

A real engine nacelle may behave closer to one of these generic descriptions than the other. The geometry, air entrance location, air and wall temperatures, agent injection location, and flow exit will impact the mixing and dispersion. For instance, the F-111 has air entering the nacelle uniformly across the radial cross-section, and exits the through an ejector at the end of the nacelle. Agent is introduced through a tee fitting located at the most forward position of the nacelle to spread the agent around its co-annular nacelle cross-section (McClure *et al.*, 1974). With this configuration, it is easy to imagine that there is no significant air or agent back flow, and the bulk of the agent would flow as a plug mixed with air. The F/A-18 on the other hand has a much different configuration. The nacelle air is introduced through an air ram located on the bottom of the aircraft and positioned between the forward and aft of the nacelle. The flow exits through two small vents located on the top and the bottom of the aircraft near the aft position (Picard *et al.*, 1993). Agent is introduced through a tube located at the forward-most position of the nacelle. Prior to agent release there must be reversed flows giving rise to recirculation zones and dead zones with no air flow. During and after agent release, the recirculation zones act as perfectly stirred regions. Instead of a plug flow of agent and air, the nacelle will undergo a rapid increase in agent concentration followed by a slower tailing. This behavior was observed qualitatively during some discharge testing with halon 1301 and HFC-125 in an F/A-18 (Leach, 1994). No specification of a smooth or rough nacelle geometry has been made in the generic models. The specific nacelle geometry is handled by the certification and fire characteristic times chosen. It was assumed that in smooth nacelles, no baffle stabilized pool fires could form and for now, the worst case fire for the smooth nacelle geometry was taken as a baffle stabilized spray flame. For rough nacelles (defined as those nacelles with ribs or other obstructions that can stabilize pool fires), the worst case fire was taken as a baffle stabilized pool fire.

9.5.2.1 Minimum Fire Suppressant Requirements. A parametric study was employed to determine the required agent amount for a range of discharge durations for the two nacelle models. The variables were nacelle type (smooth or rough which fixes the characteristic mixing times), free volume, air flow, agent density, discharge duration, and critical extinguishing concentration. The temperature and pressure were fixed at 20 °C and 101 kPa respectively. The nacelle volume range was from 0.25 m^3 to 8 m^3 in increments that double from the previous value and the air flow range was from 0.25 kg/s to 8 kg/s, also in increments that double from the previous value. These values cover the range of possible air flows and volumes in actual nacelles as listed in Table 1. In the following analysis, the incoming air flow was assumed to be a constant value; agent injection has no effect on the nacelle air flow. This would be the case when the air flow entering the nacelle is choked which can occur for a Mach number greater than one and represents the worst case scenario since dilution air flow is at its highest value. It is also assumed that during agent injection, the pressure rise inside the nacelle volume is negligible. The injection durations examined were 0.25 s, 0.5 s, 1.0 s, 1.5 s, and 2.0 s. This range covers a very rapid injection time (0.25 s) and an injection time twice the value specified in the Military Specification for halon 1301. This range will show when positive effects from rapid injection are to be expected, and when it may be possible to relax the discharge time requirements without having a drastic impact on the agent requirements. The discharge time significantly constrains hardware design (see Section 8.6 of this report). The agent mass flow rate is assumed to be a constant over the injection duration. This is a reasonable assumption given the pipe flow model results reported in Section 8.6.

For the simulations, the mixing times for the fire scenarios were fixed (not a function of air flow) and were specified to characterize worst case fires for these generic nacelles. Two different fire scenarios were considered; a baffle stabilized spray fire, and a baffle stabilized pool fire with characteristic mixing times (τ_f) taken as 0.1 s and 1.0 s, respectively. These values are consistent with the experimental measurements described in Section 9.3. The critical or maximum long injection time concentrations (X_∞) were taken as the cup burner extinction concentrations for the spray fire scenario. For the pool fire scenario, the results described in Section 9.3 served as input or in lieu of this data, the peak flammability limit of n-heptane flames was utilized (Malcolm, 1950). The peak flammability limits are a reasonable target concentration for an agent in the fire zone. This concentration insures that combustion of even the most flammable fuel/air ratio cannot occur and secures both flame suppression and the prevention of re-ignition. Note that the target concentration is for the combustion zone, not the free stream. These values are given in Table 10 along with the gas-phase density of the agent at 20 °C.

For nacelle model No. 1, an analytical expression for the minimum agent mass is given by

$$W_{ag} = \frac{\Delta t \, \rho_{ag} X_\infty \dot{W}_{air}}{\left(1 - \frac{X_\infty}{1 - e^{-\Delta t/\tau_f}}\right)\left(1 - e^{-\Delta t/\tau_f}\right)\rho_{air}} \tag{32}$$

where W_{ag} is the minimum agent mass, Δt is the injection duration, $\dot{W}_{air}$ is the mass flow of air, ρ_{ag} and ρ_{air} are the densities of agent and air at ambient conditions, and τ_f is the characteristic mixing time for the particular fire scenario. Observe that the nacelle free volume is not a variable in the equation, and thus does not impact the amount of agent for this nacelle model. For nacelle model No. 2, the minimum amount of agent is obtained by a numerical iterative procedure using Equations (28) and (31), replacing τ_3 with τ_f and solving for $X(t)=X_\infty$.

The results are presented graphically with agent mass as the dependent variable, air flow as the independent variable, and different symbols for each nacelle free volume. Results for each injection duration are presented in separate figures. Figures 62-66 are for a spray fire scenario with halon 1301 as the agent. In this and all other cases, nacelle model No. 1 (plug flow model) yielded the minimum amount of agent at any given air flow. Note also that as the volume decreased, the results for nacelle model No. 2 approached the plug flow results because the characteristic mixing time for the bulk flow approaches zero as the volume approaches zero. As the air flow approached zero, the agent mass

Table 10. Critical agent volume fraction for spray and pool fires

Agent	X_{∞}, spray fire	X_{∞}, pool fire	Agent density @ 20 °C (kg/m^3)
halon 1301	0.031	0.060	6.2
HFC-125	0.087	0.12	5.0
HFC-227	0.062	0.11	7.2
CF_3I	0.032	0.068	8.2

reached a limiting value, independent of injection time. Also, the agent requirements increased as injection time increased. What is not shown is that if the injection time were decreased below 0.25 s, a critical injection time is reached where a fire cannot be extinguished. Recall that agent mass is minimized when the free stream concentration is 100 %. But, in both nacelle models Nos. 1 and 2 the agent always mixes with air flow, therefore 100 % agent concentration cannot be achieved. In practical terms though, this result is unlikely to pose a problem since during any agent injection, there will be some spreading of agent both up and downstream. That spreading effectively increases the injection time and reduces the concentration.

Figures 67-71 are for a pool fire scenario with halon 1301. Again, as air flow decreased, the agent mass tended to a fixed value independent of injection time. The injection time that resulted in the minimum amount of agent was not the shortest injection time, but now depends on nacelle volume and falls between 0.5 s for the smaller volumes and 1.0 s for the larger volumes. In all cases the mass requirements were much higher than for the spray fire scenario.

Figures 72-76 show the results for HFC-125 in the spray fire scenario. Again, agent requirements were minimized for the 0.25 s injection as observed in the halon 1301 simulations. Figures 77-81 show the results for HFC-125 in the pool fire scenario. The minimum agent mass was obtained for injections between 0.5 s and 1.5 s, depending on the volume. In all cases, the agent mass was higher than the predicted values for halon 1301.

Figures 82-86 show the results for HFC-227 in the spray fire scenario. Agent requirements were lowest for the 0.25 s injection time. Figures 87-91 show the results for HFC-227 in the pool fire scenario. Injection durations between 0.5 s and 1.5 s minimized the agent mass requirements. As with the HFC-125 results, the agent mass requirements were higher than the halon 1301 values.

Figures 92-96 show the results for CF_3I in the spray fire scenario. Figures 97-101 show the results for CF_3I in the pool fire scenario. For the spray and pool fire cases, the injection duration that minimized the agent mass was 0.25 s and between 0.5 s and 1.5 s respectively. The agent mass requirements were still higher than halon 1301, but not as high as HFC-125 and HFC-227.

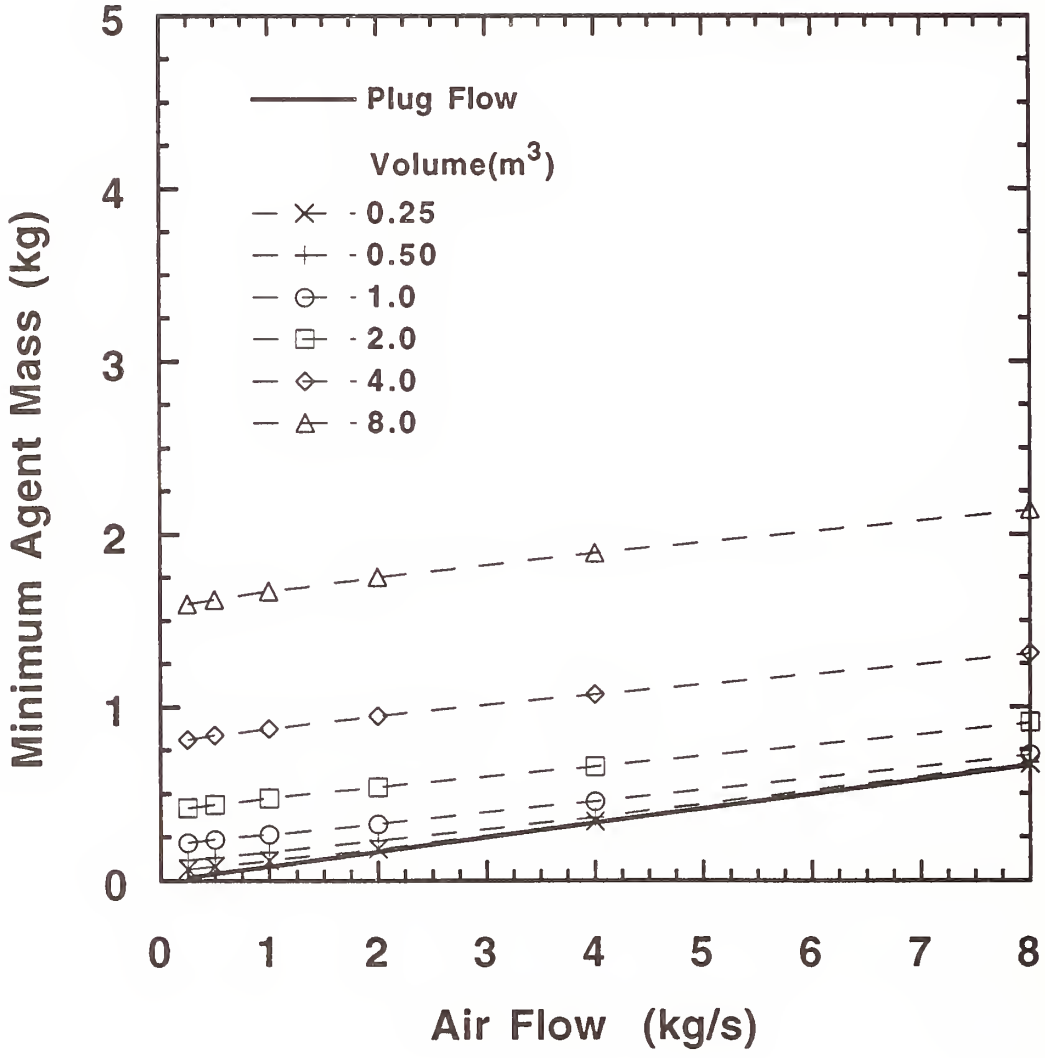

Figure 62. The minimum halon 1301 mass requirements for spray fire suppression as a function of air flow. The agent injection duration was 0.25 s.

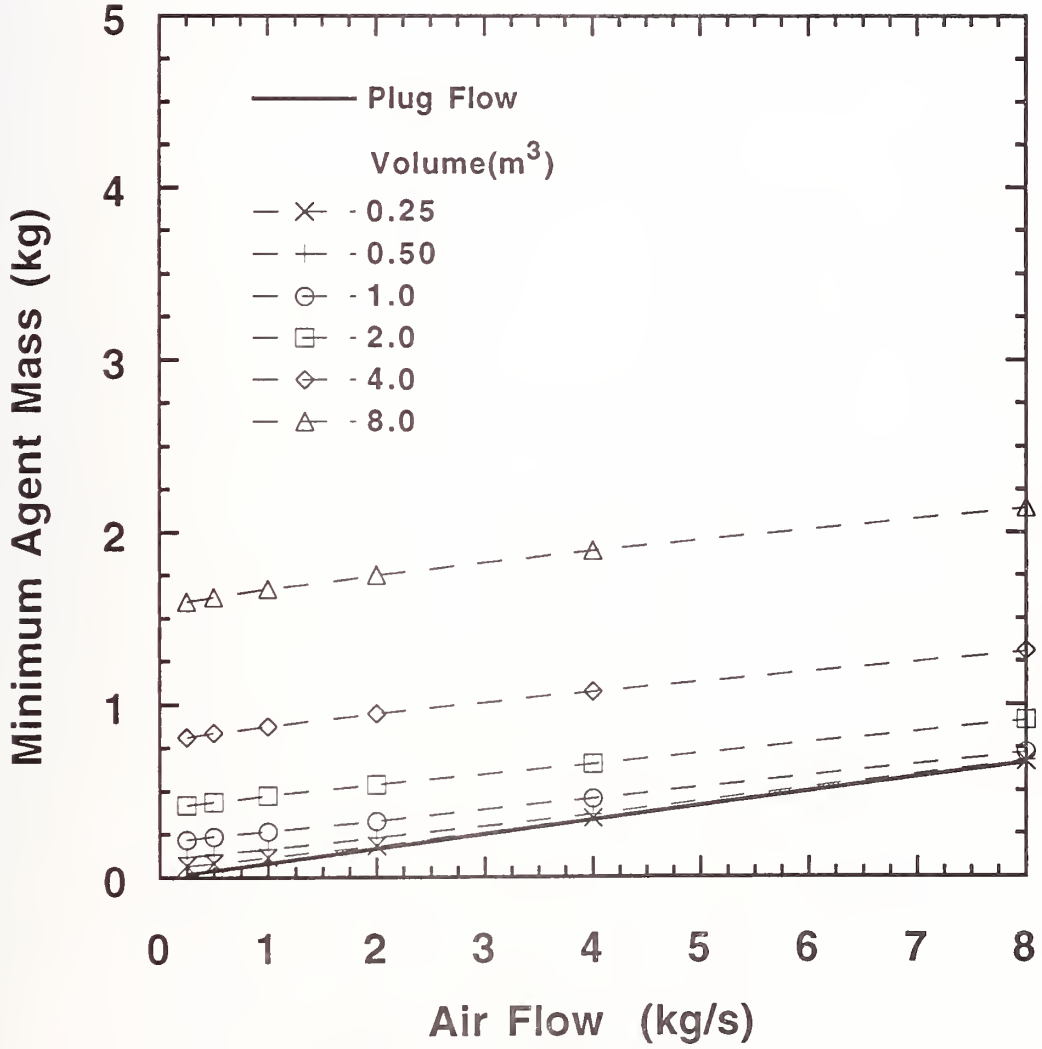

Figure 63. The minimum halon 1301 mass requirements for spray fire suppression as a function of air flow. The agent injection duration was 0.50 s.

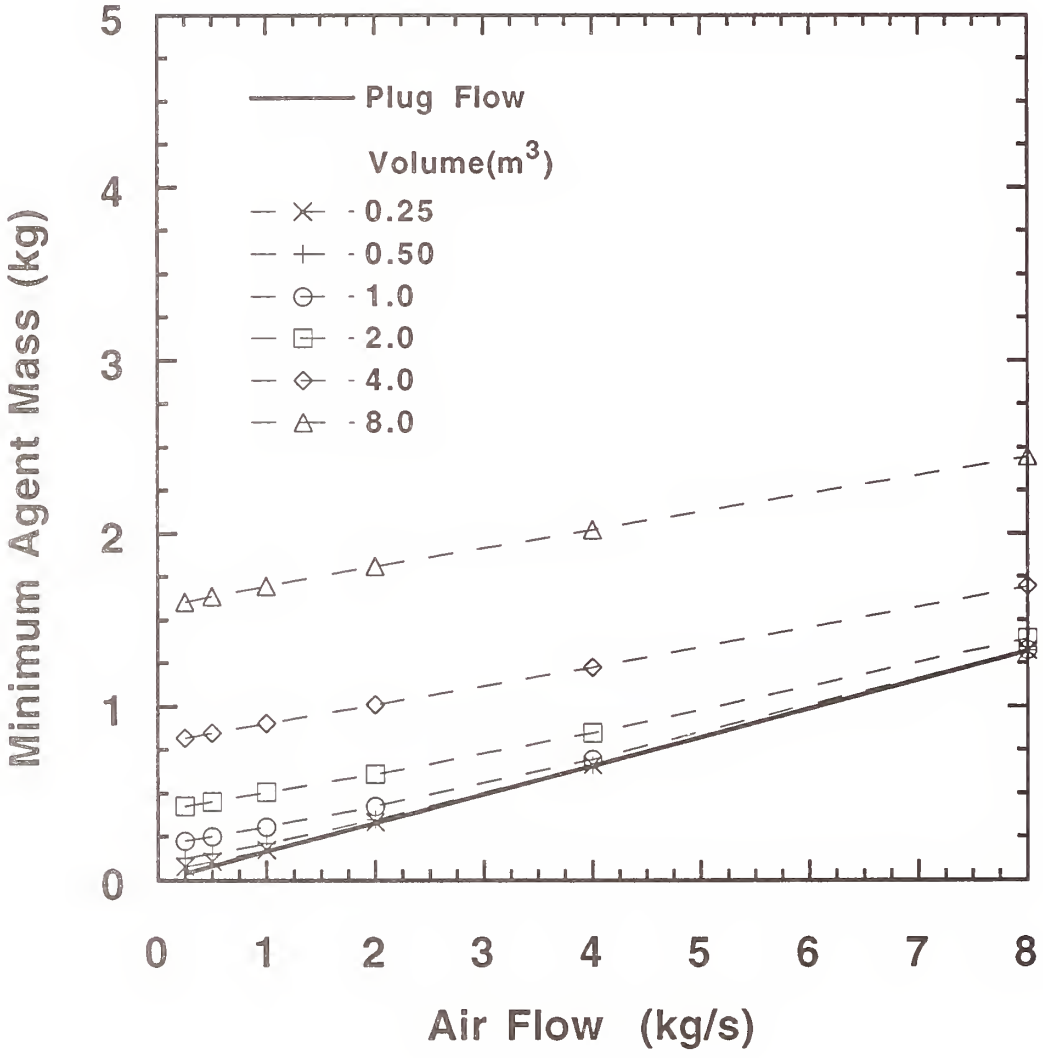

Figure 64. The minimum halon 1301 mass requirements for spray fire suppression as a function of air flow. The agent injection duration was 1.0 s.

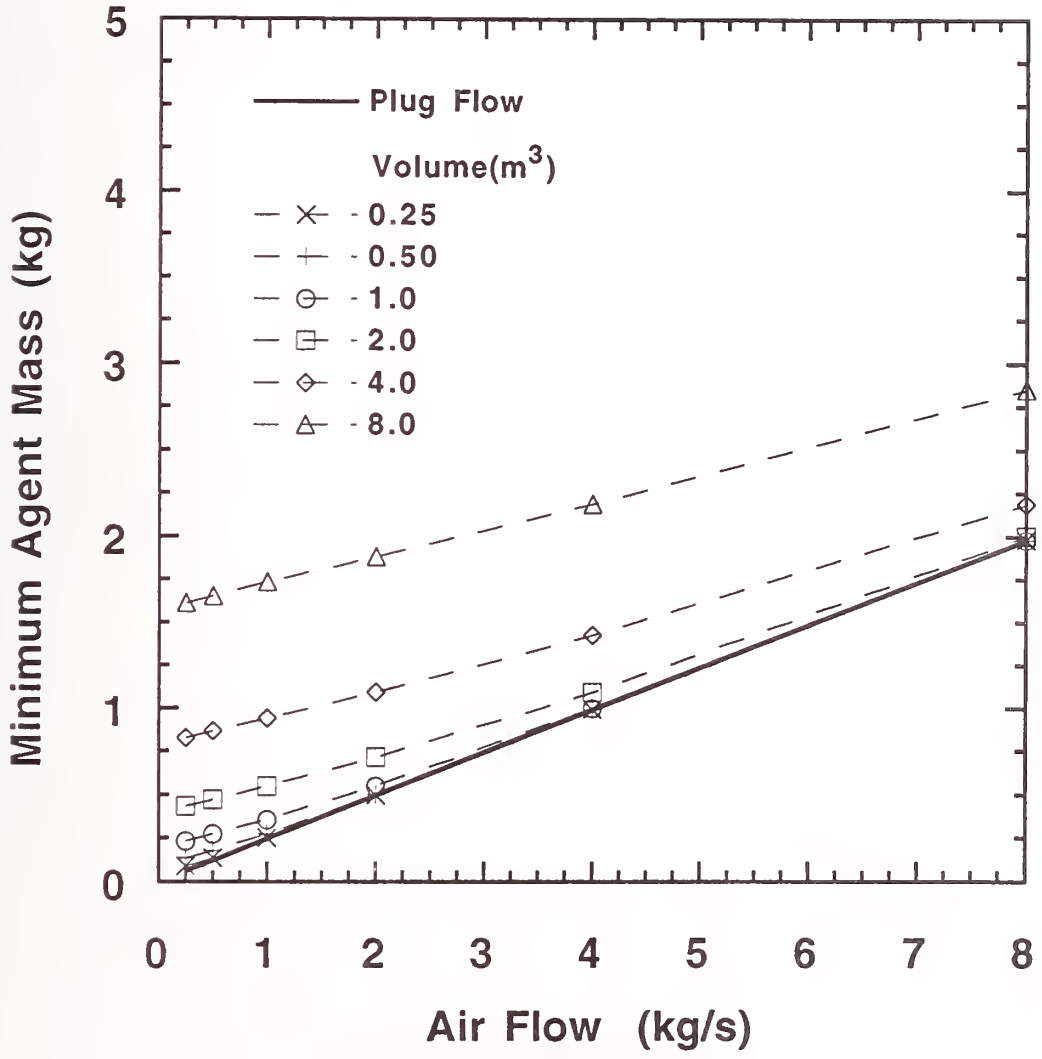

Figure 65. The minimum halon 1301 mass requirements for spray fire suppression as a function of air flow. The agent injection duration was 1.5 s.

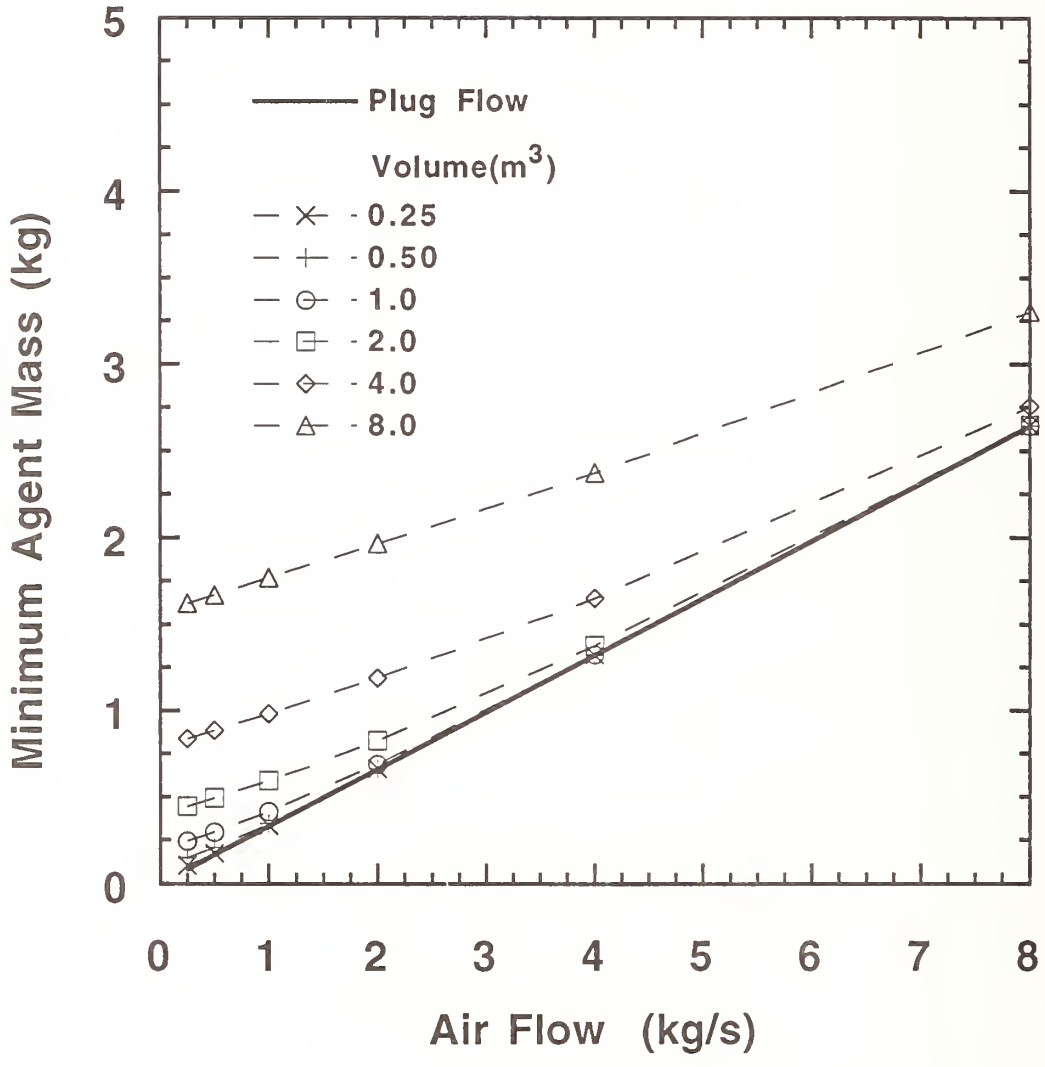

Figure 66. The minimum halon 1301 mass requirements for spray fire suppression as a function of air flow. The agent injection duration was 2.0 s.

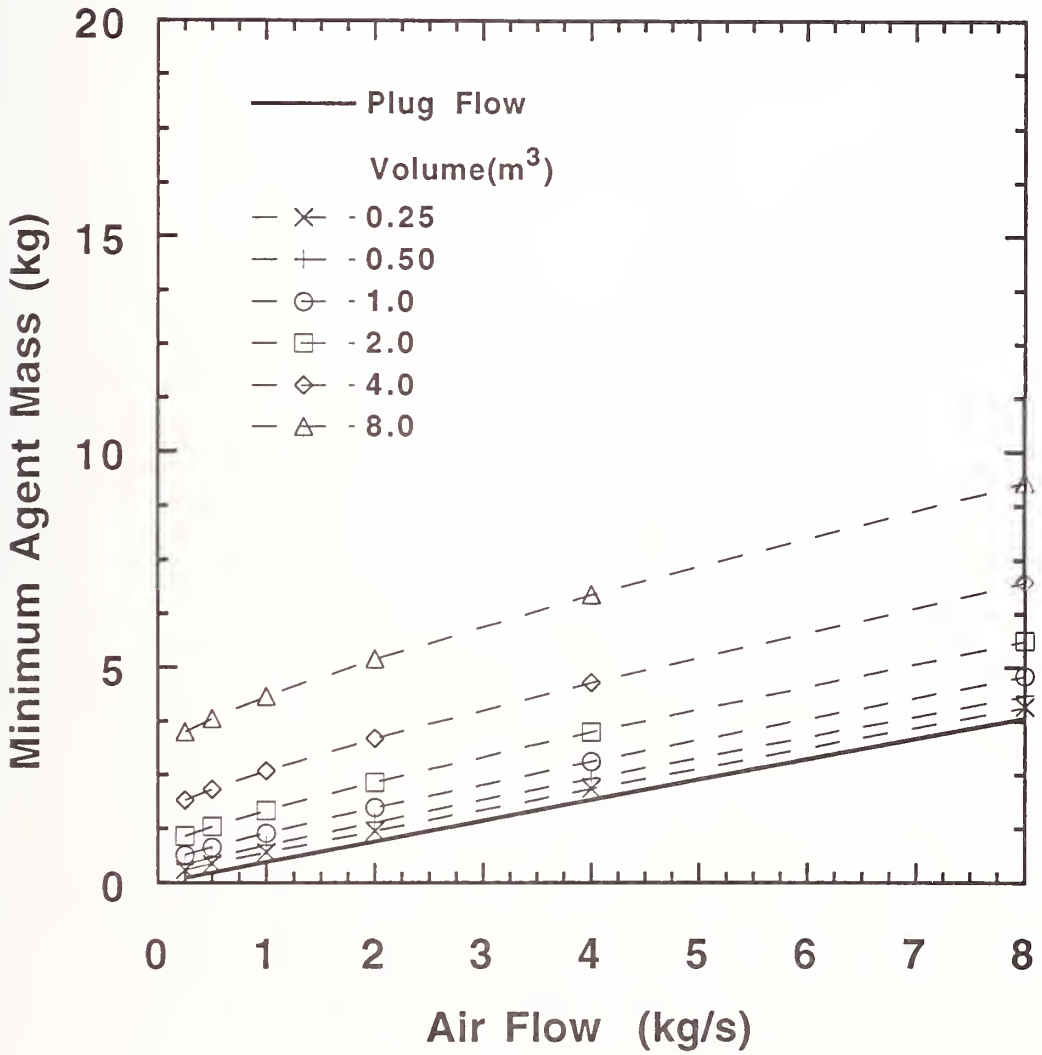

Figure 67. The minimum halon 1301 mass requirements for pool fire suppression as a function of air flow. The agent injection duration was 0.25 s.

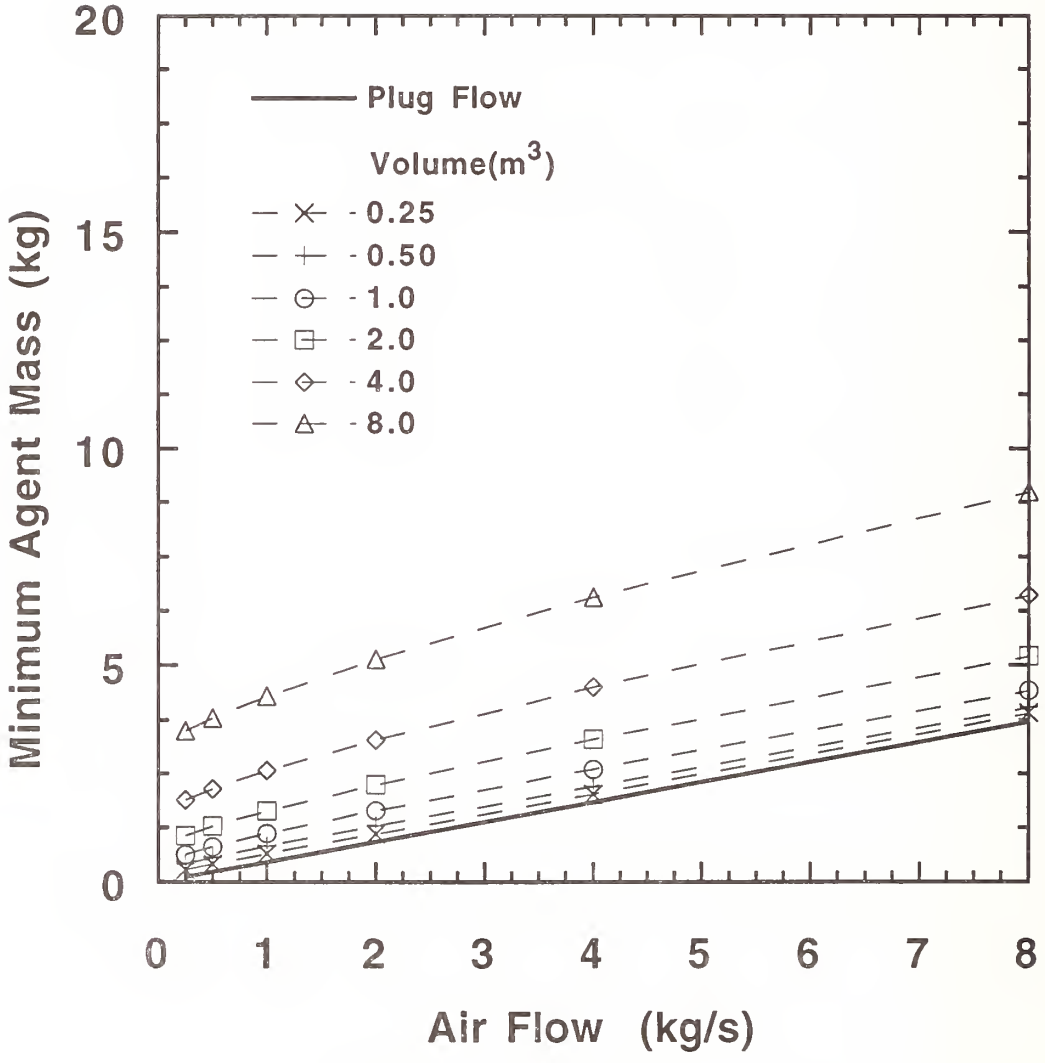

Figure 68. The minimum halon 1301 mass requirements for pool fire suppression as a function of air flow. The agent injection duration was 0.50 s.

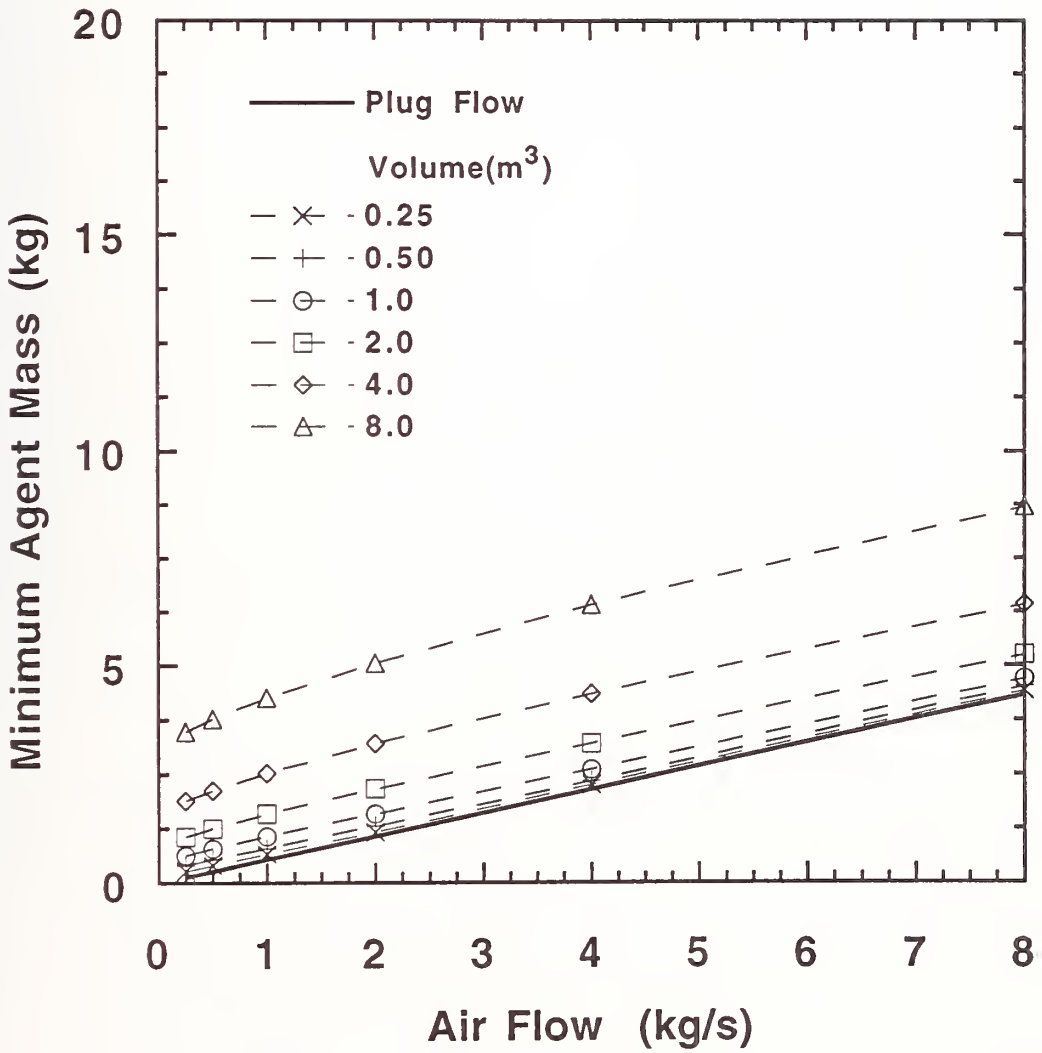

Figure 69. The minimum halon 1301 mass requirements for pool fire suppression as a function of air flow. The agent injection duration was 1.0 s.

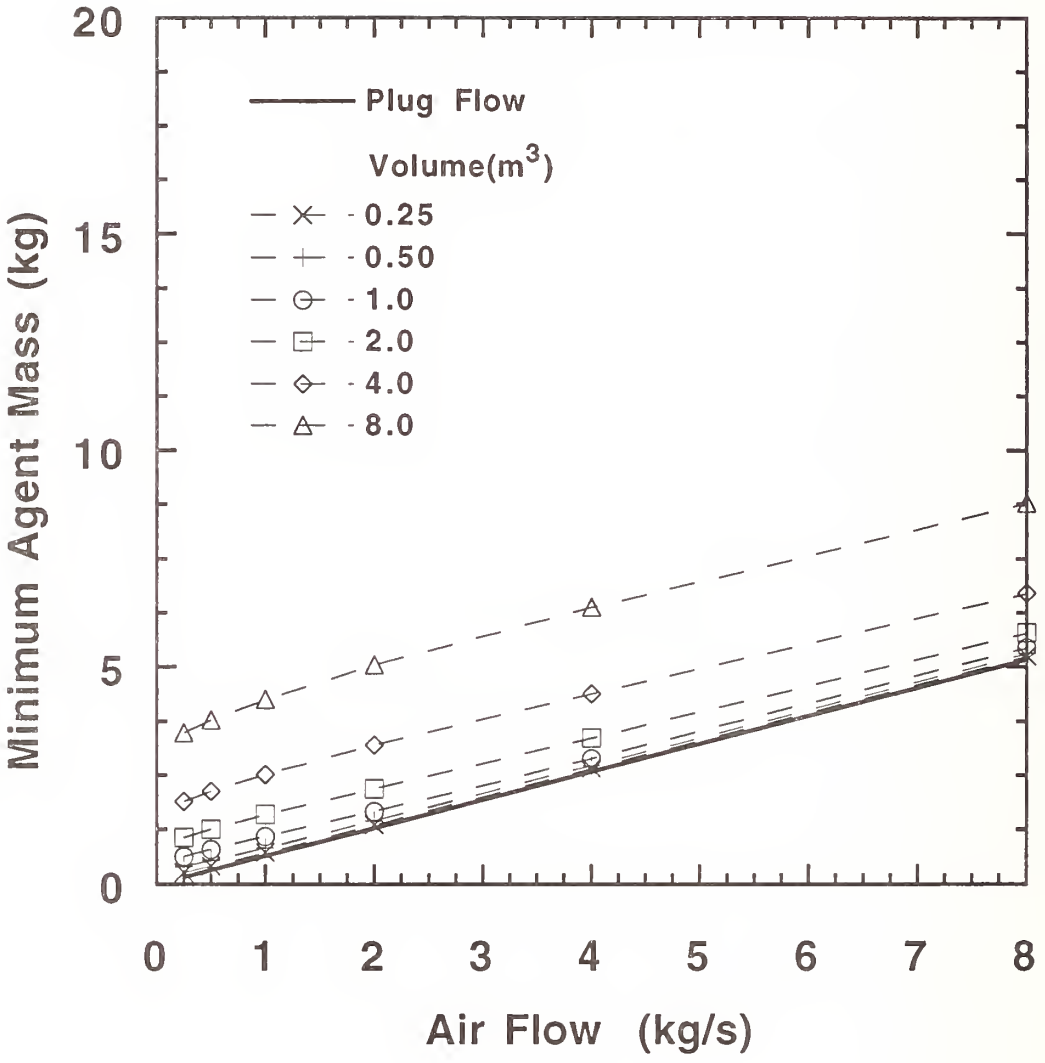

Figure 70. The minimum halon 1301 mass requirements for pool fire suppression as a function of air flow. The agent injection duration was 1.5 s.

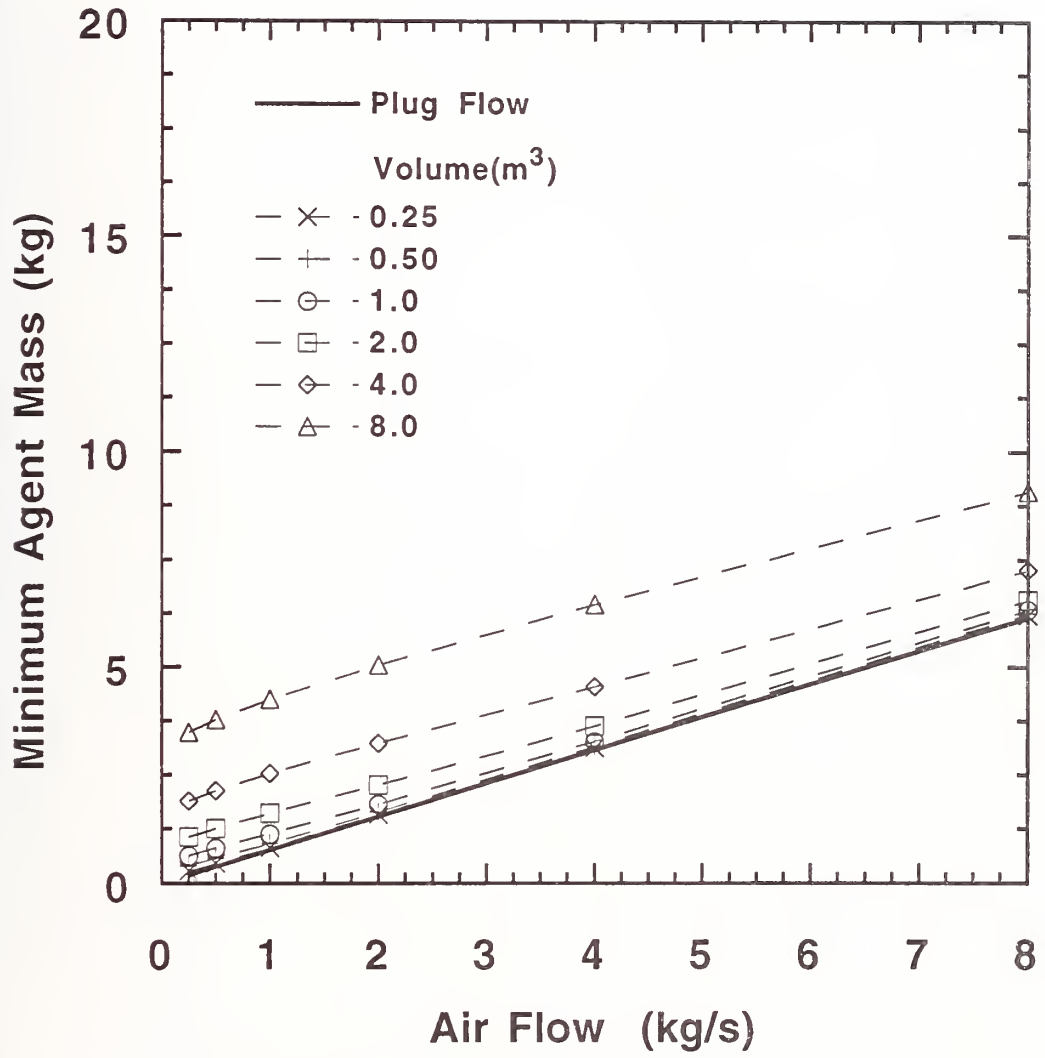

Figure 71. The minimum halon 1301 mass requirements for pool fire suppression as a function of air flow. The agent injection duration was 2.0 s.

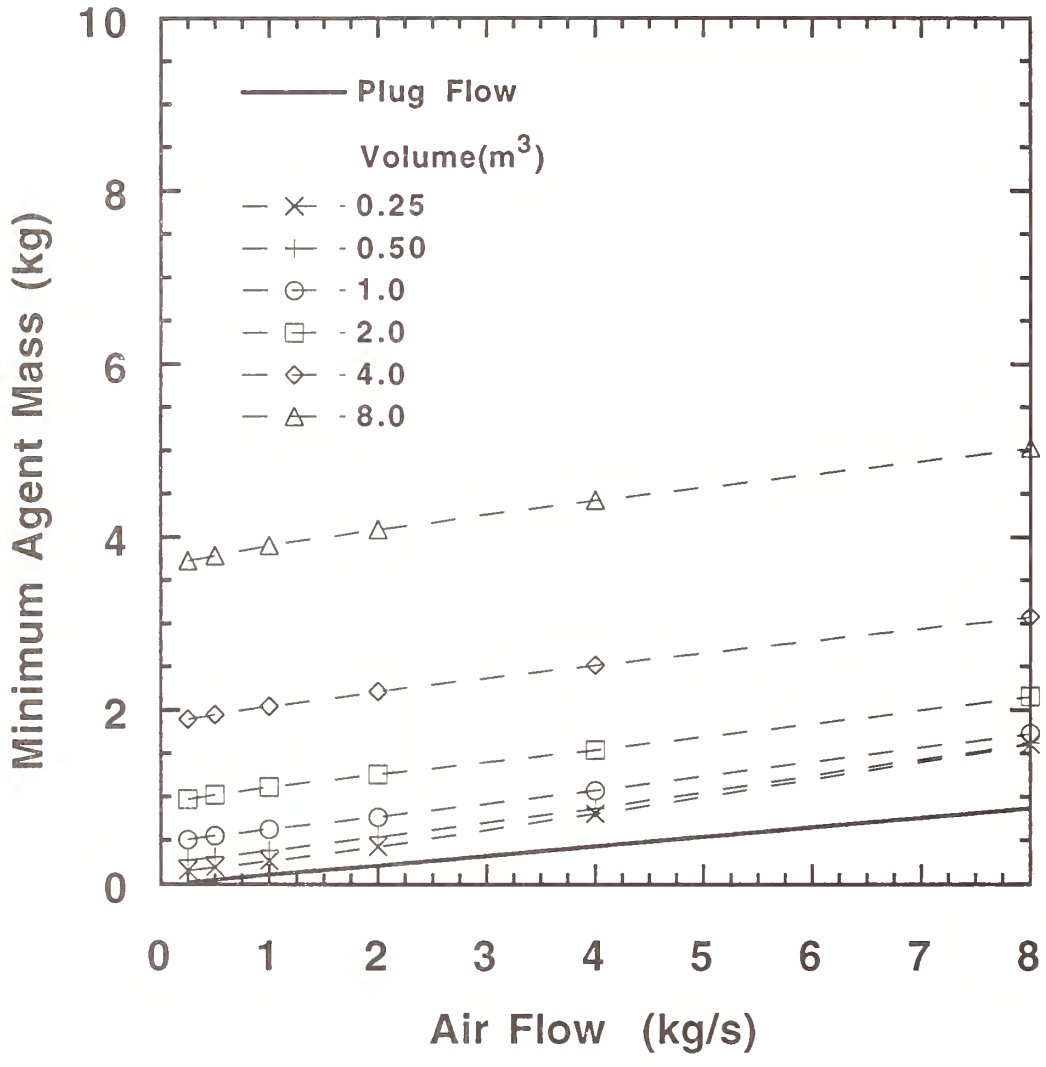

Figure 72. The minimum HFC-125 mass requirements for spray fire suppression as a function of air flow. The agent injection duration was 0.25 s.

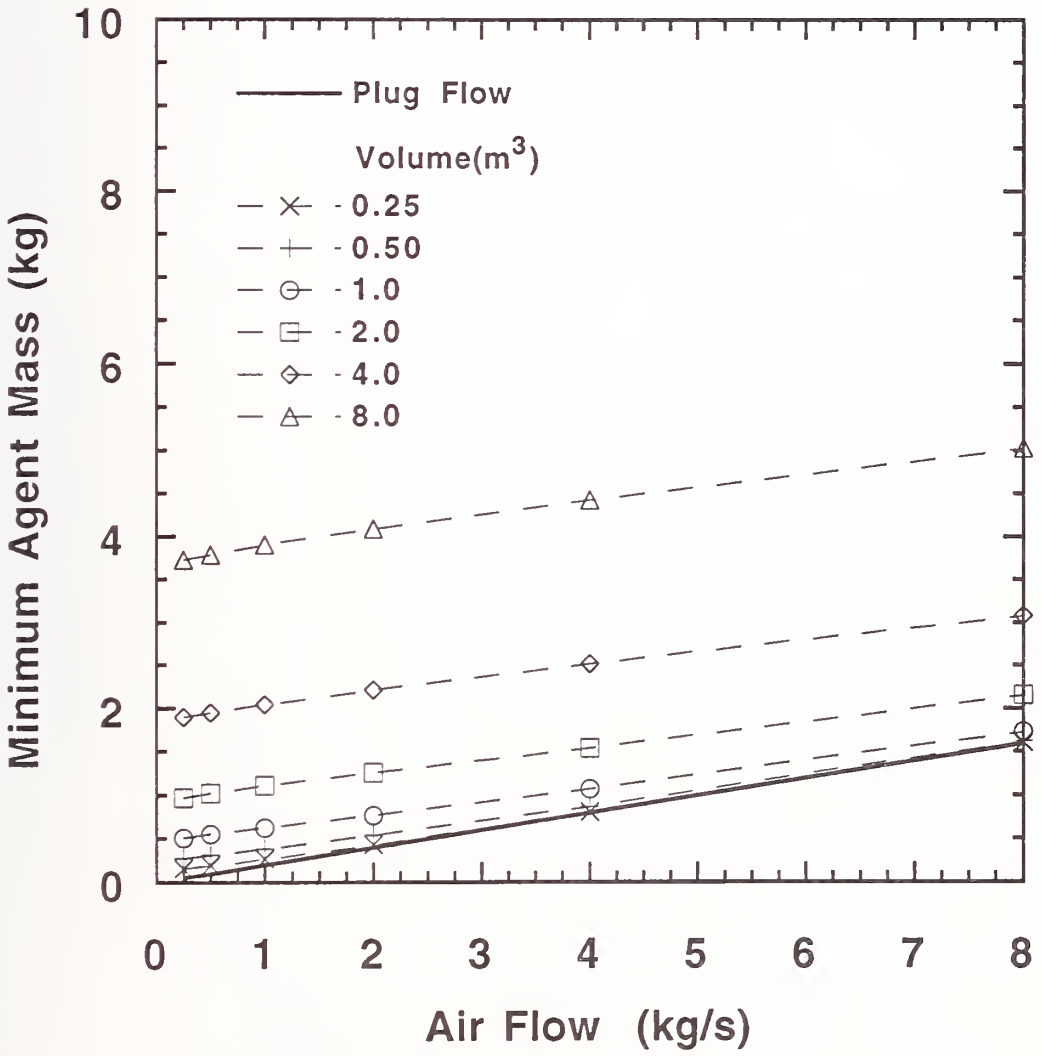

Figure 73. The minimum HFC-125 mass requirements for spray fire suppression as a function of air flow. The agent injection duration was 0.50 s.

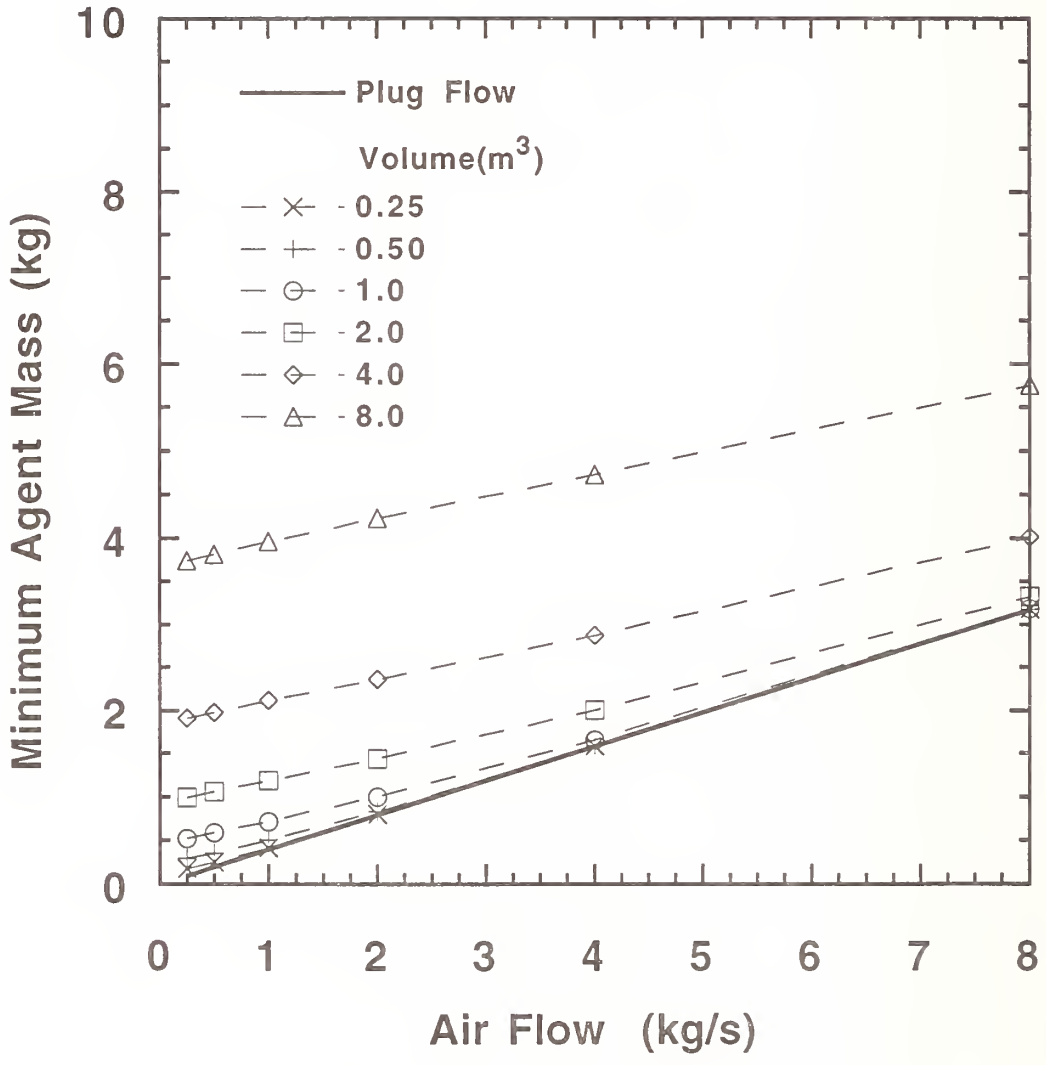

Figure 74. The minimum HFC-125 mass requirements for spray fire suppression as a function of air flow. The agent injection duration was 1.0 s.

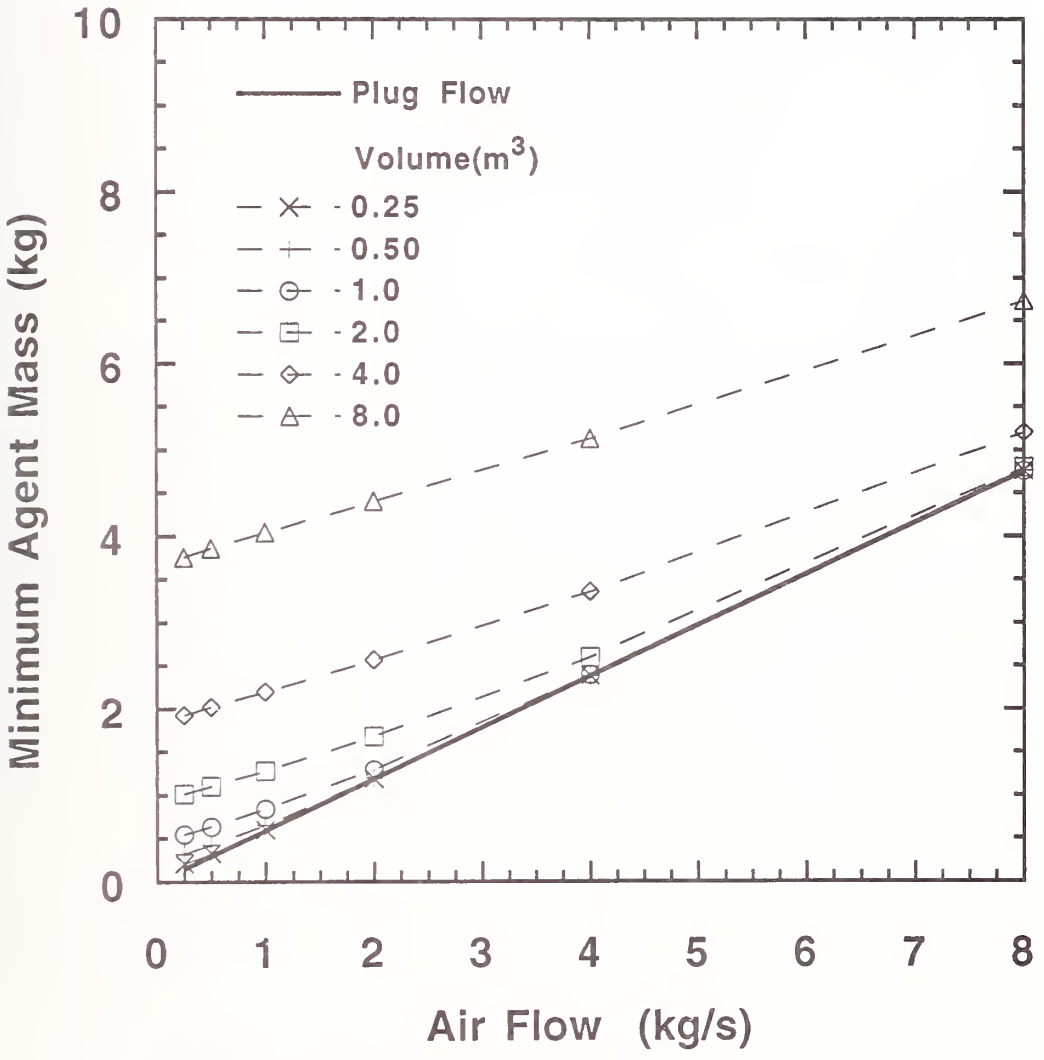

Figure 75. The minimum HFC-125 mass requirements for spray fire suppression as a function of air flow. The agent injection duration was 1.5 s.

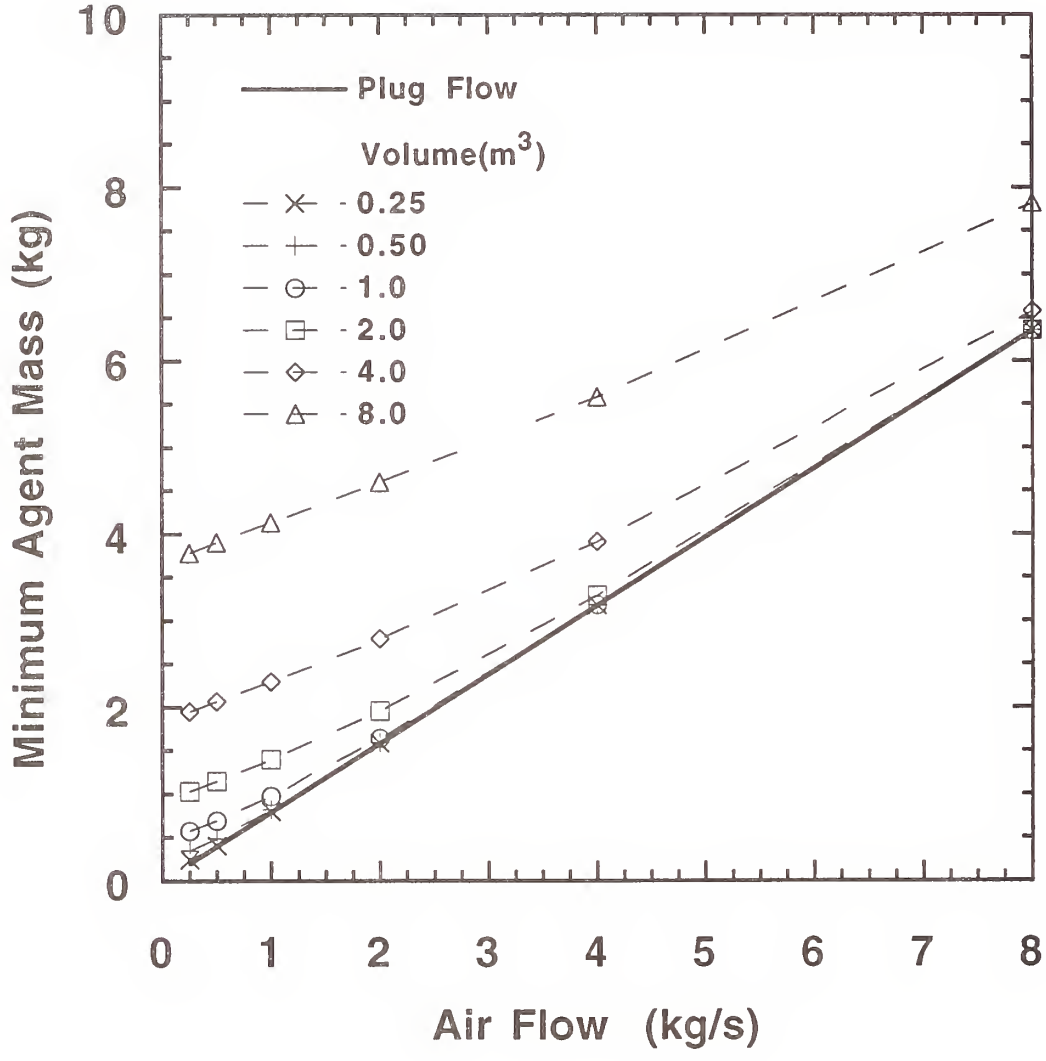

Figure 76. The minimum HFC-125 mass requirements for spray fire suppression as a function of air flow. The agent injection duration was 2.0 s.

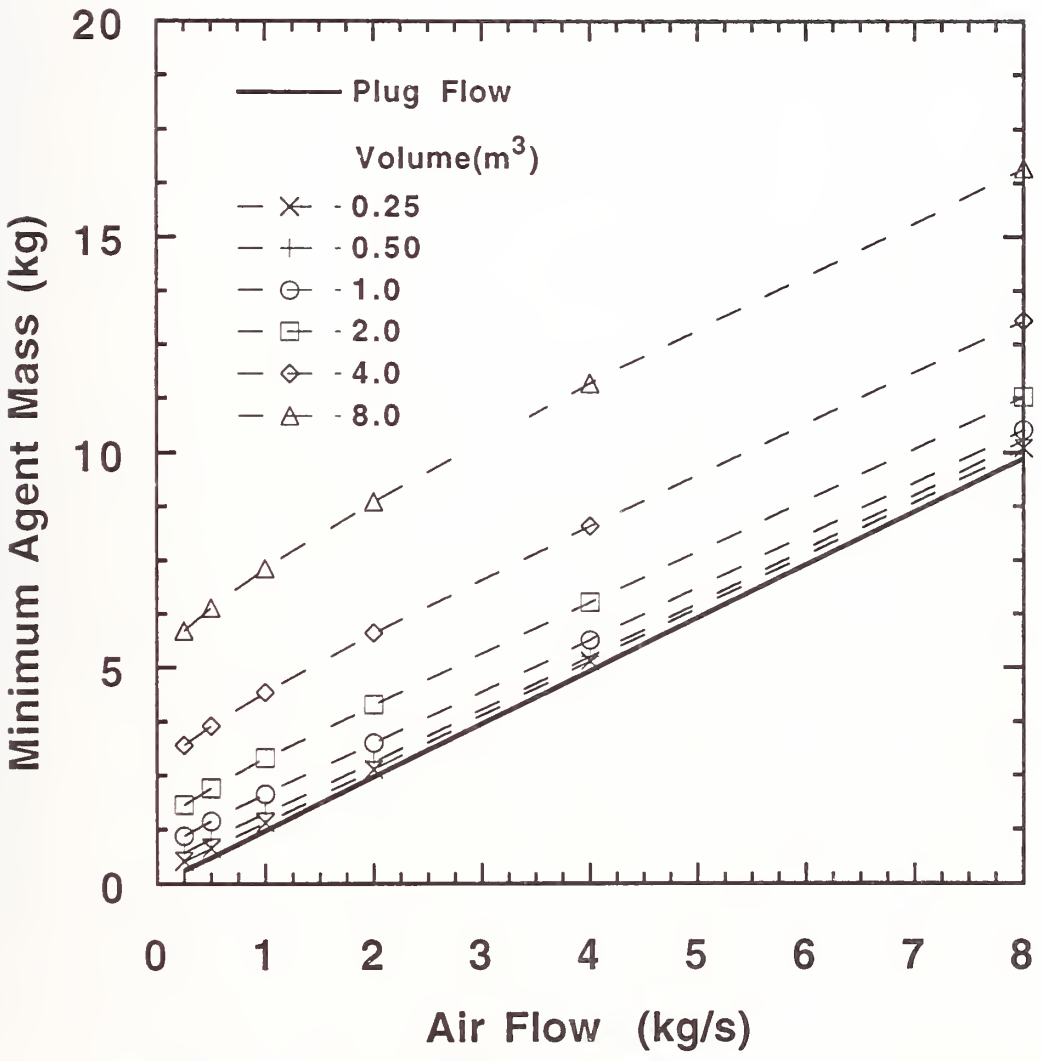

Figure 77. The minimum HFC-125 mass requirements for pool fire suppression as a function of air flow. The agent injection duration was 0.25 s.

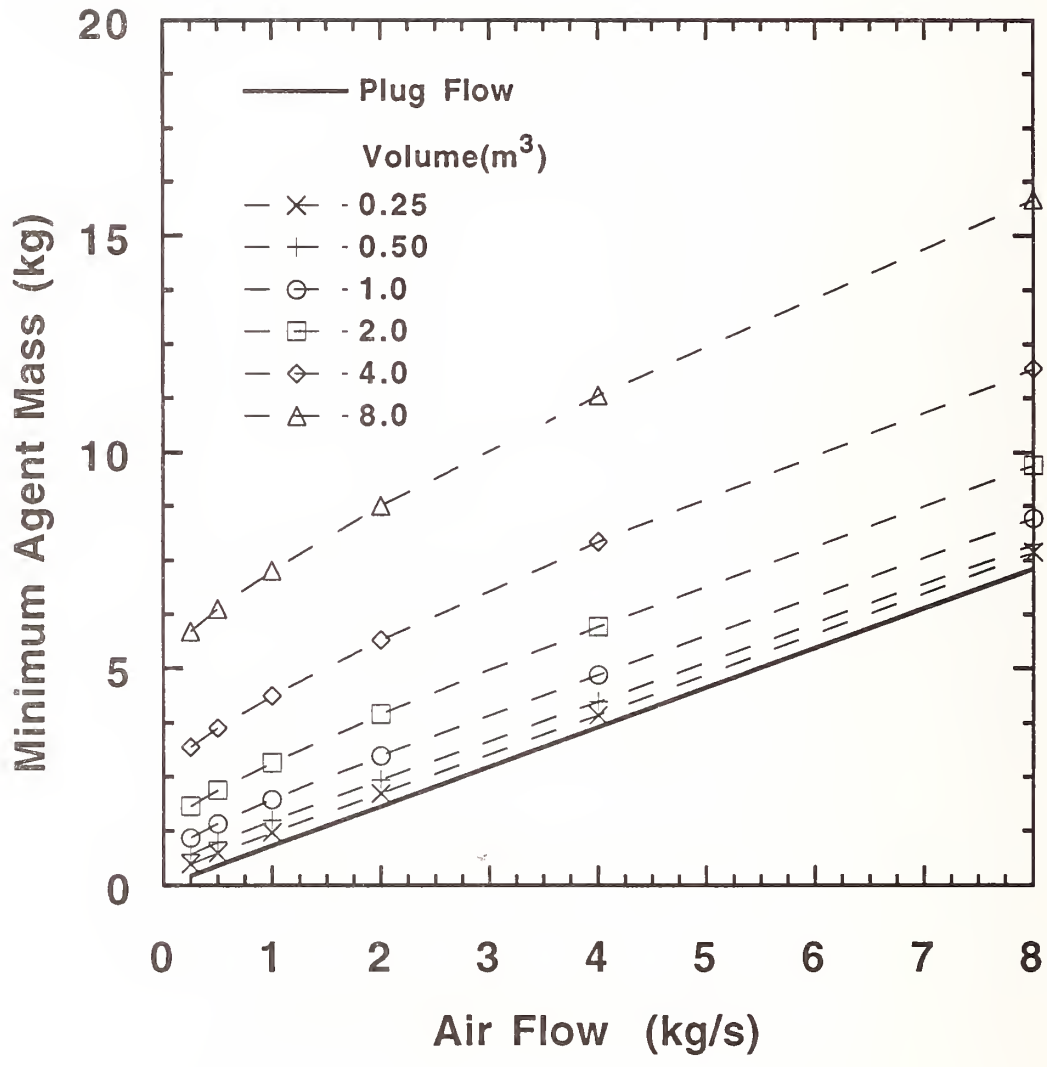

Figure 78. The minimum HFC-125 mass requirements for pool fire suppression as a function of air flow. The agent injection duration was 0.50 s.

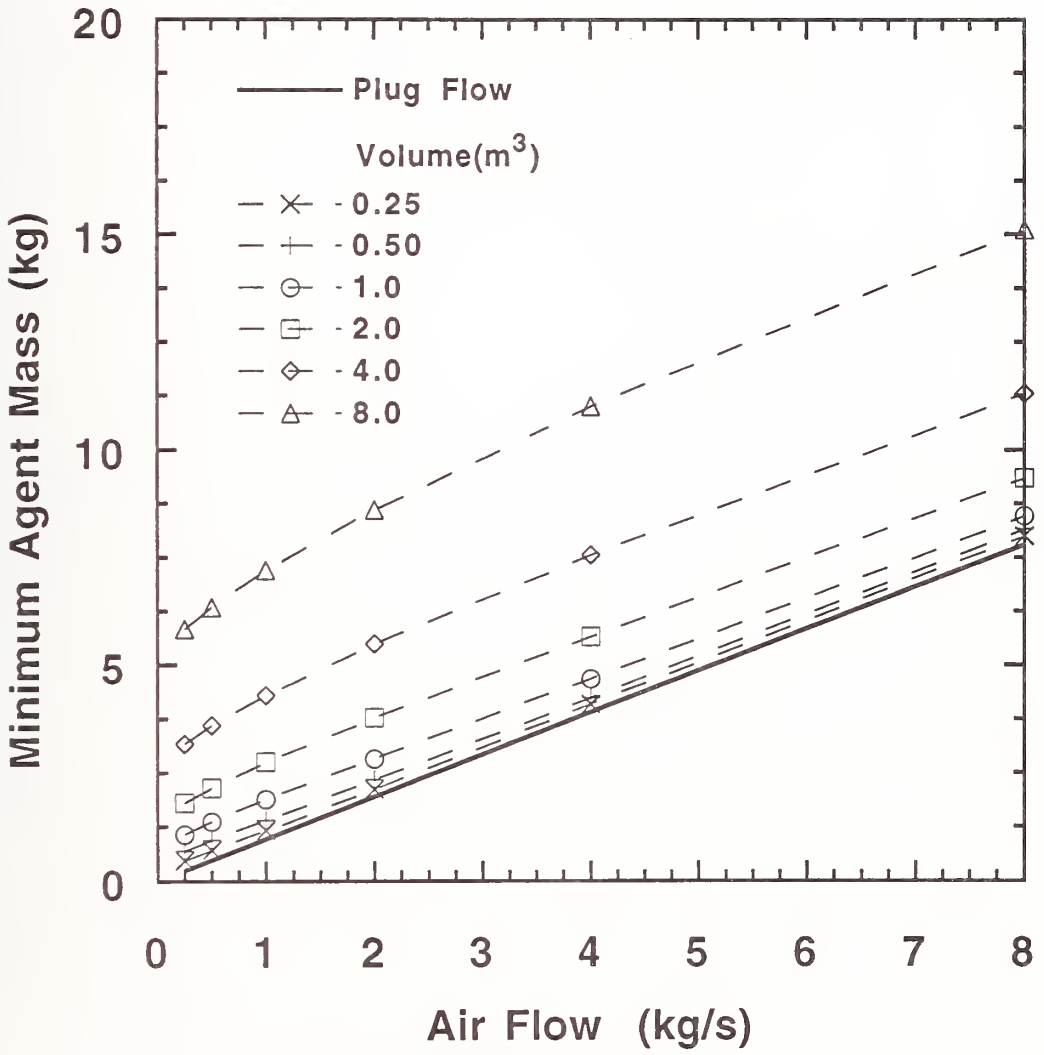

Figure 79. The minimum HFC-125 mass requirements for pool fire suppression as a function of air flow. The agent injection duration was 1.0 s.

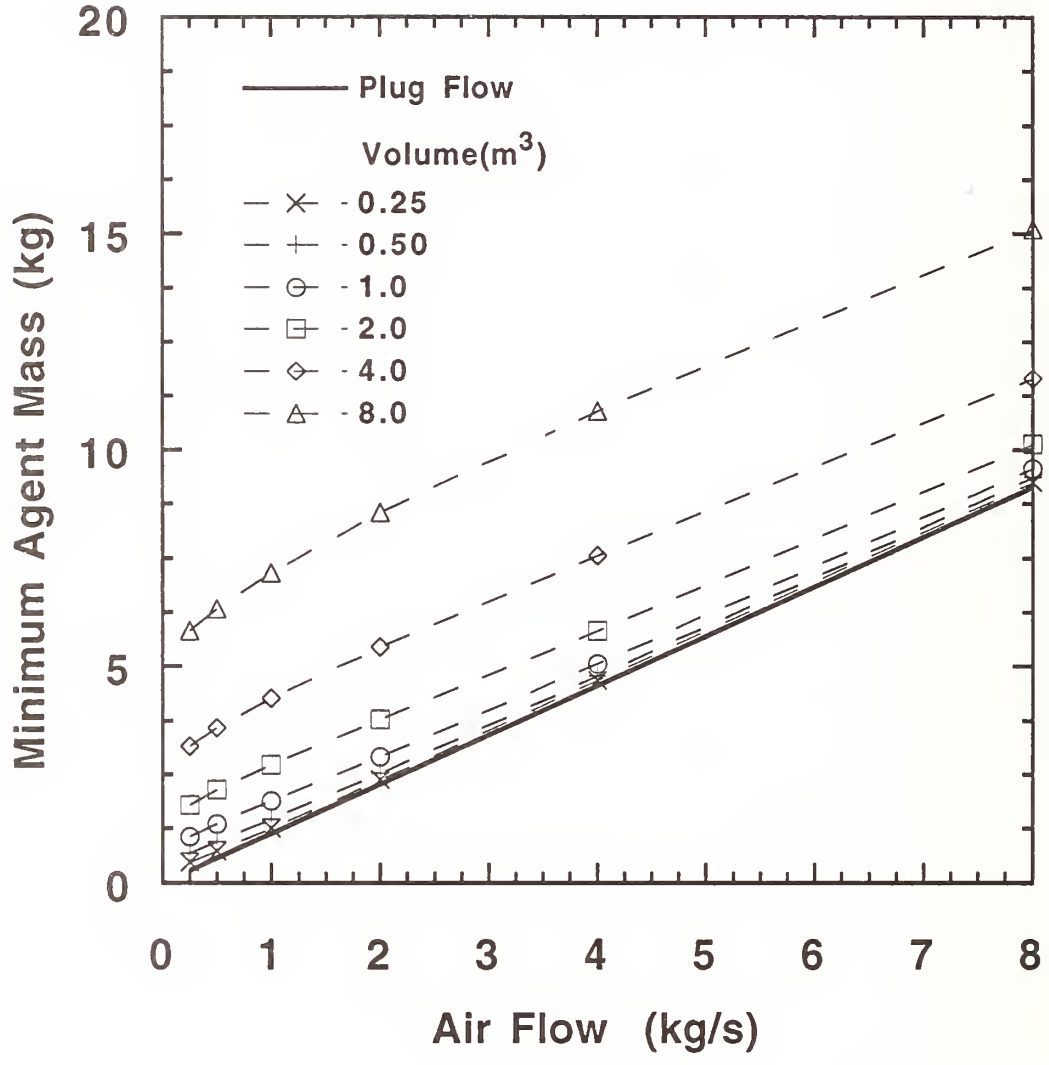

Figure 80. The minimum HFC-125 mass requirements for pool fire suppression as a function of air flow. The agent injection duration was 1.5 s.

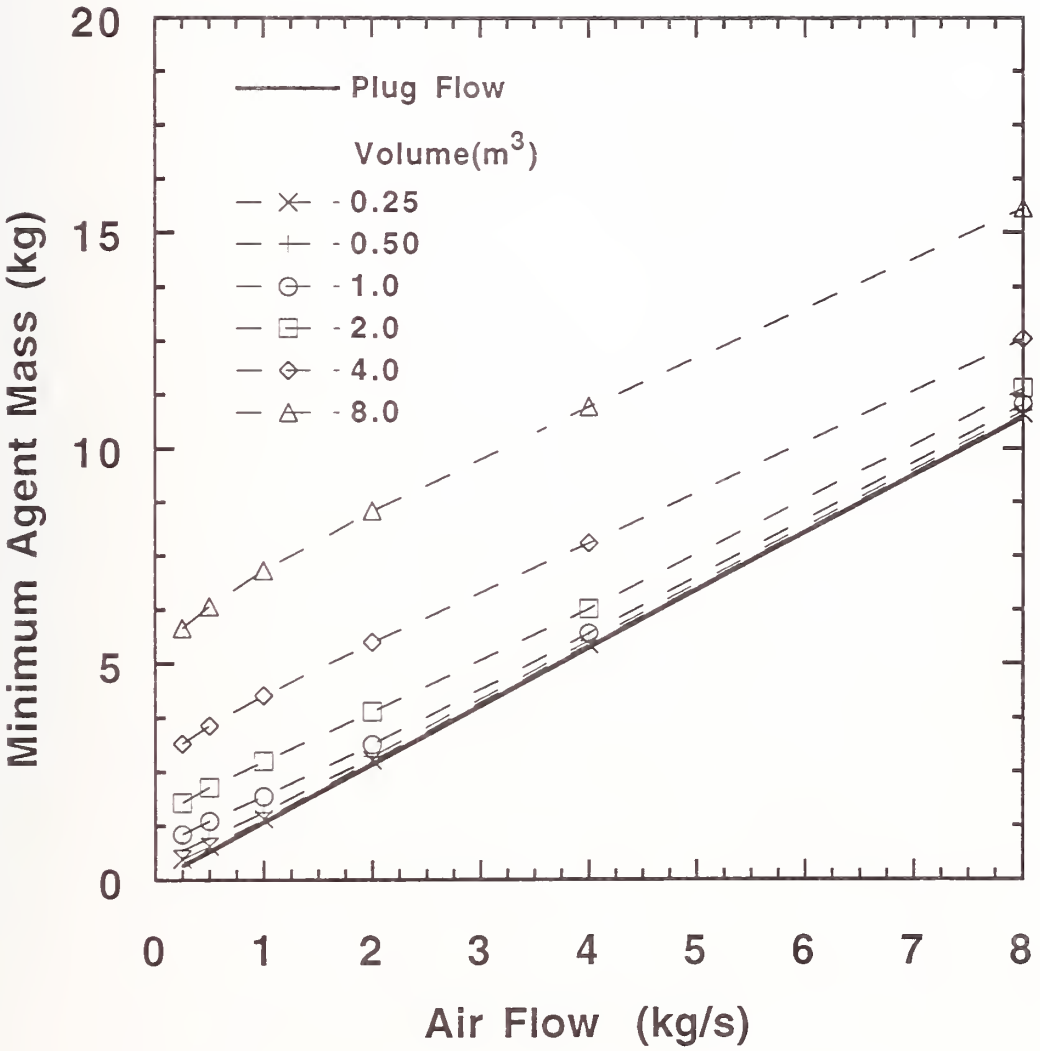

Figure 81. The minimum HFC-125 mass requirements for pool fire suppression as a function of air flow. The agent injection duration was 2.0 s.

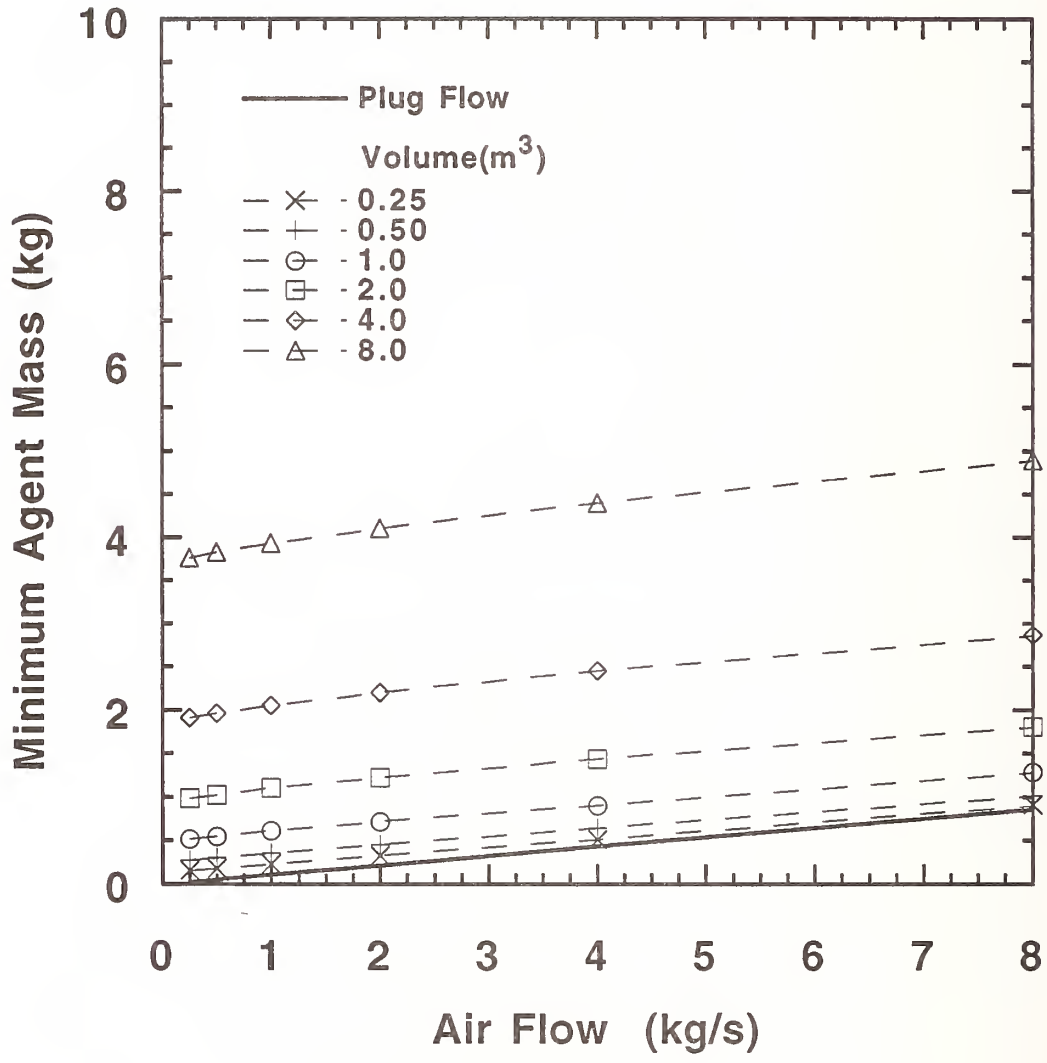

Figure 82. The minimum HFC-227 mass requirements for spray fire suppression as a function of air flow. The agent injection duration was 0.25 s.

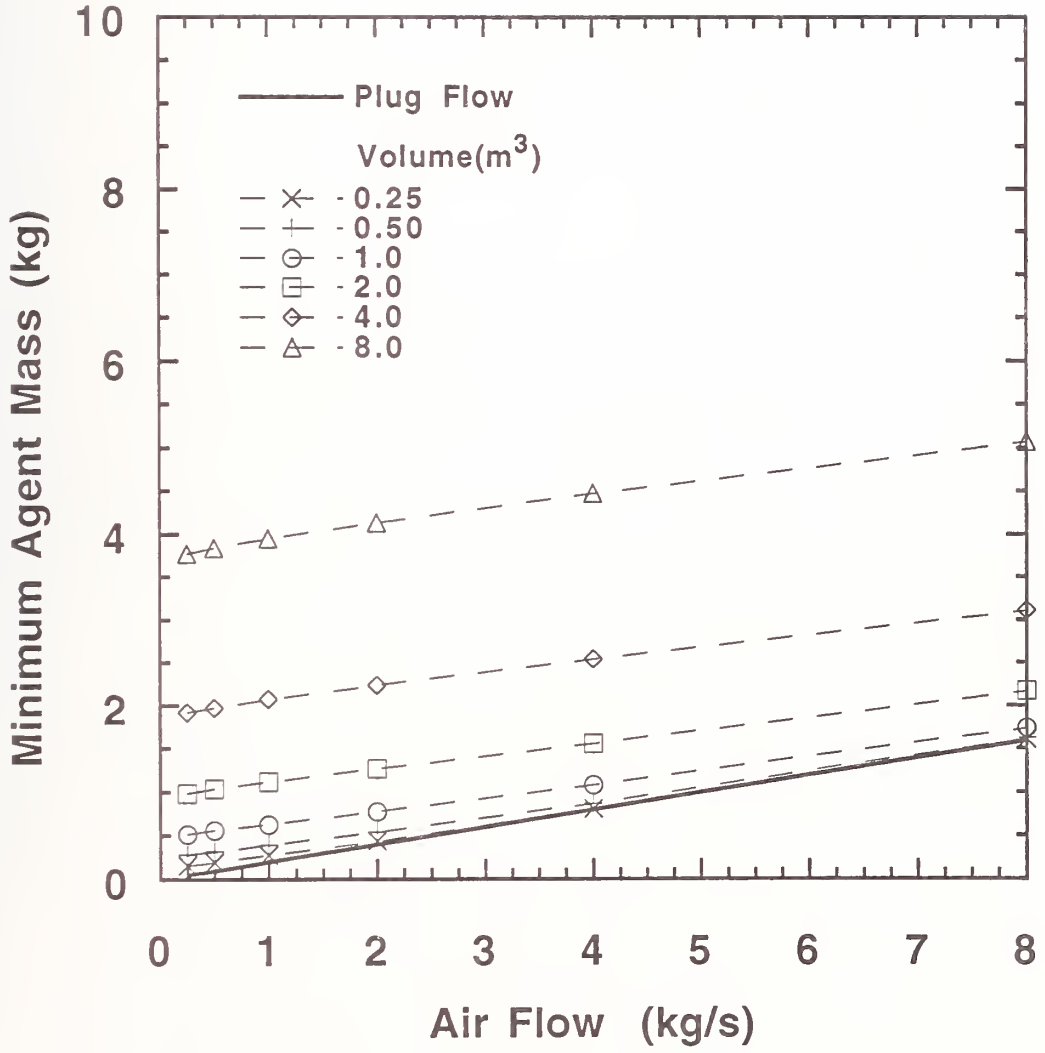

Figure 83. The minimum HFC-227 mass requirements for spray fire suppression as a function of air flow. The agent injection duration was 0.50 s.

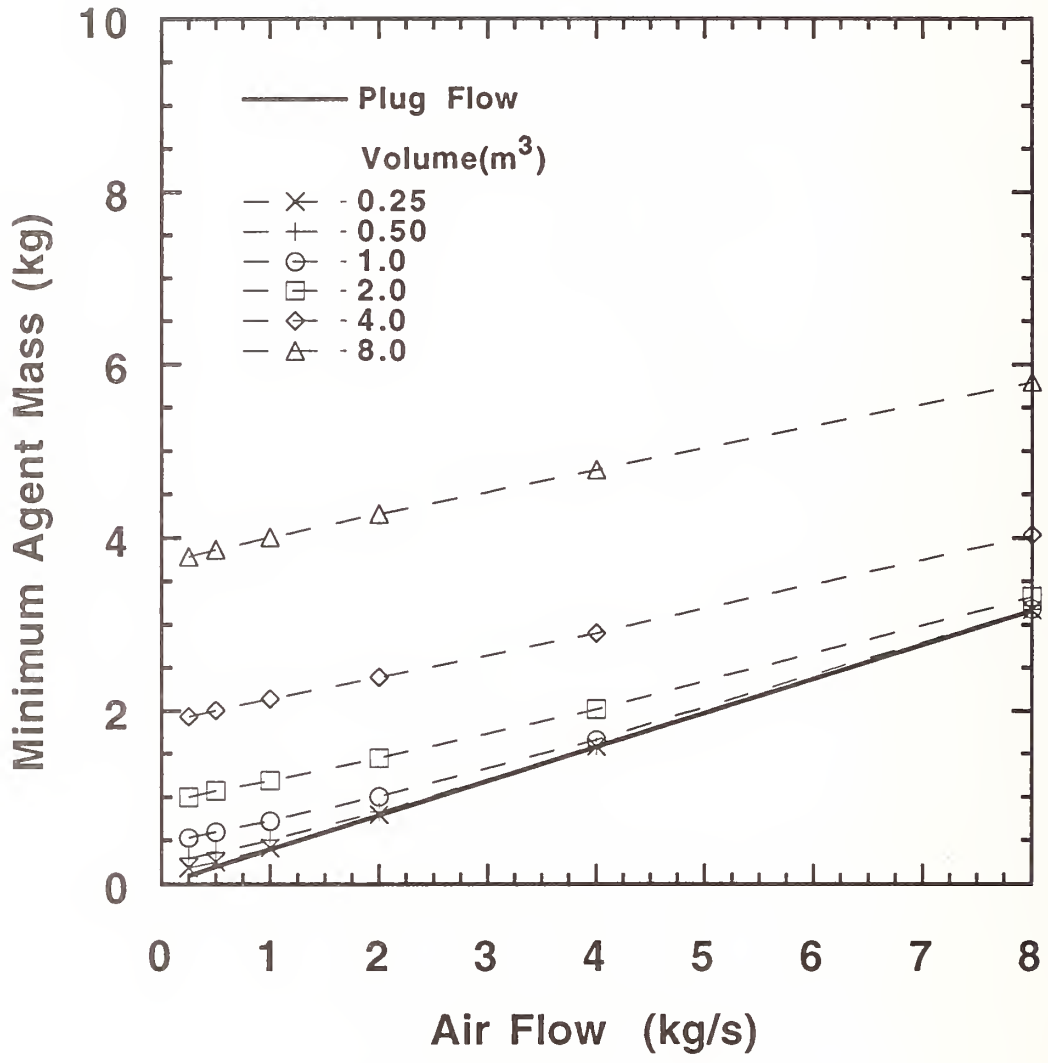

Figure 84. The minimum HFC-227 mass requirements for spray fire suppression as a function of air flow. The agent injection duration was 1.0 s.

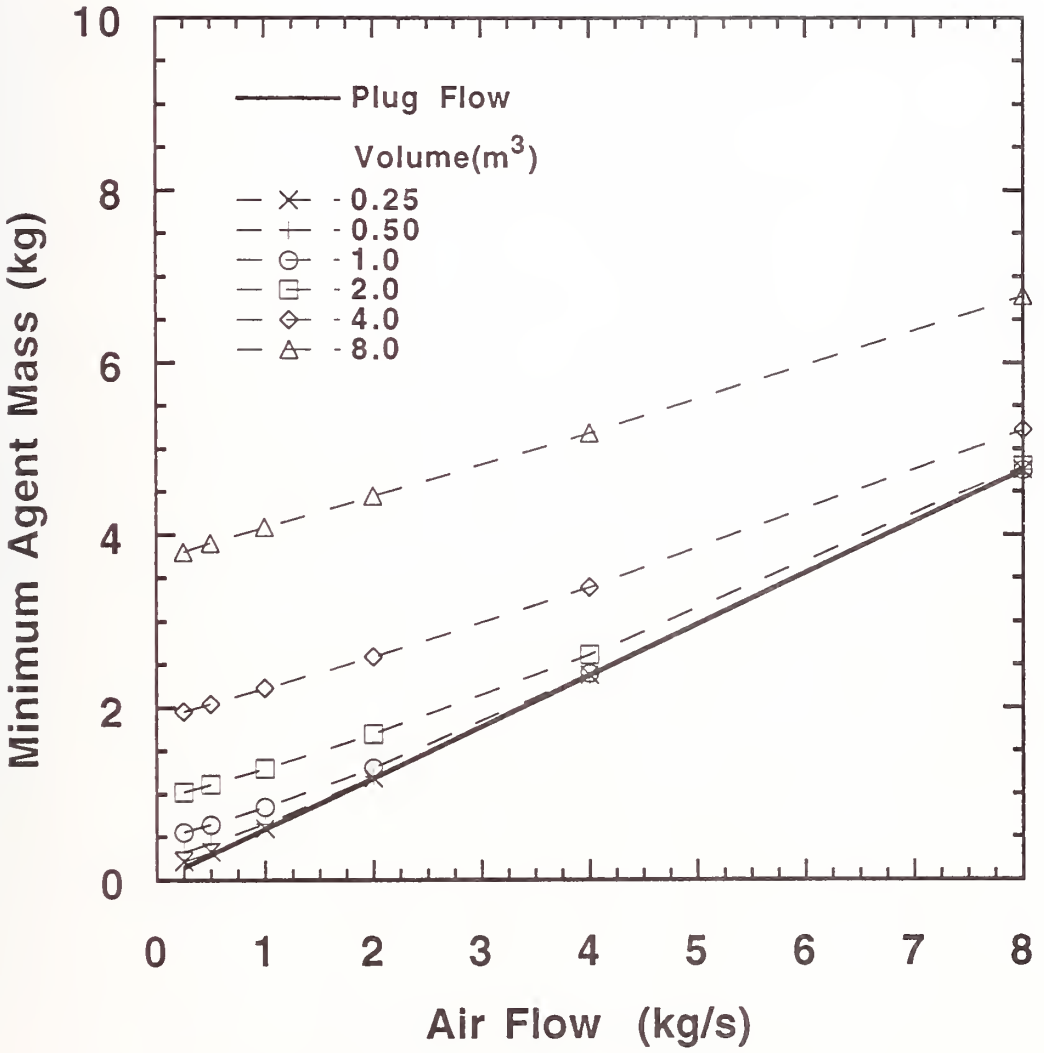

Figure 85. The minimum HFC-227 mass requirements for spray fire suppression as a function of air flow. The agent injection duration was 1.5 s.

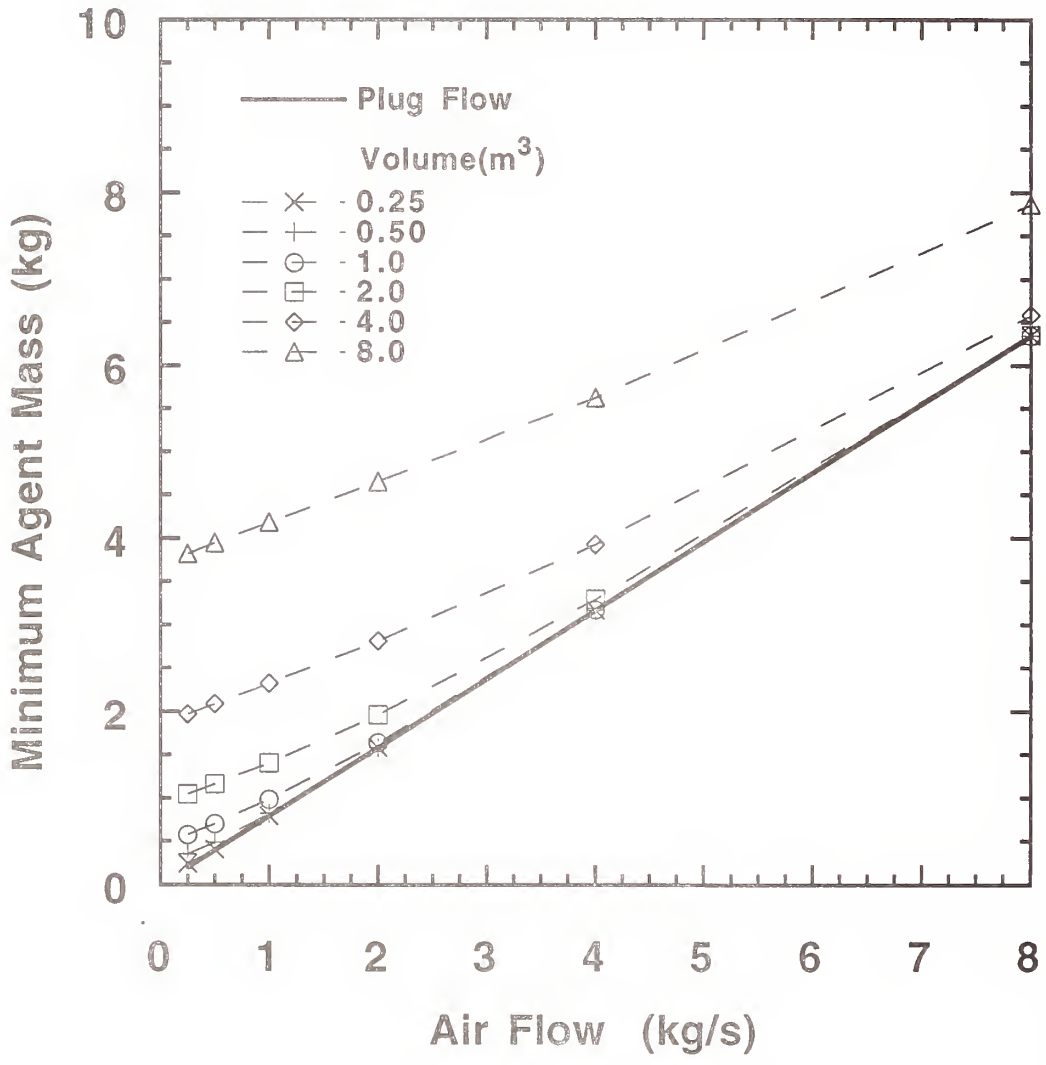

Figure 86. The minimum HFC-227 mass requirements for spray fire suppression as a function of air flow. The agent injection duration was 2.0 s.

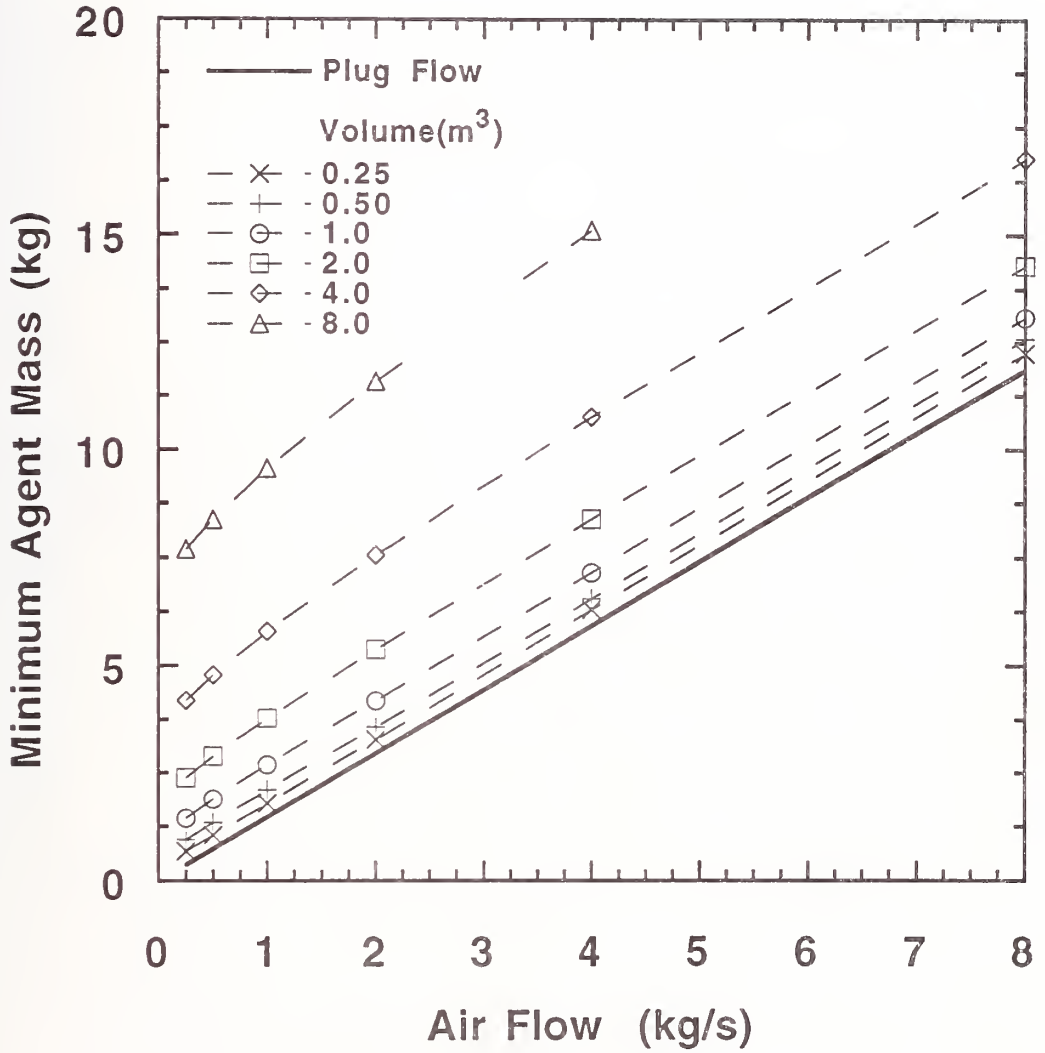

Figure 87. The minimum HFC-227 mass requirements for pool fire suppression as a function of air flow. The agent injection duration was 0.25 s.

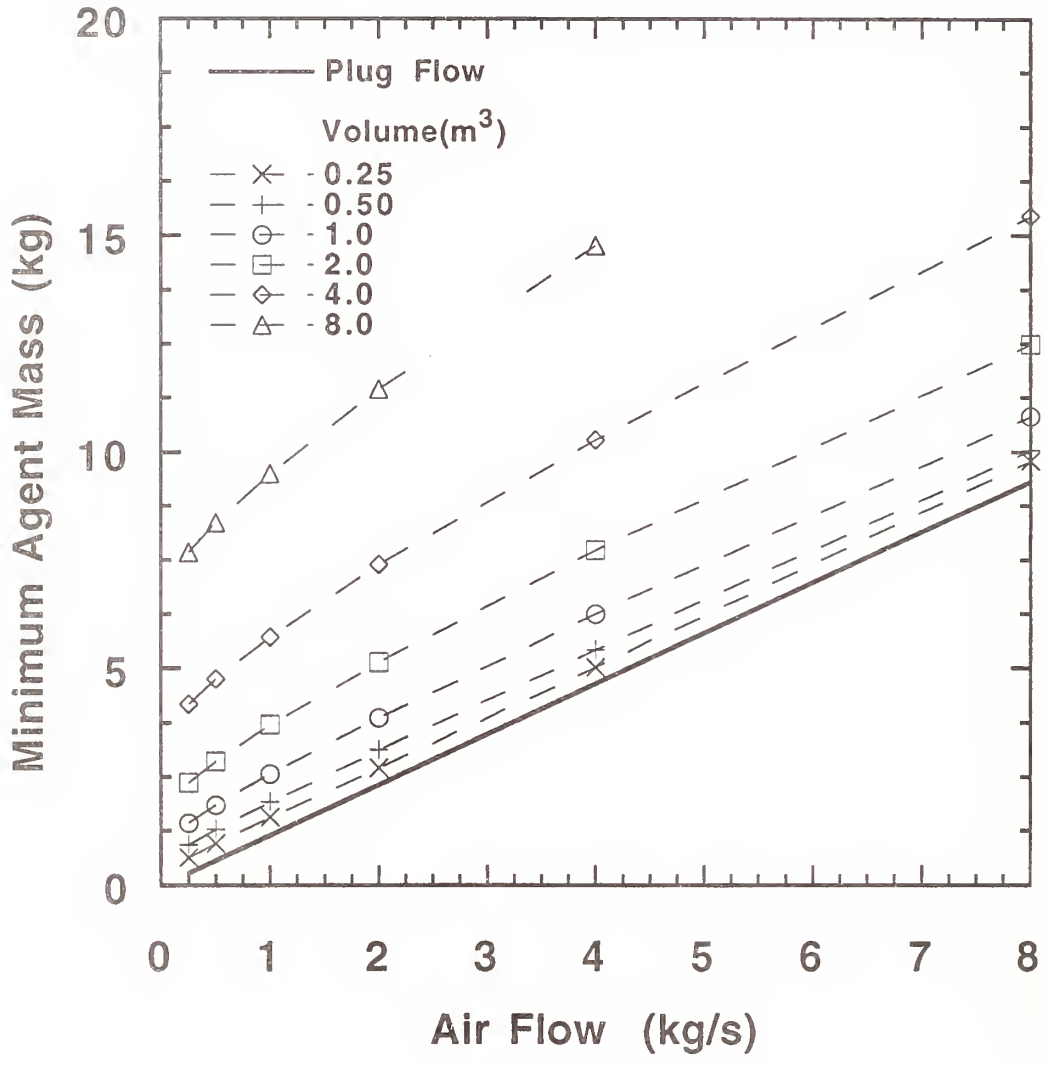

Figure 88. The minimum HFC-227 mass requirements for pool fire suppression as a function of air flow. The agent injection duration was 0.50 s.

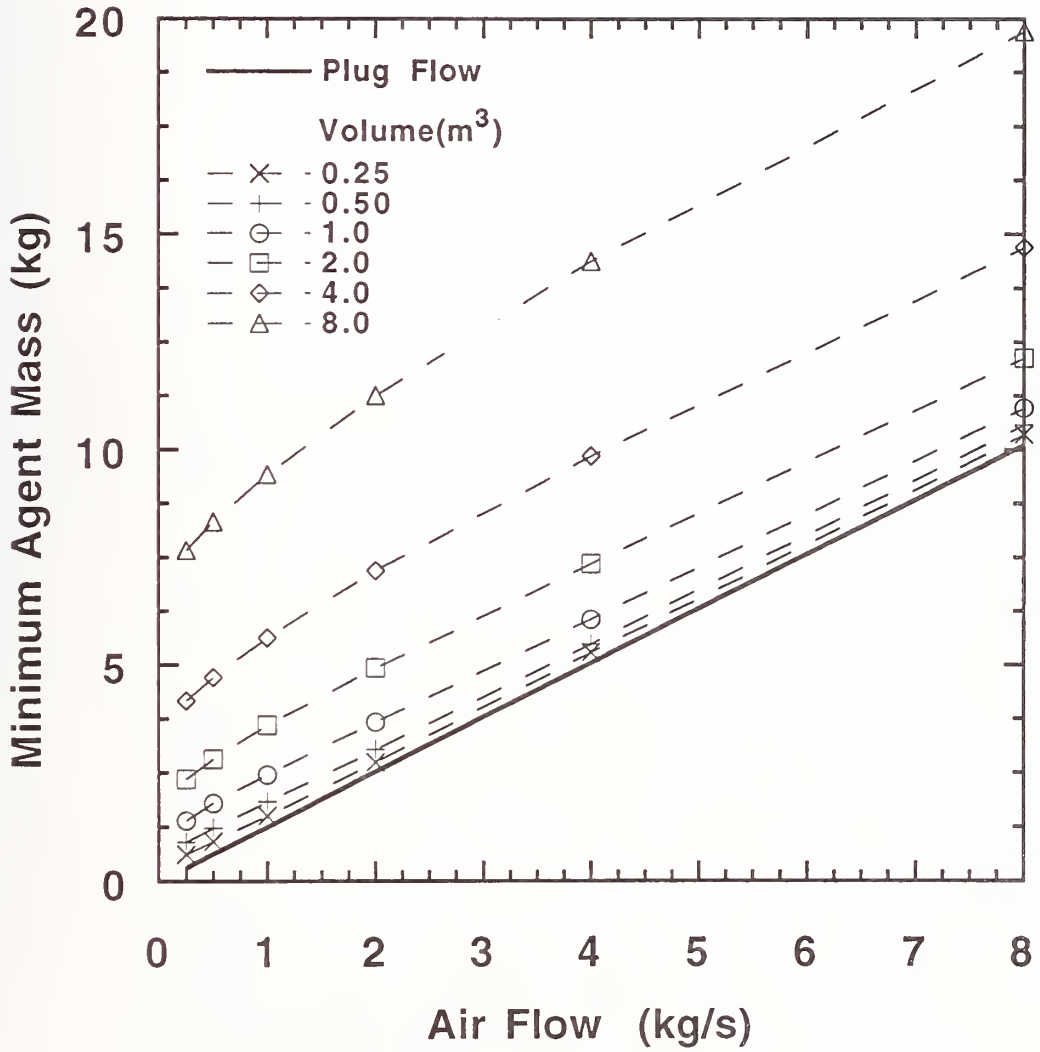

Figure 89. The minimum HFC-227 mass requirements for pool fire suppression as a function of air flow. The agent injection duration was 1.0 s.

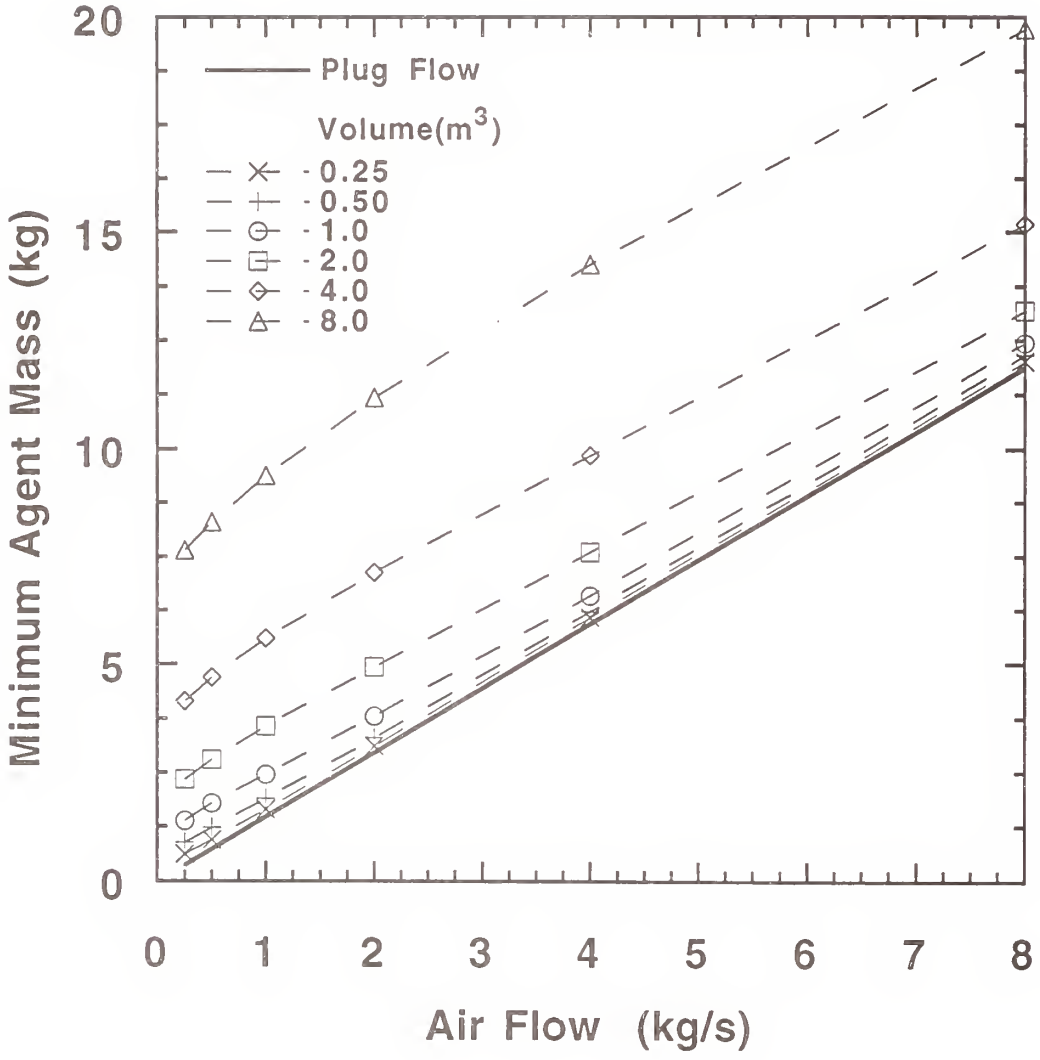

Figure 90. The minimum HFC-227 mass requirements for pool fire suppression as a function of air flow. The agent injection duration was 1.5 s.

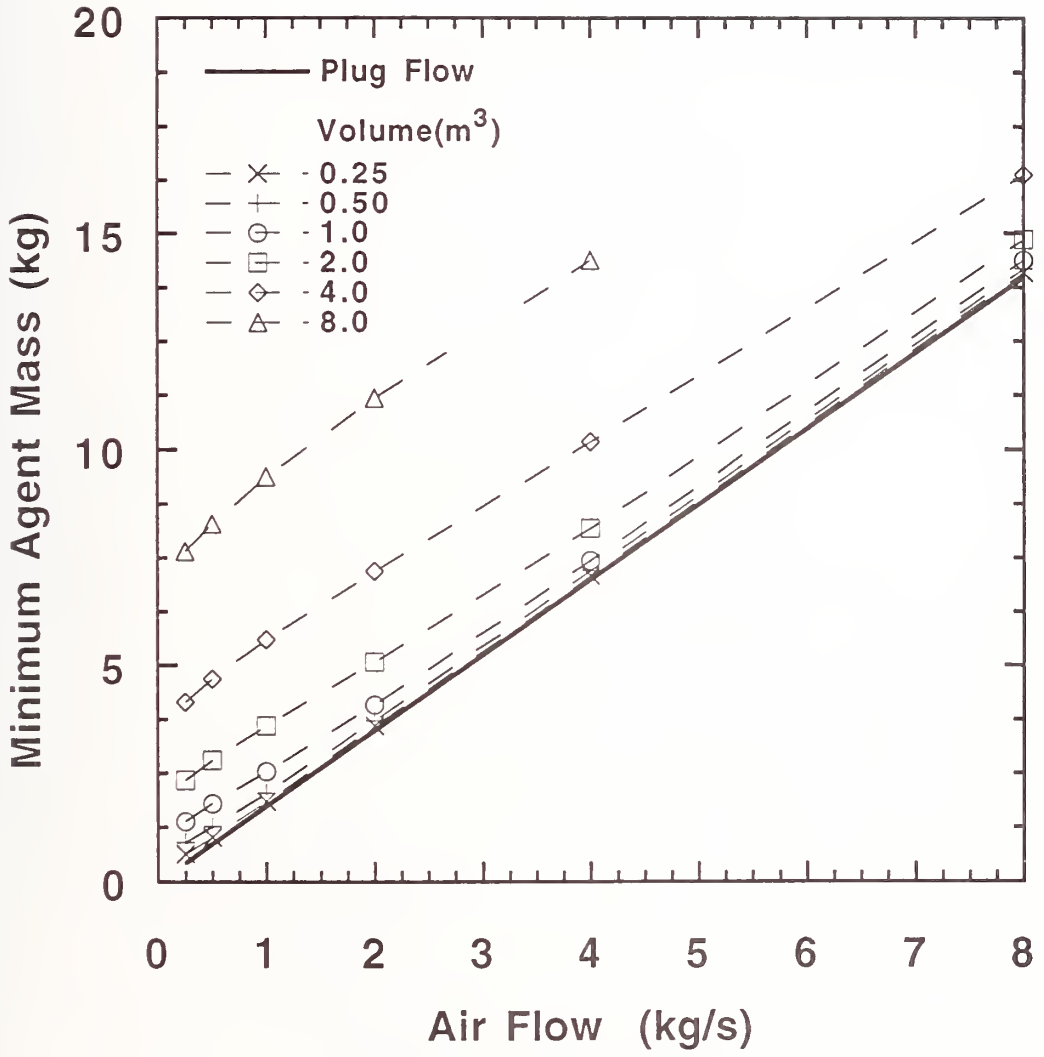

Figure 91. The minimum HFC-227 mass requirements for pool fire suppression as a function of air flow. The agent injection duration was 2.0 s.

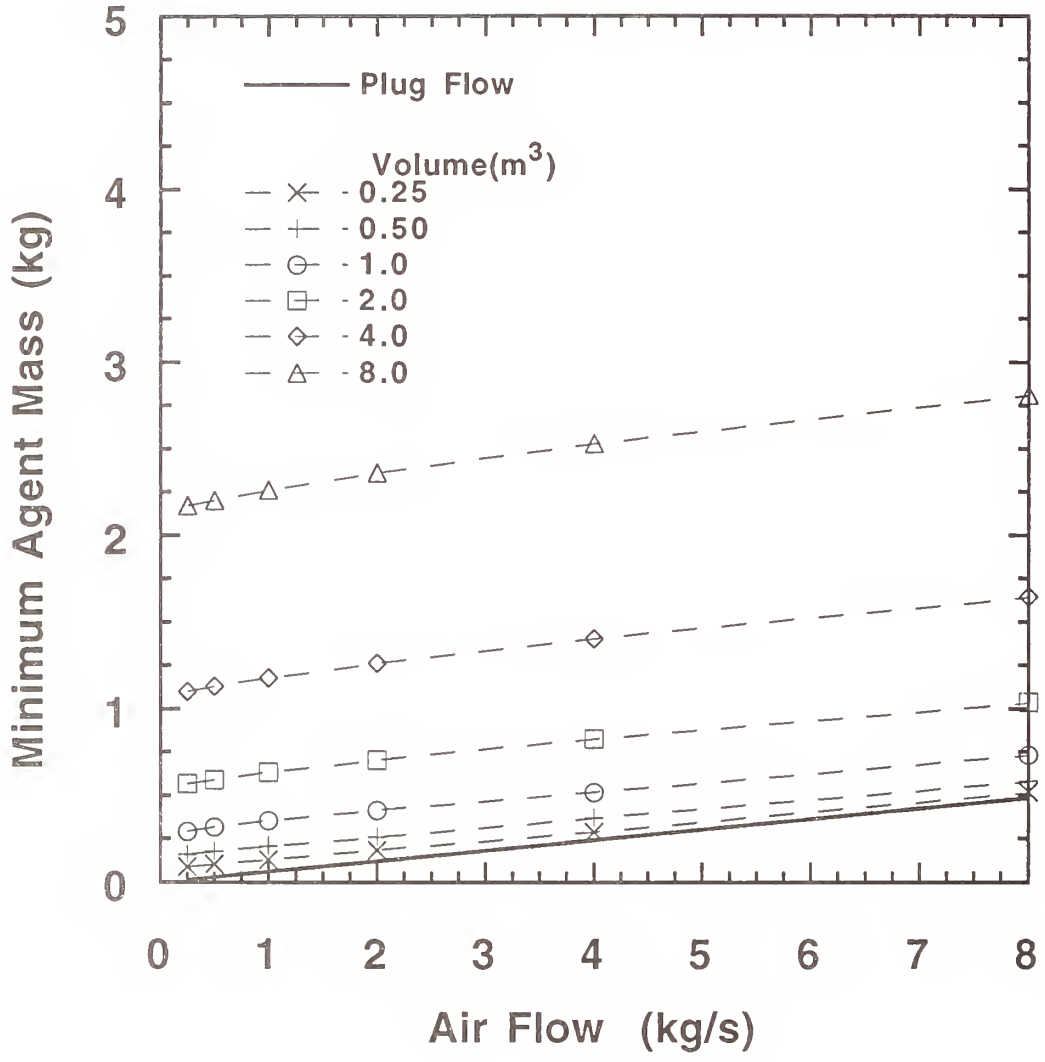

Figure 92. The minimum CF_3I mass requirements for spray fire suppression as a function of air flow. The agent injection duration was 0.25 s.

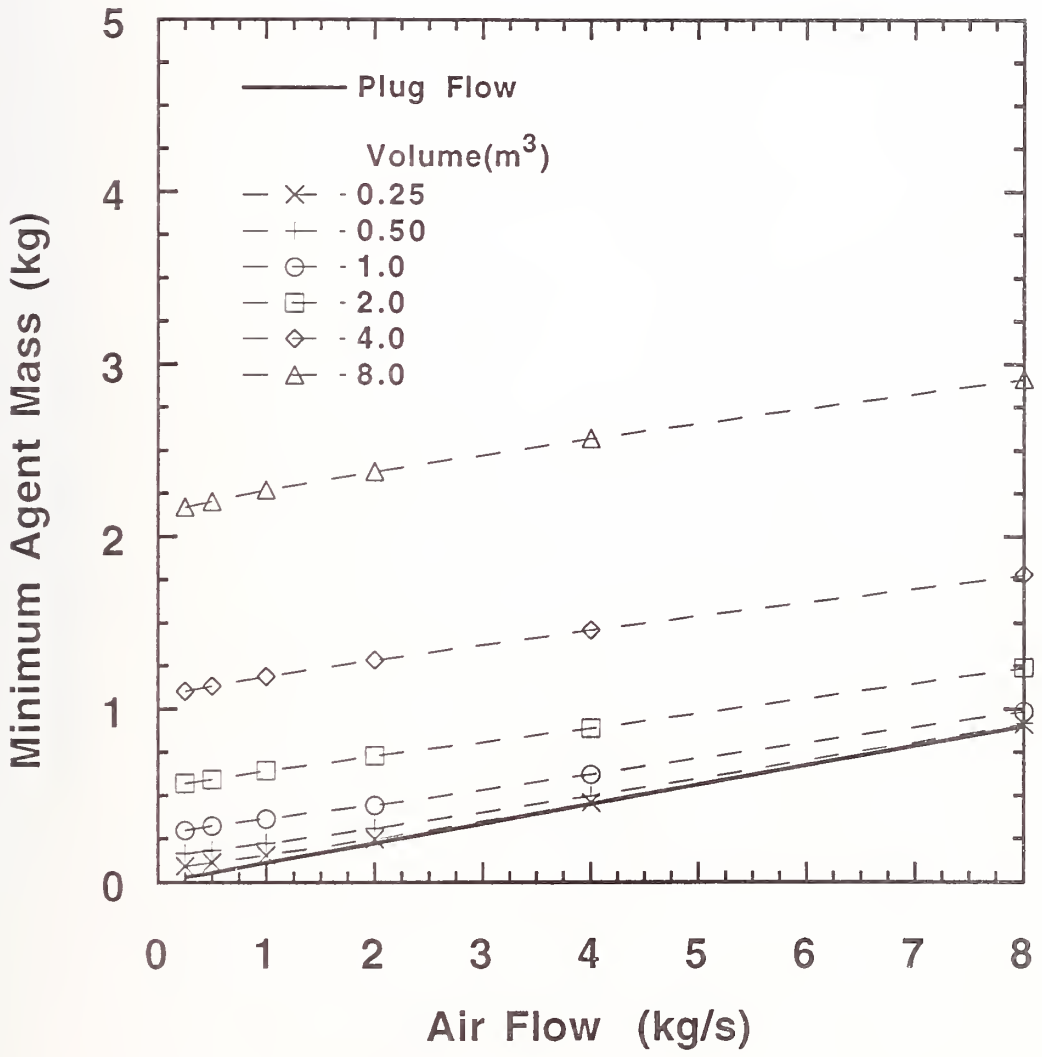

Figure 93. The minimum CF_3I mass requirements for spray fire suppression as a function of air flow. The agent injection duration was 0.50 s.

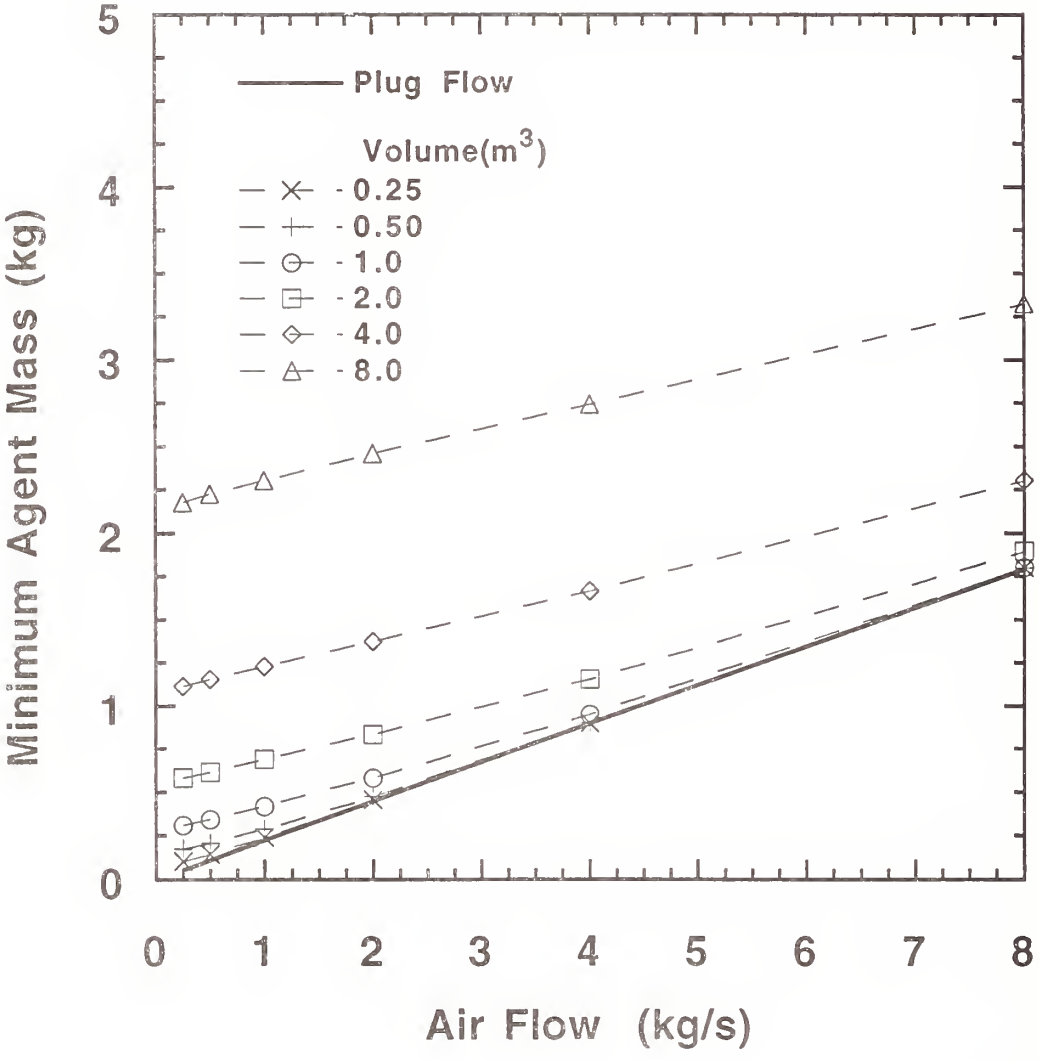

Figure 94. The minimum CF_3I mass requirements for spray fire suppression as a function of air flow. The agent injection duration was 1.0 s.

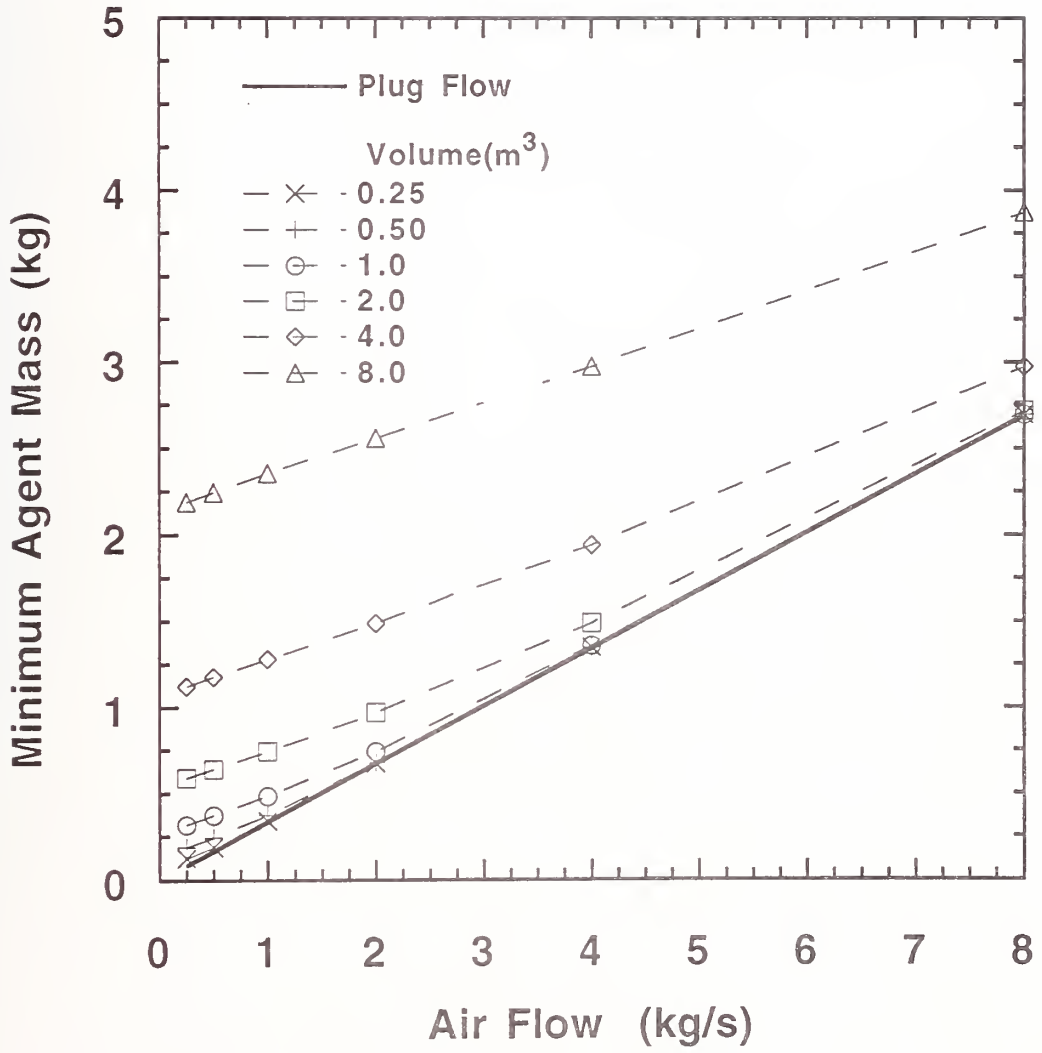

Figure 95. The minimum CF_3I mass requirements for spray fire suppression as a function of air flow. The agent injection duration was 1.5 s.

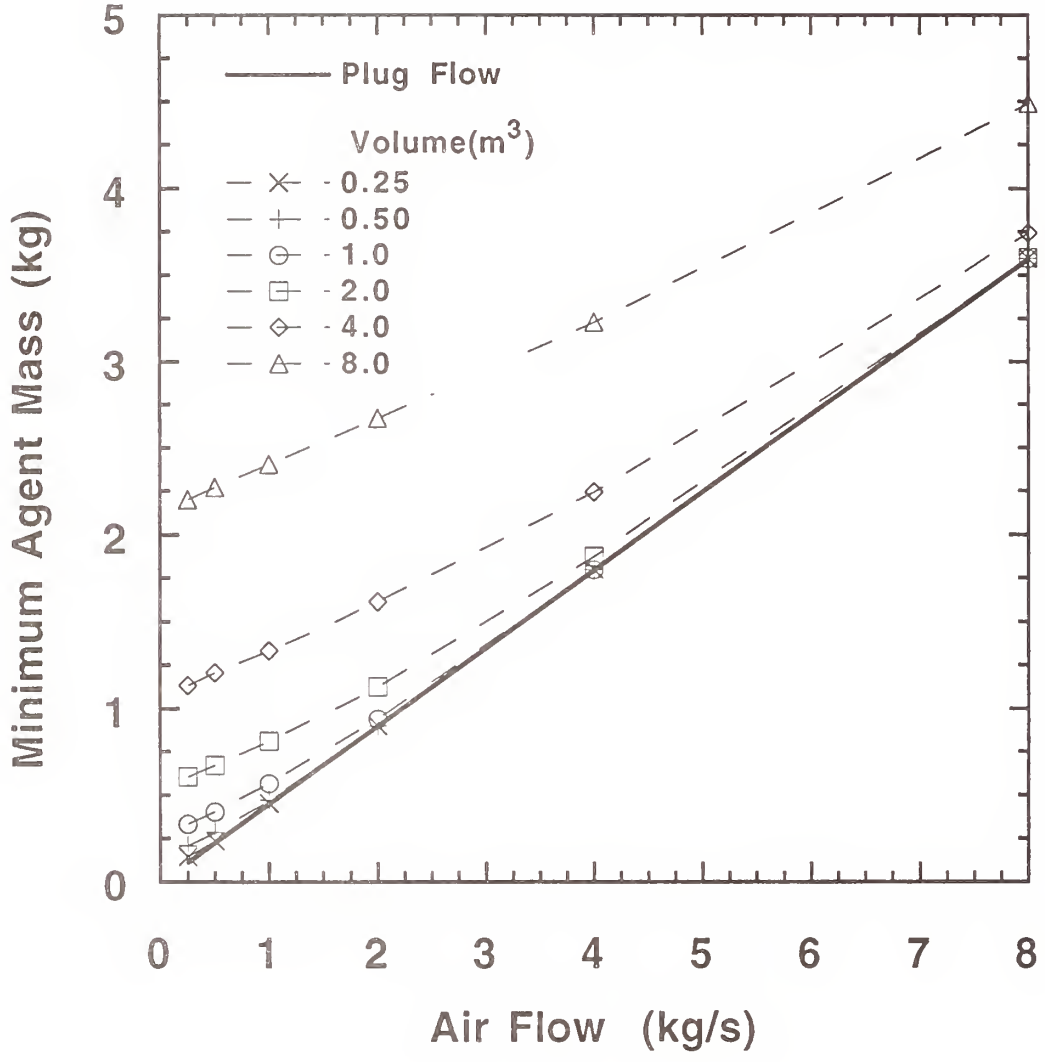

Figure 96. The minimum CF_3I mass requirements for spray fire suppression as a function of air flow. The agent injection duration was 2.0 s.

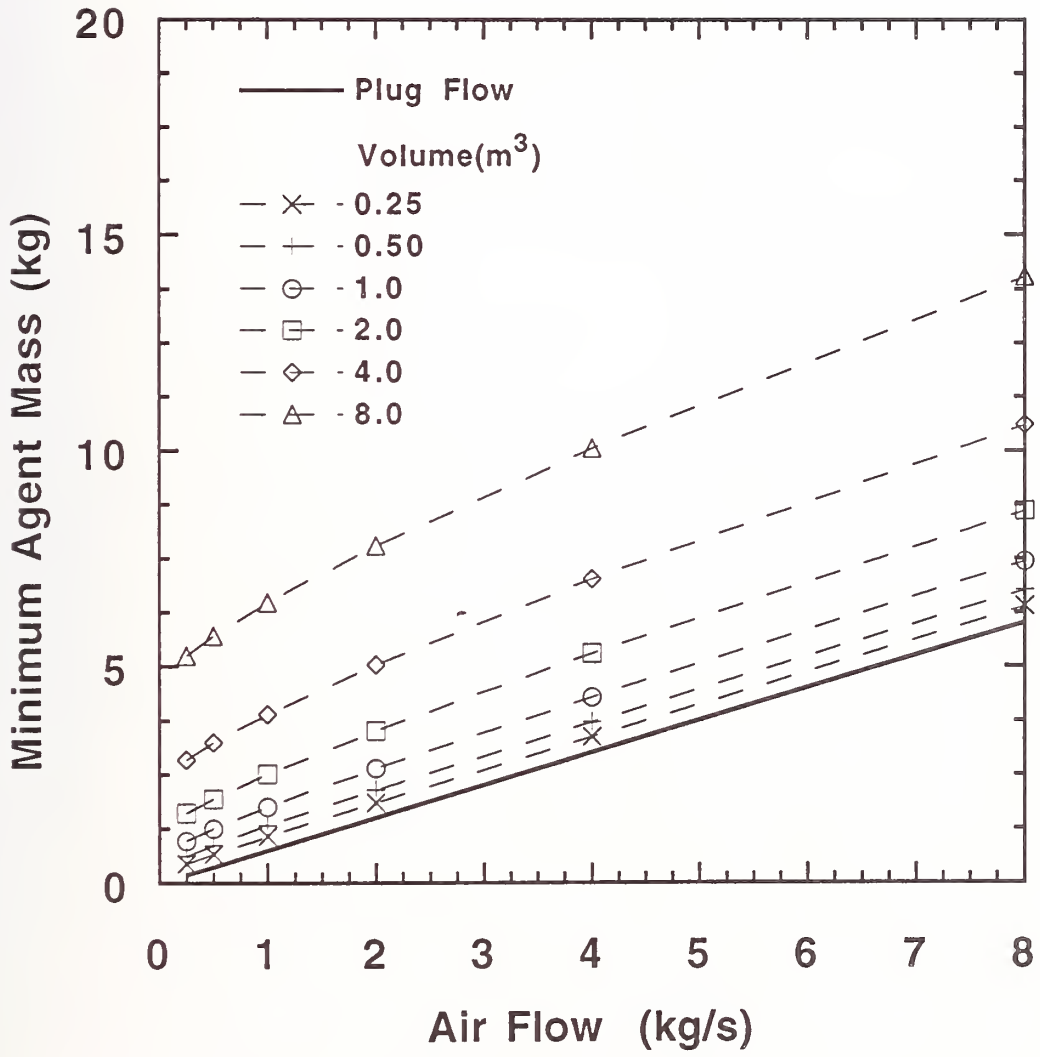

Figure 97. The minimum CF_3I mass requirements for pool fire suppression as a function of air flow. The agent injection duration was 0.25 s.

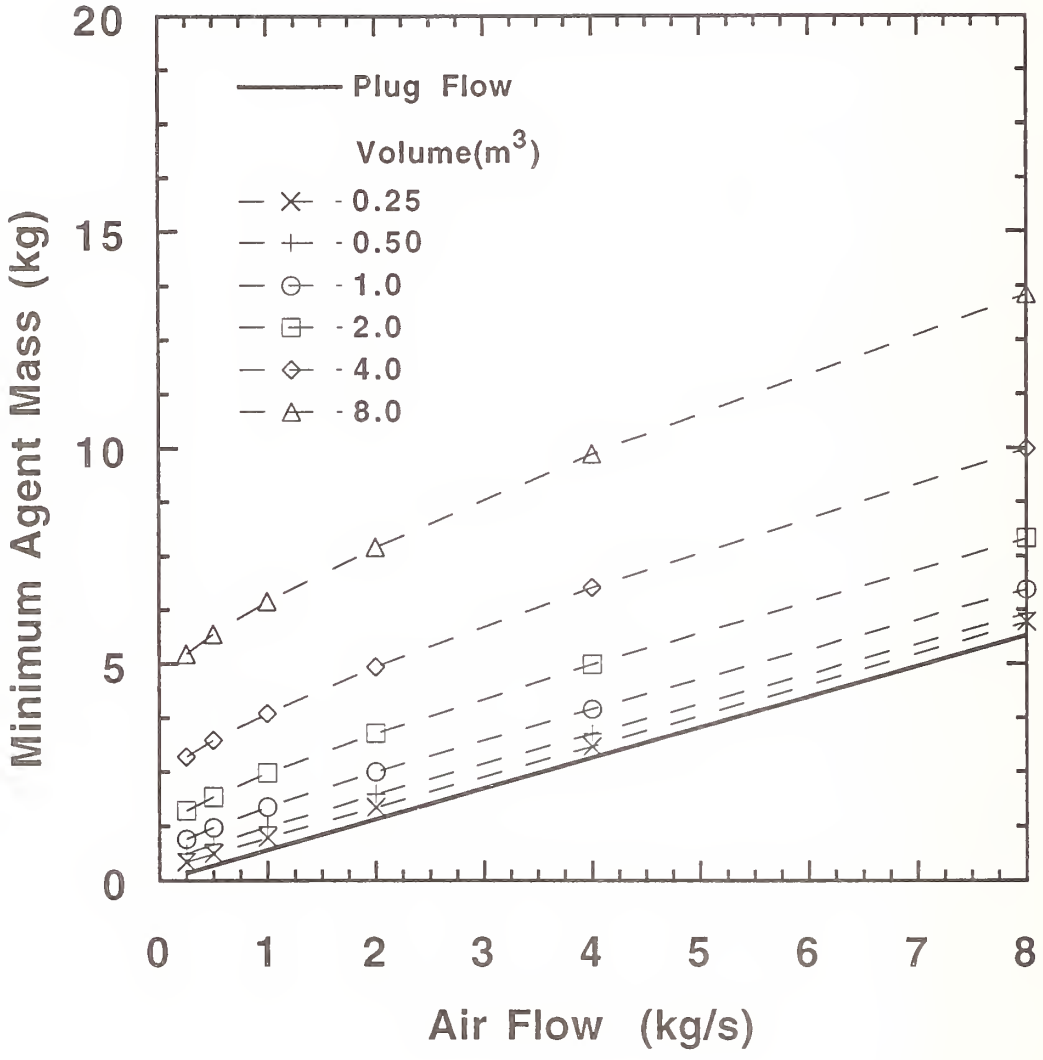

Figure 98. The minimum CF_3I mass requirements for pool fire suppression as a function of air flow. The agent injection duration was 0.50 s.

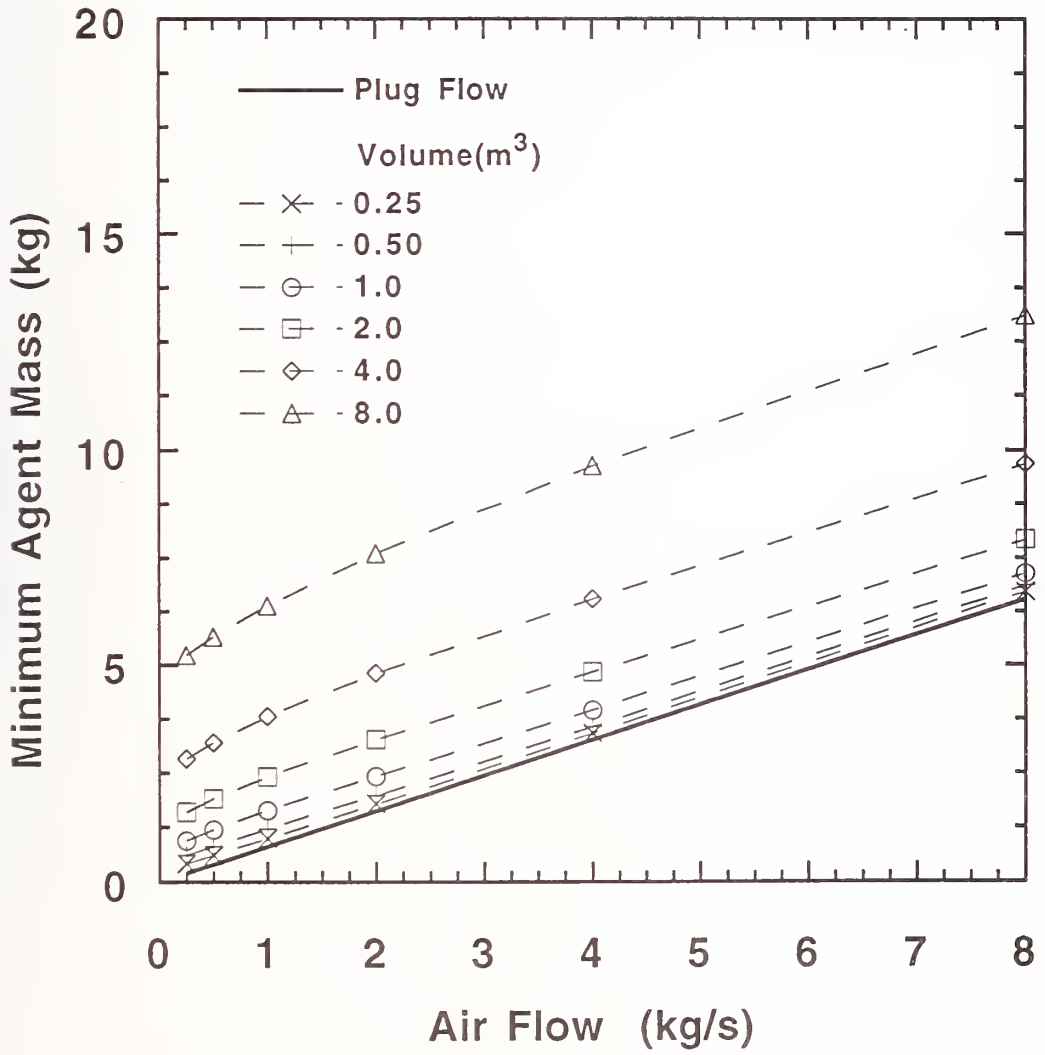

Figure 99. The minimum CF_3I mass requirements for pool fire suppression as a function of air flow. The agent injection duration was 1.0 s.

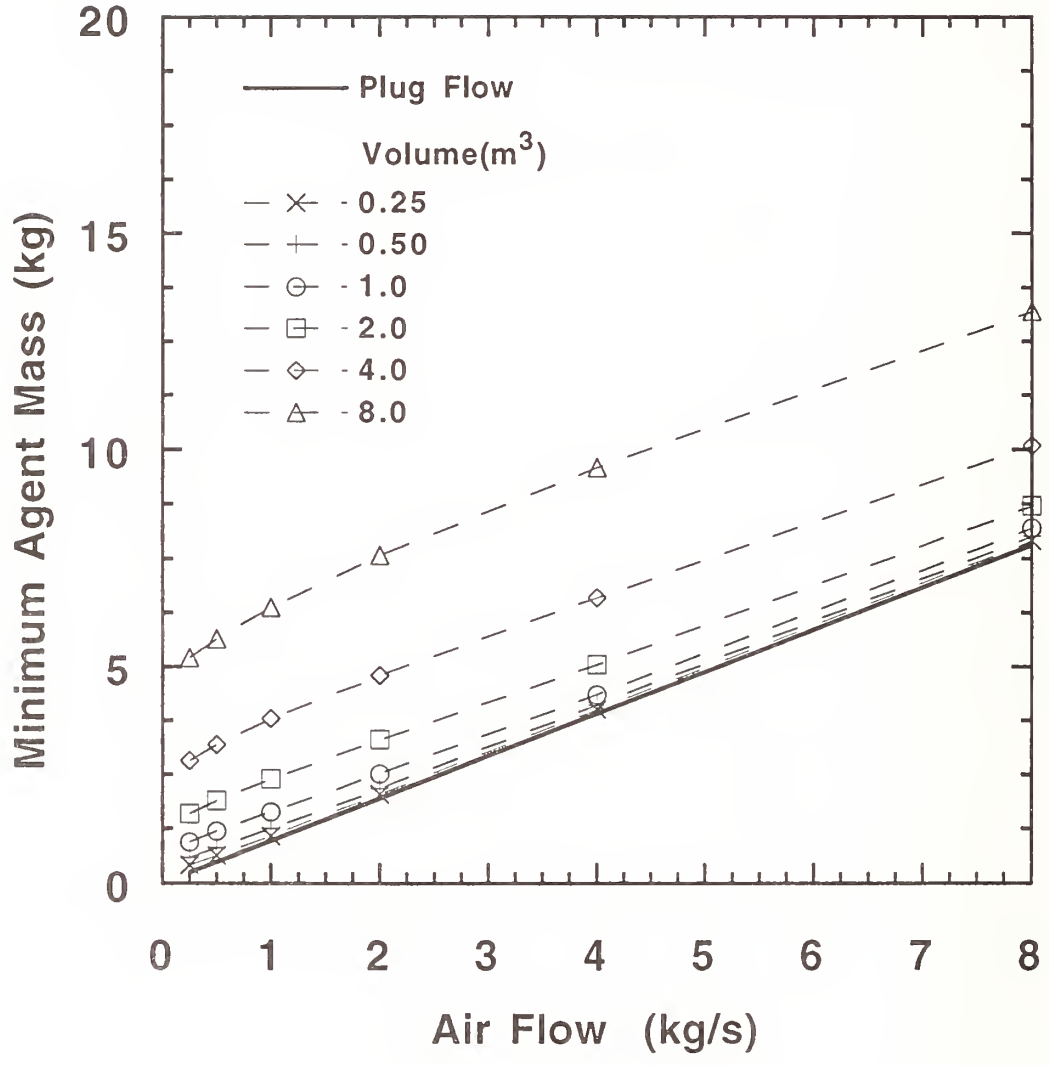

Figure 100. The minimum CF_3I mass requirements for pool fire suppression as a function of air flow. The agent injection duration was 1.5 s.

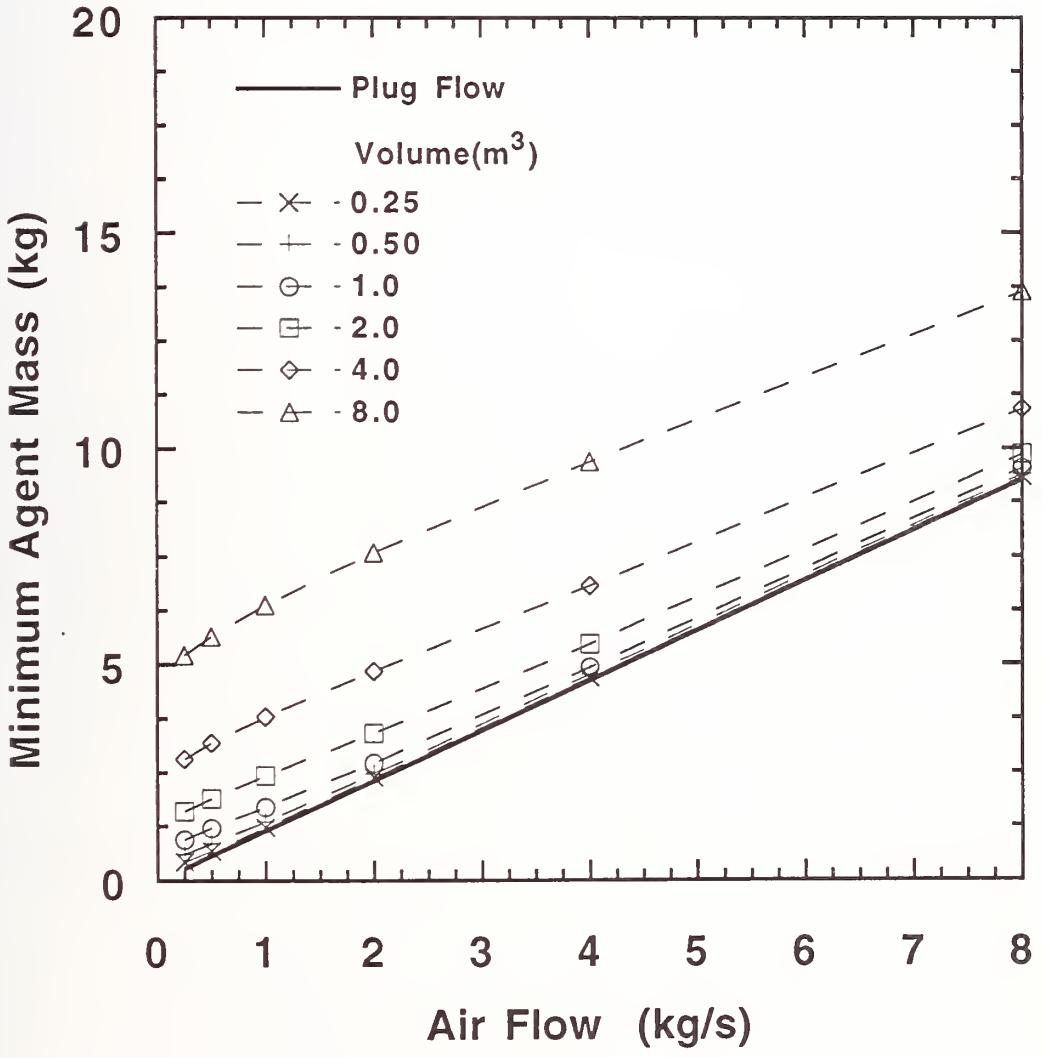

Figure 101. The minimum CF_3I mass requirements for pool fire suppression as a function of air flow. The agent injection duration was 2.0 s.

The minimum agent mass is plotted against injection time for a fixed volume (2.0 m^3) and air flow (1.0 kg/s) in Figures 102-105 to show the effect of injection time on the minimum mass requirements for the different agents, fire scenarios, and mixing modes. Figures 102 and 103 show the spray fire scenario results for plug and PSR-type mixing respectively. The injection time is seen to have a stronger impact on the relative agent mass for plug flow mixing as compared to PSR-type mixing. A comparison of the results in Figure 102 with the spray burner results in Figure 14 show identical trends between the injection time (or delivery interval) and the required mass. The agent rankings are also identical. This observation is not surprising, because the spray fire scenario and plug flow mixing mode is an excellent model for the spray burner. Johnson and Grenich (1986) reported results on the effect of agent injection duration for their "clean" nacelle fire tests in the AEN fire test simulator that are in qualitative agreement with the spray fire and plug flow mixing simulations. Their fire source was a baffle stabilized spray fire, and agent (halon 1301) was injected through a manifold to specifically provide uniform dispersion of the agent in the air flow. In Figure 103, the increase in agent mass from short to long injection times is approximately 30 %. The PSR-type mixing dampens the effect of the rate of injection. Minimum agent mass increases for both nacelle models as the injection time increases. Figure 104 shows the pool fire scenario results for the plug model. In this scenario, the injection time does not have as strong a relative impact, as compared to the spray fire/plug flow mixing model results. The minimum agent mass is a weak function of injection time for the PSR model as seen in Figure 105. Both the plug flow and PSR model results obtain minimum agent mass values at intermediate injection times in the pool fire scenario.

From Figures 102-105, it is inferred that the rate of agent injection can have either significant or negligible impact on the minimum agent mass for suppression depending on the fire scenario and mixing mode. In suppression system design, there may be applications where very short injection times significantly decrease agent mass requirements, which would benefit agent mass and volume storage considerations. Conversely, there may be applications where system constraints (constraints on storage pressure and temperature, bottle location, pipe diameter, etc.) dictate that it is impractical or impossible to achieve rapid discharge. Specific cases, where a relaxation of the discharge criterion (an increase in discharge time) would not have a significant impact on the agent mass, may benefit from flexibility in the system design. For example, in a retro-fit design, if the bottle location does not have to be changed (*i.e.*, its growth potential is sufficient), the original piping may provide an adequate discharge time. This design alternative is probably the second most desirable case, where drop-in replacement is the first.

The impact of a potential cold ambient environment on agent discharge should be considered if the discharge criterion is altered. This is especially critical when the discharge time has a significant impact on the mass of agent.

9.5.2.2 Comparison of the Model to the Military Specification for Halon 1301. The model results for halon 1301 can be compared to the guidelines presented in the Military Specification. The Military Specification used the guidelines developed from data collected by the CAA, where Hansberry (1954) reported that effective suppression occurred for agent injection durations between 0.5 s and 0.9 s. The Military Specification itself requires an injection time of 1 s or less. For comparative purposes, the injection time in the simulations was fixed at 1 s. A distinction between the smooth and rough nacelle configurations can be identified in terms of the worst case potential fire scenario, which is related to air flow and geometry. The smooth nacelle geometry has no ribs and thus pool fires will not be stabilized. In that case, the worst case fire scenario is considered to be a baffle stabilized spray fire (τ_f=0.1 s). For the rough nacelle geometry, ribs and other obstructions are available to stabilize pool fires, therefore the worst case fire is considered to be a baffle stabilized pool fire (τ_f = 1.0 s).

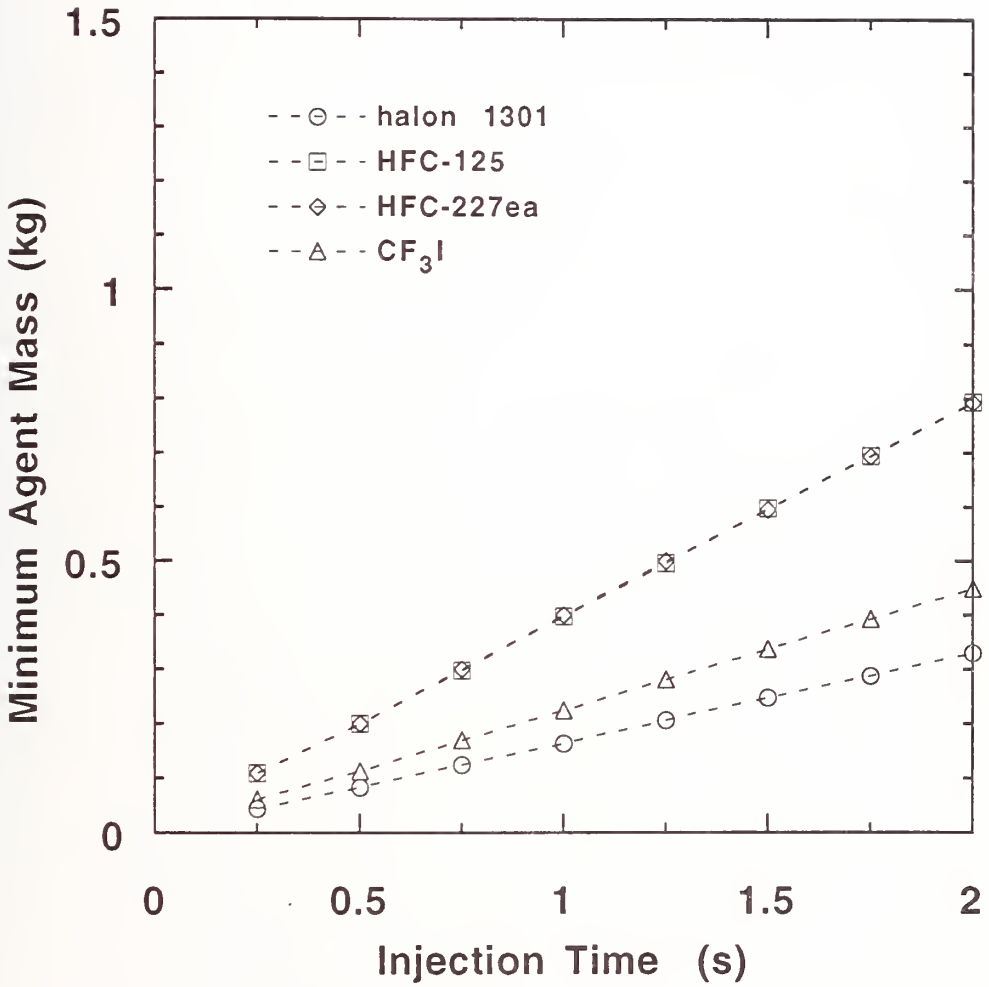

Figure 102. The minimum agent mass as a function of the injection time for the spray fire scenario with plug flow mixing. The air flow is 1 kg/s.

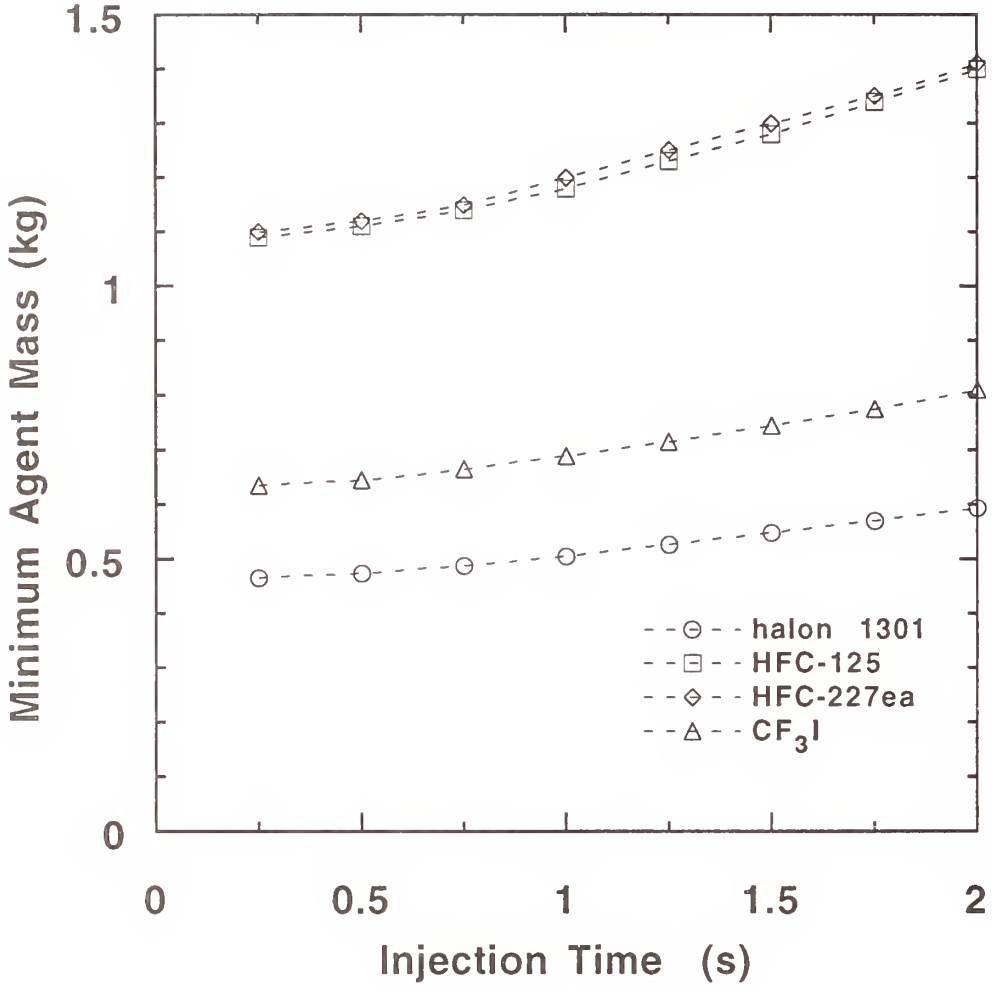

Figure 103. The minimum agent mass as a function of the injection time for the spray fire scenario with PSR mixing. The air flow is 1 kg/s and the volume is 2.0 m^3.

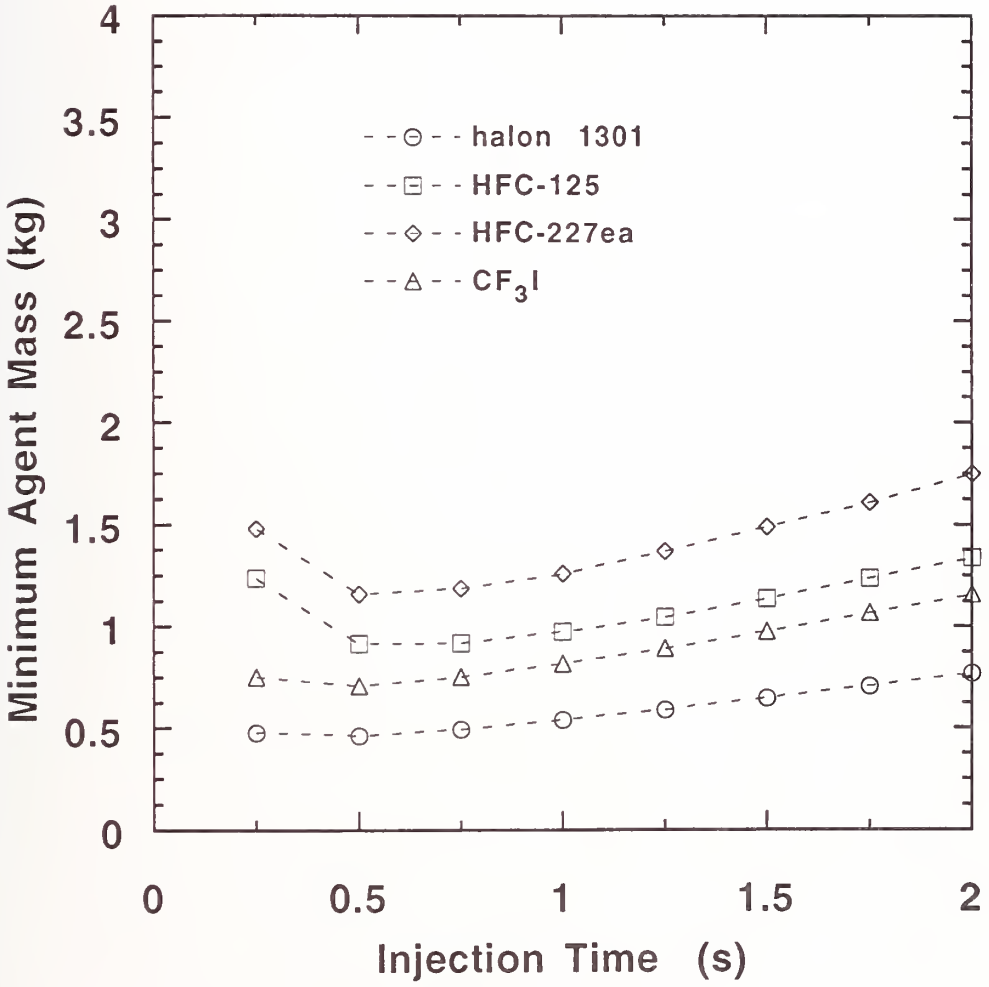

Figure 104. The minimum agent mass as a function of the injection time for the pool fire scenario with plug flow mixing. The air flow is 1 kg/s.

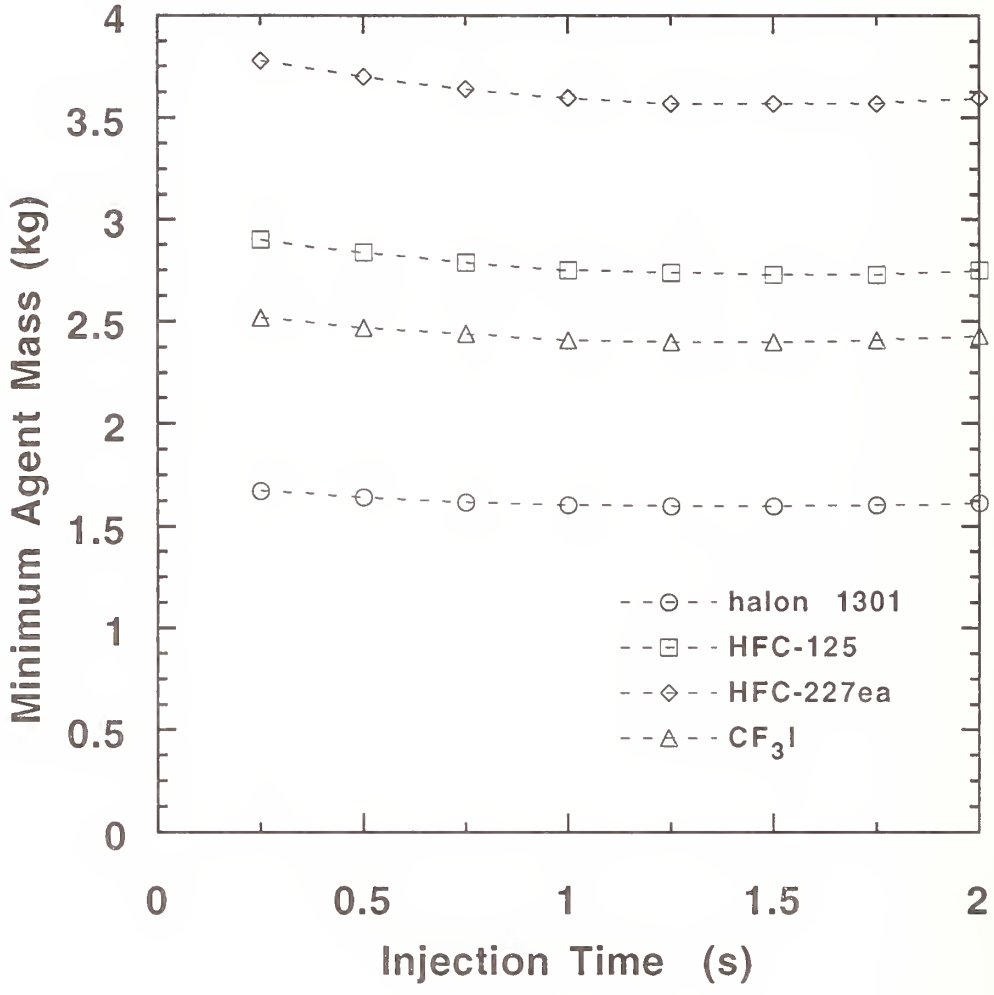

Figure 105. The minimum agent mass as a function of the injection time for the pool fire scenario with PSR mixing. The air flow is 1 kg/s and the volume is 2.0 m^3.

Figures 106-109 show the model calculations and the Military Specification agent requirements. Figures 106 and 107 show the spray fire scenario and the guideline requirements for the smooth nacelle. Notice that the Military Specification specifies more mass than predicted from the calculations; in some cases more than three times the predicted amount. If the guidelines were compared to the results for the shortest injection time then even less, and in some cases, much less agent would be predicted. Figures 108 and 109 show the pool fire scenario results compared to the guidelines for the rough nacelle geometry for air flows above 0.45 kg/s. Again the guidelines specify more agent than predicted from the model. The injection time does not have a large impact on the predicted agent requirements; thus, for shorter injection times agent mass will not be substantially less than those for 1.0 s injections and may actually be higher.

The comparison of the Military Specification's halon 1301 requirements and the model predictions indicates that the model predicted the trends as the volume and air flow increased. The fact that no allowances for imperfect mixing or other un-modeled phenomena were included in the predictions suggests that the results are consistent with the Military Specification guidelines. If such allowances were included, a model such as this may have wide applicability.

9.5.3 Comparison of Predicted Alternative Agent Requirements to Halon 1301 Requirements. The predicted alternative agent mass requirements can be compared to the predicted halon 1301 mass requirements for each given fire scenario, nacelle free volumes, air flow, and agent injection duration. Comparisons of the two fire scenarios, spray and pool fires, at the nominally best agent injection durations of 0.25 s and 1.0 s respectively are shown in Figures 110-112. These figures show the amount of alternative agent required for a given air flow and volume plotted against the amount of halon 1301. Notice that these points fall on a separate line for each fire scenario, and that the lines pass through the origin. The slopes from best fit straight lines indicate a constant multiplier to the amount of halon required to that of the alternative agent required for each fire scenario. This comparison is analogous to the Flame Suppression Number (FSN) introduced in Section 4 of NIST SP 861 (Grosshandler *et al.*, 1994) where the experimental results for the minimum halon 1301 mass required to extinguish various flames were compared to the minimum mass requirements of a number of other agents. Table 11 shows the slopes for the best-fit straight lines for each alternative agent and fire scenario.

As expected, CF_3I is the closest in terms of mass requirements to halon 1301 for both the spray and pool fire scenarios. For the spray-type flame, there is little difference between HFC-125 and HFC-227, but there is a significant difference between HFC-125 and HFC-227 for the pool fire scenario. This comparison has important practical implications. For two very different fire scenarios, there is a linear relationship between the amount of halon 1301 and alternative agent over a wide range of air flows and volumes. Even though idealized mixing and isothermal conditions were assumed, this relationship may still hold for non-idealized real fire scenarios. Therefore, knowledge gained from halon 1301 systems in terms of agent mass requirements may be directly applied to alternative agents. In addition, Table 11 suggests that HFC-125 is almost as efficient as CF_3I for the pool fire scenario. This is not surprising, after all, the input for X_∞ in the pool fire scenario was related to the peak flammability limits, which when written in terms of mass rather than mole fractions (as in Table 10) were 0.247, 0.361, 0.420 and 0.331, for halon 1301, HFC-125, HFC-227, and CF_3I respectively. This follows the same trends as the results for the pool fire scenario as seen in Table 11.

9.5.4 Comparison of the Model to Full-Scale Test Data. It is of interest to compare the model to full-scale data. Data is available from the Phase II full-scale Wright-Patterson study on halon alternatives (Bennett and Caggianelli, 1995). The tests were performed in the AEN fire test simulator, and the data included the minimum agent required to suppress a fuel spray fire. This is the only

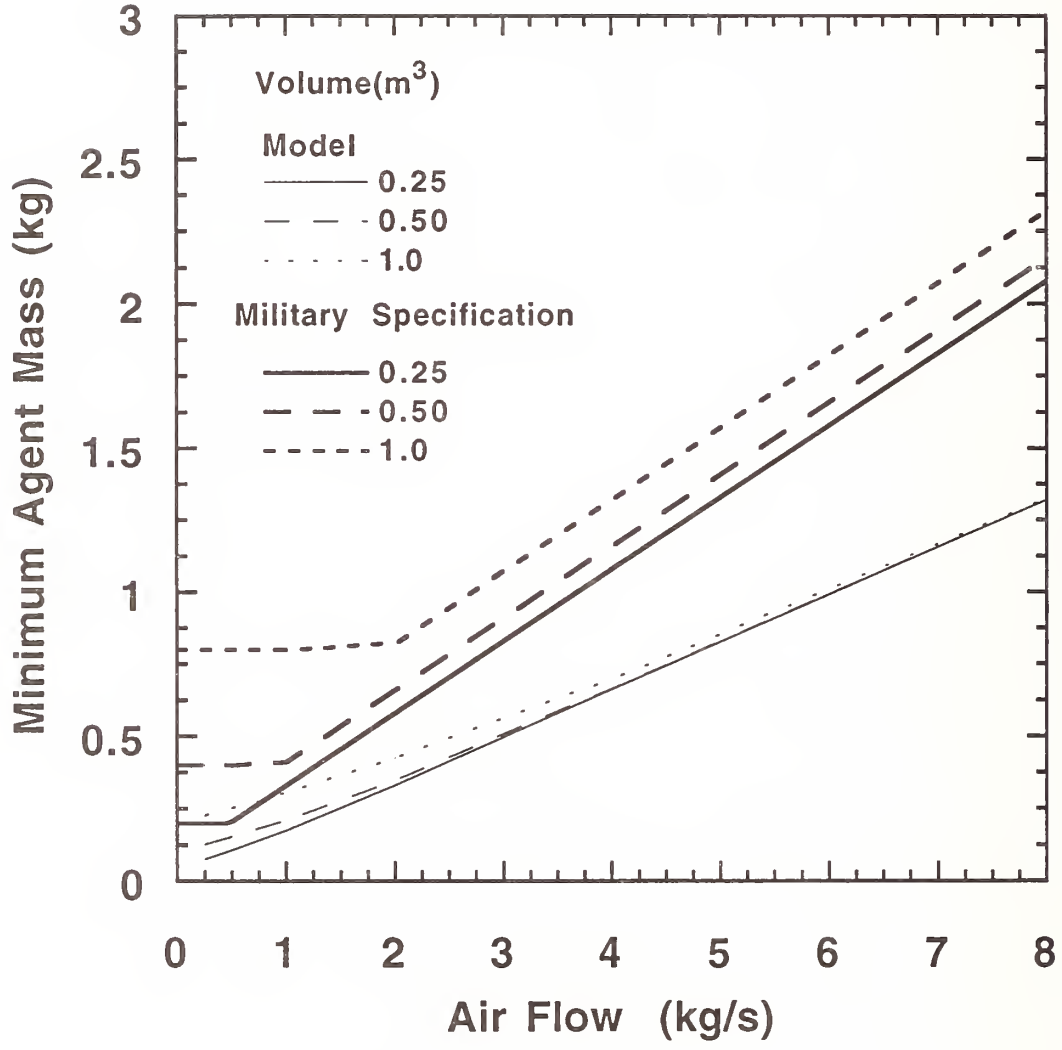

Figure 106. Comparison of calculated minimum halon 1301 mass requirements for spray fire suppression to Military Specification guidelines for low nacelle volumes.

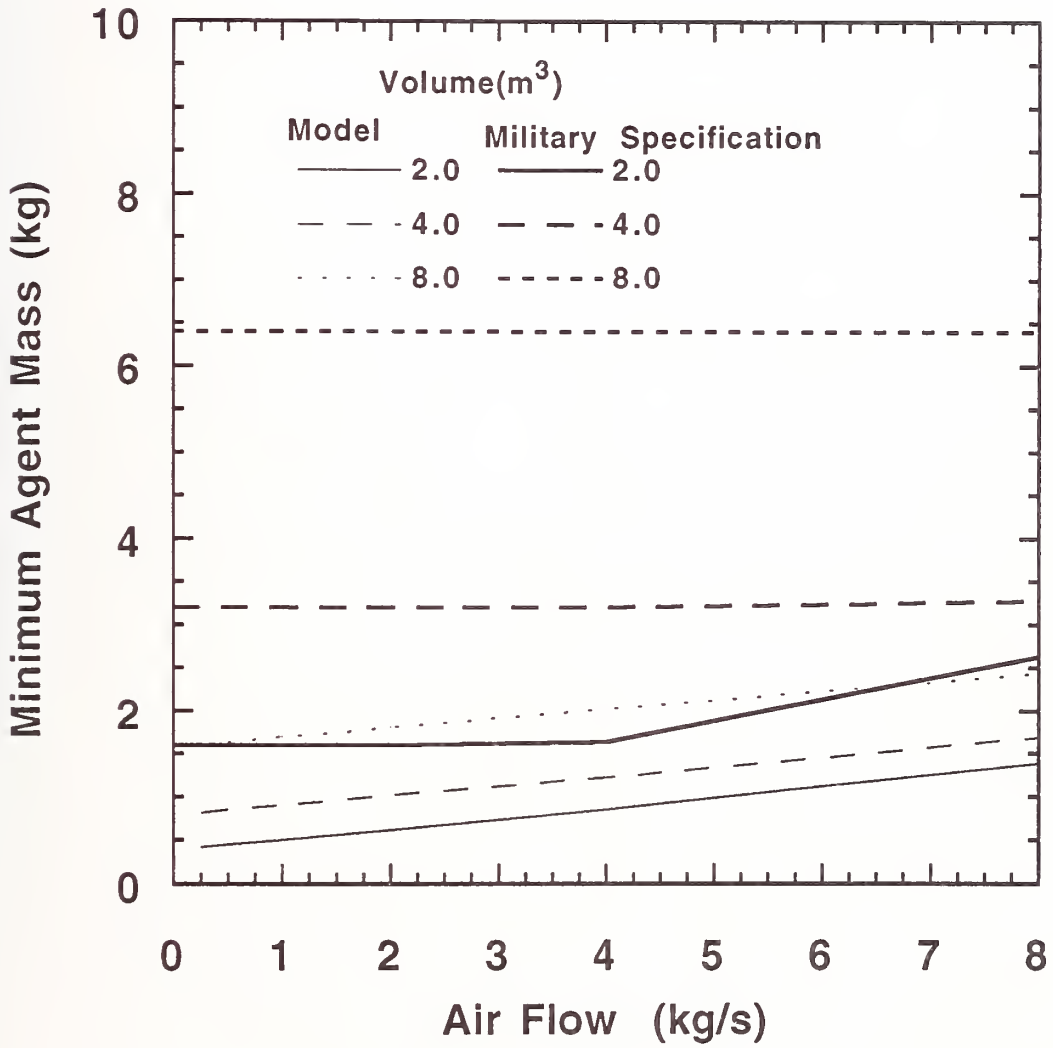

Figure 107. Comparison of calculated minimum halon 1301 mass requirements for spray fire suppression to Military Specification guidelines for high nacelle volumes.

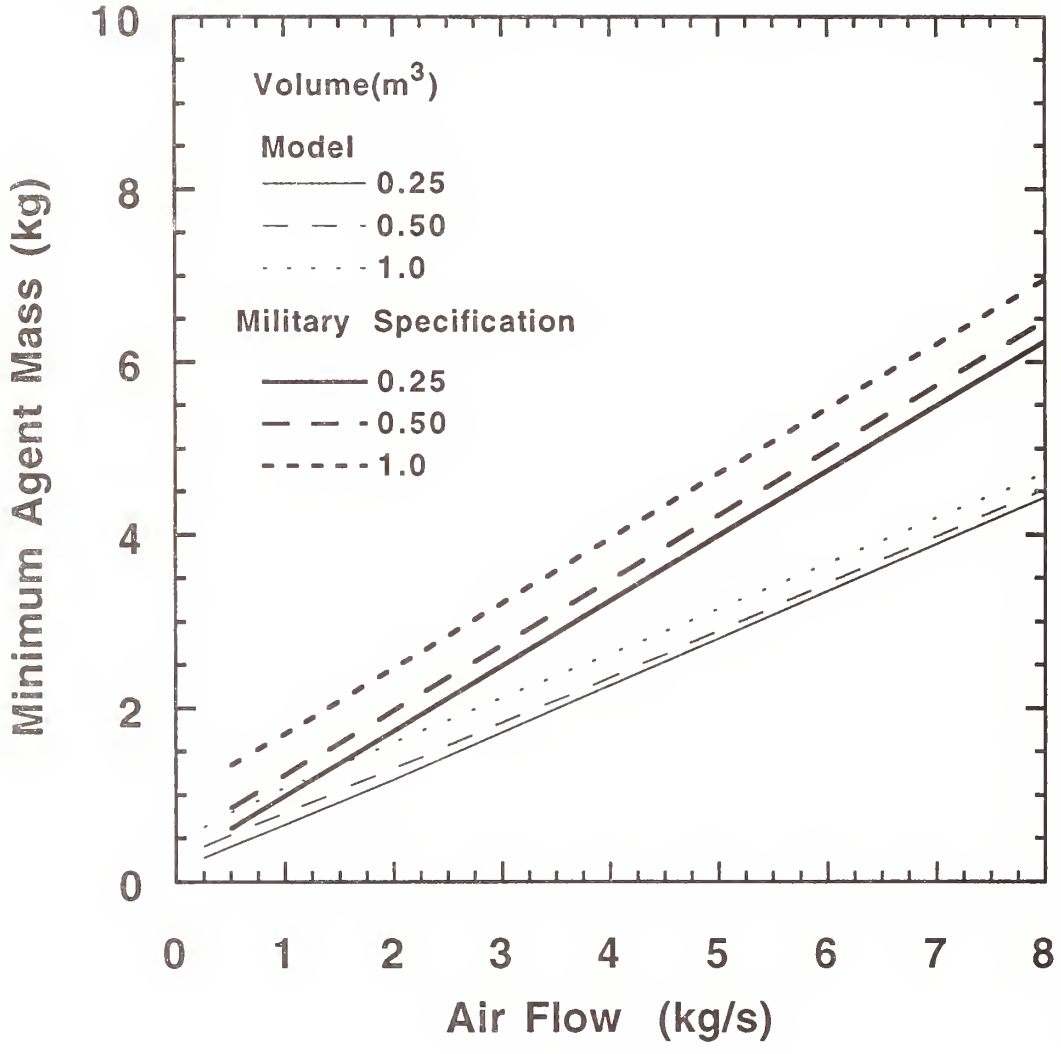

Figure 108. Comparison of calculated minimum halon 1301 mass requirements for pool fire suppression to Military Specification guidelines for low nacelle volumes.

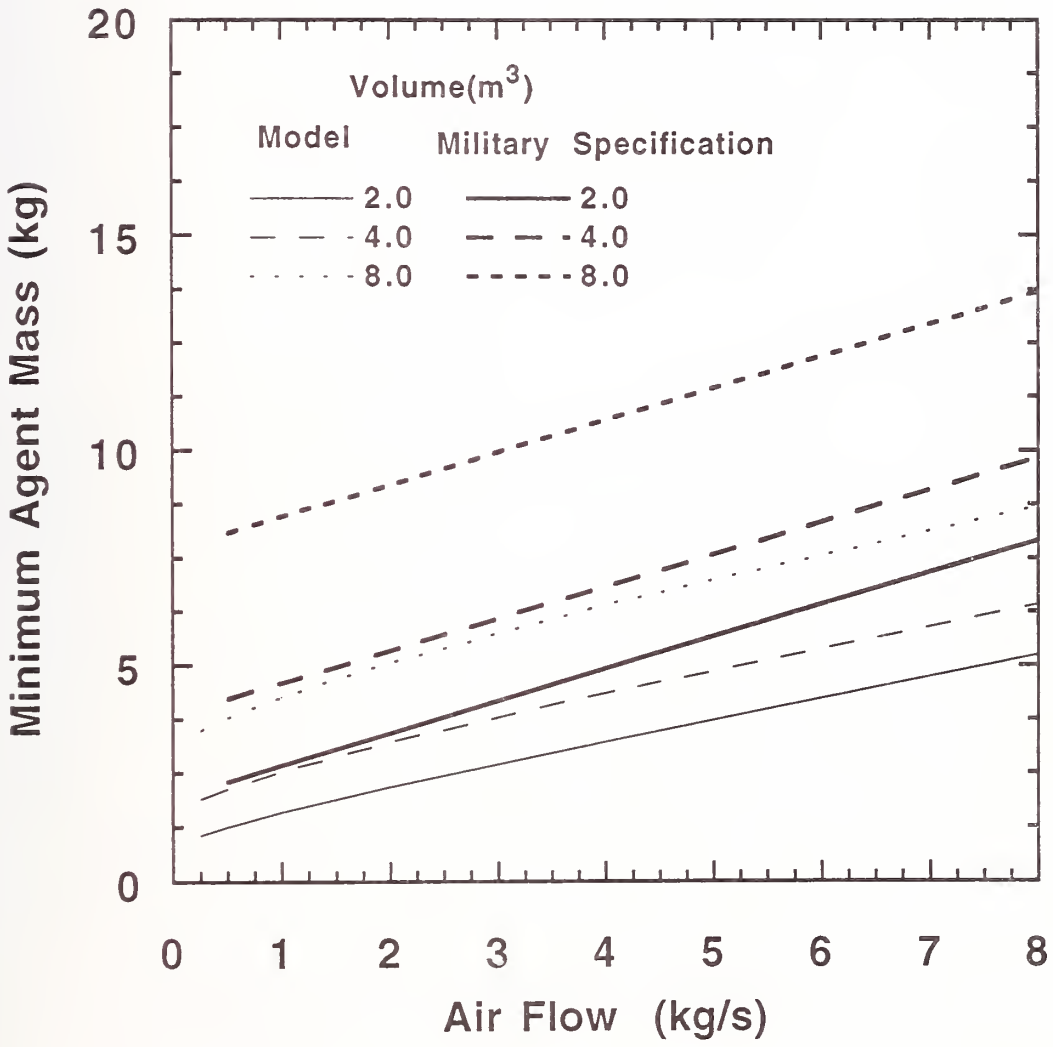

Figure 109. Comparison of calculated minimum halon 1301 mass requirements for pool fire suppression to Military Specification guidelines for high nacelle volumes.

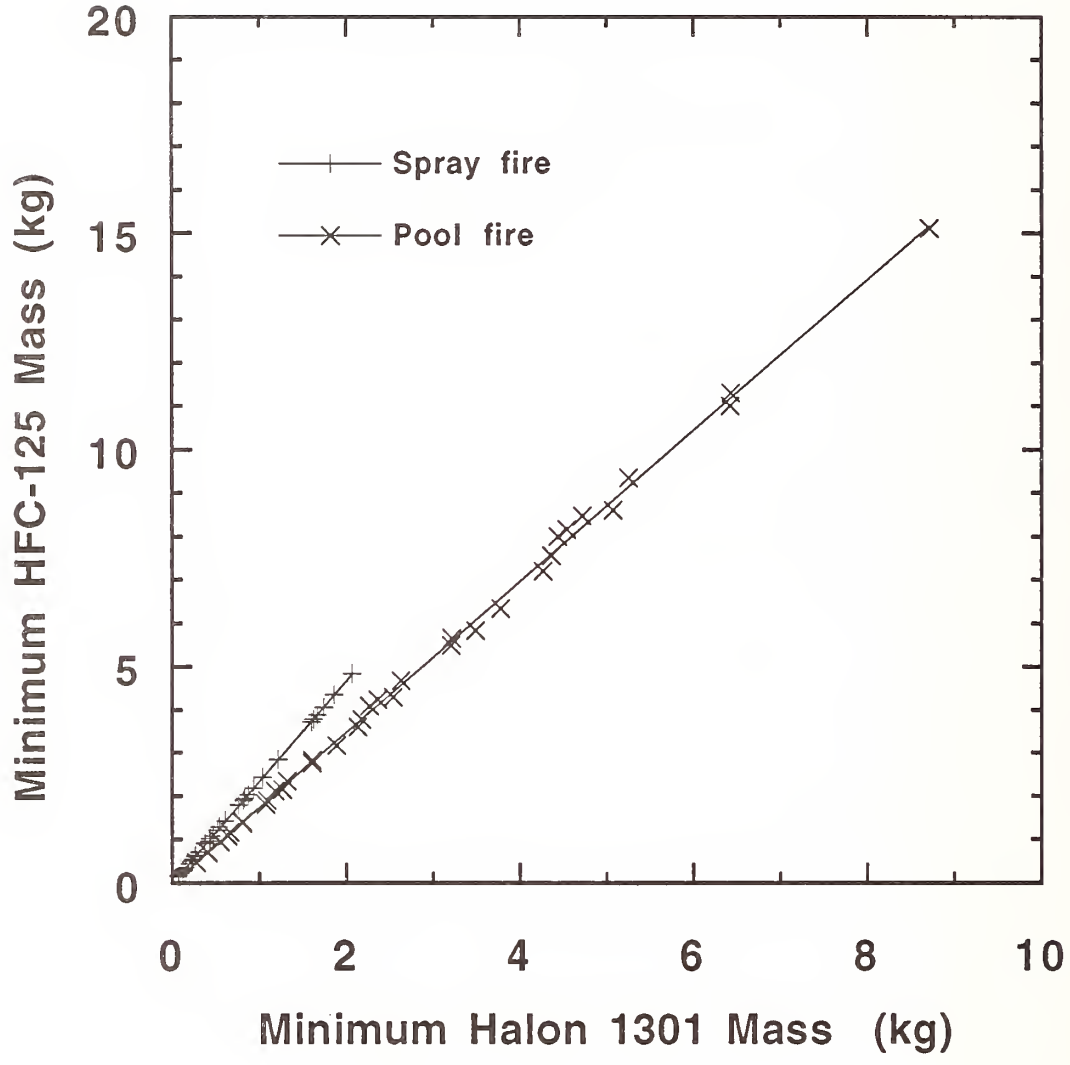

Figure 110. Comparison of minimum mass requirements of HFC-125 to halon 1301 for 0.25 s and 1.0 s injection durations in the spray and pool fire scenarios respectively. Solid lines indicate best-fits through the data.

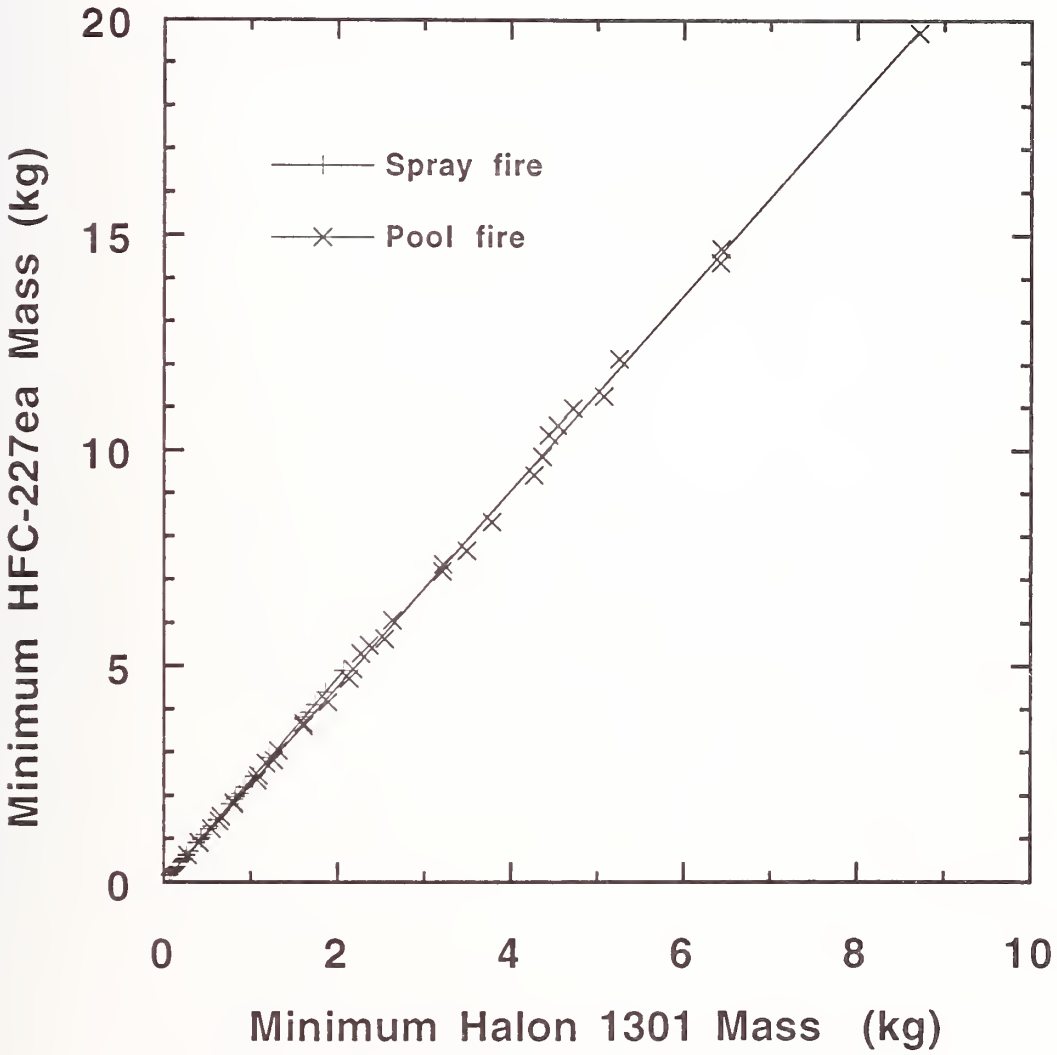

Figure 111. Comparison of minimum mass requirements of HFC-227 to halon 1301 for 0.25 s and 1.0 s injection durations in the spray and pool fire scenarios respectively. Solid lines indicate best-fits through the data.

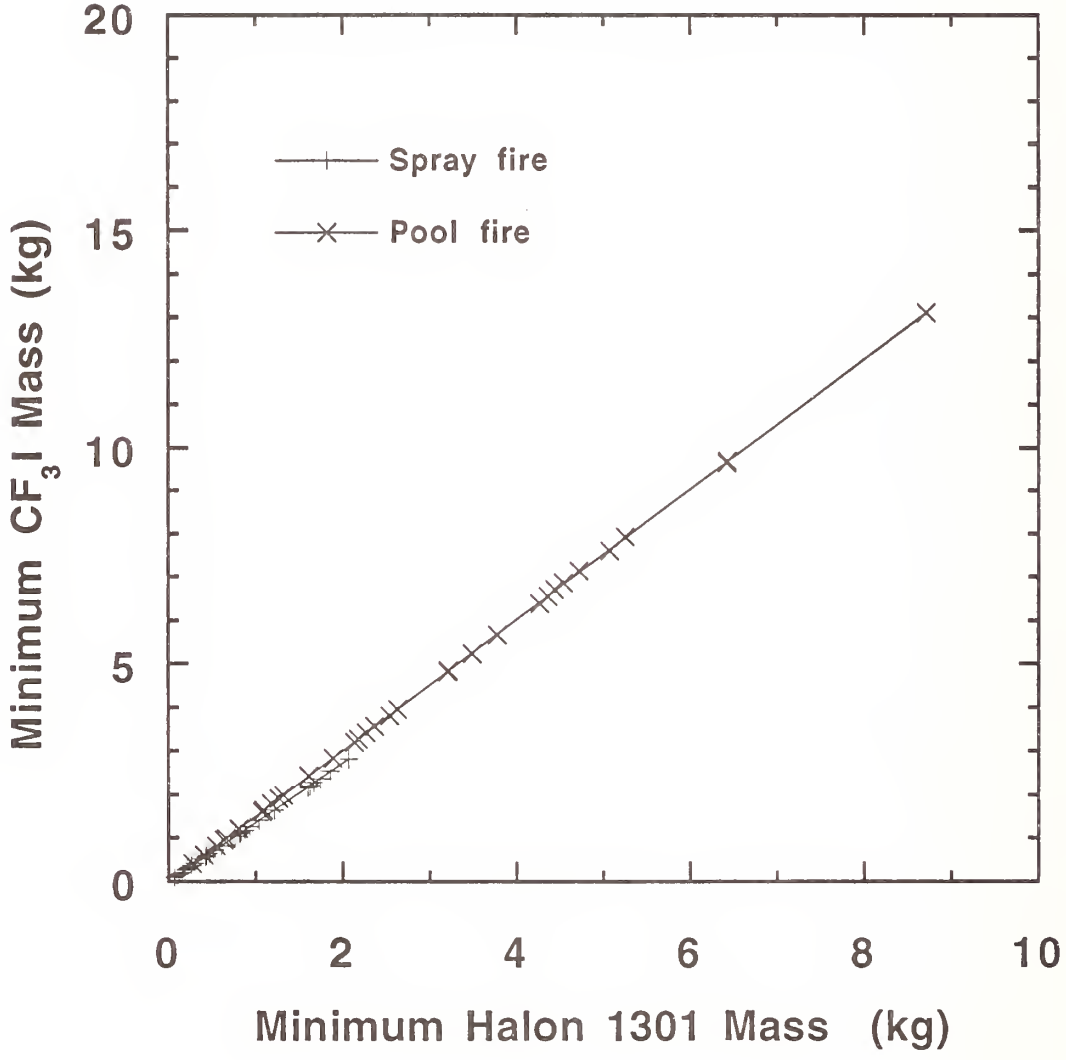

Figure 112. Comparison of minimum mass requirements of CF_3I to halon 1301 for 0.25 s and 1.0 s injection durations in the spray and pool fire scenarios respectively. Solid lines indicate best-fits through the data.

known full-scale data for the alternative agents. Model calculations were compared to this data set. Only tests where the surface temperature was not above 79 °C (175 °F) were considered since hot surface re-ignition was not included in the model at this time. Two nacelle volumes, 2.5 m^3 and 4.2 m^3, and two air flows, 0.4 kg/s and 1.2 kg/s were examined in the full-scale tests. Agent injection duration varied depending on the bottle conditions and the amount of agent required to suppress a given fire. Estimated times were in the range from 0.05 s to 0.4 s. For the purposes of comparison an effective injection time of 0.25 s was assumed, since at very rapid injection rates some spreading of the agent as it penetrates up and downstream from the injection location must occur. The data for each agent were compared to the model calculations for baffle stabilized spray and pool fire scenarios over a range of air flows and volumes. Figures 113-118 show the comparisons. The test data fall between the plug

Table 11. Best-fit Flame Suppression Number for each alternative agent and fire scenario

Agent	(Mass of agent) / (Mass of halon 1301)	
	Spray Flame (τ_f=0.1 s)	Pool Fire (τ_f=1.0 s)
HFC-125	2.34	1.74
HFC-227	2.36	2.27
CF_3I	1.36	1.51

flow results and the PSR results for the spray fire scenario. The test results lie above and then below the plug flow results for the pool fire scenario as the air flow is increased. One possible explanation of these observations is that the experimental results are consistent with a spray fire and plug flow with poor radial mixing. The details of the AEN mixing are not known, but it is unlikely that recirculation of agent and air occurs, which suggests a plug flow mixing scenario.

9.5.5 Re-ignition Suppression Requirements. Re-ignition suppression requirements are very dependent on the specific scenario. At this point, there is no reliable method to predict the optimal agent requirements to prevent it. Re-ignition is always a threat as long as fuel vapor and air can come in contact with sufficiently hot surfaces. Strategies to prevent re-ignition include removing fuel vapor, reducing surface temperatures (either through design changes or active cooling), and inerting the fuel/air mixture with a suppressant.

Fuel vapors are removed by the air flow in the nacelle, liquids are removed by drain holes or sump ejectors. Typically, before activation of the engine nacelle fire suppression system, the jet fuel and hydraulic fluid flow to the particular engine is shut down. This limits the amount of fuel in the nacelle, but it could take a relatively long time to remove the combustibles from the nacelle, especially the low vapor pressure liquids.

Surface temperatures can be reduced either by design changes such as insulating hot surfaces, or through active cooling. Air flow over hot surfaces will lower the surface temperature, but may not be available in sufficient quantity. A mechanism that should be considered is the effect of surface cooling from the agent after it is discharged into the nacelle. For instance, mass requirements for HFC-125 will probably be at least twice that of halon 1301 and, given the heat of vaporization and heat capacities for those two agents, the HFC-125 discharge would provide more cooling relative to halon 1301. It is possible, although unlikely, that cooling may be sufficient to decrease surface temperatures below ignition temperatures.

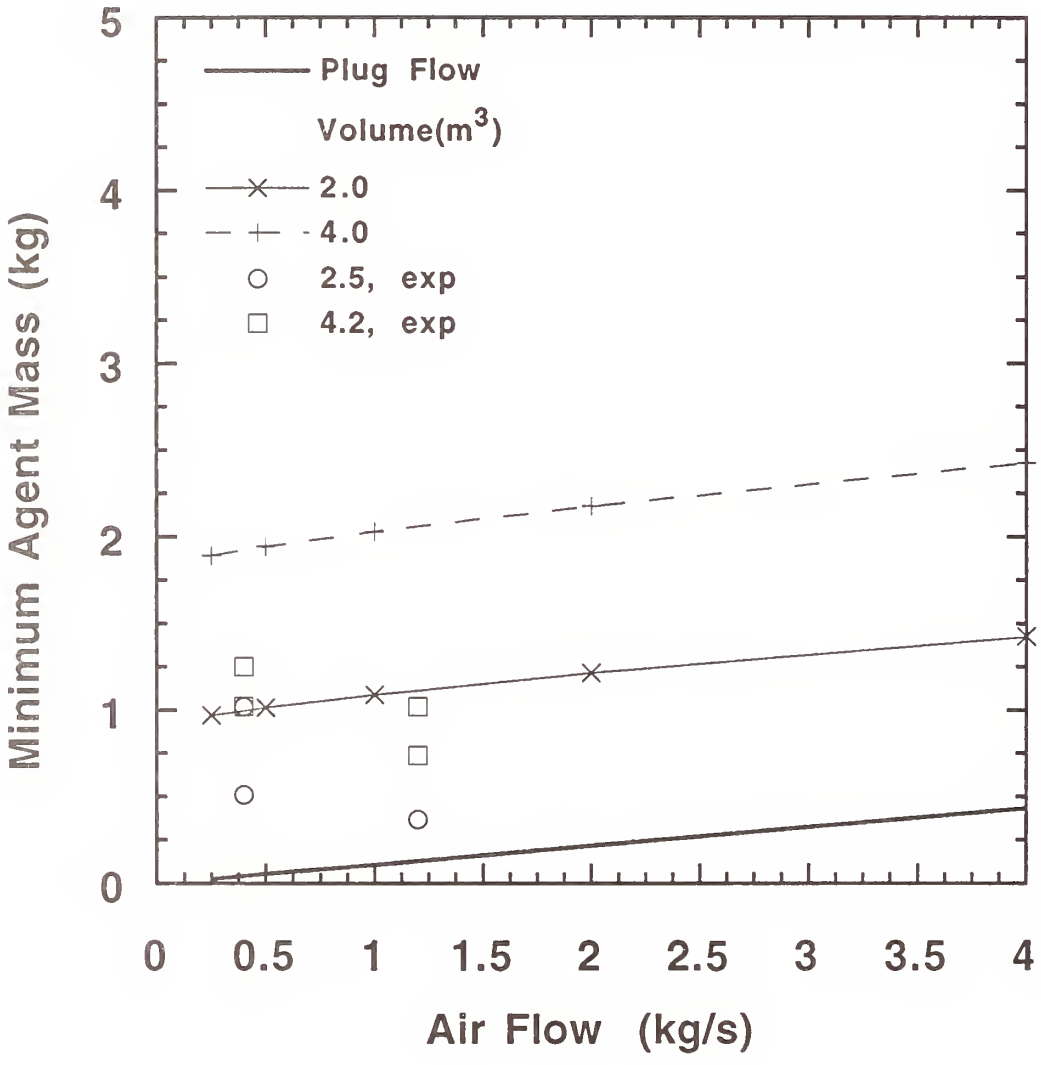

Figure 113. Minimum HFC-125 mass requirements for full-scale AEN simulator tests and the simulated spray fire scenario for an agent injection duration of 0.25 s.

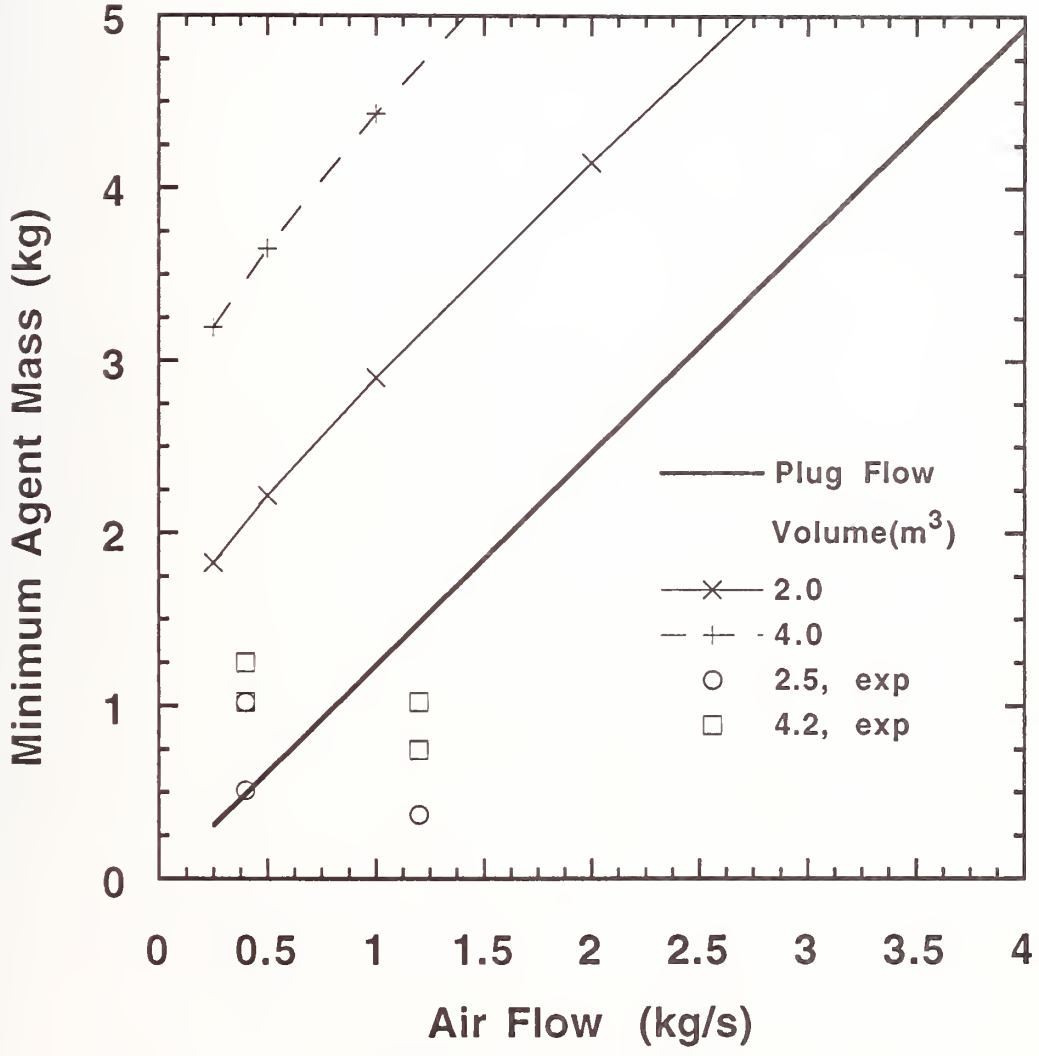

Figure 114. Minimum HFC-125 mass requirements for full-scale AEN simulator tests and the simulated pool fire scenario for an agent injection duration of 0.25 s.

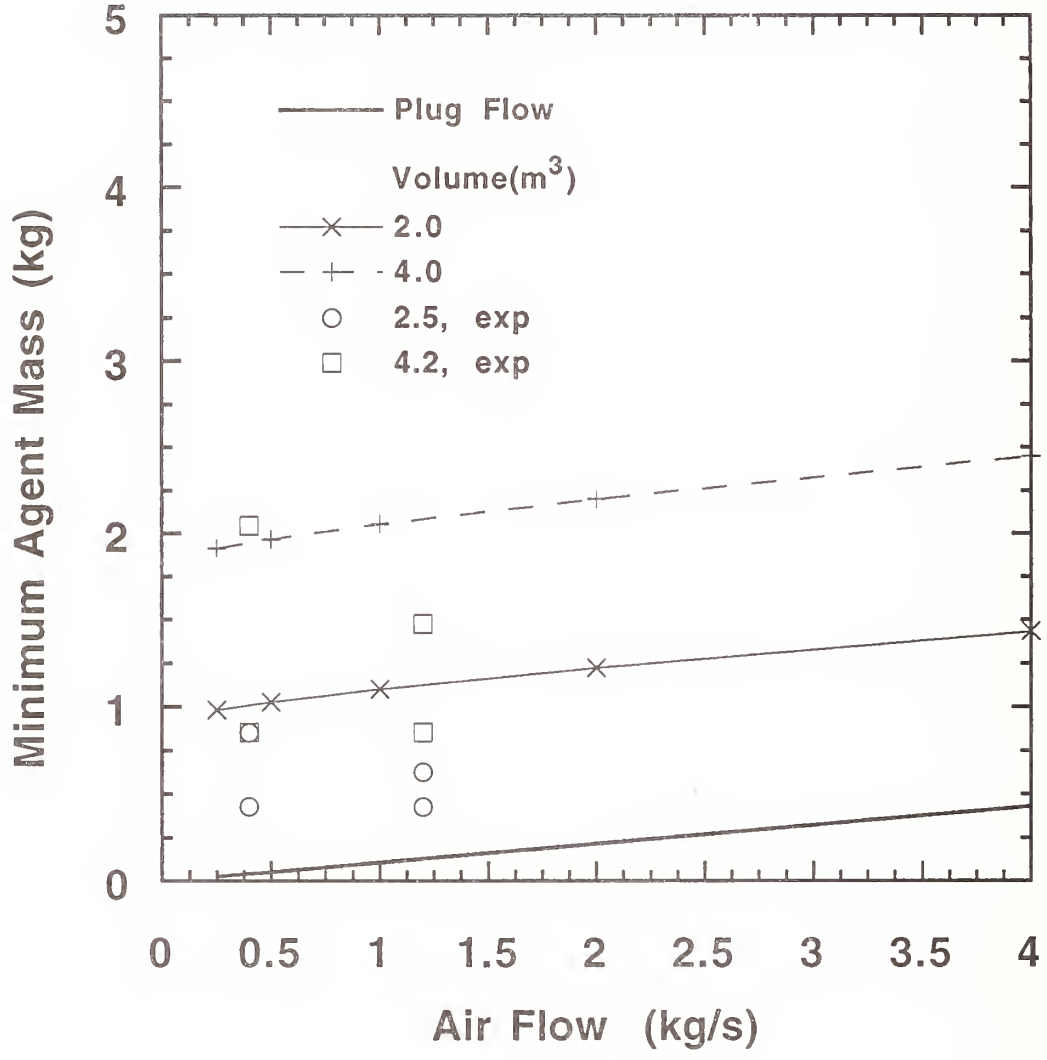

Figure 115. Minimum HFC-227 mass requirements for full-scale AEN simulator tests and the simulated spray fire scenario for an agent injection duration of 0.25 s.

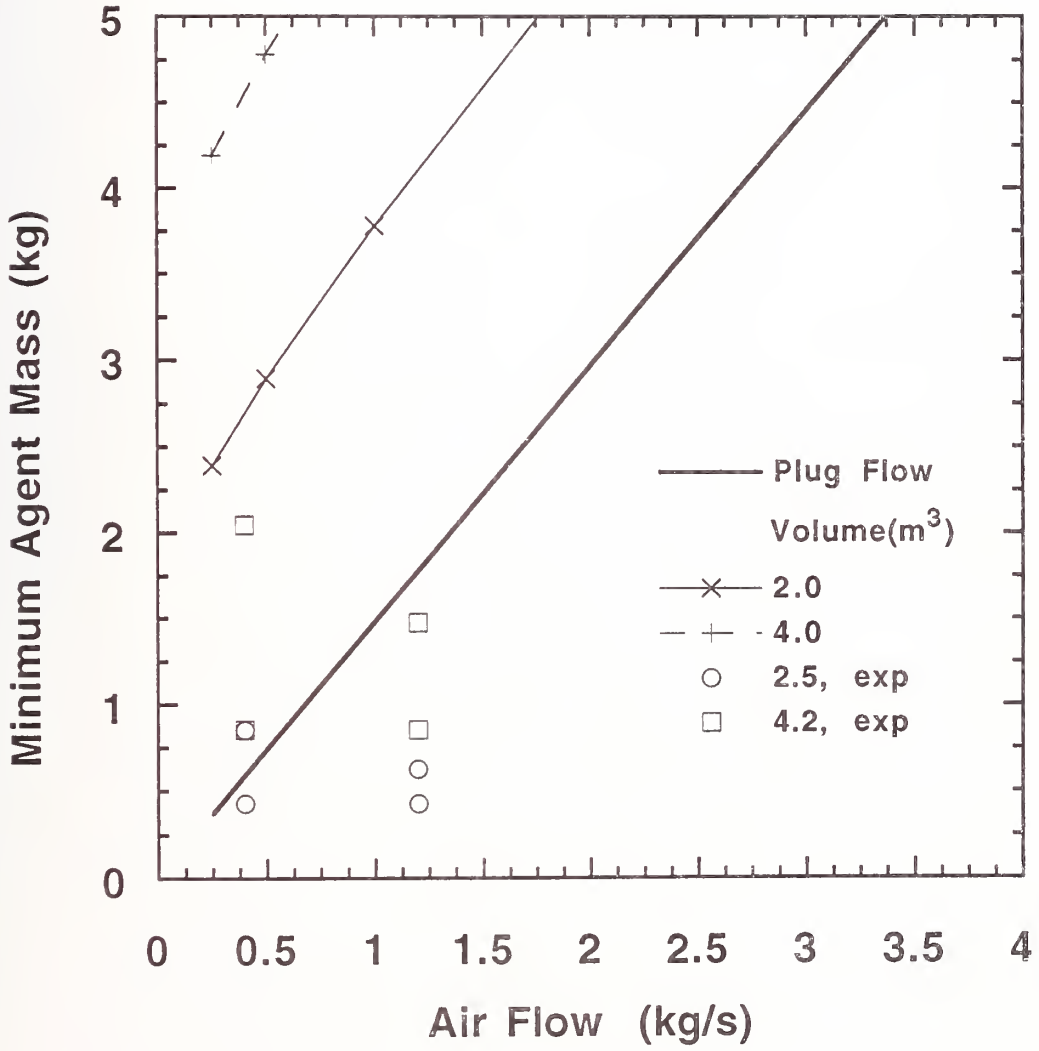

Figure 116. Minimum HFC-227 mass requirements for full-scale AEN simulator tests and the simulated pool fire scenario for an agent injection duration of 0.25 s.

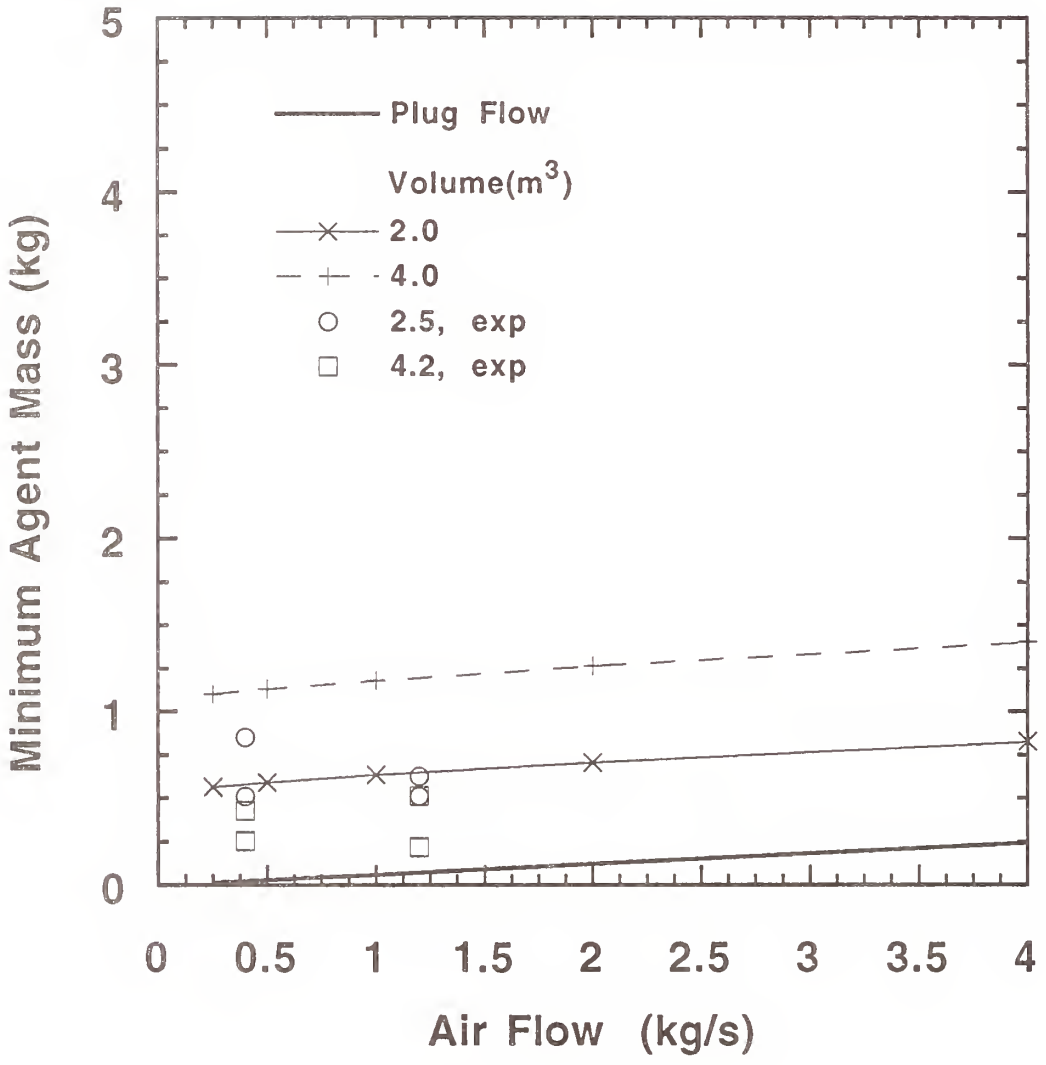

Figure 117. Minimum CF_3I mass requirements for full-scale AEN simulator tests and the simulated spray fire scenario for an agent injection duration of 0.25 s.

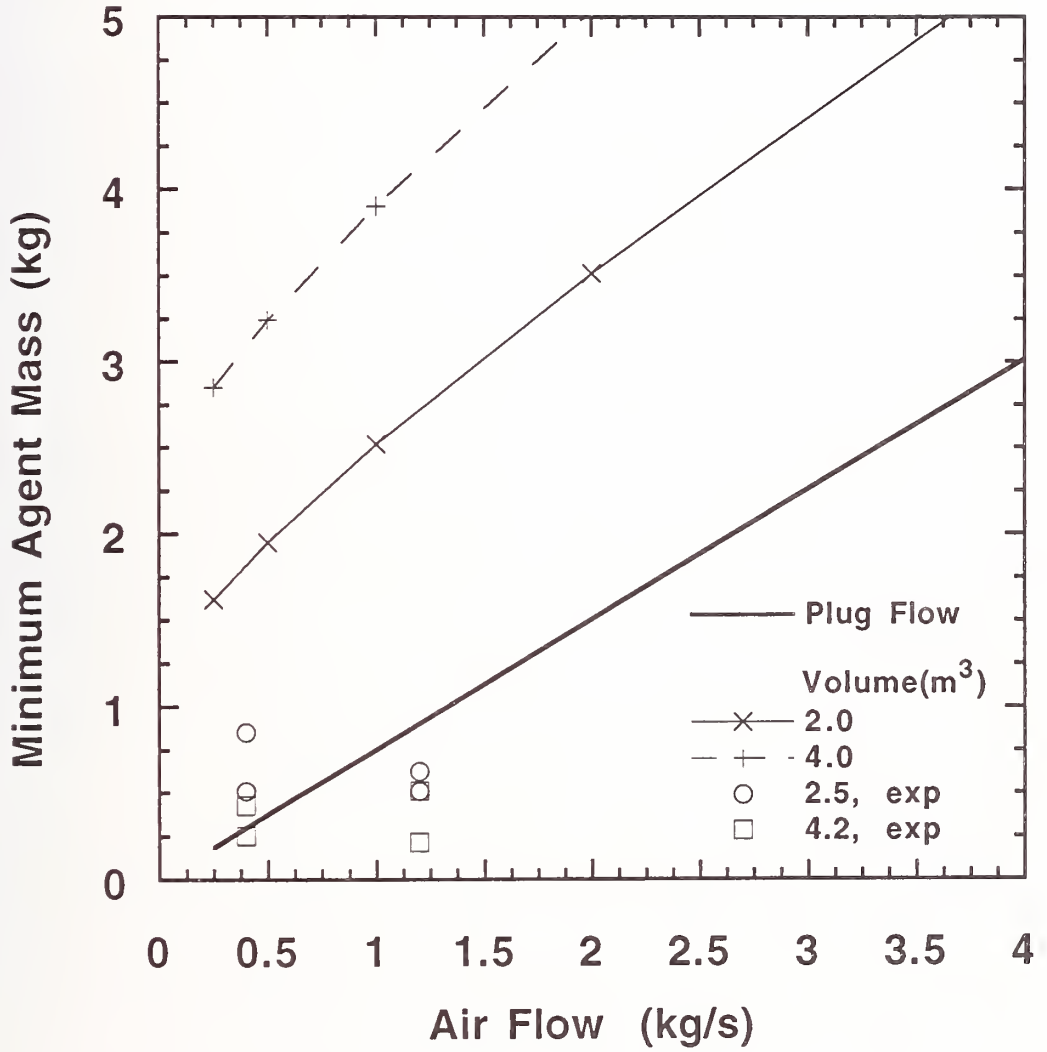

Figure 118. Minimum CF_3I mass requirements for full-scale AEN simulator tests and the simulated pool fire scenario for an agent injection duration of 0.25 s.

Unfortunately, it has been shown that the replacement agents are not very efficient in suppressing hot surface ignition at low agent concentrations as measured by relative increases in the ignition temperature (Section 9.3.4). The model developed here uses the agent concentration which inerts the peak flammability limit as a target for the combustion zone (see Section 9.5.2.1), insuring suppression of possible re-ignition. Yet, the duration of that target concentration was not specified. To insure prevention of re-ignition, a high concentration must be held until surface temperatures decrease sufficiently, or fuel vapors are removed from the nacelle.

9.5.6 Impact of Unmodeled Phenomena. In all of the model calculations above, the fire scenarios were defined by fixed characteristic mixing times and fixed critical concentrations. No allowances were made to account for the effects the local velocity has on the ease of suppression, because for the generic nacelle models, no relationship between the flow and velocity was introduced. The only constraint was that the characteristic mixing time for each fire scenario represented the worst case possible for those models. In real nacelles, geometric factors such as objects, upstream from a baffle, can significantly impact the flow field near the baffle. Therefore, it is impossible to utilize the known effects of velocity on the characteristic mixing time and flame stability unless detailed flow calculations or measurements are performed for specific nacelle configurations. See Section 9.3.6.3 for a more detailed discussion of this issue.

In the model, agent injection occurs isothermally and the agent is assumed to be in the gas phase to simplify the equations. An assumption is made that there is sufficient heat available to vaporize the agent soon after mixing with the nacelle air. Typically the agent enters the nacelle as a two-phase gas/liquid mixture and at a cold temperature due to adiabatic expansion and flash evaporation. The air flow may be approximately 20 °C during a certification discharge, or at cold or elevated temperature during flight depending on flight conditions, with the possibility of hot surfaces present. Upon mixing with air, agent will continue to vaporize while cooling the air; also heat transfer from the nacelle walls can add heat to the agent/air mixture. It is possible to numerically solve the mass and energy balance equations simultaneously to determine the impact of non-isothermal conditions for the plug flow and perfectly stirred nacelle volumes, but given the simplified mixing assumptions, such details do not significantly affect the results in terms of the predicted trends of this analysis.

9.5.7 Conservative Design Allowance. Allowances should be made to account for imperfect mixing, uncertainty in input parameters, and other un-modeled phenomena. The model calculations assume that the agent is mixed perfectly with the air flow. In reality, some areas will have relatively lower agent concentrations due to real dispersion effects; therefore, more agent must be added to protect such areas. The relative increase needed to protect such areas is configuration dependent and is not known *a priori*.

In terms of a safety factor, one question is: "Is it better to increase concentration or duration when adding additional agent mass?" Assuming that the minimum agent mass and injection time are known, to affect an increase in the agent concentration in a fire zone, the additional agent mass is injected over the original injection time. This increase in the mass injection rate will increase the turbulent mixing and local velocities in the nacelle, impacting flame stability in a favorable manner. Likewise, to increase the duration, the minimum and additional mass are injected over a longer injection time such that the mass injection rate is equal to the original mass injection rate. This increase in injection duration will increase the duration of agent at all locations. An increase in duration may be required if the nacelle volume is to be "inerted" (held at concentrations above the peak flammability limit) for a period of time. Thus, there are trade-offs associated with each choice.

9.5.8 Preliminary Agent Mass Guidelines. The model calculations show that the agent mass needed for extinguishment is not a function of the nacelle volume in the plug flow model if the cross section of the nacelle is held constant. That is to be expected since the nacelle volume does not play a role in free stream concentration or duration for the plug flow configuration. The perfectly stirred nacelle results do show variation with air flow and nacelle volume. In addition, it appears that air flow and total volume are essentially independent parameters for the ranges of air flow, free volume, and injection times examined. It follows therefore that a "design equation" of the form:

$$W = a\ V + b\ \dot{W}_{air} \tag{33}$$

could fit the model results for fixed characteristic mixing times. Here, W is the agent mass (kg), V is the nacelle free volume (m^3), and $\dot{W}_{air}$ is the mass flow of air (kg/s). Indeed, suitable equations were obtained for each agent and worst case fire scenario. This equation is of the same form as the design equations in the Military Specification (see Equations (1)-(4)). Figures 119-126 show the "new" design equation (Equation (33)) for the spray and pool fire scenarios for agent injection times of 0.25 s and 1.0 s respectively as a function of the model calculations for all of the agents. Thus, Equation (33) represents a simple algebraic equation which may be used as a design guideline. Table 12 gives the coefficients for each agent and fire scenario. The (a) coefficient is not simply the critical concentration divided by the agent density. These results approach those limiting values at very low air flows only, much lower than the flows considered here. Again, no allowances for un-modeled phenomena are included in the above design equations, and appropriate safety factors must be applied.

It should be noted that Equation (33) was developed for ambient conditions and the coefficients (a) and (b) are functions of temperature. It is anticipated that the pressure dependence is small. The temperature dependence can be obtained from calculations using the model and based on the results discussed in Section 9.3.2.3.5.

9.5.9 System Performance Criteria. For halon 1301 systems, system performance is validated through a non-combusting certification discharge test. The test involves discharging the agent into the nacelle with air flow provided to simulate cruise conditions and making temporal concentration measurements at various locations. The performance criteria specifies that the halon 1301 concentration be 6 % by volume or greater at all locations in the nacelle for a minimum of 0.5 s. Replacement agent(s) for halon 1301 will likely have to be tested in a similar manner. Here, a method to back-out agent concentration and duration requirements from flame extinction experiments is presented to provide a rational approach for the development of alternative agent system performance criteria. As presented previously, (Section 9.3) there is a relationship between the free stream agent concentration (X_f) and duration (Δt) required to suppress a given fire. Assuming a step function free stream agent concentration (plug flow), that relationship is given by Equation (14) which is re-written here as:

$$1 - \frac{X_\infty}{X_f} = e^{-\Delta t/\tau}$$

Section 9.3.2.3.4 describes this relation in detail. Figure 127 illustrates the equation as it is presented above. For conditions above the curve, a flame would be extinguished. The critical injection duration (Δt_c) shown in Figure 127 is obtained when the free stream agent concentration is equal to 100 % (see Equation (15)). Below this value, the duration is too short to extinguish the flame. For known values of X_∞ and τ, assuming that the agent and fire scenario are known, the required duration (Δt) can be

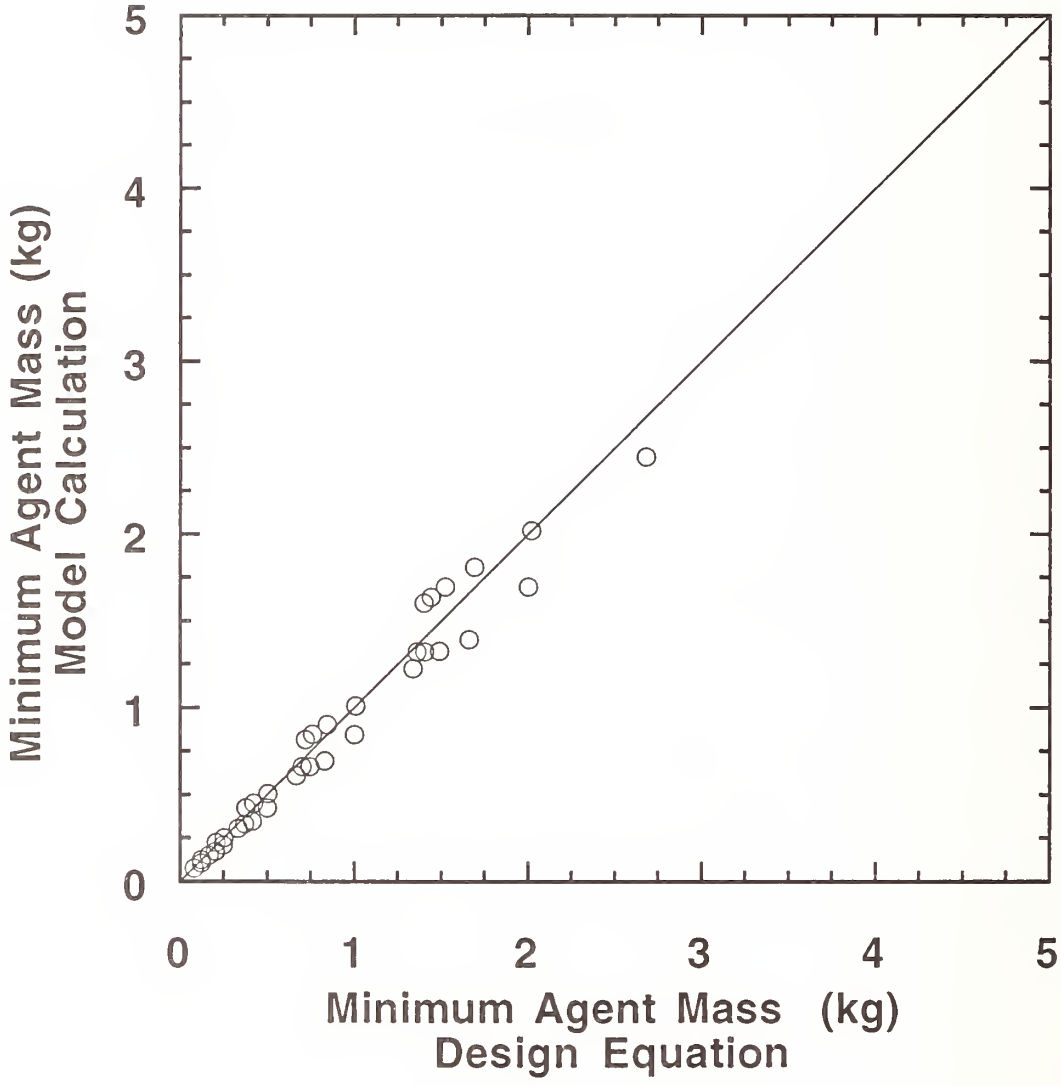

Figure 119. Comparison of the minimum halon 1301 mass from the model calculations and the "design equation" for the spray fire scenario with an agent injection duration of 0.25 s.

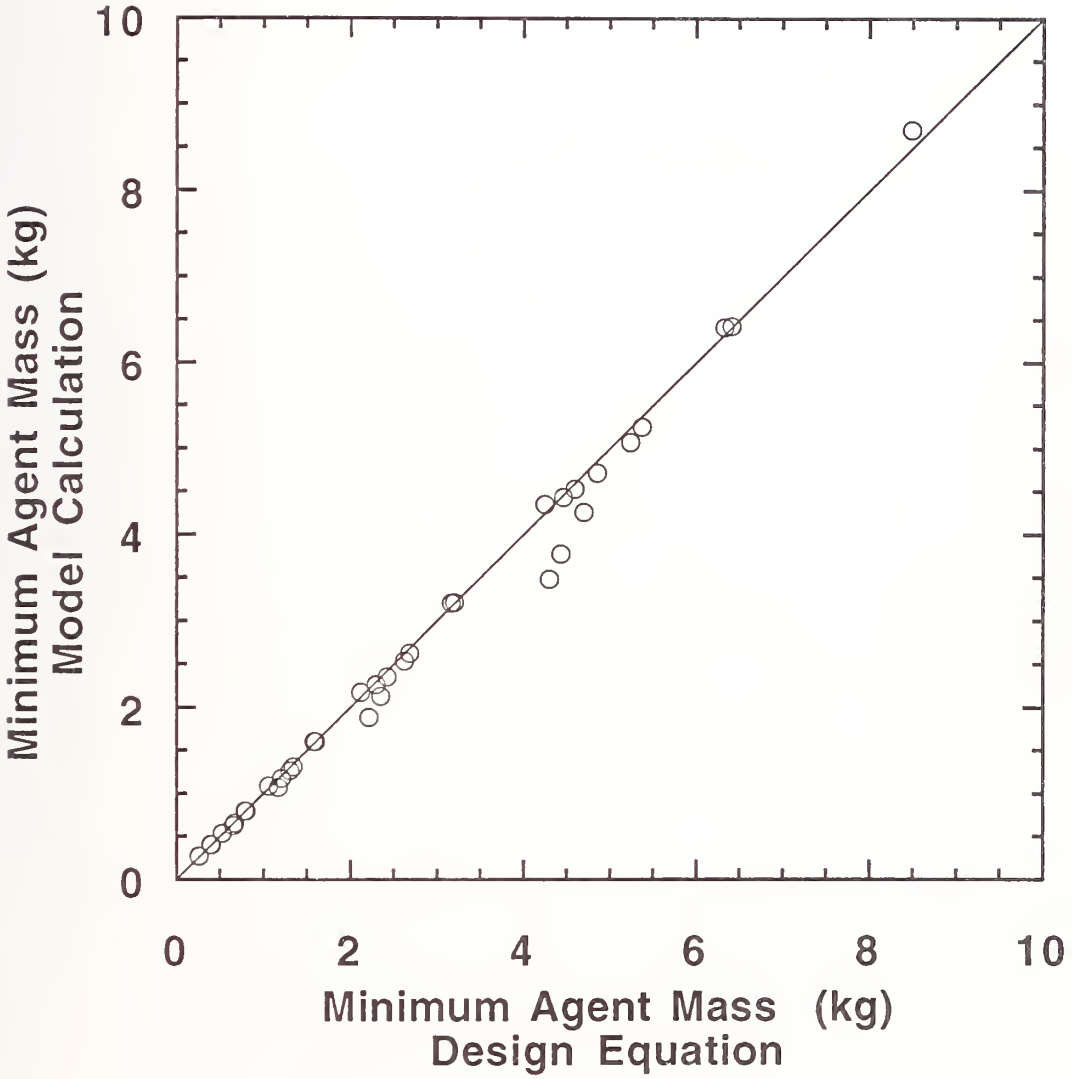

Figure 120. Comparison of the minimum halon 1301 mass from the model calculations and the "design equation" for the pool fire scenario with an agent injection duration of 1.0 s.

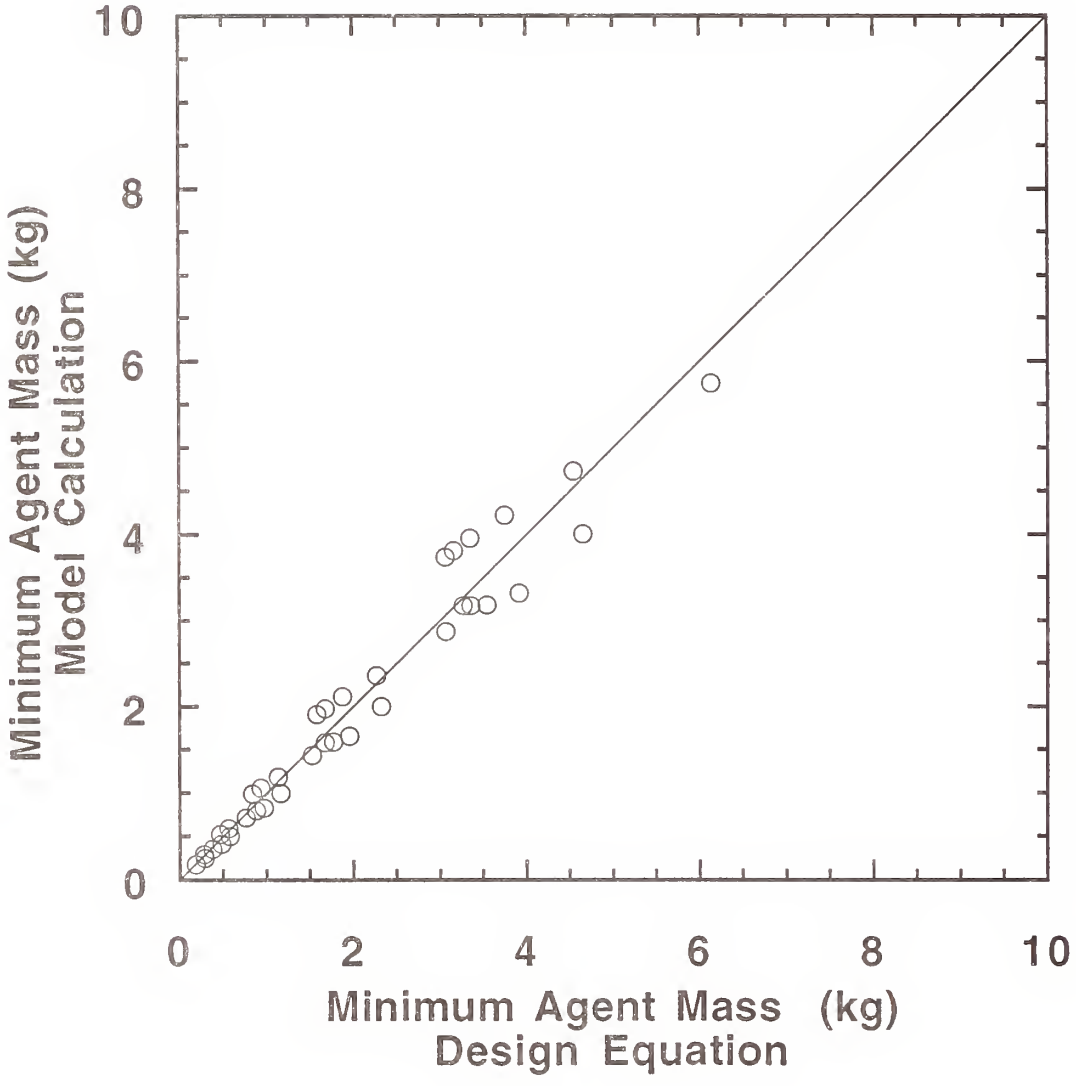

Figure 121. Comparison of the minimum HFC-125 mass from the model calculations and the "design equation" for the spray fire scenario with an agent injection duration of 0.25 s.

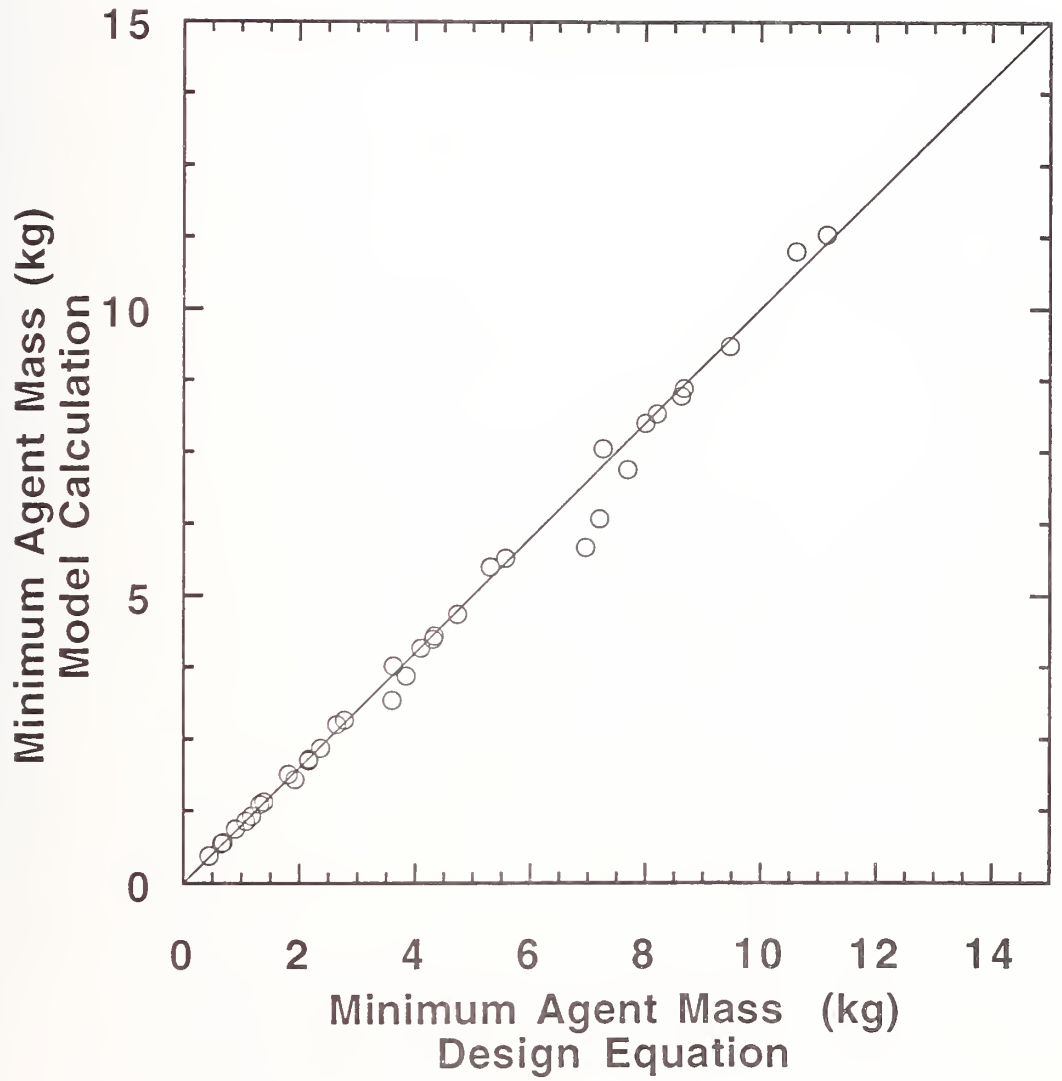

Figure 122. Comparison of the minimum HFC-125 mass from the model calculations and the "design equation" for the spray fire scenario with an agent injection duration of 1.0 s.

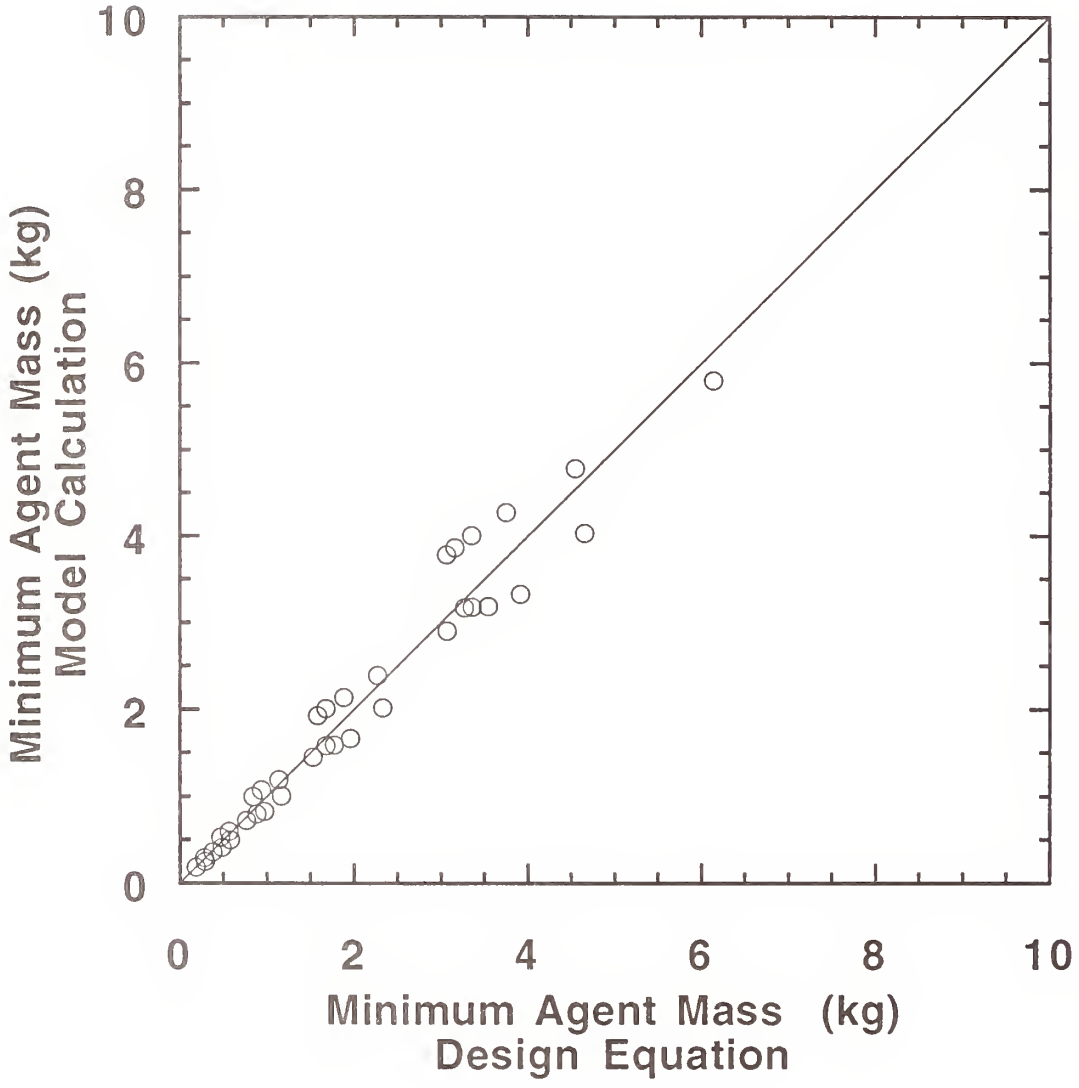

Figure 123. Comparison of the minimum HFC-227 mass from the model calculations and the "design equation" for the spray fire scenario with an agent injection duration of 0.25 s.

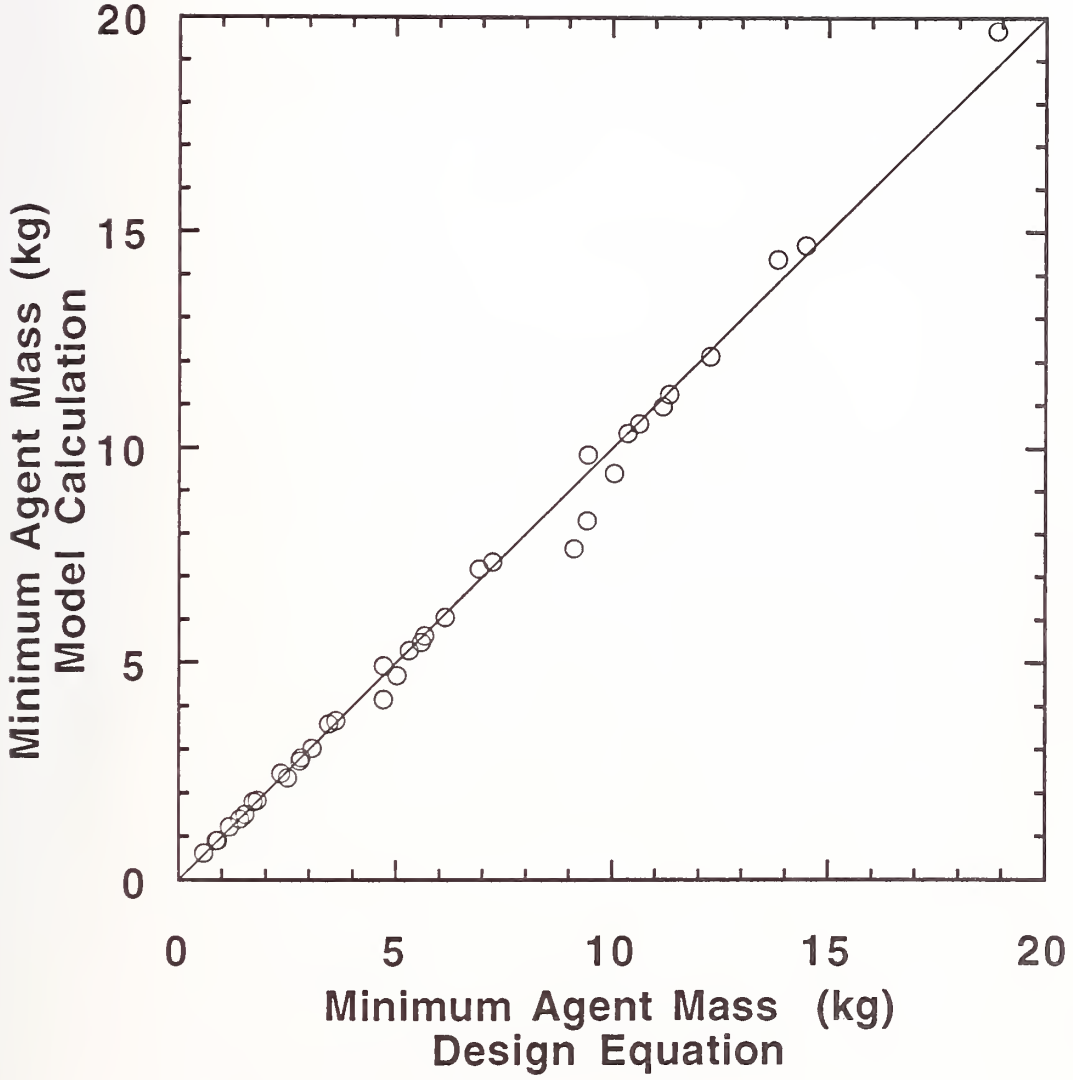

Figure 124. Comparison of the minimum HFC-227 mass from the model calculations and the "design equation" for the spray fire scenario with an agent injection duration of 1.0 s.

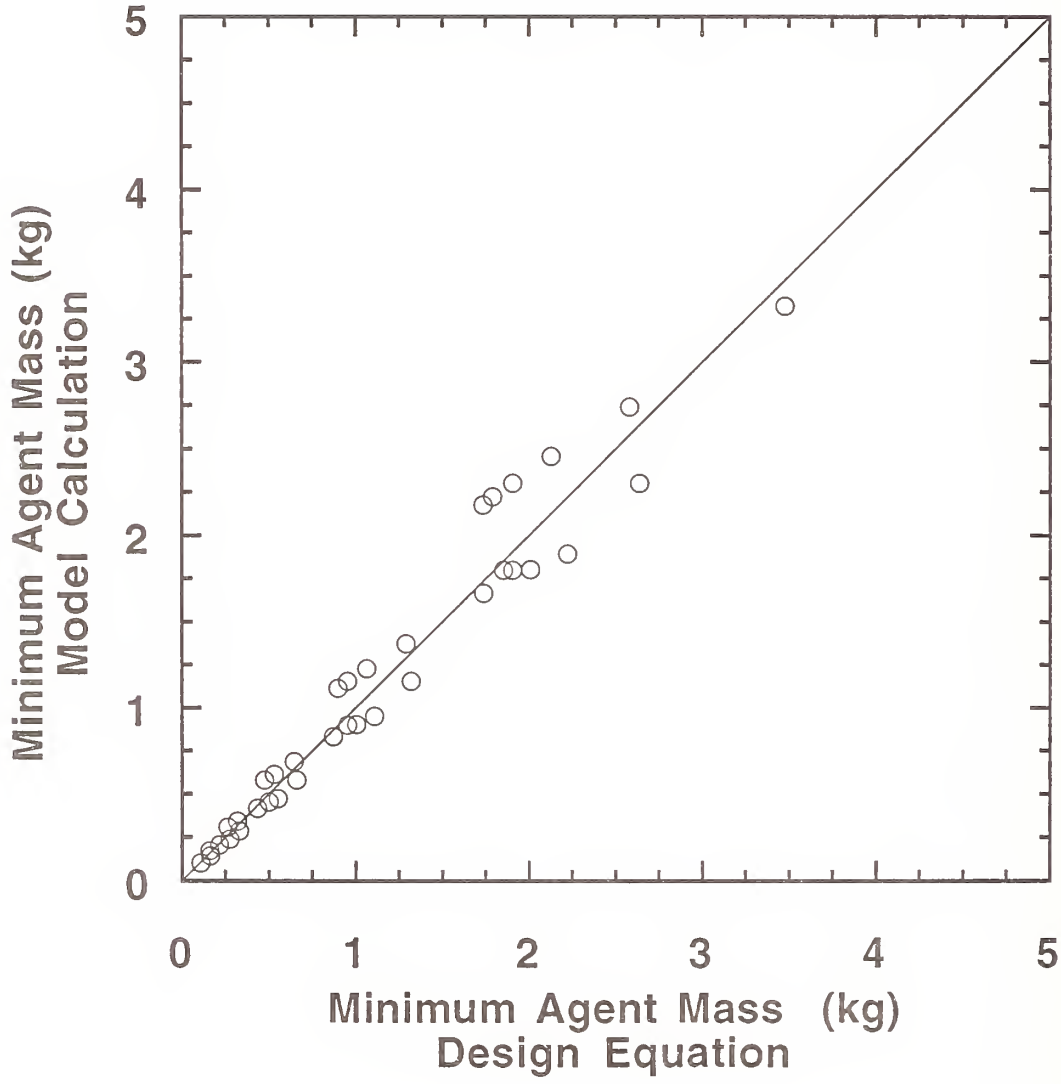

Figure 125. Comparison of the minimum CF_3I mass from the model calculations and the "design equation" for the spray fire scenario with an agent injection duration of 0.25 s.

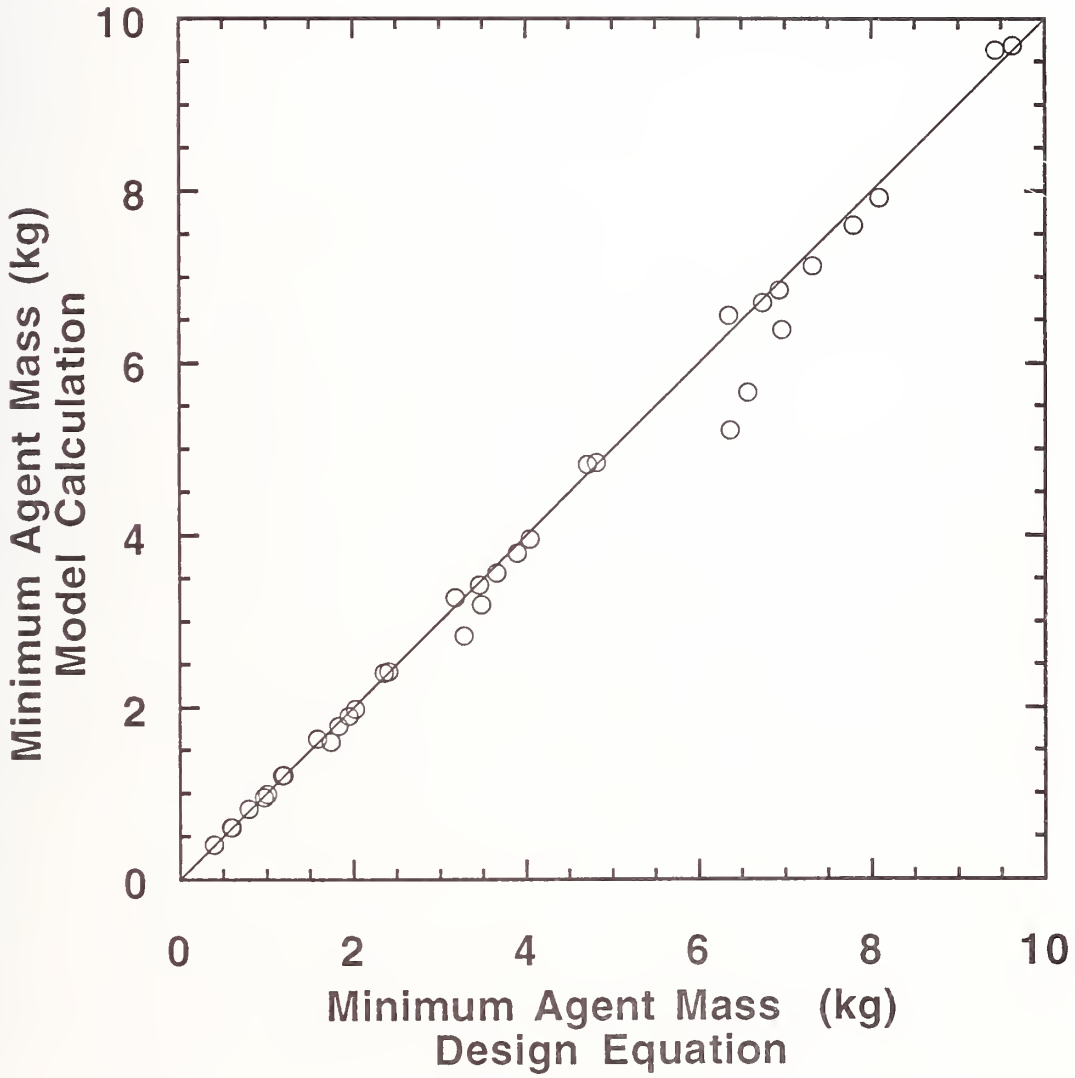

Figure 126. Comparison of the minimum CF_3I mass from the model calculations and the "design equation" for the spray fire scenario with an agent injection duration of 1.0 s.

Table 12. The coefficients in Equation (33) for each agent and fire scenario

Agent	(a) spray fire (kg/m^3)	(b) spray fire ($kg/kg_{air}/s$)	(a) pool fire (kg/m^3)	(b) pool fire ($kg/kg_{air}/s$)
halon 1301	0.17	0.165	0.52	0.542
HFC-125	0.37	0.397	0.84	0.974
HFC-227	0.37	0.397	1.1	1.26
CF_3I	0.21	0.225	0.77	0.819

obtained given the free stream concentration. For instance, if the free stream concentration is twice X_∞ then $\Delta t = 0.693\tau$. If the free stream concentration chosen is very similar to X_∞, the duration must be very long ($\Delta t \approx 3\tau$), likewise, if the free stream concentration chosen is very high, then the duration approaches the minimum (Δt_c).

The concentration/duration relationship given above, formally applies to a plug flow only, where the agent free stream concentration takes the form of a step function. It is not applicable when the free stream concentration is not constant which occurs in nacelle model No. 2 (PSR) for example, and more importantly, in real nacelles which are characterized by imperfect mixing. Because of the mixing problem, it is recommended that temporal concentration measurements be conducted in full-scale nacelles to ensure suppression system effectiveness. Following agent discharge, the transient agent concentration should be measured in the free stream near potential fire locations. In addition, temporal agent concentration measurements should be made behind bluff bodies which represent potential fire zones, as is currently the case for halon 1301 certification testing. This is of value because there is no guarantee that the free stream concentration is spatially homogeneous. These measurements made under non-combusting conditions or "cold flow" must be related to an effective free stream concentration to assess suppression system effectiveness. These issues are addressed below, yielding a generalized methodology for the determination of concentration/duration requirements for protection of a particular nacelle, fire scenario, and agent.

Real dispersion effects lead to spatial and temporal variations in the agent concentration. Fire suppression is directly related to the agent concentration in the fire zone, thus adequate free stream temporal concentrations are required at all potential fire locations. The time dependent agent concentration, initially zero in the fire zone or behind a bluff body is given by:

$$X(t) = e^{-t/\tau} \frac{1}{\tau} \int_0^t e^{t/\tau} \quad X_f(t)\, dt \tag{34}$$

which is the solution to the non-homogeneous, linear first-order differential equation describing the local mixing:

$$X_f(t) = \tau \frac{dX(t)}{dt} + X(t) \tag{35}$$

where X(t) is the agent concentration in the recirculation zone, $X_f(t)$ is the free stream concentration, and τ is the appropriate characteristic mixing time for combusting or non-combusting conditions. To

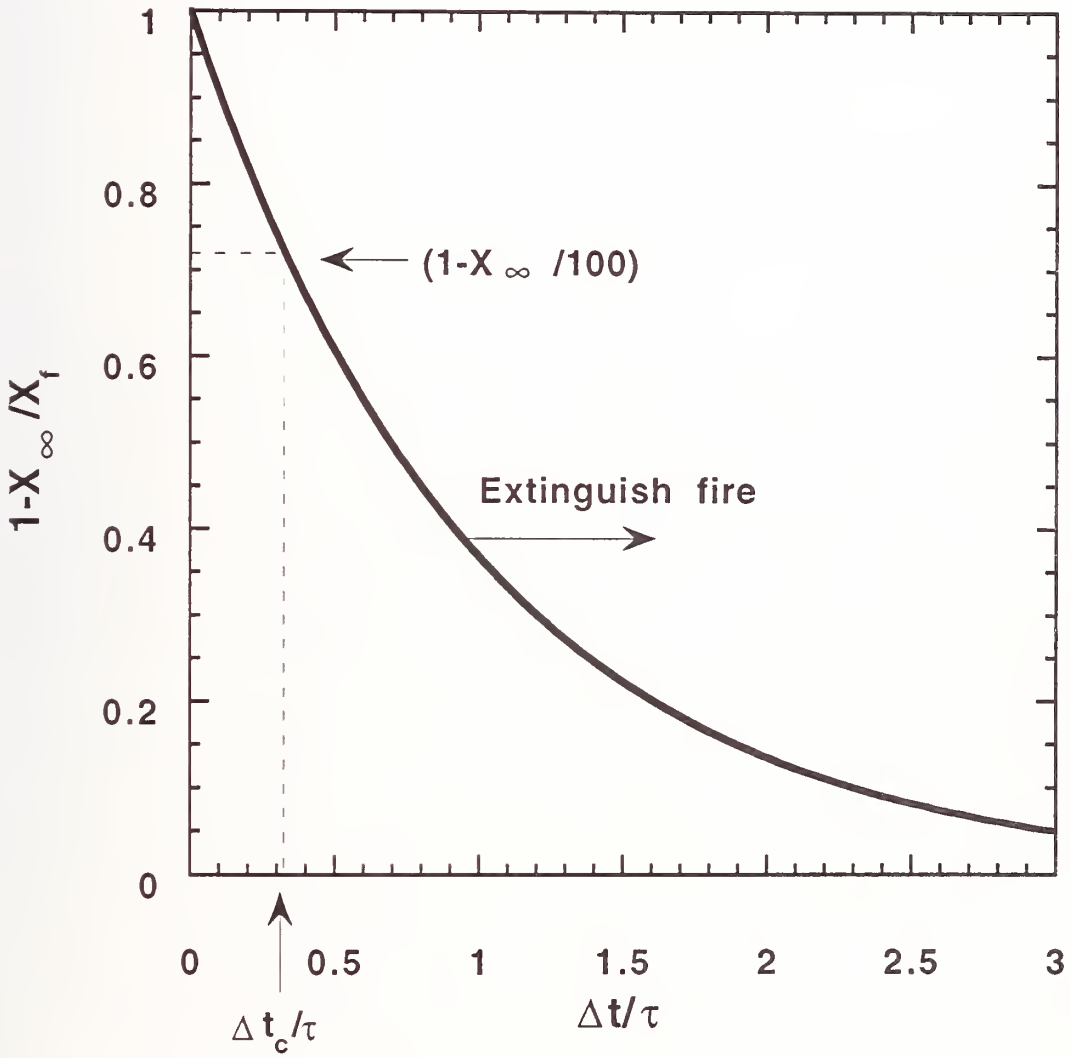

Figure 127. Concentration/duration relation for flame extinguishment assuming a steady agent plug flow.

assess whether the free stream agent concentration is sufficient to extinguish the fire, the integral in Equation (34) must be evaluated. The fire is considered extinguished if X(t) is greater than X_∞ for any discrete time interval. The relative value of $X_f(t)$ to X_∞ is irrelevant. The criteria for extinction is based on the agent concentration in the fire zone only.

The integral in Equation (34) can be evaluated either analytically or numerically. $X_f(t)$ can take any functional form, but in practice, discrete data is recorded from a concentration measuring device. If $X_f(t)$ is well represented by a facile functional form, then the integral can be evaluated and X(t) determined. If not, X(t) can be determined by piecewise integration of Equation (34) using the discrete data. For piecewise integration, given that the discrete data were collected at a regular time interval (δt), and that the curve between two data points is represented by a straight line, the concentration at time t_i is:

$$X(t_i) = \sum_{j=1}^{i} e^{-\delta t/\tau}(a - b\tau + X(t_{j-1})) + (a + b\,\delta t - b\tau) \qquad (36)$$

where $a = X_f(j-1)$ and $b = (X_f(j)-X_f(j-1))/\delta t$. As an illustration, Figure 128 shows simulated discrete agent concentration data for the free stream (with $\delta t = 0.1$ s) and the predicted concentration in the fire zone using Equation (36) for two different values of τ. At t = 0, the agent arrives just upstream of the fire zone. Notice that for the smaller value of τ (= 0.1 s), the agent concentration in the fire zone closely follows the concentration in the free stream, whereas there is a significant lag in the fire zone agent concentration for the larger value of τ (= 1 s). If the long injection concentration limit (X_∞) for these fire scenarios is taken as 12 %, then it is obvious that there is a large excess of agent for the fire zone characterized by the smaller value of τ, whereas there is just barely sufficient agent for the fire zone characterized by the larger value of τ. This example is intended to emphasize the importance of the order of magnitude difference between the values of τ measured in the baffle stabilized pool fire and in the spray flame.

Winterfeld (1965) found that the characteristic entrainment or mixing time into a baffle stabilized premixed flame is twice as long as the characteristic mixing time in an isothermal flow for the same geometry and velocities. Winterfeld's research was for obstacles in the center of the flow field. In lieu of other data, that observation could be applied to relate combusting to non-combusting characteristic mixing times. Since measurement of the characteristic mixing times (τ) in the combusting and non-combusting cases are different, the results from "cold flow" certification testing is not directly applicable to forecasting fire suppression. Given the temporal concentration in the recirculation zone, however, the free stream concentration can be deduced and then used in Equations (34) or (36) with an appropriate value of τ to assess fire suppression effectiveness. The free stream concentration, $X_f(t)$, could be calculated from solving Equation (35), where τ is the non-combusting characteristic mixing time.

For a particular nacelle, transient agent concentration measurements should be made at many possible fire locations. The performance criterion adopted above evaluates the fire suppression effectiveness at each location independently. Other performance criteria could be added to that criterion, for example requiring that all locations must be at a given concentration for a given duration simultaneously as is the case in the current halon 1301 specifications.

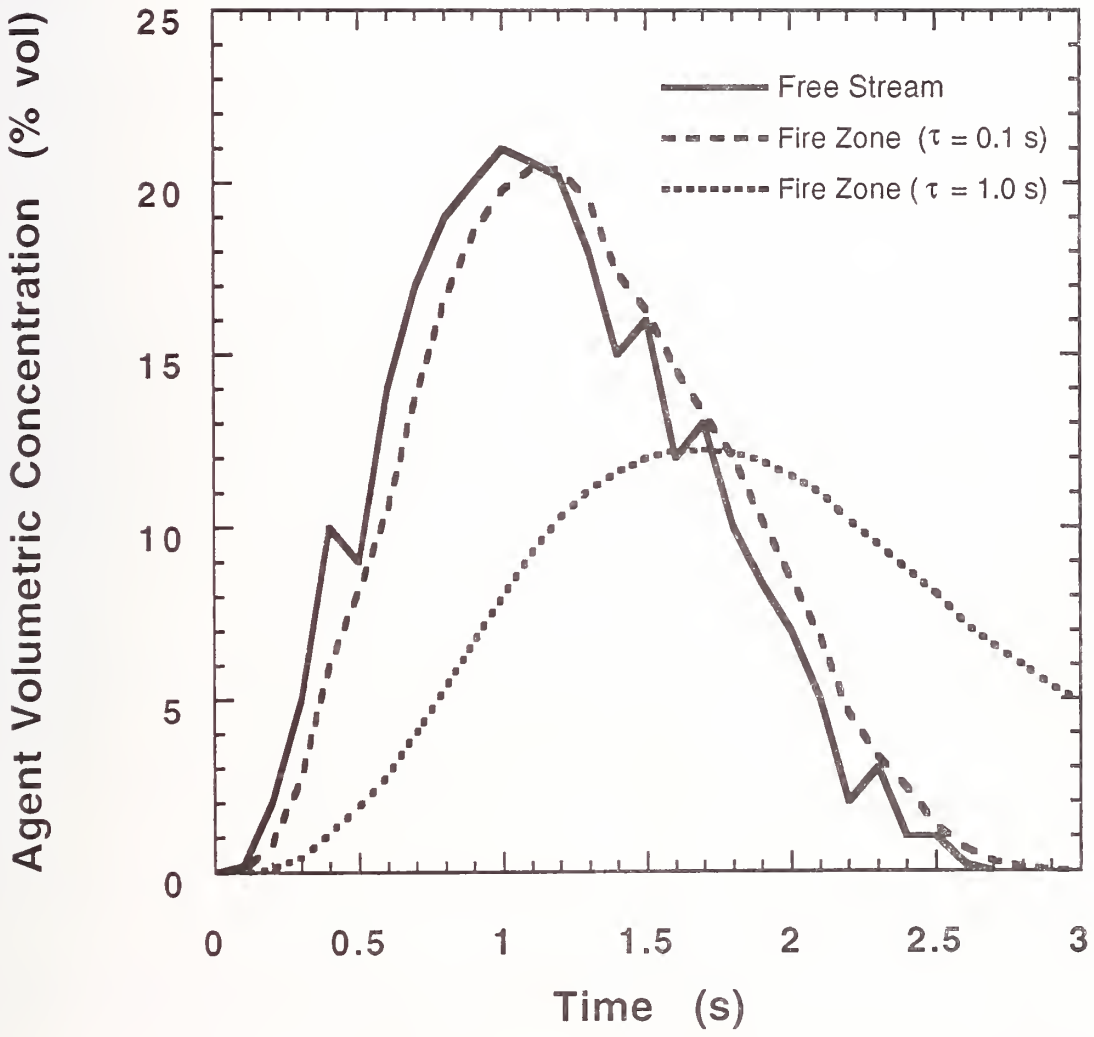

Figure 128. Simulated agent concentration data with predicted concentration build-up in specific fire zones characterized by $\tau = 0.1$ s and 1.0 s.

9.5.10 Procedure for Determination and Validation of Nacelle Fire Suppression Requirements. The following procedure outlines a methodology to determine agent requirements for fire protection and validate suppression system performance for real engine nacelles.

Step 1. Collect information regarding the nacelle volume, configuration (*e.g.*, rib sizes; locations of other obstacles), air flow, and the environment (operational temperatures and pressures). Available information regarding the nacelle air flow including measurements and/or computations would be useful in determining the type of agent mixing that would likely occur, if zones of low agent concentration ("dead zones") occur and where agent injection location(s) should be to mitigate potential problems.

Step 2. Deduce the worst-case probable fire scenarios which are inferred from the information collected in step 1. Estimate the characteristic mixing time (τ) and critical extinction concentration (X_∞) for the fire scenarios.

Two fire scenarios have been considered in the model calculations, namely baffle stabilized pool fires and spray flames. Given the configuration (the location of fuel lines, baffle sizes, geometric blockage, etc.), air flow, and environment, estimate the characteristic mixing time, τ, and the critical agent concentration, X_∞ (see Section 9.3.2.3.4). More confidence is placed on the estimates for the spray fire scenario due to the extensive testing, while much less confidence is placed on the estimates for the baffle stabilized pool fire scenario. Extrapolations to other conditions should be made conservatively until more data is gathered. Other fire scenarios have not been explicitly addressed in the modeling, most notably re-ignition of fuel from hot surfaces. The re-ignition scenario adds another dimension to the suppression system requirements.

Step 3. Calculate the minimum agent mass for a specified injection duration.

Using the appropriate design equation (Equation (32) for plug flow or Equation (33) otherwise), calculate the minimum agent mass required for fire suppression. Equation (33) should be used in concert with appropriate coefficients as described in Section 9.5.8. It is useful to check the effect of the injection duration on the minimum agent mass to determine if the injection time can be increased without a large agent mass penalty.

Step 4. Add additional mass to the agent quantity obtained in step 3 as a "safety factor." Decide whether to increase the discharge rate or injection time.

The decision to increase the discharge rate or injection time involves trade-offs (see Section 9.5.7). The decision will probably be dictated by experience after full-scale experimentation and successful system design.

Step 5. Calculate the discharge time given the agent mass, storage conditions and piping configuration.

It is prudent to integrate the discharge characteristics into this design guideline. Given the hardware requirements, assess whether the discharge of the required agent amount can be achieved in the specified injection duration (see Section 8.6 of this report). The discharge time of an agent stored at cold temperatures could be estimated to assess its impact. If a

relaxation of the discharge time is possible, potential benefits relating to hardware design can be assessed.

Step 6. Perform certification tests with the agent mass and injection rate prescribed from steps 4 and 5. Measure the agent concentration in the free stream and potential fire zones.

Step 7. Compare temporal agent concentration measurements to concentration and duration criteria.

Follow the methodology outlined in Section 9.5.9 to assess the suppression effectiveness at each measurement location. Check any other performance requirements.

Step 8. If the measured concentrations meet the criteria, then the system is properly designed. If the criteria are not met, then decide if the problem is due to inadequate mixing or insufficient agent mass. If the problem is due to inadequate mixing, then tailor the discharge (*i.e.*, by use of nozzles, tees, etc.) to improve mixing. If the problem is due to inadequate agent mass, then increase the agent amount and return to step 5.

9.5.11 Summary of the Model. There is no simple generic solution to the nacelle fire protection problem. The model developed here illustrates the importance of injection duration, air flow, nacelle free volume, fluid mixing, and fire scenario on the minimum agent suppression requirements. A comparison of the results of the model for halon 1301 suppression requirements with the current Military Specifications showed that the trends with air flow and nacelle volume were well predicted, and that the Military Specification requires larger agent mass. Comparison of the alternative agent requirements to those predicted for halon 1301 showed that a constant multiplier between them exists for each fire scenario. Comparison of the model results with full-scale fire test data for the alternative agents showed consistent trends. Preliminary guidelines in the form of simple algebraic equations were proposed for the minimum agent delivery rates. Certification specifications were discussed and the relationship between concentration and duration was given. A step-by-step procedure was proposed as a guideline for system design and certification. Before application, it is strongly advised that the model be adequately validated using full-scale testing.

9.6 Summary and Recommendations

The following conclusions are made regarding flame suppression and agent effectiveness.

1. A simple mixing model was developed that gives guidance in determining agent requirements for nacelle applications. A step-by-step procedure was proposed as a guideline for system design and certification (see Section 9.5.10).

2. In general, baffle stabilized pool fires were more difficult to extinguish than the baffle stabilized spray fires tested in this study. Larger agent concentrations and longer characteristic agent mixing times were required to achieve suppression in the pool fires due to the structure of the recirculation zone.

3. Of the candidate replacement agents evaluated in the turbulent spray burner, CF_3I was the most effective compound. CF_3I required the least amount of gaseous agent to extinguish the flames on

both a mass and volume basis. The other two alternative agents tested, HFC-125 and HFC-227, were measured to have nearly identical suppression effectiveness, and were significantly less efficient than CF_3I in extinguishing the flames. On a mass basis, none of the agents performed as well as halon 1301.

4. Agent performance measured in the turbulent jet spray burner for low air flows was very similar to the performance measured in the cup burner and in the opposed flow diffusion flame under low strain rate conditions, suggesting that a single test apparatus is sufficient for ranking the effectiveness of alternative agents.

5. The agents required more mass to extinguish flames in the turbulent spray burner when the air was heated. This trend was anticipated, since heating the air adds enthalpy to a flame, and a flame with a higher enthalpy is expected to be more stable. However, increasing the air temperature altered the agent ranking. For temperatures below 150 °C, CF_3I was the most effective agent. For temperatures above 150 °C, the three agents, CF_3I, HFC-125 and HFC-227 were approximately equally effective.

6. The system pressure and the fuel flow did not significantly impact the agent concentration required to obtain extinction over the range of conditions tested in the turbulent spray burner.

7. A model was developed that treats the recirculation zone in baffle stabilized flames as a perfectly stirred reactor, facilitating prediction of the agent concentration required for flame extinction as a function of the agent injection duration.

8. Agent type does not significantly impact mixing rates behind an obstacle in combusting or non-combusting conditions.

9. Mixing times for an agent entraining into a recirculation zone behind an obstacle under non-combusting (cold flow) conditions, such as during agent certification, are different than mixing times under combusting (suppression) conditions. In other words, the rate of fluid mixing into the recirculation zone is impacted by combustion. The mixing time also varies with the blockage ratio, the relative geometric relationship between the open and blocked area associated with a flow obstacle.

10. To achieve a target concentration in the recirculation zone behind an obstacle, the free stream concentration must be maintained for approximately three times the value of the characteristic entrainment or mixing time, τ.

11. There are trade-offs in obtaining a target concentration in the recirculation zone behind a baffle (during both flame suppression and non-combusting certification), involving the agent concentration and its duration in the free stream.

12. CF_3I was the most effective agent in suppressing the ignition of reactants flowing over a hot nickel surface. The other two agents tested, HFC-125 and HFC-227, were both measured to have nearly identical ignition suppression effectiveness, and both were significantly less efficient than CF_3I. HFC-125 was observed to marginally promote ignition in stoichiometric methane/air and propane/air mixtures.

13. A reasonable target concentration for an agent in the fire zone (not the free stream or in non-combusting tests) is the concentration which insures that the most flammable fuel/air ratio cannot occur. This agent concentration insures both flame suppression and prevention of re-ignition for a period of time on the order of the agent injection duration. After this period, however, it is likely that re-ignition will still be possible and therefore other fire prevention strategies should be considered.

A number of cautions must be made regarding utilization of the derived results for full-scale application.

1. Geometrical factors are not scaleable in a one-to-one fashion. Whereas mixing times are influenced by the Reynolds number, mixing is also impacted by the blockage ratio.

2. Fluid mixing may be impacted by changes in air flow due to agent injection itself.

3. Flame stabilization may be enhanced by a heated wall or obstacle.

4. All suppression testing was conducted with gas phase agents. Changes in the rate of agent evaporation or flashing as well as agent dispersion could also impact the relative suppression effectiveness of an agent. Therefore, changes in nacelle conditions, involving air temperature or pressure for example, could significantly impact the relative agent effectiveness in suppressing a fire.

A better understanding of a number of issues would facilitate improved design guidelines for nacelle fire protection.

1. The impact of differences in the rate of agent evaporation and agent dispersion on suppression effectiveness should be independently tested. All suppression testing in this report was conducted with gas phase agents only. This could be particularly important for discharge under low temperature conditions where droplet dynamics could impact the required agent amount.

2. The validity of Equations (16) and (17) should be tested for baffle stabilized pool flames. A large number of issues remain unresolved. Although Winterfeld (1965) studied the differences between entrainment into an eddy in isothermal and combusting flows, his study was conducted over a narrow range of Reynolds numbers and for premixed flames only. Other studies of entrainment into baffle stabilized premixed flames (Bovina, 1958; Mestre, 1966) have only considered a baffle in the middle of the flow field. The isothermal flow simulations presented here show that baffles against a wall must also be considered. Understanding agent entrainment is critical for the careful development of revised agent certification requirements.

3. Comprehensive agent dispersion measurements are needed in full-scale systems to determine the transient agent pulse shape at locations upstream and downstream of agent injection. Is the pulse shape significantly impacted by changes in the air flow induced by agent injection?

4. The peak flammability limits are a possible preliminary target for agent requirements in nacelle applications. For this reason, it would be of interest to understand the effects of initial temperature and fuel type on the peak flammability limits of halogenated agents.

5. To gain further understanding about re-ignition, it is important to model the ignition of reactants flowing over a heated plate, similar to the experiments described in Section 9.5.3. A model that considers detailed kinetics and fluid dynamics should be employed, such as that of Sano and Yamashita (1994) or Vlachos *et al.* (1994). A key element in such a model would be the kinetic and thermophysical data associated with the halogenated compounds. Such information is available for many key molecules including CF_3Br, CF_3I, and C_2HF_5 (Babushok *et al.*, 1995c). It would be beneficial to consider a range of reactant residence times, including times on the order of 1 s, where ignition may occur at relatively low temperatures.

6. Suppression testing of a baffle stabilized spray flame, with the baffle against a wall, is needed. This is a possible nacelle fire scenario and may be a more difficult to extinguish than the configurations investigated in this report. Such a study would allow a direct comparison of suppression in pool flames and spray flames.

9.7 Acknowledgments

The authors are grateful to Nelson Bryner and Kermit Smyth for many helpful discussions and use of their hot surface ignition apparatus, Bill Leach of NAVAWCLK for allowing us to view nacelle certification type testing, and to Jim Allen, Valeri Babushok, David Bagdhadi, Brett Breuel, Paula Garrett, Michael Glover, Andrew Hubbard, Darren Lowe, Roy McLane, Takashi Budda Noto, and Isaura Vazquez of NIST and Terrence Simpson and Mark Mitchell of Walter Kidde Aerospace for their technical assistance.

9.8 References

ASTM-E 659-78, "Standard Test Method for Autoignition Temperature of Liquid Chemicals," *American Society for Testing and Materials*, Philadelphia, PA, this procedure replaced the older ASTM D2155 test in 1978.

ASTM-E 681-94, "Standard Test Method for Concentration Limits of Flammability of Chemicals," *American Society for Testing and Materials*, Philadelphia, PA, 681, 1994.

Altman, R.L., Ling, A.C., Mayer, L.A., and Myronuk, D.J., "Development and Testing of Dry Chemicals in Advanced Extinguishing Systems for Jet Engine Nacelles Fires," *NASA Report JTCG/AS-82-T-002*, NASA-AMES Research Center, Mountain View, CA, (1983).

Babushok, V., personal communication, 1995.

Babushok, V., Burgess, D.R.F., Linteris, G., Tsang, W. and Miziolek, A., "Modeling of Hydrogen Fluoride Formation From Flame Suppressants During Combustion," presented at the *Halon Options Technical Working Conference*, Albuquerque, NM, May 9-11, 1995a.

Babushok, V., Noto, T., Burgess, D.R.F., Hamins, A., and Tsang, W., "Inhibitor Influence on the Bistability of a CSTR," in preparation, 1995b.

Babushok, V., Noto, T., Burgess, D.R.F., Hamins, A., and Tsang, W., "Influence of CF_3I, CF_3Br, and CF_3H on the High Temperature Combustion of Methane," submitted to *Comb. Flame*, 1995c.

Bajpai, S.N., "Extinction of Vapor Fed Diffusion Flames by Halons 1301 and 1211-Part I," *Ser. No. 22430, Factory Mutual research Corporation*, Norwood, MA, November (1974).

Ballal, D.R. and Lefebvre, A.H., "Some Fundamental Aspects of Flame Stabilization," *Fifth International Airbreathing Engine Symposium*, Bangalore, India, 1981.

Barat, R.B., Sarofim, A.F., Longwell, J.P., and Bozelli, J.W., "Inhibition of a Fuel Lean Ethylene/Air Flame in a Jet Stirred Combustor by Methyl Chloride: Experimental and Mechanistic Analyses," *Combust. Sci. Tech.* **74**, 361, (1990).

Beardsley, G., "Investigation of the Effect of Air Velocity on the Spontaneous Ignition Temperature of Kerosene Sprayed onto a Heated Tunnel Having a Rectangular Obstruction in the Airstream," Rolls Royce Ltd. Aero Engine Division, *Technical Report Rbts/RI. (FEW.10)*, Feb. 1967.

Beér, J.M. and Chigier, N.A., *Combustion Aerodynamics*, Robert Krieger Publishing Co., Malabar, FL, 1983.

Bennett, M., and Caggianelli, G., Personal Communication, 1995.

Blevins, R.D., *Applied Fluid Dynamics Handbook*, Van Nostrand & Reinhold Co., New York, p. 40, 1984.

Botteri, B., Cretcher, R., and Kane, W., "Aircraft Applications of Halogenated Hydrocarbon Fire Extinguishing Agents," *Published Proceedings of the Symposium An Appraisal of Halogenated Fire Extinguishing Agents*, Washington, DC, National Academy of Sciences, (1972).

Bovina, T.A., "Studies of Exchange Between Re-circulation Zone Behind the Flame Holder and Outer Flow," Seventh Sym. (Int.) on Combustion, *The Combustion Institute*, 692, (1958).

Clodfelter, R.G., "Hot Surface Ignition and Aircraft Safety Criteria," Proceedings of the SAE Aerospace Technology Conference and Exposition, *SAE Technical Paper Series*, Long Beach, CA, (1990).

Coward, H.F., and Jones, G.W., "Limits of Flammability of Gases and Vapors," *Bulletin 503*, Bureau of Mines, National Technical Information Service, Springfield, VA, 1939.

Cutler,D.P., "The Ignition of Gases by Rapidly Heated Surfaces," *Combust. Flame*, **22**, 105, (1974).

Demaree, J., and Dierdorf, P., "Aircraft Installation and Operation of an Extinguishing-Agent Concentration Recorder," Technical Development Report No. 403, National Aviation Facilities Experimental Center, Federal Aviation Agency, (1959).

Detz, C.F., "Threshold Conditions for the Ignition of Acetylene Gas by a Heated Wire," *Combust. Flame*, **26**, 45, (1976).

Dyer, J.H., Marjoram, M.J., and Simmons, R.F., "The Extinction of Fires in Aircraft Jet Engines - Part III," *Fire Tech.*, **13**, 126, (1977a).

Dyer, J.H., Marjoram, M.J., and Simmons, R.F., "The Extinction of Fires in Aircraft Jet Engines - Part IV," *Fire Tech.*, **13**, 223, (1977b).

Finnerty, A.E., "Effect of Halons on the Autoignition of Propane," Western States Section Meeting of the Combustion Institute, Palo Alto, CA, *Paper WSS/CI 75-27*, (1975).

Gerstein, M. and Allen, R.D., "Fire Protection Research Program for Supersonic Transport," Wright Patterson AFB, OH, *AFAPL, Report AFAPL-TR-69-66*, (1964).

Glarborg, P., Kee, R.J., Grcar, J.F., Miller, J.A., "PSR: A Fortran Program for Modeling Well-Stirred Reactors," *Sandia National Laboratories,* Report SAND86-8209, Feb. 1986.

Goodall, D.G. and Ingle, R., *Esso Air World*, **19**, 8, (1966).

Grieme, F., "Aviation Fire Protection," *NFPA Quarterly*, **35**, (No. 1), (1941).

Griffiths, J.F. Coppersthwaite, D., Phillips, C.H., Westbrook, C.K., and Pitz, W.J., "Auto-ignition Temperatures of Binary Mixtures of Alkanes in a Closed Vessel: Comparisons between Experimental Measurements and Numerical Predictions," Twenty-Third Sym. (Int.) on Combustion, *The Combustion Institute*, 1745, (1990).

Grosshandler, W., Lowe, D., Rinkinen, B., Presser, C., "A Turbulent Spray Burner for Assessing Halon Alternative Fire Suppressants," *ASME Paper No 93-WA/HT-23*, 1993.

Grosshandler, W., Gann, R.G., and Pitts, W.M., eds., "Evaluation of Alternative In-Flight Fire Suppressants for Full-Scale Testing in Simulated Aircraft Engine Nacelles and Dry Bays," *NIST Special Publication Number SP-861*, (1994).

Grosshandler, W., Lowe, D., Rinkinen, B., and Presser, C., "Assessing Halon Alternatives for Aircraft Engine Nacelle Fire Suppression," *J Heat Transfer*, **117**, 489, (1995).

Hamins, A., Trees, D., Seshadri, K., Chelliah, H.K., "Extinction of Nonpremixed Flames with Halogenated Fire Suppressants," *Combust. Flame*, **99**, 221-230 (1994).

Hansberry, H., "CAA Aircraft Fire Test Program," *NFPA Quarterly*, **42**, (No. 1), (1948).

Hansberry, H., "Aircraft Fire Extinguishment, Part V, Preliminary Report on High-Rate-Discharge Fire-Extinguishing Systems for Aircraft Power Plants," *Technical Development Report No. 260*, Civil Aeronautics Administration, (1956).

Hansberry, H., "Halogenated Extinguishing Agents, Part III, Research at the Technical Development and Evaluation Center Civil Aeronautics Administration," *NFPA Quarterly*, **45**, (No. 10), (1954).

Harwell Laboratories, "HARWELL-FLOW3D Release 3.2, User Manual," *C.D. Department, AEA Industrial Technology*, Harwell Laboratory, Oxfordshire, United Kingdom, 1992.

Hirst, R., "Aviation Fire Research," *NFPA Quarterly*, **57** (No. 2), 141, (1963).

Hirst, R. and Sutton, D., "The Effect of Reduced Pressure and Airflow on Liquid Surface Diffusion Flames," *Combust. Flame*, **5**, 319, (1961).

Hirst, R., Farenden, P.J., and Simmons, R.F., "The Extinction of Fires in Aircraft Jet Engines - Part I," *Fire Tech.*, **12**, 266, (1976).

Hirst, R., Farenden, P.J., and Simmons, R.F., "The Extinction of Fires in Aircraft Jet Engines - Part II," *Fire Tech.*, **13**, 59, (1977).

Hughes, C., "Aircraft Fire Extinguishment, Part II, The Effect of Air Flow on Extinguishing Requirements of a Jet Power-Plant Fire Zone," *Technical Development Report No. 205*, Civil Aeronautics Administration, (1953).

Johnson, A.M., and Grenich, A.F., "Vulnerability Methodology and Protective Measures for Aircraft Fire and Explosion Protection," Wright Patterson AFB, OH, *Technical Report AFWAL-TR-85-2060*, (1986).

Johnson, A.M., Roth, A.J., and Moussa, N.A., "Hot Surface Ignition of Aircraft Fluids," Wright Patterson AFB, OH, *Technical Report AFWAL-TR-88-2101*, (1988).

Kinsey, D., Personal Communication, Chief, Applied Computational Fluid Dynamics Division, Wright Patterson AFB, OH, (1994).

Klein, H., "Jet Engine Fire Protection Program," *AF Technical Report No. 5870*, U.S. Air Force Air Material Command, (1950a).

Klein, H., "New Fire Extinguishing Agents for Aircraft", *NFPA Quarterly*, **43**, (No. 4), (1950b).

Klueg, E.P., and Demaree, J.E., "An Investigation of In-Flight Fire Protection with a Turbofan Powerplant Installation," *FAA Report Na-69-26(DS-68-28)*, (1969).

Kolleck, M., Booz-Allen-Hamilton tabulated survey results of present aircraft systems and operating environments, (1993).

Kuchta, J.M., "Summary of Ignition Properties of Jet Fuels and Other Aircraft Combustible Fluids," Bureau of Mines, Pittsburgh, PA, *Report AFAPL-TR-75-70*, (1975).

Kumagai, S. and Kimura, I., "Ignition of Flowing Gases by Heated Wires," Sixth Sym. (Int.) on Combustion, *The Combustion Institute*, p. 554, 1956.

Kumar, R.K., "Ignition of Hydrogen-Oxygen Mixtures Adjacent to a Hot, Nonreactive Surface," *Combust. Flame*, **75**, 197, (1989).

Landesman, H. and Basinski, J.E., "Investigation of Fire Extinguishing Agents for Supersonic Transport," *Tech. Doc. Rept. ASD-TDR-63-804*, (1964).

Launder, B.E. and Spalding, D.B., "The Numerical Computation of Turbulent Flows," *Computer Methods in Applied Mechanics and Engineering*, **3**, 269, (1974).

Laurendeau, N., "Thermal Ignition of Methane-Air Mixtures by Hot Surfaces: A Critical Examination," *Combust. Flame*, **46**, 29, (1982).

Leach, W., Private communication, (1994).

Lefebvre, A.H., *Gas Turbine Combustion*, McGraw-Hill Book Co., New York, 1983.

Lefebvre, A.H. and Halls, G.A., "Some Experience in Combustion Scaling," *AGARD Advanced Aero Engine Testing*, Pergamon, Oxford, 177, (1959).

Lemon, L.H., Tarpley, W.B. Freeman, M.K., and Tuno, A.L., "Persistent Fire Suppression for Aircraft Engines," Wright Patterson AFB, OH 45433, *Technical Report AFAPL-TR-79-2130*, (1980).

Lewis, B., and Von Elbe, G., *Combustion, Flame and Explosions of Gases*, Academic Press, New York, 1961.

Liñan, A., "The Asymptotic Structure of Counterflow Diffusion Flames for Large Activation Energies," *Acta Astronautica*, **1**, 1007 (1974).

Longwell, J.P., Frost, E.E., and Weiss, M.A., "Flame Stability in Bluff Body Recirculation Zones," *Ind. Eng. Chem.*, **45**, 1629, (1953).

Macek, A., "Flammability Limits," *Combust. Sci. Tech.*, **21**, 43, (1979).

Malcolm, J.E., "Vaporizing Fire Extinguishing Agents," Engineer Research and Development Laboratories, Fort Belvoir, VA, *Interim Report 1177*, Project 8-76-04-003, 1950.

Mapes, D., "Development and Technical Aspects of the Aircraft-Engine Nacelle Fire Extinguishing System," *Published Proceedings Symposium on Fire Extinguishment Research and Engineering*, U.S. Naval Civil Engineering Research and Evaluation Laboratory Port Hueneme, CA, (1954).

Mestre, A., "Etudes des Limites de Stabilite en Relation avec la resistance des Obstacles a l'Ecoulement," *Combustion Researches and Reviews, 6th and 7th AGARD Meetings*, p. 72-85, Butterworths Scientific, London, 1955.

McClure, J.D., and Springer, R.J., "Environmental and Operating Requirements for Fire Extinguishing Systems on Advanced Aircraft," for Joint Technical Coordinating Group/Aircraft Survivability, Report No. *JTCG/AS-74-T-0024*, (1974).

McGrattan, K.B., Rehm, R.G., and Baum, H.R., "Fire Driven Flows in Enclosures," *Journal of Computational Physics*, **110** (2), 285, (1994).

Middlesworth, C., "Aircraft Fire Extinguishment, Part I, A Study of the Factors Influencing Extinguishing System Design," *Technical Development Report No. 184*, Civil Aeronautics Administration, (1952).

Middlesworth, C., "Determination of Means to Safeguard Aircraft From Power-Plant Fires in Flight, Part VI, The North American Tornado (Air Force XB-45)," *Technical Development Report No. 221*, Civil Aeronautics Administration, (1954).

Mulholland, J.A., Sarofim, A.F., and Beer, J.M., "Chemical Effects of Fuel Chlorine on the Envelope Flame Ignition of Droplet Streams," *Combust. Sci. Tech.*," **87**, 139, (1992).

New, J., and Middlesworth, C., "Aircraft Fire Extinguishment, Part III, An Instrument for Evaluating Extinguishing Systems," *Technical Development Report No. 206*, Civil Aeronautics Administration, (1953).

NFPA Quarterly, "Chlorobromomethane," **42**, (No. 1), (1948).

Parts, L., "Assessment of the Flammability of Aircraft Hydraulic Fluids," Wright Patterson AFB, OH, *Technical Report AFAPL-TR-79-2095*, Oct. 1980.

Perry, R.H., Green, D.W., Maloney, J.O., Eds., *Perry's Chemical Engineers' Handbook*, 6th Edition, McGraw-Hill Inc., New York, 1984.

Picard, B., Hartsig, D., and Levesque, R., "F/A-18 Engine Bay Fire Reduction," *Technical Memorandum TM 92-172 SA*, Naval Air Warfare Center Aircraft Division, Patuxent River, Maryland, (1993).

Pitts, W.M., Nyden, M.R., Gann, R.G., Mallard, W.G. and Tsang, W., "Construction of an Exploratory List of Chemicals to Initiate the Search for Halon Alternatives," *NIST Technical Note 1279*, U.S. Government Printing Office, Washington, DC, 1990.

Sano, T., and Yamashita, A., "Flame Ignition of Premixed Methane Air Mixtures on a High Temperature Plate," *JSME Int. J., Series B*, **37**, 180 (1994).

Sheinson, R.S., Penner-Hahn, J.E., and Indritz, D., "The Physical and Chemical Action of Fire Suppressants," *Fire Safety Journal,* **15**, 43 (1989).

Smyth, K.C., and Bryner, N.P., "Short-Duration Autoignition Temperature Measurements for Hydrocarbon Fuels," *National Institute of Standards and Technology Report Number NISTIR 4469*, (1990).

Snee, T.J., and Griffiths, J.F., "Criteria for Spontaneous Ignition in Exothermic, Autocatalytic Reactions: Chain Branching and Self-Heating in the Oxidation of Cyclohexane in Closed Vessels," *Combust. Flame*, **75**, 381, (1989).

Sommers, D.E., "Fire Protection Tests in a Small Fuselage-Mounted Turbojet Engine and Nacelle Installation," *Federal Aviation Administration Report RD-70-57*, (1970).

Strasser, A., Waters, N.C., Kuchta, J.M., "Ignition of Aircraft Fluids by Hot Surfaces Under Dynamic Conditions," Wright Patterson AFB, OH, *Report AFAPL-TR-71-86*, (1971).

Strehlow, R.A., *Combustion Fundamentals*, McGraw-Hill, New York, 1984.

Tedeschi, M., and Leach, W., "Halon 1301 Fire Suppression System Effectivity Aboard U.S. Naval Aircraft," *Halon Options Technical Working Conference*, pp.128-136, Albuquerque, NM, (1995).

Tucker, D.M., Drysdale, D.D. and Rasbash, D.J., "The Extinction of Diffusion Flames Burning in Various Oxygen Concentrations by Inert Gases and Bromotrifluormethane," *Combustion and Flame*, **41**, 293 (1981).

Van Wylen, G.J., and Sonntag, R.E., *Fundamentals of Classical Thermodynamics*, Second Edition, John Wiley and Sons, p. 400, 1978.

Vazquez, I., Grosshandler, W., Rinkinen, W., Glover, M., and Presser, C., "Suppression of Elevated Temperature Hydraulic Fluid and JP-8 Spray Flames," *Proceedings of the Fourth International Symposium on Fire Safety Science*, (1994).

Vlachos, D.G., Schmidt, L.D., and Aris, R., "Ignition and Extinction of Flames Near Surfaces: Combustion of CH_4 in Air," *AIChE Journal*, **40**, 1005 (1994).

Williams, F.A., "A Unified View of Fire Suppression," *Journal of Fire and Flammability*, **5**, 54 (1974).

Winterfeld, G., "On Processes of Turbulent Exchange Behind Flame Holders," Tenth Sym. (Int.) on Combustion, *The Combustion Institute*, 1265, (1965).

Womeldorf, C., King, M., and Grosshandler, W., "Lean Flammability Limit as a Fundamental Refrigerant Property," Interim Technical Report-Phase I for the Air-Conditioning and Refrigeration Technology Institute, *ARTI MCLR Project Number DE-FG02-91 CE23810*, 1995.

Yamaoka, I., and Tsuji, H., "An Experimental Study of Flammability Limits Using Counterflow Flames," Seventeenth Sym. (Int.) on Combustion, *The Combustion Institute*, p. 843, 1978.

Zabetakis, M.G., Furno, A.L., and Jones, G.W., "Minimum Spontaneous Ignition Temperatures of Combustibles in Air," *Ind. Eng. Chem.*, **46**, 2173, (1954).

Zukowski, E.E. and Marble, F.E., "The Role of Wake Transition in the Process of Flame Stabilization on Bluff Bodies," *Combustion Researches and Reviews, 6th and 7th AGARD Meetings*, pp. 167-180, Butterworths Scientific, London, 1955.

10. PREDICTION OF HF FORMATION DURING SUPPRESSION

Gregory T. Linteris
Building and Fire Research Laboratory

Grzegorz W. Gmurczyk
Science Applications International Corporation

Contents

Page

10.1 Introduction

The acid gases hydrogen fluoride, hydrogen chloride, and hydrogen bromide (HX, where X denotes a halogen), are thought to be the most damaging and dangerous of the potential decomposition products, and much study has been devoted to determining the amounts of these chemicals formed during fire suppression by CF_3Br and halon alternatives. While CF_3Br is known to readily decompose to form HF, HBr, and COF_2 in laboratory premixed and diffusion flames and in larger scale fires, the amounts were not considered to be a major threat compared to that of the fire itself. The alternative agents have been found to produce significantly more acid gas than CF_3Br, and consequently, there exists a need to understand and predict the mechanisms of formation of acid gases in laboratory flames, and ultimately, suppressed fires.

The goal of this project is to develop an ability to predict the quantity of HF formed during suppression of aircraft fires. In order to understand the formation rates of acid gases in dry bay and engine nacelle fires it is necessary to examine the thermodynamics and chemical kinetics relevant to the formation of the acid gases as well as the effects of the flow field and mixing on the chemistry. An engine nacelle fire may be similar to a steady turbulent spray diffusion flame, whereas a dry bay fire may resemble a rapidly advancing turbulent premixed flame. Because suppression of the dry bay fires occurs in a time of about 100 ms, it is also necessary to consider transient effects on the acid gas formation. The formation of toxic and corrosive by-products in flames/fires inhibited by halogenated hydrocarbons is controlled by transport rates of the agent into the flame, chemical kinetic rates, or equilibrium thermodynamics. These factors are affected by the fuel type, local mixture composition, inhibitor type and concentration, and the characteristics of the flow field such as mixing rate, strain rate, and stabilization mechanism in the case of laboratory burner flames.

The approach taken in the present work is to examine the HF production in the fire, for a range of conditions. Specifically, the effects of fuel type, fire type and size, agent chemical composition and application rate, and room humidity are considered with respect to their effect on the HF formation, both for steady-state and transient conditions. The quantity of agent required to suppress various types of fires has been used as a measure of an agent's utility. In addition, the amount of any unwanted decomposition by-products formed during fire suppression has been identified as a potentially important parameter. The rates of HF generation can then be used as a source term in more detailed models which include the effects of variable mixing rates of the inhibitor, mixing rates of post-fire gases, ventilation rates of the space, and HF condensation to surfaces.

The influence of the key parameters through systematic experiments on laboratory-scale flames has been studied. Agents were added to the air stream of co-flow diffusion flames under steady-state and transient conditions. The apparatus used to obtain these data, the results and their interpretation are presented below.

10.2 Background

The halogen acid or hydrogen halide HX (where X represents the halogen) is a thermodynamically stable product in mixtures containing hydrogen and halogen atoms. Formation of acid gases in inhibited hydrocarbon flames has been studied for many years. Nonetheless, there have been no attempts to predict the amounts of HF formed in suppressed fires which are applicable to a broad range of fire types and conditions and which are based on first principles. Since formation of HF could be an important parameter in selecting an agent to replace CF_3Br, it is essential to develop a method to estimate the amount of HF formed in suppressed fires as compared to the amount formed

with CF_3Br. Once the magnitude of the HF source (the suppressed fire) is determined, the relative importance of that amount of HF, and it's deposition and dilution rates can be determined for the particular application.

The previous research can be categorized as either global measurements of HF produced in suppressed fires, or detailed flame structure measurements. Burdon *et al.*, (1995) ignited mixtures of fuel, air, and CH_3Br in flasks, analyzed the products and found copious amounts of HBr. Numerous premixed low pressure flame studies (Wilson, 1965; Biordi *et al.*, 1973; Safieh *et al.*, 1982; VanDooren *et al.*, 1988) used mass spectroscopy to measure the profiles of hydrogen halides and other products in hydrogen, carbon monoxide, and hydrocarbon flames inhibited by CH_3Br, CF_3Br, and CF_3H. These studies indicated conversion efficiencies of the halogens in the inhibitor into halogen acids on the order of unity.

Acid gas formation in hydrocarbon-air pool fires suppressed by CF_3Br has been studied by Sheinson *et al.*, (1981); Sheinson and Alexander, (1982). His studies, in test volumes of 1.7 and 650 m_3, stressed the difficulties in probe sampling for acid gases. The latter study described an in situ IR absorption method for measuring HBr and HF. To overcome these limitations and also provide time-resolved acid gas concentration data (Smith *et al.*, 1993) developed a new HX sampling technique and obtained HX and inhibitor concentrations as functions of time for discharge of CF_3Br into a 56 m_3 space. In a series of experiments with a variety of fuels and halogenated inhibitors (Yamashika, 1973) showed that the extinction time for a compartment fire sprayed with inhibitor is dependent upon the discharge rate and room volume. He then showed (1974) that the amounts of hydrogen halides and carbonyl halides are also dependent upon the discharge rate. Using a simple model of acid gas formation based on the steady-state rates, he developed a model of transient acid gas formation to explain his results. In more recent studies (Ferreira, 1992a, 1992b) CF_3Br, C_3HF_7, and C_4F_{10} were injected into an enclosure fire and measured the HF produced using ion-selective electrodes.

Di Nenno *et al.*, (1992) introduced halon alternatives into compartment fires and measured the HF, HCl, and COF_2 produced using Fourier transform infrared spectroscopy. These studies again confirmed the importance of injection rate and fuel consumption rate on the amount of acid gas produced. Filipczak, 1993 introduced CF_2ClBr and CF_3Br into a methane flame and measured the O_2, CO_2, H_2O, HF, HCl, HBr, and unreacted inhibitor using a mass spectrometer. Hoke and Herud, (1993) are currently developing a fast-response ion-selective electrode for measuring HF and HCl produced in extinguished fires in crew compartments of combat vehicles. Previous research related to understanding acid gas formation in inhibited flames can be seen to include both detailed flame structure measurements and global measurements of HF produced in suppressed fires. The former provide the basis for obtaining a good understanding of the underlying chemical kinetics of the formation of acid gases.

The global measurements provide important information on the magnitude of the acid gases produced and allow a comparison of the relative amount of acid gases formed by new halon alternatives. There has remained a need to develop a fundamental basis for interpreting the data on acid gas formation in fires suppressed by halon alternatives and to understand the chemical kinetic rates of acid gas formation in diffusion flames inhibited by these alternative agents. In particular, there has existed a need to understand the relationship between fuel and inhibitor type, flame characteristics, agent transport rates, and the concentrations of by-products formed.

10.3 Technical Approach

The technical approach in the present project has included theoretical, numerical, and experimental components. The theoretical components have included thermodynamic calculations, numerical calculations of the flame structure of premixed flames inhibited by fluorocarbons, and development of a global model for HF formation in premixed and diffusion flames. Experiments have included premixed and diffusion flames of liquid or gaseous fuels with steady-state or transient addition of the agent. The need for and contribution of each of these components of the project are outlined below.

Equilibrium calculations are an essential first step for understanding the agent decomposition and HF formation in flames inhibited by fluorinated hydrocarbons. Although kinetic limitations are important to the formation of many products of combustion, the thermodynamics provide the driving force for reaction, and hence must be examined prior to investigating the kinetics. In order to obtain a broad understanding of the inhibited flames, numerous equilibrium calculations have been performed for a variety of fuels and agents. Presented in Section 10.4 are some representative results which illustrate the dominant features of the halogenated agents in hydrocarbon flames.

Although chemical equilibrium calculations are an essential first step towards understanding HF formation, combustion systems often display chemical kinetic limitations to the formation of final products. Consequently, it was important to consider next an inhibited flame in which chemical kinetic limitations could be considered. Premixed flames were selected for study since the complete flame structure is readily calculated using available techniques, and the computational time is not prohibitive. Once solutions are obtained, a wealth of information is available concerning the species reaction and transport in the flame, so that detailed information is available concerning byproduct formation. In order to provide a first level of validation of the kinetic mechanisms, burning velocity measurements were made and compared with the predicted burning velocities from the numerical calculations. Section 10.5 describes the modeling results for inhibited premixed flames along with comparison with experimental burning rates for initial model validation. The important implications for HF formation predicted by the modeling results are discussed for both normal and high-pressure flames.

After obtaining the necessary theoretical background from the chemical equilibrium and premixed flame structure calculations, it was possible to develop a simple model of HF production in both premixed and diffusion steady-state flames. This model was subsequently extended to transient conditions. Section 10.6 describes the physical and chemical basis of the model, presents the equations which describe the amount of HF formation, and describes phenomenologically the fate of the agent as the inhibitor concentration in the air stream increases.

In order to provide an experimental basis for the model and then test its performance, extensive measurements of HF formation in laboratory flames have been performed. In these tests, fuel flow rate, fuel type, agent type and concentration and air flow have been varied. Experiments were performed for premixed and diffusion flames, and for liquid and gaseous fuels, in both steady-state and transient conditions. The model for HF formation has been validated using these experiments. In addition, the HF formation in a large number of intermediate scale tests at the Naval Research Laboratory has been predicted by the model and compared to the actual HF measurements. The experimental configurations for all of the apparatuses are described in Section 10.7. The experimental results along with interpretation of the results are presented in Section 10.8. In Section 10.9, the model is used to predict the HF formation in intermediate-scale tests performed at the Naval Research Laboratory.

The model for predicting HF formation appears to work well. As a result, it is a useful tool for understanding the effects of various parameters on HF formation that would otherwise require much

money and time to exhaustively explore. As described in Section 10.10, we have performed extensive parametric analyses to illustrate the effects of fuel type, fire size, inhibitor type and concentration, inhibitor concentration necessary for extinction, fire-out time, and the presence of water vapor in the air. In the final section (10.11), we describe the parameters likely to be important in dry-bay and engine nacelle fires, and present the straightforward application of the model for predicting HF formation for a wide range of fire types.

10.4 Equilibrium Calculations with Halogenated Inhibitors

In order to first understand the basic driving force for reaction of the halogenated inhibitors, extensive thermodynamic equilibrium calculations were performed. These provided information on the likely product species for a variety of fuel-air mixture ratios, fuel and agent type, and agent concentration.

10.4.1 Results. Calculations have been performed for methane-air flames at various stoichiometries and concentrations of C_2HF_5. Although methane and C_2HF_5 were selected for these figures, this is arbitrary; the features of the analyses are qualitatively the same for any hydrocarbon fuel and fluorinated hydrocarbon (or perfluorocarbon) inhibitor. The results are shown in Figures 1 through 6. Detailed examination of figures such as these has illustrated the thermodynamic driving forces in hydrocarbon flames inhibited by fluorinated agents, and allowed development of an appropriate model for HF formation. Some of the pertinent characteristics of these inhibited flames are described below.

Figures 1 through 3 show the effects of increasing C_2HF_5 mole fraction on the equilibrium temperature and species mole fractions at nominal fuel-air equivalence ratios ϕ of 0.6, 0.8 and 1.0. Note that in these calculations, the equivalence ratio is calculated based on the oxygen demand of the fuel only, and does not include the oxygen demand of the inhibitor. In Figure 1, the flame is fuel lean ($\phi = 0.6$). At an inhibitor concentration of zero, the major products are H_2O and CO_2; however, the flame has an excess of oxygen, and the flame temperature is low, about 1700 K. Adding inhibitor has the effect of increasing the flame temperature since the HFC's behave, thermodynamically, much as a fuel species. As C_2HF_5 is added, the temperature increases, and the fluorine in the inhibitor forms HF, diverting some of the hydrogen away from water, so that the water concentration in the flame decreases. The additional carbon in C_2HF_5 is converted to CO_2. At an inhibitor concentration of about 5 to 6 %, the hydrogen to fluorine ratio in the flame is near unity. At this C_2HF_5 mole fraction, the temperature and $[CO_2]$ reach peak values, and water is absent as a product. Addition of more C_2HF_5 leads to COF_2 and CO formation because hydrogen and oxygen concentrations, respectively, are insufficient. The temperature decreases above 6 % C_2HF_5 because of the shortage of both hydrogen and oxygen, although HF concentration increases, at a slower rate, due to the hydrogen in the inhibitor molecule itself. For the conditions of this figure, the point of unity fluorine to hydrogen ratio, temperature peak and CO_2 peak occur at the same C_2HF_5 volume fraction (about 6 %); this is not always the case. For comparison purposes, it should be noted that a premixed stoichiometric flame in the nozzle burner described in later sections blows off at a C_2HF_5 mole fraction of about 0.09 for methane flames, and 0.05 for propane. Diffusion flames of propane blow off at a C_2HF_5 mole fraction of 0.105 in the air stream.

Figures 2 and 3, for values of ϕ of 0.8 and 1.0, show the same trends. Water disappears at the point of unity hydrogen to fluorine ratio; and CF_2O forms when water is gone. Carbon monoxide forms when there is insufficient oxygen, and the peak temperature occurs at the C_2HF_5 mole fraction where the CO production increases. This last effect implies that CO to CO_2 conversion has the largest effect on heat release, or, conversely, that the oxygen demand has more effect on peak temperature

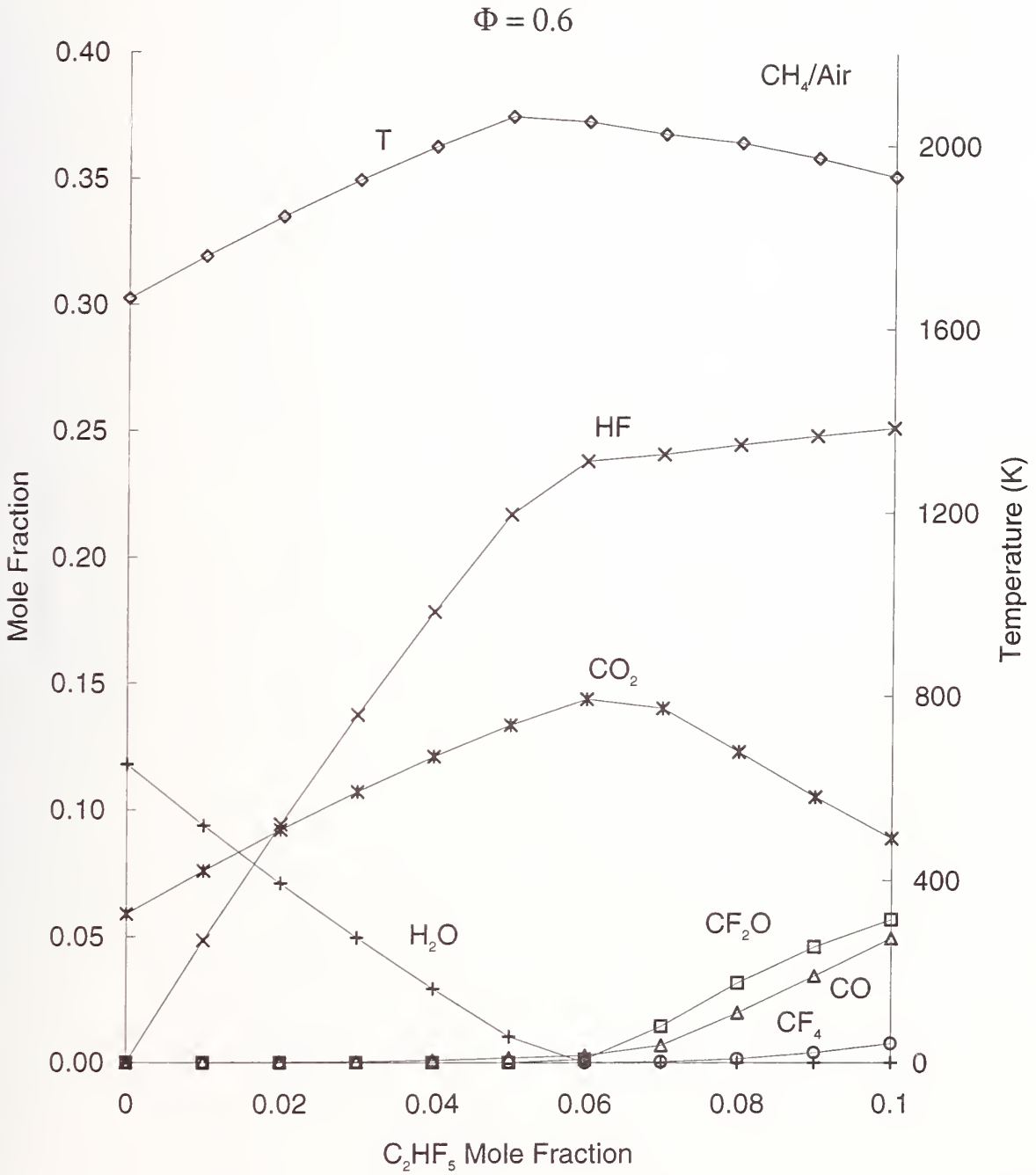

Figure 1. Equilibrium temperature and composition of combustion/inhibition products in the lean $\phi = 0.6$ CH_4/Air mixture versus C_2HF_5 mole fraction.

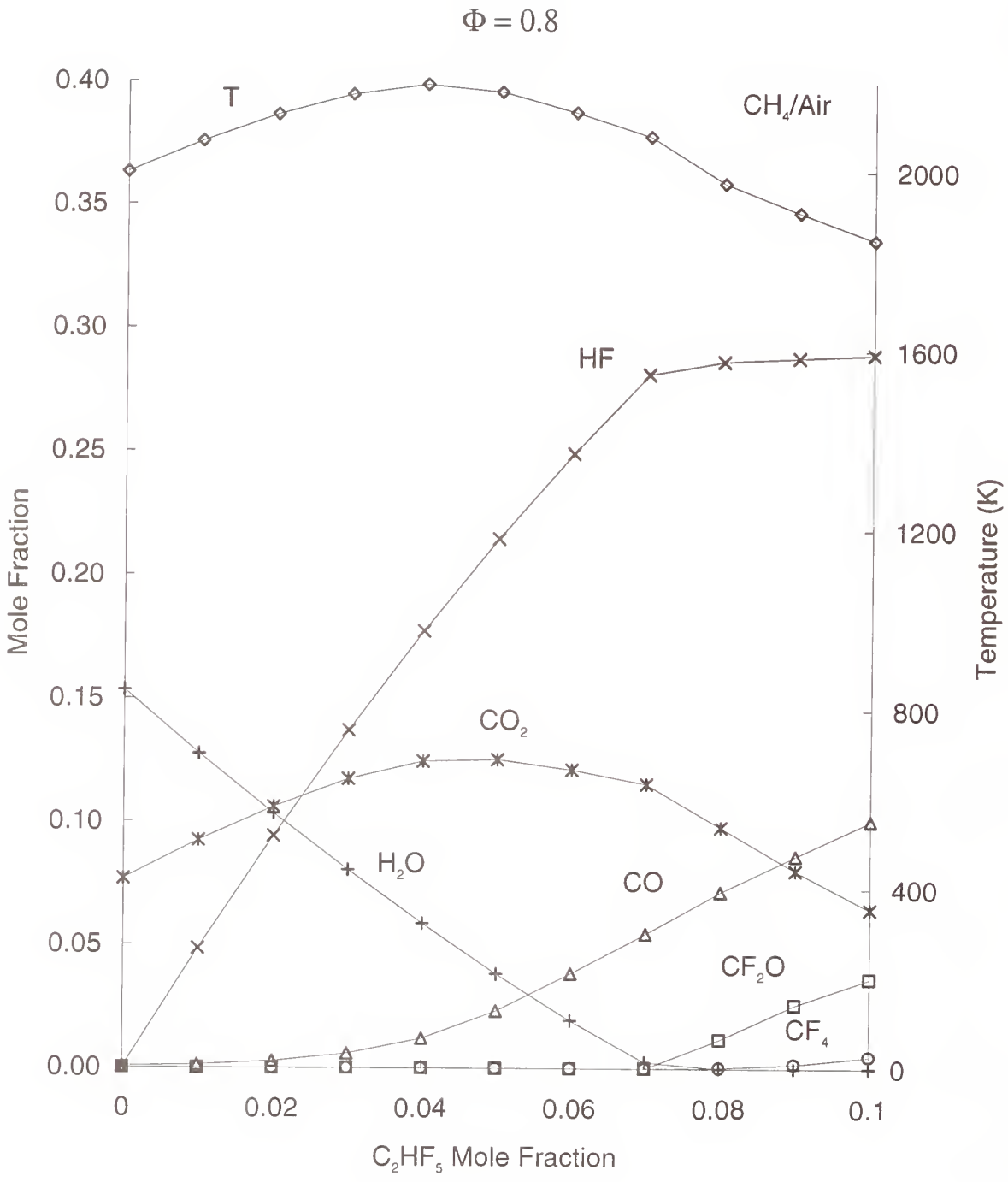

Figure 2. Equilibrium temperature and composition of combustion/inhibition products in the lean $\phi = 0.8$ CH_4/Air mixture versus C_2HF_5 mole fraction.

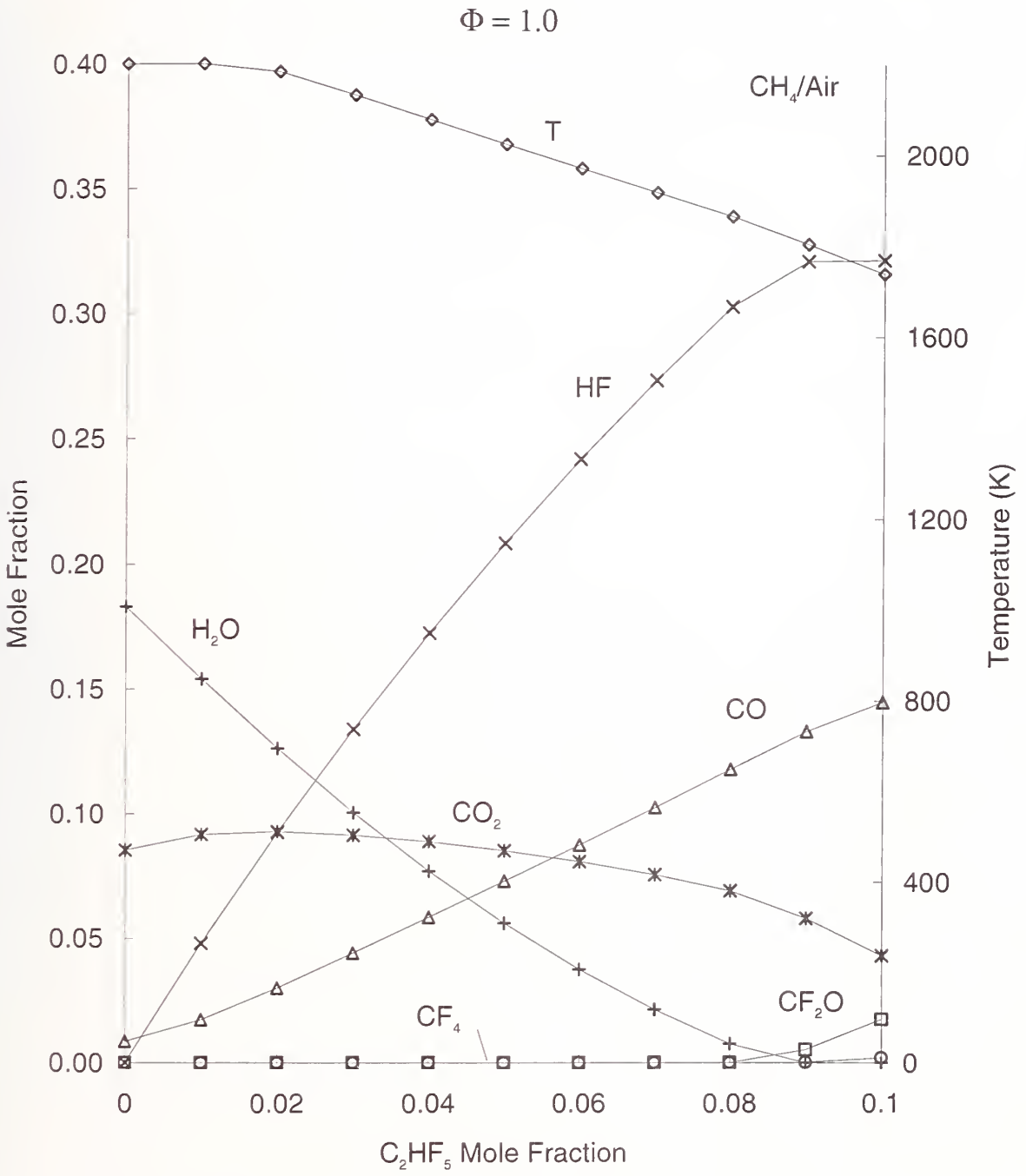

Figure 3. Equilibrium temperature and composition of combustion/inhibition products in the stoichiometric $\phi = 1.0$ CH_4/Air mixture versus C_2HF_5 mole fraction.

than the hydrogen demand. Carbonyl fluoride COF_2 forms when there is insufficient hydrogen for formation of HF. The species CF_4 appears when there is insufficient water, and either insufficient oxygen or carbon for formation of COF_2. The CF_4 concentration is typically about 20 % of the COF_2 concentration.

Figures 4, 5, 6 show the influence of a varying equivalence ratio on the equilibrium product mole fractions and temperature at a constant inhibitor mole fraction of 0.025, 0.05, and 0.10, respectively. As in ordinary hydrocarbon-air flames, the temperature is decreased for rich flames due to incomplete conversion of CO to CO_2, and for lean flames due to dilution by excess air. As described above, the peak value of the temperature occurs at lower nominal equivalence ratios as the amount of inhibitor increases (*e.g.*, Figures 1, 2, 3), due to the oxygen requirement of the inhibitor.

As for hydrogen, the primary source is the fuel, so that for richer flames, the formation of water increases, while for leaner flames, the formation of COF_2 increases. For this agent and fuel, limits to HF formation only occur at high C_2HF_5 mole fractions and leaner flames (*e.g.*, Figure 4). The greatly reduced peak temperature occurs for the lean conditions in Figure 4 due to the hydrogen limits; insufficient hydrogen forces formation of CF_2O and CF_4 rather than HF and CO_2, limiting the peak temperature.

10.4.2 Conclusions. From examination of the results of equilibrium calculations, the following characteristics have been observed for inhibited hydrocarbon-air flames:

1. Peak temperature occurs near the onset of CO formation.

2. Addition of inhibitor shifts the peak temperature to leaner nominal stoichiometries, since the agent acts as an additional fuel species.

3. For conditions typical of flames, the major product species which contain fluorine are HF and COF_2.

4. Hydrogen fluoride is formed preferentially over water as an endpoint for hydrogen.

5. Carbonyl fluoride and water do not exist at the same conditions, water exists only when [H]/[F] < 1, COF_2 when [H]/[F] >1.

6. Fuel serves as the primary source of hydrogen, which is necessary for the formation of HF.

10.5 Premixed Flame Structure Calculations and Burning Velocity Measurements

10.5.1 Introduction. It is important to recall that the above section describes thermodynamic considerations only. Generally, reactant mixtures in diffusion flames like to combine at conditions which produce the maximum temperature; however, there can be both transport and kinetic limitations. That prevents attainment of chemical equilibrium. For flames with halogens, presence of the halogen may influence the kinetic rates for consumption of the fuel and inhibitor. Consequently, there may be a competition between the tendency to move to conditions which produce high temperatures, and conditions which produce fast rates of consumption of the reactant species. For diffusion flames, the

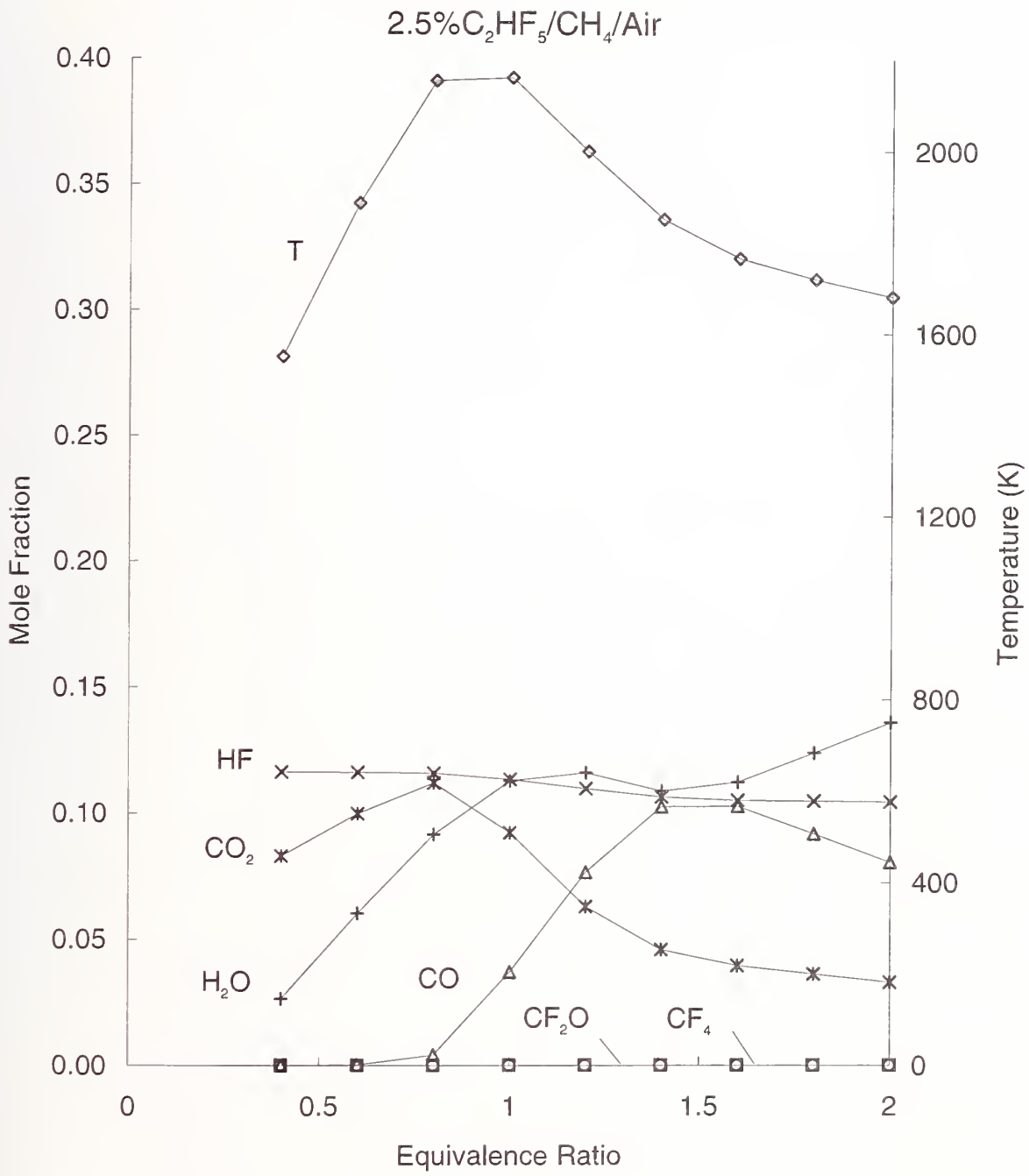

Figure 4. Equilibrium temperature and composition of combustion/inhibition products in the 2.5 % C_2HF_5/CH_4/Air mixture versus mixture equivalence ratio.

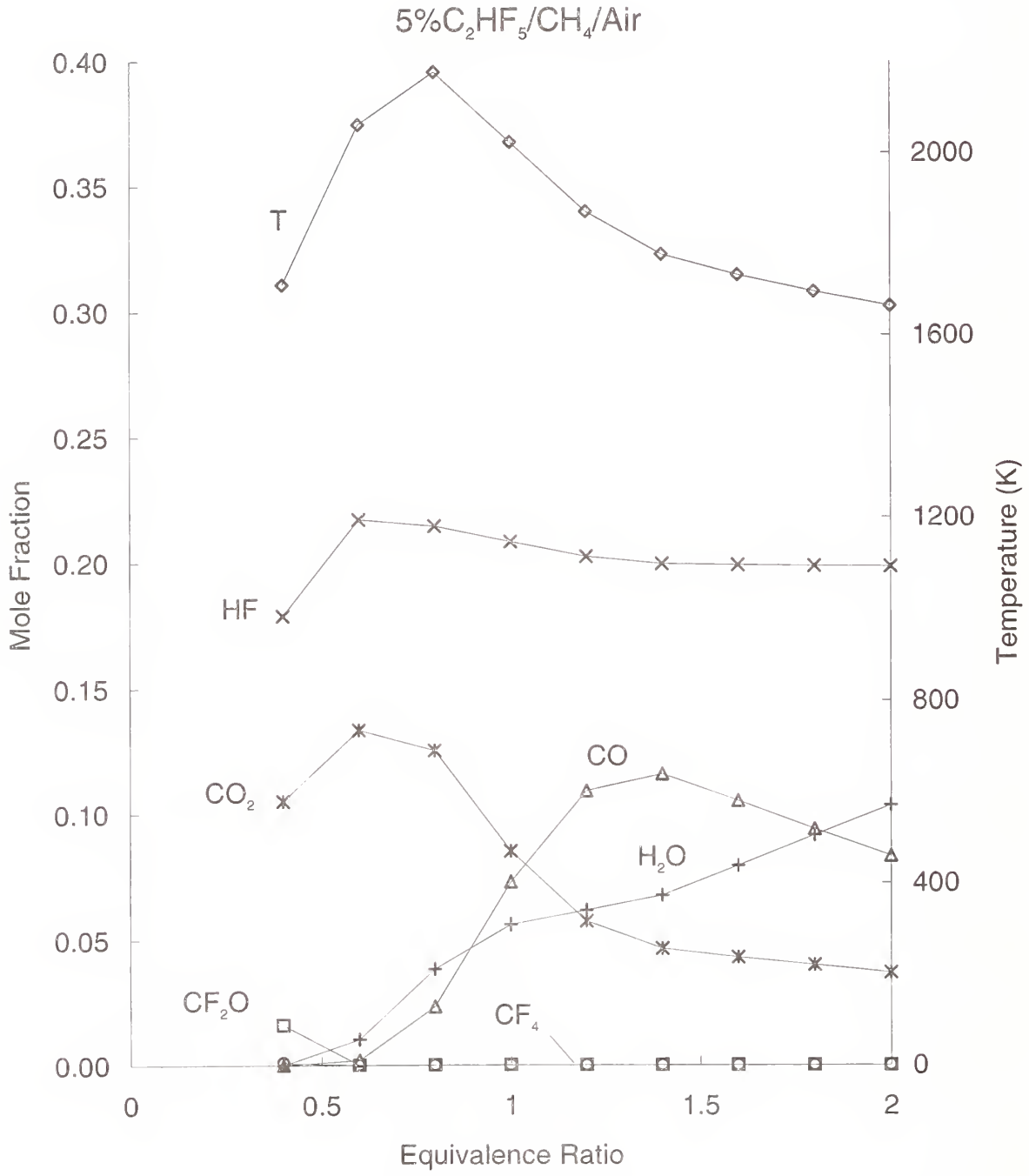

Figure 5. Equilibrium temperature and composition of combustion/inhibition products in the 5 % C_2HF_5/CH_4/Air mixture versus mixture equivalence ratio.

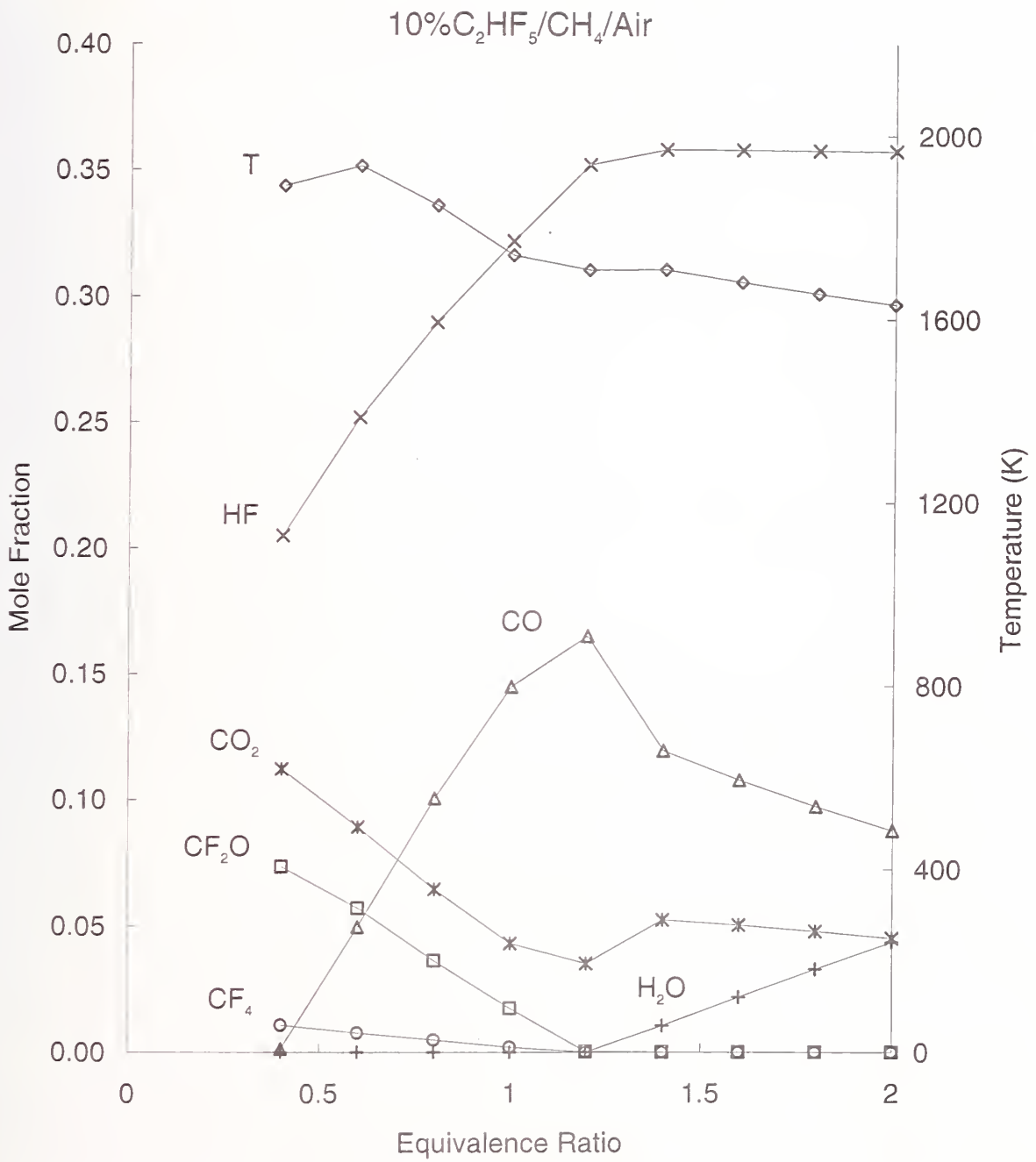

Figure 6. Equilibrium temperature and composition of combustion/inhibition products in the 10 % C_2HF_5/CH_4/Air mixture versus mixture equivalence ratio.

transport rates of species into the reaction zone depend upon the rate at which they are consumed there. Thus, species which are consumed slowly will build in concentration, which reduces the transport rate to the reaction zone. That prevents attainment of chemical equilibrium. In order to consider simultaneously the interplay of thermodynamics and kinetics in a flame (while still avoiding the added complexity of non-premixed conditions), this section describes numerical calculations of the structure of premixed flames. These calculations allow consideration of the effect of the inhibitor on the overall reaction rate (which is affected by both temperature and species concentrations). In addition, the premixed flame calculations permit examination of the exact chemical routes of formation of HF, so that additional factors which may increase of decrease HF formation rates may be considered.

In order to begin to understand the chemical kinetic limitations to HF formation, numerical modeling studies have been performed for premixed flames inhibited by the fluorinated inhibitors. The flame structure (temperature and species concentration profiles through the flame) have been calculated for premixed methane-air flames in the presence of fluorinated hydrocarbon inhibitors. From these solutions, the chemical reaction rates and the convective and diffusion transport rates of every species can be determined at each point in the flame, allowing a comprehensive understanding of HF formation for these laboratory flames. The knowledge obtained is then used to provide guidance in interpreting large-scale tests of HF formation under other flame conditions.

As a first test of the performance of the chemical kinetic mechanism, the burning velocities of methane-air flames in the presence of the inhibitors have been measured. As will be demonstrated below, the agreement is good, providing increased confidence in the capabilities of the model. Two separate experiments and the accompanying numerically analyses are presented in this section. The first set of experiments involves a nozzle burner, used to produce nearly adiabatic atmospheric pressure flames. In the second set of experiments (conducted at the Massachusetts Institute of Technology), the measurements of burning velocity are extended to higher initial pressure and temperature through the use of a constant volume combustion device (bomb) - (Hochgreb *et al.*, 1994; VanDerWege *et al.*, 1995). The predicted burning velocity reductions for each device are compared with the results of numerical calculations. The calculated flame structure is then used to understand the HF formation under both atmospheric pressure and at elevated pressures and temperatures (which may be representative of suppressed dry-bay fires).

10.5.2 Background. Early studies of the inhibitory effects of halogenated hydrocarbons on flames were conducted in premixed systems (Burgoyne *et al.*, 1948; Coleman, 1951; Belles *et al.*, 1957; Simmons *et al.*, 1956; Garner *et al.*, 1957; Rosser *et al.* 1959; Lask and Wagner, 1962). The premixed laminar burning velocity is a fundamental parameter describing the overall reaction velocity, heat release, and heat and mass transport in a flame. In addition, the reduction in the premixed flame burning velocity is useful for understanding the mechanism of chemical inhibition of fires since diffusion flames often have a stabilization region which is premixed, and good correlation has been found between the reduction in burning velocity and the concentration of inhibitors found to extinguish diffusion flames (Hastie, 1975). Premixed flame burners have flow fields which are relatively easily characterized, making interpretation of the inhibitor's effect on the overall reaction rate straightforward.

The present research extends the investigations of burning velocity reduction to fluorinated inhibitors in hydrocarbon flames and applies a newly-developed kinetic mechanism to model the experiments. The burning velocity measurements are examined as a first step in the validation of the mechanism, and the numerical results are used to study the mode of inhibition of the fluorinated agents and the mechanisms of HF formation.

10.5.3 Experiment - Nozzle Burner. Numerous techniques exist for measuring burning velocities of flames, and there are good reviews in the literature (Linnett, 1953; Andrews and Bradley, 1972). All of the flame and burner geometries employed, however, cause deviations from the desired one-dimensional, planar, adiabatic flame. In the present research, a premixed conical Bunsen-type nozzle burner is used for the atmospheric pressure experiments. This method was selected for the flame speed measurements because its simplicity allows rapid assessment of the behavior of a number of halon alternatives. The low rate of heat loss to the burner, the low strain rate, and the low curvature facilitate comparisons of the experimental burning velocity with the predictions of a one-dimensional numerical calculation of the flame structure. Although measurement of a true one-dimensional, planar, adiabatic burning velocity is difficult, the relative change in the burning velocity can be measured with more confidence. Consequently, the burning velocity reduction in the present work is normalized by the uninhibited burning velocity. For comparison with the results of other researchers, the absolute burning velocities of the uninhibited flames are also presented.

The burner consisted of a Mache-Hebra nozzle burner (Mache and Hebra, 1954; Van Wonterghem and Van Tiggelen, 1954) 27 cm long, with an inner diameter of 22 mm and wall thickness of 1.5 mm. A contraction at the top to a nozzle diameter of 1.02 (+/- 0.005 cm) occurs over a length of 3 cm. The nozzle contour is designed to produce straight-sided schlieren and visible images which are very closely parallel. The burner is placed in a square acrylic chimney 10 cm wide and 86 cm tall with provision for co-flowing air or nitrogen gas (for the present data, the co-flow velocity is zero). Gas flows are measured with digitally-controlled mass flow controllers (Sierra Model 860[1]) with a claimed repeatability of 0.2 % and accuracy of 1 %, which have been calibrated with bubble and dry (American Meter Co. DTM-200A) flow meters so that their accuracy is 1 %. The fuel gas is methane (Matheson UHP). House compressed air (filtered and dried) is used after it has been additionally cleaned by passing it through an 0.01 mm filter, a carbon filter, and a desiccant bed to remove small aerosols, organic vapors, and water vapor. The product gas temperature of the uninhibited flames is measured with Pt/Pt 6 % Rh - Pt/Pt 30 % Rh thermocouples which are coated with Yttrium oxide to reduce catalytic reaction on the thermocouple surface. Measurements with two bead diameters (344 and 139 μm) allow correction for radiation losses.

For the present data, the visible flame height is maintained at a constant value of 1.3 cm to provide similar velocities of heat loss to the burner, while the desired equivalence ratio and inhibitor concentration are preserved. An optical system provides simultaneously the visible and schlieren images of the flame. A 512 by 512 pixel CCD array captures the image which is then digitized by a frame-grabber board in an Intel 486-based computer. The flame area is determined (assuming axial symmetry) from the digitized schlieren image using custom-written image processing software. The average mass burning velocity for the flame is determined using the total area method.

10.5.4 Experiment - Bomb. For the elevated pressure experiments, a constant volume combustion device is used which is amenable to flame speed measurements at elevated and reduced pressures. The experimental apparatus consists of a spherical container 15.24 cm in diameter with one inlet port through which the combustible mixture is introduced. Ignition is provided by two extended electrodes at the center of the bomb. A pressure transducer monitors the pressure of the device as the fuel is consumed. The surface of the bomb was coated with vacuum grease to avoid corrosion by the

---

[1]Certain trade names and company products are mentioned in the text or identified in an illustration in order to specify adequately the experimental procedure and equipment used. In no case does such identification imply recommendation or endorsement by the National Institute of Standards and Technology, nor does it imply that the products are necessarily the best available for the purpose.

products of combustion. The bomb was initially evacuated, and precalculated partial pressures of inhibitor, fuel and air were added. Care was taken to remove the acid combustion products before evacuating the bomb for the next experiment. A more detailed description of the apparatus is given by Metghalchi and Keck (1980).

After introduction of the combustible mixture in the bomb, the flame is ignited at the center and a calibrated pressure trace is obtained. Given the initial conditions, it is possible to relate the pressure signal to the extent of reaction. By solving the energy and mass conservation equations, the flame speed is determined as a function of the temperature and pressure of the adiabatically compressed, unburned mixture ahead of the flame. Allowances are made for property variation in the burned and unburned gases due to temperature change and heat transfer to the wall.

10.5.5 Model. The structure of the inhibited premixed methane-air flame is calculated using currently available techniques (Kee *et al.*, 1980; Kee *et al.*, 1983; Kee *et al.*, 1988). The equations of mass, species, and energy conservation are solved numerically for the initial gas compositions of the experiments. The solution assumes isobaric, adiabatic, steady, planar, one-dimensional, laminar flow and neglects radiation and the Dufour effect (concentration gradient-induced heat transfer) but includes thermal diffusion. The calculations employ a chemical kinetic mechanism recently developed at NIST (Burgess *et al.*, 1994; Burgess *et al.*, 1995) for fluorine inhibition of hydrocarbon flames, which is based on earlier work (Burgess *et al.*, 1993; Westmoreland *et al.*, 1994; Nyden *et al.*, 1994). The 83-species mechanism uses a hydrocarbon sub-mechanism and adds C_1 (200 reactions) and C_2 (400 reactions) fluorochemistry. The hydrocarbon sub-mechanism has been updated to use GRI-Mech (31 species, 177 reactions (Frenklach *et al.*, 1994) which more closely predicts our experimental uninhibited burning velocities. The fluorinated-species thermochemistry in the references (Burgess *et al.*, 1994; Burgess *et al.*, 1995) is from the literature when available and is otherwise estimated using empirical methods (such as group additivity) and through application of ab initio molecular orbital calculations. Fluorinated species reaction rates from the literature were used when available and these were extended to wider temperature and pressure ranges using standard methods based on classic statistical mechanics and quantum mechanics. Where no rate data were available, rate constants were estimated by analogy with hydrocarbon reactions. Although all of the reactions are not necessary to describe the present flames adequately, the comprehensive full mechanism is used for these initial calculations. Reduction of the mechanism will be performed later after more experimental validation. It should be emphasized that the mechanism adopted for the present calculations should be considered only as a starting point. Numerous changes to both the rates and the reactions incorporated may be made once a variety of experimental and theoretical data are available for testing the mechanism.

10.5.6 Results. In the nozzle burner flames, the radiation-corrected temperature of the uninhibited flames is measured at 4 mm above the flame tip to be 2054, 2075, and 2050 (+/- 70 K) for ϕ = 0.95, 1.0, and 1.05 respectively, while the adiabatic flame temperature is calculated to be 2191, 2229, and 2234 K. In these experiments, the measured final temperatures at a point slightly downstream from the reaction zone are about 150 K lower than the calculated adiabatic flame temperatures. Heat losses to the burner, although important near the rim, are not expected to be large compared to the heat release integrated over the entire flame. The quartz tube of the burner was not observed to increase appreciably in temperature during the experiments. The observed heat loss may be due to non-one-dimensional effects, radiation, or chemical non-equilibrium in the post-combustion gases. Nonetheless, since the temperature difference is not too great, it seemed most appropriate to model the flame as freely-propagating rather than burner-stabilized (where heat losses, for example in a flat flame burner, are greater).

The average burning velocity is determined using the total area method described above, in which the flow rate of reactants is divided by the measured schlieren image area. Figure 7 presents the measured mass burning velocity (expressed as the equivalent flame velocity for flame propagation into reactants at 298 K) as a function of equivalence ratio for the uninhibited methane-air flame, together with the results of Rosser *et al.*, (1959) and Vagelopoulos *et al.*, (1994). The present data are about 7 % higher than the results of Rosser *et al.* (1959) for $\phi < 1.0$ and up to 30 % higher for $\phi > 1.0$. In the recent experiments of Vagelopoulos *et al.*, 1994, the measured burning velocities of premixed planar counterflow flames are extrapolated to zero stretch. For values of ϕ from 0.8 to 1.2 the present data are 3 to 7 % higher than their results. This discrepancy may result from curvature and stretch in the present flame which occurs in the conical Bunsen type flame. Figure 7 also shows the burning velocity as a function of stoichiometry calculated using the present mechanism. The agreement between the experiment and model is very good for the number of grid points used in the calculation; however, using three hundred or more grid points gives burning velocities slightly lower, so that the experimental results would be about 7 % too high for values of ϕ from 0.8 to 1.2. Nonetheless, this agreement is considered to be good, and is expected since GRI-Mech is being developed using existing experimental methane-air burning velocities and the present experimental results are close to those of other researchers.

The results for the flames inhibited by N_2, CF_4, CH_2F_2, and CF_3H are presented in Figures 8 - 11 respectively. The figures show the burning velocity of the inhibited flame (normalized by the burning velocity of the uninhibited flame) for values of ϕ of 0.9, 1.0, and 1.1 (here, the equivalence ratio is calculated based on the oxygen demand of the fuel only). The mole fraction of the inhibitor in Figure 8, as well as in all other figures, refers to the entire reactant mixture: fuel + oxidizer + inhibitor. As a baseline case, Figure 8 shows the results for a flame inhibited by N_2. The excellent agreement in Figure 8 is again a consequence of the performance of GRI-Mech. Most of the scatter in the plots of the experimental burning velocity results from flame fluctuations: the camera framing rate is 30 Hz and flame area is obtained from a single image; signal averaging would reduce this scatter.

In Figures 9 - 11, the numerical results are presented in two ways: the solid lines present solutions which allow full chemistry, while the dotted lines present solutions in which the inhibitor is constrained to be inert so that only the thermal and transport properties of the flame are modified by the inhibitor. Experimental and numerical results are presented for inhibitor mole fractions up to 0.08 when possible. Although measurements of the burning velocity reduction of even higher inhibitor mole fractions is desirable, flames could not be stabilized much beyond 8 % for most of the inhibitors. For the lean stoichiometry and the inhibitors CF_4 and CF_3H, flames could not be stabilized for inhibitor mole fractions above about 4 %. Figure 9 shows the results for CF_4. The lines are nearly coincident for the inert calculations at $\phi = 1.0$ and 1.1, and the reacting calculation at $\phi = 0.9$ and 1.0. The experiments show slightly more inhibition for richer flames; whereas the model shows more inhibition for the leaner flame. The calculation which assumes CF_4 to be inert shows slightly less inhibition than the solution which allows decomposition, but again, the difference is small. The calculated burning velocity is in excellent agreement with the numerical solution which allows reaction of CF_4. Clearly, decomposition of CF_4 in the flame is kinetically limited. Tetrafluoromethane influences the burning velocity mainly through its role as an inert species which lowers the flame temperature.

Figure 10 presents the results for CH_2F_2. Again, rich flames show more inhibition than the lean flames but the effect is large for CH_2F_2. The fuel effect of adding CH_2F_2 to lean flames increases the adiabatic flame temperature above the uninhibited case for low CH_2F_2 mole fractions, promoting a higher burning velocity. In competition with this effect is the slower kinetics caused by presence of the fluorine compounds as discussed below. Note that although the adiabatic flame temperature is higher for lean flames with up to 5 % CH_2F_2, the burning velocity is still reduced relative to the

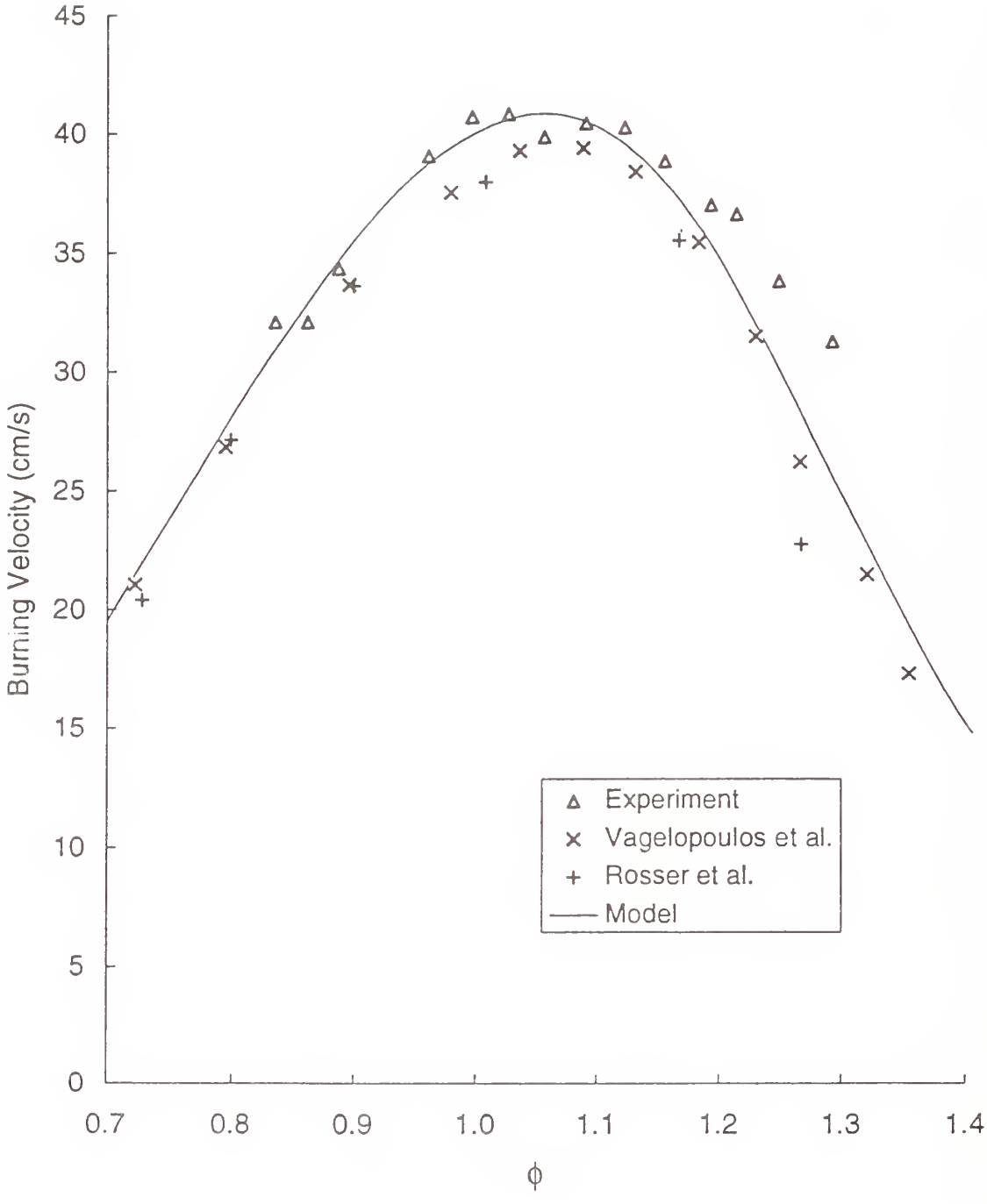

Figure 7. Burning velocity determined using the total area method from the schlieren image of the premixed methane-air flame in the nozzle burner as a function of fuel-air equivalence ratio.

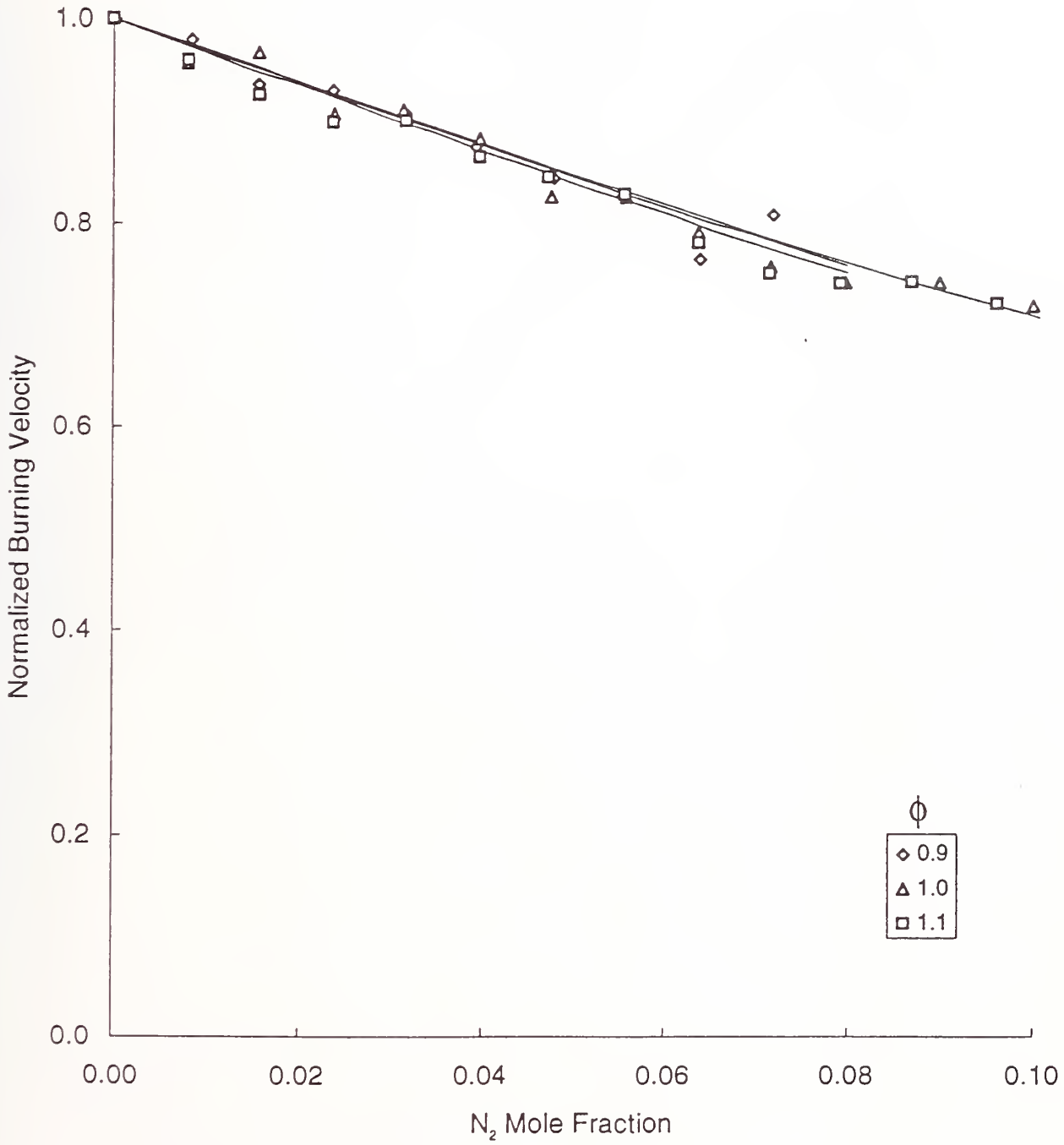

Figure 8. Normalized burning velocity of premixed methane-air flame normalized by the uninhibited burning velocity at the same stoichiometry as a function of the N_2 mole fraction of the total reactant stream.

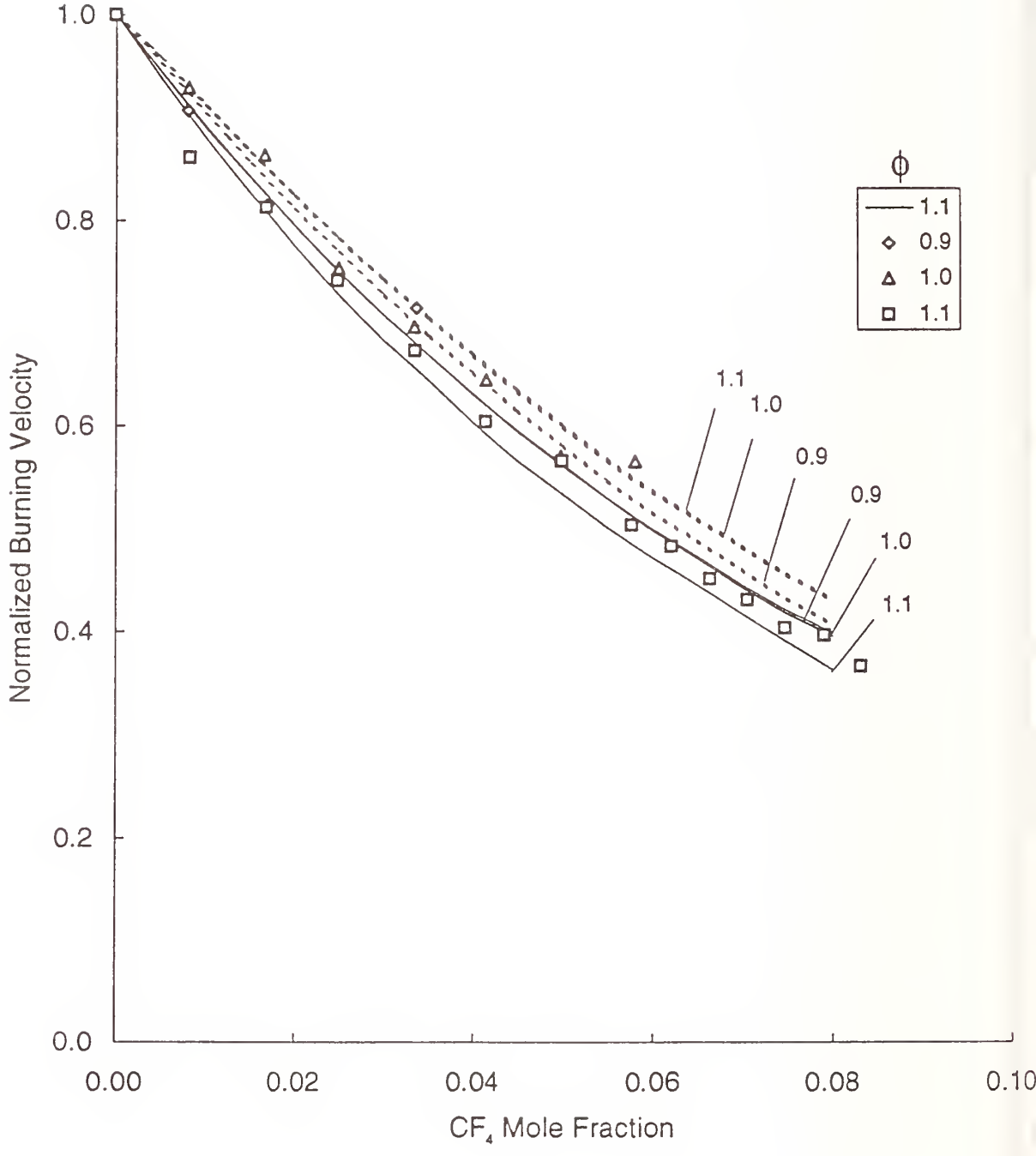

Figure 9. Normalized burning velocity of premixed methane-air flame as a function of the CF_4 mole fraction for ϕ = 0.9, 1.0, and 1.1. Symbols: experimental data; solid lines: reacting inhibitor; dotted lines: inert inhibitor.

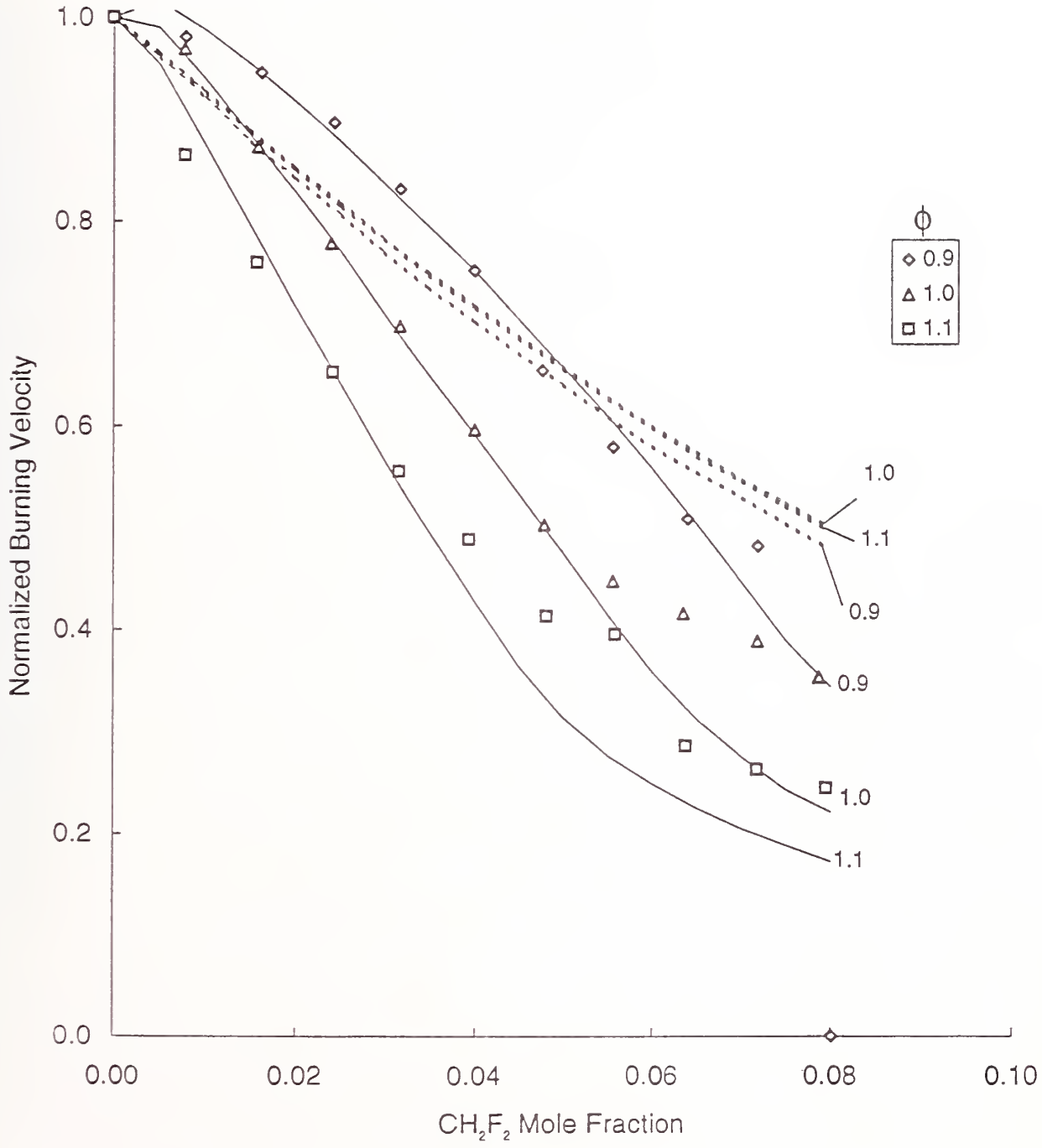

Figure 10. Normalized burning velocity of premixed methane-air flame as a function of the CH_2F_2 mole fraction for $\phi = 0.9$, 1.0, and 1.1. Symbols: exp. data; solid lines: reacting inhibitor; dotted: inert inhibitor.

uninhibited flame. The calculated burning velocities are very close to the measured values for CH_2F_2 mole fractions up to 5 %; as the inhibitor mole fractions reach 8 %, the calculations over-predict the burning velocity reductions by up to 17 %.

The results for CF_3H are shown in Figure 11. The mechanism is showing the proper qualitative features of the inhibition including the dependence on stoichiometry and the reduced inhibitory effect at higher inhibitor mole fractions; however, the calculation is showing up to 20 % more reduction in burning velocity than is observed in the experiments. Figure 12 summarizes the calculated burning velocity for inhibition by CH_4 and CF_4, CH_2F_2, and CF_3H at $\phi = 0.9$ and 1.1; a fit to experimental results for CF_3Br (Rosser *et al.*, 1994) are included for comparison. All calculations predict that the rate of reduction in the burning velocity with addition of inhibitor becomes less at higher inhibitor concentrations, and predict a strong effect of ϕ on the inhibition effect. The fluoromethanes are much less effective than CF_3Br at reducing the burning velocity of methane-air flames at these equivalence ratios. Interestingly, all of the fluoromethanes are less efficient at reducing the burning velocity of the rich methane-air flames than methane itself. For the slightly fuel lean flames, the fuel effect (increasing burning velocity of lean flames with addition of the inhibitor) is larger for methane than for the fluoromethanes, yet upon entering the fuel rich regime, the effect of methane as an inhibitor again is greater than the fluoromethanes.

Figures 13 - 15 present the burning velocity reduction caused by addition of the inhibitors C_2F_6, C_2HF_5, and $C_2H_2F_4$. As the figures show, the greatest reduction in burning velocity was obtained with the perfluorinated agent C_2F_6, followed by C_2HF_5 and $C_2H_2F_4$. For the agent C_2F_6, the burning rate calculated by assuming the agent to be inert under-predicts the burning velocity reduction by about 25 %, while the calculation which allows full reaction over-predicts by about 14 %. As shown in Figures 14 and 15, the results for C_2HF_5 and $C_2H_2F_4$ are similar. An important feature of the inhibition is its dependence on the equivalence ratio, with larger burning velocity reductions occurring in the richer flames. This dependence on the equivalence ratio becomes greater as the hydrogen content of the inhibitor increases. This feature is not captured by the inert calculations; in fact, they predict the opposite: a small decrease in inhibitor effectiveness as ϕ increases from 0.9 to 1.1. An additional observation, clearly illustrated in Figures 14 and 15, is that all of the inhibitors show reduced effectiveness as the inhibitor concentration increases. This has been observed for one-carbon fluorinated agents, where the mechanism for inhibitor consumption shifts from radical attack at low concentration, to thermal decomposition at high inhibitor concentration (Linteris, 1994). The results for the three-carbon fluorinated agents are presented in Figures 16 and 17. These agents, C_3F_8 and C_3HF_7, are about as effective, on a volume basis, as the two-carbon inhibitors, and show the same large dependence on the equivalence ratio and on the inhibitor mole fraction. However, in the case of C_3HF_7, the inhibition effect is strongest in the lean flame, whereas in all other cases the rich flames are inhibited most. The reasons for this are presently unclear but are of great interest.

As described above, the combustion bomb allows burning velocity measurements to be conducted for higher initial temperature and pressure. For the present experiments, the range of unburned gas pressures is 203 to 709 kPa (2 - 7 bar), and the temperatures, 330 to 500 K. Figure 18 shows a curve fit to the burning rate data collected in the bomb as a function of temperature and pressure. To allow comparison, the bomb results were extrapolated to the conditions of the nozzle burner described above. In the presence of the inhibitor CF_3H, the reduction in burning velocity as a function of CF_3H mole fraction is shown in Figure 19. As the figure indicates, the two experiments yield approximately the same burning rate reduction.

The measured burning rate as a function of unburned gas temperature (which is related to the unburned gas pressure) is shown in Figure 20. Experimental curves are shown for 0, 1, 2, and 5 % inhibitor at equivalence ratios near unity. The figure also shows the results of the numerical calculations of the burning rate using the kinetic mechanism described above. Although the burning

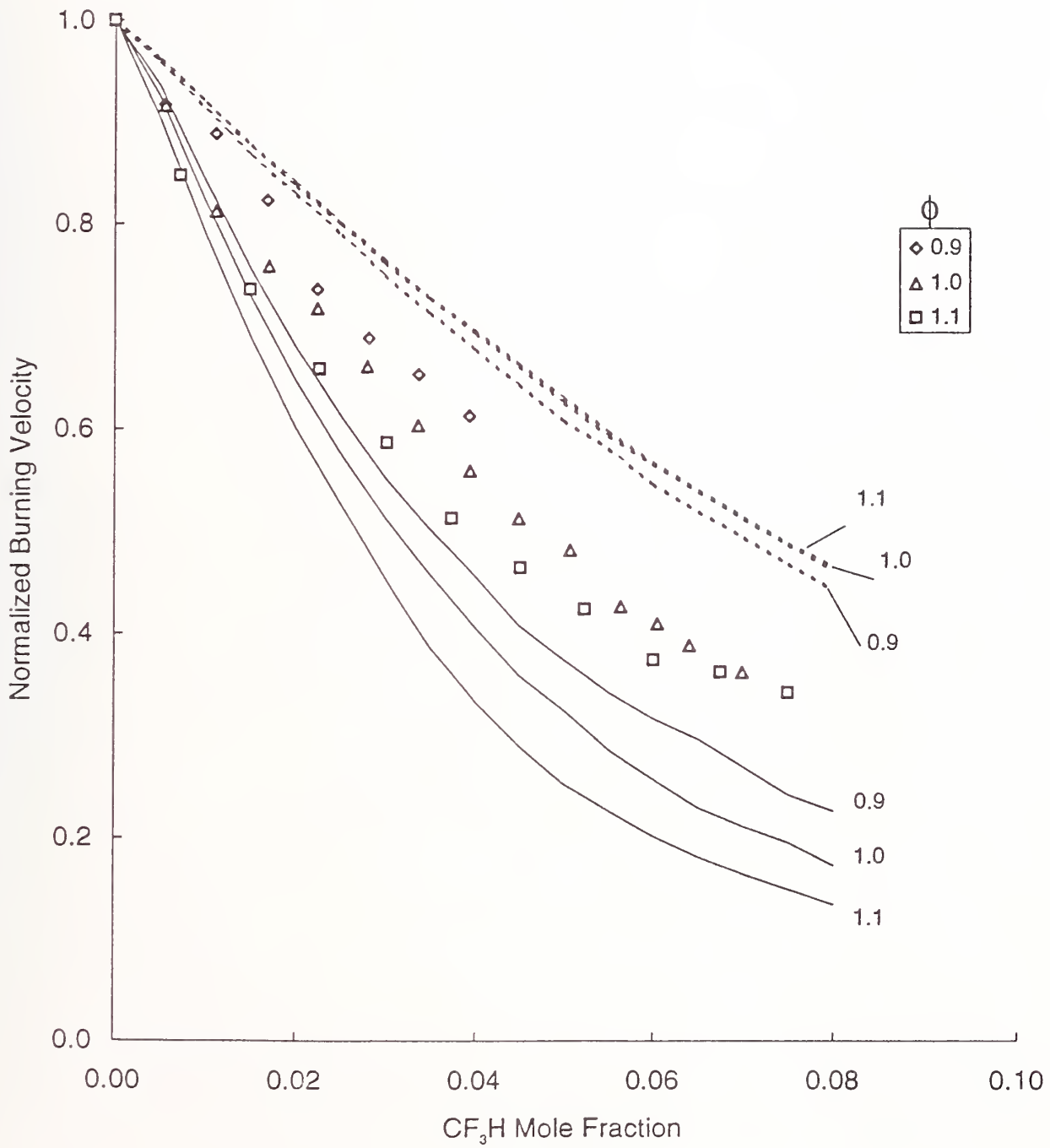

Figure 11. Normalized burning velocity of premixed methane-air flame as a function of the CF_3H mole fraction for $\phi = 0.9$, 1.0, and 1.1. Symbols: exp. data; solid lines: reacting inhibitor; dotted lines: inert inhibitor.

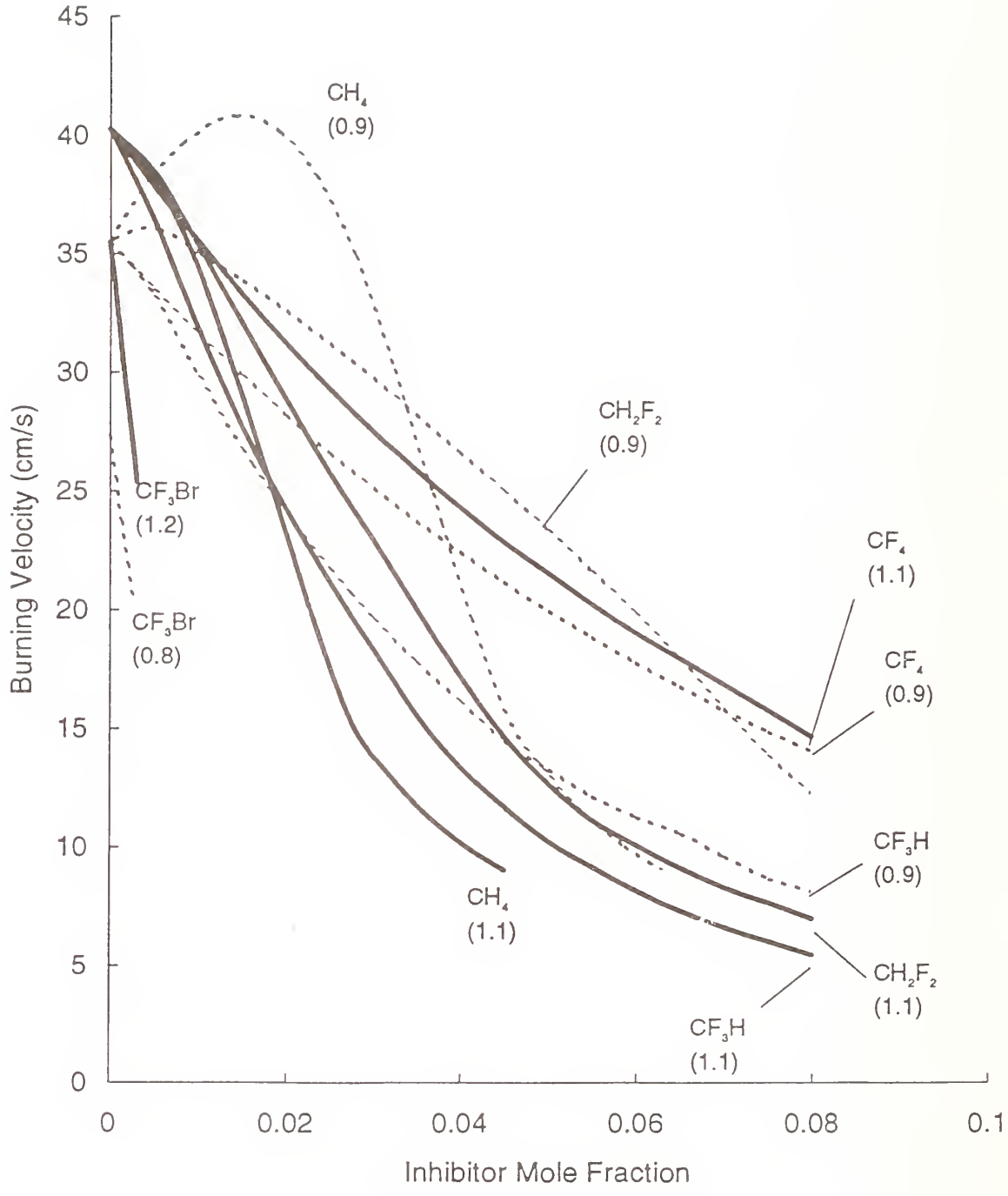

Figure 12. Calculated burning velocity of lean (dotted lines) and rich (solid lines) methane-air flames with addition of the agents CH_4, CH_2F_2, CF_3H, CF_4, and CF_3Br as flame inhibitors.

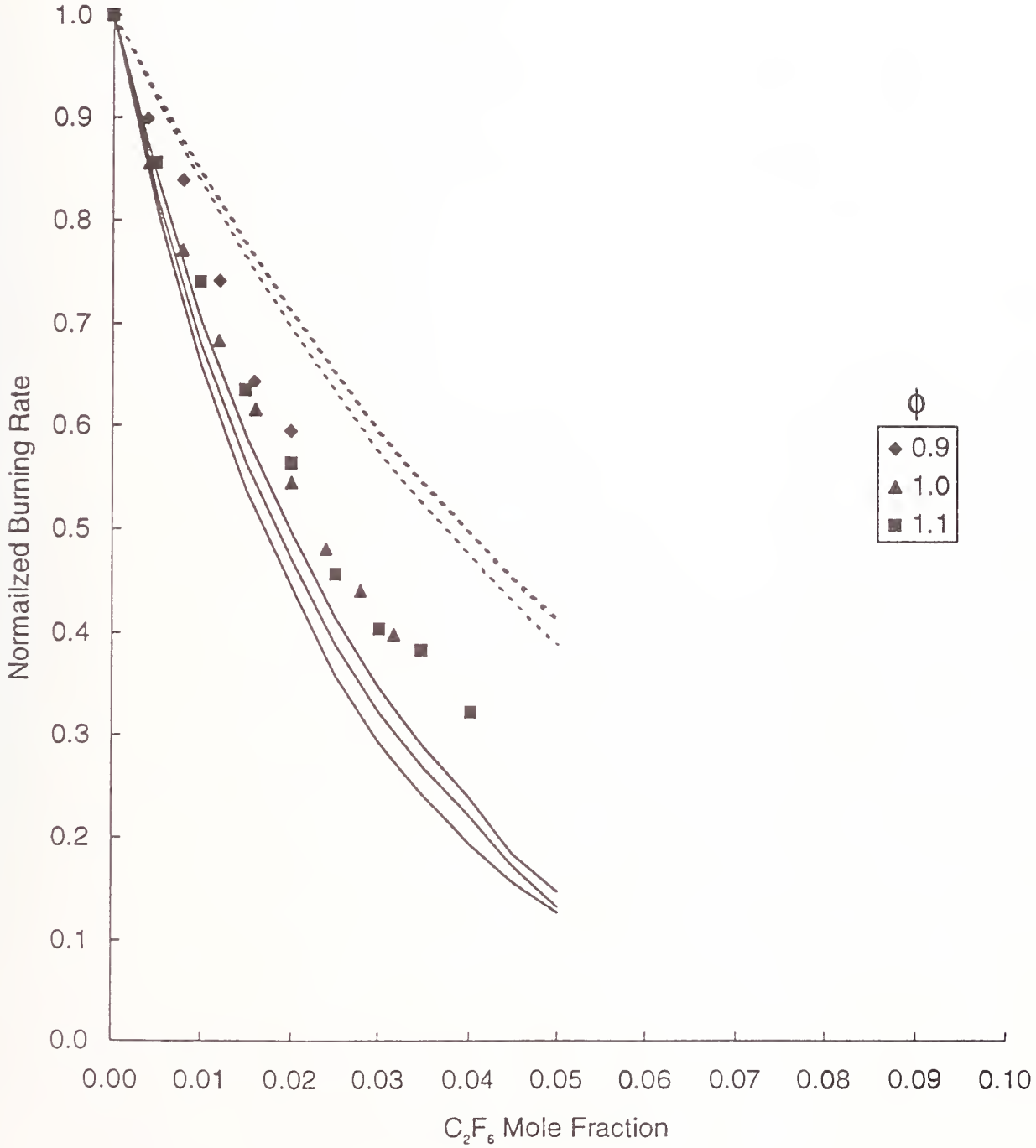

Figure 13. Normalized burning rate of premixed methane-air flame versus C_2F_6 mole fraction at ϕ = 0.9, 1.0, and 1.1. Symbols: exp. data; solid lines: numerical - full chemistry; dotted: inhibitor not reacting.

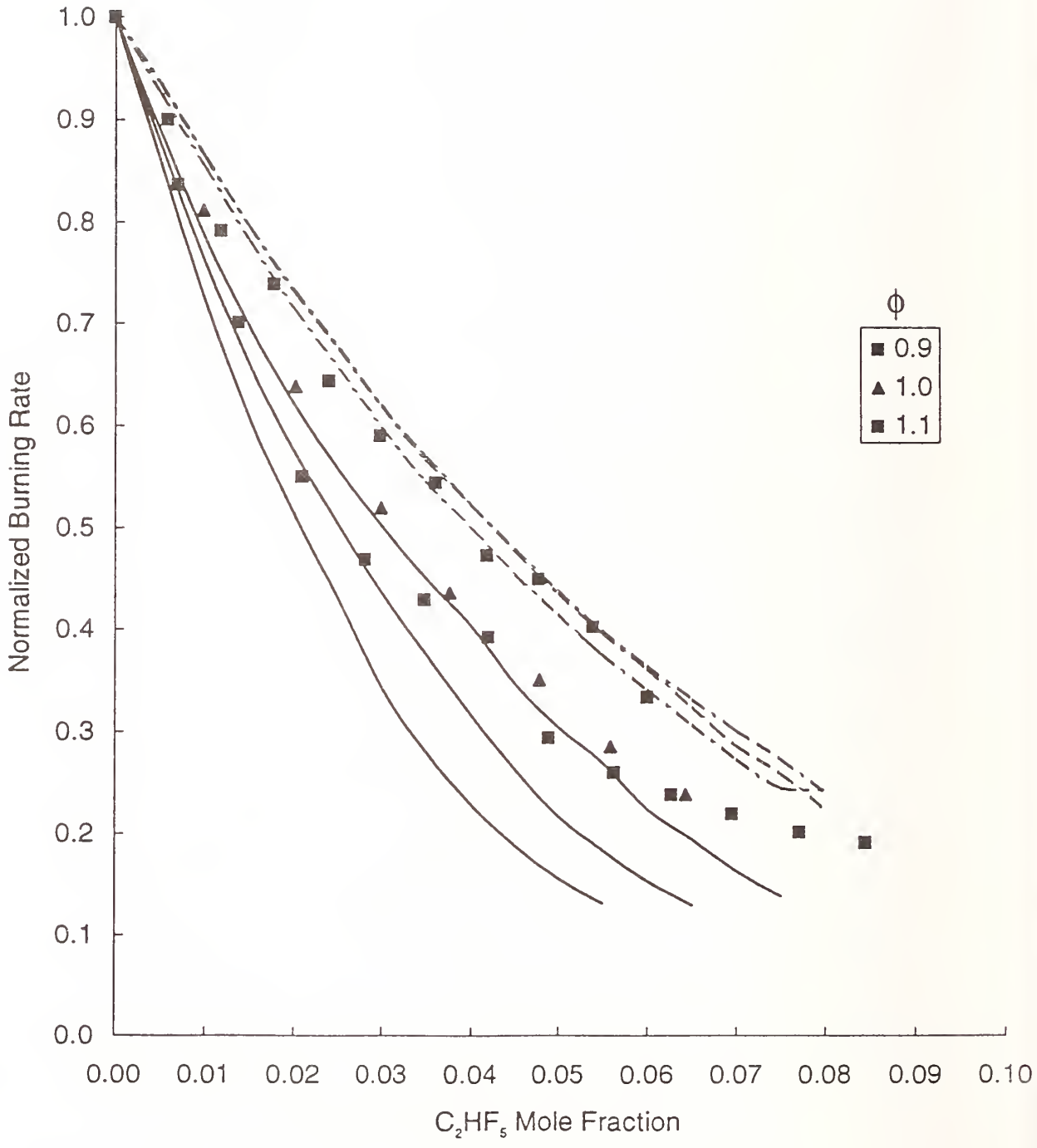

Figure 14. Normalized burning rate of premixed methane-air flame versus C_2HF_5 mole fraction at ϕ = 0.9, 1.0, and 1.1. Symbols: exp. data; solid lines: numerical - full chemistry; dotted: inhibitor not reacting.

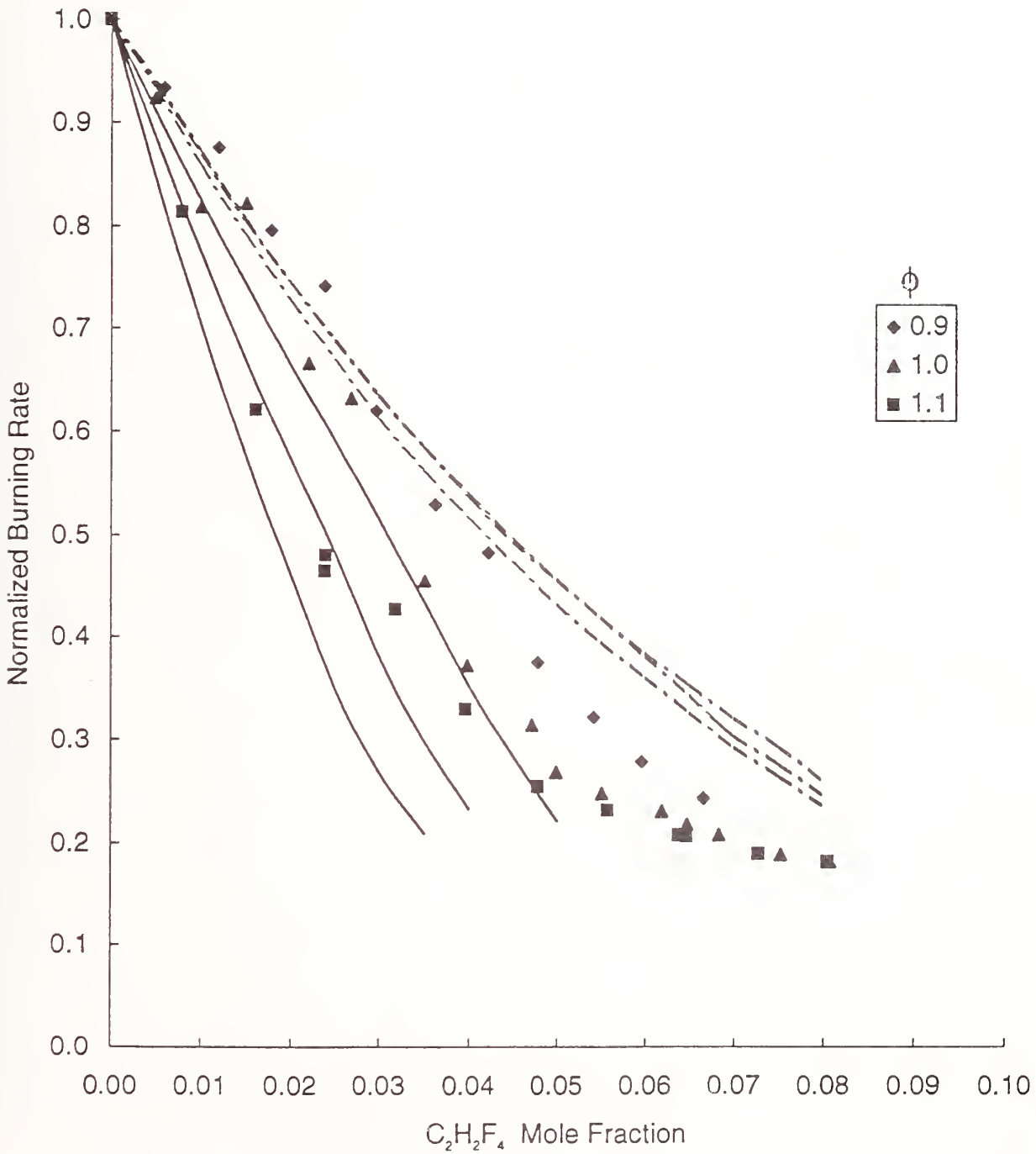

Figure 15. Normalized burning rate of premixed methane-air flame versus $C_2H_2F_4$ mole fraction at ϕ = 0.9, 1.0, and 1.1. Symbols: exp. data; solid lines: numerical - full chemistry; dotted: inhibitor not reacting.

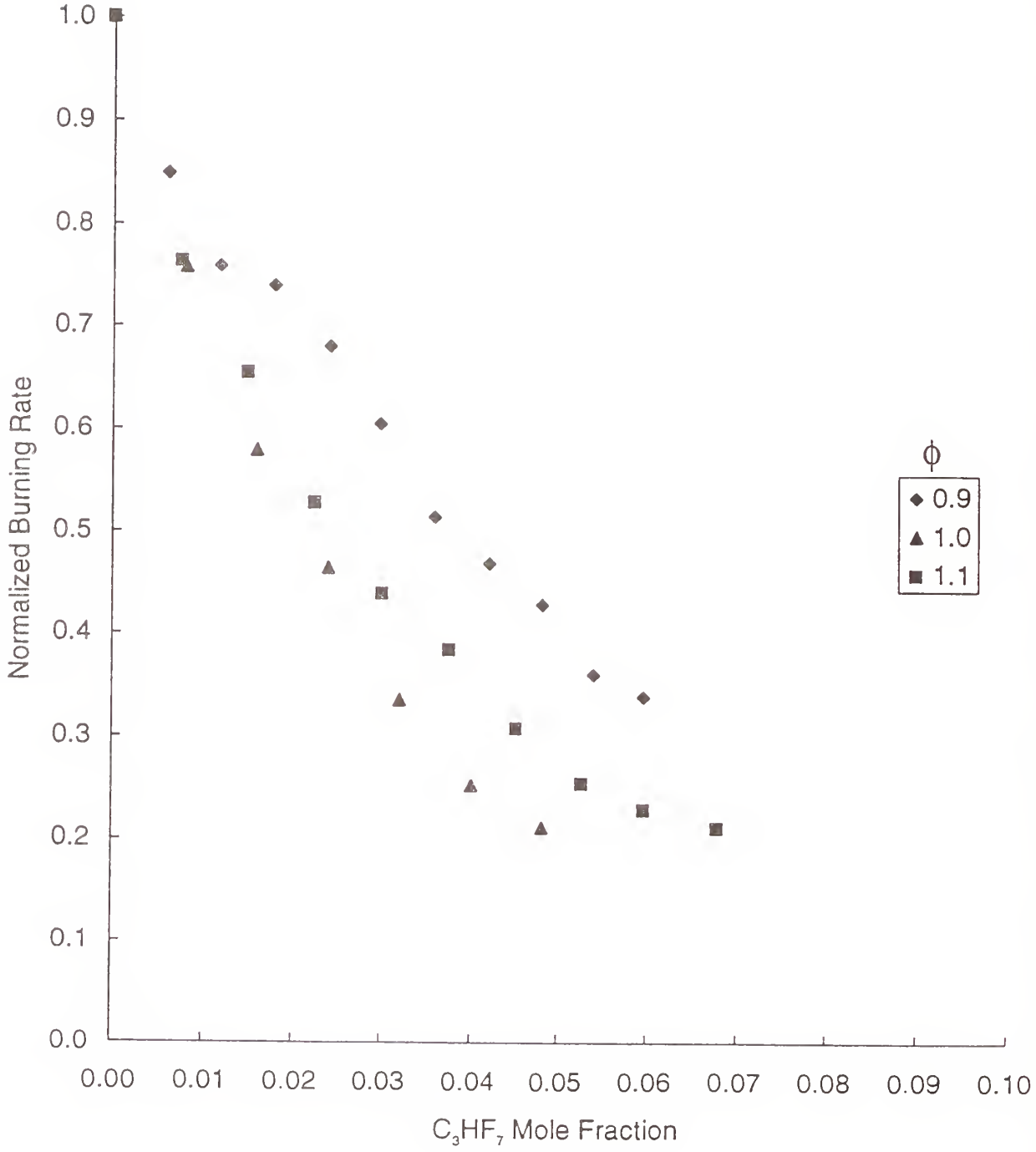

Figure 16. Normalized burning rate normalized by the uninhibited burning velocity at the same stoichiometry for the methane-air flame at fuel-air equivalence ratios of 0.9, 1.0, and 1.1 versus C_3HF_7 mole fraction.

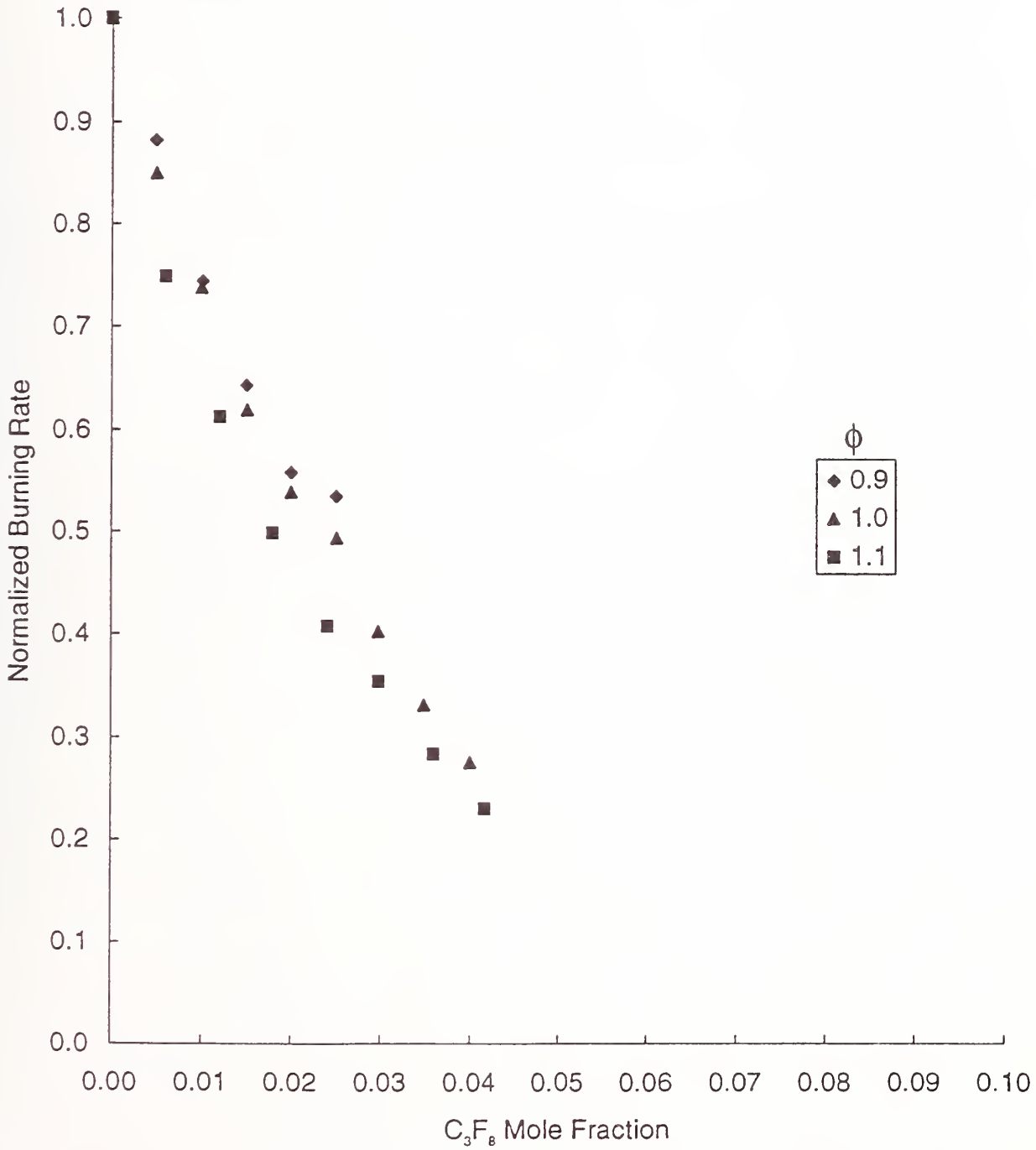

Figure 17. Normalized burning rate normalized by the uninhibited burning velocity at the same stoichiometry for the methane-air flame at fuel-air equivalence ratios of 0.9, 1.0, and 1.1 versus C_3F_8 mole fraction.

rate reduction is somewhat greater for the calculated flames as compared to the experiments, the model is able to reproduce many of the features of the flames. Both show a linear increase in the burning velocity with increased initial temperature and pressure, and similar behavior at all inhibitor concentrations.

While burning velocity comparisons are, by no means, a complete validation of the mechanism, they are an important first step. If the burning rate is wrong, the global reaction rate and flame thickness are probably wrong, and the predicted concentration profiles of the important species will be incorrect. Predicting the burning velocity is different from predicting the production of a species such as HF which has only a secondary effect on the heat release rate. Nonetheless, the reasonable agreement in the burning velocity results is reason to have more confidence in the predictive ability of the model, and to begin to use it to investigate HF formation in the present flames. Figure 21 shows the calculated species concentration profiles for methane-air flames with CF_4, CF_3H, and CH_2F_2 at a mole fraction in the unburned gases of 4 %. The temperature and the mole fractions of CH_4, agent, and HF are given as a function of position.

As the profiles for the agent mole fraction show, the agents CF_3H and CH_2F_2 behave similarly, whereas, CF_4 does not decompose appreciably in the 3 mm domain of the figure. The methane consumption is slightly slower in the inhibited flames, with CH_2F_2 slowing the consumption slightly more than CF_4, but not as much as CF_3H. On the other hand, the temperature rise is greatest for the CH_2F_2-inhibited flame and least for the CF_4-inhibited flame. Clearly, the exothermicity of the reactions of fluorine increase the final temperature for an equivalent reduction in burning rate as compared to an agent which is nearly inert (CF_4). While CF_4 is predicted to form some HF, only a small fraction of that possible (about 15 %) forms within 3 mm. An important observation is that while the inhibitors CF_3H and CH_2F_2 require slightly higher temperatures to start to decompose than methane (*i.e.*, inhibitor decomposition occurs later), their consumption is complete at about the same point as for methane. Likewise, HF formation is nearly complete near end of the fuel consumption.

Figure 22 shows the results of similar calculations for a condition of 497 K and 659 kPa in the bomb. For these conditions, the final temperature is higher and the gradients of fuel, CF_3H, HF, and temperature are greater. Less carbonyl fluoride is formed, and it decomposes faster; however, the rate of formation of HF compared to the fuel decay is similar to the 298 K 101 kPa case.

The calculated flame structures for the two-carbon inhibitors show similar trends. Figure 23 presents these results for C_2F_6, C_2HF_5, and $C_2H_2F_4$ at 2 % in stoichiometric methane-air flames. The inhibitors again decompose later, but more rapidly, than the fuel, and HF formation is fast. The perfluorinated agents, in both cases, decompose the slowest yet provide the slowest temperature rise at the end of the flame. Decreased hydrogen content in the agent tends to favor higher concentrations of COF_2 as an intermediate.

Once the initial decomposition of the agent has occurred, the reaction of the intermediates and HF formation are rapid. This is clearly seen in Figure 24, where the temperature profile and the mole fractions of some intermediate species are illustrated for C_2HF_5 inhibition. Both the formation of fluorinated-species intermediates and their consumption occur over a narrow region of the flame.

Figure 25 shows the dominant reaction pathways indicated by the numerical calculations. The conditions shown correspond to inhibition by CF_3H under laboratory conditions in the nozzle burner (298 K, 101 kPa) and at elevated temperature and pressure in the bomb (497 K, 659 kPa). The mole fractions of inhibitor are 4 % and 5 % respectively. The arrows connect species of interest; next to the arrows are the second reacting species and the percent of the first reactant which goes through that route. The top number is the result for the atmospheric pressure, 298 K flames, while the lower number is the result for the higher pressure and temperature flame. With this chart, it is possible to study the reaction sequence for consumption of an inhibitor and its fragments, and the subsequent formation of unwanted by products. For example, the reactions which form HF are indicated in bold.

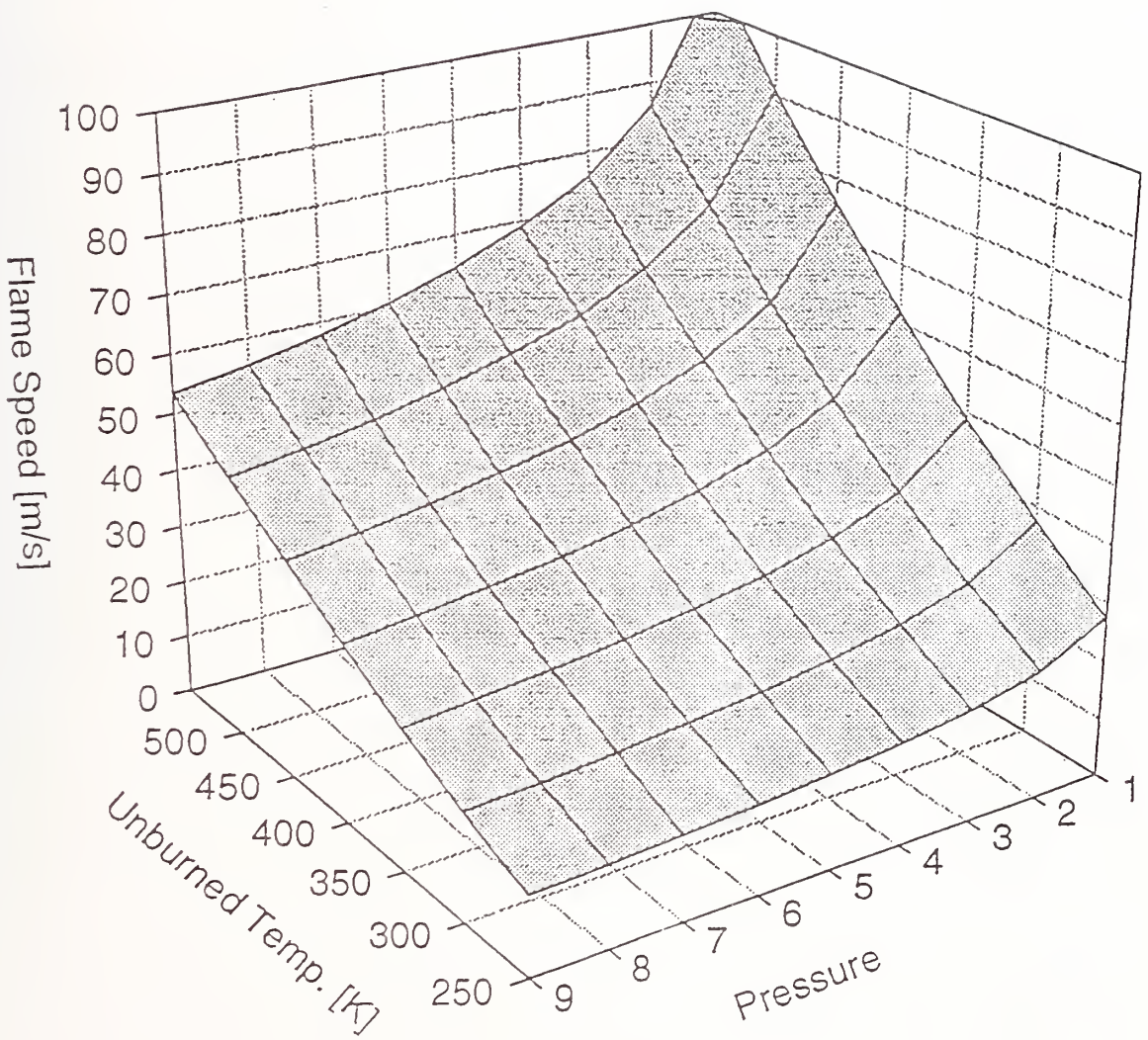

Figure 18. Curve fit to experimental burning rate velocity in combustion bomb (pressure in 10^5 Pa)

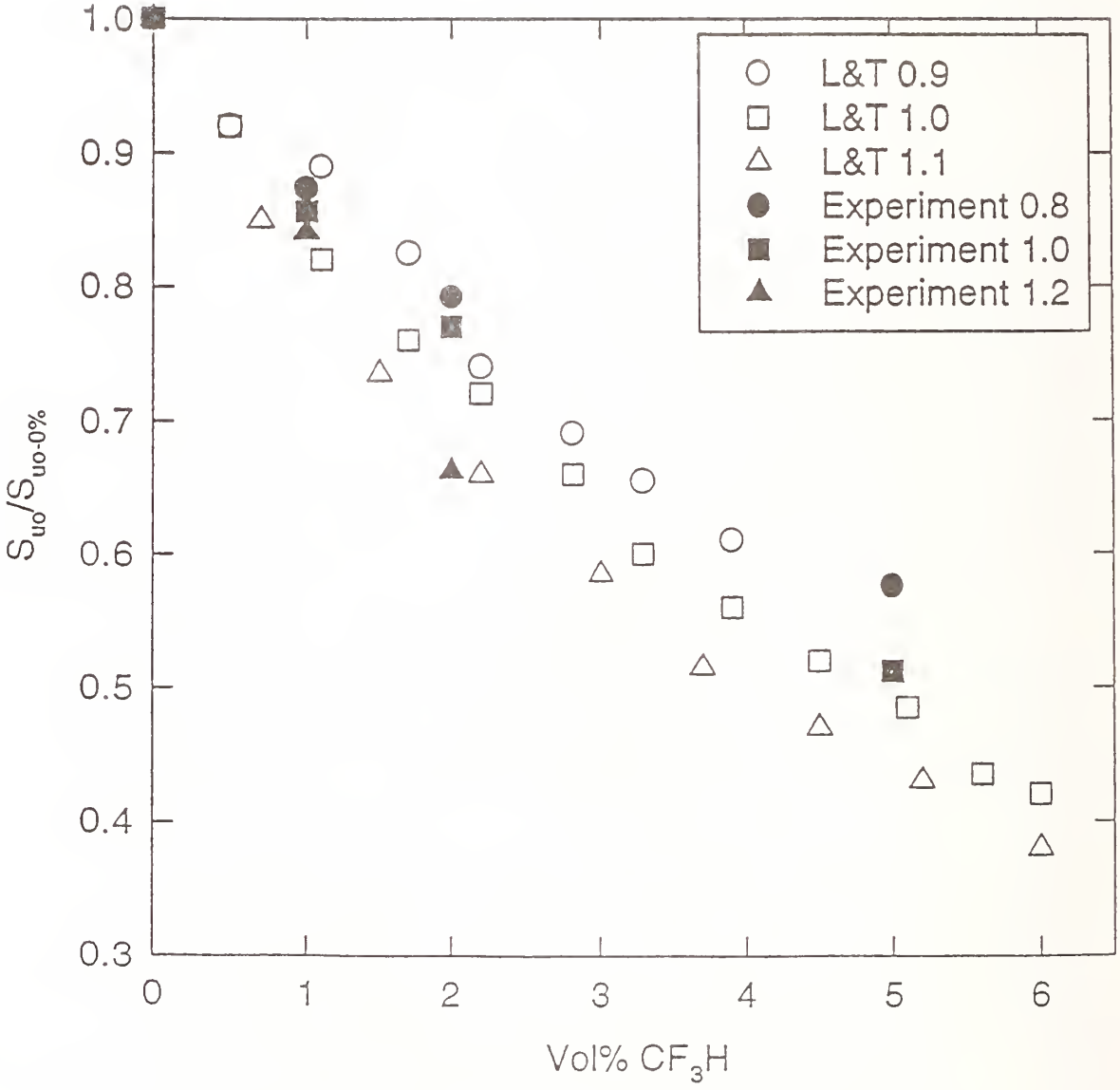

Figure 19. Normalized burning velocity of bomb experiments as a function of CF_3H mole fraction extrapolated to the conditions of the nozzle burner.

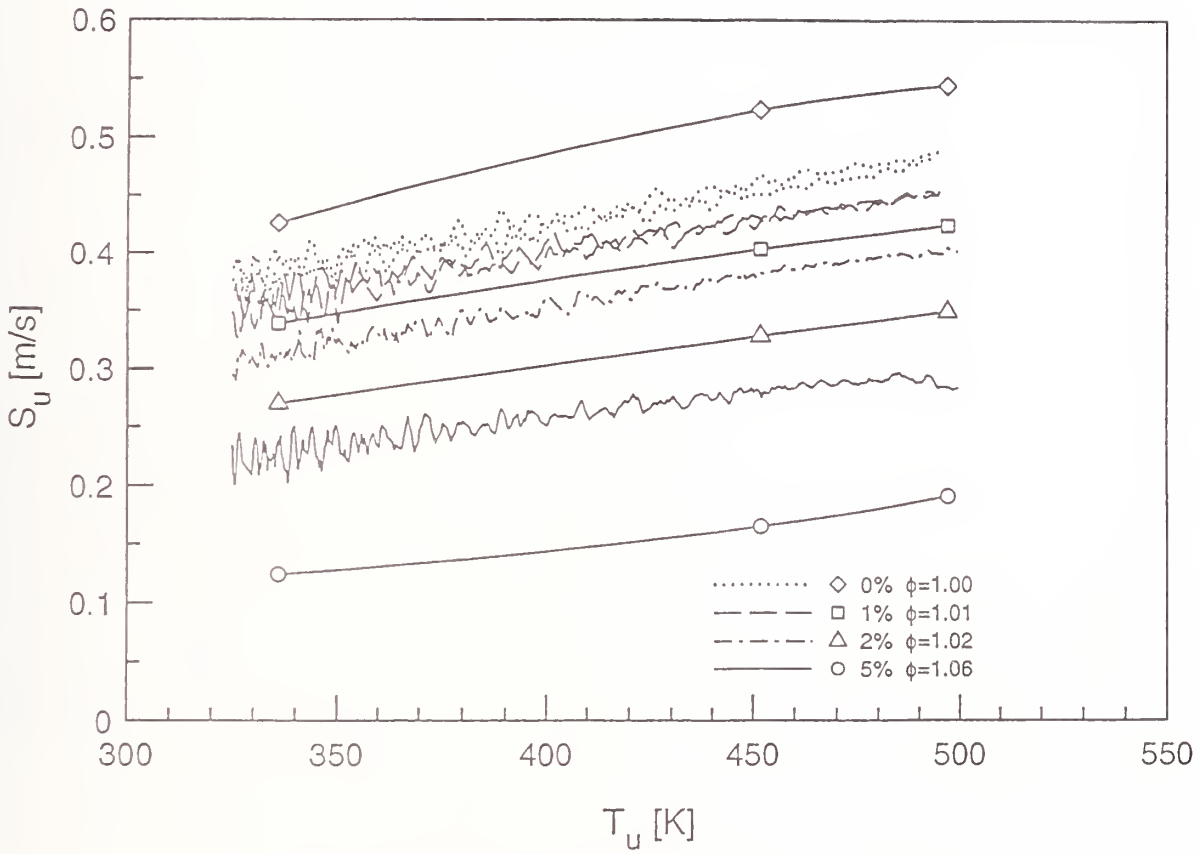

FIGURE #10 VanDerWege/Bush/Hochgreb/Linteris Combustion & Flame

Figure 20. Experimental versus calculated laminar flame speeds at a nominal equivalence ratio near 1.0 (0, 1, 2 and 5 % CF_3H in CH_4-Air; p_0 = 92.1 kPa).

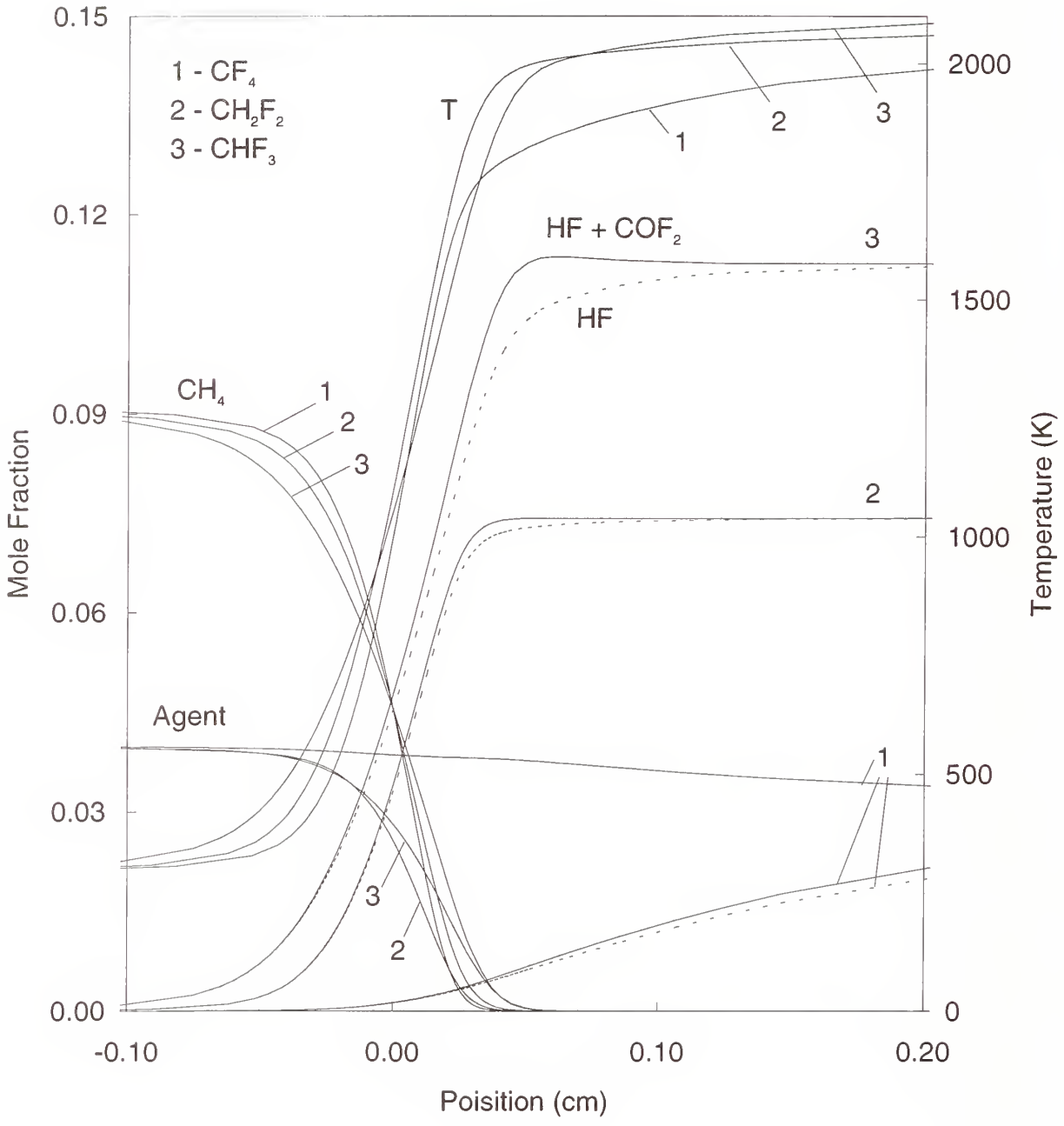

Figure 21. Calculated species mole fraction profiles for stoichiometric premixed methane-air flames with 4 % CF_4, CH_2F_2 and CHF_3.

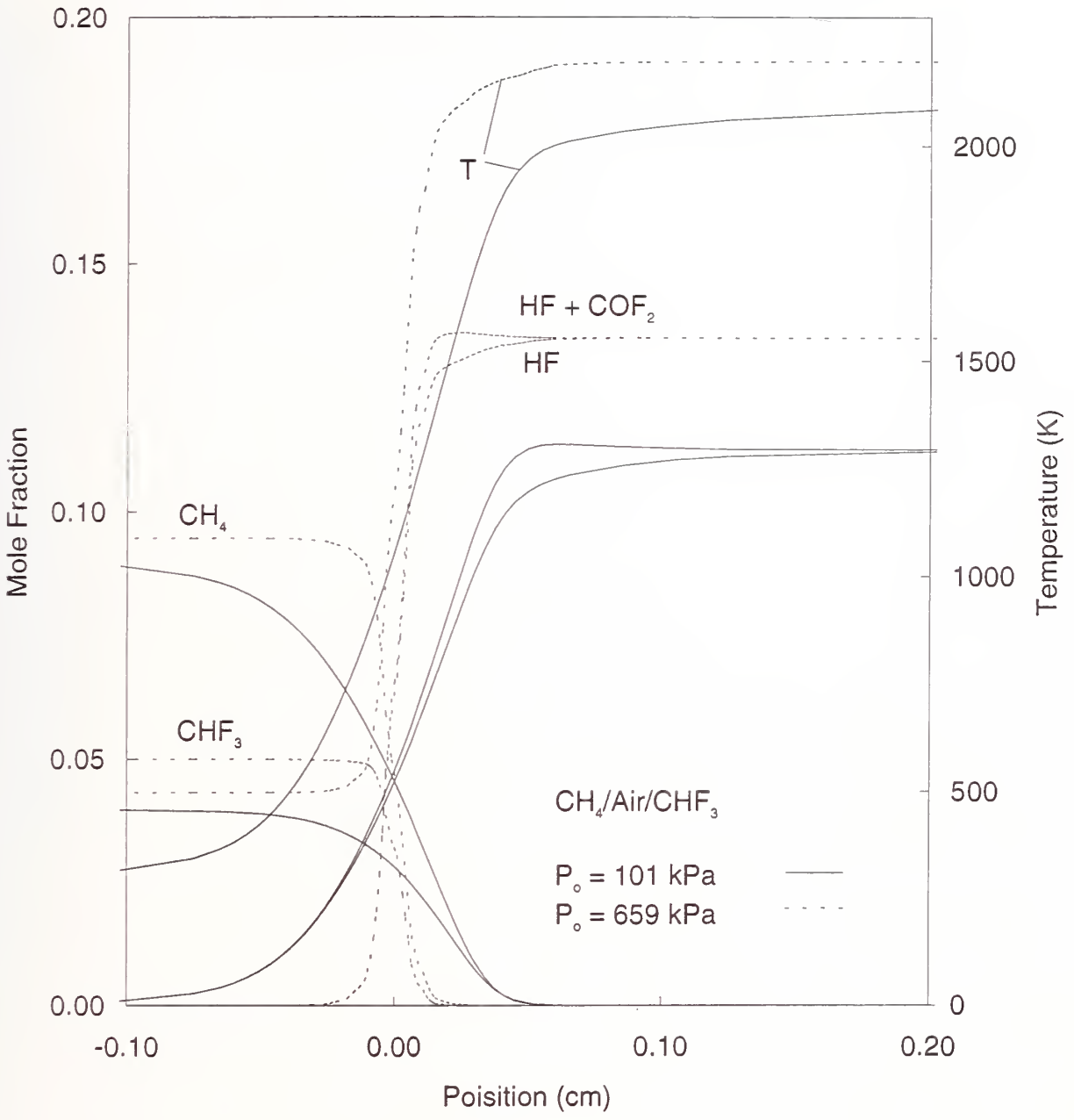

Figure 22. Calculated species mole fraction profiles for stoichiometric premixed methane-air flames with 4 % CHF_3 at 298 K, 101 kPa, and 5 % CHF_3 at 497 K and 659 kPa.

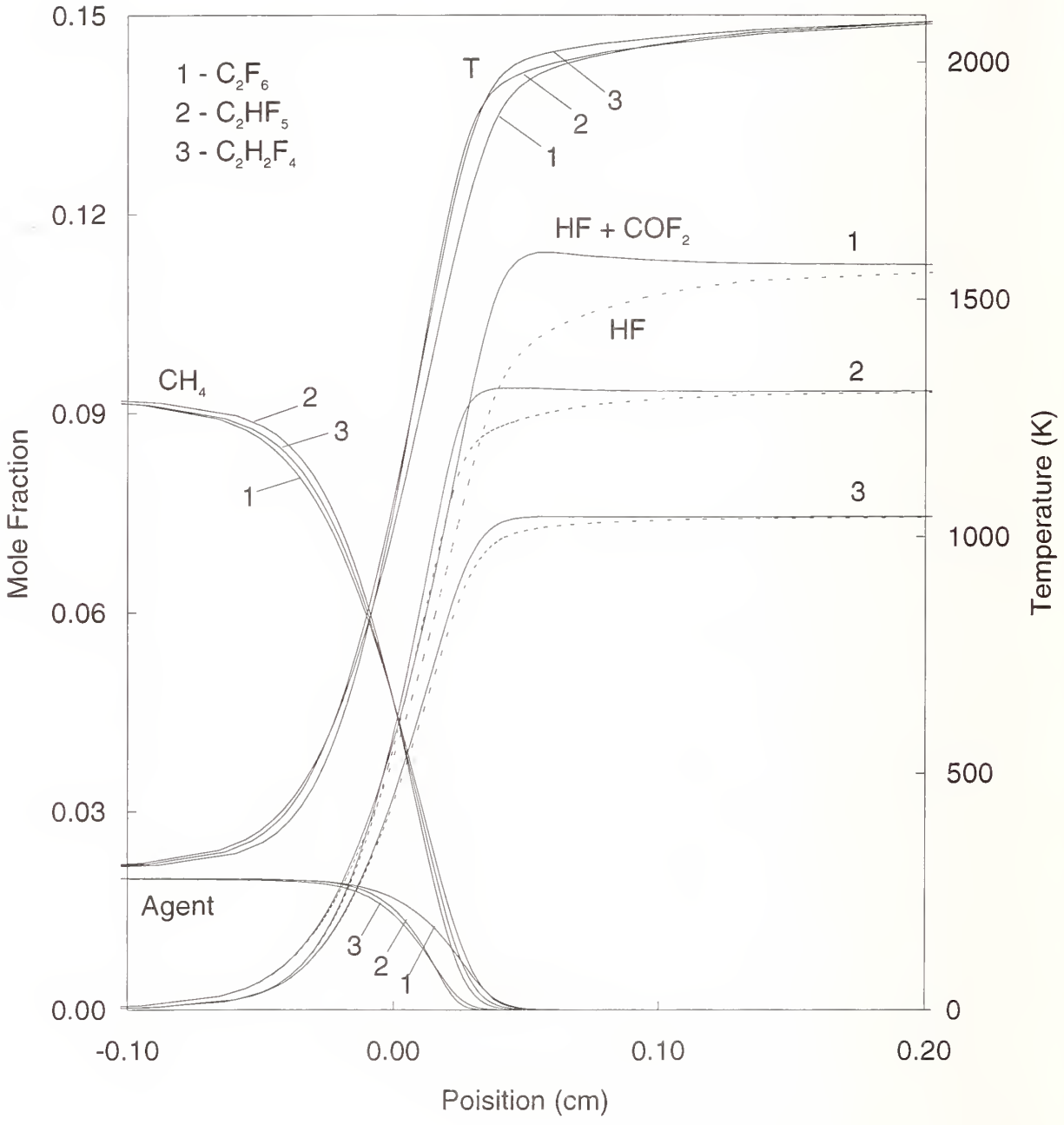

Figure 23. Calculated species mole fraction profiles for stoichiometric premixed methane-air flames with 2 % C_2F_6, C_2HF_5 and $C_2H_2F_4$.

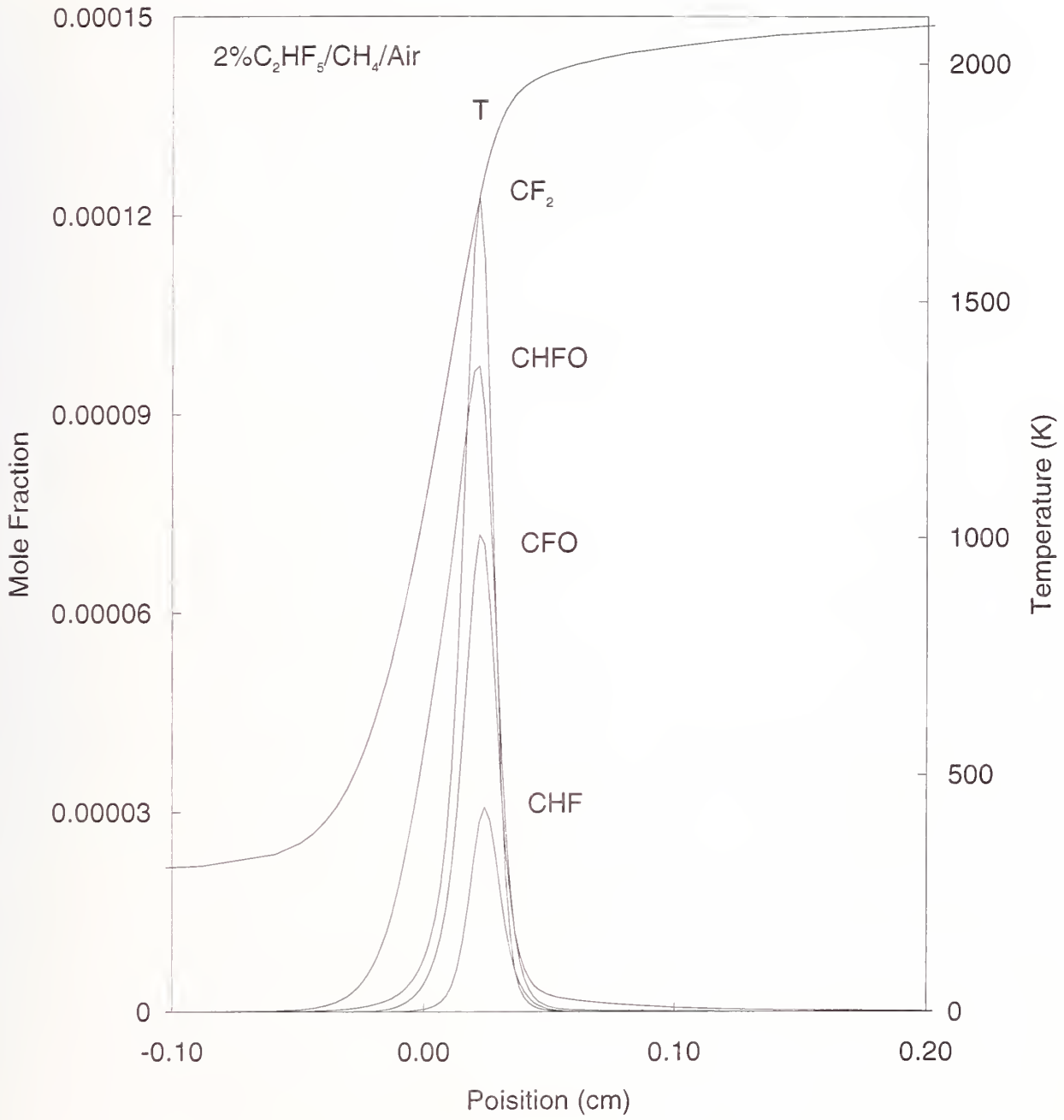

Figure 24. Calculated species mole fraction profiles of selected fluorinated intermediate species for stoichiometric premixed methane-air flames with 2 % C_2HF_5.

Table 1. Reactions responsible for formation of HF in premixed stoichiometric methane-air flames of 2 % CHF_2-CF_3 and 4 % CF_3H at atmospheric conditions, and 5 % CHF_3 at 659 kPa and 497 K in the bomb

Reaction	Fraction of HF Formation
AGENT: CHF_2-CF_3, 2 %, ϕ = 1.0, P_o= 101 kPa	
CF_2+H↔CF+HF	0.16
H_2O+F↔OH+HF	0.10
CF:O+H↔CO+HF	0.10
CHF_2+H↔CHF+HF	0.06
CF_3+H↔CF_2+HF	0.06
CF_2:O+H↔CF:O+HF	0.06
CHF_2-CF_3↔CF_2:CF_2+HF	0.06
CHF+H↔CH+HF	0.04
H_2+F↔H+HF	0.03
CH_4+F↔CH_3+HF	0.03
CH_2:CHF↔C_2H_2+HF	0.03
CF:O+OH↔CO_2+HF	0.02
CF:O+CH_3↔CH_2CO+HF	0.02
CHF_2+OH↔CHF:O+HF	0.02
CF_3+OH↔CF_2:O+HF	0.02
CHF+H_2O↔CH_2O+HF	0.02
CH_3+CHF_2↔CH_2:CHF+HF	0.02
CH_3+CF_3↔CH_2:CF_2+HF	0.02
CF+H↔C+HF	0.02
CF+OH↔CO+HF	0.02
CHF:O+M↔CO+HF+M	0.01
AGENT: CHF_3, 4 %, ϕ = 1.0, P_o= 101 kPa	
CF_2+H↔CF+HF	0.16
H_2O+F↔OH+HF	0.13
CF_3+H↔CF_2+HF	0.13
CF2:O+H↔CF:O+HF	0.08
CF:O+H↔CO+HF	0.08
CHF_3+M↔CF_2+HF+M	0.05
CH_3+CF_3↔CH_2:CF_2+HF	0.05
CF_3+OH↔CF_2:O+HF	0.04
H_2+F↔H+HF	0.03
CH_4+F↔CH_3+HF	0.03
CF+H↔C+HF	0.02
CF+OH↔CO+HF	0.02
CH_2:CHF↔C_2H_2+HF	0.02
CF:O+OH↔CO_2+HF	0.02
CH_2:CF_2↔C_2HF+HF	0.01
CF:O+CH_3↔CH_2CO+HF	0.01
CHF:O+M↔CO+HF+M	0.01

Table 1. Continued

AGENT: CHF_3, 5 %, ϕ = 1.06, P_o= 659 kPa	
CF_2+H↔CF+HF	0.17
CHF:O+M↔CO+HF+M	0.11
H_2O+F↔OH+HF	0.10
CF_3+H↔CF_2+HF	0.10
CHF_3+M↔CF_2+HF+M	0.09
CF_2:O+H↔CF:O+HF	0.07
CH_3+CF_3↔CH_2:CF_2+HF	0.06
CF:O+H↔CO+HF	0.05
CH_4+F↔CH_3+HF	0.04
CF_3+OH↔CF_2:O+HF	0.04
H_2+F↔H+HF	0.04
CH_2:CHF↔C_2H_2+HF	0.03
CH_2:CF_2↔C_2HF+HF	0.02
CHF+H↔CH+HF	0.02
CF:O+OH↔CO_2+HF	0.01

As can be seen in the figure, the higher pressure and temperature conditions decrease radical reactions of the inhibitor and its fragments and increase thermal decomposition reactions.

Table 1 lists the reactions which contribute 1 % or more to the formation of HF in flames inhibited by CF_3H, CH_2F_2, and C_2HF_5.

Clearly, the reactions which form HF are intimately related to the entire hydrocarbon oxidation mechanism. From these figures, it appears that once decomposition of the inhibitor molecule has been initiated, nearly every reaction of the intermediates forms HF or COF_2. This is expected since reaction of the inhibitor mostly involves removing fluorine from the carbon backbone, reducing fluorine to HF and oxidizing carbon to CO_2. It is important to note, however, that even for the one-carbon inhibitors, about a 20 % of the inhibitor rapidly pyrolyses to form larger (*i.e.*, two-carbon) fluorinated species, which are then decomposed in the flame.

10.5.7 Conclusions. The reduction in burning velocity has been determined experimentally and numerically for the inhibitors CF_3H, CH_2F_2, CF_4, C_2F_6, C_2HF_5, and $C_2H_2F_4$ in near-stoichiometric premixed methane-air flames at initial inhibitor mole fractions of 0 to 8 %, 298 K and 101 kPa. Even at this early stage of development, the NIST fluorine-inhibition mechanism predicts the burning velocity reduction quite well for these flames, and is a useful tool for understanding HF formation. Constant volume bomb experiments have extended the burning velocity measurements to a range of pressures of 2 to 7 bar and 330 to 500 K.

The following specific conclusions can be drawn concerning HF formation in these premixed flames:

1. Burning velocities are reduced in the inhibited flames by an amount greater than attributable to thermal dilution effects.

2. Of the six inhibitors for which calculations were performed, only CF_4 shows kinetic limitations to HF formation for premixed methane-air flames.

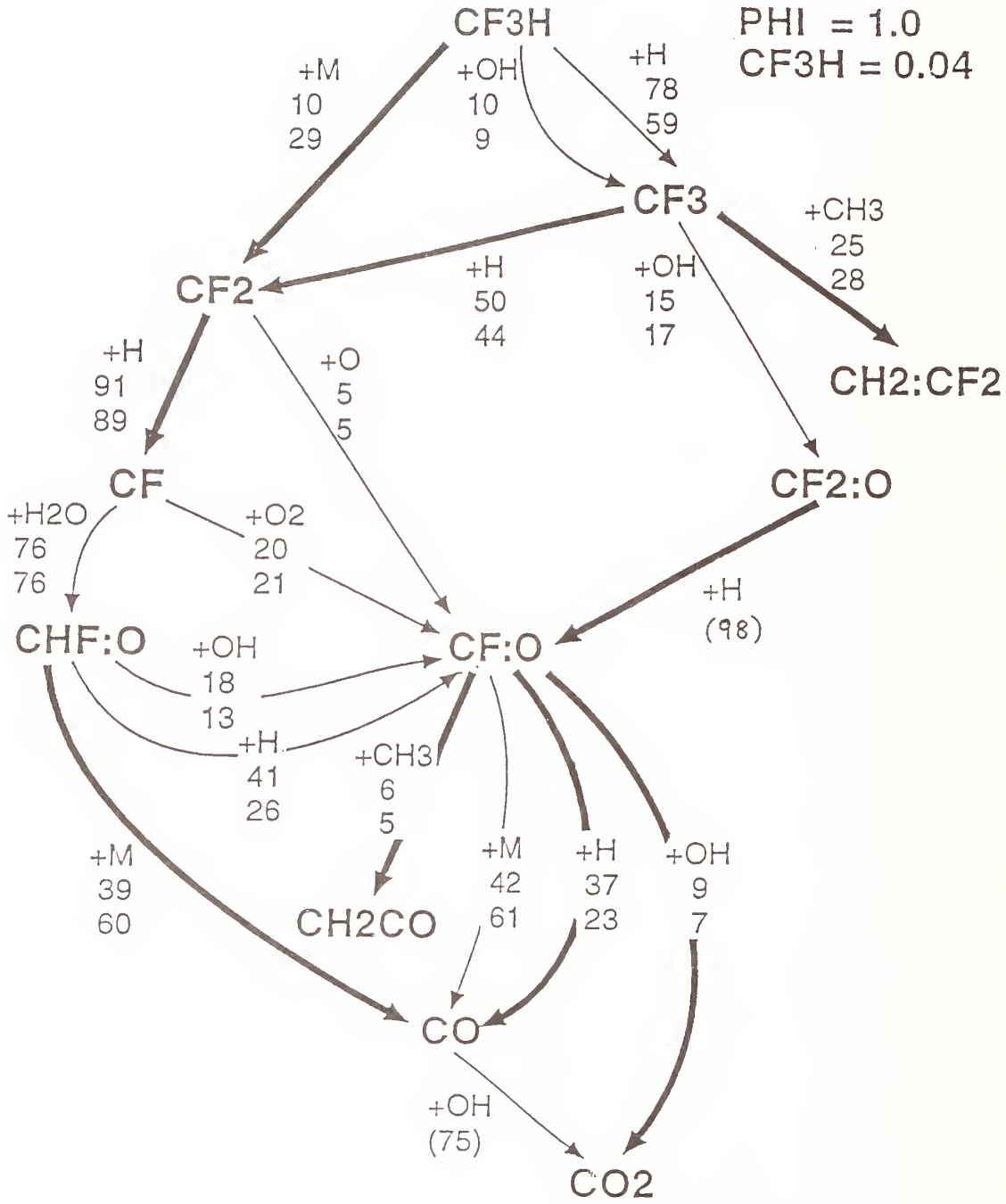

Figure 25. Dominant reaction pathways for decomposition of CF_3H in a stoichiometric premixed methane-air flame to which 4 % inhibitor has been added.

3. The inhibitors (except CF_4) are consumed in these flames as fast or faster than the fuel (methane) itself.

4. All of the fluorinated intermediates react rapidly and achieve only low concentrations except COF_2 which can persist in the product gases. Since COF_2 rapidly hydrolyses in the presence of water, its fate in the post-suppression gases will depend upon the availability of additional water from other sources besides the steady-state flame products.

5. HF is formed early in the flame, and persists at high concentrations as a final product. The amount of HF depends on the amount of hydrogen present (from the fuel and agent) and fluorine (from the agent).

6. Since the characteristic times for fuel consumption and HF formation are similar and fast, equilibrium conditions will be reached for all agents (except CF_4) in typical premixed flames.

7. Stable flames could not be obtained at fluorine loadings at or above the inhibitor concentration where the fluorine to hydrogen ratio in the flames is unity.

8. The agents appear to inhibit the flames primarily by reducing the hydrogen atom concentration well below the level which can be attributed to the temperature reduction of the flame by the agent.

10.6 Physical/Chemical Model

10.6.1 Steady-state - Premixed Flames. Although the premixed flame numerical modeling of the previous section can be used as the physical/chemical model to describe HF formation for the one- and two-carbon inhibitors, it is desirable to obtain simplifications to predict HF formation in these flames. Steady-state premixed flames are the simplest case to consider. Here, the reactants (fuel, air, and agent) are assumed to be premixed prior to interaction with the flame. This flame type most closely describes a flame ball expanding into a premixed combustible region as may occur in a dry-bay fire threat. In these cases, the mass flux of both fuel and agent into the reaction zone are well specified. As described in the section above describing the equilibrium calculations, the most abundant products of agent decomposition are CO, CO_2, HF, and COF_2. The model adopted in the present work assumes that the fluorinated agents decompose to the most thermodynamically favorable products and that finite rate kinetics are not important for HF formation. The validity of these assumptions are based on the extensive numerical modeling of premixed flames as described above (Linteris and Truett, 1995a, 1995b; Linteris, 1995a, 1995b). As will be shown below, predictions of HF formation in premixed flames based on thermodynamic equilibrium are in good agreement with measurements of HF in these flames. Hence, the model predictions for premixed flames consist essentially of the results of equilibrium calculations based on the fuel and agent species present in the flame.

10.6.2 Steady-state - Diffusion Flames. A calculation of the equilibrium concentration of HF and COF_2 in the products of a diffusion flame is not as straightforward as in a premixed flame since the amount of agent in the reactant zone is not known a priori. Consider the case of a co-flow diffusion flame in a chimney (as in Figure 26). Fuel is supplied by the center jet, and air diffuses inward, towards the high-temperature reaction zone where it is consumed. Addition of agent to the air stream

at a concentration less than the extinction concentration causes some of the agent to be consumed by the flame. Not all of the agent in the co-axial region is consumed, however; the amount consumed depends upon the relative flow rates of fuel and air. For example, if the outer chimney is very large, then only a small fraction of the agent in the coflowing region is consumed. Likewise, for a fire in a larger space, only inhibitor which is consumed in the flame will form HF. Thus it is necessary to estimate the flux of inhibitor into the reaction zone, since only this agent will decompose to form HF.

A model for acid gas formation has been developed based on a simple Burke-Schumann model (1928) of a co-flowing jet diffusion flame with fuel in the center and air co-axial. In the Burke-Schumann analysis, the fuel is assumed to be consumed at a reaction sheet, where fuel and oxidizer come together in stoichiometric proportions and the temperature reaches its highest value (which can be approximated by the adiabatic flame temperature of a stoichiometric premixed flame). The height of the flame is determined by the jet diameter and the rate at which the oxidizer can diffuse to the center-line of the fuel jet. The present flames differ in that the air stream contains inhibitor in addition to oxidizer.

In the present analysis, the inhibitor is assumed to be consumed in the reaction zone as a reactive species. This assumption is based on premixed flame measurements and modeling (Linteris *et al.*, 1994). For both brominated and fluorinated carbon compounds, complete consumption of the inhibitor is typical. In many cases, the inhibitor is consumed faster than the fuel itself. Extensive thermodynamic equilibrium calculations of the composition of fuel-air mixtures in the presence of halogenated inhibitors also indicate complete exothermic conversion of the inhibitors to HF, CO_2, COF_2, and water.

The agent can be thought of as an additional fuel species, having its own oxygen demand, yet coming from the air side of the flame. It must diffuse to the hot reaction zone which serves as a sink for the inhibitor. Thus fuel, oxygen and inhibitor are consumed in the reaction zone in stoichiometric proportions, with the stoichiometry determined from a balanced chemical reaction to the most stable products.

Transport rates of inhibitor and oxygen are based on their relative rates of diffusion (Linteris and Gmurczyk, 1995) incorporating molecular weight effects. An implicit assumption in the present analysis is that the characteristic height for reaction of the fuel with oxygen is the same as the characteristic height for decomposition and reaction of the inhibitor. For a wide variety of flames and conditions, the consumption of the inhibitor occurs more rapidly with hydrogen and oxygen atoms than through thermal decomposition (Linteris and Truett, 1995a; Linteris, 1995a, 1995b). Given the inhibitors' preference for reactions with radicals and the high concentration of these species near the flame sheet, this assumption is reasonable.

Presently, it is also assumed that there is always sufficient air for complete combustion of the inhibitor and fuel. Hence, the estimate of HF formation is an upper limit since fuel rich flames will extinguish more easily and consequently produce less HF.

The global reaction representing a combustion process in a hydrocarbon/air/water environment in the presence of a halocarbon, leading to formation of combustion/inhibition products can be formulated as follows:

$$\alpha C_a H_b + \beta C_c H_d F_e Cl_f + \mu H_2O + \gamma O_2 + \nu N_2 \rightarrow$$

$$\delta CO_2 + \lambda H_2O + \eta HF + \varphi HCl + \varepsilon COF_2 + \zeta COCl_2 + \nu N_2 \qquad (1)$$

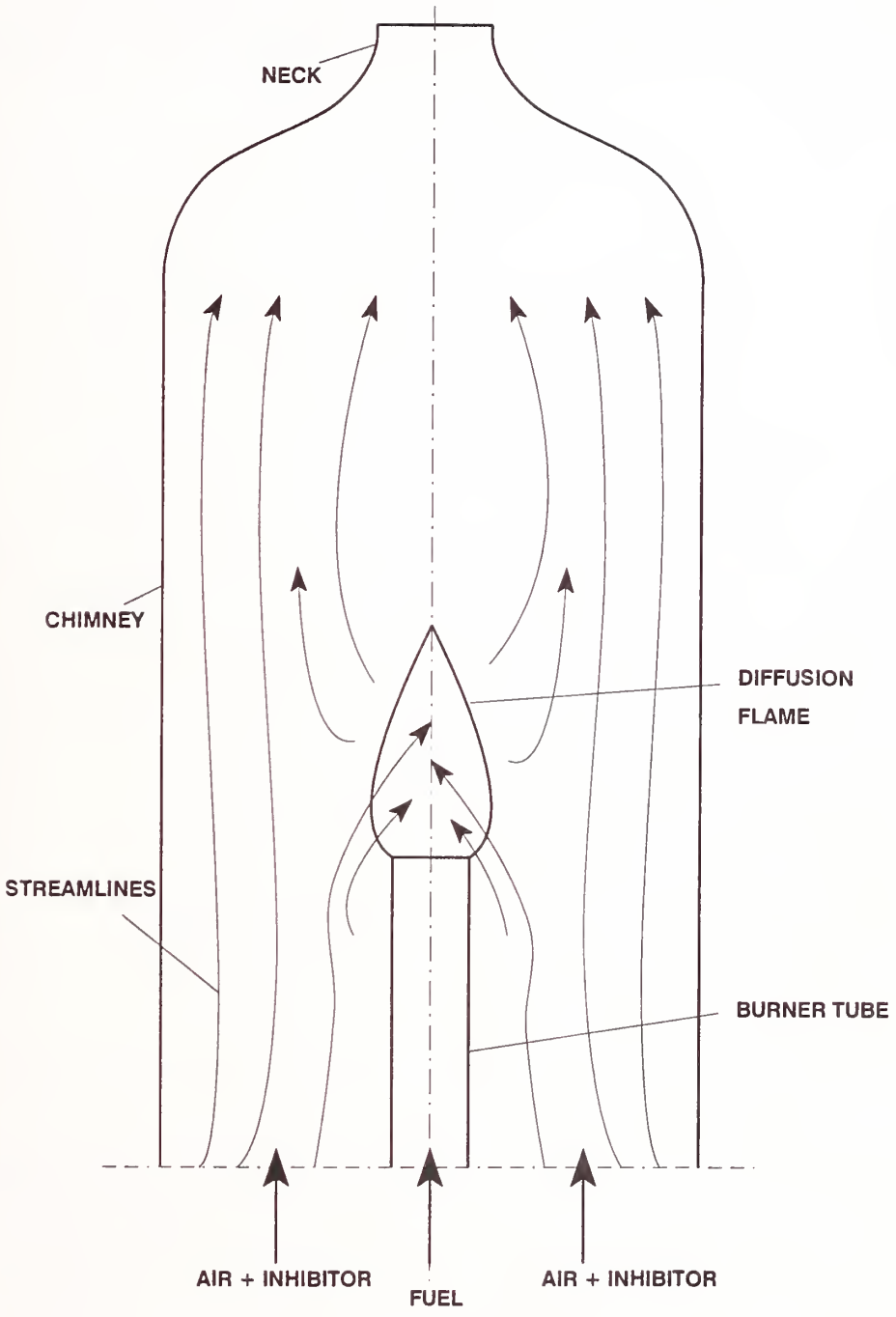

Figure 26. Illustration of the inhibitor and oxygen transport in a co-flow hydrocarbon-air diffusion flame.

where the greek symbols are the stoichiometric coefficients. In this reaction, chlorine is the second halogen, however, bromine or iodine can be used alternatively.

The fluxes of the inhibitor and water vapor to the reaction zone relative to the flux of oxygen are assumed to be proportional to the ratio of the diffusion coefficients and the concentrations, and are expressed as follows:

$$\frac{\beta}{\gamma} = \frac{[\,i\,]}{[\,O_2\,]} \times \frac{D_i}{D_{O_2}} \tag{2}$$

$$\frac{\mu}{\gamma} = \frac{[\,H_2O\,]}{[\,O_2\,]} \times \frac{D_{H_2O}}{D_{O_2}} \tag{3}$$

The molecular weight corrections for the diffusion rate of oxygen, inhibitor, and water vapor in nitrogen are:

$$D_{O_2}/D_{N_2} = \sqrt{((W_{O_2} + W_{N_2})/(W_{O_2} \times W_{N_2})} \tag{4}$$

$$D_i/D_{N_2} = \sqrt{((W_i + W_{N_2})/(W_i \times W_{N_2})} \tag{5}$$

$$D_{H_2O}/D_{N_2} = \sqrt{((W_{H_2O} + W_{N_2})/(W_{H_2O} \times W_{N_2})} \tag{6}$$

where: D_{O2}, D_{N2}, D_{H2O}, D_i are the diffusion coefficients and W_{O2}, W_{N2}, W_{H2O}, W_i are the molecular weights of oxygen, nitrogen, water vapor, and inhibitor.

For a given fuel and inhibitor, all of the subscripts (a-f) are known, so that there are seven unknown coefficients on the right side of Equation 1 and five on the left, or twelve unknowns. There are six species balance reactions (for C, O, H, N, F, and Cl) and two mass flux equations (Equations 2 and 3). The mass input of fuel is known, as is the ratio of oxygen to nitrogen in the air. The final condition is obtained from a consideration of the equilibrium results described above. Two distinct cases exist: 1 - more hydrogen than halogen in the reaction zone, and 2 - less hydrogen than halogen in the reaction zone.

Case 1 occurs for low inhibitor loadings. Hydrogen in the product gases first goes to form HF until all of the halogen has been consumed, and any remaining hydrogen forms H_2O. The concentration of COF_2 is assumed to be zero for this case, providing the needed final relation.

In the second case, there is more halogen than hydrogen. In this case, no water forms since all of the hydrogen has been tied up as HF, and the excess halogen forms COF_2. The solutions for these two cases are described below.

For the case of high halogen loading, or less hydrogen than halogen, the solution of the above equations yields the following relations describing both the flux of agent, water vapor, and oxygen into the flame (β, λ, and μ) and the amounts of product species. The fluxes of the reactants are given by:

$$\beta = \frac{\alpha(4a + b)}{\frac{4}{\rho r} + e + f - 4c - d} \tag{7}$$

$$\gamma = \frac{\beta}{\rho r} \tag{8}$$

$$\mu = \beta \rho^* \tag{9}$$

where:

$$\rho^* = \frac{\rho_{H_2O}}{\rho} \times \frac{r_{H_2O}}{r} \tag{10}$$

The fluxes of the products are expressed as follows:

$$\delta = 2\gamma - \alpha a - \beta c + \mu \tag{11}$$

$$\varphi = \delta + \alpha\left(\frac{b}{2} - a\right) + \frac{\beta}{2}(d + f + 2\mu - 2c - e) \tag{12}$$

$$\zeta = \frac{1}{2}\left[-\delta + \alpha\left(a - \frac{b}{2}\right) + \frac{\beta}{2}(2c + e + f - 2\mu - d)\right] \tag{13}$$

$$\varepsilon = \frac{1}{2}\left[\delta - 2\mu - \alpha\left(a + \frac{b}{2}\right) + \frac{\beta}{2}(e + f + 2\mu - d - 2c)\right] \tag{14}$$

$$\eta = -\delta + 2\mu + \alpha\left(a + \frac{b}{2}\right) + \frac{\beta}{2}(2c + d + e - 2\mu - f) \tag{15}$$

Note that all of the terms in the product coefficients contain α (either directly or through β), so that the amount of each product species depends upon the fuel flow rate (α).

For the condition of low halogen loading, or less hydrogen than halogen, the solution is given below:

$$\beta = \frac{\alpha(4a + b)}{\frac{4}{\rho r} + e + f - 4c - d} \tag{16}$$

$$\gamma = \frac{\beta}{\rho r} \tag{17}$$

$$\mu = \beta\rho^* \tag{18}$$

where:

$$\rho^* = \frac{\rho_{H_2O}}{\rho} \times \frac{r_{H_2O}}{r} \tag{19}$$

The fluxes of the products are expressed as follows:

$$\delta = \alpha a + \beta c \tag{20}$$

$$\varphi = \beta f \tag{21}$$

$$\eta = \beta e \tag{22}$$

$$\lambda = 2[\beta(\frac{1}{\rho r} - c) - \alpha a] + \mu \tag{23}$$

Thus, depending on the relative halogen/hydrogen ratio different pathways of formation of inhibition products are possible. When water vapor is absent in the system, the same system of equations is valid, but the terms represented by μ are equal to zero.

Basic features of the model are illustrated in Figure 27 for a steady-state propane-air cup burner diffusion flame with C_3F_8 in the air stream. In this figure, the fluxes of hydrogen and fluorine atoms into the reaction zone are depicted as a function of the C_3F_8 mole fraction in the air stream. At zero inhibitor mole fraction, all of the hydrogen input to the flame is converted to H_2O. As the inhibitor is added and fluorine becomes present in the reaction zone, hydrogen fluoride is formed preferentially over water (it is more stable). When all of the hydrogen has been consumed as HF, there is no water in the final products; any additional fluorine reaching the reaction zone shows up primarily as COF_2.

The ratio of the halogen to hydrogen concentration in the reaction zone is a useful parameter, and is obtained from the equations above as follows:

$$\frac{[\ Halogens\ ]}{[\ Hydrogen\ ]} = \frac{\beta(e + f)}{\alpha b + \beta d + 2\mu} \tag{24}$$

The crossover point for the two curves in Figure 27 corresponds to a value of unity for this parameter, and represents the switch from the first to the second solution above. This point corresponds to a critical value of the inhibitor flux into the reaction zone β_{cr} which is equal to:

$$\beta_{cr} = \frac{\alpha b + 2\mu}{e + f - d} \tag{25}$$

As illustrated in Figure 27, the HF production cannot be greater than the hydrogen or fluorine flux to the reaction zone; also, the sum of HF and COF_2 (the only significant other final species for fluorine) cannot be greater than the fluorine flux. For C_3F_8 in a propane-air flame, all of the hydrogen comes from the fuel, so that at zero inhibitor concentration there is a non-zero hydrogen flux to the reaction zone and additional inhibitor in the air stream does not increase the hydrogen flux to the reaction zone (for other inhibitors, such as C_2HF_5, increasing amounts of inhibitor slightly increase the hydrogen flux to the reaction zone).

Conversely, all of the fluorine comes from the inhibitor, so it increases nearly linearly with the inhibitor mole fraction X_i. Since COF_2 readily hydrolyses in water to form fluoride ion F^-, measurements of fluoride typically include that from both HF and COF_2. In principle, the product gases from inhibited flames near extinction could contain fluorine from both HF and COF_2. Interestingly, however, the experimental results for a number of fuels and agents (Bajpai, 1974) indicate that measured fluorine levels are rarely above the limit imposed by the hydrogen flux shown in Figure 27. These reduced fluoride levels may be due to kinetic limitations on the rate of inhibitor consumption and HF formation (Linteris, 1995).

For the present analyses, however, the predicted acid gas formation in inhibited flames is based on equilibrium thermodynamics assuming that HF (not COF_2) is the source. Provision is also made in the model for inclusion of an empirical parameter, based on the experimental results, which describes the observed deviation from the equilibrium prediction in diffusion flames for which experiments have been performed.

Based on the assumptions made in the stoichiometric model, a set of algebraic equations has been derived and a computer program has been developed to solve the set. The program uses as input: the atomic composition of a fuel and inhibitor, and the initial concentrations of the inhibitor, fuel, air, and the water vapor in the air and fuel stream. From these the estimated mole fractions of all reactants and products in the reaction zone are calculated. The program is particularly useful for parametric studies of the influence of each parameter on the predicted HF generation rate.

10.6.3 Transient State. The steady-state results are used to obtain results for transiently suppressed flames. In the present analyses, the inhibitor concentration in the air stream is assumed to increase linearly in time up to the extinction concentration for the particular flame (although any known profile of concentration versus time may be used). At each value of the inhibitor concentration, the

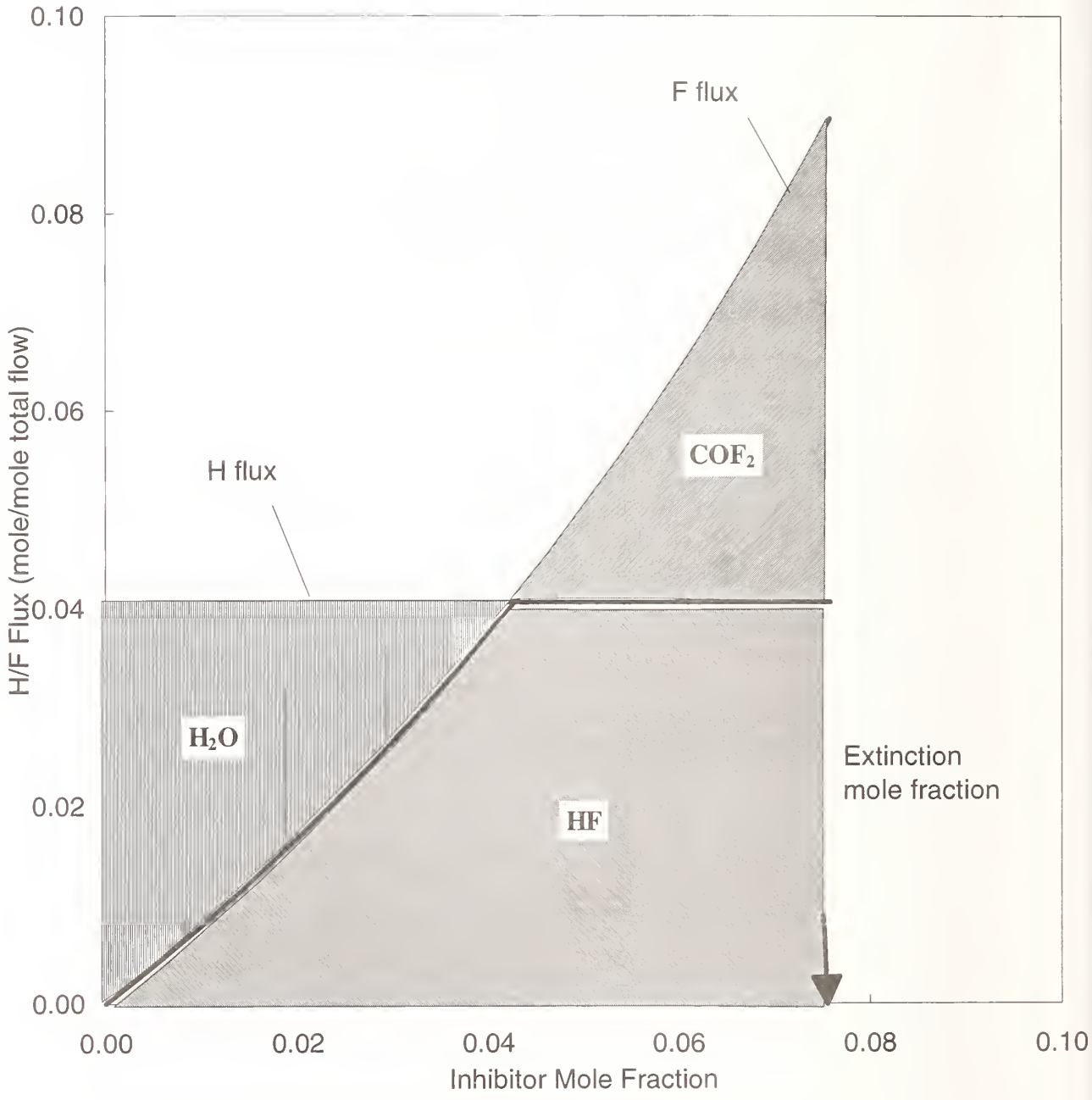

Figure 27. Stoichiometric model prediction of hydrogen and fluorine flux to the reaction zone of a propane-air diffusion flame. The fate of the hydrogen and fluorine are indicated at each inhibitor concentration.

production rate of HF is determined from the steady-state equilibrium model described above, providing a plot of the HF generation rate as a function of time. Integration of this curve provides the total HF formed during suppression of the flame. The inhibitor concentration as a function of time is provided as input, as is the concentration of inhibitor necessary to extinguish the flame.

10.7 Experiments

Laboratory experiments for HF formation were performed using several burner types, which shared some components. Three diffusion flame experiments were constructed: a propane-fueled cup burner, a propane-fueled jet burner, and a heptane-fueled cup burner. These three were used in steady-state, and the propane cup burner was also used for transient experiments. Premixed flames were used both for numerical model validation (the experiment for which is described above) and for HF measurements in steady-state. The following sections describe these experiments.

10.7.1 Propane Diffusion Flame Tests for HF. Two burner types are used for the gaseous diffusion flame experiments. The first is modelled after the cup burner described by Booth *et al.*, (1973) and Bajpai (1974). The experimental arrangement is shown in Figure 28. The burner consists of a 28 mm diameter pyrex cup positioned concentrically in a 120 mm diameter 450 mm tall chimney at about 150 mm from the base. In these experiments with propane, the cup burner was modified for use with a gaseous fuel. The cup is filled with 1 mm diameter glass beads and covered with a stainless steel screen. The second burner consisted of a 25 cm long pyrex tube with a 0.50 mm diameter opening positioned concentrically and at the same height as the cup burner, with the same chimney. The cold flow Reynolds number based on the exit velocity in the tube is 1050. This second burner, referred to here as the jet burner, is designed to provide turbulent mixing of the inhibitor in the air stream with the fuel. Although a higher jet Reynolds number would have been desirable to achieve turbulent mixing, the flame is very close to blow-off at flows with a Reynolds number of 2000, and very little inhibitor can be added before blow-off occurs. Consequently, at these flows, it is difficult to study the effects of air stream inhibitor concentration on HF formation.

The air used is shop compressed air, filtered and dried as described below. The fuel gas is propane (Matheson, CP grade) at flow rate of 0.114 l/min at 21 °C. Gas flows are measured with rotameters (Matheson 1050 series) which are calibrated with bubble and dry (American Meter Co. DTM-200A and DTM-325) flow meters. Inhibitor gases are of different purities from various suppliers.

Before measuring HF in the product gases, the concentration of inhibitor in the air stream necessary to extinguish the flame is determined. The inhibitor is then added to the co-flowing air stream at a concentration of either 50 % or 90 % of the extinguishing concentration, and the product gases are sampled for acid gas. In one series of experiments with the cup burner, the inhibitor is added to the gaseous propane stream at 70 % of the concentration which would extinguish the flame.

10.7.2 Liquid Heptane Diffusion Tests for HF. The cup burner apparatus was also used in its more usual configuration with a liquid fuel. For the purposes of this research, it is necessary to know the fuel consumption rate. To accomplish this, the overflow fuel feed system (Figure 29) was developed. In this system, a syringe pump (Harvard Apparatus Model 975) delivers the fuel at a known volumetric flow rate to the flame and the overflow tube. The flow is set to be greater than the expected fuel consumption rate of the flame, and the height of the fuel overflow tube is adjusted to provide the proper height of fuel in the cup. An electronic laboratory balance (Mettler PE360) connected to a

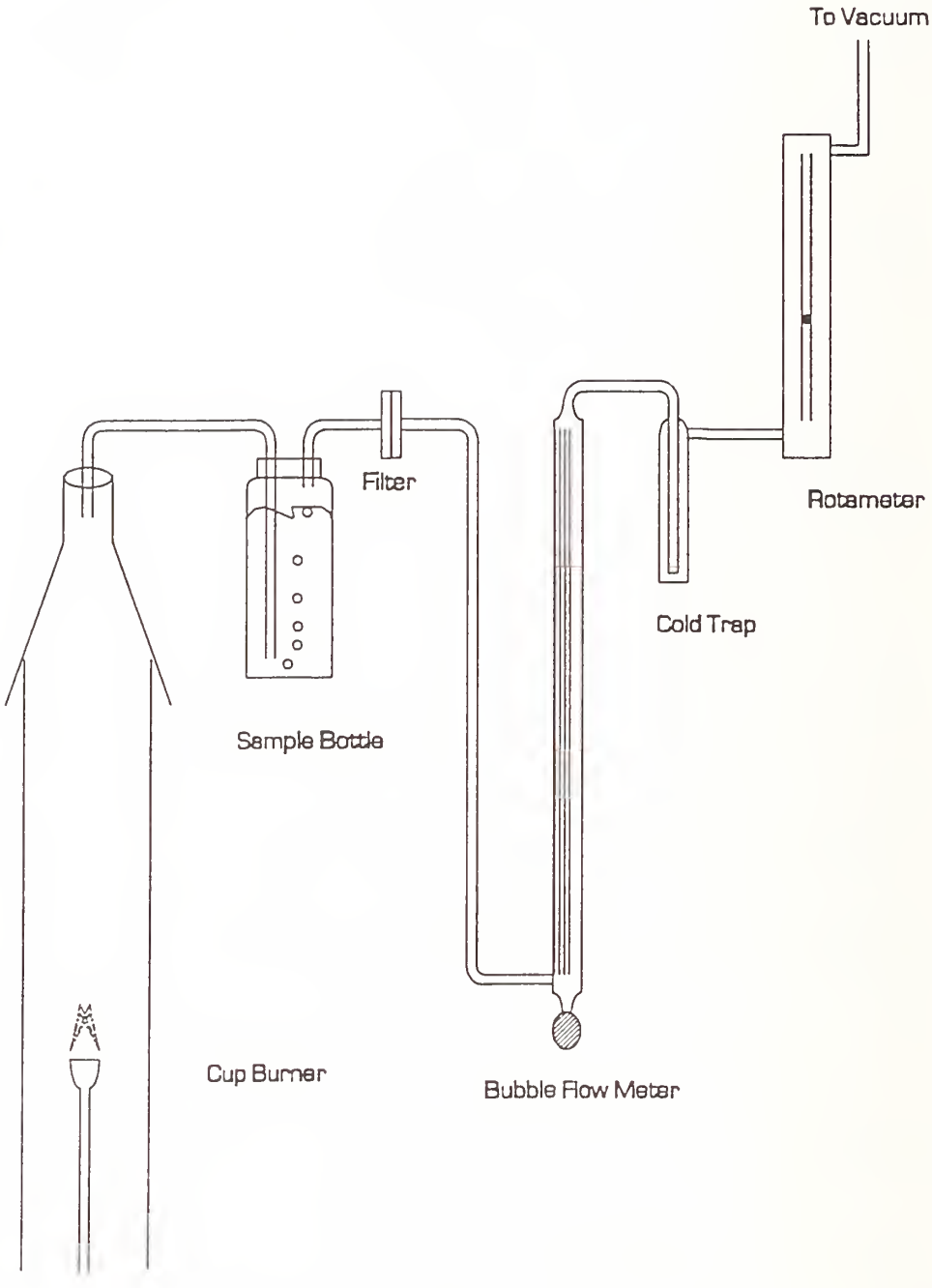

Figure 28. Experimental apparatus for co-flow diffusion flame studies of acid gas formation in inhibited propane-air diffusion flames.

computer data acquisition system, measures the mass of liquid emerging from the overflow tube. By subtracting the measured overflow rate from the supplied flow rate, the fuel consumption rate of the burner is determined. The fuel in the cup burner is adjusted to a height 1 mm below the cup rim, and this level is maintained through manual periodic adjustments during the experiment.

Heptane was used as the fuel for the liquid cup burner tests. The air cleaning and gas supply systems were identical to those described above for the premixed flame burning rate measurements. The air flow was 20.7 l/m, and the agents tested were CHF_3, C_2F_6, C_2HF_5, C_3F_8, C_3HF_7, at flow corresponding to 50 % and 90 % of the extinction concentration.

10.7.3 Premixed Flame Tests for HF. For the premixed flame tests of HF formation the same nozzle burner as in the burning velocity measurements is used. The burner consisted of a Mache-Hebra (1941) nozzle burner 27 cm long, with an inner diameter of 22 mm and wall thickness of 1.5 mm. A contraction at the top to a nozzle diameter of 1.02 (+/- 0.005 cm) occurs over a length of 3 cm. The burner tube is located concentrically in a 40 cm tall quartz chimney with an inner diameter of 7.6 cm, with contraction at the top to a 3 cm diameter. The burner produces conical flames with a height of 1.3 cm and base of 1.0 cm diameter. Air flows in the annular region at 25 l/m, while the reactant gas stream to the burner is about 2 to 5 l/m, depending upon the agent concentration and equivalence ratio. The flame height is maintained constant while the flows of oxidizer, fuel, and agent are varied to produce the desired agent concentration and equivalence ratio. The sampling of the product gases is done at the contraction in the top of the chimney as described below. The gas handling system for the premixed burner is also described below. Methane (Matheson UHP) and propane are used as the fuels, and CHF_3, C_2F_6, C_2HF_5, C_3F_8, C_3HF_7, and CF_4 are used as the agents.

10.7.4 HF Sampling Technique. A wet chemistry technique is used to measure the HF concentrations in the exhaust gases from the co-flow diffusion flames and the premixed flames. A quartz probe (6 mm O.D., 4 mm I.D., 20 cm long) is centered in the neck and extracts a measured fraction of the product gases (approximately 0.5 to 5.5 %). A vacuum pump draws the gases through polyethylene sample lines to one 250 ml polyethylene impinger and one 25 ml impinger filled with water which trap the acid gases. The second impinger was found to collect less than one percent of the total HF, but was retained for most of the experiments nonetheless. Desiccant-packed tubes or a cold finger dry the sample gas upstream of a calibrated rotameter. The steady-state experiments had sample gas flow rates of about 200 ml/m. To increase the quantity of HF collected in the short, transient experiments, the sample flow was increased to about 1.2 l/m. The sample flow is established for a total collection time of one to four minutes. The quartz probe and sample lines were washed with water which was returned to the impinger. The sample was tested for F- using ion-selective electrodes (Orion model 96-09). It should be noted that since COF_2 is known to hydrolyze rapidly in the presence of water, this technique for acid gas measurement includes F- from both HF and COF_2. To reduce the effects of sampling losses reported by other investigators, a quartz probe and polyethylene sample lines were used, the distance from the chimney top to the bubbler was kept small (~ 10 cm) and the sample lines were washed with the bubbler fluid immediately after the sample was collected.

10.7.5 Transient State Measurements. The experimental arrangement for the transient experiments is identical to the steady-state propane-air diffusion flame experiments described above. In the these experiments, the agent is added to the air flow at a concentration increasing linearly in time up to a value 25 % above the cup burner extinction concentration. The concentration ramp, implemented through computer control of the mass flow controllers, allowed effective ramp times from 5 seconds to any number of minutes. The amount of HF formed is lower than in the steady-state experiments due to the short time for interaction prior to flame extinguishment. To insure that a sufficient amount of

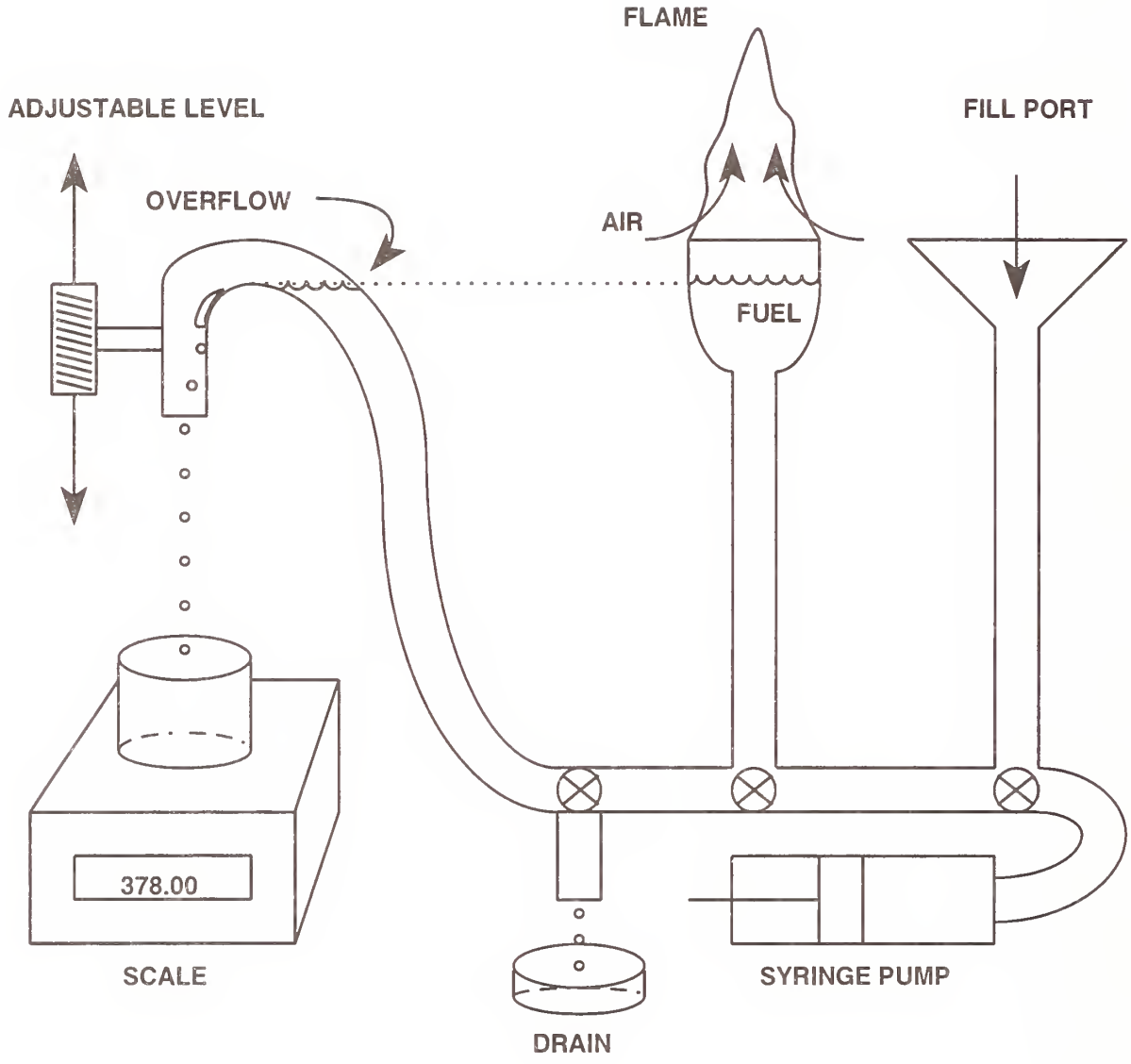

Figure 29. Experimental apparatus for co-flow diffusion flame studies of acid gas formation in inhibited heptane-air diffusion flames.

HF is collected, a higher sample gas flow is used (about 7 % of the total flow), and a second bubbler ensures that no HF is untrapped. In the experimental procedure, the gas sample flow is started, the inhibitor is ramped up in concentration to 125 % of the flame extinguishment concentration and the flame extinguished. The sample flow continues 30 seconds after extinguishment and is stopped. The sample probe consequently extracts a measured fraction of the total product gas flow, from which the total HF formed is determined.

10.8 Results

10.8.1 Steady-state - Premixed Flames. The amounts of HF measured in steady-state premixed flames are presented in Figures 30 and 31. Figure 30 shows the results for the inhibitors CF_4, CHF_3, C_2F_6, and CH_2F_2 in premixed methane-air flames, and Figure 31 shows the results for the species C_2HF_5, C_3F_8 and C_3HF_7 for propane-air flames. In these figures, the experimental results are indicated by the points, while the solid lines show the predicted HF mole fractions based on the results of equilibrium calculations. The quantities of HF produced per mole of fuel are plotted versus agent mole fraction in the reactant stream. An increase in the inhibitor mole fraction produces a linear increase in the HF generation, and there is a linear dependence on the number of fluorine atoms in the inhibitor molecule. The flames with propane show higher HF production rates per mole of fuel than do the methane-air flames, since combustion of one mole of propane requires 24 moles of air, compared to about 10 moles for methane. Since the inhibitor mole fraction is based on the sum of air and inhibitor, the resulting molar flow of inhibitor per mole of fuel is greater in the propane flames as compared to the methane flames.

For the present flames, the hydrogen to fluorine ratio is always greater than one, so that fluorine in the inhibitor molecule essentially appears only as HF in the product gases. As described above in the discussion of premixed flame modeling, the inhibitor molecule is consumed rapidly and completely in these flames to form HF. Thus, for these flames, the predicted HF molar flow in the product gases can be predicted solely from the inhibitor molar flow rate in the reactant stream and the number of fluorine atoms in the inhibitor. As the figures show, the assumption of complete inhibitor reaction to HF provides a predicted HF generation rate in good agreement with the results of experiments for all of these agents except CF_4. It is interesting to note that we were not able to produce stable flames at inhibitor loadings near or above the point of unity hydrogen to fluorine concentration in the reactant stream for any agent.

Figure 32 shows the dependence of the quantity of HF generated from C_2F_6 in the premixed methane/air flame versus equivalence ratio of the mixture. Over this narrow range of equivalence ratio, the predicted HF is in good agreement with the measured values.

As Figure 30 shows, the amount of HF formed in CF_4-inhibited premixed methane-air flames is less than half that predicted by equilibrium thermodynamics, and decreases as the inhibitor loading increases. In order to investigate this further, experiments were performed with premixed methane-air flames in which the oxygen mole fraction was changed to vary the peak final temperature of the flame.

Figure 33 shows the fractional conversion of CF_4 to HF (and COF_2) as a function of the calculated final flame temperature. As indicated, a change of final temperature of only a few hundred K produces a change in the fractional conversion of CF_4 from about 15 to 70 %. Consequently, this type of behavior was investigated numerically in premixed methane-air flames for the other inhibitors, but a strong temperature dependence for the rate of inhibitor decomposition was not observed. The

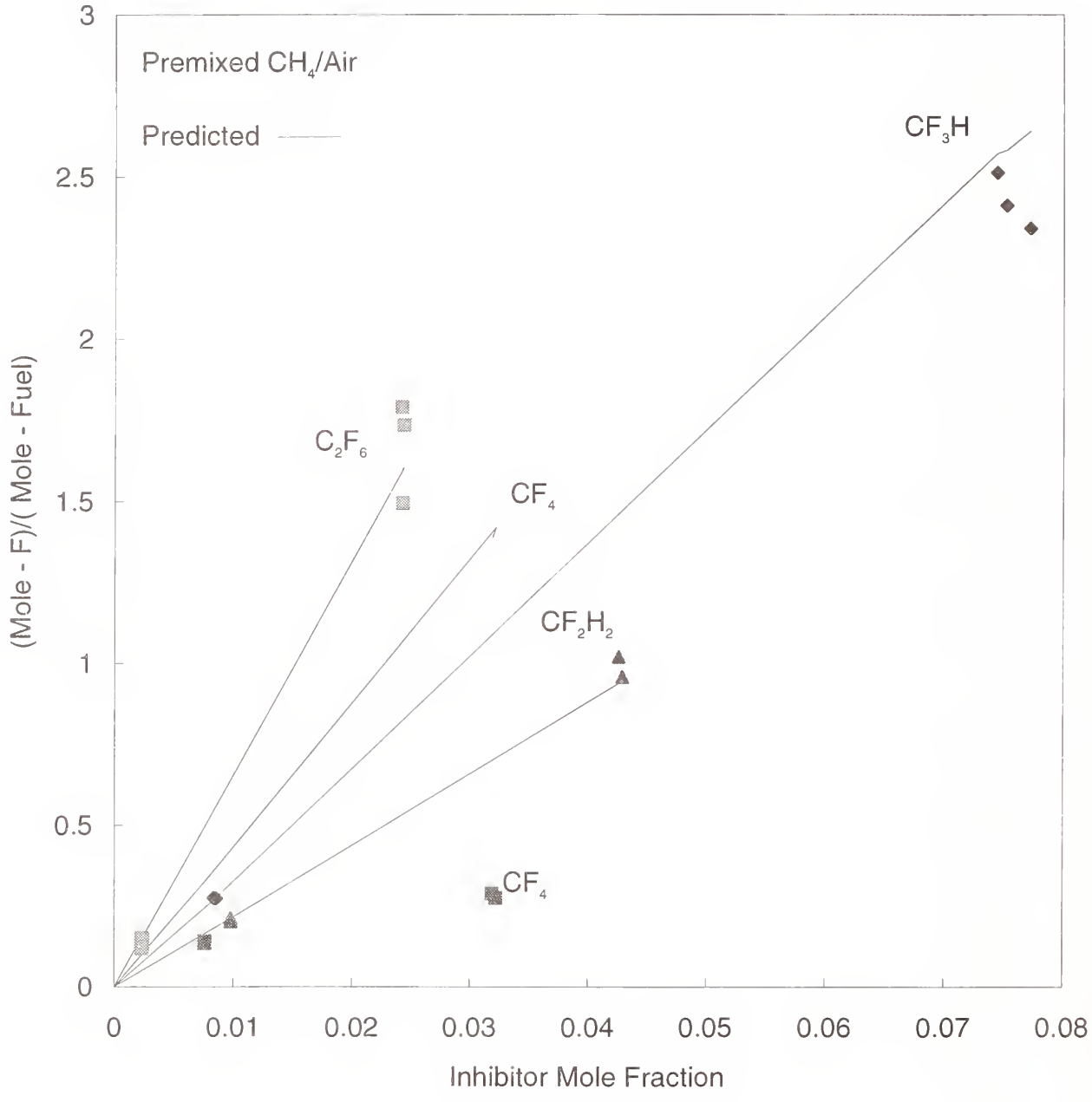

Figure 30. Measured and predicted HF in premixed methane-air flames with C_2F_6, CF_4, CHF_3, CF_2H_2.

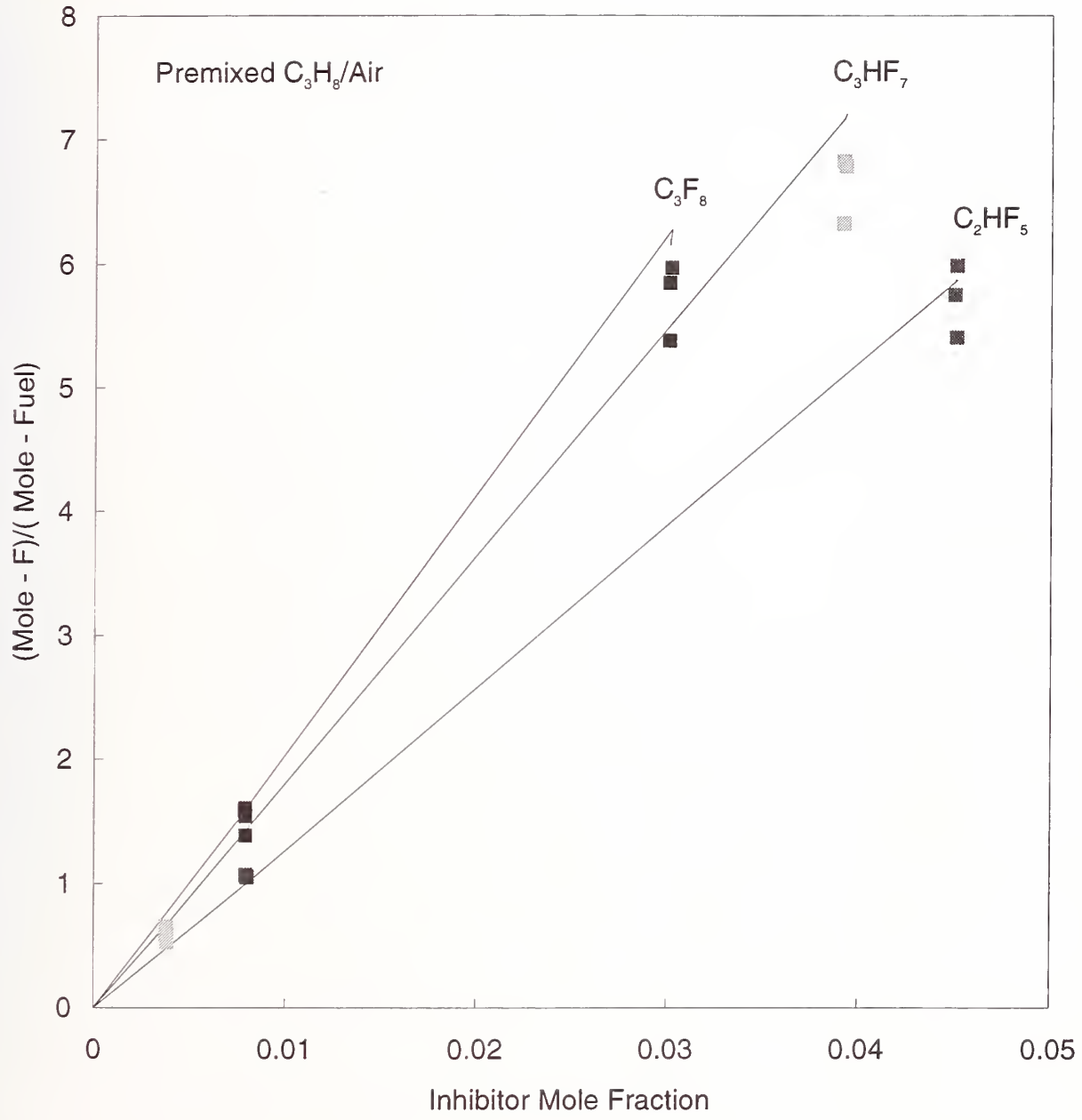

Figure 31. Measured and predicted HF in premixed propane-air flames with C_3F_8, C3HF_7, C_2HF_5.

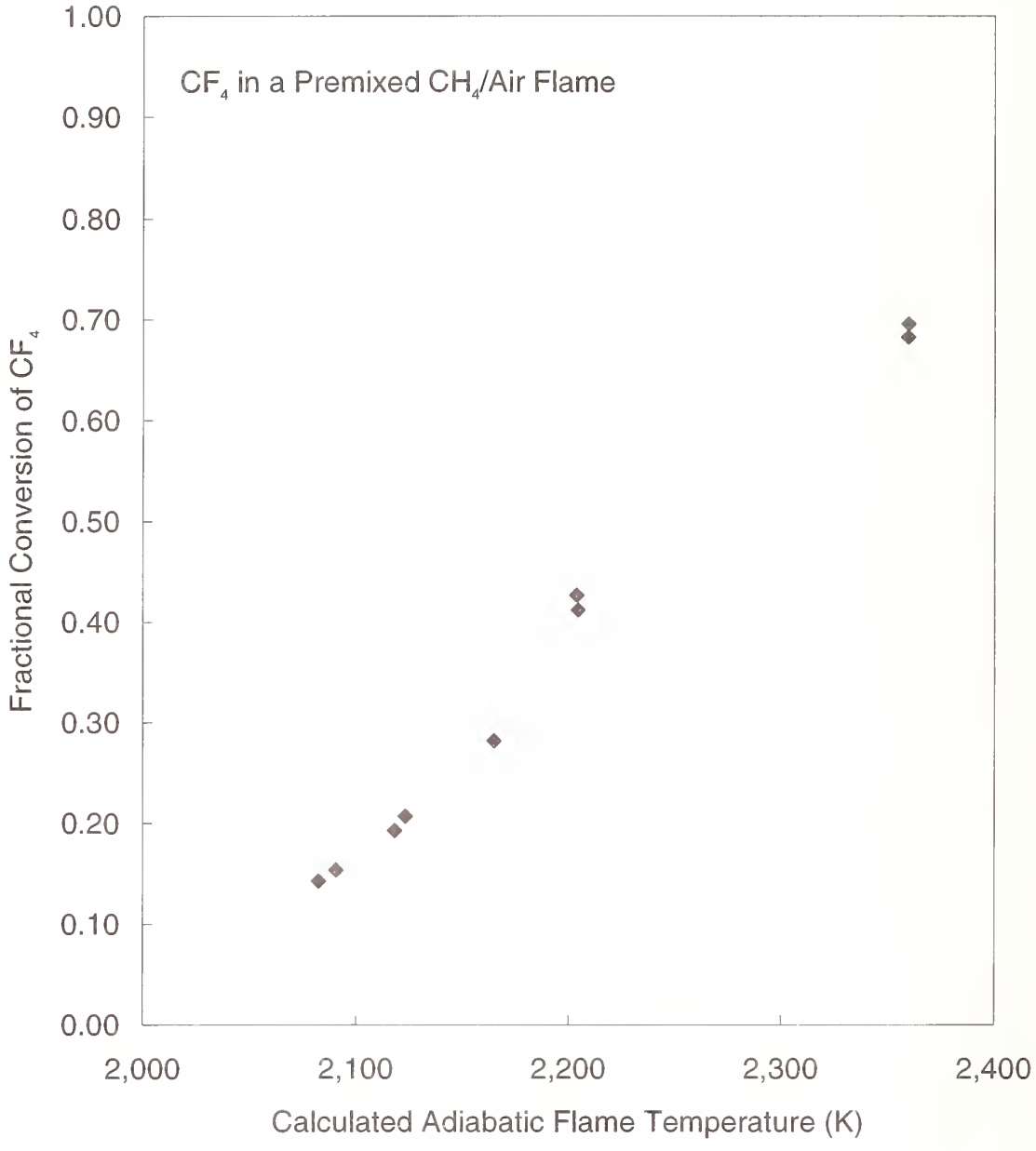

Figure 32. Fractional conversion of fluorine in CF_4 to HF in a premixed methane-air flame as a function of the calculated adiabatic flame temperature.

possibility of the effect of temperature should be kept in mind when extending the results of this study to other conditions.

It has been shown that for all of the hydrofluorocarbons tested in premixed flames, including CH_2F_2, CF_3H, C_2HF_5, and C_3HF_7, the agent completely decomposed and formed species which appeared as fluoride ion in the bubbler (*i.e.*, either HF or COF_2). This indicates that kinetic limitations are not important for these agents in these flames, and that the assumption of chemical equilibrium provides estimates of HF formation that are consistent with the experimental results. This behavior is also observed for the perfluorinated agents C_2F_6 and C_3F_8. It is important to note that all of these flames had fluorine to hydrogen ratios in the flame greater than unity. Indeed, it was not possible, in either the nozzle burner (which has narrow stability limits) or in a premixed, water-cooled, flat-flame McKenna burner (which has wide stability limits), to stabilize any premixed flame at hydrogen to fluorine ratios of one or less. Thus it appears that at agent loadings were premixed flames burn, there is nearly complete destruction of the agent and subsequent formation of HF or COF_2.

10.8.2 Steady-state - Gaseous Diffusion Flames. In the propane-air diffusion flames, the acid gases produced are measured at inhibitor concentrations of 50 % and 90 % of the concentration of inhibitor found to extinguish the flame when the inhibitor is added to the co-flowing air stream in the cup burner and jet burners. Table 2 lists the extinction concentrations for each agent for inhibitor added to the air stream of both burners. As the table indicates, the jet burner flame typically requires about 50 % less inhibitor in the air stream to extinguish the flame than the cup burner, even for identical fuel and air flows, although there are notable exceptions: CF_3Br, which requires about one fifth as much inhibitor in the jet burner than in the cup burner, and $C_2H_2F_4$ and the $CH_2F_2/C_2H_2F_4$ mixture which had nearly the same extinction concentrations. In addition to providing the necessary extinction conditions for specification of inhibitor flows at 50 % and 90 % of extinction, these results also demonstrate the sensitivity of the extinction conditions to the burner geometry.

The HF production in steady-state propane air diffusion flames was measured for the agents C_2F_6, C_3F_8, C_4F_{10}, C_4F_8, C_2HF_5, C_3HF_7, $C_2H_2F_4$, C_2HClF_4, $C_3H_2F_6$, CF_2H_2/C_2HF_5, CHF_2Cl, CF_3Br, and CF_3I; the results are presented in Figures 34 to 46, respectively. The symbols represent the experimental data, while the lines marked F and H represent estimates of the fluxes of fluorine and hydrogen into the reaction zone based on the stoichiometric model described above.

Figure 39, for example, shows the measured and estimated HF production rates in a propane-air diffusion flame for C_2F_6 in the cup and jet burners. The curve labeled F' in Figure 39 is the maximum fluoride atom molar flux into the reaction sheet of the diffusion flame calculated using the stoichiometric model described above. The curve labeled F in Figure 39 is the fluoride molar flux when the diffusion rate of the inhibitor relative to oxygen is not modified to account for preferential diffusion of oxygen. These unprimed curves are expected to more closely describe near turbulent mixing as occurs in the jet burner.

Qualitatively, the curves F and F' are seen to increase with increasing inhibitor concentration in air, and the molar flux of inhibitor into the reaction zone is lower when a lower rate of diffusion is used for the inhibitor. The curves labeled H and H' (coincident for C_2F_6) show the estimated hydrogen atom flux into the reaction zone as a function of inhibitor concentration in the air stream. Since this inhibitor does not contain hydrogen, all of the hydrogen is from the propane, and increasing inhibitor in the air stream does not increase the hydrogen flux into the flame. One would expect that the HF production rate would not be greater than the estimated flux of F or H into the reaction zone. For this inhibitor, the flame appears to be hydrogen limited above about 5 % C_2F_6 in the air stream; however, when there is not enough hydrogen, the most stable product is COF_2, which is known to rapidly hydrolyze in the presence of water, and would also appear as F- in the bubbler. Consequently,

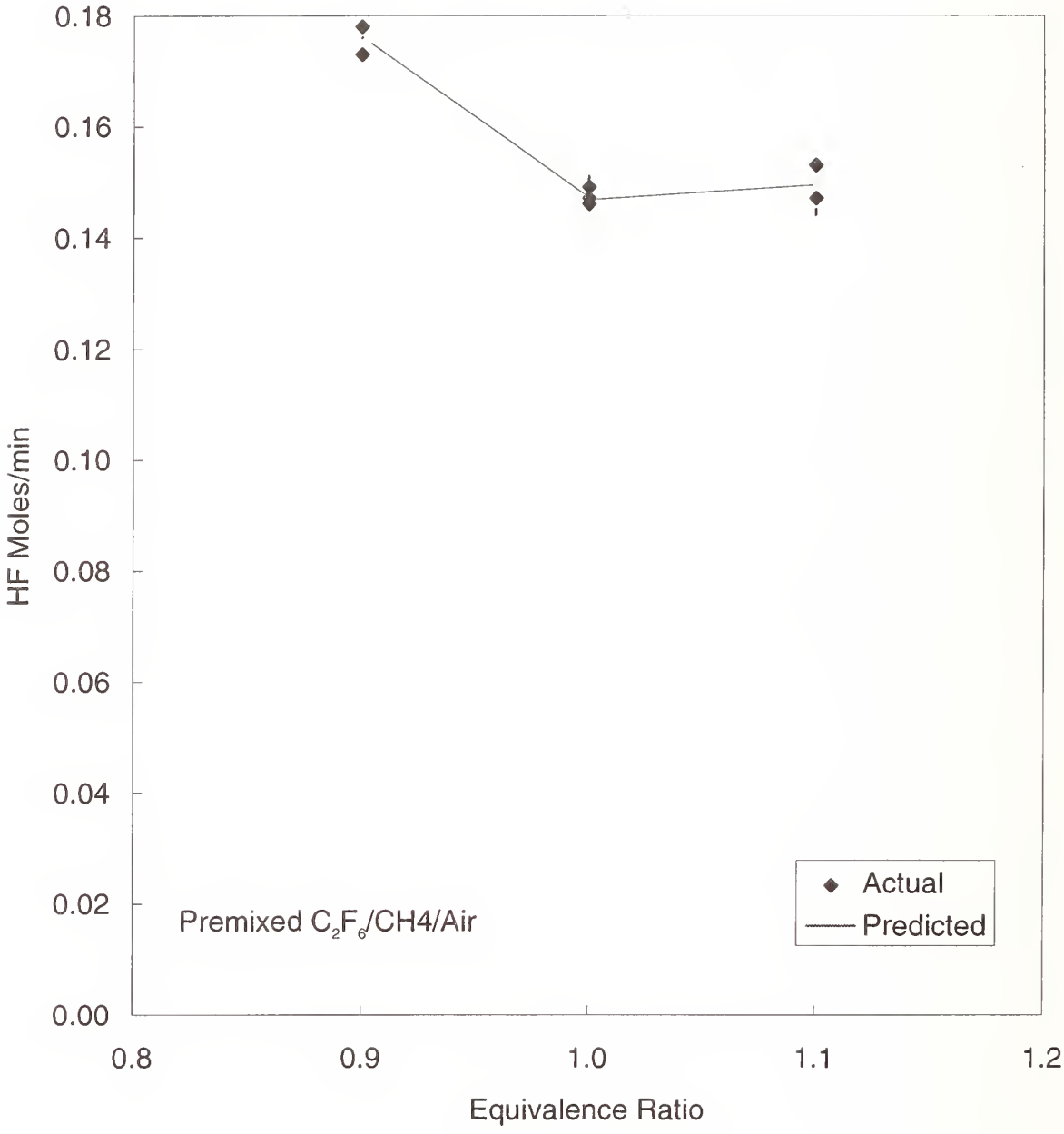

Figure 33. Measured and calculated HF production from C_2F_6 in a premixed methane-air flame for ϕ = 0.9, 1.0, and 1.1.

this hydrogen limit may or may not exist (depending upon whether the kinetics are fast enough to form COF_2 in the hydrogen-limited case).

Also shown in the figure are the experimentally measured HF production rates for the jet and cup burners (labeled c and j respectively) at 50 % and 90 % of the extinction concentration of C_2F_6. As indicated, the measured quantities of HF are lower than both the fluorine and hydrogen limits, and the measured values are closer to the estimated limits when the effects of preferential diffusion (H' and F') are included as described above.

Although the cup and jet burner results are plotted together, the phenomenological behavior of jet burner is distinctly different from that of the cup burner. Because the flame of the jet burner first stabilizes as a co-flow diffusion flame anchored at the outlet of the jet, the heated gases have a much lower Reynolds number, keeping the flow laminar. As inhibitor is added to the air stream, the flame grows in length (as it would in increasing the fuel flow rate). Eventually, the flame lifts off the burner surface by about 5 cm to form a lifted jet diffusion flame. With further inhibitor addition, the flame eventually blows off. These blow-off concentrations are referred to as the extinction concentrations (see Table 1) and are found to be much lower (about half) of the values determined for the cup burner. In the tests at 50 % extinction, the flow is laminar, whereas at 90 % of extinction, the flow is nearly turbulent and the flame is lifted. Transport of the agent into the flame is estimated in the stoichiometric model assuming molecular diffusion.

The goal of these experiments is to compare the model's prediction of HF formation for a diffusion flame where more vigorous mixing occurs, and identify if the enhanced mixing increases the HF production. Figures 34 to 45 show that HF production in the turbulent burner at 90 % of extinction is higher relative to the model prediction than the cup burner results at 90 % (except for C_2F_6 and C_4F_8), but that the jet burner HF production rates are still not above the estimate of the fluorine flux based on equal transport for O_2 and the inhibitor (the curve labeled F). When viewed as in Figures 34 - 45, the behavior of the alternative inhibitors falls into three categories. In the first category are the inhibitors C_2F_6, C_3F_8, C_4F_{10}, C_3F_8, C_2HF_5, and C_3HF_7 (Figures 34 - 39). For these inhibitors, at the highest inhibitor concentration tested (cup burner at 90 % of extinction) the estimated hydrogen flux into the reaction zone is lower than the fluorine flux. The ratio of hydrogen to total halogen flux ranges from 0.31 to 0.68, and the H flux is not a strong function of the inhibitor concentration. For these inhibitors, the HF produced does not increase significantly when the inhibitor concentration in the air stream increases above that necessary for a hydrogen/fluorine ratio in the reaction zone of about unity (the region of where the lines marked F and H or F' and H' cross in Figures 34 to 43).

A second category includes those inhibitors ($C_2H_2F_4$, C_2HClF_4, $C_3H_2F_6$, and CH_2F_2/C_2HF_5; Figures 40 to 43) for which the estimated H and X fluxes are closer, with H/X ratios of 0.68 to 0.85. For these inhibitors, the amount of HF produced increases with increasing inhibitor concentration in the air, but the highest concentration tested corresponds F/H ratio of about unity in the reaction zone. The last category consists of CF_3Br and $CHClF_2$ (Figures 44 and 45) for which the estimated hydrogen flux is much higher than halogen flux (in a ratio of 2.3 and 1.1, respectively), and there is estimated always to be more hydrogen than halogen in the reaction zone. For these agents, the HF produced is always increasing with higher agent concentration in the air stream. Although the stoichiometric model is simple and is only expected to provide an upper limit on the amount of HF formed, it is instructive to investigate the possible reasons that the measured HF production rates might be lower than the estimates. Lower HF may be measured in the experiments due to experimental difficulties, for example: loss of HF to the chimney walls, loss in the sampling system, HF undetected by the ion-selective electrodes, or imperfect mixing in the product gases. Based on parametric tests, however, these loss mechanisms are found to be minor. The predicted values of the

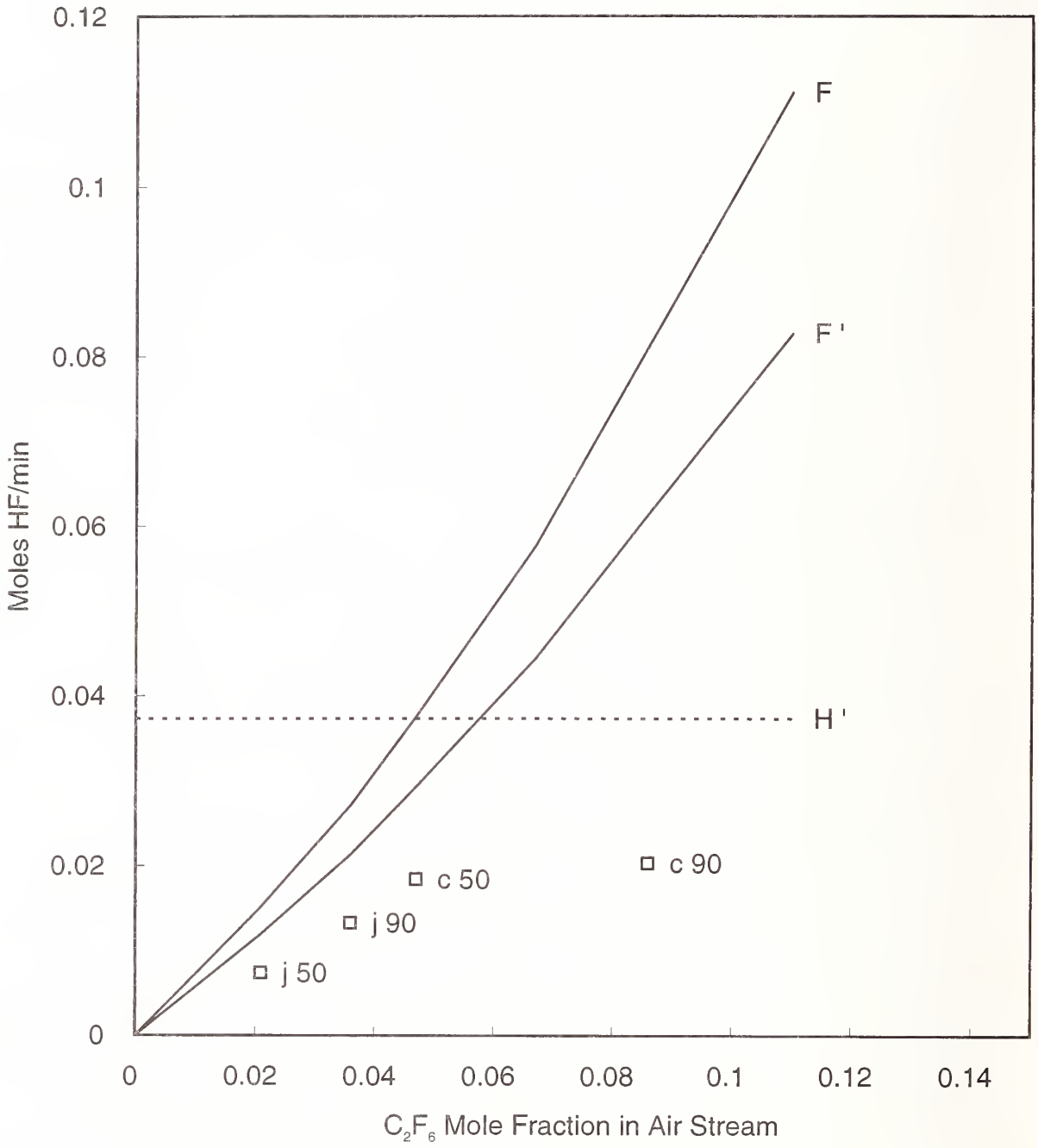

Figure 34. Measured HF production rates in co-flow propane-air diffusion flames inhibited by C_2F_6 with estimated fluorine and hydrogen fluxes to the reaction zone.

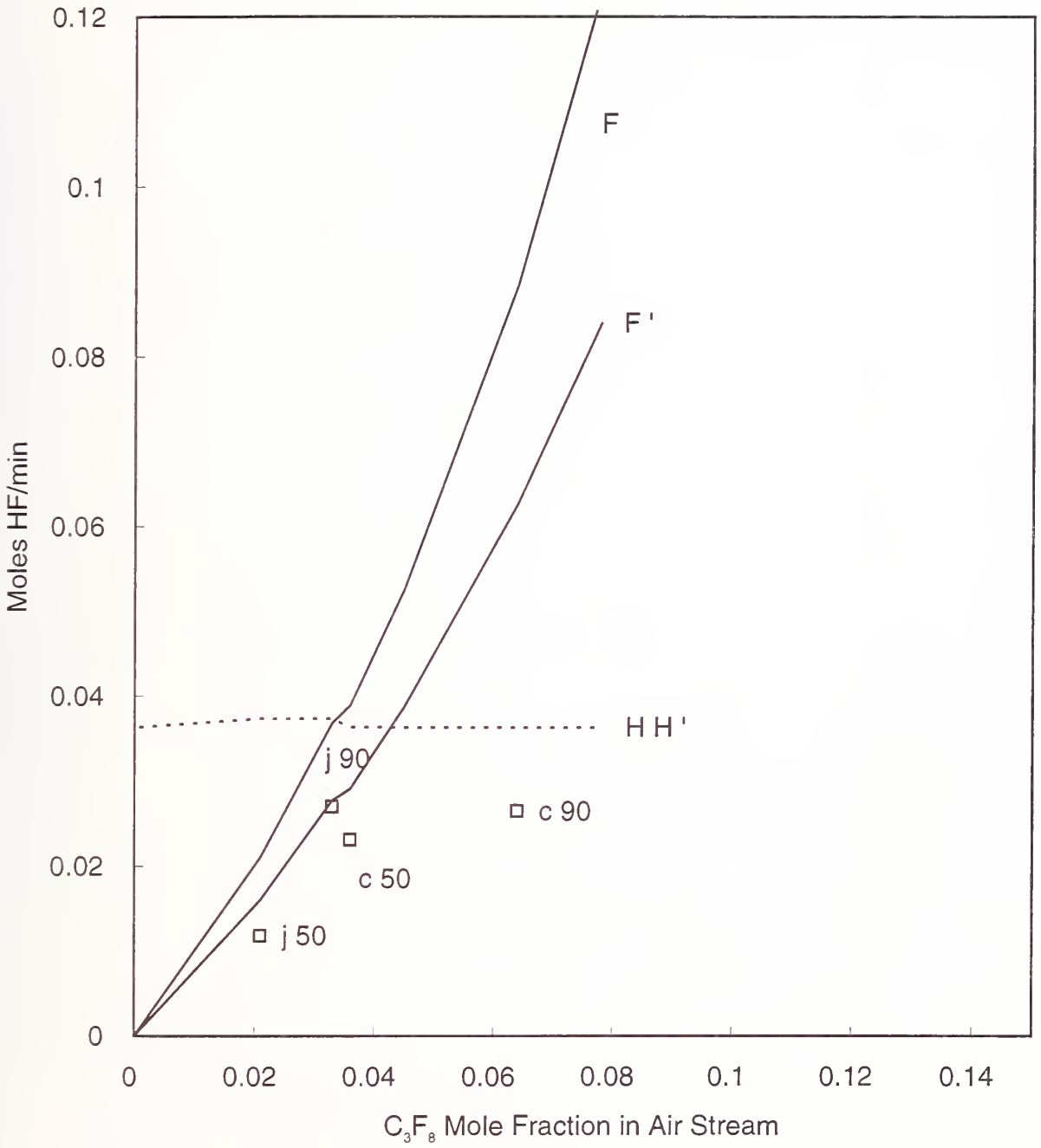

Figure 35. Measured HF production rates in co-flow propane-air diffusion flames inhibited by C_3F_8 with estimated fluorine and hydrogen fluxes to the reaction zone.

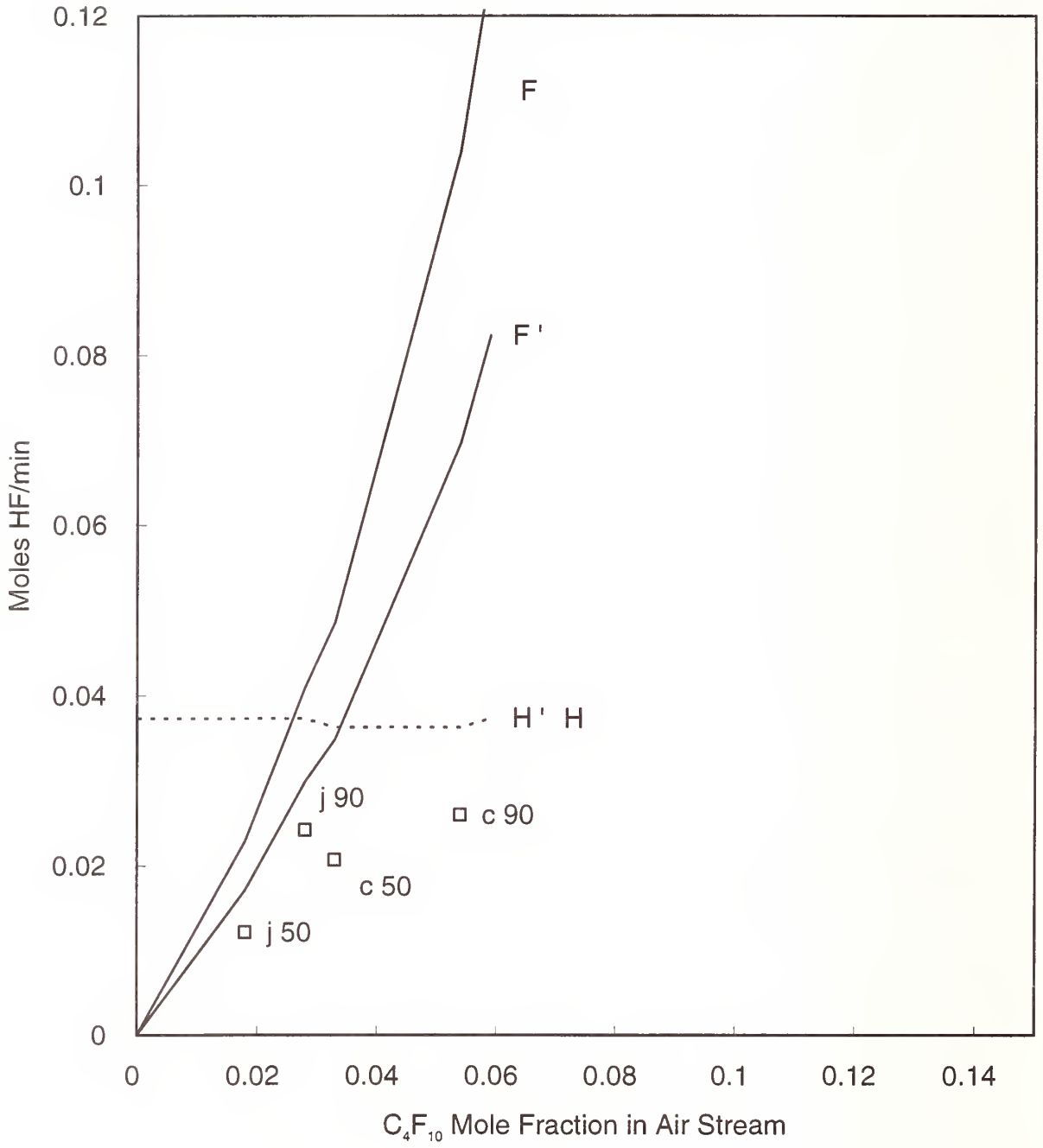

Figure 36. Measured HF production rates in co-flow propane-air diffusion flames inhibited by C_4F_{10} with estimated fluorine and hydrogen fluxes to the reaction zone.

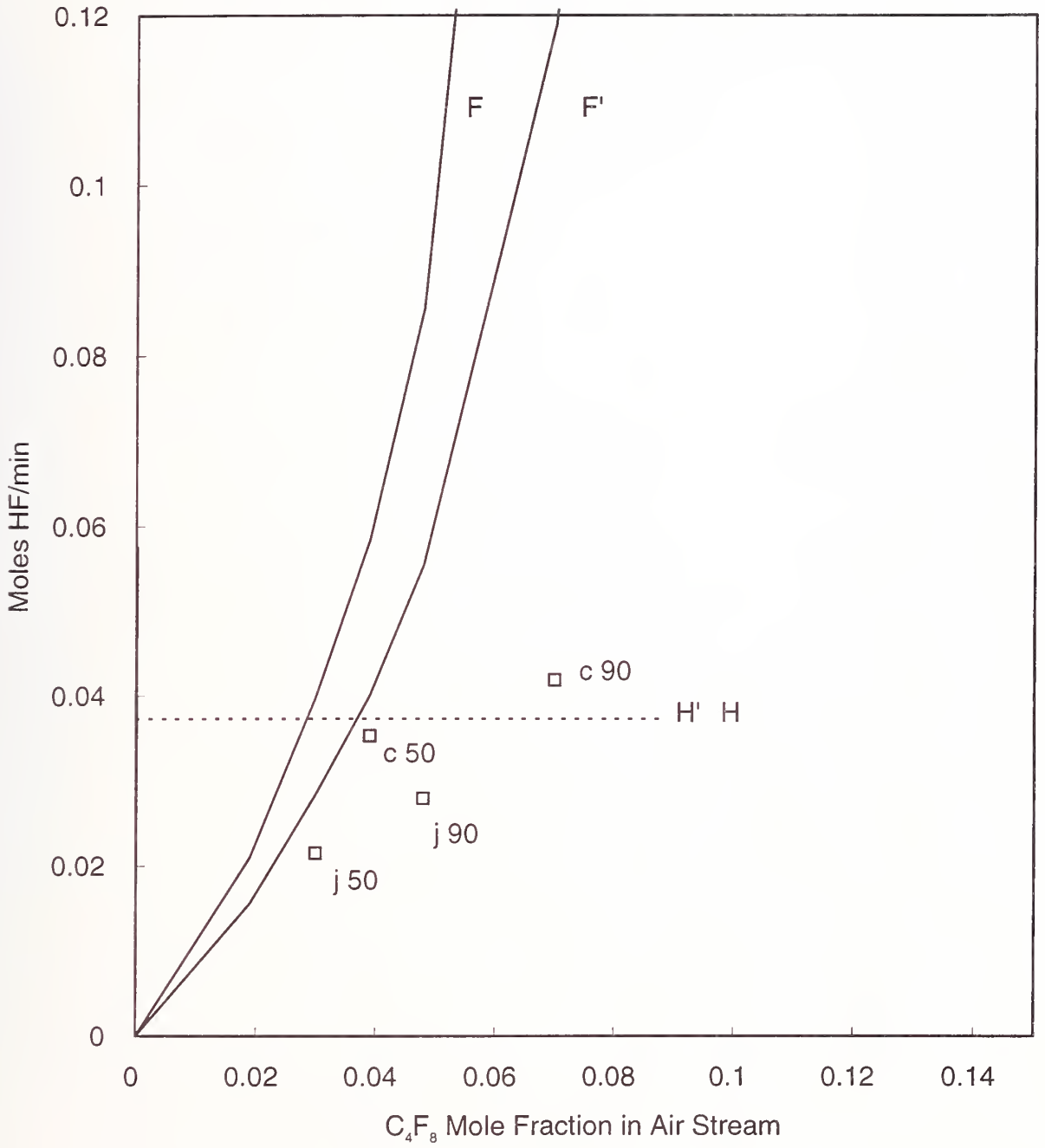

Figure 37. Measured HF production rates in co-flow propane-air diffusion flames inhibited by C_4F_8 with estimated fluorine and hydrogen fluxes to the reaction zone.

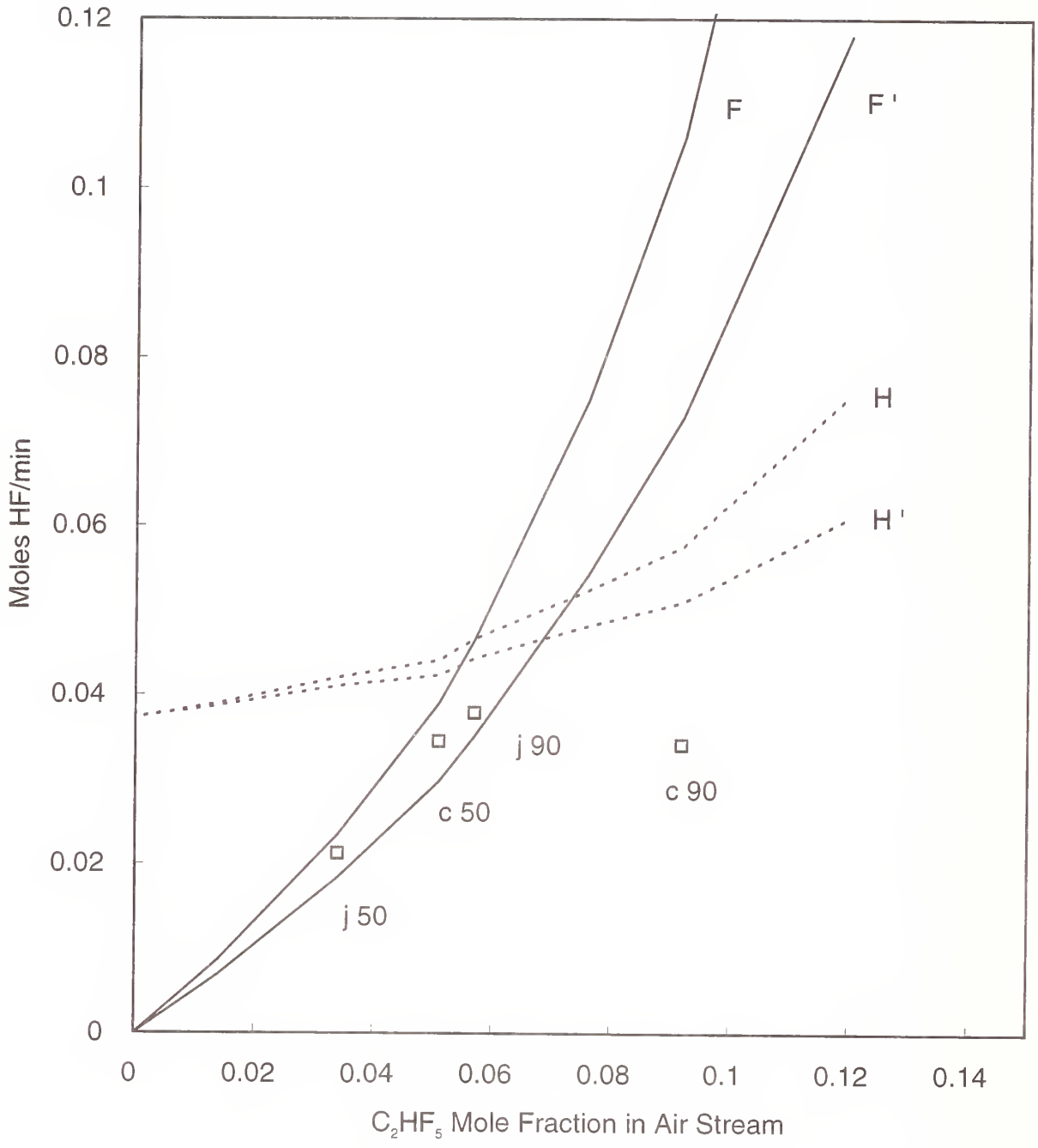

Figure 38. Measured HF production rates in co-flow propane-air diffusion flames inhibited by C_2HF_5 with estimated fluorine and hydrogen fluxes to the reaction zone.

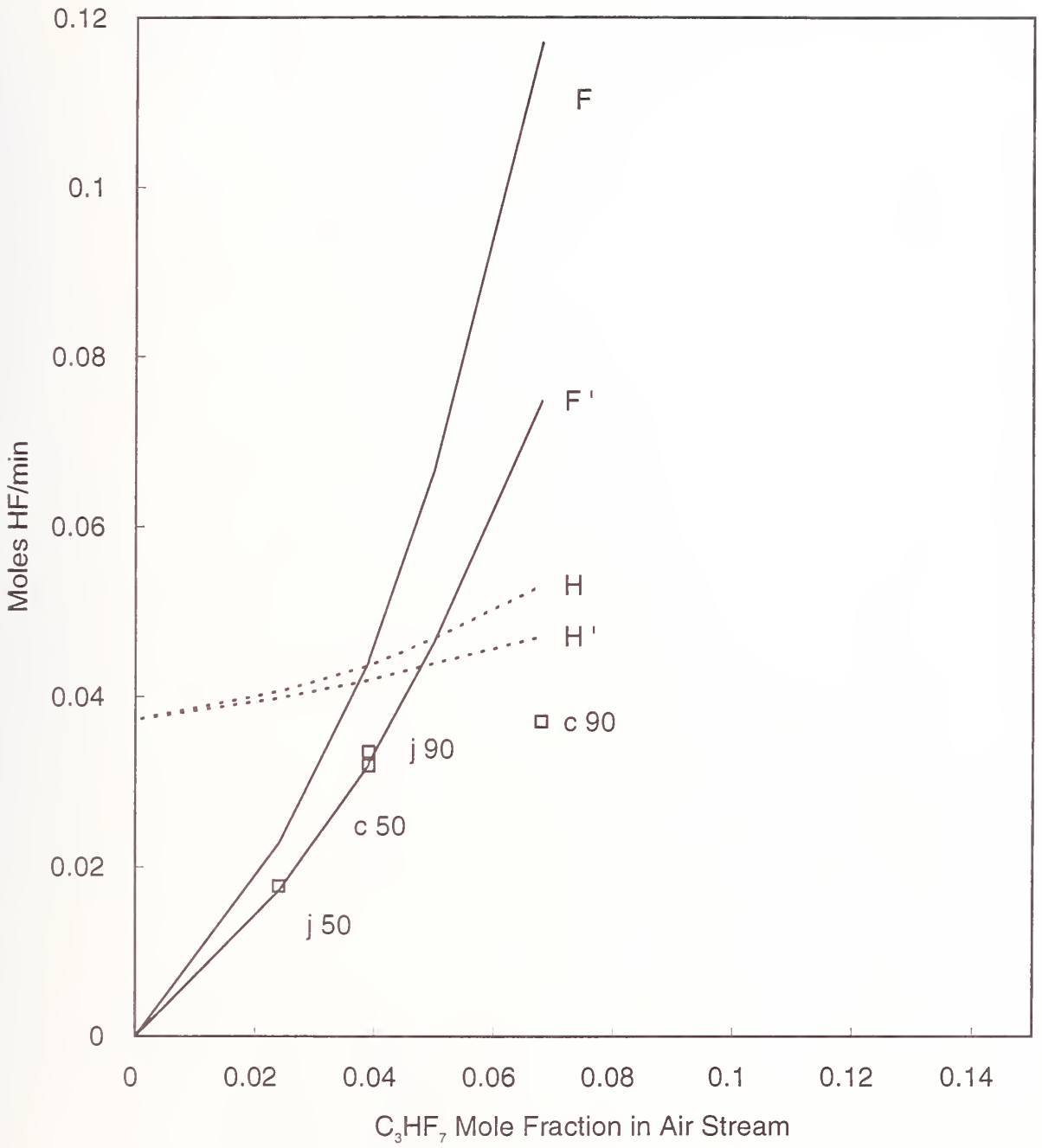

Figure 39. Measured HF production rates in co-flow propane-air diffusion flames inhibited by C_3HF_7 with estimated fluorine and hydrogen fluxes to the reaction zone.

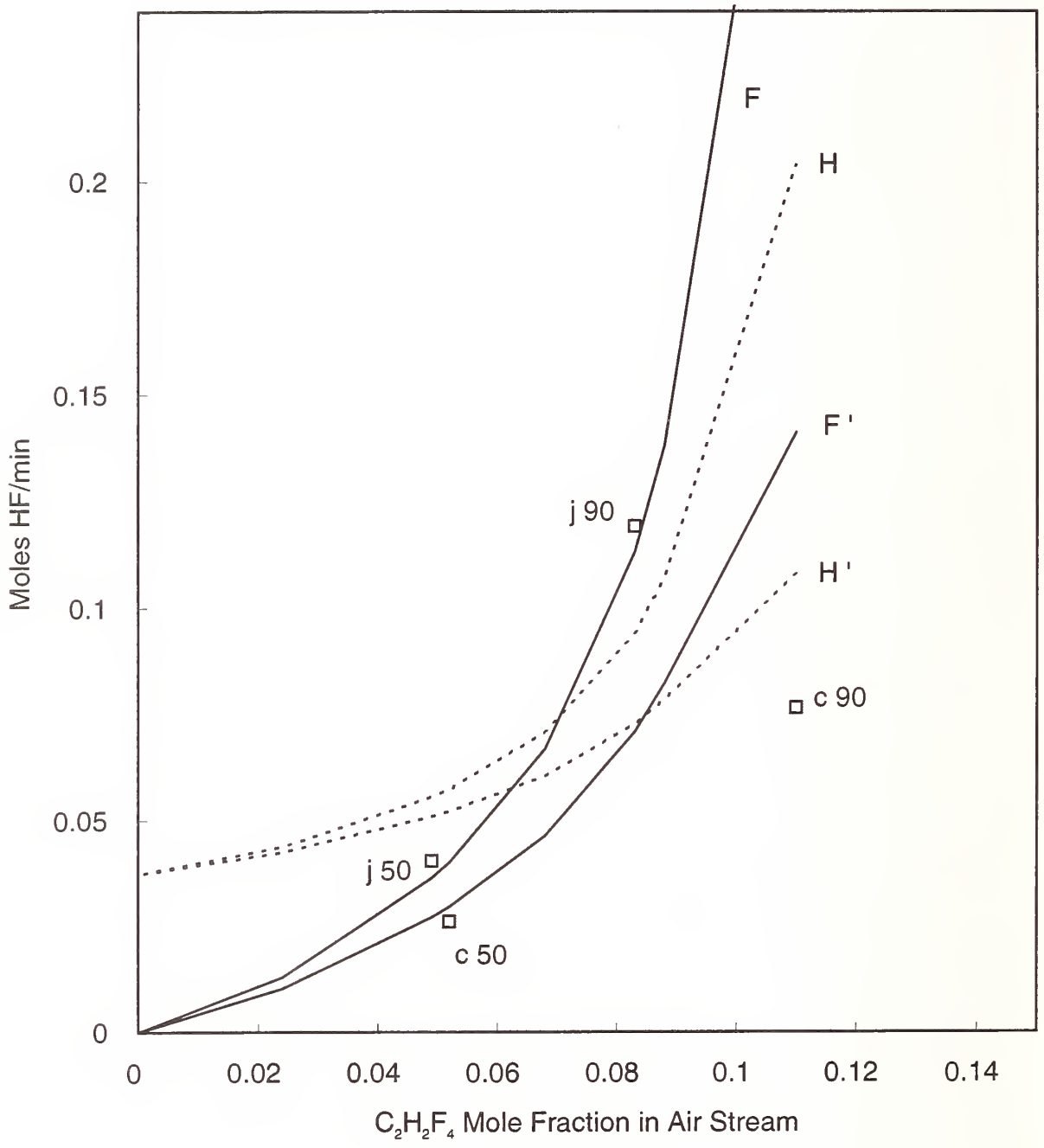

Figure 40. Measured HF production rates in co-flow propane-air diffusion flames inhibited by $C_2H_2F_4$ with estimated fluorine and hydrogen fluxes to the reaction zone.

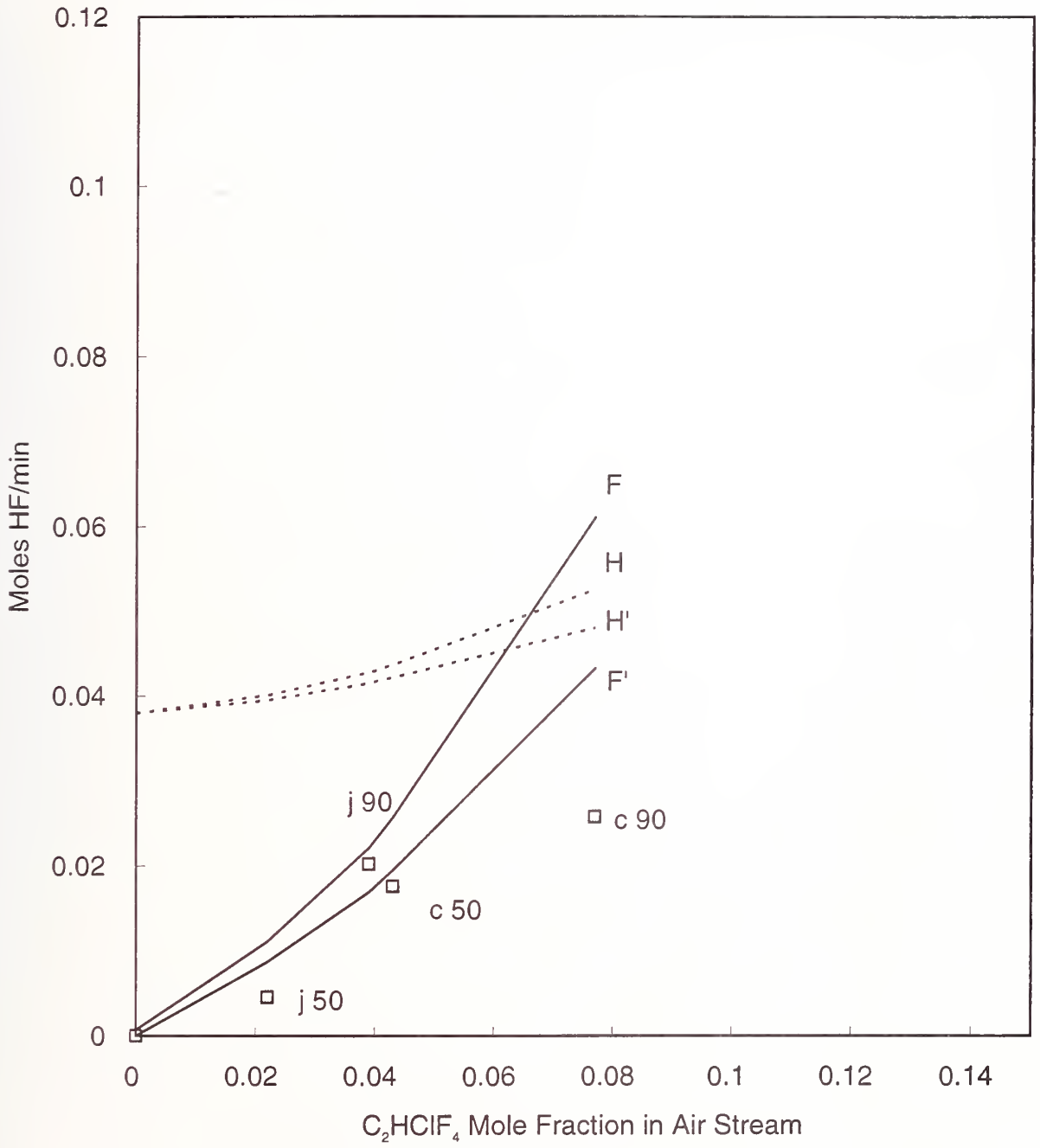

Figure 41. Measured HF production rates in co-flow propane-air diffusion flames inhibited by C_2HClF_4 with estimated fluorine and hydrogen fluxes to the reaction zone.

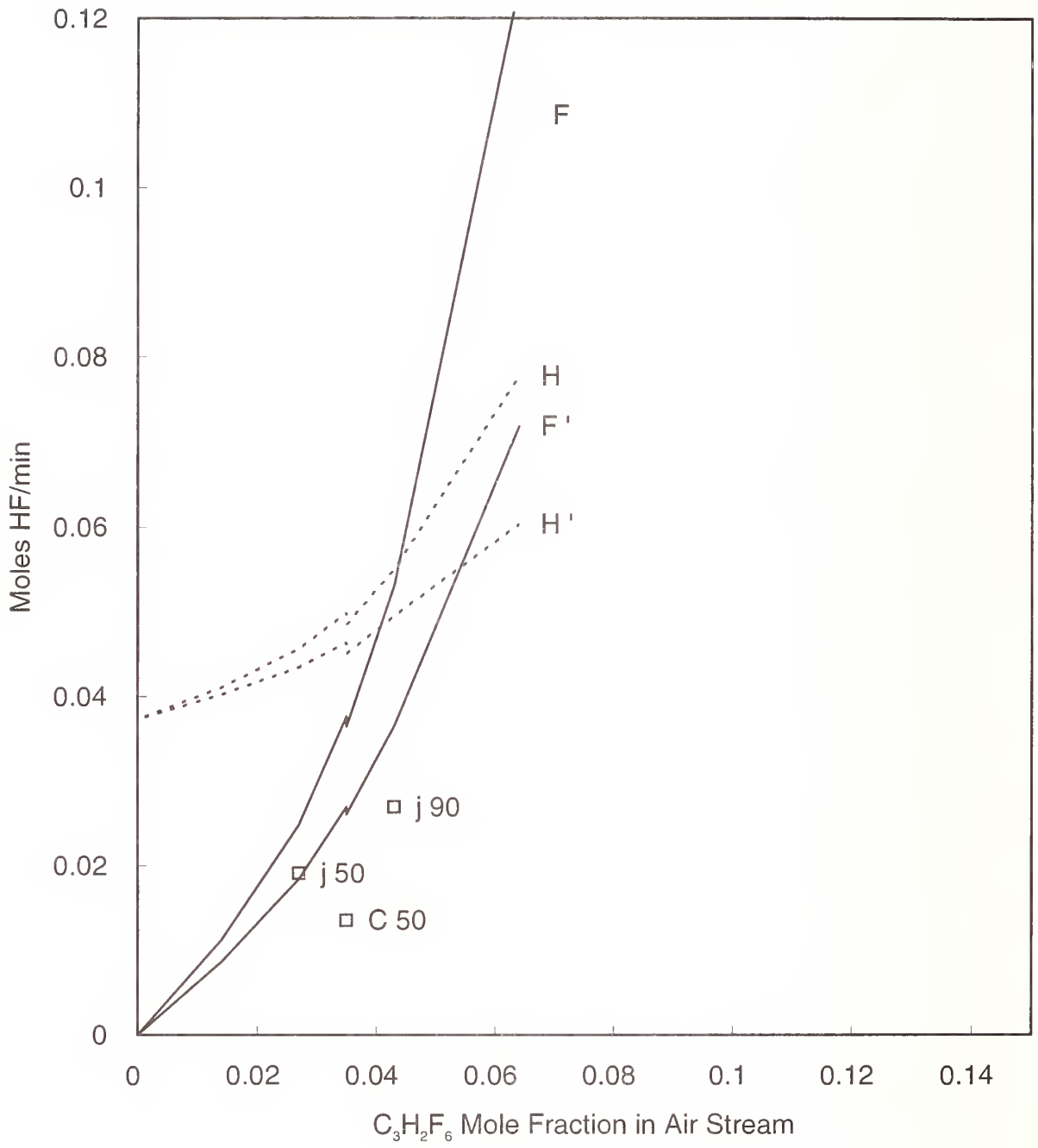

Figure 42. Measured HF production rates in co-flow propane-air diffusion flames inhibited by $C_3H_2F_6$ with estimated fluorine and hydrogen fluxes to the reaction zone.

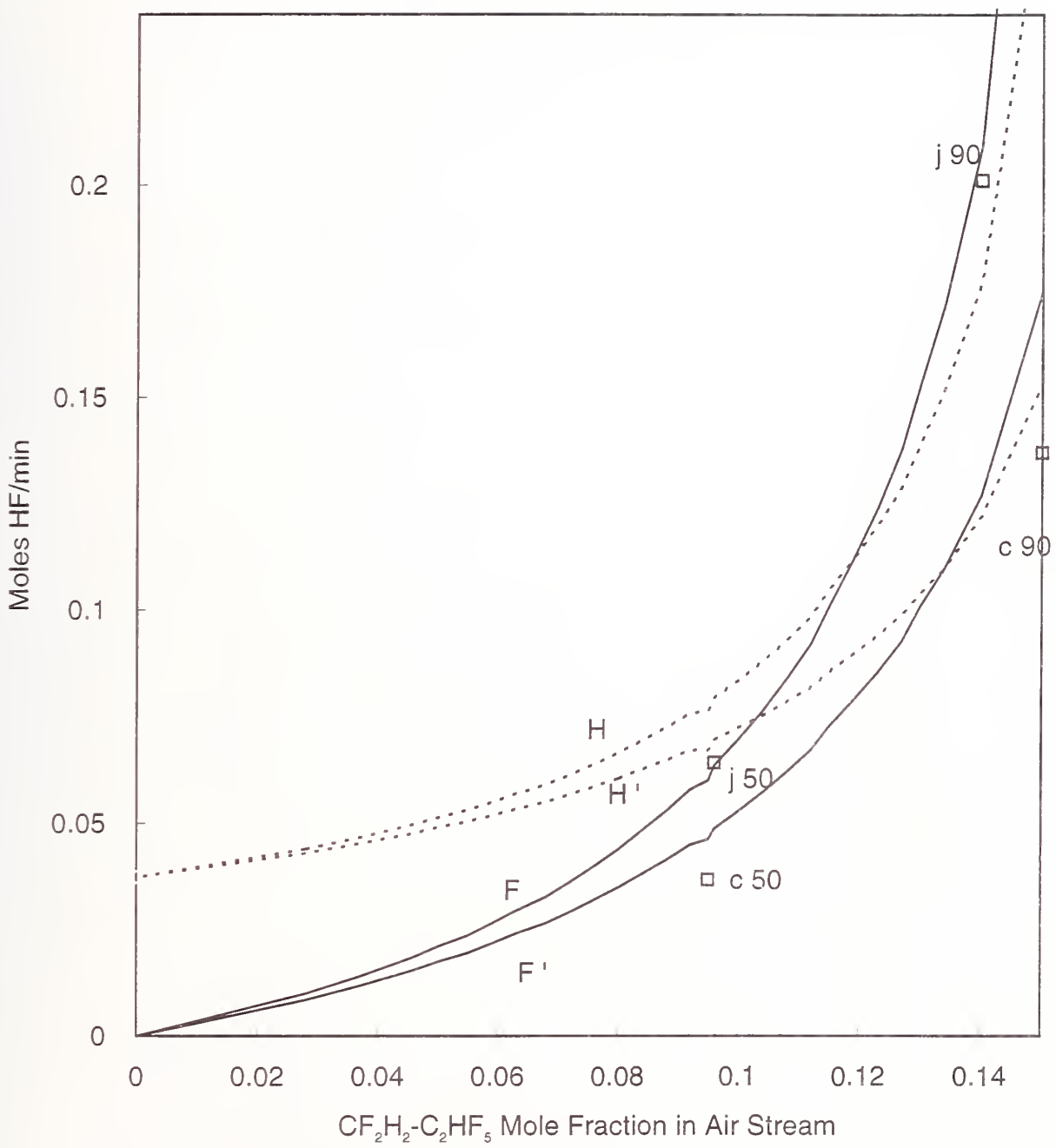

Figure 43. Measured HF production rates in co-flow propane-air diffusion flames inhibited by CF_2H_2-C_2HF_5 with estimated fluorine and hydrogen fluxes to the reaction zone.

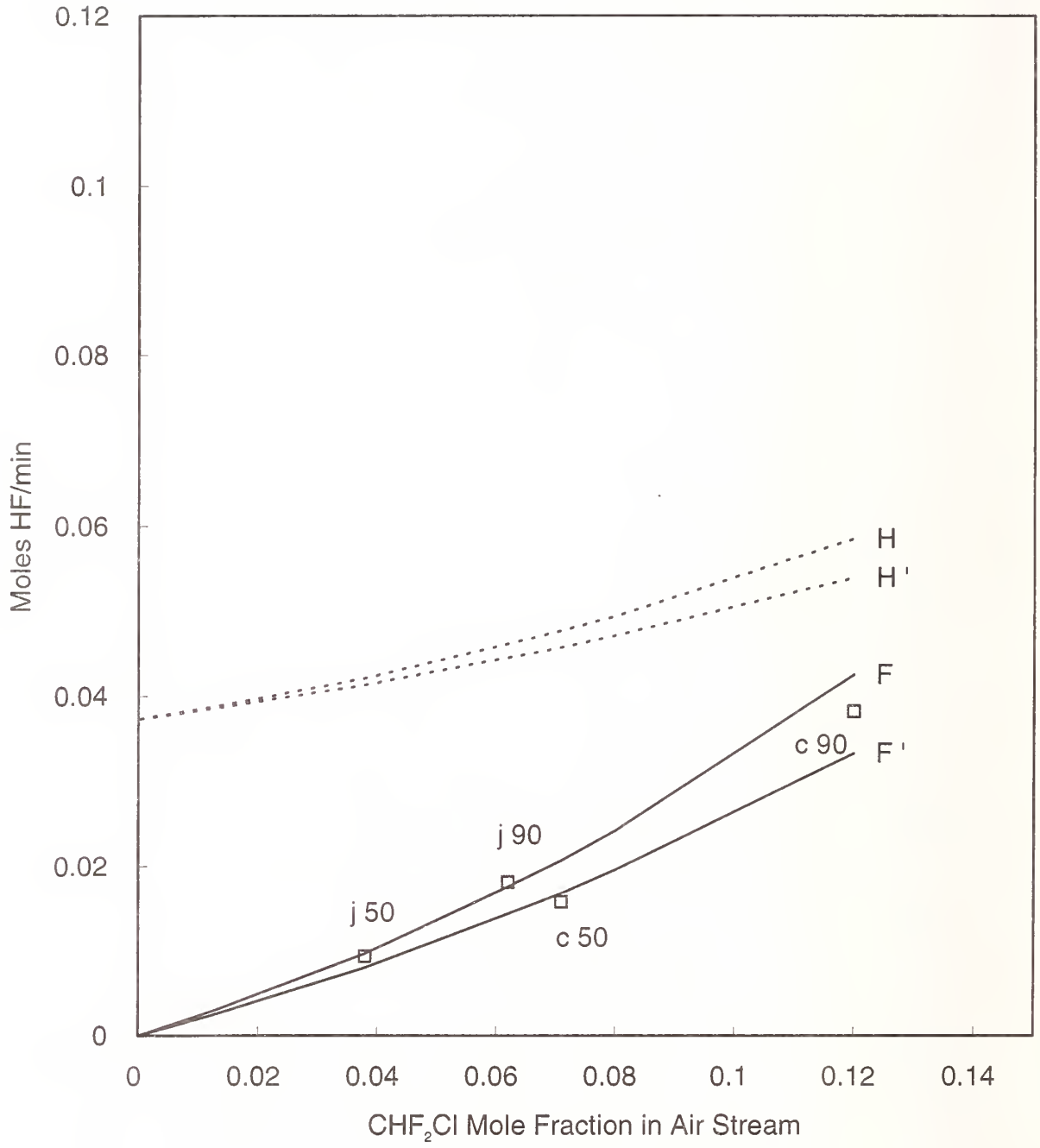

Figure 44. Measured HF production rates in co-flow propane-air diffusion flames inhibited by CHF_2Cl with estimated fluorine and hydrogen fluxes to the reaction zone.

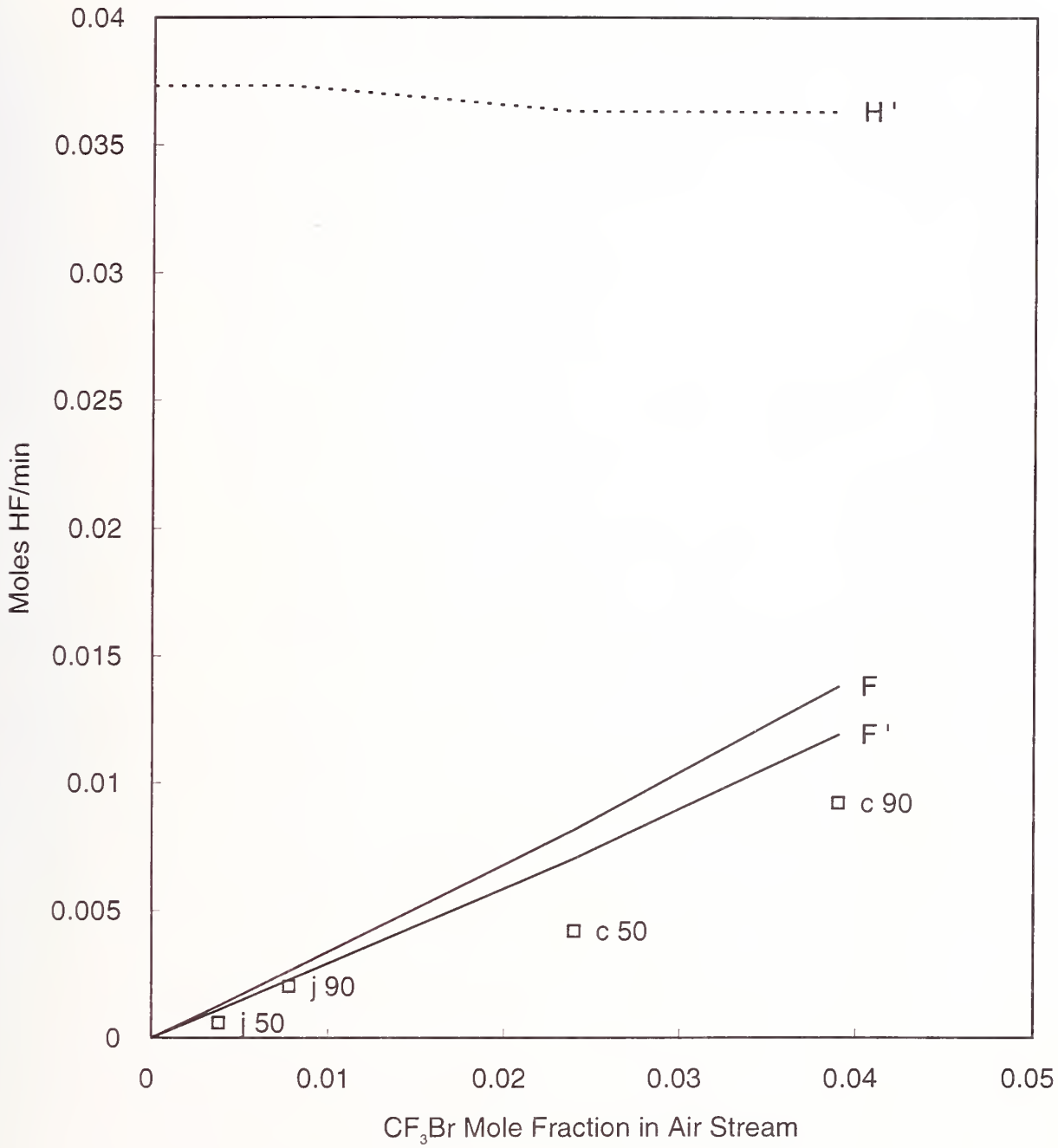

Figure 45. Measured HF production rates in co-flow propane-air diffusion flames inhibited by CF_3Br with estimated fluorine and hydrogen fluxes to the reaction zone.

Table 2. Extinction conditions for halon alternatives added to the air stream of co-flow propane-air cup burner and jet burner flames

Inhibitor	Extinction Concentration in Air (mole percent)	
	jet	cup
C_2F_6	3.8	9.4
C_3F_8	3.8	7.5
C_4F_{10}	3.2	5.0
C_4F_8	5.1	7.6
C_2HF_5	6.2	10.2
C_3HF_7	4.2	7.6
$C_2H_2F_4$	9.5	11.1
C_2HClF_4	4.2	8.6
$C_3H_2F_6$	4.0	7.2
CH_2F_2/C_2HF_5	15.5	15.2
CF_3Br	0.8	4.3
$CHClF_2$	6.7	13.8

HF production do not include chemical kinetic limitations; this is believed to the likely source of the discrepancy.

The experimental results are typically within 30 % of the prediction for the hydrogenated fluorocarbons, which is good considering the simplicity of the model. Perfluorinated agents produce HF at rates significantly less, up to 50 %, than predicted based on equilibrium thermodynamics. These agents are believed to react more slowly in the flame. A detailed understanding of the apparent chemical kinetic limitations to HF formation for the perfluorinated agents at all concentrations as well as for hydrofluorocarbons at high fluorine loading should be possible using a recently developed chemical kinetic mechanism for fluorine inhibition of hydrocarbon flames (Burgess *et al.*, 1994) together with a diffusion flame model. For the present analyses, however, the predicted acid gas formation in inhibited flames is based on equilibrium thermodynamics assuming that HF (not COF_2) is the source.

The measured HF for CF_3I is shown in Figure 46. For CF_3Br, the experimental results are about 30 % lower than the prediction, although both are significantly lower than for the HFCs. On the other hand, CF_3I makes about twice as much HF as is predicted by the model (which was not developed for CF_3I), or about three times as much HF as CF_3Br in these diffusion flames. The reasons for this is believed to be due to the relative weakness of the C-I bond in CF_3I. It is likely that CF_3I enters the hot region near or above the flame and undergoes thermal decomposition much more easily than the other agents tested, so that the net amount of HF formed is higher (and higher than predicted from the model which assumes no additional decomposition in the region above the flame).

10.8.3 Steady-state - Liquid Diffusion Flames. For the liquid-fueled cup burner experiments the consumption rate of the fuel is found to be a strong function of the inhibition concentration. Figure 47 shows the measured burning rate (g/s) for heptane as a function of the C_2HF_5 mole fraction in the air stream. The measured HF formation rates for liquid cup burner flames of heptane are shown in Figures 48 to 51 for C_2HF_5, C_3HF_7, $C_2H_2F_4$, and C_3F_8. As in Figures 34 to 46, the solid lines

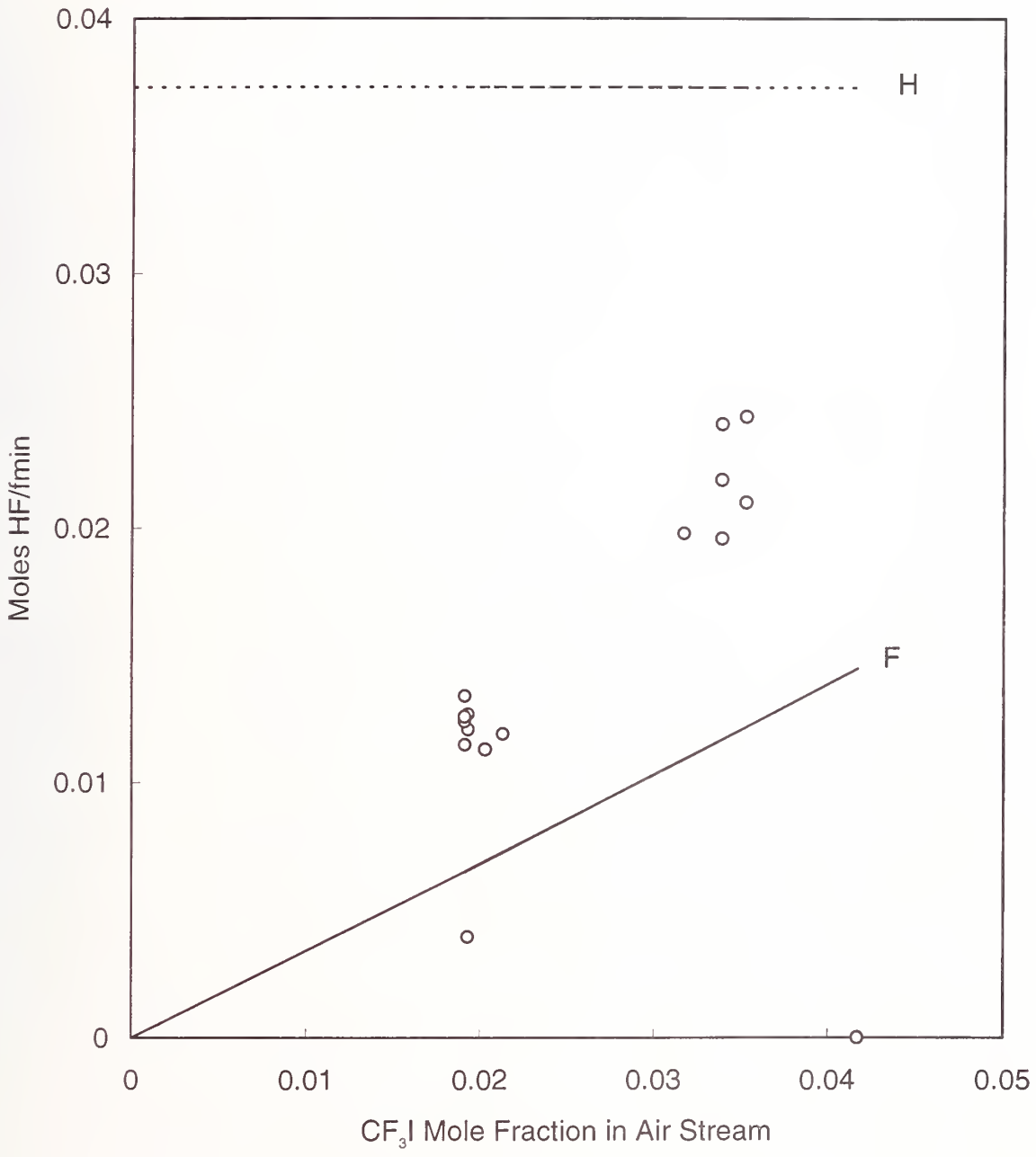

Figure 46. Measured HF production rates in co-flow propane-air diffusion flames inhibited by CF_3I with estimated fluorine and hydrogen fluxes to the reaction zone.

indicate the predicted flux of F and H into the flame. The measured HF production rate for these steady-state flames is within 16 % of the lower of the F or H flux for all of the inhibitors except C_2HF_5. For this agent, the measured HF production rate is about 30 % higher than the estimated hydrogen flux, and is well predicted by the fluorine flux. The reasons for this discrepancy are unclear, but may be related to details of the reaction mechanism for this particular agent and fuel. It is important to emphasize that the "hydrogen limit" is really a kinetic argument. As illustrated in Figure 27, when there is not enough hydrogen to form HF as an equilibrium product, the thermodynamically-favored product is COF_2. This species also appears in the bubbler as fluoride ion, and is thus indistinguishable from HF. Thus, when the hydrogen to fluorine ratio drops below unity, the argument is that the kinetics slow down such that the stages of inhibitor consumption which form either COF_2 or HF are impeded. Given the premixed modeling results described above, as well as the experimental results for inhibitor addition to premixed flames, this interpretation seems appropriate.

Nonetheless, it is remarkable that the rather simple stoichiometric model is still able to predict the HF formation within 30 % for this liquid pool flame when the agent is present at 90 % of the extinction value and the heat feedback and kinetics are affected to such an extent that the burning rate is reduced by about a factor of 2.5. This lends support for the basic assumptions in the model that the products are controlled primarily by the quantities of hydrogen and fluorine in the flame, and that these are controlled primarily by the fuel type and consumption rate and the inhibitor type and mole fraction in the air stream. The final assumption of equal characteristic flame height for both fuel and inhibitor consumption also appears to be good.

10.8.4 Transient-state - Gaseous Diffusion Flames. As described above, HF formation in the propane-air cup burner flames was also measured when the inhibitor was added in a transient fashion, rather than in steady-state, and the flames were extinguished. The concentration of inhibitor varied linearly from zero to 125 % of the extinction concentration, and the injection rate of inhibitor was varied to produce flame-extinguishment times of 5 to 18 seconds. Experiments were conducted for the agents C_2HF_5, C_3HF_7, C_3F_8.

The results are shown in Figures 52 - 54 respectively, where the total mass of F- produced during the extinction event is plotted as a function of the extinction time. Also indicated in the figures are the predicted HF formed using the stoichiometric model assuming equilibrium products (solid lines), and using the model in which the steady-state HF production rates are determined from empirically determined deviations from full equilibrium based on the steady-state results. As the figures show, in either case, the model is able to predict the results within the experimental scatter. The uncertainty in Figures 52 to 54 is essentially shown by the experimental variation for similar conditions. Most of this is variation is believed to occur from differences in the mixing of product gases with co-flowing air in the chimney prior to sampling. While the degree of mixing varies from run to run, the magnitude of the fluctuations are difficult to specify due to the turbulent nature. The relatively short experiment times (only a factor of three of four greater than the mixing times) accentuates the problem. Unfortunately, signal averaging (which would be achieved through longer experimental times) is not possible as in the steady-state experiments.

10.9 HF Production in Larger Scale Tests

The stoichiometric model developed above from consideration of laboratory flames allows an estimation of the HF generation based on the fuel consumption rate and transport of the agent in the flame. However, the quantities of acid gases formed in a large-scale suppressed fire will depend upon

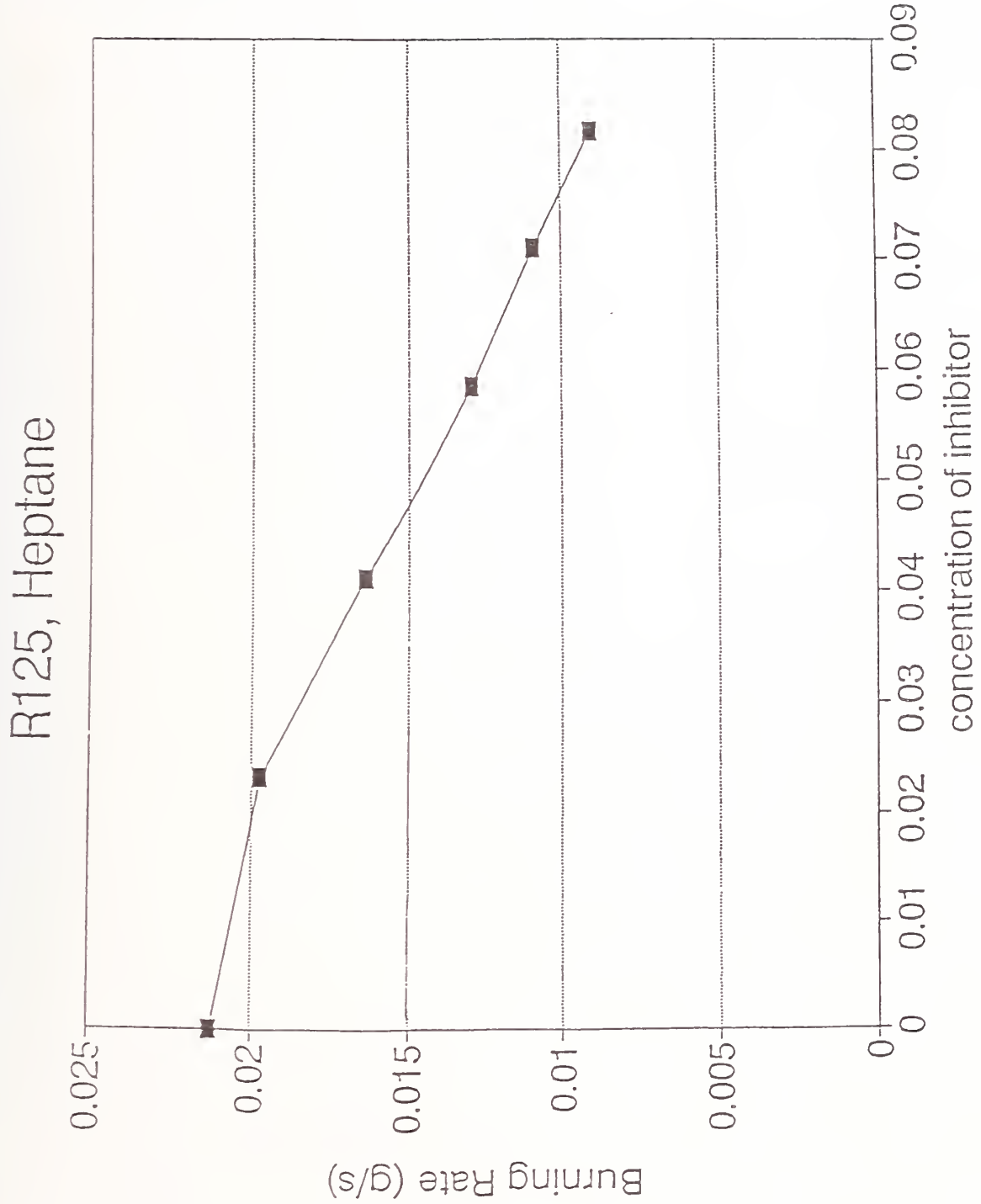

Figure 47. Burning rate of heptane in cup burner as a function of C_2HF_5 mole fraction in the air stream.

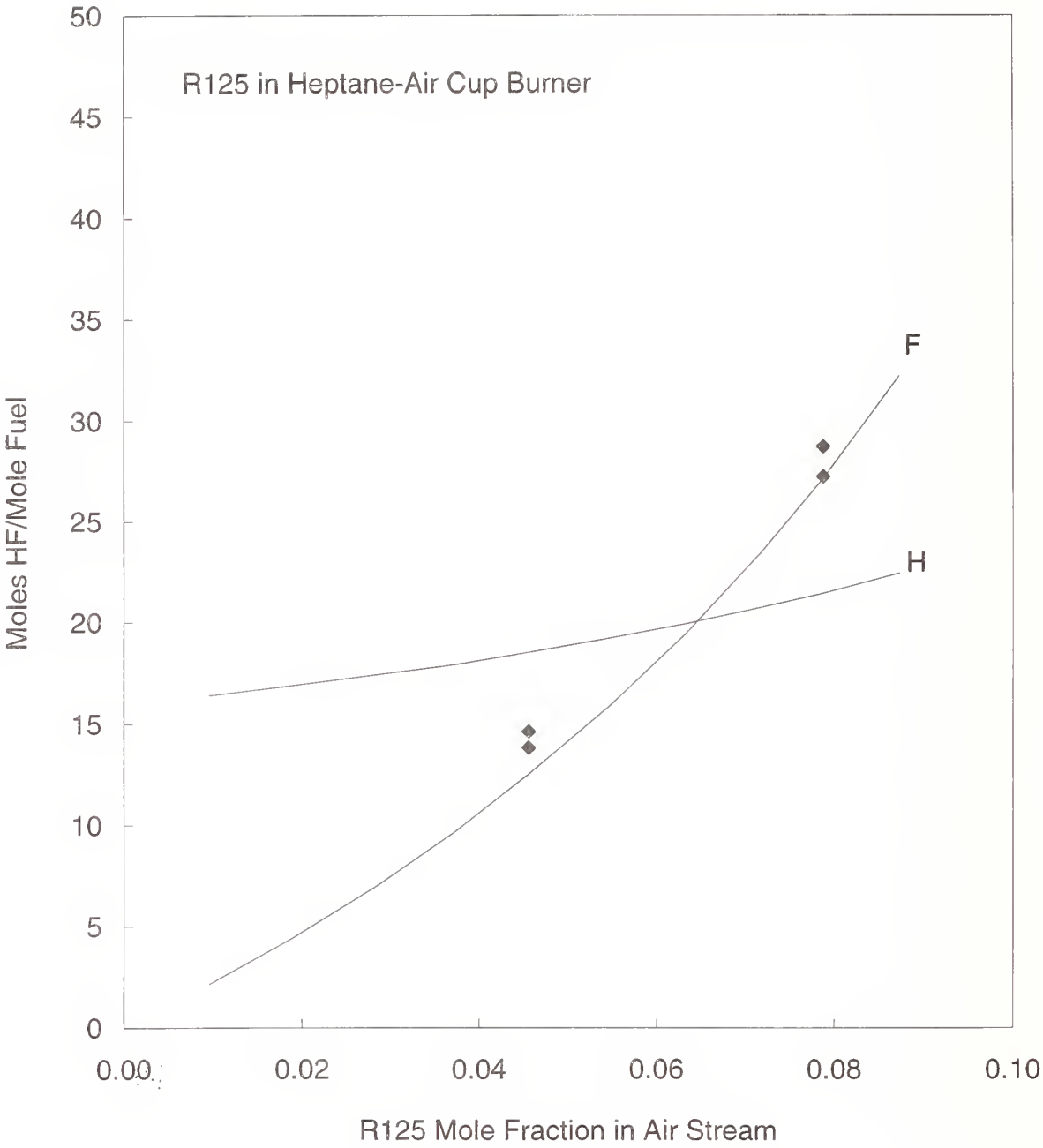

Figure 48. Measured HF production rates in co-flow heptane-air diffusion flames inhibited by C_2HF_5 with estimated fluorine and hydrogen fluxes to the reaction zone.

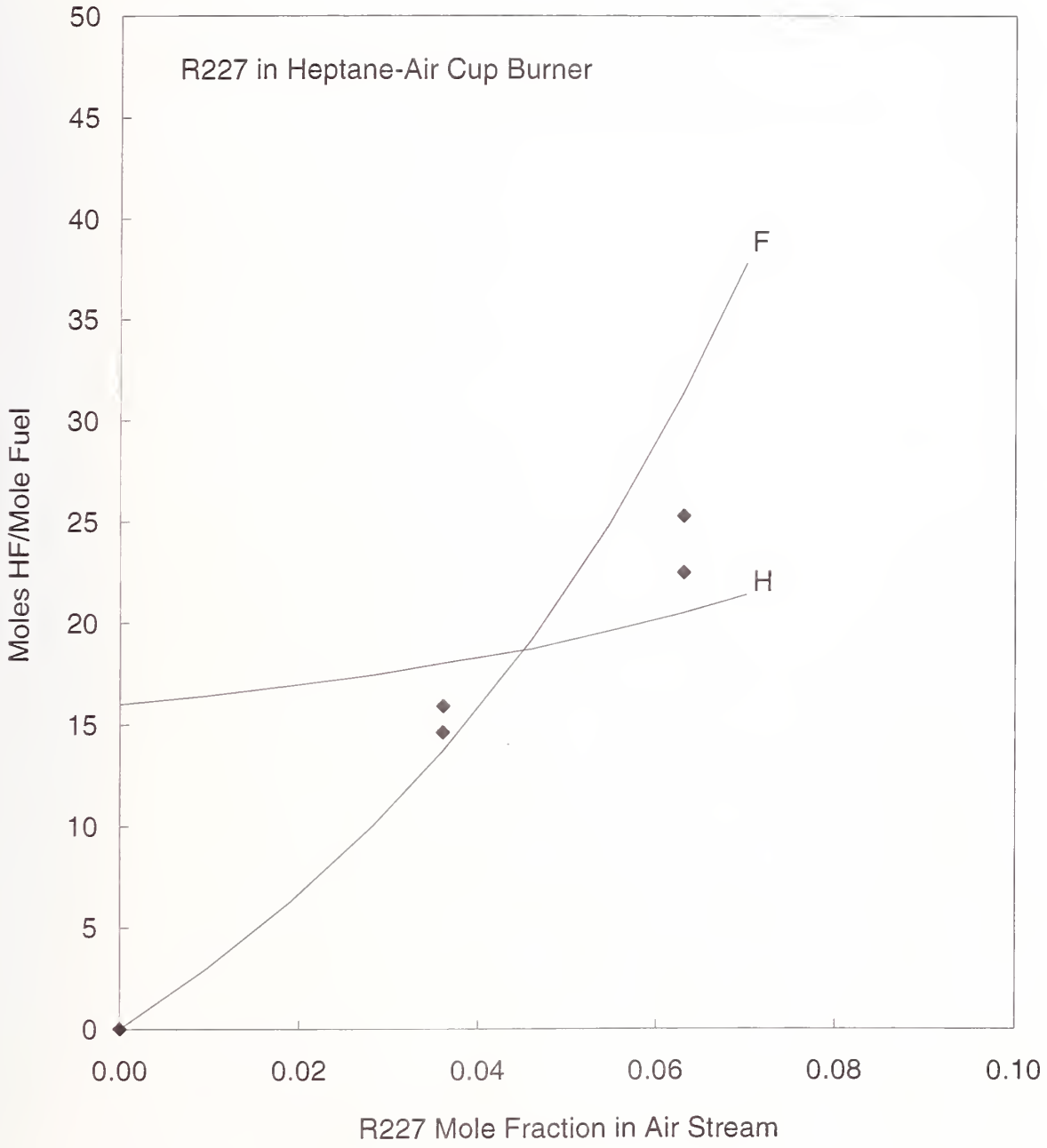

Figure 49. Measured HF production rates in co-flow heptane-air diffusion flames inhibited by C_3HF_7 with estimated fluorine and hydrogen fluxes to the reaction zone.

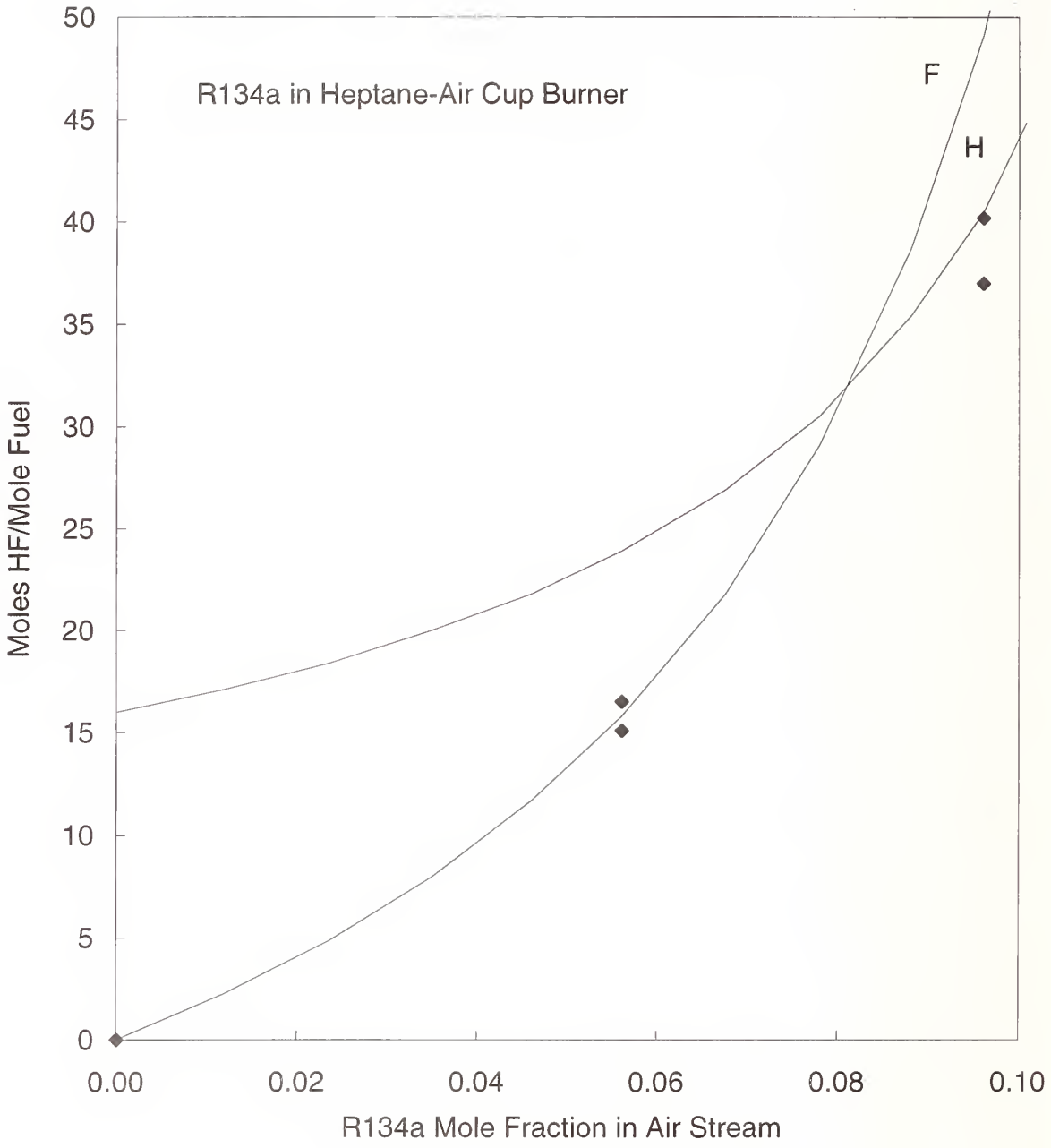

Figure 50. Measured HF production rates in co-flow heptane-air diffusion flames inhibited by $C_2H_2F_4$ with estimated fluorine and hydrogen fluxes to the reaction zone.

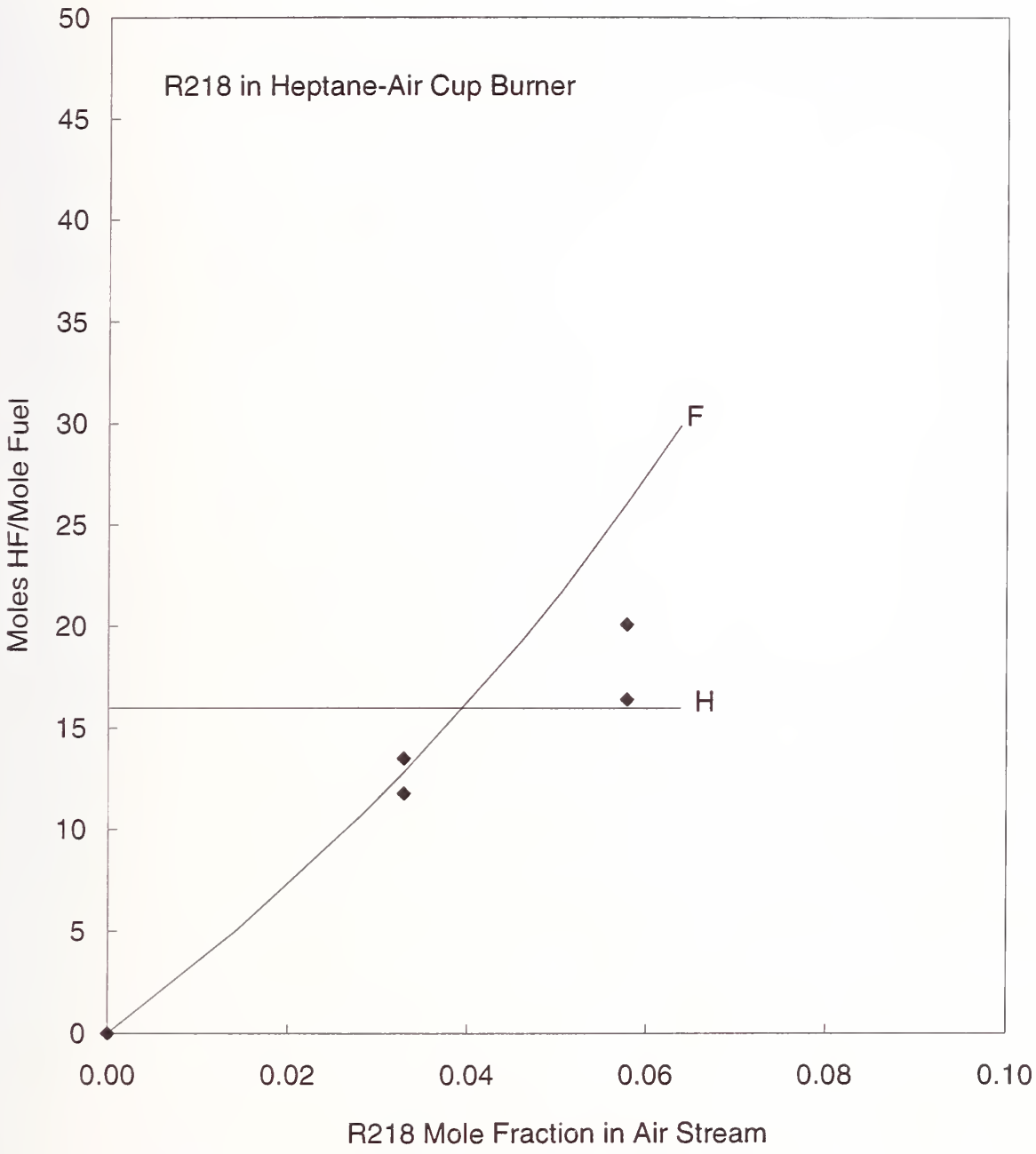

Figure 51. Measured HF production rates in co-flow heptane-air diffusion flames inhibited by C_3F_8 with estimated fluorine and hydrogen fluxes to the reaction zone.

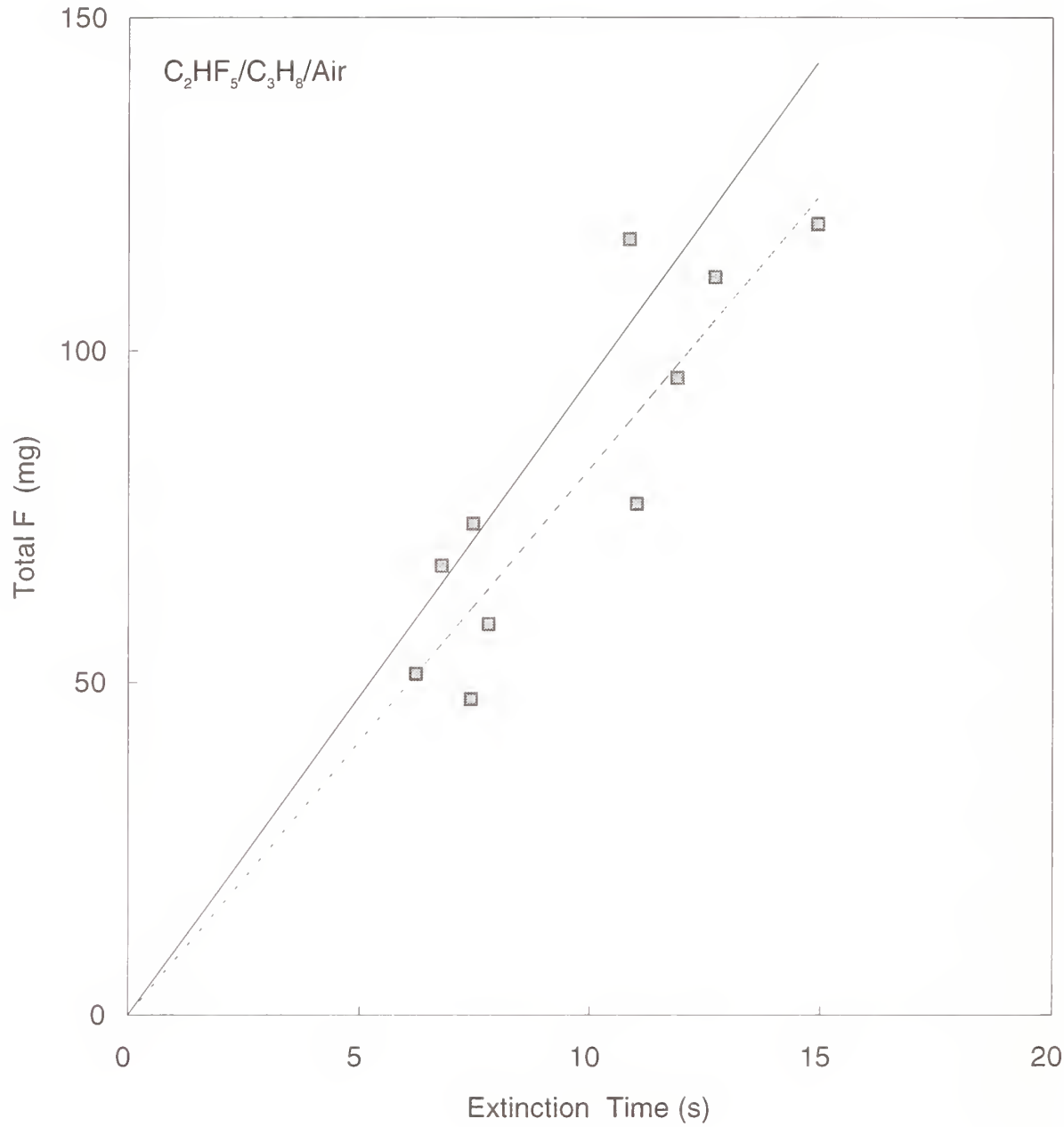

Figure 52. Total fluoride produced (points) during suppression of a cup burner propane-air diffusion flame for various extinction times, together with model predictions (solid line: calculations; dotted line: steady-state results).

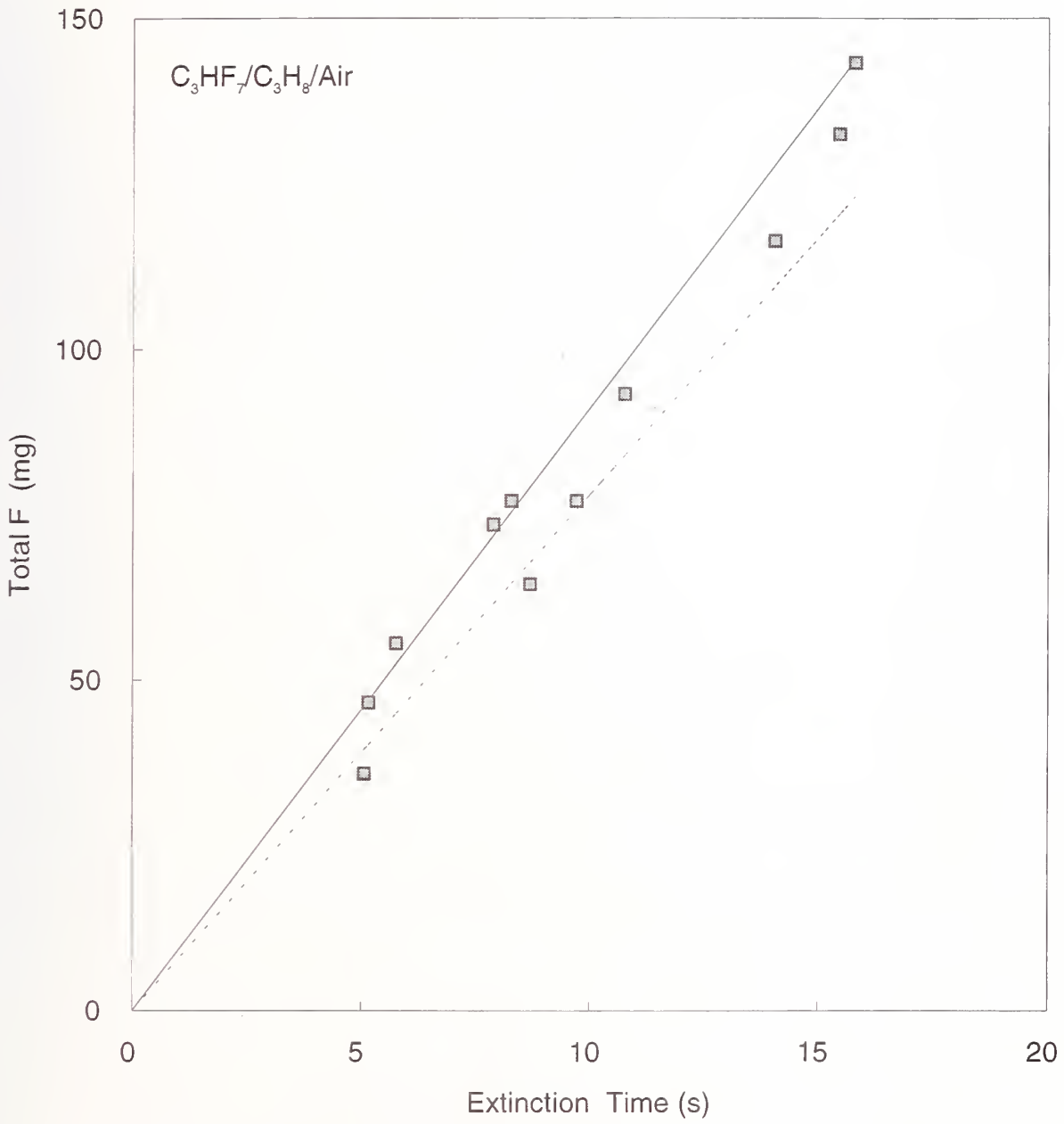

Figure 53. Total fluoride produced (points) during suppression of a cup burner propane-air diffusion flame for various extinction times, together with model predictions (solid line: calculations; dotted line: steady-state results).

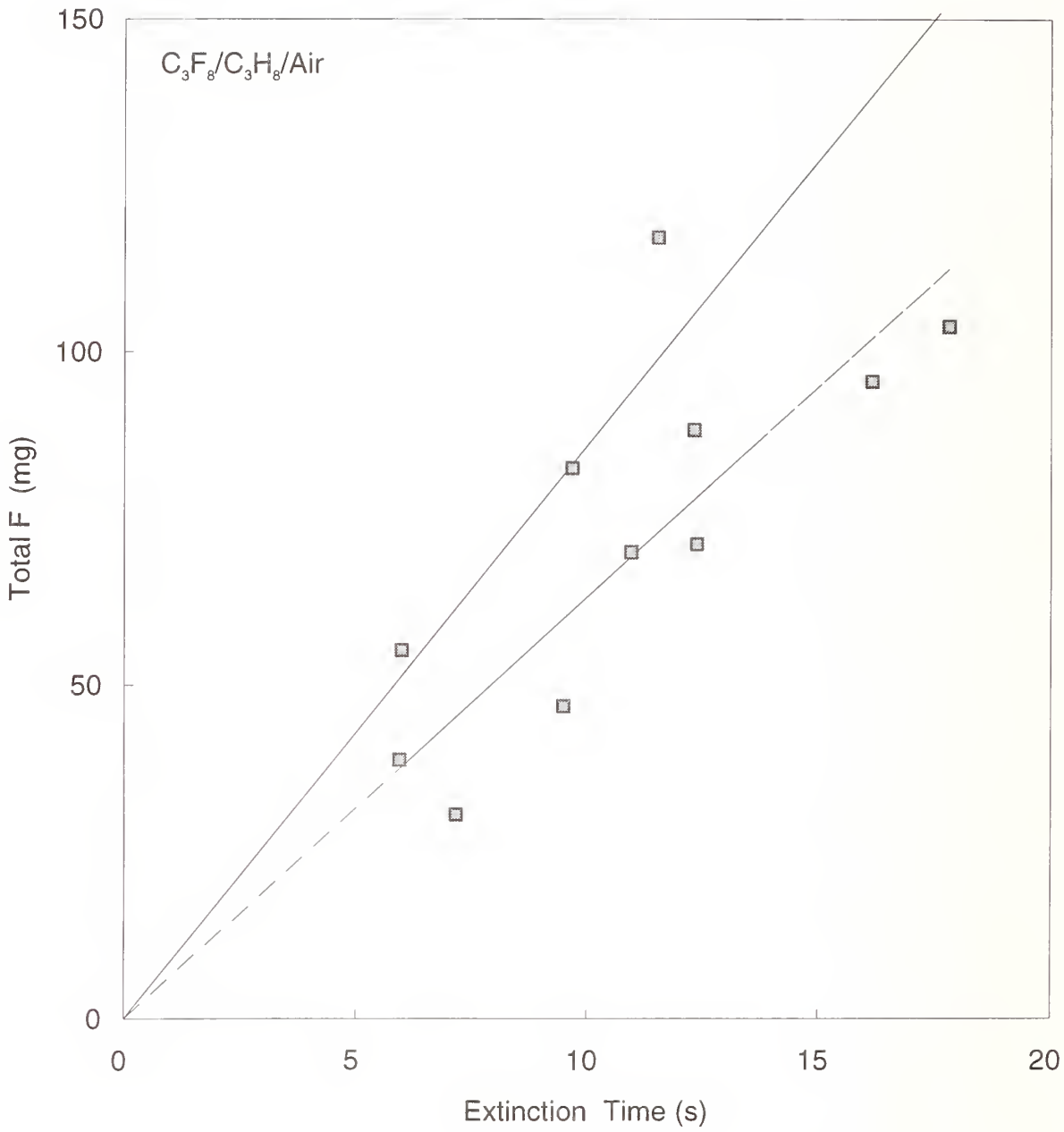

Figure 54. Total fluoride produced (points) during suppression of a cup burner propane-air diffusion flame for various extinction times, together with model predictions (solid line: calculations; dotted line: steady-state results).

the properties of the fire itself, characteristics of the agent delivery system, and fate of the acid gases after their formation. The fire is essentially the source term for acid gas formation, since high temperatures are required for rapid agent decomposition. The amount of HF formed will depend upon the fire size, fuel type, and flame type (premixed or diffusion). In addition, ease of extinguishment of the fire will be crucial, since for a given inhibitor, different fire types will extinguish at different concentrations for the same inhibitor. An additional feature of larger scale fires is the presence of hot surfaces. These could provide a high enough local temperature to cause thermal decomposition of the inhibitor molecule, and possibly result in HF formation. Given the apparent lack of decomposition of the inhibitor in the hot post-combustion region above the laboratory diffusion flames, this is not believe to be a major source for HF formation.

Flame extinguishment ease will be affected by the stabilization mechanisms, the flow field, and sources of re-ignition. The characteristics of the agent delivery system which will affect the quantity of HF formed include the agent type and the concentration at which it extinguishes the flame. The rate of introduction of the agent is important, as are the mixing rates in the protected volume and the delivery rate to the stabilization region of the flame. Finally, after formation of HF by the fire, the dispersion of the acid gas throughout the protected space and on surfaces will affect its peak and average concentrations.

The space volume as compared to the fire size, the ventilation rate, and the presence of surfaces for acid gas condensation will influence the HF concentrations, which will vary both spatially and temporally. The rate of air mixing in the protected space may have a large effect on the final measured HF concentrations. Both the characteristics of the agent delivery to the fire and the fate of the HF after fire suppression - while greatly affecting the quantities of HF formed, may vary widely for different applications. Because this potentially wide variation, they are difficult to specify. Nonetheless, it is of great interest to attempt to predict HF formation in larger-scale tests using the present model.

10.9.1 Comparison with Predictions. Extensive intermediate-scale tests of HF production by CF_3Br and halon alternatives have been reported by Sheinson *et al.*, (1994). In order to further test the present model, we have attempted to predict the HF formed in their experiments. The experiments consisted of 0.23 and 1.1 m^2 heptane pool fires extinguished by CF_3Br, CHF_3, C_2HF_5, and C_4F_{10}. The agents were injected at varying rates and to different final inhibitor concentrations in the 56 m^3 protected space. The reported HF concentrations represent the peak measured values at a single fixed location. The results of their experiments (for the 0.23 m^2 pools) are shown in Figure 55, which provides the measured HF mole fraction (in ppmv) as a function of the fire out time for the four agents. Although the experimental data represent different agent injection rates and final design concentrations of inhibitor, we have included all of the data in a single plot.

The large scatter in the experimental results probably occurs from the effects of these additional parameters. Of these three parameters, injection rate, design concentration, fire-out time, we believe the latter to be most important in determining the HF production and have made it the independent parameter. The results of the stoichiometric model predictions based on achievement of full equilibrium are given by the solid line. Each of the four lines in the figure refers to the predicted HF for one of the agents CF_3Br, CHF_3, C_2HF_5, and C_4F_{10}; the symbol at the end of the line serves to identify the line with the proper data. In these calculations, the model predicts the total mass of HF produced. In order to allow a comparison, it is necessary to assume a spatial distribution of HF. Although there will be gradients of HF concentration in the room, uniform distribution has been assumed. As the figure shows, the predicted HF concentration agrees well with the experimental results. Having gained confidence in the ability of the model to predict some experimental results, we now proceed to investigate the effect of several parameters on HF production in suppressed fires.

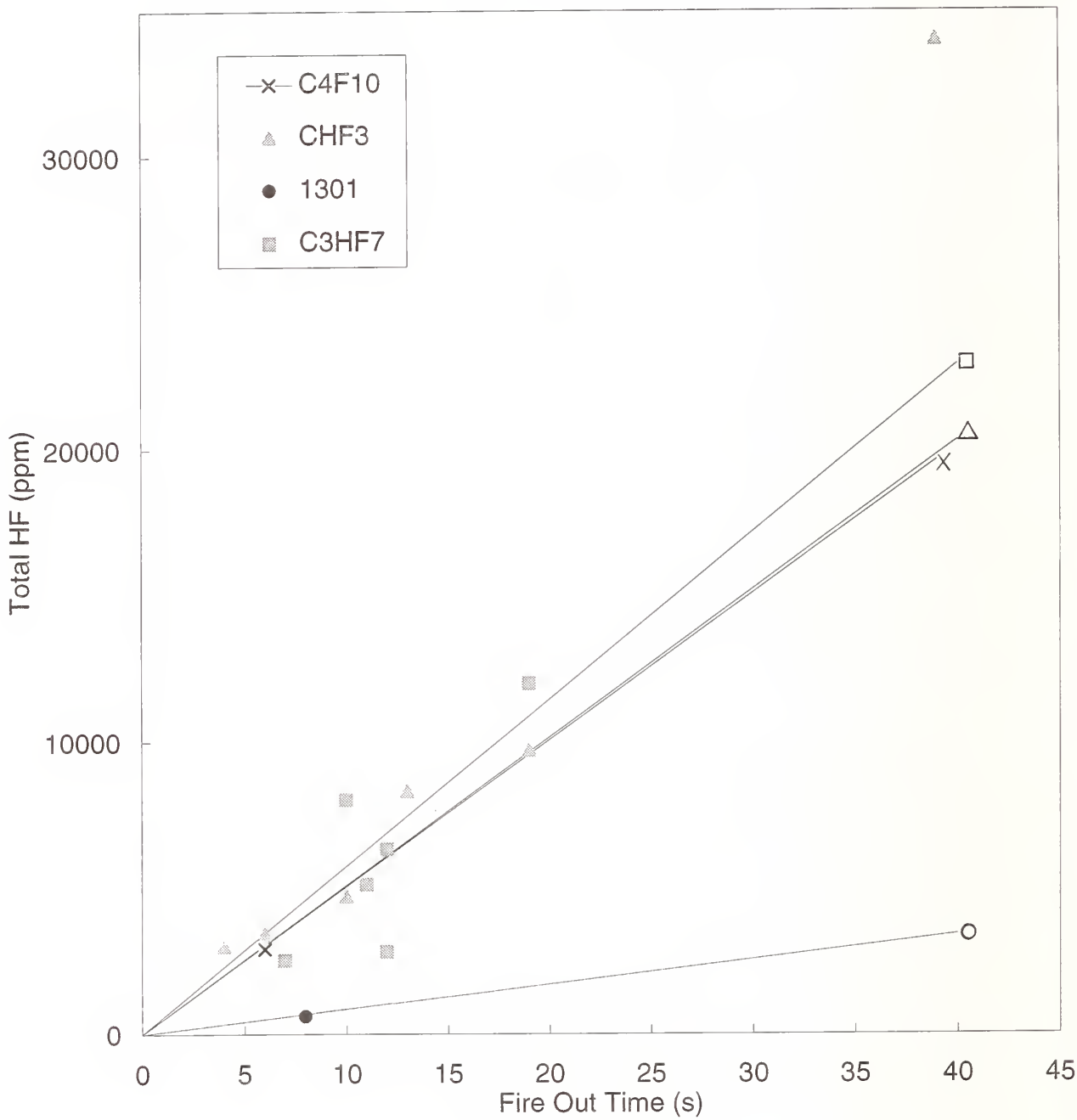

Figure 55. Experimental data of Sheinson *et al.* for intermediate-scale tests of HF production in heptane pool fires, with the model predictions for CF_3Br, CF_3H, C_2HF_5, and C_4F_{10}.

10.10 Parametric Analysis

The effect of various parameters on the production of HF can be examined using the stoichiometric model. First, it should be emphasized that in the present model, the HF generation rate is linearly proportional to the fuel consumption rate. Hence, in all subsequent figures in this section, the HF generation rate is normalized by the fuel consumption rate, so that this parameter need not be specified for each figure. Analyses are presented for the six inhibitors C_2HF_5, C_3HF_7, $C_2H_2F_4$, C_2F_6, C_3F_8, and CF_3Br as well as the four hydrocarbon fuels methane, propane, heptane, and JP8.

It has been assumed in these calculations that the extinction occurs at the cup burner extinction concentration for the particular fuel with dry air. Clearly, extinction at an inhibitor concentration larger or smaller than the cup burner value will affect the generation of HF; this is treated in a final figure.

10.10.1 Results. In Figures 56, 57, and 58 we examine the influence of inhibitor type, inhibitor concentration, fuel type, and the presence of water vapor in the air on the HF generation rate, all for steady-state flames. These calculations refer to a condition where the agent is added at a concentration lower than the extinction concentration, so that the flame continues to burn, but produces copious amounts of HF. These figures are shown to illustrate the influence of the fuel and agent type, inhibitor concentration, and moisture content of the air on steady flames. The results will be extended to transiently suppressed fires in subsequent figures.

Figure 56 shows the calculated steady-state HF production rate (g-HF/g-fuel) as a function of the agent mole fraction in the air stream for the one-carbon suppressants CF_3Br and CHF_3, the two-carbon suppressants C_2F_6, C_2HF_5, and $C_2H_2F_4$, and the three-carbon suppressants C_3HF_7 and C_3F_8. The results are calculated for heptane, and the calculations are performed for dry air. As the figure shows, the each curve has a distinctive change in slope (which occurs at the inhibitor concentration where the flux of fluorine into the flame equals that of hydrogen). The curves are grouped according to the number of carbon atoms in the inhibitor, which correlates with the number of fluorines and the molecular weight, both of which influence the flux of fluorine into the flame, and hence the HF generation rate. Surprisingly, for agents which extinguish the flame at approximately the same concentration, for example C_3F_8 and C_3HF_7, the agent with more hydrogen atoms is predicted to make more HF. This occurs because above a certain concentration (about 3.5 % agent in the figure), the HF production is limited by hydrogen, not fluorine. The agent CF_3Br makes less HF because at a given mole fraction, the molecule carries fewer fluorine atoms into the flame than the larger halocarbons, and because it puts the flame out at a much lower concentration.

Each curve is truncated at the extinction concentration in a heptane cup burner flame for that inhibitor. The area under each curve from zero inhibitor up to the extinction concentration represents the total HF formed for an extinguished flame (in g-HF/g-fuel consumed). If the fuel consumption rate is larger or the inhibitor injection rate is slower, the total fuel consumed during the extinction event is larger, and the HF formed is proportionally greater.

The effect of water vapor in the air stream is indicated in Figure 57 which shows the steady-state production rate of HF as a function of inhibitor mole fraction for CF_3Br, C_3F_8, and C_2HF_5. Curves are shown for dry air (dotted lines) and for air with 2.3 mole percent water vapor (solid lines), corresponding to 100 % R.H. at 25 °C, and assuming that wet and dry flames extinguish at the same concentration. The effect of water vapor is small when the agent concentration is low, since under these conditions, the limitation on the amount of HF is the fluorine flux into the flame, not the

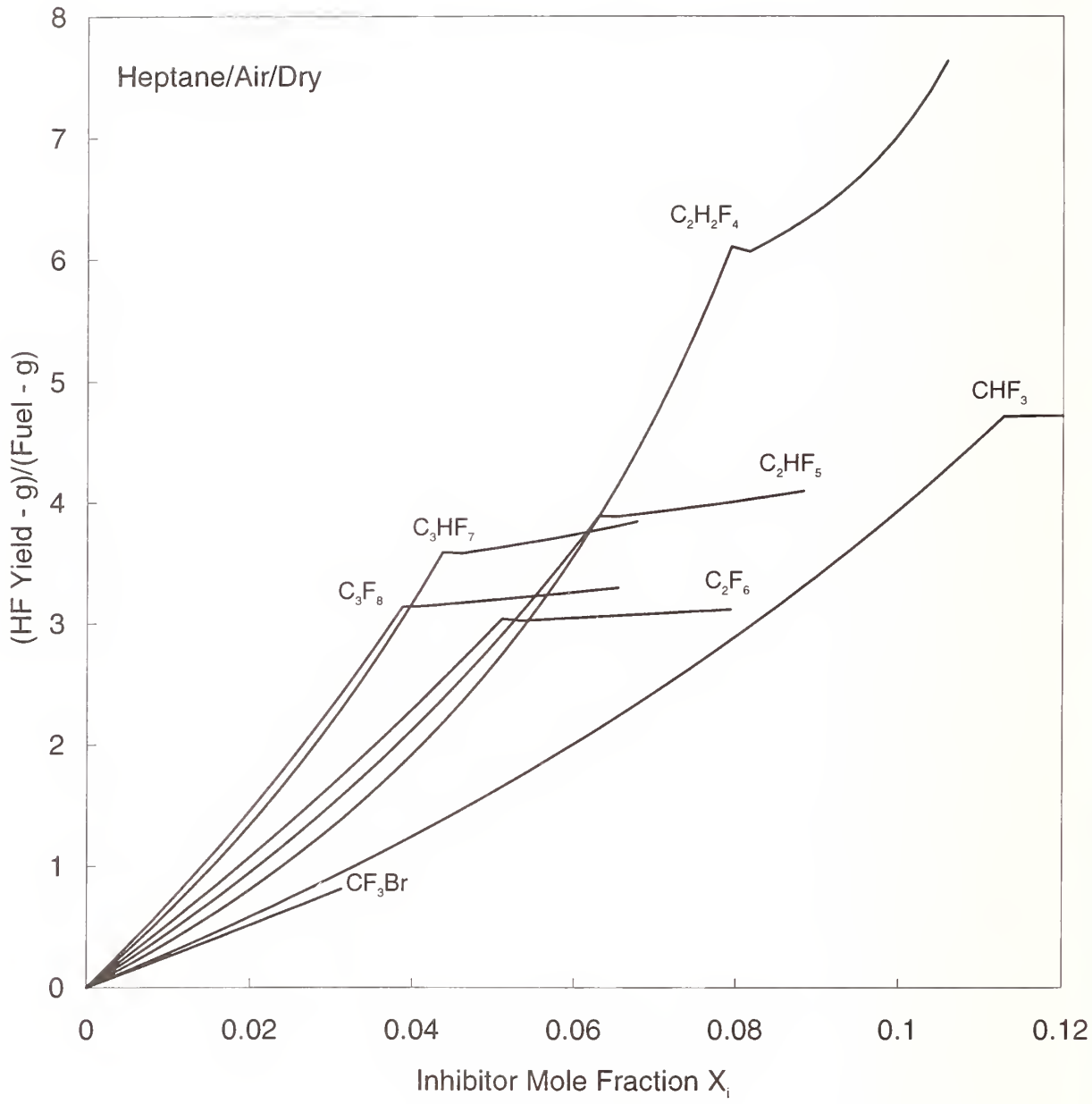

Figure 56. Stoichiometric model predictions of the HF formed in heptane-air flames under steady-state with CHF_3, C_2HF_5, $C_2H_2F_4$, C_3HF_7, C_2F_6, C_3F_8, and CF_3Br.

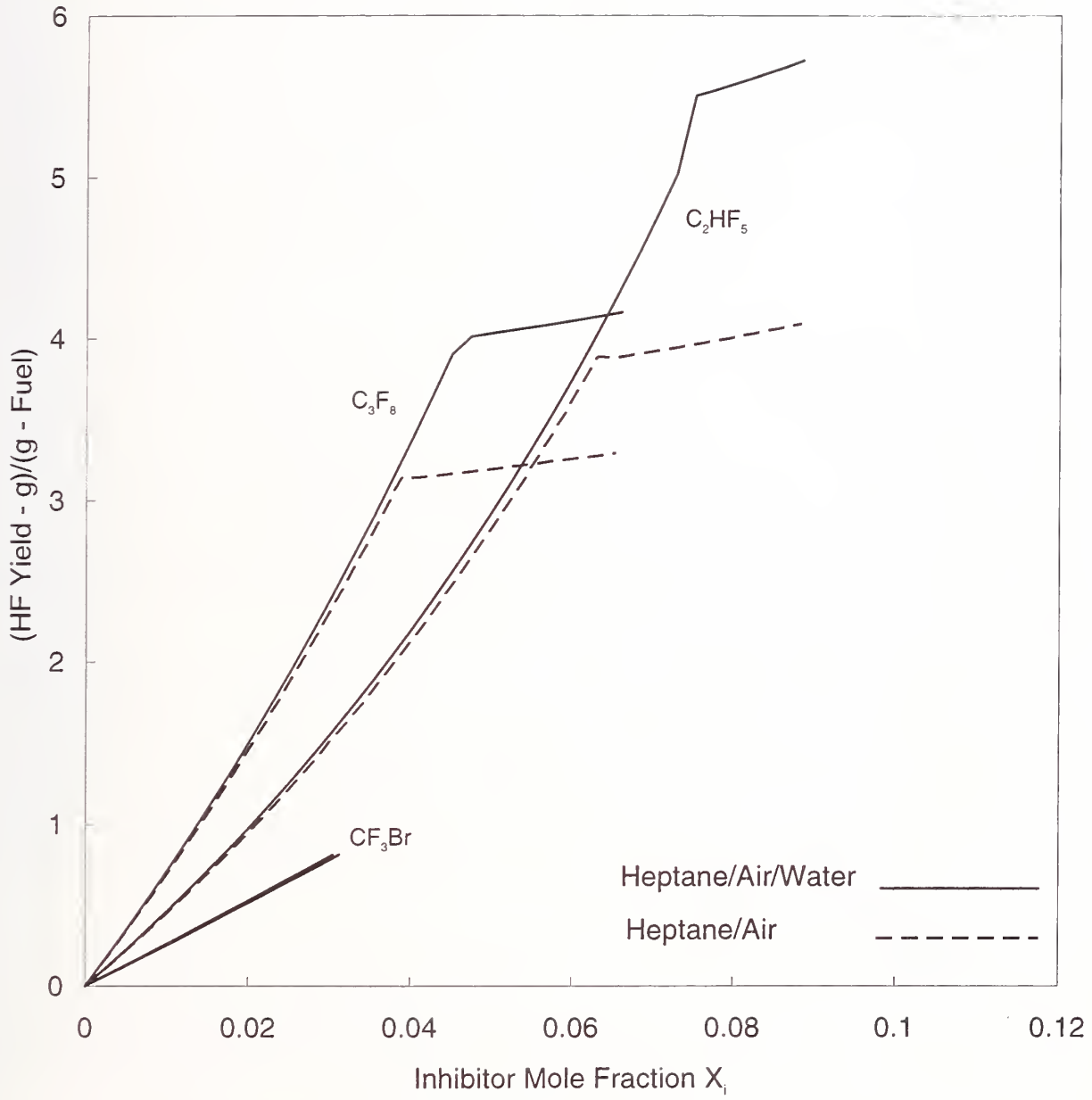

Figure 57. Stoichiometric model predictions of HF formed in heptane-air flames at steady-state with C_2HF_5, C_3F_8, and CF_3Br. Dotted lines: dry air; solid lines: wet air.

hydrogen flux. At high inhibitor loading, however, there becomes more fluorine than hydrogen in the flame, and any additional hydrogen from water vapor can increase the production rate of HF.

Figure 58 illustrates the effect of fuel type on the steady-state HF production in flames inhibited by C_2HF_5 by showing curves for JP8, heptane (C_7H_{16}), propane (C_3H_8), and methane (CH_4). The different fuels have a different carbon to hydrogen ratio, which affects the HF production rate, since the fuel is the major source of hydrogen in the flame, and hydrogen is necessary for the efficient production of HF (the kinetic rates get much slower in hydrogen-starved flames as described above). The amount of HF formed is lowest for JP8, followed by heptane, propane and methane. Note that the amount of HF formed in transient flames is represented by the area under the curves in Figure 59, so that the differences in HF formation between the fuel types can be quite large.

As discussed above in the description of the model for HF formation, transiently suppressed fires produce HF according to the area under the steady-state generation curve as in Figure 56. For a given inhibitor, fuel type, water vapor concentration, and extinction condition, the area under the curve will be a constant.

Two additional factors can affect the total quantity of HF formed: 1) the fuel consumption rate, and 2) the time for the fire to be extinguished. The first of these is obvious since the HF production rate is normalized by the fuel consumption rate. Fuel consumption is the driving force for transport of inhibitor and air to the reaction zone, so that increased fuel consumption increases HF production proportionally. The effect of the inhibitor injection rate (or alternatively, the fire out time, since they are strongly related) is to change the fuel consumption. That is, if the flame is extinguished slowly, more HF is produced because during the longer time, more fuel is consumed.

Figure 59 indicates the total HF produced during extinguishment of a heptane air flame by CF_3Br, CHF_3, C_3F_8, C_3HF_7, C_2HF_5, and $C_2H_2F_4$ in dry air. As the figure shows, the quantity of HF produced in linearly proportional to the extinction time.

Finally, the effect of extinguishment at lower inhibitor concentrations is described. In the above figures, the extinction condition of the fire was assumed to be equal to the cup burner extinction value for the agent and fuel. If the flame is more easily extinguished, less acid gas will be produced during extinction. This is because if a flame extinguishes more easily, the curves in Figures 56 will be integrated up to a lower concentration, and the area under the curve (which represents the total HF produced) will be proportionally less. This is illustrated in Figure 60 which shows the quantity of HF produced by heptane-air flames with dry air extinguished by CHF_3, CF_3Br, C_2HF_5, C_3HF_7, and C_3F_8 as a function of the flame's extinction concentration for a constant fire out time (10 s). As the figure illustrates, flames which extinguish at lower concentrations of inhibitor produce less HF, in an approximately linear fashion.

It should be emphasized that the analyses demonstrated above examine the effects of several parameters on the HF source, the fire, under the assumption of thermodynamic equilibrium. As shown previously in Figures 34 - 38 for propane flames, there can be significantly less HF formed than predicted by chemical equilibrium, although for heptane, the agreement is excellent. Consequently, the predictions described here are upper limit estimates probably with about 30 % of actual results.

10.10.2 Conclusions. The following conclusions can be drawn based on the diffusion flame experiments, modeling, and parametric analysis:

1. The stoichiometric model, based on relatively simple but fundamental assumptions, is a useful tool for understanding HF formation in suppressed fires. The predictions of the model provide good estimates of the upper limit for formation of HF, and are valid for both steady-state and transient modes of inhibition.

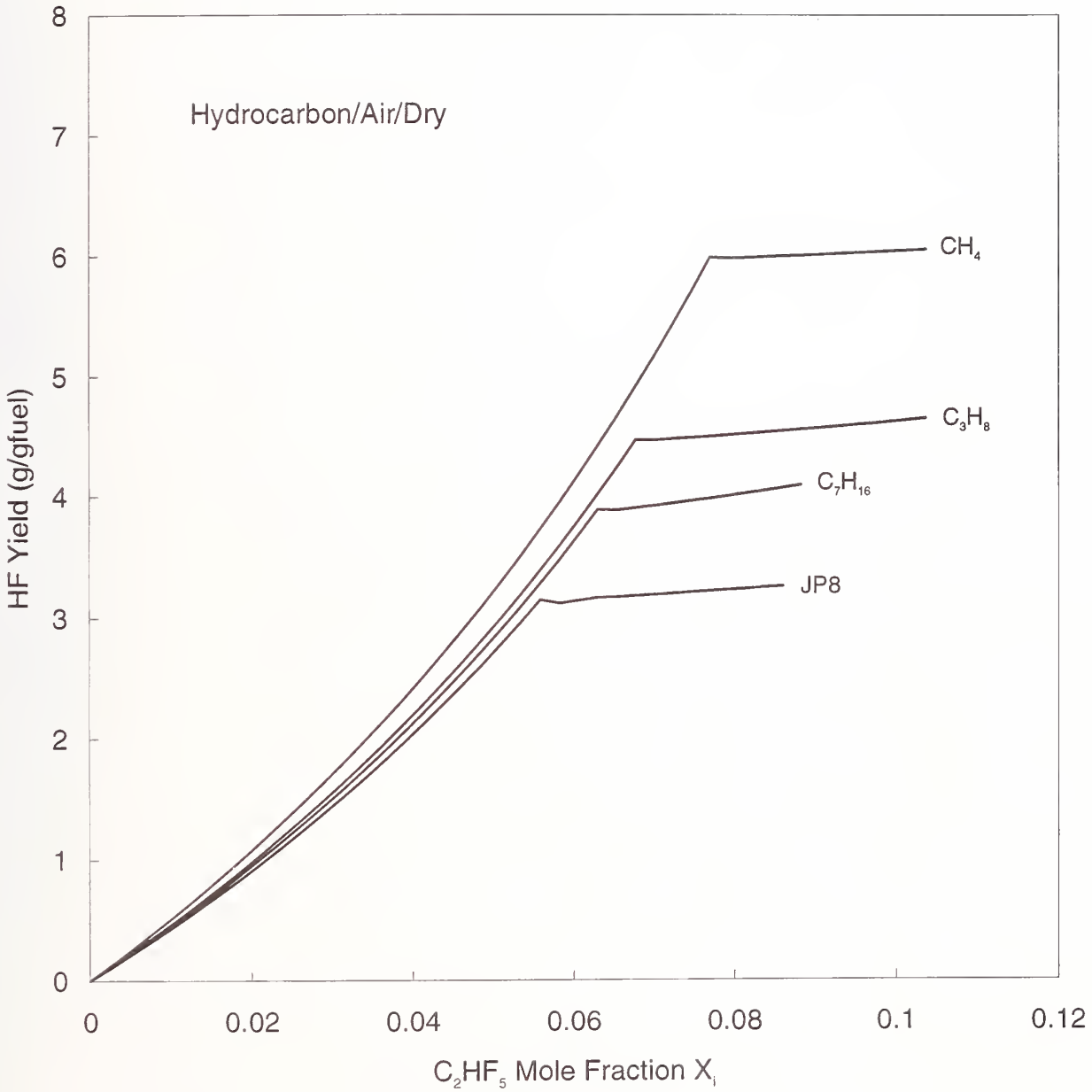

Figure 58. Stoichiometric model predictions of HF formed in heptane-air flames at steady-state with C_2HF_5 added to air stream with various fuels (CH_4, C_3H_8, C_7H_{16}, and JP8).

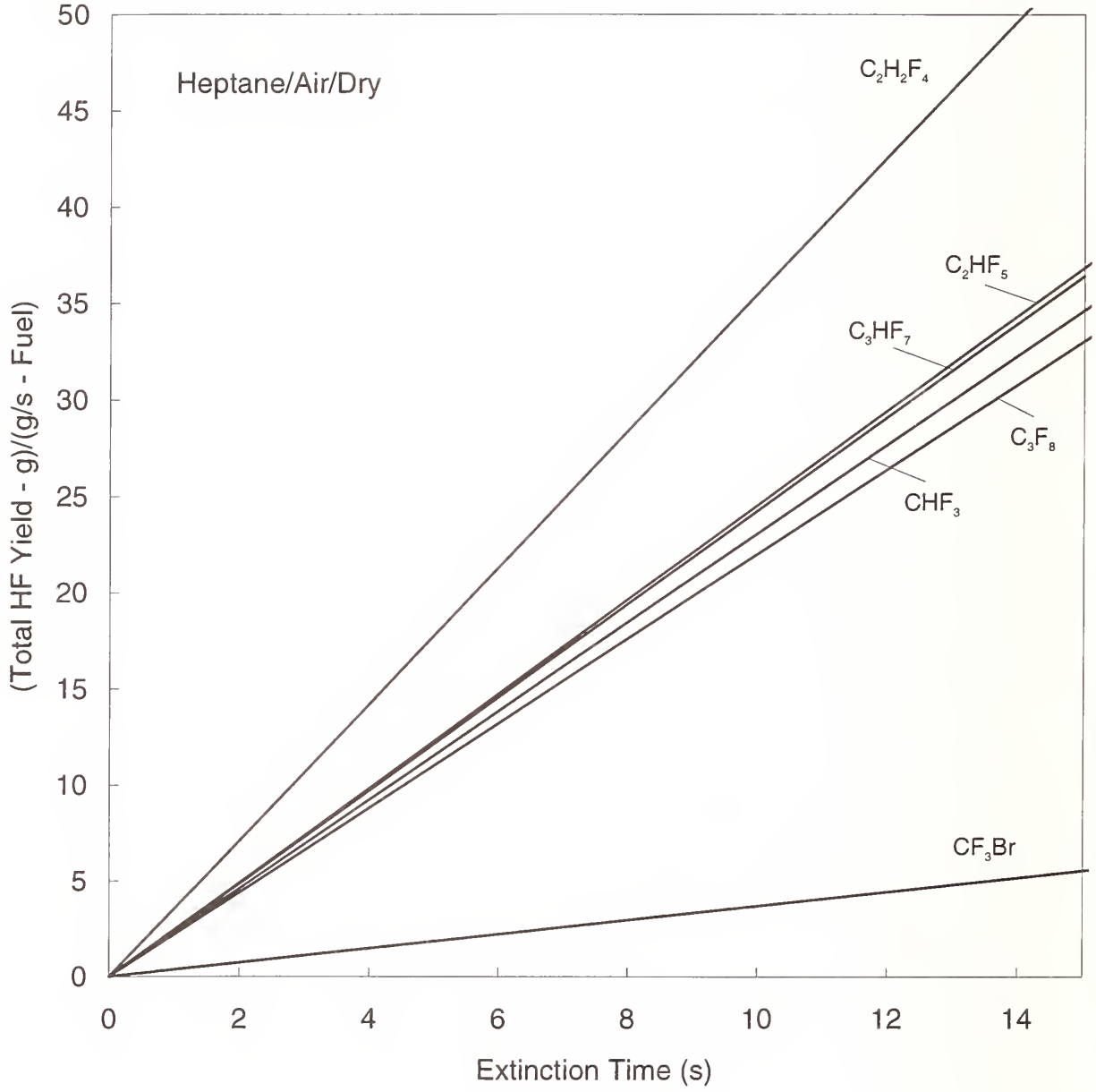

Figure 59. Total HF predicted during extinguishment of heptane-air flames for CHF_3, C_2HF_5, C_3HF_7, C_3F_8, CF_3Br versus extinction time.

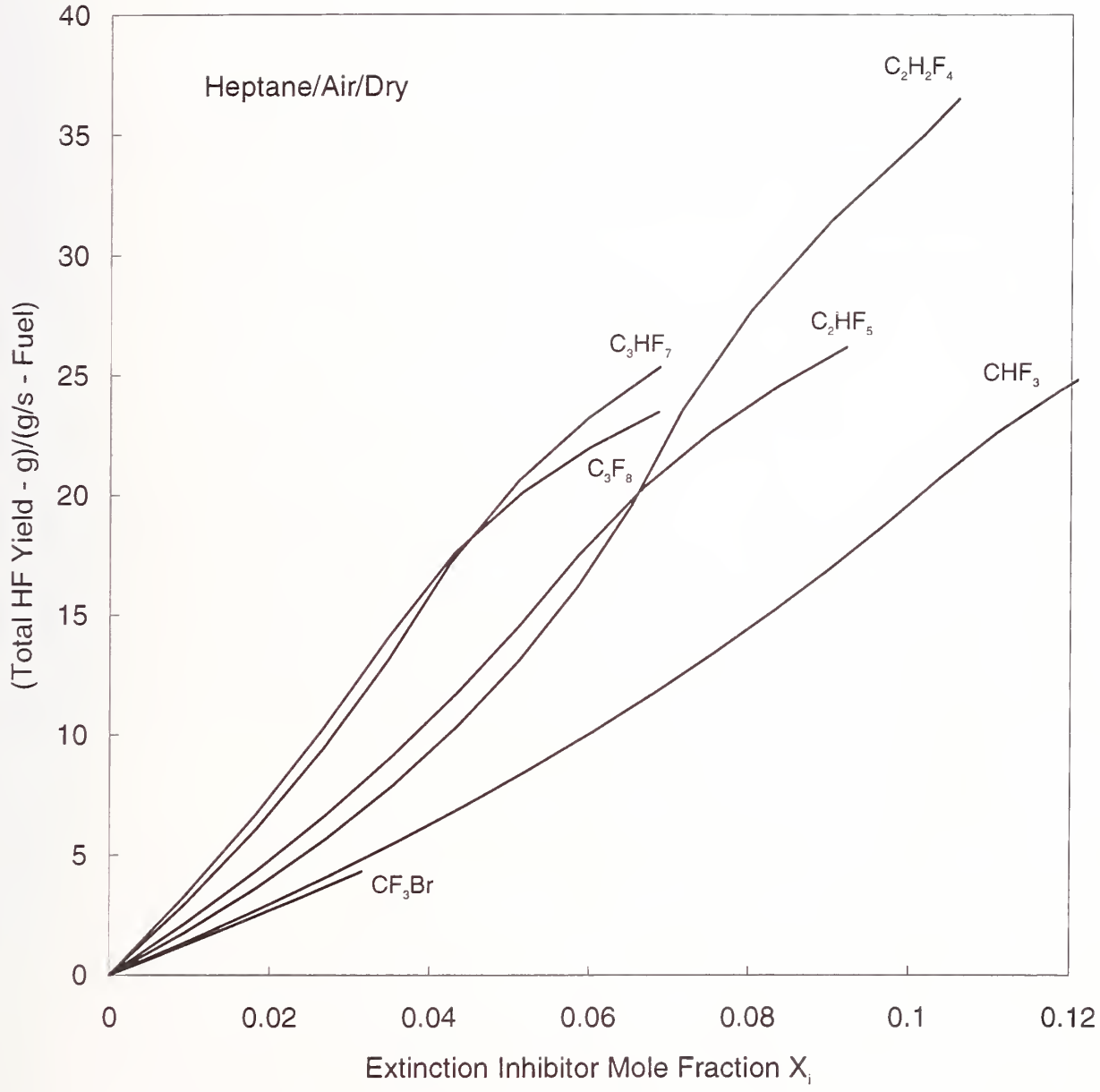

Figure 60. Total HF predicted during extinguishment of heptane-air flames for CHF_3, C_2HF_5, $C_2H_2F_4$, C_3HF_7, C_3F_8, CF_3Br versus extinction concentration.

2. The predictive model indicates that HF formation increases approximately linearly with fire size and extinguishing time and decreases approximately linearly with extinction concentration of the inhibitor.

3. The formation of HF is affected somewhat by the hydrogen to carbon ratio of the fuel, hydrogen to fluorine ratio in the agent, and the water vapor content of the air.

4. While predictions of HF produced in suppressed flames and intermediate scale fires are within about 25 % of the experimental results (which have large scatter), the estimated quantities of HF formation based on chemical equilibrium can overestimate the steady-state HF production by up to a factor of two for some agents.

5. Based on the analyses above, it should be possible to predict the HF formation by any arbitrary fluorocarbon which has a chemical structure similar (but not identical) to those agents analyzed above.

10.11 Predicting HF in Dry-Bay and Engine Nacelle Fires

Dry-bay and engine nacelle fires are expected to be distinctly different from each other, and as a result, the estimation of HF formation in each will require application of different methods. In the engine nacelle fire threat, the most likely scenario is expected to be a broken fuel or hydraulic line spraying into the nacelle region, with an attached, stabilized spray diffusion flame. Conversely, the dry-bay fire threat will most like occur from an incendiary device rupturing the fuel tank, creating a large rapidly advancing turbulent flame progressing into the basically premixed dry-bay region. Because the model for HF formation developed above is based on first principles, it is possible to apply it to the cases of engine nacelle and dry-bay fires. For each fire type, the important parameters controlling HF formation will be discussed, and specific methods for estimating the amount of HF produced during suppression will be presented.

10.11.1 Engine Nacelle Fires. A likely scenario for a engine nacelle fire is that of a spray diffusion flame of a liquid fuel. The time for fire suppression in this case is assumed to be seconds. In many respects, the flame will resemble a laboratory diffusion flame of a hydrocarbon fuel. Typically, the burning rate of a diffusion flame is controlled by the rate of transport of oxidizer to the reaction zone. In a similar way, the production of HF is also controlled by the rate of transport of inhibitor to the reaction zone. Although equilibrium calculations described in Section 10.4 above indicate that complete decomposition of the inhibitors to HF, COF_2, and CO_2 is favored, it is necessary to estimate the flux of the inhibitor to the reaction zone to determine the amount of reactants available. In addition, kinetic limitations to HF formation must be considered since complete and rapid destruction of the inhibitors is not assured at the high inhibitor concentrations typical of the extinction concentrations for diffusion flames, and in addition, slower rates of destruction reduce the transport rate to the reaction zone.

In the model for HF production described in Section 10.6 above, the inhibitor is assumed to be consumed in the reaction zone as a reactive species. The agent can be thought of as an additional fuel species, having its own oxygen demand, yet coming from the air side of the flame. It must be transported to the hot reaction zone which serves as a sink for the inhibitor. Thus fuel, oxygen and inhibitor are consumed in the reaction zone in stoichiometric proportions, with the stoichiometry

determined from a balanced chemical reaction to the most stable products. Total HF production is often limited by the availability of atomic hydrogen both for formation of HF itself and as an important intermediate which permits rapid decomposition of the inhibitor.

The predictive model for HF formation described in Section 10.6 indicates that HF formation in diffusion flames will increase approximately linearly with fire size, extinguishing time, and the concentration at which the flame extinguishes. In addition, HF formation will be affected somewhat by the hydrogen to carbon ratio of the fuel, hydrogen to fluorine ratio in the agent, and the water vapor content of the air.

Fire size influences the HF production rate for two main reasons. First, the fuel serves as the source of hydrogen, which is necessary for HF formation and for production of H-atoms which promote the rapid reaction of both the fuel and agent. Second, the fuel reaction produces the high temperatures necessary for inhibitor thermal decomposition and for production of H, O, and OH radicals which are the main promoters of inhibitor decomposition.

For similar reasons, the longer it takes for the inhibitor to build to the concentration which extinguishes the flame, the more HF that will be produced, since the fire is the driving force for inhibitor decomposition and HF formation. Thus, the HF production is linearly proportional to the fire-out time. The concentration at which the inhibitor extinguishes the flame is also directly related to the amount of HF produced during extinction. Since the HF production is linearly related to the concentration of inhibitor in the air stream, high extinction concentrations cause correspondingly higher HF production rates. As described above in Section 10.10, fuels or agents with higher hydrogen contents, or water vapor in the air stream typically cause higher production rates of HF. This is true because, to a large extent, trapping of the hydrogen atoms available from any source is how the agents reduce the reaction rate (and extinguish the flame) and also produce HF. For the present fluorinated agents, the amount of HF is often controlled more by the supply of hydrogen than by the amount of fluorine.

Application of the model for HF formation follows that outlined in Section 10.6. The necessary inputs are:

- the fuel type,
- fuel consumption rate m_f,
- agent type,
- fire-out time t_{out},
- concentration of agent at which the fire is extinguished C_{ext}.

While the values for these parameters may not be immediately available, they can be estimated from the characteristics of the aircraft. For example, the fire fuel may be aircraft jet fuel (JP8), and the flow rate could be estimated from the fuel line size and pressure. The most difficult parameters to specify then are the fire-out time and the extinction concentration. The fire-out time can be left as a variable; an estimate for the extinction concentration is the cup-burner extinction value. It should be noted that actual extinction concentrations can be higher or lower.

With the above information, prediction of the HF becomes possible with the present model.

$$HF\ (g) = G\ (g/g\ fuel) \cdot m_f\ (g/s) \cdot t_{out}\ (s) \cdot C_{ext}/C_{ext,cup}$$

where the HF generation parameter G is a function of the fuel and inhibitor type. Values for G for heptane and JP8 for CF_3H, C_2HF_5, C_3HF_7, C_3F_8, and CF_3Br are given in Table 3.

Table 3. The generation parameter G for heptane and JP8

Inhibitor	Heptane		JP8	
	Dry	Wet	Dry	Wet
CHF_3	2.3	2.3	2.2	2.2
C_2HF_5	2.5	2.8	1.7	1.7
C_3HF_7	2.4	2.8	1.6	1.7
C_3F_8	2.2	2.5	1.5	1.6
CF_3Br	0.4	0.4	0.1	0.1

10.11.2 Dry-Bay Fires. The dry-bay fire threat is harder to specify, but is envisioned to be a very rapidly expanding fireball driven by an incendiary device. These fires can be described as a rich, premixed turbulent flame, rapidly accelerating. As such, the conditions for HF formation are those of a premixed flame as described above in Sections 10.5 and 10.6.1. In these cases, the mass flux of both fuel and agent into the reaction zone are well specified.

As described in the section above describing the equilibrium calculations, the most abundant products of agent decomposition are CO, CO_2, HF, and COF_2. The model adopted in the present work assumes that the fluorinated agents decompose to the most thermodynamically favorable products and that finite rate kinetics are not important for HF formation. The validity of these assumptions are based on the extensive numerical modeling of premixed flames as described above. Complete conversion of the inhibitor to HF in premixed flames has been demonstrated above for conditions where the inhibitor is present at concentrations such that the atomic hydrogen to fluorine ratio is less than unity. As described in Section 10.5 above, complete conversion to HF may also be expected for higher temperature and pressure flames since the mechanism for agent decomposition becomes more dependent upon thermal decomposition under these conditions. In addition, there will be residual water vapor present in the dry-bay from the combustion which occurred prior to agent injection; this water vapor will hydrolyse COF_2 (which is the favored product in the absence of sufficient hydrogen) to produce HF.

The time for extinction of dry-bay fires is expected to be much shorter (tens of milliseconds) as compared to engine nacelle fires. Consequently, it is necessary to discuss the influence of these short times on the HF formation. Premixed flames have propagation rates on the order of 1 m/s and flame thicknesses of about a millimeter. This corresponds to a characteristic time on the order of 1 ms. However, the reaction zone in a premixed flame is typically about a tenth of the flame thickness, so that the characteristic chemical time is less than a millisecond. Since the chemical time is much shorter than the extinction time, the effects of the transient extinction do not influence the chemical considerations; results which describe steady-state flame are also applicable to transient suppression.

Essentially, all of the agent which is encountered by the expanding flame is expected to be converted to HF. To estimate the amount of HF formed, it is only necessary to specify:

- the volume of the space, V
- the agent type and number of fluorines/molecule, n_F
- the design mole fraction of agent in the space, X_i
- the fraction of the space over which the flame interacts with the inhibitor/air mixture prior to extinguishment, χ.

$$HF\ (g) = 19 \cdot V \cdot X_i \cdot n_F \cdot \chi / (22.4 \cdot T/273 \cdot 101/P)$$

where P is the pressure (kPa) and T is the temperature (K).

Note that in these fire threats, the time is so short and the process so rapid that the volume of the space becomes more important than the time of the process or the fuel consumption rate. If the time is long, then the HF formation should be treated as in the engine nacelle case described above.

10.12 Summary

Comprehensive chemical equilibrium calculations for hydrocarbon-air flames with halogenated inhibitors have been performed. These calculations, followed by detailed flame structure calculations for premixed flames have provided a theoretical basis for development of a simple model for HF formation.

Extensive tests for HF production have been performed in laboratory flames. In these carefully designed and executed experiments, the HF formation rates in steady-state premixed and diffusion flames have been determined. The experiments encompass both gaseous and liquid fuels, including methane, propane, and heptane. Transient experiments for HF formation have been performed for propane-air diffusion flames. These data provide an experimental basis for comparing the agents and for testing the stoichiometric model which was developed. In addition the model was tested against intermediate-scale tests of HF production conducted at the Naval Research Laboratory.

Dry-bay fires most likely resemble a rapidly accelerating turbulent premixed flame. For these flames, numerical calculations of the flame structure indicate that there will be complete conversion of the fluorine in the agent in the protected space to HF. Premixed experiments at elevated pressures and the accompanying modeling also indicate complete conversion of the inhibitor to HF.

Engine nacelle fires are expected to resemble turbulent diffusion flames. For these flames, the stoichiometric model which has been developed is able to predict HF formation in transiently suppressed flames within about 30 % of the experimental results for all the data against which it has been tested.

The formation rate of HF in diffusion flames is strongly influenced by the mass flux of inhibitor into the flame sheet. For diffusion flames with the inhibitor added to the air stream, there appear to be kinetic limitations to the rate of HF formation for most but not all of the agents tested which increase as the inhibitor concentration in the air stream increases. Many of the agents (for example $C_2H_2F_4$, C_2HClF_4, $C_3H_2F_6$, CH_2F_2/C_2HF_5, CF_3Br and $CHClF_2$) produced HF at rates within about 25 % of that given by equilibrium thermodynamics in the diffusion flames tested. Most of the perfluorinated agents tested (C_2F_6, C_3F_8, and C_4F_{10}) and the agents C_4F_8, C_2HF_5 and C_3HF_7 produced 0 to 35 % less than the equilibrium values except when the estimated fluorine to hydrogen flux into the flame goes above unity when they show no further increase with increasing inhibitor concentration in the air stream.

The stoichiometric model, based on relatively simple but fundamental assumptions, is a useful tool for understanding HF formation in suppressed fires. The predictions of the model provide good estimates of the upper limit for formation of HF, and are valid for both steady-state and transient modes of inhibition.

The following conclusions can be drawn concerning HF formation in suppressed fires - for diffusion flames:

1. HF formation increases linearly with fire size (*i.e.*, fuel consumption rate) for any given fuel and suppressant.

2. Assuming a constant agent injection rate, the HF formation increases approximately linearly with the time it takes for the fire to extinguish, for any given fuel and suppressant

3. For a given agent and fuel, the HF produced decreases approximately linearly with the concentration at which the flame is extinguished. That is, flames that are extinguished at lower inhibitor concentrations produce correspondingly less HF.

4. The hydrogen to carbon ratio of the fuel can influence the amount of HF produced by up to a factor of two for a given agent, with the higher hydrogen fuels making more HF.

5. The agents C_2HF_5, C_3HF_7, and C_3F_8 will make about four times as much HF as will CF_3Br for heptane flames for the same fire-out time. If the fire goes out faster (which will probably occur with CF_3Br since a lower concentration is required to extinguish the flame and that can probably be attained faster), the amount of HF will be proportionally less.

6. Large differences in the amount of HF produced by the agents C_2HF_5, C_3HF_7, are C_3F_8 are not expected.

7. The hydrogen to fluorine content of the agent influences the HF formation, with higher hydrogen content agents making more HF.

8. Water vapor in the air will increase the HF formation slightly.

and for premixed flames:

1. Complete conversion of the fluorine in the inhibitor to HF is expected.

2. The amount of HF produced depends upon: a) the volume of air consumed by the fire before extinction; b) the concentration of agent in that volume.

The predictions of the stoichiometric model are summarized in Figure 61. This figure presents the mass of HF formed (g) per gram of fuel consumed, and shows the cup burner extinction value for heptane. The effect of the fuel type is shown, as well as the effects of the agent type and presence of water vapor in the air. The prediction assumes a 10 second extinction time and cup burner extinction concentrations. For shorter extinction times or lower extinction concentrations, the amount of HF is reduced proportionally.

While predictions of HF produced in suppressed flames and intermediate scale fires are within about 25 % of the experimental results (which have large scatter), the estimated quantities of HF formation based on chemical equilibrium can overestimate the steady-state HF production by up to a factor of two for some agents. An examination of the chemical kinetics of suppressed diffusion flames can lead to an understanding of the relevant phenomena, and may indicate approaches for reduction of the HF production by halon alternatives.

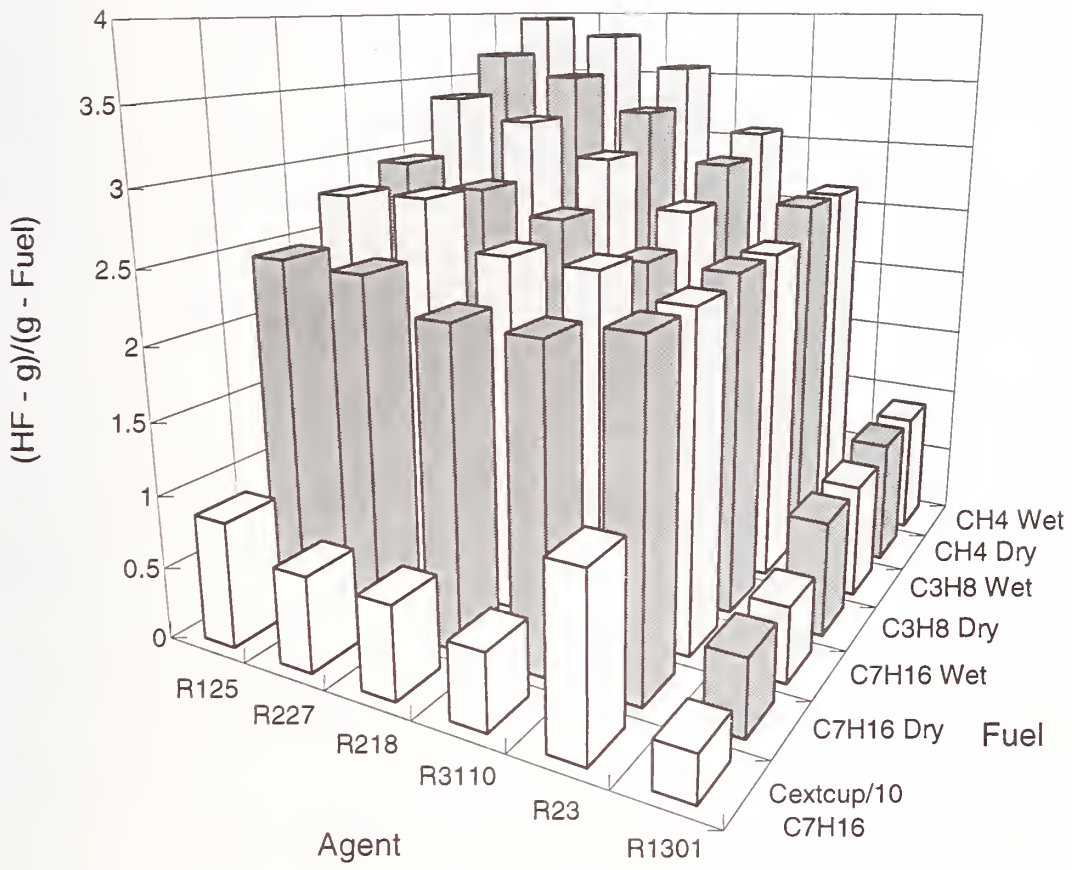

Figure 61. Predicted HF production (g) per gram of fuel consumed during the suppression. Effects of fuel and inhibitor type and wet and dry air are shown. The first row shows the cup burner extinction concentration (divided by 10) for heptane.

10.13 Acknowledgments

This research was supported by the U.S. Naval Air Systems Command; U.S. Army Aviation and Troop Command; Federal Aviation Administration Technical Center; and the U.S. Air Force. The author especially appreciates the support and technical direction of Mr. J. Michael Bennett at the Wright Patterson AFB Flight Dynamics Laboratory, Survivability Enhancement Branch. The authors are grateful to Drs. D. Burgess, W. Tsang, P. Westmoreland, and M. Zachariah for helpful conversations and for making their mechanism and publications available prior to publication; to Drs. J. Vandooren and P. Van Tiggelen for helpful suggestions concerning the experimental techniques; and to Dr. J. Hodges for help with the image processing; and to Dr. K. Smyth for helpful conversations throughout the project. It is a pleasure to acknowledge the collaboration with L. Truett in making the measurements, and the assistance of Mr. Arnold Liu and Miss Cynthia Yu in writing the data acquisition and image processing software, performing the numerical calculations, and reducing the data. The authors are grateful to M. King, R. Harris, Y.E. Hsin, C. Womeldorf, and A. Liu for careful performance of the experiments. Helpful conversations with Dr. R. Sheinson at the Naval Research Laboratory concerning the intermediate-scale experiments are gratefully acknowledged.

10.14 References

Andrews, G.E. and Bradley, D. *Combust. Flame* 18, 133-153 (1972).

Bajpai, S.N. J. *Fire and Flammability*, 1974, 5, 255.

Belles, F.E. and O'Neal, C. Jr., *Sixth Symposium (Int'l) on Combustion*, The Combustion Institute, Pittsburgh, PA, 1957, 806.

Biordi, J.C., Lazzara, C.P., and Papp, J.F. *XIVth Symposium (Int'l) on Combustion*, The Combustion Institute, Pittsburgh, PA, 1973, 367.

Biordi, J.C.; Lazzara, C.P.; Papp, J.F. *XIVth Symposium (Int'l) on Combustion*, The Combustion Institute, Pittsburgh, PA, 1973, 367-381.

Biordi, J.C., Lazzara, C.P., and Papp, J.F. *XVth Symposium (Int'l) on Combustion*, The Combustion Institute, Pittsburgh, PA, 1974, 917.

Biordi, J.C., Lazzara, C.P., and Papp, J.F. 1976, *J. Phys. Chem.* 80, 1042-1048.

Biordi, J.C., Lazzara, C.P., and Papp, J.F. 1977, *J. Phys. Chem.* 81, 1139-1145.

Biordi, J.C., Lazzara, C.P., and Papp, J.F. 1978, *J. Phys. Chem.* 82, 125.

Booth, K.; Melina, B.J.; Hirst, R. 1973, *Imperial Chemical Industries Limited*, Mond Division, Cheshire UK, 31 August.

Burdon, M.C.; Burgoyne, J.A.; Weinberg, F.J. *Vth Symposium (Int'l) on Combustion*, Reinhold Publishing Corp., New York, NY, 1955, 647-651.

Burgess, D., Jr., Tsang, W., Westmoreland, P.R., Zachariah, M.R. *Third International Conference on Chemical Kinetics*, July 12-16, 1992, Gaithersburg, MD, 1993, p. 119.

Burgess, D.R.F.; Jr., Zachariah, M.R.; Tsang, W.; and Westmoreland, P.R. *Thermochemical and Chemical Kinetic Data for Fluorinated Hydrocarbons in Flames*, National Institute of Standards and Technology, Gaithersburg MD, 1994, NIST Technical Note, submitted.

Burgess, D.R.F., Jr., Zachariah, M.R., Tsang, W., and Westmoreland, P.R. *Thermochemical and Chemical Kinetic Data for Fluorinated Hydrocarbons in Flames*, National Institute of Standards and Technology, Gaithersburg MD, 1994, NIST Technical Note, submitted.

Burgess, D.R.F., Jr., Zachariah, M.R., Tsang, W., and Westmoreland, P.R. Thermochemical and Chemical Kinetic Data for Fluorinated Hydrocarbons, to appear as a special issue of *Progress in Energy and Combustion Science*, 1995.

Burgoyne, J.H. and Williams-Lier, G., *Proceedings of the Royal Society*, A193, 525, (1948).

Burgoyne *et al.*, 1948; Coleman, 1951; Belles *et al.*, 1957.

Burke, S.P.; Schumann, T.E.W. 1928, *Ind. Eng. Chem.* a4 20, 998.

Coleman, E.H., *Fuel*, 30, 114, (1951).

Di Nenno, P.J.; Forssell, E.W.; Peatross, M.J.; Wong, J.T.; Maynard, M. *Halon Alternatives Technical Working Conference*, New Mexico Engineering Research Institute, Albuquerque, NM, May 11-13, 1992.

Ferreira, M.J.; Hanauska, C.P.; Pike, M.T. *Halon Alternatives Technical Working Conference*, New Mexico Engineering Research Institute, Albuquerque, NM, May 11-13, 1992.

Ferreira, M.J.; Hanauska, C.P.; Pike, M.T. *Halon Alternatives Technical Working Conference*, New Mexico Engineering Research Institute, Albuquerque, NM, May 11-13, 1992.

Filipczak, R.A. *Halon Alternatives Technical Working Conference*, New Mexico Engineering Research Institute, Albuquerque, NM, May 11-13, 1993, 149-159.

Filipczak, R.A. *Halon Options Technical Working Conference*, New Mexico Engineering Research Institute, Albuquerque, NM, May 3-5, 1994, 165-176.

Frenklach, M., Wang, H., Bowman, C.T., Hanson, R.K., Smith, G.P., Golden, D. Gardiner, W. Lissianski, V., Poster 3-26, *Twenty-fifth Symposium (Int'l) on Combustion*, The Combustion Institute, Pittsburgh, PA, 1994.

Gann, R.G., Ed., Halogenated Fire Suppressants; *ACS Symposium Series* No. 16, The American Chemical Society, Washington, DC, 1975.

Garner, F.H., Long, R., Graham, A.J., and Badakhshan, A., *Sixth Symposium (Int'l) on Combustion*, The Combustion Institute, Pittsburgh, PA, 1957, 802.

Grosshandler, W.L.; Gann, R.G.; Pitts, W.M.; Eds. *Evaluation of Alternative In-Flight Fire Suppressants for Full-Scale Testing in Simulated Aircraft Engine Nacelles and Dry Bays*, National Institute of Standards and Technology, Gaithersburg, MD, 1994; NIST SP 861.

Hastie, J.W., High Temperature Vapors: *Science and Technology*, New York, NY, 1975, Academic Press, 332.

Hochgreb, S., Hsin, Y.E., and Linteris, G.T., *Laminar Flame Speeds of CF3H-Propane-Air Mixtures at Elevated Pressures*, NIST Annual Conference on Fire Research, Oct. 17-20, 1994, Gaithersburg, MD.

VanDerWege, B., Bush, M.T., Hochgreb, S., and Linteris, G.T., "Inhibition of CH4 Laminar Flame Speeds by CF3H and C2F6 in a Combustion Bomb," to be submitted to Combustion Science and Technology, July, 1995.

Kee, R.J., Miller, J.A. and Jefferson, T.H. *CHEMKIN: a General-Purpose, Transportable, Fortran Chemical Kinetics Code Package*, Sandia National Laboratories Report, 1980, SAND80-8003.

Kee, R.J., Warnatz, J., Miller, J.A. *A Fortran Computer Code Package for the Evaluation of Gas-Phase Viscosities, Conductivities, and Diffusion Coefficients*, Sandia National Laboratories Report, 1983, SAND83-8209.

Kee, R.J., Grcar, J.F., Smooke, M.D. and Miller, J.A. *A Fortran Program for Modeling Steady Laminar One-dimensional Premixed Flames*, Sandia National Laboratories Report, 1991, SAND85-8240.

Kee, R.J., Warnatz, J., Miller, J.A. *A Fortran Computer Code Package for the Evaluation of Gas-Phase Viscosities, Conductivities, and Diffusion Coefficients*, Sandia National Laboratories Report, 1983, SAND83-8209.

Lask, G., Wagner, H.G., *Thirteenth Symposium (Int'l) on Combustion*, Williams and Wilkins Co., Baltimore, 1962, 432.

Linnett, J.W. *Fourth Symposium (Int'l) on Combustion*, Williams & Wilkins, Baltimore, 1953, p. 20.

Linteris, G.T.; King, M.D.; Liu, A.; Womeldorf, C.; Hsin, Y.E. *Halon Options Technical Working Conference*, New Mexico Engineering Research Institute, Albuquerque, NM, May 3-5, 1994, 177-190.

Linteris, G.T.; Gmurczyk, G.W. Parametric Study of Hydrogen Fluoride Formation in Suppressed Fires, *Halon Options Technical Working Conference*, Albuquerque, NM, 1995.

Linteris, G.T., and Truett, L.F., Inhibition of Premixed Methane-Air Flames by Fluoromethanes, accepted for publication in *Combustion and Flame*, June, 1995a.

Linteris, G.T. and Truett, L., Inhibition of Premixed Methane-Air Flames by Halon Alternatives, *Proc. of International Conf. on Fire Research and Engineering*; Sept. 10-15, 1995b; Orlando, FL.

Linteris, G.T., Effect of inhibitor concentration on the inhibition mechanism of fluoromethanes in premixed methane-air flames, to appear in "Halon Replacements: Technology and Science," *American Chemical Society Symposium Series* (A.W. Miziolek, and W. Tsang, Eds.), Washington, DC, 1995a.

Linteris, G.T., Acid gas production in inhibited propane-air diffusion flames, to appear in Halon Replacements: Technology and Science, *American Chemical Society Symposium Series* (A.W. Miziolek, and W. Tsang, Eds.), Washington, DC, 1995b.

Linteris, G.T., Numerically predicted flame structure and burning rates of premixed CO-Ar-O2-H2 flames inhibited by CF3H, submitted to *Combustion and Flame*, Feb. 1995b.

Mache, H. and Hebra, A. Sitzungsber. *Osterreich. Akad. Wiss.*, Abt. IIa, 150, 157 (1941).

Metghalchi, M. and Keck, J. C., *Combust. Flame* 38, 143 (1980).

Moore, T.A.; Dierdorf, D.S.; Hanauska, C. *Halon Options Technical Working Conference*, New Mexico Engineering Research Institute, Albuquerque, NM, May 3-5, 191.

Nyden, M.R., Linteris, G.T., Burgess, D.R.F., Jr., Westmoreland, P.R., Tsang, W., and Zachariah, M.R., in *Evaluation of Alternative In-Flight and Dry Bays*, (W.L. Grosshandler, R.G. Gann, and W.M. Pitts, Eds.), National Institute of Standards and Technology, Gaithersburg MD, 1994, NIST SP 861, p. 467.

Pitts, W.M.; Nyden, M.R.; Gann, R.G.; Mallard, W.G.; Tsang, W. *Construction of an Exploratory List of Chemicals to Initiate the Search for Halon Alternatives*; National Institute of Standards and Technology, Gaithersburg MD, 1990; NIST SP 1279.

Rosser, W. A., Wise, H., and Miller, J., *Seventh Symposium (Int'l) on Combustion*, Butterworths Scientific Publications, Butterworths, London, 1959, 175.

Safieh, H.Y.; Vandooren, J.; Van Tiggelen, P.J. *XIXth Symposium (International) on Combustion*, The Combustion Institute, 1982, Pittsburgh, PA, 117-127.

Sheinson, R.S.; Musick, J.K.; Carhart, H.W. 1981, *Journal of Fire and Flammability*, 12, 229.

Sheinson, R.S; Alexander, J.I. Fall Meeting, *Eastern States Section Meeting*/The Combustion Institute, 1982, Pittsburgh, PA, Paper 62.

Sheinson, R.S., Penner-Hahn, J.E., and Indritz, D. 1989, *Fire Safety Journal* 15, 437.

Sheinson, R.S.; Eaton, H.G.; Black, B.; Brown, R.; Burchell, H.; Smith, W.D. *Halon Options Technical Working Conference*, New Mexico Engineering Research Institute, Albuquerque, NM, May 3-5, 1994, 43-53.

Simmons, R.F. and Wolfhard, H.G., *Transactions of the Faraday Society*, 52, 53 (1956).

Simmons *et al.*, 1956; Garner *et al.*, 1957; Rosser *et al.* 1959; Lask and Wagner, 1962.

Smith, W.D.; Sheinson, R.S.; Eaton, H.G.; Brown, R.; Salmon, G.; Burchell, H.; St. Aubin, H.J. *Sixth International Fire Conference*, Interflam '93, Interscience Communications Limited, 1993, 757-764.

Thorpe, R.K., Gmurczyk, G.W.: *Technical Support Services and Assistance to the Halon Compatibility Project." Science Applications International Corporation*, Report for the National Institute of Standards and Technology, Contract No. 52SBNB4C8144, 1995.

Yamashika, S. 1973, *Report of Fire Research Institute of Japan*, 36, 7.

Yamashika, S.; Hosokai, R.; Morikawa, T. 1974, *Report of Fire Research Inst. of Japan*, 38, 1.

Vagelopoulos, C.M., Egolfopoulos, F.N., and Law, C.K, *Twenty-fifth Symposium (Int'l) on Combustion*, The Combustion Institute, Pittsburgh, 1994, p. 1341.

VanDerWege, B., Bush, M.T., Hochgreb, S., and Linteris, G.T., *Inhibition of CH4 Laminar Flame Speeds by CF3H and C2F6 in a Combustion Bomb*, to be submitted to Combustion Science and Technology, July, 1995.

Vandooren, J. F.; da Cruz, N.; P. *Van Tiggelen XXIInd Symposium (International) on Combustion*, The Combustion Institute, Pittsburgh, PA, 1988, 1587-1595.

Van Wonterghem, J. and Van Tiggelen, A. *Bull. Soc. Chim. Belg.* 63, 235-260 (1954). Van Wonterghem and Van Tiggelen, 1954.

Westbrook, C.K. *Combust. Sci. and Tech.* 1983, 34, 201.

Westmoreland, P.R., Burgess, D.F.R. Jr., Tsang, W., and Zachariah, M.R. *XXVth Symposium (Int'l) on Combustion*, The Combustion Institute, Pittsburgh, PA, 1994.

Wilson, W.E., Jr. *Xth Symposium (International) on Combustion*, The Combustion Institute, Pittsburgh, PA, 1965, 47-54.

World Meteorological Organization, 1989, *Scientific Assessment of Stratospheric Ozone: 1989," Report No. 20, Alternative Fluorocarbon Environmental Acceptability Study* (AFEAS).

Zallen, D.M., 1992, *Halon Replacement Study*, SBIR Report No. ZIA-92-001 to Aeronautical Systems Division, Wright-Patterson AFB, Zallen International Associates.

Appendix A. The Computer Program Predicting Formation of HF

```
c     The Computer Program:
c     Composition of Combustion/Inhibition Products
c     For the Reaction of Hydrocarbon/Air/Water/Halocarbon
c     with Species Diffusion and Convection Transport - 4/12/95
c*****************************************************************
c
c     Greg W. Gmurczyk
c     SAIC c/o NIST
c     Building and Fire Research Laboratory
c     Gaithersburg, MD 20899
c     phone: (301) 975-6888
c     e-mail: gmurczyk@tiber.nist.gov
c*****************************************************************
c
c     List of Variables:
c
c     al - alfa (fuel moles)
c     be - beta (halocarbon moles)
c     becr - beta critical
c     ga - gamma (oxygen moles)
c     ni - nie (nitrogen moles)
c     et - eta (hf moles)
c     ph - phi (hcl moles)
c     ep - epsylon (cof2 moles)
c     dz - dzeta (cocl2 moles)
c     de - delta (co2 moles)
c     la - lambda (product h2o moles)
c     mu - miu (substrate h2o moles)
c     q*i - inlet species volume flow (slpm)
c     q* - outlet species volume flow (slpm)
c     d*i - inlet species densities (kg/m3)
c     d* - outlet species densities (kg/m3)
c     m*i - inlet species mass flow (g/s)
c     m* - outlet species mass flow (g/s)
c     X*i - inlet species mole fractions (l/l)
c     X* - outlet species mole fractions (l/l)
c     Y*i - inlet species mass fractions (kg/kg)
c     Y* - outlet species mass fractions (kg/kg)
c     w* - species molecular mass (kg/kmole)
c     *r - species consumed/generated in flame (slpm)
c     *u - species unreacted in flame (slpm)
c     roi - ro (inhibitor/oxygen(fuel) diff.coeff.rat.)
c     row - ro (water/oxygen(fuel) diff.coeff.rat.)
c     ron - ro (nitrogen/oxygen(fuel) diff.coeff.rat.)
c     ros - ro (star)
```

```
c     ri - r (inhibitor/oxygen(fuel) flow rat.)
c     rw - r (water/oxygen(fuel) flow rat.)
c     rn - r (nitrogen/oxygen(fuel) flow rat.)
c     a,b,c,d,e,f - a,b & c,d,e,f (fuel & inhibitor composition)
c     vm = 24.415 (l/mole)
c     si = 0.0 (standard case)
c     hl = 0.0 (low h2: la=0.0), 1.0 (high h2: ep=0.0, dz=0.0)
c*************************************************************
c
      program coeff
      implicit double precision (a-h,j-z)
c
      common /atom/ a,b,c,d,e,f
      common /coef/ al,be,becr,ga,de,ep,dz,ph,et,la,mu
      common /w/ wo2,wn2,wair,wc,wh,wf,wcl,wco2,wh2o,
     &           whf,whcl,wcof2,wcocl2,wfu,win,wmi,wm
      common /rat/ ri,rw,roi,row,ros,hl,si
      common /dif/ do2n2,dfun2,dinn2,dh2on2
      common /therm/ vm,lm3,p,t,ru,cm
      common /qi/ qini,qh2oi,qfui,qo2i,qn2i,qairi,qti,dq
      common /di/ dini,dfui,do2i,dn2i,dco2i,dh2oi,dhfi,dhcli,dcof2i,
     &            dcocli,denmi,dmi
      common /mi/ mini,mfui,mo2i,mn2i,mco2i,mh2oi,mhfi,mhcli,mcof2i,
     &            mcocli,mti
      common /Xi/ Xini,Xh2oi,Xfui,Xo2i,Xn2i
      common /Yi/ Yini,Yh2oi,Yfui,Yo2i,Yn2i
      common /qr/ qinr,qfur,qo2r,qn2r,qco2r,qh2or,qhfr,qhclr,qcof2r,
     &            qcoclr,qr
      common /dr/ dinr,dfur,do2r,dn2r,dco2r,dh2or,dhfr,dhclr,dcof2r,
     &            dcoclr,denmr,dmr
      common /mr/ minr,mfur,mo2r,mn2r,mco2r,mh2or,mhfr,mhclr,mcof2r,
     &            mcoclr,mtr
      common /Xr/ Xinr,Xfur,Xo2r,Xn2r,Xco2r,Xh2or,Xhfr,Xhclr,Xcof2r,
     &            Xcoclr
      common /Yr/ Yinr,Yfur,Yo2r,Yn2r,Yco2r,Yh2or,Yhfr,Yhclr,Ycof2r,
     &            Ycoclr
      common /q/ qin,qfu,qo2,qn2,qco2,qh2o,qhf,qhcl,qcof2,
     &           qcocl2,qt
      common /d/ din,dfu,do2,dn2,dco2,dh2o,dhf,dhcl,dcof2,
     &           dcocl2,denm,dm
      common /m/ min,mfu,mo2,mn2,mco2,mh2o,mhf,mhcl,mcof2,
     &           mcocl2,mt,mhffu
      common /n/ nin,nfu,no2,nn2,nco2,nh2o,nhf,nhcl,ncof2,
     &           ncocl2,nt,nti,dn
      common /X/ Xin,Xfu,Xo2,Xn2,Xco2,Xh2o,Xhf,Xhcl,Xcof2,Xcocl2
      common /Y/ Yin,Yfu,Yo2,Yn2,Yco2,Yh2o,Yhf,Yhcl,Ycof2,Ycocl2
c
      open(unit=1, file='i', form='formatted', status='old')
```

```
      open(unit=2, file='o', form='formatted', status='unknown')
*
*************************************************************************
*     input data
*     fuel and inhibitor composition
*     inlet species volume flows, flame configuration
*     inlet pressure and temperature
*************************************************************************
*
      read(1,*) a,b,c,d,e,f
      read(1,*) qinit,qh2oi,qfui,qairi,si
c
      qini=0.0d0
 5000 qini=qini+0.02d0*qinit
*
******inlet pressure and temperature*****************************************
*
      ru=8313.0d0
      p=1.0d5
      t=298.0d0
      dmi=p/(ru*t)
*
******conversion factors*****************************************************
*
      vm=24.415d0
      lm3=1.0d-3
      if(si) 1250,15,17
   15 al=1.0d0
      go to 19
   17 ga=1.0d0
*
******species molecular weights**********************************************
*
   19 wo2=32.0d0
      wn2=28.0d0
      wair=29.0d0
      wc=12.0d0
      wh=1.0d0
      wf=19.0d0
      wcl=35.5d0
      wco2=44.0d0
      wh2o=18.0d0
      whf=20.0d0
      whcl=36.5d0
      wcof2=66.0d0
      wcocl2=99.0d0
c
      wfu=a*wc+b*wh
```

```
      win=c*wc+d*wh+e*wf+f*wcl
*
******species diffusion coefficient corrections*************************
*
      do2n2=dsqrt((wo2+wn2)/(wo2*wn2))
      dfun2=dsqrt((wfu+wn2)/(wfu*wn2))
      if(win) 1250,1,2
    1 dinn2=0.0d0
      go to 3
    2 dinn2=dsqrt((win+wn2)/(win*wn2))
    3 dh2on2=dsqrt((wh2o+wn2)/(wh2o*wn2))
*
******inlet species mole fractions*************************************
*
      qti=qini+qh2oi+qfui+qairi
      qo2i=0.21d0*qairi
      qn2i=0.79d0*qairi
      Xini=qini/qti
      Xh2oi=qh2oi/qti
      Xfui=qfui/qti
      Xairi=qairi/qti
      Xo2i=qo2i/qti
      Xn2i=qn2i/qti
*
******inlet species mole flows*****************************************
*
      nti=qti/vm
      nini=qini/vm
      nh2oi=qh2oi/vm
      nfui=qfui/vm
      nairi=qairi/vm
      no2i=qo2i/vm
      nn2i=qn2i/vm
*
******inlet species densities******************************************
*
      wmi=Xini*win+Xh2oi*wh2o+Xfui*wfu+Xo2i*wo2+Xn2i*wn2
      denmi=dmi*wmi
      dini=dmi*win
      dfui=dmi*wfu
      dh2oi=dmi*wh2o
      do2i=dmi*wo2
      dn2i=dmi*wn2
      dairi=dmi*wair
*
******inlet species mass flows*****************************************
*
      mti=qti*denmi*lm3*1.0d3/60.0d0
```

```
      mini=qini*dini*lm3*1.0d3/60.0d0
      mfui=qfui*dfui*lm3*1.0d3/60.0d0
      mh2oi=qh2oi*dh2oi*lm3*1.0d3/60.0d0
      mo2i=qo2i*do2i*lm3*1.0d3/60.0d0
      mn2i=qn2i*dn2i*lm3*1.0d3/60.0d0
      mairi=qairi*dairi*lm3*1.0d3/60.0d0
*
******inlet species mass fractions*****************************************
*
      Yini=Xini*win/wmi
      Yfui=Xfui*wfu/wmi
      Yh2oi=Xh2oi*wh2o/wmi
      Yo2i=Xo2i*wo2/wmi
      Yn2i=Xn2i*wn2/wmi
      Yairi=Xairi*wair/wmi
*
*******************************************************************************
*                  m a i n   c o m p u t a t i o n s
*******************************************************************************
*
*  a) no inhibitor in the system
*******************************************************************************
*
      if(si) 1250,4,5
*
*******************************************************************************
*      1. standard case: with/without water, fuel inside, o2/n2 outside
*******************************************************************************
*
    4 rw=qh2oi/qo2i
      row=dh2on2/do2n2
      if(qini) 1250,6,9
    6 call noins
      go to 1300
*
    5 rw=qh2oi/qfui
      row=dh2on2/dfun2
      if(qini) 1250,7,9
    7 call noini
      go to 1350
*
*******************************************************************************
*  b) inhibitor in the system
*******************************************************************************
*
    9 if(si) 1250,50,650
*
*******************************************************************************
```

```
*     2. standard case: inhibitor outside, fuel inside, o2/n2 outside
*************************************************************************
*
   50 ri=qini/qo2i
      rw=qh2oi/qo2i
      roi=dinn2/do2n2
      row=dh2on2/do2n2
c
      call betas
      if(be.le.becr) then
        hl=1.0d0
      else
        hl=0.0d0
      endif
c
      if(mu) 1250,100,400
*
******3.1 no h2o in substrates: mu=0.0************************************
*
  100 if(hl) 1250,200,300
*
**    3.1.1 low level of hydrogen: la=0.0
*
  200 call coefls
      go to 1300
*
**    3.1.2 high level of hydrogen: ep=0.0, dz=0.0
*
  300 call coefhs
      go to 1300
*
******3.2 h2o in substrates*************************************************
*
  400 if(hl) 1250,500,600
*
**    3.2.1 low level of hydrogen: la=0.0
*
  500 call coefls
      go to 1300
*
**    3.2.2 high level of hydrogen: ep=0.0, dz=0.0
*
  600 call coefhs
      go to 1300
*
  650 ri=qini/qfui
      rw=qh2oi/qfui
      roi=dinn2/dfun2
```

```
      row=dh2on2/dfun2
c
      call betai
      if(be.le.becr) then
        hl=1.0d0
      else
        hl=0.0d0
      endif
c
      if(mu) 1250,700,1000
*
******4.1 no h2o in substrates: mu=0.0************************************
*
  700 if(hl) 1250,800,900
*
**    4.1.1 low level of hydrogen: la=0.0
*
  800 call coefli
      go to 1350
*
**    4.1.2 high level of hydrogen: ep=0.0, dz=0.0
*
  900 call coefhi
      go to 1350
*
******4.2 h2o in substrates*************************************************
*
 1000 if(hl) 1250,1100,1200
*
**    4.2.1 low level of hydrogen: la=0.0
*
 1100 call coefli
      go to 1350
*
**    4.2.2 high level of hydrogen: ep=0.0, dz=0.0
*
 1200 call coefhi
      go to 1350
c
 1250 write(*,*) ' '
      write(2,*) ' '
      write(*,*) '  1250 negative value  '
      write(2,*) '  1250 negative value  '
      go to 1600
*
*****************************************************************************
*     flows of species consumed/generated in flame
*     flows of species unreacted
```

```
*     outlet volume and mass flows, mole and mass fractions
*************************************************************************
*
 1300 qfur=qfui
      qinr=qfur*be/al
      qo2r=qfur*ga/al
      qn2r=qfur*3.762d0*ga/al
      qco2r=qfur*de/al
      qh2or=qfur*(la-mu)/al
      qhfr=qfur*et/al
      qhclr=qfur*ph/al
      qcof2r=qfur*ep/al
      qcoclr=qfur*dz/al
c
      qfuu=0.0d0
      qinu=qini-qinr
      qo2u=qo2i-qo2r
      qn2u=qn2i-qn2r
      qh2ou=qh2oi-qh2or
      qco2u=0.0d0
      qhfu=0.0d0
      qhclu=0.0d0
      qcof2u=0.0d0
      qcoclu=0.0d0
c
      qin=qinu
      qfu=0.0d0
      qo2=qo2i-qo2r
      qn2=qn2i
      qh2o=qh2oi+qh2or
      qco2=qco2r
      qhf=qhfr
      qhcl=qhclr
      qcof2=qcof2r
      qcocl2=qcoclr
c
      call molef
c
      call massf
c
      call molefl
c
      go to 1550
c
 1350 qo2r=qo2i
      qinr=qo2r*be/ga
      qfur=qo2r*al/ga
      qn2r=qn2i
```

```
      qco2r=qo2r*de/ga
      qh2or=qo2r*(la-mu)/ga
      qhfr=qo2r*et/ga
      qhclr=qo2r*ph/ga
      qcof2r=qo2r*ep/ga
      qcoclr=qo2r*dz/ga
c
      qinu=qini-qinr
      qfuu=qfui-qfur
      qo2u=0.0d0
      qn2u=0.0d0
      qh2ou=qh2oi-qh2or
      qco2u=0.0d0
      qhfu=0.0d0
      qhclu=0.0d0
      qcof2u=0.0d0
      qcoclu=0.0d0
c
      qin=qinu
      qfu=qfuu
      qo2=0.0d0
      qn2=qn2i
      qh2o=qh2oi+qh2or
      qco2=qco2r
      qhf=qhfr
      qhcl=qhclr
      qcof2=qcof2r
      qcocl2=qcoclr
c
      call molef
c
      call massf
c
      call molefl
*
*************************************************************************
*     output data
*************************************************************************
*
 1550 write(*,*) ' fu     o2     in     h2os   co2    h2op   hf     hcl
     & cof2  cocl2 (coeff)'
      write(*,1500) al,ga,be,mu,de,la,et,ph,ep,dz
      write(2,*) ' fu     o2     in     h2os   co2    h2op   hf     hc
     &l    cof2  cocl2 (coeff)'
      write(2,1500) al,ga,be,mu,de,la,et,ph,ep,dz
      write(*,*) ' qin    qfu    qo2    qn2    qco2   qh2o   qhf    qhcl
     &qcof2 qcocl2 (slpm)'
      write(*,1500) qin,qfu,qo2,qn2,qco2,qh2o,qhf,qhcl,qcof2,qcocl2
```

```
      write(2,*) ' qin   qfu   qo2   qn2   qco2  qh2o  qhf   qhcl
     &  qcof2 qcocl2 (slpm)'
      write(2,1500) qin,qfu,qo2,qn2,qco2,qh2o,qhf,qhcl,qcof2,qcocl2
      write(*,*) ' min   mfu   mo2   mn2   mco2  mh2o  mhf   mhcl
     &  mcof2 mcocl2 (g/s)'
      write(*,1500) min,mfu,mo2,mn2,mco2,mh2o,mhf,mhcl,mcof2,mcocl2
      write(2,*) ' min   mfu   mo2   mn2   mco2  mh2o  mhf   mhcl
      write(2,1500) min,mfu,mo2,mn2,mco2,mh2o,mhf,mhcl,mcof2,mcocl2
      write(*,*) ' Xin   Xfu   Xo2   Xn2   Xco2  Xh2o  Xhf   Xhcl
     &  Xcof2 Xcocl2'
      write(*,1500) Xin,Xfu,Xo2,Xn2,Xco2,Xh2o,Xhf,Xhcl,Xcof2,Xcocl2
      write(2,*) ' Xin   Xfu   Xo2   Xn2   Xco2  Xh2o  Xhf   Xhcl
     &  Xcof2 Xcocl2'
      write(2,1500) Xin,Xfu,Xo2,Xn2,Xco2,Xh2o,Xhf,Xhcl,Xcof2,Xcocl2
      write(*,*) ' Yin   Yfu   Yo2   Yn2   Yco2  Yh2o  Yhf   Yhcl
     &  Ycof2 Ycocl2'
      write(*,1500) Yin,Yfu,Yo2,Yn2,Yco2,Yh2o,Yhf,Yhcl,Ycof2,Ycocl2
      write(2,*) ' Yin   Yfu   Yo2   Yn2   Yco2  Yh2o  Yhf   Yhcl
     &  Ycof2 Ycocl2'
      write(2,1500) Yin,Yfu,Yo2,Yn2,Yco2,Yh2o,Yhf,Yhcl,Ycof2,Ycocl2
      write(*,*) ' nin   nfu   no2   nn2   nco2  nh2o  nhf   nhcl
     &  ncof2 ncocl2 (mole/min)'
      write(*,1500) nin,nfu,no2,nn2,nco2,nh2o,nhf,nhcl,ncof2,ncocl2
      write(2,*) ' nin   nfu   no2   nn2   nco2  nh2o  nhf   nhcl
     &  ncof2 ncocl2(mole/min)'
      write(2,1500) nin,nfu,no2,nn2,nco2,nh2o,nhf,nhcl,ncof2,ncocl2
      write(*,*) ' nt    deltan  qt    deltaq    mhffu '
      write(*,1590) nt,dn,qt,dq,mhffu
      write(2,*) ' nt    deltan  qt    deltaq    mhffu '
      write(2,1590) nt,dn,qt,dq,mhffu
c
      if(qini.lt.qinit) go to 5000
c
 1400 format(6f7.4)
 1500 format(10f12.5)
 1590 format(5f8.4)
c
 1600 stop
      end
*
*************************************************************************
*                    s u b r o u t i n e s
*************************************************************************
*
*************************************************************************
*     a) standard case, no inhibitor - with/without water combustion products
*************************************************************************
*
```

```
      subroutine noins
      implicit double precision (a-h,j-z)
      common /atom/ a,b,c,d,e,f
      common /coef/ al,be,becr,ga,de,ep,dz,ph,et,la,mu
      common /rat/ ri,rw,roi,row,ros,hl,si
c
      ga=al*(a+0.25d0*b)
      de=al*a
      la1=rw*row*(a+0.25d0*b)
      la2=0.5d0*al*b
      la=la1+la2
      mu=rw*row*al*(a+0.25d0*b)
      be=0.0d0
      becr=0.0d0
      et=0.0d0
      ph=0.0d0
      ep=0.0d0
      dz=0.0d0
      return
      end
*
**********************************************************************
*     b) no inhibitor - with/without water combustion products
**********************************************************************
*
      subroutine noini
      implicit double precision (a-h,j-z)
      common /atom/ a,b,c,d,e,f
      common /coef/ al,be,becr,ga,de,ep,dz,ph,et,la,mu
      common /rat/ ri,rw,roi,row,ros,hl,si
c
      al=ga/(a+0.25d0*b)
      de=ga/(1.0d0+b/(4.0d0*a))
      mu=al*rw*row
      be=0.0d0
      becr=0.0d0
      et=0.0d0
      ph=0.0d0
      ep=0.0d0
      dz=0.0d0
      return
      end
*
**********************************************************************
*     a) standard case, hydrogen/halocarbon limit - with/without water
**********************************************************************
*
      subroutine betas
```

```
      implicit double precision (a-h,j-z)
      common /atom/ a,b,c,d,e,f
      common /coef/ al,be,becr,ga,de,ep,dz,ph,et,la,mu
      common /rat/ ri,rw,roi,row,ros,hl,si
c
      be1=al*(4.0d0*a+b)
      be2=4.0d0/(roi*ri)
      be3=e+f-4.0d0*c-d
      be=be1/(be2+be3)
      ros=(row*rw)/(roi*ri)
      mu=be*ros
      ga=be/(ri*roi)
      be4=al*b+2.0d0*mu
      if(e+f-d) 10,20,10
   10 be5=e+f-d
      go to 30
   20 be5=e+f-d+0.01d0
   30 becr=be4/be5
      return
      end
*
**********************************************************************
*     b) hydrogen/halocarbon limit - with/without water
**********************************************************************
      subroutine betai
      implicit double precision (a-h,j-z)
      common /atom/ a,b,c,d,e,f
      common /coef/ al,be,becr,ga,de,ep,dz,ph,et,la,mu
      common /rat/ ri,rw,roi,row,ros,hl,si
c
      be1=4.0d0*ga
      be2=4.0d0*c+d-e-f
      be3=4.0d0*(a+b/4.0d0)/(ri*roi)
      be=be1/(be2+be3)
      ros=(row*rw)/(roi*ri)
      mu=be*ros
      al=be/(ri*roi)
      be4=al*b+2.0d0*mu
      if(e+f-d) 10,20,10
   10 be5=e+f-d
      go to 30
   20 be5=e+f-d+0.01d0
   30 becr=be4/be5
      return
      end
*
**********************************************************************
*     inhibitor in - with/without water combustion/inhibition products
```

```
*     a) low hydrogen level
**********************************************************************
*
      subroutine coefls
      implicit double precision (a-h,j-z)
      common /atom/ a,b,c,d,e,f
      common /coef/ al,be,becr,ga,de,ep,dz,ph,et,la,mu
c
      la=0.0d0
      de=2.0d0*ga-al*a-be*c+mu
      if(f.gt.0.0d0) then
        ph1=al*(0.5d0*b-a)
        ph2=0.5d0*be*(d+f+2.0d0*mu-2.0d0*c-e)
        ph=de+ph1+ph2
        dz1=al*(a-0.5d0*b)
        dz2=0.5d0*be*(2.0d0*c+e+f-2.0d0*mu-d)
        dz=0.5d0*(-de+dz1+dz2)
      else
        ph=0.0d0
        dz=0.0d0
      endif
      et1=al*(a+0.5d0*b)
      et2=0.5d0*becr*(2.0d0*c+d+e-2.0d0*mu-f)
      et3=-de+2.0d0*mu+et1+et2
      et=et
      ep=et3-et
      return
      end
*
**********************************************************************
*     inhibitor in - with/without water combustion/inhibition products
*     b) low hydrogen level
**********************************************************************
*
      subroutine coefli
      implicit double precision (a-h,j-z)
      common /atom/ a,b,c,d,e,f
      common /coef/ al,be,becr,ga,de,ep,dz,ph,et,la,mu
c
      la=0.0d0
      de=2.0d0*ga-al*a-be*c+mu
      if(f.gt.0.0d0) then
        ph1=al*(0.5d0*b-a)
        ph2=0.5d0*be*(d+f+2.0d0*mu-2.0d0*c-e)
        ph=de+ph1+ph2
        dz1=al*(a-0.5d0*b)
        dz2=0.5d0*be*(2.0d0*c+e+f-2.0d0*mu-d)
        dz=0.5d0*(-de+dz1+dz2)
```

```
      else
        ph=0.0d0
        dz=0.0d0
      endif
      et1=al*(a+0.5d0*b)
      et2=0.5d0*becr*(2.0d0*c+d+e-2.0d0*mu-f)
      et3=-de+2.0d0*mu+et1+et2
      et=et
      ep=et3-et
      return
      end
*
**********************************************************************
*     inhibitor in - with/without water combustion/inhibition products
*     c) standard case, high hydrogen level
**********************************************************************
*
      subroutine coefhs
      implicit double precision (a-h,j-z)
      common /atom/ a,b,c,d,e,f
      common /coef/ al,be,becr,ga,de,ep,dz,ph,et,la,mu
c
      ep=0.0d0
      dz=0.0d0
      de=al*a+be*c
      ph=be*f
      et=be*e
      la=2.0d0*ga-2.0d0*de+mu
      return
      end
*
**********************************************************************
*     inhibitor in - with/without water combustion/inhibition products
*     d) high hydrogen level
**********************************************************************
*
      subroutine coefhi
      implicit double precision (a-h,j-z)
      common /atom/ a,b,c,d,e,f
      common /coef/ al,be,becr,ga,de,ep,dz,ph,et,la,mu
c
      ep=0.0d0
      dz=0.0d0
      de=al*a+be*c
      ph=be*f
      et=be*e
      la=2.0d0*ga-2.0d0*de+mu
      return
```

```
      end
*
*************************************************************************
*     outlet species mole flows
*************************************************************************
*
      subroutine molefl
      implicit double precision (a-h,j-z)
      common /qi/ qini,qh2oi,qfui,qo2i,qn2i,qairi,qti,dq
      common /q/ qin,qfu,qo2,qn2,qco2,qh2o,qhf,qhcl,qcof2,
     &           qcocl2,qt
      common /X/ Xin,Xfu,Xo2,Xn2,Xco2,Xh2o,Xhf,Xhcl,Xcof2,Xcocl2
      common /therm/ vm,lm3,p,t,ru,cm
      common /n/ nin,nfu,no2,nn2,nco2,nh2o,nhf,nhcl,ncof2,
     &           ncocl2,nt,nti,dn
c
      qt=qin+qfu+qh2o+qo2+qn2+qco2+qhf+qhcl+qcof2+qcocl2
      nt=qt/vm
      dn=nt-nti
      nin=qin/vm
      nfu=qfu/vm
      no2=qo2/vm
      nn2=qn2/vm
      nco2=qco2/vm
      nh2o=qh2o/vm
      nhf=qhf/vm
      nhcl=qhcl/vm
      ncof2=qcof2/vm
      ncocl2=qcocl2/vm
      return
      end
*
*************************************************************************
*     outlet species mole fractions
*************************************************************************
*
      subroutine molef
      implicit double precision (a-h,j-z)
      common /qi/ qini,qh2oi,qfui,qo2i,qn2i,qairi,qti,dq
      common /q/ qin,qfu,qo2,qn2,qco2,qh2o,qhf,qhcl,qcof2,
     &           qcocl2,qt
      common /X/ Xin,Xfu,Xo2,Xn2,Xco2,Xh2o,Xhf,Xhcl,Xcof2,Xcocl2
c
      qt=qin+qfu+qh2o+qo2+qn2+qco2+qhf+qhcl+qcof2+qcocl2
      dq=qt-qti
      Xin=qin/qt
      Xfu=qfu/qt
      Xo2=qo2/qt
```

```
      Xn2=qn2/qt
      Xco2=qco2/qt
      Xh2o=qh2o/qt
      Xhf=qhf/qt
      Xhcl=qhcl/qt
      Xcof2=qcof2/qt
      Xcocl2=qcocl2/qt
      return
      end
*
**********************************************************************
*
*     outlet species mass fractions and flows
**********************************************************************
      subroutine massf
      implicit double precision (a-h,j-z)
      common /therm/ vm,lm3,p,t,ru,cm
      common /mi/ mini,mfui,mo2i,mn2i,mco2i,mh2oi,mhfi,mhcli,mcof2i,
     &            mcocli,mti
      common /w/ wo2,wn2,wair,wc,wh,wf,wcl,wco2,wh2o,
     &           whf,whcl,wcof2,wcocl2,wfu,win,wmi,wm
      common /X/ Xin,Xfu,Xo2,Xn2,Xco2,Xh2o,Xhf,Xhcl,Xcof2,Xcocl2
      common /Y/ Yin,Yfu,Yo2,Yn2,Yco2,Yh2o,Yhf,Yhcl,Ycof2,Ycocl2
      common /q/ qin,qfu,qo2,qn2,qco2,qh2o,qhf,qhcl,qcof2,
     &           qcocl2,qt
      common /d/ din,dfu,do2,dn2,dco2,dh2o,dhf,dhcl,dcof2,
     &           dcocl2,denm,dm
      common /m/ min,mfu,mo2,mn2,mco2,mh2o,mhf,mhcl,mcof2,
     &           mcocl2,mt,mhffu
c
      wm=Xin*win+Xfu*wfu+Xo2*wo2+Xn2*wn2+Xco2*wco2+Xh2o*wh2o+
     &   Xhf*whf+Xhcl*whcl+Xcof2*wcof2+Xcocl2*wcocl2
      Yin=Xin*win/wm
      Yfu=Xfu*wfu/wm
      Yo2=Xo2*wo2/wm
      Yn2=Xn2*wn2/wm
      Yco2=Xco2*wco2/wm
      Yh2o=Xh2o*wh2o/wm
      Yhf=Xhf*whf/wm
      Yhcl=Xhcl*whcl/wm
      Ycof2=Xcof2*wcof2/wm
      Ycocl2=Xcocl2*wcocl2/wm
c
      qt=qin+qfu+qh2o+qo2+qn2+qco2+qhf+qhcl+qcof2+qcocl2
      mt=mti
      dm=mt/(qt*wm)
      min=qin*win*dm
      mfu=qfu*wfu*dm
```

```
      mo2=qo2*wo2*dm
      mn2=qn2*wn2*dm
      mco2=qco2*wco2*dm
      mh2o=qh2o*wh2o*dm
      mhf=qhf*whf*dm
      mhcl=qhcl*whcl*dm
      mcof2=qcof2*wcof2*dm
      mcocl2=qcocl2*wcocl2*dm
c
      if(mfui.le.0.0d0) then
        mhffu=0.0d0
      else
        mhffu=mhf/mfui
      endif
c
      return
      end
```

11. REAL-TIME SUPPRESSANT CONCENTRATION MEASUREMENT

William M. Pitts, George W. Mulholland, Brett D. Breuel,
Erik L. Johnsson, Steve Chung, Richard H. Harris
Building and Fire Research Laboratory

David E. Hess
Chemical Science and Technology Laboratory

Contents

11.1 Introduction

An aspect of fire extinguishment which has not received a great deal of attention is the role that the dispersion and evaporation characteristics of the agent play in fire-fighting effectiveness. The reason for this lack of interest in the past was that these properties have been nearly optimized by the use of halon 1301 for total flooding applications and halon 1211 for spray applications. With regard to total flooding applications, which are of most interest for this study, the low boiling point of halon 1301 has ensured that, for the majority of applications, it can be dispersed and vaporized very rapidly into a space. The dispersal effectiveness of halon 1301 is a direct result of the rapid evaporation which occurs when the agent is released from a pressurized vessel. The rapid evaporation not only effectively converts liquid agent to the gaseous state, but also results in a strong "flashing" which aids greatly in the distribution of the agent within the volume. Due to the effectiveness of dispersal of halon 1301, designers of total flooding systems generally have focused on the use and placement of hardware designed to ensure all areas of an enclosure quickly receive concentrations of the agent sufficient to extinguish the fire.

The fire fighting applications which are the focus of the current investigation--nacelle and dry-bay fires on aircraft--have different requirements with respect to these agent characteristics. Due to the nature of dry-bay fires, detection and extinguishment is generally required within tens of milliseconds. On the other hand, nacelle fires tend to have burned for longer periods before extinguishment, and a premium is placed on the achievement of extinguishing concentrations which can be maintained for a period of time following extinguishment to prevent relight on heated surfaces. Effective dispersion throughout the volume is required, but the dispersion can take place over longer periods of time than for the dry-bay application.

Even though the physical mixing processes involved are not generally considered in designs of halon fire-fighting systems, they are crucial. The important processes can be characterized into three major categories--release rate, dispersion and mixing, and evaporation. The release rate determines the minimum time required to extinguish a fire. If the release is very slow, it is possible that the fire may never be extinguished.

In order to determine the characteristics of an agent's dispersion behavior which are most important in determining extinguishment efficiency, it is necessary to have the means to make accurate concentration measurements on the time scales of interest. As new agents are incorporated into fire-extinguishment systems, it will also be necessary to make quantitative measurements in order to certify that these new systems are meeting their design goals. Development of the capability for making the necessary concentration measurements for 1) the design of dispersion systems and 2) the certification of new systems is the focus of this effort.

At the present time, instruments sensitive to variations in viscosity which occur with changes in concentration are used to certify fire-extinguishing systems based on halon 1301, 1211, 1202 and CO_2. Two similar devices of this type are known as the Statham analyzer and Halonyzer. See the discussion in Section 11.4 for further details. Response times for these instruments configured in the standard way have been listed as 0.25 s (New and Middlesworth, 1953; Pacific Scientific, 1988a). These times are clearly too long to allow their use for making measurements in dry-bay applications where the entire event is generally over in less than 0.1 s. Furthermore, the existing instruments have not been tested for their response to potential halon alternatives, and their sensitivity for certain chemicals may be poor.

Recognizing the need for improved instrumentation to make concentration measurements of halon 1301 and alternatives, the Air Force, Navy, Army, and Federal Aviation Administration jointly funded the project summarized in this section. The objective of this effort was "to evaluate possible methods

for real-time measurements of concentrations of alternative fire fighting agents for dry-bay and nacelle fire applications. If one or more feasible approaches are identified early in the investigation, a demonstration system will be developed for characterization under actual test situations." The major tasks were:

1. Review of the Concentration Measurement Literature
2. Evaluate and Test Instrumentation Developed with Air Force Funding
3. Evaluate and Test Hot-Film Probes
4. Development of Operating Procedures (Optional)

During the recent project on *Evaluation of Alternative In-Flight Fire Suppressants for Full-Scale Testing in Aircraft Engine Nacelles and Dry Bays* (Grosshandler *et al.*, 1994) an aspirated hot-film sensor was used to detect the presence of halon alternatives during releases of the pressurized agents (Pitts *et al.*, 1994). Commercial versions of these probes have been developed for concentration measurement (see the discussion in Section 11.2.1.2) which are capable of making measurements on a millisecond time scale. It was believed that these devices offered the best promise of commercially available measurement systems for making concentration measurements in full-scale dry-bay and nacelle test facilities. One component of the work described here was to test this hypothesis.

Wright-Patterson AFB staff members had anticipated the need for an instrument capable of detecting the presence of an alternative agent. A Small Business Innovation Research contract had been awarded to John Brown Associates to develop a device based on infrared absorption which would respond to transient concentrations of halons and alternative agents containing fluorine. The instrument could also be configured to respond to carbon dioxide. Several instruments, referred to as Fire Extinguishment Agent Sensors (FEAS), were delivered to the Air Force by John Brown Associates. At the request of the program sponsors, testing of these instruments for their potential to make quantitative concentration measurements was incorporated into the current research program.

In addition to testing of the two types of instrumentation, a literature review was to be carried out to identify additional techniques which might be employed for making the concentration measurements.

Very early in the investigation it was found that neither of the probes to be tested could be used to make the required measurements without substantial modification. With the agreement of the sponsors, the program was substantially extended to include the redesign and testing of modified approaches. Two instruments (a combined aspirated hot-film/cold-wire probe and an infrared absorption probe denoted as the Differential Infrared Rapid Agent Concentration Sensor (DIRRACS)) were developed and appeared promising enough that testing was carried out in the full-scale dry-bay test facility at Wright-Patterson AFB.

The following two sections describe the development and testing of the two instruments as well as providing the background necessary to understand their operation. Brief summaries and recommendations for additional research are included. These sections are followed by one describing the Statham analyzer and Halonyzer. The final section of this chapter contains a literature review assessing other potential techniques for making the required concentration measurements. A summary and recommendations for considering other possible techniques are included.

11.2 Development and Testing of a Combined Aspirated Hot-Film and Cold-Wire Probe

11.2.1 Background

11.2.1.1 Hot-Film Anemometry. Hot-wire and hot-film anemometers are devices which are normally used to measure velocity in flows of liquids or gases. Many books and monographs contain extensive discussions of their use and applications (*e.g.*, see Corrsin, 1963; Hinze, 1975; Bradshaw, 1971; Comte-Bellot, 1976; Fingerson and Freymuth, 1983; Perry, 1982). The principle of operation is fairly simple. An electric current passing through the conductive probe heats the sensor to a temperature higher than that of the ambient surroundings. Fluid flow over the sensor removes heat with the rate of heat transfer increasing with fluid-flow rate. Calibration of the amount of heat loss as a function of known flow velocity allows the velocity of an arbitrary flow of the fluid to be determined by measuring the heat loss of the sensor.

There are a number of different types, sizes, and shapes of probes which have been used. See the review articles listed above for details. In this paper we will only consider a hot-film anemometer operated in a constant-temperature mode. The hot-film detector is formed by depositing a thin film of platinum onto a 50 μm diameter quartz rod. The active length of the probe is specified by depositing an approximately 6.4 μm thick layer of gold at either end. The nominal active length is 1.0 mm. In order to limit oxidation, the entire probe is sealed with a thin layer of alumina.

During operation a current is passed through the probe sufficient to heat the sensor to a temperature well above the ambient. The resistance of the probe depends on temperature, generally increasing with temperature. Over the typical range of operating temperatures for hot films, the dependence of resistance on temperature is linear. The resistance of the probe can therefore be written as

$$R_{op} = \alpha_p(T_{op}-T_{ref}) + R_{ref} , \tag{1}$$

where R_{op} is the operating resistance of the probe, T_{op} is the nominal operating temperature, R_{ref} is the resistance of the probe at the reference temperature, T_{ref}, and α_p is the thermal coefficient for the probe resistance. For a constant voltage across the probe, the current (i_f) through the sensor varies with temperature.

As a fluid flow passes over the surface of the sensor, heat is convected away and the probe begins to cool. The amount of heat loss to the fluid per unit time (H) can be written as

$$H = h\pi d_f l_f(T_{op}-T_\infty) , \tag{2}$$

where h is the heat transfer coefficient, d_f is the sensor diameter, l_f is the active length of the sensor, and T_∞ is the ambient temperature of the fluid. In order to maintain the resistance of the probe (and hence the nominal temperature) constant it is necessary that heat be added to the sensor (*i.e.*, the amount of resistive heating must be adjusted by varying the flow of current to the sensor to balance the heat loss due to convection). A constant-temperature anemometer uses electronics to ensure that the resistance of the sensor remains constant at a preset value. The output signal of the electronics is a voltage which is proportional to the current flowing through the probe. Since values of h generally increase with velocity, the voltage output also increases with flow velocity.

Heat transfer correlations for heated cylinders are typically written in terms of the nondimensional Nusselt number (Nu), defined as

$$Nu = \frac{hd_f}{k_o} , \tag{3}$$

and have the general form

$$Nu = fun(Re, Pr, Gr, wire\ properties) , \tag{4}$$

where

$$Re = \frac{U_o d_f}{\nu_o} , \tag{5}$$

$$Pr = \frac{c_p \mu_o}{k_o} , \tag{6}$$

and

$$Gr = \frac{g\rho_o^2 d_f^3 \beta (T_{op} - T_\infty)}{\mu_o^2} . \tag{7}$$

Undefined variables are the thermal conductivity of the fluid, k_o, Reynolds number (Re), flow velocity over the hot film, U_o, kinematic viscosity of the fluid, ν_o, the Prandtl number, Pr, constant pressure heat capacity for the fluid, c_p, dynamic viscosity for the fluid, μ_o, the Grashof number, Gr, gravitational constant, g, the fluid density, ρ_o, and the coefficient of thermal expansion of the gas, β.

The most commonly used heat-transfer law for cylindrical hot-film anemometers is known as King's (1914) Law,

$$Nu = C_1(Pr) + C_2(Pr)Re^n , \tag{8}$$

where C_1 and C_2 are constants which depend on Pr. King originally set the exponent n to ½, but here it is treated as a parameter since experiments have demonstrated that it varies with flow conditions and gas.

The overheat ratio for a hot-film anemometer is defined as $(T_{op}-T_\infty)/T_\infty$. For normal operating overheats Gr effects can be neglected. Furthermore, the dependence of the heat transfer on Pr is generally weak. From the above equations it becomes clear that the heat loss from the cylinder should vary linearly with the overheat ratio and roughly as the square root of the velocity.

Recall that the heat loss from a hot-film sensor operated in the constant-temperature mode must be balanced by adding heat to the sensor by resistive heating. Since the amount of heat provided to

the cylinder is $(i_f)^2 R_{op,}$ and the output voltage of the sensor is proportional to the hot-film current i_f, the output voltage for a constant overheat is expected to obey the following relation,

$$E^2 = A + BU_o^n \,, \tag{9}$$

where E is output voltage and A and B are constants. Equation (9) is known to be an approximation. Many other parameters can affect the output of a hot-film anemometer. A detailed discussion of such effects can be found in Pitts and McCaffrey (1986).

11.2.1.2 Hot-Film Sensitivity to Composition. Hot-film anemometers are most commonly used for velocity measurements in which the composition of the fluid does not change. The device response to changes in velocity is simply calibrated for the fluid of interest. It is well known that such calibrations are sensitive to the composition of the fluid which can be understood in the terms of the simplified description of hot-film response provided in the last section. Equations (3) - (7) contain molecular constants which vary with composition. In particular, the response of a hot film should depend strongly on the thermal conductivity and kinematic viscosity of the fluid surrounding the hot film.

The sensitivity of the hot-film anemometer to gas composition is a decided drawback when making velocity measurements. It is effectively impossible to make velocity measurements in a flow where the composition is varying with time using a single probe, since the response is a function of both velocity and an unknown composition. The same is true for flow fields in which temperature is fluctuating.

Several groups have developed probes which are capable of measuring concentration and velocity simultaneously by using two probes with very different responses (Way and Libby, 1970, 1971; McQuaid and Wright, 1973, 1974; Aihara *et al.*, 1974). Since two sets of measurements are available which have different dependencies on velocity and concentration, the signals can be deconvoluted to give velocity and concentration. These probes require extensive and tedious calibration in order to make quantitative measurements. They have only been used for constant-temperature flows. In order to operate them in situations where the temperature is also varying, it would be necessary to calibrate both sensors as functions of temperature and to provide an independent measurement of temperature at the sampling location during the measurement.

Other workers have attempted to use the sensitivity of hot wires and films to concentration to develop probes for measurements in binary mixtures based on single sensors. One of the earliest investigations is due to Adler (1972) who describes a system in which a hot wire is placed in a flow created by withdrawing gases from the sampling volume. The flow system incorporates a heater to ensure that the temperature of the gases is constant and a supersonic orifice is used to control the velocity. Since the flow velocity in the sampling volume is a function of the pressure in the volume and composition only, the hot-wire response is expected to be independent of gas temperature and velocity. Proper calibration allowed quantitative concentration measurements to be made. Adler does not report the time response of the instrument, but does indicate that "rapid response is ensured because of the high response of the hot wire." It is interesting that the design of this instrument is very similar to that for the Statham and Halonyzer instruments described in Section 11.4. The major difference is that the concentration response in the latter instruments is provided by measuring the pressure drop across a subsonic orifice. Of relevance to the later discussion, Adler pointed out the need to use this probe in a clean environment since probe contamination would change the probe

response. Response times for Statham and Halonyzer instruments have been characterized as being too long for the current application in Section 11.4.

Other researchers have developed probes based on hot-wires or hot-films in which single sensors are placed in choked flows of the gas to control the velocity, but for which the sensor and choke point are located very close to the probe sampling volume. These probes have the advantage of maximizing the time response since the flow only has to flow over a small distance before reaching the sensor.

The first report of such a sensor was by Blackshear and Fingerson (1962). This probe incorporated a unique cylindrical hot-film probe in which a small pyrex tube (0.15 mm outside diameter (o.d.), 0.10 mm inside diameter (i.d.)) was used as the cylindrical rod. The platinum film was deposited on the outside of the tube. Water was passed through the sensor to provide cooling. In this way it was possible to use the probe in highly heated flows. The probe was mounted at the entrance of a tube with a cap containing a sonic orifice. Dimensional details of the probe are not provided, but the overall o.d. of the probe was 8 mm.

The probe was found to respond to external velocity fluctuations even though ideally it should have been insensitive to such fluctuations. The sensitivity of the probe to velocity fluctuations was characterized by placing the probe on the centerline of an axisymmetric turbulent air jet fifteen diameters downstream of the exit and measuring the response of the probe to the external velocity fluctuations, which had a root-mean-square (rms) value equal to 0.17 of the average velocity. The fluctuations recorded by the probe increased with the ratio of the velocity in the probe and the average external air velocity. On the other hand, the velocity fluctuations were shown to be independent of the ratio of areas for the opening into the probe and the choked orifice. Blackshear and Fingerson reported that the velocity fluctuations at the probe were reduced by a factor of thirteen over those observed in the free stream.

Measurements using the probe were demonstrated for two very different systems. The first was as a temperature measurement device in flame globules created by discharging a voltage across a pair of electrodes located in a flowing combustible gas mixture. The measured rise time of the temperature using the aspirated probe was roughly 0.1 ms which was in good agreement with the expected temperature gradients for the flames. In the second experiment, the probe was used to measure either the concentration of helium or the temperature of heated air in axisymmetric turbulent jets. Radial profiles of the rms for the concentration and temperature fluctuations were reported. According to the authors, with the exception of measurements based on Mie scattering from seed particles, these results represented the first direct time-resolved measurements of concentration in turbulent flows.

The next reported use of an aspirated concentration probe was a study by Brown and Rebollo (1972). These researchers mounted a 12.7 μm diameter hot wire across the 2 mm diameter of a tube which had been drawn down to a fine tip with an opening of 25 μm. A vacuum was attached to the other end of the tube, and gases were withdrawn through the orifice. The vacuum was sufficient to ensure that the flow through the orifice was choked and therefore only depended on external pressure, temperature, and composition. Assuming constant temperature and pressure, the response of the hot-wire should only be a function of concentration.

Since the wire was located only 1.6 mm from the orifice and internal gas flow velocities were high, the probe was expected to have a rapid response time. It was experimentally demonstrated that actual response times were less than one ms. The authors also contended that the response of the probe was insensitive to the external flow velocity. The probe was calibrated for mixtures of helium, argon, and krypton in nitrogen. Measurements of helium concentration in a mixing layer formed between flows of helium and nitrogen were demonstrated.

Aihara *et al.* (1974) reported the use of a similar probe for helium concentration measurement. In their probe the velocity of the fluid at the sensor was reduced to a low level by passing the sampled

gases through a large area expansion. They reported that the output voltage of the hot wire was quite insensitive to velocity.

Perry (1977) performed an analysis of the flow over and through a Brown-Rebollo-type probe and estimated the frequency response as 10 kHz.

Ahmed and So (1986) developed a probe which was similar to that of Brown and Rebollo, but which incorporated a pumping port and BNC connector for the anemometer electronics. The glass tube was contained within a stainless steel tube. The hot wire used by Brown and Rebollo was replaced with a 50 μm diameter hot film. The hot film was located 12.7 mm downstream of the 130 μm diameter sonic orifice. Figure 1 is a schematic of the probe based on Figure 1 in their paper. These authors designed the probe for use in a swirled flow and were therefore concerned about the response of the probe to variations in upstream (*i.e.*, sampled gas) pressure with sampling position. By calibrating the response across the flow they showed that the probe was nearly insensitive to the stagnation pressure. This finding has important implications with regard to the findings of the current investigation.

The probe developed by Ahmed and So was used to measure helium concentrations in a variety of flows. These include a model cylindrical combustor (Ahmed and So, 1986) and a jet discharge into a swirled flow (So and Ahmed, 1987). Later the technique was combined with laser Doppler anemometry (LDV) to allow simultaneous measurements of concentration and velocity in a variety of helium/air flows (Zhu *et al.*, 1988, 1989; So *et al.* 1990, 1991). These later studies showed that the probe response was not sensitive to the presence of the roughly 1 μm diameter 50 % water/50 % glycerine droplets used to seed the flow field for the LDV measurements.

A commercial aspirating hot-film probe, designated as Model 1440, was developed and marketed by Thermo-Systems Inc. (now known as TSI, Inc.) several years prior to 1979 (Jones and Wilson, 1979). A schematic of the Model 1440 is shown in Figure 2. Note that this design differs significantly from that reported by Brown and Rebollo (1972) in that the hot-film probe is mounted upstream of the sonic orifice, and the flow must pass down a tube before flowing through the sonic orifice.

Jones and Wilson (1979) have provided a detailed analysis of the flow through the device and the response of the hot-film to variations in gas composition. They pointed out that by holding the upstream dynamic pressure and temperature constant, the mass flow through the nozzle becomes only a function of the molecular weight of the gas. Using an expression similar to Equation (9) and standard expressions for electrical heating and heat loss, they derived the following expression for hot-film response,

$$\frac{E^2}{R_{op}} = \frac{\pi d_f k_o}{4}(T_{op}-T_\infty)\left[A+\left(B\frac{d_f \beta(\rho V)^*}{\mu_o}\right)^n\right], \tag{10}$$

where β is the ratio of the nozzle area to the area of the tube containing the hot film and $(\rho V)^*$ is the maximum mass-flow rate of fluid per unit area through the supersonic orifice which can be calculated using

$$(\rho V)^* = \sqrt{\frac{\gamma MW}{RT_o}}P_o\left[\left(\frac{2}{\gamma+1}\right)^{\frac{\gamma+1}{2(\gamma-1)}}\right]. \tag{11}$$

P_o and T_o are the fluid pressure and temperature upstream of the nozzle, γ is the ratio of the constant pressure and volume specific heats, MW is the molecular weight of the gas, and R is the universal gas constant.

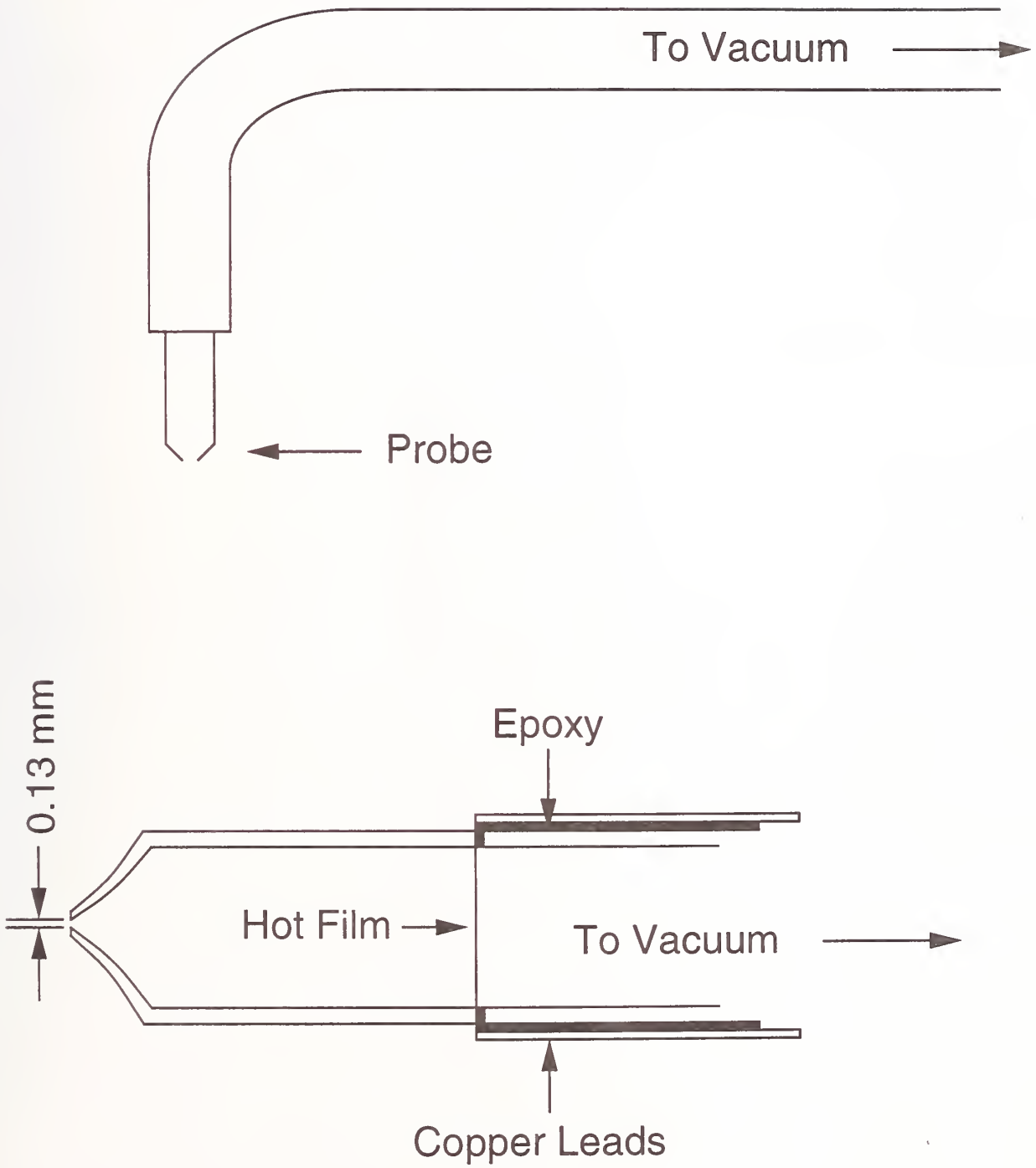

Figure 1. Schematic of the concentration probe developed by Ahmed and So (1986) based on Figure 1 of their paper.

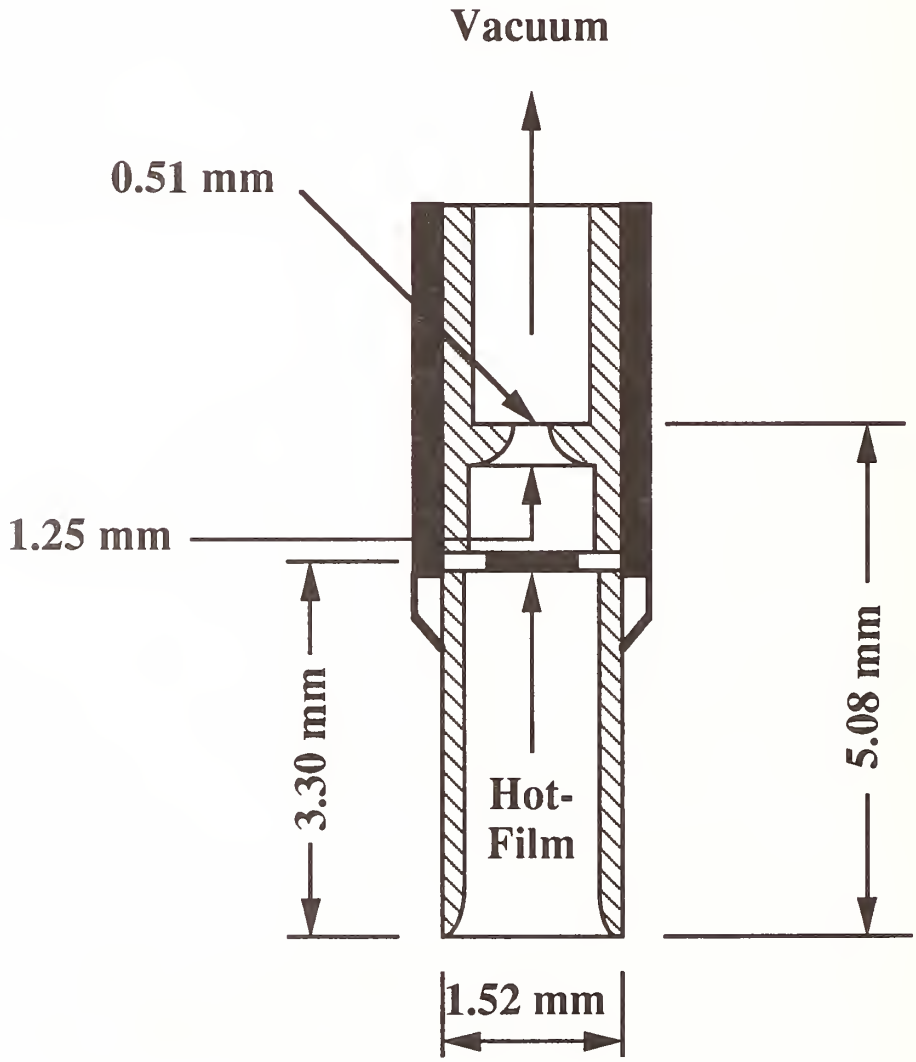

Figure 2. Schematic diagram of the TSI, Inc. Model 1440 aspirated hot-film probe.

The authors showed that Equation (10) provided a fairly good prediction of the observed variation in hot-film output for a range of helium-argon concentrations. They attributed much of the difference between the observed and calculated values of hot-film voltage to the neglect of end effects where the probe transfers heat to its supports. A detailed discussion of such effects can be found in Pitts and McCaffrey (1986).

Jones and Wilson were interested in making measurements in flow fields in which both the concentration and temperature were varying. As Equation (10) shows, the hot-film response varies with the ambient temperature, T_∞. In order to correct for this temperature variation an independent temperature measurement is required. They obtained temperature measurements by installing a second 50 μm diameter probe within the sampling tube 250 μm upstream of the standard hot film. This second hot film was operated with a very low overheat such that its output was sensitive to temperature (LaRue *et al.*, 1975). In this way it was possible to record the temperature and correct the response of the primary hot film for temperature variations.

By recognizing that k_o and ν_o are approximately proportional to the square root of temperature and that the mass flow is inversely proportional to temperature, Equation (10) can be used to show that

$$\left.\frac{E^2}{R_{op}}\right|_{T_1} = \left.\frac{E^2}{R_{op}}\right|_{T_2} \times \frac{T_{op}-T_1}{T_{op}-T_2} \; . \tag{12}$$

This equation allows the hot-film response to be predicted for a temperature T_1 when it is known for a second temperature T_2. Experiments with variable temperature flows of argon, helium, and mixtures of these two gases indicated that Equation (12) predicts the observed changes in anemometer output voltage quite well. Jones and Wilson concluded that the aspirated hot-film could be used to make concentration measurements having an accuracy of 1 %.

Wilson and Netterville (1981) reported the development of an aspirated hot-film concentration probe based on a very different design. Figure 3 shows a schematic for their probe. In their system the gases to be sampled were drawn into a 1.7 mm diameter tube, which then expanded into a 2.4 mm diameter tube. The larger tube contained a short plug of cigarette-filter material. The filter was intended to dampen out turbulent stagnation pressure fluctuations by providing a pressure drop of nearly 50 kPa through what amounts to a bundle of parallel capillary tubes. After passing through the filter, the lower pressure flow continued down the tube where it ultimately reached a hot-film anemometer. After the hot film the flow entered a region containing a 600 μm diameter sonic orifice. A pump lowered the pressure on the downstream side of the orifice to a sufficient level to ensure supersonic flow through the orifice. The authors pointed out the need to have the hot-film as close as possible to the sonic orifice in order to minimize the lag time between changes in sampling velocity at the orifice due to composition and heat transfer from the sensor. A novel configuration was used in which the flow from the hot film to the sonic orifice was through an angled channel. This modification from other probes of this type was designed to minimize velocity fluctuations within the device.

This new probe was calibrated for its response to helium and CFC-12 (CF_2Cl_2) concentrations[1] in air. The calibrations covered the narrow concentration range of 0 % to 1 %. Differences in concentration smaller that 0.1 % were easily distinguishable for both gases, and both calibrations were

[1]For the purposes of this section concentration of agents will be expressed either as mole fractions or as percentages of agent (*i.e.*, mole fraction × 100)

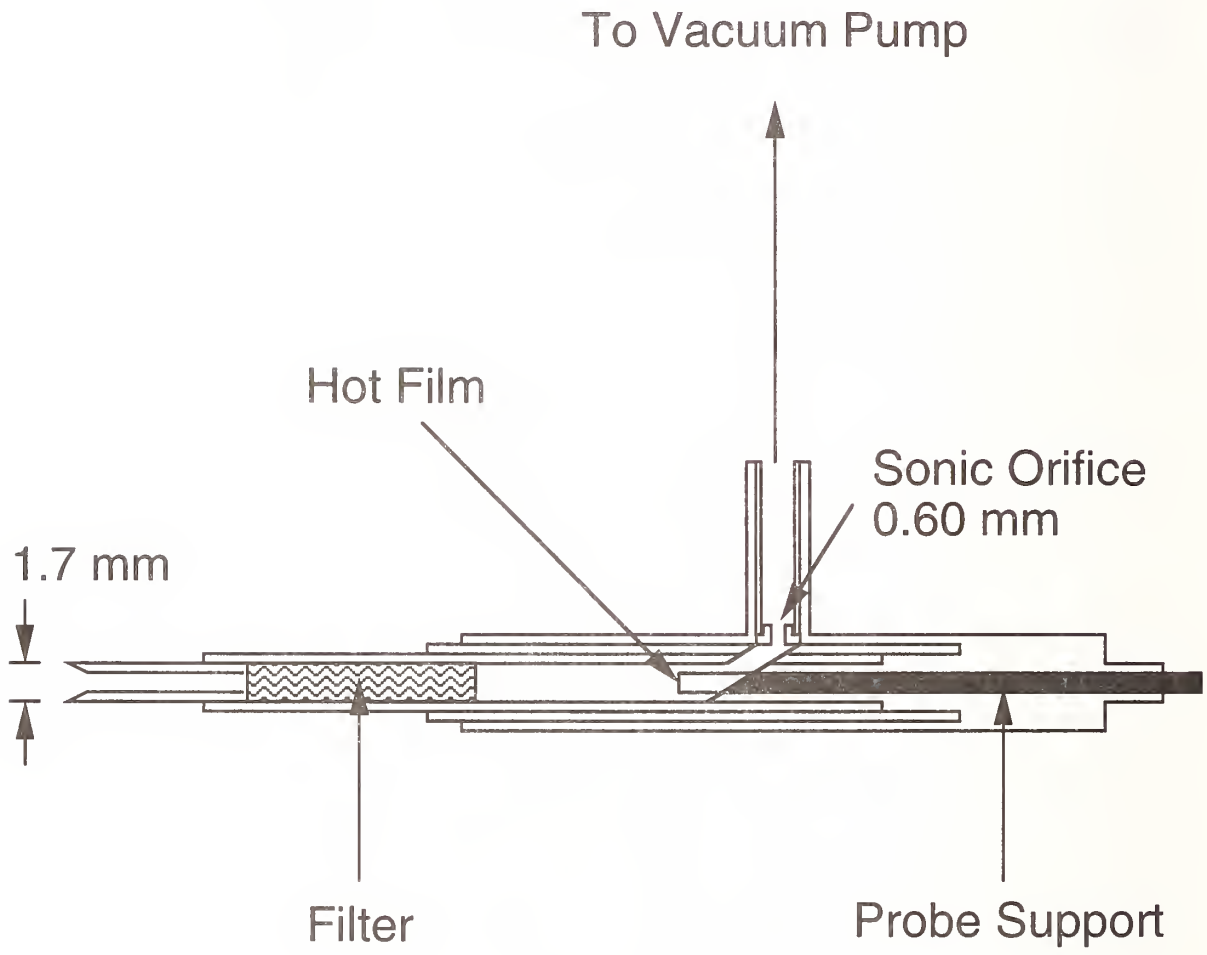

Figure 3. Schematic diagram of the aspirated hot-film probe developed by Wilson and Netterville (1981).

linear over this limited range. The lower detection limit for helium was reported to be 0.01 %. The slope of the calibration curve for helium was positive and had an absolute magnitude five times higher than the negative slope found for CF_2Cl_2.

The time response of the probe was investigated by placing the probe on the end of a pendulum and swinging it rapidly through a jet flow of 1 % helium in air and recording the transient response. The probe entered the flow sufficiently fast that the concentration change with time was effectively a step function. The response time was determined to be 500 μs and was successfully modeled as consisting of a time constant associated with the flow through the filter and the response of the hot-film anemometer to changes in concentration and velocity. Wilson and Netterville used their probe to monitor concentration fluctuations in a turbulent boundary flow doped with helium. The probe response time was sufficient to fully resolve the concentration fluctuations.

Fedyaev *et al.* (1990) reported the fabrication of a probe similar in construction to that originally developed by Blackshear and Fingerson (1962). A three mm diameter steel tube was sealed at one end, and a 20 μm diameter sonic orifice was machined into the end. Instead of placing the probe upstream of the orifice, as in the case of Blackshear and Fingerson, a 5 μm diameter hot wire was mounted downstream of the orifice on the low-vacuum side of the probe. The hot wire was operated in the constant-temperature mode. The response of the probe to velocity fluctuations on the centerline of an axisymmetric jet of air was investigated. They found that the probe output was essentially independent of velocity and its fluctuations for velocities less than 20 m/s. At higher velocities a distinct response to velocity was observed, which increased with increasing velocity. The authors discussed how such noise levels can limit the resolution of an experimental measurement of concentration. The probe was used to measure helium concentration upon injection of helium into the turbulent boundary layer of a wind tunnel.

Ninnemann and Ng (1992) have reported still another design for an aspirated hot-wire probe for recording helium concentration in supersonic shear flows. The 51 μm diameter hot film was placed downstream of a 28 μm diameter opening into a tapered tube which opened to 1.2 mm. At a much larger downstream distance the flow in the tube passed through a 56 μm diameter orifice which choked the flow. The probe was calibrated as functions of helium concentration, temperature, and pressure. The sensitivity of the constant-temperature anemometer output as a function of the angle of the probe to the flow direction of a supersonic air jet was shown to introduce errors in the concentration measurement of a few percent. In order to use the probe for quantitative concentration measurements, it was necessary to know the local stagnation pressure. For these experiments this was recorded using a low-frequency-response pressure probe. For this reason, only time-averaged helium concentration values were reported.

An earlier paper by Ng and Epstein (1983) discussed the development of a related probe designed to provide temperature and pressure measurements in unsteady high-speed flows. The design incorporated two hot wires into an aspirated probe having a 1.5 mm i.d. This paper is particularly relevant because it contains an excellent discussion of many of the design considerations which must be taken into account when designing aspirated hot-wire or hot-film probes.

All of the measurements discussed thus far have focused on the use of aspirated hot wires or films to record concentration in mixtures of helium with heavier gases. These are particularly advantageous cases since the thermal conductivity, and hence expected probe response, of helium is much larger than for heavier molecular weight gases. Birch *et al.* (1986) were the first to consider the response of an aspirated probe to mixtures of a wide range of gases (helium, natural gas, ethylene, argon, and Freon 12 (CF_2Cl_2)) with air. They used the TSI, Inc Model 1440 aspirating probe described above. Calibration curves for large numbers of mixtures are presented. Unlike the study of Wilson and Netterville (1981), calibration curves are provided for mole fractions of the gas of interest in air varying from 0 to 1.

The calibration curves for each gas were very well defined with little variation for a given concentration. The response of the probe varied widely with the gas mixed with air. Increasing concentrations of ethylene, natural gas, and helium led to increasing voltage outputs, while decreasing voltage outputs were observed for argon and Freon 12. As expected, the largest response was found for helium, while the remaining four gases had similar signal magnitudes. The output voltages for natural gas and argon varied linearly with concentration while the other three gases yielded curves with definite curvature.

The calibrated Model 1440 probe was used to make concentration measurements in an axisymmetric jet of natural gas flowing into air. The concentration behavior in this same jet had been reported earlier using Raman spectroscopy (Birch *et al.*, 1978). Time-averaged centerline concentrations measured with the aspirated probe were shown to be in excellent agreement with the earlier measurements. Root-mean-square (rms) values were also reported for the concentration fluctuations along the centerline of the jet. In the far field the agreement was excellent, while in the near field the rms values measured by the aspirated probe were somewhat lower. Birch *et al.* attributed the lower values to a high-frequency cutoff in the response of the aspirated probe which resulted in some averaging of the concentration fluctuations. Based on their results, they estimated the frequency response of the probe as 500 Hz.

Birch *et al.* also reported the development of a much simpler and ruggedized aspirating probe. The probe was based on a TSI, Inc. Model 1291 probe which consists of a hot-film sensor built into a Swagelok fitting. A tube having a 6.4 mm diameter tube with a length of 25 mm was inserted into one end of the swagelok. The end of the tube was closed by a disk having a centered orifice of 0.25 mm diameter which formed the sonic orifice and also served as the sampling port. The other end of the sensor was connected to a vacuum line. Note that this sensor was configured with the sensor downstream of the sonic orifice. Calibration curves for this sensor were very similar to those for the Model 1440. However, the response time was seriously degraded, being on the order of 10 Hz. A system for multi-point measurements of concentration consisting of 64 of these ruggedized probes was described.

An array of five of the ruggedized probes were subsequently used to record concentration fluctuations within a turbulent jet of natural gas entering an air cross flow. The noise level of these probes was reported as corresponding to a methane mole fraction of 0.0025.

11.2.2 Design Considerations. In developing a probe for measuring halon 1301 and alternative agents in real-scale facilities we relied heavily on observations of a series of tests carried out during the study on *Evaluation of Alternative In-Flight Fire Suppressants for Full-Scale Testing in Simulated Aircraft Engine Nacelles and Dry Bays* (Grosshandler *et al.*, 1994). As part of this investigation, many releases of nitrogen-pressurized (typically 4.1 MPa) vessels containing liquid agents were investigated (Pitts, 1994). A number of parameters were measured during the tests, but the two which are most relevant for the current study are aspirated hot-film response and dynamic pressure measurements within the flow generated by the release.

Flow visualization showed that the agents typically "flashed" on exiting the containment vessel and formed a rapidly expanding two-phase flow. The two-phase flow traveled over long distances. A piezoelectric pressure transducer located on the centerline of the flow 1.3 m from the vessel exit was used to record the dynamic pressures generated by the passage of the flow. Measured dynamic pressures varied with agent, but were generally on the order of several MPa. Pressures of this magnitude can only be due to the arrival of a high speed two-phase (high-density) flow. Such high pressures exert significant forces which have the potential to destroy sensors or other objects placed in the flow.

Flashing of an agent occurs when a pressurized agent is suddenly opened to atmospheric surroundings. Since the boiling points of the tested agents were generally below the ambient temperature, the release of the pressure generated a condition in which the liquid was superheated, *i.e.*, the liquid was at a temperature (ambient) which was significantly higher than its boiling point. The response of the liquid was to begin boiling very rapidly and, in the process, extract sufficient heat from the remaining liquid to lower the temperature to the boiling point. The mass fraction of the liquid which can be vaporized is determined by the amount of heat stored in the liquid and is characterized by the Jacob number, *Ja*, defined as

$$Ja = \frac{\Delta h}{\Delta H_{vap}} , \tag{13}$$

where ΔH_{vap} is the heat of vaporization for the liquid and

$$\Delta h = \int_{T_{amb}}^{T_{sat}} c_{p,l}(T) dT . \tag{14}$$

$c_{p,l}$ is the constant pressure heat capacity for the liquid which varies slightly with temperature and T_{amb} and T_{sat} are the ambient temperature and liquid boiling point, respectively. Generally, the agents having smaller values of *Ja* resulted in higher overpressures.

An uncalibrated TSI Model 1440 aspirated hot-film probe was mounted at the same location as the pressure transducer, and its voltage output was recorded during the releases. Arrival of the agent at the measurement location resulted in large voltage changes for all agents. In many cases the response was much greater than expected for a change in concentration of a gas. It was concluded that the large response occurred when a two-phase flow was present. This suggested that the aspirated hot film could be used to detect the presence of two-phase flow.

As noted above, during the release of a superheated liquid, the fluid is expected to cool very rapidly to its boiling point. This suggests that there are likely to be large temperature excursions associated with measurements of agent concentration. Recall that this presents a difficulty in applying aspirated hot films for concentration measurements since they respond to temperature fluctuations as well as concentration changes.

In designing the system for agent concentration measurements major characteristics which had to be considered were:

1. The ability to record continuous records of time-resolved concentration with the desired response time of 1 ms,
2. The need to record measurements in flows subject to velocity and temperature fluctuations,
3. The need for the probe to be robust enough to survive high-velocity flows and significant overpressures in two-phase flows, and
4. The need to have an efficient and easily implemented calibration system.

The first decision was the type of aspirated probe to use for the system. Several different designs are discussed in the previous section. Given the short period of the project, it was concluded that insufficient time was available to design, fabricate, and test a probe based on one of the designs available in the literature, and that it was desirable to use a commercially available probe. The only

commercial aspirated probes that were identified were those produced by TSI[2], Inc. For this reason, the decision was made to use Model 1440 aspirated hot-film probes manufactured from TSI, Inc. as the basis for the instrument. There were numerous descriptions of the use of these probes in the literature which provided confidence that they had sufficient time response and insensitivity to velocity fluctuations to be useful for our purpose. Since a probe of this type was used in the earlier investigation of two-phase flows (Pitts *et al.*, 1994), it was known that they were capable of surviving the environment generated by an agent release from a pressurized bottle.

In order to correct the response of the probe for temperature variations, it was necessary to record the fluid temperature at a location very near the hot-film sensor with a frequency response of at least 1 kHz. A number of approaches were considered including thermistors, thermocouples, and cold wires. Generally, the time responses for commercially available thermistors and thermocouples were too slow for this application. It was concluded that the use of a cold wire was the most viable approach for measuring temperature. Note that this approach had been adopted earlier by Jones and Wilson (1979). At the time this decision was made we were unaware of this previous work.

The operating principle of the cold wire is fairly simple. As shown by Equation (1), the resistance of a cold wire or film is a function of temperature. The resistance of the wire can be quantified by passing a small constant current through the wire sufficient to cause a measurable voltage drop, but too small to cause significant resistive heating of the sensor. The voltage output is therefore proportional to sensor resistance. Note that these measurements are done in the "constant-current" mode unlike the velocity and concentration measurements discussed earlier which generally employ the "constant-temperature" (*i.e.*, constant resistance) mode.

Due to the small heating of the wire, the sensor output voltage is nearly independent of the flow velocity across the sensor. However, the frequency response to temperature changes is a function of velocity. This is due to the need to transfer heat to or from the sensor when the temperature changes. As discussed in Section 11.2.1.2, the amount of heat transferred from a fluid is a function of the velocity as well as the fluid properties. Antonia *et al.* (1981) discuss the theory which can be used to estimate the frequency response and report measurements for cold wires of 0.63 μm, 1.3 μm, and 2.5 μm diameter as a function of velocity of air. Response frequencies were found to vary nearly linearly with velocity. For the smallest wire, the frequency response was greater than 1 kHz.

Having decided which approach to use for the proposed measurements, the next step was to actually design and procure the required probes. The design work was done in collaboration with staff from TSI, Inc. Three members of the research team (W. Pitts, D. Hess, and B. Breuel) traveled to Minneapolis and met with Jagadish Buddhavarapu, Skip Kiland, and Steve Hoff of TSI for two days. A number of topics were discussed including the viability of the chosen approach, potential problems in the manufacture of the probes, and pricing. It was agreed that the best approach was to modify a standard Model 1440 aspirating hot-film probe by locating the cold wire just outside of the entrance to the probe.

The decision to locate the cold wire outside of the aspirating probe raised a potential problem. In order to have an adequate time response, the diameter of the cold wire was required to be on the order of a few microns. It was not at all clear whether or not such a small probe could survive the severe environment generated by the two-phase flow formed by the release of the fire-fighting agents. In order to determine whether or not such probes were robust enough, a test was run in which single cold

---

[2]Certain trade names and company products are mentioned in the text or identified in an illustration in order to specify adequately the experimental procedure and equipment used. In no case does such identification imply recommendation or endorsement by the National Institute of Standards and Technology, nor does it imply that the products are necessarily the best available for the purpose.

wires (Models 1210-T1.0 and 1210-T1.5, diameters of 2.5 μm and 3.8 μm, respectively) were placed in the flow generated by the release of FC-218 (C_3F_8) from a vessel pressurized to 4.1 MPa. This test was run in the same facility used previously for investigating releases of fire-fighting agents (Pitts *et al.*, 1994). The probes were located 1.3 m from the vessel opening. Neither cold wire was operated during the test. Both were found to be operational after the superheated liquid was released.

Later releases were performed in which the Model 1210-T1.5 probe was operated with the cold-wire current set to 1 mA. Figure 4 shows an example of the signal recorded during one of these preliminary releases. The dynamic pressure measured during this test at the temperature measurement position reached approximately 9 MPa. The probe was not carefully calibrated, but a voltage change of 1 V corresponds roughly to a temperature change of 6 °C. The plot indicates that there was a rapid drop of approximately 55 °C when the discharge reached the cold wire. This is consistent with the boiling point of FC-218 (-37 °C) for an initial starting temperature of 21 °C. After the passage of the two-phase flow, the temperature increased again, but still remained below the initial room temperature. This experiment demonstrates that the temperature does vary during releases of the agent, and that cold-wire probes can survive the harsh environment created by an agent released from a pressurized bottle striking the probe.

An experiment was run in which a cold wire was located at various distances from the entrance of an operating aspirated hot-film. The results indicated that the response of the cold wire was insensitive to the separation from the cold-wire to the aspirated probe. On the basis of these experiments, an order was placed with TSI, Inc. to design and construct a probe consisting of an aspirated hot film with a cold wire mounted just outside of the tube.

Figure 5 shows a schematic of the probe designed by TSI, Inc. It incorporates a standard hot film and a standard hot wire operated as a cold wire. The hot film sensor, designated as "-20", consists of a cylindrical quartz substrate having a diameter of 51 μm with a thin layer of platinum deposited on the surface which conducts and serves as the heating element. The probe is overcoated with a thin protective layer of alumina. The hot-wire designation is "T1.5." It is made from tungsten wire having a 4.0 μm diameter. A thin layer of platinum is overcoated on the wire to limit surface oxidation of the tungsten.

11.2.3 Combined Aspirated Hot-Film/Cold-Wire Probe Electronics and Operation. The combined aspirated hot-film/cold-wire probe requires two sets of control electronics in order to make measurements. The hot-film is operated by a constant-temperature anemometer and the cold wire by a constant-current anemometer. A TSI, Inc. IFA 100 modular system was used for both types of measurements. The overall system is contained within a system cabinet (Model 158) which includes a microprocessor that aids in setting up the instruments and provides slots and power for up to four constant-current and/or constant-temperature anemometers. A keypad on the cabinet allows all of the major function of the system to be accessed. Remote access by RS-232 signals is also possible, but was not utilized in the current study.

The constant-temperature anemometer was a Model 150. It was paired with a Model 157 signal conditioner which provided frequency filters, a high-gain amplifier, and DC offsets. As discussed above, this is a circuit designed to maintain the resistance of the probe at a preset constant level by varying the current flow through, and hence the heating within, the probe in response to variations in heat losses from the probe. This is generally done by placing the probe in one leg of a four-leg Whetstone bridge as indicated in Figure 6. The particular circuit used for this study was a 5:1 bridge. The control resistance is set to a value five times greater than desired as the operation resistance for the probe. The control amplifier varies the current through the resistors in such a way that the bridge is balanced (*i.e.*, there is no flow of current into the amplifier). Thus the setting of the control resistance actually determines the operating resistance of the probe. A voltage output is available from

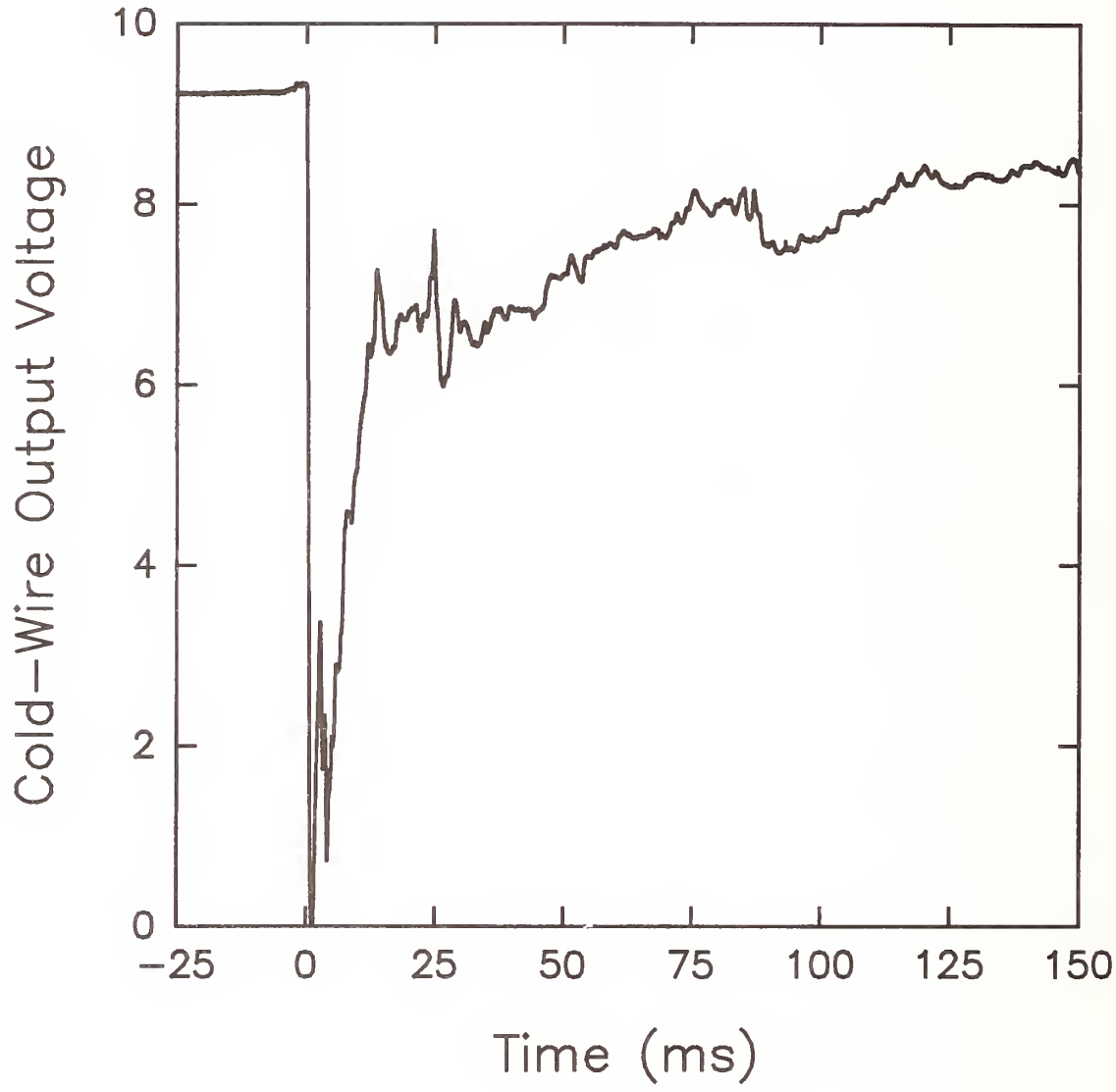

Figure 4. An example of the time-resolved voltage output from a cold wire recorded during a release of FC-218. A voltage change of 1 V corresponds roughly to 6 °C.

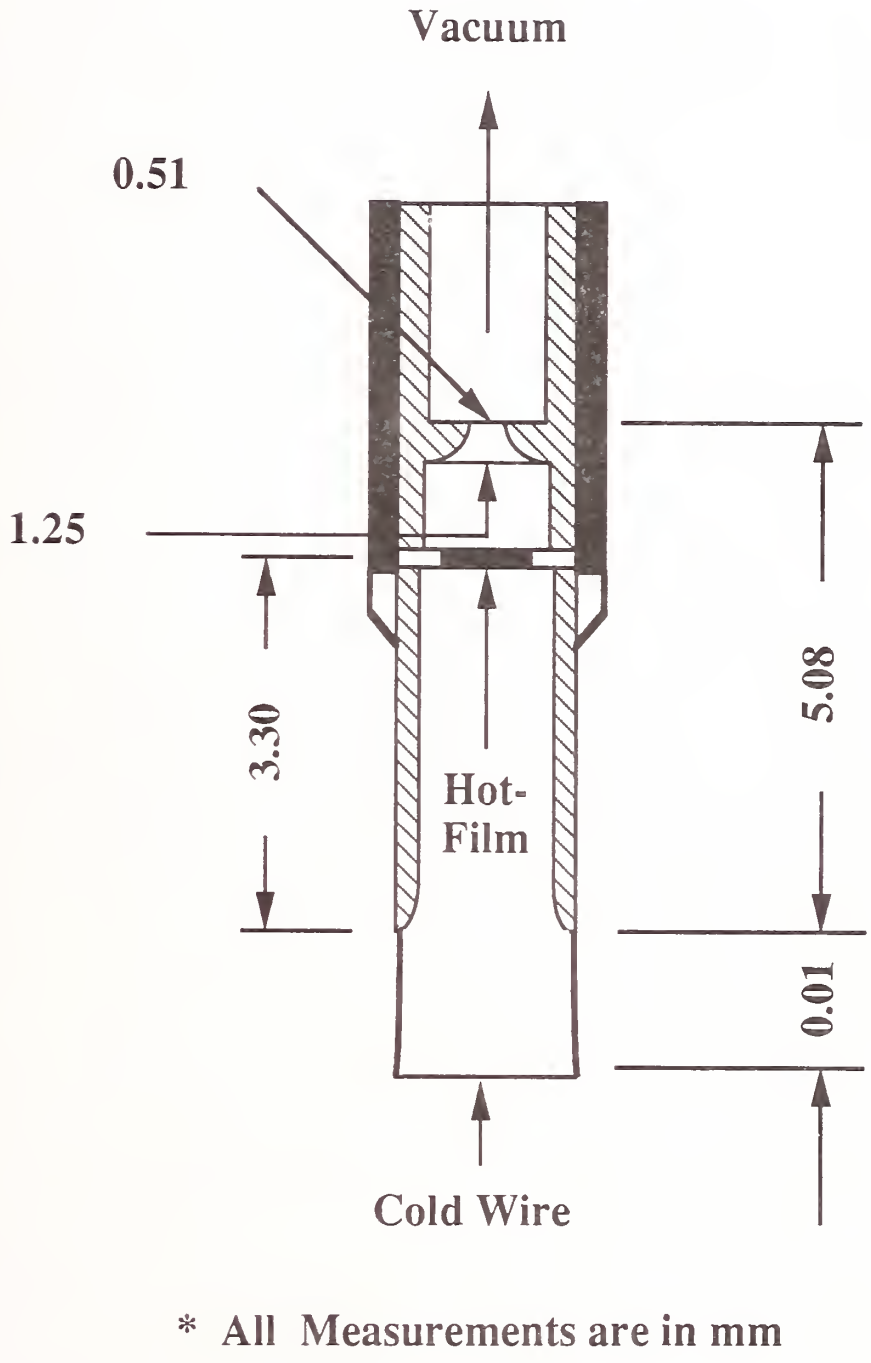

Figure 5. Schematic diagram of the TSI, Inc. combined aspirated hot-film/cold-wire probe which is designated by TSI, Inc. as a Model 1440S aspirated hot-film probe.

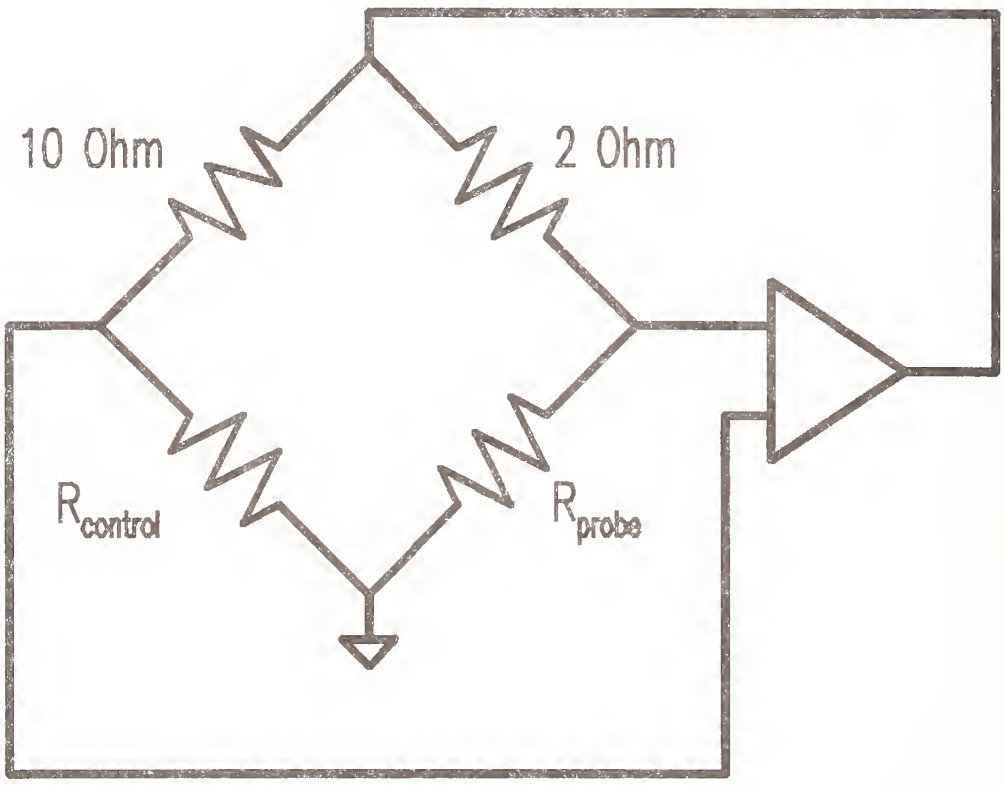

Figure 6. A schematic of the bridge circuit used for the constant-temperature anemometer is shown.

the Model 150 which is directly related to the heat loss of the sensor.

The aspirated hot film requires that the volume downstream of the supersonic nozzle be evacuated to a low enough pressure to ensure choked flow. For the ambient conditions of these experiments this required a pump capable of pumping 7 L/min at 33 kPa. A Thomas Industries, Inc. Model 905CA18 single cylinder, oil-less vacuum pump was used. The pump was connected to the aspirated probe through a stainless-steel tube attached to the 3.2 mm Swagelok vacuum connection of the probe.

The constant-current anemometer was a TSI Model 145 which was mounted in the Model 158 system cabinet. This module provides a preset constant current to the probe which is small enough to ensure that heating of the probe is minimal. It outputs a voltage which is proportional to the resulting voltage drop across the probe. The output signal is directly proportional to the resistance of the probe which, for small temperature changes, varies linearly with temperature. The Model 145 allows the voltage output to be adjusted such that a 0 V output corresponds to a reference temperature and the gain (50 to 1000) can be adjusted so that the ± 5 V output corresponds to the temperature range of interest.

11.2.4 Calibration System. Even though theories and models are available which have been used to predict the response of hot films and cold wires (see the discussion in Section 11.2.1.1), in practice, it is necessary to perform extensive calibrations of these devices, fit the calibrations, and then use the observed response of an instrument to an unknown condition along with the appropriate calibrations to deduce a value for the desired variable. The need for calibration presented a severe challenge for the proposed combined aspirated hot-film/cold-wire system since it had to be calibrated for variations in both agent concentration and temperature. Efficient algorithms were also required to convert the observed voltage outputs of the hot-film and cold-wire electronics to measurements of temperature and concentration using the calibration results.

In order to obtain meaningful calibrations, it was necessary to develop a system for generating known agent concentrations and temperatures over the full ranges of interest to this investigation. These ranges were chosen to be zero to one mole fraction of agent and -58 °C (the boiling point of halon 1301 (CF_3Br)) to 40 °C (a relatively high ambient temperature) for temperature. The agents to be tested included the three alternative agents recommended for testing in full-scale systems (Grosshandler *et al.*, 1994), FC-218 (C_3F_8), HFC-125 (C_2HF_5), and HFC-227ea (C_3HF_7), and halon 1301 for comparison purposes.

A unique computer-controlled calibration system was designed, constructed, and tested during the project. An overall schematic for the flow calibration system is shown in Figure 7. The major components are 1) sources for the air and agent, 2) mass-flow controllers for both the air and agent, 3) a mixing chamber to effectively mix the flows of agent and air, 4) a thermal bath capable of accurately controlling the temperature, 5) a heat exchanger to ensure the gas flow and bath temperature were equilibrated (not shown in Figure 7), 6) the test section where the probe was located, 7) a thermocouple to measure the temperature in the thermal bath, and 8) the computer control and measurement system. A personal computer interfaced to the calibration system was used to calculate the required flows of agent and air for a preset concentration, set the mass-flow controllers, open the appropriate solenoid valves, and record the voltage outputs of the aspirated hot film, cold wire, and thermocouple. The individual components of the calibration system are described in the following sections.

11.2.4.1 Test Section. The first step in the design process was to specify the calibration test section where the gas mixtures would be extracted by the aspirating probe. The mass-flow rate for gases extracted by the aspirated probe was first estimated for the agents and air using the equation for isentropic adiabatic flow of an ideal gas through a sonic orifice, Equation (11). Note that the mass-

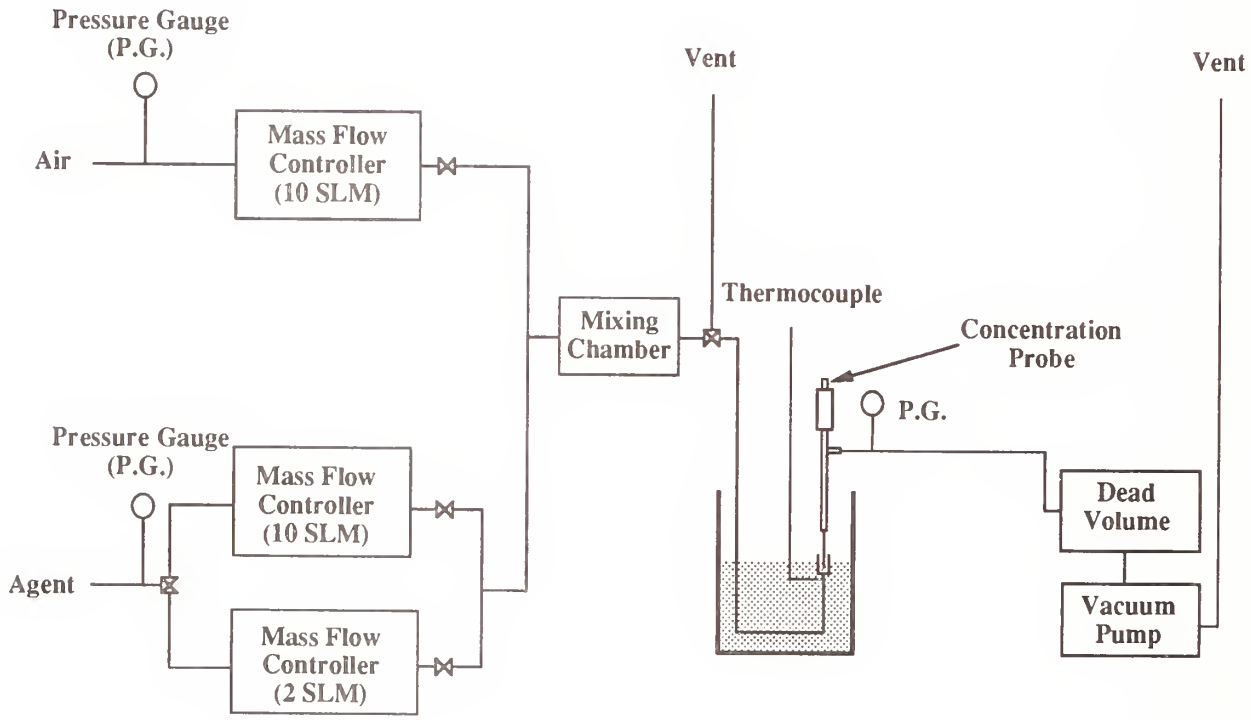

Figure 7. Overall schematic for the calibration facility used to generate flows of known agent concentration and temperature.

flow rate for the supersonic nozzle used in the aspirated probe is calculated by dividing $(\rho V)^*$ by the area of the nozzle, 0.02027 mm^2. Gas temperatures were varied over the range from the boiling points of the individual agents (-60 °C for air) to 40 °C. For comparison purposes, the mass-flow rates are expressed in comparable standard (0 °C, 101 kPa) liters per minute of nitrogen (slmn), the unit of measure for the mass-flow controllers used in the experiment. The gas correction factors required for the calculation (see ahead) were those recommended by the manufacturer. A FORTRAN program, included as Appendix A, was written to perform the calculations.

Table 1 lists the results. It can be seen that the values fall in a range of 2.25 slmn to 4.55 slmn. To ensure that the gas flow rate exceeds the withdrawal rate of the aspirated probe and to provide an excess flow to prevent backstreaming of gas from downstream of the probe, values of the actual flow rates must exceed the values listed in Table 1.

In order to accurately control the temperature of the gas at the probe entrance, it was necessary that the volume to be sampled be surrounded by the liquid of the temperature bath. This required the probe to be "plunged" into the flow since it was impractical to incorporate the probe into a closed flow system. In choosing an appropriate test section it was desirable to have a large cross section at the measurement location to limit flow velocities and to have a narrow exit from the test section to the atmosphere to create higher velocities and prevent backflow of air into the volume. A Whitey 304L-HDF4-50 sample cylinder was used to form the test section. This is a stainless-steel cylinder having a length of 95.2 mm with an i.d. of 34 mm. The inside dimensions are smoothly tapered at either end to 6.4 mm pipe-threaded exits. The cylinder was mounted vertically onto a pipe which was part of the mixing and flow system. The upper end of the test section was open to the air.

A lever designed for use with a drill press was placed near the test section. The probe to be tested was mounted on the lever. In this way it was possible to position the probe outside of and above the test section when the lever was in the "up" position, or manually lower the probe into the test section where it could be locked in place.

11.2.4.2 Mixing Chamber. Mixtures of agents in air were required having mole fractions ranging from zero to one. In order to ensure that the concentrations were constant, it was necessary to mix the gases uniformly before they were cooled and transported to the test section. A specially designed chamber was used for this purpose. Figure 8 shows a schematic of a horizontal cross-sectional cut through the gas mixer. It consists of a volume with baffles forming four sections that stir and mix the two gas stream flowing into the first section. The outside dimensions of the mixer are 51 mm (w) × 86 mm (l) × 51 mm (h). The outer walls are 6.4 mm thick and the baffle walls are 3.2 mm thick. Corners are curved on 6.4 mm radii. A single block of stainless steel was machined to form the inner volume of the mixer and a cover was then welded onto the block. Figure 9 is photograph of the machined mixer and its cover before final welding.

Four holes threaded for 6.4 mm pipe were drilled into the mixer. Three of these were centered in the three outer walls of the first section and the fourth in the opposite wall of the fourth section. 6.4 mm diameter stainless-steel pipe-to-BNC connectors were inserted in each of these positions. Figure 8 indicates the positions where air and agent flows enter the mixer. Note that the two gas streams enter perpendicular to each other which promotes efficient mixing. The third flow position in this section was capped. The mixed gases exit at the far end.

Subsequent experiments showed that this design was very effective in mixing the gas streams and that any fluctuations in concentration were too small to detect.

11.2.4.3 Mass-Flow Controllers. Three mass-flow controllers were used to provide the flows of air and agent required to prepare the gas mixtures. Note that mass-flow controllers are designed to deliver a known mass of gas, but that they are generally calibrated in terms of the volume flow rate

Table 1. Flow Volumes Required for Gases Listed in Mass-Flow Controller Units of Standard Liters Per Minute Nitrogen (slmn). Calculations for the Lower Temperatures Listed and 20 °C

Gas	Lower T	Lower T required flow	20 °C required flow
air	-60 °C	2.64 slmn	2.25 slmn
HFC-227ea	-16 °C	4.55 slmn	4.26 slmn
FC-218	-36 °C	4.89 slmn	4.40 slmn
HFC-125	-48 °C	4.12 slmn	3.61 slmn
halon 1301	-58 °C	2.78 slmn	2.38 slmn

(Q_{slm}) of gas delivered for standard conditions (0 °C, 101 kPa). Actual flow volumes delivered can be calculated by correcting the slm reading for the actual conditions using

$$Q_{actual} = Q_{slm} \times \frac{T_{actual}}{273.15\ K} \times \frac{101\ kPa}{P_{actual}}\ , \tag{15}$$

where Q_{actual}, T_{actual}, and P_{actual} are the volume flow rate, temperature, and pressure for ambient conditions.

Figure 10 shows a schematic of the flow-control system. MKS Instruments, Inc. Type 1359C mass-flow controllers were chosen for the system because of their high accuracy (± 0.5 % of full scale), resolution (0.1 % of full scale), and control range (1.0 % to 100 % of full scale). The flow system was designed to cover a concentration range from 0 to 1 mole fraction of air with a resolution of 0.01. The flow calculations described earlier indicated that a range of 10 slmn would be sufficient for the air mass-flow controller. Since the calibration curves for a flow meter using air or nitrogen are nearly identical, a single flow meter having a maximum flow rate of 10 slmn (Model 1359C-10000SN) was adequate for air. However, when using gases having properties which are different than those for nitrogen, the actual flow rate of the gas is equal to

$$Q_x = F \times Q_{full,N_2} \times GCF_x\ , \tag{16}$$

where Q_x is the volume flow rate for gas x, F is the fraction of full-scale setting for the mass-flow controller, $Q_{full,N2}$ is the nominal full-scale range of the flow meter for nitrogen, and GCF_x is the gas correction factor for gas x. Table 2 shows the gas correction factors recommended by MKS Instruments for the gases of interest. From these values it is clear that a mass-flow controller having a range of 10 slmn cannot accurately provide the flow required to create a 1 % agent concentration (*i.e.*, the required setting for the mass-flow controller will be less than 1 %). For this reason, a second mass-flow controller was included in the agent stream so that lower flow rates of agent could be generated accurately. A meter having a full-scale range of 2 slmn (Model 1359C-02000SN) was chosen. The mass-flow controllers were connected to a MKS Type 247C 4-Channel Readout. The

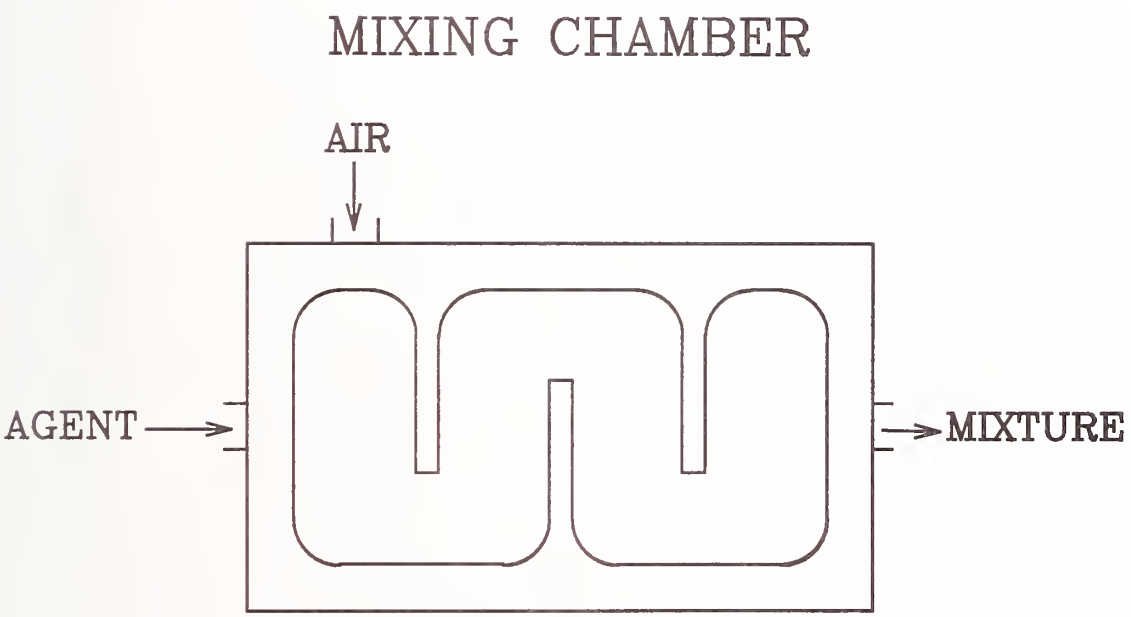

Figure 8. Cross-sectional view of the gas mixer for flows of an agent and air.

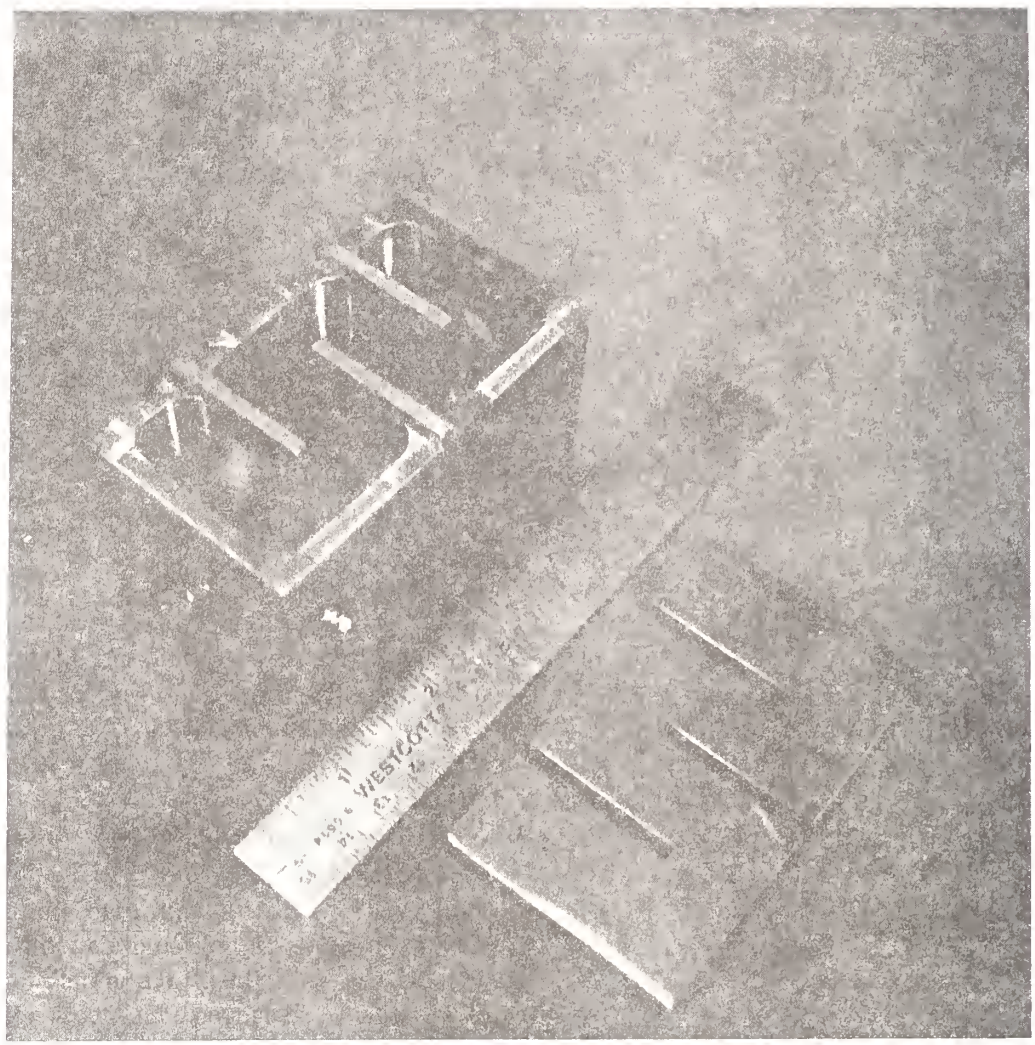

Figure 9. Photograph of the gas mixer showing the machined body and top before welding.

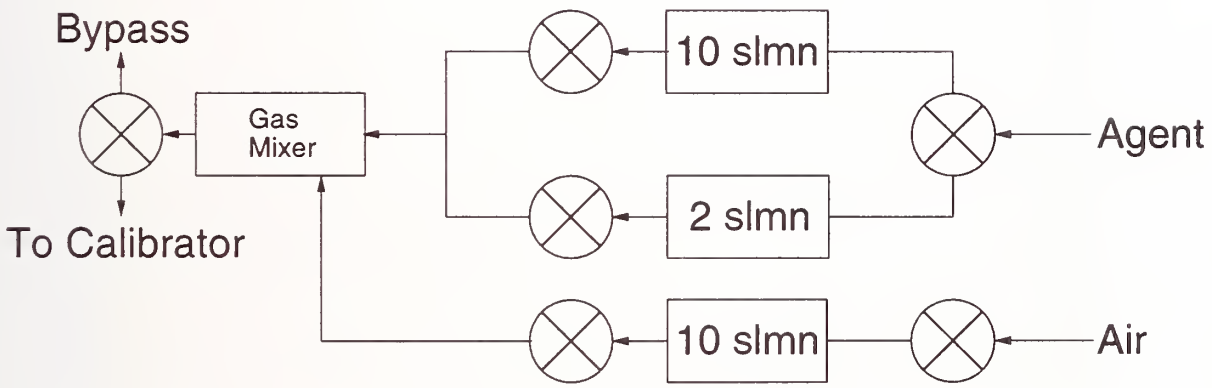

Figure 10. A schematic diagram of the flow meters and electro-pneumatic-actuated ball values used to control agent and air flows for the variable-temperature concentration calibration system.

Table 2. Gas Correction Factors Recommended by the Mass-Flow Controller Manufacturer for the Gases Investigated

Gas	*GCF*
air	1.00
HFC-227ea	0.18
FC-218	0.17
HFC-125	0.30
halon 1301	0.37

readout system acted as the power supply, analog readout, and set point source for each of the three mass-flow controllers. In particular, the Type 247C accepts 0 V - 5 V analog inputs which act as set points for the selected mass-flow controllers. This allows the mass-flow controllers to be remotely set by computer.

Mass-flow controllers are sensitive to changes in temperature. In order to limit calibration changes due to temperature variations, the three mass-flow controllers were placed on a thermostated block of aluminum containing thermistors and two small heaters. The temperature of the block was set to be slightly higher (32 °C) than room temperature.

The mass-flow controllers were carefully calibrated for each of the gases to be used. Volume-flow rates of air and the agents were measured using a Humonics, Inc. Model 730 Digital Soapfilm Flowmeter. The accuracy of this device was checked by using a NIST standard piston prover. The accuracy was within 1 % over the entire range of the flowmeter. The gas to be calibrated was connected to the chosen mass-flow controller, a range of set point voltages were applied to the appropriate Type 247C 4-Channel Readout input, and the resulting volume-flow rate was recorded with the soap film flow meter. The temperature of the flow was recorded simultaneously.

In order to convert the volume-flow rate measured by the Humonics to standard L/min it was necessary to correct for pressure and temperature differences using Equation (15). Values for Q_{slm} are derived by substituting actual values of volume-flow rate, temperature, and pressure into this expression. The pressure correction was not made during the calibrations. Figure 11 shows an example of a calibration curve for the agent 10 slmn mass-flow controller using HFC-227ea as the test gas. For nitrogen at standard conditions, the full-scale voltage would be 5 V giving a slope of 2 slmn/V. The actual slope of 0.387 requires that the gas correction factor (GCF) be 0.194. GCFs were determined for the 2 slmn and 10 slmn agent mass-flow controllers in the same way. Table 3 lists the results for the four agents investigated. In most cases, the results are averages of two determinations. Comparison of Table 2 and Table 3 shows that the values of GCF determined experimentally agree well with those recommended by the mass-flow-controller manufacturer.

Since mass-flow controllers were utilized in the system, the flow system was designed to deliver a constant mass-flow rate. A value of 0.210 g/s was used because this corresponds to nearly the full-scale value of the air mass-flow controller (10 slmn) and provides sufficient volume flow rates for all mixtures to more than meet the extraction requirements of the aspirating probe.

A three-way (on-off, two flow directions) electro-pneumatic-actuated ball valve (Whitey Model SS-62XTS4-F4-N-51DD) was used to route the agent flow to the proper mass-flow controller. In

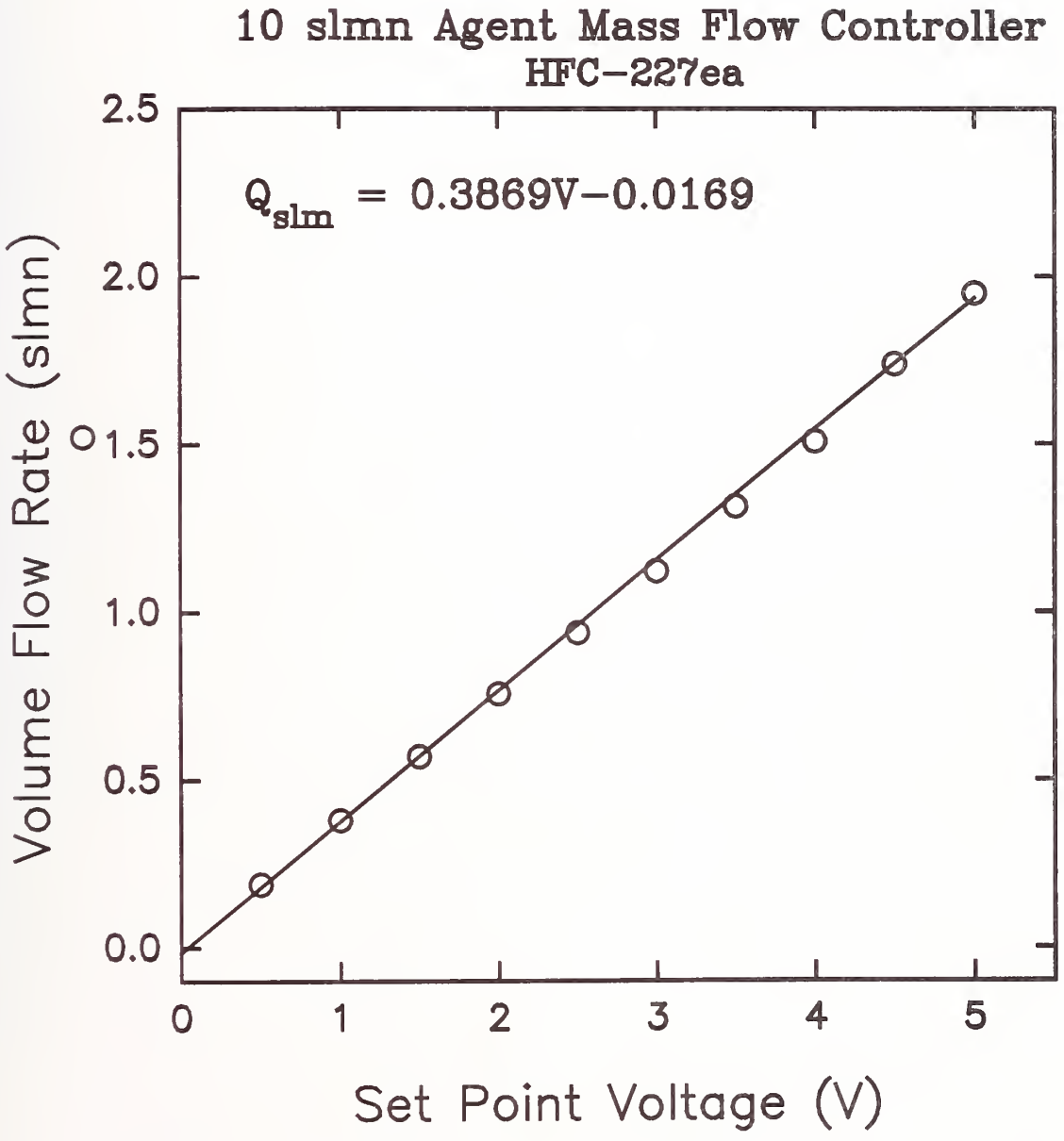

Figure 11. An example of the calibration results for HFC-227ea using the 10 slmn agent mass-flow controller.

Table 3. Experimental Gas Correction Factors for the Gases Investigated

Agent	2 slmn *GCF*	10 slmn *GCF*
HFC-227ea	0.190	0.192
FC-218	0.177	0.176
HFC-125	0.273	0.276
halon 1301	0.373	0.385

order to provide additional flow control and safety, a set of three two-position (on-off) electro-pneumatic actuated ball valves (Whitey Model SS-62TS4-N-31CD) were placed on the flow outlets of the mass-flow controllers. The ball valves were actuated by coupling 120 V ac to the proper connection of the actuator.

A second three-way valve was placed on the downstream side of the gas mixer. One of the outputs of the valve directed the gas flow to the test section. The second was connected to a line which simply dumped the flow into the hood where it was exhausted.

The valves were actuated by applying 120 V ac to the appropriate inputs. Small lamps connected to the valve power supplies were mounted on the top of each valve. When the valves were energized, the lamps would light and provide an indication that the valve had been opened or switched. A house 680 kPa air line was used to pressurize the electro-pneumatic actuated ball valves.

Pressurized bottles of air and the agent to be tested were coupled to the input solenoids. Regulated pressures were set to 137 kPa.

11.2.4.4 Thermal Bath and Heat-Transfer Coil. The temperature of the gas was controlled by passing the flow through a heat-transfer coil contained within a temperature-controlled bath of polydimethylsiloxane (Dow Corning Corporation Syltherm XLT Heat Transfer Fluid). The temperature bath was contained in a 7.75 L Agitainer-B vessel from Neslab Instruments, Inc. which provides a magnetic stirrer to mix the working fluid. In order to ensure that the fluid was well mixed and, therefore, at a uniform temperature, a second mechanical stirrer was added to the bath.

Temperature control was achieved by simultaneously heating and cooling the bath liquid. Cooling was provided by an immersion cooler (Neslab Instruments, Inc. CC-100II) equipped with a small diameter probe ("FV") for sensing temperature in the bath fluid. This cooler is capable of cooling to -90 °C with no thermal load. Over the temperature range of interest, it extracts more than 120 W of heat. The desired temperature for the bath was obtained by using a Neslab Exatrol Digital Temperature Controller in combination with a 250 W heater. The FV sensor measures the bath temperature, and the controller uses a feedback circuit to determine when it is necessary to add heat to the system and turns on the heater until the desired temperature is reached. A second 700 W heater was included in the system which was only used when it was required to rapidly raise the temperature from a lower value to a higher one. Once the desired temperature was reached, the second heater was turned off. Temperatures were adjusted simply by setting the desired temperature on the Exatrol controller.

A Type E thermocouple was placed in the bath fluid to provide an accurate measurement of the temperature. It was calibrated using ice- and boiling-water baths in conjunction with thermometers

calibrated by NIST. Temperatures were read using the computer system described below. It was determined that the bath temperature remained constant to within ± 0.5 °C.

The temperature of the gas to be calibrated must be brought to the bath temperature before entering the test section. In order to achieve this the gas must flow through a pipe for a sufficient period of time to ensure that the gas temperature reaches the same temperature as the pipe walls (*i.e.*, the bath temperature). Standard formulas are available (Pitts and Sissom, 1977) which allow the heat transfer to a gas flow within a pipe to be calculated assuming a constant wall temperature and either laminar or turbulent pipe flow. These formulas were used to solve for the pipe length required for the gas to come to the pipe wall temperature using a FORTRAN program named COIL.FOR, which is included as Appendix B. Table 4 lists the calculated lengths of a 6.35 mm diameter pipe required assuming either laminar or turbulent flow conditions along with minimum Reynolds numbers for the flows. Pipe flows are expected to be turbulent for Reynolds numbers greater than 2000. Therefore, it can be concluded that a pipe of 0.6 m length should be sufficient to cool these gases to the bath temperature.

A total pipe-flow length of 1 m was provided by coiling a 6.35 mm length of pipe and placing it at the bottom of the thermal bath. Swageloks on either end of this section were used to connect the coil to tubing joined to the gas mixing chamber and the measurement test section.

The temperature bath was placed on a x-y positioner controlled by manual micrometers. This positioner allowed the test section within the thermal bath to be accurately positioned relative to the lever arm used to lower the probe into the test section. In this way it was possible to lower the probe into the test section without risk of damage.

11.2.4.5 Data Acquisition and Control. All of the control and data acquisition functions required for the calibration of the combined aspirated hot-film/cold-wire probe, except for setting the temperature of the silicon oil bath, were automated. Central control was provided by a TCP 486-DX personal computer having a clock speed of 66 Mhz, 8 Mbytes of RAM, and a 250 Mbyte hard drive. Two plug-in modules--a Flash-12 Model 1 data-acquisition board and a ACAO-12-2 analog and digital output board--from Strawberry Tree were installed in computer bus slots and provided interfaces for the experiments. Workbench PC data acquisition software was used to provide overall control.

The Flash-12 Model 1 board has 16 single-ended or 8 differential analog inputs which can be digitized at a total rate up to 1 MHz. Eight TTL-compatible input/output lines are also available. The board is set up to provide thermocouple cold-junction compensation and linearization. An optional "daughter board" (Model DB03) was installed which provides on-board memory sufficient for recording one million samples. The daughter board allows large data sets to be recorded with the full temporal resolution of the digitizer. It also provides two 12-bit digital-to-analog converter outputs. Digital ribbon cable was used to connect the Flash-12 to a T21B terminal board which provided convenient electrical connections for the calibration system.

The ACAO-12-2 has two 12-bit digital-to-analog converters which have switch selectable ranges of 0 V - 10 V, 0 V - 5 V, ± 5 V, or 4 mA - 20 mA. Eight digital I/O lines which can be individually configured as either inputs or outputs are also available. This board was connected through digital cable to a T-31 general-purpose interface board.

A special interface box containing the T21B and T31 interface boards was constructed. Connections to the calibration system were made through these interface boards. Appendix C lists the various electrical connections to the output signals of the interface boards.

An icon-based work sheet named ACTRL3.WBB was assembled to control the calibration process. A copy of this work sheet is included as Appendix D. This work sheet provided all of the calculations and controls necessary to turn on and set the mass-flow controllers, open and close the proper valves, provide indicator lights on the calibration system, automatically step through a series of

Table 4. Calculated Lengths of 6.35 mm Diameter Pipe to Cool Air and Agent Flows to Temperature of Thermal Bath. Calculations Assume Laminar and Turbulent Pipe Flow. Reynolds Numbers are Calculated for the Lowest Flow Velocities.

Agent	Required pipe length (m) for laminar flow	Required pipe length (m) for turbulent flow	Reynolds number
air	1.41	0.51	2710
HFC-227ea	2.27	0.60	3850
FC-218	2.18	0.59	3710
HFC-125	2.15	0.58	3690
halon 1301	1.85	0.56	3200

concentrations, and record measurements of the bath temperature and the voltage outputs for the aspirated hot-film and cold-wire controllers. The entire process was controlled by "pushing" the appropriate buttons using a mouse on a computer-screen "control panel" created by the work sheet. An example of the control panel is shown in Appendix E.

The following events occurred when a calibration sequence was started. The data acquisition logs for the system were first enabled. Then commands were sent to open the electro-pneumatic valve on the air outlet and to switch the three-way solenoid valve to let gas pass through the test section. Simultaneously, a flag was set on the computer-screen control panel indicating that a test had started, and a logical pulse generator was triggered which generated a pulse every 42 s. The output of the pulser then traveled two paths. The first was to a counter which simply counted the number of pulses received. This number was multiplied by 0.1 to give the current air mass fraction for the calibration. When the air mass fraction became greater than one, a trigger was fired which halted further data collection. The second pathway from the pulse generator started a 20 s timer which then triggered a second one-shot pulse generator with a 20 s output. The end of the second 20 s period caused the current analog-to-digital values (see ahead) to be frozen in memory and triggered a 1 s one shot which requested the computer to record data. In this way a 40 s period was allowed for the flow to stabilize before the data was recorded. After the data was recorded, the pulse generator fired and the cycle repeated until the air mass fraction became greater than one. Note that the sequence of the test was through mass fractions of air of 0.0, 0.1, 0.2, . . ., 0.9, and 1.0.

The current mass-fraction setting for air (Y_{air}) was used to set the air mass-flow controller. This value was displayed on the computer-screen control panel. The air mass-flow controller was set to $Y_{air} \times 9.745$ slmn since 9.745 slmn is the air flow rate required for a mass-flow rate of 0.210 g/s. This value was also displayed on the control panel. Since the air mass-flow controller has a range of 0 slmn - 10 slmn and requires a set point of 0 V - 5 V, the number of slmn was divided by two to generate the number which was fed to the digital-to-analog converter connected to the voltage set point for the air mass-flow controller. This voltage was displayed on the control panel.

The next stage was to calculate the required agent flow rate, determine whether to use the 2 slmn or 10 slmn range agent mass-flow controller, and calculate the required voltage set point for the mass-flow controller. These calculations were implemented through a series of pathways which changed

depending on the agent being tested. Pathways exist for FC-218, HFC-125, HFC-227ea, CF_3Br, and CF_3I. The gas to be tested was chosen by modifying connections on page 1 (see Appendix D) of the icon worksheet.

The mass-flow rate of agent was determined by requiring that the total mass-flow rate of agent and air remain constant at 0.210 g/s. For an agent mass fraction of one, the mass-flow rate was therefore equal to 0.210 g/s. The required agent volume-flow rate (Q_{agent}) for $Y_{agent} = 1$ was therefore

$$(Q_{agent})_{Y_{agent}=1} = 9.745\frac{\rho_{air}}{\rho_{agent}} . \tag{17}$$

where ρ_{air} and ρ_{agent} are the air and agent densities. The volume flow rate for the agent was obtained by multiplying this value by the mass fraction of the agent,

$$Q_{agent} = (1-Y_{air})(Q_{agent})_{Y_{agent}=1} . \tag{18}$$

The result of this calculation was output on the computer-screen control panel.

The calculated agent volume-flow rate was in L/min. It had to be converted to slmn using the calibration curves previously determined, and these, in turn, had to be converted to set-point voltages for the agent mass-flow controllers. These steps were combined into overall equations which depended on both the chosen gas and flow meter. Table 5 lists the conversion formulas used for both flow meters with each of the agents. Whether the 2 slmn or 10 slmn meter was used depended on whether or not the calculated agent volume-flow rate fell above or below the full-scale range of the 2 slmn mass-flow controller. Values of standard L/min of agent corresponding to full-scale values for the 2 slmn meter are included in Table 5. The results of these calculations were a decision as to which agent mass-flow controller to use and the set-point voltage for that controller.

The calculated set point for the agent mass-flow controller was output to both the 2 slmn and 10 slmn controllers. However, when the 2 slmn controller was chosen the electro-pneumatic-actuated ball valve for this controller was opened and the lamp indicating the valve was open was turned on, while the valve for the 10 slmn remained closed, and the indicator light was off. The opposite occurred when the 10 slmn controller was required. The computer-screen control panel indicated which agent mass-flow controller had been turned on as well as the voltage set point being transmitted to the mass-flow controller.

An algorithm was included in the work sheet which converted the agent mass fraction into a mole fraction (X_{agent}) which was ultimately saved with the other results of the measurements. The calculation implemented this equation:

$$X_{agent} = \frac{(1-Y_{air})}{Y_{air}\left(\frac{\rho_{agent}}{\rho_{air}}-1\right)} . \tag{19}$$

The calculated agent mole fraction was displayed on the computer-screen control panel.

Data acquisition was initiated following the 40 s period allowed for the new mass-flow conditions to come into a steady state. Analog-to-digital converters continuously read the voltage outputs of the hot-film anemometer and cold-wire constant-current anemometer as well as the temperature measured

Table 5. Formulas Used to Convert slm for Given Mass Fraction of Agent (Q_{ag}) to Set Point Voltages for Agent Mass-Flow Controllers. Formulas for the 2 slmn Controller Are Listed First

Agent	Maximum agent standard L/min for 2 slmn controller	Conversion formula
FC-218	0.348	$14.54Q_{ag}$-0.074
		$-0.239Q_{ag}^3+0.553Q_{ag}^2+2.495Q_{ag}+0.0608$
halon 1301	0.745	$-3.670Q_{ag}^3+4.212Q_{ag}^2+5.518Q_{ag}+0.058$
		$-0.018Q_{ag}^3+0.032Q_{ag}^2+1.378Q_{ag}-0.048$
HFC-125	0.540	$-0.055Q_{ag}^3+0.192Q_{ag}^2+1.650Q_{ag}+0.032$
		$9.336Q_{ag}$-0.049
HFC-227ea	0.374	$-0.179Q_{ag}^3=0.424Q_{ag}^2+2.375Q_{ag}+0.028$
		$13.551Q_{ag}$-0.080

by the coil thermocouple at data rates of 10 Hz. A running average of each of these outputs was calculated over 10 s periods (*i.e.*, 100 samples). Current values were updated on the computer-screen control panel. After a signal was received to sample-and-hold the averaged data, several different parameters were written into two hard-disk files. Values of the agent mole fraction, the voltage output of the hot-film anemometer, and the thermal bath temperature (*i.e.*, the gas temperature in the test section) were stored in the first file. The second file contained the thermal bath temperature and the voltage output of the constant-current anemometer. A flag on the computer-screen control panel was enabled during the period when data was recorded.

The mass-flow controllers generate voltages which are proportional to the actual flow rates through the instruments. Voltages generated by the 10 slmn air, 10 slmn agent, and 2 slmn mass-flow controllers were digitized and averaged over a running period of 1 s. The three voltages were then displayed on the computer-screen control panel. These outputs served to confirm the proper operation of the calibration system.

The work sheet incorporates three additional capabilities which could be implemented on the computer-screen control panel with push buttons. The first was "Air Enable" which turned on the air flow and allowed it to flow continuously through the test section. The remaining buttons were "Pause" and "Emerg. Stop" which could be activated during actual testing. The "Pause" temporarily halted testing until the button was pushed again, while the "Emerg. Stop" button aborted the test and turned off the gas flows when it was depressed. Status boxes were included on the computer-screen control panel which indicated the current state of a calibration.

11.2.4.6 Calibration Procedures. Calibration of the combined probe to variations in agent concentration and temperature were fairly simple with the calibration system. Appendix F contains the detailed procedure which was followed during a calibration. Briefly, a regulated pressure bottle of the

agent to be investigated was connected to the calibration system as was a tank of breathing-quality air. The instrumentation was turned on and allowed to warm up for half an hour. The temperature bath was set to the desired temperature and allowed to equilibrate. The calibration sequence was initiated by "pushing" the appropriate button on the computer-screen control panel. The calibration sequence acquiring probe-response data for a series of concentrations was then repeated for as many different temperature settings as desired. The system was then shut down.

11.2.5 Calibration Results and Probe Characterization

11.2.5.1 Calibration Results. The calibration system and the behavior of individual cold wires and aspirated hot films were characterized before the combined aspirated hot-film/cold-wire probe was delivered by TSI, Inc. Measurements were made separately for a TSI Model 1440R aspirated hot film and a Model 1210-T1.5 hot wire operated as a cold wire. The behaviors of these probes should be similar, but not identical, to those for the combined probe which are described below.

The cold-wire current was set to 1.00 mA. Figure 12 shows an example of the voltage output of the constant-current anemometer operated in the cold-wire mode. These measurements were recorded by placing the cold wire in a heated water bath while recording the temperature with a calibrated thermometer. As expected, the dependence on temperature is linear, and the sensitivity to temperature changes is quite good.

The resistance (R_{250} = 9.129 Ω) of the aspirated hot-film probe was set to a value corresponding to an operating temperature (T_{op}) of 250 °C. Some difficulties were encountered when calibration of the aspirated hot film was initiated. Initially, the probe was held outside and only plunged into the test section when measurements were to be taken. The measurements were very irreproducible. This was ultimately traced to water condensation on the probe when it was removed from the cold test section. In order to overcome this problem, the probe was maintained in a flow of dry air or agent mixture at all times during a calibration sequence. Calibrations performed in this manner were reproducible. The first calibration measurements were done in a pipe instead of the vessel test section described above. A display of the constant-temperature anemometer voltage output showed that there was a very low noise level when no flow was present, but that the noise increased dramatically when the flow was started. This observation was very surprising because the literature indicated the output of an aspirated hot film should be insensitive to velocity fluctuations. By replacing the pipe with the vessel described above, it was possible to lower the flow velocity in the test section and decrease the measurement noise. The sensitivity of the probe to flow velocity remained a problem and is discussed in more detail shortly.

Once the above problems were solved, it was possible to record reproducible calibrations. Figure 13 to Figure 16 show calibration results for FC-218, HFC-125, HFC-227ea, and halon 1301 as a function of temperature and agent concentration. Several general points should be noted concerning the results. For a given temperature, the plots of hot-film voltage versus mole fraction of agent fall on well defined smooth curves. For a given concentration of agent, the voltage output of the anemometer increases as the temperature decreases. This is to be expected based on Equation (10) which predicts that the output voltage is proportional to the difference in the operating temperature of the probe and the ambient temperature. Since the operating temperature of the hot film is held constant during a calibration, the voltage increases as the ambient temperature is lowered. In general, the voltage changes with temperature depend somewhat on concentration, *e.g.*, the change in output voltage for a given change in temperature is found to be different for the pure agents as compared to those observed for air. The nonlinear dependence on temperature is most likely the result of the molecular properties (particularly thermal conductivity and kinematic viscosity) of air and the agents having different dependencies on temperature. These properties appear in Equation (10).

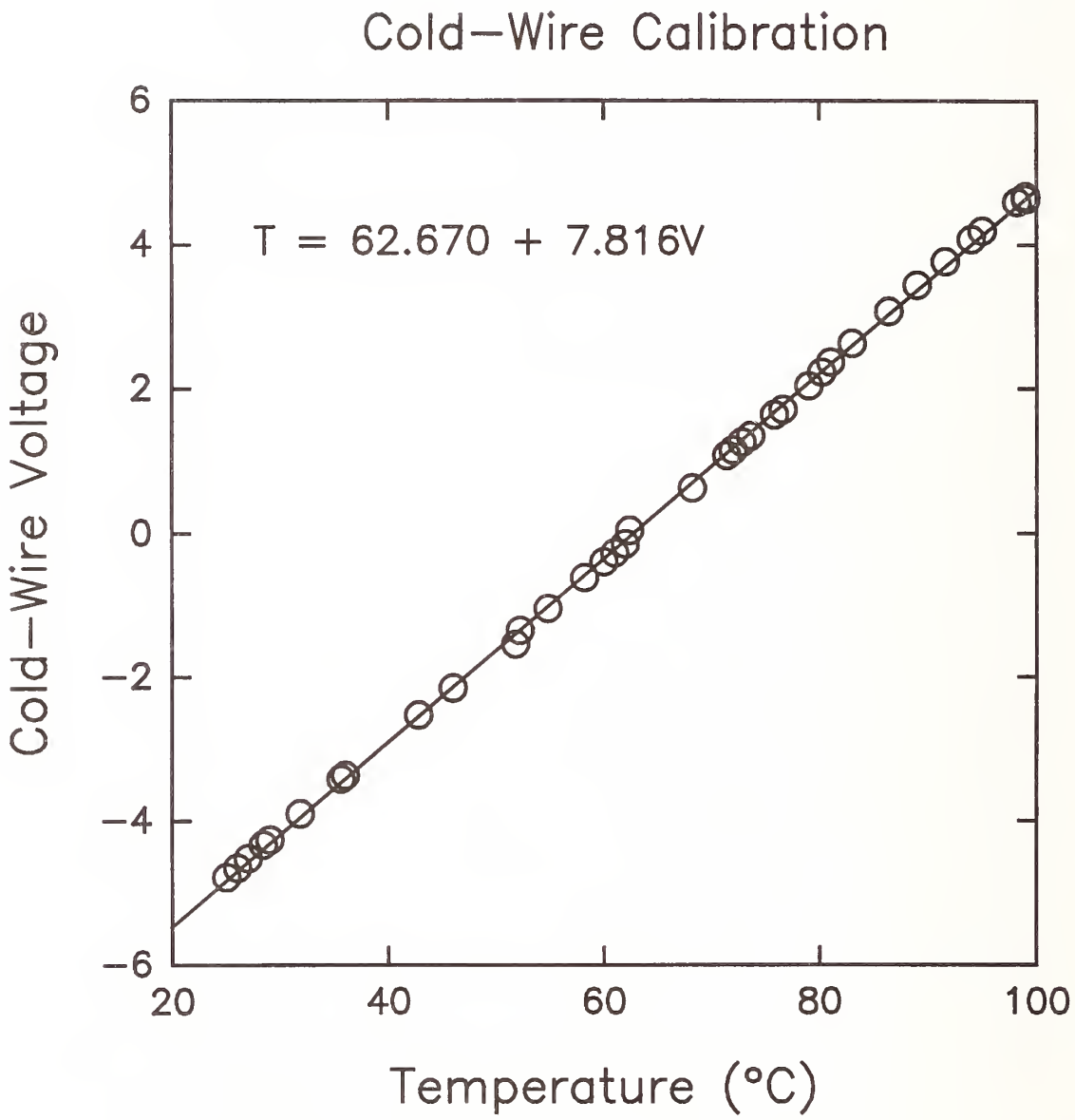

Figure 12. Voltage output as a function of temperature for a TSI Model 1210-T1.5 hot-wire probe operated as a cold wire with a 1.00 mA current. Measurements recorded in a heated water bath.

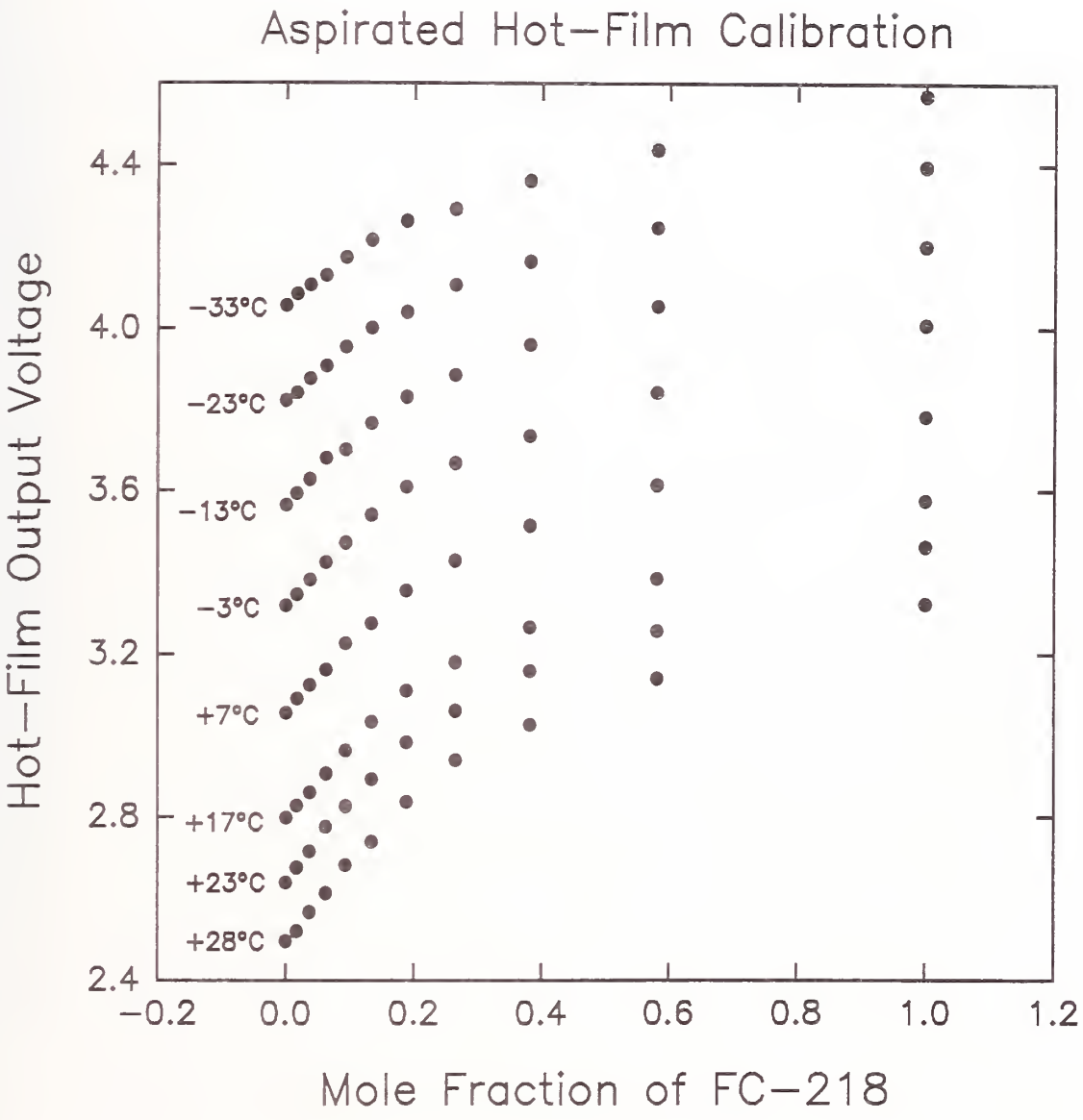

Figure 13. Voltage output of aspirated hot-film anemometer as a function of FC-218 concentration and temperature. The bridge voltage has been offset by 2 volts and a gain of 6 has been applied.

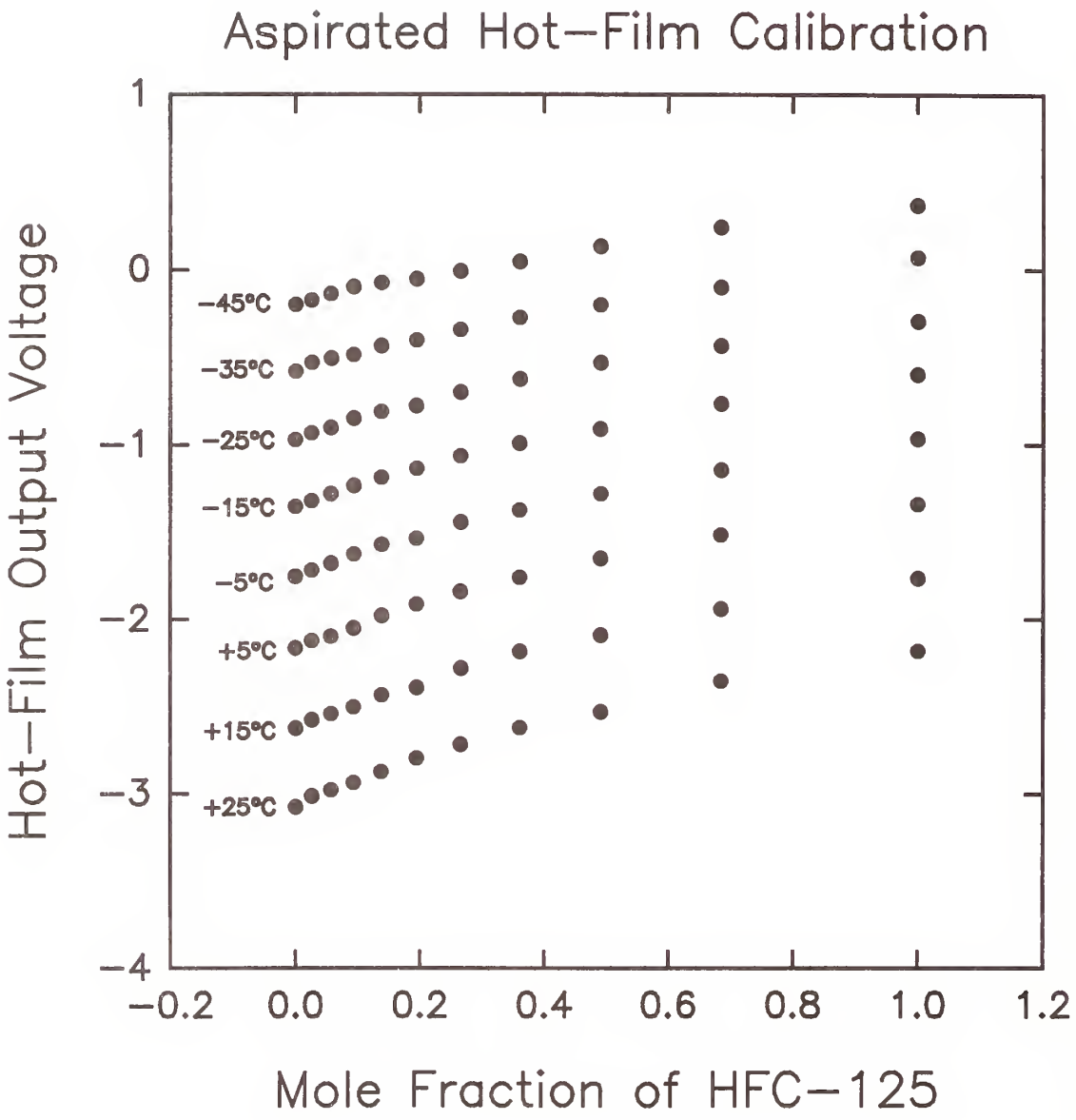

Figure 14. Voltage output of aspirated hot-film anemometer as a function of HFC-125 concentration and temperature. The bridge voltage has been offset by 3 volts and a gain of 10 has been applied.

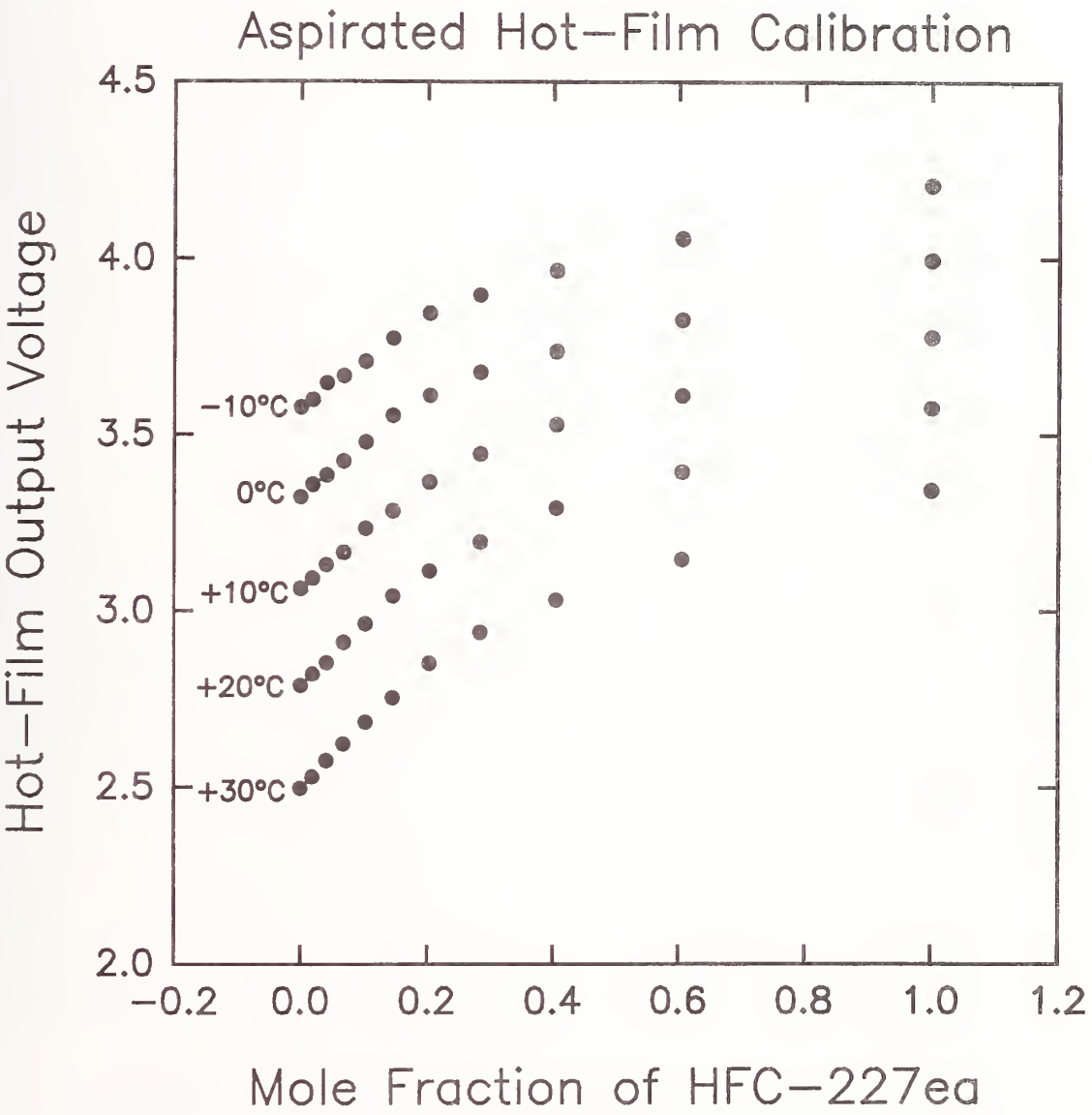

Figure 15. Voltage output of aspirated hot-film anemometer as a function of HFC-227ea concentration and temperature. The bridge voltage has been offset by 2 volts and a gain of 6 has been applied.

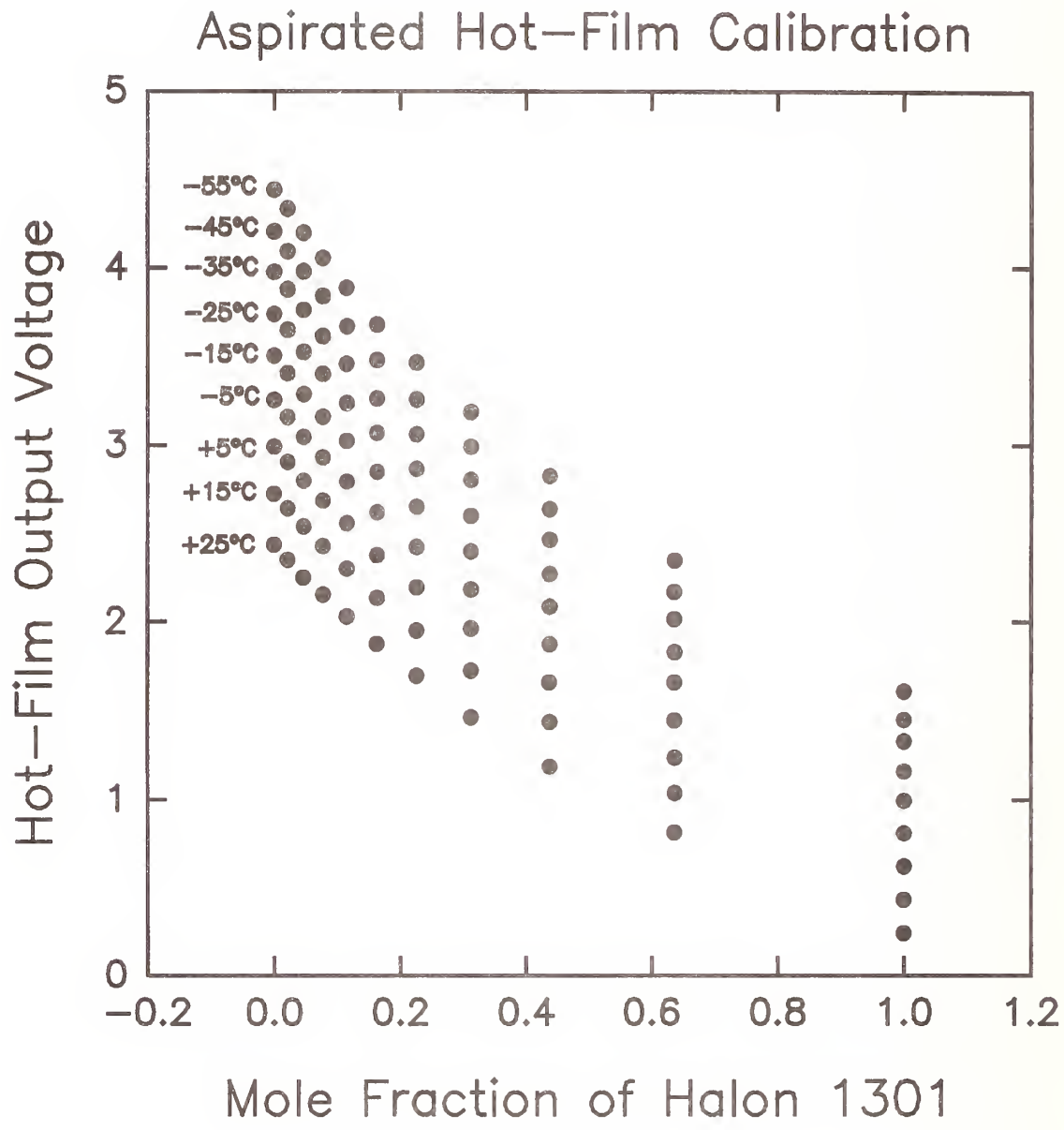

Figure 16. Voltage output of aspirated hot-film anemometer as a function of halon 1301 concentration and temperature. The bridge voltage has been offset by 2 volts and a gain of 6 has been applied.

Perhaps the most important characteristic of the calibration curves is the change in voltage as a function of agent concentration for a given temperature. Some immediate differences are apparent by comparing Figure 13 to Figure 16. The voltage is found to decrease with increasing halon 1301 concentration while it increases for FC-218, HFC-125, and HFC-227ea. The absolute magnitudes of changes in the voltage output on going from air to pure agent also depend on the agent. This is an important property because it ultimately determines the accuracy and precision which is possible using these probes for concentration measurements. Figure 17 shows the responses of the aspirated probe to concentration for the four agents at 24.5 °C. The voltage plots have been normalized such that the voltage is defined to be zero when the agent concentration is zero, and the voltage change has been by divided by the gain used to record the signal. This transformation allows direct comparison of the probe responses for the four agents on the same scale. The largest response is for halon 1301. The responses for FC-218 and HFC-227ea are roughly equal, but more than a factor of two smaller than observed for halon 1301. The smallest response was observed for HFC-125, which was a factor of two smaller than those observed for FC-218 and HFC-227ea.

In principle it should be possible to predict the results shown in Figure 17 using Equations (10) and (11). In practice, quantitative predictions are difficult. By combining Equations (10) and (11) and assuming that the external temperature and pressure are constant, the dependence of the hot-film voltage on molecular properties can be written as

$$E^2 \sim k_o \left[A + B \left(\frac{\sqrt{\gamma MW} \left(\frac{2}{\gamma + 1} \right)^{\frac{\gamma+1}{2(\gamma-1)}}}{\mu_o} \right)^n \right] . \tag{20}$$

A and B are often assumed to be constants. For finite probe lengths their values actually depend on molecular properties (Pitts and McCaffrey, 1986). For the purposes of this discussion they will be assumed to be constant. The relative slopes of E^2 versus velocity (U) for agent x normalized by the slope for air ($(\Delta E^2)_x/(\Delta E^2)_{air}$) can be calculated using Equation (20). Table 6 lists the results of these calculations for each of the four agents. Note that the exponent n in Equation (20) has been set to 0.40. This is based on findings for the response of a hot-film probe described in Pitts and McCaffrey (1986). These slopes are in qualitative agreement with the experimental observations if variations in the constant A are neglected. For instance, since the ratio is less than one for halon 1301, the voltage output for this agent should be lower than that measured for air. Similarly, voltage changes for the other three agents should be positive. The results of this simple calculation also predict the experimental observations that FC-218 and HFC-227ea have similar voltage behaviors which are somewhat higher than for HFC-125. However, close examination shows that even though the relative differences are captured, the approach fails to accurately predict the magnitudes of the effects. For instance, the calculations suggest that the absolute voltage change would be smallest on going from air to halon 1301, when it is in fact the largest. This suggests that additional factors not captured by this simple approach, such as varying A factors or probe end-loss effects, are also important. This conclusion is important because it implies that the relative responses can be modified somewhat by changing the probe design (*e.g.*, by varying the probe diameter or the area ratio of the tube containing the probe and the sonic orifice). In this way it may be possible to design a probe in such a way as to maximize its response to changes in concentration of a particular gas pair.

11.2.5.2 Characterization of Probe Response to Velocity Fluctuations. During the calibrations discussed in the last section it was noted that the noise in the output voltage increased somewhat when

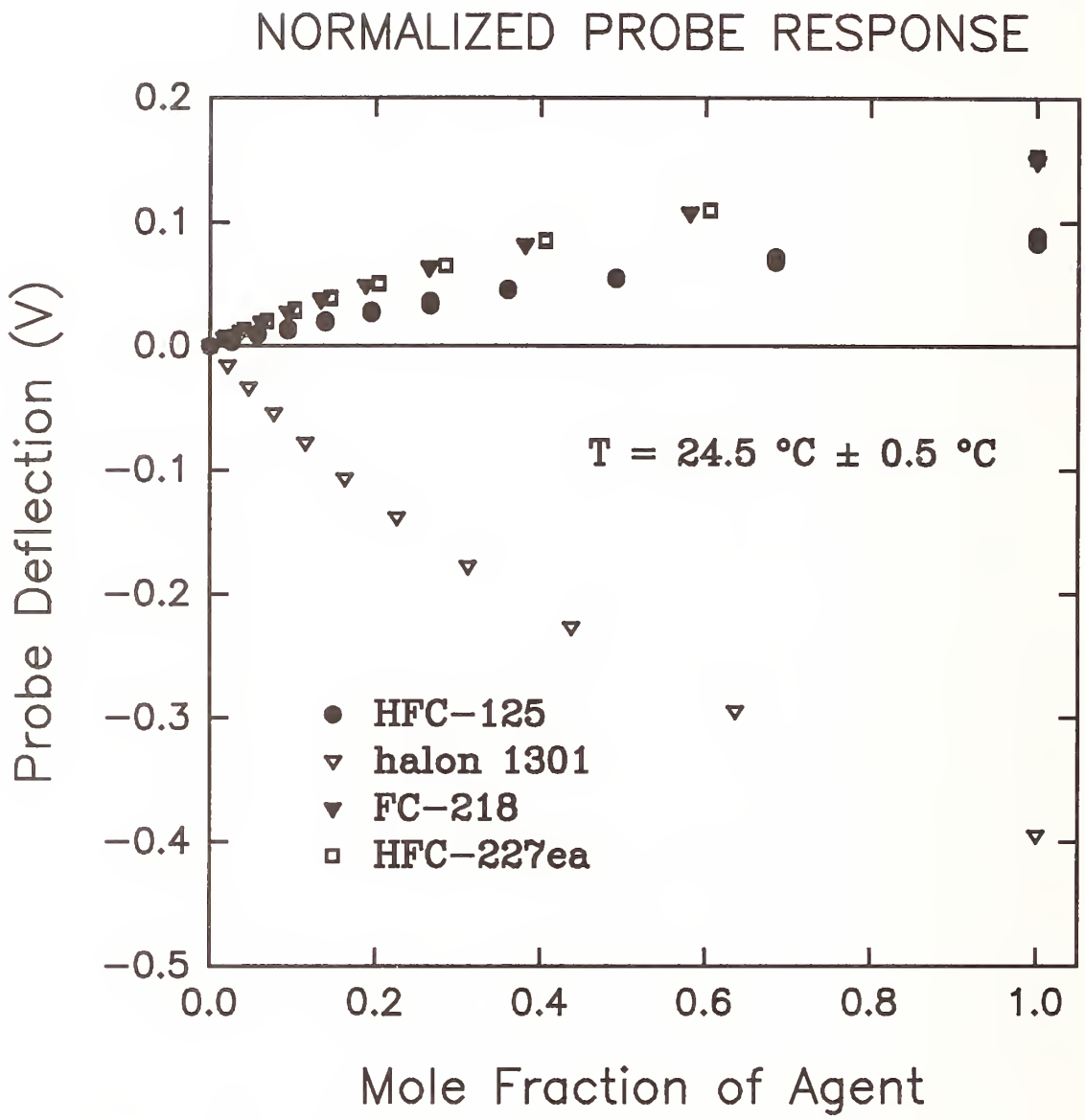

Figure 17. Voltage output of aspirated hot-film anemometer as a function of concentration for the four agents investigated. Normalized to be zero at zero agent concentration. Recorded voltages are divided by the applied gain.

Table 6. Predicted Values of Slopes of Plots of E^2 Versus U^n for the Agents Normalized by the Value for Air. n Has Been Assumed To Equal 0.40

Agent	$((\Delta E^2)_x/(\Delta E^2)_{air}$
HFC-227ea	1.48
FC-218	1.48
HFC-125	1.44
halon 1301	0.94

the flow in the test section was initiated. When the probe was removed from the test section and placed in open air, it was found that there was a slight difference in the output voltage as compared to that predicted based on the air calibrations at room temperature. Both of these observations suggested that the probe was sensitive to velocity to some degree. This was unexpected since the literature indicated quite clearly that such sensitivity should be minimal.

In order to characterize the sensitivity of the hot-film response to velocity a series of tests in an air flow were run. Measurements were made in the flow generated by a TSI, Inc. Model 1125 Flow Calibrator. This system consists of a well contoured nozzle which generates a uniform flow at the exit. Measurement of the pressure drop across the orifice allows the exit velocity to be determined accurately. The aspirated hot-film probe was placed in the flow at positions near the nozzle where velocity fluctuations were very small, as well as at a larger distance (centerline, 51 mm downstream of the nozzle) where the flow had developed into a turbulent jet and therefore had considerable velocity fluctuations.

Figure 18 shows examples of the time records observed in the nonturbulent and turbulent regions of the flow field. The probe was oriented parallel to the flow direction. It is clear that the anemometer signal is much noisier in the presence of the turbulent flow. Figure 19 and Figure 20 show plots of average and rms voltage versus flow velocity at the two positions for the probe oriented parallel (vertical) and perpendicular (horizontal) to the flow. The time-averaged voltages indicate that the response of the hot-film anemometer is slightly dependent on flow velocity and more so on the probe orientation. Interestingly, the output voltage seems to decrease slightly as the velocity increases. If this velocity sensitivity were due to a dynamic pressure on the probe it would be expected to increase with velocity.

The aspirated hot-film response to turbulent velocity fluctuations is more complicated. As suggested by the results in Figure 18, the rms voltage is very low when the flow is laminar and the probe is oriented parallel to the flow. However, when the probe is oriented parallel to the flow, the rms voltage increases dramatically with velocity. We attribute this behavior to a resonant frequency as the air "whistles" by the opening of the aspirated probe. Also consistent with Figure 18, the rms for the probe located parallel to the flow increases significantly when the probe is moved into the turbulent region of the flow. Strangely, the rms seems to be independent of flow velocity. This is difficult to understand since the absolute magnitude of the turbulent velocity fluctuations must increase with flow velocity. However, the finding is encouraging because it suggests that a single rms value (0.04 V) can be used to characterize the noise which results from locating the probe perpendicular to a turbulent flow. On the other hand, the rms values measured at the downstream position with the probe oriented perpendicular to the flow again increase with velocity. This provides further confirmation

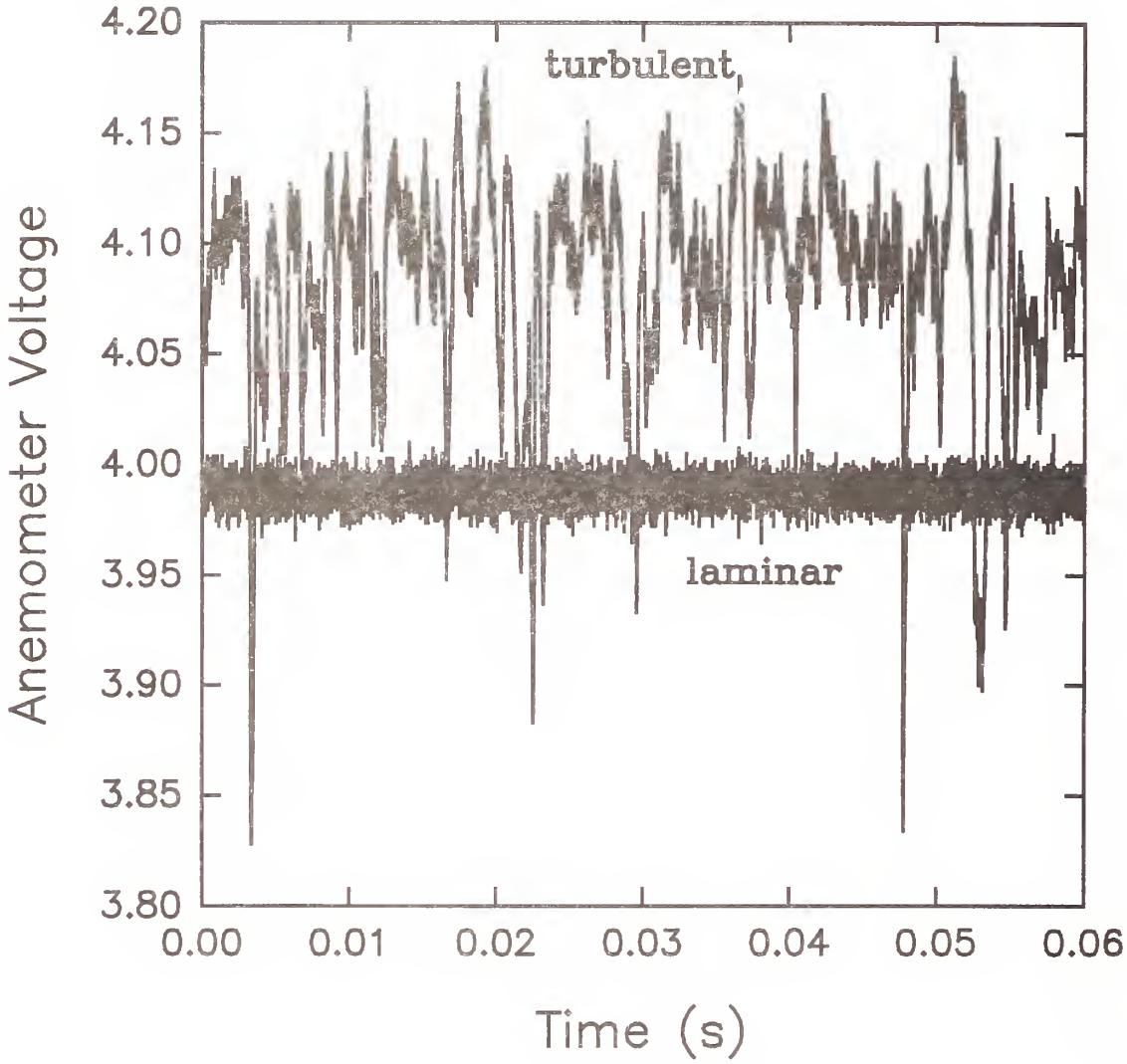

Figure 18. Time records of aspirated hot-film voltage for an air jet having a velocity of 15.0 m/s at the jet exit. Measurements were recorded at the jet exit (laminar) and 51 mm downstream (turbulent). A gain of 10 and offset of 2 V was used.

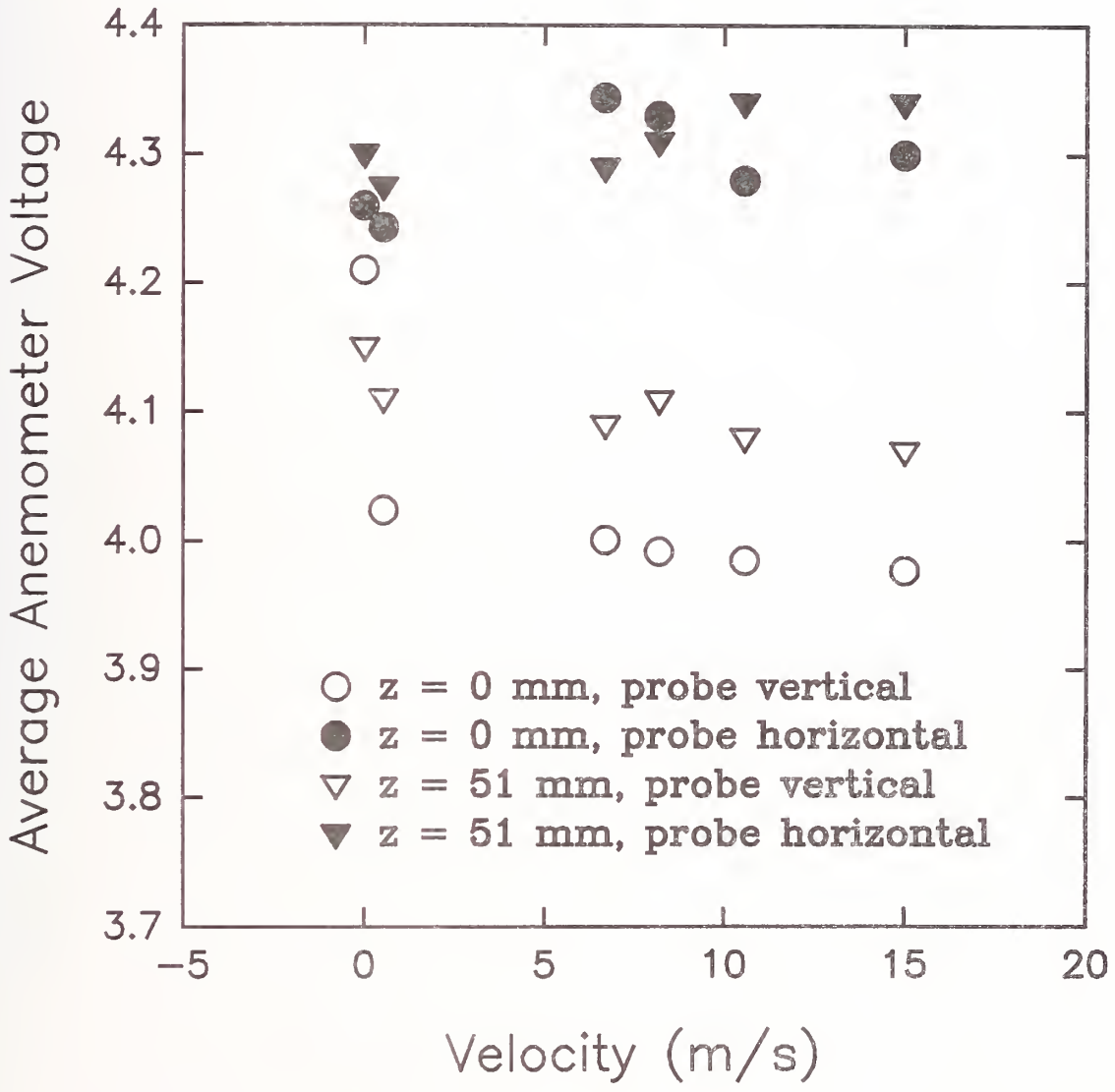

Figure 19. Time-averaged voltages for the aspirated hot-film probe oriented parallel and perpendicular to an air flow of 15.0 m/s at the calibration-jet exit. Measurements were recorded at the exit and 51 mm downstream. Gain of 10, offset of 2 V used.

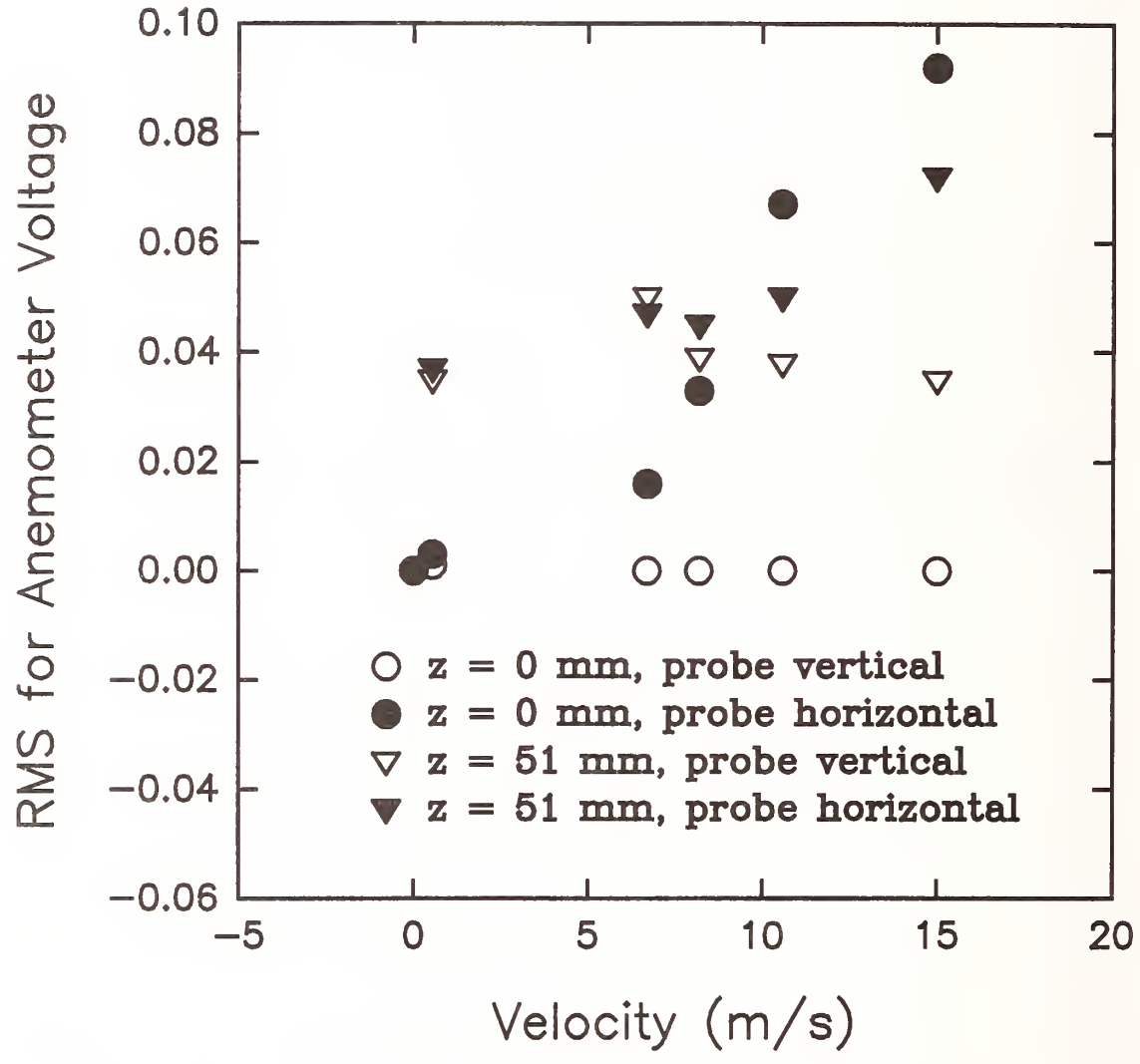

Figure 20. rms voltages for the aspirated hot-film probe oriented parallel and perpendicular to an air flow of 15.0 m/s at exit. Measurements were recorded at the jet exit and 51 mm downstream. Gain of 10, offset of 2 V used.

that the variations in response observed for the two probe orientations result from different flow effects.

These results were discussed with Professor Ronald So of Arizona State University and Anthony Birch of the British Gas Corporation. These researchers have used aspirated hot-film probes extensively for concentration measurements. Both expressed surprise at the sensitivity to velocity observed in the current work. At the present time it is impossible to determine whether this is a new observation characteristic of aspirated hot films in general, or an effect limited to the particular probe that was tested. The implications of the velocity sensitivity for the accuracy of real-time concentrations measurements is discussed in the following section.

Two additional tests were performed in an effort to understand the sensitivity of the probe to velocity fluctuations. A check was made to ensure that the flow at the sonic orifice of the aspirated probe was choked. The condition required for choked flow is

$$\frac{P}{P_o} \leq \left(\frac{2}{\gamma+1}\right)^{\frac{\gamma}{\gamma-1}}, \tag{21}$$

where P is the pressure on the downstream side of the sonic orifice. For air this requires $P/P_o \leq 0.53$. A valve and pressure gauge were installed in the pump line to allow control and measurement of the pressure downstream of the sonic orifice. The aspirated hot-film probe was placed 51 mm downstream of the flow calibrator and a flow of air with a velocity of 10.6 m/s at the nozzle exit was passed over the probe. The average and rms probe voltages were then recorded as a function of P/P_o. Figure 21 and Figure 22 show the results. It can be seen that both the average and rms voltages remain nearly constant for $P/P_o \leq 0.45$. The average voltage begins to drop and the rms voltage begins to rise at higher pressure ratios. These are the expected behaviors when the downstream pressure is insufficient to choke the orifice. The value of P/P_o where the flow is no longer choked is slightly lower than predicted by Equation (21), but the agreement must still be considered excellent. Since the probe is normally operated with no valve in the pump line, it is clear that the sonic orifice is choked during routine use.

Since the hot-film anemometer is sensitive to changes in temperature, it was possible that the apparent velocity sensitivity to turbulent fluctuations was, in fact, the result of temperature variations due to turbulence. In order to investigate this possibility, the calibrated constant-current anemometer operated as a cold wire was used to record temperatures in room air and at the nozzle of the flow calibrator for a range of air flow velocities. The average temperature of the ambient air was recorded as 24.4 °C while measurements of the temperature in the air flow were in the range 24.4 °C - 24.8 °C This suggests that the maximum temperature fluctuations to be expected in the turbulent air flow (which is a mixture of jet and ambient air) are on the order of 0.5 °C with a somewhat smaller rms. Based on the calibrations shown in Figure 13 to Figure 16, the change in voltage output with temperature (assuming a gain of 10) is in the range of 30 mV/°C - 46 mV/°C. This suggests that the rms voltage change which can be associated with temperature fluctuations is less than 15 mV. The 40 mV rms observed in Figure 20 is much larger than this value, which indicates that the probe is indeed responding to velocity fluctuations.

11.2.5.3 Estimation of Uncertainty in Concentration Measurements Introduced by Probe Sensitivity to Turbulent Fluctuations. The response of the aspirated hot film to velocity fluctuations introduces a noise into the concentration measurements since they are interpreted as concentration fluctuations. Using the observed rms noise for a probe oriented parallel to a flow (0.04 mV with a

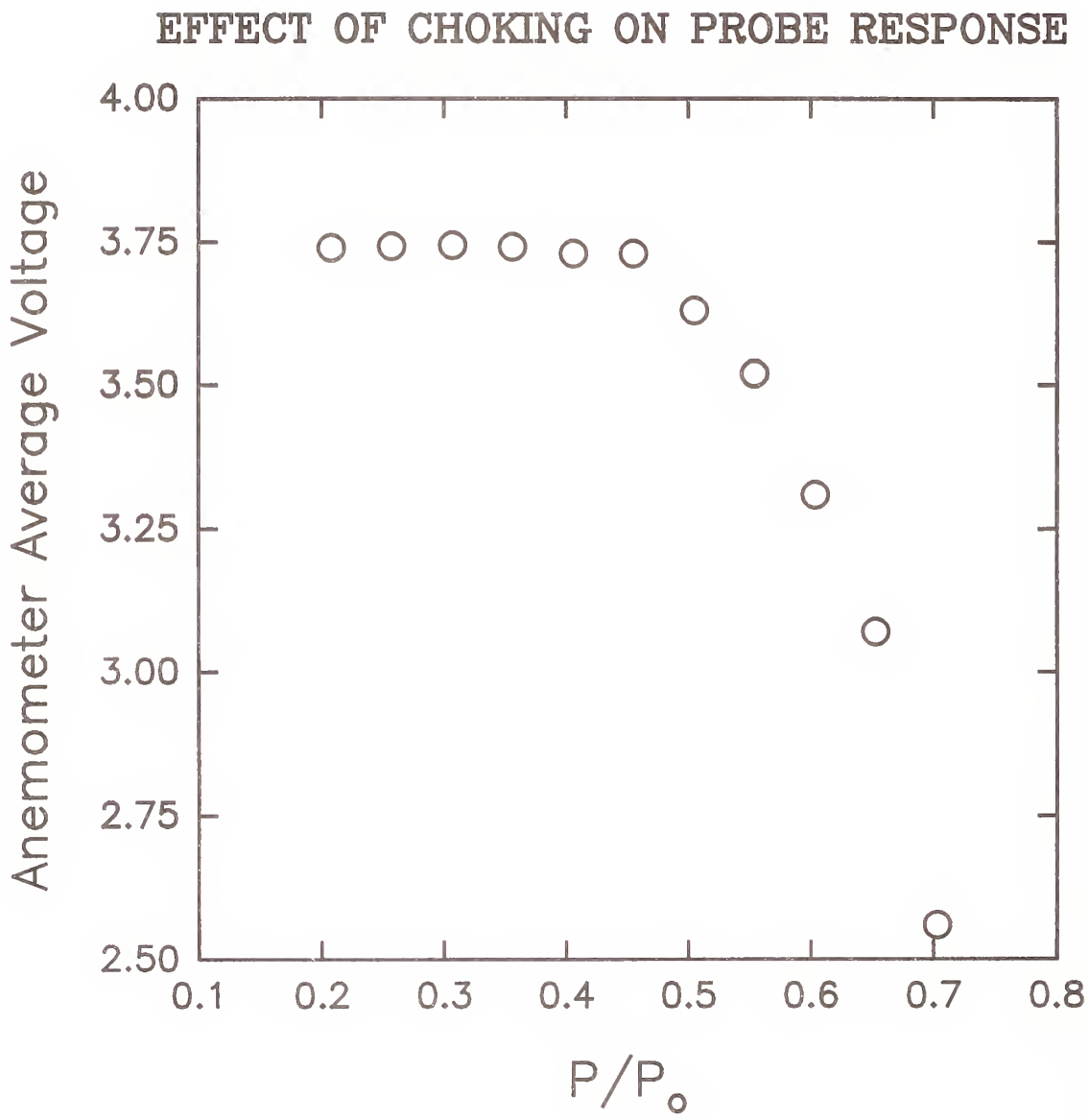

Figure 21. Average voltage output of hot-film anemometer as a function of the pressure ratio downstream of sonic orifice and ambient with probe located in a turbulent flow. A gain of 10 and offset of 2 V was used.

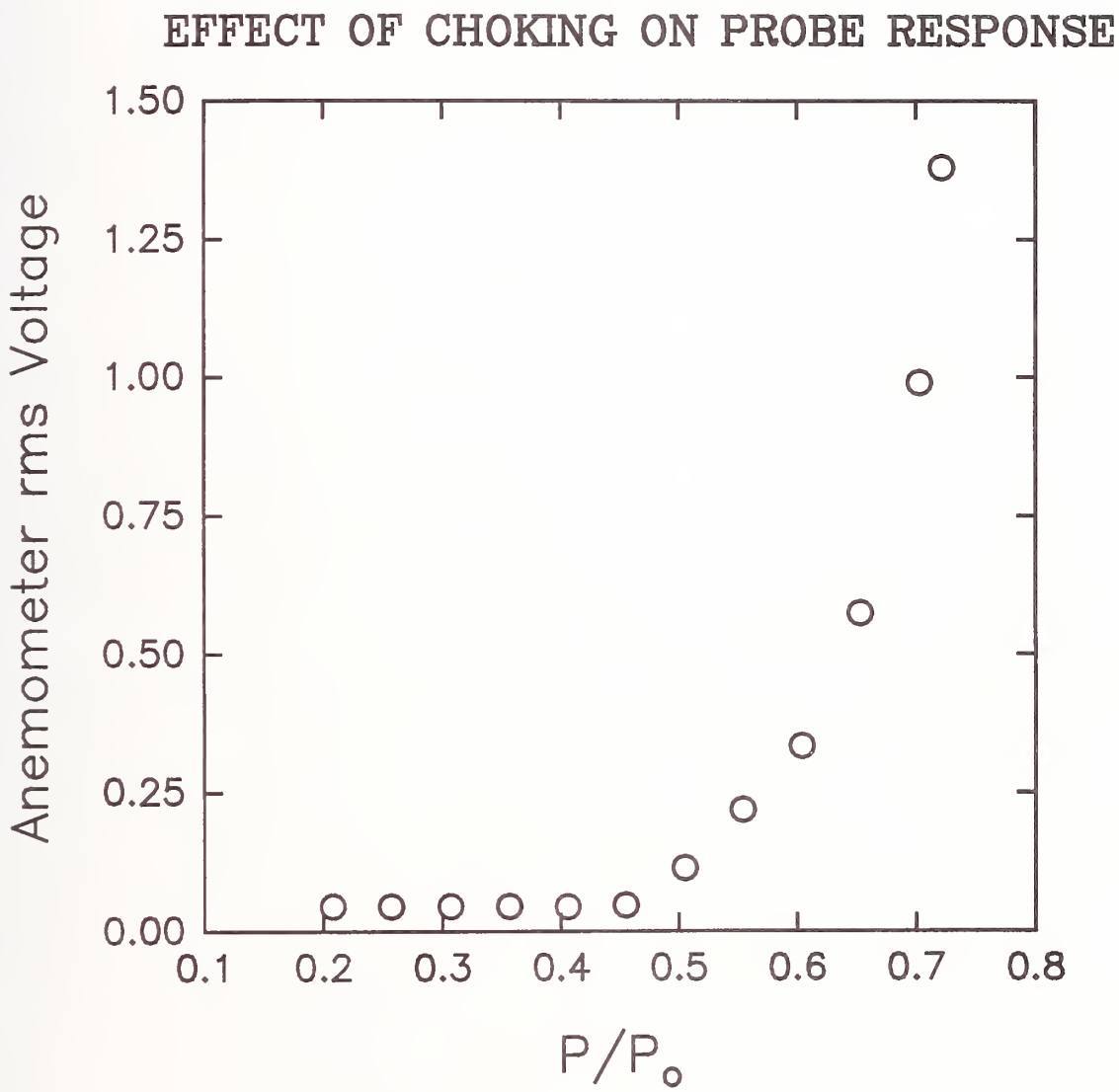

Figure 22. rms voltage output of aspirated hot-film anemometer as a function of the pressure ratio downstream of sonic orifice and ambient with probe located in a turbulent flow. A gain of 10 and offset of 2 V was used.

gain of 10) and the room-temperature calibration curves recorded for each agent, it is possible to estimate the uncertainty in individual time-resolved concentration measurements as the result of the velocity sensitivity. The results for agent mole fractions of 0.01, 0.05, and 0.10 are listed in Table 7. As expected, the predicted errors for a given mole fraction are largest for HFC-125, which has the smallest change of output voltage on going from air to pure agent. For a constant mole fraction of 0.01 the uncertainty in an individual measurement is ± 0.03, a very inaccurate measurement. For a HFC-125 mole fraction of 0.1 the uncertainty in an individual measurement is approaching 30 %. On the other hand, the expected uncertainties for halon 1301 (for which the probe sensitivity is highest) are much smaller. For a 0.01 mole fraction the relative uncertainty in an individual measurement is 50 % and drops to 6 % for a 0.10 mole fraction. This is considered acceptable for the current purposes. The uncertainties for FC-218 and HFC-227ea are intermediate. It can be concluded that the aspirated hot-film probe should provide time-resolved concentration measurements for halon 1301 with good accuracy, for FC-218 and HFC-227ea with moderate accuracy, and for HFC-125 with poor accuracy.

Another way to characterize the sensitivity of the aspirated hot-film probe to velocity fluctuations is to calculate the minimum mole fraction of an agent required to give a signal-to-noise ratio of 1. Values have been calculated assuming a noise rms of 0.004 V (no gain) and using the experimental calibration curves shown in Figure 17. The results are tabulated in Table 8. The same conclusions concerning the relative accuracies of concentration measurements for the four agents are reached.

11.2.6 Aspirated Hot-Film Concentration Measurements During Releases of Pressurized Agents. The next stage of testing was to calibrate the combined aspirated hot-film/cold-wire probe and attempt to use it for measurements in actual releases of agents. Measurements were carried out in three different experimental systems. This section summarizes the experimental methods used, the data analysis techniques, and the experimental findings.

11.2.6.1 Experimental System and Data Analysis for Concentration Measurement. The calibration system and its use has been described in previous sections. The result of these calibrations is an array of aspirated hot-film and cold-wire voltages versus agent concentration for a number of different temperatures. In order to record concentration in an actual release it is necessary to mount the probe at the desired measurement location, record the voltage outputs of the hot-film and cold-wire anemometers at a sufficient data rate during the period of interest, and convert these voltages to time records of temperature and concentration.

A special mount was fabricated to position and support the combined aspirated hot-film/cold-wire probe in the flow field. The mount consisted of a solid 25 mm aluminum rod which was cut in half and milled along the center such that the probe could be placed inside and held tightly. Set screws were used to join the two halves of the rod. The end of the rod was machined to a cone shape to minimize flow interferences. In general, the end of the probe would extend several tens of millimeters beyond the mounting rod. The holder could be bolted to a perpendicular plate for mounting in the experiment.

The same Flash-12 data acquisition system used for the calibrations was used to record the voltage outputs for the two anemometers. This system is described in detail in Section 11.2.4.5. The configuration of the data-acquisition system is somewhat simpler for experimental measurements than that required for the calibration system. All that is needed is the ability to "trigger" the system to start data acquisition and to record two voltage signals at the desired data rate for the desired period of time.

A second T21 terminal panel was used for experiments. It was mounted in an aluminum box equipped with eight BNC connectors. The BNCs were connected to the eight differential inputs of the

Table 7. Expected Uncertainties in Agent Mole Fraction for Three Average Values. rms Estimates Based on rms Voltage of 0.04 V from Figure 20 and Experimental Calibration Curves of Voltage Versus Mole Fraction

Agent	Assumed average mole fraction		
	0.01	0.05	0.10
HFC-227ea	0.0136	0.0145	0.0162
FC-218	0.0123	0.0138	0.0160
HFC-125	0.0285	0.0277	0.0283
halon 1301	0.0052	0.0058	0.0065

analog-to-digital converter. A digital ribbon cable was used to connect the interface box to the Flash-12. In order to switch from probe calibration to data acquisition, it was only necessary to disconnect the digital ribbon cable for the calibration interface box from the Flash-12 and replace it with that for the experimental measurement interface box.

An icon-based work sheet such as SHOT.WBB shown in Appendix G was used to control the experiment. The work sheet sets up the hardware to accept a trigger from the experiment on analog-to-digital input channel 1 which initiates data collection following a 0.8 s delay. The work sheet provides for recording three input voltages. Two of these are the outputs of the aspirated hot-film (channel 6) and cold-wire (channel 7) anemometers. The third channel was used for the Differential Infrared Rapid Agent Concentration Sensor (DIRRACS) described in Section 11.3. Three seconds following the trigger, data collection was halted and the data was written out to the hard disk. Note that the total data collection time using this work sheet was 2.2 s.

Since the physical processes of interest are quite fast, the data must be recorded at a high rate. Typically 20 kHz was used. With the current data-acquisition hardware, this requires that the data be recorded directly into memory located on the daughter board using the so-called "fast mode." Only after completion of acquisition is data transferred to the personal computer and stored to disk. The total number of data points which could be stored was limited by the daughter board memory to 1 000 000. For the 2.2 s sampling time, the total data sampling rate was 60 kHz and the total number of measurements recorded was 132 000, which was well within the limits of the device.

At the conclusion of an experiment the data was stored in a file containing two columns of readings corresponding to time records of the hot-film and cold-wire anemometer voltage outputs. It was necessary to convert these voltages to time records of temperature and concentration using the appropriate calibration curves. There are a number of ways in which this could have been done. Since the response of a cold wire has a linear dependence on temperature, the approach chosen was to directly calculate the temperature from the cold-wire voltages using an intercept and slope calculated by a least squares curve fit to the calibration data. Once the temperature was available, it was necessary to calculate the concentration knowing the output voltage of the aspirated hot film and the temperature. For this purpose a least squares fit of a concentration surface (either in mole fraction (X) or mass fraction (Y) terms) to the calibration values of temperature (T) and aspirated hot-film output voltage (E_{hf}) was used.

The general form of such a surface of order m can be written as

Table 8. Minimum Mole Fraction of an Agent Required To Give a Signal-To-Noise Ratio of 1. Voltage rms of 0.04 (No Gain) Has Been Assumed

Agent	Minimum mole fraction
HFC-227ea	0.015
FC-218	0.016
HFC-125	0.028
halon 1301	0.006

$$X = \sum_{i=0}^{m} \sum_{j=0}^{m} a_{i,j} T^j E_{hf}^i , \tag{22}$$

where the coefficients $a_{i,j}$ are determined by a least squares fit to the calibration data. As examples, for $m = 1$ Equation (22) would be written as

$$X = a_{0,0} + a_{0,1} T + a_{1,0} E_{hf} + a_{1,1} T E_{hf} , \tag{23}$$

while for $m = 2$ the expression becomes

$$X = a_{0,0} + a_{0,1} T + a_{0,2} T^2 + a_{1,0} E_{hf} + a_{1,1} T E_{hf} + a_{1,2} T^2 E_{hf} + a_{2,0} E_{hf}^2 + a_{2,1} T E_{hf}^2 + a_{2,2} T^2 E_{hf}^2 . \tag{24}$$

A Fortran code (SURFFIT.FOR, included as Appendix H) was written to determine the coefficients $a_{i,j}$ for a file of input values of temperature, hot-film voltage, concentration, and a predetermined m. Once the values of $a_{i,j}$ were available, Equation (22) could be used to calculate values of concentration from arbitrary pairs of temperatures and aspirated hot-film voltages. A Fortran program named CONCEN.FOR (included as Appendix I) read a file containing a time series of the voltage pairs and by using Equation (22), along with the input values of $a_{i,j}$ from SURFFIT.FOR and the experimental dwell time at which the data was recorded, generated an output file containing listings of time, temperature, and concentration. Once the reduced data for temperature and concentration as a function of time were available, they could be plotted or analyzed further.

11.2.6.2 Measurement of Halon 1301 Concentration Following Release From a Pressurized Vessel into an Open Room. As an initial test of the experimental system and procedures, an attempt was made to measure the time behaviors of agent concentration and temperature during the release of halon 1301 from a pressurized vessel. The experimental system used to release the agent was that described in Section 8. The particular experimental configuration included the stainless-steel cylindrical vessel developed at NIST during our previous work on the selection of agents (Pitts *et al.*, 1994) with an attached Marotta solenoid valve. The vessel was oriented vertically, and, since the

valve turns the flow 90°, the fluid exited the vessel horizontally. The transmission behaviors of the photo-diode-detected laser beams described in Section 8 were recorded during the release. The extinction of the beam from laser No. 1, located at the vessel exit, was used to define a time of 0.000 s for the release.

The combined aspirated hot-film/cold-wire probe was mounted on the axis of the release valve 1.85 m from the valve exit. The DIRRACS infrared sensor described in Section 11.3 was also mounted at the same downstream distance and was operated during the test. A signal from the system used to initiate the release of the agent provided a trigger for the data acquisition system for the probe. The work sheet SHOT.WBB (Appendix 6) was used to control the data acquisition. Signals for both the aspirated hot-film/cold-wire probe as well as the DIRRACS were recorded simultaneously. Note that the data acquisition rate was 20 kHz per channel for 2.2 s following trigger detection.

A complete calibration of the combined aspirated hot-film/cold-wire probe was carried out for the first time the day before the agent was released. The results of the calibrations were used to generate the fits required in order to use CONCEN.FOR to calculate the temperature and concentration histories of the release at the measurement location. Figure 23 shows the results of the calibration for the cold wire. The least-squares fit of the experimental data to a line is included on the graph. The coefficients of the line were used as inputs for CONCEN.FOR. Figure 24 shows the corresponding data for the calibration of the aspirated hot-film probe. SURFFIT.FOR was used to calculate least-squares surface fits of halon 1301 mole fraction to the aspirated hot-film voltage and temperature for a range of surface orders, m. The case with $m = 3$ was determined to be the most appropriate for fitting the data. Figure 25 shows the calculated mole fraction surface as a function of temperature and observed aspirated hot-film anemometer voltage. Note that nonphysical values (*e.g.*, mole fractions > 1 or < 0) are shown, but, voltages corresponding to these values should not be observed experimentally. The coefficients used to generate the surface of Figure 25 were input to CONCEN.FOR.

For the release, the vessel was filled two-thirds full (0.605 kg) with liquid halon 1301. The liquid agent was saturated with nitrogen with the nitrogen pressure above the liquid increased to 4.1 MPa. Measurements of the pressure behavior within the vessel indicated that the total release time for the liquid was on the order of 45 ms.

Figure 26 and Figure 27 show the voltage outputs of the constant-current (cold-wire) and constant-temperature (aspirated hot-film) anemometers for 200 ms following the release of the halon 1301. Both signals show strong responses at around 30 ms following the start of the release. This corresponds to the time required for the agent to travel from the vessel to the location of the probe (*i.e.*, a distance of 1.85 m). Very strong oscillations in the voltage outputs are observed during the period from 30 to 80 ms following release. After this time the voltages are still significantly different than those observed before the agent reached the measurement location, but the magnitudes and intensities due to the presence of the agent are much smaller than recorded earlier. It is significant that the largest voltages and fluctuations occur over a period which is roughly the same as that required to expel the liquid agent from the vessel. It seems certain that the strong signals and fluctuations are associated with the forced flow of agent driven from the pressurized vessel.

The voltage signals displayed in Figure 26 and Figure 27 along with the coefficients derived from fits to calibrations of the probe response as a function of concentration and temperature were used to calculate the temperature and concentration of halon 1301 as a function of time. Figure 28 and Figure 29 show the measured temperatures and mole fractions of halon 1301 following release of the agent from the pressurized bottle at 0 s. Some very interesting behaviors are observed in the data.

The temperature data look very reasonable. Before the agent reaches the probe at roughly 34 ms following the release, the recorded temperature is on the order of 23 °C which is reasonable for the experimental room. Careful scrutiny of Figure 28 shows that there appears to be a very small increase in temperature with a maximum at 29.4 ms just before the temperature begins to drop rapidly. At

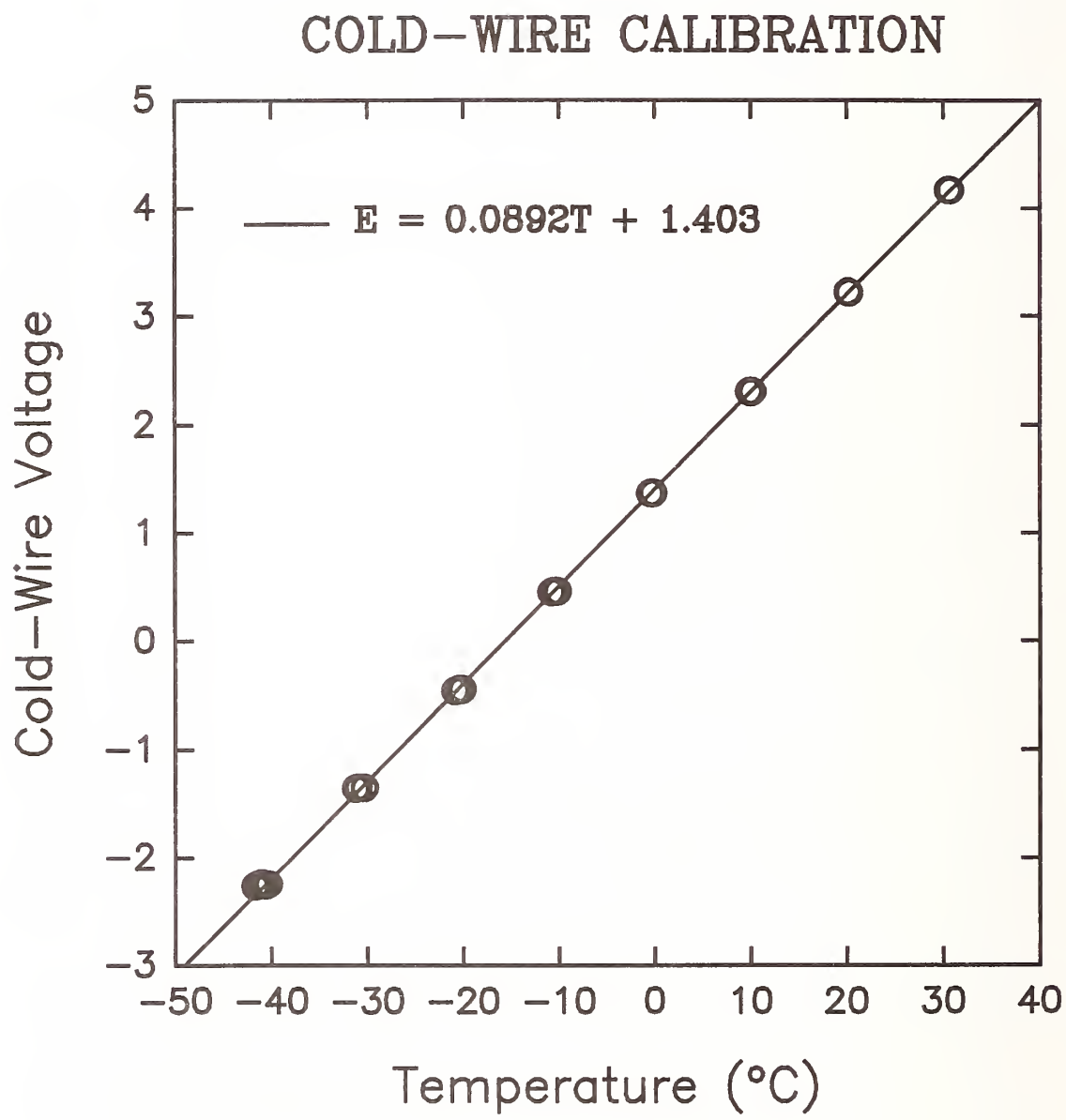

Figure 23. Values of constant-current anemometer voltage are plotted as a function of temperature. Note that eleven measurements were made for each nominal temperature. The line is a linear-least-squares curve fit of the experimental data.

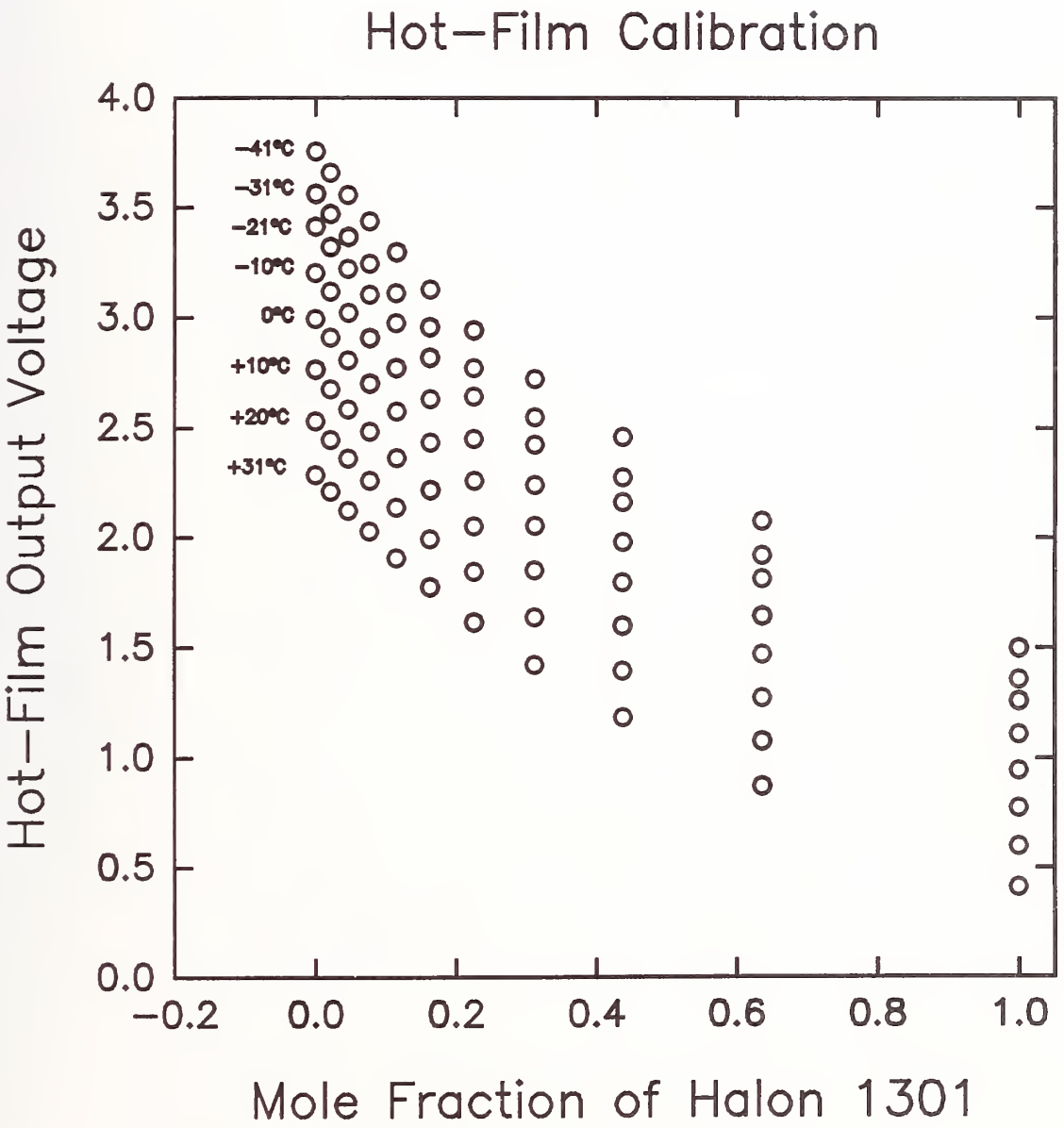

Figure 24. Values of aspirated hot-film anemometer voltage are plotted as a function of halon 1301 mole fraction for a range of temperatures.

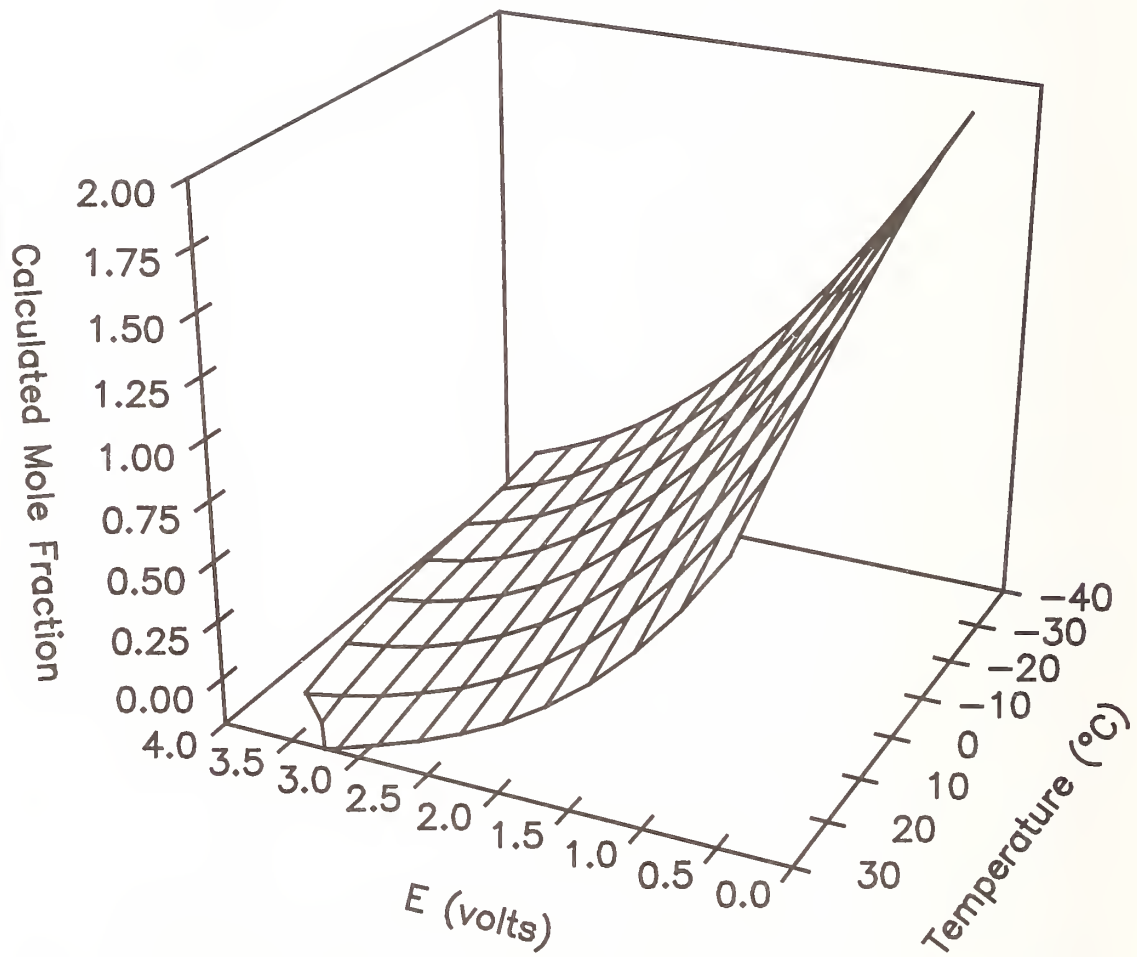

Figure 25. Plot of the mole fraction of halon 1301 surface calculated as a function of temperature and aspirated hot-film voltage based on a fit of a third-order surface to the data shown in Figure 24.

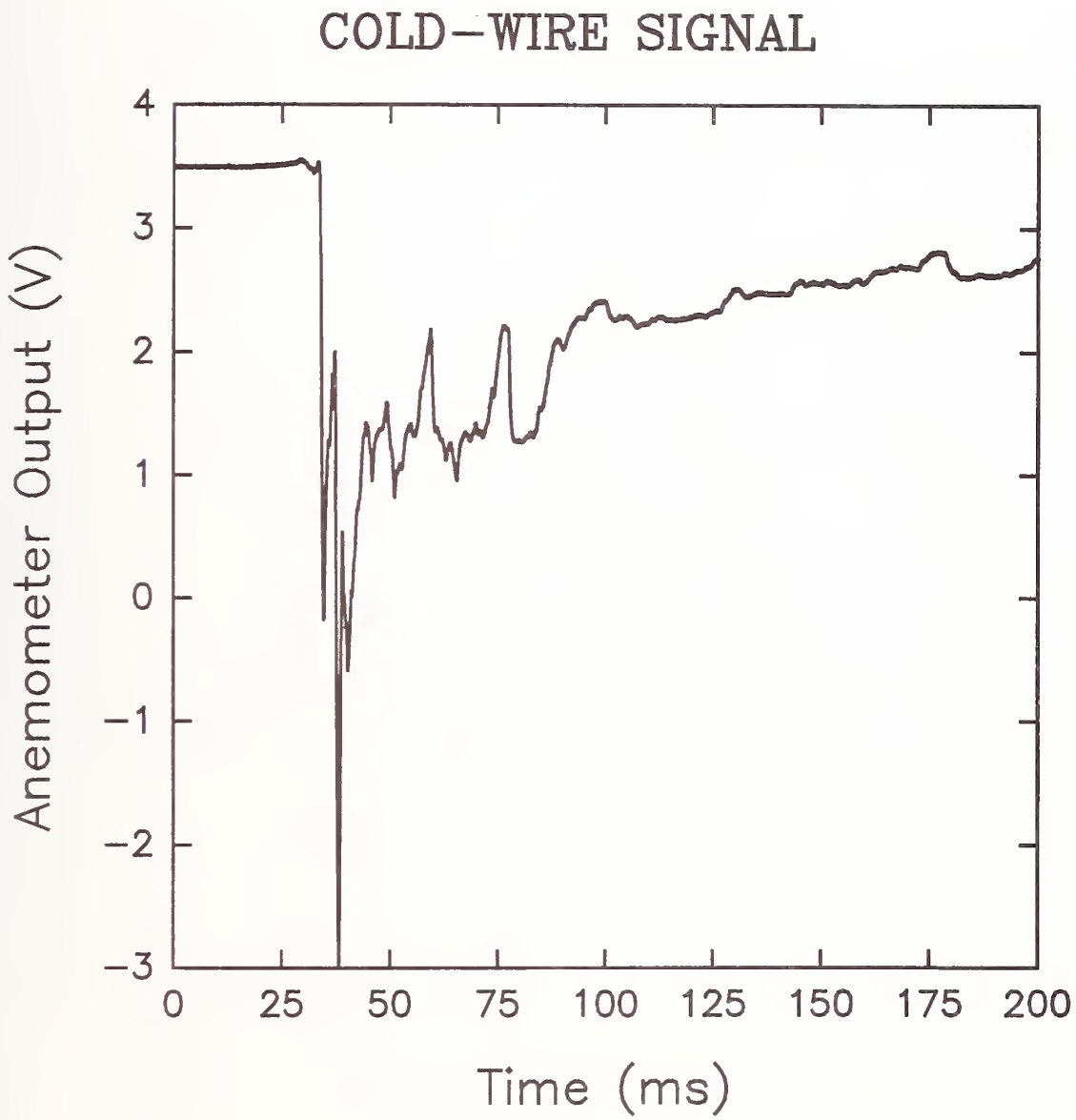

Figure 26. The output voltage of the constant-current anemometer is shown as a function of time following the release of halon-1301 from a pressurized vessel.

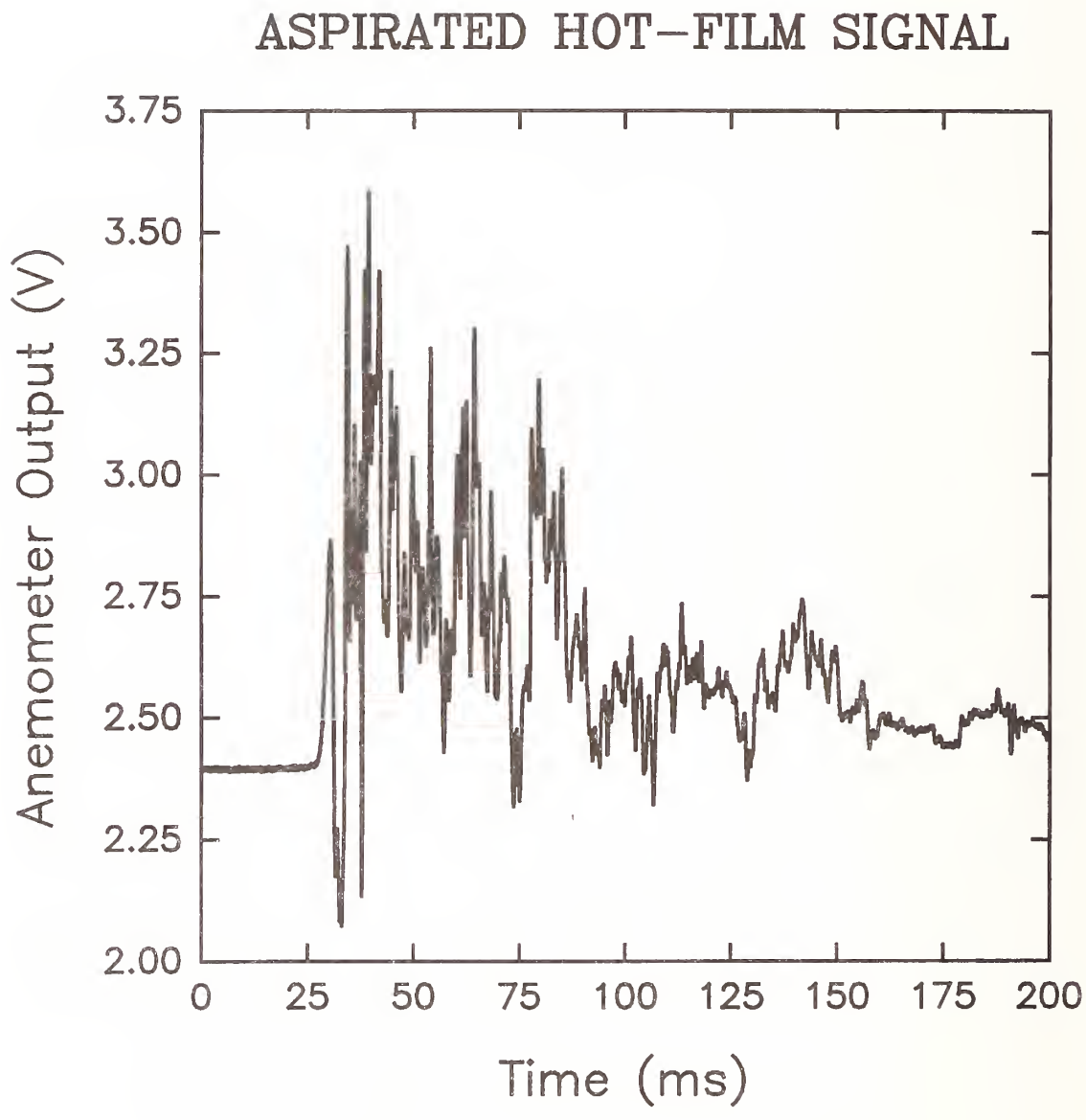

Figure 27. The output voltage of the constant-temperature anemometer is shown as a function of time following the release of halon 1301 from a pressurized vessel.

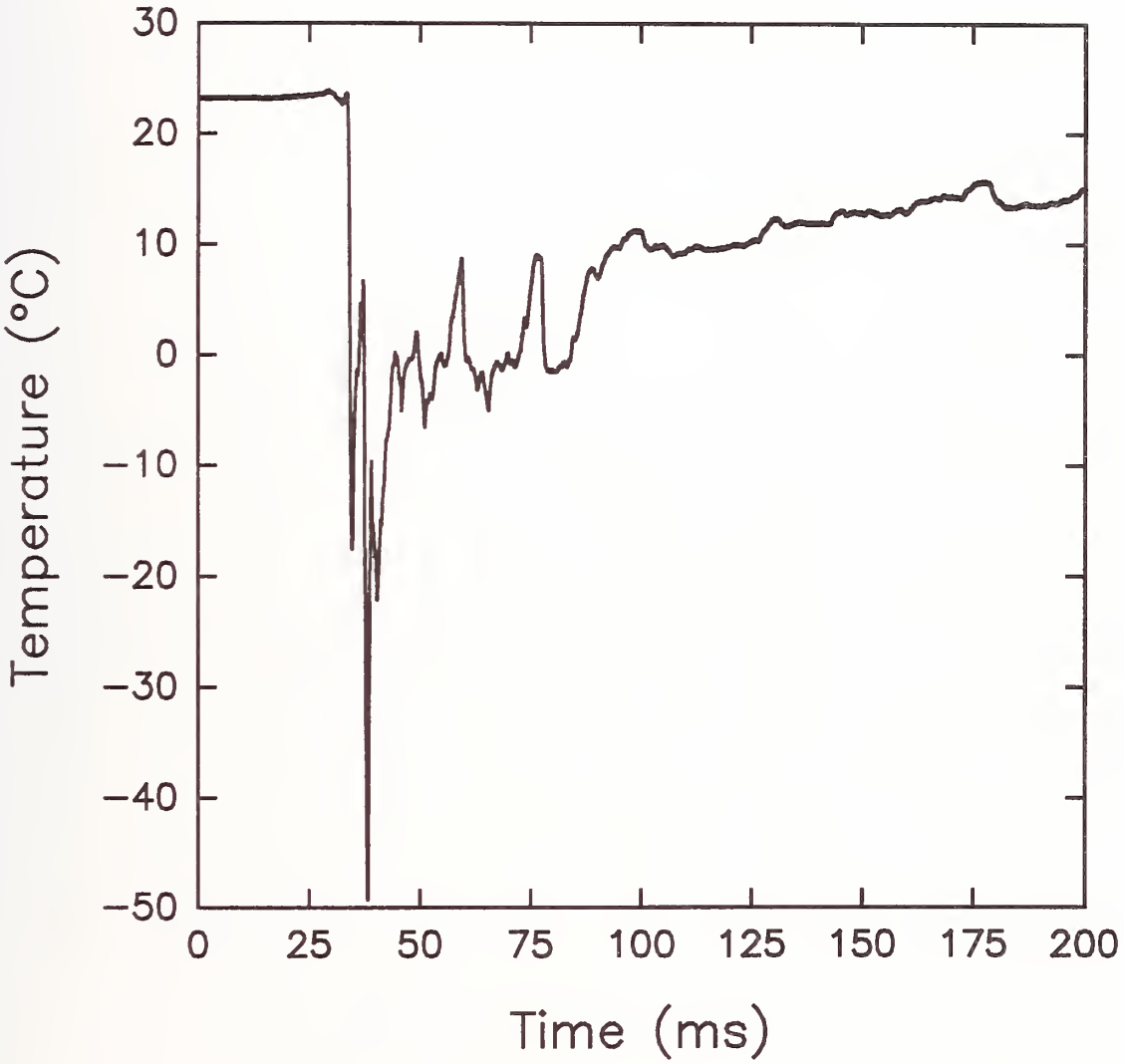

Figure 28. Measured temperature is shown as a function of time following the release of halon 1301 from a pressurized vessel. The probe was located 1.85 m from the vessel exit.

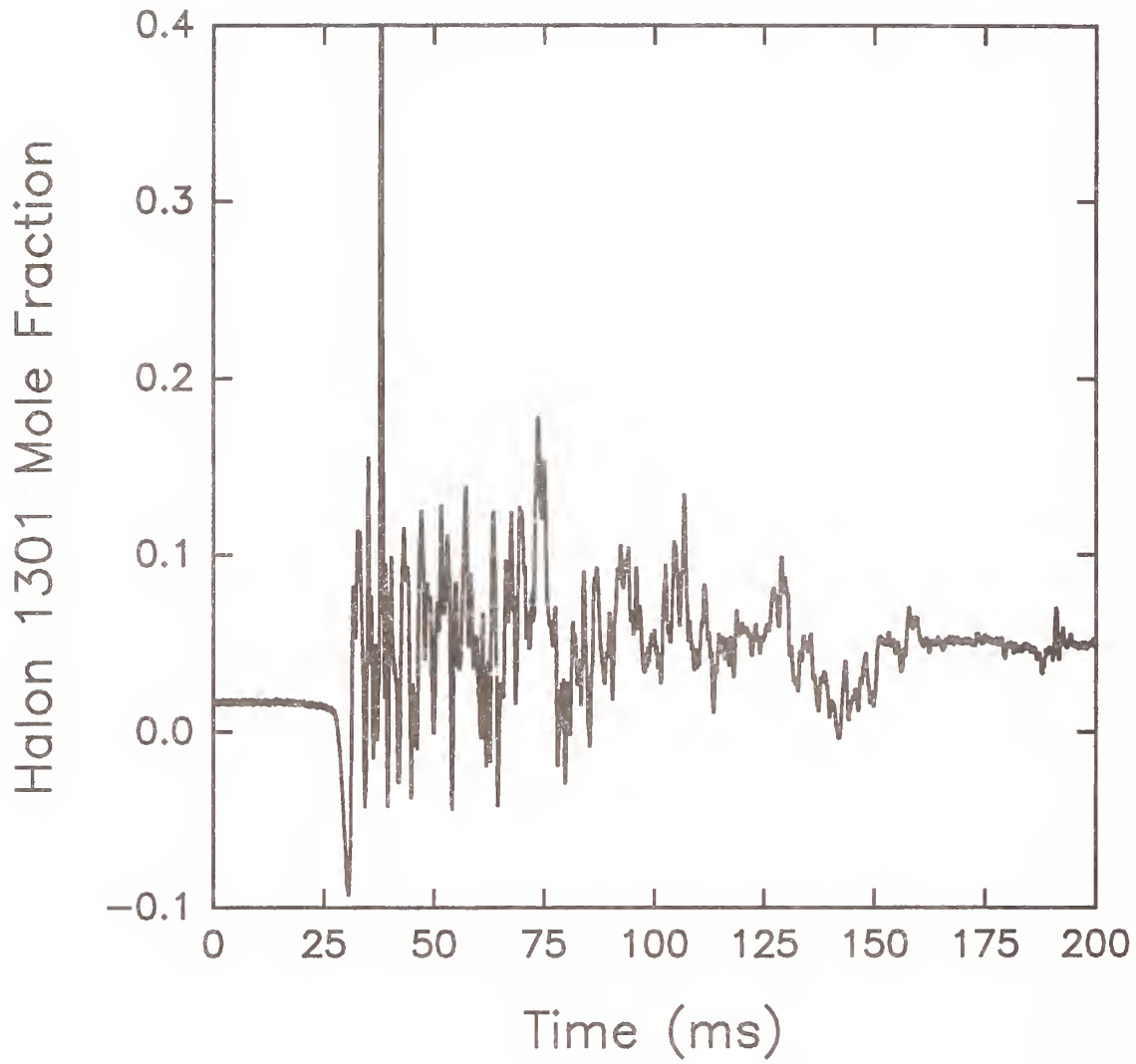

Figure 29. Measured halon 1301 mole fraction is shown as a function of time following release of the agent from a pressurized vessel. The probe was located 1.85 m from the vessel exit.

33.6 ms following release the temperature shows a sharp drop falling to -17.5 °C at 34.7 ms. There is a small increase in temperature before the temperature drops rapidly to -49.3 °C at 38.2 ms. This temperature is very nearly as low as the halon 1301 boiling point of -57.8 °C. The temperature remains at these very cold levels only briefly before rising to values on the order of 0 °C. Following the passage of the released agent, the temperature begins rising slowly, reaching 11 °C at 100 ms, 15 °C at 200 ms, and 21.8 °C recorded at the end of experiment, 2 s following the release (not shown).

In considering the concentration data in Figure 29 a problem is immediately evident. In the period before the agent release reaches the probe, concentrations on the order of 0.016 are calculated, even though there is no agent present. This demonstrates there is some uncertainty in the calibrations. The source of this uncertainty is difficult to identify. It could be due to small changes in probe response due to flow effects as described above. The probe is calibrated in flows of agent/air mixtures, while the probe was located in ambient air when these measurements were recorded. Another possible source of error is the quality of the fit concentration surface to the experimental calibration data. Whatever the source, the results suggests that there will be an offset in the results corresponding to a mole fraction of 0.016.

An even more troubling aspect of the concentration data is the observation of physically unrealistic negative values at times earlier than the temperature measurement indicates the agent reached the probe. The negative concentration results reach a minimum at 30.5 ms following release. Based on the calibration results in Figure 24, such negative concentrations must correspond to voltages which are higher than those for air alone. Interestingly, the period of negative concentrations corresponds closely to the time when a very small temperature rise was observed. The actual cause of these observations is uncertain, but a reasonable hypothesis can be proposed. When the agent is released from the vessel it accelerates rapidly in the direction of the probe. As it does so it "pushes" air in front of it. If the flow velocities are high enough, the pressure of the air will increase, and it will be heated. When the compressed air reaches the probe it will be detected as a higher temperature by the cold wire, and the aspirated hot film will lose heat more rapidly due to the increased pressure, which will increase the voltage output and appear to correspond to a negative concentration.

During the period from roughly 34 ms to 75 ms, corresponding to the release period of the agent from the vessel offset by the passage time from the vessel to the probe, the mole-fraction data are very noisy and even occasionally display negative values. In a previous investigation (Pitts *et al.*, 1994) such behavior was attributed to the presence of two-phase flow at the measurement point. The same explanation is likely for the current data. Once this period is over, the data has a smoother appearance and looks more reasonable. At 100 ms the measured mole fractions are on the order of 0.11 (0.09 assuming an offset of 0.02) and by 200 ms have dropped to 0.05 (0.03 assuming an offset of 0.02). By the end of the period during which data was recorded (2 s), the concentration had dropped back nearly to the ambient levels recorded before the agent/air mixture reached the probe.

This series of tests was repeated at a later time. The results were somewhat different, but in general the overall behaviors were consistent with those described above.

It is impossible to say whether the measured concentration time history accurately reflects the true concentration behavior without an independent measurement of the concentration. Such a measurement was not possible for these experiments. However, the observed concentration behavior is consistent with the observed temperature changes which were recorded independently. Both indicate that significant concentrations of cooled agent are present during the passage of the flow generated by the release of the agent. Following this passage, the concentration rapidly drops, and additional mixing of the gas left behind by the agent release occurs with the surrounding air.

Although the quantitative findings of this test must be considered suspect due to the offset in concentration observed for ambient air, overall the results demonstrate that the combined aspirated hot-

film/cold-wire probe has the required time response and sensitivity to temperature and concentration of halon 1301 to allow accurate quantitative measurements at high data rates.

11.2.6.3 Attempt to Measure Halon 1301 Concentration Following Release From Pressurized Vessels into a Simulated Dry Bay. As noted in Section 11.1, a decision was made mutually with the program sponsors to test the combined aspirated hot-film/cold-wire probe during releases of agent into the dry-bay test facility at Wright-Patterson AFB, Dayton, OH. During the week of July 18, 1994, members of the BFRL research staff traveled to Dayton, OH and performed the tests which are summarized here. The goal of these tests was to assess the performance of the new probe for agent concentration measurement under "real-world" conditions (*i.e.*, in an environment where actual measurements are required).

All of the equipment required to perform the tests, including the calibration system, was transported from NIST and reassembled at Wright-Patterson AFB. The TSI, Inc. Model 1440S (SN 943064) combined aspirated hot-film/cold-wire probe was used. Figure 30 and Figure 31 show calibration curves for the cold-wire and aspirated hot-film probes recorded prior to testing in the simulated dry-bay facility. Also included in the figures are calibration results recorded immediately following the tests. Reasons for the differences in the two sets of curves are discussed below.

Following calibration, the combined aspirated hot-film/cold-wire probe was mounted in the dry-bay simulation facility. The tests were carried out in the large dry bay which is 6.1 m (long) × 1.5 m (high) × 0.30 m (deep). Figure 75 in Section 11.3.9.1 shows a schematic drawing of the facility. Small fans were located on the right edge of the dry bay which blew a constant volume of air into the facility. Three vents were located on the lower left edge. During the tests an additional opening of 0.30 m × 0.30 m, which was intended to represent an opening due to battle damage, was placed near the base in the center of the dry-bay front wall. The facility was equipped with a "high-clutter environment" which significantly blocked free flow within the dry bay. The agent to be released was stored in two vessels, which were placed on either side of the centerline, mounted at the top of the dry bay. The agent was released by firing "squib" charges which were exploded electronically under computer control.

Normally the dry-bay facility is used to perform fire tests under simulated battle and flight conditions. During these tests aviation fuel is located in a tank on the back side of the dry bay. An external high-speed air flow is passed along the front side of the dry bay. A fire is initiated by firing a high-explosive incendiary (HEI) antiaircraft round through a plate on the front. This round pierces the fuel tank and generally starts a fire. The result of the test is whether or not the agent extinguishes the fire upon release. During the current tests the dispersion of the agent was monitored under ambient conditions. The only air flow was the internal ventilation flow. There was no fuel, fire, or HEI rounds used.

The probe was mated to the facility using the mounting system described in Section 11.2.6.1. A hole of sufficient diameter to pass the probe and its mount was cut in the aluminum back panel of the dry bay along with holes for securing the plate which holds the mount. The probe was inserted to the center of the dry bay (*i.e.*, 0.15 m from the back wall). By creating a number of such mounting positions, it was possible to make measurements at different locations within the dry bay.

The outputs of the cold-wire and aspirated hot-film anemometers were recorded using the data-acquisition system described above. A trigger for the data-acquisition system was provided by the computer used to control the release of the agent into the dry bay. This trigger arrived approximately 0.2 s before the squib charges were fired. The Workbench PC work sheet for the experiment was set up to record voltages from both the cold wire and hot film. Additionally, voltage outputs were recorded for the two DIRRACS probes described in Section 11.3. Data were taken at 20 kHz/channel with a total data-acquisition time of 10.2 s. Note that this required that 816 000 measurements be

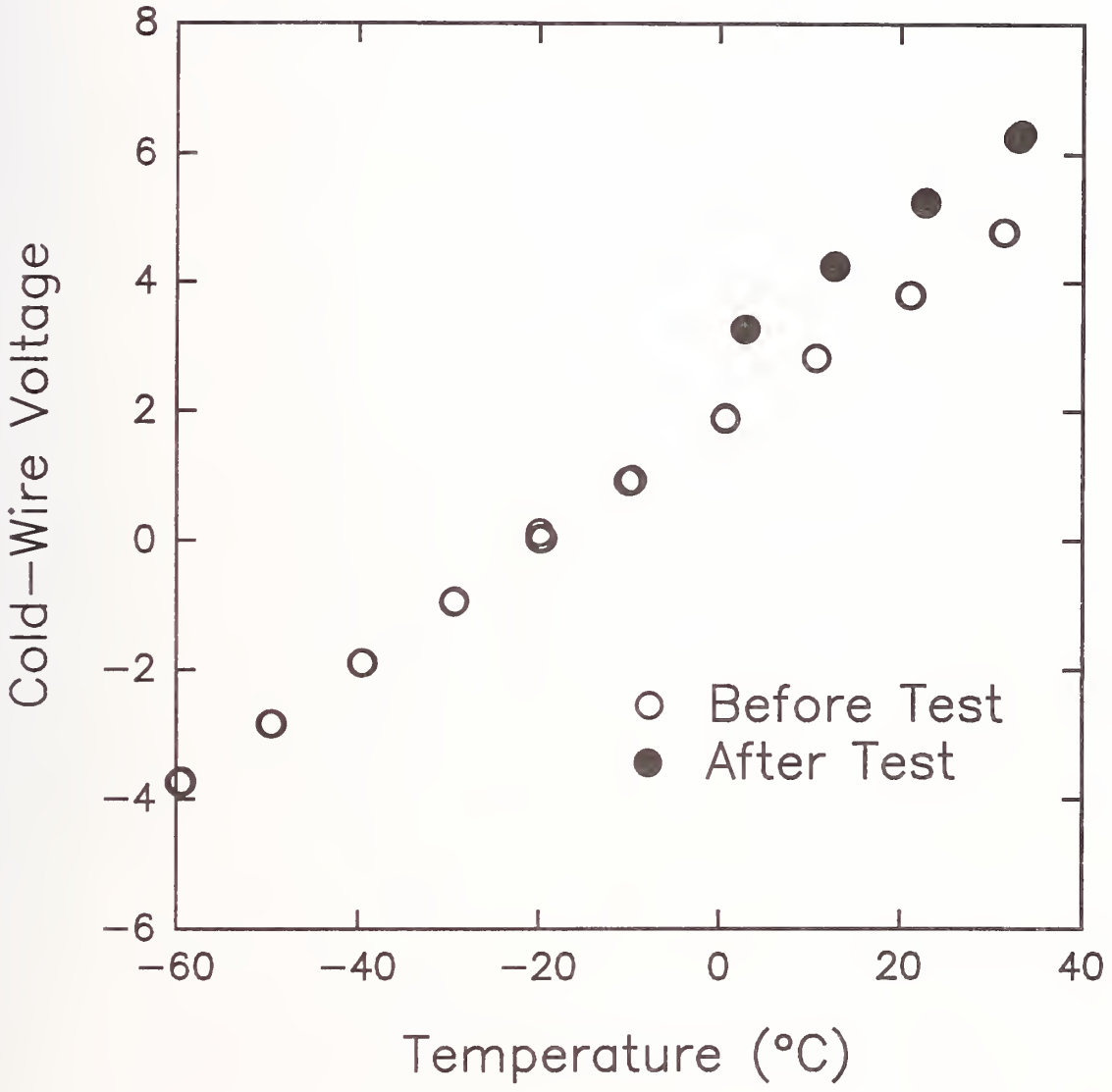

Figure 30. Calibrations of the cold wire before and after a series of measurements in the simulated dry-bay facility. See text for a discussion of reasons for the change in response.

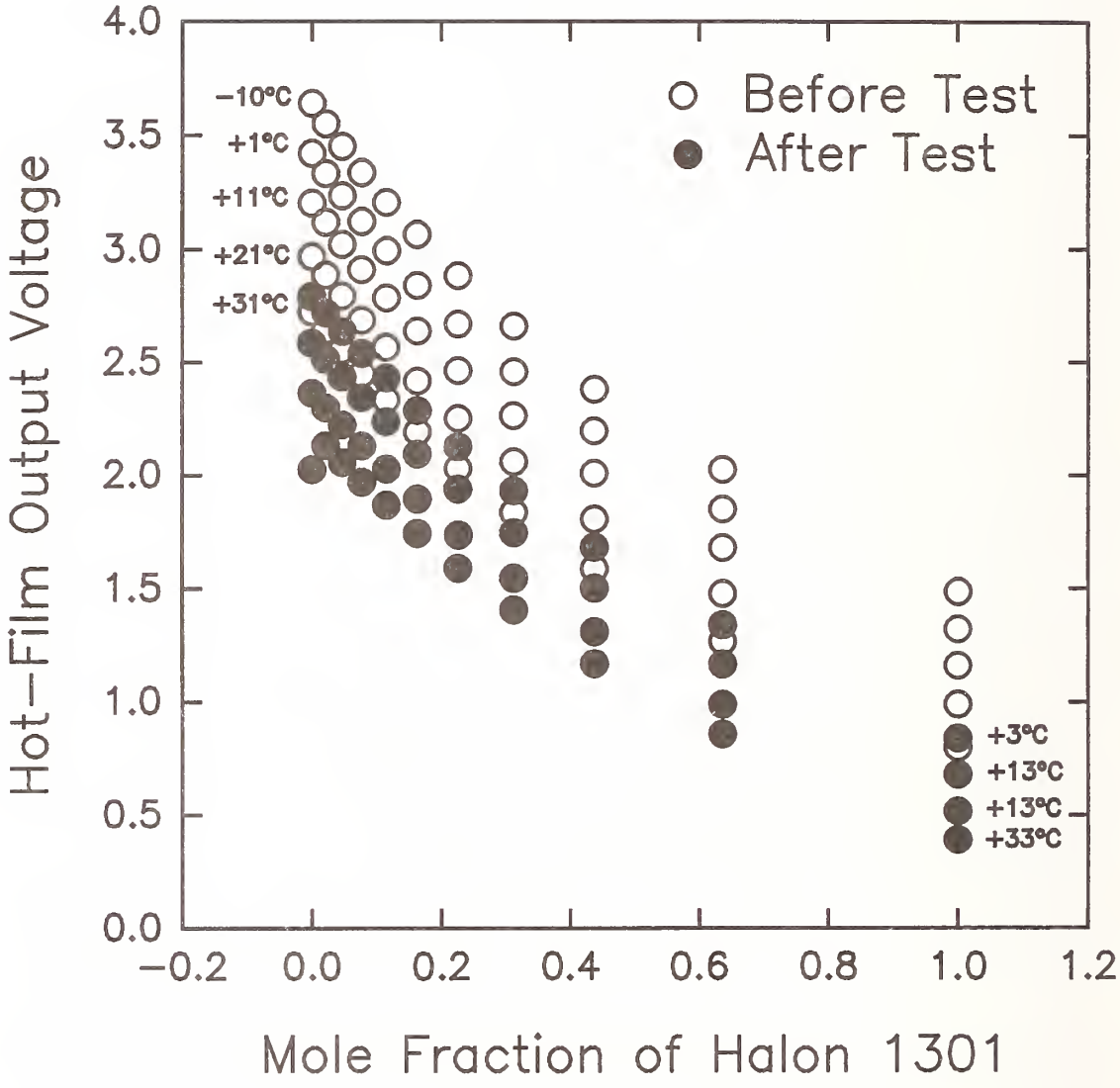

Figure 31. Calibrations of the aspirated hot-film before and after a series of measurements in the simulated dry-bay facility. See text for a discussion of reasons for the change in response.

made during a single experiment.

A total of six releases of halon 1301 were carried out. For one set of data the trigger was missed so only five sets were saved. During releases the probe location and amounts of agent were varied as indicated in Table 9. For reasons which will become obvious, only the results of the first release are summarized here. Figure 32 and Figure 33 show the cold-wire and aspirated hot-film voltages observed following initiation of halon 1301 release No. 1. Close inspection of Figure 32 shows a sharp voltage spike at 0.21 s after data collection was initiated. This is a noise signal associated with the firing of the squib charges and provides an accurate indication of the release time for the agent. No changes in the cold-wire output are observed until roughly 1.8 s following the release of the agent. At this time the voltage begins to rise slowly (indicating a temperature rise), reaching a maximum roughly 3.5 s following the release. The overall voltage increase is small indicating a small temperature change.

The voltage output for the aspirated hot film has a very different behavior. It remains nearly constant for the first 2 s following initiation of the experiment, but then begins to drop. The drop in voltage continues at a relatively constant rate for the remaining 8 s that data was recorded. The decrease in hot-film voltage is relatively large.

The raw voltage signals were converted to measured values of temperature and concentration using the CONCEN.FOR program described earlier. A third-order surface fit was used to fit the concentration data. The results are shown in Figure 34 and Figure 35. The initial temperature of roughly 36.6 °C seems somewhat high since the air temperature outside of the dry bay was recorded as 28 °C. It seems likely, however, that temperatures in the dry bay were somewhat higher since the clear-walled facility was located in the open on a bright sunny day. Even though the release of halon 1301 occurred at 0.21 s, no changes in temperature were detected until nearly 1.8 s following the discharge. The earlier tests had shown that the release of pressurized agents leads to a strong cooling since the superheated liquids cool to their boiling points (-57.8 °C for halon 1301). Despite this expected cooling, only a small temperature increase of roughly 0.7 °C was detected 4 s following release. After the maximum, the temperature began to decay back toward the original ambient levels. As discussed below, the measured temperature rise may be associated with a change in cold-wire calibration and may not be real. However, it does seem clear that there is no large temperature drop at the measurement position associated with the halon 1301 release. This observation requires either that the agent did not reach the detector, or that a large amount of heat transfer to the dry-bay walls and baffles occurred before it did.

The recorded time behavior of halon 1301 mole fraction shown in Figure 35 is nonphysical. Initially negative mole fractions on the order of -0.05 were recorded. Recall that negative values were also observed during the earlier tests of agent release at NIST. This is possibly due to the sensitivity of the aspirated hot-film calibrations to velocity. At roughly 1.8 s following release, the calculated agent concentration began a relatively constant rise, and by 10 s following the release, the measured mole fraction was slightly higher than 0.10. Including the negative offset, this indicates the halon 1301 concentration rose by 0.15 during the test. If the initial mass of halon 1301 were distributed evenly throughout the dry bay, the average concentration would be 0.014. The measured increase therefore seems very unreasonable.

The unusual behavior of the aspirated hot-film response continued after the conclusion of release No. 1. Data recorded prior to later releases (*i.e.*, in air) yielded calculated mole fractions of halon 1301 which were on the order of 0.10. As the later tests progressed, the voltage output for the cold-wire anemometer in air continued to increase while that for the aspirated hot-film anemometer continued to decrease. The voltage variations were so large that the operators suspected that the calibration curves for the probe were undergoing large changes. Following release No. 6 the probe was inspected. It seemed to be coated with black particles. It was believed that the residue was black

Table 9. Locations of the Combined Aspirated Hot-Film/Cold-Wire Probe and Masses of Released Halon-1301 for Dry-Bay Tests

Test #	Location (m)[1]	Total mass halon 1301 (kg)
1	0.20 × 0.58	0.23
2	0.20 × 0.58	0.91
3	3.05 × 0.36	0.23
4	3.05 × 0.36	0.91
5	5.89 × 0.51	0.91

[1]Measured from lower left-hand corner of the dry-bay test facility

powder which was released during the firing of the squib charges used to release the agent.

Immediately following the dry-bay tests the probe was returned to the calibration facility, and the calibration runs were repeated. The results are included in Figure 30 and Figure 31 where they are represented by the filled symbols. It is clear that the temperature calibration has been shifted upwards by over a volt. Note that this means the resistance of the wire has increased between the two sets of calibrations. At the same time the slope of the plot has changed less than 10 %. For a given voltage, the change in calibration represents a temperature difference of nearly 15 °C. Clearly this is unacceptable.

The changes in the response of the aspirated hot film were equally dramatic. For a given temperature, the output voltage for the constant-current anemometer was 0.6 V lower than prior to the test. In fact, the change in calibration corresponded to roughly 1/3 of the entire voltage difference observed between air and halon 1301 at a given temperature. Again, it is clear that such dramatic changes in probe response make accurate measurements of concentration impossible.

The modifications in response observed during the dry-bay tests were a complete surprise. Even though minor changes in calibration curves are often observed experimentally, they tend to be small. Test experiments at NIST had indicated that such changes were small, despite severe experimental conditions. Based on the use of squibs to release the agent and the observation of a black residue on the probe, it is most likely that contamination by black powder is the cause of the shifts in calibration curves for the two sensors. Deposition of a conducting solid on the cold wire would be expected to increase its resistance. This is consistent with the increased voltage output of the constant-current anemometer observed for a given temperature. Deposition of a solid on the sonic orifice of the aspirated probe would reduce the diameter and, therefore, the mass flow through the orifice. Since the mass flow is reduced, the flow velocity over the hot-film sensor would also be decreased. This would result in a smaller heat loss and a decrease in the output voltage as observed experimentally. Based on the observations, it seems certain that the deposition of a black residue as the result of squibs firing was the source of the shifts in calibration curves for the combined aspirated hot-film/cold-wire probe.

Following this short series of tests it was necessary to return the probe to TSI and have it repaired.

Since these tests indicated that it would be impossible to use the aspirated hot-film/cold-wire probe for measurements in the dry-bay configuration, the decision was made to abandon further

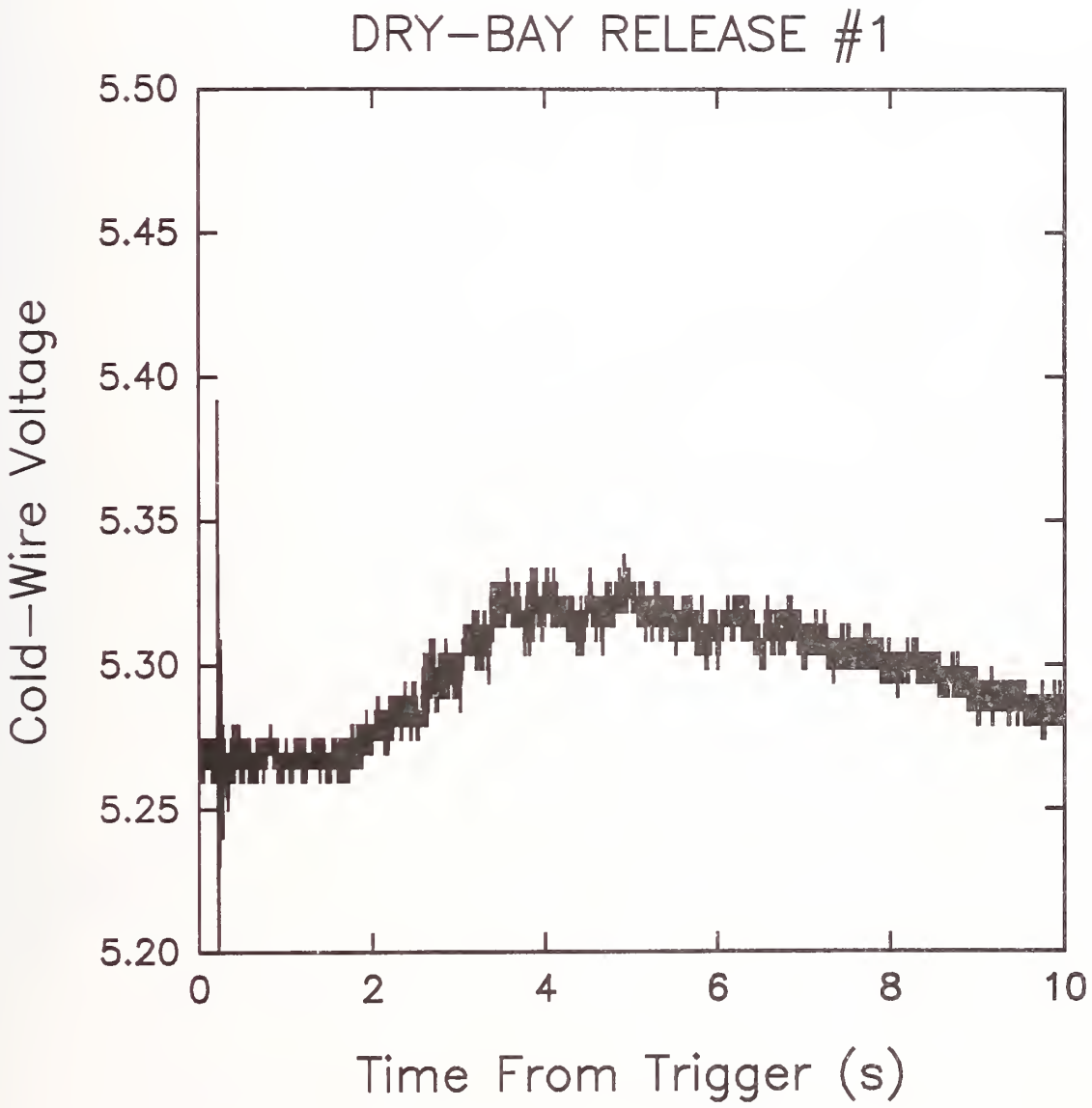

Figure 32. The voltage output of the cold-wire anemometer is plotted as a function of time following release No. 1 of halon 1301 into the dry bay. Data are plotted at 1 ms intervals.

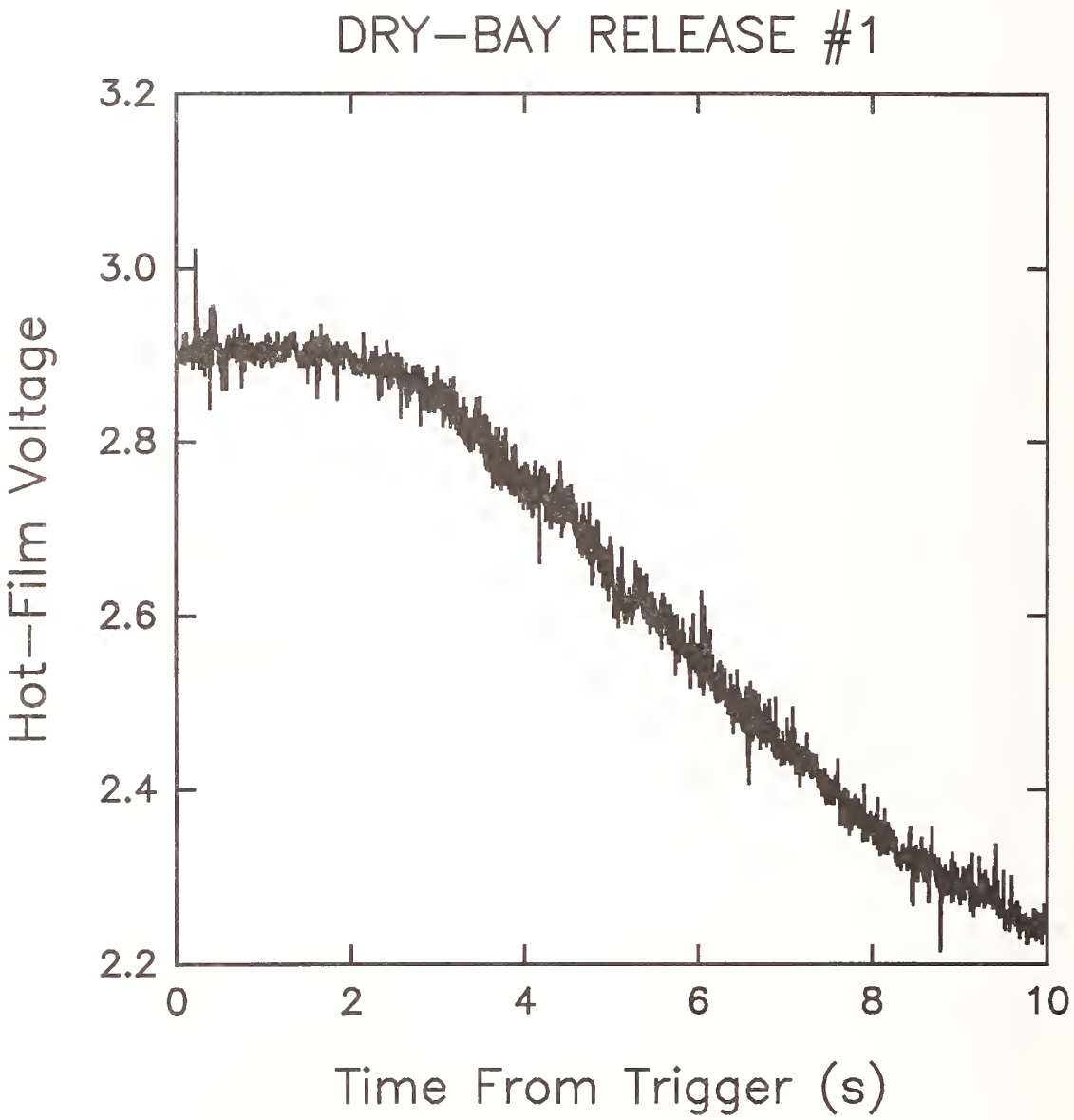

Figure 33. The voltage output of the aspirated hot-film anemometer is plotted as a function of time following release No. 1 of halon 1301 into the dry bay. Data are plotted at 1 ms intervals.

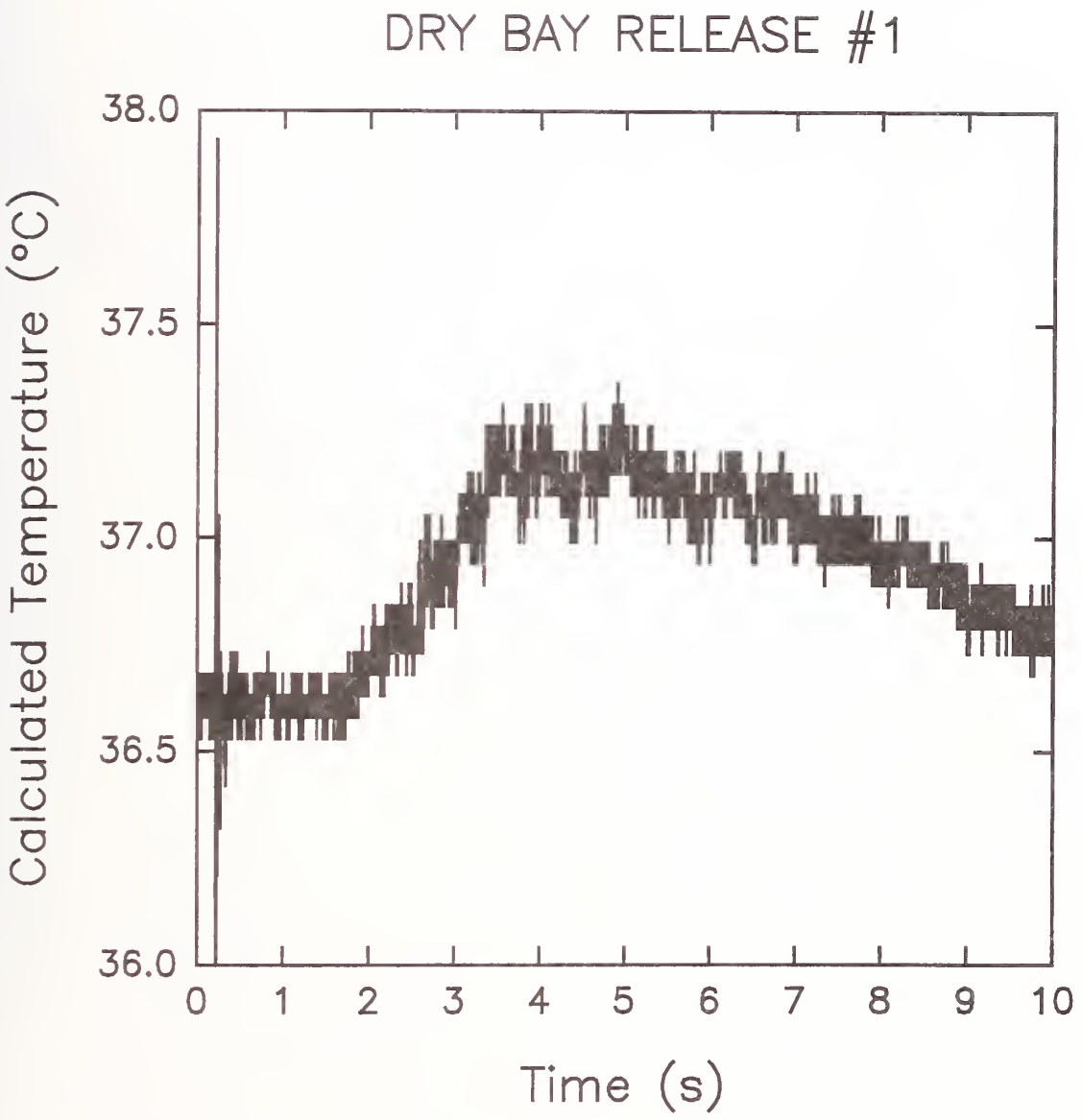

Figure 34. Calculated temperature is shown as a function of time following release of the agent into the dry bay at 0.21 s. The probe was located in the lower left-hand corner of the facility. Data are shown for 1 ms intervals.

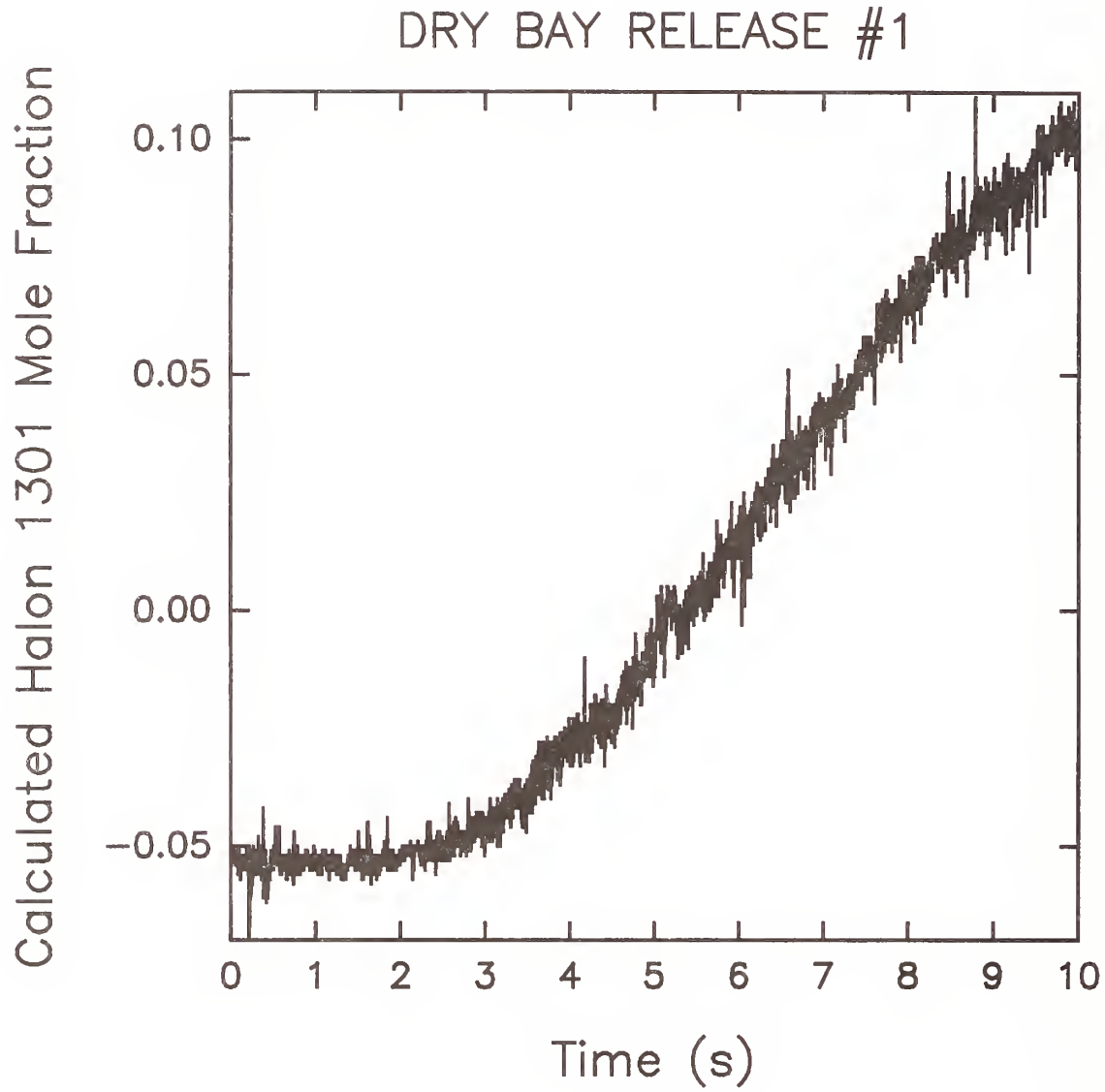

Figure 35. Calculated halon 1301 mole fraction is shown as a function of time following release of the agent into the dry bay at 0.21 s. The probe was located in the lower left-hand corner of the facility. Data are shown for 1 ms intervals.

development of these probes and focus our efforts on completing development of the DIRRACS discussed in Section 11.3.

11.2.6.4 Measurement of Halon 1301 Concentration Following Release Into a Turbulent Spray-Flame Burner. The turbulent spray-flame burner is a facility which has been utilized to investigate the extinction of bluff-body-stabilized turbulent flames by halon 1301 and various replacement agents (Hamins *et al.*, 1994). The system is discussed in detail elsewhere in this report (see Section 9), and only a brief description is provided here. Figure 36 is a schematic diagram of the turbulent spray-flame burner facility. It consists of a 0.5 m long, 73 mm diameter stainless-steel tube containing an air flow for which the velocity and temperature can be varied. A 6 mm diameter fuel tube capped by a liquid pressure-jet spray nozzle is centered in the air pipe with the nozzle outlet located at the open end of the outer pipe. A 35 mm diameter steel disk located just downstream of the nozzle serves to stabilize the flame. The gaseous agents to be added to the air flow were injected impulsively 0.5 m upstream of the nozzle through two 6 mm diameter tubes. Screens were placed downstream of the injection port to aid mixing. By recording the dynamic pressure drop inside the vessel used to hold the agents, it was possible to estimate the average mass-flow rate of the agent into the air flow as a function of time.

Even though this burner and an earlier version (Hamins *et al.*, 1994) had been used extensively for testing fire-fighting agents, the time behavior and spatial distribution of agent in the air flow had not been experimentally characterized. As a test of the aspirated hot film for concentration measurements and to characterize the temporal and spatial concentration of the agent near the pipe exit, a series of measurements of halon 1301 mole fraction were carried out. These measurements were made at room temperature in the absence of a fuel flow or combustion. The air flow velocity was varied over a range of 2.5 m/s - 10.0 m/s. Due to the presence of the stabilization disk and the relatively large diameter of the air-flow tube, the flow at the stabilization point is expected to be turbulent. Measurements downstream of the stabilization disk were found to be very noisy due to high turbulence and recirculating flow. For this reason measurements were made 25 cm upstream of the disk.

Since the temperature was not expected to change during these experiments, a single aspirating probe without the cold wire was used. The probe was designated as a TSI, Inc. Model 1440R-20 (Serial #941102). Halon 1301 was the agent added to the air flow. Measurements were made at various locations in the air flow by moving the probe horizontally across the pipe. Table 10 summarizes the radial locations where data were recorded. The output of the aspirated hot film was digitized and stored using Workbench PC and the Flash-12 analog-to-digital converter described in Section 11.2.4.5. Data were recorded at 1 kHz.

The response of the aspirated hot film was calibrated by measuring the anemometer output voltage as a function of halon 1301 mole fraction. The calibration temperature was chosen to closely match that in the laboratory where the turbulent flame burner was located. Figure 37 shows the calibration results plotted as mole fraction versus the constant-temperature anemometer voltage. The data were fit to a third-order polynomial for which the result is included and compared with the data in Figure 37. The calibration curve reproduces the experimental data quite well. During the actual measurements in the turbulent spray-flame burner, small variations in the voltage recorded when only air was present were noted. During data analysis these were corrected by adding or subtracting a small voltage such that the average halon 1301 mole fraction in the presence of air was 0.00. Over 30 measurements were made for various conditions in the burner. Only a few are summarized here in order to provide an indication of the quality of the measurements using the aspirated hot-film probe.

Figure 38 shows an example of the time behavior of halon 1301 concentration following release into the air coflow of the burner. It can be seen that the noise level for the concentration measurement is quite good. No halon 1301 is detected until 0.8 s after the start of the release. This corresponds to

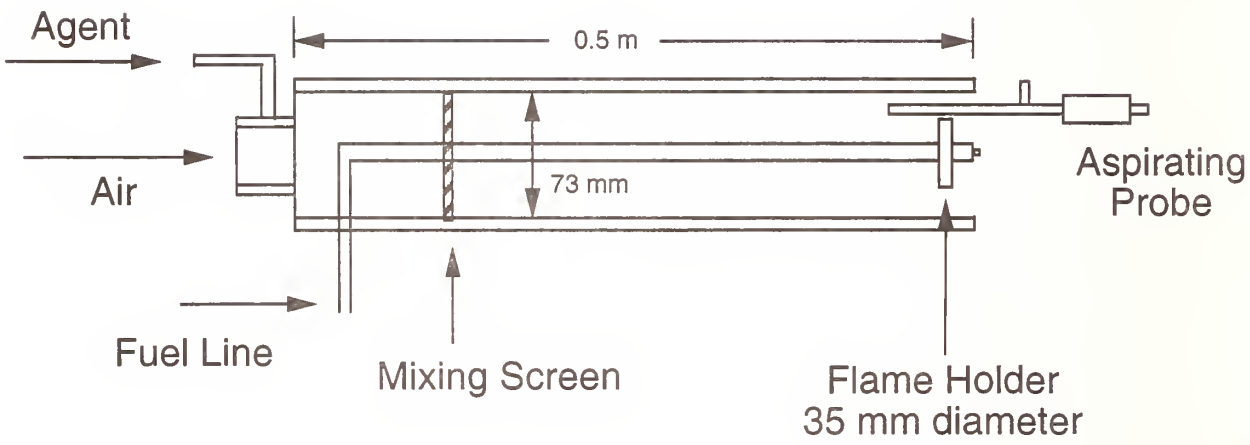

Figure 36. Schematic diagram of the turbulent spray-flame burner. The aspirated hot-film probe was used to monitor halon 1301 concentration at various positions in the air coflow.

Table 10. Positions of the Aspirated Hot-Film Probe for Agent Concentration Measurements in the Turbulent Spray-Flame Burner. Positions Relative to the Left-Hand Edge of the Coflow Air Tube

Position #	Radial Location (mm)
1	0.5
2	4.6
3	15.9
4	17.3
5	53.3
6	61.1
7	67.4
8	70.1

the period required for the agent to flow from the release point to the probe. The data show that a finite period of roughly 50 ms is required for the concentration of the agent to increase to a relatively constant level, where it remains for a period close to the nominal time during which the valve is open. When the valve is closed, there is a tailing of the agent mole fraction which suggests that the closing time for the solenoid valve used to release the agent is somewhat longer than the period required to open. The measured mole fraction is in good agreement with the mole fraction calculated assuming that the agent is released as a square-wave pulse.

The measured concentrations for a series of tests in which the nominal concentration of the release was varied by changing the pressure in the agent containment vessel are shown in Figure 39. All of these experiments had release times on the order of 230 ms. It can be seen that the measured concentrations increase with the nominal concentrations. A detailed comparison of the measured and nominal concentrations is provided below.

Figure 40 shows the time behaviors recorded for releases of halon 1301 in which the release times were varied. It is clear that for the shortest time release the concentration does not reach a clear plateau, but instead appears as a spike. For intermediate release times the halon 1301 mole fractions do attain relatively constant values. However, as the release times are lengthened further, the concentration shows a distinct drop with time. The concentration fall off is the result of the pressure drop which occurs in the halon 1301 holding tank during a release. As the pressure falls off the release rate decreases and the concentration falls. In order to hold the concentration at a given level for a longer period it would be necessary to increase the size of the holding tank.

Average concentrations for the releases were calculated by averaging the measured concentrations over periods of time after a nearly constant concentration was achieved. A series of these measurements were made across the turbulent burner at the positions which were accessible on either side of the stabilization disk. Figure 41 shows the results. Even though there appears to be slight asymmetry in the distribution with higher concentrations on the right, it does appear that the agent is distributed relatively uniformly across the entire flow.

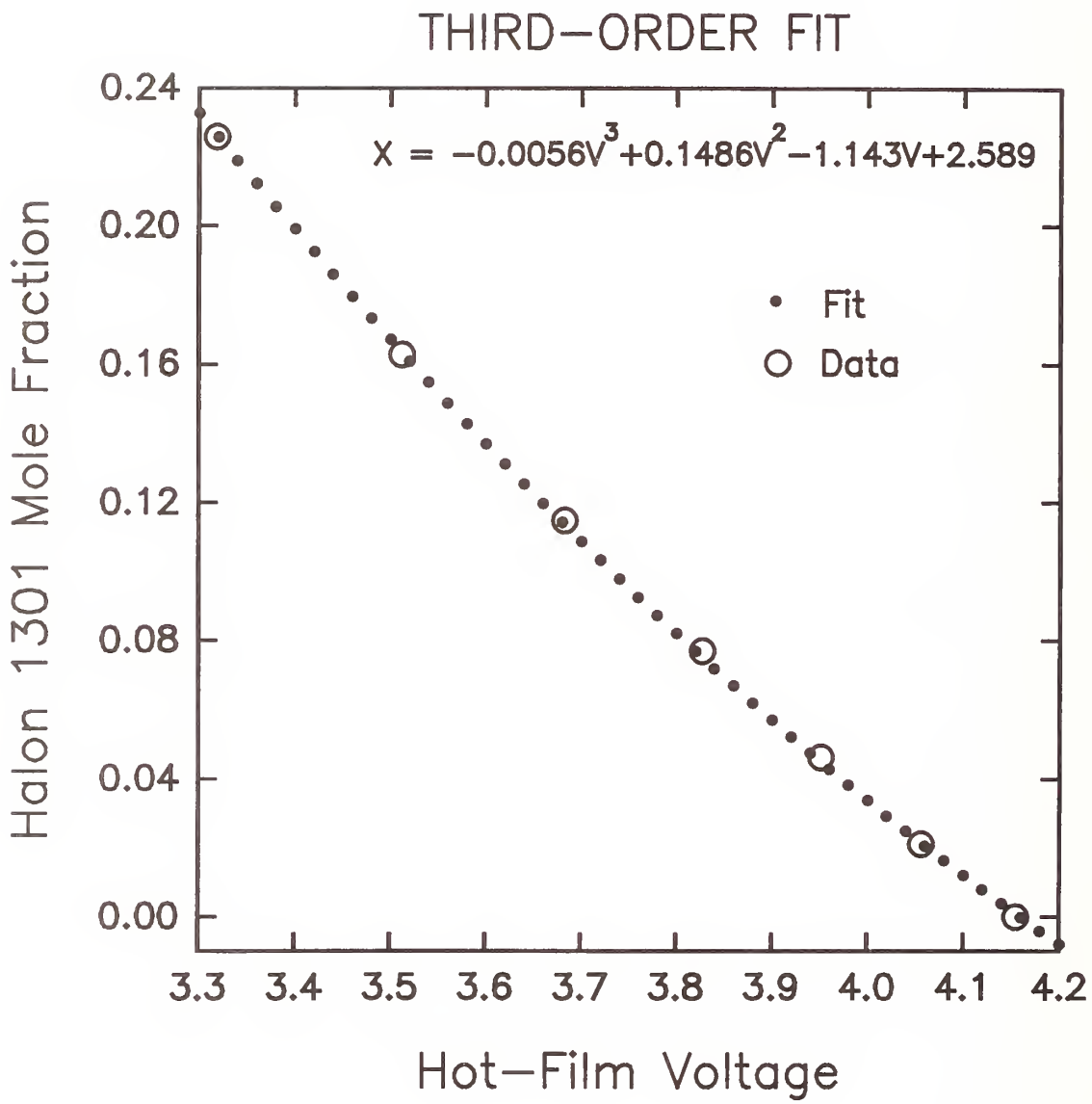

Figure 37. Halon 1301 mole fraction is plotted as a function of the output voltage of the constant-temperature anemometer . These values are compared with a least squares fit of a third-order polynomial to the data.

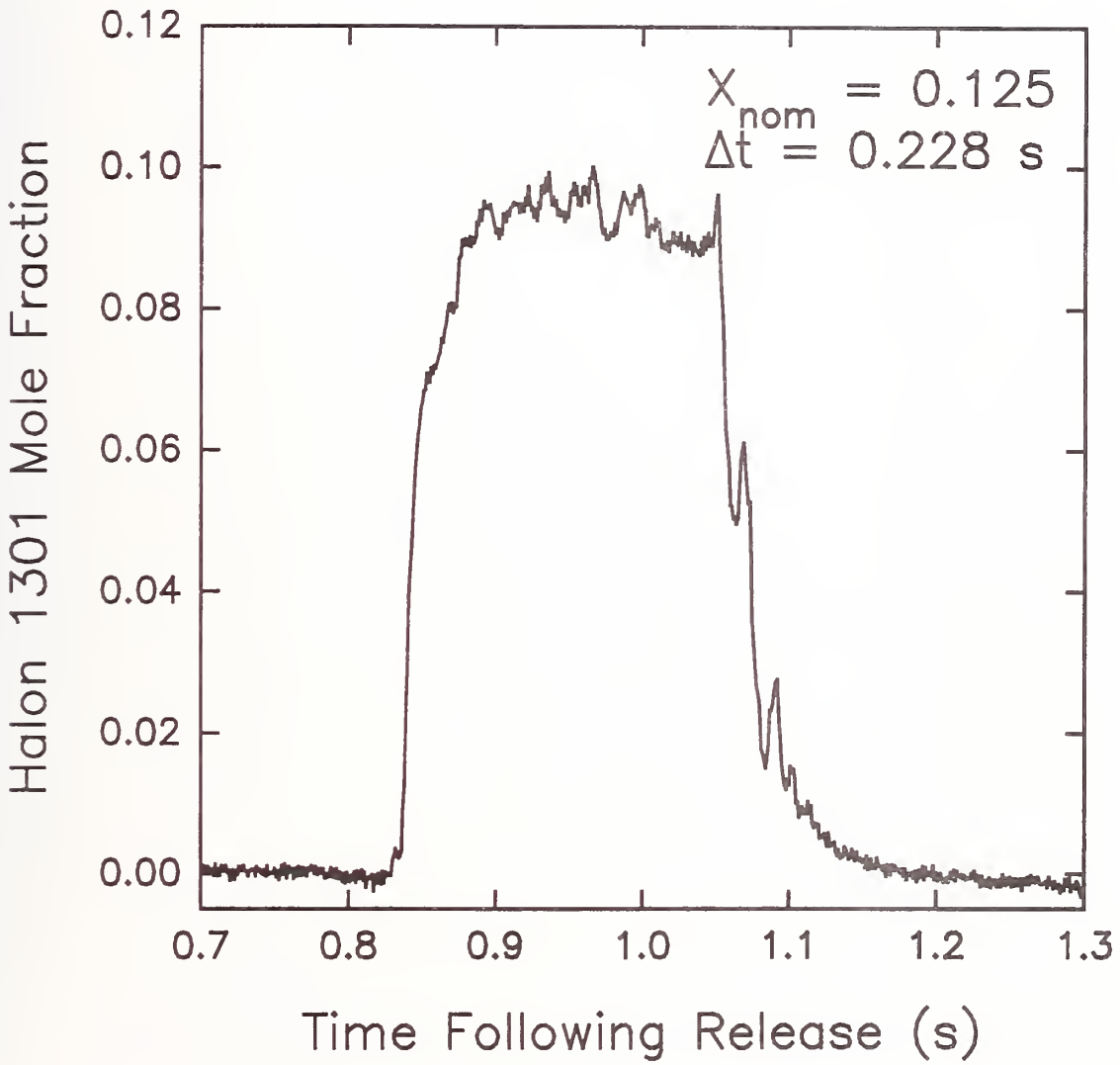

Figure 38. Halon 1301 concentration as a function of time following release of the agent into the air coflow of the turbulent spray-flame burner. The nominal mole fraction and period of the release were 0.125 and 0.228 s, respectively.

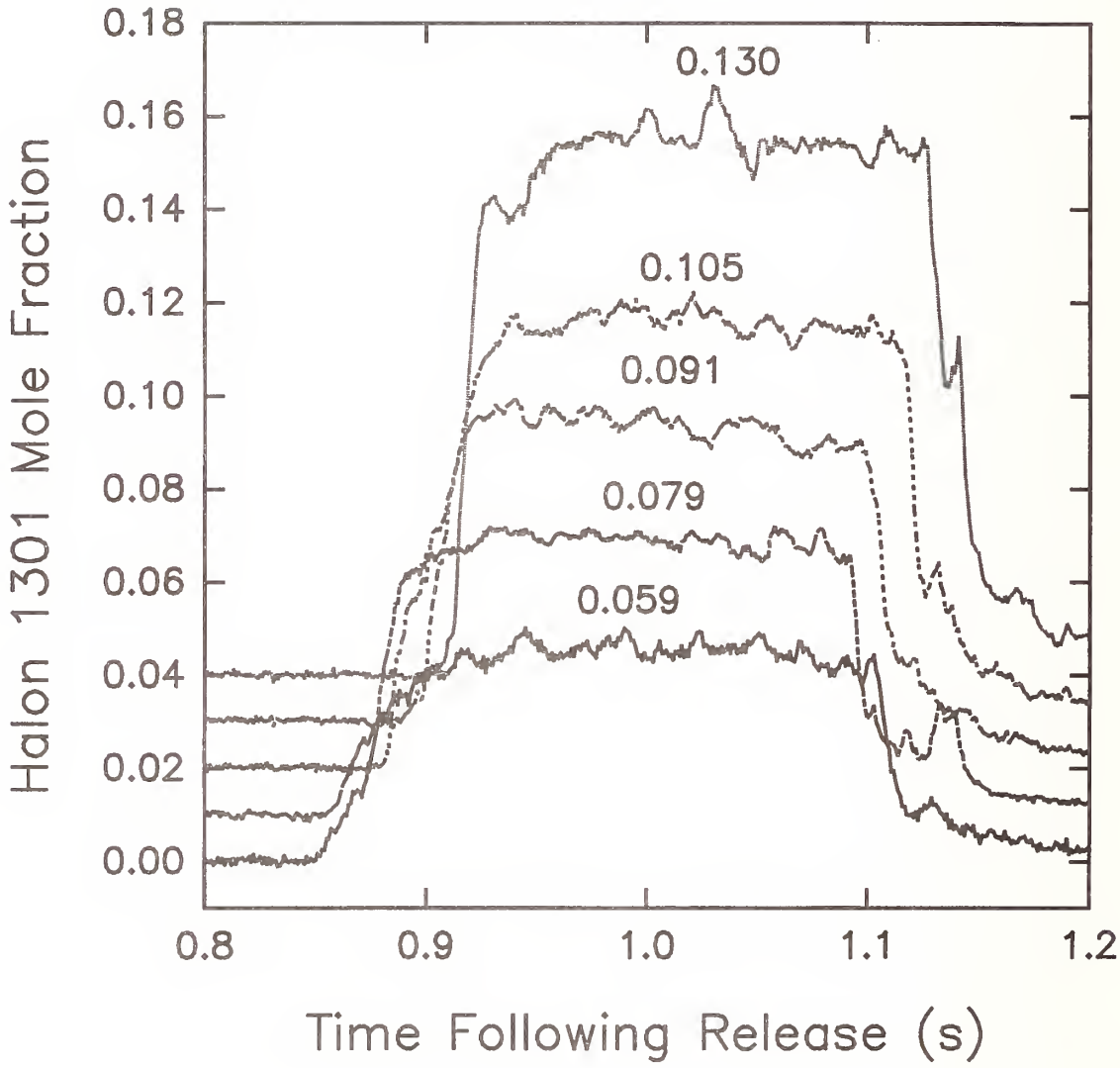

Figure 39. Halon 1301 mole fraction as function of time following release of varying mole fractions (indicated by numbers on the plot) into the air coflow of the turbulent spray-flame burner. Nominal release periods of 0.230 s. Plots offset by 0.01.

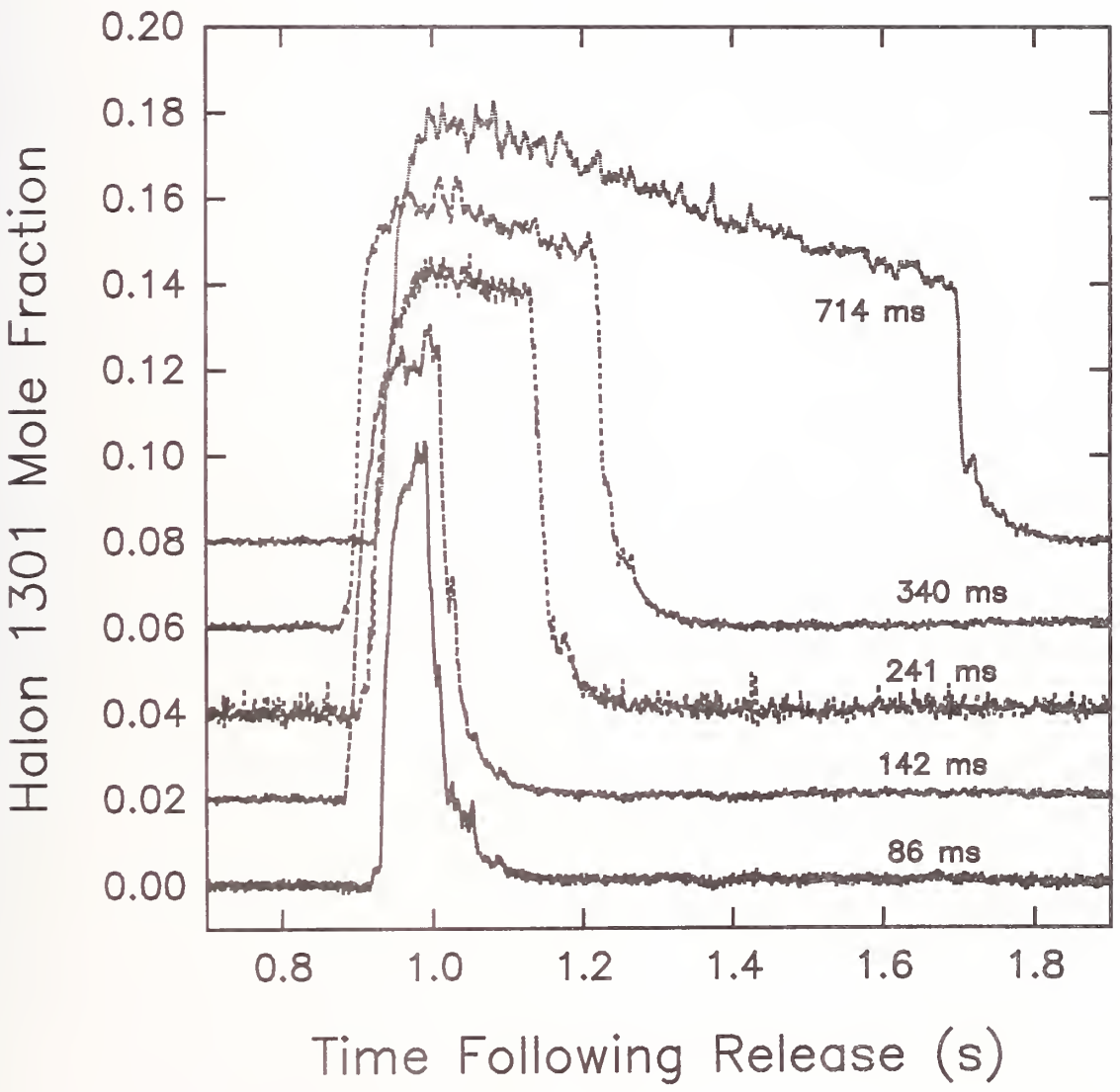

Figure 40. Halon 1301 mole fraction as function of time following release with varying release periods (indicated on the plot) into the air coflow of the turbulent spray-flame burner. Nominal mole fractions were 0.10. Plots offset by 0.02.

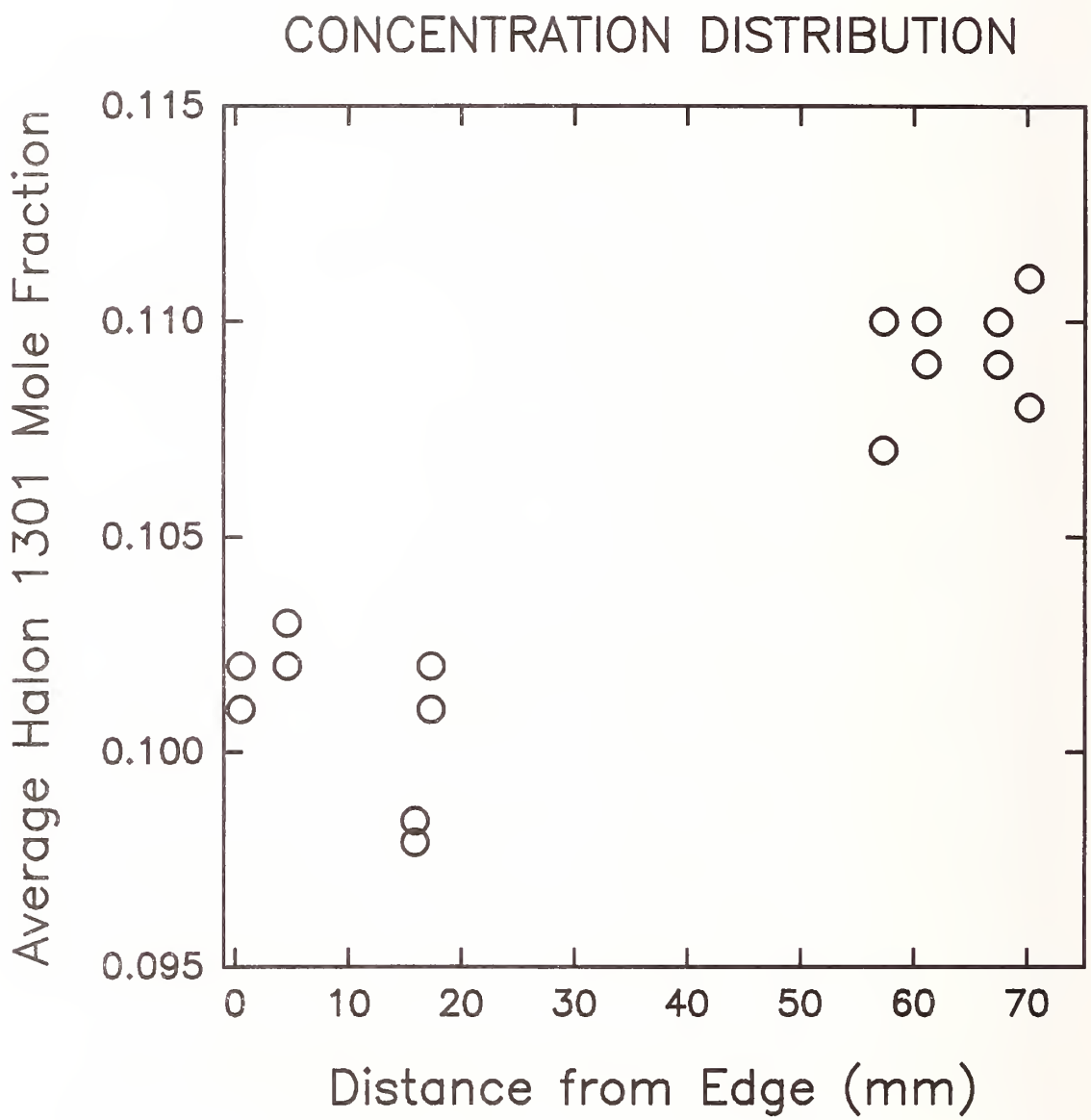

Figure 41. Average halon 1301 concentration is plotted as a function of location across the turbulent spray-flame burner as measured from left to right. Nominal halon 1301 mole fractions based on pressure measurement were 0.104.

Comparison of the measured concentrations with nominal concentrations based on pressure drops in the agent vessel provides an opportunity to assess the accuracy of the measurement technique. Figure 42 shows a comparison of the measured average mole fractions of halon 1301 with those estimated using the pressure drop within the containment vessel. Even though the general agreement is good, some scatter is obvious. In particular, some of the measured mole fractions seem to be systematically offset to lower values from the estimated values. These measurements were the first recorded during the experiment, but we have been unable to provide an explanation as to why they should be different than later results. On the basis of this plot, we conclude that the aspirated hot film does respond well to changes in halon 1301 concentration and that measured values are accurate to within 20 %. More definite statements concerning accuracy will require more careful experiments.

This brief series of experiments has demonstrated that the aspirated hot film is capable of recording accurate agent concentrations with high temporal resolution. At the same time, it has provided a useful characterization of the efficiency of mixing of an agent into the air flow of the turbulent spray-flame burner.

11.2.7 Summary and Recommendations. During the work described in this section it was demonstrated that a combined aspirated hot-film/cold-wire probe can be utilized to record simultaneous temperature and agent concentration measurements with high temporal ($\approx$ 1 ms) and spatial resolution $\approx$ (1 mm^3). A unique facility was developed which allowed the probe to be calibrated over a wide range of temperature (-65 °C to 40 °C) and a full range of concentration for five fire suppressants. At the same time, an unexpected sensitivity of the aspirated hot film to velocity fluctuations was identified and characterized. This sensitivity to velocity limited the accuracy of concentration measurements to such a degree that the current approach does not seem feasible for FC-125, and the accuracy for the other agents was compromised. Measurements of halon 1301 concentration in the turbulent flame burner demonstrated that aspirated hot films are capable of accurate quantitative concentration measurements with good temporal resolution.

When the probe was tested in the dry-bay test facility at Wright-Patterson AFB, it was found that a black residue generated by the facility clogged the probe and prevented accurate measurements. For this reason, further development of the probe was halted, and our further efforts were focused on the development of the DIRRACS system.

There are several modifications which could be made to the aspirated hot-film/cold-wire probe which would be likely to improve its performance. It is possible that the velocity sensitivity observed during the current effort was due to the design of the system which placed the hot-film probe within a narrow tube at a significant distance from the tube entrance and the downstream sonic orifice. Alternative probe designs discussed in Section 11.2.1.2 might well have much lower sensitivity to velocity. It is also possible that experimental conditions could be identified which would improve the response of the hot film to changes in concentration of the fire-fighting agents and therefore improve the accuracy of the measurements.

The contamination of the probe in the dry-bay test facility was ultimately the factor which led us to halt further work on the development of this measurement approach. Wilson and Netterville (1981) have described an aspirated hot-film probe containing a filter, but which still provides good time response. The use of a filter might be expected to dampen velocity fluctuation sensitivity. It is also possible that the filter could remove the contaminant present in the dry-bay experiment and allow the concentration measurements to be made in this environment.

The success of any or all of the above changes in the probe design could lead to the development of more effective combined aspirated hot-film/cold-wire probes for the measurement of concentration. Unfortunately, the additional design and experimental studies required were beyond the fiscal and time constraints of the current effort. While we feel that there is a reasonable probability that such

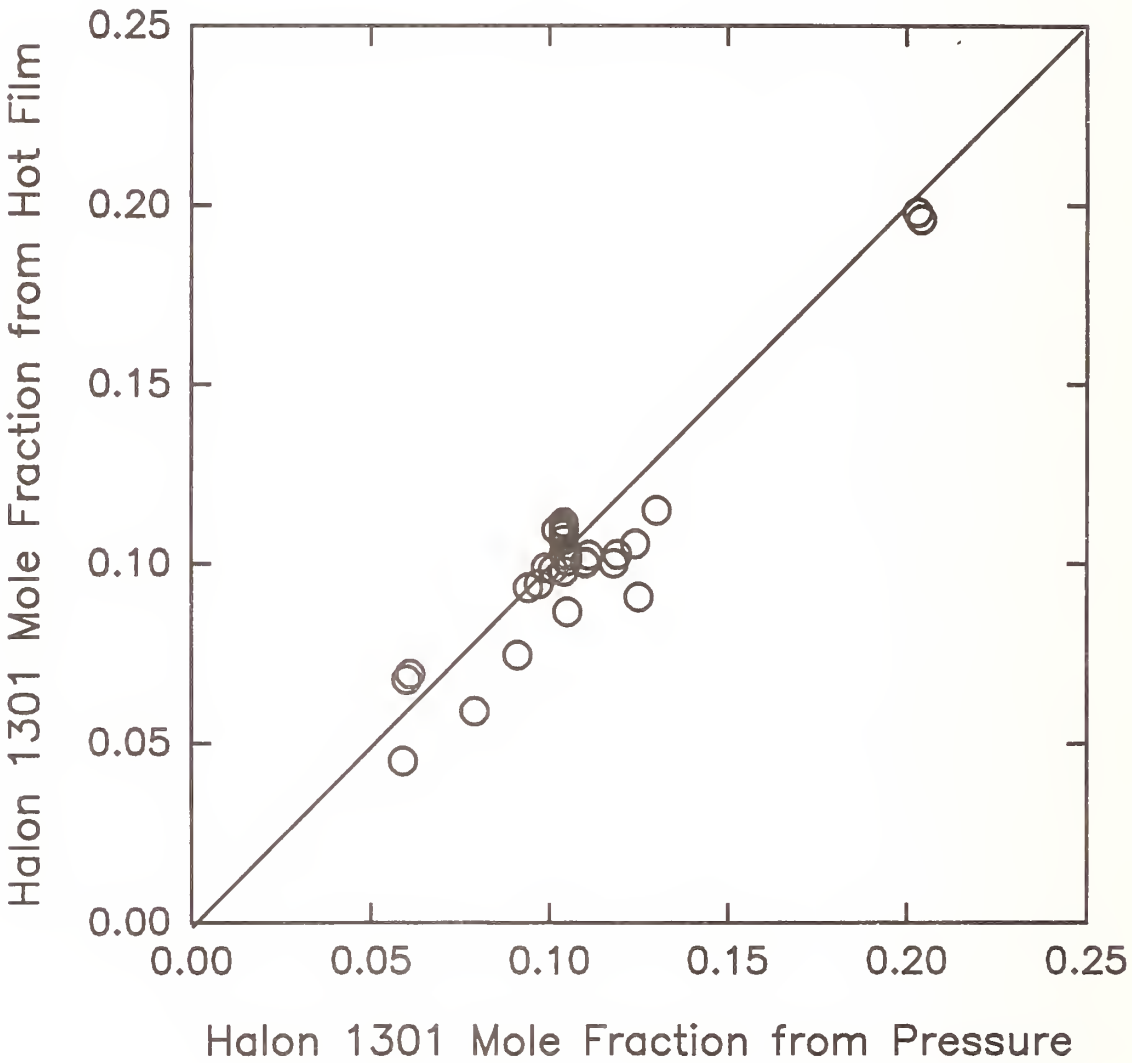

Figure 42. Average measured halon 1301 mole fraction is plotted as a function of nominal halon 1301 mole fraction estimated using the measured pressure drop. The solid line represents perfect agreement.

modifications would lead to the desired measurement capability, it would be impossible to guarantee success. Any future decision to continue further development of this type of probe must keep this in mind.

11.3 Evaluation of Infrared Sensing For Rapid Measurement of Halon Replacement Chemicals

11.3.1 Background. As discussed in Section 11.1, there is a need for monitoring the concentration of potential halon replacement chemicals with millisecond response time. One scenario of great concern to the sponsors is the penetration of an enemy shell into the fuel tank of an aircraft. To prevent structural damage to the aircraft wing or fuselage to the point where the plane would crash, the sponsors and NIST consider it crucial that the fire extinguishing agent be distributed throughout the interior region surrounding the fuel tank, the so-called dry-bay, in less than 30 ms. The existing instrumentation for monitoring the concentration of halon 1301, including the Statham analyzer and the Halonyzer (Yanikoski, 1952), have response times on the order of 200 ms or longer. Clearly they are not capable of monitoring the spread of the agent in a dry-bay type environment. So there is the need for a much faster time response instrument for monitoring potential halon replacement chemicals. The design goal is an instrument with a response time of 1 ms that could be used with a variety of fire suppression agents over a concentration range from 1 % - 20 % with an accuracy of ± 10 % of the nominal value. The Fire Extinguishing Agent Sensor (FEAS) was developed by John Brown Associates (Brown and DeStefano, 1992) to provide a fast time response instrument capable of detecting the presence of an agent. The original intention of the current study was to test the FEAS and determine its suitability for field measurement of agent concentration. The scope of the project was broadened with the sponsors' agreement to include redesign and testing of a modified instrument. The report includes calibration results of the improved device and field testing of the unit at Wright-Patterson AFB.

11.3.2 Description of FEAS. The FEAS sensing head illustrated in Figure 43 contains an incandescent wire as the infrared (IR) source behind a germanium window, a sensing gap of about 3 cm, a narrow bandpass IR filter, a pyroelectric detector, and an operational amplifier to couple the detector signal to a data collection console. Six detector heads can be run from a single power supply unit which provides ± 15 V dc for the detector and amplifier and a separate AC power supply for the incandescent wires. The narrow-pass IR filter has a peak transmission of 73 % at a wavelength of 8.2 μm; the transmission drops to 50 % of the peak value at wavelengths of 8.116 μm and 8.231 μm. This wavelength range corresponds to strong absorption bands of fire-extinguishing agents containing carbon-fluorine bonds.

The basic idea of an IR absorption measurement is that the flux of IR radiation is reduced as the agent concentration is increased. Standard IR detectors yield a signal directly related to the IR flux. So a high flux would give a high signal and a lower flux resulting from increased IR absorption from the agent would produce a lower signal. A key concept behind the FEAS is the use of a pyroelectric detector. Such a detector produces no signal for a steady source intensity independent of whether the IR flux is strong or weak. Instead the detector responds to changes in the IR radiation reaching the detector. Potential advantages of this type of detector are immunity to ambient light levels or slow drifts, and a chopper with associated electronics is not required. Below we present a more detailed description of the phenomenology of the pyroelectric detector and the mathematical relationship between the detector output and the IR intensity. The reader interested in the calibration results only may skip to Section 11.3.2.5.

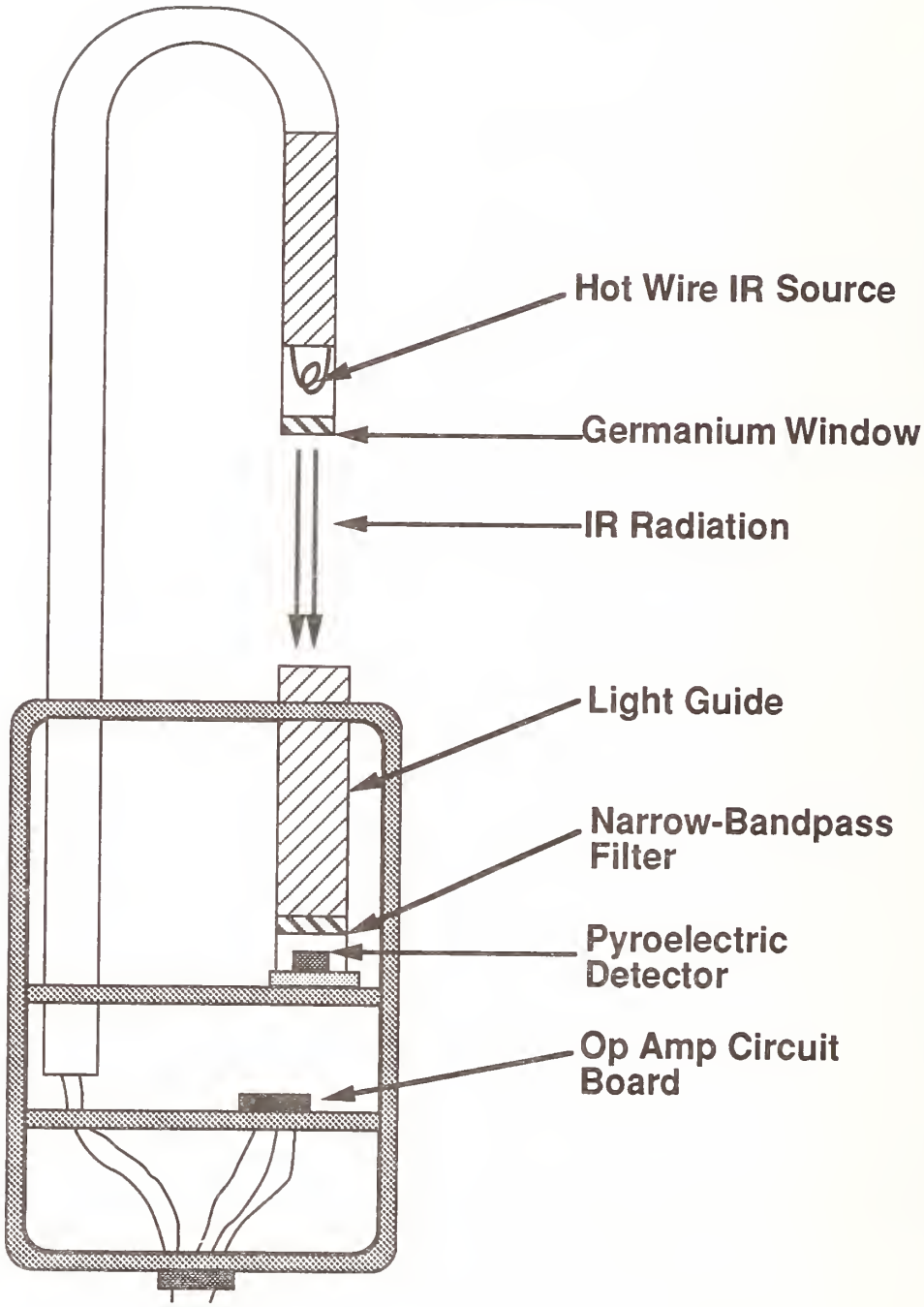

Figure 43. Schematic of the sensing head of the Fire Extinguishing Agent Sensor (FEAS).

11.3.2.1 Phenomenology of a Pyroelectric Sensor. A pyroelectric material is an electric analog to a magnetic material. A magnetic material such as iron or nickel has a large magnetization, which is a measure of the net magnetic moment per unit volume. The "atomic magnets" (originating from the unpaired electrons of the iron or nickel atoms) are aligned in one direction leading to a strong magnetic field. As the temperature of the magnetic material increases, the field from the magnet and its magnetization decrease due to thermal motion breaking up the alignment of the magnetic domains until it reaches zero at the Currie temperature. Above the Currie temperature, the magnetization is zero. For a pyroelectric material, the center of positive and negative charges in each unit cell of the crystal is slightly displaced leading to a dipole moment. In analogy to the magnetic case, the polarization, which is the electric dipole field per unit volume, is temperature dependent. As the temperature changes, there are slight changes in the positions of the atoms in the crystal lattice resulting in a change in the polarization (Putley, 1970; Lang, 1974). However, an external electric field is not normally observed, because stray charges are attracted and trapped on the surface until the surface charge associated with the polarization is neutralized. The charge distribution produced in this way near the surface of an insulator is relatively stable, unable to respond quickly to sudden changes of the internal dipole moment. When there is a sudden change in temperature of the material resulting from a change in the intensity of radiant energy absorbed by the material, there will be a variation in the polarization, and this will result in an observable electric field at the detector surface. So even though the polarization is not directly observed, its temperature coefficient, $p = dP/dT$, is observable. The material used in the FEAS pyroelectric sensor, $LiTaO_3$, has a pyroelectric coefficient at 25 °C of 6×10^{-9} C cm^{-2} K^{-1}, where C refers to Coulombs. For a 5 mm diameter detector, a 1 μ°C temperature generates a charge of 1.2×10^{-15} C, which can be measured with state-of-the-art electrometers.

Figure 44 provides a schematic representation of how a pyroelectric detector functions. The IR radiation impinges on the surface of the pyroelectric where it is absorbed by the thin (typically on the order of 20 μm) detector. The heating of the detector changes the polarization of the material leading to an excess of positive charge on one surface and negative charge on the other. To neutralize the charge, current flows through an RC circuit, where the resistance and capacitance represent the combined values for both the device itself and a preamplifier. The values of R and C determine the electronic time constant, $\tau_e = RC$, which is generally much smaller than the thermal time constant for the device. If the radiant flux remains constant, the temperature reaches a steady-state value and the current decreases toward zero. This is why the pyroelectric device will not respond to a steady source. It is only useful for a changing source intensity. To show how the instrument output can be related to the radiant flux incident on the device, the appropriate heat-transport modelling is discussed in the next section.

11.3.2.2 Heat Transfer for a Pyroelectric Sensor. The pyroelectric device is a thin plate of material on the order of 20 μm thick with a heat capacity H. As the radiant flux is absorbed by the pyroelectric device, the temperature increase is determined by the heat capacity of the plate together with the thermal conductance G. The thermal conductance includes both conductive losses through leads to a heat sink and radiative losses. From a heat balance (Putley, 1970) the following equation is obtained for a time-dependent radiant source $\phi(t)$:

$$\phi(t) = H\frac{d\Delta T}{dt} + G\Delta T \quad , \tag{25}$$

where ΔT is the plate temperature minus the temperature of the heat sink. One can see from Equation (25) that if the rate of temperature change is fast enough, and the magnitude of the change is small,

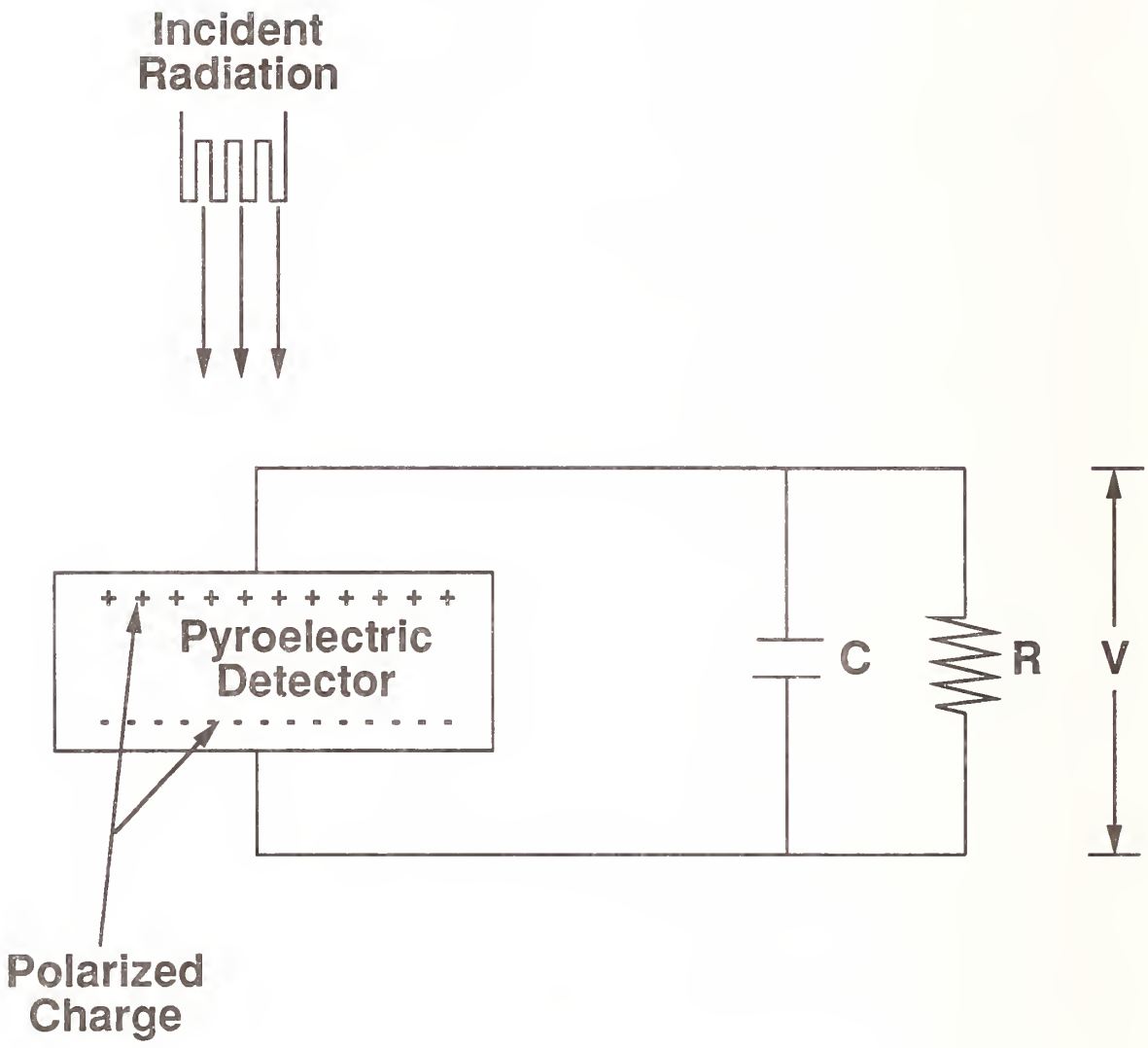

Figure 44. Illustration of the operating principle for a pyroelectric sensor. The changing incident radiation heats the sensor leading to a polarization of the charge on the device. The output signal is taken from the voltage drop across a resistor.

the heat-conductance term can be ignored relative to the heat-capacity term. Under these conditions the rate of change of the temperature is directly proportional to the source intensity, $\phi(t)$. Furthermore, the rate of change of the temperature difference is directly related to the pyroelectric current i, dq/dt, via the following equation involving the pyroelectric temperature coefficient:

$$i = pAd\Delta T/dt \quad . \tag{26}$$

A is the surface area of the sensor. In this limit of negligible heat conductance, the pyroelectric current provides a direct measure of the time-dependent source intensity. A limitation of the pyroelectric device is also evident from Equations (25) and (26). For a steady source intensity ϕ, ΔT is constant and the current vanishes. So, as pointed out above, the pyroelectric device by itself is not useful for monitoring the radiant output of a constant source.

Below the heat transfer equation is solved for two assumed source-intensity time behaviors. The first is for a Gaussian pulse in order to assess the range of conditions for which the second term on the right-hand side of Equation (25) can be ignored. The second is a harmonic time-dependent source, which is important in the design of the new IR absorption-type instrument to be described subsequently.

11.3.2.3 Response to a Gaussian Thermal Pulse. To make the previous discussion quantitative, we consider the specific case of a Gaussian source intensity $\phi(t)$ with half width τ_s and peak intensity ϕ_0,

$$\phi(t) = \phi_0 \exp[-(t/\tau_s)^2] \quad . \tag{27}$$

Solving the linear differential equation given by Equation (25) for the source intensity given by Equation (27), we obtain:

$$\Delta T(t) = \frac{\phi_0}{H} \tau_s \exp[1/4(\tau_s G/H)^2 - Gt/H] \int_{-\infty}^{\beta} \exp(-w^2) dw \quad , \tag{28}$$

where the integration limit β is given by:

$$\beta = \frac{t}{\tau_s} - \frac{\tau_s G}{2H} \quad . \tag{29}$$

Computing the differential $d\Delta T/dt$ we obtain:

$$\frac{d\Delta T}{dt} = \frac{\phi_0}{H} \exp[-(t/\tau_s)^2] - \frac{\phi_0 \tau_s}{H\tau_T} \exp[1/4(\tau_s/\tau_T)^2 - t/\tau_T] \int_{-\infty}^{\beta} \exp(-w^2) dw] \quad . \tag{30}$$

where the thermal time constant τ_T is equal to H/G.

It can be seen from Equation (30) that for a pulse width much smaller than the thermal relaxation time, the first term in the equation will be larger than the second for small values of reduced time. This is true since the exponential terms and the Gaussian integral will be of order unity for these conditions. This result confirms the intuitive explanation given above for why the rate of temperature change is proportional to the radiant source for a fast enough rate of temperature change. A

quantitative comparison of the rate of change of the temperature and the source function for a wide range of conditions is shown in Figure 45. The results are presented for a thermal time constant of 500 ms and for τ_s values of 10 ms, 30 ms, 100 ms, and 250 ms. The plots are expressed in terms of a reduced rate of temperature change, $(d\Delta T/dt)_r$, and reduced time, t_r, defined as:

$$(d\Delta T/dt)_r = \frac{H}{\Phi_0}\frac{d\Delta T}{dt} \tag{31}$$

and

$$t_r = t/\tau_s \quad . \tag{32}$$

This choice of variables allows direct comparison of time dependencies of the source intensity and the rate of change of temperature. The agreement is good for pulse half widths of 30 ms or less, and the difference becomes greater for the longer times. At 100 ms, the difference in the peak heights is 17 %. So the proportionality between source intensity and rate-of-temperature change is quantitative only in the limit of small pulse widths.

The analysis presented above is really only half the story. The other half concerns the electronics used to characterize the response of the detector. An important question is: How fast can the electronics respond to a temperature change? A measure of the electronic time response of the sensor is the effective *RC* time constant (see Figure 44). The approximate values of the capacitance and resistance of the pyroelectric device used in the FEAS were 75 pF and 1×10^8 Ω, respectively, leading to a time constant of 7.5 ms. The useful operation range therefore corresponds to times less than 100 ms set by the thermal response and times longer than 20 ms set by the electronic cutoff. This is a rather narrow window of operation.

11.3.2.4 A Periodic Source Intensity. It is of interest to consider the response of the pyroelectric device to a periodic signal for two reasons. First it is convenient to test the FEAS performance by using a chopper. Secondly, a chopper is used in a new IR absorption type instrument developed in this study. The analysis given below is similar to Putley's study (1970).

Equation (25) is solved for the following harmonic source:

$$\Phi(t) = \Phi_0 e^{j\omega t} \quad , \tag{33}$$

where j equals $(-1)^{1/2}$. After solving Equation (25) by standard linear differential equation analysis, we take the time derivative and obtain the following expression for long enough time that transients have died out:

$$\frac{d\Delta T}{dt} = \frac{j\omega\Phi_0 e^{j\omega t + j\theta}}{G(1+\omega^2 H^2/G^2)^{1/2}} \quad , \tag{34}$$

where θ is the phase angle between the harmonic source and the resulting rate of temperature change wave form, which is expressed as

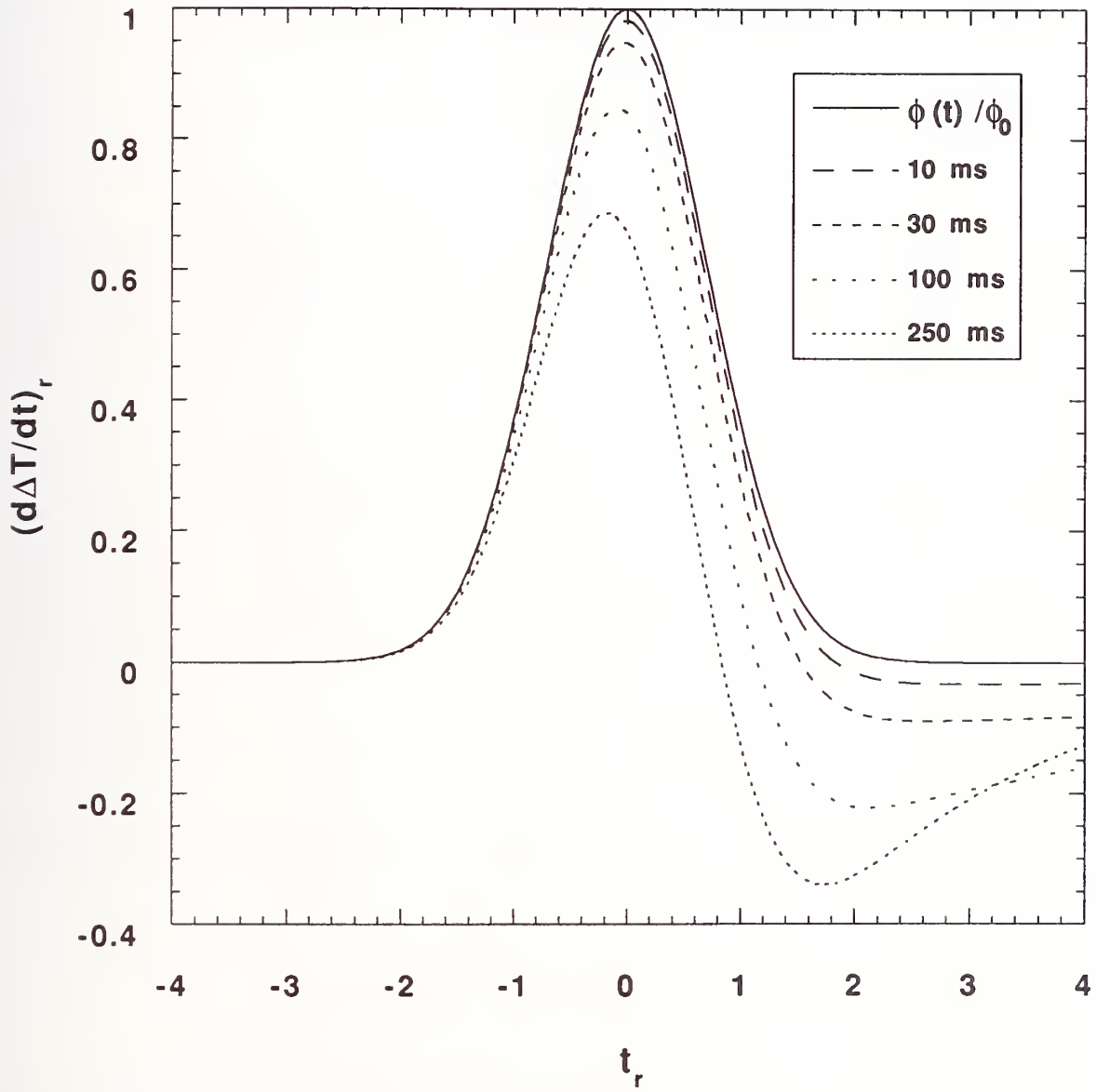

Figure 45. Reduced rate of temperature rise is plotted versus reduced time, t/τ, for a thermal relaxation time of 500 ms for various pulse widths. The solid line is the source function.

$$\tan^{-1}\theta = \omega H/G \quad . \tag{35}$$

This time-varying temperature produces a time-varying current obtained from Equations (24) and (34) as:

$$i = \frac{j\omega pA\phi_0 e^{j\omega t + j\theta}}{G(1+\omega^2 H^2/G^2)^{1/2}} = i_0 e^{j\omega t} \quad , \tag{36}$$

where i_0 is the combination of terms multiplying the exponential time dependent term.

What is ultimately measured is the voltage, which can be deduced from the circuit illustrated in Figure 44 which has a capacitance and resistor in parallel. Using Kirchhoff law, the current from the pyroelectric element is equal to the sum of the currents through the capacitor and resistor:

$$C\frac{dV}{dt} + \frac{V}{R} = i_0 e^{j\omega t} \quad . \tag{37}$$

This differential equation is of the same form as the thermal equation given by Equation (25). Solving by the same method we obtain the following expression for the voltage:

$$V = \frac{i_0 R e^{j\omega t + j\theta_1}}{(1+\omega^2 R^2 C^2)^{1/2}} \quad , \tag{38}$$

where

$$\tan^{-1}\theta_1 = \omega RC \quad . \tag{39}$$

The performance of the pyroelectric device is often expressed in terms of its responsivity, R_v, which is the amplitude of the signal divided by the source intensity flux ϕ_0. From Equations (36) and (38), we obtain:

$$R_v = \frac{\omega pAR}{K(1+\omega^2 H^2/K^2)^{1/2}(1+\omega^2 R^2 C^2)^{1/2}} \quad . \tag{40}$$

In Figure 46, the reduced responsivity, $R_v' = R_v/pAR$, is plotted versus ω for a thermal time constant equal 0.5 s and RC time constant equal 10 ms. We see that for small ω, R_v' increases with ω, becomes flat around 5 Hz due to the 0.5 s thermal relaxation time constant, remains flat to about 50 Hz, above which the 10 ms time constant for the electronic circuit leads to a $1/\omega$ dependence. Of course, the ideal system would have a flat frequency response to more than 1000 Hz. In the next section we present the measured frequency response of the FEAS Instrument.

11.3.2.5 Characterization of FEAS Performance. First a qualitative test was carried out to determine whether the FEAS would respond to an agent release. Using the same facility as was previously used for measuring agent dispersion (Pitts *et al.*, Section 3.5, 1994), 189 g of C_3HF_7 (HFC-227ea) were released towards a pressure transducer and 3 FEASs located near the floor, 1.3 m from the release point. The pressure transducer was directly below the discharge point while the

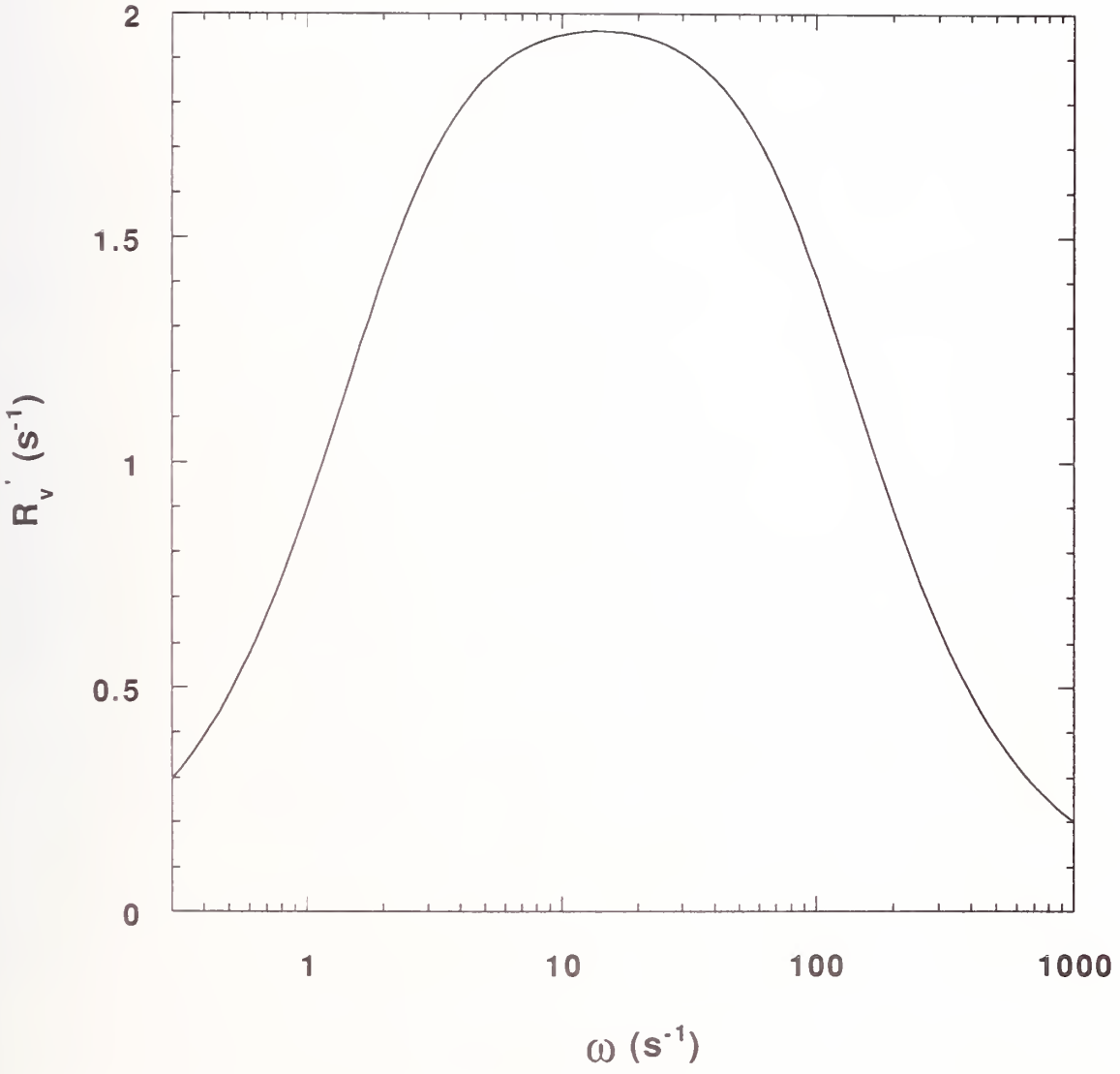

Figure 46. Plot of the frequency response of the reduced responsivity function, R_v', for a thermal time constant = 0.5 s and *RC* time constant = 10 ms.

FEASs were about 60 cm off the centerline. The response of one of the three units is shown in Figure 47. Two spikes are observed in the voltage output shortly following the agent release at 0 s. The first spike reaches 10 V at about 20 ms. This can be compared to a time of about 30 ms for which the pressure transducer output peaks. The time interval between the narrowly spaced saturation readings of the FEAS is approximately 20 ms compared to a 30 ms release time obtained from a pressure transducer reading in the release vessel. Two characteristics of the FEAS signal are the large noise, on the order of 2 V, and the saturation of the output. It is not known whether the peaks around 200 ms are artifacts or not.

The performance of the FEAS was evaluated by measuring the instrument response as a function of frequency. A chopper was positioned between the source and the detector. It was necessary to replace the 10 000 × amplifier in the FEAS with a 100 × amplifier to avoid saturation of the output signal. The output from the amplifier was read with an oscilloscope triggered on the chopper. A typical plot of peak-to-valley voltage versus frequency is shown in Figure 48. There is a peak in the frequency response at about 10 Hz and then a decrease with increasing frequency with a five-fold reduction in signal at 75 Hz. However, based on the analysis in the previous section, a flat frequency response over the frequency range of interest is required to relate the instrument output to the change in radiant flux.

To obtain a flatter frequency response, an 18 MΩ resistor was added in parallel with the 100 MΩ load resistor of the pyroelectric sensor in order to reduce the overall resistance to 15.3 MΩ. Equation (40) predicts that a decrease in the output resistance will flatten the detector's frequency response. The frequency responses with and without the added resistor are plotted in Figure 49. With the added resistor the frequency response is relatively flat out to a frequency of 450 Hz, with about a factor of two decrease in signal over this frequency range. Without the added resistor, there is about a 15-fold reduction in signal as the frequency is increased from 10 Hz to 450 Hz. There is a penalty to pay in using a lower resistance. The output signal is lower. According to Equation (40), the responsivity is proportional to the resistance. So the output signal with the reduced resistance is flatter but it is also smaller, especially at the lower frequencies.

We summarize the FEAS performance and its potential for improvement. The modelling indicates that semi-quantitative results can be obtained for time scales fast compared to the thermal time constant, H/G, and slow compared to the electronic time constant, RC. Operationally it is possible to improve the time response by decreasing the load resistance. Still the response is not perfectly flat. Even a slight deviation can be significant, because, as we show below, the relation between voltage and concentration is non-linear so that even a few percent change in signal could correspond to a change in concentration from 10 % to 20 %. Another problem is the calibration of the device, which would require changing both the concentration and the rate at which the concentration is changed. The great advantage of the device is its simplicity. It could be useful for qualitative applications, but it does not meet the requirements of accuracy and time response needed for a satisfactory instrument for monitoring the agent concentration in a dry bay. Below an alternative design is presented which is more quantitative, responds faster, and is easier to calibrate.

11.3.3 Description of An Improved Differential Infrared Rapid Agent Concentration Sensor (DIRRACS)

11.3.3.1 Design Improvements. The existing FEAS, even with a modified amplifier and added resistor, was shown to be unsatisfactory for making quantitative concentration measurements with a time response of a few milliseconds. The basic idea motivating the new design was to add an optical chopper, which was operated at high enough frequency to obtain the desired time response. This method of collecting data at a fixed frequency has the following major advantages:

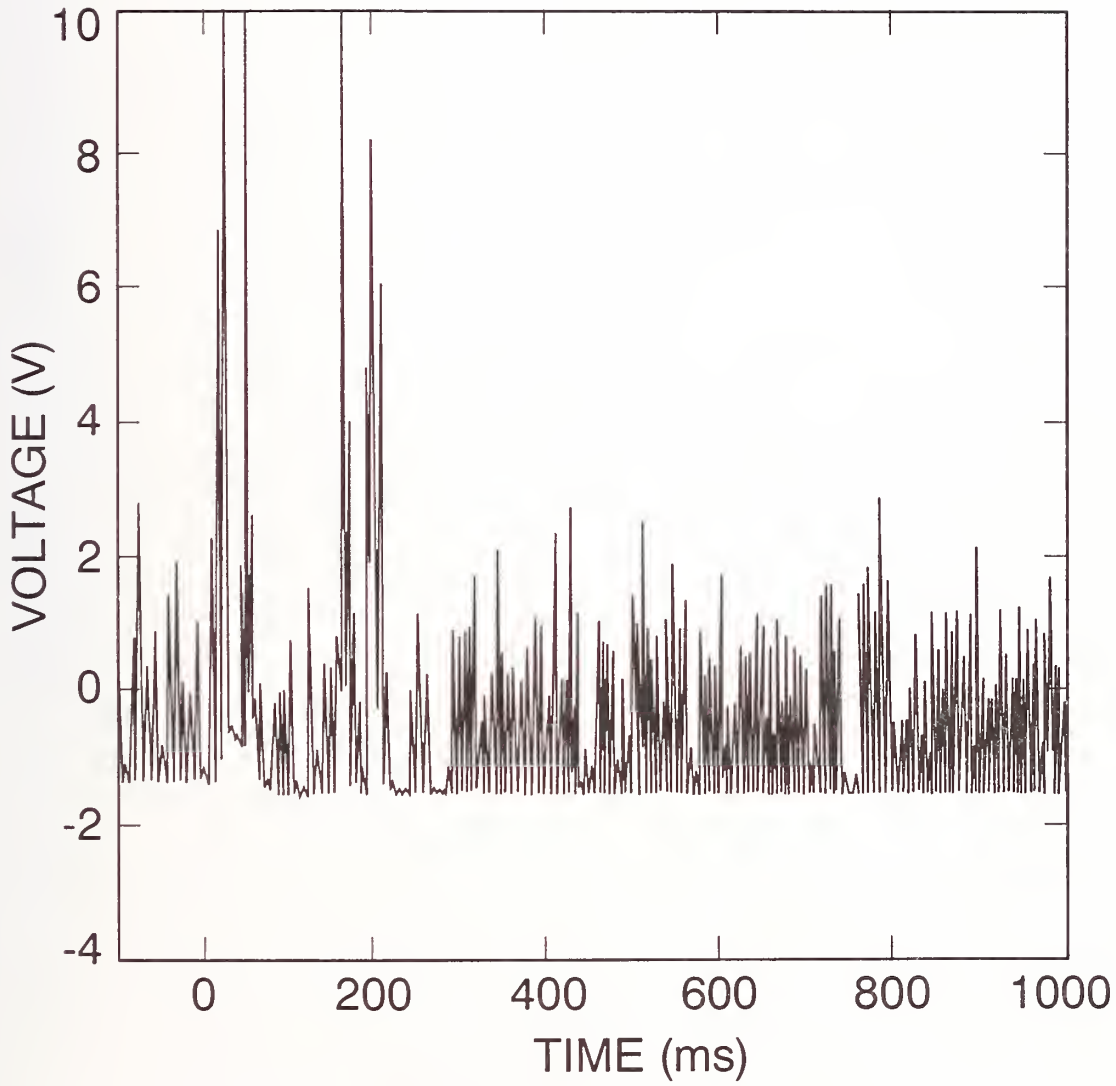

Figure 47. The response of a FEAS to a release of 190 g of HFC-227ea. The FEAS was located 1.3 m below the release point and about 0.6 m off the centerline.

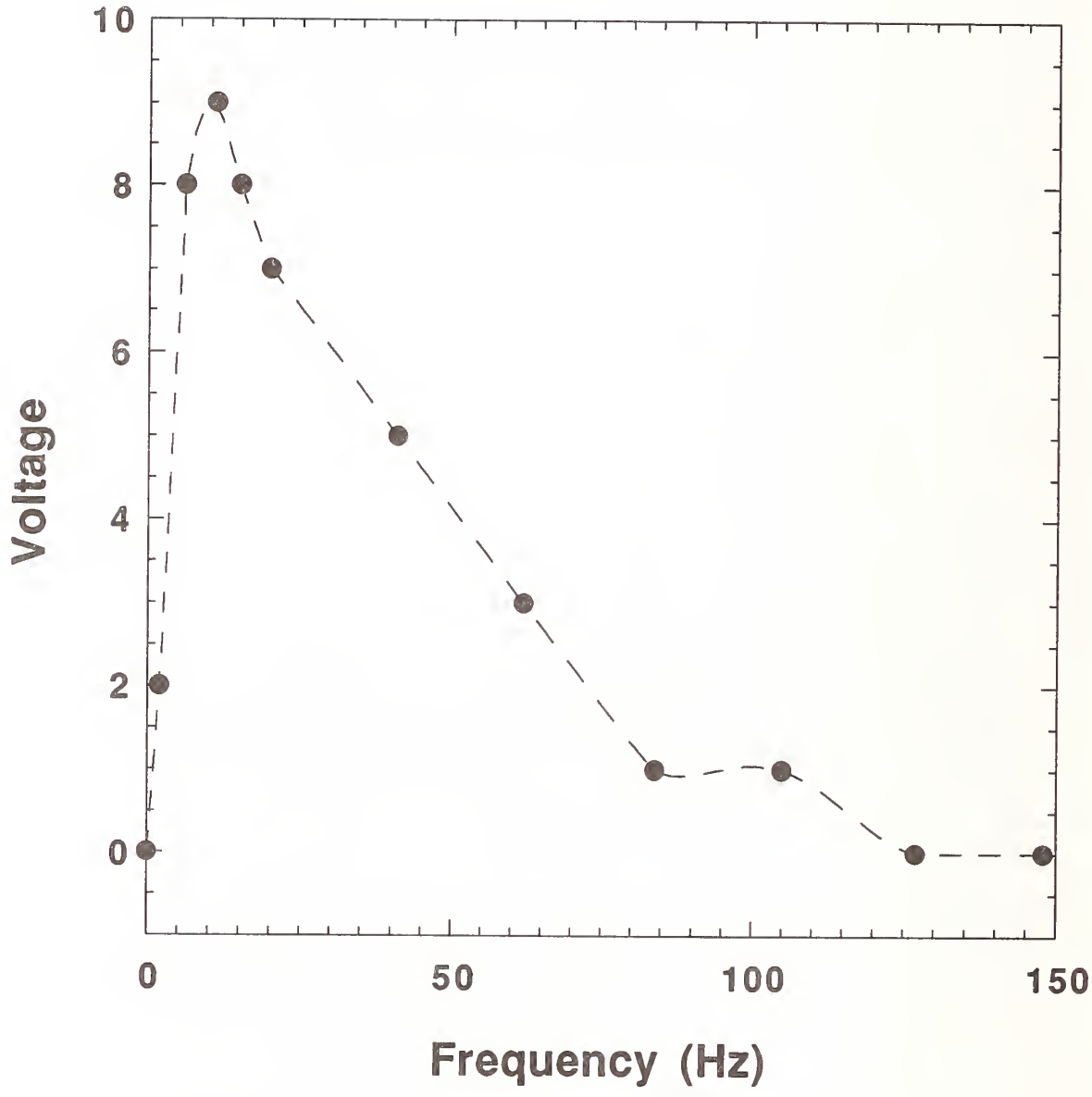

Figure 48. Frequency response of the FEAS measured in air using an optical chopper.

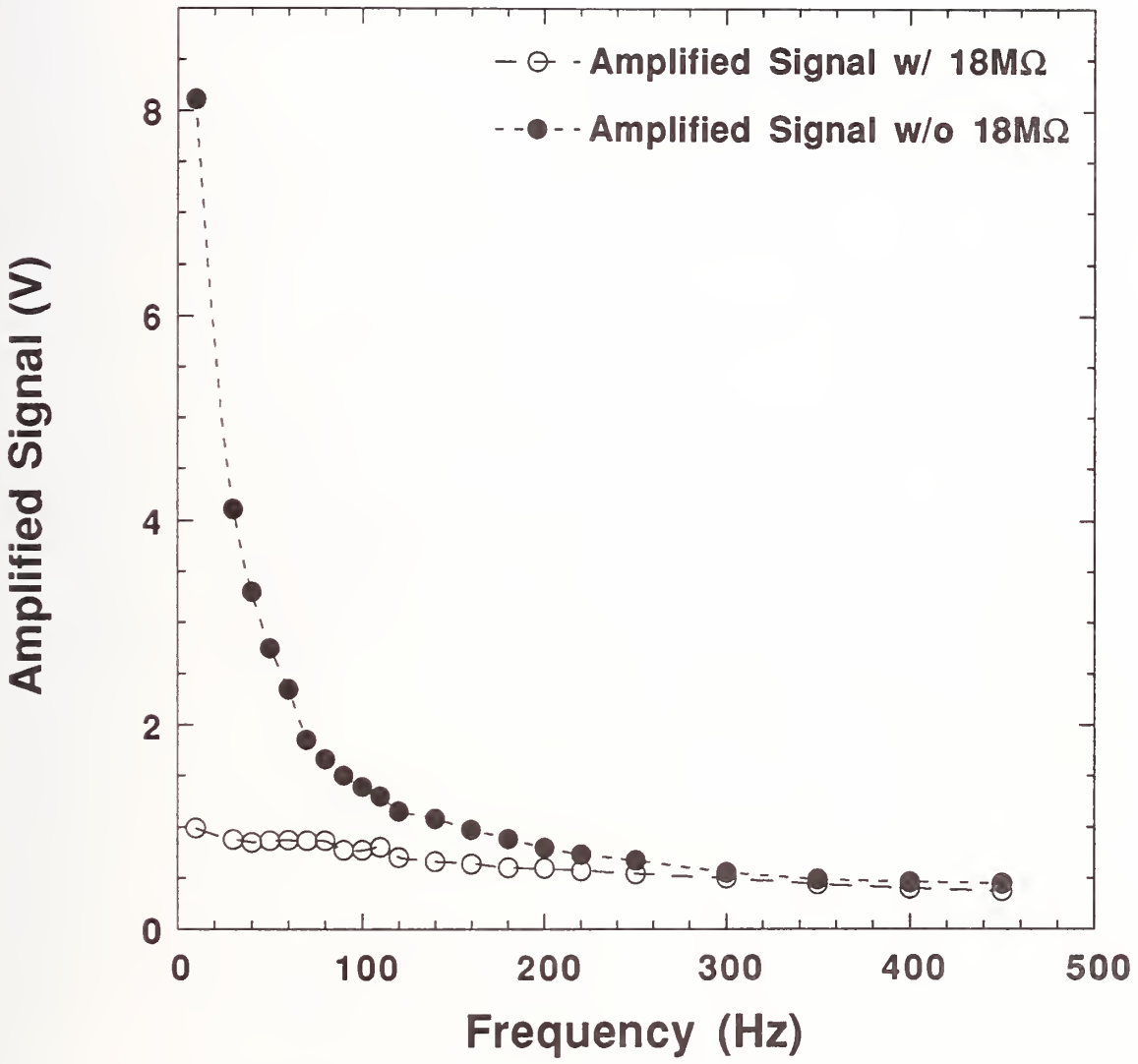

Figure 49. Frequency response of the FEAS for two overall output resistances differing by a factor of 6.5. An 18 MW external resistor is used to lower the overall output resistance.

1. Calibration data need only be collected for one frequency.
2. The signal-to-noise ratio can be increased by use of a single frequency.
3. There is no need for the pyroelectric detector to have a flat frequency response.

In order to obtain a good signal-to-noise ratio at 1000 Hz it was necessary to increase the radiant flux reaching the detector beyond that available in the FEAS. This was accomplished by increasing the size of the source, increasing the width of the IR band pass filter, and increasing the detector size. Below we provide a detailed description of the instrument design.

11.3.3.2 Instrument Design. An overall schematic of the Differential Infrared Rapid Agent Concentration Sensor (DIRRACS) is shown in Figure 50. All of the components of the device are listed in Appendix J. The instrument is designed so that the tube assembly can extend about 15 cm inside an engine nacelle or dry bay with the agent flowing through the 2.8 cm long test section located next to the IR source. For rigidity of design and alignment, the IR source chamber, sample volume, and IR transmission tube are assembled from a single 3.18 cm OD brass tube with a length of about 20 cm. A major design challenge was to assemble a system that could fit through a 1 1/4 inch NPT fitting into an engine nacelle simulator and allow monitoring of the agent near the nacelle wall.

The IR source was a 120 V cable heater. The 1.57 mm diameter element was coiled in a cylindrical shape to fit within the 3.2 cm long section of the 3.02 cm ID brass tube. An elliptical cross section was used to contain the 61 cm cable without allowing it to touch the brass housing. A 2.8 cm diameter ZnSe window was attached to the source housing with high temperature RTV. It was found during testing that the seal leaked and agent entered the source housing. To prevent this leakage of agent into the housing a small flow of nitrogen, on the order of 0.3 cm^3/s, was fed into the housing. Flexible stainless steel tubing (1.6 mm diameter) such as is commonly used with gas chromatographs was silver soldered to the housing wall and was routed with the heater cables along the tube assembly and through the 1 1/4 inch NPT fitting. The nitrogen exited the source chamber through a 1 mm diameter hole in the end of the housing.

Next to the source was a 2.8 cm length of the brass tubing which had been milled out leaving four 6 mm wide segments to connect with the source housing. The agent flowed through this region during a test. The IR radiation passed through the sample region, through a 1 mm thick ZnS window, and then through an IR version of a light transmission tube with the light reflecting off the walls of the brass tube. The interior of the tube was cleaned with solvent and tissue to improve its reflectivity. The ZnS window was sealed with RTV to a retaining ring that had been soldered into the tube. In a later version of the DIRRACS, a wide-bandpass IR filter was added at the end of the IR transmission tube just before the chopper to remove IR radiation over the 10 μm - 14 μm range. A standard 1 1/4 inch pipe fitting was soldered to the brass tube for mounting purposes. Three small holes were drilled through the fitting for the nitrogen purge line and the heater cables.

The IR radiation then passed through the frequency-controlled optical chopper operating at 500 Hz. The IR radiation was filtered with a narrow band-pass filter, which passed radiation from 8.396 μm to 8.913 μm. This narrow wavelength range of radiation entered a conical collector, which focused the IR radiation onto the $LiTaO_3$ pyroelectric sensor with a 5 mm active diameter. The design of the collector is illustrated in Figure 51.

The electronics board with detector was attached directly to the collector. The pyroelectric detector has an FET built into the device. Additional amplification was provided by a 100 × low-noise amplifier designed for use in the DIRRACS. The circuit for the amplifier is shown in Figure 52. To further reduce noise, the voltage signal was passed through a low-frequency filter with 24 dB per octave filter set at about 300 Hz.

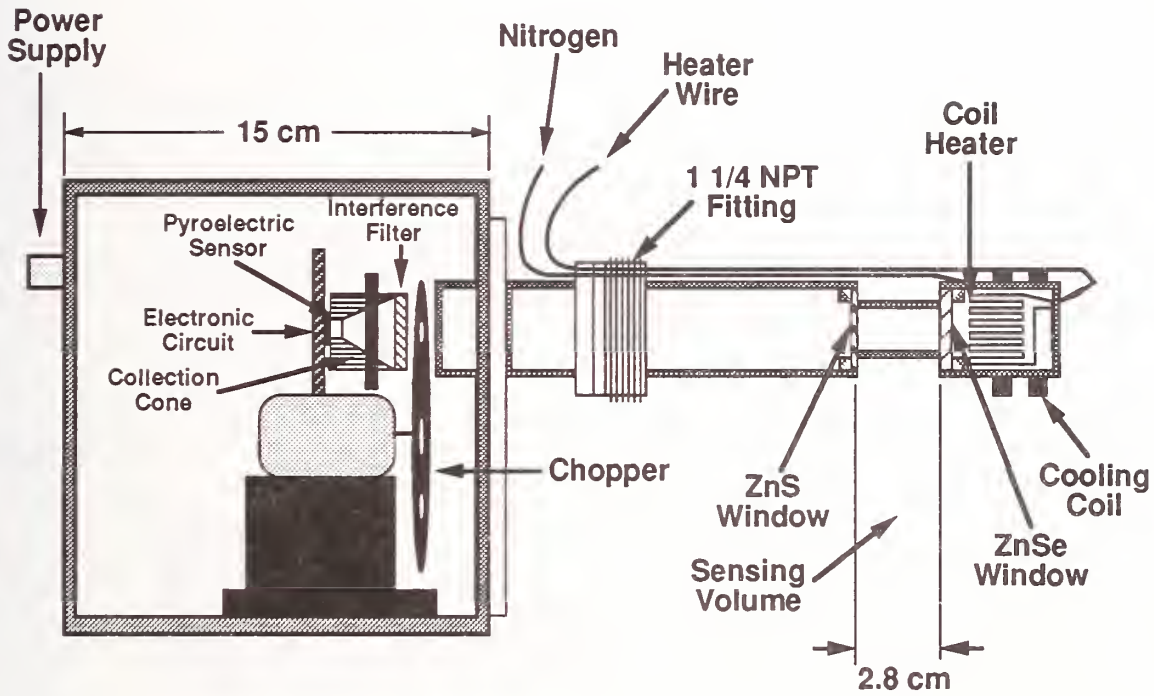

Figure 50. Overall schematic of the Differential IR Rapid Agent Concentration Sensor (DIRRACS).

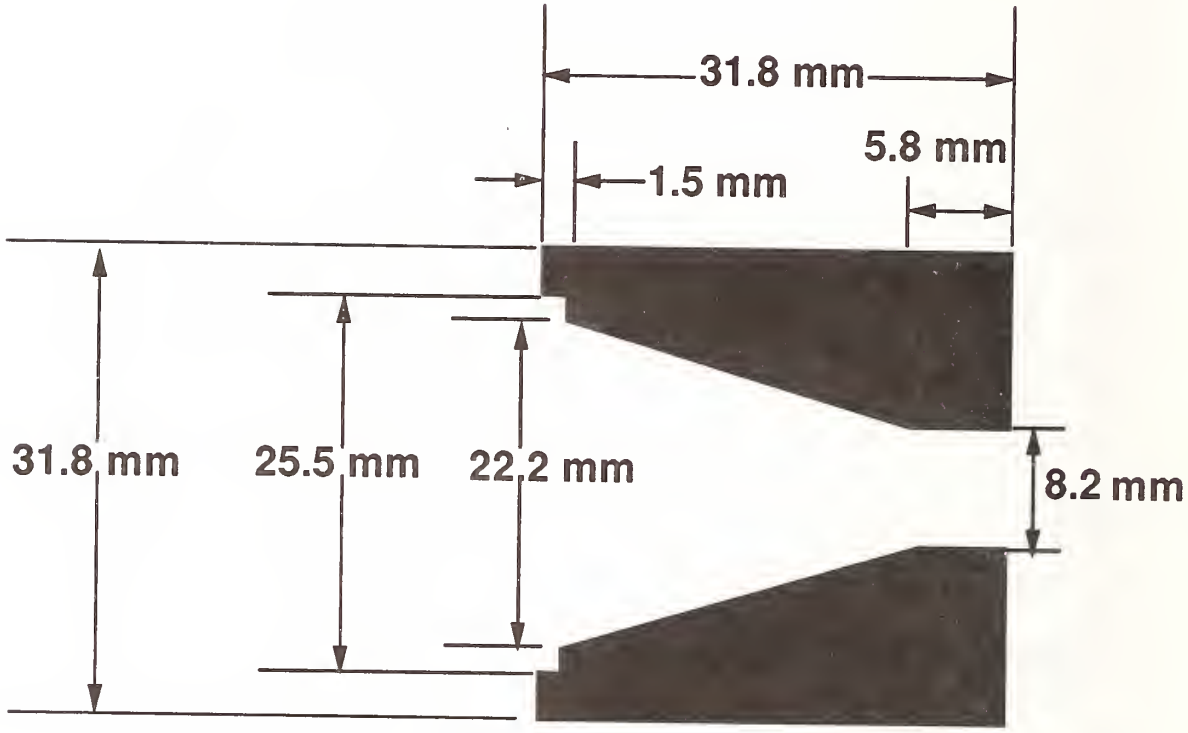

Figure 51. Design of collection cone for focussing the IR radiation from a diameter of 15 mm to about 8 mm. The cone was machined from brass with the narrow-bandpass filter attached at left and the detector inserted at the right.

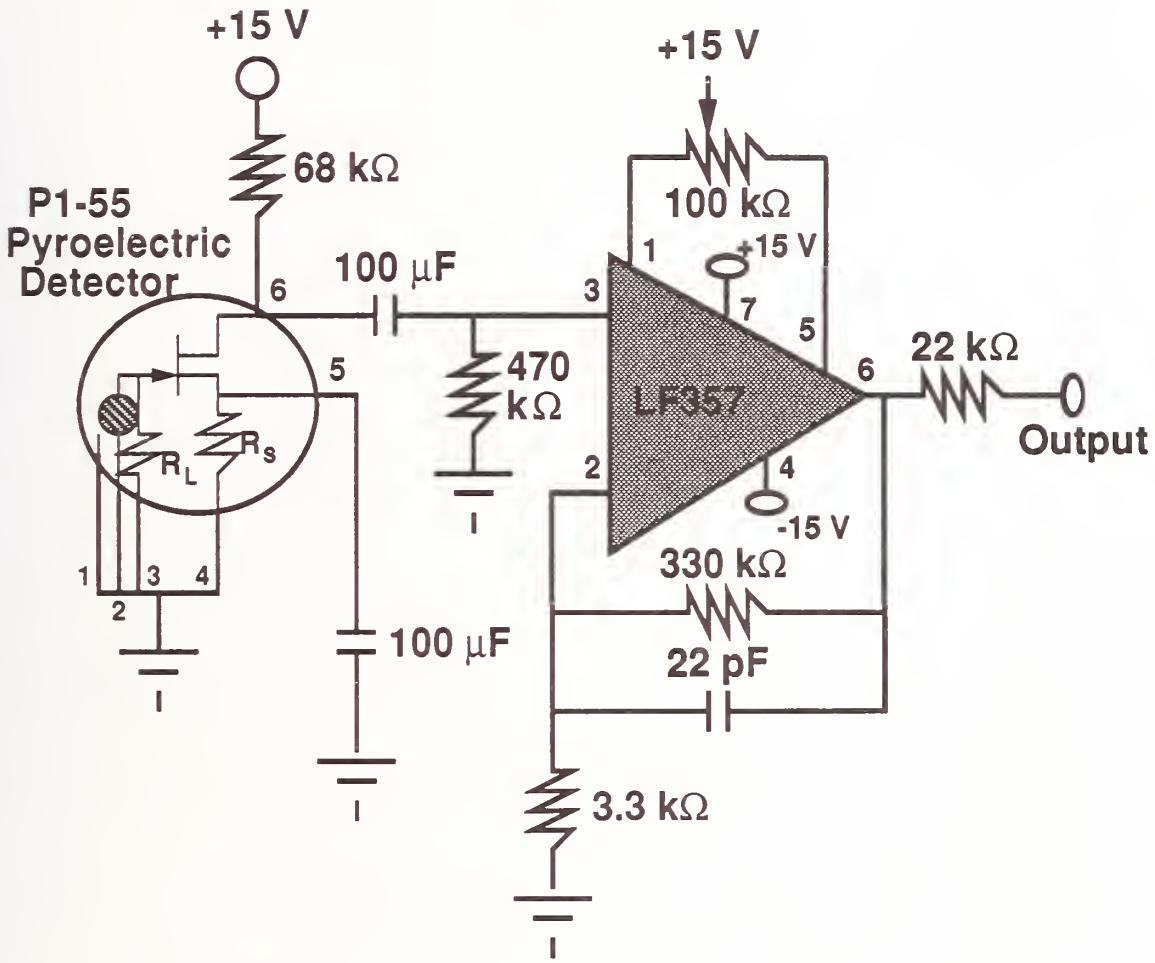

Figure 52. Design of the 100 × low-noise amplifier used with the DIRRACS.

Two DIRRACS with nominally identical designs were fabricated and are referred to in the text as the "blue" and the "black" units for the color of the boxes housing the electronics and chopper.

11.3.4 Theory of Operation. A schematic of the optical system for the DIRRACS is shown in Figure 53. The radiation from the heated wire is emitted in all directions striking the ZnSe window with about 20 % reflection loss. Some fraction of the IR radiation is absorbed by the agent depending on the concentration and pathlength and is then transmitted through the ZnS window with reflection loss before passing through the transmission tube. The remaining optical components through which the IR radiation passes before reaching the detector are the wide-band-pass filter, chopper blade with a limiting slot size, narrow-band-pass filter, and conical collector. Each one of these optical components has losses that reduces the IR radiation reaching the detector.

The choice of optics was in large part an effort to increase the signal detected relative to the original FEAS device. The signal of the FEAS with the improved amplifier was measured at a chopper frequency of 500 Hz and was found to have a value of about 100 mV with a noise of roughly 20 mV. We increased the signal by about a factor of 20 to improve the signal-to-noise ratio. This increase was obtained by increasing the source size from 6 mm to 18 mm, increasing the width of the narrow-band-pass filter by a factor of 5, and increasing the diameter of the detector from 1 mm to 5 mm. The factor of 3 longer pathlength in the DIRRACS compared to the FEAS, the addition of a conical collector to focus the IR radiation on the detector, and the addition of a wide-band-pass filter were competing factors that reduced the IR flux in the DIRRACS relative to the FEAS. It was found empirically that these changes increased the signal to a value of about 1 V for one device and about 2 V for the second. By using a 300 Hz low-pass filter, the noise was 10 mV to 20 mV so that signal-to-noise ratios were typically about 100.

As the agent enters the sensing volume, the IR radiation is absorbed by the agent reducing the flux of radiation reaching the detector. The higher the concentration, the lower the flux reaching the detector. The IR spectrum of HFC-125 (C_2HF_5) is plotted in Figure 54 for a concentration of 6.3×10^{-3} moles/m^3 with a 10 m pathlength along with the spectrum of the narrow-band-pass filter. The HFC-125 spectrum was taken in a 10 m multipass cell at a partial pressure of about 16 Pa. It is seen that the region where the filter passes IR radiation is also a region of strong IR absorption by HFC-125. There is also strong IR absorption, resulting from C-F stretch vibrational modes, in the same spectral region for other agents with C-F bonds including HFC-227ea (C_3HF_7), FC-218 (C_3F_8), halon 1301 (CF_3Br), and CF_3I. The spectra plotted in Figure 55 illustrate that both HFC-125 and halon 1301 have strong absorption features over the 8.4 μm to 8.9 μm wavelength region of the narrow-band-pass filter. The strong absorption peak in halon 1301 at 9.2 μm corresponds to a symmetric stretch of the CF_3 (symmetry type A_1, frequency assignment ν_1) (McGee *et al.*, 1952). While the absorption peak for halon 1301 is slightly outside of the wavelength range for the narrow-band-pass filter, the peak for HFC-125 is within the range of the filter. As discussed below, this leads to a greater sensitivity of the DIRRACS to HFC-125 relative to halon 1301. These are the two agents tested in this study.

The starting point for modelling the IR transmission through the agent is Bouger's law, which relates the intensity of incident monochromatic light of wavelength λ, I_λ^0, and the intensity of the radiation I_λ transmitted through a pathlength L of the agent,

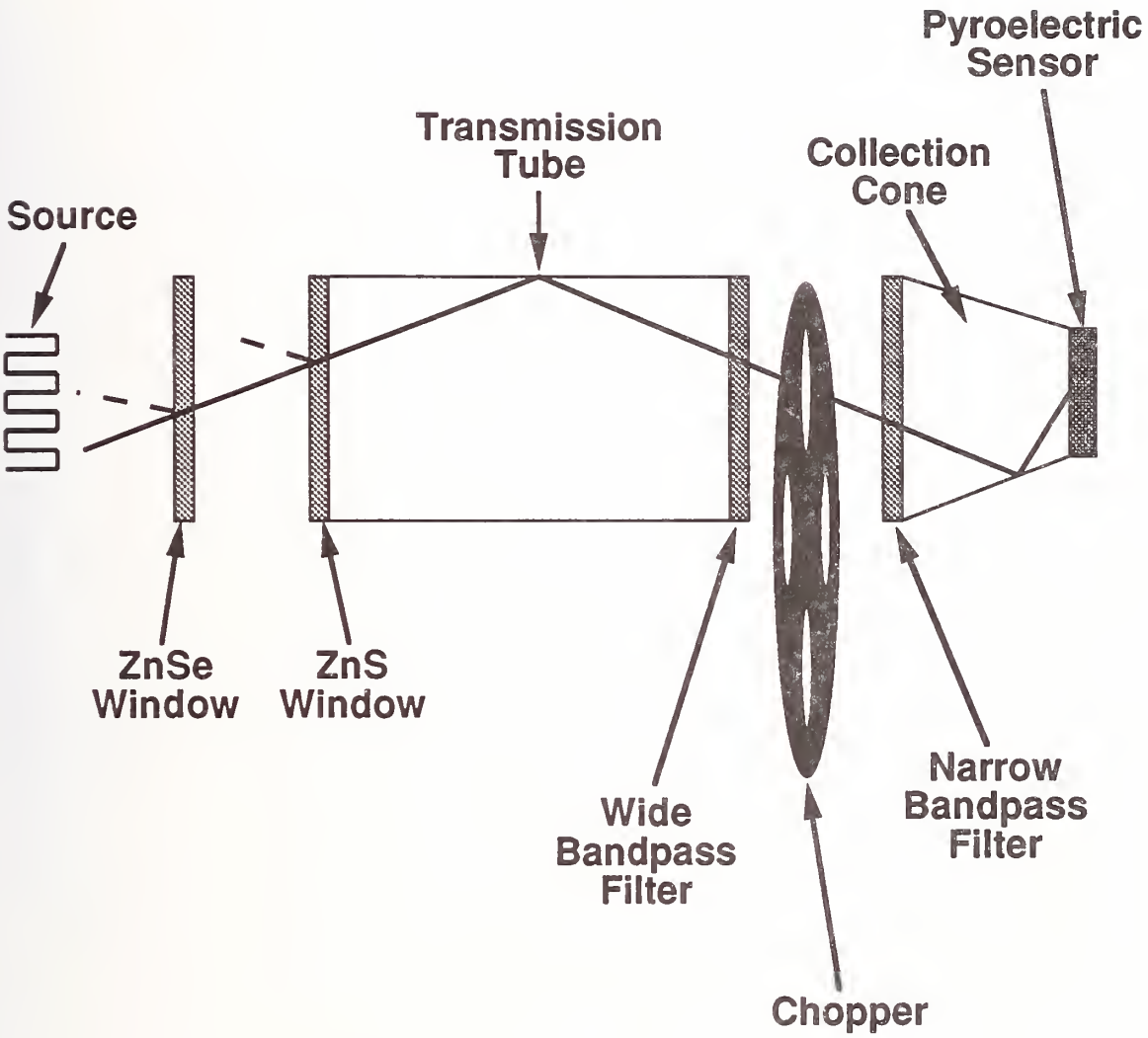

Figure 53. Schematic (not to scale) of the optical system of the DIRRACS. The dashed lines represent reflected IR radiation.

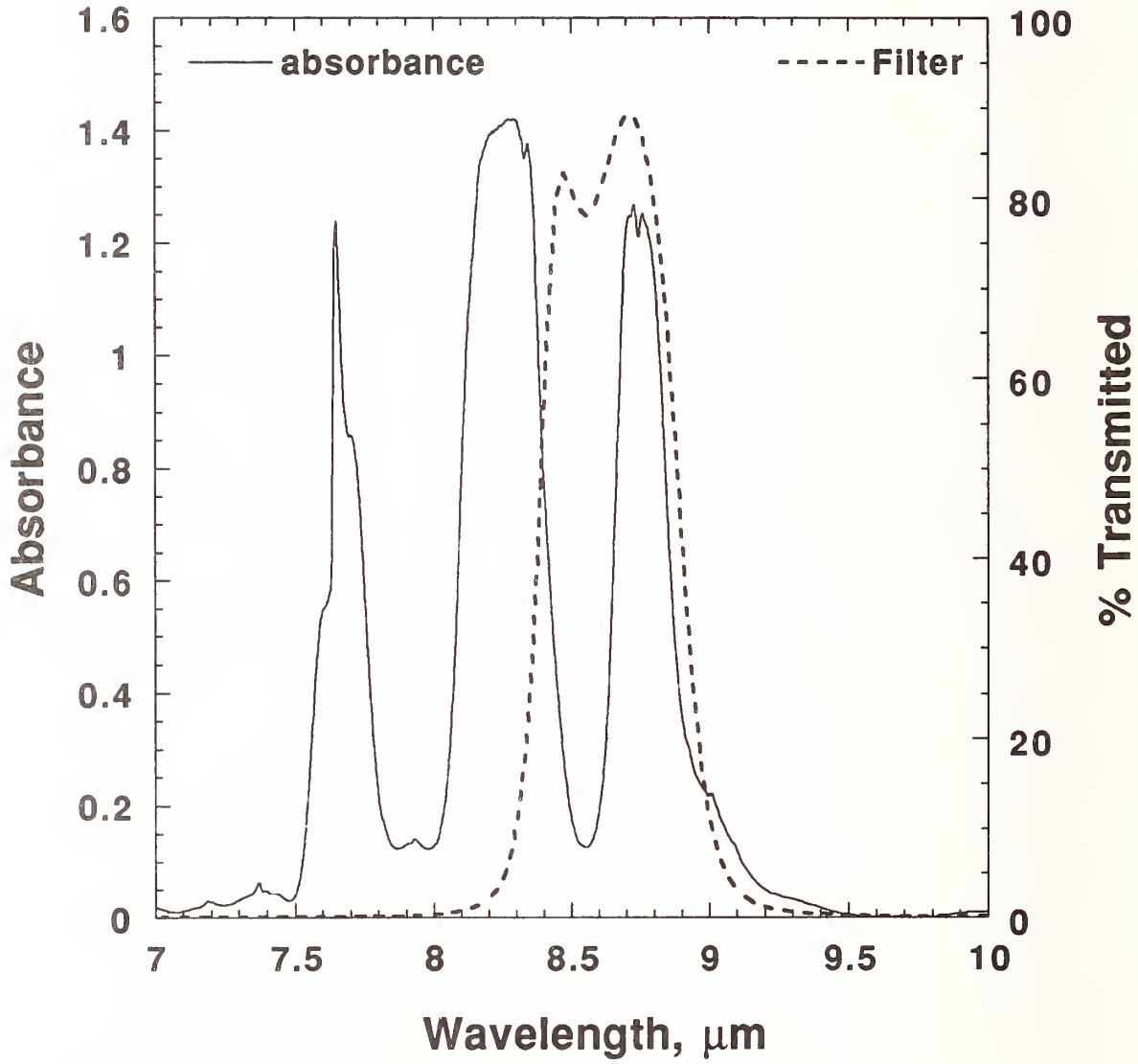

Figure 54. IR absorbance spectra of HFC-125 and of the narrow-band-pass filter.

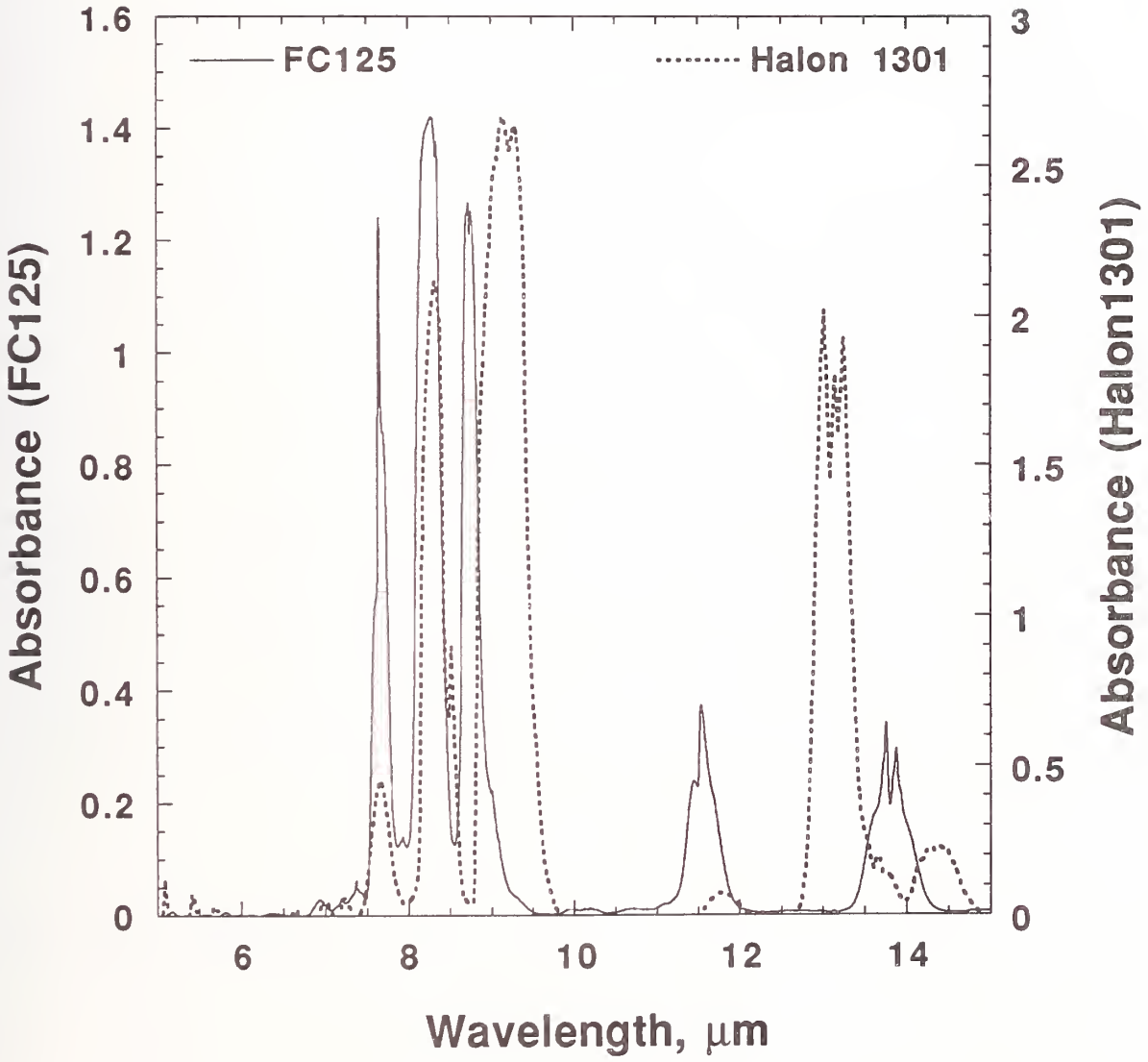

Figure 55. Absorption spectra are plotted for HFC-125 and halon 1301. Both agents have absorption features over the wavelength region of the narrow-band-pass filter (8.4 μm - 8.9 μm).

$$I_\lambda / I_\lambda^0 = e^{-K(\lambda)CL} \quad , \tag{41}$$

where C is the molar concentration of the agent. The quantity $K(\lambda)$ is the wavelength dependent absorption coefficient of the agent. The absorbance, $A(\lambda)$, is simply related to the transmittance, I_λ/I_λ^0:

$$A(\lambda) = -\log_{10}(I_\lambda / I_\lambda^0) \quad . \tag{42}$$

From Equations (41) and (42), we obtain the following relation between $K(\lambda)$ and $A(\lambda)$:

$$K(\lambda) = \frac{2.3A(\lambda)}{CL} \quad . \tag{43}$$

We make use of this relation in deriving $K(\lambda)$ from the absorbance measurements made for HFC-125 (C_2HF_5).

The cable-heater IR source is approximated as a so called "blackbody" radiation source. The blackbody spectral radiance L_λ, which has the units of Watts per steradian, per cubic meter, is given by the following equation (Dereniak and Crowe, 1984):

$$L_\lambda = \frac{2hc^2}{\lambda^5 (e^{\frac{hc}{\lambda kT}} - 1)} \quad . \tag{44}$$

In this expression h is Planck's constant (6.63×10^{-34} W s^2), c is the speed of light (3.00×10^8 m s^{-1}), k is Boltzmann's constant (1.38×10^{-23} W s K^{-1}), and λ is the wavelength of light (m). In Figure 56 the spectral distributions are plotted for three temperatures including the estimated source temperature, 800 K, and the IR source housing temperature, 330 K. We see that while the higher temperature source has a greater radiance at all λ, the fractional increase is smaller as the wavelength increases.

We are interested in estimating the effect of agent concentration on the radiant heat flux reaching the IR transmission tube. If the source diameter and the transmission-tube diameter are both small relative to the separation distance, the radiant flux incident on the window of the transmission tube is given by:

$$\Phi = L_\lambda A_s \Omega_d \quad , \tag{45}$$

where A_s is the cross-sectional area of the source and Ω_d is the solid angle subtended by the transmission tube. The radiant intensity without agent present I_λ^0, defined as the flux per solid angle, is given by:

$$I_\lambda^0 = L_\lambda A_s \quad . \tag{46}$$

In our case, diameters of both the source and the transmission tube are comparable to the pathlength so that Equations (45) and (46) are not exact. A full treatment of this optical arrangement would involve integrating over both the source area and the cross section of the transmission tube. However, Equation (46) is a useful approximation for studying the effects of wavelength and temperature on the radiant intensity reaching the detector. Besides the source, the optical components most sensitive to the wavelength are the narrow and wide-band-pass filters. We use the quantity $F(\lambda)$ to represent the

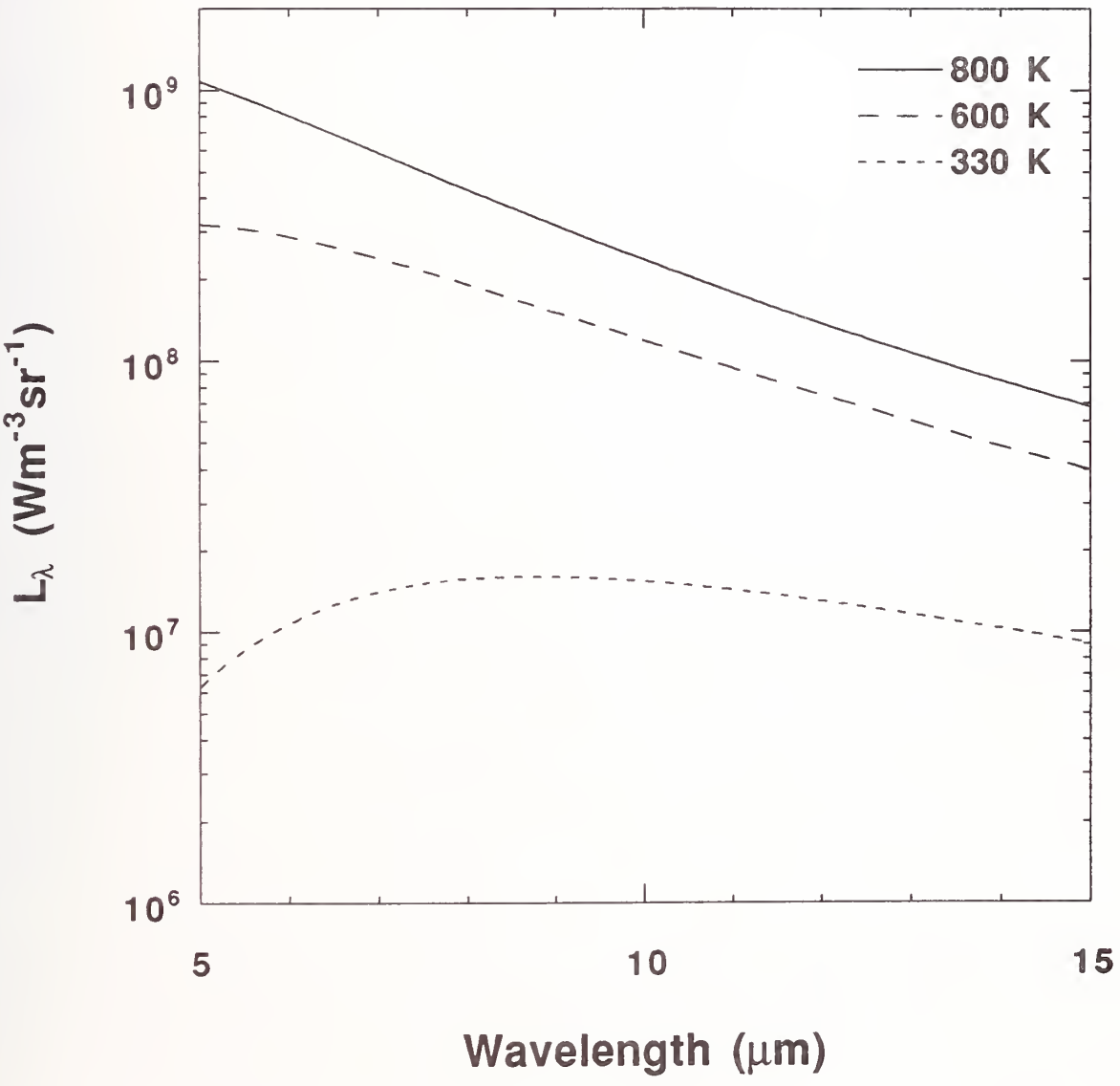

Figure 56. Effect of temperature on blackbody radiance L_λ.

combined wavelength dependent filter function for both filters. The windows, transmission tube, conical collector, and chopper affect the amount of radiation passing through the device, but are not very sensitive to wavelength.

Now it is possible to compute the total radiant intensity I_t reaching the transmission tube as a function of agent concentration. This involves integrating the expression for the transmitted intensity over wavelength. The following expression is obtained for the ratio of the total transmitted radiant intensity I_t with agent present to the intensity I_t^0 in the absence of agent:

$$\frac{I_t}{I_t^0} = \frac{\int_{\lambda_1}^{\lambda_2} e^{-K(\lambda)CL} I_\lambda^0 F(\lambda) d\lambda}{\int_{\lambda_1}^{\lambda_2} I_\lambda^0 F(\lambda) d\lambda} \tag{47}$$

A FORTRAN program, which is listed in Appendix K, was developed to compute I_t/I_t^0 based on Equation (47). The program returns the theoretical output of the device for a given concentration of agent. The program first reads in the filename for the blackbody absorbance of the agent, the agent concentration, the temperature, and the path length. Next, the program reads the filter transmittance and the absorbance as a function of wavelength. A conversion is made of the absorbance function from a basis of inverse centimeters to meters.

An integration loop with a step size of 0.01 μm is started wherein three terms are calculated and combined to generate the light intensities transmitted through the agent and through air. The terms are an exponential term based on the agent concentration, an intensity term based on the wavelength, and a filter transmittance term also based on the wavelength. The wavelength is incremented each time through the loop. The filter function is indexed when its next wavelength-transmittance pair is applicable. Each term is calculated using the trapezoidal rule. The light intensity through the agent is calculated by multiplying the exponential, intensity, and filter terms by the wavelength step size and adding this to the previous sum. The light intensity through air is calculated by multiplying the intensity and filter terms by the wavelength step size and adding to the previous sum. When the integration loop is complete, the two intensity terms are summed and then divided to generate the fraction of light transmitted through the agent mixture relative to that which would have passed through air. The ratio is written to the screen as well as intermediate sums of the two intensities.

The integration was performed over the wavelength range from 5 μm to 10 μm for a pathlength of 2.8 cm. The calculated intensity ratio is plotted in Figure 57 as a function of HFC-125 mole fraction for three source temperatures. It is seen that the source temperature has very little effect on the intensity ratio. In Figure 58 the intensity ratio is plotted for a hypothetical narrow-band-pass filter that only allows passage of the radiation at the peak in the absorbance of 1.2 for λ equal 8.75 μm. In this case of a single wavelength, Equation (47) reduces to Equation (41) (Bouger's Law). The exponential decrease in the intensity ratio with respect to concentration limits the concentration range that could be measured relative to using the wider band-pass filter. Another advantage of a wider band-pass is the ability to use one instrument for several agents.

In the above analysis it is assumed that there is no long wavelength radiation with $\lambda > 10$ μm reaching the detector. The spectra of the narrow-band-pass filter and of the ZnS window are shown in Figure 59 for λ up to 25 μm. It is seen that both optical elements transmit a significant fraction of light over the wavelength range from 12 μm to 15 μm. The product of these two transmission curves is computed to obtain the combined filter function, $F'(\lambda)$. This function is substituted into Equation (47) and the integration is performed from 5 μm to 15 μm. No molecular absorption for λ greater than 10 μm is assumed in this simplified example, though a more detailed analysis would account for the two absorption features above 10 μm for HFC-125. The intensity ratio versus mole fraction for source

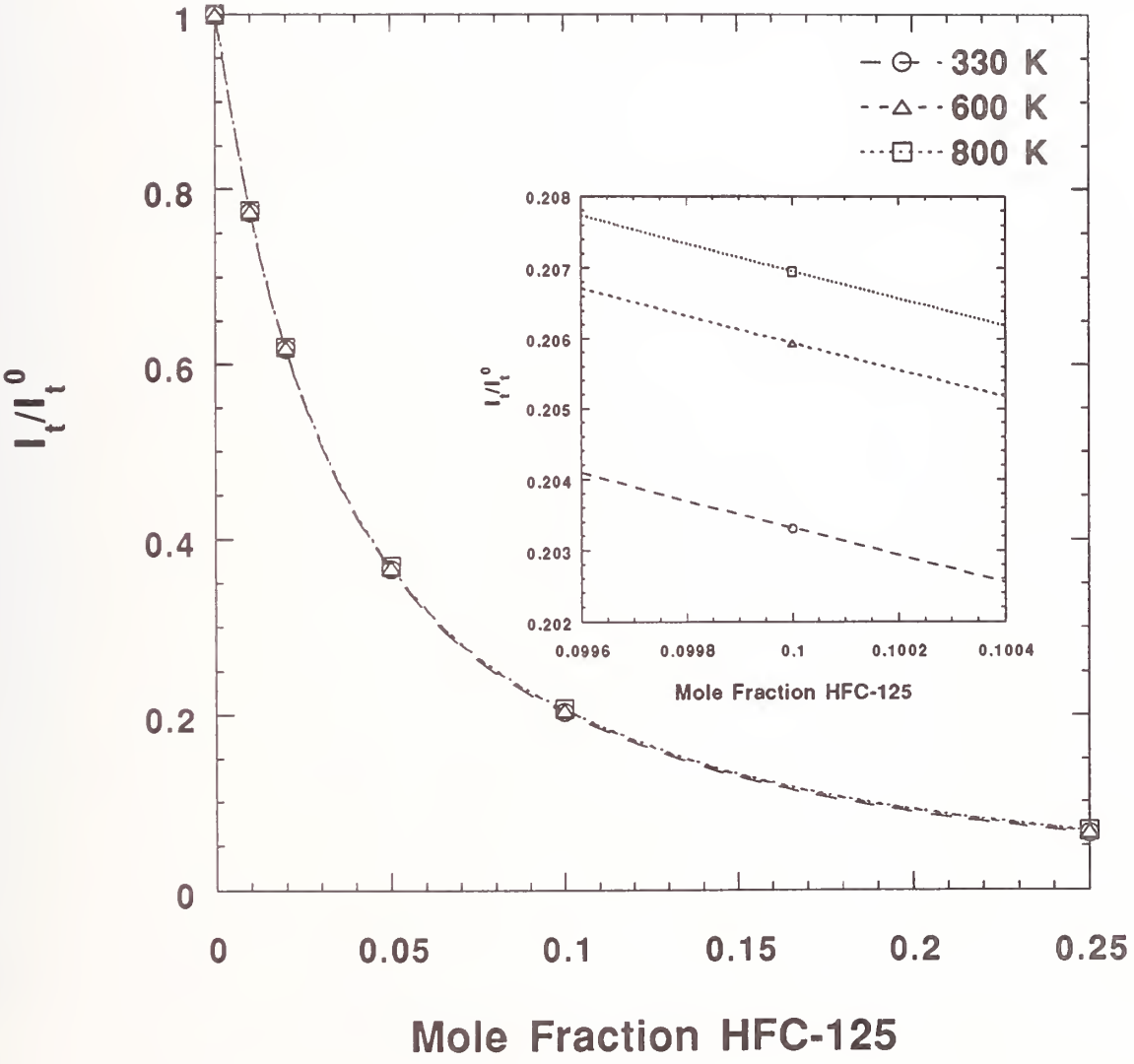

Figure 57. Predicted ratio of the wavelength integrated intensity of the transmitted IR radiation and the incident IR radiation versus mole fraction of HFC-125 for three IR source temperatures.

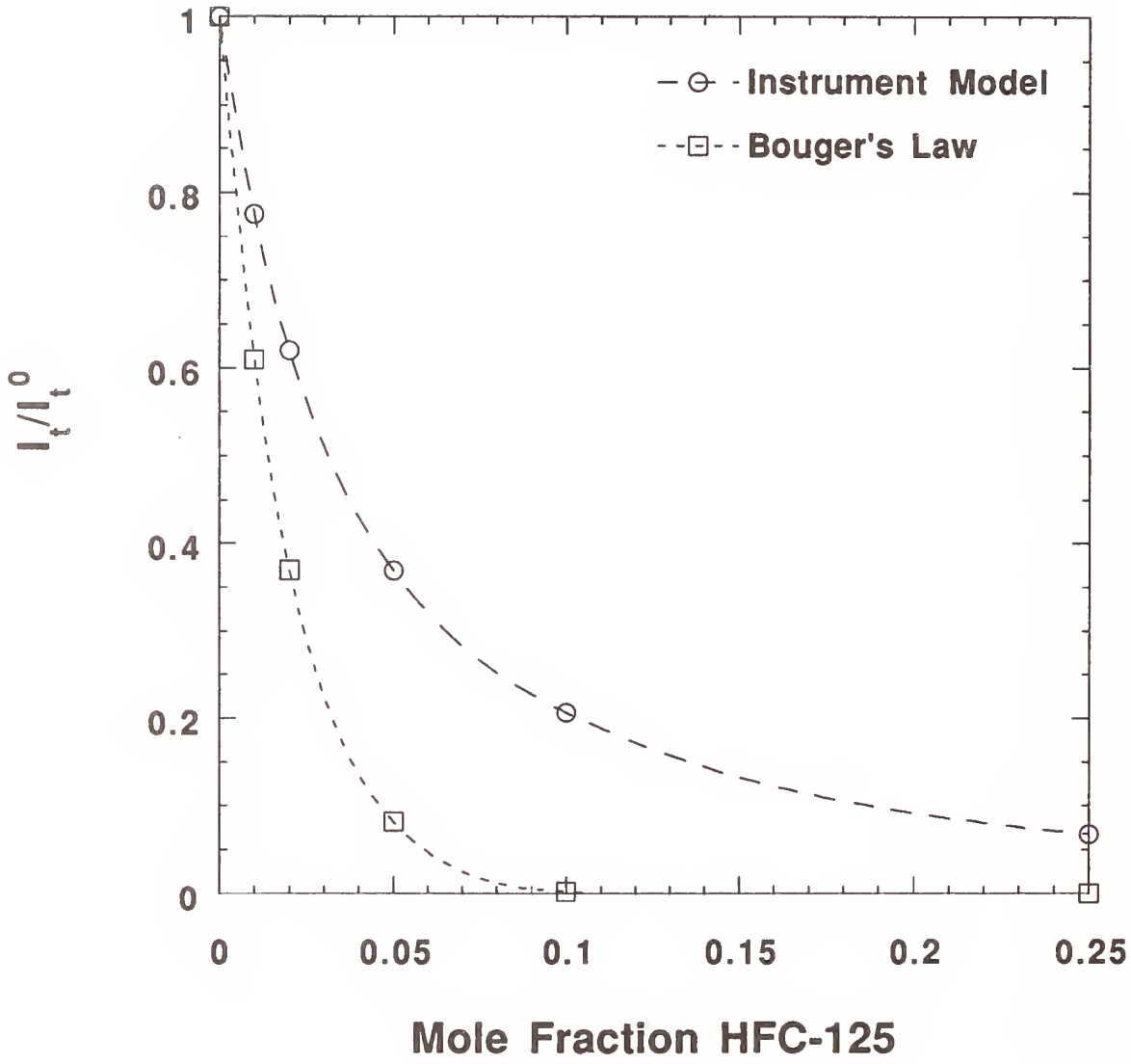

Figure 58. Comparison of the intensity ratio for the instrument (DIRRACS) model and Bouger's law.

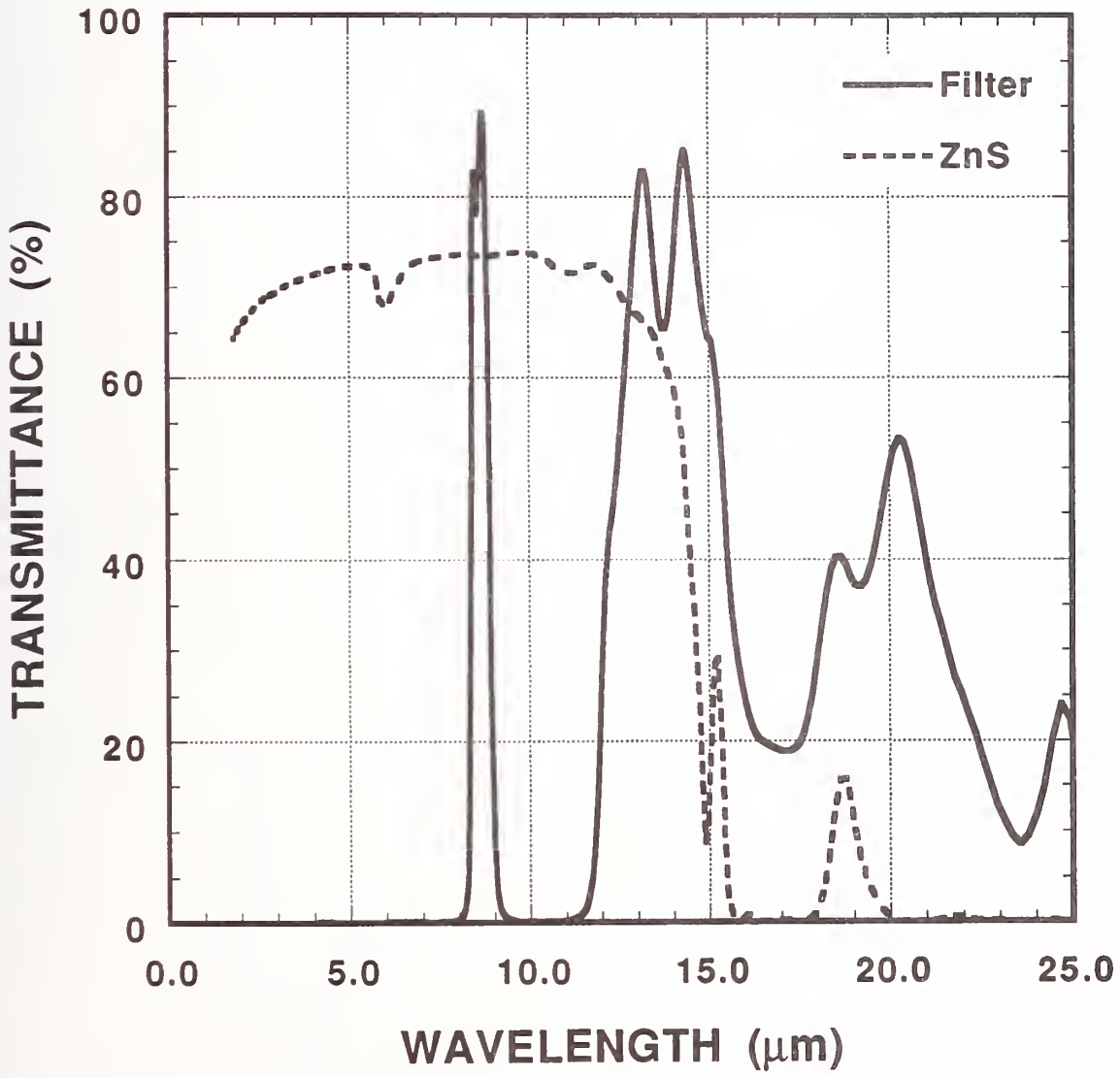

Figure 59. Transmittance versus wavelength for the narrow-band-pass filter and for the ZnS window.

temperature of 800 K are compared with the results with the reduced integration region in Figure 60. It is seen that the unfiltered light penetrating the filter results in a higher value of the transmitted ratio for all concentrations.

There are a number of secondary factors not included in the analysis that may be important to the instrument's performance. As the source heated up to about 500 °C, the temperature of the housing was found to increase to a temperature of about 70 °C over a 30 min period, and even the temperature of the conical collection tube was heated from 25 °C to about 30 °C. The significance of this heating on the performance of the instrument will be discussed in the calibration section. Other factors important for quantitative modeling of the system include the spatial distribution of the source radiance, the transmission characteristics of the ZnSe and ZnS windows, and the transmission characteristics of the IR transmission tube and conical collector.

11.3.5 Data Acquisition. Two methods of data acquisition were used. As illustrated in Figure 61, the output signal from the 100 × amplifier was filtered with a low-band-pass filter and analyzed with a digital oscilloscope with 8 bit resolution. The scope was triggered by the controller for the chopper. The DIRRACS voltage output has a cosine shape as can be seen in Figure 62. The scope provided peak-to-valley (Pk-Vy) voltages of the oscillatory signal. Typically 100 sweeps with a single peak and valley per sweep were taken and the average and standard deviation, σ, were computed from these values. This was the primary method for data acquisition during the calibration of instrument response versus agent mole fraction.

A TCP 486DX personal computer having a clock speed of 66 MHz, 8 Mbytes of RAM, and a 250 Mbyte hard drive was used for data acquisition. The same data acquisition and control system as described in detail in Section 11.2.4.5 was used. Two of the channels were used for acquiring data from the two DIRRACS. As described above, the system included two plug-in modules--a Flash 12 Model 1 data-acquisition board and a ACAO-12-2 analog and digital output board--from Strawberry Tree which were installed in computer-bus slots and provided interfaces for the experiments. The standard configuration involved operating at a data-acquisition rate of 20 000 Hz for 1 s to 10 s after a trigger signal.

The data acquisition/analysis involved several steps. First the output voltage versus time data was acquired. Then the data were transferred from a multi-channel output to a single file for subsequent analysis. An algorithm was developed for determining the peaks and valleys in the voltage for each cycle. The infrared detector output data was reduced with a FORTRAN program listed in Appendix L that returns normalized voltages and concentrations for a given set of raw voltages. The program begins by reading the input and output filenames and the operating parameters of chopping frequency, sampling frequency, zero-concentration peak-to-peak voltage, and whether the blue or black DIRRACS is the source of the data. The number of data points is determined from the data file. The number of points per cycle and total number of cycles are then calculated. A loop is started to read the voltages and store the minimum and maximum values and their times for each cycle in an array.

The program next calculates agent concentrations based on a concentration versus Pk-Vy equation fit to the data for either the blue or black detector. The calibration methodology is described in the Instrument Calibration Section. Pk-Vy voltage differences are calculated and normalized by the appropriate zero-concentration value. The appropriate calibration function is applied to each normalized voltage. If a normalized voltage is below the 100 % agent value, 100 % is assigned to that cycle. If a normalized voltage is greater than one, 0 % is assigned to that cycle. The time of the cycle, maximum and minimum voltages, peak-to-valley voltage, normalized peak-to-valley, and concentration are written to a file for each cycle.

The shape of the normalized voltage plot in Figure 62 is close to a cosine function. This is more apparent from the expanded plot in Figure 63 where the reduced voltage output of the DIRRACS is

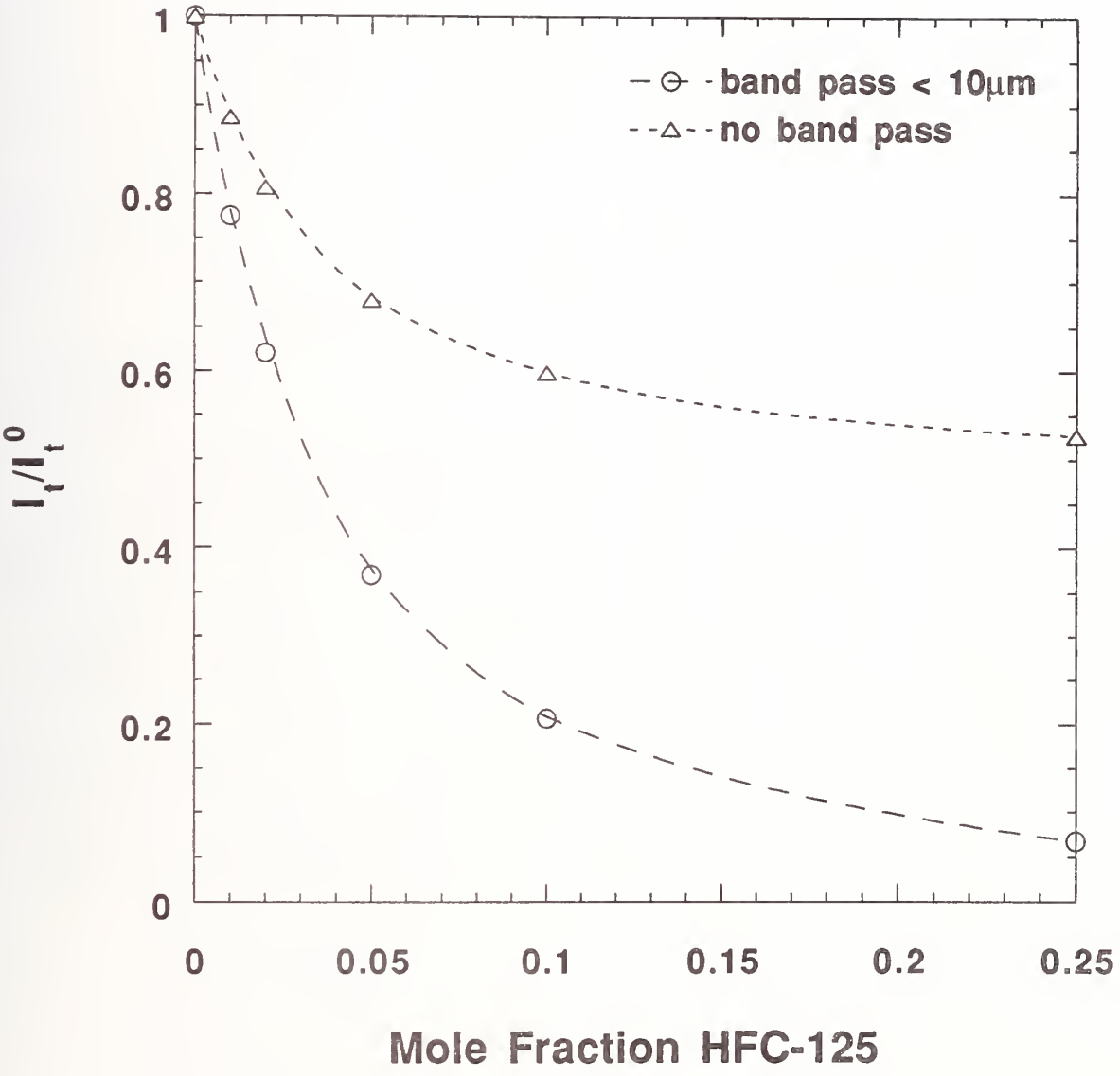

Figure 60. Effect of the integration range of λ on the predicted intensity ratio (5μm - 10 μm, added band pass, 5 μm - 15 μm, no band pass).

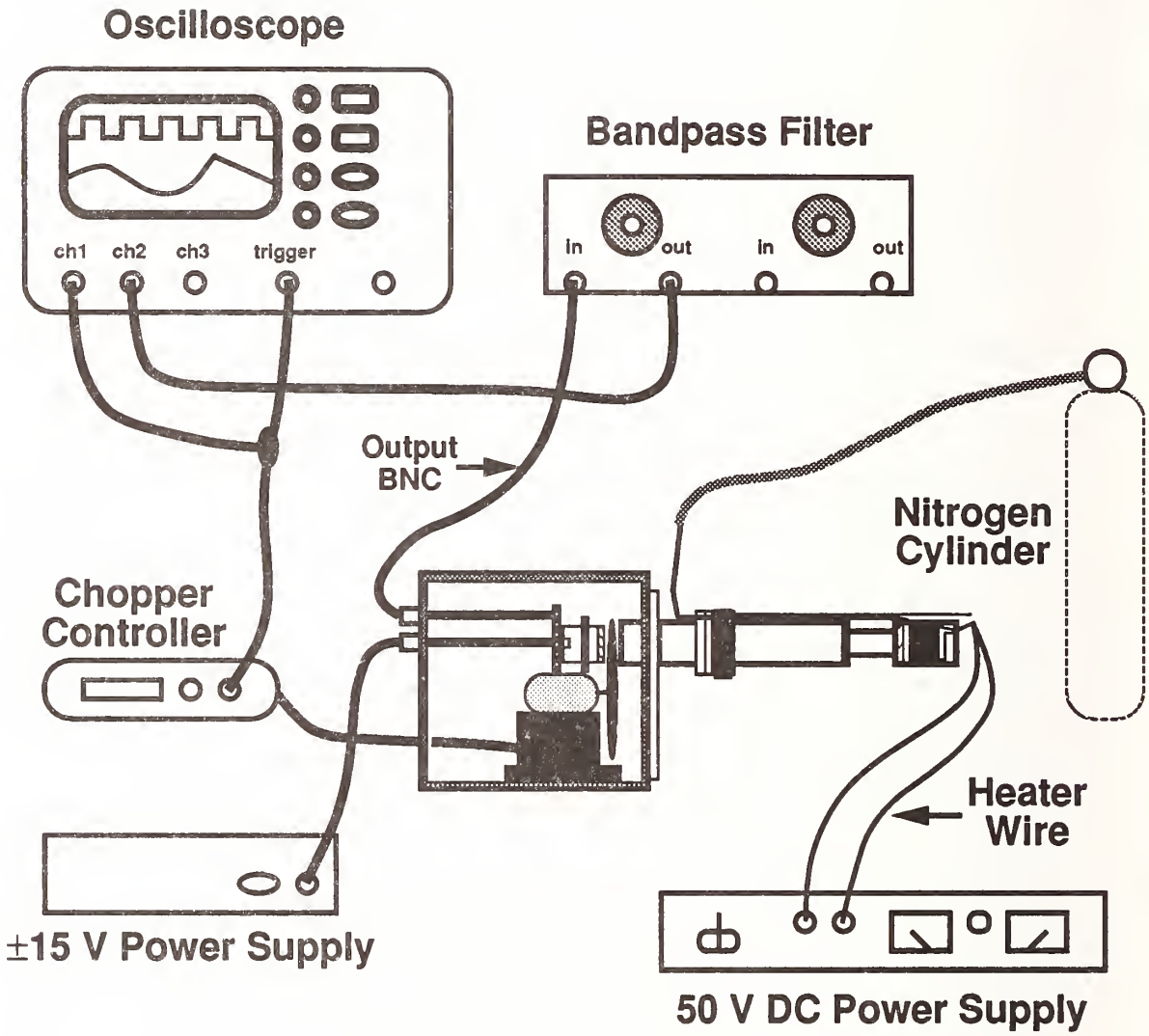

Figure 61. Schematic of experimental setup including data acquisition.

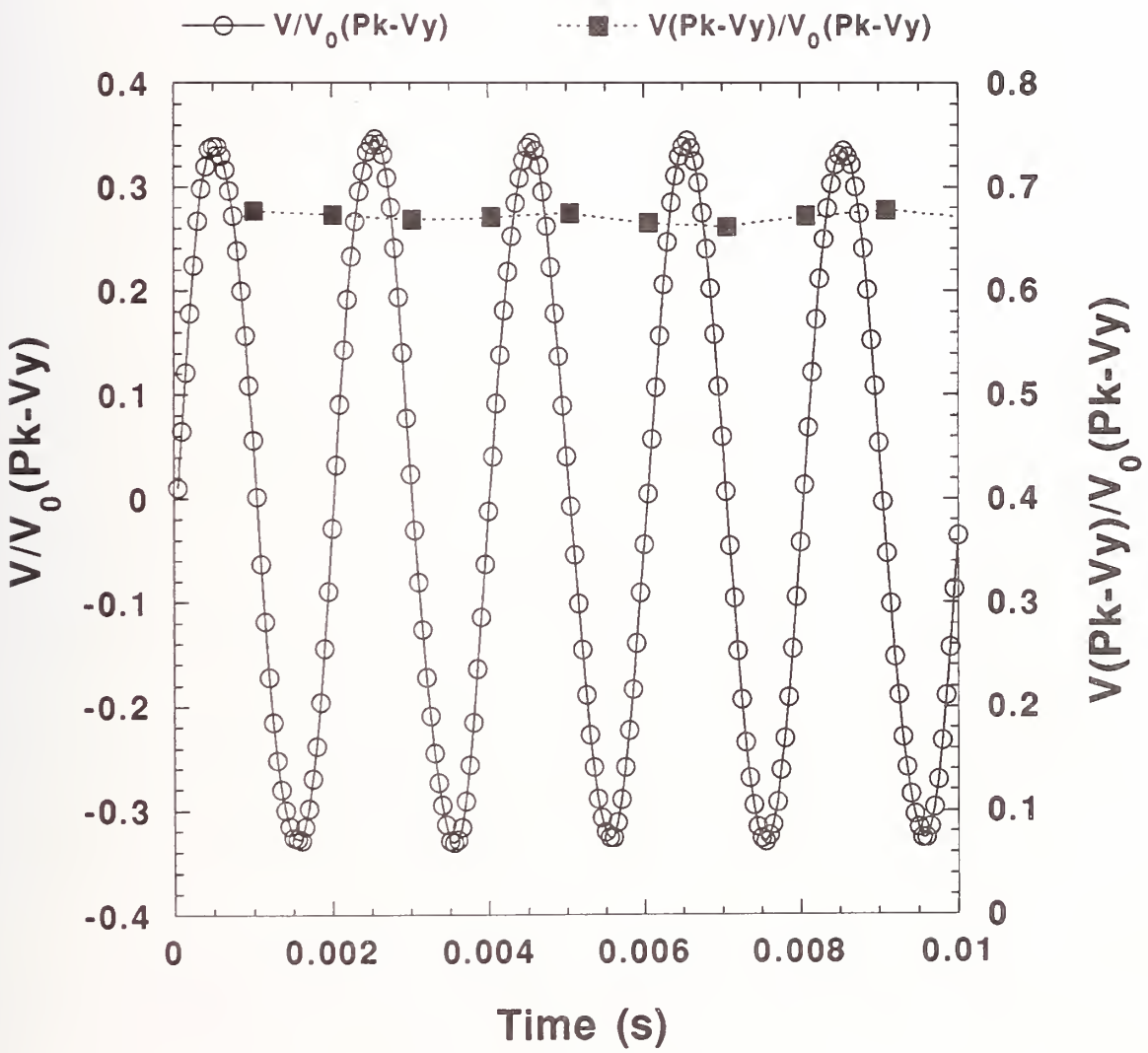

Figure 62. Plots of DIRRACS output voltage normalized by the Pk-Vy signal in air and the normalized Pk-Vy voltages versus time for 0.10 mole fraction HFC-125.

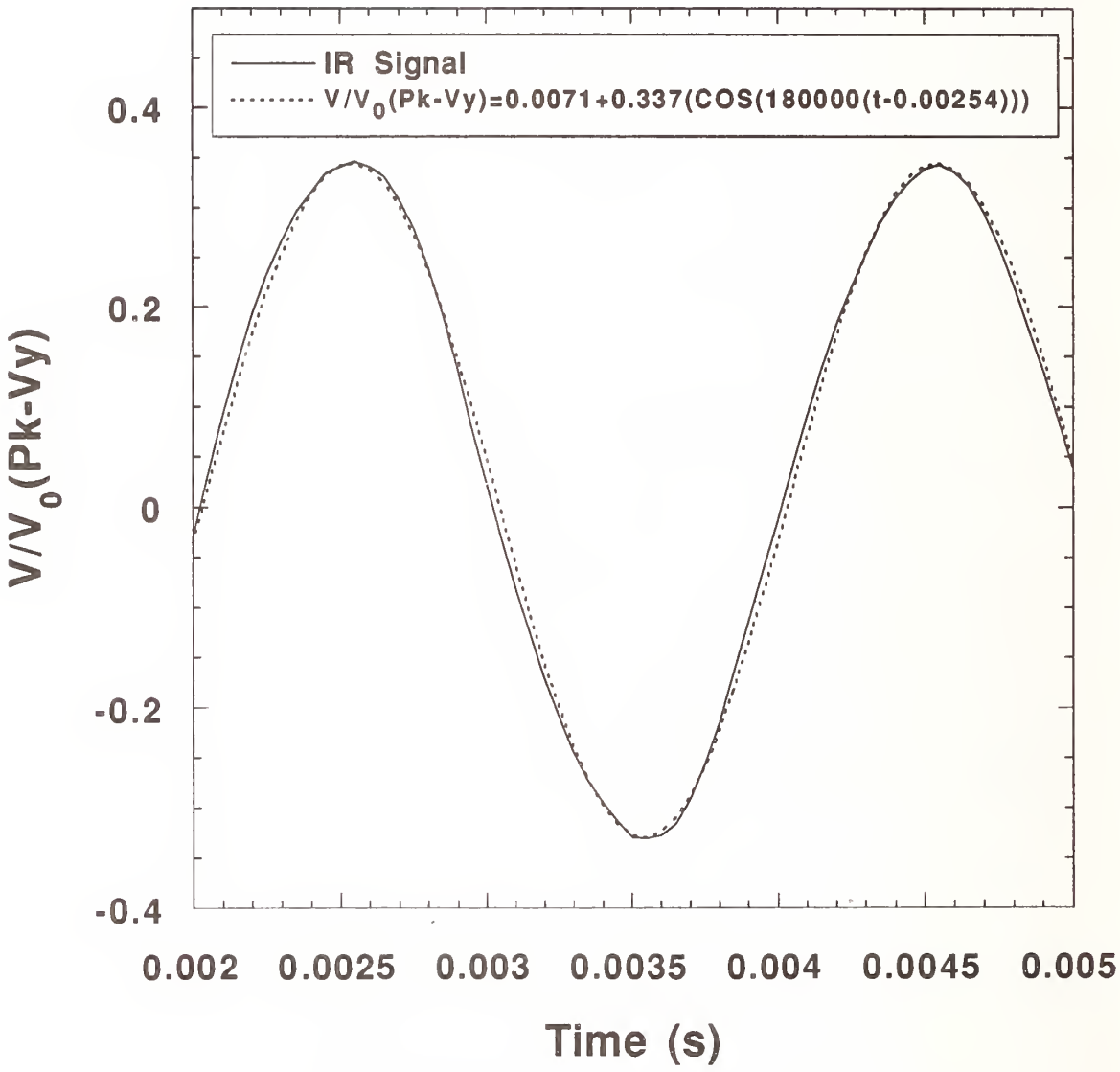

Figure 63. The reduced voltage signal from the DIRRACS is compared with a cosine function on an expanded time scale.

compared with the following expression:

$$V/V_0(Pk-Vy) = 0.0071 + 0.337\cos[180000(t-0.00254)]. \quad (48)$$

The cosine behavior arises from the IR beam leaving the wide-band-pass filter being approximately the same size as the opening on the chopper blade. As a result, as the blade rotates, first an increasing fraction and then a decreasing fraction of the IR radiation passes through the opening. This pattern differs from the case of a beam narrow relative to the chopper opening where the voltage increases linearly with time while the beam passes through the opening in the chopper and then decreases linearly while the beam is blocked (Molectron, 1994). We show that this linear time dependence can be derived from the equations given above for the pyroelectric detector operation. In the limit of time short compared to the thermal time constant, one finds from Equations (25) and (26) that the pyroelectric current is constant for a step increase in the radiant flux. The voltage output of the pyroelectric detector is obtained from Equation (37) with the right hand side replaced with a constant current as indicated below:

$$C\frac{dV}{dt} + \frac{V}{R} = i = \frac{V_0}{R} \quad . \quad (49)$$

Solving for V, we obtain

$$V = V_0(1 - e^{-t/(RC)}) \quad . \quad (50)$$

For the small time limit of Equation (50), the voltage increases linearly with time. When the beam is blocked a similar analysis yields a linearly decreasing signal.

The DIRRACS response to HFC-125 at a mole fraction of 0.1 is plotted in Figure 62. The output signal is normalized by the Pk-Vy voltage in the absence of the agent. The voltage difference between peak to valley is computed and then valley to peak etc. as shown in Figure 62. Using this procedure we obtain 1000 values per second even though we are operating the chopper at 500 Hz. Finally, these results are expressed in terms of mole fraction versus time by use of a concentration calibration curve.

11.3.6 Temporal and Spatial Resolution. The unique feature of the DIRRACS is its high speed of data acquisition. One data point is obtained every millisecond based on the peak-to-valley analysis method. The instrument is therefore capable of measuring the average concentration within the observation volume at 1 kHz. However, the effective temporal resolution can be degraded significantly by the relatively large sampling volume of the current instrument.

The volume sampled by the DIRRACS is a cylinder having a length of 2.8 cm and a diameter of 3 cm. The probe is designed such that the sampled gas must flow through the partially blocked sampling volume. In order to understand how sampling volume can limit temporal resolution, consider an idealized two-dimensional flow of gas perpendicular to the probe consisting of air which instantaneously increases to pure agent (*i.e.*, a step increase). Assuming no flow blockage, a period, τ_p, equal to

$$\tau_p = \frac{d_p}{U} \quad , \quad (51)$$

where d_p is the probe diameter and U is the flow velocity, is required for the step increase to cross from one side of the sampling volume to the other. A flow velocity of 30 m/s yields τ_p = 1 ms. If

the velocity is less than 30 m/s, the concentration will be averaged and the step increase will not be completely temporally resolved. For example, if the flow velocity is 1 m/s, a period of 30 ms will be required for the measured agent concentration to monotonically increase from 0 % to 100 %. In this case, the effective temporal resolution is on the order of 30 ms. Note that the direction of the flow is important. A similar concentration gradient oriented parallel to the flow direction would result in a constant concentration measurement which would depend on the location of the step increase within the observation volume. Partial blockage of the flow will tend to degrade the effective temporal resolution still further. A determination of the effective temporal resolution in a given experimental configuration requires a detailed understanding of the flow velocity. Such spatial averaging effects will tend to average (*i.e.*, smooth) agent concentration fluctuations except in the case of high-speed flows.

11.3.7 Signal-to-Noise Behavior. It is the standard deviation, σ, associated with the peak height that is the relevant measure of noise for the highest speed operation, since this is the quantity measured at 1000 Hz. We expected that a signal-to-noise ratio of at least 100 would be required to obtain adequate instrument performance when expressed in terms of agent concentration. The Pk-Vy voltages for the blue DIRRACS were about 2.0 V and about 1 V for the black DIRRACS with no agent present when operating the IR source at 50 V, which corresponded to about 60 W. When using a low-band-pass filter with 24 db per octave set at 300 Hz to remove low frequency noise, the signal-to-noise was found to be in the range 100-140. A possible negative feature of the low-band-pass filter is to distort the instrument response for a slowly changing concentration. Results presented below in Section 11.3.9.2 suggest that the low-band-pass filter does not substantially effect the response of the DIRRACS for a release lasting about 240 ms.

The manufacturer's specification for the noise of the pyroelectric detector is 1.1 μV at a frequency of 15 Hz. The unamplified signal corresponding to a 1 V output of the DIRRACS is 10 mV. Assuming a noise equal to 0.7 % of the signal corresponds to 70 μV. So the apparent noise is a factor of 70 greater than the manufacturer's specification. The difference in frequency between the manufacturer's specification and our measurement is not the source of the difference, since the dominant detector related noise sources, the Johnson noise of the detector itself and the noise associated with the preamplifier (Putley, 1970), should decrease with increasing frequency. Other contributions to the noise could be mechanical vibration from the chopper and lack of temperature control of the detector housing. The amplified signal at 500 Hz with the IR source off is about 40 mV with a dc offset from zero of about 50 mV compared to a signal of 1 V to 2 V with the source on.

The responsivity of the detector is approximately 1 V/W at 500 Hz. The nominal 10 mv to 20 mV unamplified detector output corresponds to a radiant flux of 10 mW. The maximum power rating for the detector is about 50 mW, so it is operated well below this limit. For an 800 K blackbody source, the total flux emitted from a unit surface area integrated over all wavelengths is obtained from the Stefan-Boltzmann law:

$$\Phi(T) = \sigma_e T^4 \quad , \tag{52}$$

where σ_e is the Stefan-Boltzmann constant (5.67×10^{-8} WK^4/m^2). This corresponds to 2.32 W/cm^2 or a total of about 8.4 W for the total source area of 3.6 cm^2. The total heat produced by the heater is estimated as 60 W when operated at 50 V dc. To estimate the radiant flux emitted and transmitted by the narrow-band-pass filter, we assume a flat source area A_s of 3.6 cm^2, that the source is 3.0 cm from the collection tube with a 2.86 cm diameter, and that the source is Lambertain. Every point on the source is treated as if it has the same collection angle as the center of the disk,

$$\Phi(\Delta\lambda) = 0.19\pi L_{\lambda} A_s \Delta\lambda \quad . \tag{53}$$

The simplified wavelength dependence results form the small variation in L_λ with a nominal value of 1.8×10^8 W sr^{-1} m^{-3} for the small change in λ, $\Delta\lambda = 0.517$ μm. The resulting value is 20 mW, which is twice the 10 mW flux actually detected. Additional loss terms not accounted for include reflection losses by the windows, losses in the transfer tube, losses at the chopper, losses in the collector, and reflection of some radiation from the detector.

11.3.8 Instrument Calibration. The calibration of the DIRRACS was a major component of this study. The approach was to flow a known concentration of agent through the sample volume and to measure the Pk-Vy signal. A unique computer-controlled calibration system described in Section 11.2.4 was used to generate flows of agent having a specified concentration. In operating the system one would simply enter the desired concentration and the software/interface would change the air and agent mass-flow controller settings to give the desired concentration within a few seconds. The ability to rapidly change the concentration was an important feature because of the possibility of drift in the source or detector over a long period of time. The system was designed to provide a constant mass-flow rate. The volumetric flow rates varied from about 167 cm^3/s (10 L/min) for pure air to about 67 cm^3/s (4 L/min) for pure agent.

After leaving the mixing chamber, the agent/air mixture entered the cell surrounding the sensing volume of the DIRRACS. Three different cells were fabricated for containing the agent/air mixture as it flowed through the DIRRACS. The first device consisted of a rectangular plastic chamber having dimensions of 20 cm × 20 cm × 40 cm. In the development phase, all of the components of the DIRRACS were located in the cell. There was a small fan to provide mixing within the chamber. Later this facility was modified so that only the tube assembly was in the cell. Because of the long time required to reach a constant concentration, on the order of 10 min with a nominal flow of 167 cm^3/s (10 L/min), a smaller chamber was designed as illustrated in the top portion of Figure 64. The total volume was reduced to 320 cm^3. In this case 5 s were required for displacing the cell volume (the total volume of the flow to equal the chamber volume) at the minimum flow of 67 cm^3/s (4 L/min). However, experimentally, we observed that the time required to reach steady-state behavior was up to 100 s. It was thought that the long time resulted from poor mixing in the measurement volume. A third cell was fabricated allowing direct flow of the agent through the cell. It consisted of a cylindrical tube with a diameter slightly larger than the pathlength of the DIRRACS. Oversized openings were machined to allow clearance for the heater wires and purge tube, and the cell was sealed to the DIRRACS using fiberglass tape. A subsequent addition of a cooling coil to the IR sensor housing required that the cell be split in half along the axis of flow to allow mounting to the DIRRACS, since it could no longer slip on over the housing. Screens were placed near the inlet and outlet of the cell to ensure uniform flow. With a cell volume of 90 cm^3, only 1.3 s was required for displacing the cell volume. Empirically it was found that 10 s was sufficient time to reach a steady state. Some fraction of the 10 s is the settling time of the flow controllers to a new voltage setting.

The standard calibration procedure was to allow 10 min after energization for the IR source to reach a steady temperature. Figure 65 includes data on temperature versus time for a similar IR source to the one located in the DIRRACS. The ZnSe window was removed to provide access. The thermocouple was attached to the heating coil with high-temperature cement. The temperature typically varied by less than ± 2 °C over a period of 5 min, which is longer than the period required for a typical calibration. We verified that the system was in steady state by requiring that two Pk-Vy readings taken 1 min apart with air flowing through the cell agreed within 0.5 %. Following achievement of a steady state, the Pk-Vy output was measured for increasing agent concentrations, allowing

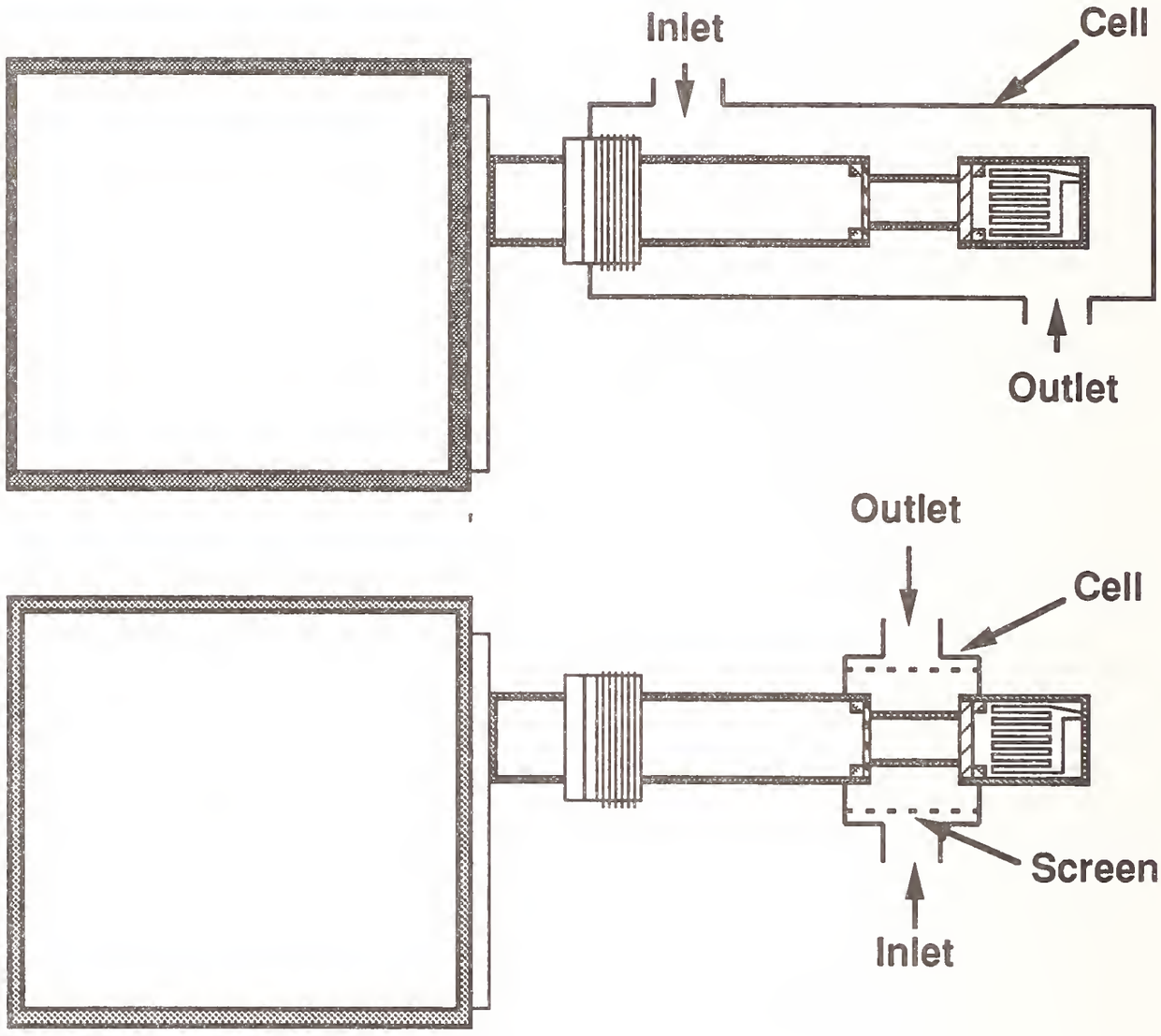

Figure 64. Illustrations of two of the cells used for calibrating the DIRRACS.

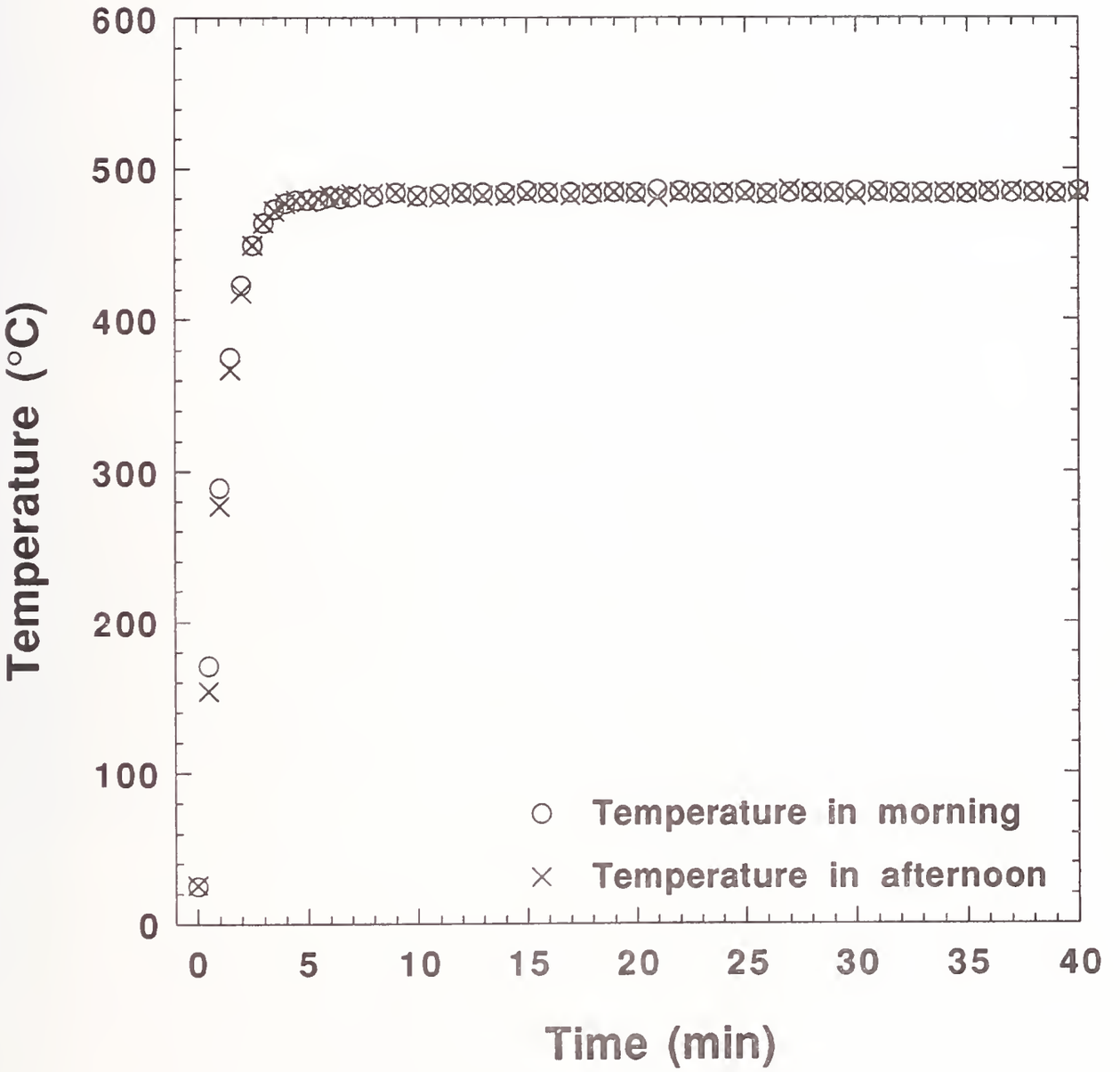

Figure 65. Temperature versus time for IR source with window removed.

about 30 s per concentration; after measuring the highest concentration, a final measurement was made for air to verify the output for air was unchanged. Five to seven concentrations could be measured in 3 min to 5 min. Typical mole fractions were 0.01, 0.02, 0.05, 0.10, 0.25, 0.50, and 1.00. This entire procedure was repeated three times to determine variations in the calibration curve. Typical data are shown for four repeats for HFC-125 in Figure 66 for mole fractions up to 0.25. These results show that the instrument sensitivity is much higher at low concentrations. Calibration data for halon 1301 is plotted in Figure 67. By comparing the two calibration curves, it is seen that the DIRRACS is slightly more sensitive to HFC-125 than halon 1301. This is consistent with the much stronger absorption features for HFC-125 compared to halon 1301 over the wavelength range of the narrow-pass filter (see Figure 54 and Figure 55)

An important quantity for characterizing the performance of the DIRRACS is the uncertainty in the concentration for a given concentration, ΔC, divided by the concentration. The standard deviation based on three repeat calibrations is used as ΔC. Figure 68 shows results based on two repeat series of calibrations for both DIRRACS. We see in all cases that the value of $\Delta C/C$ is less than 0.1. One expects high $\Delta C/C$ for both small C because of the small denominator and for large C because of the flatness of the calibration curve, and one expects the lowest $\Delta C/C$ over the middle range. The decrease in $\Delta C/C$ for a mole fraction of 0.25 for the one test is the opposite of our expectation. Below we provide estimates of $\Delta C/C$ for a rapid release.

During our testing it was noticed that changing the air flow across the detector housing affected the DIRRACS response. A flow effect is of concern since high flows are produced as an agent is released in a dry bay and engine nacelle. A series of measurements were performed to quantify this effect. A small fan with a 10 cm diameter blade was positioned about 5 cm from the IR source housing resulting in an estimated velocity of 5 m/s. Figure 69 illustrates the effect of this flow on the calibration curve. The effect is especially pronounced for high concentrations. For example, for a 0.20 mole fraction, using the calibration curve for the case of no external air flow would lead to a measured mole fraction of 0.35.

A number of measurements were performed to try to determine the cause of the shift in the calibration curve. One conjecture was that the increased air flow cooled the IR source housing and reduced the source temperature. Calibration measurements were carried with filament voltages of 45 V and 50 V corresponding to IR source temperatures of about 450 °C and 500 °C. As shown in Figure 70, there was essentially no detectable change in the calibration curves. This result of no temperature effect is also consistent with the model calculation presented in Figure 57.

A second conjecture for the cause of the discrepancy was based on the difference between the predicted and measured voltage ratios at large concentration. As indicated in Figure 57, the predicted voltage ratio for a mole fraction of 0.25 is less than 0.1, while the measured value is greater than 0.5. It was suspected that the narrow-band-pass filter was allowing longer wavelength radiation to pass to the detector. In our initial spectral measurements, we were limited to wavelengths less than about 15 μm by the optics of the Fourier transform infrared instrument which was used. Later spectra taken with an infrared absorption spectrometer allowed measurements from 2 μm to 25 μm. The results are included in Figure 59. It is clearly seen that there is radiation in the range 11 μm - 15 μm that is transmitted though both the narrow-band-pass filter and the ZnS window. To block the 11 μm to 15 μm radiation, a wide-band-pass filter which transmits radiation in the 8 μm - 10 μm range but blocks at least 99 % of the radiation in the 11 μm - 15 μm range was installed at the end of the IR transmission tube near the chopper. Figure 71 shows a comparison of the original results and the results with the additional band-pass filter installed. We see that there is almost a factor of two decrease in the signal for an agent mole fraction equal 1. This indicates that previously half the radiation was transmitted through this long wavelength region. The spectrum for HFC-125 from 7 μm to 15 μm shown in Figure 55 indicates that the agent absorbs over a portion of the 11 μm to 15 μm

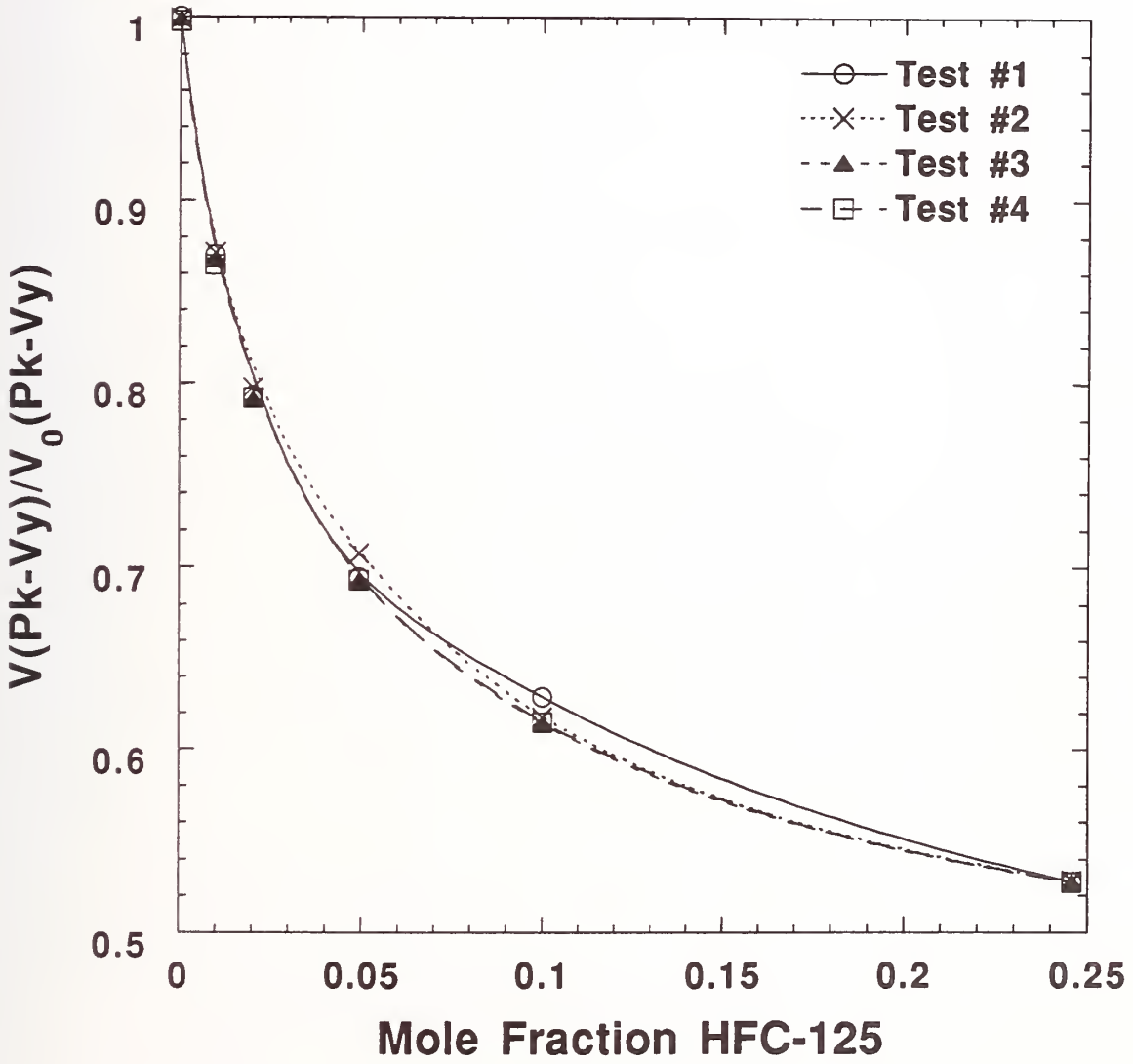

Figure 66. The ratio of the Pk-Vy voltage with various agent/air mixtures versus the mole fraction of HFC-125. Results are presented for four repeat tests.

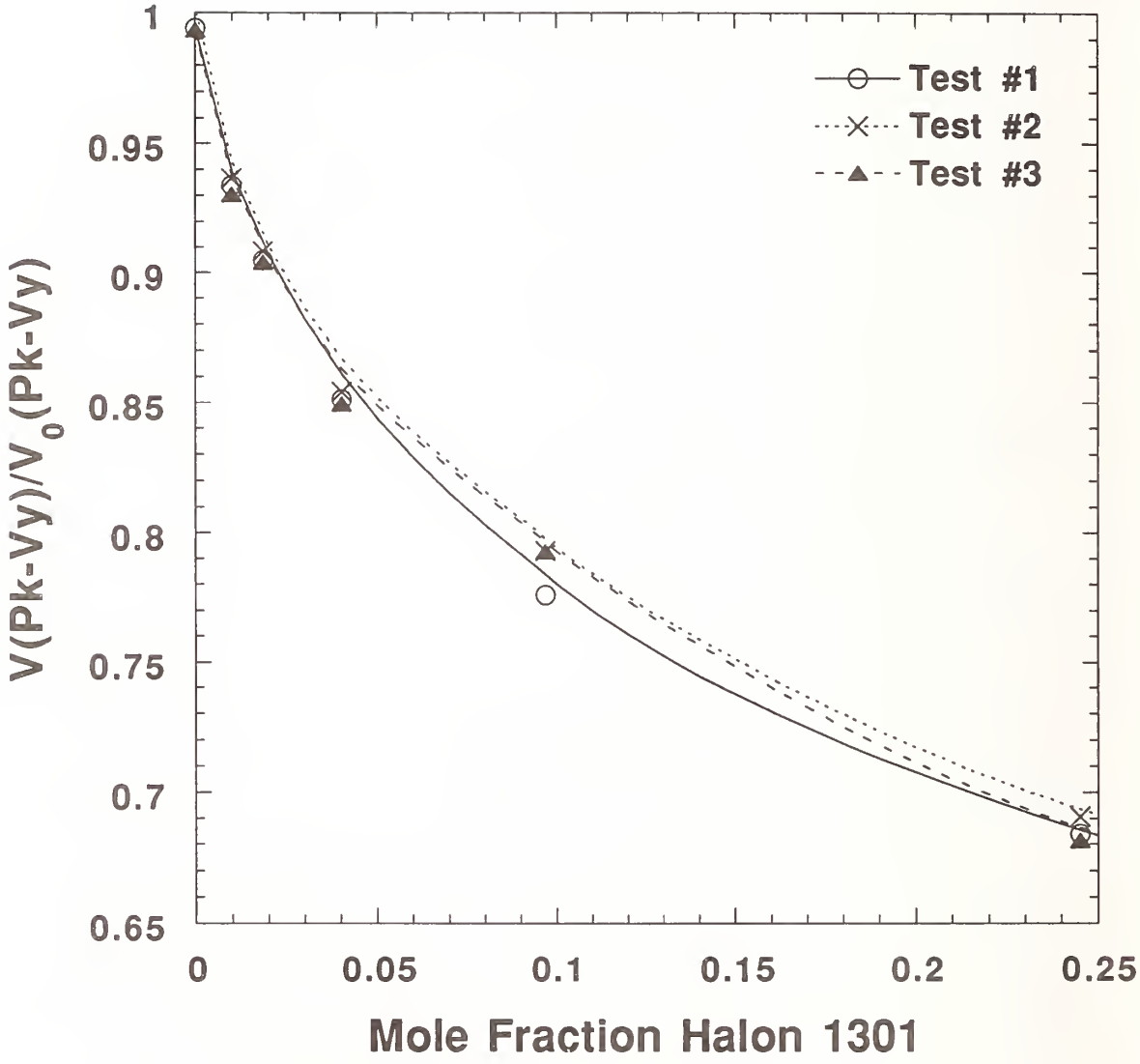

Figure 67. Calibration curves for halon 1301 based on three repeat tests.

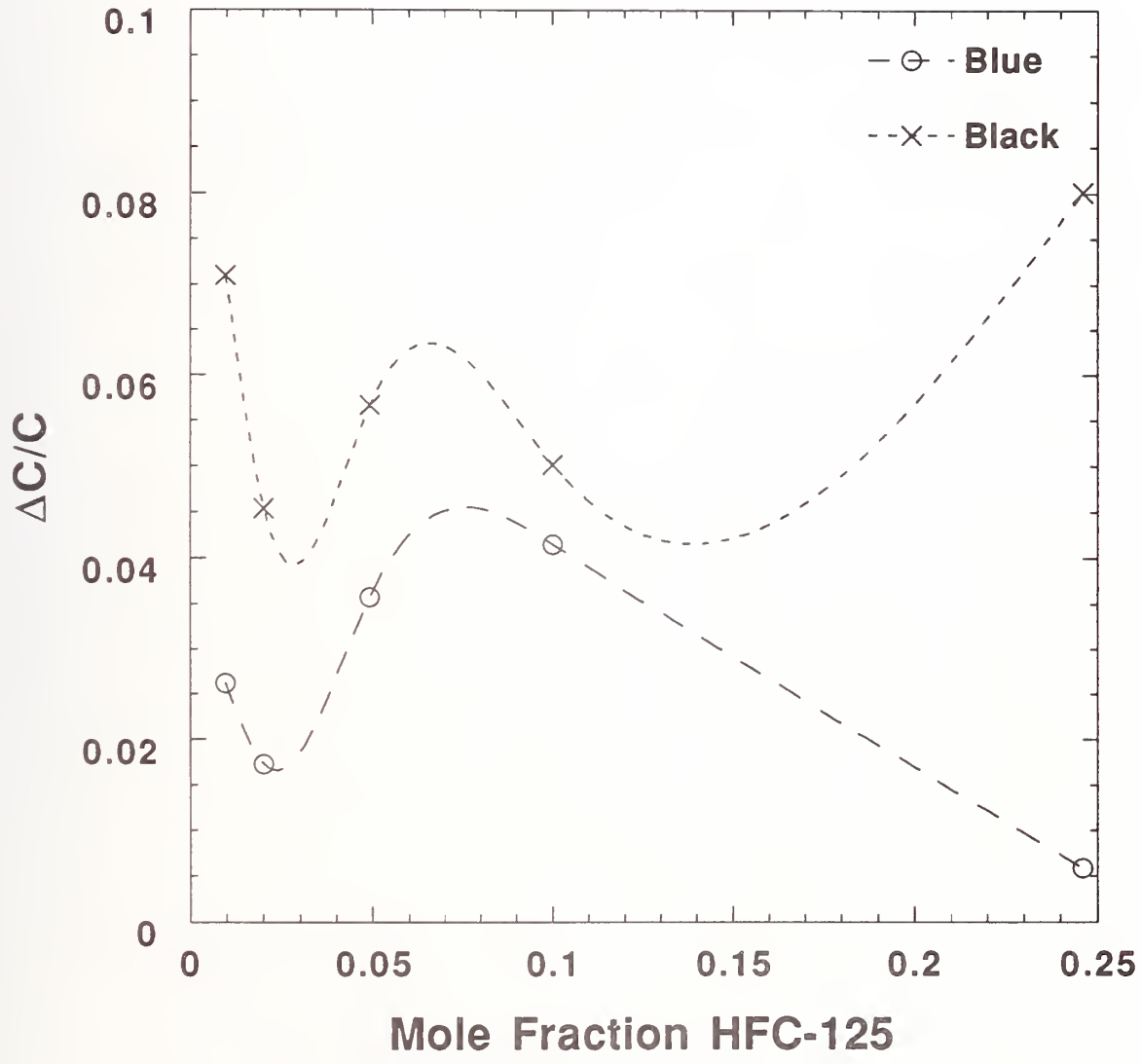

Figure 68. ΔC/C versus C based on three repeat calibrations for both the "black" and the "blue" DIRRACS with HFC-125.

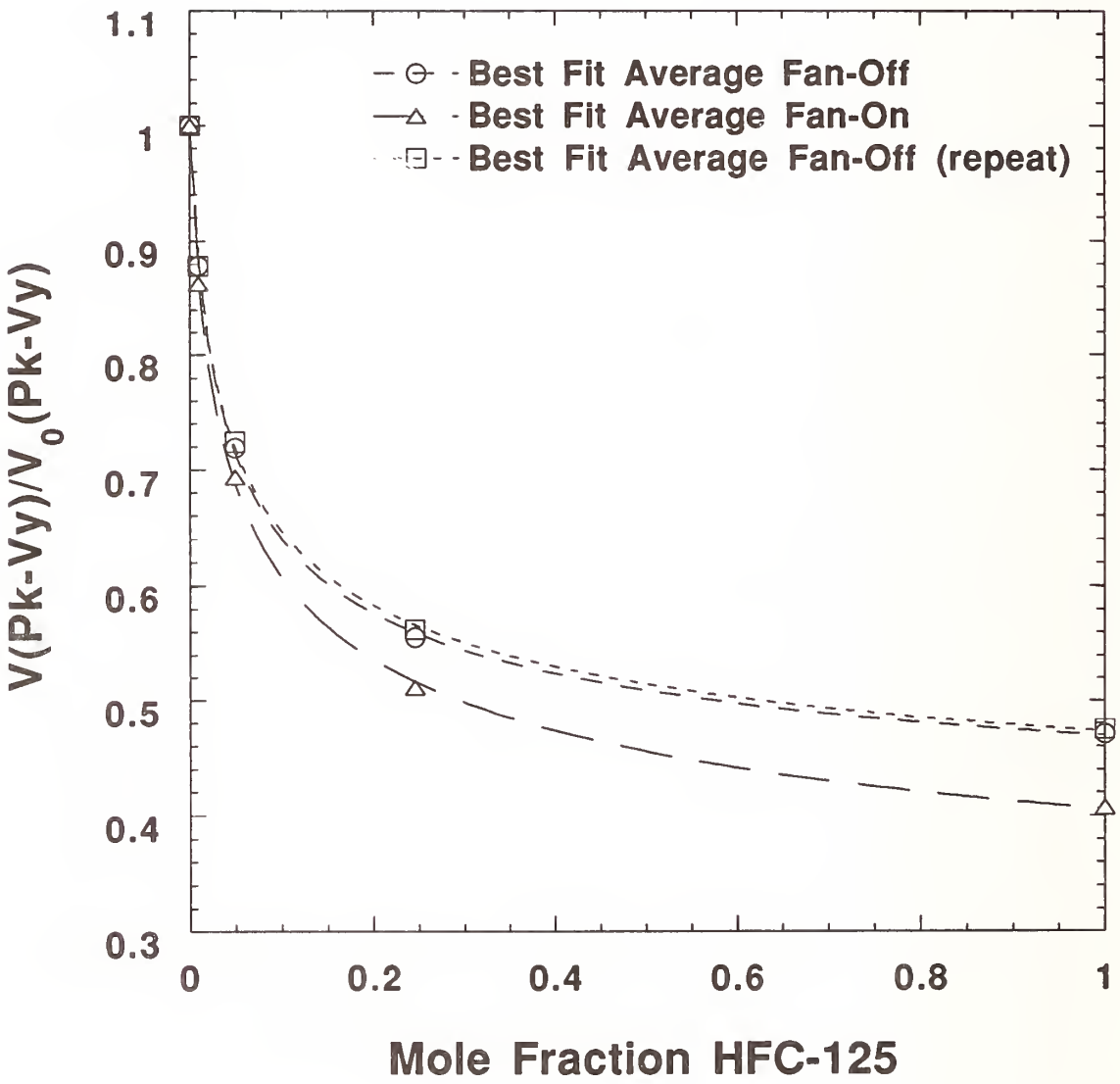

Figure 69. The effect of air flow on the DIRRACS calibration.

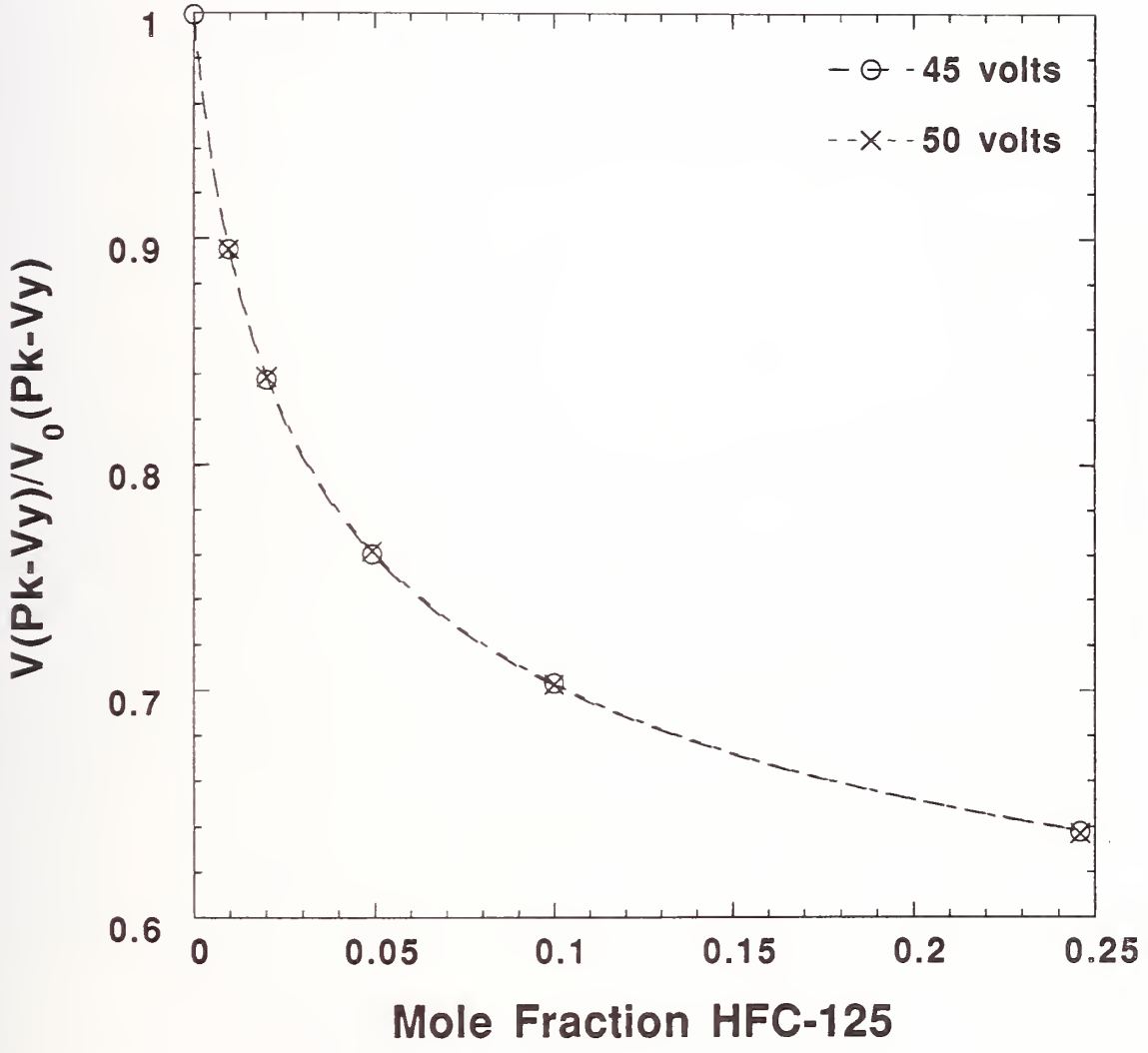

Figure 70. The effect of the source temperature on the calibration curve. Voltage settings of the IR source of 45 V and 50 V correspond to source temperatures of approximately 450 °C and 500 °C.

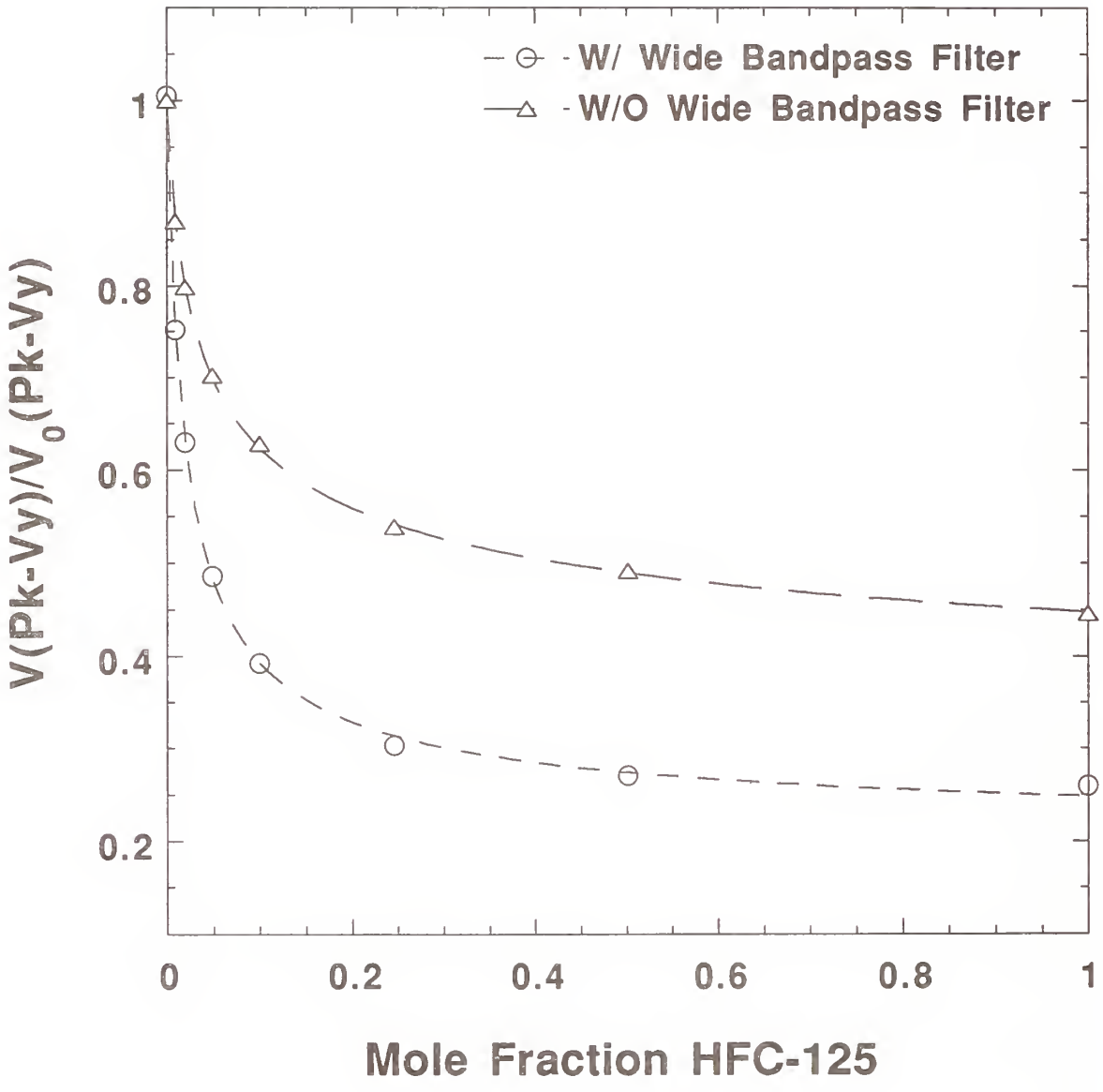

Figure 71. Comparison of the calibration curves with and without the addition of the wide-band-pass filter.

region. The addition of the filter decreased the output signal by about a factor of 3 and also appeared to decrease the signal-to-noise ratio. We also point out that the measured value of about 0.3 at a mole fraction of 0.25 is still larger than the predicted value of 0.07. Possible causes for the remaining discrepancy include the DC offset of the detector and uncertainty in the spectral data of HFC-125.

In Figure 72 it is shown that even with the addition of a band-pass filter there is still a flow effect of about the same order of magnitude as before. Additional temperature measurements were made of the source housing and of the metal collection cone holding the detector. It was observed that the temperature of the housing increased to about 80 °C without the flow and to only about 50 °C with the flow. The resulting temperature change of the agent/air passing through the sensing volume is at most 10 °C. The study of Edgell and May (1953) indicate that an increase in temperature from 30 °C to 160 °C changes the percent transmission at 13.5 μm from about 40 % to 50 %. A gas temperature change of 10 °C is estimated to change the percentage of transmission by approximately 1 % and thus can not account for the observed change in calibration curve with an external flow.

The cone temperature increased by about 5 °C over a 30 min period as a result of heat transmitted down the brass tube through the box and then convectively heating the interior components. Since the pyroelectric coefficient and the band-pass filter transmission curves are temperature dependent, this could lead to a change in response. Figure 73 shows calibration curves for two different temperatures of the conical collector obtained by placing the DIRRACS chassis without lid in the large calibration cell and heating the air in the chamber with a heat gun. This is not an ideal test since there is also flow, however, it does show that heating of the pyroelectric sensor and optical components could be an issue. There was also concern that there could be a gradual heating of the detector from the incident IR radiation. To assess the significance of this effect, the output was monitored, then the beam was blocked for 1 min - 5 min and the output again monitored. It was found that the detector signal changed by no more than 0.5 %. The manufacturers' reported detector drift is 0.2 %/1 °C and interference filter drift is also 0.2 %/1 °C. So the expected effect of a 5 °C temperature drift is at most 2 % which does not account for the measured 6 % change.

Since it could not be determined which thermal effect was responsible for the change in the instrument response, an empirical approach was taken of trying to limit heat transfer from the source to other parts of the DIRRACS by cooling the area around the IR source. Three turns of 3.2 mm diameter copper tubing were soldered to the IR source housing. The water flow through the coil was set at approximately 5 cm^3/s. Figure 74 shows the effect of cooling the housing. It is seen that in this case the same results are obtained both with the fan on and off! Unfortunately, the modified system in its present form is not consistent with the use in an engine nacelle test facility because of the addition of the cooling coil. Below we present field testing results of the units before the inclusion of the cooling coil.

11.3.9 Field Testing of DIRRACS. Two types of testing were performed with the DIRRACS. The first was carried out at the simulated dry-bay test facility at Wright-Patterson AFB. The second was testing with controlled agent releases at NIST in the turbulent spray flame facility.

11.3.9.1 Dry-Bay Testing at Wright Patterson AFB. During the week of July 19-22, 1994, two DIRRACS were tested at Wright-Patterson with releases of halon 1301 in the simulated dry-bay facility. The dry-bay configuration shown in Figure 75 had dimensions of 6.0 m × 1.5 m × 0.3 m (20 ft × 5 ft × 1 ft). One of the DIRRACS was positioned close to the extinguisher on the left side and the second monitor was positioned near the exhaust close to the lower left hand corner. The probe assemblies were mounted to aluminum plates, and the plates were attached to the metal plate on the back of the simulated dry bay. A total of 10 locations were prepared for positioning the DIRRACS. A second opening was cut in the plate for use of a combined aspirated hot-film/cold-wire

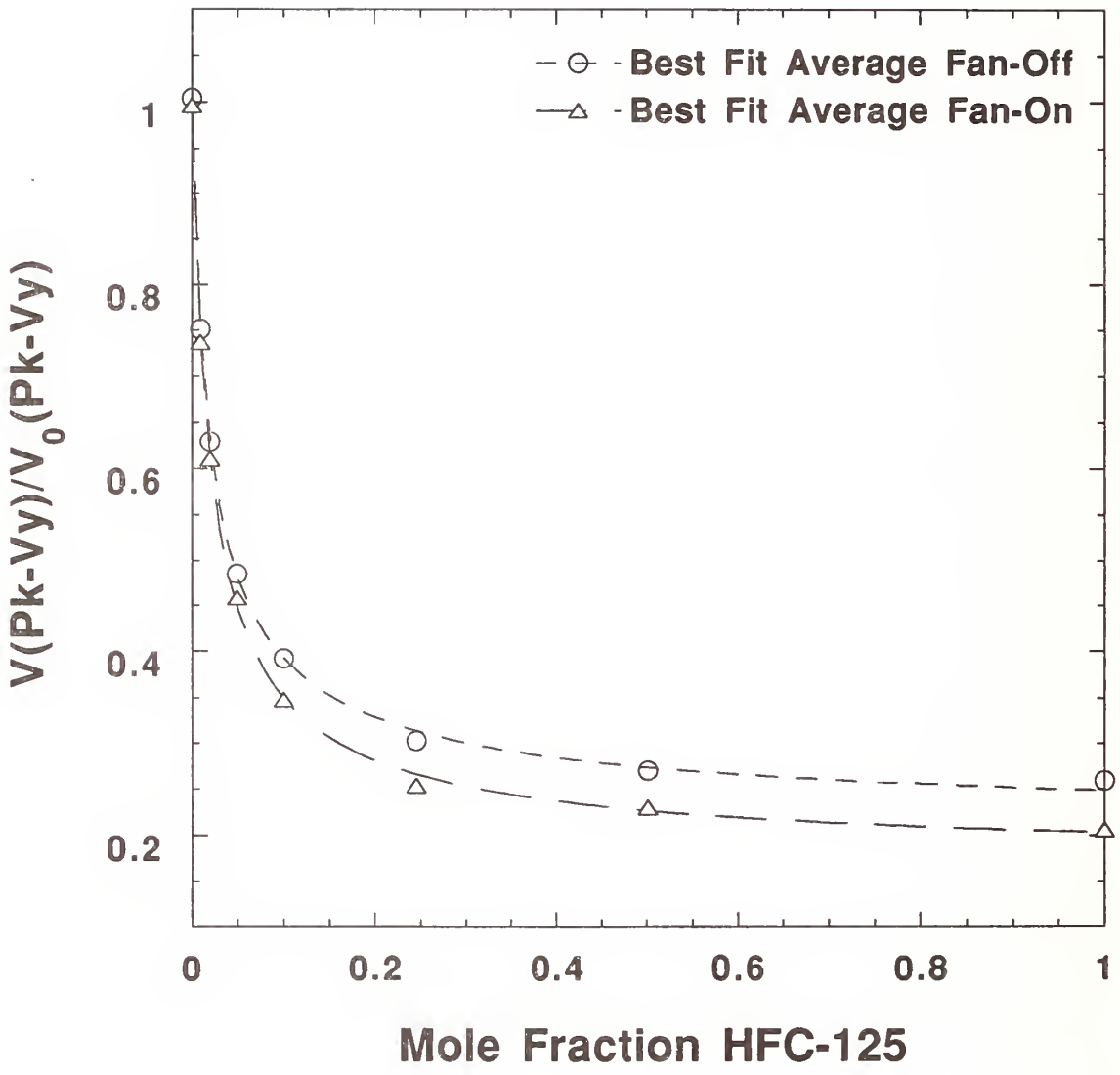

Figure 72. The effect of air flow on the calibration curve of the DIRRACS modified with a wide band-pass filter.

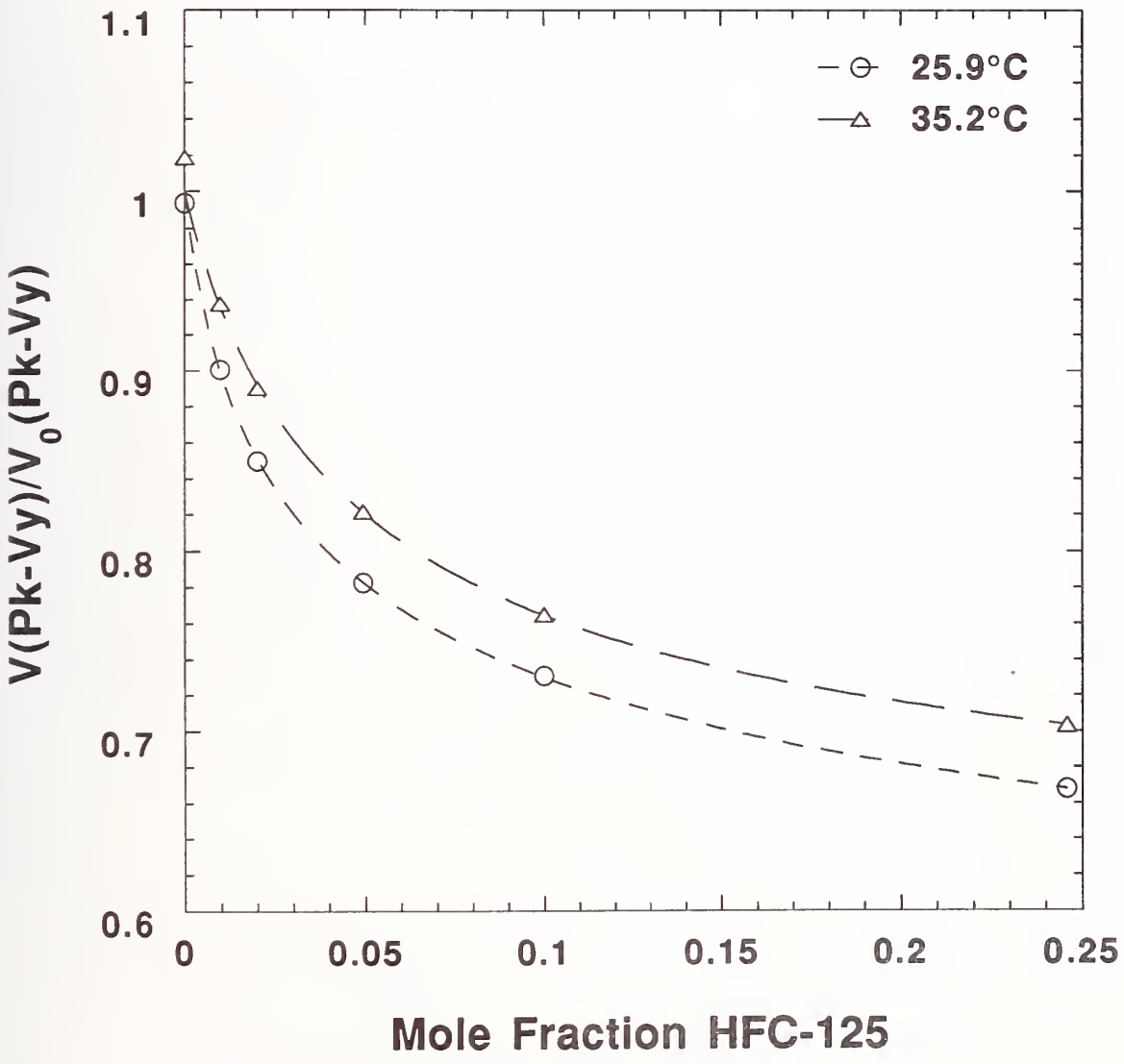

Figure 73. Effect of temperature within the "box" chamber on the DIRRACS calibration.

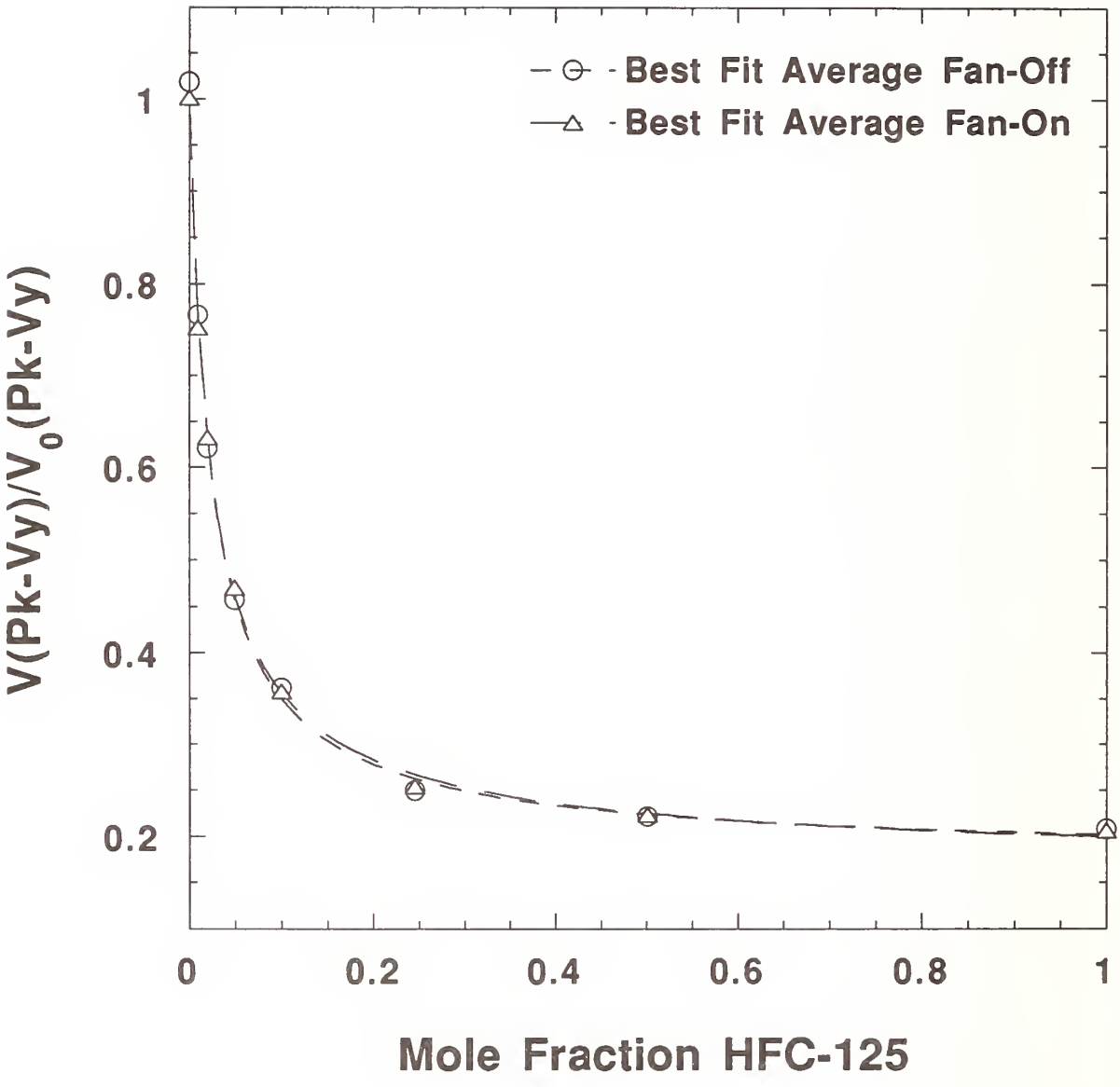

Figure 74. Effect of air flow with water-cooled IR source housing on the DIRRACS calibration.

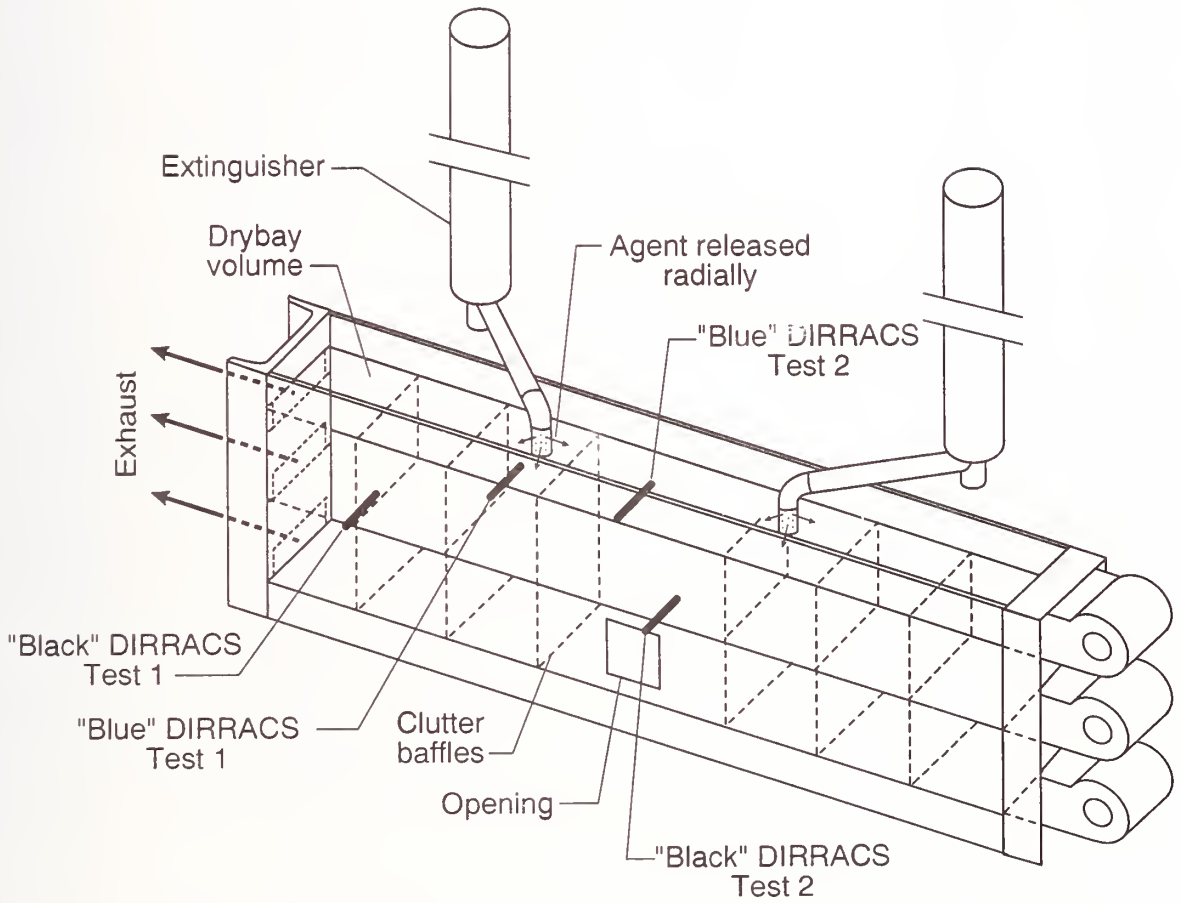

Figure 75. Illustration of simulated dry bay at Wright-Patterson, AFB.

agent concentration probe, which was tested at the same time (See Section 11.2.6).

Figure 76 shows smoothed concentration data versus time as 0.23 kg (0.5 lb) of the agent were released. The agent was released simultaneously from two extinguishers by the firing of squibs, one each, positioned below metal diaphragms. An electrical discharge fired the squibs, which perforated the diaphragms allowing the agent to be discharged. If the agent had been uniformly distributed throughout the volume, the concentration would have been 1.3 % by volume. Initially there is a spike in the readings which may be caused by electrical noise associated with the firing of the squib used to release the agent. Approximately 1 s after release the DIRRACS near the discharge recorded a peak concentration of about 4 %, while the DIRRACS near the exhaust required about 8 s to reach a 1 % concentration. At least 2 s after agent release is required before a noticeable increase in concentration is observed near the exhaust. This time far exceeds the desired 30 ms time to extinguish a dry-bay fire. If the test fires are suppressed by an agent released far from the fire, our results would suggest that the flame extinction is not a direct suppression effect of the agent on the fire.

We also show a second set of data where the DIRRACS probes were moved so that one was near the opening used to simulate the entry point of a projectile into the dry bay and the second was located directly above it nearer the discharges. In this case, the mass of agent released was increased by a factor of four to 0.9 kg (2 lb). It is seen in Figure 77 that there is a momentary 9 % spike in the concentration near the exhaust for about 100 ms and then a decrease to about 1 %; on the other hand, near the discharge the concentration builds up to about 40 % 2 s after the discharge. We suspect that the value of 40 % may be a factor of two higher than actually present based on the flow effect discussed in the previous section. It is noteworthy that these are the first time-resolved dry-bay measurements that have been made!

In the course of carrying out the tests we encountered several difficulties. There was a problem with false-trigger signals apparently arising from the high noise on the transmission line from the Wright-Patterson control system to the NIST data-acquisition system. We ran a total of six tests, but only two gave useful data. Secondly, there appeared to be electrical interference arising from the squib firing, which initiated the agent release. At the time, the DIRRACS was grounded to the instrument chassis; however, the squib is grounded to the dry bay, which is in physical contact with the instrument chassis. To correct the problem, we now have a separate instrument ground. The final problem was an apparent leak around the ZnS window on the light transmission tube for one of the DIRRACS, which was corrected back at NIST.

While no engine nacelle testing was performed, it was found that the DIRRACS was compatible with the opening in the engine nacelle test facility.

11.3.9.2 Testing in the Turbulent Spray Burner Facility at NIST. The turbulent spray burner facility (see Section 9 of this report) at NIST allows the release of a pulse of agent from a 6.5 cm diameter tube. Both the concentration and duration of the pulse can be controlled. A combination of radial injection ports for the agent into the air stream and two sets of screens ensured uniform mixing of the agent with the air. Typical test conditions were an agent release mole fraction of 0.08 for 200 ms. Both DIRRACS probes were placed in series just downstream of the flame stabilization disk. The air-flow velocity was on the order of 20 m/s. Figure 78 shows the peak-to-valley voltages recorded during one of these tests for HFC-125 with the agent first flowing through the "black" DIRRACS and then the "blue" DIRRACS. Using the appropriate calibration curves the data is converted into concentration versus time. The resulting curves are shown in Figure 79 and 29 point smoothed curves are shown in Figure 80. The solid horizontal line is the expected concentration based on the known amount of agent released during the test (0.088 mole fraction). It is seen that the blue DIRRACS result is about 33 % greater than the actual concentration while the black DIRRACS is about 90 % greater. The differences between the measured and predicted results are thought to result

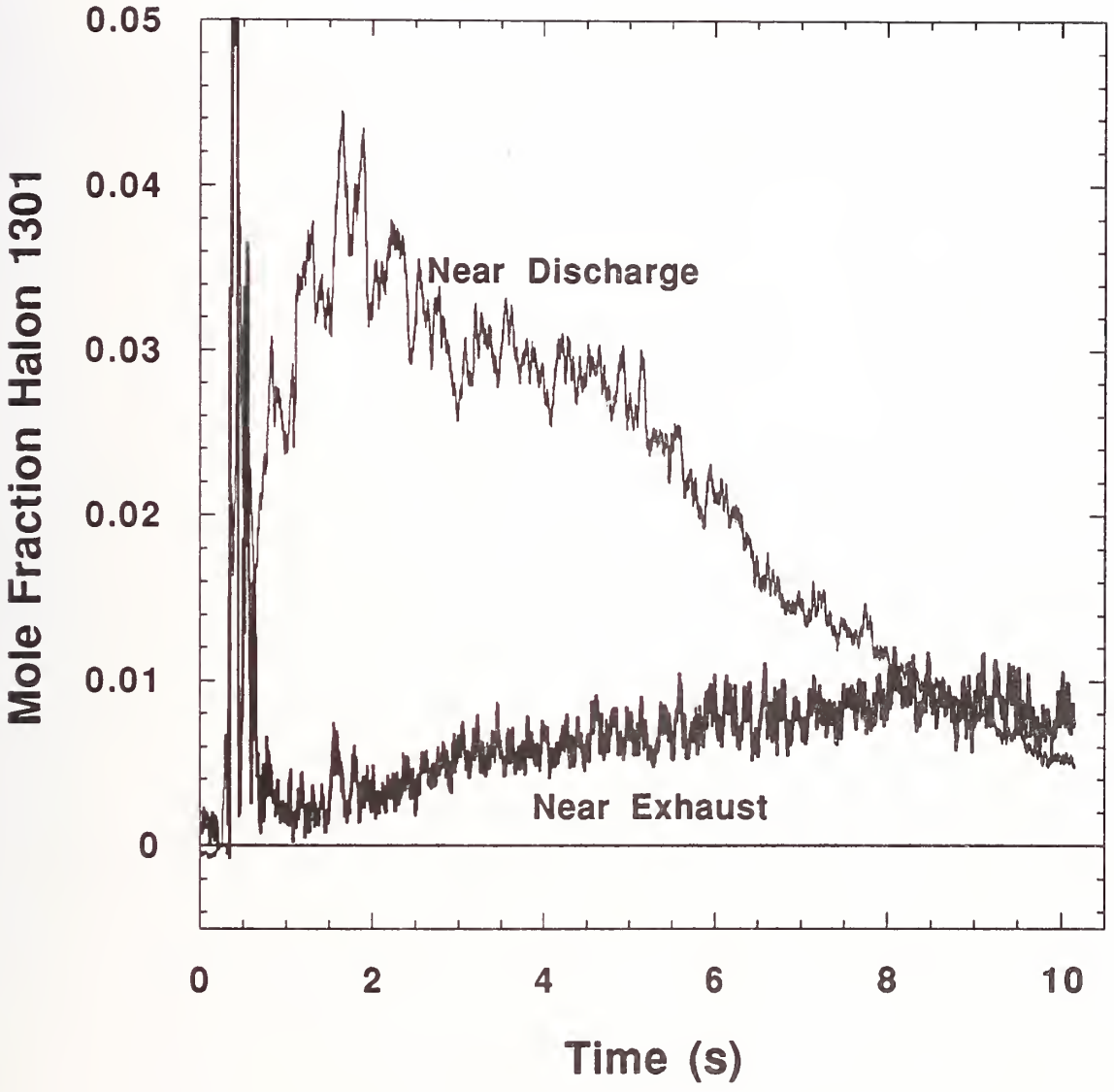

Figure 76. Concentration versus time for the total release of 0.23 kg (1/2 lb) of halon 1301. A 29 point smoothing of the data has been used. The exhaust position is at the far left side of the facility.

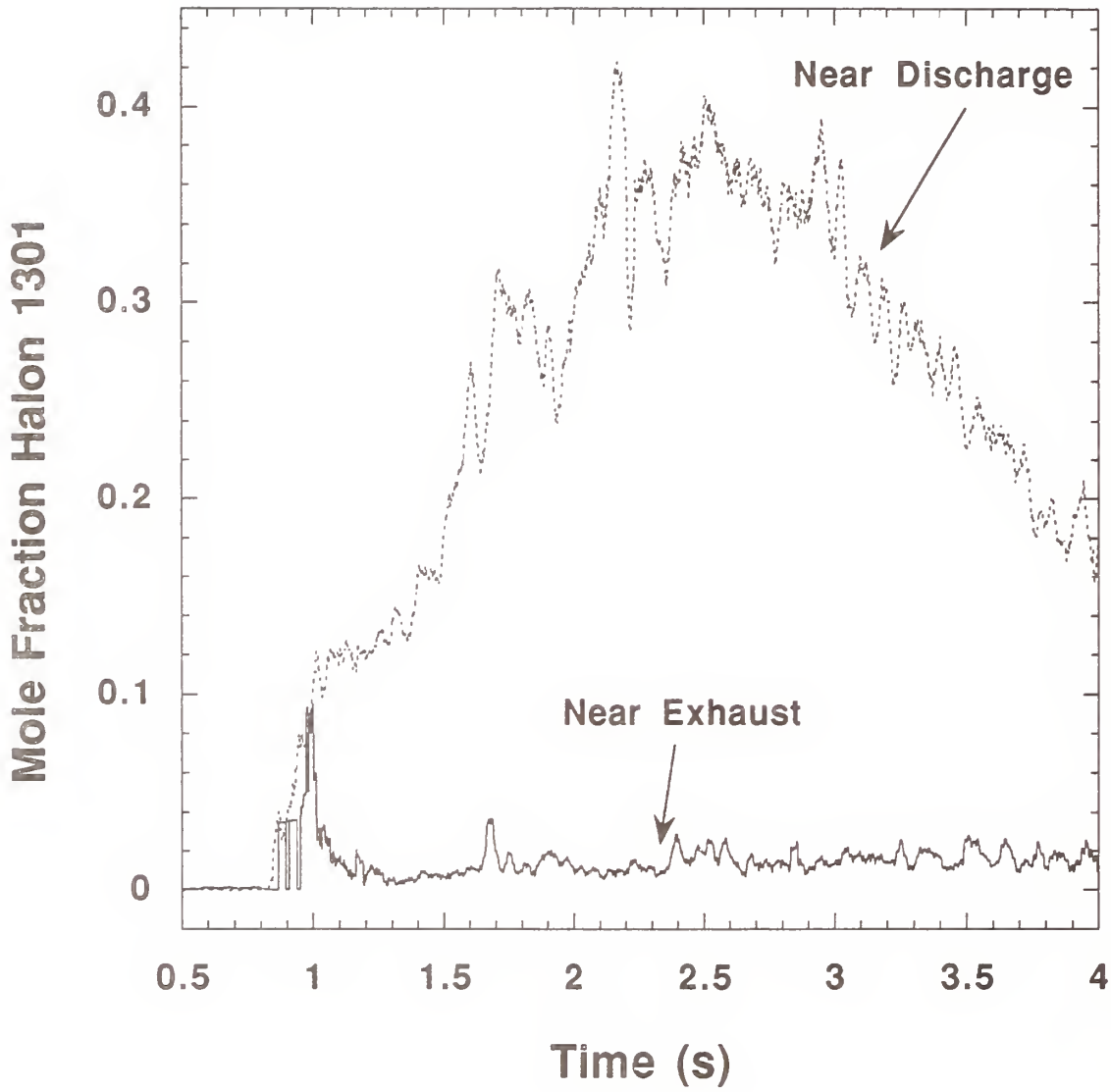

Figure 77. Concentration versus time for the total release of 0.9 kg (2 lb) of halon 1301. The exhaust position corresponds to the opening in the front center of the facility.

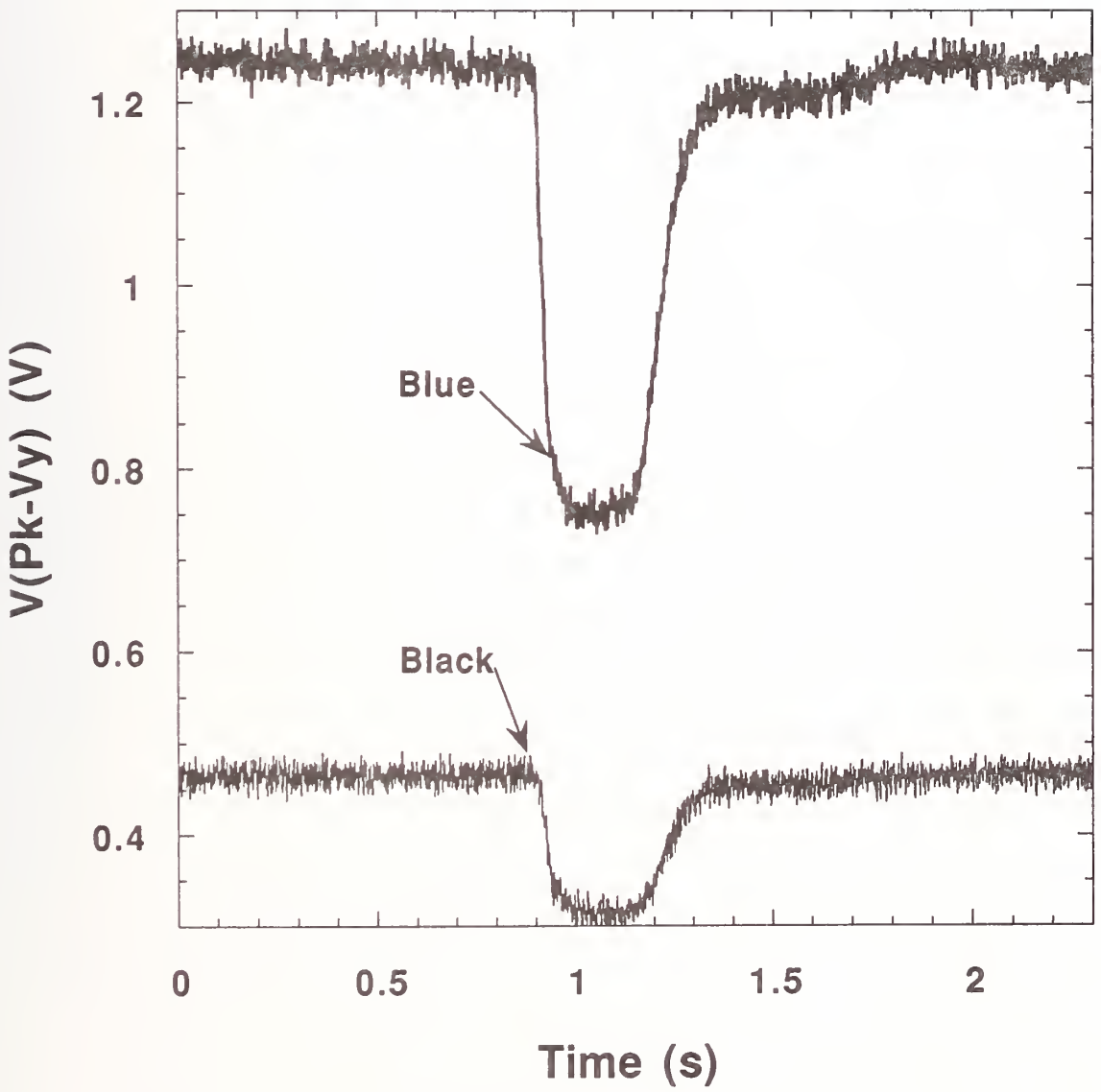

Figure 78. The Pk-Vy voltage is plotted versus time for a release of HFC-125/N_2 mixture from a 6.5 cm diameter pipe at a velocity of about 20 m/s.

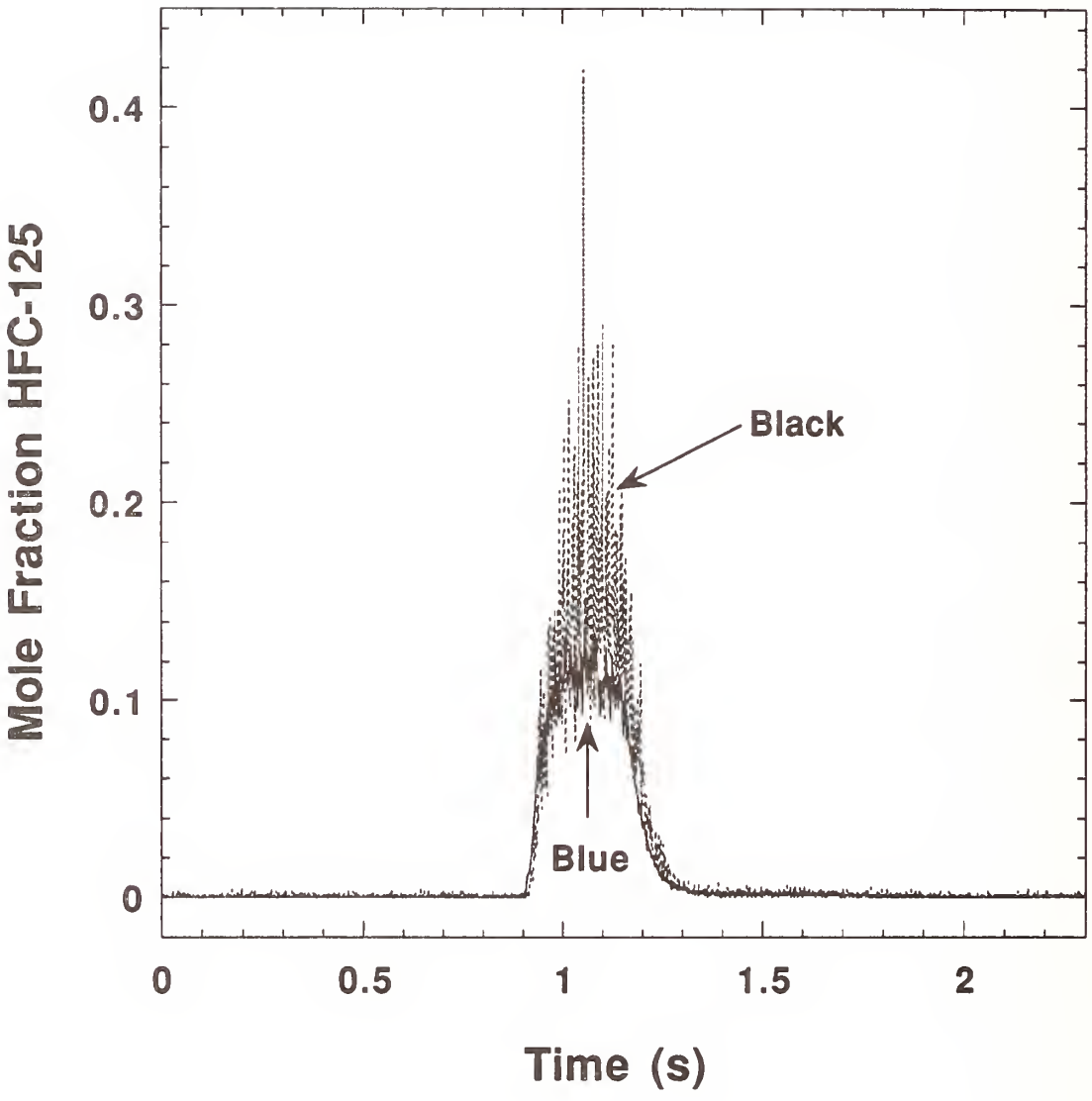

Figure 79. Concentration versus time for a HFC-125 release into the turbulent spray flame burner based on the analysis of the data in the previous figure. The data is not smoothed.

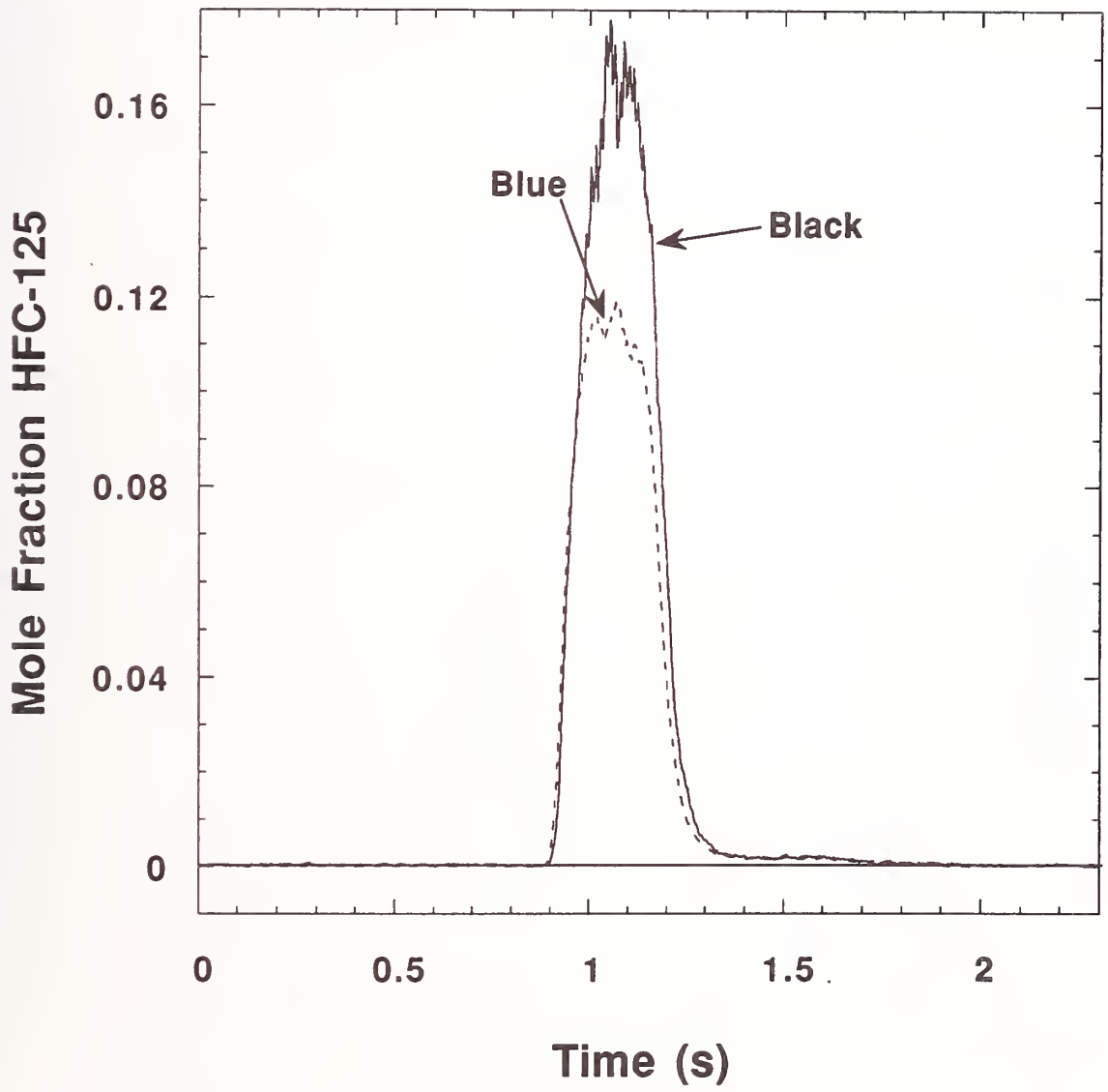

Figure 80. A 29 point smoothing of the data in the previous figure for a HFC-125 release. The solid line represents the nominal concentration for the release.

from the calibrations for the instruments being effected by the flow as discussed in the instrument calibration section.

While the absolute concentration is in error, the duration of the concentration pulse measured by the DIRRACS of 240 ms was in good agreement with both the predicted response time and the output of the combined aspirated hot-film/cold-wire agent concentration probe. Furthermore, this good agreement indicates that the low-band-pass filter used with the DIRRACS does not qualitatively distort the response for the conditions of this release. The peak for the DIRRACS concentration is rounded while the combined probe measured concentration has a trapezoidal shape with an extended flat section. We speculate that the difference is caused by the much larger probe volume of the DIRRACS compared to the combined sensor.

The value of $\Delta C/C$ is 0.12 for the blue unit and 0.34 for the black unit based on 30 ms of unsmoothed data over the flat period. The value for the blue unit is about 3 times larger than the value of $\Delta C/C$ obtained for the calibration curves, and the value for the black unit is about 6 times larger. The cause of this large decrease in performance during actual testing is not known. One possible factor is that the agent uniformly fills the sensing volume during the calibration but does not during the test release.

An effort was made to perform a final test with a cooled sensor, but the results were not conclusive. Components were used from both devices because the heating element burned out in the blue DIRRACS and the only wide-band-pass filter was mounted on the blue DIRRACS. The noise level was high, but the results indicated an instrument signal appreciably greater than the expected value. One possible reason is that the cooling coil is not adequate to fully cool the infrared source housing. The flow in the burner, which is faster than that present during the calibration measurements, may cause additional cooling of the source housing, thus affecting the output of the instrument.

11.3.10 Summary and Recommendations. The concept of using an incandescent source and a pyroelectric sensor for a millisecond time response fire-agent concentration measurement has been validated, even though the original instrument developed on this principle, the Fire Extinguishing Agent Sensor (FEAS), was found lacking in performance. The sensor output signal of the FEAS was dependent on frequency and had a low signal-to-noise ratio. Modelling of a modified FEAS with a flat frequency response indicated possible application as a qualitative probe.

An improved system, designated as the DIRRACS, was developed which has a stronger infrared source, larger area detector, and wider IR band-pass filter compared to the FEAS. The use of an optical chopper produces a millisecond time response, but the sample size can limit the effective time response for velocities less than 30 m/s. The total cost of the components is less than $5,000. The DIRRACS is compatible with both dry-bay and engine-nacelle test facility at Wright-Patterson AFB.

The current design has an average uncertainty, $\Delta C/C$, in the repeatability of the concentration calibrations of 0.05 for the blue unit and 0.12 for the black unit at the 95 % confidence interval. However, data collected during an actual release indicated larger uncertainties of $\Delta C/C$ of 0.15 and 0.40 respectively. A more comprehensive uncertainty analysis is not warranted until the large effect of flow on the instrument response is eliminated.

This study includes the first measurements of the dispersal time of an agent in the dry-bay test facility at Wright-Patterson AFB. The preliminary measurements indicate a relatively long time on the order of a few seconds for dispersal of the agent throughout the large dry bay. This information has important implications about the mechanism of extinguishment when the fire is far from the release point of the agent. If the fire is extinguished under these conditions, the mechanism must not involve a direct interaction of the agent with the fire if one assumes the presence of the fire does not affect the distribution of the agent. More research is needed to understand what the controlling mechanism is for flame extinction.

One major obstacle which must be overcome before the DIRRACS can be used for quantitative concentration measurements is the effect of the surrounding flow on the instrument response. Because of the large flow effect, the DIRRACS output could be in error by 50 % at high flow velocities for agent concentrations in the range 30 % - 100 %. We attempted to cool the source housing to minimize the effect of the flow velocity on the housing temperature. The results were encouraging, but not conclusive. Additional development of the cooling system may greatly reduce the flow effect on the instrument output.

A second desired improvement is to reduce the sampling volume of the instrument in order to improve the effective temporal resolution. Such a reduction is feasible, though a number of refinements may be needed to offset the reduction in signal. These include providing a constant temperature for the detector housing, improved acoustic isolation of the sensor, coated windows, polished light-transmission tube, and optimized collection cone. The first two of these refinements were crucial in the development of an accurate CO_2 gas monitor using a pyroelectric detector by Takeuchi *et al.* (1993).

Another issue to be resolved is the possible effect of the use of a low-band-pass filter on the temporal response of the DIRRACS.

11.4 Review of Statham and Halonyzer Extinguishing-Agent Concentration Recorders

Two instruments have been certified by the FAA for measuring halon 1301 concentrations within a nacelle during certification of fire-extinguishment systems. These are the Statham analyzer manufactured by Statham Laboratories of Los Angeles, CA under contract from the United States Air Force and the Halonyzer which is based on similar design principles as the Statham analyzer and was produced by the HTL Division of Pacific Scientific of Duarte, CA.

The early history of the development of these instruments can be traced through a 1947 Air Force report and a patent (Yanikoski, 1952) filed October 18, 1946 and issued on Feb. 26, 1952. In the original patent application the device was referred to as a "Gas Analysis Apparatus." The basic operating principles of these devices are straight forward. The patent application provides a good description of the basis for the devices in use today.

Figure 81 shows the drawings included in the patent filing. The gas to be analyzed is generally drawn through a tube into the instrument. The instrument inlet is denoted by "5" in drawing "Fig. 1" of Figure 81. The insulated instrument is maintained at a constant temperature using a thermostated heater. The flow enters a heat exchanger (denoted "6" in the drawing) which heats the gas flow rapidly to a predetermined temperature. Once the gas has been heated it enters a restriction made of porous material ("13" in the drawing) which ensures viscous flow and results in a pressure drop as a result of its resistance to flow. For these flow conditions the resulting pressure drop, ΔP, is

$$\Delta P = c_2 \mu Q \ , \tag{54}$$

where μ is the dynamic viscosity, Q is the volumetric flow rate and c_2 is a constant. Fittings "17" and "18" are placed just before and just after the flow restriction to allow the pressure drop to be measured. Any device capable of differential pressure measurement may be used. In the drawing a manometer, "19", is shown.

A second restriction, marked "20" in the drawing, is placed in the flow downstream of the first restriction. This restriction is designed to be a sonic orifice which provides the maximum possible

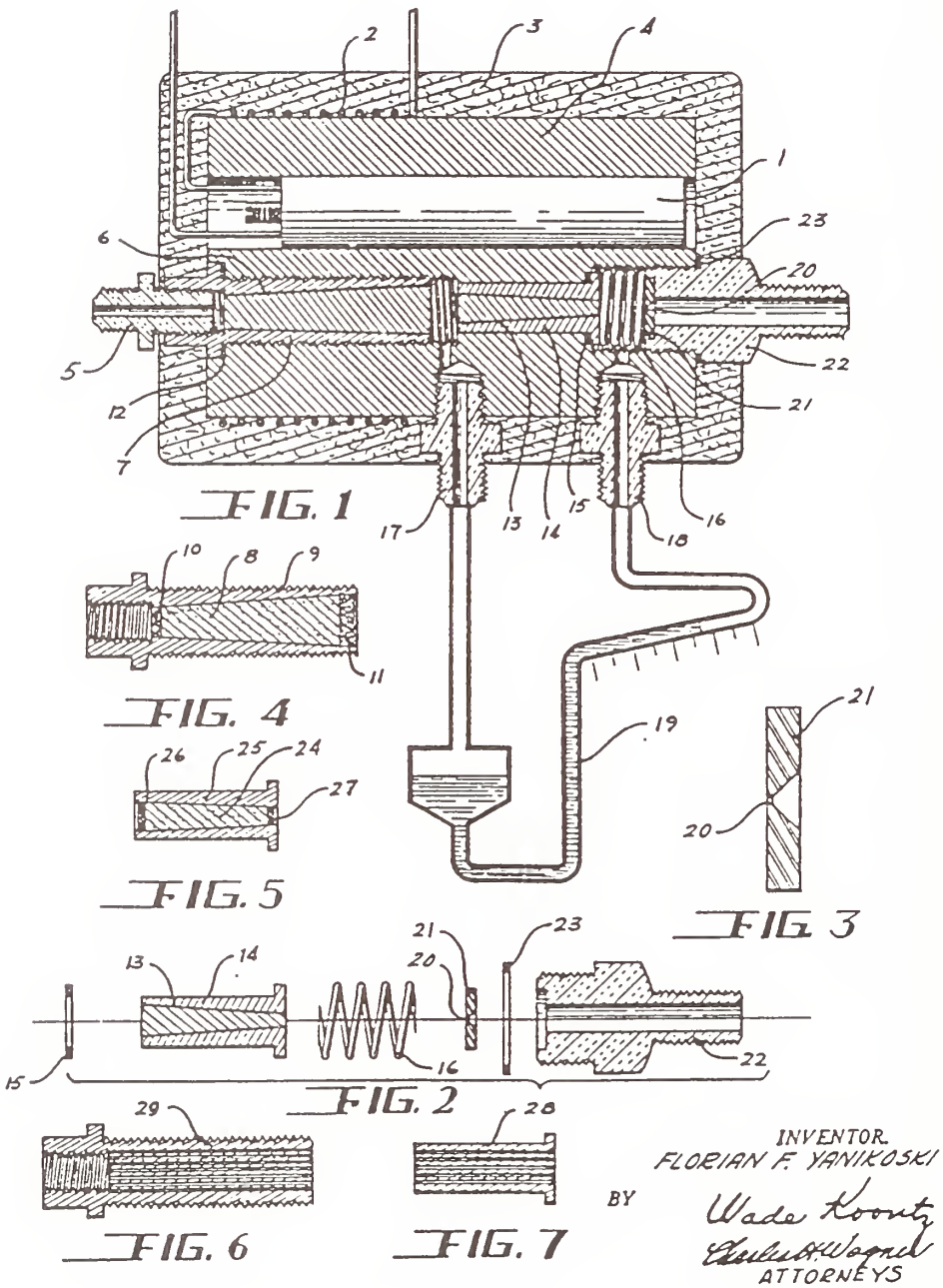

Figure 81. Schematic for a "Gas Analysis Apparatus" reproduced from the United States patent of Yanikoski (1952).

volume-flow rate when the flow is choked, which is generally true when the pressure downstream of the sonic orifice is maintained at less than one half the upstream pressure. The volume-flow rate through a choked orifice can be written as

$$Q = c_2 \frac{\pi d_{so}^2}{4} \sqrt{\frac{gTR}{MW} \gamma \left(\frac{2}{\gamma + 1} \right)^{\frac{\gamma+1}{\gamma-1}}} , \tag{55}$$

where c_2 is a constant, d_{so} is the diameter of the orifice, MW is the molecular weight of the gas, g is the gravitational constant, T is the temperature, R is the universal gas constant, and γ is the ratio of the constant pressure and constant volume heat capacities of the gas. Note that Equation (55) is a different form of Equation (11) introduced in Section 11.2.1.2 during the discussion of aspirated hot-film concentration probes.

Since the temperature is a constant, the volume flow rate through the sonic orifice is only a function of the square root of the product of the gas γ and the inverse molecular weight. The value of Q which appears in Equation (54) should therefore be a unique function of concentration for a given binary gas mixture. In general, values of μ depend on molecular composition and will vary with concentration in binary gas mixtures. By substituting Equation (55), Equation (54) can be rewritten as

$$\Delta P = c_3 \frac{\mu}{\sqrt{MW}} \sqrt{\gamma \left(\frac{2}{\gamma + 1} \right)^{\frac{\gamma+1}{\gamma-1}}} , \tag{56}$$

where MW, μ, and γ all depend on the concentration of species 1 in the binary mixture. Note that one or both of the components can actually be a well defined mixture of gases such as air.

Equation (56) allows the expected variation in pressure drop across the first flow restriction to be predicted when the required molecular properties are known for the pure gases and mixtures. Note that the overall response is a function of a number of variables. In practice, it is common to calibrate the response of the analyzer by recording the measured pressure drop for the pure gases and assuming a linear dependence of pressure change on concentration (such a measurement is often referred to as "Relative Concentration") or by calibrating the pressure drops for a number of known mixtures and curve fitting the resulting pressure changes to the known concentrations.

A discussion concerning the response time of the instrument was not provided by Yanikoski, but it was stated that "One object of the invention is to provide a gas analysis apparatus capable of very high speeds in responding to a change in the composition of the sample."

New and Middlesworth (1953) reported extensive characterization tests of the first Statham analyzer (Model GA-1) delivered to the Air Force. They reported that the specifications for the instrument were:

1. An instrument capable of continuous recording of agent concentration for gases drawn from eighteen regions,
2. A response time of 0.1 s to a concentration change of 100 %,
3. A measurement error not to exceed ± 3 % over the full concentration range,
4. Accurate measurements over normal ranges of temperature and pressure, and
5. Capable of being operated on flying aircraft.

Figure 82 reproduces a schematic for a typical analyzer cell taken from the report. The primary features discussed in the patent can be seen. The flow enters the heated metal block of the cell as

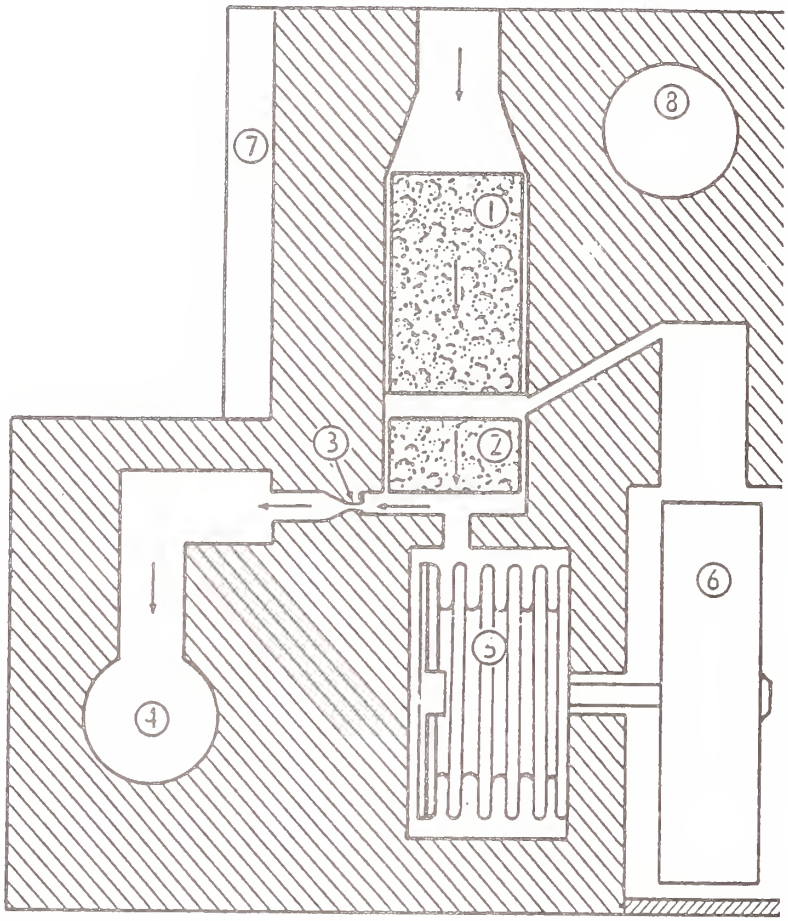

Figure 82. Schematic for a single analyzer cell of a Statham gas analyzer reproduced from the report of New and Middlesworth (1953).

shown. The heat exchanger is a porous plug ("1" in the figure) which is followed by a second porous plug ("2") over which the pressure drop is measured. In this design the pressure change is measured using a pressure-sensitive bellows attached to a Statham strain gage which outputs an electrical signal proportional to the displacement of the bellows. The volume flow rate is controlled by a sonic orifice ("3"). Vacuum was applied through a manifold machined into the metal block. The voltage outputs of the strain gages were recorded using a remotely controlled oscillograph.

The overall analyzer unit consisted of eighteen analyzer cells assembled in two groups which allowed eighteen simultaneous measurements to be recorded. Samples were drawn into the analyzers through electrically heated 1.8 m lengths of copper tubing. New and Middlesworth reported that a period of 0.10 s was required for the instrument to respond (defined as the period required to attain 95 % of the maximum displacement) to an instantaneous increase of carbon dioxide concentration from 0 % to 100 % when the gas was introduced directly into the instrument. When the 1.8 m sample line was used the response time increased to 0.25 s. The increase in response time was attributed to molecular diffusion in the sample line during the period required for flow from the sampling point to the instrument.

The response of the instrument was analyzed using Equations (54) - (56). The expected response for a particular gas was characterized by calculating the expected pressure change ratio for the test gas relative to that for air using Equation (56). Unfortunately, the authors did not report the operating temperature of the analyzer. Three fire-fighting agents; carbon dioxide, methyl bromide, and bromochloromethane; were considered. Table 11 lists the predicted ratios of ΔP for the three agents. Note that substantial differences in ΔP are predicted on going from air to high concentrations of the agents.

By recording the instrument response for air and the agents, experimental values were determined for these ratios. The results are included in Table 11. It can be seen that while the theoretical predictions reproduce the general trends observed for changes in the ratios with agent, the quantitative agreement is poor. The reason for the poor agreement between the theoretical and actual response of the instrument was not determined, but it was speculated that it may have been due to departures from the ideal gas law.

The response of the instrument to changes in concentration was assumed to be linear. With this assumption, the percentage of agent in air could be calculated using

$$\% \ Agent = 100 \frac{\Delta P_{air} - \Delta P_{mix}}{\Delta P_{air} - \Delta P_{agent}} , \tag{57}$$

where the subscripts refer to measurements for air, the agent, and the unknown mixture. In practice, the values which were used in Equation (57) were the displacements of the recorded response which should be proportional to ΔP. A number of tests were run on known concentrations of carbon dioxide in air varying from 25 % to 75 %. Measured values were found to agree within 5 %.

The sensitivity of the instrument to variations in ambient pressure and relative humidity were discussed. In general, these parameters require small, but significant, corrections.

The instrument was tested during simulated fire testing on a B-45 nacelle using carbon dioxide. Reliable concentration measurements were obtained which allowed an evaluation of the extinguishing system. Measurements were also performed during actual flights and found to be satisfactory.

Hough (1959) considered the response of the Statham analyzer in more detail. His work was an outgrowth of an uncited study by the Federal Aeronautics Administration which indicated that the response of the instrument was not linear as assumed in deriving Equation (57). Both theoretical and experimental results are presented.

Table 11. Various Values of $\Delta P_{agent}/\Delta P_{air}$ Reported in the Literature for the Statham Analyzer.

Agent	Predicted (New and Middlesworth)	Observed (New and Middlesworth)	Predicted (Hough)	Observed (Demaree and Dierdorf)
CO_2	0.64	0.73	0.729	0.717
CH_2BrCl	0.375	0.51	0.400	0.395
CH_3Br	0.316	0.40	-	0.466
CF_3Br	-	-	0.403	0.401
CF_2Br_2	-	-	0.328	0.319

The analyzer considered in this case was slightly different than the original system described by New and Middlesworth (1953). Instead of eighteen cells it contained twelve. The operating temperature of the instrument was reported to be 116 °C.

In order to understand the nonlinear behavior Hough started with Equation (56). He used known values of μ, γ, and MW to calculate expected values of $\Delta P_{agent}/\Delta P_{air}$ for CF_3Br, CF_2Br_2, CH_2BrCl, and CO_2. The results of the calculations are included in Table 11. Similar calculations were carried out for intermediate concentrations (10 %, 20 %, 40 %, 60 %, and 80 %) of the agents. The data were plotted in such a way that variations due to changes in μ and γ with concentration were emphasized. The analysis showed that the variation of μ introduced some nonlinearity into the expected response. The degree of nonlinearity was least for CO_2 and increased in the order CH_2BrCl, CF_3Br, and CF_2Br_2. Values of γ were assumed to vary linearly with concentration. When these values were incorporated into Equation (56) it was demonstrated that the dependence on γ also introduced nonlinear dependencies on concentration into the predicted response curves.

The deviation of the theoretical response from a linear dependence resulted in large errors when a linear response, which was the basis for Equation (57), was assumed. An indication of the large errors is obtained from the results listed in Table 12 taken from Hough (1959), where concentration values (in %) which were obtained using Equation (57) are listed as functions of the assumed actual concentrations for the four agents. In some cases the differences are greater than 100 %.

As part of the analysis, values of concentration for mixtures of air and CF_3Br recorded using the Statham analyzer and Equation (57) were compared to the actual concentrations for the mixtures. The differences in actual and measured values were large, but the differences were well explained by the analysis discussed above. On this basis the author provided four charts which were used to convert measurements of an agent's relative concentration using Equation (57) to corrected values. The uncertainty in a concentration measurement following correction was estimated to be less than 1 %. A brief discussion indicated that the analysis also did a good job of predicting the nonlinear behaviors observed in the earlier FAA tests.

Demaree and Dierdorf (1959) have provided a detailed account of the operating and installation procedures for a Model GA-2A Statham Analyzer. This instrument is different than the earlier model discussed above in that it utilizes 12 cells arranged in three analyzer units. The theory and principles

Table 12. Predicted Relative Mole Per Cent (Assuming Linear Response of Statham Analyzer) as Function of Actual Mole Per Cent in Various Agent/Air Mixtures Based on the Calculations of Hough (1959)

Actual agent mole per cent	Prediction of indicated agent mole per cent			
	CF_3Br	CF_2Br_2	CH_2BrCl	CO_2
0.00	0.00	0.00	0.00	0.00
10.0	27.3	31.9	22.5	14.8
20.0	45.6	50.0	38.3	23.6
40.0	67.5	70.7	60.8	45.8
60.0	82.3	83.5	76.8	65.7
80.0	91.8	92.7	89.4	83.4
100.0	100.0	100.0	100.0	0.319

for operation of the device are the same as discussed by New and Middlesworth (1953). Instructions were provided for mounting the equipment for flight tests. This included the use of 6.4 mm copper tubes for extracting samples. It was noted that, in order to prevent the analyzer cells from becoming clogged with fine suspensions carried by the gas, a filter was used to at the end of each sampling line to remove particles.

The initial data treatment was identical to that described above. Equation (57) was used to calculate relative concentrations for the agent. The authors noted that it was not necessary to calibrate the instrument for a given agent before a test. Experimental ratios of ΔP_{agent} and ΔP_{air} were deemed constant enough to be used. These values are included in Table 11. Note that these values differ somewhat from those recommended by Hough (1959). Once relative concentration values were available, it was necessary to use calibration curves for the various agents to convert the results to either volume or mass percentages. Calibration curves were provided for CO_2, CH_3Br, CH_2BrCl, CF_2Br_2, and CF_3Br. Comparison of the calibrations curves for CO_2, CH_2BrCl, CF_2Br_2, and CF_3Br with those provided by Hough shows that they are qualitatively similar, but that there are significant quantitative differences. As above, the use of Equation (57) without correction would lead to large errors in concentration measurements.

The report lists the concentrations of the agents required for extinguishment of a nacelle fire. The criteria for a system to be considered adequate was that all twelve sampling positions maintain the minimum required concentration at the same time for not less than 0.5 s.

A later FAA report by Chamberlain (1970) deals primarily with installation and test procedures for the Statham analyzer under actual testing conditions, but it does provide some details concerning the instrumentation, as well as discussing a number of findings from earlier test series. The instrument utilized was the same Model GA-2A discussed by Demaree and Dierdorf (1959). The operating temperature of the analyzer was listed as 121 °C. A schematic of one of the individual cells is included in the report which is identical to Figure 82 reproduced from New and Middlesworth (1953)

for the Model GA-1 Statham Analyzer. This suggests that there had been very little change in the cell configuration on going from the Model GA-1 to the Model GA-2. At the time of the report, the later version of the instrument had been in use for over 10 years.

A useful plot included in the report shows the delay time in the response of the analyzer to a concentration change as a function of the length of tubing used for sampling. The increase with tube length was roughly linear with a delay of 4.4 s for a 9.1 m length of tubing. The results indicate that the flow velocity in the tube was roughly 2.1 m/s.

The data analysis procedure recommended by Chamberlain was the same as that discussed by Demaree and Dierdorf. A detailed description of the procedure is given. An important recommendation was that concentration values be determined manually from the continuous recordings at 0.5 s intervals. Note that such plots will have very poor temporal resolution.

These authors concluded that the Statham Analyzer was at the time "the most comprehensive and practical means available for the determination of aircraft fire-extinguishing system performance."

From 1959 to 1968 the Federal Aviation Administration was actively engaged in the evaluation of fire-extinguishment systems for nacelles. After this time, this function was turned over to private contractors. In 1977 (Ferrarese) an advisory circular was issued which summarized the measurement approach. In addition to a discussion of earlier reports, this document incorporated several useful tables and graphs. One of these tables included the required extinguishing concentrations in weight per cent, volume percent, and relative concentration percent. This table is reproduced as Table 13.

Since this time a revised Statham Analyzer had been designed and constructed by Pacific Scientific (1988a, 1988b). This newer instrument is known as the Halonyzer. Its design principles are similar to those of the Statham Analyzer, but several design modifications have been incorporated into the newer instrument. One of the more significant changes is the replacement of the porous plug used for the pressure drop measurement with a series of capillary tubes. Instead of recording the instrument response as an analog output, a computer data-acquisition system has been included which is capable of recording data at a rate as high as 100 Hz. Additionally, calibration curves have been incorporated into the data analysis, so it is possible to obtain the results directly as either volume or mass percents of agent. This is in contrast to the Statham Analyzer, where relative concentrations were corrected manually using calibration curves. Current FAA procedures recommend the use of volume fraction for testing of fire-fighting agents. The documentation for the instrument indicates that the system is only certified for use with halon 1301 (Pacific Scientific, 1988a).

Documentation for the Halonyzer (Pacific Scientific, 1988a) indicates the system is designed to respond to a change from 100 % air to 100 % halon 1301 in 250 ms. William Meserve and Duane Van Ostrand of Pacific Scientific were kind enough to provide the authors with the results of a test designed to characterize the experimental time-response behavior of the instrument. For this test, three of the inputs for the Halonyzer were connected through different lengths of tubing (0.91 m, 3.7 m, and 7.6 m) to a flow system which could be rapidly switched from air to halon 1301 using a quick-dump valve. In this way, it was possible to characterize crudely the time response of the instrument.

Two different aspects of the response of the Halonyzer are relevant. The first is the period required for the agent to flow from the source to the detector. The second, and more important, time period is that required for the sensor to respond to the assumed step function increase in concentration. For the purposes of the current discussion, this period will be characterized by the time required for the measured halon 1301 concentration to increase from zero to 95 % following its earliest detection by the Halonyzer. Figure 83 shows a plot of the measured time of first detection of halon 1301 as a function of tube length. The data lie roughly on a straight line. The result of a linear least-squares-curve fit of the data is included on the figure. Note that the plot indicates that the flow was initiated at 390 ms which is consistent with the manner in which the experiment was performed (*i.e.*, the Halonyzer data scan was initiated just prior to switching the quick-dump valve). The slope of the line

Table 13. Required Concentrations of Various Fire-Fighting Agents for Aircraft Nacelles Taken from Ferrarese (1977)

Agent	Weight percent	Volume percent	Relative concentration
CO_2	49	37	40
CH_3Br	30	11	15
CH_2BrCl	36	11	25
CF_2Br_2	26.5	5	15
CF_3Br	22	6	15

indicates that the delay time increases with tubing length at roughly 389 ms/m. This value is similar to the value of 480 ms/m which can be derived from the results of Chamberlain (1970) for a Statham Analyzer.

By subtracting the time for first detection from the actual time, it is possible to plot the Halonyzer response for different sampling-tube lengths on a normalized time plot. The results are shown in Figure 84. It is clear that the period required for the instrument to respond fully to the change in concentration is increasing with the tubing length. This is quantified in Figure 85 where the time required to reach 95 % of the actual concentration change is plotted as a function of the tubing length. This plot shows clearly that the response time increases with tubing length. This observation is consistent with the occurrence of molecular diffusion within the sample during the time required to flow from the sampling position to the instrument as first suggested by New and Middlesworth (1953). The response time reported in this earlier work is somewhat shorter than shown in Figure 85, for which the shortest response time is extrapolated to be on the order of 600 ms, but definite conclusions can not be made because it is not known how fast the valve could be closed in the Pacific Scientific experiments.

The experimental results shown in Figure 83 to Figure 85 confirm the literature findings that significant delay times are required for the agent to flow from the sampling point, and that the longer the sampling tubes used, the longer is the response time of the instrument to a step increase in concentration. Practical minimum response times are significantly longer than 100 ms.

11.5 Literature Search For Additional Diagnostics for High-Speed Alternative-Agent Concentration Measurement

As part of the overall program on alternative-agent concentration measurement, a literature search was performed to identify possible alternative approaches to the combined aspirated hot-film/cold-wire probe and the Differential Infrared Rapid Agent Concentration Sensor already discussed in this report. The preceding section summarizes the characteristics of Statham Analyzers and Halonyzers which are currently used for certifying halon 1301 fire-extinguishing systems in aircraft nacelles. It was concluded that these devices do not have sufficient time response to meet the design goals of the

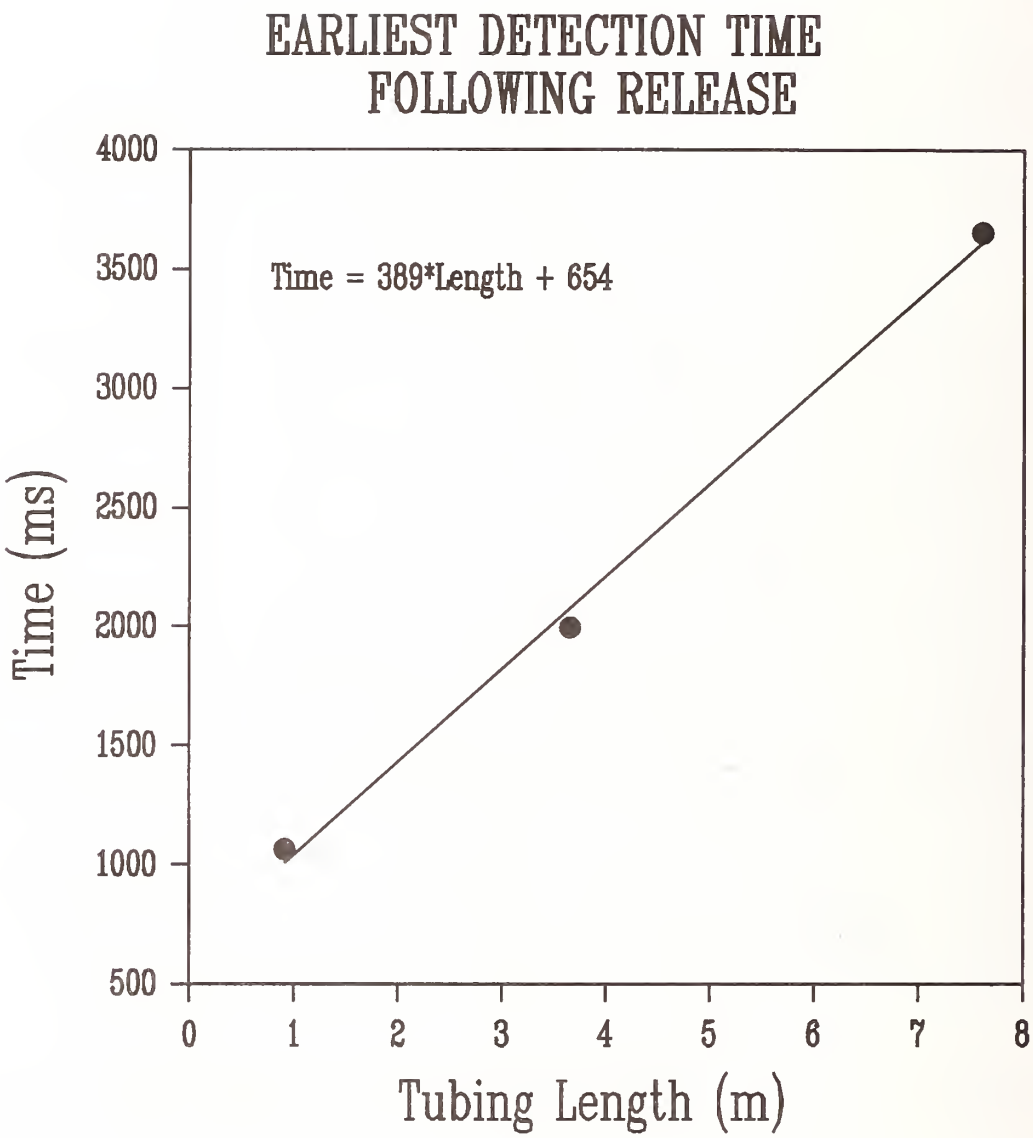

Figure 83. The period required for a Halonyzer to first respond to a step change in halon 1301 concentration from 0 to 100% as a function of sampling tube length. Data provided by W. Meserve and D. Van Ostrand of Pacific Scientific.

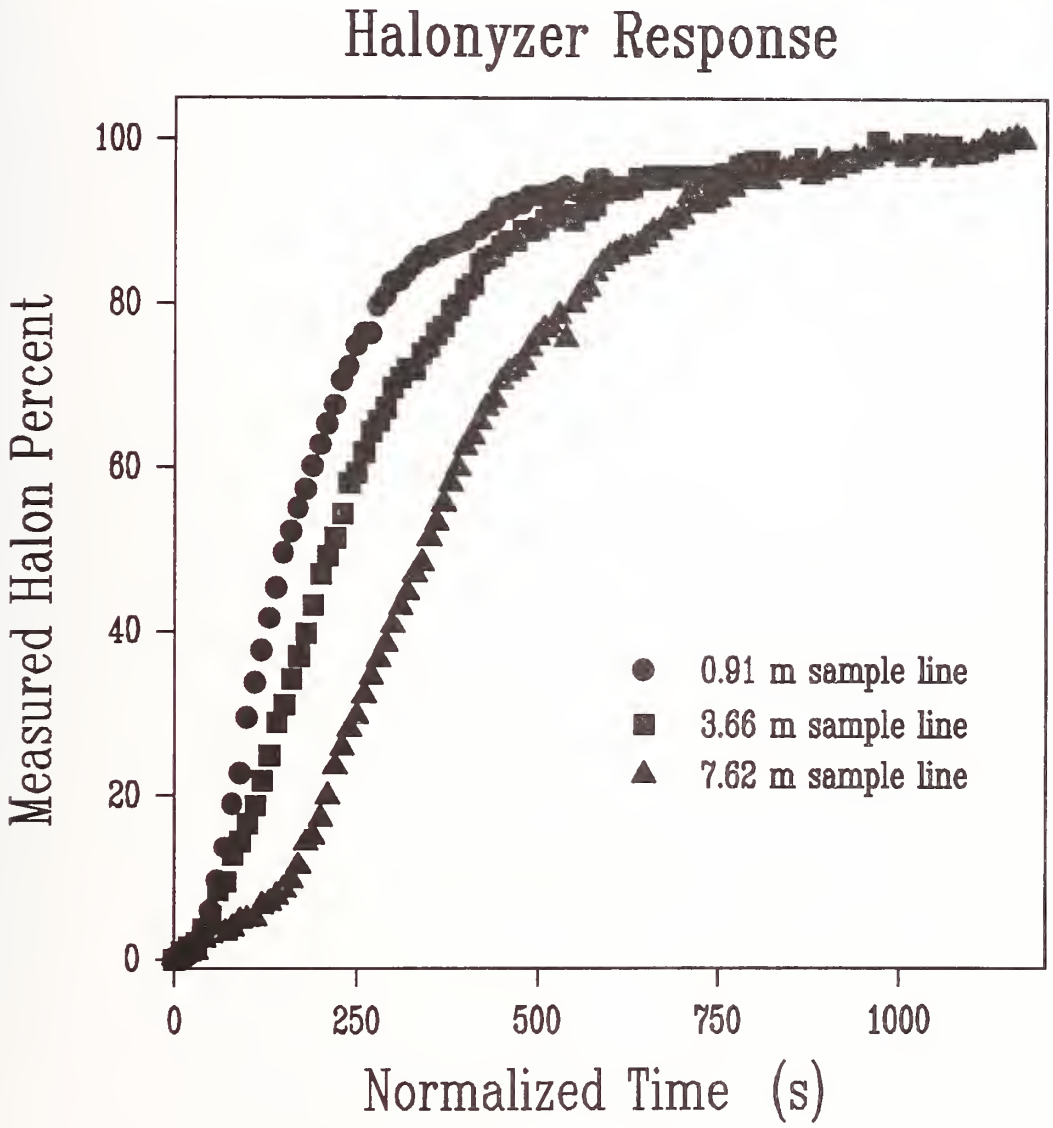

Figure 84. Measured halon 1301 mole percent as a function of normalized time for three different lengths of sampling tube. Data provided by W. Meserve and D. Van Ostrand of Pacific Scientific.

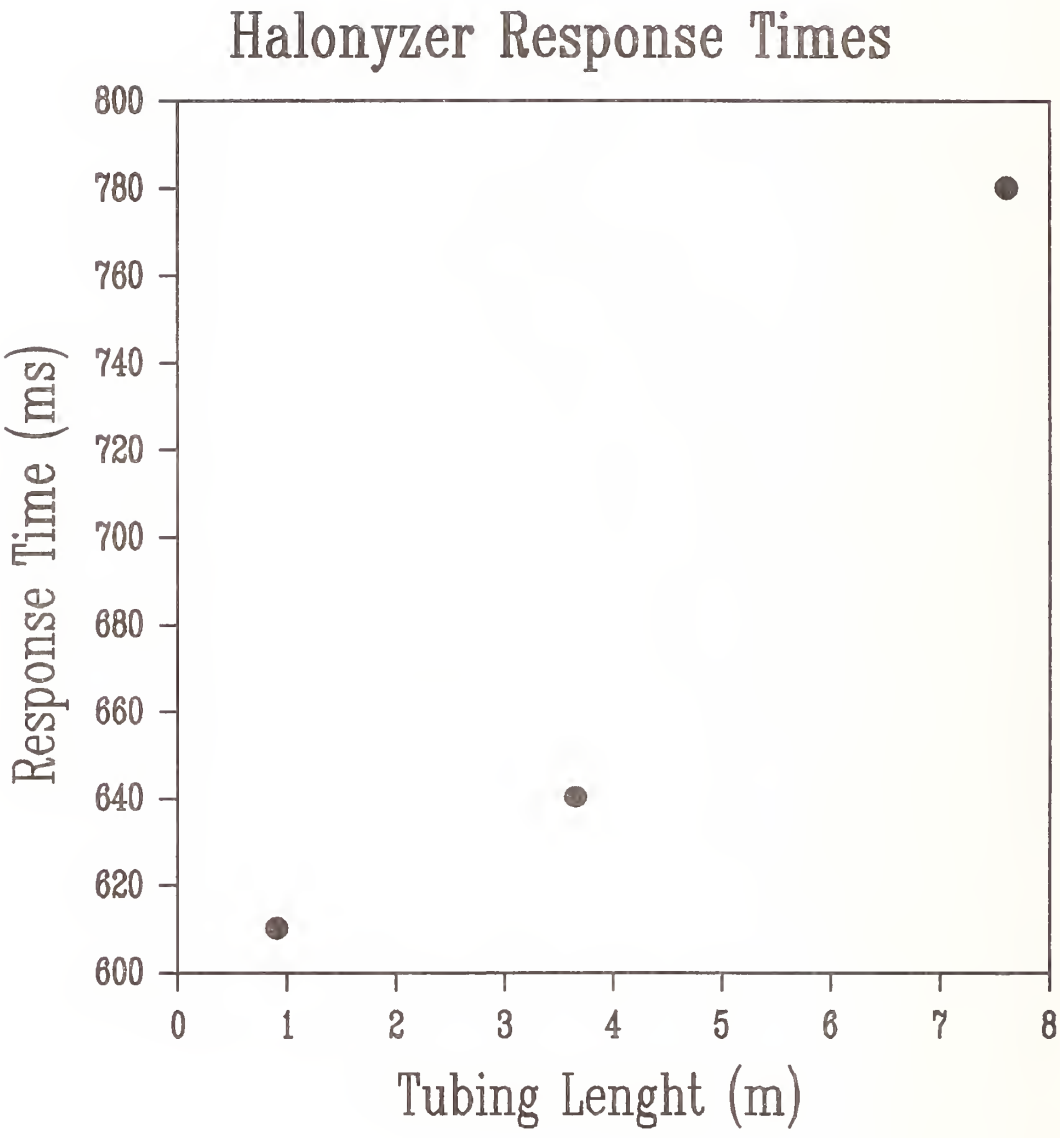

Figure 85. Response times for a Halonyzer concentration reading to change from 0 to 0.95 for a step increase in halon 1301 mole fraction to 1 as a function of sampling tube length. Data provided by W. Meserve and D. Van Ostrand of Pacific Scientific.

current effort. In this chapter other possible concentration measurement techniques are discussed and assessed as to their potential for making the required measurements.

Recall that accurate real-time measurements of the proposed halon 1301 alternatives--FC-218, HFC-227ea, HFC-125, and halon 1301--are desired with a time resolution of 1 ms. As discussed, this temporal resolution requirement places constraints on the sampling volume as well. Generally, sample volumes on the order 1 mm^3 are desirable. These parameters severely limit the existing concentration diagnostics which might be applicable. This section summarizes the possible approaches which have been considered during the literature review.

11.5.1 Introduction. The development of measurement techniques for concentration is one of the most active areas in chemistry. Nearly an infinite number of techniques have been described for measurements in a wide variety of systems. Numerous monographs are available which describe chemical instrumentation and analysis methods. Clearly such a literature is too extensive to review in depth. For the purposes of this project we have chosen to limit ourselves to gas measurement techniques which may have applicability for the measurement of halon 1301 and its potential replacements.

A useful starting point for discussion is the monograph by Strobel and Heineman (1989). This book provides discussions of a wide range of instrumentation used for chemical characterization. Several of the methods are useful for measuring gas concentrations. These include widely used techniques such as absorption spectrometry, mass spectrometry, x-ray fluorescence spectrometry, and gas chromatography. Many of these techniques are discussed below.

It is interesting that many concentration-measurement techniques which are useful for binary mixtures are not included in this list. Such techniques include two instruments--the Statham analyzer and the combined aspirated hot-film/cold-wire probe--which have already been discussed. These probes function by sensing changes in physical properties such as viscosity, heat capacity, or thermal conductivity which are dependent on concentration. Such techniques will not generally be applicable to mixtures of multiple gases because insufficient information is available to fully characterize the concentration of each species.

The ability to follow concentration changes in time is often not a requirement in making chemical concentration measurements. The sample is available and it can be analyzed at ones leisure. However, there are a number of areas where time-resolved concentration measurements are required. Examples include studies of chemical kinetics where changes in concentration result from chemical reaction and turbulent flows and combustion systems where fluid-flow fluctuations lead to rapid changes in concentration at a given sampling point. Many of the techniques which are discussed below have been developed for these specialized applications. The time-scale range important in these applications is large, varying from femtoseconds for very fast chemical reactions to days or years for slowly changing processes. Clearly the technique chosen for a particular application must depend on the time resolution required.

Several characteristics of concentration measurements are relevant to the discussion. An "in situ" concentration measurement is one which is made within the system of interest while an extractive technique requires that a sample be removed for analysis. For instance, the Differential Infrared Rapid Agent Concentration Sensor can be considered an in-situ concentration probe because it was designed to operate within nacelles and dry bays. The Statham analyzer and Halonyzer are extractive techniques since the sample is removed to a remote location for measurement. Another important property of a measurement technique is whether it behaves intrusively or nonintrusively. If a measurement is made which does not modify the system under study it is said to be nonintrusive, while measurements which change, or have the potential to change, the system, are said to be intrusive. Any physical probe will generally be intrusive even though the perturbations to the system under study can be quite

small. On the other hand, many remote sensing optical techniques are characterized as nonintrusive because the measurement has minimal effects on the system.

In the following section the possible application of standard chemical analysis methods for the measurements of halon replacements will be considered. This will be followed by a discussion of several possible specialized techniques which have been developed primarily for measurements of concentration in turbulent flows of isothermal binary mixtures or chemically reacting species.

11.5.2 "Standard" Chemical-Analysis Techniques

11.5.2.1 Gas-Solid and Gas-Liquid Chromatography. Gas chromatography is a chemical-analysis technique which separates and quantitatively measures concentrations of gases (or liquids) in a sample. In its simplest form the sample to be analyzed is injected into a flow of "carrier gas" which then passes through a chromatographic column. The column contains either a solid substrate such as alumina (gas-solid) or a solid substrate coated with a high-boiling liquid (gas-liquid). As the sample passes along the column its components are absorbed or dissolved on the substrate and then released back into the gas flow repeatedly. As a result, their progress along the column is slowed. The relative amounts of time spent in the gas or attached to the substrate is temperature dependent, so the ability to vary the temperature of the column is generally provided. Different components of a mixture interact with the substrate differently, so as a mixture moves along the column the components begin to separate in space along the column. If the experimental conditions are chosen appropriately, by the time the various components reach the end of the column they will be well separated in time and space. The time required for a particular component to move along the column is known as its "retention time." For a given set of experimental conditions, each species in the mixture will have a characteristic retention time which can be quantified by injecting the individual gas onto the column. The last major component of a chromatograph is a suitable detector which can be any of a number capable of sensing the presence of small amounts of materials in a carrier gas. Flame-ionization, thermal-conductivity, and electron-capture detectors are three of the most common types.

This method of chemical analysis is intrusive and extractive since it is necessary to withdraw a sample from the region of interest. However, sample requirements are generally small and it should be possible to design probes which have minimal effects on the types of flows of current interest.

Chromatographic techniques are well developed and widely used. They are certainly capable of separating and quantifying fire-extinguishing agent concentrations in air. However, a major drawback with this approach for the current application is the time required to make an individual measurement. Normally a period of several seconds is required due to the need for flow through the column. This clearly prohibits real-time concentration measurements with the required temporal resolution. An approach which is sometimes used to improve the response time is to take a series of "grab bag" samples at selected times and analyze the samples at a later time. For the current application the number of samples required would be prohibitive, and the analysis would be very costly. On this basis, we conclude that chromatographic techniques are not a viable alternative for real-time measurement of fire-fighting agent concentration.

11.5.2.2 Mass Spectrometry. Mass spectrometry is a technique which is widely used for the identification and quantification of chemical species. In this method the gas-phase species to be analyzed are injected into a region of low pressure (on the order of 10^{-2} Pa) and ionized. The resulting charged particles are then electrically accelerated and physically separated according to their mass-to-charge ratio by one of a number of possible approaches. The separated ionized species are then detected which can be very efficient since charged species are easily observed and quantified. The technique can be made quantitative by proper calibration. Mass spectrometry is capable of

identifying molecular components in a mixture since the mass-to-charge distributions of fragments formed from a particular species is generally unique. Interferences do occur when two or more species generate ions having the same mass-to-charge ratio.

A number of sources have been used to ionize molecular species. The most common is an electron beam generated by a heated filament. The energetic electrons interact with the low-pressure species and create positive ions which are then analyzed. A drawback of this approach is that the energetic electrons not only ionize a molecular species, but also tend to break up the species into smaller charged molecular fragments. As a result, a single molecular species may result in the formation of fragments having a number of mass-to-charge ratios. A second approach is chemical ionization in which a simple molecular species is first ionized by electron impact. The ionized species is then accelerated and interacts with the sampled gas where it results in ionization of the sample. This method generally results in less fragmentation than electron impact. Other methods which are used less frequently include laser desorption/ionization and photoionization.

Once the ions have been generated, they can be accelerated to a high velocity by application of an electric field. All of the accelerated ions are accelerated to the same energy. For singly charged species (generally the most common by far) the kinetic energy and electrical energy are equivalent, which can be written as

$$\tfrac{1}{2}mv^2 = eV\,, \tag{58}$$

where m is the mass of the ion, v is the velocity, e is the charge on an electron, and V is the electric-field applied potential. Accelerated ions having different m/e ratios can now be separated in a number of ways. One such mass selector is known as a magnetic-sector analyzer. This approach is based on the fact that a charged species in a magnetic field will follow a curved path having a radius which depends on the strength of magnetic field and the mass of the ion. By adjusting the magnetic field, it is possible to select the particular mass-to-charge-ratio ions which will reach a detector. A second type of analyzer uses a curved electric field to separate the ions. As for the magnetic-sector analyzer, the curvature of the ion path can be adjusted by varying the electric field strength and the spatial location of a particular mass ion can be selected.

Another type of analyzer known as the time-of-flight approach uses the time required for the accelerated ions to cover a known distance to infer the mass. From Equation (58), it is clear that if the ions are impulsively accelerated along a free path, the time required to reach a certain distance will be inversely proportional to ion velocity and therefore its mass. By recording the ion arrival times using a suitable detector, the mass can be measured accurately.

The approach most widely used today for mass separation is the quadrupole mass analyzer. The quadrupole analyzer consists of four metal rods which are arranged parallel to each other in the shape of a diamond. A combination of dc and ac radio-frequency electric fields are applied to the rods which cause ions moving between the rods to undergo a series of oscillations. These oscillations can grow to the point where the ions strike a rod and are lost. Whether or not this occurs depends on the magnitudes of the applied fields. For a given combination of fields only a narrow range of m/e ions can traverse the analyzer for detection at the end. For this type of analyzer, the velocity of the ions entering the analysis region is unimportant, and the ions do not need to be accelerated to the high velocities required for the other types of analyzers described above.

Several different detectors have been developed to detect the charged species. The two most common are briefly described here. A Faraday cup is a sloping plate electrode formed in the shape of a metal cup. When a charged species strikes the cup it generates secondary electrons which are collected and detected as a current. Most mass spectrometers today employ electron multipliers. These devices are similar to Faraday cups in that the energetic ions strike a metal surface to generate

electrons. The difference is that once the electrons are created, they are accelerated in an electric field and strike a second metal surface which generates still more electrons. This process can be repeated many times so that the detection of a single ion can lead to the generation of a large number of electrons. In other words, the device provides a great deal of amplification and a current which is easily measurable.

Most mass spectrometers are designed to perform mass analysis on molecular species. For all of the analyzers discussed above, except the time-of-flight system, the sample is usually introduced continuously into the spectrometer and the detected mass is swept by changing the applied magnetic or electric fields to generate a mass spectrum of the sample which consists of the detected ion signal as a function of *m/e*, or, assuming a charge of one electron, the mass of the ions. As mentioned above, the analysis is often complicated by the fact that an individual molecular species may fragment into a number of different ions. The mass spectrum for complicated chemical mixtures can be quite complex indeed. For this reason, it is common to perform chemical separation on a mixture before performing mass analysis. Mass spectrometry is often combined with the chromatographic techniques mentioned above. In this method it is necessary to record the mass spectrum fast enough to resolve the individual species which are leaving the chromatographic column. This has led to the development of mass spectrometers which can be swept quite rapidly. (White and Wood, 1986)

In its standard configuration a mass spectrometer is unlikely to be a suitable device for quantitative measurements of real-time fire-fighting agent concentration. The period required to scan the mass spectrum is simply too long. However, the instruments have been modified to allow on-line sampling of composition of particular species. This is done by setting the spectrometer to a particular *m/e* of interest and recording the resulting ion signal as a function of time. Since the mass does not need to be scanned, quite rapid measurements are possible. By using a mass analysis method which provides spatial separation of ions, it is possible to place multiple ion detectors in the instrument and monitor several species at once. (White and Wood, 1986; Whistler and Schaefer, 1983; Savin *et al.*, 1983)

Even though mass spectrometry has not been tested for the current application, it seems to offer possibilities for the real-time measurement of fire-fighting agent concentrations. Since very small samples are required, it should be possible to develop sampling systems which perturb the sampled system very little and which allow accurate measurements of concentration with good temporal resolution. Major drawbacks of using mass spectrometry for this application are its relative complexity and cost. The components and electronics of a mass spectrometer must be carefully designed and manufactured. The system generally requires a very good vacuum system capable of high pumping speeds. As a result, the systems tend to be fairly expensive (on the order of tens of thousands of dollars), bulky, and difficult to operate and maintain. These considerations should be carefully considered before designing a system to make the required measurements.

11.5.2.3 Standard Optical Absorption Techniques. Optical techniques are widely used in chemical analysis. The mostly frequently employed methods involve the absorption or emission of electromagnetic radiation by molecules. Interactions between matter and electromagnetic energy occur over a very wide energy range from low-energy radio waves to high-energy gamma rays. Various analytical techniques based on absorption or emission of electromagnetic energy have been developed which use different portions of the electromagnetic spectrum. Table 14 lists some of these techniques and includes the types of molecular energy transitions which are responsible.

Many of the spectroscopic methods listed in Table 14 are rarely used for quantitative measurements in the gas phase. These include nuclear magnetic resonance, electron spin resonance, microwave spectroscopy, x-ray spectroscopy, and gamma-ray spectroscopy. These techniques will not be discussed further here, but the reader should keep in mind that it is possible that quantitative analysis

Table 14. Various Types of Molecular Spectroscopies Are Listed Along With The Relevant Electromagnetic Spectrum Region and the Molecular Motion Responsible for the Transitions

Type of spectroscopy	Energy range	Molecular interaction
Nuclear magnetic resonance	Radio	Nuclear spin
Electron spin resonance	Radio	Electron spin
Rotational	Microwave	Rotational
Infrared absorption	Mid-infrared	Vibrational
Near-infrared absorption	Near infrared, Visible	Vibrational overtones
Raman	Visible, ultraviolet	Vibrational
Electronic absorption	Visible, ultraviolet	Electronic
Fluorescence	Visible, ultraviolet	Electronic
X ray	X ray	Inner-shell electronic
γ ray	γ ray	Nuclear

techniques for fire-fighting agents based on some of these approaches might be feasible following a significant development effort.

The remaining spectroscopic methods included in Table 14 have been used extensively for quantitative concentration measurements of gas-phase species. These techniques are discussed in more detail below.

Infrared absorption spectroscopy is widely used for chemical identification and concentration measurement. The technique normally refers to the absorption of infrared electromagnetic energy (usually defined as having wavelengths from 0.75 μm to 400 μm) which lies in the mid-infrared range of 2.5 μm to 16 μm. In infrared work the positions of absorption bands are often reported in wavenumber units (cm^{-1}) which are the inverse of the wavelength of light and are proportional to the energy of the light. The mid-infrared region extends from 4000 cm^{-1} to 625 cm^{-1}.

The reason for the great importance of infrared absorption techniques is that the vibrational energy-level separations of the vast majority of molecules lie in this energy range, and the molecules can absorb infrared energy during allowed transitions from a lower lying vibrational energy level to a higher lying level. A discussion of transition rules is beyond the scope of this discussion, but suffice it to say that most molecules which are not linear and symmetrical will have at least one allowed infrared absorption. The energy required for absorption is highly dependent on the atoms in the molecule as well as the molecular structure. It is this strong dependence on molecular structure which allows infrared spectroscopy to be such an excellent technique for molecular identification.

The concentration of an absorbing species can be quantified using Beer's law which states that the logarithm of the ratio of infrared power at a given wavelength transmitted through a space containing an absorbing species (P) to the power transmitted in the absence of the species (P_o) is equal to the product of the absorption coefficient of the absorbing species (ε), the pathlength over which the energy travels (ℓ), and the concentration of the species (c),

$$\log\frac{P}{P_o} = \epsilon \ell c \ . \tag{59}$$

A variety of units may be used for the terms in Equation (59), and care must be used to ensure that the units are consistent. When the pathlength and absorption coefficient are known for a species, a measurement of the light transmission allows the concentration to be determined.

Infrared absorption measurements are normally recorded using either dispersive or Fourier transform spectrometers. The older of the two is the dispersive type. In this approach a narrow wavelength range of a continuous source of infrared radiation, such as a heated filament, is isolated with a dispersive element such as a prism or grating. The selected radiation is then passed through a cell containing the sample of interest. Following passage through the sample, the infrared energy strikes a detector which records the intensity of the transmitted light. It is common to use a second unabsorbed beam of light as a reference for I_o.

The Fourier transform infrared (FTIR) spectrometer is a more recent development. This instrument is typically formed from a Michaelson interferometer in which one of the optical legs is replaced by a mirror which can be scanned back and forth with time. The infrared radiation exiting the interferometer first passes through an absorption cell containing the sample, and the intensity is then measured with a suitable detector. Unlike a dispersive spectrometer, all wavelengths of interest are passed through the interferometer simultaneously. The detected light varies at the frequency of the scanned mirror, and the resulting interferogram includes information concerning frequency components of the absorption spectra. The normal infrared spectrum in terms of wavelength or energy is recovered by Fourier transforming using the fast Fourier transform (FFT) algorithm from the frequency space of the measurement to wavelength (energy) space. Additional details can be found in numerous textbooks (*e.g.*, Strobel and Heineman, 1989).

Dispersive infrared and FTIR spectrometers are similar in that both usually use absorption cells which are inserted into the instruments. For making time-resolved measurements, it is necessary to flow gases through the cell with a sufficient volume-flow rate that the volume is completely flushed at a rate equal to the required time resolution. Additionally, the instruments require finite times to record a resolved spectrum. Due to these requirements, commercial infrared spectrometers are generally not used to record concentrations having time resolutions on the order of 1 ms. As a result, commercial infrared spectrometers are not recommended for time-resolved agent concentration measurements.

As noted above, the energies of most vibrational bands in molecules result in strong allowed molecular absorptions which have energies corresponding to the mid-infrared portion of the electromagnetic spectrum. In reality, the vibrational energy levels of molecules are like a step ladder, with the energy separation increasing with the number of steps separating the levels. For most molecules, the probability of absorption of a photon is much higher for a step size of one (*i.e.*, $\Delta v = 1$, where v is known as the vibrational quantum number) than for larger steps. However, there are often small probabilities of electromagnetic absorption occurring for step sizes larger than one. Such transitions have a higher energy and often fall in an energy range known as the near-infrared which lies in the 0.75 μm to 2.5 μm wavelength range.

The near-infrared has been used very little for quantitative concentration measurement using standard spectrometers due to the weak absorption of molecules in this spectral range. However, as discussed below, there are potential advantages for making concentration measurements in this wavelength range. However, measurements using standard commercial spectrometers will be subject to the same limitations described above for mid-infrared measurements and, as a result, are unlikely to be applicable for high-speed applications.

As one moves to higher energy in the electromagnetic spectrum, one comes to the visible and ultraviolet regions where photons have energies sufficient to induce transitions between electronic states of a molecule. The actual wavelengths where these transitions occur depend strongly on the structure and symmetry of the particular molecule. Electronic transitions can be quite strong and, when they occur, are quite useful for analytical measurements.

For the purposes of the following discussion we will subdivide the visible and ultraviolet portions of the electromagnetic spectrum into three regions: the visible from 350 nm to 750 nm, the quartz ultraviolet from 200 nm to 350 nm, and the vacuum ultraviolet from 100 nm to 200 nm. The names are quite literal. The visible region corresponds roughly to wavelengths which can be detected by the human eye, the quartz ultraviolet corresponds to wavelengths which are transmitted by quartz, and the vacuum ultraviolet corresponds to a region of the spectrum which is strongly absorbed by oxygen in the air and therefore normally requires a vacuum for efficient transmission. This classification follows Pasto and Johnson (1969).

A review of the literature reveals that halon 1301 and the replacement agents are transparent at visible wavelengths (*i.e.*, absorption is either very weak or totally absent). On the other hand, CF_3Br and CF_3I have relatively strong absorptions in the quartz ultraviolet. CF_3Br has a broad absorption which begins in the vacuum ultraviolet and reaches a maximum at roughly 205 nm (Roxlo and Mandl, 1980; Molina *et al.*, 1982). CF_3I has a moderately weak, but broad absorption which peaks near 268 nm and extends out to 317 nm (Calvert and Pitts, 1966). This molecule also has a relatively sharp, strong absorption band with a maximum at 174 nm (Roxlo and Mandl, 1980). The absorption bands in the quartz ultraviolet offer possibilities for quantitative analysis. However, standard absorption spectrometers are too slow to allow highly time-resolved measurements (however, see the section on the Ultra-Violet Halonyser below). On this basis, it is concluded that standard absorption spectrometry is not appropriate for the current application.

The remaining alternative agents, *i.e.*, C_2F_5H, C_3F_8, and C_3F_7H, all have electronic absorption bands which lie is the vacuum ultraviolet and would be difficult to quantify in air using standard spectroscopic analysis.

11.5.3 Fiber-Optic-Based Measurements of Concentration. A variety of techniques have been demonstrated or are under development which utilize fiber-optic probes for concentration measurements. In some cases these probes are simple absorption techniques where the fiber optics are used to convey the light to and from an open-path sample volume. In other cases the chemical to be sensed is used to induce changes in the light transmission characteristics of the fiber, and concentration is monitored by changes in light transmitted by the fiber. Examples of each approach are discussed below.

11.5.3.1 Introduction To Fiber Optics. Simply speaking, an optical fiber is a long, thin filament of a transparent, dielectric material, such as glass or plastic, used for the transmission of light over long distances with very little loss. If the diameter of this fiber is large relative to the wavelength of the transmitted light, then simple geometrical optics may be used to describe the light transmission in the fiber. The key principle is that of total internal reflection. If the fiber is modeled as a cylinder of glass surrounded by air, then a ray of light within the fiber striking a wall will be totally internally reflected (that is, all of the light remains in the reflected ray with no refracted ray

escaping through the wall) when the incident angle (measured from the normal to the wall) is greater than a critical angle given by

$$\theta_c = \sin^{-1}\frac{n_o}{n_1} , \tag{60}$$

where n_o is the index of refraction for the fluid surrounding the fiber and n_1 is the index of refraction for the fiber material (chosen such that $n_1 > n_o$). Thus, rays of light coupled into an optical fiber may undergo many thousands of reflections per meter and still remain trapped within the fiber. However, one can easily see that if moisture, dust, or oils come into contact with the surface of the fiber, then the critical angle at the air/fiber interface is altered, and light may well leak through the fiber. Furthermore, if large numbers of fibers are packed together in a bundle, light may leak from one fiber to another (crosstalk). To prevent these rather common problems, currently manufactured optical fibers are equipped with a thin, transparent sheath of material with a lower index of refraction than the core material. This sheath is known as cladding. Typical index of refraction values are 1.62 for the core material and 1.52 for the cladding although other values are commonly available. A fiber with two discrete values for the index of refraction of the core and cladding is known as a step-index fiber. A graded-index fiber has a continuous distribution of values for the index of refraction proceeding from the centerline of the fiber to the boundary. The presence of cladding prevents many of the types of leakage described above, but it cannot prevent leakage resulting from sharp bends or kinks in the fiber. In general, fibers have a minimum bend radius specification on the order of 5 cm for glass and 2.5 cm for fused-silica fibers.

Light is coupled into the fiber by directing rays into one of the end faces. There exists a maximum for the incident angle (measured from the normal to the end face and denoted by η_{max}) of these input rays in order for the ray to strike an interior wall of the fiber at an angle greater than the critical angle for total internal reflection. Rays entering the end face of the fiber with an incident angle greater than this maximum angle will be partially refracted at each encounter with the core-cladding interface and will quickly leak out of the fiber. Thus, η_{max} represents the half-angle of a cone centered on the fiber axis for which light within this acceptance cone will be transmitted through the fiber, whereas light outside of the cone will not. This maximum angle may be determined from

$$\sin\theta_{max} = \frac{\left(n_1^2 - n_2^2\right)^{1/2}}{n_o} , \tag{61}$$

where n_o is the index of refraction for the fluid surrounding the fiber (air), n_1 is the index of refraction for the fiber core material, and n_2 is the index of refraction for the fiber cladding. As with lenses, one may define a numerical aperture, the square of which is a measure of the light gathering power of the system,

$$NA = n_o\sin\theta_{max} = \frac{1}{2f\#} , \tag{62}$$

where *f/#* is the f-number of the system. For air ($n_o \approx 1$), the numerical aperture cannot exceed 1 which corresponds to $\theta_{max} = 90°$ and a condition in which all light entering the end face of the fiber is transmitted through it. Commercially available fibers may be obtained with numerical apertures ranging from 0.2 up to and including 1.0.

In order to be flexible, single fibers must have a small diameter (typically 200 μm to 1 mm); however this makes them inefficient for the collection of light from large, incoherent, non-laser sources. To overcome this limitation, fibers packed in a bundle may be obtained. These bundles provide both flexibility as well as a larger physical aperture (several millimeters) in which to focus the input beam. If no attempt is made to order the individual fibers within a bundle into some sort of ordered array, they are said to form an incoherent bundle and are useful only for the transmission of light from one location to another. On the other hand, when the fibers are carefully arranged such that their terminations occupy the same relative positions at both ends of the bundle, then this coherent fiber may be used for the transmission of images. In addition, bundles that are bifurcated or trifurcated are readily available, and they allow beam splitting to be performed without the aid of lenses. Although the transmittance through single fibers is nearly 100 %, the transmittance through a bundle is usually much less (50 % - 70 % for a length of about 0.3 m). This fiber-bundle transmittance is usually expressed in dimensionless form as the ratio of the bundle transmittance to the transmittance of a single fiber with the same physical aperture and is a function of the wavelength of the transmitted light and the length of the bundle. Single glass fibers are commonly available and transmit light over a range of wavelengths from 500 nm to about 1600 nm in the near-infrared. Single fused-silica fibers may also be obtained and can extend this range from about 300 nm in the UV range out to about 2000 nm. Bundles may be obtained in these wavelength ranges as well, but transmittances tend to fall off rapidly for lengths exceeding about 0.3 m.

Single fibers may be multimode or single mode. This refers to the number of axial laser modes (which comprise a single laser line) which a fiber can guide. The number of modes drops as the fiber core diameter or the numerical aperture is reduced. For small enough values of either, only one fiber mode exists, and the fiber is referred to as single mode. Single-mode fibers are generally more expensive, are more difficult to obtain, and are of very small diameter (4 μm to 8 μm with *NA*s of about 0.2). They are generally used for communication over long distances.

11.5.3.2 Spatially Resolved Absorption Concentration Measurements Using Fiber Optics. Numerous systems have been developed which utilize fiber optics to allow absorption measurements over small regions of space and, therefore, allow spatially resolved concentration measurements. In order to provide the reader an understanding of such an approach, several early applications are described.

Batt (1977) has reported the use of a fiber-optic probe in his study of the turbulent structure and diffusive characteristics associated with the mixing of both a passive and reacting species in a two-dimensional free turbulent shear layer. Specifically, Batt used a vertically oriented recirculating wind tunnel to deliver the primary (core) flow which consisted of dry air that had been cooled to -20 °C by means of liquid-nitrogen injection and then seeded with dilute concentrations of nitrogen tetroxide (N_2O_4). He then made use of the decomposition of nitrogen tetroxide to give nitrogen dioxide gas by the reaction

$$N_2O_4 + N_2 \leftrightarrow 2NO_2 + N_2 \,. \tag{63}$$

The primary flow was exhausted into the larger test section chamber of the tunnel containing a secondary source of dry air at room temperature and forming a two-dimensional free turbulent shear layer at the interface. Due to the mixing of N_2O_4-rich cold eddies in the mixing layer with the hot (ambient temperature) eddies of the secondary fluid, the dissociation of N_2O_4 to generate NO_2 was favored. Thus, this configuration allowed the study of the mixing of chemically reacting species. However, a unique feature of this reaction was the fact that when the temperature of the primary gas was increased from -20 °C to room temperature, the degree of dissociation varied from 0.3 to 0.96.

This required that the dissociation was essentially complete immediately after significant mixing into the primary flow, and with this configuration, the author could study the mixing of a passive species. The author made point measurements of velocity using constant-temperature hot wires, measurements of temperature using constant-current cold wires, and measurements of the concentration of NO_2 gas with the fiber-optic probe.

The light-sensor probe was constructed by splitting the light from a tungsten-filament lamp into two beams which were then chopped at 1 Hz by a rotating chopper wheel. The resulting beams were directed through optical high-pass filters (with a cut-off wavelength at 380 nm) and then focused into two optical fibers. One fiber was routed to the measurement location in the mixing layer and the other to a reference location in the secondary ambient air. At each of these locations the fibers were terminated and fitted with a glass lens. A fixture was then employed to position a second fiber, also fitted with a glass lens, immediately adjacent to the first fiber with only a 2.5 mm gap separating them. The other end of this second fiber was directed to a photomultiplier tube. The idea, then, was that light from the lamp exited the fiber through the lens, was attenuated upon passing through eddies of dark-brown NO_2 gas instantaneously present in the gap, then proceeded into the second fiber and terminated at the photomultiplier tube where the transmitted light was measured. Due to the fact that the nitrogen dioxide gas strongly absorbed at a wavelength of 400 nm, whereas the other species in the flow were transparent to this wavelength, the light attenuation in the gap was a measure of the gas concentration. To eliminate problems associated with stray light, the measurements were acquired in complete darkness. The relationship between the transmission of light in the gap and concentration of NO_2 gas is described by the Beer-Lambert law,

$$\frac{I}{I_o} = \frac{E}{E_o} = 10^{-\beta l_f c} , \tag{64}$$

where I is the transmitted light intensity, E is the photomultiplier voltage, the subscript o refers to the transmitted light intensity or voltage with no absorption, β is the molar extinction coefficient for nitrogen dioxide gas in cm^2/mole, l_f is the gap spacing, and c is the concentration of NO_2 gas in mole/cm^3. Note that Equation (64) is simply another way to write Equation (59). Since only dilute concentrations were measured, Equation (64) could be simplified into the following linear relation as

$$\frac{\Delta E}{E_o} = -2.3\beta l_f c , \tag{65}$$

where ΔE represents the difference in photomultiplier voltages resulting from the reference and attenuated light signals.

The purpose of the chopper wheel was to provide a means for monitoring the reference-signal strength and the extent of any drift in the source intensity that may have occurred during the course of the measurement. It was activated immediately before a concentration measurement, then turned off while the concentration data was obtained, then reactivated immediately afterward. This probe exhibited a sensitivity of 300 mV per percent of NO_2 in N_2, had a bandwidth of approximately 2 kHz, and a signal-to-noise ratio of 70 dB. In addition to the mean and fluctuating values of concentration that could be obtained with this sensor, Batt reported simultaneous correlation measurements of concentration and velocity or temperature by positioning a hot-wire or cold-wire sensor in the gap of the light probe, but displaced a small amount from the gap center in a lateral direction to avoid disturbing the transmitted light signal.

The origins of the light sensor probe employed by Batt (1977) may be found in the earlier papers of Lee and Brodkey (1964) and Nye and Brodkey (1967a). The first paper describes the original light-

sensor probe developed for the specific case of the measurement of turbulent concentration fluctuations in high Schmidt-number flows. Recall that the Schmidt number is the ratio of momentum diffusivity to mass diffusivity, and a high Schmidt-number case corresponds to the mixing of mass in a liquid stream. The authors had pointed out that the existing hot-wire techniques for resolving concentration fluctuations in low Schmidt-number flows could not be adapted to the high Schmidt-number case, and this deficiency necessitated the development of a new experimental technique. The experimental configuration consisted of the axial injection of dye in the form of a turbulent jet on the centerline of a co-flowing water stream in a 7.8 cm pipe. Further details of the experimental apparatus may be found in Lee and Brodkey (1964).

The light probe of Lee and Brodkey (1963) consisted of a pair of optical fibers of diameter 0.75 mm which were separately encased in 1 mm diameter, thin-wall metal tubes for support. The two metal tubes were spaced 1 mm apart and rigidly housed inside a probe body constructed of a 6.3 mm diameter Monel tube with a length of 16.5 cm. At one end of the probe body, the Monel tube was tapered, and the metal tubes containing the optical fibers extended from the probe housing for a distance of about 12 mm. At the very end of the two metal tubes, small prisms were attached to the ends of the optical fibers such that the optical paths were directed inward by 90° to meet each other across the 1 mm gap. At the other end of the probe body, the optical fibers were directed into flexible, waterproof, plastic tubes of diameter 2.5 mm and with a length of over 1.5 m which allowed light to be transported into and out of the experimental facility. The spatial resolution was computed to be the volume obtained by extending the fiber optical cross-section of 0.56 mm^2 across the 1 mm gap for a probe volume of 5.6×10^{-4} cm^3. The light source was an intense white light from a lamp. As in the paper by Batt, the principle is that of light attenuation in the gap due to the presence of dilute concentrations of gentian violet dye injected into the flow. The relationship between dye concentration and light attenuation is again governed by the Beer-Lambert law, Equation (64). Measurement of light intensity was accomplished by means of a 9-stage photomultiplier tube, and the frequency response of the probe was approximately 10 kHz.

The goal of the investigation was to report on the general shape of the concentration spectrum and to compare it to predictions from theory. The resulting measurements were generally inconclusive, which was deemed to be the result of deficiencies in the design of the light sensor. Improvements such as a smaller probe volume and increased light level resulting from a higher intensity light source and a reduction in the length of the 1.5 m optical fibers for transporting the beams were suggested as a means for increasing the signal-to-noise ratio. These improvements were the basis of a second-generation sensor described in the paper by Nye and Brodkey (1967a).

The second-generation light sensor was entirely revamped. It was constructed by bringing two optical fibers, of diameters 0.25 mm and 0.38 mm, enclosed in metal tubing and with small glass windows cemented to their ends, face to face across a gap of 0.25 mm. This was accomplished by means of a supporting mount which suspended the two optical fibers, encased in tubes, in a U-arrangement. The probe volume was calculated by using the cross-sectional area of the 0.25 mm fiber and extending it across the 0.25 mm gap to obtain 1.2×10^{-5} cm^3. This was a reduction in volume relative to the previous sensor of about 46. A much stronger white light source was also employed. The dye was also changed, and higher concentrations were used. The net result of these changes to the probe and system was a signal-to-noise ratio ten times better than that obtained by Lee and Brodkey (1963). The concentration spectra obtained with the new probe were considered to be satisfactory, and full details of the data and the concomitant comparison to theory may be found in the paper of Nye and Brodkey (1967b).

The optical sensors discussed to this point have been able to acquire point measurements due to the relatively high concentrations of contaminant that were introduced. The method, however, can be extended to the measurement of extremely low, mean concentrations by increasing the gap spacing so

that a greater distance is traversed through the fluid to be measured. One then obtains an integrated line-of-sight measurement as opposed to a point measurement.

This approach finds application as an economical and safe way for the implementation of remote sensing of various dangerous, explosive, and toxic gases at strategic locations within enclosed environments such as factories, fuel-storage facilities, tunnels, ships and buildings. Since electrical sensors are inappropriate in these kinds of hostile environments, optical techniques based on absorption spectroscopy appear to be the most suitable. However, implementation of such an optical technique was hampered by the fact that most hydrocarbon gases have weak absorption coefficients in the near-infrared region where conventional fused silica optical fibers remain transparent. The use of light in the near-infrared requires long path lengths within the measured gas in order to obtain sufficient attenuation of the signal. Such a method was pursued by Chan *et al.* (1984) for the measurement of low levels of propane (C_3H_8). They employed ultra-low-loss silica fibers transmitting light at 1.68 μm, but were required to have a path length through the gas of 0.5 m!

On the other hand, as discussed in Section 11.5.2.3, hydrocarbon gases display strong absorption bands in the mid-infrared, but conventional optical fibers exhibit large transmission losses in this region. Tai *et al.* (1987) employed standard silica fibers transmitting mid-infrared radiation at 3.392 μm for the detection of methane, but they were forced to keep the fiber length to less than 40 cm in order to avoid large transmission losses. (They used a very interesting arrangement, however, in which a portion of the fiber itself formed the transducer. We will return to this feature below.) Saito *et al.* (1988) seem to have found a better solution. They have developed a system exploiting the properties of novel optical fibers made from chalcogenide glasses such as arsenic sulphide (As_2S_3) and arsenic selenide (As_2Se_3).

Specifically, the optical fiber consisted of a 0.5 mm core of As_2S_3 glass and a 70 μm thick cladding of Teflon FEP. The transmissivity of the fiber was a maximum (63 % to 67 %) at the 3.39 μm wavelength used in the study. Furthermore, the methane (CH_4) gas examined in this investigation (as well as most hydrocarbon molecules) has a very strong absorption band in this part of the spectrum. The experimental configuration consisted of a 4 mW He-Ne laser as the light source. Light from this source was conveyed through an As_2S_3 fiber (1.0 m to 1.5 m long) to a cell containing the gas to be measured. A second fiber routed the light transmitted through the cell to a liquid-nitrogen-cooled InSb detector which transduced the radiation into an electrical signal. This configuration, however, was sensitive to fluctuations or drift in the source intensity of the laser. Indeed, this was checked, and fluctuations as large as 10 % were found. To remove this effect from the system, a clever combination of a chopper wheel and interrupter wheel was used to alternately direct the beam from the laser through the fiber to the gas cell or to send the beam directly to the detector, bypassing the gas cell completely. This allowed the detector to produce a voltage instantaneously proportional to the source intensity immediately followed by a voltage quantifying the concentration of gas within the cell. Division of the latter quantity by the former had the effect of removing the dependence on source intensity from the system. The modified signal showed a small fluctuation level on the order of 2 % which was attributed to vibrations of the chopper disk and represented the noise floor of the system.

Saito *et al.* (1988) used this system to detect methane levels ranging from a predesigned maximum of 5700 ppm down to 300 ppm (which represents 0.6 % of the lower explosion limit) in a gas cell of length 100 mm. When using a shorter cell of only 50 mm in length, the lowest resolvable concentration was 700 ppm. The optical path lengths used in this study, 50 mm and 100 mm, are large compared to the point measurements made by Batt and by Brodkey and his coworkers. When these lengths are placed into the inverse exponential Beer-Lambert law, one can immediately see that the concentration levels that can be discerned with this technique are of much smaller magnitude and are therefore most appropriate for these leak detection studies.

Saito *et al.* (1992) reviewed the attractive features of chalcogenide glass fibers and recent applications in thermometry and gas monitoring using these fibers. Details from this paper include the fact that the fibers have large numerical apertures allowing them to accept a large amount of radiation from a large field of view. The As_2S_3 fiber has a transmission wavelength range of 1 μm - 6 μm and a minimum optical loss of 0.06 dB/m, whereas the As_2Se_3 has a wavelength range of 1 μm - 10 μm and a minimum loss of 0.3 dB/m. Furthermore, these fibers have a minimum bending radius less than 50 mm when the core diameter of the fiber is less than 0.7 mm, and this is primarily a mechanical specification as the transmissivity of the fibers is relatively unaffected by bending. The authors also describe a coherent As_2S_3 fiber bundle containing 1000 individual fibers with cores of 20 μm and an outer bundle diameter of 1 mm. This bundle was successfully utilized for thermal imaging applications during the monitoring of a Tokomak fusion reactor.

Gregory (1993) describes infrared fibers which are available commercially. For wavelengths longer than 3 μm these include Fluoride ZBLAN (0.4 μm - 5 μm), chalcogenide (1 μm - 11 μm), polycrystalline (4 μm - 15 μm) and hollow glass (7 μm - 9.4 μm), metal (5 μm - 5.5 μm, 10 μm - 13 μm) and sapphire (10 μm - 17 μm) fibers. With the exception of chalcogenide, losses are generally greater than 0.5 dB/m in this region. Work is continuing on the development of mid-infrared fibers. It has recently been reported (Laser Focus World, 1994) that tellurium-containing glass fibers with an attenuation of 0.11 dB/m at 6.6 μm and less than 1 dB/m over a range of 5.25 μm - 9.5 μm have been fabricated.

The discussion above suggests that fiber-optic based diagnostics may be suitable for developing a high-speed probe for the measurement of replacement-agent and halon 1301 concentrations. Based on the discussion in Section 11.5.2.3, the mid-infrared and near-infrared regions of the spectrum seem to offer the best possibilities, even though the ultraviolet region is also feasible for halon 1301 and CF_3I. Here we will focus on the possibility of developing fiber-optic probes based on absorption of infrared radiation.

In many ways a fiber-optic-based concentration probe is similar to the DIRRACS system described earlier in that the absorption of an infrared band is monitored to infer concentration, and that the pathlength of the light beam is used to define the absorption volume. However, there are potentially several advantages for a fiber-based measurement technique. Fibers tend to have fairly small diameters (values less than 1 mm are common) so the sampling volume as well as the probe size itself can be quite small. As a result one would expect a fiber-optic-based probe to sample a smaller volume and to be less intrusive than the DIRRACS. Both the detector and light source can be isolated from the measurement volume so that heating problems such as those encountered during the current study can be eliminated.

Since the absorption of mid-infrared light is strongest and the most commonly used approach, fiber optic systems employing this wavelength range are discussed first. This is followed by a discussion of near-infrared methods.

As mentioned above, incoherent light sources are difficult to couple into single fiber optics. If available, lasers offer a much better alternative as a light source. There are a number of tunable lasers which operate in the mid-infrared region. Several of these are reviewed by Eng and Ku (1982). The best candidates which are currently available for the application under discussion are known as tunable lead-salt diode lasers (TDLs). Eng *et al.* (1980) list some of the unique features of TDLs as narrow linewidths ($< 10^{-4}$ cm^{-1}), broad and continuous tunability, ease of rapid amplitude modulation and wavelength scanning, operation throughout the 3 μm to 30 μm spectral range, and extremely small emitting areas.

TDLs are formed from lead-salt semiconductors and their ailoys with SnSe, SnTe, CdS, and other materials. Laser action is induced by optical transitions across the bandgap between the nearly empty conduction band and the nearly full valence band existing across a p-n junction. The laser wavelength

is dependent on a number of system parameters including composition, hydrostatic pressure, magnetic fields, operating temperature, and bias current. One major disadvantage of TDLs is that they require cryogenic cooling in order to operate. The requirement for cooling substantially complicates the operation of these devices.

TDLs have been used for spectroscopy measurements in a wide variety of molecules (Eng *et al.*, 1980; Eng and Ku, 1982). The devices have also been widely used for making line-of-sight measurements of concentrations for a range of molecules. As an example, Sell (1983) measured the concentration of CO in the exhaust of an operating engine by line-of-sight absorption of TDL laser light at 4.70 μm. Measurements over a concentration range of 0.1 to 1.5 volume percent were discussed. Particularly significant was the ability to make accurate measurements of CO concentration in the presence of water vapor. The time response of the instrument was reported as 25 ms.

Hanson (1983) has summarized a series of TDL measurements in systems relevant to combustion. Due to the ability to compare on- and off-resonance signals, it was shown that molecular absorption measurements can be made in the presence of concentrated soot fields, which also strongly absorb the infrared light. Many of the measurements discussed were line-of-sight applications, but of particular relevance to the current discussion is the use of TDL absorption measurements for local time-resolved measurements of concentration. Schoenung and Hanson (1982a) demonstrated two techniques for making such measurements in nonreacting and combusting turbulent flows of CO. Absorption measurements were carried out in the region of the 4.6 μm band center of CO. In one case, 8 mm diameter cooled hollow light pipes constructed from brass and aluminum were used to transport the IR laser beam to and from an open absorption path typically having a length of 5 mm. With this probe it was possible to make CO concentration measurements having a signal-to-noise ratio of 1 for a 0.1 mole percent concentration of CO. Response times for the measurements were estimated to be 0.5 ms.

In a second approach, Schoenung and Hanson (also discussed in 1982b) rapidly extracted a sample of the flow through a miniature water-cooled quartz sampling probe having a choked orifice of 0.04 cm diameter. The gases then passed into a room-temperature sample cell having a 1.4 cm pathlength. TDL absorption measurements were then carried out in the cell. With this configuration, it was possible to detect CO concentrations as low as mole fractions of 0.000001. Both experiments and modeling indicated that the response time for this probe was on the order of 0.5 ms with a sampling length of roughly 5 mm for room-temperature gases and 2.0 cm in the flame.

As an indication of the response times achievable using TDL absorption spectroscopy, consider the work of Hanson (1977) who reported a line-of-sight measurement of CO heated by a shock tube. It was reported that measurements could be recorded in less than 100 μs.

Based on the above discussion, it would appear that a TDL system in conjunction with either a properly designed extractive probe or IR fiber optics could be used to make concentration measurements with the required temporal resolution. Kuznetsov *et al.* (1992) have demonstrated the feasibility of fiber-based measurements by coupling lead-salt diode lasers with infrared halide and chalcogenide fibers. The system for coupling the lasers and fiber optics is described. Measurements are reported for ammonia at 10 μm, water at 7.3 μm, and carbon monoxide at 4.7 μm.

Given the ability of the technique to quantify small absorptions and the known strengths of absorption lines in halon 1301 (Baldacci *et al.* 1982), it should be possible to record halon 1301 concentration measurements for very short path lengths. Similar IR absorption strengths at slightly different spectral locations are to be expected for the other replacement agents. Based on these characteristics, the sampling volume for such a system could be made considerably smaller than the current version of the DIRRACS. As discussed earlier, there is a strong interaction between sampling volume, flow velocity, and the ability to time resolve concentration fluctuations. The capability of making concentration measurements in the presence of an absorbing and scattering medium suggests

that measurements should be possible in dirty environments and, perhaps, even in the presence of a two-phase flow of the agent.

It should be noted that the use of lead-salt TDLs does have some drawbacks. Significant complications are introduced by the need for cryogenic cooling. They are fairly complicated devices which require significant training to use appropriately. Additionally, their cost remains relatively high. Often it is necessary to calibrate the output wavelength using known absorptions. Wavelength scans can be nonlinear, and it is common to use a Fabry-Perot etalon to determine the scanning behavior. Occasionally, the frequency output is stabilized by passing part of the beam through a cell with a known absorber. These characteristics suggest that a concentration measurement system for halon alternatives is likely to be costly to construct and operate.

Development work on mid-infrared lasers is continuing. For example, Faist *et al.* (1994a; 1994b) have recently reported the development of a new type of semiconductor laser known as a quantum cascade laser. The laser demonstrated operated near 4.35 μm, but the authors conclude that by varying the band structure of the semiconductor it should be possible to construct lasers having wavelengths throughout the mid-infrared and extending out to the submillimeter wave region. The new laser requires cooling, but operation has been demonstrated for temperatures above that of liquid nitrogen (77 K) suggesting that cooling of these lasers would be somewhat easier than for mid-infrared TDLs which generally must be cooled to substantially lower temperatures. The authors suggest that it may even be possible to operate quantum cascade lasers at higher temperatures.

It is clear that additional development of this new technology is required before a combination of mid-infrared lasers and fiber optics can be used for making concentration measurements in gas mixtures containing replacement halons. However, the advances made thus far in both fiber optics and lasers suggest that in the future it should be possible to quantitatively measure many molecular species, including replacement fire-fighting agents, with high spatial and temporal resolution using a fiber-optic based, mid-infrared absorption probe.

Until recently, the near-infrared has been used very little for quantitative concentration measurements due to the weak absorption of most molecules in this spectral range. However, there are potential advantages for making concentration measurements in this wavelength region. In the mid-infrared the number of lasers and sensitive detectors has been very limited. On the other hand, numerous tunable and nontunable lasers have been developed for near-infrared work, and quantum detectors capable of amplification exist for these wavelengths. The availability of a number of communication lasers operating in the spectral region has driven a great deal of development. These lasers are inexpensive, come in small packages, require low input power, can be efficiently modulated at high frequencies, and require little or no cooling.

Recent research has shown that it is possible to use near-IR absorption techniques for sensitive concentration measurements. A few of these studies are summarized here to give a flavor of the possibilities. One of the earliest studies was by Lenth (1983) who used a GaAlAs diode laser to detect a water-vapor absorption line at a wavelength of 0.8167 μm. In order to increase the sensitivity, a technique known as optical heterodyne spectroscopy was employed. The details of this approach are beyond the scope of the current discussion. It will suffice to point out that the method involves rapid scanning of the laser wavelength over the spectral region of the transition under investigation. This turns out to be relatively simple since the GaAlAs laser can be scanned by varying either the operating temperature or "injection current" for the laser. Lenth used temperature to adjust the laser to operate at a wavelength of 0.8167 μm and then modulated the injection current at a microwave frequency of 2.6 GHz. An absorption cell having a 1 m pathlength containing 2.4 kPa of water vapor was used to provide a 5 % absorption which was easily detected using the experimental configuration.

Later investigators have employed a frequency modulation technique in which two well defined, but closely spaced frequencies are superimposed on the injection current. This approach is known as

two-tone frequency modulation spectroscopy (TTFMS) and has been discussed in detail by Cooper and Warren (1987). Wang *et al.* (1989) applied the technique to record water concentration using overtone absorptions near 0.8171 μm. It was demonstrated that absorptions as small as 3×10^{-7} could be measured. Based on data provided in the paper, it can be shown that such high sensitivity is sufficient to accurate measure water vapor at pressures less than 1 kPa for a 1 mm pathlength. Stanton and Silver (1988) reported similar measurements using the third overtone absorption band of hydrogen chloride. A InGaAsP laser operating at 1.2 μm was used for these measurements. The minimum detectable absorption was 4×10^{-6}, but it was argued that relatively straight-forward modifications to the experimental system would be expected to lower this value below 10^{-6}.

Very recently, Bomse (1994) has suggested that near-infrared diode laser spectroscopy could be used to measure a number of species relevant to fire extinguishment including hydrogen fluoride, hydrogen chloride, hydrogen bromide, hydrogen iodide, water, methane, carbon dioxide, carbon monoxide, hydrogen cyanide and oxygen. Furthermore, he speculated that the technique could be developed for measuring halon replacement concentrations. This manuscript also contains a good introduction of the technology which is used for these measurements.

Very efficient optical fibers have been developed for communication applications, and it was a natural extension to couple the newly developed sensitive near-infrared absorption techniques with optical-fiber transport of the laser beam. Carlisle and Cooper (1990) used TTFMS to record a 10^{-4} absorption of water at 1.3 μm following transport of the laser beam through 100 m of optical fiber. After passing through the optical fiber, the laser beam was collimated with a lens, passed through a sample cell containing the water vapor, and was detected with a InGaAs photodiode. A two-beam method was employed in which a reference beam was split from the laser beam before entering the absorption cell. The signal levels indicated the minimum detectable absorption was 5×10^{-7}.

The use of fiber optics makes it possible to multiplex two or more laser beams into a single fiber. Arroyo *et al.* (1994) used two separate lasers operating at 1.393 μm and 1.394 μm to record two individual absorption lines of water vapor heated to 1293 K in a shock tube. Frequency modulation techniques were not used for this experiment. Instead, the two laser were simply scanned at high rates at different times, and the absorption of each beam was measured by comparing transmitted light with a reference signal. The scans could be recorded at a 3 kHz rate. Since the two water transitions were for different rovibronic states, temperature measurements could be derived from the ratio of integrated intensities for the two transitions. The inferred temperature was within 4 % of the actual temperature.

Baer *et al.* (1994) extended the multiplexing technique further by demonstrating that three laser beams could be used to simultaneously measure water concentration, oxygen concentration, and temperature. In this case, two of the laser beams, operating at 1.347 μm and 1.392 μm, were used to measure water vapor temperature in the same way as above. The third laser was operated near 0.76065 μm and was used to measure the absorption of a weak electronic transition of oxygen. The multiplexed beams were transported to the observation region by the optical fiber and then allowed to pass through either a heated static cell or a 236 cm long room-temperature air path. After passing through the observation volume, the beams were separated using a diffraction grating and detected by three individual photodetectors. Note that since the beams were physically separated, it was not necessary to scan the lasers at different times. Absorption measurements of the water lines were made in a standard way using dual beam approaches, while the oxygen absorption was measured using TTFMS. All three measurements were recorded with a repetition rate of 2 kHz. Measurements showed that the concentration and temperature measurements could be made with good accuracy.

The near-infrared investigations discussed thus far would all be classified as line-of-sight experiments and therefore are not directly applicable to measurements having high spatial resolution. However, Bomse (1994) discusses two approaches which could be used to provide short pathlengths and, therefore, high spatial resolution. The first is referred to as "pitch and catch" in which a laser

beam is transported to the observation volume by a fiber optic, is then passed through the observation volume, and then enters a second fiber optic which transports the beam to a detector. He indicates that collection efficiencies of 25 % - 50 % are possible with this configuration. In the second arrangement, the transmitted laser beam is allowed to strike a detector directly after passing through the observation volume. This is the same approach used in the fiber-optic experiments discussed above. It may be possible to obtain high spatial resolution by reducing the separation between the fiber and detector.

Based on the above discussion, it is clear that fiber-optic-based infrared absorption methods in both the near- and mid-infrared have excellent potential for highly spatial and temporally resolved measurements of fire-fighting agents. Considerable research and development would be required to demonstrate the viability of these approaches and develop a system for field use.

11.5.3.3 Other Fiber-Optic-Based Concentration Measurement Approaches. As mentioned previously, simple geometrical optics may be used to describe the light transmission in an optical fiber if the diameter is large relative to the wavelength of the transmitted light. As the diameter becomes small, however, the transmission tends to behave according to wave-guide theory. In other words, the wave nature of light must be taken into account. Furthermore, for small diameter fibers, light propagates not only in the core but also in the cladding. This latter component is known as the evanescent wave, and it decays rapidly in a direction away from the axis of the fiber. If a fiber has no cladding, the evanescent wave penetrates into the fluid outside of the fiber, and, if the fluid strongly absorbs at the wavelength of the transmitted light, the power of the propagating light in the evanescent wave is decreased. Thus, if the fiber is of very small diameter, and the gas surrounding the fiber is a strong absorber, gas sensing can be performed by using an unclad portion of the optical fiber itself as the transducer and employing evanescent wave coupling.

On the other hand, as the fiber diameter gets larger, geometrical optics assumes increasing importance, and the transmission of light behaves according to total internal reflection. For this case, with a gas surrounding the fiber, the core index of refraction, n_1, is much greater than the index of refraction for the gas, n_2, and the fiber becomes highly guiding in the sensing region with a corresponding reduction in evanescent wave power and a resulting loss in detection sensitivity. For liquids, a larger fiber with the cladding stripped from a small sensing region performs better due to the relatively higher indices of refraction for liquids. This latter principle for the detection of chemical species is referred to as attenuated total internal reflection (ATR).

The former case of using a very small fiber and taking advantage of evanescent wave coupling to a gas was demonstrated by Tai *et al.* (1987) using fibers transmitting mid-infrared radiation at 3.392 μm for the detection of methane. The authors used standard fused-silica fibers with a core of 50 μm and a cladding thickness of 125 μm. Then, by heating the fiber and drawing a portion of it to a much smaller diameter (1.8 μm), they fashioned a 10 mm long sensing region and were able to generate an evanescent wave of 5 % to 40 % of the total propagating power outside of the fiber. The minimum detectable concentration of methane using this configuration was reported to be about 1 %.

Expanding upon the idea of ATR, an optical fiber may incorporate fluorocarbon polymers or silicones as cladding materials. Due to their high refractive indices (weak guiding of the core light), the evanescent fields can penetrate deeply into the cladding. These cladding materials, however, are quite porous, and the evanescent field may interact with any gas present in the pores. A power loss at a particular wavelength can then be used to infer the concentration of gas present. Ruddy and Lardner (1993) have modeled the time-dependent attenuation of the optical power in a multimode, step-index fiber due to Fickian diffusion of a fluid through its porous cladding. They proceeded to derive sensor sensitivity, response time, and the product of minimum detectable concentration and sensing length in terms of the fiber parameters, the absorptivity of the fluid, and the diffusion coefficient in the cladding

material. A large number of results are reported in the form of a table listing many common gases. For each gas, an absorption coefficient at a particular wavelength is used to estimate the evanescent power attenuation for typical fiber parameters, and these data yield a value of the product of minimum detectable concentration and sensing length which is reported in the table for each gas. A disadvantage for a technique such as this is the fact that diffusion of the absorbing gas into the fiber is a slow process. Time-response estimates provided by the model are reported in the form of a parameter, t_{90}, which represents the time required for the attenuation to reach 90 % of the saturation value. Predicted t_{90} values for typical fiber dimensions were in the range of 20 s to 30 min. The paper also contains numerous references to other ATR and evanescent wave coupling investigations.

An interesting variation on the porous cladding technique was reported by Zhou *et al.* (1989) in which a copolymerization process was used to create a fully porous, plastic fiber with a pore size range from 5 nm to 10 nm and a surface area of 100 m^2/g. A small 5 mm length of the porous fiber, representing the sensing area, was then spliced into a length of standard, nonporous, plastic fiber. A strongly absorbing gas was then allowed to permeate fully into the sensor core and direct in-line absorption occurred. The authors claim that this sort of sensor has much greater sensitivity than those based on evanescent wave coupling. Furthermore, they assert that the porous fiber exhibits high gas permeability as well as high liquid impermeability, making it particularly suitable for gas concentration measurements in aqueous samples (such as blood gas sensing, for example). An additional advantage was the high flexibility and ease of use for plastic fibers relative to glass fibers. Disadvantages for this technique include the fact that some light gets scattered out of the porous section of the fiber, the calibration curve is nonlinear, and response times are on the order of minutes.

Wenquan *et al.* (1992) describe the application of a tin oxide (SnO_2) film to an optical fiber, and the resulting increase in transmission when the fiber is immersed in differing concentrations of such gases as methanol, acetone vapor, and ammonia vapor. They present data in the form of transmission spectra for various concentrations of these gases and show that the increases occur in the visible and near-infrared ranges.

The concentration-measurement approaches discussed in this section are under active development. It must be concluded, however, that they have not yet been developed sufficiently to allow real-time concentration measurements of halon replacements. However, as advances are made, it is possible that these techniques could become quite useful for this application.

11.5.4 Additional Optical-Based Techniques. There are a number of additional optical techniques beyond the standard absorption and fiber-optic-based approaches discussed thus far which have been used for rapid concentration measurement of gas-phase species. Several of these are discussed in the following sections.

11.5.4.1 Raman Spectroscopy. Raman light scattering refers to the nonresonant scattering of light by a molecule in which the energy of the scattered light is shifted by an amount corresponding to differences between the rotational, vibrational, or electronic energy levels of the molecule. When the scattered light has a longer wavelength (lower energy) than the light incident on the molecule it is known as Stokes scattering, and when the scattered wavelength is shorter (higher energy) it is known as anti-Stokes scattering. The most common form of Raman light scattering involves vibrational transitions, and this type will be the focus of the current discussion. Eckbreth (1988) provides a good discussion of Raman light scattering and its use for measurements in combustion environments.

The physical mechanisms responsible for Raman scattering are relatively weak, and very intense lasers are generally required to scatter sufficient radiation for easy detection. The intensity of scattering increases with the photon energy to the fourth power. As a result, visible and even ultraviolet lasers are commonly used to induce Raman scattering. Since the effect causes wavelength

shifts which are characteristic of a particular vibrational transition, it can be selective. As the shifts in wavelength are characteristic of vibrational transitions, they have energies which correspond to mid-infrared transitions. Such energy shifts are small compared to the initial energy of the photons for the light source. The light scattering process also generates light which is unshifted in wavelength from the light source (*i.e.*, resonance or Rayleigh scattering which will be discussed shortly) and which is generally many times more intense than the Raman scattering. As a result, it is typically necessary that the Raman scattered light be isolated from the Rayleigh light scattering in some manner (*e.g.*, by using a spectrograph or a narrow-band spectral filter). The need for spectral isolation complicates the experimental set up.

Raman light scattering can be used for concentration measurements since the intensity of the scattered light is proportional to the number of molecules in the scattering volume. Time-resolved measurements are generally made using high-power pulsed laser which generate sufficient scattered light intensities to provide accurate concentration measurement. A significant drawback of the use of pulsed lasers is that the repetition rates tend to be low (< 100 Hz), and the pulse-to-pulse variations can be large requiring that the laser intensity be measured for each pulse. Copper vapor lasers have recently become available having pulse rates greater than 1000 Hz and sufficient power levels for Raman scattering studies.

It is our opinion that an experimental system could be developed using Raman light scattering for the measurement of halon-replacement concentrations at the required data rate. However, the system would be very expensive to construct and maintain, would require high levels of operator training, and would require that the system in which the measurements were to be made allow adequate optical access for the laser beam and the collection of scattered light. As a result, we conclude that Raman light scattering is not a practical approach for the current application.

11.5.4.2 Coherent Anti-Stokes Raman Spectroscopy (CARS). Coherent anti-Stokes Raman spectroscopy (CARS) is a complicated nonlinear optical effect which leads to the generation of an intense coherent beam when two laser beams are "mixed" with the proper phases in an appropriate medium. The effect occurs when two laser beams have a frequency difference ($\omega_1 - \omega_2$, with $\omega_1 > \omega_2$) corresponding to a vibrational transition frequency of a molecule in the volume where the laser beams cross. The resulting coherent beam has a frequency, ω_3, given by

$$\omega_3 = 2\omega_1 - \omega_2 \ . \tag{66}$$

The beam which is generated has a higher energy than either of the original laser beams which is why it is known as anti-Stokes scattering. Due to the phase-matching requirements of the technique, the coherent beam which is generated propagates in a different direction than either of the input laser beams.

Since the optical effect which leads to CARS is nonlinear, very high laser intensities are required to induce the effect, but once a threshold power is reached, the intensity of the generated beam increases rapidly. CARS has several advantages over the Raman scattering technique described in the last section. First, the coherent CARS beam can have an intensity many times higher than obtainable from simple incoherent Raman scattering. Second, the fact that the CARS beam is coherent means that it can be transported over a long distance before detection. As a result, it can be spatially separated from potential interferences such as the laser beams used to induce the effect. Third, due to the coherence of the generated beam, CARS measurements can be carried out in flows which are heavily laden with particles. Eckbreth (1988) and Goss (1993) provide excellent reviews of CARS techniques.

CARS has been widely employed for temperature measurements in combustion and other types of systems. In some laboratories it is used quite routinely, and systems have been developed which are sufficiently hardened that they can be used in quite harsh environments (*e.g.*, Eckbreth *et al.*, 1984). Proper calibration allows the technique to be used for concentration measurements as well. It is likely that CARS could be developed as a technique for monitoring suppression-agent concentrations. However, there are several drawbacks which could potentially limit the use of CARS for the current application. Perhaps the most detrimental problem is the complexity and cost of a CARS system. Normally a high powered pulsed Nd^{+3}/YAG-pumped dye laser is combined with the doubled output of the solid-state laser at 532 nm to provide the two laser beams. Such a laser system with the associated hardware and detection equipment normally runs well in excess of a 100 000 dollars. In order to record multiple measurements multiple CARS systems would be required. Additionally, the use of a CARS system is far from turn-key, and a qualified professional is required to operate the system. Similar to the Raman measurements discussed earlier, the ability to record measurements every millisecond is likely to be limited by the maximum pulse rate of the laser system. Generally measurements are make at 10 Hz - 20 Hz. Apparently, no measurements have been made at 1000 Hz. Finally, optical access to the region of interest is required. Due to the coherent nature of the laser beams and the generated CARS beam, it would be possible to design systems with relatively small windows for optical access.

Due to the cost, complexity, and relatively low frequency of the CARS approach, we do not recommend this technique for routine concentration measurements of alternative agents. However, it could prove very effective for special measurements under certain circumstances. In particular, it would appear that CARS measurements could be performed during an actual fire-extinction event.

11.5.4.3 Rayleigh Light Scattering. As mentioned above, Rayleigh light scattering refers to light scattering by molecules in which the wavelength (energy) of the scattered light is unchanged from that of the light source. The intensity of scattered light is generally at least a 1000 times greater than observed for Raman scattering. As for Raman scattering, the intensity of scattering light increases as the inverse fourth power of light wavelength. Rayleigh light scattering can easily be observed using commercial high-power CW lasers such as argon ion lasers. Scattering can also be induced using pulsed lasers.

Rayleigh light scattering occurs as the result of the interaction of light with all atoms and molecules in a volume. However, the intensity of scattered light depends on the polarizability of the atom or molecule, and the intensity for different molecules varies widely. The rate of photon detection (R_p) for Rayleigh scattered light can be written as

$$R_p = KN\sum_{j=1}^{M} \sigma_j X_j \,, \tag{67}$$

where K is a constant whose value depends on the laser intensity, the optics used, and the quantum efficiency of the detector, N is the total number of molecules in the observation region, σ_j is the Rayleigh light scattering cross section for species j which is a measure of the efficiency of the molecule for scattering light, and X_j is the mole fraction of species j.

For gas mixtures containing three or more species, Equation (67) alone does not provide sufficient information to determine values of X_j. However, in mixtures of two gases, *e.g.*, air and a halon replacement, the sum of the two mole fractions must equal 1, and it is possible to measure mole fractions for the two species. If calibrations are carried out for the pure gases, denoted as 1 and 2, Equation (67) can be rewritten as

$$X_2(t) = \frac{I(t)-I_1}{I_2-I_1}, \tag{68}$$

with $X_2(t)$ being the time-dependent concentration of species 2, $I(t)$ the observed time-dependent Rayleigh light scattering intensity from the observation volume, and I_1 and I_2 the observed scattering intensities from pure gases 1 and 2.

Rayleigh light scattering has been widely used to record time-resolved concentration measurements in turbulent flows of binary gas mixtures (*e.g.*, Pitts and Kashiwagi, 1984; Dowling and Dimotakis, 1990). It has been demonstrated that measurements are possible for a variety of gas pairs which have data rates in excess of 20 kHz and sampling volumes as small as 0.0003 mm^3. The technique has been applied to molecules such as CF_4 and SF_6 (Pitts, 1991) which are similar to the replacement agents in molecular structure. Concentrations of halon 1301 have been recorded during unpublished work at NIST. (Pitts, 1984)

There is no doubt that Rayleigh light scattering could be used to make accurate measurements of the replacement agent concentrations given the proper experimental conditions. In fact, Rayleigh light scattering was considered as a serious candidate for such measurements during the planning for the current project. It was ultimately rejected due to its sensitivity to stray scattered light. As discussed above, Rayleigh light scattering occurs at the same wavelength as the laser which induces it. Scattering from particles, known as Mie scattering, also occurs at this same wavelength. Unfortunately, unless special precautions are taken, particles are always present in air with sufficient size to induce Mie scattering from a single particle which is much stronger than the Rayleigh light scattering measured for all of the molecules in the observation volume. As a result, Rayleigh light scattering concentration measurements are nearly impossible unless these small particles are removed in some way. Additionally, any surfaces which are near the observation region can reflect or scatter stray laser light (known as glare) at the same wavelength. For the worst cases, glare can completely overwhelm the Rayleigh light-scattering signal.

A facility for the investigation of turbulent flows has been constructed at NIST which nearly totally eliminates problems associated with the presence of particles and glare. (Bryner *et al.*, 1992) However, such an approach was deemed impractical for field studies of agent releases and Rayleigh light scattering was eliminated from consideration for the current application.

11.5.4.4 Fluorescence Concentration Measurements. It was noted earlier that quite strong absorption of light is often observed for transitions between the electronic states of molecules and atoms. These strong absorptions are referred to as "allowed" transitions. The result of the absorption of light is that a molecule ends up in an excited state. The energy which is absorbed is eventually given up by the absorbing species, and the system returns to a lower energy state. There are a number of ways that an electronically excited species can lose energy. One of these is by the release of a photon. The resulting electromagnetic energy can either have the same energy as the photon which was absorbed (*i.e.*, it can return to the same lower energy state from which it came by a process known as resonance fluorescence), or it can result from a transition to a different lower lying state, in which case the emitted photon will be at a different energy than the absorbed photon. Unless absorption occurred from relatively high lying energy states, the transition is most likely to occur to energy states which lie higher than the state from which absorption occurred. As a result, the emitted photon will have a lower energy than the absorbed photon (*i.e.*, the emitted photon is red-shifted).

Fluorescence can be used for selective detection since the absorption and emission wavelengths for a particular molecule are determined by the electronic structure of the molecule which is generally unique. By careful selection of the absorption wavelength and spectral isolation of the emitted energy,

it is possible to isolate the fluorescence from an individual species in complicated mixtures. Generally, electronic transitions of molecules and atoms correspond to photon energies in the visible and ultraviolet portions of the electromagnetic spectrum. Very efficient light sources for absorption and detectors for observing fluorescence have been developed. As a result, species which strongly fluoresce can be detected and measured nonintrusively with good sensitivity using laser-induced fluorescence (LIF). Techniques based on LIF can have excellent temporal and spatial resolution.

The details of the fluorescence behavior of molecules and atoms is a complex subject which is beyond the scope of the current review. Excellent discussions are available in numerous monographs (*e.g.*, Calvert and Pitts, 1966; Eckbreth, 1988). It is sufficient to point out that fluorescence techniques are widely used to measure species in very complicated systems including combustion (*e.g.*, see Eckbreth, 1988). LIF is sufficiently sensitive that images can be recorded for two-dimensional sheets (Seitzman and Hanson, 1993).

As noted above, with the exception of CF_3Br and CF_3I, the agents considered in the current study do not have strong electronic absorptions at energies lower than those corresponding to the vacuum ultraviolet. As a result, it would be extremely difficult to apply fluorescence techniques to the direct measurements of these agents. However, there is another approach based on fluorescence detection which could be applicable.

For measurements of concentration for species which do not fluoresce, it is common to add small amounts of species which strongly fluoresce as tracers. Examples of species which might be added are acetone and iodine. If the tracer species is uniformly mixed with the molecule of interest, then a measure of the tracer species also provides a good approximation for the concentration of the desired species. Such measurements have not been reported for halon 1301 or its possible replacements considered in this study, but it is possible that a tracer fluorescing species could be dissolved in the agent at low concentrations and used to monitor the agent concentration.

The development of a LIF-based measurement approach for agent concentration measurements would require a large research and development effort. A successful conclusion could not be guaranteed. On this basis, it is suggested that this approach be utilized only if more well developed methods do not prove feasible.

11.5.4.5 Mie Scattering Concentration Measurements. A light scattering technique for the noninvasive point measurement of mean and fluctuating concentration fields within mixtures was pioneered by Rosensweig, Hottel and Williams (1961). A standard implementation of the technique calls for one of the components to be seeded with passive marker particles (or naturally occurring particles may be used, if appropriate) prior to entering the mixing region. An optical probe in the form of an incident light beam is then propagated into the mixture, and the colloidal suspension of particles in the path of the beam scatters light in all directions. Some of that light is collected by a lens outside of the measurement chamber and directed to a field stop (a slit) which passes light scattered from only a short segment of the incident beam. This defines a probe-measurement volume that is then imaged onto a photomultiplier tube where the collected photons are transduced into an electrical current. The current from the transducer is proportional to the number of particles instantaneously contained within the probe volume, in other words, to the particle concentration.

Strictly speaking, marker concentration is an accurate measure of the marked component concentration only when the diffusivity of the marker in the mixture is the same as the diffusivity of the marked species within the mixture. A measure of the two diffusivities can be obtained by comparing the marker Schmidt number with the Schmidt number of the marked component. Normally, the marker Schmidt number is substantially higher. This condition will not affect the measurement of mean concentration, but it will necessitate that caution be used in the interpretation of concentration fluctuations, particularly those that occur very rapidly. So, in addition to the rather

obvious requirement that the particles have light scattering properties, such as size, shape, and refractive index, that remain invariant from the point of introduction into the flow field to the measurement location, the method further requires that the marker particles faithfully follow the motion of the marked fluid.

The latter constraint leads to a choice of particle diameters typically in the range of 0.2 μm to 2.0 μm. The scattering of light from particles in this size range is described by the Mie equations, which are based on a general solution of Maxwell's equations, and, for this reason, the method is often referred to as an application of Mie scattering. However, H.A. Becker, one of the early pioneers of the procedure, combined the Greek word nephele (meaning cloud) with meter and coined the alternate phrase "marker nephelometry" in his 1977 review paper describing the technique.

Indeed, the exhaustive introduction to marker nephelometry by Becker (1977) remains an excellent initial entry point into the literature for the reader unfamiliar with the procedure. This paper describes the state of the art of the marker-scattered-light technique prevailing at that time. Becker gives a rigorous and general treatment of the theory and reviews the experimental efforts up to the time of publication. In particular, he examines the suitability of using marker concentration as an accurate measure of marked component concentration, and he provides theoretical estimates that demonstrate the validity of the claim when a characteristic length scale of the probe measurement volume (the diameter of a sphere with the same volume, say) is much smaller than the largest length scale over which concentration fluctuations occur in the flow field. The author summarizes the following advantages of the technique: noninvasive, applicable in hostile environments, minimal need for calibration, inherent linearity, and good frequency response.

With the exception of a few key papers, no attempt will be made to repeat the extensive review of the literature prior to 1977 conducted by Becker. Instead, selected relevant papers, which serve to provide an overview of the progress in the field up to the present time, will be discussed. The reader is urged to consult Becker (1977) for earlier investigations.

The initial investigation using this technique was that of Rosensweig *et al.* (1961). The experimental configuration consisted of an air jet marked with smoke particles discharging from a 12.7 mm diameter round nozzle into ambient air. The probe measurement volume was defined by the cross section of the incident light beam and by the width of the slit positioned just in front of the photomultiplier tube. The beam diameter at the measurement location was 1.6 mm and the slit width was 1.8 mm. If we assume that the magnification of the collection optics was equal to one, a probe measurement volume of 3.62 mm^3 can be calculated. The frequency response of the system was reported to be flat out to 2.5 kHz. The authors noted that primary scattering was weak, and that the smoke concentration was dilute so that secondary scattering was negligible. Smoke particles with diameters of 1 μm were used. These smoke particles must be small enough to follow the flow. A criterion for evaluating this condition may be found by evaluating the ratio of particle maximum velocity to fluid maximum velocity for a state of steady sinusoidal fluctuation. A brief analysis which yields this criterion follows.

Consider a spherical smoke particle suspended in an air flow of velocity u which is sinusoidally oscillating at frequency f with a maximum velocity U,

$$u = U\sin(2\pi ft) \ , \tag{69}$$

and acted on with a force (F) given by Stokes' expression (modified by the Cunningham correction) for viscous drag in creeping flow, namely

$$F = \frac{3\pi\mu D_p u_{rel}}{1+\frac{K_g l}{D_p}} , \tag{70}$$

where D_p is the particle diameter, μ is the fluid kinematic viscosity, u_{rel} is the relative velocity between the particle and the fluid, K_g is the Cunningham correction factor (= 1.8 for air), l is the molecular mean free path, and l/D_p is the Knudsen number. Note that the Cunningham correction assumes importance only when the particle diameter becomes small enough to approach the size of the molecular mean free path. If the weight of the particle is negligible relative to this drag force, then the equation of motion becomes

$$m_p \frac{dv}{dt} = \frac{3\pi\mu D_p(v-u)}{1+\frac{K_g l}{D_p}} , \tag{71}$$

where $m_p = (\pi/6)\rho_p D_p^3$ is the particle mass for particle density ρ_p, v is the particle velocity, and $u_{rel} = (v-u)$. The solution of this equation is of the form

$$v = V\sin(2\pi ft+\theta) , \tag{72}$$

and one can then form the ratio

$$\frac{V}{U} = \left[1+\left(\frac{2\pi f}{a}\right)^2\right]^{-1/2} , \tag{73}$$

where

$$a = \frac{18\mu}{\rho_p D_p^2\left(1+\frac{K_g l}{D_p}\right)} . \tag{74}$$

For values of this ratio that are very nearly equal to one, the particle is considered to follow the fluid motion. Thus, upon specification of the fluid and the particle density, one may compute a frequency for a given particle size which yields a specified value of the ratio. For the 1 μm diameter particles used by Rosensweig *et al.* (1961), the ratio was 0.997 at a frequency of 5 kHz. Note that the Stokes drag expression used above is valid only when the Reynolds number based on particle diameter is within the creeping flow regime (less than 1). The authors claimed that this condition was satisfied.

Rosensweig *et al.* (1961) used their experimental system to compute mean concentration, concentration intensity (concentration rms divided by mean concentration), frequency spectra,

autocorrelation functions, two-point spatial correlation functions, and integral length scales at various locations throughout the axisymmetric jet. The measurements established the feasibility of the technique and defined the capabilities and limitations of the system. Becker *et al.* (1967a, 1967b) established a large portion of the theory, refined the experimental technique, and carried out an extensive study of the round free jet configuration with the goal of characterizing its behavior as accurately as possible. Once again the authors measured mean concentration, rms concentration, concentration intermittency factor, spectra, and two-point spatial correlation functions at various locations throughout the jet. A general conclusion drawn from the study was that marker nephelometry applied to gas mixing yields a substantial amount of information in the convective region of the concentration fluctuation spectrum, but cannot give information for spatial scales where molecular diffusion is important because the marker particles do not mimic gas behavior at this level.

Grandmaison *et al.* (1982) repeated the earlier measurements of Becker *et al.* (1967a, 1967b) in the round, free turbulent jet configuration. They used a much larger jet, however. Because of the large scale of the jet, the ratio of turbulence integral length scale to probe measurement volume (a measure of spatial resolution) was quite large. The results were therefore used as a check of the accuracy of earlier measurements. In addition, the authors acquired measurements of the skewness and kurtosis of the concentration fluctuations, the probability density function and wave-number spectra extending into the viscous-convective subrange of the concentration fluctuation spectrum.

With the exception of the experiment by Grandmaison *et al.* (1982), all of the experiments reviewed to this point were conducted with systems employing conventional light sources. Shaughnessy and Morton (1977) appear to have been the first to introduce the use of a laser as the light source for the system. The 2 W argon-ion laser beam employed in this study reduced the electronic-shot-noise level in the detector to levels lower than previously attained. The resulting low detector-noise level allowed the study of another type of noise process: marker shot noise. This noise arises as the result of the random arrival in the control volume of the particles which mark the flow field and is usually referred to as ambiguity noise. The intent of the experiment was to explore the limitations imposed by ambiguity noise on the light scattering technique, and, therefore, the well-documented experimental configuration of a round turbulent jet of air marked with smoke particles and exhausting into a secondary air flow was chosen for the study. The authors detected ambiguity noise and determined that it provided a fundamental limitation on spectral measurements. They furnished theoretical estimates of the ambiguity noise spectrum and its dependence on the size of the control volume and on particle concentration. They also presented experimental measurements to support the theoretical predictions. This paper is also a good source for additional references to the literature before 1977.

Gad-el-Hak and Morton (1979) combined the techniques of laser-Doppler velocimetry (LDV) and marker nephelometry to obtain a probe capable of simultaneous measurement of both concentration and velocity fluctuations at a point. They employed this system for the study of the downstream evolution of smoke released in an isotropic, turbulent flow field. Specifically, the experimental configuration consisted of a biplanar grid of rods with diameter 2.4 mm and mesh size 12 mm mounted in the 20 cm × 30 cm test section of a wind tunnel. Air, flowing at a velocity of 4 m/s, created a nearly isotropic turbulent flow field after passing through the grid. Smoke was released upstream of the grid. The smoke had a mean particle diameter of 0.3 μm and consisted of dioctal phthalate polydispersed particles produced by a smoke generator. The probe consisted of a standard LDV arrangement in which two equal intensity beams from a laser were crossed in the flow field forming a fringe system at the intersection volume. Forward scattered light was collected and focused onto a 1 mm diameter pinhole (spatial filter) where it then passed to a photomultiplier tube. The output from the photomultiplier tube was amplified and low pass filtered at 5 kHz to yield a voltage that was directly proportional to the concentration of smoke, whereas for velocity measurements, the

tube output was band pass filtered between 300 kHz and 3 MHz, amplified, and then directed to a circuit which removed amplitude information. The resulting frequency modulated signal was passed through a phase-locked loop in order to demodulate the Doppler frequency shift and to convert it to a voltage directly proportional to the velocity component normal to the bisector of the two crossed beams. Note that velocity measurements were possible only when smoke was present. The spatial resolution of the system was about 2 mm, and the signal-to-noise ratio was about 100 for the axial velocity component and 200 for the concentration signal. The system was used for the acquisition of mean and rms velocity and concentration profiles, concentration autocorrelation functions, spectra, scales, intermittencies, probability density functions and concentration-velocity cross correlations. These data were obtained for a selection of downstream locations. An earlier note by Catalano *et al.* (1976) describes similar measurements using the same techniques for an examination of the development of an axisymmetric jet exhausting into a co-flowing airstream.

The work of Long *et al.* (1981) dramatically extended the application of marker nephelometry by simultaneously acquiring the instantaneous concentration field at 10 000 spatial locations in a plane intersecting a turbulent jet flow. The output beam from a 2.5 W argon-ion laser was first focused using a long-focal-length spherical lens (in order to minimize the thickness of the sheet produced in the next step) and then diverged by means of a cylindrical lens. The resulting laser sheet was 0.15 mm thick. The sheet was directed into the seeded jet, and scattered light was collected and imaged onto the active area of a computer-controlled, low-light-level TV camera. In order to freeze the motion, the camera was gated on for a period of 10 μs after which the image was digitized and the values transferred to computer memory and then onto magnetic tape. The digitization was performed on a 100 × 100 array so that the scattered light intensity as a function of position was recorded at 10 000 locations. The lenses were selected such that the area imaged onto the camera corresponded to a 2 cm × 2 cm region of the jet with each pixel of the image corresponding to a volume given by 0.2 mm × 0.2 mm × 0.15 mm. The smallest resolvable length scale was therefore 0.2 mm. The frequency corresponding to this smallest scale at the Reynolds numbers typically used was 7.5 kHz resulting in a minimum resolvable time scale of about 130 μs, which was much longer than the 10 μs time during which the camera was gated on. Thus, each image was essentially a realization of the instantaneous concentration distribution within the flow. The time required to digitize the 10 000 point array and transfer the results to tape was about 1 s, which was much longer than the longest characteristic time scale of the flow. This implied that successive images were independent events and that statistical quantities could be calculated by means of ensemble averaging. The results included plots of mean and rms concentration surfaces varying in two space dimensions over a longitudinal plane passing through the axis of the jet and covering a region extending from three to eight diameters downstream of the jet. Furthermore, a rotation of the laser sheet also allowed data to be acquired for a plane oriented normal to the jet flow. Further results included spatial covariance information and temporal information along a line in the flow field which resulted from an interesting variation on the technique. Additional discussion of the mixing mechanism and the structure of the jet mixing layer as revealed by these measurements was provided by Long and Chu (1981). An earlier paper by Long *et al.* (1979) gives an initial brief introduction to the experimental technique.

Marker nephelometry provides an accurate and sensitive means for measuring concentration in time-varying flows. It is generally considered nonintrusive. Optical access is required, but the experimental configuration is relatively simple. The required lasers and optics are relatively inexpensive and simple to operate. With regard to the current application, however, a major drawback is the need to seed the flow with a uniform concentration of small particles. We have identified no investigations in the literature where a released superheated liquid has been seeded with particles, such that the vaporized liquid has a uniform distribution of particles. A possible alternative would be to seed the air flow. However, this approach would be very difficult to implement in the full-scale dry-

bay and nacelle test facilities at Wright-Patterson AFB. On this basis, marker nephelometry is not recommended for measurements of agent concentration.

11.5.4.6 Specialized Concentration Measurements Based on Optical Absorption. In this section two techniques are discussed which can be utilized for concentration measurements of specific species or for binary mixtures which are known to consist of only two gases such as the halon 1301 and replacement-agent mixtures in air discussed in this report.

An infrared absorption technique known as the nondispersive infrared (NDIR) approach is widely used for quantitative concentration measurements. Various configurations are used, but the most relevant is the Luft-type NDIR analyzer. (Strobel and Heineman, 1989) These devices are often employed for measurements of carbon dioxide and carbon monoxide. In this approach two heated nichrome wires are used as IR sources, and their output is chopped so that light passes first through a sample cell and then a reference cell. Light transmitted by the cells falls on a Golay detector formed by placing the gas of interest in a volume containing a flexible membrane. When radiation is absorbed by the gas in the detector, the volume changes and causes movement of the membrane which can be detected optically or by changes in capacitance. The resulting alternating signal has an amplitude which can be related to the concentration of the gas in the sample cell. Proper calibration results in an instrument which has low noise levels and very little drift. A major drawback of these instruments for the current application is that their time response is on the order of 3 s to 5 s and that gas samples must be extracted and passed through the sample cell. Significant engineering would be required to produce an instrument based on this principle having a millisecond time response.

Kidde-Graviner company (1992) has developed an instrument, named the Ultra-Violet Halonyser, for measuring concentrations of halon 1211 and 1301 based on ultraviolet absorption. It consists of a sensing head having dimensions of 18 cm × 12.5 cm × 8.5 cm which is placed in the flow of interest. The sensing head contains two ultraviolet sources which are transmitted over a pathlength of roughly one cm. One source falls in a wavelength range which is absorbed by the species of interest, while the second is not absorbed. The transmitted beams are then detected by solar blind (one which does not respond to visible wavelengths) detectors. By comparing the two transmitted beam intensities, the concentration of absorbing species can be determined. The presence of the second beam allows the measurement to be corrected for the presence of dust or condensed water.

The specifications for the instrument indicate that it has excellent accuracy, stability, linearity, and temperature insensitivity. The response time is listed as 1 ms. Note that this instrument will be subject to the same geometric constraints as the DIRRACS which were discussed earlier. A 1 ms response time will only be possible if the detection volume is swept out during this period.

The operating wavelengths are not given, but it is certain that the ultraviolet radiation must have longer wavelengths than the vacuum ultraviolet which is strongly absorbed by air. Of the replacement agents, only CF_3I has strong absorption is this region. For this reason, this instrument could not be used for C_2F_5H, C_3F_8, or C_3F_7H. Measurements could be made by mixing a species such as halon 1301 into the agent which would act as a tracer. (Hillman, 1994)

The Ultra-Violet Halonyser seems to offer potential for the direct measurement of halon 1301 and CF_3I. Drawbacks of the current system include the large size of the sampling head, the large sampling volume, and limitations on the number of agents which can be sampled. It would be worthwhile to consider further development of this approach to see if these limitations could be overcome.

11.5.4.7 Optical Speckle Technique. An optical speckle technique was utilized by Oberste-Lehn and Merzkirch (1993) for the indirect measurement of density fluctuations which can then be related to temperature fluctuations by assuming a constant pressure, ideal-gas flow. Because the method directly measures the deflection of light caused by gas density fluctuations, it is also suitable

for the measurement of concentration fluctuations. Recall that speckle refers to the granular appearance that arises when laser light is reflected from a diffuse surface. Because of the rough texture of the diffusely reflecting surface, two wavelets arriving at a point in space that are scattered from different bumps on the surface undergo an optical path length difference. For most light sources, the coherence length is so small that overlapping wave trains change rapidly and randomly, thereby have washing out any interference pattern that might have been set up. Conversely, most lasers enjoy a relatively large coherence length (at least much greater than the height of the surface imperfections) such that when the two wavelets meet at a point in space as described above, a constant phase difference is maintained and a large-scale interference pattern can be sustained. In other words, the spatially coherent light scattered from a diffuse surface fills the surrounding region with a stationary interference pattern.

Oberste-Lehn and Merzkirch made use of this technique to study the turbulent temperature field developed downstream of a turbulence generating grid through which a heated mixture of methane and air was passed. Specifically, methane was injected into the air flow at the grid location by passing the methane gas through injection holes in the tubes which formed the structure of the grid. The gas mixture was then stably burned at the grid location. The grid itself served as the flame holder producing a nearly planar and stable flame front. The investigators determined that a homogeneous turbulent scalar field was produced as a result of this technique beginning at a distance of 15 mesh lengths downstream from the grid. Furthermore, rms values of temperature fluctuations as high as 33 K were produced which were an order of magnitude higher than any achieved by earlier investigations. This fact allowed the experimenters to investigate the question of whether or not a turbulent scalar field remains passive (*i.e.*, it does not affect the turbulence dynamics) at such high fluctuation amplitudes. This question was the motivation for the experiment.

The experimental arrangement for the optical speckle technique employed the light from a pulsed ruby laser. The beam was expanded to a diameter of 90 mm and was then transmitted as a parallel beam through the test section downstream of the grid. After exiting from the test section, the beam passed through a lens which formed a half-size image of a vertical plane in the test section on a ground glass plate placed after the lens. The ground glass served as the diffusely reflecting surface for the generation of a speckle pattern. The light exiting the ground glass plate was then imaged onto a photographic plate. The experimental procedure required that a double exposure be recorded on the photographic plate: the first exposure resulted from a 50 ns pulse transmitted through the test section with no flow, and the second exposure was acquired after passing the pulsed beam through a flow with density variations. The density variation in the turbulent temperature field deflected light resulted in a displaced speckle pattern with respect to the first reference pattern. The local displacement Δ at a point furnished a measure of the light deflection angle ε at a point in the flow field. Subsequent point-by-point interrogation of the double exposure (the specklegram) with a thin laser beam produced a Young's fringe pattern at each location. Evaluation of the fringe pattern permitted the recovery of the local displacement Δ at each point, and thus the light deflection angle ε at each point in the field of view. Finally, this information was used to recover such information as the spatial correlation of the density fluctuations $r_{\rho\rho}$, macro and micro integral length scales Λ_ρ and λ_ρ, as well as one-dimensional energy spectra of the density and temperature fields. By comparing the experimental data with the theoretical models of Rotta (1972) and of Driscoll and Kennedy (1985), the authors determined that even at very large fluctuation magnitudes, the turbulent temperature field could still be regarded as a passive scalar field.

This technique is very interesting because it allows the entire flow field to be analyzed simultaneously. However, we feel that the technique is not appropriate for the current application since it requires significant optical access and a very high degree of experimental sophistication. It would be difficult to record data in real time.

11.5.4.8 Miniature Mach-Zehnder Interferometer. Fabricius *et al.* (1992) discuss the use of a miniature gas sensing system for the measurement of gas concentrations as small as 0.000001 mole fraction. The centerpiece of this system is a small chip (4 cm x 1 cm) which, by employing integrated optics, incorporates a miniature Mach-Zehnder interferometer. As with most interferometry techniques, the input light path is split into two arms (paths) and then brought back together. If the optical path lengths of the two arms are not identical, then the coherent light will form an interference pattern, thereby altering the intensity of the output beam. Light is directed through the chip by means of surface wave guides which are single-mode structures on the order of 4 μm. Now, if one of the arms of the interferometer is coated with a gas-sensitive polymer layer (polysiloxane) which is sensitive to the vapors of organic solvents, then the presence of one of these gases will produce a continuous change in the refractive index of the polymer layer and, in turn, alter the optical path length of one arm of the interferometer. Thus, the phase shift imparted to the signal in one arm induces an interference pattern, and the output intensity of the signal is reduced. The phase shift of the signal is a function of the type of gas and the concentration. To complete the miniature sensor system, light at 788 nm from a semiconductor laser was coupled into the interferometer chip, and the output light was guided by a 50 μm multimode optical fiber to a diode array detector. The authors investigated the response of the system to the presence of various hydrocarbons, chlorohydrocarbons and aromatic compounds. They found the calibration curve (phase shift versus concentration) to be linear, and the response time to be on the order of seconds. Possible drawbacks could include: a lack of reproducibility resulting from difficulties in controlling the thickness and adhesion of the polymer layer and a sensitivity issue due to the fact that light must penetrate a short distance into the polymer layer from within the wave guide and therefore light interaction with the gas-sensitive material is limited.

11.5.5 Acoustic Absorption. A review of the literature indicates that the measurement of concentration of a contaminant within a binary gas mixture can be made by means of acoustic techniques by taking advantage of the direct dependence of sound absorption in gas mixtures on mole fraction. When a sound wave propagates through a fluid or solid medium, it loses some of its energy due to losses in the medium and at the boundaries of the medium. More specifically, following Temkin (1981), the passage of an acoustic wave serves to drive individual fluid particles into oscillation about their mean positions, and because of this motion, the pressure, density, temperature and entropy vary for each fluid particle. The sound wave performs a net amount of work on each fluid particle at the expense of the acoustic energy. In other words, the loss of acoustic energy of the wave becomes an increase in the internal energy of the fluid particles. In general, attenuation within the medium is a result of many factors: viscous losses, heat conduction effects, and diffusive processes, as well as losses associated with molecular exchanges of energy. If the medium is bounded, then losses at the boundaries can also occur as a result of the combination of the effects of reflection, refraction, diffraction and scattering. For the measurement of concentration, the basic experimental arrangement would require an acoustic source which transmits a signal which is attenuated upon passage through the fluid medium of variable concentration to a receiver where the intensity of the signal would be monitored. This basic setup could then be improved with the addition of a second transmitter-receiver pair which propagates a reference signal through a portion of the same fluid medium, but for which the concentration is held constant. Division of the attenuated signal by the reference signal would serve to remove the effects of drift resulting from changes in source intensity as well as variations in the fluid medium itself due to effects other than a changing concentration (humidity variations, *etc.*). Furthermore, techniques based upon the propagation of an acoustic beam vis a vis the transmission of an optical beam enjoy the additional advantage that the fluid medium may be optically opaque. A

brief review of pertinent theory and experiments will be followed by a probative calculation serving to illustrate the feasibility of the method.

The subject of acoustic wave propagation in fluids has been treated by many authors over a period of 150 years. An exhaustive history of the oldest work may be found in Truesdell (1953). In addition, Truesdell develops, with considerable detail and rigor, the classical viscothermal theory describing the propagation of a plane acoustic wave into a Newtonian viscous fluid obeying Fourier's law of heat conduction. The extension of the theory to nonreacting, binary mixtures undergoing various diffusive processes may be found in the papers by Kohler (1949), Huang (1973), and Margulies and Schwarz (1985). In addition, the latter authors extend the theory further by discussing the case of a nondiffusive, equilibrium mixture with coupled chemical reactions as well as the case of a single component viscoelastic material. Bass *et al.* (1984) discuss the classical theory, but augment it with a lengthy discourse on molecular relaxation processes which are of importance for the general case of absorption of sound by the atmosphere. For further information on relaxation processes and their relation to sound propagation in fluids, the interested reader is referred to Lindsay (1982). Several experimental investigations are available which serve to gage the range and validity of the theory. Angona (1953) measured absorption in CO_2, CS_2, C_2H_4O and in mixtures of CS_2 and C_2H_4O for frequencies ranging from 2 kHz to 10 kHz. He reported that differences between theory and the observed attenuation were less than 5 %. Greenspan (1956) performed measurements of sound absorption in monatomic gases such as He, Ne, Ar, Kr, and Xe and Greenspan (1959) extended the measurements to such polyatomic gases as N_2, O_2 and dry air. He reports that the classical theory is verified for monatomic gases, but differences between theory and observed attenuation are somewhat larger in the case of diatomic gases. He provides an extensive review of theory and experiment in Greenspan (1965). Law *et al.* (1966) examined the behavior of sound absorption in mixtures of He in Ar and He in Kr at a single frequency of 70 kHz. They plotted the variation in the absorption coefficient versus mole fraction of He and showed excellent agreement with theory over the entire range. Prangsma *et al.* (1970) performed measurements of sound absorption in mixtures of Ar in He for frequencies ranging from 108 Hz to 1010 Hz. Their data is in good agreement with theory over the lower half of their frequency range. Finally, in the area of detection of acoustic waves in fluids, Bucaro *et al.* (1982) review the state of the art in the use of optical fibers for the purpose of creating acoustic sensors as well as the related issues of acoustic modulation of optical field parameters such as phase, intensity, and polarization. In order to illustrate the nature of the theory and to lay the groundwork for the calculation to follow, the classical viscothermal case will be reviewed below.

The simplest one-dimensional problem concerns the forced propagation of planar, infinitesimal, acoustic waves into a semi-infinite, single component, homogeneous fluid, otherwise at rest. The variables in this perturbed system will be considered to consist of an equilibrium value (I_o) and an acoustic contribution (I^a). The decomposition is represented by

$$I = I_o + I^a \tag{75}$$

where I represents any of the system variables such as velocity, pressure, temperature, *etc.* If one positions a reference coordinate system such that the x-axis points in the propagation direction, then the acoustic contribution oscillates the yz-plane of fluid at $x = 0$ according to

$$I^a = \Re[I_o^a e^{i\omega t}] , \tag{76}$$

where ω is the radian frequency of the oscillation, t is time, and $\Re$ indicates the real part of the expression. This disturbance then propagates in the x-direction as a damped harmonic oscillation governed by the complex propagation constant

$$\chi = -(\alpha + ik) = -\left(\alpha + i\frac{\omega}{c}\right) , \tag{77}$$

where the imaginary part, the wave number k, describes the spatial variation in the propagation direction, and the real part, the absorption coefficient α, is a measure of the change in amplitude with distance. c is the phase speed of the wave. The full description of the damped longitudinal wave is, therefore, given by

$$I^a = \Re[I_o^a e^{\chi x + i\omega t}] . \tag{78}$$

The attenuation and dispersion (variation of phase speed with wavelength) of this acoustic wave are found by solving the balance equations for the fluid such as: conservation of mass, momentum and energy, and with the use of such constitutive relations as: Newton's law (the linear relationship between stress and rate of strain) and Fourier's law, for example. Considerable simplification of the problem follows from the linearization of the field equations that results from the introduction of the infinitesimal acoustic contributions as described by Equation (75) for each variable and then neglecting products of acoustic quantities. Into this set of linear partial differential equations, one substitutes the acoustic disturbance (Equation (78)) for each variable to obtain a set of algebraic equations in terms of the acoustic amplitude variables χ. In order to obtain a nontrivial solution, the determinant of the coefficients of the equations is set to zero. This process yields a biquadratic characteristic equation in the dimensionless variable χ/k_o, where $k_o = \omega/k_o$. Note that c_o is a fixed, reference sound speed which is conventionally obtained by neglecting the effects of viscosity and heat conduction. For this case, fluid pressure is a function of density alone, and $(c_o)^2 = (\partial p/\partial \rho)_s$ (constant entropy). Expressed in dimensionless form, this equation is referred to as the Kirchhoff-Langevin equation and is given by

$$[(i - \gamma X)XY]\left(\frac{\chi}{k_o}\right)^4 + [1 + iX(1 + \gamma Y)]\left(\frac{\chi}{k_o}\right)^2 + 1 = 0 , \tag{79}$$

where the dimensionless variables are

$$X = StVi = \frac{\omega \eta_o Vi}{\rho_o c_o^2} \quad (\textit{Frequency Number}) , \tag{80}$$

$$Y = \frac{1}{PrVi} = \frac{k_\theta}{\eta_o C_p Vi} \quad (\textit{Thermoviscous Number}) , \tag{81}$$

$$\gamma = \frac{C_p}{C_v} \quad (\textit{Specific Heat Ratio}) , \tag{82}$$

$$St = \frac{\omega \eta_o}{\rho_o c_o^2} \quad (\textit{Stokes Number}) , \tag{83}$$

$$Vi = \frac{4}{3} + \frac{\kappa_o}{\eta_o} \quad (\textit{Viscosity Number}) , \tag{84}$$

and

$$Pr = \frac{\eta_o/\rho_o}{k_\theta/\rho_o C_p} = \frac{\eta_o C_p}{k_\theta} \quad (\textit{Prandtl Number}) . \tag{85}$$

Additional quantities referred to in the dimensionless groups are radian frequency, ω, dynamic viscosity, η, density, ρ_o, reference phase speed, c_o, thermal conductivity, k_θ, specific heat at constant pressure, C_p, specific heat at constant volume, C_v, and bulk viscosity, κ_o.

The roots of the Kirchhoff-Langevin equation are found by means of the quadratic formula. The simplest expressions are obtained by solving for the alternative quantity $(k_o/\chi)^2$ yielding the two pairs of roots:

$$\left(\frac{k_o}{\chi}\right)^2 = \frac{-[1+iX(1+\gamma Y)] - \{1-X^2(1-\gamma Y)^2 + 2iX[1-(2-\gamma)Y]\}^{1/2}}{2}$$

and (86)

$$\left(\frac{k_o}{\chi}\right)^2 = \frac{-[1+iX(1+\gamma Y)] + \{1-X^2(1-\gamma Y)^2 + 2iX[1-(2-\gamma)Y]\}^{1/2}}{2} .$$

Note that in this expression, of the two possible values for the square root of the complex quantity within the braces, one uses the principal value, that is, the value for which the argument of the complex number expressed in polar form lies between $-\pi \leq \theta \leq \pi$. Furthermore, of the two pairs of roots in Equation (86), only one root from each pair may be retained, namely the root for which a positive value is obtained for α corresponding to real attenuation. This analysis yields two solutions. The first, referred to as type I waves, corresponds to typical compressional sound waves and is obtained from the first equation in Equation (86), whereas the second is denoted as type II waves, commonly referred to as thermal waves, and derived from the latter expression in Equation (86). Unfortunately, due to the complexity of the expressions in Equation (86), one cannot easily interpret the behavior of α and c. However, for fluids such that $Y < 1/(2 - \gamma)$ and for low frequencies $X << 1$, one may employ a power series expansion to yield an approximation to the solutions in Equation (86). For this approximation, only the pressure wave solution survives (the attenuation of the type II waves is very large at low frequencies) and one obtains

$$\frac{\alpha}{k_o} = \frac{X}{2}[1+(\gamma-1)Y] \quad \textit{and} \quad c = c_o \ . \tag{87}$$

This approximation predicts no dispersion and a simple form for the absorption coefficient due to Kirchhoff (1868). In dimensional form, the absorption coefficient becomes

$$\alpha = \frac{2\pi^2 f^2}{c_o^3}\left[\frac{\kappa_o+\frac{4}{3}\eta_o}{\rho}+\frac{\gamma-1}{\gamma}\frac{k_\theta}{\rho}C_v\right], \tag{88}$$

where f is the frequency of the acoustic wave in Hz. Unfortunately, due to the many assumptions and approximations employed in its derivation, this expression has only limited utility and is most accurate only for low frequencies where the absorption is proportion to f^2.

The extension of the derivation to binary mixtures undergoing various diffusive processes requires the generalization of the balance and constitutive equations used. For example, Fick's equation describing diffusion due to a concentration gradient (Fick, 1855) must be added to the derivation and should, for low frequency number, be extended to include, at the very least, terms describing pressure diffusion and thermo-diffusion (the Soret effect). The pressure diffusion effect describes the tendency for a preferential diffusion of the component with the greater molecular weight toward the region of higher pressure in a local pressure gradient. The thermo-diffusion or Soret effect occurs with a local temperature gradient and describes the tendency for heavier molecules to diffuse toward regions of low temperature. In other words, following Bass *et al.* (1984), when there is a local pressure or temperature gradient, less massive molecules with their higher thermal speeds move toward a condition of equilibrium more rapidly than heavier molecules. The diffusion due to the pressure gradient is accompanied by preferential diffusion of the lighter molecules due to the thermal gradient. Fourier's law must also be supplemented with a term which yields additional heat transfer as a result of diffusion. This effect, called the diffusion-thermo effect, tends to have the opposite effect to that of thermo-diffusion. This sort of generalized Fick's law was developed in the dissertation of Huang (1973) and allows for finite propagation of concentrations at large distances from a diffusing source.

Now, following the more complete derivation of Margulies and Schwarz (1985), the constitutive equations along with the balance equations for the fluid such as conservation of mass, momentum, and energy, are once again combined and linearized as before. A solution in the form of Equation (78) is again assumed and substituted into the equations to yield a set of algebraic equations in the variable χ. The resulting characteristic equation for the determinant of the coefficients becomes a sixth-order polynomial and admits three pairs of roots. Retaining the root from each pair that yields a positive value for α (real attenuation) produces three possible solutions, types I, II and III waves. Once again employing a power series expansion valid for $X << 1$, we can obtain explicit expressions for α and c for the sole surviving type I wave. The form obtained when one assumes a binary mixture of perfect, monatomic gases is given by

$$\alpha = \frac{2\pi^2 f^2}{c_o^3}\left[\frac{k_o+\frac{4}{3}\eta_o}{\rho}+\frac{\gamma-1}{\gamma}\frac{k_\theta}{\rho C_v}+D_{AB}x_A x_B\gamma\left(\frac{M_B-M_A}{M}+\frac{\kappa_T(\gamma-1)}{x_A x_B\gamma}\right)^2\right] \tag{89}$$

and

$$c = c_o ,$$

where the undefined variables in the equation are the diffusion coefficient due to a concentration gradient, D_{AB}, mole fractions of components A and B, x_A and x_B, molecular weights for components A and B, M_A and M_B, molecular weight for the mixture, $M = x_A M_A + x_B M_B$, and the thermodiffusion coefficient, κ_T. This approximation also predicts no dispersion, and the classical form for the absorption coefficient is extended to include diffusion effects. This form of the equation was also found by Kohler (1949).

The absorption coefficient α is more precisely termed an amplitude attenuation coefficient and has units of nepers per meter. Note that a neper (Np) is a dimensionless unit of *level* often used in the acoustics community. More specifically, the American Institute of Physics Handbook defines the level of a quantity as the logarithm of the ratio of that quantity to a reference quantity of the same kind. The neper, then, is a unit of level when the logarithm is to the napierian base e. This attenuation coefficient is not to be confused with the *energy attenuation coefficient*. The latter is related to α because the acoustic energy is proportional to the square of the wave's amplitude. Thus, the energy of the wave will decay with an exponential constant, the energy attenuation coefficient, equal to 2α. We can express this precisely in terms of the acoustic intensity I which is defined as the average rate of flow of energy through a unit area normal to the direction of propagation and has units of W/m^2. The difference in intensity level as the wave propagates from 0 to x is given by

$$I(x) = I(0)e^{-2\alpha x}$$

or

$$2\alpha x = \ln\frac{I(0)}{I(x)} . \tag{90}$$

This quantity, also in nepers per meter, can be expressed in the more conveniently measured units of dB per m by calculating the quantity (see Kleppe, 1989)

$$\begin{aligned} 10\ \log_{10}\left(\frac{I(0)}{I(x)}\right) &= 10\ \log_{10}(e^{2\alpha x}) \\ &= 10\ \log_{10}(e)\ln(e^{2\alpha x}) \\ &= 10\ \log_{10}(e)(2\alpha x) \\ &= 8.686\ \alpha x . \end{aligned} \tag{91}$$

Summarizing, then, α expressed in Np/m can be converted to the more easily measured units of dB/m by multiplying by 8.686.

Some experimental data is available to document the range of validity of Equation (89). Specifically, the experiments of Prangsma *et al.* (1970), Law *et al.* (1966), and Greenspan (1956) are particularly useful. The mixture data of Prangsma *et al.* (1970) and Law *et al.* (1966) show good agreement with theory for relatively low frequencies, and the data of Greenspan (1956) in monatomic

gases displays excellent agreement with Equation (89) up to a frequency number of about $X = 0.1$. Furthermore, in a plot revealing the relative contributions to the absorption coefficient from the effects of viscosity, heat conduction, and diffusion effects, Law *et al.* (1966) showed that for $x_{He} > 0.25$ (He in Ar) and for $x_{He} > 0.15$ (He in Kr), concentration dependent diffusive effects dominate the relative contributions to the absorption coefficient and were attributed to the large differences in molecular weights for the two components. Equation (89), therefore, appears to be a good predictor of the behavior of the absorption coefficient for acoustic waves in a binary mixture of gases with frequency numbers $X < 0.1$.

With this in mind, a probative calculation using Equation (89) was performed to determine the variation in the absorption coefficient of a planar acoustic wave propagating through mixtures of halon replacement agents and air. Although these agents are not monatomic, nor do they follow a perfect gas equation of state, the calculation should, nevertheless, reveal the nature of the variation of the absorption coefficient with mole fraction and should serve as a reasonable guide for the determination of the feasibility of a potential acoustic absorption experiment. The bulk viscosity κ_o and the thermodiffusion coefficient κ_T were both assumed to be zero for the purposes of this calculation. All other material parameters for the fluid were taken to be those for dry air at 20 °C. The acoustic wave was chosen to have a frequency of 1 MHz corresponding to a frequency number $X = 0.001$. The precise diffusivity value to use was unknown. However an examination of experimental diffusivities for various gas mixtures found in such texts as Bird *et al.* (1960) shows that a value of $D_{AB} = 1 \times 10^{-5}$ m^2s^{-1} is reasonable. Note that the various fluid parameters such as η_o, k_θ, and D_{AB} should actually be values calculated for the mixture and should thus be a function of mole fraction. The functional behavior with mole fraction for these values can, with some difficulty, be calculated from the Chapman-Enskog theory described in Hirschfelder *et al.* (1964) or from the more complete two-fluid theory of Goldman and Sirovich (1967, 1969). However, simply using constant values for dry air at 20 °C will provide a relatively accurate first approximation. Finally, the result from Equation (89) was multiplied by 8.686 as explained above in order to obtain units of dB/m. The results are shown in Figure 86, and the program used for the calculation may be found in Appendix M. The figure shows that for each agent, the absorption $\alpha(x_{agent})$ rises to a maximum for $0.1 \leq x_{agent} \leq 0.3$ and then slowly decays back to its starting level. The inverse function $x(\alpha)$ is double valued. It is very sensitive for small mole fractions and less sensitive for larger mole fractions. Except for mole fractions close to the maximum value where some ambiguity could arise, determining the mole fraction based upon sound absorption appears to be quite feasible. Topics which will need to be investigated further include the effects of humidity and the presence of particles on the absorption coefficient.

Even though the analysis provided here suggests that sound absorption has the potential to measure concentration in binary mixtures of air and fire-fighting agents, we have not identified examples where such measurements have been made. For this reason, it is concluded that a great deal of development would be required before this technique would be available for the current application. On this basis, it is recommended that this approach not be developed until other, more developed approaches have been tried.

11.5.6 Summary and Recommendations. During the course of the literature review summarized above we have identified no analytical techniques which could be used to record agent concentrations with high temporal and spatial resolution without a significant development and testing effort. This is true despite the fact that a large and wide variety of possibilities were considered. In fact, none of the techniques surveyed appear to be more promising than the two approaches (combined aspirated hot-film/cold-wire probe and DIRRACS) considered during the current effort.

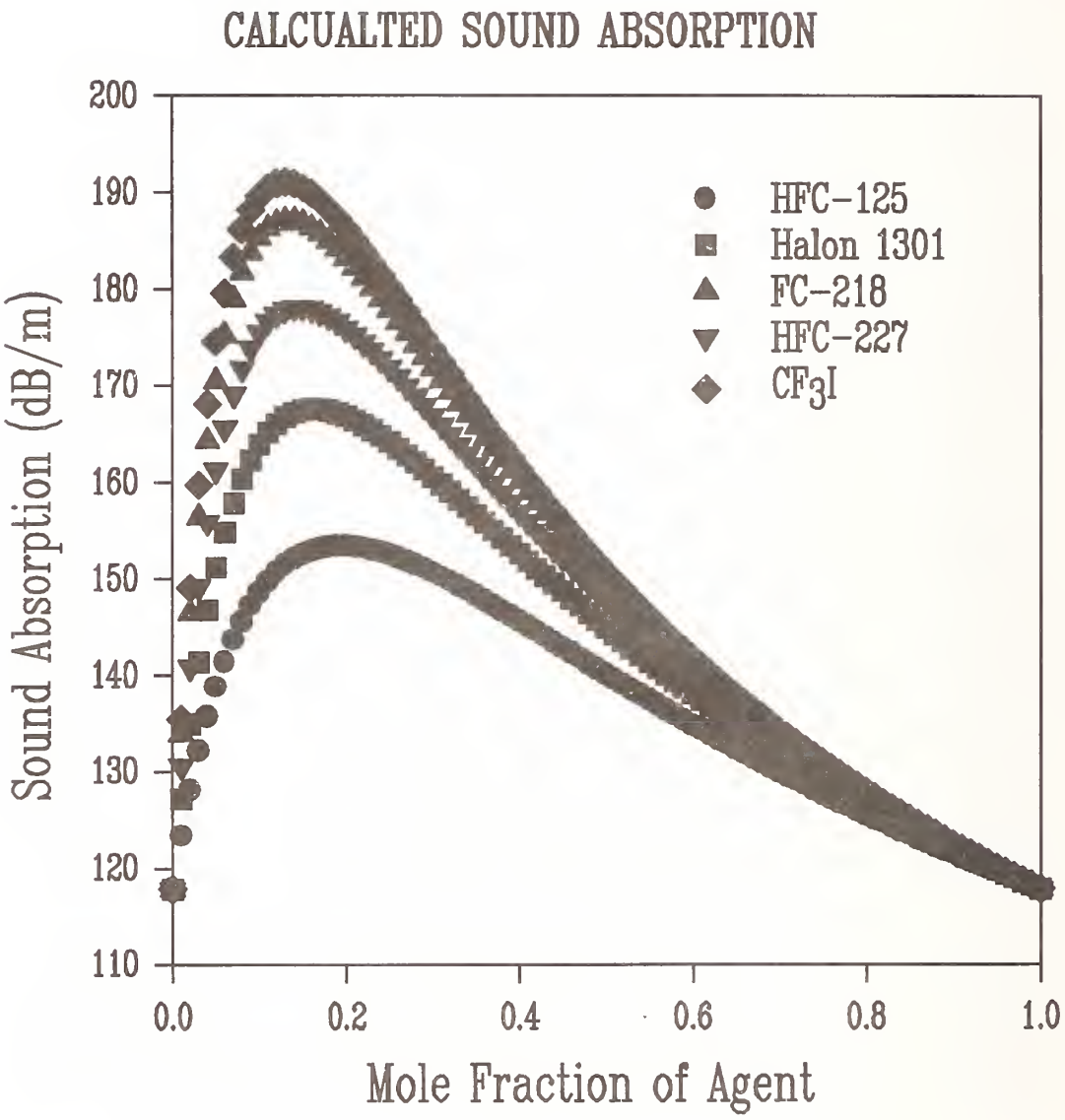

Figure 86. Values of sound absorption (dB/m) as a function of mixture fraction for HFC-125, halon 1301, FC-218, HFC-227ea, and CF_3I in air calculated using Equation (89).

On the other hand, it is also clear that some of the techniques surveyed are more promising than others. In particular, we have concluded that time-resolved mass spectrometry, and mid- and near-infrared absorption used in conjunction with fiber optics (to provide easy access and spatial resolution) are the most promising approaches considered during our literature search. If it is necessary to expand the search for suitable diagnostics, these approaches should be assessed very early in the effort.

11.6 Acknowledgments

This project was supported by the Air Force, Navy, Army, and the Federal Aviation Administration. A large number of people made contributions to our efforts by providing guidance, data, advice, and information. We are very grateful to all for the help we received. Lt. Gretchen Brockfeld of Wright-Patterson AFB served as the project manager. Her advice and support was very much appreciated. Our specifications of the combined aspirated hot-film/cold-wire probe was greatly aided by our discussions with Jagadish Buddhavarapu, Skip Kiland, and Steve Hoff of TSI, Inc. George Kluoda, Jim Norris, and Bill Dorko of the Chemical Science and Technology Laboratory at NIST provided advice for the design of the calibration system. Dr. Dean Ripple, George Burns, and Dr. Billy Mangum of the Physics Laboratory at NIST provided guidance in the calibration and use of thermocouples. Dr. Calvin Stainback of NASA Langley provided understanding of compressible flow through a nozzle. Dr. George Mattingly of the Chemical Science and Technology Laboratory suggested the use of a soap bubble meter for calibrating our mass-flow controllers and helped with the calibration of the soap-bubble meter. Dick Jacobs of MKS Instruments, Inc. helped with details concerning the mass flow controllers and the use of gas correction factors. Dr. Jiann Yang of BFRL at NIST was very helpful with regard to the computer work sheets used in calibration and data acquisition. Professor Ronald So of Arizona State University and Anthony Birch of the British Gas Corporation provided useful information concerning the response of aspirated hot-films to velocity fluctuations. We are grateful for the efforts of Mike Glover in assembling the DIRRACS, Yonas Makai for assembling an amplifier and assisting with the optical design of the DIRRACS, Darren Lowe for design and electronics assistance, Mike Smith for his testing of the FEAS, and Zhuomin Zhang for characterizing various optical components of the DIRRACS. We are appreciative of the capable and timely support we received at Wright Patterson AFB under the direction of Captain Gregg Caggianelli during experiments in the dry-bay test facility; including set up and testing support by Russ Cornetet, William Humphries, and Frank Feldman from Systems Research Laboratory, and the availability of Ron Britton's laboratory for calibration work. Several experts provided information concerning the Statham analyzer and the Halonyzer. These included William Meserve and Duane Van Ostrand of Pacific Scientific, Paul Boris of the Federal Aviation Administration, Steve Lamb of Walter Kidde Aerospace, and Joe Petkus of Boeing Aerospace Corporation. Special thanks go to William Meserve and Duane Van Ostrand who provided experimental results for the time response of the Halonyzer. Tom C. Hillman of Walter Kidde Aerospace provided insights concerning the Ultra-Violet Halonyzer. Dr. Tim Margulies of the Environmental Protection Agency suggested the acoustical technique for concentration measurements and provided many helpful discussions.

11.7 References

Adler, D., "A Hot Wire Technique for Continuous Measurement in Unsteady Concentration Fields of Binary Gaseous Mixtures," *J. Phys. E. Scientific Ins. 5*, 163 (1972).

Ahmed, S.A., and So, R.M.C., "Concentration Distributions in a Model Combustor," *Exp. Fluids 4*, 107 (1986).

Aihara, Y., Koyama, H., and Morishita, E., "Effects of an Air Stream on Turbulent Diffusion of a Helium Jet from a Small Nozzle," *Phys. Fluids 17*, 665 (1974).

Angona, F.A., 1953 "The Absorption of Sound in Gas Mixtures," *J. Acoustical Soc. Am. 25*, 1116 (1953).

Antonia, R.A., Browne, L.W.B, and Chambers, A.J., "Determination of Time Constants of Cold Wires," *Rev. Sci. Instrum. 52*, 1382 (1981).

Arroyo, M.P., Birbeck, T.P., Baer, D.S., and Hanson, R.K., "Dual Diode-Laser Fiber-Optic Diagnostic for Water-Vapor Measurements," *Optics Lett. 19*, 1091 (1994).

Bass, H.E., Sutherland, L.C., Piercy, J., and Evans, L., "Absorption of Sound by the Atmosphere," *Physical Acoustics XVII*, 145 (1984).

Baer, D.S., Hanson, R.K., Newfield, M.E., and Gopaul, N.K.J.M., "Multiplexed Diode-Laser Sensor System for Simultaneous H_2O, O_2, and Temperature Measurements," *Optics Lett. 19*, 1900 (1994).

Baldacci, A., Passerini, A., and Ghersetti, S., "Infrared Absorption Studies in the Vapor Phase of CF_3Br: Spectra Between 1800 and 400 cm^{-1}," *J. Mol. Spectros. 91*, 103 (1982).

Batt, R.G., "Turbulent Mixing of Passive and Chemically Reacting Species in a Low-Speed Shear Layer," *J. Fluid Mech. 82*, 53 (1977).

Becker, H.A., Hottel, H.C., and Williams, G.C., "On the Light-Scatter Technique for the Study of Turbulence and Mixing," *J. Fluid Mech. 30*, 259 (1967a).

Becker, H.A., Hottel, H.C., and Williams, G.C., "The Nozzle-Fluid Concentration Field of the Round, Turbulent, Free Jet," *J. Fluid Mech. 30*, 284 (1967b).

Becker, H.A., "Mixing, Concentration Fluctuations, and Marker Nephelometry," in *Studies in Convection: Theory, Measurement, and Applications, Volume 2*, Launder, B.E., Ed., pp. 45-139, Academic, New York, 1977.

Birch, A.D., Brown, D.R., Dodson, M.G., and Thomas, J.R., "The Turbulent Concentration Field of a Methane Jet," *J. Fluid Mech. 88*, 431 (1978).

Birch, A.D., Brown, D.R., Dodson, M.G., and Swaffield, F., "Aspects of Design and Calibration of Hot-Film Aspirating Probes Used for the Measurement of Gas Concentration," *J. Phys. E. Scientific Ins. 19*, 59 (1986).

Bird, R.B., Stewart, W.E., and Lightfoot, E.N., *Transport Phenomena*, Wiley, New York, 1960.

Blackshear, Jr., P.L. and Fingerson, L., "Rapid-Response Heat Flux Probe for High Temperature Gases," *ARS J. 32*, 1709 (1962).

Bomse, D.S., *Real Time Detection of Halon Replacement Decomposition Products Using Near-Infrared Diode Laser Spectroscopy*, A White Paper for the Halon Replacement RDT&E Community, Southwest Sciences, Inc., September 19, 1994.

Bradshaw, P., *An Introduction to Turbulence and Its Measurement*, Pergamom, New York, 1971.

Brown, G.L., and Rebollo, M.R., "A Small, Fast-Response Probe to Measure Composition of a Binary Gas Mixture," *AIAA J. 10*, 649 (1972).

Brown, J.A., and DeStefano, R.J., "Fire Extinguishing Agent Sensor (FEAS)," Wright Laboratories, Wright-Patterson AFB., Ohio 45433-6553, 1992 .

Bryner, N., Richards, C.D., and Pitts, W.M., "A Rayleigh Light Scattering Facility for the Investigation of Free Jets and Plumes, *Rev. Sci. Instrum. 63*, 3629 (1992).

Bucaro, J.A., Lagakos, N., Cole, J.H., and Giallorenzi, T.G., "Fiber Optic Acoustic Transduction," *Physical Acoustics XVI*, 385 (1982).

Calvert, J.G., and Pitts, J.N., *Photochemistry*, Wiley, New York, 1966.

Carlisle, C.B., and Cooper, D.E., "Tunable Diode Laser Frequency Modulation Spectroscopy Through an Optical Fiber: High-Sensitivity Detection of Water Vapor," *Appl. Phys. Lett. 56*, 805 (1990).

Catalano, G.D., Morton, J.B., and Humphris, R.R., "Experimental Investigation of an Axisymmetric Jet in a Coflowing Airstream," *AIAA J. 14*, 1157 (1976).

Chamberlain, G., *Criteria for Aircraft Installation and Utilization of an Extinguishing Agent Concentration Recorder*, Federal Aviation Administration Report No. FAA-DS-70-3, March, 1970.

Chan, K., Ito, H., and Inaba, H., "All-Optical Remote Monitoring of Propane Gas Using a 5-km-Long, Low-Loss Optical Fiber Link and an InGaP Light-Emitting Diode in the 1.68 μm Region," *Appl. Phys. Letters 45*, 220 (1984).

Comte-Bellot, G., "Hot-Wire Anemometry," *Annual Review of Fluid Mechanics 8*, 209 (1976).

Cooper, D.E., and Warren, R.E., "Two-Tone Optical Heterodyne Spectroscopy with Diode Lasers: Theory of Line Shapes and Experimental Results," *J. Opt. Soc. Am. B 4*, 470 (1987).

Corrsin, S., "Turbulence: Experimental Methods," in *Handbuck der Physik, Vol. 8/2*, Flugge, S., and Truesdell, C., Eds., pp. 523-590, Springer Verlag, Berlin, 1963.

Demaree, J.E., and Dierdorf, P.R., *Aircraft Installation and Operation of an Extinguishing-Agent Concentration Recorder*, National Aviation Facilities Experimental Center Technical Development Report No. 403, September 25, 1959.

Dereniak, E.L, and Crowe, D.G., *Optical Radiation Detectors*, Wiley, New York, 1984. The expression given in the book is for the spectral radiant emittance which is π times the spectral radiance.

Dowling, D.R., and Dimotakis, P.E., "Similarity of the Concentration Field of Gas-Phase Turbulent Jets," *J. Fluid Mech. 218*, 109 (1990).

Driscoll, R.J., and Kennedy, L.A., "A Model for the Spectrum of Passive Scalars in an Isotropic Turbulence Field," *Phys. Fluids 28*, 72 (1985).

Eckbreth, A.C., Dobbs, G.M., Stufflebeam, J.H., and Tellex, P.A., "CARS Temperature and Species Measurements in Augmented Jet Engine Exhausts," *Appl. Optics 23*, 1328 (1984).

Eckbreth, A.C., *Laser Diagnostics for Combustion Temperature and Species*, Abacus, Cambridge, MA, 1988.

Edgell, W.F. and May, C.E., "Raman and Infrared Spectra of CF_3Br and CF_3I," *J. Chem. Phys. 22* 1808 (1953).

Eng, R.S., Butler, J.F., and Linden, K.J., "Tunable Diode Laser Spectroscopy: An Invited Review," *Opt. Eng. 19*, 945 (1980).

Eng, R.S., and Ku, R.T., "High Resolution Linear Laser Absorption Spectroscopy-A Review," *Spectros. Letters 15*, 803 (1982).

Fabricius, N., Gauglitz, G., and Ingenhoff, J., "A Gas Sensor Based on an Integrated Optical Mach-Zehnder Interferometer," *Sensors and Actuators B 7*, 672 (1992).

Faist, J., Capasso, F., Sivco, D.L., Sirtori, C., Hutchinson, A.L., and Cho, A.Y., "Quantum Cascade Laser," *Science 264*, 553 (1994a).

Faist, J., Capasso, F., Sivco, D.L., Sirtori, C., Hutchinson, A.L., and Cho, A.Y., "Quantum Cascade Laser: An Intersub-band Semiconductor Laser Operating Above Liquid Nitrogen Temperature," *Electron. Letters 30*, 865 (1994b).

Fedyaev, A.A., Mironov, A.K., and Sergievskiy, E.D., "An Experimental Investigation of Binary Turbulent Boundary Layer Structures," *Dantec Information 9*, 13 (September, 1990).

Ferrarese, J.A., *General Guidelines for Measuring Fire-Extinguishing Agent Concentrations in Powerplant Compartments*, Federal Aviation Administration Advisory Circular AC No. 20-100, September 21, 1977.

Fick, A., "Über Diffusion," *Annalen Phy. Chem. 94*, 59 (1855).

Fingerson, L.M., and Freymuth, P., "Thermal Anemometers," in *Fluid Mechanics Measurements*, Goldstein, R.J., Ed., pp. 99-154, Hemisphere, Washington, 1983.

Gad-el-Hak, M., and Morton, J.B., "Experiments on the Diffusion of Smoke in Isotropic Turbulent Flow," *AIAA J. 17*, 558 (1979).

Goldman, E., and Sirovich, L., "Equations for Gas Mixtures," *Phys. Fluids 10*, 1928 (1967).

Goldman, E., and Sirovich, L., "Equations for Gas Mixtures II," *Phys. Fluids 12*, 245 (1969).

Goss, L.P., "CARS Instrumentation for Combustion Applications," in *Instrumentation for Flows with Combustion*, Taylor, A.M.K.P., Ed., pp. 251-322, Academic, New York, 1993.

Grandmaison, E.W., Rathgeber, D.E., and Becker, H.A., "Some Characteristics of Concentration Fluctuations in Free Turbulent Jets," *Can. J. Chem. Eng. 60*, 212 (1982).

Greenspan, M., "Propagation of Sound in Five Monatomic Gases, *J. Acoustical Soc. Am. 28*, 644 (1956).

Greenspan, M., "Rotational Relaxation in Nitrogen, Oxygen and Air," *J. Acoustical Soc. Am. 31*, 155 (1959).

Greenspan, M., 1965 "Transmission of Sound Waves in Gases at Very Low Pressures," *Phys. Acoustics II*, 1 (1965).

Gregory, C.C., "IR Fibers Shed Poor Reputation at Longer Wavelengths," *Photonics Spectra 27(7)*, 103 (July, 1993).

Grosshandler, W.L., Gann, R.G., and Pitts, W.M., *Evaluation of Alternative In-Flight Fire Suppressants for Full-Scale Testing in Simulated Aircraft Engine Nacelles and Dry Bays*, National Institute of Standards and Technology Special Publication SP-861, April, 1994.

Hamins, A., Gmurczyk, G., Grosshandler, W., Presser, C., and Seshadri, K., "Flame Suppression Effectiveness," in *Evaluation of Alternative In-Flight Fire Suppressants for Full-Scale Testing in Simulated Aircraft Engine Nacelles and Dry Bays*, Grosshandler, W.L., Gann, R.G., and Pitts, W.M., Eds., pp. 345-465, National Institute of Standards and Technology Special Publication SP-861, April, 1994.

Hanson, R.K., "Shock Tube Spectroscopy: Advanced Instrumentation with a Tunable Diode Laser," *Appl. Optics 16*, 1479 (1977).

Hanson, R.K., "Tunable Diode Laser Measurements in Combustion Gases," in *Tunable Diode Laser Development and Spectroscopy Applications, Proceedings of SPIE, Volume 438*, Lo, W., Ed., pp. 75-83, The Society of Photo-Optical Instrumentation Engineers, Bellingham, WA, 1983.

Hillman, T.C., Walter Kidde Aerospace, Personal Communication, February, 1994.

Hinze, J.O., *Turbulence Second Edition*, McGraw-Hill, New York, 1975.

Hirschfelder, J.O., Curtiss, C.F., and Bird, R.B., *Molecular Theory of Gases and Liquids*, Wiley, New York, 1964.

Hough, R.L., *Critical Analysis of the Statham Gas Analyzer Method*, Wright Air Development Center Technical Memorandum WCLE-TM-59-14, March 18, 1959.

Huang, M.-N., *Ultrasound and Light Scattering in a Diffusing and Chemically Reacting Binary Mixture of Fluids*, Ph.D. Dissertation, The John Hopkins University, 1973.

Jones, B.G., and Wilson, R.J., "Gas Concentration Measurements with a Temperature Compensated Aspirating Probe," in *Symposium on Turbulence*, Patterson, G.K., and Zakin, J.L., Eds., pp. 205-210, Science Press, Princeton, 1979.

Kleppe, J.A., *Engineering Applications of Acoustics*, Artech House Acoustics Library, Artech House, Norwood, MA, 1989.

Kidde-Graviner, Ltd., *Ultra-Violet Halonyser*, Data Sheet, September, 1992.

King, L.V., "On the Convection of Heat from Small Cylinders in a Stream of Fluid: Determination of the Convection Constants of Small Platinum Wires with Applications to Hot-Wire Anemometry," *Phil. Trans. R. Soc. London A214*, 373 (1914).

Kirchhoff, G.R., "Über den Einfluß der Wärmeleitung in einem Gase auf die Schallbewegung," *Annalen Phys. Chem. 134*, 177 (1868).

Kohler, M., "Schallabsorption in Binären Gasmischungen," *Zeits. Physik 127*, 41 (1949).

Kuznetsov, A.I., Nadezhdinskii, A.I., and Stepanov, E.V., "Tunable Diode Laser Spectroscopy Accessories Based on Middle IR Halide and Chalcogenide Fibers," in *Tunable Diode Laser Applications*, Nadezhdinskii, A.I., and Prokhorov, A.M., Eds., pp. 104-118, The Society of Photo-Optical Instrumentation Engineers, Bellingham, WA (1992).

Lang, S.B., *Sourcebook of Pyroelectricity,* Gordon and Breach, New York, 1974.

Laser Focus World 30(9), 13 (September, 1994), "Purification Lowers IR-Fiber Loss to 0.11 db/m."

LaRue, J.C., Deaton, T., and Gibson, C.H., "Measurement of High-Frequency Turbulent Temperature," *Rev. Sci Instrum. 46*, 757 (1975).

Law, A.K., Koronaios, N., and Lindsay, R.B., "Effect of Diffusion on Ultrasonic Attenuation in Mixtures of the Rare Gases, *J. Acoustical Soc. Am. 41*, 93 (1966).

Lee, J., and Brodkey, R.S., "Light Probe for the Measurement of Turbulent Concentration Fluctuations," *Rev. Sci. Instrum. 34*, 1086 (1963).

Lee, J., and Brodkey, R.S., "Turbulent Motion and Mixing in a Pipe," *A.I.Ch.E. J. 10*, 187 (1964).

Lenth, W., "Optical Heterodyne Spectroscopy with Frequency- and Amplitude-Modulated Semiconductor Lasers," *Optics Lett. 8*, 575 (1983).

Lindsay, R.B., "Relaxation Processes in Sound Propagation in Fluids: A Historical Survey," *Physical Acoustics XVI*, 1 (1982).

Long, M.B., and Chu, B.T., "Mixing Mechanism and Structure of an Axisymmetric Turbulent Mixing Layer," *AIAA J. 19*, 1158 (1981).

Long, M.B., Webber, B.F., and Chang, R.K., "Instantaneous Two-Dimensional Concentration Measurements in a Jet Flow by Mie Scattering," *Appl. Phys. Letters 34*, 22 (1979).

Long, M.B., Chu, B.T., and Chang, R.K., "Instantaneous Two-Dimensional Gas Concentration Measurements by Light Scattering," *AIAA J. 19*, 1151 (1981).

Margulies, T.S., and Schwarz, W.H., 1985 "Acoustic Wave Propagation in Fluids," in *Frontiers in Fluid Mechanics, A Collection of Research Papers Written in Commemoration of the 65th Birthday of Stanley Corrsin*, Davis, S.H., and Lumley, J.L., Eds., pp. 219-280, Springer-Verlag, New York (1985).

McGee, P.R., Cleveland, F.F., and Miller, S.I., "Infrared Spectral Data and Tentative Assignments for CF_3Br and CF_3I," *J. Chem. Phys. 20*, 1044 (1952).

McQuaid, J., and Wright, W., "The Response of a Hot-Wire Anemometer in Flows of Gas Mixtures," *Int. J. Heat Mass Transfer 16*, 819 (1973).

McQuaid, J., and Wright, W., "Turbulence Measurements with Hot-Wire Anemometry in Non-Homogeneous Jets," *Int. J. Heat Mass Transfer 17*, 341 (1974).

Molectron Application Note, *P1-Series Pyroelectric Detector/Amplifier*, Molectron Detector Incorporated, Portland, OR, 1994.

Molina, L.T., Molina, M.J., and Rowland, F.S., "Ultraviolet Absorption Cross Sections of Several Brominated Methanes and Ethanes of Atmospheric Interest," *J. Phys. Chem. 86*, 2672 (1982).

New, J.D., and Middlesworth, C.M., *Aircraft Fire Extinguishment. Part III. An Instrument for Evaluating Extinguishing Systems*, Civil Aeronautics Administration Technical Development and Evaluation Center Technical Development Report No. 206, Indianapolis, IN, June, 1953.

Ng, W.F., and Epstein, A.H., "High-Frequency Temperature and Pressure Probe for Unsteady Compressible Flows," *Rev. Sci. Instrum. 54*, 1678 (1983).

Ninnemann, T.A., and Ng, W.F., "A Concentration Probe for the Study of Mixing in Supersonic Shear Flows," *Exp. Fluids 13*, 98 (1992).

Nye, J.O., and Brodkey, R.S., "Light Probe for Measurement of Turbulent Concentration Fluctuations," *Rev. Sci. Instrum. 38*, 26 (1967a).

Nye, J.O., and Brodkey, R.S., "The Scalar Spectrum in the Viscous-Convective Subrange," *J. Fluid Mech. 29*, 151 (1967b).

Oberste-Lehn, K., and Merzkirch, W., "Speckle Optical Measurement of a Turbulent Scalar Field With High Fluctuation Amplitudes," *Expts. Fluids 14*, 217 (1993).

Pacific Scientific HTL Division, *Halonyzer II Operation/Maintenance*, Document No. 57180001, September, 1988a.

Pacific Scientific HTL Division, *Calibration Certification Plan for HTL P/N 60000009-2 Model Halonyzer II with Halon 1301 Extinguishant*, Document No. 57710001, September, 1988b.

Pasto, D.J., and Johnson, C.R., *Organic Structure Determination*, Prentice-Hall, Englewood Cliffs, NJ, 1969.

Perry, A.E., *Hot-Wire Anemometry*, Oxford University Press, Oxford, 1982.

Perry, A.E., "The Time Response of an Aspirating Probe in Gas Sampling," *J. Phys. E. Scientific Ins. 10*, 898 (1977).

Pitts, D.R., and Sissom, L.E., *Schaum's Outline of Theory and Problems of Heat Transfer*, McGraw-Hill, New York, 1977.

Pitts, W.M., "Effects of Global Density Ratio on the Centerline Mixing Behavior of Axisymmetric Turbulent Jets," *Expts. Fluids 11*, 125 (1991).

Pitts, W.M., and Kashiwagi, T., "The Application of Laser-Induced Rayleigh Light Scattering to the Study of Turbulent Mixing," *J. Fluid Mech. 141*, 391 (1984).

Pitts, W.M., and McCaffrey, B.J., "Response Behaviour of Hot Wires and Films to Flows of Different Gases," *J. Fluid Mech. 169*, 169 (1986).

Pitts, W.M., unpublished work (1984).

Pitts, W.M., Yang, J.C., Gmurczyk, G., Copper, L.Y., Grosshandler, W.L., Cleveland, W.G., and Presser, W.G., "Section 3. Fluid Dynamics of Agent Discharge" in *Evaluation of Alternative In-Flight Fire Suppressants for Full-Scale Testing in Simulated Aircraft Engine Nacelles and Dry Bays*, Grosshandler, W.L., Gann, R.G., and Pitts, W.M., Eds., pp. 37-343, National Institute of Standards and Technology Special Publication SP-861, April, 1994.

Prangsma, G.J., Jonkman, R.M., and Beenakker, J.J.M., "Sound-Absorption Measurement in Helium-Argon Mixtures in the 'Burnett Region'" *Physica 48*, 323 (1970).

Putley, E.H., "The Pyroelectric Detector," In *Semiconductors and Semimetals*, Vol. 5, Willardson, R.K., and Beers, A.C., Eds., pp. 259-285, Academic Press, New York, 1970.

Rosensweig, R.E., Hottel, H.C., and Williams, G.C., "Smoke-Scattered Light Measurement of Turbulent Concentration Fluctuations," *Chem. Eng. Science 15*, 111 (1961).

Rotta, J.C., *Turbulente Strömungen*, B. G. Teubner, Stuttgart, 1972.

Roxlo, C., and Mandl, A., "Vacuum Ultraviolet Absorption Cross Sections for Halogen Containing Molecules," *J. Appl. Phys. 51*, 2969 (1980).

Ruddy, V., and Lardner, K., "Porous Clad Fibres as Sensor Probes," *Int. J. Optoelect. 8*, 87 (1993).

Saito, M., Takizawa, M., Ikegawa, K., and Takami, H., "Optical Remote Sensing System for Hydrocarbon Gases Using Infrared Fibers," *J. Appl. Phys. 63*, 269 (1988).

Saito, M., Miyagi, M., Kuritani, T., and Tanei, F., "Radiation Thermometry and Gas Sensor Using Chalcogenide Glass Fibres," *Int. J. Optoelect. 7*, 375 (1992).

Savin, O.R., Shkurdoda, V.F., and Simonovsky, V.I., "Mass Spectrometers for Technological Control in Industry," *Int. J. Mass Spect. Ion Phys. 46*, 163 (1983).

Schoenung, S.M., and Hanson, R.K., "Laser Absorption Sampling Probe for Temporally and Spatially Resolved Combustion Measurement," *Appl. Optics 21*, 1767 (1982a).

Schoenung, S.M., and Hanson, R.K., "Temporally and Spatially Resolved Measurements of Fuel Mole Fraction in a Turbulent CO Diffusion Flame," *Nineteenth Symposium (International) on Combustion*, pp. 449-458, Combustion Institute, Pittsburgh, 1982b.

Seitzman, J.M., and Hanson, R.K., "Planar Fluorescence Imaging in Gases," in *Instrumentation for Flows with Combustion*, Taylor, A.M.K.P., Ed., pp. 405-466, Academic, New York, 1993.

Sell, J.A., "Tunable Diode Laser Measurements of Carbon Monoxide in Engine Exhaust," in *Tunable Diode Laser Development and Spectroscopy Applications, Proceedings of SPIE, Volume 438*, Lo, W., Ed., pp. 67-74, The Society of Photo-Optical Instrumentation Engineers, Bellingham, WA, 1983.

Shaughnessy, E.J., and Morton, J.B., "Laser Light-Scattering Measurements of Particle Concentration in a Turbulent Jet," *J. Fluid Mech 80*, 129 (1977).

So, R.M.C., and Ahmed, S.A., "Helium Jets Discharging Normally into a Swirling Air Flow," *Expts. Fluids 5*, 255 (1987).

So, R.M.C., Zhu, J.Y., Ötugen, M.V., and Hwang, B.C., "Some Measurements in a Binary Gas Jet," *Exp. Fluids 9*, 272 (1990).

So, R.M.C., Zhu, J.Y., Ötugen, M.V., and Hwang, B.C., "Behavior of Probability Density Functions in a Binary Gas Jet," *Exp. Fluids 11*, 227 (1991).

Stanton, A.C., and Silver, J.A., "Measurements in the HCl $3 \leftarrow 0$ Band Using a Near-IR InGaAsP Diode Laser," *Appl. Optics 27*, 5009 (1988).

Strobel, H.A., and Heineman, W.R., *Chemical Instrumentation: A Systematic Approach, Third Edition*, Wiley, New York, 1989.

Tai, H., Tanaka, H., and Yoshino, T., "Fiber-Optic Evanescent-Wave Methane-Gas Sensor Using Optical Absorption for the 3.392-μm line of a He-Ne Laser," *Opt. Letters 12*, 437 (1987).

Takeuchi, K., Tanaka, T., Ikeda, M., Shibata, K., Sakauchi, Y., Yamada, Y., and Nakano, S., "Highly Accurate CO_2 Gas Sensor Using a Modulation-Type Pyroelectric Infrared Detector," *Jpn. J. Appl. Phys. 32*, 221 (1993).

Temkin, S., *Elements of Acoustics*, Wiley, New York, 1981.

Truesdell, C., "Precise Theory of the Absorption and Dispersion of Forced Plane Infinitesimal Waves According to the Navier-Stokes Equations," *J. Rational Mech. Analysis 2*, 643 (1953).

Wang, L.-G., Tate, D.A., Riris, H., and Gallagher, T.F., "High-Sensitivity Frequency-Modulation Spectroscopy with a GaAlAs Diode Laser," *J. Opt. Soc. Am B 6*, 871 (1989).

Way, J., and Libby, P.A., "Hot-Wire Probes for Measuring Velocity and Concentration in Helium-Air Mixtures," *AIAA J. 8*, 976 (1970).

Way, J. and Libby, P.A., "Application of Hot-Wire Anemometry and Digital Techniques to Measurements in a Turbulent Helium Jet," *AIAA J. 9*, 1567 (1971).

Wenquan, L., Sigan, G., and Shunxuan, Z., "Study of Optical Characteristics of SnO_2 as Optical Fiber Sensing Material," *Chinese Phys. Lasers 19*, 215 (1992).

Whistler, W.J., and Schaefer, K., "Design Considerations and Applications of Mass Spectrometers for Process Measurement and Control," *Int. J. Mass Spect. Ion Phys. 46*, 159 (1983).

White, F.A., and Wood, G.M., *Mass Spectrometry Application in Science and Engineering*, Wiley, New York, 1986.

Wilson, D.J., and Netterville, D.D.J., "A Fast-Response, Heated-Element Concentration Detector for Wind-Tunnel Applications," *J. Wind Eng. Ind. Aerodynamics 7*, 55 (1981).

Yanikoski, F.F., *Gas Analysis Apparatus*, United States Patent Office Patent Number 2,586,899, February, 26, 1952.

Zhou, Q., Kritz, D., Bonnell, L., and Sigel, Jr., G.H., "Porous Plastic Optical Fiber Sensor for Ammonia Measurement," *Appl. Optics 28*, 2022 (1989).

Zhu, J.Y., So, R.M.C., and Ötugen, M.V., "Turbulent Mass Flux Measurements Using a Laser/Hot-Wire Technique," *Int. J. Heat Mass Transfer 31*, 819 (1988).

Zhu, J.Y., So, R.M.C., and Ötugen, M.V., "Mass Transfer in a Binary Gas Jet," *AIAA J. 27*, 1131 (1989).

Appendix A. FORTRAN Program NOZZLE.FOR to Estimate Volume-Flow Rates of Agents and Air Extracted By Aspirating Hot-Film Probe

```
*    Isentropic flow through a nozzle.  (NOZZLE.FOR)

*    David E. Hess
*    Fluid Flow Group - Process Measurements Division
*    Chemical Science and Technology Laboratory
*    National Institute of Standards and Technology
*    January 31, 1994
*    Updated on May 21, 1994 - incorporates calibration data.

*    This routine computes various data corresponding to the
*    sonic nozzle contained within the TSI Model 1440 Aspirating
*    probe for the measurement of concentration or temperature.
*    Three modes of operation are provided :

*      1. The full set of conditions are computed and displayed
*         to the screen for stagnation pressure set to 1 atm
*         and a user-selected temperature.

*      2. The variation in a subset of nozzle parameters is
*         computed for stagnation pressure set to 1 atm and
*         a user-selected range of temperatures.  The data
*         are written to a data file [.PRN].

*      3. The variation in a subset of nozzle parameters is
*         computed for stagnation temperature set to 20 °C and
*         a user-selected range of pressures.  The data
*         are written to a data file [.PRN].

      IMPLICIT    REAL*8 (A-H,M,O-Z), INTEGER*2 (I-L,N)
      PARAMETER     (NUMO=2)
      LOGICAL*1  ST
      CHARACTER*1  INP
      CHARACTER*4  FEXT
      CHARACTER*10     GAS
      CHARACTER*12     FNAMO

      COMMON /GPROP/  MW,RHOSTAND,GAMMA,GCF,RUNIV
      COMMON /AREA/   A,ASTAR,ARAT
      COMMON /STAG/   RHOZERO
      COMMON /ENTR/   P,T,RHO,M,C,U,MRATE1,QRATE1,QN1
      COMMON /THROAT/ PSTAR,TSTAR,RHOSTAR,MSTAR,CSTAR,
     +                USTAR,MRATE2,QRATE2,QN2,PSTPSI,PSTMM
```

```
      DATA          D1,D2 / 1.2192D-3, 0.508D-3 /   ! meters
      DATA          FEXT  /'.PRN'/

*     Initialization.

      PI=2.0D0*DASIN(1.0D0)    ! Formula for pi
      RUNIV=8314.36D0          ! Universal gas constant - J / kmol K
      ARAT=D1**2/D2**2  ! Area ratio
      A=PI*D1**2/4.0D0
      ASTAR=PI*D2**2/4.0D0

*     Display list of gases.

5     WRITE (*,'(/16X,A/16X,A)') 'ISENTROPIC, ADIABATIC FLOW OF A',
     +                          ' PERFECT GAS THROUGH A NOZZLE'
      WRITE (*,'(/16X,A)')  'Choose from the following gases : '
      WRITE (*,'(/16X,A)')  '          1. AIR'
      WRITE (*,'(16X,A)')   '          2. CF3I'
      WRITE (*,'(16X,A)')   '          3. HFC-227'
      WRITE (*,'(16X,A)')   '          4. FC-218'
      WRITE (*,'(16X,A)')   '          5. HFC-125'
      WRITE (*,'(16X,A)')   '          6. HALON-1301'
      WRITE (*,'(/16X,A\)') 'Enter choice (1-6) : '
      READ (*,*) IGAS
      WRITE (*,'( )')

      GO TO (10,20,30,40,50,60) IGAS
      GO TO 5

*     Get gas properties.  (SI Units)

*     ************* AIR **************

10    MW=28.966D0          ! Molecular weight - kg / kmol
      RHOSTAND=1.29304D0   ! Density (at 273 K and 1 atm) - kg / m3
      GAMMA=1.4D0          ! Specific heat ratio
      GCF=1.0D0            ! Gas correction factor (from MKS)
      GAS='AIR      '
      GO TO 70

*     ************* CF3I *************

20    MW=195.911D0         ! kg / kmol
      RHOSTAND=9.0439D0    ! kg / m3
      GAMMA=1.149D0        ! Specific heat ratio
      GCF=0.34D0           ! Gas correction factor (from MKS)
      GAS='CF3I     '
      GO TO 70
```

```
*     ********** HFC-227 ***********

30    MW=170.03D0          ! kg / kmol
      RHOSTAND=7.92544D0    ! kg / m3
      GAMMA=1.075D0          ! Specific heat ratio
      GCF=0.19D0        ! Gas correction factor (from cal)
      GAS='HFC-227   '
      GO TO 70

*     ********** FC-218 ***********

40    MW=188.017D0         ! kg / kmol
      RHOSTAND=8.68268D0    ! kg / m3
      GAMMA=1.068D0          ! Specific heat ratio
      GCF=0.176D0          ! Gas correction factor (from cal)
      GAS='FC-218    '
      GO TO 70

*     ********** HFC-125 ***********

50    MW=120.02D0          ! kg / kmol
      RHOSTAND=5.47635D0    ! kg / m3
      GAMMA=1.103D0          ! Specific heat ratio
      GCF=0.275D0          ! Gas correction factor (from cal)
      GAS='HFC-125   '
      GO TO 70

*     ********** HALON 1301 **********

60    MW=148.91D0          ! kg / kmol
      RHOSTAND=6.77643D0    ! kg / m3
      GAMMA=1.145D0          ! Specific heat ratio
      GCF=0.38D0        ! Gas correction factor (from cal)
      GAS='HALON-1301'

*     This section of code calculates the variation in nozzle
*     parameters as a function of stagnation pressure (barometric
*     pressure) for a single temperature (20 °C).  I allow for a
*     worst case variation of 29.0 to 31.0 in Hg which corresponds
*     to a variation of 98.0 k Pa to 104.8 kPa or 14.2 psia to 15.2 psia.

70    WRITE (*,'(10X,A\)')
     +    'Enter (A)tmospheric press or (M)any pressures : '
      READ (*,'(A)') INP
      WRITE (*,'( )')
      GO TO (70,72) ILET(INP,'MA')

*     Compute data for SINGLE pressure.
```

```
      PZERO=101300.0D0  ! Stagnation pressure - Pa
      GO TO 75

*     Compute data for MANY pressures.

72    WRITE (*,'(16X,A,A,A\)')
     +    'Enter name of output file [',FEXT,']: '
      READ (*,'(A)') FNAMO
      WRITE (*,'( )')

*       Concatenate file extension to FNAMO (if necessary)
*       and then open the file.

      IPD=INDEX(FNAMO,'.')
      IF (IPD .GT. 9) GO TO 80
      IF (IPD .EQ. 0) THEN
        IEND=LEN_TRIM(FNAMO)
        FNAMO(IEND+1:IEND+4)=FEXT
      ENDIF

      OPEN (NUMO,FILE=FNAMO,STATUS='UNKNOWN')

      TEMPC=20.0D0        ! Room temp (°C)
      TZERO=TEMPC+273.15D0       ! Kelvin

      WRITE (*,'(16X,A\)') 'Enter Pstart, Pstop, Pstep (in Hg) : '
      READ (*,*) PSTART,PSTOP,PSTEP
      WRITE (*,'( )')

      NVAL=NINT((PSTOP-PSTART)/PSTEP)+1
      PSTART=PSTART*3379.978D0        ! Pa
      PSTOP=PSTOP*3379.978D0          ! Pa
      PSTEP=PSTEP*3379.978D0          ! Pa
      PZERO=PSTART-PSTEP

      IEND=LEN_TRIM(GAS)
      WRITE (NUMO,'(21X,A,A,A/)')
     +      'NOZZLE CONDITIONS FOR ',GAS(:IEND), ' :'
      WRITE (NUMO,'(5X,A,A)')
     +    'P0 (inHg)  T0 (°C)   U (m/s)  P* (psi)   T* (°C)  Q (slmN)',
     +    '   m (kg/s)'
      WRITE (NUMO,'(5X,A,A)')
     +    '---------  -------  -------  --------  -------  --------',
     +    '  ---------'

      DO I=1,NVAL
        PZERO=PZERO+PSTEP
        CALL NOZCALC (PZERO,TZERO)
```

```
      WRITE (NUMO,'(5X,6(F8.3,2X),1P,E9.3)')
     +     PZERO/3379.978D0,TZERO-273.15D0,U,PSTPSI,
     +     TSTAR-273.15D0,QN1,MRATE1
      ENDDO
      CLOSE (NUMO)
      STOP ' '

*     Compute data for single temperature or many temperatures.

75    WRITE (*,'(16X,A\)') 'Enter (S)ingle temp or (M)any temps : '
      READ (*,'(A)') INP
      WRITE (*,'( )')
      GO TO (75,80) ILET(INP,'MS')

*     Get SINGLE stagnation temperature.

      WRITE (*,'(16X,A\)')
     +    'Enter the stagnation temperature (in °C) : '
      READ (*,*) TEMPC
      WRITE (*,'( )')
      NVAL=1
      TSTEP=1.0D0
      TZERO=TEMPC-TSTEP+273.15D0   ! Kelvin
      ST=.TRUE.
      GO TO 90

*     Get data to compute for MANY stagnation temperatures.

80    WRITE (*,'(16X,A,A,A\)')
     +    'Enter name of output file [',FEXT,']: '
      READ (*,'(A)') FNAMO
      WRITE (*,'( )')

*       Concatenate file extension to FNAMO (if necessary)
*       and then open the file.

      IPD=INDEX(FNAMO,'.')
      IF (IPD .GT. 9) GO TO 80
      IF (IPD .EQ. 0) THEN
        IEND=LEN_TRIM(FNAMO)
        FNAMO(IEND+1:IEND+4)=FEXT
      ENDIF

      OPEN (NUMO,FILE=FNAMO,STATUS='UNKNOWN')

      WRITE (*,'(16X,A\)') 'Enter Tstart, Tstop, Tstep (in °C) : '
      READ (*,*) TSTART,TSTOP,TSTEP
      WRITE (*,'( )')
```

```
      NVAL=NINT((TSTOP-TSTART)/TSTEP)+1
      TZERO=TSTART-TSTEP+273.15D0        ! Kelvin
      ST=.FALSE.

      IEND=LEN_TRIM(GAS)
      WRITE (NUMO,'(21X,A,A,A/)')
     +     'NOZZLE CONDITIONS FOR ',GAS(:IEND), ' :'
      WRITE (NUMO,'(5X,A,A)')
     +   'P0 (kPa)   T0 (°C)   U (m/s)  P* (psi)   T* (°C)  Q (slmN)',
     +   '   m (kg/s)'
      WRITE (NUMO,'(5X,A,A)')
     +   '--------  -------  -------  --------  -------  --------',
     +   '  ---------'

90    DO I=1,NVAL
        TZERO=TZERO+TSTEP
        CALL NOZCALC (PZERO,TZERO)
        IF (.NOT. ST) WRITE (NUMO,'(5X,6(F8.3,2X),1P,E9.3)')
     +     PZERO/1000.0D0,TZERO-273.15D0,U,PSTPSI,
     +     TSTAR-273.15D0,QN1,MRATE1
      ENDDO
      IF (.NOT. ST) CLOSE (NUMO)

*     Display results.

      IF (ST) THEN
        WRITE (*,'(25(/))')
        IEND=LEN_TRIM(GAS)
        WRITE (*,'(26X,A,A,A/)')
     +     'NOZZLE CONDITIONS FOR ',GAS(:IEND), ' :'

        WRITE (*,'(16X,A,8X,A/)')
     +     'Stagnation Properties : ',      'Gas Properties : '
        WRITE (*,'(16X,A,F8.3,A,12X,A,F8.3)')
     +     'P0   = ',PZERO/1000.0D0,'  kPa','Γ    = ',GAMMA
        WRITE (*,'(16X,A,F8.3,A,13X,A,F8.3)')
     +     'T0   = ',TZERO-273.15D0,'  °C', 'MW   = ',MW
        WRITE (*,'(16X,A,F8.3,A,10X,A,F8.3,A)')
     +     'Rho0 = ',RHOZERO,'  kg/m3',     'RhoS = ',RHOSTAND,'  kg/m3'
        WRITE (*,'(48X,A,F8.3/)')          'GCF  = ',GCF

        WRITE (*,'(16X,A,10X,A/)')
     +     'Entrance Properties : ',      'Throat Properties : '
        WRITE (*,'(16X,A,F8.3,A,12X,A,F8.3,A)')
     +     'P    = ',P/1000.0D0,'  kPa','P*   = ',PSTAR/1000.0D0,'  kPa'
        WRITE (*,'(16X,A,F8.3,A,13X,A,F8.3,A)')
     +     'T    = ',T-273.15D0,'  °C', 'T*   = ',TSTAR-273.15D0,'  °C'
        WRITE (*,'(16X,A,F8.3,A,10X,A,F8.3,A)')
```

```
     +    'Rho  = ',RHO,'  kg/m3',     'Rho* = ',RHOSTAR,'  kg/m3'
          WRITE (*,'(16X,A,F8.3,A,12X,A,F8.3,A)')
     +    'M    = ',M,'  m/s',         'M*   = ',MSTAR,'  m/s'
          WRITE (*,'(16X,A,F8.3,A,12X,A,F8.3,A)')
     +    'C    = ',C,'  m/s',         'C*   = ',CSTAR,'  m/s'
          WRITE (*,'(16X,A,F8.3,A,12X,A,F8.3,A)')
     +    'U    = ',U,'  m/s',         'U*   = ',USTAR,'  m/s'
          WRITE (*,'(16X,A,1P,E9.3,A,11X,A,E9.3,A)')
     +    'mdot = ',MRATE1,' kg/s',    'mdot = ',MRATE2,' kg/s'
          WRITE (*,'(16X,A,F8.3,A,12X,A,F8.3,A)')
     +    'Qdot = ',QRATE1,' slm',     'Qdot = ',QRATE2,' slm'
          WRITE (*,'(16X,A,F8.3,A,10X,A,F8.3,A/)')
     +    'Qdot = ',QN1,' slm-N',  'Qdot = ',QN2,' slm-N'
          WRITE (*,'(16X,A,F5.3,A/16X,A,F6.3,A,F5.3,A,F6.2,A)')
     +     'The vacuum pump must draw at least ',QN1,' slm-N at ',
     +     'a pressure ≤ ',PSTAR/1000.0D0,' kPa = ',PSTPSI,
     +     ' psia = ',PSTMM,' mm Hg abs.'
          ENDIF

          END

          SUBROUTINE NOZCALC (PZERO,TZERO)

          IMPLICIT    REAL*8 (A-H,M,O-Z), INTEGER*2 (I-L,N)
          PARAMETER     (ITMAX=99,EPS=1.0D-6)

          COMMON /GPROP/  MW,RHOSTAND,GAMMA,GCF,RUNIV
          COMMON /AREA/   A,ASTAR,ARAT
          COMMON /STAG/   RHOZERO
          COMMON /ENTR/   P,T,RHO,M,C,U,MRATE1,QRATE1,QN1
          COMMON /THROAT/ PSTAR,TSTAR,RHOSTAR,MSTAR,CSTAR,
     +                    USTAR,MRATE2,QRATE2,QN2,PSTPSI,PSTMM

     *    The entrance and throat diameters of the nozzle are known.
     *    Solve for the Mach number (M) by iteration.

          M=0.1D0
          MDIFF=1.0D0
          ITER=0
          EX=(GAMMA+1.0D0)/(GAMMA-1.0D0)/2.0D0

          DO WHILE (MDIFF .GT. EPS .AND. ITER .LE. ITMAX)
            ITER=ITER+1
            MGUESS=( 2.0D0/(GAMMA+1.0D0) *
     +             (1.0D0+(GAMMA-1.0D0)/2.0D0*M**2) )**EX / ARAT
            MDIFF=DABS(MGUESS-M)
            M=MGUESS
          ENDDO
```

```
*     Compute stagnation density from Perfect Gas equation of state.
*     This gives densities which are in error by 1% to 3%.

      R=RUNIV/MW                ! Gas constant - J / kg K
      RHOZERO=PZERO/(R*TZERO)           ! Stagnation density - kg / m3

*     Compute properties at entrance to nozzle.

      T=TZERO/(1.0D0+(GAMMA-1.0D0)/2.0D0*M**2)
      TRAT=T/TZERO
      P=PZERO*TRAT**(GAMMA/(GAMMA-1.0D0))
      RHO=RHOZERO*TRAT**(1.0D0/(GAMMA-1.0D0))
      C=DSQRT(GAMMA*R*T)
      U=M*C
      MRATE1=RHO*U*A                        ! kg / s
      QRATE1=MRATE1/RHOSTAND*60000.0D0   ! slm of agent
      QN1=QRATE1/GCF                    ! slm of nitrogen

*     Compute properties at throat of nozzle.

      FACTOR=2.0D0/(GAMMA+1.0D0)
      TSTAR=TZERO*FACTOR
      PSTAR=PZERO*FACTOR**(GAMMA/(GAMMA-1.0D0))
      PSTPSI=PSTAR/6894.76D0            ! PSTAR in psi
      PSTMM=PSTAR/133.07D0        ! PSTAR in mm Hg
      RHOSTAR=RHOZERO*FACTOR**(1.0D0/(GAMMA-1.0D0))
      CSTAR=DSQRT(GAMMA*R*TSTAR)
      USTAR=CSTAR
      MSTAR=1.0D0
      MRATE2=RHOSTAR*USTAR*ASTAR          ! kg / s
      QRATE2=MRATE2/RHOSTAND*60000.0D0   ! slm of agent
      QN2=QRATE2/GCF                    ! slm of nitrogen

      RETURN
      END

      FUNCTION ILET (INP,STRING)  ! (ILET.FOR)

      IMPLICIT    INTEGER*2 (I-N)
      CHARACTER*1  INP
      CHARACTER*(*)    STRING

*     First, convert INP to uppercase if it is lowercase.  If it
*     is uppercase, leave it unchanged.

      IF (ICHAR(INP) .GE. 97 .AND. ICHAR(INP) .LE. 122) THEN
        IHOLD=ICHAR(INP)-32
```

```
      INP=CHAR(IHOLD)
    ENDIF

*   Determine the position of INP in STRING, then add one to get
*   ILET which determines label to use in computed GO TO statement.

    IPOS=INDEX(STRING,INP)
    ILET=IPOS+1

    RETURN
    END
```

Appendix B. FORTRAN Program COIL.FOR to Estimate Length of Pipe Required For Laminar and Turbulent Flows in Pipes to Achieve Pipe-Wall Temperature

```
*     Laminar and Turbulent Heat Transfer in a Pipe  (COIL.FOR)

*     David E. Hess
*     Fluid Flow Group - Process Measurements Division
*     Chemical Science and Technology Laboratory
*     National Institute of Standards and Technology
*     February 3, 1994

      IMPLICIT      REAL*8 (A-H,O-Z), INTEGER*2 (I-N)
      REAL*8        MOUT

      DATA          MOUT  / 2.1D-4 /

*     Display list of gases.

10    WRITE (*,'(/16X,A/16X,A)') 'LAMINAR AND TURBULENT HEAT',
     +                           ' TRANSFER IN A PIPE FLOW'

      WRITE (*,'(/16X,A\)') 'Enter pipe diameter (in) : '
      READ (*,*) D
      WRITE (*,'( )')
      D=D*25.4D0/1.0D3        ! Convert from inches to meters

      WRITE (*,'(/16X,A)')  'Choose from the following gases : '
      WRITE (*,'(/16X,A)')  '          1. AIR'
      WRITE (*,'(16X,A)')   '          2. CF3I'
      WRITE (*,'(16X,A)')   '          3. HFC-227'
      WRITE (*,'(16X,A)')   '          4. FC-218'
      WRITE (*,'(16X,A)')   '          5. HFC-125'
      WRITE (*,'(16X,A)')   '          6. HALON-1301'
      WRITE (*,'(16X,A)')   '          7. ALL OF THE ABOVE'
      WRITE (*,'(/16X,A\)') 'Enter choice (1-7) : '
      READ (*,*) ICHOICE
      WRITE (*,'( )')

      IF (ICHOICE .GE. 1 .AND. ICHOICE .LE. 6) THEN

        CALL COILCALC (ICHOICE,MOUT,D)

      ELSEIF (ICHOICE .EQ. 7) THEN

        DO I=1,6
```

```
      CALL COILCALC (I,MOUT,D)
      WRITE (*,'( )')
     ENDDO

    ELSE

     GO TO 10

    ENDIF

    STOP ' '
    END

    SUBROUTINE COILCALC (IGAS,MOUT,D)

    IMPLICIT        REAL*8 (A-H,O-Z), INTEGER*2 (I-N)
    PARAMETER       (ITMAX=99,EPS=1.0D-8)
    REAL*8          MW,K,MUB,MUW,MURAT,NU,L,LDIFF,LGUESS
    REAL*8          K1,K2,N,MOUT,NUINF,LT
    CHARACTER*10    GAS

    COMMON /GPROP/  MW,GAMMA,GCF,RHO,RHOI,RHOO,RHOS,CP,K,
   +                MUB,MUW,NU,TB,TW,TBI,TBO,GAS

    EXTERNAL        GASPROP

    DATA  NUINF,K1,K2,N / 3.656D0,0.0668D0,0.04D0,0.6667D0 /

*     Get the gas properties.

    CALL GASPROP(IGAS)

*     Calculate average velocity.

    PI=2.0D0*DASIN(1.0D0)   ! Formula for pi
    A=PI*D**2/4.0D0         ! Pipe cross-sectional area - m2
    CTOK=273.15D0           ! Convert °C to K
    UOUT=MOUT/(RHOO*A)
    UIN=MOUT/(RHOI*A)
    UM=(UIN+UOUT)/2.0D0

*     Calculate various dimensionless parameters.

    RE=UM*D/NU                  ! Reynolds number
    ALPHA=K/(RHO*CP)            ! Thermal diffusivity
    PR=NU/ALPHA                 ! Prandtl number
    PE=RE*PR                    ! Peclet number
    MURAT=(MUB/MUW)**0.14D0     ! Viscosity ratio
```

```
*     Calculate length for laminar heat transfer.

      TWK=TW+CTOK
      TBK=TB+CTOK
      TBOK=TBO+CTOK
      TBIK=TBI+CTOK
      F1=RHO*UM*CP*D*(TBOK-TBIK)/(4.0D0*(TWK-TBK))
      F2=NUINF*K/D
      F3=K1*MURAT*K*PE
      L=1.0D0
      LDIFF=1.0D0
      ITER=0

      DO WHILE (LDIFF .GT. EPS .AND. ITER .LE. ITMAX)
        ITER=ITER+1
        DENOM=1.0D0+K2*(PE*D/L)**N
        LGUESS=F1/(F2+F3/L/DENOM)
        LDIFF=DABS(LGUESS-L)
        L=LGUESS
      ENDDO

*     Calculate length for laminar heat transfer.

      H=0.023D0*MURAT*K/D*RE**0.8D0*PR**0.333D0
      LT=F1/H

*     Calculate the pressure drop for turbulent flow.

      P=PDROP (UM,1.0D0,D)

*     Display the results.

      IEND=LEN_TRIM(GAS)
      WRITE (*,'(16X,A,A,A/)')
     +      'COMPUTED COIL LENGTHS FOR ',GAS(:IEND), ' :'

      WRITE (*,'(16X,A,1P,E9.3,A)') 'Mout = ',MOUT,' kg / s'
      WRITE (*,'(16X,A,F6.3,A,F5.4,A/)')
     +    'D    = ',D*1.0D3,' mm = 0',D*1.0D3/25.4D0,' in'
      WRITE (*,'(16X,A,F6.3,A,5X,A,F6.0)')
     +    'Uin  = ',UIN,' m / s', 'RE = ' ,RE
      WRITE (*,'(16X,A,F6.3,A,5X,A,F4.3)')
     +    'Uout = ',UOUT,' m / s','PR = 0',PR
      WRITE (*,'(16X,A,F6.3,A,5X,A,F6.0)')
     +    'Uavg = ',UM,' m / s',  'PE = ' ,PE

      WRITE (*,'(/16X,A,F8.5,A)') 'Laminar   : L = ',L ,' m'
      WRITE (*,'(16X,A,F8.5,A)')  'Turbulent : L = ',LT,' m'
```

```
      WRITE (*,'(/16X,A,F8.3,A,F7.3,A/16X,A)')
     +    'Pdrop = ',P/1.0D3,' kPa = ',P/6894.76D0,' psi',
     +    '(based on a length of 1 m of coiled tubing)'

      RETURN
      END

      FUNCTION PDROP (U,L,D)

      IMPLICIT        REAL*8 (A-H,O-Z), INTEGER*2 (I-N)
      REAL*8          MW,K,MUB,MUW,NU,L,L2
      CHARACTER*10    GAS

      COMMON /GPROP/  MW,GAMMA,GCF,RHO,RHOI,RHOO,RHOS,CP,K,
     +               MUB,MUW,NU,TB,TW,TBI,TBO,GAS

*     Calculate the friction factor for turbulent flow through a pipe.

      RE=U*D/NU
      F=0.184D0/RE**0.2D0

*     Compute the pressure drop.  Double (?) the pipe length used
*     in the calculation because the pipe is coiled, not straight.

      L2=2.0D0*L
      PDROP=F*L2*RHO*U**2/(2.0D0*D)   ! Result in Pa

      RETURN
      END

      SUBROUTINE GASPROP (IGAS)

      IMPLICIT        REAL*8 (A-H,O-Z), INTEGER*2 (I-N)
      REAL*8          MW,K,MUB,MUW,NU
      CHARACTER*10    GAS

      COMMON /GPROP/  MW,GAMMA,GCF,RHO,RHOI,RHOO,RHOS,CP,K,
     +               MUB,MUW,NU,TB,TW,TBI,TBO,GAS

      GO TO (10,20,30,40,50,60) IGAS

*     Get gas properties.  (SI Units)

*     ************  AIR  **************

10    MW    =  28.966000D+0  ! Molecular weight - kg / kmol
      GAMMA =   1.400000D+0  ! Specific heat ratio
      GCF   =   1.000000D+0  ! Gas correction factor (from MKS)
```

```
      RHO   =    1.397970D+0  ! Density (at TB and 1 atm) - kg / m3
      RHOI  =    1.209650D+0  ! Density (at TBI and 1 atm) - kg / m3
      RHOO  =    1.745990D+0  ! Density (at TBO and 1 atm) - kg / m3
      RHOS  =    1.293040D+0  ! Density (at 273 K and 1 atm) - kg / m3
      CP    =    1.005300D+0  ! Specific heat - kJ / kg·K
      K     =    2.252000D-5  ! Thermal conductivity - kJ / s·m·K
      MUB   =    1.519000D-5  ! Dynamic viscosity - (kg / m·s)
      MUW   =    1.338900D-5  ! Dynamic viscosity - (kg / m·s)
      TB    = -20.000000D+0  ! Bulk temperature - (°C)
      TW    = -60.000000D+0  ! Wall temperature - (°C)
      TBI   =  20.000000D+0  ! Inlet bulk temperature - (°C)
      TBO   = -60.000000D+0  ! Outlet bulk temperature - (°C)
      GAS   = 'AIR       '
      GO TO 70

*     ************ CF3I ************

20    MW    =  195.911000D+0  ! Molecular weight - kg / kmol
      GAMMA =    1.149000D+0  ! Specific heat ratio
      GCF   =    0.340000D+0  ! Gas correction factor (from MKS)
      RHO   =    9.059290D+0  ! Density (at TB and 1 atm) - kg / m3
      RHOI  =    8.339090D+0  ! Density (at TBI and 1 atm) - kg / m3
      RHOO  =    9.943630D+0  ! Density (at TBO and 1 atm) - kg / m3
      RHOS  =    9.043900D+0  ! Density (at 273 K and 1 atm) - kg / m3
      CP    =    0.363263D+0  ! Specific heat - kJ / kg·K
      K     =    6.524410D-6  ! Thermal conductivity - kJ / s·m·K
      MUB   =    1.371780D-5  ! Dynamic viscosity - (kg / m·s)
      MUW   =    1.266080D-5  ! Dynamic viscosity - (kg / m·s)
      TB    = - 1.000000D+0  ! Bulk temperature - (°C)
      TW    = -22.000000D+0  ! Wall temperature - (°C)
      TBI   =  20.000000D+0  ! Inlet bulk temperature - (°C)
      TBO   = -22.000000D+0  ! Outlet bulk temperature - (°C)
      GAS   = 'CF3I      '
      GO TO 70

*     *********** HFC-227 ************

30    MW    =  170.030000D+0  ! Molecular weight - kg / kmol
      GAMMA =    1.075000D+0  ! Specific heat ratio
      GCF   =    0.180000D+0  ! Gas correction factor (from MKS)
      RHO   =    7.837960D+0  ! Density (at TB and 1 atm) - kg / m3
      RHOI  =    7.260000D+0  ! Density (at TBI and 1 atm) - kg / m3
      RHOO  =    8.509880D+0  ! Density (at TBO and 1 atm) - kg / m3
      RHOS  =    7.925440D+0  ! Density (at 273 K and 1 atm) - kg / m3
      CP    =    0.793461D+0  ! Specific heat - kJ / kg·K
      K     =    1.128140D-5  ! Thermal conductivity - kJ / s·m·K
      MUB   =    1.093770D-5  ! Dynamic viscosity - (kg / m·s)
      MUW   =    1.014750D-5  ! Dynamic viscosity - (kg / m·s)
```

```
      TB    =   2.000000D+0  ! Bulk temperature - (°C)
      TW    = -16.000000D+0  ! Wall temperature - (°C)
      TBI   =  20.000000D+0  ! Inlet bulk temperature - (°C)
      TBO   = -16.000000D+0  ! Outlet bulk temperature - (°C)
      GAS   = 'HFC-227   '
      GO TO 70

*     ********** FC-218 **********

40    MW    = 188.017000D+0  ! Molecular weight - kg / kmol
      GAMMA =   1.068000D+0  ! Specific heat ratio
      GCF   =   0.170000D+0  ! Gas correction factor (from MKS)
      RHO   =   8.962690D+0  ! Density (at TB and 1 atm) - kg / m3
      RHOI  =   7.987000D+0  ! Density (at TBI and 1 atm) - kg / m3
      RHOO  =  10.257900D+0  ! Density (at TBO and 1 atm) - kg / m3
      RHOS  =   8.682680D+0  ! Density (at 273 K and 1 atm) - kg / m3
      CP    =   0.752860D+0  ! Specific heat - kJ / kg·K
      K     =   1.111450D-5  ! Thermal conductivity - kJ / s·m·K
      MUB   =   1.131740D-5  ! Dynamic viscosity - (kg / m·s)
      MUW   =   1.005830D-5  ! Dynamic viscosity - (kg / m·s)
      TB    = - 8.000000D+0  ! Bulk temperature - (°C)
      TW    = -36.000000D+0  ! Wall temperature - (°C)
      TBI   =  20.000000D+0  ! Inlet bulk temperature - (°C)
      TBO   = -36.000000D+0  ! Outlet bulk temperature - (°C)
      GAS   = 'FC-218    '
      GO TO 70

*     ********** HFC-125 **********

50    MW    = 120.020000D+0  ! Molecular weight - kg / kmol
      GAMMA =   1.103000D+0  ! Specific heat ratio
      GCF   =   0.300000D+0  ! Gas correction factor (from MKS)
      RHO   =   5.788080D+0  ! Density (at TB and 1 atm) - kg / m3
      RHOI  =   5.057000D+0  ! Density (at TBI and 1 atm) - kg / m3
      RHOO  =   6.807060D+0  ! Density (at TBO and 1 atm) - kg / m3
      RHOS  =   5.476350D+0  ! Density (at 273 K and 1 atm) - kg / m3
      CP    =   0.753624D+0  ! Specific heat - kJ / kg·K
      K     =   1.127550D-5  ! Thermal conductivity - kJ / s·m·K
      MUB   =   1.137060D-5  ! Dynamic viscosity - (kg / m·s)
      MUW   =   9.828150D-6  ! Dynamic viscosity - (kg / m·s)
      TB    = -14.000000D+0  ! Bulk temperature - (°C)
      TW    = -48.000000D+0  ! Wall temperature - (°C)
      TBI   =  20.000000D+0  ! Inlet bulk temperature - (°C)
      TBO   = -48.000000D+0  ! Outlet bulk temperature - (°C)
      GAS   = 'HFC-125   '
      GO TO 70

*     ********** HALON1301 **********
```

```
60     MW    =  148.910000D+0  ! Molecular weight - kg / kmol
     GAMMA =    1.145000D+0  ! Specific heat ratio
     GCF   =    0.370000D+0  ! Gas correction factor (from MKS)
     RHO   =    7.309030D+0  ! Density (at TB and 1 atm) - kg / m3
     RHOI  =    6.263000D+0  ! Density (at TBI and 1 atm) - kg / m3
     RHOO  =    8.829990D+0  ! Density (at TBO and 1 atm) - kg / m3
     RHOS  =    6.776430D+0  ! Density (at 273 K and 1 atm) - kg / m3
     CP    =    0.443921D+0  ! Specific heat - kJ / kg·K
     K     =    7.729630D-6  ! Thermal conductivity - kJ / s·m·K
     MUB   =    1.312610D-5  ! Dynamic viscosity - (kg / m·s)
     MUW   =    1.110830D-5  ! Dynamic viscosity - (kg / m·s)
     TB    =  -19.000000D+0  ! Bulk temperature - (°C)
     TW    =  -58.000000D+0  ! Wall temperature - (°C)
     TBI   =   20.000000D+0  ! Inlet bulk temperature - (°C)
     TBO   =  -58.000000D+0  ! Outlet bulk temperature - (°C)
     GAS   =  'HALON 1301'

70     NU    =  MUB / RHO     ! Kinematic viscosity - m2 / s

     RETURN
     END
```

Appendix C. Electrical Connections of Interface Boards and Components of Flow Calibration System

Signal Type	Computer Module Connection	Connections for Calibration System
ACAO-12 Interface Board		
Analog Output	Analog Output 1 (#1 on ACAO-12)	Set Point for Agent 10 slmn Mass-Flow Controller (Channel 3, Pin 6)
Flash-12 Interface Board		
Analog Output	Analog Output 3 (#1 on Flash-12)	Set Point for Air 10 slmn Mass-Flow Controller (Channel 1, Pin 4)
Analog Output	Analog Output 4 (#2 on Flash-12)	Set Point for Agent 2 slmn Mass-Flow Controller (Channel 2, Pin 5)
Digital Output	Digital Output 9 (#1 on Flash-12)	Enable to Switch Two-Way Electro-Pneumatic Valve and Light for Flow of Agent to Agent 2 slmn Mass-Flow Controller
Digital Output	Digital Output 10 (#2 on Flash-12)	Enable for Air 10 slmn Electro-Pneumatic Valve and Light
Digital Output	Digital Output 11 (#3 on Flash-12)	Enable for Agent 2 slmn Electro-Pneumatic Valve and Light
Digital Output	Digital Output 12 (#4 on Flash-12)	Enable for Agent 10 slmn Electro-Pneumatic Valve and Light
Digital Output	Digital Output 13 (#5 on Flash-12)	Enable for Vent/Test Electro-Pneumatic Valve and Light
Digital Output	Digital Output 14 (#6 on Flash-12)	Enable for 10 slmn Air Mass-Flow Controller (Channel 1, pin 12)
Digital Output	Digital Output 15 (#7 on Flash-12)	Enable for Agent 2 slmn Mass-Flow Controller (Channel 2, pin 10)
Digital Output	Digital Output 16 (#8 on Flash-12)	Enable for Agent 10 slmn Mass-Flow Controller (Channel 3, pin 11)
Analog Input	Analog-to-Digital Input #1	Thermocouple for Pump Temperature Measurement
Analog Input	Analog-to-Digital Input #2	Voltage Output for Air Mass-Flow Controller (Channel 1, pin 2)

Analog Input	Analog-to-Digital Input #3	Voltage Output for Agent 2 slmn Mass-Flow Controller (Channel 2, pin 14)
Analog Input	Analog-to-Digital Input #4	Voltage Output for Agent 10 slmn Mass-Flow Controller (Channel 2, pin 16)
Analog Input	Analog-to-Digital Input #5	Thermocouple for Coil Temperature Measurement
Analog Input	Analog-to-Digital Input #6	Voltage Output for Constant-Temperature Aspirated Hot Film
Analog Input	Analog-to-Digital Input #7	Voltage Output for Constant-Current Cold Wire

Appendix D. Workbench PC Icon-Based Worksheet ACTRL3.WBB for Controlling Calibration System, Digitizing Voltages During Calibrations, and Storing Results to Files

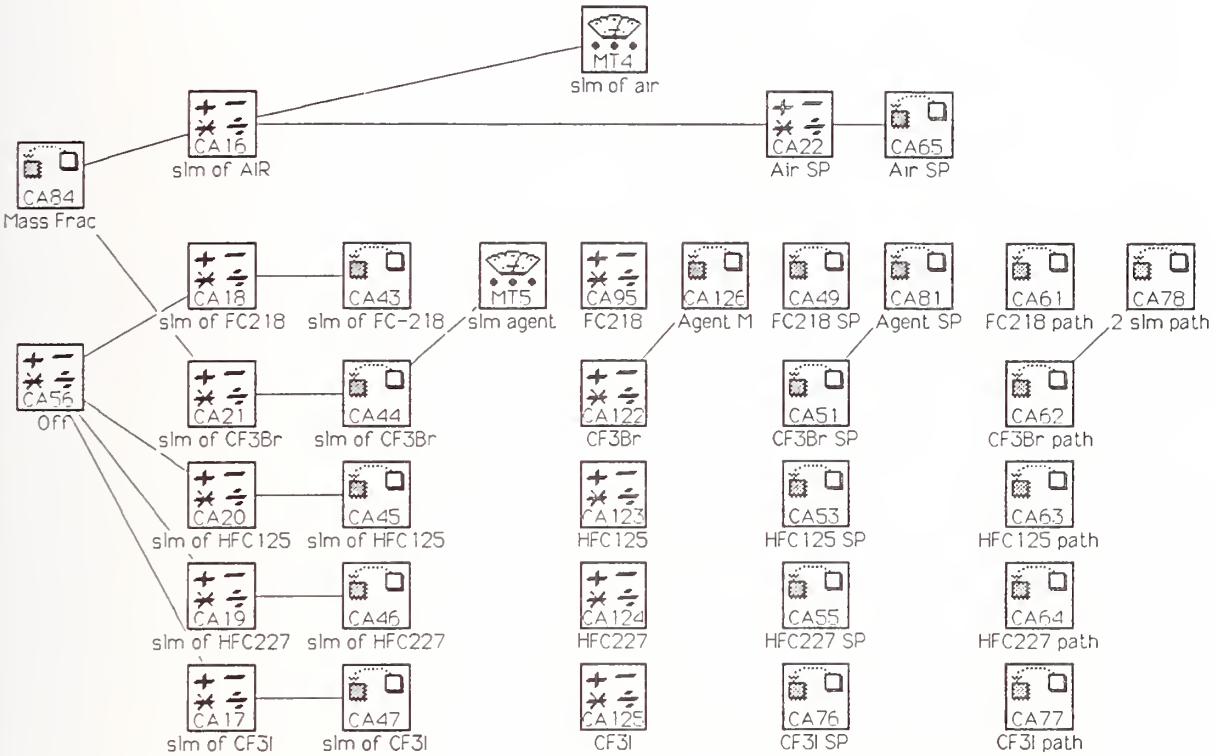

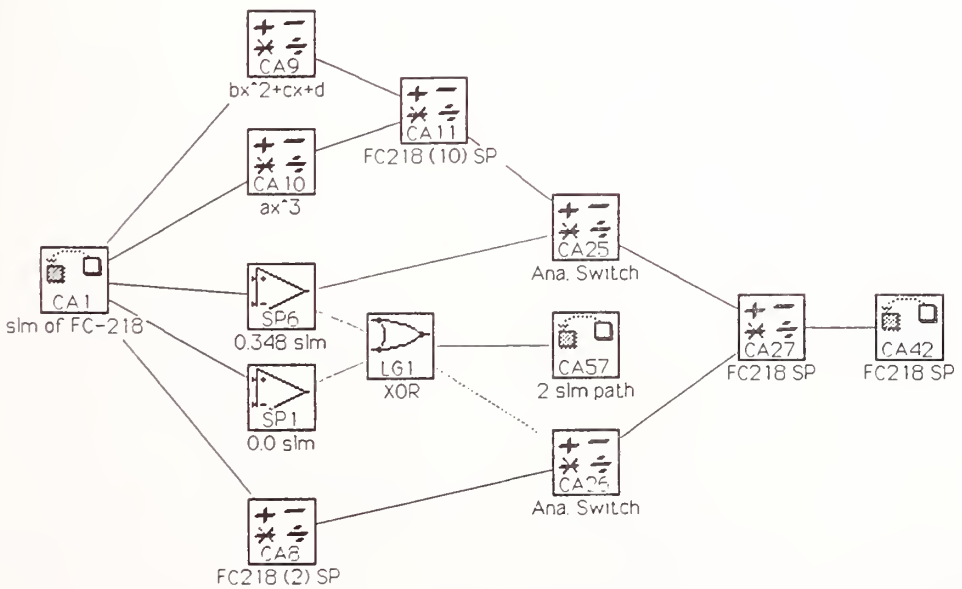

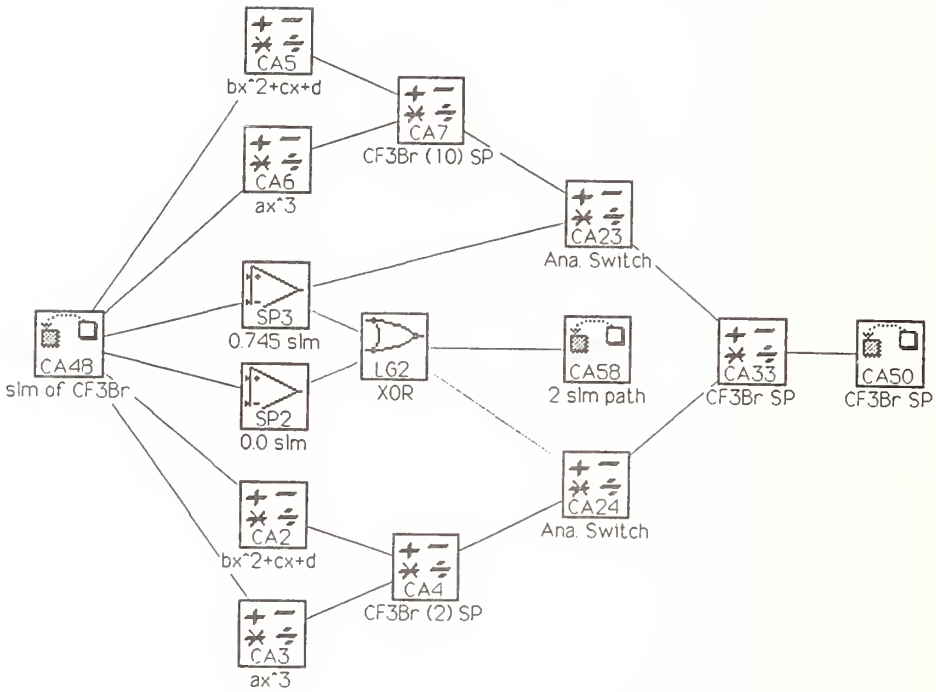
CA5
bx^2+cx+d
CA7
CF3Br (10) SP
CA6
ax^3
CA23
Ana. Switch
SP3
0.745 slm
LG2
XOR
CA58
2 slm path
CA33
CF3Br SP
CA50
CF3Br SP
CA48
slm of CF3Br
SP2
0.0 slm
CA24
Ana. Switch
CA2
bx^2+cx+d
CA4
CF3Br (2) SP
CA3
ax^3

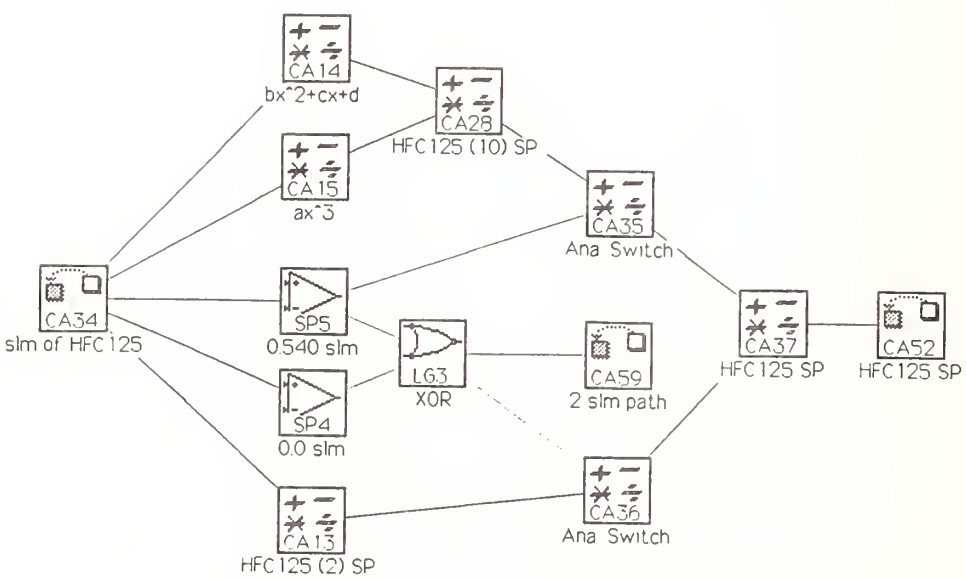
CA14
bx^2+cx+d
CA28
HFC 125 (10) SP
CA15
ax^3
CA35
Ana. Switch
CA34
slm of HFC 125
SP5
0.540 slm
LG3
XOR
CA59
2 slm path
CA37
HFC 125 SP
CA52
HFC 125 SP
SP4
0.0 slm
CA36
Ana. Switch
CA13
HFC 125 (2) SP

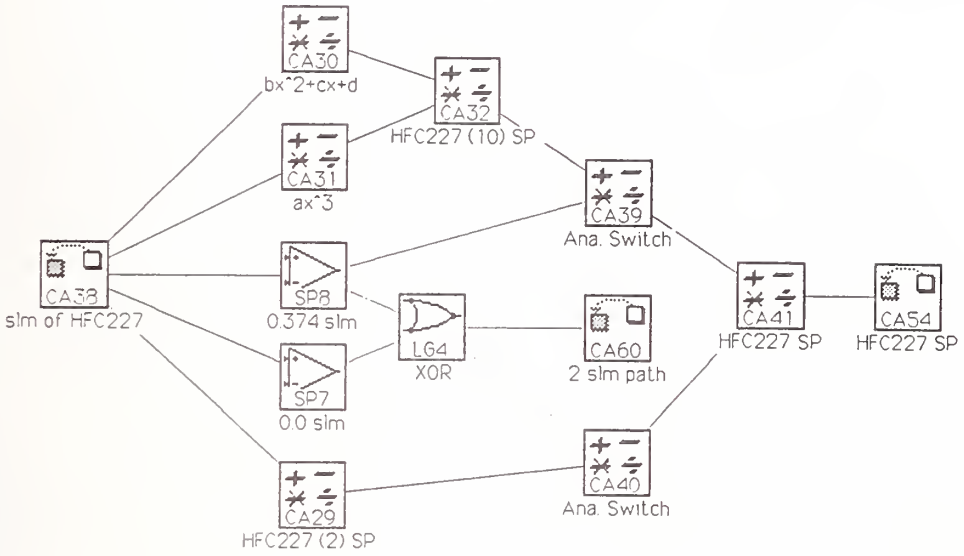
CA30
bx^2+cx+d
CA32
HFC227 (10) SP
CA31
ax^3
CA39
Ana. Switch
CA38
slm of HFC227
SP8
0.374 slm
LG4
XOR
CA60
2 slm path
CA41
HFC227 SP
CA54
HFC227 SP
SP7
0.0 slm
CA40
Ana. Switch
CA29
HFC227 (2) SP

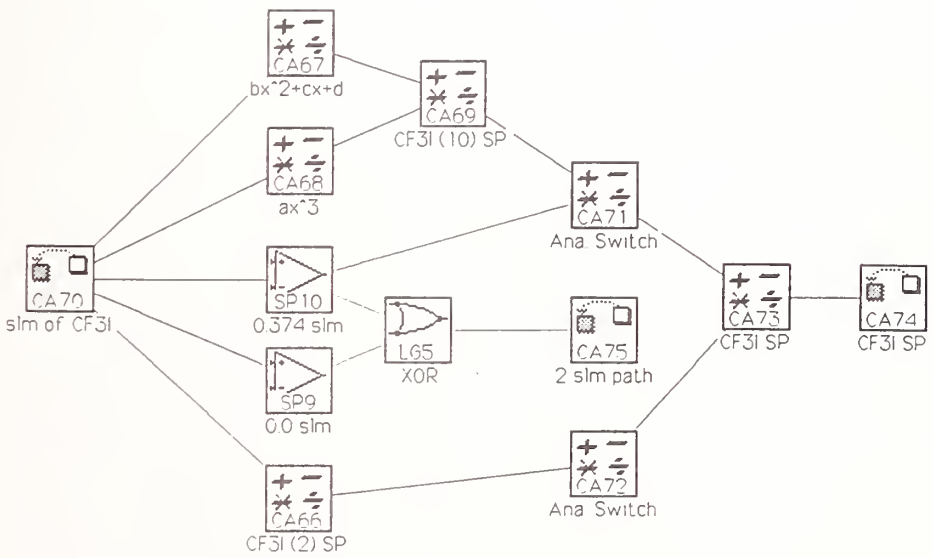
CA67
bx^2+cx+d
CA69
CF3I (10) SP
CA68
ax^3
CA71
Ana. Switch
CA70
slm of CF3I
SP10
0.374 slm
LG5
XOR
CA75
2 slm path
CA73
CF3I SP
CA74
CF3I SP
SP9
0.0 slm
CA72
Ana. Switch
CA66
CF3I (2) SP

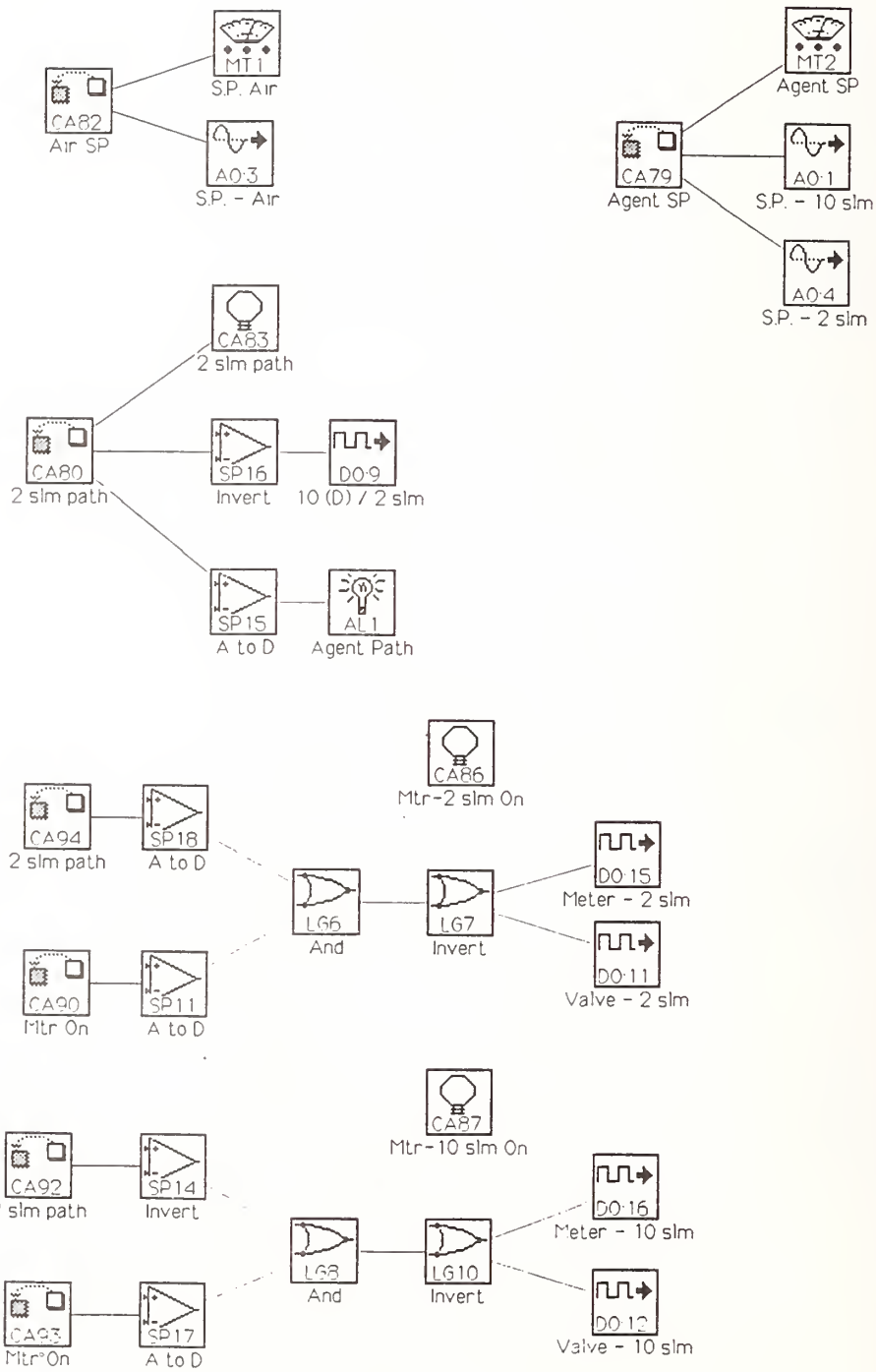
MT1
S.P. Air
CA82
Air SP
AO:3
S.P. - Air
MT2
Agent SP
CA79
Agent SP
AO:1
S.P. - 10 slm
AO:4
S.P. - 2 slm
CA83
2 slm path
CA80
2 slm path
SP16
Invert
DO:9
10 (D) / 2 slm
SP15
A to D
AL1
Agent Path
CA86
Mtr-2 slm On
CA94
2 slm path
SP18
A to D
LG6
And
LG7
Invert
DO:15
Meter - 2 slm
DO:11
Valve - 2 slm
CA90
Mtr On
SP11
A to D
CA87
Mtr-10 slm On
CA92
2 slm path
SP14
Invert
LG8
And
LG10
Invert
DO:16
Meter - 10 slm
DO:12
Valve - 10 slm
CA93
Mtr On
SP17
A to D

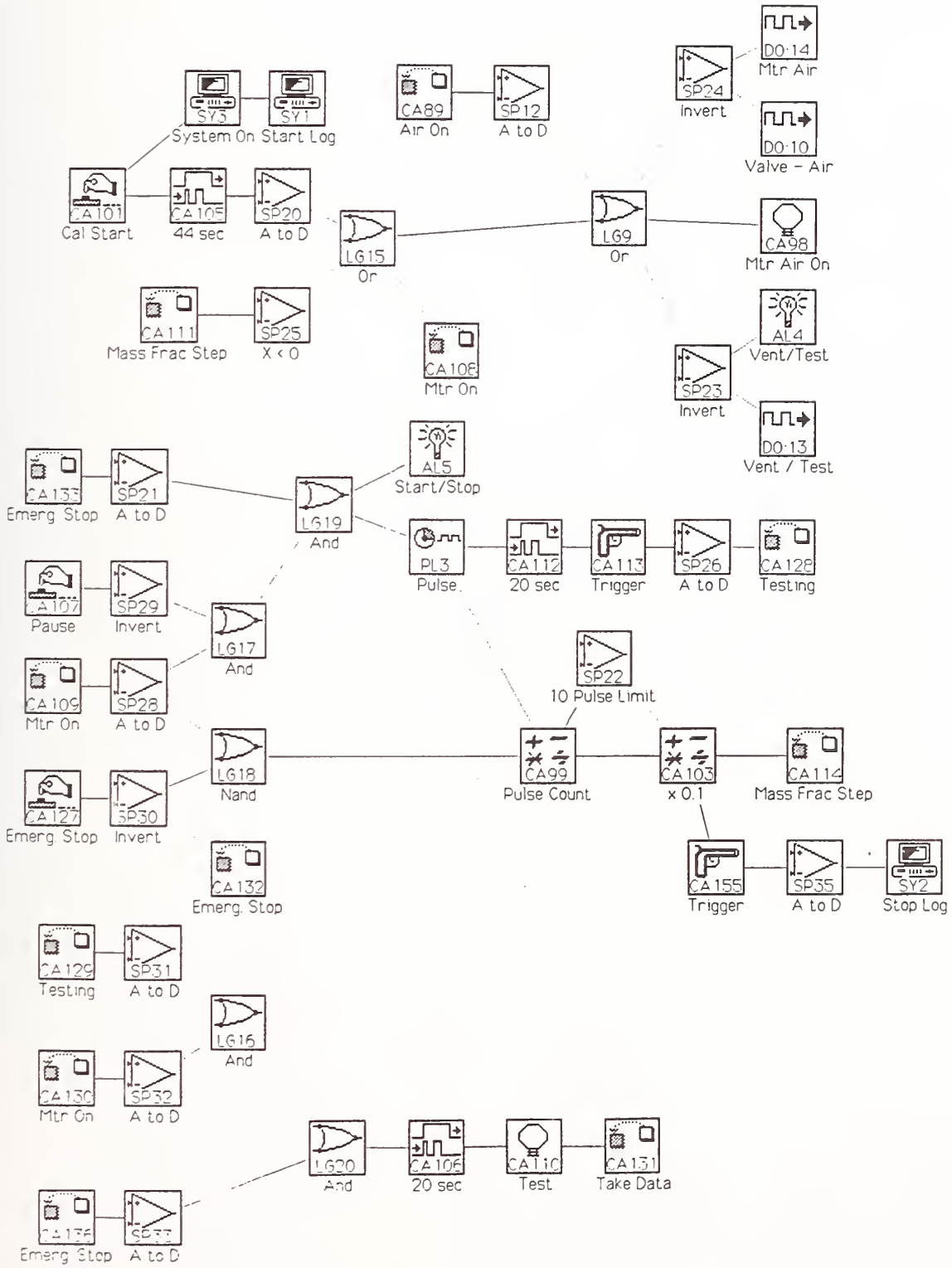
SY5
System On
SY1
Start Log
CA89
Air On
SP12
A to D
SP24
Invert
DO·14
Mtr Air
DO·10
Valve - Air
CA101
Cal Start
CA105
44 sec
SP20
A to D
LG15
Or
LG9
Or
CA98
Mtr Air On
CA111
Mass Frac Step
SP25
X < 0
CA108
Mtr On
AL4
Vent/Test
SP23
Invert
DO·13
Vent / Test
AL5
Start/Stop
CA133
Emerg. Stop
SP21
A to D
LG19
And
PL3
Pulse
CA112
20 sec
CA113
Trigger
SP26
A to D
CA128
Testing
A107
Pause
SP29
Invert
LG17
And
SP22
10 Pulse Limit
CA109
Mtr On
SP28
A to D
LG18
Nand
CA99
Pulse Count
CA103
x 0.1
CA114
Mass Frac Step
CA127
Emerg. Stop
SP30
Invert
CA132
Emerg. Stop
CA155
Trigger
SP35
A to D
SY2
Stop Log
CA129
Testing
SP31
A to D
LG16
And
CA130
Mtr On
SP32
A to D
LG20
And
CA106
20 sec
CA110
Test
CA131
Take Data
Emerg. Stop
A to D

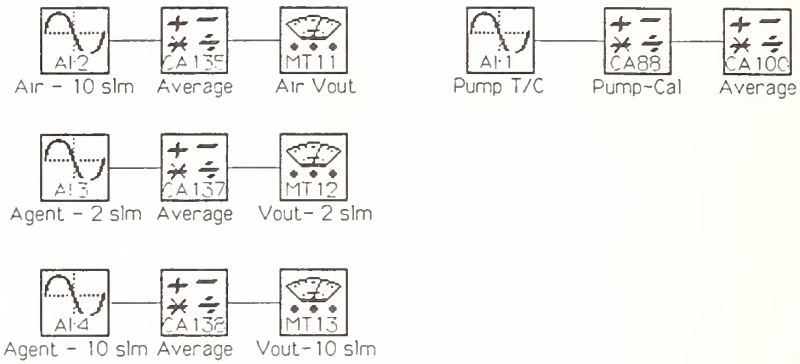
AI:2
Air - 10 slm
CA135
Average
MT11
Air Vout
AI:1
Pump T/C
CA88
Pump-Cal
CA100
Average
AI:3
Agent - 2 slm
CA137
Average
MT12
Vout- 2 slm
AI:4
Agent - 10 slm
CA138
Average
MT13
Vout-10 slm

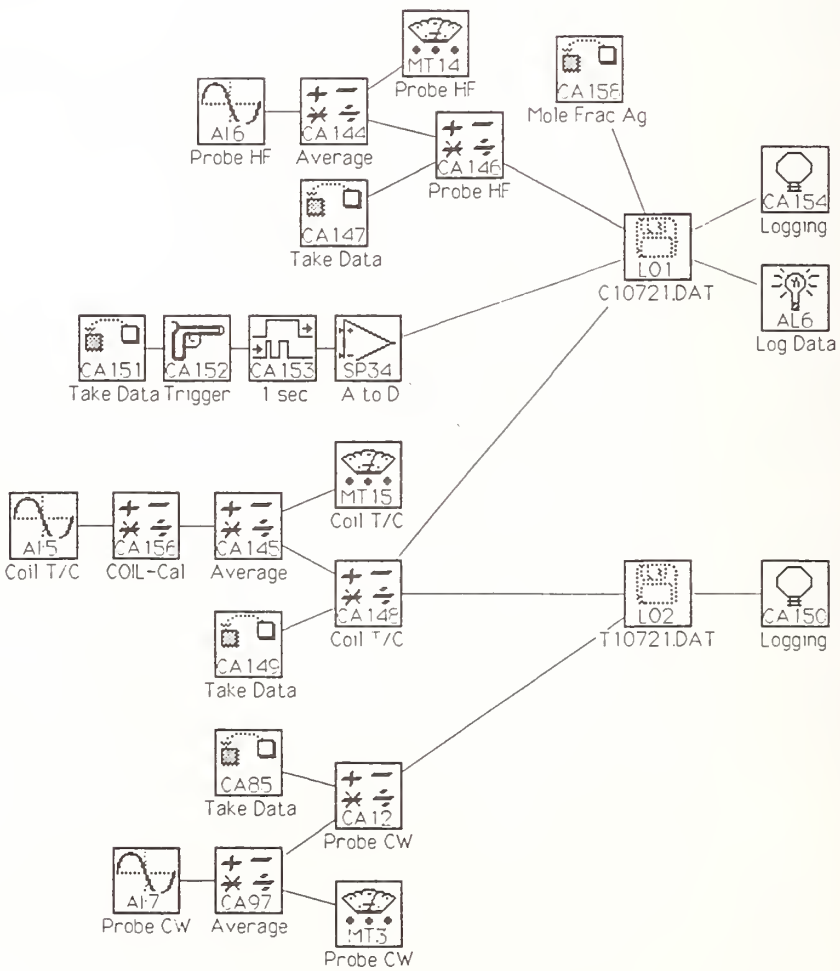
MT14
Probe HF
CA156
Mole Frac Ag
AI6
Probe HF
CA144
Average
CA146
Probe HF
CA147
Take Data
CA154
Logging
LO1
C10721.DAT
AL6
Log Data
CA151
Take Data
CA152
Trigger
CA153
1 sec
SP34
A to D
MT15
Coil T/C
AI:5
Coil T/C
CA156
COIL-Cal
CA145
Average
CA148
Coil T/C
CA149
Take Data
LO2
T10721.DAT
CA150
Logging
CA85
Take Data
CA12
Probe CW
AI:7
Probe CW
CA97
Average
MT3
Probe CW

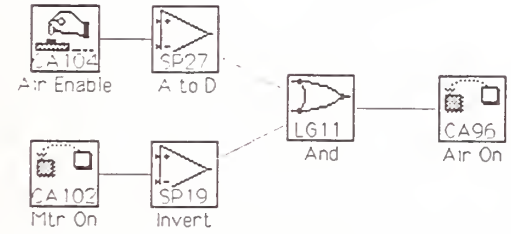
CA104
Air Enable
SP27
A to D
LG11
And
CA96
Air On
CA102
Mtr On
SP19
Invert

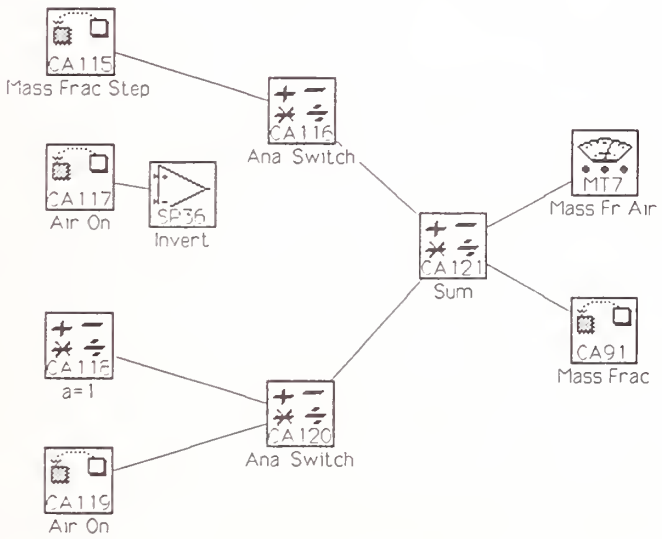
CA115
Mass Frac Step
CA116
Ana Switch
CA117
Air On
SP36
Invert
MT7
Mass Fr Air
CA121
Sum
CA91
Mass Frac
CA118
a=1
CA120
Ana Switch
CA119
Air On

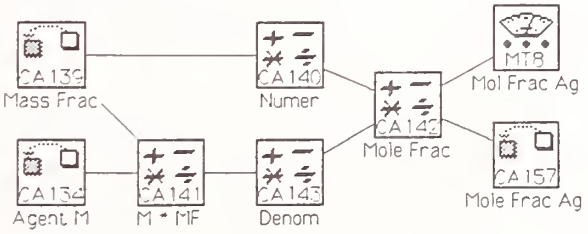
CA139
Mass Frac
CA140
Numer
MT8
Mol Frac Ag
CA142
Mole Frac
CA157
Mole Frac Ag
CA134
Agent M
CA141
M * MF
CA143
Denom

Appendix E. Workbench PC Computer-Control Panel for Calibration System. Panel Is Controlled By worksheet ACTRL3.WBB Shown in Appendix D

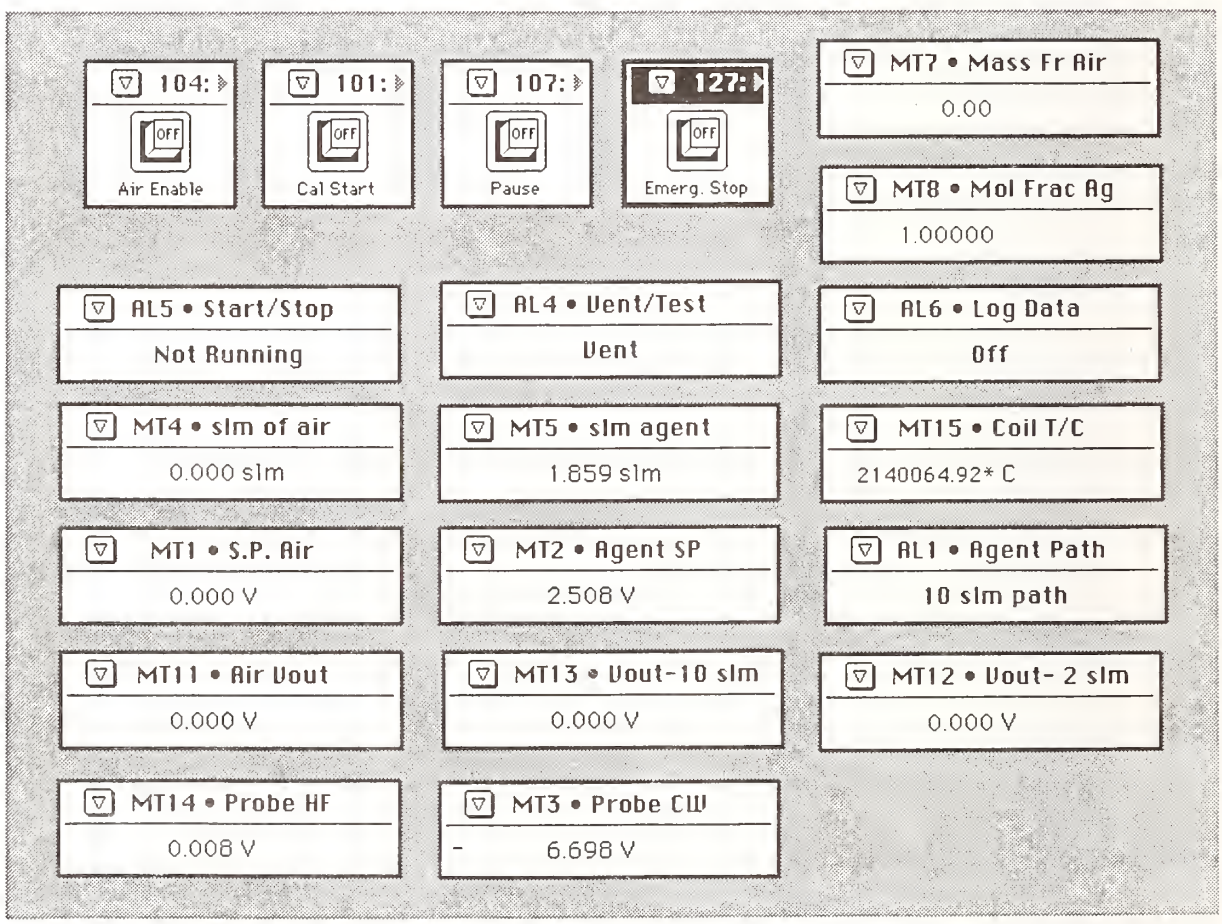

Appendix F. Detailed Operating Procedures for Calibration of Combined Aspirated Hot-Film/Cold-Wire Probe

TURN ON AND OPERATING PROCEDURE FOR CALIBRATION FACILITY

1. Turn on light in hood.

2. Check Syltherm level and fill if necessary. The fill line is located where the contraction of the nozzle straightens out.

3. Turn on the computer.

4. Turn on the power strip for the board, mixer, Agitainer, Exatrol, pump, and heaters. At this point do not plug in the pump.

5. Set up the IFA 100 anemometer.
   a. Refer to TSI Reference Manual
   b. Set up operating resistance
   c. Perform frequency response tuning.

6. Position aspirating probe
   a. Attach aspirating probe to drill press mount such that the end of the probe is approximately two inches from the steel block.
   b. Tighten the screws uniformly.
   c. Make sure the aspirating probe does not bend.
   d. Mount the drill press holder on the vertical steel rod.
   e. Locate the tip of the probe just above the exit of the nozzle. (This was done to reduce the chance of hitting the probe against the walls of the nozzle.
   f. Locate the tip near the center of the nozzle. The X-Y translation stage provides an adjustment to center the probe.
   g. Connect pump to aspirating probe.
   h. Move drill press handle to lower the aspirating probe into the nozzle.
   i. Place U-shaped bracket so that the dill press remains in the down position. We typically used the longest bracket.

7. Check that the set point on the Exatrol for the heater is below the lowest desired temperature. This will prevent overheating the liquid. **Note:** Do not connect the cooler to an outlet on the power strip described in 4 because the outlet will become overloaded.

8. While the fluid is transparent, check the operation of the magnetic stirrer.

9. Turn on the motor-driven stirrer. Set to approximately 60 to ensure smooth operation.

10. Turn on 100 psi air to valves.

11. Check the following on the Model 247C Readout:
    a. All the toggle switches except for the power switch are in the down position.
    b. Cables to flow meters:
        Channel 1-10 slmn Air
        Channel 2-2 slmn Agent
        Channel 3-10 slmn Agent
        Channel 4-Not used
    c. Ribbon cable connects "Interface Channel 1-4" to box containing A/D boards (blue connector).

12. After warm-up time of 1/2 hr., zero the outputs on the Model 247C 4-Channel Readout. This is accomplished by adjusting the pot labelled Z.

13. Call up the appropriate worksheet (ACTRL3.WBB).

14. Enter the filename for the data into the log icon.

15. Set up worksheet for gas to be tested.
    a. Connect global feedback CA84 to appropriate agent box CA17, CA18, CA19, CA20, or CA21.
    b. Connect appropriate calculation icon CA43, CA44, CA45, CA46, or CA47 to MT5.
    c. Connect appropriate global feedback icon CA49, CA51, CA53, CA55, or CA76 to global-feedback icon CA81.
    d. Connect appropriate global-feedback icon CA61, CA62, CA63, CA64, or CA77 to global-feedback icon CA78.

16. Pressurize air and agent flow lines. Set pressures to 20 psig.

17. Turn on cooler.

18. Turn on dry air to prevent condensation. To do this press "air enabled" on the worksheet.

19. Check that Fenwall unit which controls the temperature of the plate is set to 28 °C.

20. Start all logs (This is automatically done in ACTRL3.WBB).

21. Wait for the Syltherm fluid to attain set-point temperature and stabilize.

22. Turn on pump.

23. Check pressure gauge to ensure that the probe is choked.

24. Set IFA 100 to "Run."

25. Press "Cal Start" on the worksheet.

27. Adjust the set point on the Exatrol to the next temperature setting. The 700 W heater can be used in addition to the 250 W heater during this period to accelerate heating of the liquid. Do not

leave the 700 W heater on for long periods because it heats quickly. Be careful!!! Do not leave the 700 Watt heater on.

28. When the temperature has stabilized to 0.1 °C press "Cal Start."

29. Check to make sure that the software is operating properly.
    a. Make sure MT1 "S.P. Air" and MT11 "Air Vout" are approximately the same for a specified mass fraction.
    b. Make sure MT2 "Ag S.P." and MT13 "Vout slm" or MT12 "Vout 2slm" are the same for a specified mass fraction.

30. Then heat Sylthern up to next temperature and proceed as before.

31. When the calibration is completed begin the shut down procedure.

SHUT DOWN PROCEDURE

1. Set IFA 100 Anemometer to "standby."

2. Unplug pump.

3. Turn off cooler.

4. Adjust set point on Exatrol to a low temperature. This will avoid heating when the exatrol is turned on again.

5. Make sure the 700 W heater is off.

6. Turn off the motor-driven stirrer.

7. Turn off agent flow. Get MCTRL2.WBB worksheet, set mass fraction on slider to 0.0 and press "MTR ON" to bleed agent out of the lines.

8. Flush system with air.
    a. Turn off black knob on air tank.
    b. Hook up air line to agent line.
    c. Set mass fraction on slider to 0.0, turn black knob on air tank on. Turn "MTR ON." This flushes out the 10 slmn path.
    d. Set mass fraction to 0.78 to flush out the 2 slmn path.
    e. Shut off air. The pressure will drop. Turn off meter.

9. Turn off 100 psi air supply. Flip vent on and off a few times. This will remove the air pressure from the line.

10. Turn off power strip.

11. Return air line to air pipe and agent line to agent pipe.

12. Turn off light in hood.

13. Turn off computer.

Appendix G. Workbench PC Icon-Based Worksheet SHOT.WBB for Triggering Data Acquisition, Digitizing Hot-Film and Cold-Wire Voltages and Output of DIRRACS, and Storing Results to Files

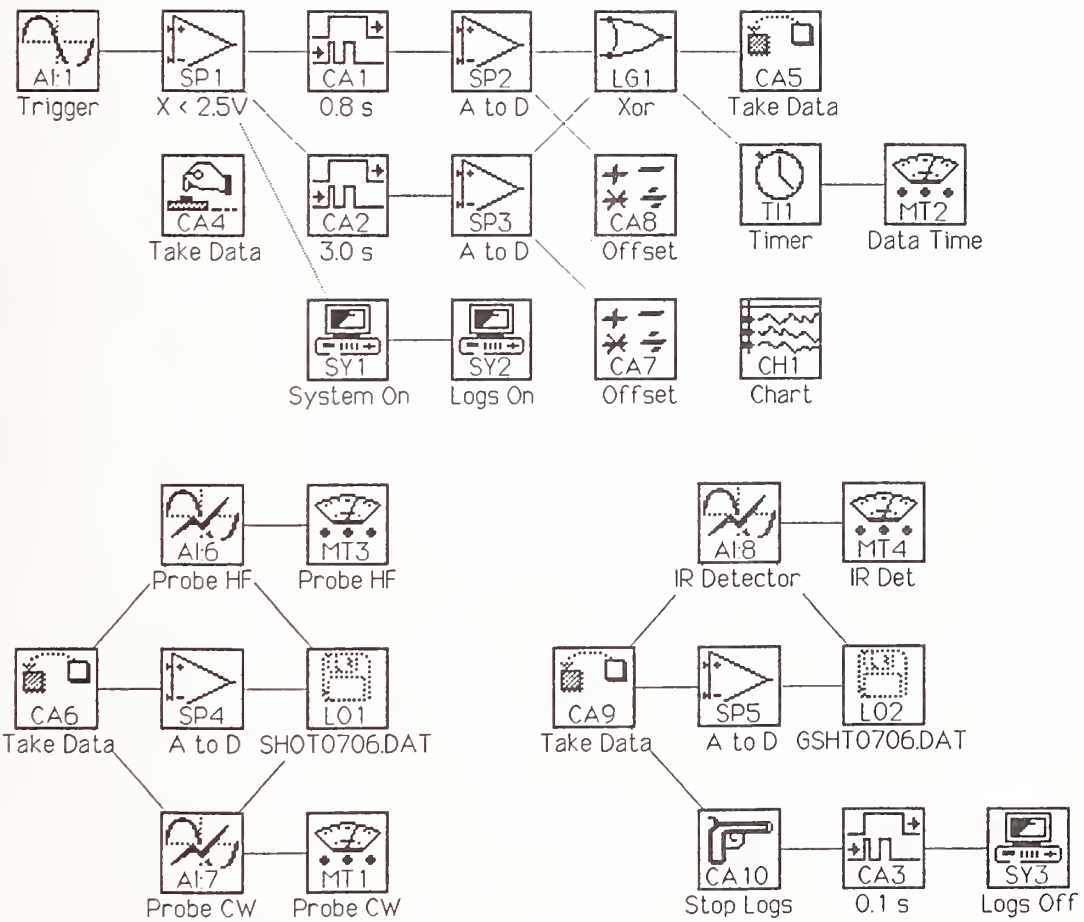

Appendix H. FORTRAN Program SURFFIT.FOR to Calculate Least Squares Fit to Surface of Order m Representing Agent Concentration. Surface is Fit of Agent Concentrations As Function of Temperature and Aspirated Hot-Film Voltage

```
*     Fit a surface to calibration data.  (SURFFIT.FOR)

*     David E. Hess
*     Fluid Flow Group - Process Measurements Division
*     Chemical Science and Technology Laboratory
*     National Institute of Standards and Technology
*     June 8, 1994

*     This routine is designed to accept three quantities:
*           X(k), Y(k) and Z(k)  for k = 1 to N.
*     The data may be typed in at the keyboard or read from a file.

*     The filename must be of the form :
*     C // 1 digit test number // 4 digit date // .DAT (appended)

*     There is no specific limit to the number of values N except
*     that imposed by memory constraints.  Note that the parameter
*     NMAX must be greater than the largest anticipated value of N
*     when reading data from a file.

*     The program then uses a least square fit analysis to
*     determine the Mth order surface: Z(X,Y).  The (M+1)**2
*     coefficients for the fit are stored in A.  An error analysis
*     for the fit is performed, and the output is stored in a file.

      IMPLICIT    REAL*8 (A-H,O-Z), INTEGER*2 (I-N)
      PARAMETER     (NMAX=150)
      PARAMETER     (NUMI=1,NUMO=2)
      INTEGER*2  DAT,TN
      INTEGER*4  BYTES
      CHARACTER*1   INP,FILKEY
      CHARACTER*4   FEXT,FEXT2,FEXT3
      CHARACTER*10     FNAMI,FNAME,FNAMA

      REAL*8          Z [ALLOCATABLE] (:)   , ZTEMP [ALLOCATABLE] (:)
      REAL*8          X [ALLOCATABLE] (:)   ,     Y [ALLOCATABLE] (:)
      REAL*8  XTEMP [ALLOCATABLE] (:)   , YTEMP [ALLOCATABLE] (:)
      REAL*8         XY [ALLOCATABLE] (:,:) ,   XYT [ALLOCATABLE] (:,:)
      REAL*8  XYTXY [ALLOCATABLE] (:,:) ,  XYTZ [ALLOCATABLE] (:,:)
      REAL*8       ZEQS [ALLOCATABLE] (:,:) ,     A [ALLOCATABLE] (:)
      REAL*8       ZEST [ALLOCATABLE] (:)   , ZFEST [ALLOCATABLE] (:)
```

```
      REAL*8      ZDEL [ALLOCATABLE] (:)  ,  ZREL [ALLOCATABLE] (:)

      DATA        EPS, INDIC / 1.0D-10, 1 /
      DATA        FEXT, FEXT2, FEXT3 / '.DAT', '.ERR', '.COE' /

*     Title of routine.

      WRITE (*,'(25(/))')
      WRITE (*,'(18X,A//18X,A)')
     +   '      L E A S T   S Q U A R E S',
     +   'S U R F A C E   F I T T I N G   R O U T I N E'
      WRITE (*,'(11(/))')

*     Get the order of the surface to fit.

      WRITE (*,'( )')
      WRITE (*,'(16X,A\)') 'Enter order of surface M : '
      READ (*,*) M
      WRITE (*,'( )')

      MP1=M+INT2(1)
      MP1SQ=(MP1)**2
      MP1SQP1=MP1SQ+INT2(1)

*     Read in X, Y and Z from a file or from the keyboard ?

10    WRITE (*,'(16X,A\)') 'Enter (F)ile input or (K)eyboard input: '
      READ (*,'(A)') FILKEY
      WRITE (*,'( )')
      GO TO (10,40) ILET(FILKEY,'FK')

*     Keyboard input section ****************************************
*     Get values of X, Y and Z from keyboard.

20    WRITE (*,'(16X,A\)') 'Enter # of calibration values (N) : '
      READ (*,*) N
      WRITE (*,'( )')

*     Estimate space required for arrays for this choice of M and N.

      SPACE=DBLE(BYTES(M,N))/1024.0D0

      WRITE (*,'(13X,A,F7.2,A/)')
     +      'Amount of space required for arrays = ',SPACE,' kB.'
      PAUSE
     +   '                Press enter to allocate arrays and continue.'

*     Allocate space for the necessary arrays.
```

```
      ALLOCATE (X(N), Y(N), Z(N), STAT=IERR)
      IF (IERR .NE. 0) STOP 'Can't allocate input arrays in main.'

      ALLOCATE (XY(N,MP1SQ), XYT(MP1SQ,N), STAT=IERR)
      IF (IERR .NE. 0) STOP 'Can't allocate XY & XYT arrays in main.'

      ALLOCATE (XYTXY(MP1SQ,MP1SQ), STAT=IERR)
      IF (IERR .NE. 0) STOP 'Can't allocate XYTXY array in main.'

      ALLOCATE (XYTZ(MP1SQ,1), STAT=IERR)
      IF (IERR .NE. 0) STOP 'Can't allocate RHS array in main.'

      ALLOCATE (ZEQS(MP1SQP1,MP1SQP1), STAT=IERR)
      IF (IERR .NE. 0) STOP 'Can't allocate ZEQS array in main.'

      ALLOCATE (A(MP1SQ), STAT=IERR)
      IF (IERR .NE. 0) STOP 'Can't allocate coeff arrays in main.'

      ALLOCATE (ZEST(N),ZFEST(N),ZDEL(N),ZREL(N), STAT=IERR)
      IF (IERR .NE. 0) STOP 'Can't allocate error arrays in main.'

*     Now, get the data.

      DO I=1,N
        WRITE (*,30) I,I,I
30      FORMAT (16X,'Enter X(',I2,') , Y(',I2,') and Z(',I2,') : '\)
        READ (*,*) X(I),Y(I),Z(I)
      ENDDO
      WRITE (*,'( )')

      GO TO 70

*     File input section ******************************************

40    WRITE (*,'(16X,A,I3,A)')
     +      'Program will read up to ',NMAX,' points.'
50    WRITE (*,'(16X,A,A,A\)')
     +   'Enter name of input file [',FEXT,']: '
      READ (*,'(A)') FNAMI
      WRITE (*,'( )')

*     Concatenate file extension to FNAMI.

      IPD=INDEX(FNAMI,'.')
      IF (IPD .GT. 9) GO TO 50
      IF (IPD .EQ. 0) THEN
        IEND=LEN_TRIM(FNAMI)
        FNAMI(IEND+1:IEND+4)=FEXT
```

```
      ENDIF

*     Create the other filenames.

      IPD=INDEX(FNAMI,'.')
      FNAME  = FNAMI(:IPD-1) // FEXT2
      FNAMA  = FNAMI(:IPD-1) // FEXT3

*     Get the input file.

      OPEN (NUMI,FILE=FNAMI,STATUS='OLD')

*     First determine # of values of X, Y and Z in the file.

      DO I=1,NMAX
        READ (NUMI,*,END=60) XTST,YTST,ZTST
      ENDDO
60    N=I-1
      REWIND(NUMI)

*     Estimate space required for arrays for this choice of M and N.

      SPACE=DBLE(BYTES(M,N))/1024.0D0

      WRITE (*,'(13X,A,F7.2,A/)')
     +       'Amount of space required for arrays = ',SPACE,' kB.'
      PAUSE
     +  '              Press enter to allocate arrays and continue.'

*     Allocate space for the necessary arrays.

      ALLOCATE (X(N), Y(N), Z(N), STAT=IERR)
      IF (IERR .NE. 0) STOP 'Can't allocate input arrays in main.'

      ALLOCATE (XY(N,MP1SQ), XYT(MP1SQ,N), STAT=IERR)
      IF (IERR .NE. 0) STOP 'Can't allocate XY & XYT arrays in main.'

      ALLOCATE (XYTXY(MP1SQ,MP1SQ), STAT=IERR)
      IF (IERR .NE. 0) STOP 'Can't allocate XYTXY array in main.'

      ALLOCATE (XYTZ(MP1SQ,1), STAT=IERR)
      IF (IERR .NE. 0) STOP 'Can't allocate RHS array in main.'

      ALLOCATE (ZEQS(MP1SQP1,MP1SQP1), STAT=IERR)
      IF (IERR .NE. 0) STOP 'Can't allocate ZEQS array in main.'

      ALLOCATE (A(MP1SQ), STAT=IERR)
      IF (IERR .NE. 0) STOP 'Can't allocate coeff arrays in main.'
```

```
      ALLOCATE (ZEST(N),ZFEST(N),ZDEL(N),ZREL(N), STAT=IERR)
      IF (IERR .NE. 0) STOP 'Can't allocate error arrays in main.'

*     Get values of X, Y and Z from file.

      DO I=1,N
        READ (NUMI,*) X(I),Y(I),Z(I)
      ENDDO
      CLOSE (NUMI)

*     Display these values on the screen for verification.

70    CALL DISPLAY_CALDATA (X,Y,Z,N,*130)

*     Fix, Insert, Delete an entry or Continue.

80    WRITE (*,'(16X,A\)') '(F)ix, (I)nsert, (D)elete '
      WRITE (*,'(A\)') 'an entry or (C)ontinue? '
      READ (*,'(A)') INP
      WRITE (*,'( )')
      GO TO (80,90,110,130) ILET(INP,'IDCF')

*     Routine to fix bad keyboard entry ****************************

      WRITE (*,'(16X,A\)') 'Enter array subscript of bad value: '
      READ (*,*) I
      WRITE (*,30) I,I,I
      READ (*,*) X(I),Y(I),Z(I)
      GO TO 70

*     Insert an entry ***********************************************

*       First, create some temporary space.

90    ALLOCATE (XTEMP(N+1), YTEMP(N+1), ZTEMP(N+1), STAT=IERR)
      IF (IERR .NE. 0)
     +    STOP 'Can't allocate XTEMP, YTEMP and ZTEMP in INSERT.'

*       Copy old values into temporary area.

      DO I=1,N
        XTEMP(I)=X(I)
        YTEMP(I)=Y(I)
        ZTEMP(I)=Z(I)
      ENDDO

*       Throw away old arrays.
```

```
      DEALLOCATE (X,Y,Z, STAT=IERR)
      IF (IERR .NE. 0)
     +    STOP 'Can't deallocate X, Y and Z in INSERT.'

  100    WRITE (*,'(16X,A\)') 'Insert after which array subscript? '
      READ (*,*) J
      IF (J .LT. 0 .OR. J .GT. N) GO TO 100
      N=N+1
      JP2=J+2
      DO I=N,JP2,-1
        IM1=I-1
        XTEMP(I)=XTEMP(IM1)
        YTEMP(I)=YTEMP(IM1)
        ZTEMP(I)=ZTEMP(IM1)
      ENDDO
      JP1=J+1
      WRITE (*,30) JP1,JP1,JP1
      READ (*,*) XTEMP(JP1),YTEMP(JP1),ZTEMP(JP1)

*       Create space for X, Y and Z arrays.

      ALLOCATE (X(N), Y(N), Z(N), STAT=IERR)
      IF (IERR .NE. 0)
     +    STOP 'Can't allocate X, Y and Z in INSERT.'

*       Copy X, Y and Z values into permanent arrays.

      DO I=1,N
        X(I)=XTEMP(I)
        Y(I)=YTEMP(I)
        Z(I)=ZTEMP(I)
      ENDDO

*       Delete temporary space and display values.

      DEALLOCATE (XTEMP,YTEMP,ZTEMP, STAT=IERR)
      IF (IERR .NE. 0) STOP
     +    'Can't deallocate XTEMP, YTEMP and ZTEMP in INSERT.'

      GO TO 70

*     Delete an entry ********************************************

*       First, create some temporary space.

  110 ALLOCATE (XTEMP(N), YTEMP(N), ZTEMP(N), STAT=IERR)
      IF (IERR .NE. 0)
     +    STOP 'Can't allocate XTEMP, YTEMP and ZTEMP in DELETE.'
```

```
*       Copy old values into temporary area.

        DO I=1,N
          XTEMP(I)=X(I)
          YTEMP(I)=Y(I)
          ZTEMP(I)=Z(I)
        ENDDO

*       Throw away old arrays.

        DEALLOCATE (X,Y,Z, STAT=IERR)
        IF (IERR .NE. 0)
       +    STOP 'Can't deallocate X, Y and Z in DELETE.'

120     WRITE (*,'(16X,A\)') 'Delete which subscript? '
        READ (*,*) J
        IF (J .LT. 1 .OR. J .GT. N) GO TO 120
        NM1=N-1
        DO I=J,NM1
          IP1=I+1
          XTEMP(I)=XTEMP(IP1)
          YTEMP(I)=YTEMP(IP1)
          ZTEMP(I)=ZTEMP(IP1)
        ENDDO
        N=N-1

*       Create space for X, Y and Z arrays.

        ALLOCATE (X(N), Y(N), Z(N), STAT=IERR)
        IF (IERR .NE. 0)
       +    STOP 'Can't allocate X, Y and Z in DELETE.'

*       Copy X, Y and Z values into permanent arrays.

        DO I=1,N
          X(I)=XTEMP(I)
          Y(I)=YTEMP(I)
          Z(I)=ZTEMP(I)
        ENDDO

*       Delete temporary space and display values.

        DEALLOCATE (XTEMP,YTEMP,ZTEMP, STAT=IERR)
        IF (IERR .NE. 0) STOP
       +    'Can't deallocate XTEMP, YTEMP and ZTEMP in DELETE.'

        GO TO 70
```

```
*     Create an input file ****************************************

130 WRITE (*,'(16X,A\)') 'Create an input file? (Y/N) : '
    READ (*,'(A)') INP
    WRITE (*,'( )')
    GO TO (130,140) ILET(INP,'NY')
      CALL PRINT2 (N,X,Y,Z,FEXT)

*     Calculate all possible products of X and Y.

140 CALL COEFF (X,Y,XY,N,M)

*     Compute the transpose XYT of the XY array.

    DO K=1,N
      DO J=1,MP1SQ
        XYT(J,K)=XY(K,J)
      ENDDO
    ENDDO

*     Compute coefficient array: XYTXY = XYT * XY
*     Compute right hand sides : XYTZ = XYT * Z

    CALL MATMLT (XYT,XY,XYTXY,MP1SQ,N,  MP1SQ)
    CALL MATMLT (XYT, Z, XYTZ,MP1SQ,N,INT2(1))

*     Create the augmented matrix ZEQS.

    DO I=1,MP1SQP1
      DO J=1,MP1SQP1
        ZEQS(I,J)=0.0D0
      ENDDO
    ENDDO

    DO I=1,MP1SQ
      DO J=1,MP1SQ
        ZEQS(I,J)=XYTXY(I,J)
      ENDDO
    ENDDO

    DO I=1,MP1SQ
      ZEQS(I,MP1SQP1)=XYTZ(I,1)
    ENDDO

*     Solve the set of MP1SQ eqs in MP1SQ unknowns for A.

    DETERZ=SIMUL(MP1SQ,ZEQS,A,EPS,INDIC,MP1SQP1)
    WRITE (*,'(16X,A,D16.5/)') 'Deter for Z = ',DETERZ
```

```
      IF (DETERZ .EQ. 0.0D0) THEN
        WRITE (*,'(16X,A)') 'Z matrix is singular, no solution.'
        GO TO 160
      ENDIF

*     Store the coefficients in a file.

      OPEN (NUMO,FILE=FNAMA,STATUS='UNKNOWN')
        WRITE (NUMO,'(D25.15)') (A(I),I=1,MP1SQ)
      CLOSE (NUMO)

*     Perform error analysis on Z.

160   IF (DETERZ .EQ. 0.0D0) GO TO 180
      CALL ERRANAL (X,Y,Z,XY,A,N,M,
     +      ZEST,ZFEST,ZDEL,ZREL,ZMAX,ZAV,ZDEV,ZAVR,ZDEVR,SZXY,R)

*     Generate filenames if keyboard option was selected.

      IF (FILKEY .EQ. 'K') THEN

*       Get date and generate filenames.

        WRITE (*,'( )')
        WRITE (*,'(1X,A\)') 'Enter date (mmdd) : '
        READ (*,*) DAT
        WRITE (*,'( )')

        WRITE (*,'(1X,A\)') 'Enter test number (#) : '
        READ (*,*) TN
        WRITE (*,'( )')

        WRITE (FNAMI,'(A1,I1,I4.4,A4)') 'C',TN,DAT, FEXT
        WRITE (FNAME,'(A1,I1,I4.4,A4)') 'C',TN,DAT,FEXT2
        WRITE (FNAMA,'(A1,I1,I4.4,A4)') 'C',TN,DAT,FEXT3
      ENDIF

*     Save data in a file.

      CALL STORE_ERRDATA ('Z',Z,FNAME,M,N,DETERZ,
     +      ZEST,ZFEST,ZDEL,ZREL,ZMAX,ZAV,ZDEV,ZAVR,ZDEVR,SZXY,R)

180   STOP ' '
      END

      FUNCTION ILET (INP,STRING)  ! (ILET.FOR)

      IMPLICIT    INTEGER*2 (I-N)
```

```
      CHARACTER*1  INP
      CHARACTER*(*)    STRING

*     First, convert INP to uppercase if it is lowercase.  If it
*     is uppercase, leave it unchanged.

      IF (ICHAR(INP) .GE. 97 .AND. ICHAR(INP) .LE. 122) THEN
        IHOLD=ICHAR(INP)-32
        INP=CHAR(IHOLD)
      ENDIF

*     Determine the position of INP in STRING, then add one to get
*     ILET which determines label to use in computed GO TO statement.

      IPOS=INDEX(STRING,INP)
      ILET=IPOS+1

      RETURN
      END

      FUNCTION BYTES (M,N)

      IMPLICIT    INTEGER*2 (A-Z)
      INTEGER*4  BYTES

      MP1=M+1
      MP1SQ=(MP1)**2
      MP1SQP1=MP1SQ+1

      BYTES=3*8*N                    ! X, Y, Z
      BYTES=BYTES+2*8*N*MP1SQ              ! XY, XYT
      BYTES=BYTES+8*MP1SQ*MP1SQ            ! XYTXY
      BYTES=BYTES+8*MP1SQ                ! XYTZ
      BYTES=BYTES+8*MP1SQP1*MP1SQP1          ! ZEQS
      BYTES=BYTES+8*MP1SQ                ! A
      BYTES=BYTES+4*8*N              ! ZEST, ZFEST, ZDEL, ZREL
      BYTES=BYTES+8*MP1              ! C in F
      BYTES=BYTES+3*2*N              ! IROW,JCOL,JORD in SIMUL
      BYTES=BYTES+8*N                    ! Y in SIMUL

      RETURN
      END

      SUBROUTINE DISPLAY_CALDATA (X,Y,Z,N,*)

      IMPLICIT    REAL*8 (A-H,O-Z), INTEGER*2 (I-N)
      REAL*8          X(N), Y(N), Z(N)
```

```
      WRITE (*,'( )')
      WRITE (*,10) 'I','X(I)','Y(I)','Z(I)'
      WRITE (*,10) '-','----','----','----'
10    FORMAT (10X,A1,9X,A4,12X,A4,11X,A4)
      KOUNT=0
      KTST=18
      DO I=1,N
        WRITE (*,20) I,X(I),Y(I),Z(I)
20      FORMAT (8X,I3,4(F14.5,2X))
        KOUNT=KOUNT+1
        IF (KOUNT .EQ. KTST) THEN
          KOUNT=0
          KTST=20
          IF (N .EQ. I) CYCLE
          WRITE (*,'( )')
          WRITE (*,'(/16X,A,A\)') 'Press Enter for next page',
     +                            ' or (C)ontinue : '
          READ (*,'(A)') INP
          WRITE (*,'( )')
          IF (INP .EQ. 'C' .OR. INP .EQ. 'c') RETURN 1
          WRITE (*,10) 'I','X(I)','Y(I)','Z(I)'
          WRITE (*,10) '-','----','----','----'
        ENDIF
      ENDDO
      IF (KOUNT .LT. KTST) THEN
        DO I=KOUNT-1,KTST
          WRITE (*,'( )')
        ENDDO
      ENDIF

      RETURN
      END

      SUBROUTINE STORE_ERRDATA (LETTER,Z,FNAM,M,N,DETERZ,
     +      ZEST,ZFEST,ZDEL,ZREL,ZMAX,ZAV,ZDEV,ZAVR,ZDEVR,SZXY,R)

      IMPLICIT    REAL*8 (A-H,O-Z), INTEGER*2 (I-N)

      PARAMETER     (NUM=1)
      REAL*8        Z(N),ZEST(N),ZFEST(N),ZDEL(N),ZREL(N)
      CHARACTER*1   LETTER
      CHARACTER*10    FNAM

      OPEN (NUM,FILE=FNAM,STATUS='UNKNOWN')
        WRITE (NUM,'(35X,A/)') FNAM
        WRITE (NUM,'(8X,A,6X,A,8X,A,8X,A,8X,A)')
     +        'M','N','Deter','Std Err','R'
        WRITE (NUM,'(8X,A,6X,A,8X,A,8X,A,8X,A)')
```

```
     +         '-','-','-----','-------','-'
       WRITE (NUM,'(8X,I1,4X,I3,D15.5,2X,D12.5,2X,G12.5)')
     +              M,N,DETERZ,SZXY,R
       WRITE (NUM,'( )')
       WRITE (NUM,'(8X,A,7X,A,7X,A,6X,A,8X,A)')
     +         'Max Err','Avg Err','S.D. Err','Avg %','S.D. %'
       WRITE (NUM,'(8X,A,7X,A,7X,A,6X,A,8X,A)')
     +         '-------','-------','--------','-----','------'
       WRITE (NUM,'(5X,5(G12.5,2X))')
     +            ZMAX,ZAV,ZDEV,ZAVR,ZDEVR
       WRITE (NUM,'( )')
       WRITE (NUM,'(4X,A,5X,A,9X,A,8X,A,10X,A,8X,A)')
     +       'I',LETTER // '-act',LETTER // '-fit',
     +       LETTER // '-func',LETTER // '-diff','Err (%)'
       WRITE (NUM,'(4X,A,5X,A,9X,A,8X,A,10X,A,8X,A)')
     +       '-','-----','-----','------','------','-------'
       WRITE (NUM,'(2X,I3,2X,G12.5,2X,G12.5,2X,
     +           G12.5,2X,G12.5,2X,G12.5)')
     +           (I,Z(I),ZEST(I),ZFEST(I),ZDEL(I),ZREL(I),I=1,N)
       CLOSE (NUM)

       RETURN
       END

       SUBROUTINE COEFF (X,Y,XY,N,M)      ! (COEFF.FOR)

*      Inputs:

*         X  - array containing X
*         Y  - array containing Y
*         N  - # of elements = (# of Q's) * (# of Alphas)
*         M  - order of surface used in fit (most often 3 or 4)

*      Outputs:

*         XY - array containing all possible X * Y products

       IMPLICIT    REAL*8 (A-H,O-Z), INTEGER*2 (I-N)
       REAL*8           X(N),Y(N)
       REAL*8           XY(N,(M+1)**2)

*      Initialization.

       MP1=M+INT2(1)
       MP1SQ=(MP1)**2

       DO K=1,N
```

```
*     Calculate first MP1 elements which have X's and no Y's.

      XY(K,1)=1.0D0
      DO J=2,MP1
        XY(K,J)=X(K)*XY(K,J-1)
      ENDDO

*     Calculate remaining elements which have X's and Y's.

      DO J=MP1+1,MP1SQ
        I=J-MP1
        XY(K,J)=Y(K)*XY(K,I)
      ENDDO

    ENDDO

    RETURN
    END

    SUBROUTINE MATMLT (A,B,C,M,N,P)   ! (MATMLT.FOR)

*   Ref: Carnahan, B., Luther, H.A., Wilkes, J.O., Applied
*        Numerical Methods, Wiley, New York, 1969, pp.210-217.

*   Inputs:

*       A     - first input array
*       B     - second input array
*       M,N,P - #'s of elements in various arrays
*               A (M x N), B (N x P), C (M x P)

*   Outputs:

*       C  - resultant array is product of A and B

*                          1
*       Formula:   Cij = SUM (Aik Bkj)
*                          N

    IMPLICIT    REAL*8 (A-H,O-Z), INTEGER*2 (I-N)
    INTEGER*2  P
    REAL*8             A(M,N),B(N,P),C(M,P)

*   Zero the C array.

    DO I=1,M
      DO J=1,P
        C(I,J)=0.0D0
```

```
      ENDDO
    ENDDO

*   Perform the multiplication.

    DO I=1,M
      DO J=1,P
        DO K=1,N
          C(I,J)=C(I,J)+A(I,K)*B(K,J)
        ENDDO
      ENDDO
    ENDDO

    RETURN
    END

    SUBROUTINE ERRANAL (X,Y,Z,XY,A,N,M,
   +          ZEST,ZFEST,ZDEL,ZREL,ZMAX,ZAV,ZDEV,ZAVR,ZDEVR,SZXY,R)

*   Inputs:

*       X  - array containing X
*       Y  - array containing Y
*       Z  - array containing Z
*       XY - array containing all possible X * Y products
*       A  - array containing fit coeffs A (for Z)
*       N  - # of elements = (# of Q's) * (# of Alphas)
*       M  - order of surface used in fit (most often 3 or 4)

*   Outputs:

*       ZEST  - array containing Z estimated
*               from fit coeffs * X * Y products
*       ZFEST - array containing Z estimated
*               from function subroutines.
*       ZDEL  - array containing differences between Z and ZEST
*       ZREL  - array containing percent errors between Z and ZEST
*       ZMAX  - maximum absolute value of ZDEL array
*       ZAV   - average ZDEL value
*       ZDEV  - standard deviation of ZDEL array.

    IMPLICIT    REAL*8 (A-H,O-Z), INTEGER*2 (I-N)
    REAL*8          X(N),Y(N),Z(N),A((M+1)**2)
    REAL*8          XY(N,(M+1)**2)
    REAL*8          ZEST(N),ZFEST(N),ZDEL(N),ZREL(N)

*   Initialization.
```

```
      MP1=M+INT2(1)
      MP1SQ=(MP1)**2
      E2=0.0D0
      ZM=0.0D0
      ZSUM=0.0D0
      ZRSUM=0.0D0
      ZVARSUM=0.0D0
      ZVARSUMR=0.0D0

*     Calculate various arrays.

      DO K=1,N

        ZFEST(K)=F(X(K),Y(K),A,M) ! Calculate u's from function

        ZEST(K)=0.0D0
        DO J=1,MP1SQ              ! Calculate u's from fit coeffs
          ZEST(K)=ZEST(K)+A(J)*XY(K,J)
        ENDDO

        ZDEL(K)=Z(K)-ZEST(K)      ! Calculate differences
        E2=E2+ZDEL(K)*ZDEL(K)     ! Calculate sum of squared diffs.
        ZM=ZM+Z(K)                ! Calculate avg Z

        IF (Z(K) .EQ. 0.0) THEN ! Don't divide by zero
          ZREL(K)=0.0D0
        ELSE
          ZREL(K)=ZDEL(K)/Z(K)*100.0D0    ! Calculate percents
        ENDIF

        IF (K .EQ. 1) ZMAX=DABS(ZDEL(K))
        ZMAX=DMAX1(DABS(ZDEL(K)),ZMAX)  ! Calculate largest ZDEL value

        ZSUM=ZSUM+DABS(ZDEL(K))
        ZRSUM=ZRSUM+DABS(ZREL(K))

      ENDDO

*     Calculate standard error and mean value of Z(K).

      IF (N .LE. 2) THEN
        SZXY=DSQRT(E2)
      ELSE
        SZXY=DSQRT(E2/DBLE(N-2))
      ENDIF

      ZM=ZM/DBLE(N)
```

```
*    Calculate unbiased std. dev. of Z(I). (N-1 Method)

     SZ=0.0D0
     DO K=1,N
       SZ=SZ+(Z(K)-ZM)**2
     ENDDO

     IF (N .EQ. 1) THEN
       SZ=DSQRT(SZ)
     ELSE
       SZ=DSQRT(SZ/DBLE(N-1))
     ENDIF

*    Calculate the correlation coefficient as R=SQRT(1-SZXY^2/SZ^2).
*    This is given in Ref. 2.

     IF (SZ .LE. 0.0D0) THEN
       WRITE (*,'(16X,A/)') 'Note SZ = 0. Forced R = 1.'
       PAUSE
       R=1.0D0
       RETURN
     ENDIF

     R=DSQRT(1.0D0-SZXY**2/SZ**2)

*    Calculate the average ZDEL and ZREL values.

     ZAV=ZSUM/DBLE(N)          ! Average of ABS(ZDEL)
     ZAVR=ZRSUM/DBLE(N)        ! Average of ABS(ZREL)

*    Calculate the standard deviation of ZDEL and ZREL.

     DO K=1,N
       ZVARSUM=ZVARSUM+(DABS(ZDEL(K))-ZAV)**2
       ZVARSUMR=ZVARSUMR+(DABS(ZREL(K))-ZAVR)**2
     ENDDO
     ZDEV=DSQRT(ZVARSUM/DBLE(N))     ! Std. Dev. of ABS(ZDEL)
     ZDEVR=DSQRT(ZVARSUMR/DBLE(N))       ! Std. Dev. of ABS(ZREL)

     RETURN
     END

     FUNCTION F(X,Y,A,M)   ! (F.FOR)

*    Inputs:

*       X - X value
*       Y - Y value
```

```
*       A - array containing fit coeffs A (for Z)
*       M - order of surface used in fit (most often 3 or 4)

*   Output:

*       F - value of Z

      IMPLICIT    REAL*8 (A-H,O-Z), INTEGER*2 (I-N)
      REAL*8          A((M+1)**2)
      REAL*8          C[ALLOCATABLE](:)

*   Initialization.

      MP1=M+INT2(1)
      MP1SQ=(MP1)**2

      ALLOCATE (C(MP1), STAT=IERR)
      IF (IERR .NE. 0) STOP 'Can't allocate C in F function.'

*   Note: C's (collections of A's and X's) multiply Y's
*   and A's multiply X's.  Calculate first C "coefficient."

      C(MP1)=A(MP1SQ)
      DO K=MP1SQ-1,M*MP1+1,-1
        C(MP1)=C(MP1)*X+A(K)
      ENDDO
      F=C(MP1)

*   Enter double loop multiplying X's and Y's.

      DO J=M,1,-1
        C(J)=A(J*MP1)
        DO K=J*MP1-1,(J-1)*MP1+1,-1
          C(J)=C(J)*X+A(K)
        ENDDO
        F=F*Y+C(J)
      ENDDO

      DEALLOCATE (C, STAT=IERR)
      IF (IERR .NE. 0) STOP 'Can't deallocate C in F function.'

      RETURN
      END

*************************************************************************
*                                                                       *
      SUBROUTINE PRINT2 (N,X,Y,Z,FEXT)
*                                                                       *
```

```
*     David E. Hess                                          *
*     August 17, 1992                                        *
*                                                            *
*     This subroutine stores the input data in a new sequential      *
*     formatted .PRN file for easy access by LOTUS and LSFIT.        *
*                                                            *
*************************************************************************

      IMPLICIT    REAL*8 (A-H,O-Z), INTEGER*2 (I-N)
      PARAMETER     (NUM=2)
      REAL*8        X(N),Y(N),Z(N)
      CHARACTER*4   FEXT
      CHARACTER*12    FILNAM

*     Get name of input file.

10    WRITE (*,'(16X,A,A,A\)')
     +    'Enter name of input file [',FEXT,']: '
      READ (*,'(A)') FILNAM
      WRITE (*,'( )')

*     Concatenate file extension to FILNAM.

      IPD=INDEX(FILNAM,'.')
      IF (IPD .GT. 9) GO TO 10
      IF (IPD .EQ. 0) THEN
        IEND=LEN_TRIM(FILNAM)
        FILNAM(IEND+1:IEND+4)=FEXT
      ENDIF

      OPEN (NUM,FILE=FILNAM,STATUS='UNKNOWN')

*     Write results to file.

      DO I=1,N
        WRITE (NUM,*) X(I),Y(I),Z(I)
      ENDDO

      CLOSE (NUM)
      RETURN
      END

*************************************************************************
*                                                            *
      FUNCTION SIMUL (N,A,X,EPS,INDIC,NRC)
*                                                            *
*     Ref: Carnahan, B., Luther, H.A., Wilkes, J.O., Applied         *
*          Numerical Methods, Wiley, New York, 1969, pp.290-291.     *
```

```
*                                                                     *
*    When INDIC is negative, SIMUL computes the inverse of the N      *
*    by N matrix A in place. When INDIC is zero, SIMUL computes       *
*    the N solutions X(1)...X(N) corresponding to the set of          *
*    linear equations with augmented matrix of coefficients in        *
*    the N by N+1 array A and in addition computes the inverse of     *
*    the coefficient matrix in place as above. If INDIC is            *
*    positive, the set of linear equations is solved but the          *
*    inverse is not computed in place. The Gauss-Jordan complete      *
*    elimination method is employed with the maximum pivot            *
*    strategy. Row and column subscripts of successive pivot          *
*    elements are saved in order in the IROW and JCOL arrays          *
*    respectively. K is the pivot counter, PIVOT the algebraic        *
*    value of the pivot element, MAX is the number of columns in      *
*    A and DETER the determinant of the coefficient matrix. The       *
*    solutions are computed in the (N+1)st column of A and then       *
*    unscrambled and put in proper order in X(1)...X(N) using the     *
*    pivot subscript information available in the IROW and JCOL        *
*    arrays. The sign of the determinant is adjusted, if              *
*    necessary, by determining if an odd or even number of            *
*    pairwise interchanges is required to put the elements of the     *
*    JORD array in ascending sequence where JORD(IROW(I))=JCOL(I).    *
*    If the inverse is required, it is unscrambled in place using     *
*    Y(1)...Y(N) as temporary storage. The value of the deter-        *
*    minant is returned as the value of the function. Should the      *
*    potential pivot of largest magnitude be smaller in magnitude     *
*    than EPS, the matrix is considered to be singular and a true     *
*    zero is returned as the value of the function.                   *
*                                                                     *
***********************************************************************

      IMPLICIT    REAL*8 (A-H,O-Z), INTEGER*2 (I-N)
      INTEGER*2  IROW[ALLOCATABLE](:)
      INTEGER*2  JCOL[ALLOCATABLE](:)
      INTEGER*2  JORD[ALLOCATABLE](:)
      REAL*8           Y[ALLOCATABLE](:)
      REAL*8           A(NRC,NRC),X(N)

*     Set up space for arrays used only in SIMUL.

      ALLOCATE (IROW(N), JCOL(N), JORD(N), Y(N), STAT=IERR)
      IF (IERR .NE. 0) STOP 'Can't allocate arrays in SIMUL.'

*     Initialization.

      MAX=N
      IF (INDIC .GE. 0) MAX=N+1
```

```
*     Begin elimination procedure.

      DETER=1.0D0
      DO 40 K=1,N
       KM1=K-1

*      Search for the pivot element.

       PIVOT=0.0D0
       DO 30 I=1,N
        DO 20 J=1,N

*         Scan IROW and JCOL arrays for invalid pivot subscripts.

          IF (K .EQ. 1) GO TO 10

          DO ISCAN=1,KM1
           DO JSCAN=1,KM1
            IF (I .EQ. IROW(ISCAN)) GO TO 20
            IF (J .EQ. JCOL(JSCAN)) GO TO 20
           ENDDO
          ENDDO

10        IF (DABS(A(I,J)) .GT. DABS(PIVOT)) THEN
           PIVOT=A(I,J)
           IROW(K)=I
           JCOL(K)=J
          ENDIF

20       CONTINUE
30      CONTINUE

*     Ensure that selected pivot is larger than EPS.

      IF (DABS(PIVOT) .LE. EPS) THEN
       SIMUL=0.0D0
       DEALLOCATE (IROW, JCOL, JORD, Y, STAT=IERR)
       IF (IERR .NE. 0) STOP 'Can't deallocate arrays in SIMUL.'
       RETURN
      ENDIF

*     Update the determinant value.

      IROWK=IROW(K)
      JCOLK=JCOL(K)
      DETER=DETER*PIVOT

*     Normalize pivot row elements.
```

```
      DO J=1,MAX
        A(IROWK,J)=A(IROWK,J)/PIVOT
      ENDDO

*     Carry out elimination and develop inverse.

      A(IROWK,JCOLK)=1.0D0/PIVOT

      DO 40 I=1,N
        AIJCK=A(I,JCOLK)
        IF (I .EQ. IROWK) GO TO 40
        A(I,JCOLK)=-AIJCK/PIVOT

        DO J=1,MAX
          IF (J .NE. JCOLK) A(I,J)=A(I,J)-AIJCK*A(IROWK,J)
        ENDDO

40    CONTINUE

*     Order solution values (if any) and create JORD array.

      DO I=1,N
        IROWI=IROW(I)
        JCOLI=JCOL(I)
        JORD(IROWI)=JCOLI
        IF (INDIC .GE. 0) X(JCOLI)=A(IROWI,MAX)
      ENDDO

*     Adjust sign of determinant.

      INTCH=0
      NM1=N-1
      DO I=1,NM1
        IP1=I+1
        DO J=IP1,N
          IF (JORD(J) .GE. JORD(I)) CYCLE
          JTEMP=JORD(J)
          JORD(J)=JORD(I)
          JORD(I)=JTEMP
          INTCH=INTCH+1
        ENDDO
      ENDDO

      IF (INTCH/2*2 .NE. INTCH) DETER=-DETER

*     If INDIC is positive, return with results.

      IF (INDIC .GT. 0) THEN
```

```
      SIMUL=DETER
      DEALLOCATE (IROW, JCOL, JORD, Y, STAT=IERR)
      IF (IERR .NE. 0) STOP 'Can't deallocate arrays in SIMUL.'
      RETURN
    ENDIF

*   If INDIC is negative or zero, unscramble the inverse.
*   ..... First by rows .....

    DO J=1,N

      DO I=1,N
        IROWI=IROW(I)
        JCOLI=JCOL(I)
        Y(JCOLI)=A(IROWI,J)
      ENDDO

      DO I=1,N
        A(I,J)=Y(I)
      ENDDO

    ENDDO

*   ..... then by columns.....

    DO I=1,N

      DO J=1,N
        IROWJ=IROW(J)
        JCOLJ=JCOL(J)
        Y(IROWJ)=A(I,JCOLJ)
      ENDDO

      DO J=1,N
        A(I,J)=Y(J)
      ENDDO

    ENDDO

*   Return for INDIC negative or zero.

    SIMUL=DETER
    DEALLOCATE (IROW, JCOL, JORD, Y, STAT=IERR)
    IF (IERR .NE. 0) STOP 'Can't deallocate arrays in SIMUL.'
    RETURN
    END
```

Appendix I. FORTRAN Program CONCEN.FOR Used to Calculate Time Records of Concentration and Temperature From Digitized Records of Cold-Wire and Aspirated Hot-Film Voltages

```
*     Convert voltage traces into concentration.  (CONCEN.FOR)

*     David E. Hess
*     Fluid Flow Group - Process Measurements Division
*     Chemical Science and Technology Laboratory
*     National Institute of Standards and Technology
*     July 7, 1994

      IMPLICIT    REAL*8 (A-H,O-Z), INTEGER*2 (I-N)
      INTEGER*4   I,N,NMAX
      REAL*8            A [ALLOCATABLE] (:), B(2)
      REAL*8            HF (8192), CW (8192)
      REAL*8            TIME (8192), T (8192), C (8192)
      CHARACTER*1 INP
      CHARACTER*4 FEXT,FEXT2,FEXT3
      CHARACTER*12      COEF1,COEF2,FNAMI,FNAMO

      PARAMETER   (NUMI=1,NUMO=2,NMAX=1000000)
      DATA              FEXT, FEXT2, FEXT3 / '.DAT', '.COE', '.OUT' /

*     Title of routine.

      WRITE (*,'(25(/))')
      WRITE (*,'(10X,A,A)')
     +    'Convert Voltage Traces to Temperature',
     +    ' and Concentration Traces'
      WRITE (*,'(11(/))')

*     Get the order of the fitted surface.

      WRITE (*,'( )')
      WRITE (*,'(16X,A\)') 'Enter order M of fitted surface : '
      READ (*,*) M
      WRITE (*,'( )')
      MP1SQ=(M+1)**2

*     Get the sampling rate.

      WRITE (*,'(16X,A\)') 'Enter data sampling rate (sps) : '
      READ (*,*) SAMPRATE
      WRITE (*,'( )')
      DELT=1.0D0/SAMPRATE
```

```
*     Allocate coefficient array.

      ALLOCATE (A(MP1SQ), STAT=IERR)
      IF (IERR .NE. 0) STOP 'Can't allocate coeff array in MAIN.'

*     Get the surface fit coefficient data file.

5     WRITE (*,'(1X,A,A,A\)')
     +    'Enter name of surface fit coefficient file [',FEXT2,']: '
      READ (*,'(A)') COEF1
      WRITE (*,'( )')

*     Concatenate file extension to COEF1.

      IPD=INDEX(COEF1,'.')
      IF (IPD .GT. 9) GO TO 5
      IF (IPD .EQ. 0) THEN
        IEND=LEN_TRIM(COEF1)
        COEF1(IEND+1:IEND+4)=FEXT2
      ENDIF

*     Get the surface fit coefficient data.

      OPEN (NUMI,FILE=COEF1,STATUS='OLD')
        READ (NUMI,*) (A(I), I=1,MP1SQ)
      CLOSE (NUMI)

*     Get the temperature fit coefficient data file.

6     WRITE (*,'(1X,A,A,A\)')
     +    'Enter name of temperature fit coefficient file [',FEXT2,']: '
      READ (*,'(A)') COEF2
      WRITE (*,'( )')

*     Concatenate file extension to COEF2.

      IPD=INDEX(COEF2,'.')
      IF (IPD .GT. 9) GO TO 6
      IF (IPD .EQ. 0) THEN
        IEND=LEN_TRIM(COEF2)
        COEF2(IEND+1:IEND+4)=FEXT2
      ENDIF

*     Get the temperature fit coefficient data.

      OPEN (NUMI,FILE=COEF2,STATUS='OLD')
        READ (NUMI,*) (B(I), I=1,2)
      CLOSE (NUMI)
```

```
*     Get the input data file.

      WRITE (*,'(1X,A,I7,A)')
     +       'Program will read up to ',NMAX,' points.'
10    WRITE (*,'(1X,A,A,A\)')
     +    'Enter name of input data file [',FEXT,']: '
      READ (*,'(A)') FNAMI
      WRITE (*,'( )')

*     Concatenate file extension to FNAMI.

      IPD=INDEX(FNAMI,'.')
      IF (IPD .GT. 9) GO TO 10
      IF (IPD .EQ. 0) THEN
        IEND=LEN_TRIM(FNAMI)
        FNAMI(IEND+1:IEND+4)=FEXT
      ENDIF

*     Create the other filename.

      IPD=INDEX(FNAMI,'.')
      FNAMO  = FNAMI(:IPD-1) // FEXT3

*     Open the input and output files.

      OPEN (NUMI,FILE=FNAMI,STATUS='OLD')
      OPEN (NUMO,FILE=FNAMO,STATUS='UNKNOWN')

*     Enter # of data points or determine from file.

20    WRITE (*,'(1X,A\)')
     +    '(E)nter # of data points or (R)ead from file : '
      READ (*,'(A)') INP
      WRITE (*,'( )')
      GO TO (20,30,45) ILET(INP,'RE')

*     First determine # of values of X in the ascii file.

30    DO I=1,NMAX
        READ (NUMI,*,END=40) XTST
      ENDDO
40    N=I-1
      REWIND(NUMI)
      WRITE (*,'(/1X,A,I7,A/)')
     +    'Read ',N,' data values from file.'
      GO TO 50

*     Enter the number of data points.
```

```
45  WRITE (*,'(1X,A\)') 'Enter the number of data points : '
    READ (*,*) N
    WRITE (*,'( )')

*   Divide N into sets 8192 REAL*4 values and calculate remainder.

50  IFULL=N/8192
    IPART=N-IFULL*8192

*   Loop over full sets of 8192 data points.

    DO J=1,IFULL

*     Get values of hot-film voltage and
*     cold-wire voltage from file.

      READ  (NUMI,*) (HF(I), CW(I), I=1,8192)

*     Convert cold-wire voltages into temperatures using straight
*     line fit.  Then, use surface fit to get concentrations from
*     temperature and hot-film voltage data.

      DO I=1,8192
        TIME(I)=((J-1)*8192+I-1)*DELT
        T(I)=B(1)+B(2)*CW(I)
        C(I)=F(T(I),HF(I),A,M)
      ENDDO

*     Store the data to the output file.

      WRITE (NUMO,'(3(G17.7,2X))')
     +     (TIME(I), T(I), C(I), I=1,8192)

    ENDDO

*   Now do the remaining partial set of points.

    IF (IPART .NE. 0) THEN

*     Get values of hot-film voltage and
*     cold-wire voltage from file.

      READ  (NUMI,*) (HF(I), CW(I), I=1,IPART)

*     Convert cold-wire voltages into temperatures using straight
*     line fit.  Then, use surface fit to get concentrations from
*     temperature and hot-film voltage data.
```

```
      DO I=1,IPART
        TIME(I)=(IFULL*8192+I-1)*DELT
        T(I)=B(1)+B(2)*CW(I)
        C(I)=F(T(I),HF(I),A,M)
      ENDDO

*     Store the data to the output file.

      WRITE (NUMO,'(3(G17.7,2X))')
     +     (TIME(I), T(I), C(I), I=1,IPART)

    ENDIF

    CLOSE (NUMI)
    CLOSE (NUMO)

*     Deallocate array.

    DEALLOCATE (A, STAT=IERR)
    IF (IERR .NE. 0) STOP 'Can't deallocate coeff array in MAIN.'

    STOP ' '
    END

    FUNCTION ILET (INP,STRING)  ! (ILET.FOR)

    IMPLICIT    INTEGER*2 (I-N)
    CHARACTER*1  INP
    CHARACTER*(*)    STRING

*   First, convert INP to uppercase if it is lowercase.  If it
*   is uppercase, leave it unchanged.

    IF (ICHAR(INP) .GE. 97 .AND. ICHAR(INP) .LE. 122) THEN
      IHOLD=ICHAR(INP)-32
      INP=CHAR(IHOLD)
    ENDIF

*   Determine the position of INP in STRING, then add one to get
*   ILET which determines label to use in computed GO TO statement.

    IPOS=INDEX(STRING,INP)
    ILET=IPOS+1

    RETURN
    END

    FUNCTION F(X,Y,A,M)   ! (F.FOR)
```

```
*    Inputs:

*        X - X value
*        Y - Y value
*        A - array containing fit coeffs A (for Z)
*        M - order of surface used in fit (most often 3 or 4)

*    Output:

*        F - value of Z

     IMPLICIT    REAL*8 (A-H,O-Z), INTEGER*2 (I-N)
     REAL*8           A((M+1)**2)
     REAL*8           C[ALLOCATABLE](:)

*    Initialization.

     MP1=M+INT2(1)
     MP1SQ=(MP1)**2

     ALLOCATE (C(MP1), STAT=IERR)
     IF (IERR .NE. 0) STOP 'Can't allocate C in F function.'

*    Note: C's (collections of A's and X's) multiply Y's
*    and A's multiply X's.  Calculate first C "coefficient".

     C(MP1)=A(MP1SQ)
     DO K=MP1SQ-1,M*MP1+1,-1
       C(MP1)=C(MP1)*X+A(K)
     ENDDO
     F=C(MP1)

*    Enter double loop multiplying X's and Y's.

     DO J=M,1,-1
       C(J)=A(J*MP1)
       DO K=J*MP1-1,(J-1)*MP1+1,-1
         C(J)=C(J)*X+A(K)
       ENDDO
       F=F*Y+C(J)
     ENDDO

     DEALLOCATE (C, STAT=IERR)
     IF (IERR .NE. 0) STOP 'Can't deallocate C in F function.'

     RETURN
     END
```

Appendix J. Components of DIRRACS

IR Source: Cable heater from Watlow, 120 V, 240 W, 1.57 mm diameter, 61 cm long; coiled with elliptical cross section to fit within tube.

Optical Components:

Narrow bandpass filter from Optical Coating Laboratory, Inc. with center wavelength 8.654 μm, half-power points 8.396 and 8.913 μm, peak transmission 86%, 2.54 cm diameter, 1 mm thick. Attached at entrance of conical collector.

Wide-bandpass filter from Optical Coating Laboratory, Inc. with center wavelength 9.191 μm, half power points 7.853 μm and 10.529 μm, peak transmission 95.4%, less than 0.1 % transmission out to 15.75 μm, 2.54 cm diameter, 1 mm thick. Attached at exit of IR transmission tube.

ZnSe window, 2.80 cm diameter, 3.1 mm thick. Attached to IR source housing.

ZnS window, 2.54 cm diameter, 1 mm thick. Attached to entrance of IR transmission tube.

Detector: 5 mm diameter pyroelectric detector/FET Preamp from Molectron (P1-55) made from $LiTaO_3$ with 5 mm diameter. Specifications for two units: Voltage responsivity 27.3 and 29.1 V/W, voltage noise 1.1×10^{-6} and 1.2×10^{-6}, and noise equivalent power 40×10^{-9} and 41×10^{-9} all measured at 15 Hz. Attached to far end of IR collection cone.

Optical Chopper: Chopper with controller from Stanford Research Systems (Model SR 540), 10.2 cm diameter, six slot blade with 2.13 cm aperture (5 slot portion taped over), operated at 500 Hz.

Power Supplies:

15 V DC power supply (low power) for the pyroelectric detectors.

0-50 V, 100 W Sorensen DC power supply for the heater.

Electronics:

100× amplifier (see Figure 50 for schematic).

High bandpass filter operated at 300 Hz (Ithaco 4302 Dual 24 db/Octave filter).

Hardware Components:

15.2 cm long cubical steel chassis box enclosing the chopper, collection cone, detector and electronics.

3.18 cm diameter, 1.6 mm thick, 20 cm long brass tube containing the source, the open area where the agent flows through, and IR transmission section. The end of tube where source is located was machined out to an ID of 3.02 mm and an end cap was silver soldered to the tube.

1 1/4 NPT soldered to the brass tube for connecting to the dry bay and the engine nacelle facilities at Wright Patterson AFB.

1.6 mm diameter flexible stainless steel tubing for N_2 purge line.

14 cm long, 7.5 cm wide, 6.4 thick brass support plate for rigid mounting of brass tube.

lens mounting plates: rings soldered into tube for mounting the ZnSe and ZnS windows; a plastic mounting was used for the wide-bandpass filter.

Appendix K. Infrared Detector Model

```
************************************************************************
*                                                                      *
*    PROGRAM:        INFRARED DETECTOR MODEL                           *
*                       IR.FOR/EXE                                     *
*                                                                      *
*    PROGRAMMER:     RIK JOHNSSON                                      *
*                       SMOKE DYNAMICS RESEARCH GROUP                  *
*                       ROOM B256 BLDG 224 NIST                        *
*                       GAITHERSBURG, MD 20899                         *
*                                                                      *
*    DATE:           5/12/94                                           *
*                                                                      *
*    PROJECT:        HALON REPLACEMENT                                 *
*                                                                      *
*    VARIABLE DEFINITIONS:                                             *
*                                                                      *
*    A( )      -   ABSORBANCE                                          *
*    AC        -   AGENT CONCENTRATION                                 *
*    AF        -   AGENT ABSORBANCE COEFFICIENT                        *
*    AL( ) -   ABSORBANCE WAVELENGTH                                   *
*    ALTMP( )  -   TEMPORARY VARIABLE FOR AL                           *
*    ATMP      -   TEMPORARY VARIABLE FOR A                            *
*    C         -   SPEED OF LIGHT                                      *
*    DENSUM    -   DENOMINATOR INTEGRATED SUM                          *
*    ENDF2     -   LAST RECORD NUMBER OF FILE 2                        *
*    EX        -   EXPONENTIAL TERM                                    *
*    EX1       -   LOWER WAVELENGTH PART OF EXPONENTIAL TERM           *
*    EX2       -   HIGHER WAVELENGTH PART OF EXPONENTIAL TERM          *
*    F( )      -   FILTER TRANSMITTANCE FUNCTION                       *
*    FF        -   FILTER FUNCTION TERM                                *
*    FL( )     -   FILTER TRANSMITTANCE WAVELENGTH                     *
*    H     -   PLANCK'S CONSTANT                                       *
*    I         -   DUMMY VARIABLE                                      *
*    IL        -   INTENSITY TERM                                      *
*    IL1       -   LOWER WAVELENGTH PART OF INTENSITY TERM             *
*    IL2       -   HIGHER WAVELENGTH PART OF INTENSITY TERM            *
*    J         -   DUMMY VARIABLE                                      *
*    KB        -   BOLTZMAN CONSTANT                                   *
*    L         -   DUMMY VARIABLE                                      *
*    M         -   DUMMY VARIABLE                                      *
*    NUMSUM    -   NUMERATOR INTEGRATED SUM                            *
*    PI        -   CONSTANT PI                                         *
*    PL        -   PATH LENGTH                                         *
*    T         -   TEMPERATURE                                         *
```

```
*     TRAT        -     RATIO TRANSMITTED INTENSITY TO BACKGROUND       *
*                                                                        *
**************************************************************************
C
C VARIABLE TYPE DEFINITIONS AND DIMENSIONING OF ARRAYS
C
      CHARACTER FNAME*12,TNAME*12
      REAL C,KB,H,PI,AC,T,PL,AL(2000),A(2000),AF,F(344),FL(344),EX,EX1
     +,EX2,IL,IL1,IL2,FF,NUMSUM,DENSUM,TRAT,ATMP(2000),ALTMP(2000)
      INTEGER I,L,M,ENDF2
C
C VARIABLE INITIALIZATION
C
      ENDF2=0.
      EX1=0.
      EX2=0.
      EX=0.
      IL1=0.
      IL2=0.
      IL=0.
      FF=0.
      F(0)=0.
      M=1
      NUMSUM=0.
      DENSUM=0.
C
C CONSTANT ASSIGNMENTS
C
      C=3.0E+8
      KB=1.38E-23
      H=6.626E-34
      PI=3.1415926
C
C INPUT OF EXPERIMENTAL PARAMETERS
C
C     WRITE(*,105)
C     READ(*,110)FNAME
      WRITE(*,115)
      READ(*,*)AC
      WRITE(*,120)
      READ(*,*)T
C     WRITE(*,125)
C     READ(*,*)PL
C     WRITE(*,130)
C     READ(*,*)AF
C     WRITE(*,132)
C     FNAME='C3.DAT'
C     FNAME='C13.DAT'
```

```
C     FNAME='CF3I.DAT'
      FNAME='FC125MAC.DAT'
C     WRITE(*,101)
C     READ(*,102)TNAME
C     AC=2.
C     T=800.
      PL=0.028
C     AF=94.7
C     AF=56.79
C     AF=98.75
      AF=36.45
C
C READING OF FILTER FUNCTION
C
      WRITE(*,*)'THE FILTER FUNCTION'
      WRITE(*,*)'WAVELENGTH TRANSMITTANCE'
      OPEN (UNIT=1,FILE='FILWIN.15')
10      READ (1,135,END=11)(FL(I),F(I),I=1,344)
11      WRITE(*,*)I
        DO 12, I=1,344
12        FL(I)=FL(I)/1000000.
C       WRITE(*,140)(FL(I),F(I),I=1,344)
      CLOSE (1)
C
C READING OF ABSORBANCE DATA
C
      OPEN (UNIT=2,FILE=FNAME)
      DO 20 J=1,2000
        READ (2,145,END=21)AL(J),A(J)
C
C CONVERSION OF INVERSE CM TO M
C
20      AL(J)=1./(AL(J)+.00000001)/100.
21      WRITE(*,*)
        ENDF2=J-1
        WRITE(*,*)
        WRITE(*,*)ENDF2
      CLOSE (2)
C
C INVERSION OF DATA FOR INCREASING WAVELENGTH
C
      DO 30 I=1,ENDF2
        J=ENDF2-I+1
        ALTMP(J)=AL(I)
30      ATMP(J)=A(I)
      DO 40 I=1,ENDF2
        AL(I)=ALTMP(I)
40      A(I)=ATMP(I)
```

```
      WRITE(*,*)
      WRITE(*,*)'DATA'
      WRITE(*,*)'WAVELENGTH ABSORBANCE'
C     WRITE(*,150)(AL(J),A(J),J=1,ENDF2)
C
C INTEGRATION LOOP
C
      WRITE(*,*)' RECORD    WAVELENGTH      NUMERATOR       DENOMINATO
     +R'
      DO 50 L=1,ENDF2-1
C
C EXPONENTIAL TERM CALCULATION
C
       EX1=EXP(-AC*PL*AF*A(L))
       EX2=EXP(-AC*PL*AF*A(L+1))
       EX=(EX1+EX2)/2.
C
C INTENSITY TERM CALCULATION
C
       IL1=H*C**2./AL(L)**5./(EXP(H*C/AL(L)/KB/T)-1.)
       IL2=H*C**2./AL(L+1)**5./(EXP(H*C/AL(L+1)/KB/T)-1.)
       IL=(IL1+IL2)/2.
       IF(AL(L).GE.FL(M+1))M=M+1
C       IF(FL(M).GE.10./1000000.)THEN
C         F(M)=0.
C         F(M+1)=0.
C       ENDIF
C
C FILTER FUNCTION TERM CALCULATION
C
       FF=(F(M)+F(M+1))/2.
       IF(FL(M).GT.15./1000000.)FF=0.
C
C SUMMING OF NUMERATOR AND DENOMENATOR
C
       NUMSUM=NUMSUM+(EX*IL*FF)*(AL(L+1)-AL(L))
       DENSUM=DENSUM+(IL*FF)*(AL(L+1)-AL(L))
       AL(L)=10**6*AL(L)
C       OPEN(3,FILE=TNAME)
C       WRITE(3,154)AL(L),IL
       R=L-10.*INT(L/10.)
50      IF(R.EQ.0.)WRITE(*,155)L,AL(L),NUMSUM,DENSUM
C     CLOSE (3)
C
C CALCULATION OF RATIO OF TRANSMITTED INTENSITY TO BACKGROUND
C
     TRAT=NUMSUM/DENSUM
     WRITE(*,*)
```

```
      WRITE(*,160)TRAT
101   FORMAT(/'INPUT THE BLACKBODY FILE NAME AS filename.ext',1X)
102   FORMAT(A12)
105   FORMAT(/'INPUT THE DATA FILE NAME AS filename.ext',1X)
110   FORMAT(A12)
115   FORMAT(/'INPUT THE AGENT CONCENTRATION IN moles/m^3',1X)
120   FORMAT(/'INPUT THE TEMPERATURE IN K',1X)
125   FORMAT(/'INPUT THE PATH LENGTH IN m',1X)
130   FORMAT(/'INPUT THE ABSORBANCE COEFFICIENT IN m^2/mole',1X)
132   FORMAT(/'INPUT THE ABSORBANCE DECREASE',1X)
135   FORMAT(F7.4,1X,F7.5)
140   FORMAT(F11.9,4X,F5.3)
145   FORMAT(F7.2,1X,F6.4)
150   FORMAT(E10.4,3X,F6.4)
154   FORMAT(F9.6,2X,E12.7)
155   FORMAT(I4,6X,F9.4,1X,F15.5,4X,F15.5)
160   FORMAT(/,'THE RATIO OF THE TRANSMITTED INTENSITY THROUGH THE GAS'
     +,/,'SAMPLE TO THE INTENSITY THROUGH AIR IS',2X,F8.6,1X,'.')
      END
```

Appendix L. DIRRACS Data Reduction Program

```
************************************************************************
*                                                                      *
*   PROGRAM:      DIRRACS DATA REDUCTION PROGRAM                       *
*                 SIG.FOR/EXE                                          *
*                                                                      *
*   PROGRAMMER:   RIK JOHNSSON                                         *
*                 SMOKE DYNAMICS RESEARCH GROUP                        *
*                 ROOM B256 BLDG 224 NIST                              *
*                 GAITHERSBURG, MD 20899                               *
*                                                                      *
*   DATE:         JUNE 1994                                            *
*                                                                      *
*   REVISED:      DR. DAVID HESS, JULY 1994                            *
*                                                                      *
*   PROJECT:      HALON REPLACEMENT                                    *
*                                                                      *
*   VARIABLE DEFINITIONS:                                              *
*                                                                      *
*   BLACK    -    LOGICAL STATE FOR BLACK DETECTOR                     *
*   BLKLOW   -    LOWER VOLTAGE LIMIT FOR BLACK DETECTOR               *
*   BLUE     -    LOGICAL STATE FOR BLUE DETECTOR                      *
*   BLUELOW  -    LOWER VOLTAGE LIMIT FOR BLUE DETECTOR                *
*   BOX      -    DETECTOR IDENTITY                                    *
*   C        -    CONCENTRATION                                        *
*   CHFR     -    CHOPPER FREQUENCY                                    *
*   DBLCYC   -    NUMBER OF HALF CYCLES                                *
*   FEXT     -    INPUT FILE EXTENSION                                 *
*   FEXT2    -    OUTPUT FILE EXTENSION                                *
*   FNAMEI   -    INPUT FILE NAME                                      *
*   FNAMEO   -    OUTPUT FILE NAME                                     *
*   I        -    DO LOOP COUNTER FOR DATA                             *
*   IEND -    LENGTH OF FILENAME BEFORE EXTENSION                     *
*   IPD      -    INDEX OF FILENAME                                    *
*   J        -    CYCLE COUNTER                                        *
*   K    -    HALF-CYCLE COUNTER                                      *
*   LIMIT    -    LOWER VOLTAGE LIMIT OF DETECTOR                      *
*   NMAX     -    MAXIMUM NUMBER OF DATA POINTS ALLOWED                *
*   NOCYC    -    NUMBER OF CYCLES                                     *
*   NUMI     -    INPUT FILE NUMBER                                    *
*   NUMO     -    OUTPUT FILE NUMBER                                   *
*   PKPK     -    DIFFERENCE OF HALF CYCLE MAX & MIN VOLTAGES          *
*   PT       -    CYCLE POINT COUNTER                                  *
*   PTSCYC   -    NUMBER OF POINTS PER CYCLE                           *
*   SMPFR    -    SAMPLING FREQUENCY                                   *
*   TMIN     -    TIME MINIMUM VOLTAGE OCCURS FOR A CYCLE              *
```

```
*     TMAX      -    TIME MAXIMUM VOLTAGE OCCURS FOR A CYCLE          *
*     TOTPTS    -    TOTAL NUMBER OF DATA POINTS                      *
*     TV        -    TIME ASSIGNED TO CYCLE                           *
*     V     -    VOLTAGE FOR SPECIFIC DATA POINT                  *
*     V0        -    PEAK-TO-PEAK VOLTAGE FOR AIR                     *
*     VMAX      -    MAXIMUM VOLTAGE FOR A CYCLE                      *
*     VMIN      -    MINIMUM VOLTAGE FOR A CYCLE                      *
*     VOLD      -    PREVIOUS DATA POINT VOLTAGE VALUE                *
*     VV0       -    NORMALIZED PEAK-TO-PEAK VOLTAGE                  *
*                                                                      *
************************************************************************
C
C VARIABLE TYPE DEFINITIONS AND DIMENSIONING OF ARRAYS
C
      PARAMETER          (SIZE=12000)
      INTEGER            I,J,TOTPTS,DBLCYC
      REAL*4                V,NOCYC,LIMIT
      REAL*4                VMAX [HUGE] (SIZE/2.0) , VMIN [HUGE] (SIZE/2.0)
      REAL*4                PKPK [HUGE] (SIZE) , VV0  [HUGE] (SIZE)
      REAL*4                TMIN [HUGE] (SIZE) , TMAX [HUGE] (SIZE)
      REAL*4                TV   [HUGE] (SIZE) , C    [HUGE] (SIZE)
      REAL*4                PT   [HUGE] (SIZE/10.0)
      LOGICAL*1          BLACK,BLUE
      CHARACTER*1     BOX
      CHARACTER*4     FEXT,FEXT2
      CHARACTER*12       FNAMEI,FNAMEO
C
      PARAMETER          (NUMI=1,NUMO=2,NMAX=1048576)
      PARAMETER          (BLKLOW=0.6000,BLUELOW=0.5000)
      DATA               FEXT, FEXT2 / '.DAT', '.OUT' /
C
C TITLE OF ROUTINE
C
      WRITE (*,'(25(/))')
      WRITE (*,'(24X,A)')
     +  'Infrared Halon Detection Routine'
      WRITE (*,'(12(/))')
C
C GET THE INPUT FILENAME
C
      WRITE (*,'(1X,A,I7,A)')
     +  'Program will read up to ',NMAX,' points.'
10    WRITE (*,'(1X,A,A,A\)')
     +  'Type the input data file name [',FEXT,'] : '
      READ (*,'(A)') FNAMEI
      WRITE (*,'( )')
C
C CONCATENATE FILE EXTENSION TO FNAMEI
```

```
C
      IPD=INDEX(FNAMEI,'.')
      IF (IPD .GT. 8) GO TO 10
      IF (IPD .EQ. 0) THEN
        IEND=LEN_TRIM(FNAMEI)
        FNAMEI(IEND+1:IEND+4)=FEXT
      ENDIF
C
C GET THE OUPUT FILENAME
C
20    WRITE (*,'(1X,A,A,A\)')
     +  'Type the output data file name [',FEXT2,'] : '
      READ (*,'(A)') FNAMEO
      WRITE (*,'( )')
C
C CONCATENATE FILE EXTENSION TO FNAMEO
C
      IPD=INDEX(FNAMEO,'.')
      IF (IPD .GT. 8) GO TO 20
      IF (IPD .EQ. 0) THEN
        IEND=LEN_TRIM(FNAMEO)
        FNAMEO(IEND+1:IEND+4)=FEXT2
      ENDIF
C
C GET NEEDED INPUT PARAMETERS
C
      WRITE (*,'(1X,A\)')
     +  'Enter the chopping frequency (Hz) : '
      READ (*,*) CHFR
      WRITE (*,'( )')
C
      WRITE (*,'(1X,A\)')
     +  'Enter the sampling frequency (Hz) : '
      READ (*,*) SMPFR
      WRITE (*,'( )')
C
      WRITE (*,'(1X,A\)')
     +  'Enter the zero concentration PK-PK voltage (V) : '
      READ (*,*) V0
      WRITE (*,'( )')
C
      WRITE (*,'(1X,A\)')
     +  '(B)lack or B(L)ue detector box : '
      READ (*,'(A)') BOX
      WRITE (*,'( )')
      IF (BOX .EQ. 'b') BOX='B'
      IF (BOX .EQ. 'l') BOX='L'
      IF (BOX .EQ. 'B') THEN
```

```
      BLACK=.TRUE.
      BLUE =.FALSE.
      ENDIF
      IF (BOX .EQ. 'L') THEN
      BLACK=.FALSE.
      BLUE =.TRUE.
      ENDIF
C
C GET THE INPUT DATA
C
      WRITE (*,'(/1X,A/)') 'Counting data points...'
      OPEN (NUMI,FILE=FNAMEI,STATUS='OLD')
      OPEN (NUMO,FILE=FNAMEO,STATUS='UNKNOWN')
      DO I=1,NMAX
        READ (NUMI,*,END=30) XTST
      ENDDO
30    TOTPTS=I-1
      REWIND (NUMI)
      WRITE (*,'(/1X,A,I7,A/)')
     +  'Read ',TOTPTS, ' data values from file.'
C
      PTSCYC=SMPFR/CHFR
      NOCYC=TOTPTS/PTSCYC
C
      J=0
      VMAX(1)=0.
      VMIN(1)=0.
      V=0.
      PT(J)=0
C
C LOOP TO READ VOLTAGE, FIND MAX, MIN PER CYCLE
C
      WRITE(*,'(/1X,A/)')'Finding cycle peak-to-peaks...'
      DO I=0,TOTPTS-1
        VOLD=V
        READ(1,*)V
        PT(J)=PT(J)+1
        IF(V.GT.VMAX(J))THEN
          VMAX(J)=V
          TMAX(J)=I/SMPFR
          ENDIF
        IF(V.LT.VMIN(J))THEN
          VMIN(J)=V
          TMIN(J)=I/SMPFR
          ENDIF
C
C FINDS BEGINNING OF A NEW CYCLE
C
```

```
      IF(V.GT.0..AND.VOLD.LT.0..AND.PT(J).GT.INT(PTSCYC-3.))THEN
        J=J+1
        PT(J)=0
        VMAX(J)=0.
        VMIN(J)=0.
C
C IN CASE OF NO SIGN CHANGE INITIATES NEW CYCLE
C
      ELSEIF(PT(J).GT.INT(PTSCYC))THEN
        TMAX(J)=TMAX(J-1)+PTSCYC/SMPFR
        TMIN(J)=TMIN(J-1)+PTSCYC/SMPFR
        J=J+1
        PT(J)=0
        VMAX(J)=0.
        VMIN(J)=0.
        VOLD=0.
      ELSE
        CONTINUE
      ENDIF
    ENDDO
C
C CALCULATION OF CONCENTRATIONS
C
    WRITE(*,'(/1X,A/)')'Calculating concentrations...'
    DBLCYC=2*(J-1)
C
    DO 23 K=1,DBLCYC-1,2
      L=(K+1)/2
      PKPK(K)=VMAX(L)-VMIN(L)
      VV0(K)=PKPK(K)/V0
      TV(K)=(TMAX(L)+TMIN(L))/2.
C
      IF (BLACK) LIMIT=BLKLOW
      IF (BLUE)  LIMIT=BLUELOW
C
      IF (VV0(K) .LT. LIMIT) THEN
        C(K)=100.0
        GOTO 21
      ENDIF
C
      IF(VV0(K).GT.1.0001)THEN
        C(K)=0.0
        GOTO 21
      ENDIF
C
    IF (BLACK) C(K)=.42531+.13956/(.010587+VV0(K))**.31119
    IF (BLUE)  C(K)=.26614+.16948/(.011903+VV0(K))**.33076
C
```

```
21     CONTINUE
C
       PKPK(K+1)=VMAX(L+1)-VMIN(L)
       VV0(K+1)=PKPK(K+1)/V0
       TV(K+1)=(TMAX(L+1)+TMIN(L))/2.
C
       IF (VV0(K+1) .LT. LIMIT) THEN
         C(K+1)=100.0
         GOTO 22
       ENDIF
C
       IF(VV0(K+1).GT.1.0001)THEN
         C(K)=0.0
         GOTO 22
       ENDIF
C
     IF (BLACK) C(K)=.42531+.13956/(.010587+VV0(K+1))**.31119
     IF (BLUE)  C(K)=.26614+.16948/(.011903+VV0(K+1))**.33076
C
22     CONTINUE
C
C WRITING OUTPUT TO FILE
C
       IF(K.EQ.DBLCYC-1)WRITE(*,'(/1X,A/)')'Saving to file...'
       WRITE(NUMO,140)TV(K),PKPK(K),VV0(K),C(K)
       WRITE(NUMO,140)TV(K+1),PKPK(K+1),VV0(K+1),C(K+1)
C
23    CONTINUE
C
     CLOSE (NUMI)
     CLOSE (NUMO)
C
     WRITE(*,'(/1X,A,1X,A)')'The output is in column form in this order
    +:','TIME  PEAK  V/Vo  CONCENTRATION'
C
101   FORMAT(25(/)1X'TYPE THE DATA INPUT FILE NAME AS filename.ext',1X)
111   FORMAT(A12)
102   FORMAT(/1X'TYPE THE DATA OUTPUT FILE NAME AS filename.ext',1X)
103   FORMAT(/1X'ENTER THE TOTAL NUMBER OF POINTS',1X)
104   FORMAT(/1X'ENTER THE SAMPLING FREQUENCY (Hz)',1X)
105   FORMAT(/1X'ENTER THE CHOPPING FREQUENCY (Hz)',1X)
106   FORMAT(/1X'ENTER THE ZERO CONCENTRATION PK-PK VOLTAGE (V)',1X)
135   FORMAT(F8.6)
140   FORMAT(F8.5,2X,F7.4,1X,F7.4,1X,F9.3)
141   FORMAT(1X' TIME    MIN    MAX    PEAK    V/Vo     CONC')
      END
```

Appendix M. FORTRAN Program SOUND.FOR Used to Calculate Sound Attenutation As a Function of Fire-Fighting Agent Concentration in Air

```
*     Computes absorption coefficient versus  (SOUND.FOR)
*     a user-specified abscissa.

*     David E. Hess
*     Submarine Dynamics Branch - Code 564
*     Ship Dynamics Department, Hydromechanics Directorate
*     David Taylor Model Basin
*     Naval Surface Warfare Center - Carderock
*     May 15, 1995

*     The following variables must be defined in an external ASCII
*     file.  I have provided an example of the file; it has the file
*     extension [.NML] because it is a NAMELIST.  All of these
*     variables are for dry air at 20 °C.  A nice feature of namelists
*     is that the values of variables may be changed without having
*     to recompile the source code.  The name of this first namelist
*     is AIR_PROP.

*     RHO   kg / m^3   density
*     GAMMA      dim'less       ratio of specific heats (Cp / Cv)
*     C   m / s            speed of sound
*     ETA0  Pa - s         dynamic viscosity
*     MW    dim'less       molecular weight of air
*     K   W / m - K        thermal conductivity
*     CP      kJ / kg - K      specific heat at constant pressure (air)

*     A second namelist entitled OTHER_PROP contains quantities which
*     may be used as the abscissa of a graph.  The user selects the
*     chosen abscissa in the code below, then, the quantities NOT
*     chosen as the abscissa are defined with the values in this
*     namelist.

*     F   Hz          acoustic frequency
*     D   m^2 / s          mass diffusivity of agent in air
*     X   dim'less    mole fraction of agent in air

      IMPLICIT     REAL*8 (A-H,O-Z), INTEGER*2 (I-N)

      PARAMETER      (NUMI=1, NUMO=2)

      REAL*8            MW_AGENT, MW_AIR, K
      LOGICAL*1  EXISTS
```

```
      CHARACTER*12     FILNAM

      NAMELIST  /AIR_PROP/ RHO, GAMMA, C, ETA0,
     +                     MW_AIR, K, CP

      NAMELIST  /OTHER_PROP/ F, D, X

      COMMON    /AIR/    RHO, GAMMA, C, ETA0, MW_AIR, K, CP, MW_AGENT

*     Initialization.

      PI=2.0D0*DASIN(1.0D0)

*     Check for existence of namelist file.

      INQUIRE (FILE='PROPS.NML', EXIST=EXISTS)
      IF (.NOT. EXISTS) THEN
        WRITE (*,'( )')
        STOP 'Namelist file PROPS.NML not present in root directory.'
      ENDIF

*     Open the namelist file and read in data.

      OPEN (NUMI, FILE='PROPS.NML')
        READ (NUMI, NML=AIR_PROP, IOSTAT=IERR)
        READ (NUMI, NML=OTHER_PROP, IOSTAT=IERR)
        IF (IERR .NE. 0) THEN
          WRITE (*,'( )')
          STOP 'Error reading the namelist file.'
        ENDIF
      CLOSE (NUMI)

*     Display list of gases.

5     WRITE (*,'(/16X,A)') 'Calculation of Absorption Coefficient'
      WRITE (*,'(/16X,A/)') 'Choose from the following gases : '
      WRITE (*,'(16X,A)')   '          1. CF3I'
      WRITE (*,'(16X,A)')   '          2. HFC-227'
      WRITE (*,'(16X,A)')   '          3. FC-218'
      WRITE (*,'(16X,A)')   '          4. HFC-125'
      WRITE (*,'(16X,A)')   '          5. HALON-1301'
      WRITE (*,'(/16X,A\)') 'Enter choice (1-5) : '
      READ (*,*) IGAS
      WRITE (*,'( )')

*     Initialize MW_AGENT with appropriate number.

      SELECT CASE (IGAS)
```

```
      CASE (1)
      MW_AGENT = 195.91D0          ! CF3I

      CASE (2)
      MW_AGENT = 170.03D0          ! HFC-227

      CASE (3)
      MW_AGENT = 188.02D0          ! FC-218

      CASE (4)
      MW_AGENT = 120.02D0          ! HFC-125

      CASE (5)
      MW_AGENT = 148.91D0          ! HALON-1301

      CASE DEFAULT
      WRITE (*,'(16X,A/)') 'Using HFC-125.'
      MW_AGENT = 120.02D0          ! HFC-125

    END SELECT

*   Select data to plot.

    WRITE (*,'(16X,A/)')  'Choose from the following: '
    WRITE (*,'(16X,A)')   '      1. Alpha views F'
    WRITE (*,'(16X,A)')   '      2. Alpha views D'
    WRITE (*,'(16X,A)')   '      3. Alpha views X'
    WRITE (*,'(16X,A)')   '      4. Single value'
    WRITE (*,'(/16X,A\)') 'Enter choice (1-4) : '
    READ (*,*) IPLOT
    WRITE (*,'( )')

*   Get output filename.

    IF (IPLOT .EQ. 1 .OR. IPLOT .EQ. 2 .OR. IPLOT .EQ. 3) THEN
      WRITE (*,'(16X,A\)') 'Enter output filename: '
      READ (*,'(A)') FILNAM
      WRITE (*,'( )')
      OPEN (NUMO, FILE=FILNAM, STATUS='UNKNOWN')
    ENDIF

*   Perform selected task.

    SELECT CASE (IPLOT)

      CASE (1)    ! Alpha views F

*       Get Fstart, Fstop and Fstep.
```

```
      WRITE (*,'(16X,A\)') 'Enter Fstart, Fstop and Fstep: '
      READ (*,*) FSTART, FSTOP, FSTEP
      WRITE (*,'( )')

*     Calculate alphas for this range of frequencies.

      IMAX=NINT((FSTOP-FSTART)/FSTEP)+1
      F=FSTART-FSTEP
      DO I=1,IMAX
        F=F+FSTEP
        A=ALPHA(F,D,X)
        XNUM = 8.0D0 / 3.0D0 * PI * F * ETA0 / (RHO * C**2)
        WRITE (NUMO,*) F,A,XNUM
      ENDDO
      CLOSE (NUMO)
      STOP ' '

    CASE (2)   ! Alpha views D

*     Get Dstart, Dstop and Dstep.

      WRITE (*,'(16X,A\)') 'Enter Dstart, Dstop and Dstep: '
      READ (*,*) DSTART, DSTOP, DSTEP
      WRITE (*,'( )')

*     Calculate alphas for this range of frequencies.

      IMAX=NINT((DSTOP-DSTART)/DSTEP)+1
      D=DSTART-DSTEP
      XNUM = 8.0D0 / 3.0D0 * PI * F * ETA0 / (RHO * C**2)
      WRITE (NUMO,*) XNUM
      DO I=1,IMAX
        D=D+DSTEP
        A=ALPHA(F,D,X)
        WRITE (NUMO,*) D,A
      ENDDO
      CLOSE (NUMO)
      STOP ' '

    CASE (3)   ! Alpha views X

*     Get Xstart, Xstop and Xstep.

      WRITE (*,'(16X,A\)') 'Enter Xstart, Xstop and Xstep: '
      READ (*,*) XSTART, XSTOP, XSTEP
      WRITE (*,'( )')

*     Calculate alphas for this range of frequencies.
```

```
      IMAX=NINT((XSTOP-XSTART)/XSTEP)+1
      X=XSTART-XSTEP
      XNUM = 8.0D0 / 3.0D0 * PI * F * ETA0 / (RHO * C**2)
      WRITE (NUMO,*) XNUM
      DO I=1,IMAX
        X=X+XSTEP
        A=ALPHA(F,D,X)
        WRITE (NUMO,*) X,A
      ENDDO
      CLOSE (NUMO)
      STOP ' '

    CASE (4)    ! Single value

      A=ALPHA(F,D,X)
      XNUM = 8.0D0 / 3.0D0 * PI * F * ETA0 / (RHO * C**2)
      WRITE (*,'(16X,A,G17.8,A/)') 'Alpha = ', A, ' dB / m.'
      WRITE (*,'(16X,A,G17.8,A/)') 'Xnum  = ', XNUM,'.'
      STOP ' '

    CASE DEFAULT     ! Single value

      A=ALPHA(F,D,X)
      XNUM = 8.0D0 / 3.0D0 * PI * F * ETA0 / (RHO * C**2)
      WRITE (*,'(16X,A,G17.8,A/)') 'Alpha = ', A, ' dB / m.'
      WRITE (*,'(16X,A,G17.8,A/)') 'Xnum  = ', XNUM,'.'
      STOP ' '

  END SELECT

  END

  FUNCTION ALPHA (F, D, X)

  IMPLICIT    REAL*8 (A-H,O-Z), INTEGER*2 (I-N)
  REAL*8          MW_AGENT, MW_AIR, MW_MIX, K, KNEW

  COMMON   /AIR/   RHO, GAMMA, C, ETA0, MW_AIR, K, CP, MW_AGENT

*   Initialization.

  PI = 3.141592653589793D0
  MW_MIX = X * MW_AGENT + (1.0D0-X) * MW_AIR

*   Convert K from (W / m - K) to (kW / m - K) = (kJ / m - s - K)
*   in order to have consistent units with Cp.

  KNEW = K / 1000.0D0
```

```
*     Compute various parts of governing equation.

      SCALE = 2.0D0 * PI**2 * F**2 / C**3
      TERM1 = ETA0 * 4.0D0 / 3.0D0 / RHO
      TERM2 = (GAMMA - 1.0D0) * KNEW / RHO / CP
      TERM3 = D * X * (1.0D0 - X) * GAMMA
     +        * ( (MW_AIR - MW_AGENT) / MW_MIX )**2
      ALPHA = SCALE * (TERM1 + TERM2 + TERM3)

*     Convert alpha from (nepers / m) to (dB / m).

      ALPHA = 8.7 * ALPHA

*     Debug code.

*     WRITE (*,'(16X,A,1P,E17.8)') 'Scale    = ', SCALE
*     WRITE (*,'(16X,A,1P,E17.8)') 'Term1    = ', TERM1
*     WRITE (*,'(16X,A,1P,E17.8)') 'Term2    = ', TERM2
*     WRITE (*,'(16X,A,1P,E17.8/)') 'Term3   = ', TERM3

*     WRITE (*,'(16X,A,1P,E17.8)') 'Rho      = ', RHO
*     WRITE (*,'(16X,A,1P,E17.8)') 'Gamma    = ', GAMMA
*     WRITE (*,'(16X,A,1P,E17.8)') 'C        = ', C
*     WRITE (*,'(16X,A,1P,E17.8)') 'Eta0     = ', ETA0
*     WRITE (*,'(16X,A,1P,E17.8)') 'K        = ', K
*     WRITE (*,'(16X,A,1P,E17.8)') 'Cp       = ', CP
*     WRITE (*,'(16X,A,1P,E17.8)') 'MW_agent = ', MW_AGENT
*     WRITE (*,'(16X,A,1P,E17.8)') 'MW_air   = ', MW_AIR
*     WRITE (*,'(16X,A,1P,E17.8/)') 'MW_mix  = ', MW_MIX

*     WRITE (*,'(16X,A,1P,E17.8)') 'F = ', F
*     WRITE (*,'(16X,A,1P,E17.8)') 'D = ', D
*     WRITE (*,'(16X,A,1P,E17.8)') 'X = ', X
*     WRITE (*,'(16X,A,1P,E17.8/)') 'A = ', ALPHA
*     PAUSE '              Press enter to continue.'

      RETURN
      END
```

12. SELECTION OF A CF_3Br SIMULANT FOR USE IN ENGINE NACELLE CERTIFICATION TESTS

Carole A. Womeldorf and William L. Grosshandler
Building and Fire Research Laboratory

Contents

12.1 Introduction

This section describes the requirements and selection of a simulant of CF_3Br for the purpose of certification testing engine nacelle fire suppression systems. To illustrate the storage, delivery, and distribution requirements of CF_3Br, relevant characteristics of engine nacelle fire suppression systems and certification tests are briefly summarized. An initial screening of over 1300 chemicals based on the boiling point, critical temperature, and molecular weight of CF_3Br is described, and the nine potential candidate simulants that were found are listed. Three final candidates (SF_6, C_2HF_5, and $CHClF_2$) were selected for experimental testing based upon their saturated vapor pressures, Jakob numbers, and the requirements of this application: ozone depletion potential, flammability, corrosiveness, toxicity, stability, and atmospheric lifetime. To evaluate the hydraulic properties of the simulants, as compared to CF_3Br, pressure traces of discharges through a piping system into cooled recovery bottles and to atmosphere are compared with like tests of CF_3Br. To compare the discharge spray distribution of the simulants with CF_3Br, high speed movies of the plumes at the end of the piping system were taken and are described. Results and conclusions from comparisons of the three candidate simulants with CF_3Br are presented and discussed.

12.1.1 Background. The Department of Defense and the Federal Aviation Administration require certification testing of the fire suppression system for each aircraft engine design to ensure that the required concentration of halon 1301 is distributed throughout the nacelle. Historically all halon 1301 systems have been tested by discharging an installed bottle of halon 1301 into the engine nacelle. The concentration of the agent is then measured to determine whether the system passes the certification test. The Montreal Protocol of 1987 increased awareness of the harmful effect of halon 1301 on the environment; consequently national (European Communities Regulation 3093/94, 22 December 1994) and local regulations (e.g., South Coast Air Quality Management District Rule 1418, Section (d)(2)(B), 10 January 1992) are bringing this procedure to an end.

Given the continued need to test engine nacelle fire suppression systems, the United States Navy initiated a search for a simulant of halon 1301 that would have an acceptable (preferably zero) ozone depletion potential (ODP). An effective simulant would need to mimic halon 1301 and could be used during system development or a certification test to evaluate the discharge performance of the fire suppression system. The Building and Fire Research Laboratory of the National Institute of Standards and Technology was contracted to identify and test three possible simulants and make a final recommendation to the Navy for an appropriate simulant. This section describes the work defining the requirements of a simulant, a review of relevant thermophysical properties to identify three candidates, and experimental testing which led to the selection of C_2HF_5 (HFC-125) as a simulant of halon 1301 for certification and development testing.

12.1.2 Engine Nacelle Fire Suppression Systems. Though the details of engine nacelle fire suppression systems vary from aircraft to aircraft, their fundamental configuration is basically the same. The agent is stored in a spherical or cylindrical pressure vessel with a volume as small as 0.7 L or as large as 15.5 L. The N_2 pressurization is in the range of 2.5 MPa to 6.4 MPa at 21 °C. The *percent liquid fill*, which describes the volume of CF_3Br present in liquid phase at room temperature divided by the total volume of the bottle, is usually between 40 % and 75 % and typically 50 % on Navy aircraft. When a bottle is only 40 % filled with liquid there is a sizable weight and space penalty on board an aircraft. At the other extreme, when a bottle is filled to 75 %, less N_2 is available to propel the agent from the bottle and into the nacelle. The fill conditions of the bottle are determined by the size and

geometry of the nacelle and the volume of air flowing through it, as well as the distance the bottle is stored from the nacelle. In practice designers refer to the *fill density* of the storage bottle which is the total mass of the agent divided by the volume of the bottle, rather than the percent liquid fill. The fill density when given in U.S. Customary Units, pounds per cubic foot, is nearly identical to the percent liquid fill because the density of CF_3Br at saturation pressure and room temperature is 97.3 lb/ft^3 (1.56 x 10^3 kg/m^3). If the density is rounded up to 100 lb/ft^3 then the fill density divided by 100 lb/ft^3 gives a ratio very close to the percent liquid fill.

Once the design parameters are selected for a particular engine and nacelle, a fire bottle is filled with the correct mass of CF_3Br and pressurized with the appropriate amount of N_2 to achieve the desired pressure at room temperature. During this process the bottle is agitated to equilibrate the N_2 with the CF_3Br. The charged bottle is then mounted in an aircraft with the discharge head usually pointed downward. This is done to allow the N_2 gas to force the agent out from above when the aircraft is flying level, as is required when the engine nacelle fire protection system is triggered by the pilot.

The agent release mechanism is typically a small explosive device, known as a squib, which ruptures a small closure disk and produces an opening that allows the agent-N_2 mixture to flow through the discharge head and into the tubing. The N_2 that was in solution at the higher storage pressure begins to degas, while the CF_3Br boils. At atmospheric pressure, the boiling point of CF_3Br is -57.8 °C. The detonation of the squib also promotes nucleation in the N_2-saturated agent. This turbulent, highly transient mixture of dense vapor and evaporating liquid travels through usually less than 3 m of pipe, though as much as 24 m, from the storage location to the targeted nacelle. The mixture sprays into the nacelle through tubes, sometimes with supplementary holes, mounted in the nacelle and located to distribute the CF_3Br simultaneously and evenly throughout fire zones in the nacelle.

12.1.3 Suppression System Certification. Based upon years of testing and experience, a system that generates a 6 % by volume concentration of CF_3Br, held for at least 0.5 s during the test procedure, has been found sufficient in practice to extinguish an engine nacelle fire under most conditions (Tedeschi and Leach, 1995). Any redesign of an engine nacelle with a halon fire suppression system requires that tests be run to re-certify that the 6 % level can still be maintained throughout the nacelle for the 0.5 s requirement. Military aircraft are tested according to the Military Specification MIL-E-22285, while the Federal Aviation Administration is responsible for the certifying of commercial aircraft. The FAA test requires that a 6 % concentration be achieved with the bottle cooled to -54 °C (FAA Advisory Circular Number 20-100). For the military certification process, the discharge of the calculated amount of agent must occur in one second or less, timed from the entrance of the agent into the nacelle.

The concentration of agent is usually measured using 12 probes located throughout the nacelle while in flight or with air flow conditions to simulate in-flight conditions. The probes are attached to a halon analyzer, (see Section 11, this publication) which measures the change in concentration of the air-agent mixture. Any change in concentration affects the fluid properties of the mixture and causes a pressure variation that is detected by a strain gauge mounted on a bellows. The strain gauge resistance is calibrated against a known concentration of CF_3Br. The required concentration must be reached at all 12 probes and held for 0.5 s simultaneously for the system to pass the certification test.

During the process of certifying an aircraft, as many as 50 bottles of CF_3Br can be discharged to the atmosphere. The specific number discharged depends on the type of aircraft, the different flight attitudes, velocities, altitudes, and bottle temperatures that the certifying agency requires, as well as the amount of design modification required to achieve a successful certification test. The Environmental Protection Agency has defined the certification process to be a "non-essential" atmospheric discharge

of the very high ozone depletion potential chemical, CF_3Br. Because of the significant amounts of CF_3Br used, its deleterious effect on the environment, and resultant regulations, it is important that any simulants identified for modeling CF_3Br during future certification procedures possess an ODP defined as acceptable by the 1990 amendment to the Clean Air Act with a value of 0.2 or less.

12.1.4 Previous Simulant Work. Previous studies (Moore, 1989; DiNenno *et al.*, 1990; BA^{e}SEMA, 1992) have examined different halocarbons and refrigerants to determine their suitability as CF_3Br simulants. $CHClF_2$ and SF_6 were both tested for use in shipboard room flooding applications as simulants of CF_3Br by the Navy (DiNenno *et al.*, 1989, 1990). This work found that SF_6 outperformed $CHClF_2$. Though $CHClF_2$ was not selected, the Navy tests demonstrated that its pipe flow behavior (i.e., the slope of pressure decline) was similar to that of CF_3Br, although the absolute timing was different. Only BA^{e}SEMA (1992) tested C_2HF_5 as a simulant. BA^{e}SEMA and the British Ministry of Defense were also concerned with a total flooding application and also selected SF_6. For engine nacelle fire suppression systems, the dynamic flow characteristics are more important than the suspension-in-air characteristics. These earlier studies concerned total flooding applications where leakage and suspension-in-air timing, on the order of 30 seconds to 15 minutes, were of primary importance. For the current application in engine nacelles, the time scales are much shorter, on the order of 500 ms, and the dynamic pipeline properties and spray plume characteristics dominate the process.

12.2 Thermophysical Screening of Candidate Simulants

12.2.1 Thermophysical Comparison and Analysis. Given the dynamic phase change, from a liquid saturated with N_2 to a gas detected by a halon analyzer, any simulant should match as closely as possible the thermophysical characteristics of CF_3Br listed in Table 1. In an effort to broaden the scope and focus on essential physical properties, NIST selected explicit criteria for an extensive search. These physical properties were molecular weight, normal boiling point, and critical temperature. The molecular weight was selected as the broadest of screening tools to eliminate those chemical compounds that were less suitable than the two previously tested simulants: SF_6 and $CHClF_2$. A range of ± 65 g/mol about the molecular weight of CF_3Br was selected, based upon the difference between the molecular weights of CF_3Br and $CHClF_2$. The normal boiling point and the critical temperature of CF_3Br were selected as the other two criteria based on their contributions to the phase change process. The acceptable range about both these temperatures was defined as ± 25 °C.

An examination of the halogenated compounds and other refrigerants listed in REFPROP (Gallagher *et al.*, 1993), a database complied by NIST, located three new candidates in addition to the previously tested $CHClF_2$ and C_2HF_5. A second, more general database, DIPPR (Daubert and Danner, 1993) was searched also. This covered 83 different families of chemicals, including all classes of pure hydrocarbons; hydrocarbons containing halogens, nitrogen, sulfur, and/or oxygen; as well as silanes and inorganics. From these two databases only nine chemicals met the screening criteria: $CHClF_2$, C_2ClF_5, C_2HF_5, $C_2H_3F_3$, C_3F_6, C_3OF_6, C_3F_8, ClO_3F, and SF_6. Their properties are summarized in Table 1.

In addition to the candidates' resemblance to CF_3Br, they must also be appropriate for the application, a discharge into an engine nacelle. For broad acceptance a candidate to be discharged into the atmosphere must possess an ozone depletion potential less than 0.2, preferably zero. C_2ClF_5 was removed from consideration because it has an ODP of 0.4. For discharge into the fire zones of a running aircraft engine, it is important that the chemical be non-flammable. $C_2H_3F_3$ is not suitable

Table 1. Thermophysical Properties of CF_3Br and Potential Candidate Simulants

Candidate Simulants Chemical Compounds	Chemical Formulas	Refrigerant Number	Molecular Weight (kg/kmol)	Normal Boiling Point[R,D] (°C)	Critical Temperature[R,D] (°C)
Bromotrifluoromethane	CF_3Br	R13B1	148.9	-57.8	67.1
Chlorodifluoromethane	$CHClF_2$	R22	86.5	-40.9	96.2
Chloropentafluoroethane	C_2ClF_5	R115	154.5	-39.2	79.9
Pentafluoroethane	C_2HF_5	R125	120.0	-48.6	66.2
1,1,1-Trifluoroethane	$C_2H_3F_3$	R143a	84.0	-47.4	73.1
Hexafluoropropene	C_3F_6	R216	150.0	-29.7‡	94.8
Hexafluoroacetone	C_3OF_6	-	166.0	-27.3	83.9
Octafluoropropane	C_3F_8	R218	188.0	-36.8	72.0
Perchloryl Fluoride	ClO_3F	-	102.5	-46.7	95.2
Sulfur Hexafluoride	SF_6	-	146.1	-64.0	45.5

The reliability is better than 5 %, except where noted.

References/Key:
R REFPROP: Gallagher *et al.*, 1993.
D DIPPR: Daubert and Danner, 1985.
‡ Reliability quoted in reference as < 10 % error on a Kelvin scale.

because it has a lower flammability limit of 13 % by volume in air (MSDS, 1994), and as such it could be a fire hazard during testing. In addition, the chemical must not be corrosive, unstable, nor toxic. Both C_3OF_6 and ClO_3F fail on these points because of the ease with which they hydrolyze into highly toxic and corrosive acids: HF and HCl (MSDS, 1994).

The five remaining candidates were evaluated based on saturated vapor pressure, Jakob number, experimental history, and atmospheric lifetime (Refer to Table 2). Saturated vapor pressure is an indicator of the relative pressure reached during a discharge in the pipeline and the force that will expel the chemical in addition to the nitrogen. At 22 °C, both C_3F_6 and C_3F_8 have saturated vapor pressures more than 46 % lower than CF_3Br. As a result, these candidates may not achieve the same pipeline pressures as CF_3Br. At the other extreme, SF_6 has a saturated vapor pressure 50 % greater than CF_3Br. This may result in SF_6 dispensing more quickly than CF_3Br. Of all the five possible candidates, C_2HF_5 has the saturated vapor pressure closest to CF_3Br.

The Jakob number (*Ja*) (Pitts *et al.*, 1994) is the difference in enthalpy of a liquid between the normal boiling point and the ambient temperature (evaluated by the integral of the heat capacity of the liquid over that temperature range), divided by the heat of vaporization at the boiling point:

$$Ja = \frac{\int_{T_{bp}}^{T_{ambient}} C_{p,l}(T)dT}{\Delta H_{vap}(T_{bp})}$$

Table 2. Thermophysical and Environmental Properties of CF_3Br and Potential Candidate Simulants

Chemical Formulas	Vapor Pressure[R,D] (kPa) at 22 °C	Jakob Number[P] at 22 °C	Ozone Depletion Potential[B]	Atmospheric Lifetime[B] (years)	Reasons for Exclusion
CF_3Br	1496	0.51	16	110	*Baseline*
$CHClF_2$	957	0.31	0.05	16	*Selected*
C_2HF_5	1271	0.52	0	41	*Selected*
C_3F_6	603	0.40	0	< 1[†]	Low VP & Low Jakob
C_3F_8	805	0.59	0	10,000	Low VP & High ALT
SF_6	2268	0.66[A]	0	3200	*Selected*

Reliability of values is better than 5 %.

References/Key:
R REFPROP: Gallagher *et al.*, 1993.
P Pitts *et al.*, 1994.
B Braun *et al.*, 1994.
D DIPPR: Daubert and Danner, 1985.
A Jakob Number was calculated using thermodynamic values from AlliedSignal Chemicals.
VP Vapor Pressure
ALT Atmospheric Lifetime. For these chemicals ALT is a predictor of global warming effects.
† Correspondence with Scott Thomas, 3M Specialty Chemicals Division and Robert Huie, NIST.

This dimensionless number is a measure of the fraction of a pure liquid that will flash to vapor when depressurized instantaneously. The *Ja* numbers for these candidates at 22 °C vary from 0.31 for $CHClF_2$ to 0.66 for SF_6, compared to a value of 0.51 for CF_3Br.

Another consideration was the environmental impact of the chemicals based upon their atmospheric lifetime (ALT). Ideally, the selected candidate should have a very short atmospheric lifetime and very low global warming potential (GWP). Global warming gases have been identified by the Environmental Protection Agency as an area of serious concern, although as of yet, chemicals are not regulated based on their GWP. The values in Table 2 show that SF_6 and C_3F_8 have ALTs greater than a millennium. In addition, their S-F and C-F chemical bonds indicate that they will absorb infrared effectively (Ravishankara *et al.*, 1993). The possible advantages of either of these global warming gases as a simulant must be balanced against the possibility of future regulation.

12.2.2 Three Final Candidates. Based on the above thermophysical, application specific, and environmental criteria, C_2HF_5 (also known as HFC-125 or R125), $CHClF_2$ (HCFC-22 or R22), and SF_6 were selected as the three candidate simulants for experimental testing. None of these candidates is flammable, corrosive, toxic, or unstable, and there is sufficient commercial availability of each. $CHClF_2$ has a non-zero ozone depletion potential, at 0.05. The atmospheric lifetime of SF_6 is greater than the 110 years of CF_3Br. Thus, of the three, C_2HF_5 is the most appropriate candidate based on its environmental impact properties: a zero ODP and lower ALT. Because of this and its close thermophysical similarities to CF_3Br, C_2HF_5 was considered the strongest candidate of the three.

12.3 Experimental Testing of Candidate Simulants

Though evaluation of the chemical compounds based upon their thermophysical properties is a strong indicator of their suitability as simulants for CF_3Br in the certification testing process, the relative importance of the thermophysical differences between the candidates and CF_3Br has not been quantified. Accordingly, comparative experiments were performed. NIST performed tests on CF_3Br as a baseline, C_2HF_5, SF_6, and $CHClF_2$, which focused on distinct aspects of the discharge process. An initial round of tests compared dynamic pressures of the compounds to evaluate their behavior inside the fire suppression distribution system. A second set of tests evaluated the discharge characteristics from a simulated fire suppression system through a T-fitting using a high speed movie camera. The width and duration of these plumes are a qualitative indication of how the chemicals will distribute throughout the nacelle relative to CF_3Br. Additional pressure measurements were taken during the spray discharge filming. In the discussion below, the general test methodology and initial conditions will be presented. The pressure traces of the pipeline flow tests and selected prints from the spray tests follow.

12.3.1 Test Methodology. To model an aircraft engine nacelle fire suppression system, these tests used the same basic apparatus described in Section 8.6 (this publication) and earlier work by Cleary *et al.* (1994). Generally it consisted of a fixed cylindrical storage vessel of 4.19 L, charged with a specified mass of CF_3Br and pressurized with N_2 gas. The N_2 gas was slowly bubbled through the agent to pressurize the vessel to 4.41 MPa and to maximize the dissolution of N_2. The vessel was attached to a discharge head and a 3 m long straight piping system, similar in length to a typical Navy aircraft delivery system. The agent release mechanism was a manually engaged, plunger-type solenoid valve. Once the plunger was released, the agent-N_2 mixture traveled through the discharge head, turned 90°, entered a smooth reducing section, into the pipe with a 15.9 mm inner diameter for the entire length. The pressures in the vessel and along the piping were measured by pressure transducers sampling at 1000 Hz. A total of five pressure transducers recorded the pressure decay within the vessel and in the pipeline. Locations are shown at the bottom of Figure 1. The total time of a discharge was no more than 2000 ms.

The first set of tests to compare pipeline behavior used a closed system as in Section 8. The 3 m pipe was terminated into four recovery cylinders in a freezer cooled with dry ice to approximately -57 °C. This temperature, at the pipeline final pressure of about 1 MPa, was sufficient to condense the tested compounds. Two or more shots of compound were discharged, the first with the chemical directly from a supply bottle, the second with chemical condensed and recovered from the freezer cylinders. By recovering and recycling the chemicals less agent was required to run the series of tests. Some minor variation was observed between new agent and recycled agent, as discussed below.

A second set of tests were performed without the recovery tanks attached. These discharges were released through a T-fitting with 7.0 mm diameter outlets to the atmosphere (as shown in Figure 1). The upward plume of each agent was filmed using a 16 mm high speed movie camera at 500 frames per second. The T-fitting used was an actual discharge nozzle provided by Walter Kidde Aerospace, that can be found in some aircraft fire suppression systems. Figure 1 illustrates the location of the pressure transducers and the discharge T-fitting.

12.3.2 Fill Conditions. Previous simulant work for use in shipboard testing for both the Naval Research Laboratory (DiNenno *et al.*, 1989, 1990) and the British Ministry of Defense (BA^{c}SEMA, 1992) matched the moles of the potential simulants with the initial moles of CF_3Br in order to achieve the same concentration by volume in the test chambers. In each test, SF_6 was selected over either

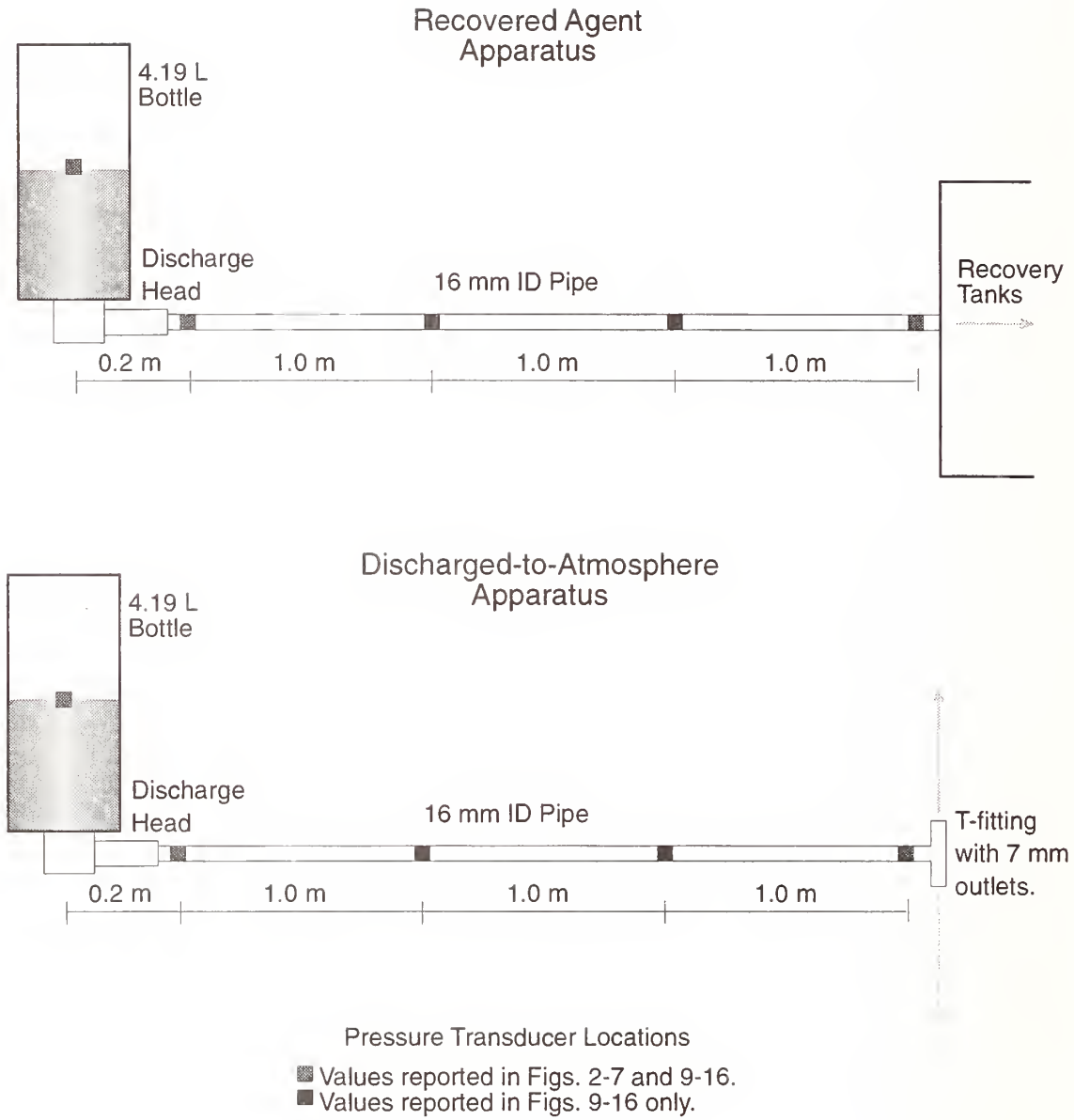

Figure 1. The discharge apparatus with storage vessel and pressure transducers in both configurations, with recovery tanks and with discharge T-fitting.

$CHClF_2$ or C_2HF_5. These tests matched the number of moles in an effort to have 6 % of the simulant equal 6 % of CF_3Br, thereby requiring no rescaling. A significant drawback to this method is that the amount of simulant in liquid volume may be quite different than the corresponding amount of CF_3Br, and as a result there may be either an increase or a decrease in the amount of compressed nitrogen gas available for the discharge process. For example, a four liter bottle with 21 mol (3.2 kg) of CF_3Br at 4.41 MPa has roughly 2 L of liquid and an equal volume of gas. The same bottle filled with the same number of moles of $CHClF_2$ (1.9 kg) will have approximately 20 % less liquid and 20 % more gaseous N_2, due to the difference in liquid molar densities. This increase in gaseous N_2 will significantly impact the discharge pressure and affect the distribution and timing of the discharge independent of the simulant selected.

In these tests the percent liquid fill of CF_3Br was matched rather than the number of moles, thereby conserving the amount of gaseous N_2. Using the chemical's liquid density calculated at saturation pressure and 22 °C, a 51 % liquid fill condition was matched for CF_3Br and each of the different candidates. (The small contribution of the nitrogen in solution and agent in vapor was neglected.) As a result, the volume of agent-N_2 vapor available to force the agent through the pipes was nearly the same for each agent. For each chemical the 51 % liquid fill required a different mass. Specific fill conditions used in both the recovered and the discharged-to-atmosphere tests are described in Table 3.

12.4 Results

12.4.1 Comparison of Pressure Results. The time history of the pressure of each candidate and CF_3Br at different locations in the storage and piping system permits characterization of the complex dynamics that take place during a discharge. These measurements permit quantitative comparison of the magnitude of the pressures as well as the timing of the discharges of the candidates with CF_3Br. Two or more tests of each candidate were performed with the recovery tanks attached. Based on the scatter about the zero points and numerous similar tests with the same apparatus, there is less than 5 % uncertainty in the values presented.

In Figure 2 the pressure traces of both $CHClF_2$ and CF_3Br are plotted. The top pair of lines are the values that were recorded inside the storage vessel. The next pair were recorded at 0.2 m downstream of the discharge head. The lowest pair of traces were taken at the end of the 3.0 m pipe, just before the recovery tanks. (For clarity only these three of the five pressure measurements are shown here.) Figures 3 and 4 show the pressures measured at the same locations for CF_3Br with C_2HF_5 and SF_6, respectively. From an initial inspection, the pressure magnitude and trend of CF_3Br is most nearly matched by C_2HF_5. It is apparent that the close Jakob number and vapor pressures have accurately predicted the pipeline flow similarities of this candidate and CF_3Br.

Table 4 lists the timing and peak pressure values measured at the 3.0 m pressure transducer (PT). These values were calculated by averaging the peaks of each test and their time from discharge. The range is inclusive of pressures and times for all of the peaks of a particular chemical compound. An uncertainty value of about 5 % reflects the human and mechanical variability inherent in the system. The values confirm was what evident by inspection. C_2HF_5 most closely simulates the discharge of CF_3Br. The difference between the peaks is about 2 %. $CHClF_2$ is about 11 % lower and the next closest; while SF_6 is more than 15 % greater.

In addition to these quantitative values there is a qualitative trend that distinguishes the candidates. Inside the storage vessel the initial condition is always 4.41 MPa and the final pressure is approximately 1 MPa, as a result of the back pressure in the recovery tank. The storage vessel

Table 3. Initial Conditions for Both Recovered and Discharged-to-Atmosphere Tests

Properties & Initial Conditions	CF_3Br^R	$SF_6{}^D$	$C_2HF_5{}^R$	$CHClF_2{}^R$
Liquid density‡ (kg/m^3), at saturation pressure, 22 °C	1574	1354	1207	1204
Mass (kg) used to match 51% liquid fill. ±0.02 kg	3.36	2.93	2.58	2.57
Fraction of CF_3Br mass	1.00	0.87	0.77	0.76
Number of Moles‡	22.6	20.1	21.5	29.7
Fraction of CF_3Br moles	1.00	0.89	0.95	1.31

References/Key:
R REFPROP: Gallagher *et al.*, 1993.
D DIPPR: Daubert and Danner, 1985.
‡ Estimated error is less than 1 %.

pressure traces for $CHClF_2$, C_2HF_5, and CF_3Br have a noticeable inflection point at about 500 ms. It is not present in the SF_6 curves, though there is a short rough plateau at about 100 ms. From the discussion in Section 8, these inflection points are attributable to the delayed degassing of the N_2 within the storage vessel. Due to the lower solubility of N_2 in SF_6 (Huber, 1994) degassing is much less pronounced and occurs earlier in SF_6. The similarity of C_2HF_5 and $CHClF_2$ with respect to the degassing of N_2 is a subtle but possibly important quality of a good simulant.

For both of the pipeline pressure traces at 0.2 m and 3.0 m, there is a steep initial rise in the pressure just after the discharge is initiated. (Refer to Figure 1 for PT locations.) This reflects the swift release of the agent. For the rest of the discharge these curves follow the trend of the vessel pressure trace, at a reduced pressure. The difference between the peaks of these tests and those which were discharged to atmosphere (Table 5) is consistently 0.285 ± 0.013 MPa for each chemical. Consequently the tests with recovery tanks provide reliable predictors of the flow behavior when discharged to atmosphere.

In Figures 5 through 7 pressure traces recorded during the discharges through the T-fitting to atmosphere are plotted. Again each candidate is plotted with CF_3Br for the same three PT locations. Qualitatively, both sets of tests show the same general results. Even the difference in the peaks at the 3.0 m PT is the same, though there is an offset to the tests in which the agent was recovered such that the peaks are about 0.3 MPa higher. Table 5 lists the peak values of the 3.0 m PT of the discharges that were released through the T-fitting to atmosphere. Only one of each of these tests was conducted. Figure 8 is a bar chart of the values tabulated in Tables 4 and 5. The similarity between CF_3Br and C_2HF_5 for both sets of tests is clearly greater than for any of the other candidates. Additionally the differences among SF_6, $CHClF_2$, and CF_3Br are much larger than the error.

Additional tests and the remaining pressure transducer values are plotted in Figures 9 through 13 for both the recovered tests and those discharged to atmosphere. Figure 9 shows the same run of CF_3Br plotted in Figure 2 as well as the run that came before it with the agent directly from the supply bottle. The difference between the two curves is only distinguishable between 500 and 700 ms, and at that point it is less than 0.1 MPa. In Figure 10 three curves from $CHClF_2$ are plotted, one with new agent and two with agent that was recycled. A small amount of variation can be seen toward the end of the test near the end of the discharge at about 900 ms. Three tests of C_2HF_5 are plotted in Figure 11. Here the difference between new and once recycled is more noticeable. This inflection

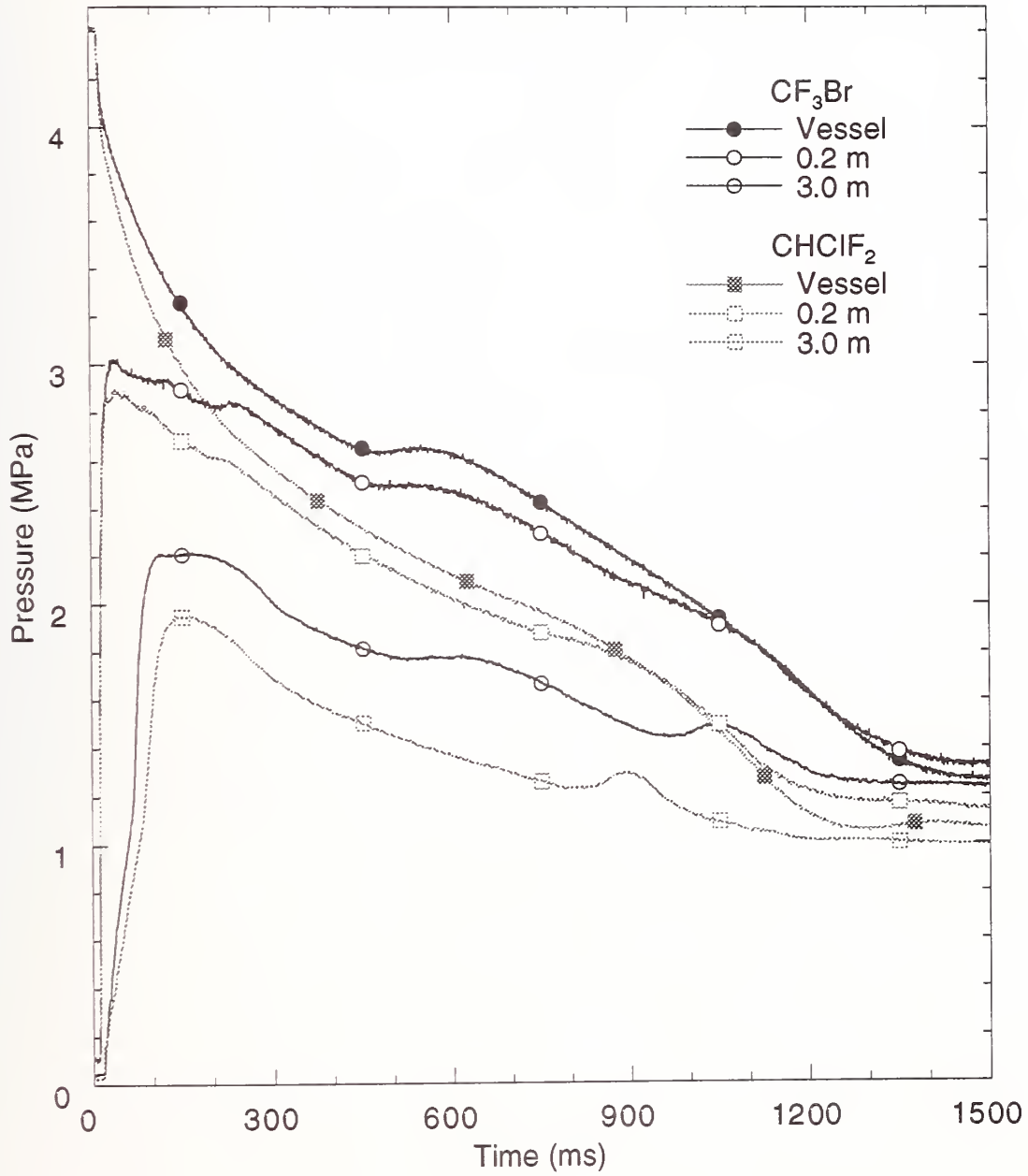

Figure 2. Pressure traces measured in the storage vessel (filled symbols), and at the 0.2 m and 3.0 m pressure transducers for recovered discharges of recycled $CHClF_2$ and CF_3Br.

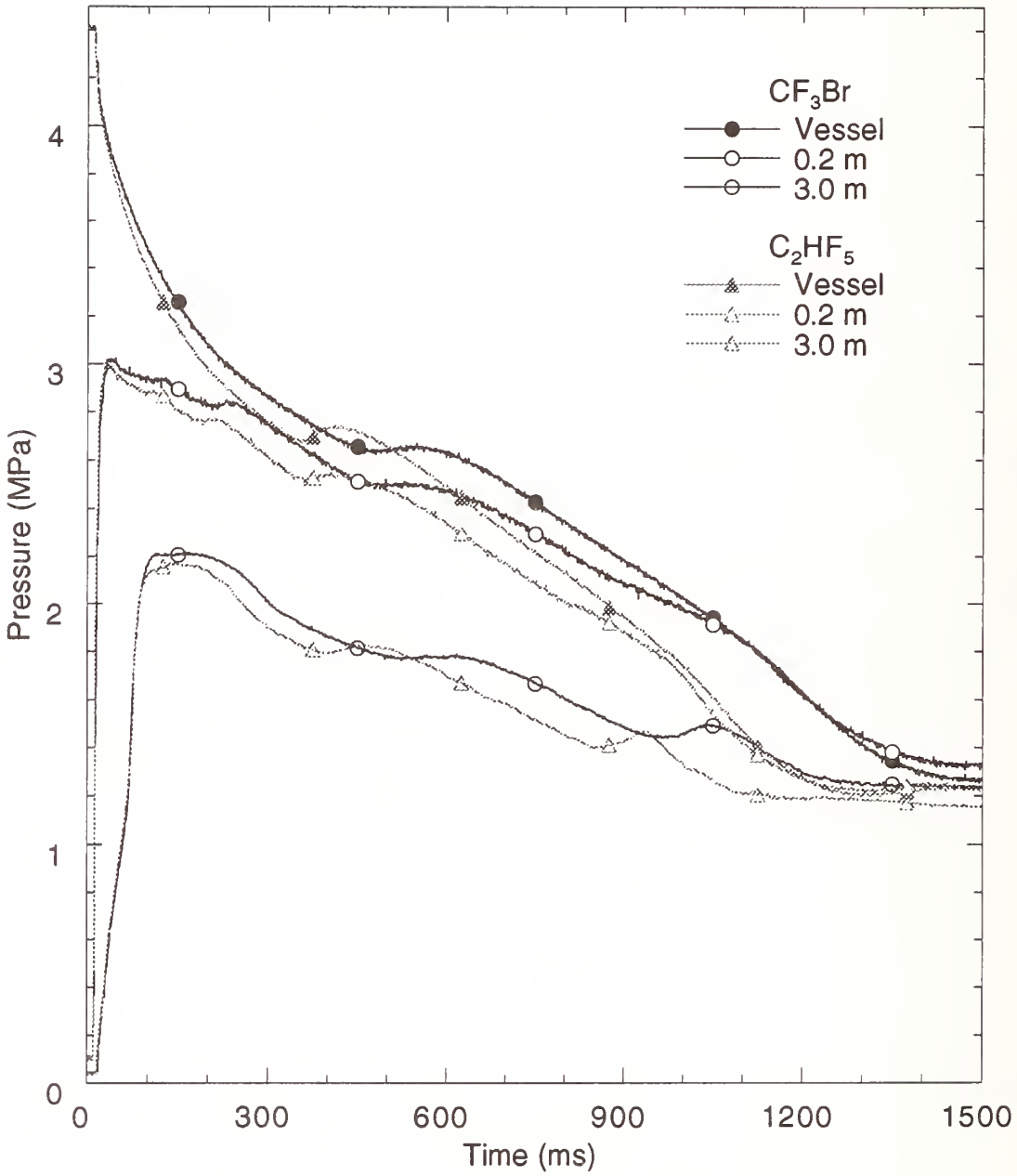

Figure 3. Pressure traces measured in the storage vessel (filled symbols), and at the 0.2 m and 3.0 m pressure transducers for recovered discharges of recycled C_2HF_5 and CF_3Br.

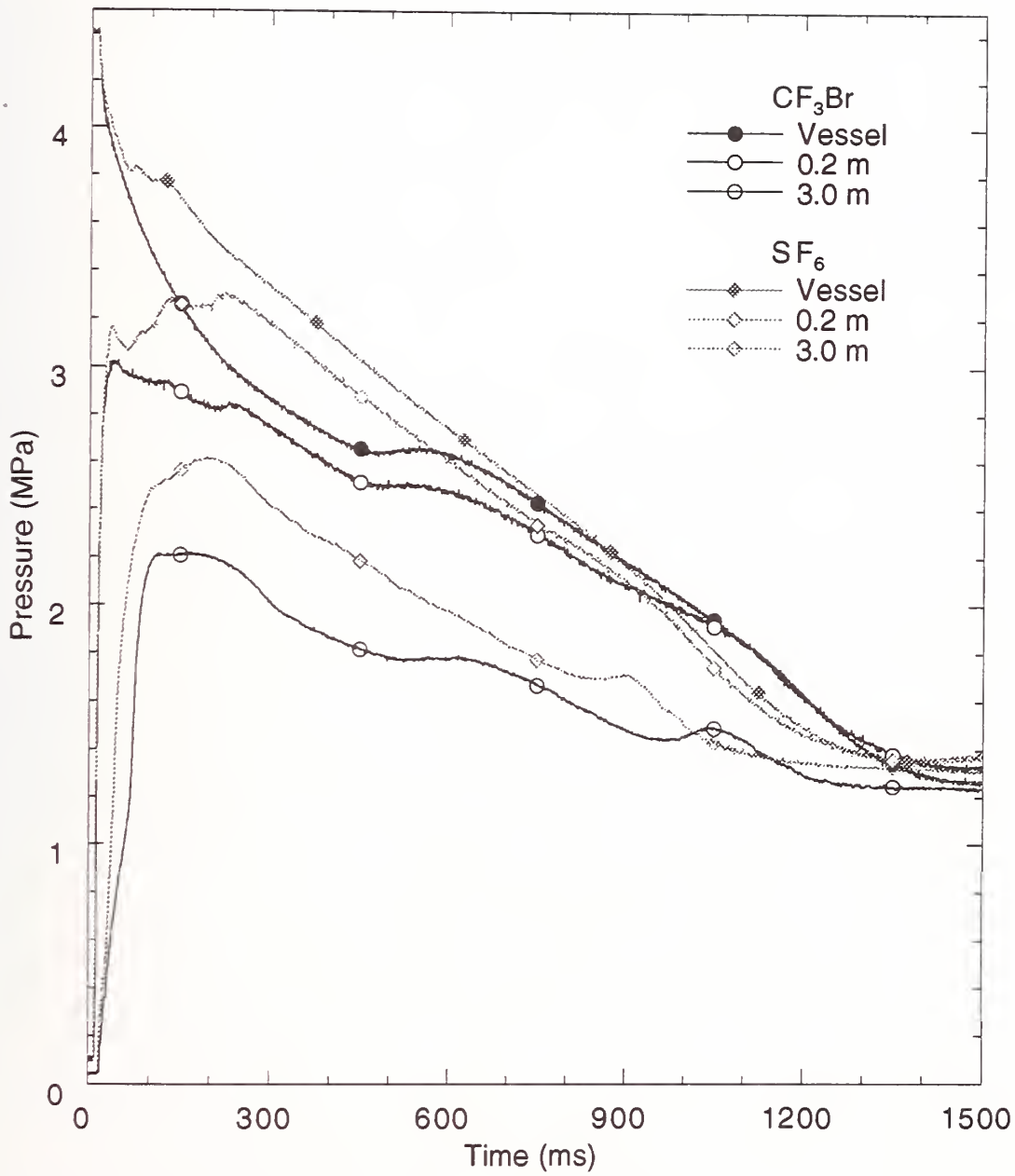

Figure 4. Pressure traces measured in the storage vessel (filled symbols), and at the 0.2 m and 3.0 m pressure transducers for recovered discharges of recycled SF_6 and CF_3Br.

Table 4. Peak Values of 3 m Pressure Transducer for All Tests with Recovery Tanks Attached

Chemical Formula	Peak values (MPa)	Scatter of pressure values (MPa)	Time from release (ms)	Scatter in peak timing (ms)	Number of tests	Subset of tests which were recycled
CF_3Br	2.21	±0.01	135	±20	2	1
$CHClF_2$	1.96	±0.02	145	±5	3	2
C_2HF_5	2.16	±0.03	140	±10	5	3
SF_6	2.61	±0.01	180	±5	2	1

point occurs during the dense vapor phase of the flow and may represent a variation in saturation condition with N_2 gas; however it is clear from the peak values from all of the pipeline pressure transducers and the close timing of the final drop off at 900 ms that the differences among chemicals recycled a different number of times has not affected the overall characteristics of this discharge. Figure 12 contains two curves of SF_6, one the first time it was used and the other after it was recycled once. There is no detectable difference between the recycled and initial run. (Note that the pressure transducers at 1.0 m and 2.0 m were not reading the peak pressures properly during the SF_6 discharge.)

Figures 13 through 16 contain pressure plots of all of the tests with discharges to atmosphere. The chemical used in every one of these tests was recycled once before. As it was shown in the tests where the chemical was recovered, there is little difference between tests run with fresh or recycled agent. Figure 13 shows the details of the CF_3Br discharge-to-atmosphere baseline test. The pressure transducer at 1.0 m did not work properly during this test. $CHClF_2$ results are plotted in Figure 14. All transducers appear to have operated properly. Traces from the tests with C_2HF_5 are plotted in Figure 15 and no problems were observed with the pressure transducers during these tests. In Figure 16, SF_6 results are plotted. The same plateau was reached with the pressure transducers located at 1.0 and 2.0 m during these tests, as was seen during the tests with the recovered chemical.

12.4.2 Spray Discharge Results. The second part of the experiment was designed to evaluate and compare the spray characteristics of CF_3Br and the simulants. In this part of the comparison the upward outlet of the T-fitting was filmed for each chemical using a high speed movie camera. Prints of frames taken at 200 ms and 900 ms after the plume began exiting the T-fitting are shown in Figures 17 and 18. Figure 17 represents the discharge during its fully developed phase, just after the peak value was measured at the 3.0 m pressure transducer. Figure 18 shows the discharge near its end.

At 200 ms (Figure 17) the sprays of C_2HF_5 and SF_6 have nearly the same appearance as that of CF_3Br, with C_2HF_5 slightly wider and SF_6 somewhat narrower. The spray discharge of $CHClF_2$ is significantly wider than the CF_3Br discharge. If one recalls the values of the Jakob number for each of these chemicals (*Ja* equals 0.51 for CF_3Br, 0.66 for SF_6, 0.52 for C_2HF_5, and 0.31 for $CHClF_2$) the wider spread of $CHClF_2$ and the narrower spread of SF_6 appears counter-intuitive. A reasonable explanation is that the chemicals with the higher *Ja* are flashing primarily inside the piping. The $CHClF_2$, on the other hand, does not possess the internal energy to flash in the confined environment

Table 5. Peak Values of 3.0 m Pressure Transducer for All Tests Discharged Through T-fitting to Atmosphere

Chemical Formulas	Peak values (MPa)	Time from release (ms)	Number of tests	Number of times recycled
CF_3Br	1.94	109	1	1
$CHClF_2$	1.66	129	1	1
C_2HF_5	1.87	115	1	1
SF_6	2.33	100	1	1

and elevated pressures of the pipe. $CHClF_2$ flashes fully only when it is exposed to atmospheric pressure at the exit of the pipe.

At 900 ms (Figure 18) it is evident that the stronger flashing of SF_6 has either emptied the bottle faster, or it has gasified the agent more rapidly so that it is no longer visible exiting the T-fitting. In either case, the dense vapor cloud of CF_3Br is poorly represented by the SF_6 at this time. The $CHClF_2$ still has a fairly large cloud, but its more conical shape indicates a weaker jet than that of either the CF_3Br or the C_2HF_5. Finally, the jet from the C_2HF_5, though smaller than the CF_3Br, best represents the flashing spray characteristics of the CF_3Br at 900 ms as well as 200 ms.

12.5 Conclusion

The results for this model fire suppression system are conclusive. C_2HF_5 filled to 77 % of the mass of CF_3Br provides an excellent simulant for development and certification purposes. $CHClF_2$ and SF_6 both have similarities, but are inappropriate for reasons brought out by this testing. SF_6 reaches significantly higher pressures in the pipeline, its degassing behavior is unique in these tests, and from the observable spray plumes, it empties or vaporizes too quickly. $CHClF_2$ has a significantly reduced pressure in the pipelines, and though it does have a similar degassing inflection point, the broader spreading of its spray could lead to different distribution when directed into a nacelle.

The similarity between the thermophysical parameters of C_2HF_5 and CF_3Br, particularly the Jakob number, reinforces the conclusion that C_2HF_5 should be an excellent simulant for CF_3Br in different engine nacelle fire suppression systems. Subsequent field testing of C_2HF_5 alongside CF_3Br with a halon analyzer by the Naval Air Warfare Center and Walter Kidde Aerospace (Leach and Homan, 1995), the Boeing Corporation (Kaufmann *et al.*, 1995), and Short Brothers of N. Ireland (Riordan, 1995) has provided additional evidence for the suitability of C_2HF_5 as a simulant in different systems and operating conditions. On February 3, 1995, the U.S. Naval Air Systems Command officially certified an aircraft with C_2HF_5 for the first time. Boeing, at the time of publication, has requested that the Federal Aviation Administration accept C_2HF_5 as simulant for certification purposes on the Rolls Royce 777 engine. The use of C_2HF_5 in sustained total flood applications remains a possible extension of this work.

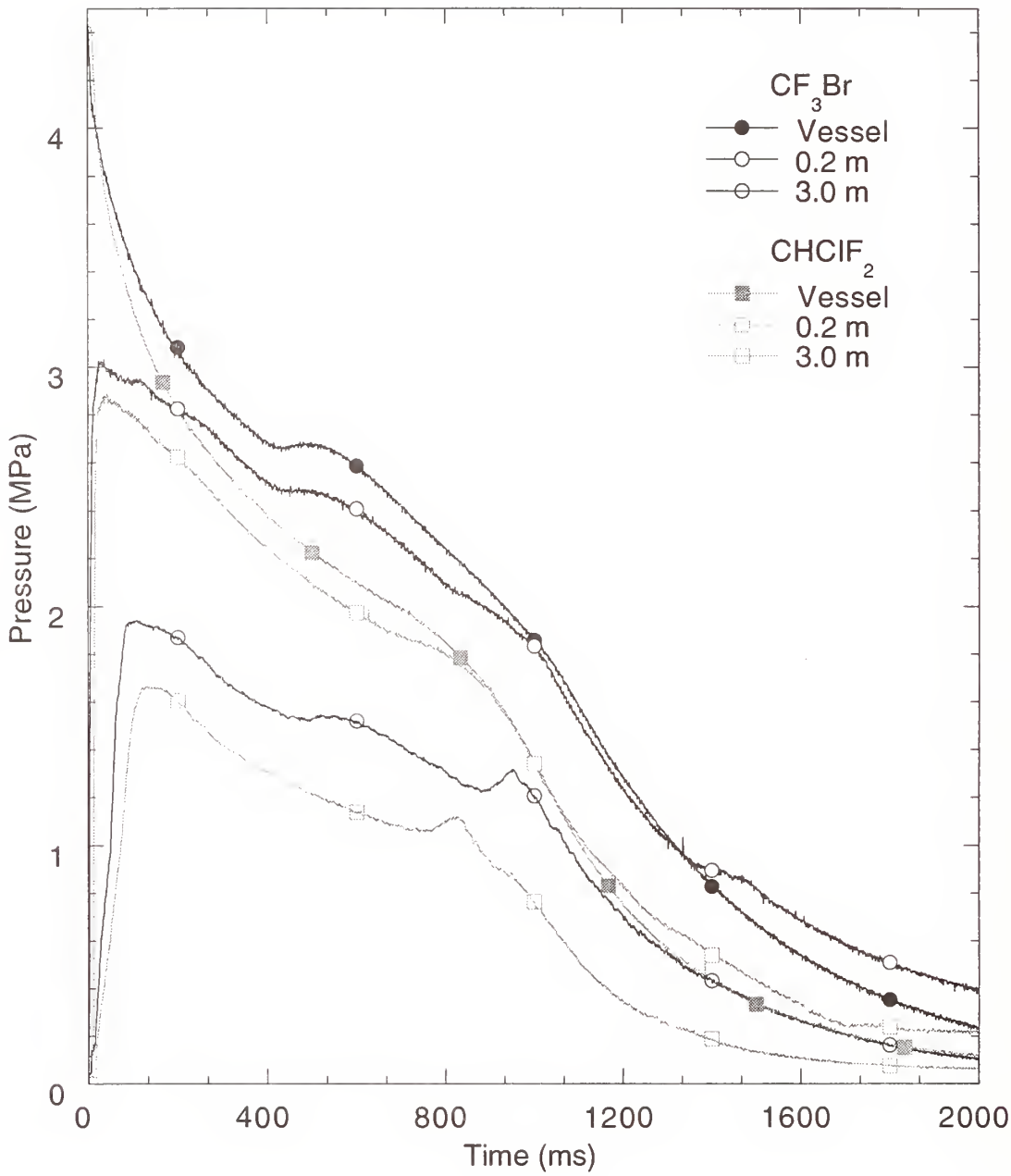

Figure 5. Pressure traces measured in the storage vessel (filled symbols), and at the 0.2 m and 3.0 m pressure transducers for the discharges to atmosphere of recycled $CHClF_2$ and CF_3Br.

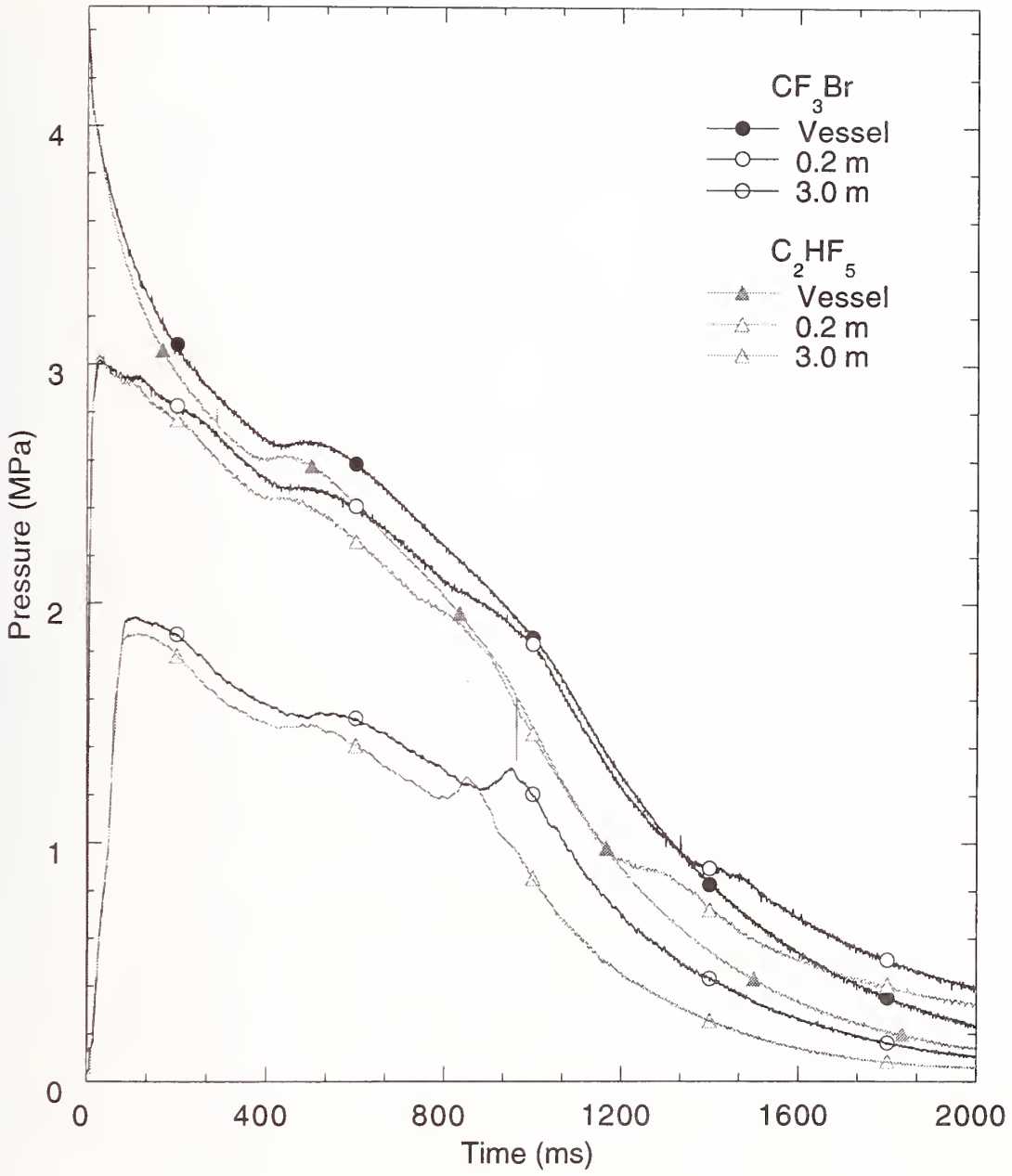

Figure 6. Pressure traces measured in the storage vessel (filled symbols), and at the 0.2 m and 3.0 m pressure transducers for the discharges to atmosphere of recycled C_2HF_5 and CF_3Br.

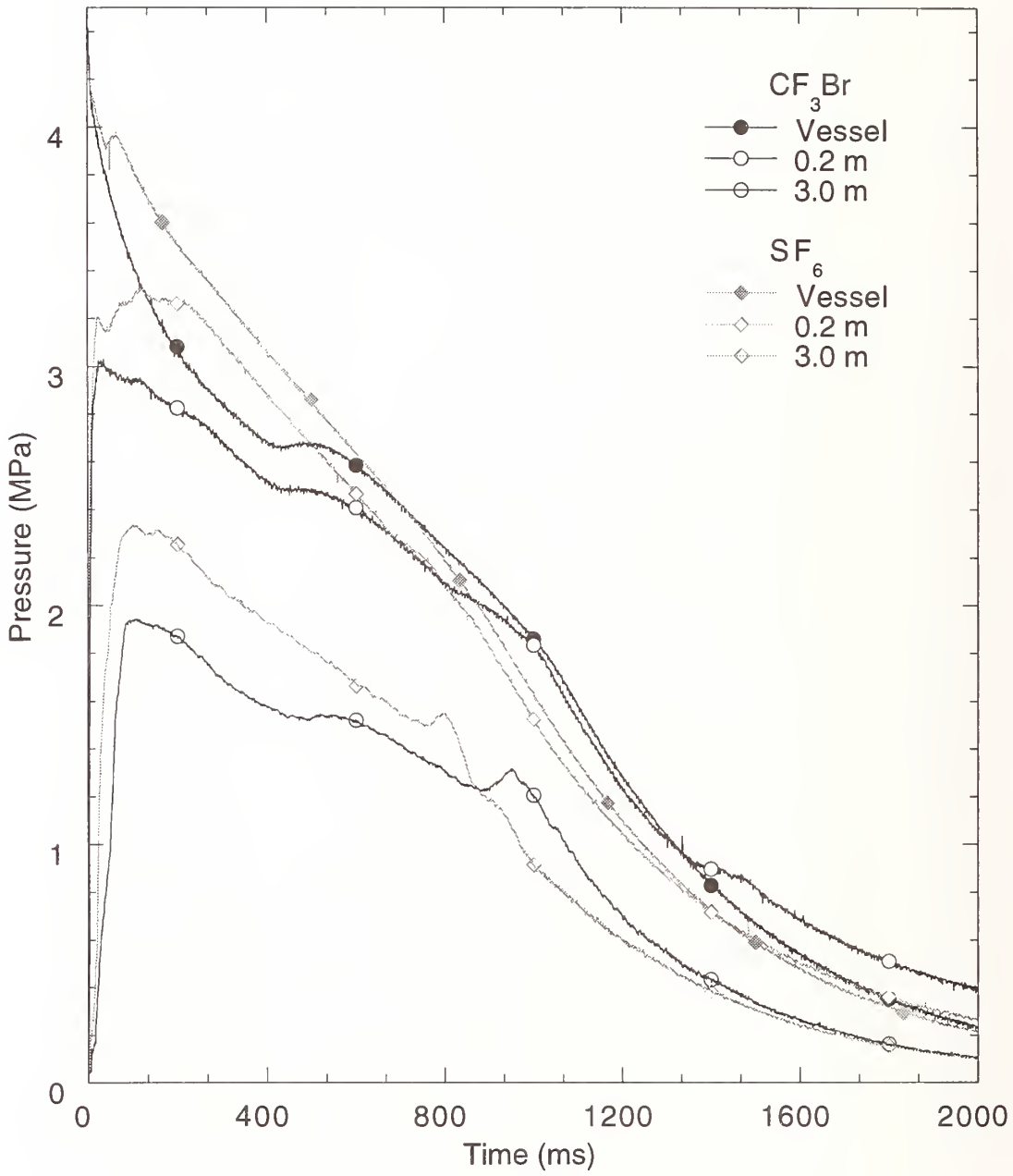

Figure 7. Pressure traces measured in the storage vessel (filled symbols), and at the 0.2 m and 3.0 m pressure transducers for the discharges to atmosphere of recycled SF_6 and CF_3Br.

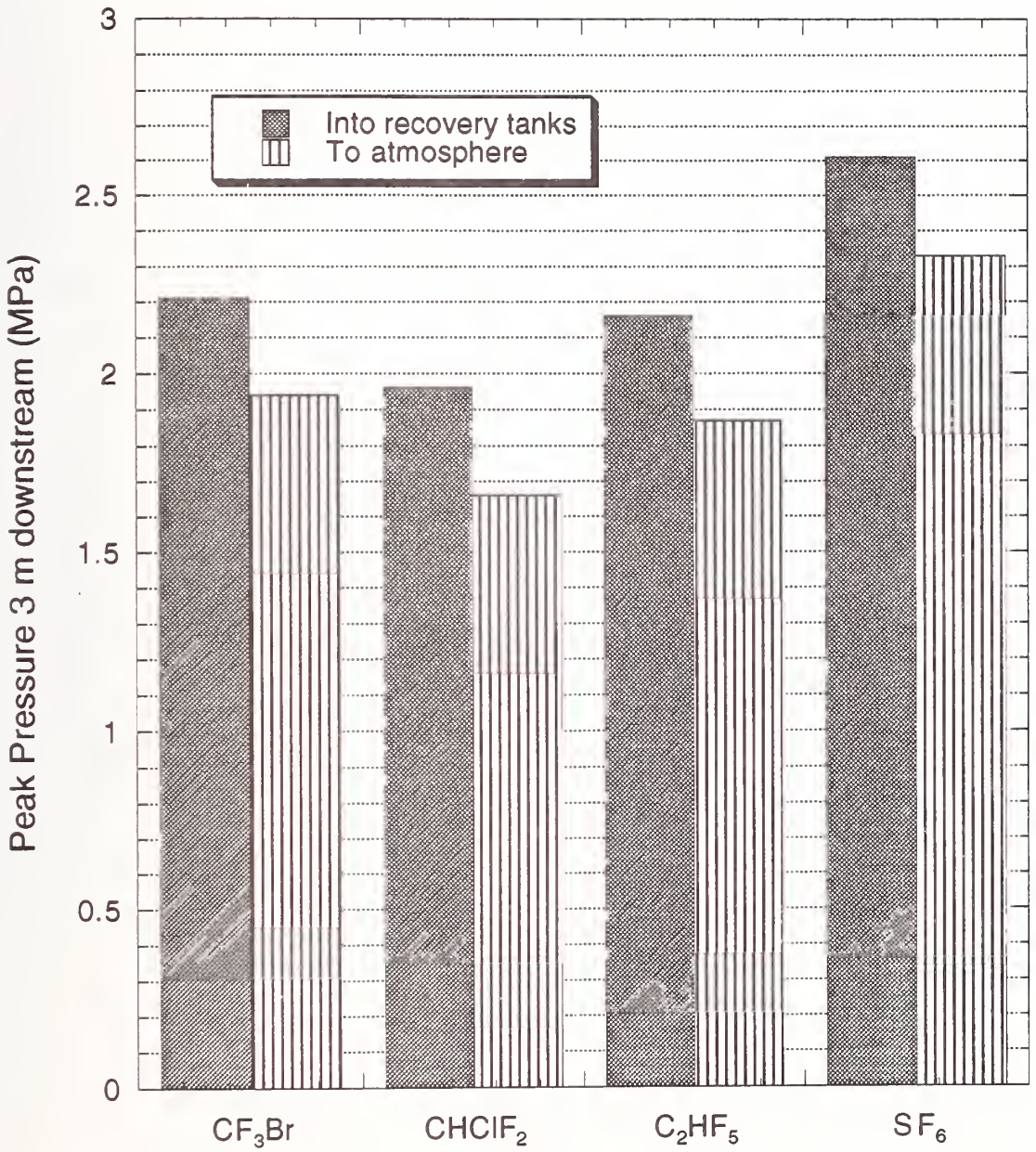

Figure 8. Graph of peak pressures 3.0 m downstream for recovered and discharged-to-atmosphere tests.

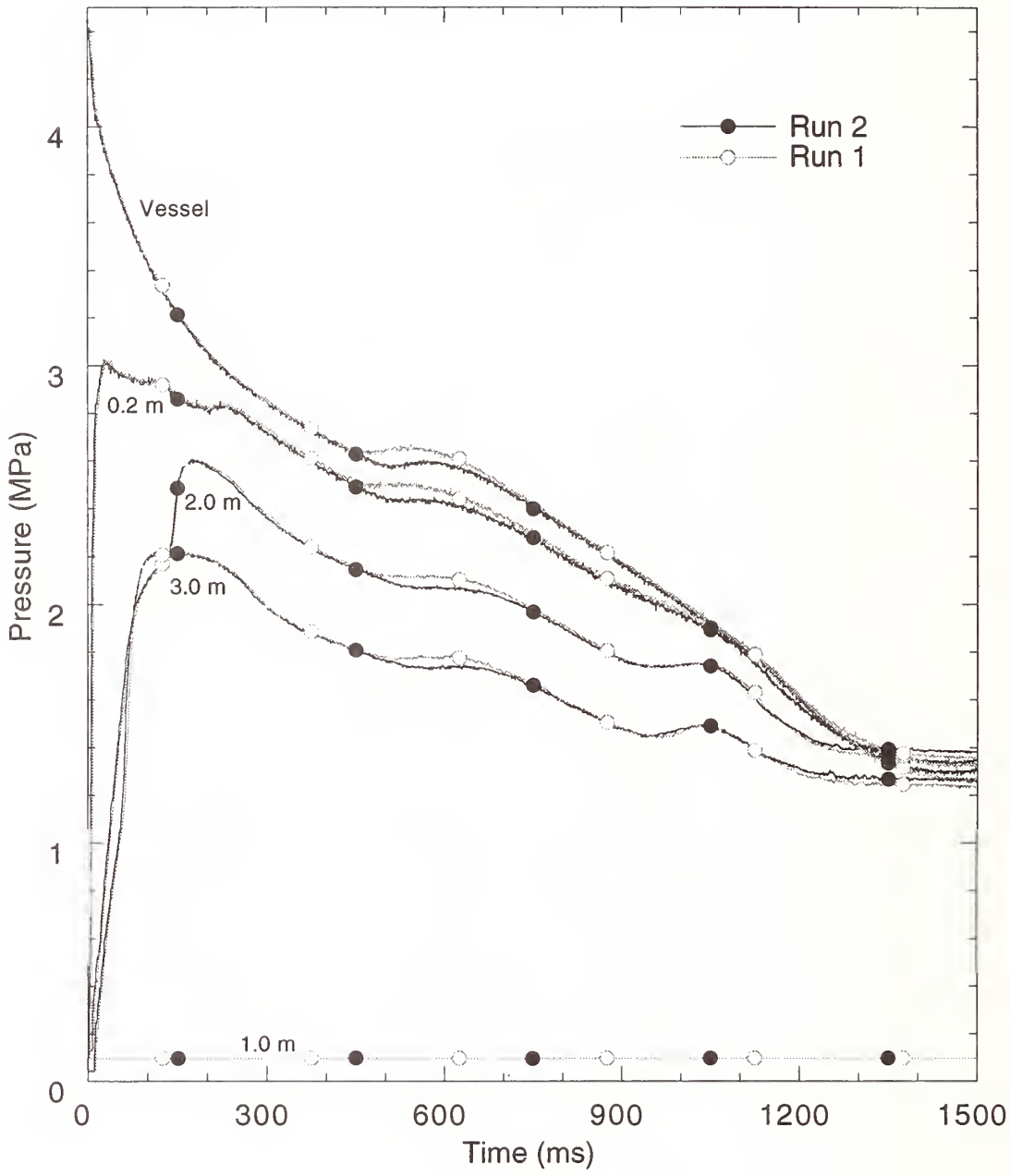

Figure 9. Pressure curves of CF_3Br at five locations using both new (Run 1) and once recycled (Run 2) agent.

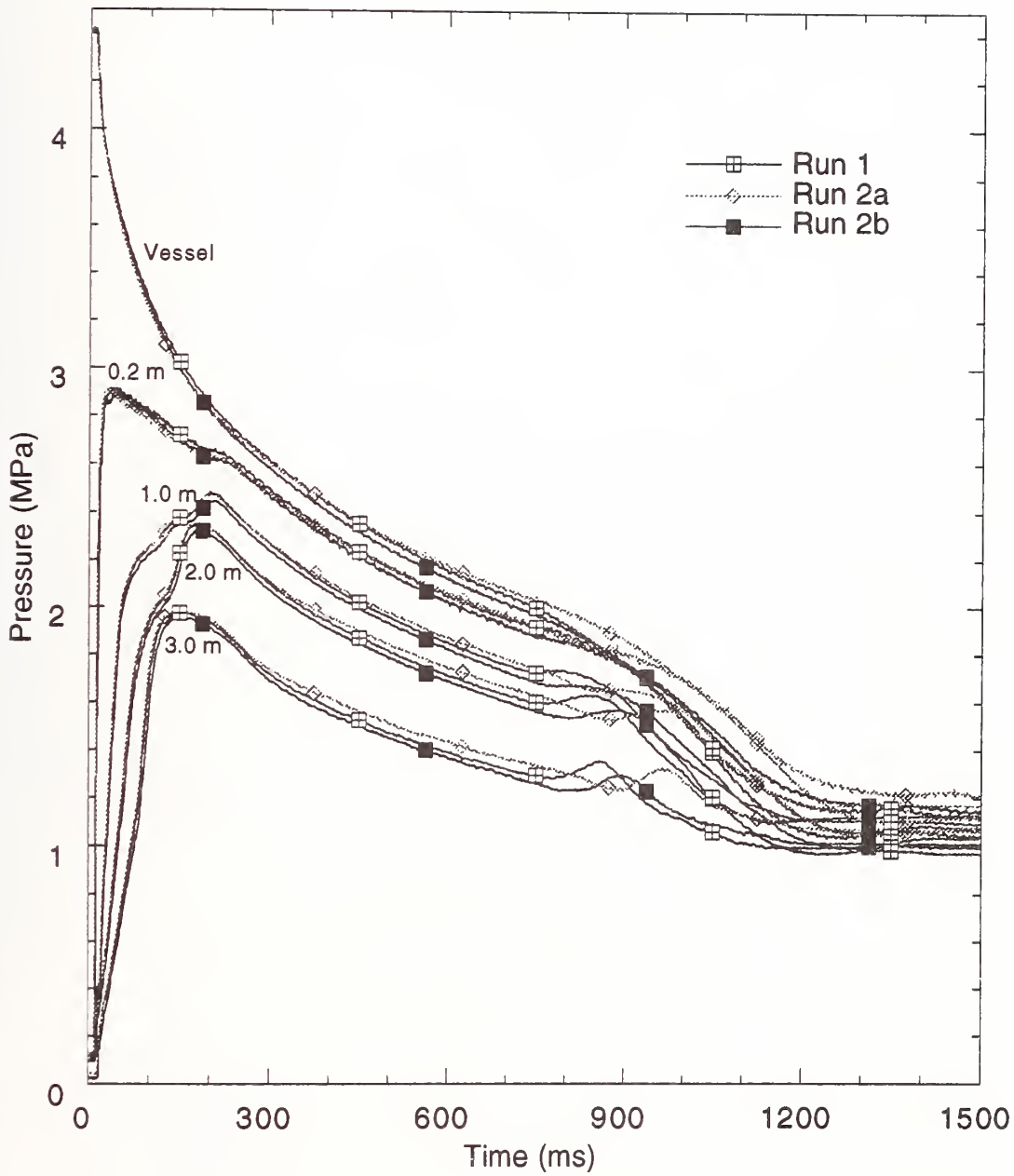

Figure 10. Pressure curves of $CHClF_2$ at five locations using both new (Run 1) and once recycled (Run 2a and 2b) chemical.

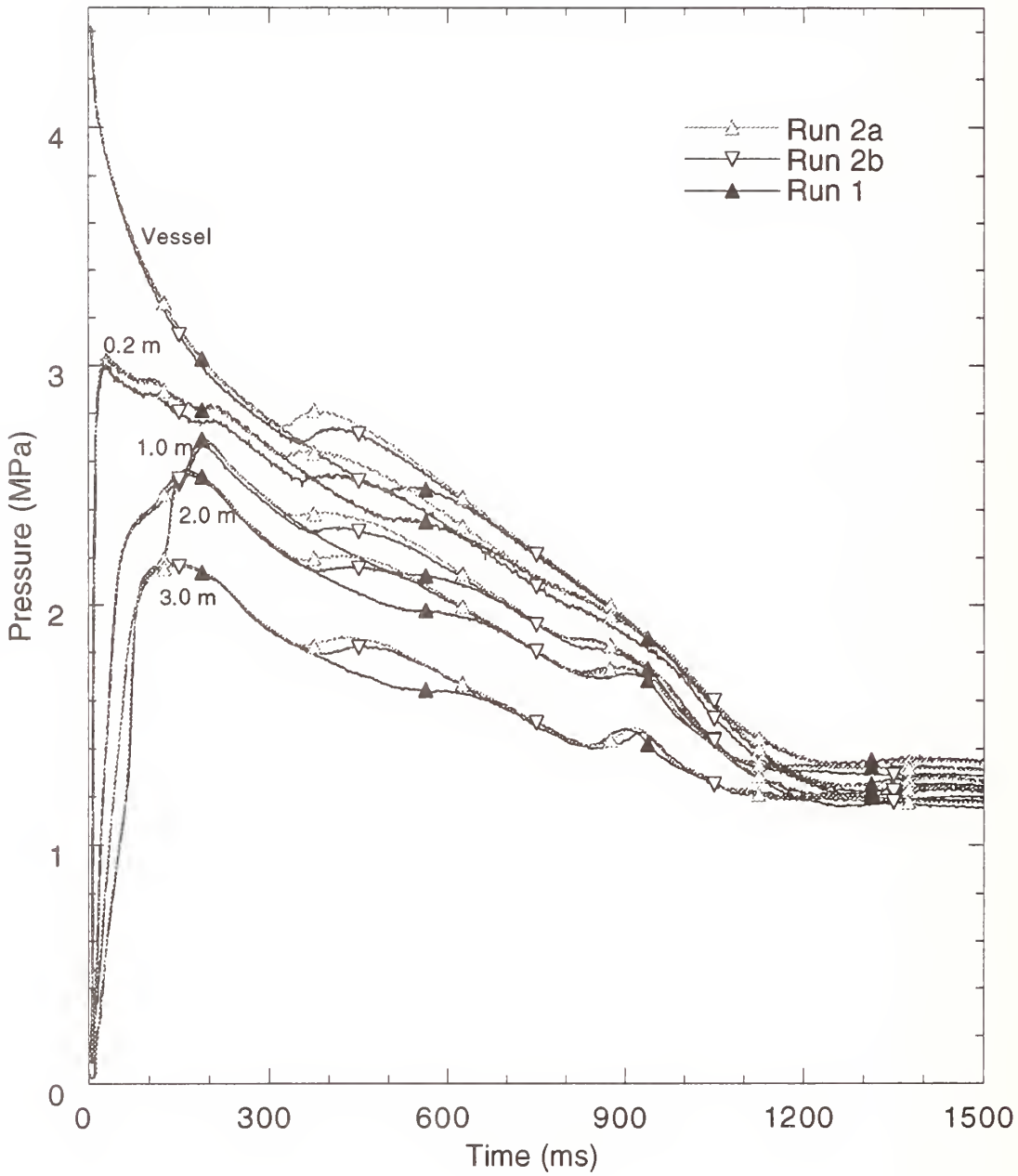

Figure 11. Pressure curves of C_2HF_5 at five locations using both new (Run 1) and once recycled (Run 2a and 2b) chemical.

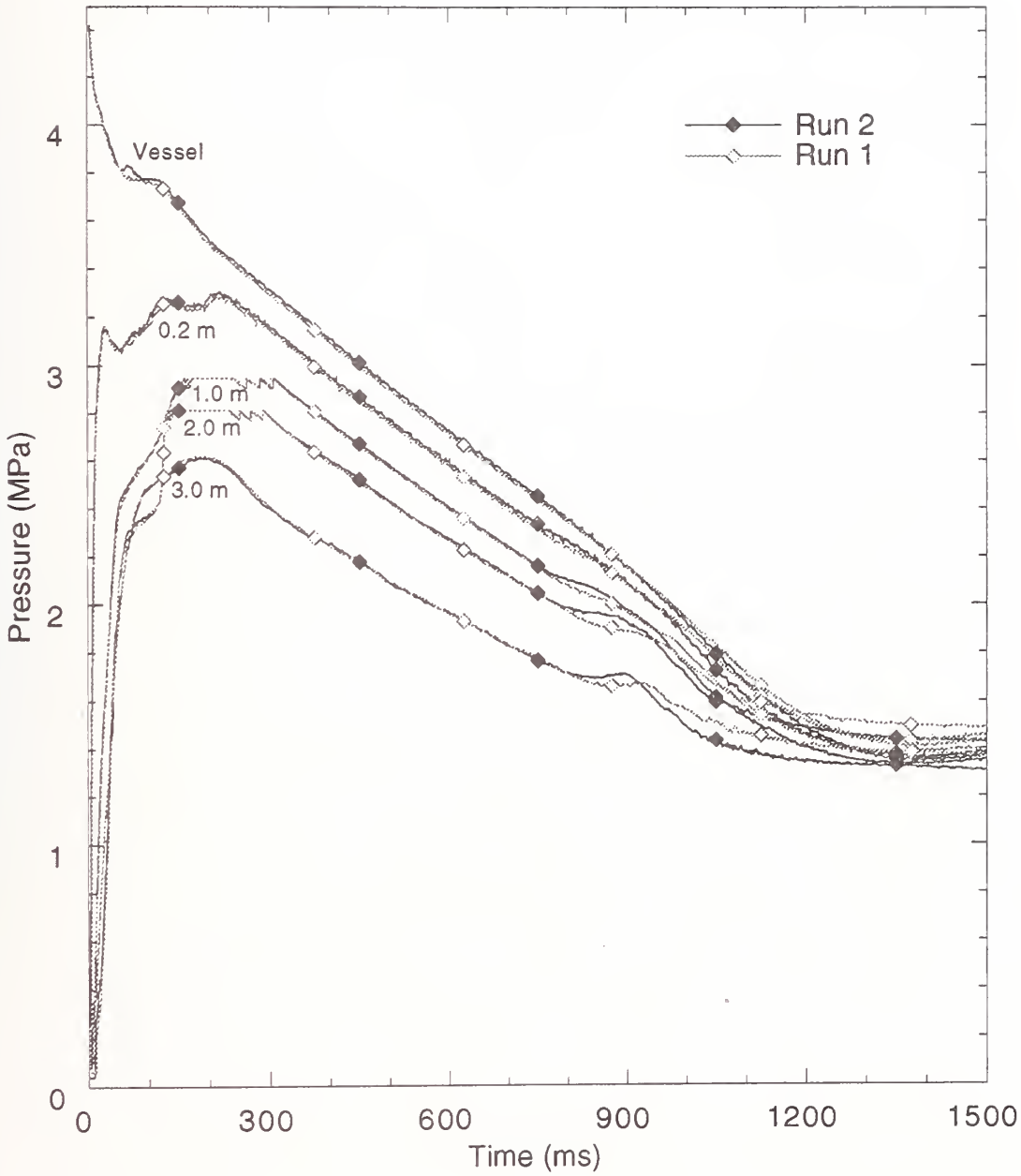

Figure 12. Pressure curves of SF_6 at five locations using both new (Run 1) and once recycled (Run 2) chemical.

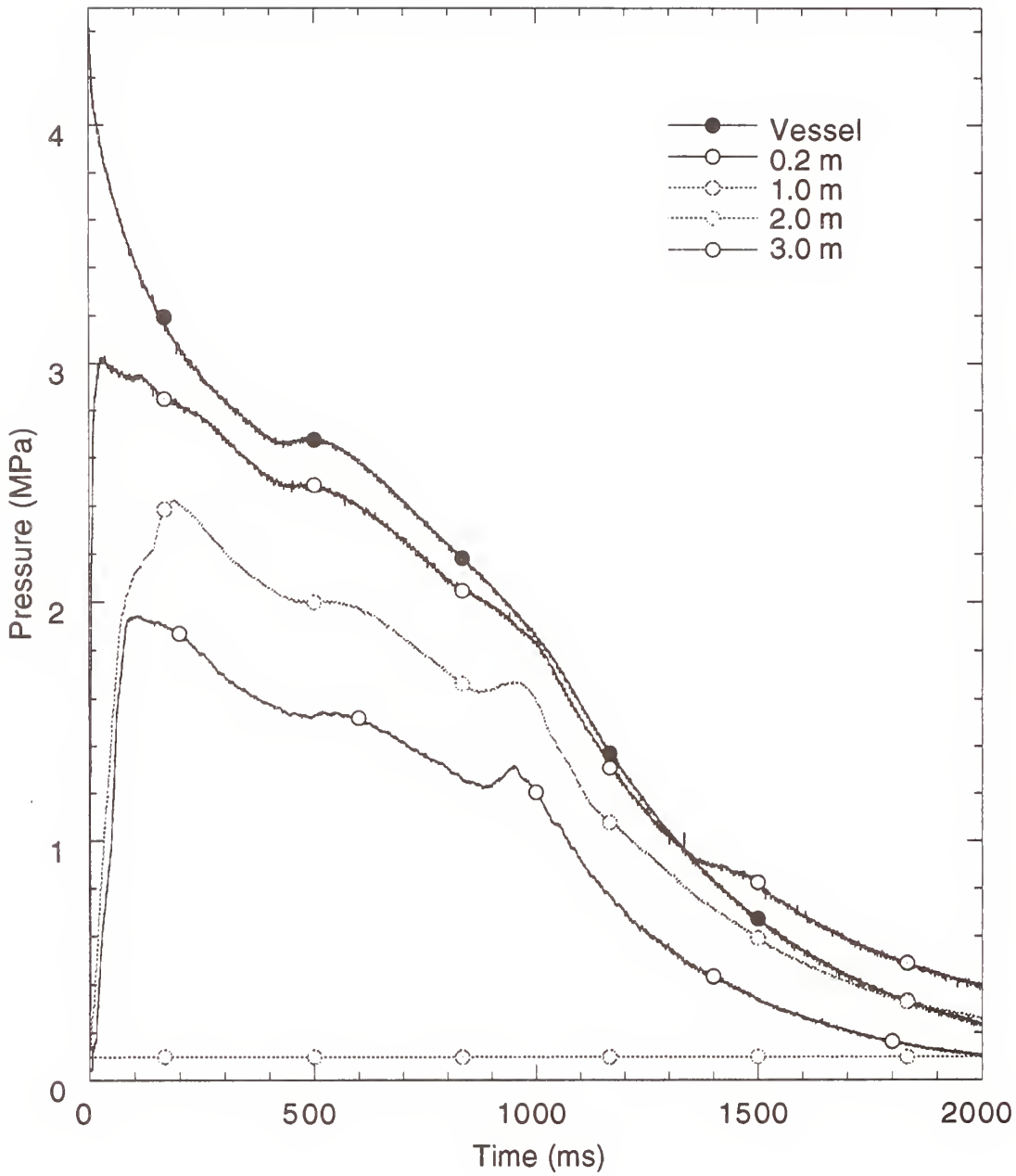

Figure 13. Pressure curves of CF_3Br discharged to atmosphere for five locations with agent that was recycled once. (Note that the 1.0 m pressure transducer malfunctioned.)

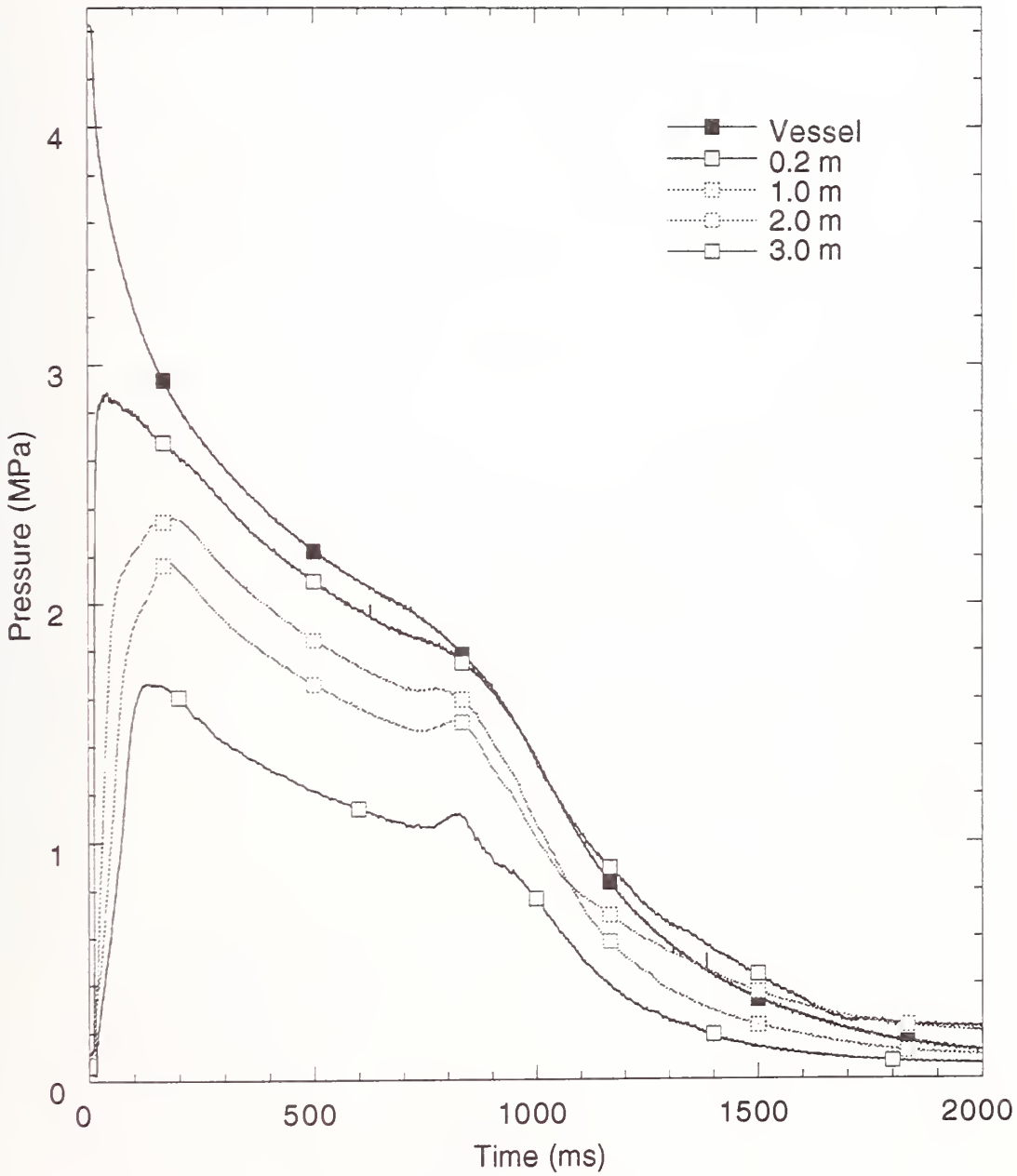

Figure 14. Pressure curves of $CHClF_2$ discharged to atmosphere for five locations with chemical that was recycled once.

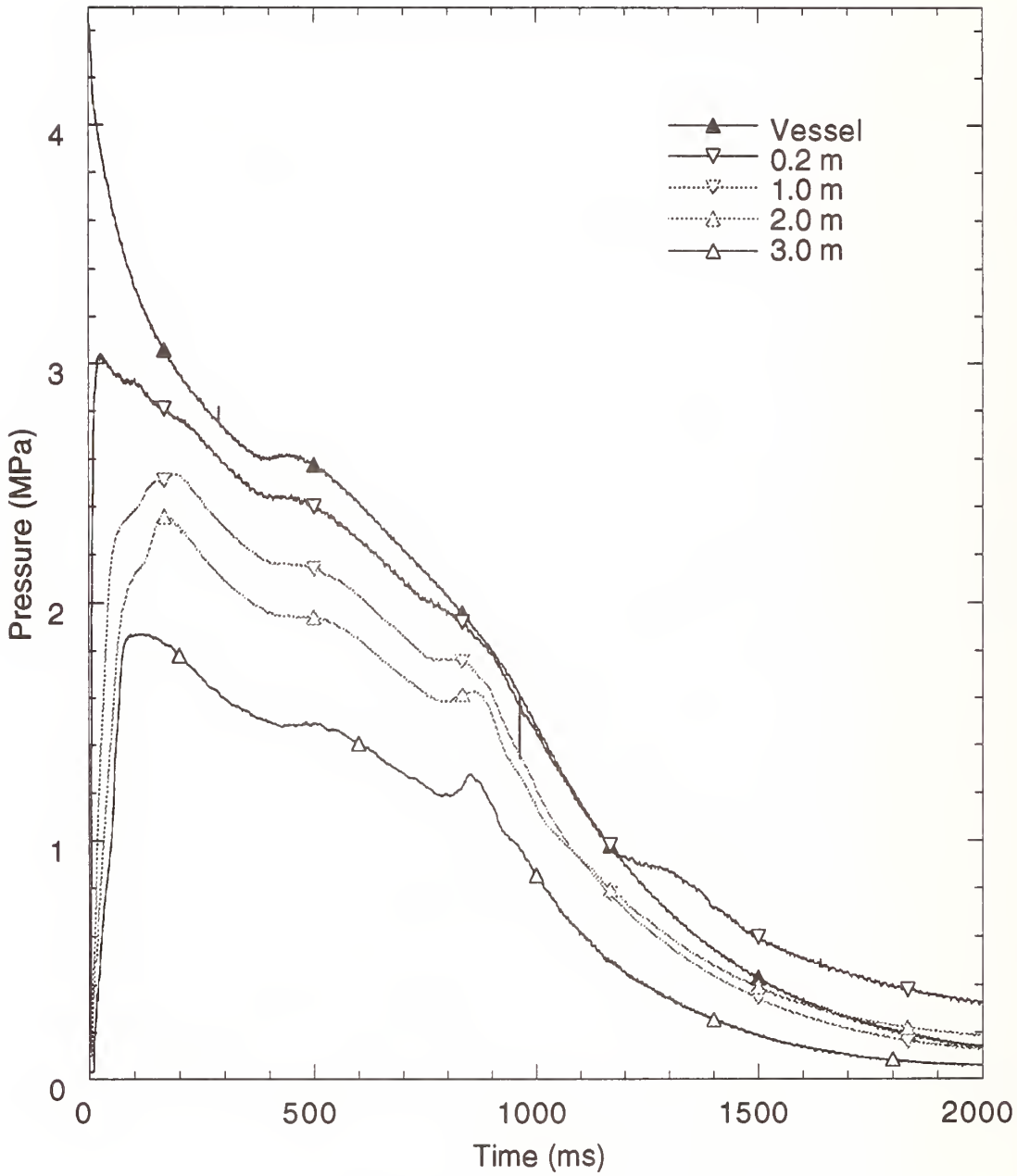

Figure 15. Pressure curves of C_2HF_5 discharged to atmosphere for five locations with chemical that was recycled once.

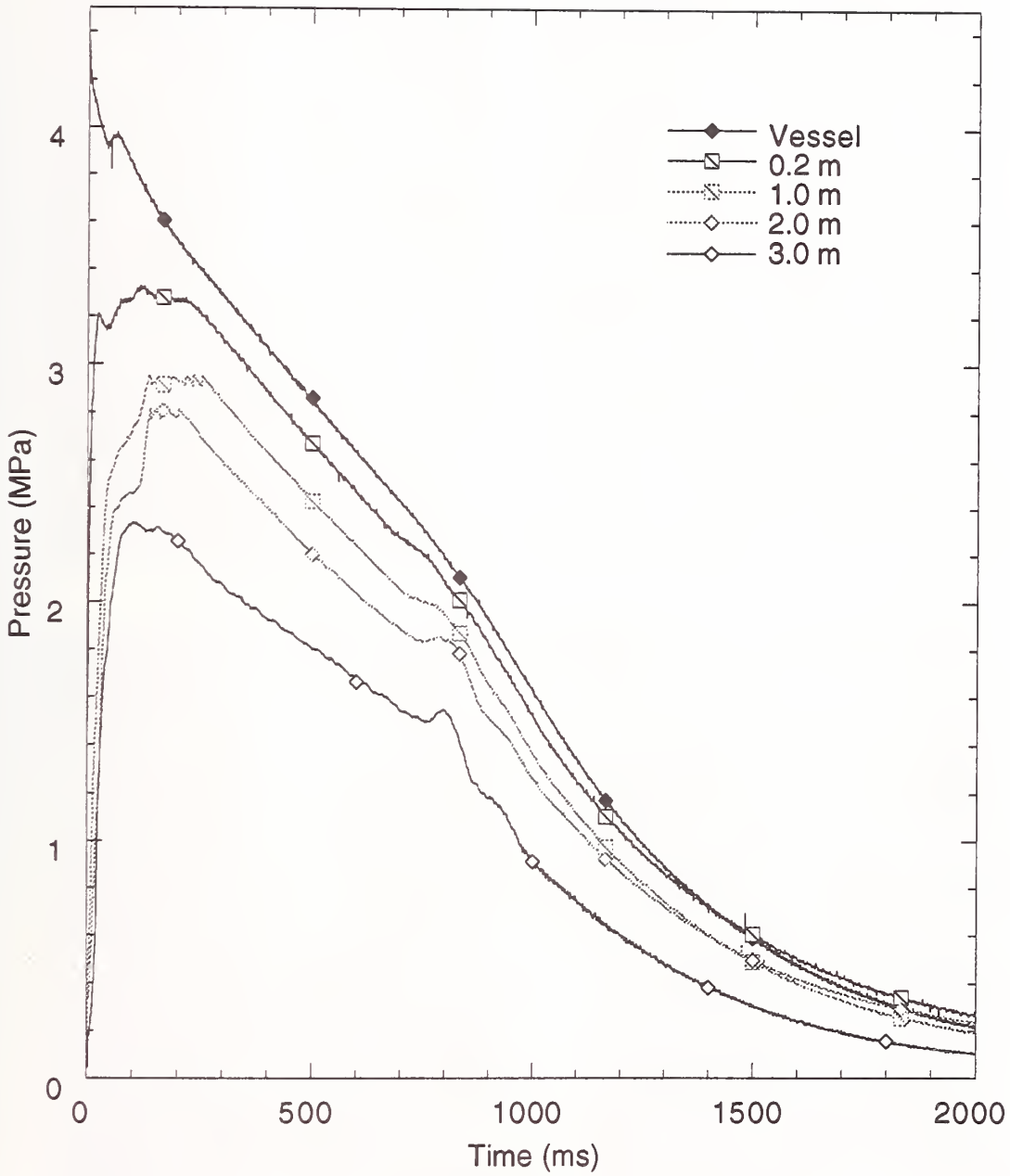

Figure 16. Pressure curves of SF_6 discharged to atmosphere for five locations with chemical that was recycled once.

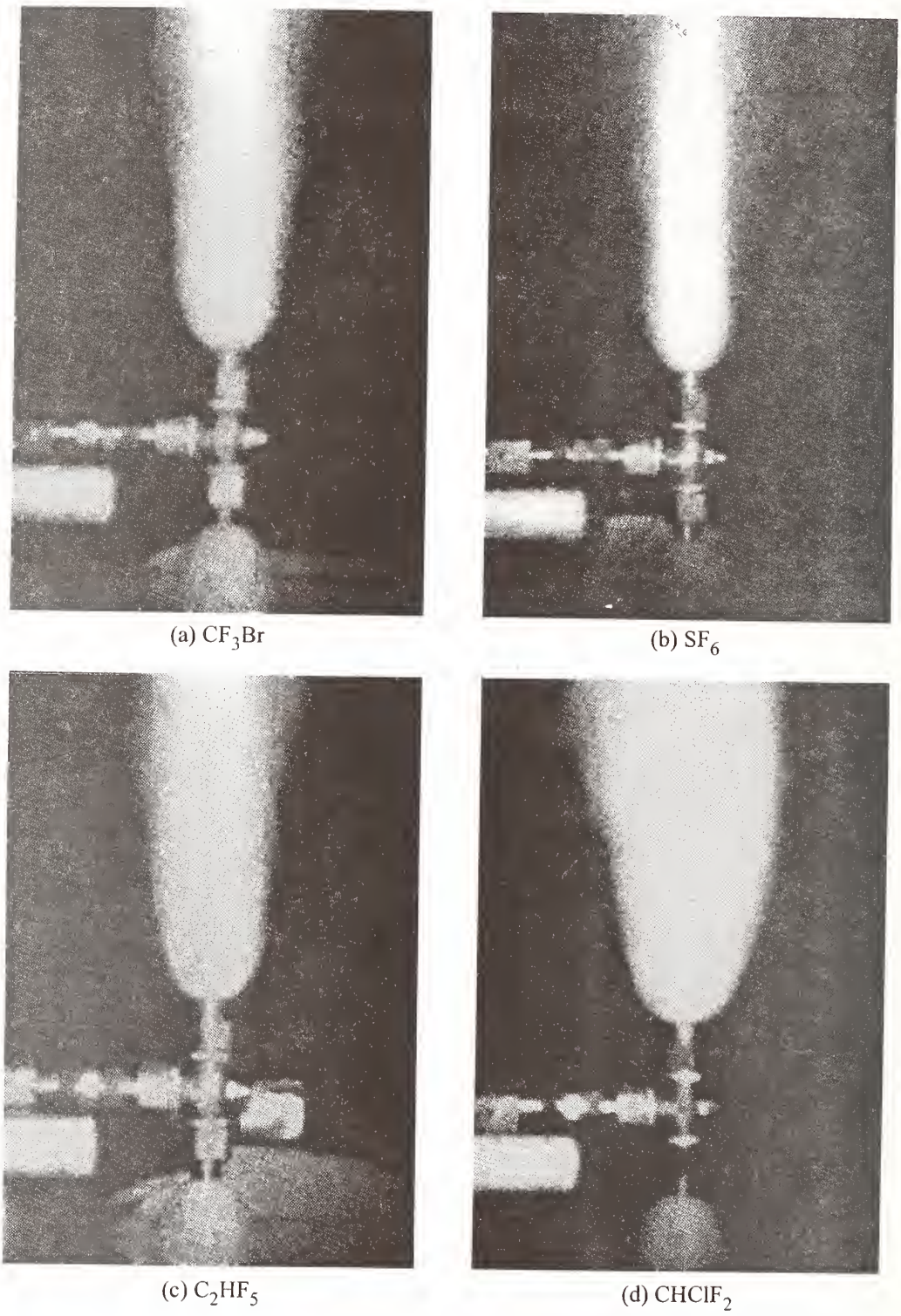

(a) CF_3Br (b) SF_6

(c) C_2HF_5 (d) $CHClF_2$

Figure 17. Prints of the spray plumes discharged to atmosphere through the T-fitting after 200 ms for (a) CF_3Br, (b) SF_6, (c) C_2HF_5, and (d) $CHClF_2$.

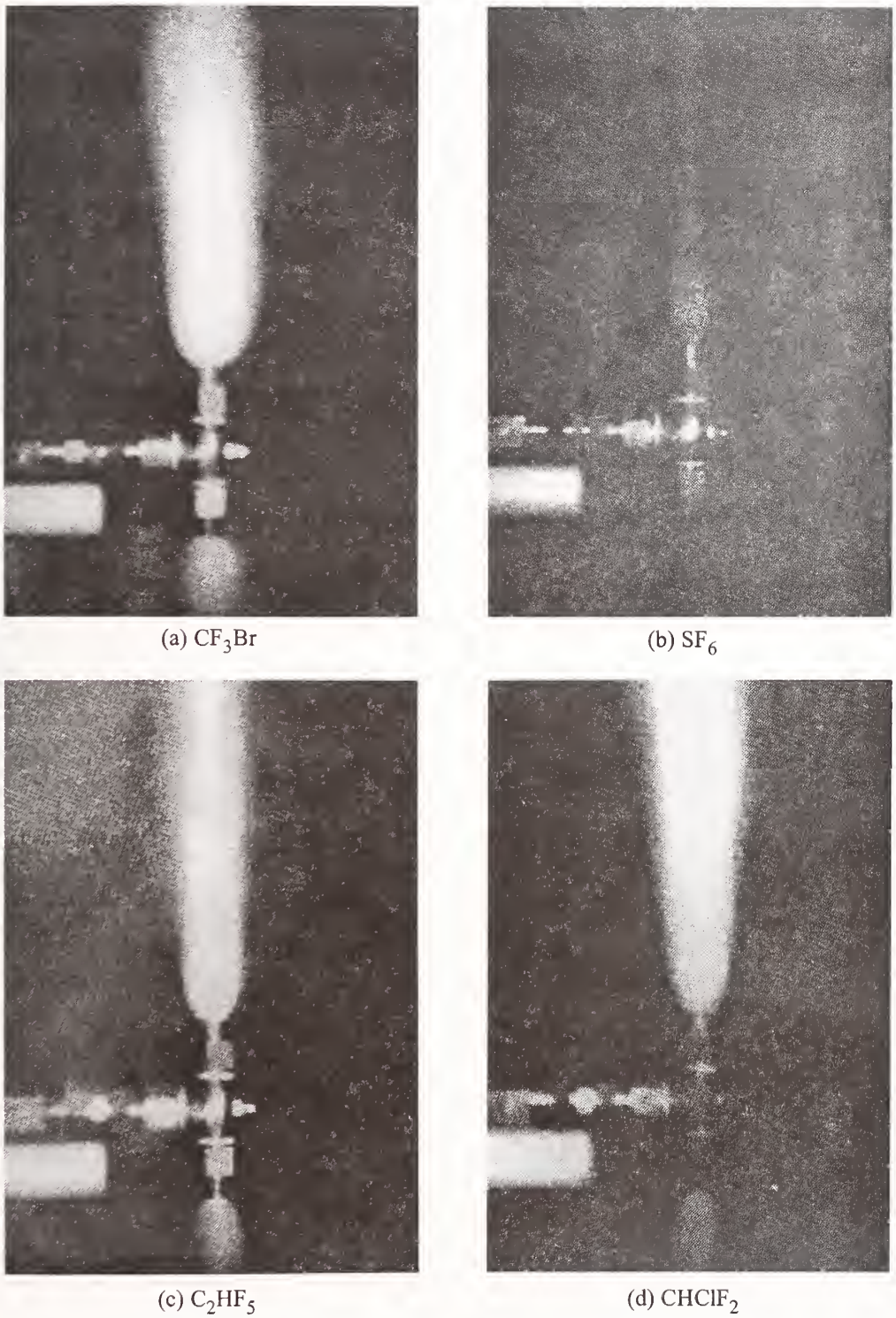

(a) CF_3Br (b) SF_6

(c) C_2HF_5 (d) $CHClF_2$

Figure 18. Prints of the spray plumes discharged to atmosphere through the T-fitting after 900 ms for (a) CF_3Br, (b) SF_6, (c) C_2HF_5, and (d) $CHClF_2$.

12.6 Acknowledgments

This work was sponsored by the U.S. Naval Air Warfare Center at Lakehurst, New Jersey under the direction of Mr. William Leach. Concurrent work at Walter Kidde Aerospace by Mr. Mark Mitchell provided valuable insight into specifics of aircraft suppression systems and the aircraft certification process. In addition the authors are grateful to Mr. Mitchell for supplying the T-fitting that was used in the above simulant spray tests. Ms. Lois Ellis of AlliedSignal provided valuable information about the properties of SF_6. We appreciate the work of Ms. Marcia Huber of NIST in Boulder, Colorado for adding SF_6 to her software program PROFISSY. At NIST in Gaithersburg, Maryland, we would like to thank Mr. Charles Boyer who performed numerous discharge tests, and Mr. Tom Cleary and Dr. Jiann Yang who greatly facilitated the use of their experimental discharge apparatus for this work. Finally, we would like to acknowledge those who have contributed to the general knowledge in this field by an open exchange of their ongoing work: Mr. Ken Kaufmann, Mr. Gregg Wosniak, and Dr. Harendra Mehta of the Boeing Corporation and Mr. David Riordan of Short Brothers.

12.7 References

BA^{e}SEMA, *Substitutes for Halons for use in Shipboard Discharge Tests - Final Report*, BA^{e}SEMA Ltd., Report No. YD 4852, 1992.

Braun, E., Peacock, R.D., Forney, G.P., Mulholland, G.W., Levin, B.C., "Human Exposure and Environmental Impact," in *Evaluation of Alternative In-Flight Fire Suppressants for Full-Scale Testing in Simulated Aircraft Engine Nacelles And Dry Bays*; Grosshandler, W.L., Gann, R.G., Pitts, W.M., Eds.; NIST SP 861, 813-826, April 1994.

Cleary, T.G., Grosshandler, W.L., Yang, J.C., "Flow of Alternative Agents in Piping," *Proceedings of the Halon Options Technical Working Conference*, Albuquerque, NM, May 3-5, 1994.

Daubert, T.E., Danner, R.P., Eds., "DIPPR *Data Compilation of Pure Chemicals*," Version 8.0; NIST Standard Reference Database 11, Design Institute for Physical Property Data American Institute of Chemical Engineers, 1993.

Department of Transportation Federal Aviation Administration Advisory Circular Number 20-100, "General Guidelines for Measuring Fire-Extinguishing Agent Concentrations in Powerplant Compartments"; September 21, 1977.

DiNenno, P.J., Forssell, E.W., Starchville, M.D., Carhart, H.W., "Evaluation of Halon 1301 Test Gas Simulants: Enclosure Leakage," *Fire Technology* 25, No. 1, 24-40 (1989).

DiNenno, P.J., Forssell, E.W., Starchville, M.D., Carhart, H.W., Leonard, J.T., "Hydraulic Performance Test of Halon 1301 Test Gas Simulants," *Fire Technology* 26, No. 1, 121-140 (1990).

European Communities Regulation 3093/94, 22 December 1994.

Gallagher, J., McLinden, M., Morrison, G., Huber, M., "REFPROP 4.0 *NIST Thermodynamic Properties of Refrigerants and Refrigerant Mixtures,*" NIST Standard Reference Database 23, 1993.

Huber, M. L., "NIST Program PROFISSY - Version 0.03: PROperties of FIre Suppression SYstems," NIST Thermophysics Division, 1994.

Kaufmann, K. J., Miller, M.P., Woznaik, G., Mitchell, M., "Results of Halon 1301, HFC-125, and SF_6 Concentration Tests in a Large Commercial Aircraft Engine," *Proceedings of the Halon Options Technical Working Conference*, Albuquerque, NM, May 3-5, 1995.

Leach, W., Homan, J., "U.S. Navy Halon Simulant Identification Program," *Proceedings of the Halon Options Technical Working Conference*, Albuquerque, NM, May 3-5, 1995.

Material Safety Data Sheet (MSDS); Occupational Health Services, Inc., New York, NY, 1994.

Military Specification MIL-E-22285 (Wep): "Installation and Test of Extinguishing System, Fire Aircraft, High-Rate-Discharge Type," 11 December 1959, and "Amendment - 1," 27 April 1960.

Moore, D.W., "Alternate Test Agent for Halon Systems," DuPont Fluoroproducts, 1989.

Pitts, W.M., Yang, J.C., Gmurczyk, G., Cooper, L.Y., Grosshandler, W.L., Cleveland, W.G., and Presser, C., "Fluid Dynamics of Agent Discharge," in *Evaluation of Alternative In-Flight Fire Suppressants for Full-Scale Testing in Simulated Aircraft Engine Nacelles And Dry Bays*, Grosshandler, W.L., Gann, R.G., Pitts, W.M., Eds.; NIST SP 861, 291-295, April 1994.

Ravishankara, A.R., Soloman, S., Turnipseed, A.A., Warren, R.F., "Atmospheric Lifetimes of Long-Lived Halogenated Species"; *Science* 259, 194-199 (1993).

Riordan, D., correspondence to C. Womeldorf, NIST, on May 25, 1995 and conversation with C. Womeldorf, NIST, on June 16, 1995. Short Brothers Plc, Nacelle Systems Division, Belfast, Northern Ireland.

South Coast Air Quality Management District Rule 1418, Section (d)(2)(B), 10 January 1992.

Tedeschi, M. and Leach, W., "U.S. Navy Aircraft Halon 1301 Effectivity Analysis," *Proceedings of the Halon Options Technical Working Conference*, Albuquerque, NM, May 3-5, 1995.

13. CONCLUSION

Richard G. Gann
Building and Fire Research Laboratory

Contents

13.1 Background

This report presents the results of two years of research in support of the objective to identify and make ready for use the optimal near-term fluid to replace halon 1301 for in-flight fire suppression in aircraft engine nacelles and dry bays. At the time the work presented in this report was begun, the Technology Transition Team of the sponsors, the Air Force, Army, Navy, and FAA, had selected the following candidates for consideration:

Engine Nacelle	Dry Bay
C_2HF_5 (HFC-125, pentafluoroethane)	C_2HF_5 (HFC-125, pentafluoroethane)
C_3HF_7 (HFC-227ea, 1,1,1,2,3,3,3-heptafluoropropane)	CF_3I (trifluoroiodomethane)
CF_3I (trifluoroiodomethane)	C_3F_8 (FC-218, octafluoropropane)

The NIST research results in Part 1 of this report were directed at helping to reduce each of these lists to a single chemical. The results in Part 2 are to assist in the development of engineering design criteria and suppressant system certification.

13.2 Knowledge to Help Select the Optimal Currently-Available Alternate Fire Suppressant

13.2.1 Fire Suppression Efficiency

Most of the laboratory-scale information was reported in Grosshandler *et al.*, (1994). From the deflagration/detonation tube results presented here, FC-218 provides the most consistent performance over the widest range of fuel/air mixtures and tube geometries. CF_3I has the greatest positive impact at low addition levels, but shows non-monotonic behavior of combustion wave speed and shock pressure at higher levels. HFC-125 produces higher peak pressures than either CF_3I or FC-218, but the more moderate conditions investigated in the current study do not yield the excessive overpressures note previously.

Also presented here are comprehensive fire suppression efficiency measurements in a turbulent spray burner. CF_3I was found to be more efficient than either HFC-125 or HFC-227ea. However, at elevated temperature of 150 °C, the three chemicals performed equally on a mass basis.

13.2.2 Stability During Storage

There should be no problems with designing long-term storage capability for any of the four agents.

- The stability of HFC-125, HFC-227ea, and FC-218 was excellent after storage for 48 weeks at 150 °C and 4.2 MPa in the presence of a range of possible metals for use in the storage bottles: Nitronic 40, Ti-15-3-3-3, C4130, and Inconel 625. In all cases, there was no noticeable loss of agent, and no new spectral features appeared in the post-exposure analyses.

- Samples of CF_3I were observed to be stable at 23 °C for 52 weeks in the presence of the same metals. However, during exposure at 100 °C and especially at 150 °C, some CO_2 and an unknown chemical appeared whose concentration increased with exposure time. Identification was by the appearance of a sharp peak at 950 cm^{-1} in the spectrum of the degraded CF_3I. The peak appeared in all of the samples, and was not significantly affected by the nature of the metals present. It did not appear when moisture or metallic copper (reputed to retard the degradation of iodides) were added to the storage atmosphere at 150 °C. Our efforts to identify the product chemical from its telltale peak have been unsuccessful. The degree of CF_3I degradation was small, even if extrapolated to a 5-year storage time. However, should this unknown chemical be toxic, its presence might be an additional reason for care in discharging CF_3I in occupied areas.

Each of the four chemicals is compatible with a choice of materials for the storage containers: elastomers, lubricants, and metals.

- The compatibility of the four candidate suppressants with organic materials potentially found in fire suppression systems was evaluated by swelling experiments. Seven elastomers and three greases were exposed to each of the agents at pressures up to 5.86 MPa and temperatures up to 105 °C. The tests measure the extent to which the agent dissolves in the material, a behavior that is undesirable if excessive. Each agent caused only relatively minor swelling in at least three of the elastomers and at most moderate swelling in the greases. HFC-125, FC-218, and CF_3I all showed only limited solubility in two of the greases.

- The long-term stability of the seven elastomers was evaluated using compression set measurements and tensile testing of o-ring materials. Exposures in CF_3I were performed to 58 weeks, and the other three agents were tested for times as long as 74 weeks. The testing temperature was 75 °C. Compression set evaluates the resistance of the elastomers to excessive permanent deformation, and the results showed that at least two elastomers are compatible with each of the candidate agents. Tensile testing was performed to evaluate the retention of mechanical strength of the elastomer. However, these results were inconclusive due to large variability in the data. The testing also showed anomalous behavior of the CF_3I, suggesting some agent degradation.

- After immersion of five types metal coupons (Nitronic 40, Ti-15-3-3-3, C4130, 304 stainless steel, and aluminum alloy 6061-T6) for 12 months at 150 °C and 5.86 MPa in each of the four candidate agents plus halon 1301, the mass changes for these alloys were relatively minor, although some slight pitting was observed, particularly on the C4130 steel. In addition, CF_3I showed some small interaction with three of the metals, none with Nitronic 40, and significant interaction with C4130. Under the same conditions at 20 °C, little or no interaction was seen except for three pairs: halon 1301 with the aluminum alloy, and CF_3I and HFC-125 with the C4130 steel.

- Slow strain rate tests of the five above agents with Nitronic 40, 304 stainless steel, and Ti-15-3-3 at 150 °C and 5.86 MPa showed no difference from metal samples immersed in inert argon. The one exception was CF_3I and the titanium alloy. Two of these three titanium samples fractured distinctively early, indicating potential incompatibility between the two. At 20 °C all the agents were similar to argon (an inert gas) in their effects on the metals.

13.2.3 Safety Following Discharge

- While accidentally-discharged CF_3I will decompose under both normal outdoor and indoor lighting, laboratory measurements and dispersion modeling show that the concentrations of potentially toxic photolysis products (HF, COF_2) are not likely to be sufficient to hinder prompt escape. HFC-125, HFC-227ea, and FC-218 are not photosensitive to normal lighting.

- The production of HF (during fire suppression) from all four of the chemicals can now be predicted. The principles for this have been verified using HF concentration data from laboratory flames and room fires. Fires in dry bays are suppressed sufficiently quickly that only small amounts will be formed regardless of which of these agents is used. For engine nacelle fires, the model developed here predicts that HFC-227ea, HFC-125 and FC-218 would produce similar amounts, while the more efficient CF_3I would produce far less. Exposure to surfaces heated by the fire would produce more HF from CF_3I than from the other three chemicals.

- Samples of aircraft materials (6061-T6 aluminum alloy, Inconel alloy 718, Inconel alloy 903, 410 stainless steel, titanium alloy Ti-8-1-1-1, titanium grade 5 alloy, Haynes alloy 188, and a 3501-6/AS4 graphite-epoxy composite) that might be located near or downstream of an engine nacelle fire were immersed in 1 % or 10 % aqueous HF and then stored at 100 % relative humidity for 30 days at 22 °C. In both cases, no significant corrosion occurred after the initial exposures to the HF.. However, actual deployments in service will contain particulates and/or other compounds that could significantly alter the corrosion behavior of these alloys.

- The excessively high overpressures previously observed when HFC-125 suppressed high speed combustion waves in a deflagration tube do not occur under conditions more typical of those observed in the live-fire dry bay tests at WPAFB. The data indicate that none of the three candidates should be eliminated from consideration based on this criterion.

13.2.4 Discharge Performance

- All four of the chemicals can be expected to discharge and disperse well from their storage and distribution systems at temperatures near 20 °C.

- Data from this report and the prior work indicate that at the lower temperatures experienced during high altitude flight or cold weather operation, CF_3I and HFC-227ea, with their high boiling points, would not distribute as uniformly as the other two chemicals.

13.2.5 Recommendation

Based on the results available in October, 1994, we recommended the selection of HFC-125 as the optimal candidate for Phase III examination for both engine nacelle and dry bay fire suppression. FC-218 is not distinctively more efficient than the other chemicals and possesses an extremely long environmental lifetime. While CF_3I is the most efficient suppressant, being virtually a drop-in replacement for halon 1301 in some tests, it is unfavorable in three aspects. First, its inhalation toxicity in cardiac sensitization testing (performed elsewhere) is such that it is not usable in occupied areas. Second, at the time the decision was to be made, the stability and materials compatibility data were inconclusive. Third, its relatively high boiling point makes it less likely to discharge and disperse well (especially around obstructions) at the low temperatures encountered when flying at high

altitudes or operating in cold weather. HFC-227ea has a similar boiling point, and thus would show similar behavior. This is the principal distinguishant from HFC-125, whose boiling point is far closer to that of CF_3Br. In other respects, the two HFCs are comparable in their performance measures. The knowledge that has accrued in the final year of the project has not changed our perspective on this recommendation.

During the fall, 1994 meetings of the Technology Transition Team, these data and the results of an extensive and carefully-constructed series of real-scale live-fire tests at Wright Patterson Air Force Base were discussed. The Team recommended HFC-125 as the candidate for Phase III evaluation for both applications.

13.3 Knowledge to Assist in the Development of Engineering Design Criteria and Suppression System Certification

13.3.1 Agent Discharge Behavior

The rate at which a suppressant will emerge from its storage container depends on the thermodynamic properties of the stored fluid and any pressurizing gas as well as the initial conditions in the container. Effective design of the suppression hardware requires quantitative performance measures for these chemicals.

- The computer code PROFISSY accurately calculates binary vapor-liquid equilibria within the storage bottle. This will aid hardware designers by providing useful and reliable data on the pressure/temperature characteristics of the selected agent/nitrogen mixtures.

- Laboratory data show that the nitrogen dissolved in the stored liquid agent significantly affects the agent discharge whether in a direct release system for dry bays or a piping system for engine nacelles.

- The storage bottle discharge model developed here, which incorporates nitrogen degassing, generally predicts agent discharge times to within a factor of two, but occasionally a factor of four. The only required input for the model is the initial conditions in the vessel.

- The prediction of the detailed structure of a highly transient flashing spray is still exploratory. Some very preliminary results are reported using state-of-the-art computer codes.

- For plumbed engine nacelle systems, a new, validated model can be used to facilitate transient pipe-flow calculations for two-phase flow.

- We have developed a flow chart to organize the use of these tools into a coherent process for optimal design of a new discharge system.

13.3.2 Engine Nacelle Fire Suppression Guidance

The selection of the mass of the alternative agent to be stored on an aircraft should be based on the amount needed to quench the worst realistic fire.

- For engine nacelles with ribs and other obstructions, experiments show that under similar flow conditions, a baffle-stabilized pool fire requires higher agent concentrations and longer mixing times than a baffle-stabilized spray flame.

- As anticipated, heating the air stream increases the mass of agent need for flame extinction. The system pressure and fuel flow had no significant effect on the mass of agent needed for suppression.

A step-by-step procedure has been developed that gives guidance in determining fire suppressant concentrations and discharge times for flame extinguishment. It shows the importance of agent injection duration, air flow and velocity, agent/air mixing mode, and fire scenario. A reasonable target concentration for an agent in the fire zone is that needed to quench the most flammable fuel/air mixture, ensuring both flame suppression and preventing re-ignition.

13.3.3 Real-Time Concentration Measurement

Determination of the dispersion of the suppressant following discharge requires measurements of its concentration that are well-resolved in both time and space. We examined two instruments in order to assess their ability to perform *in situ* measurements with the ~1 ms time resolution needed for dry bay applications. Neither performed well. Both were re-designed with the following results:

- An aspirated hot-film/cold-wire probe has been shown capable of recording simultaneous temperature and agent concentration measurements with high temporal (~1 ms) and spatial (~1 mm^3) resolution. However, the film is sensitive to velocity fluctuations and the small diameter, sonic orifice is readily clogged by small particles, leaving the probe unfit for practical use in its current version. There is a reasonable probability that these limitations could be overcome with further work.

- An infrared absorption probe (DIRRACS) with an incandescent source, narrow bandpass filter, pyroelectric sensor and an optical chopper can also record simultaneous temperature and agent concentration measurements. As developed, the air/agent mixture is observed as it flows between the source and the detector, a volume which manifests as a cylinder of 2.8 cm length and 3 cm diameter. Further, in its current design, the instrument response is sensitive to the flow velocity over it. Thus, this device also requires additional engineering to reduce both the sample volume and the flow dependence.

- A review of the sensing literature shows a number of alternative approaches, but none that could be accurately adapted to this application without a significant development and testing effort. The most promising are time-resolved mass spectrometry and mid- and near-infrared absorption combined with fiber optics to provide easy access and the needed spatial resolution.

13.3.4 Certification Guidance

- The mixing time for agent entrainment behind an obstacle is different under non-fire conditions than for fire conditions. A method for using the non-fire data to approximate the fire suppression concentration has been developed.

- HFC-125 closely replicates the physical and dispersion properties of halon 1301. Thus it is an excellent simulant for hardware development and can be used to certify those engine nacelle fire suppression systems that still rely on halon 1301.

13.3.5 Interaction with Metal Fires

In laboratory experiments, none of the four alternative chemicals nor halon 1301 showed exacerbation of burning of magnesium or titanium rods. It is not explicitly known why the flare-ups observed during the introduction of halon 1301 to real metal fires were not observed here. However, it may be useful to know that in the circumstances replicated in the laboratory tests, the alternative agents did not worsen the combustion relative to that with halon 1301 present.

13.4 Concluding Remarks

This report brings to a conclusion the laboratory-scale research and screening method development in support of the portion of the Department of Defense Technology Development Plan devoted to finding the optimal current replacement for halon 1301 for suppressing in-flight fires. The recommendation by the Technology Transition Team of HFC-125 for Phase III testing for both engine nacelle and dry bay use demonstrates the present state of this field: today's commercial technology only offers suppressants that are distinctly less acceptable than halon 1301. It will remain the task of a further search already about to begin, to find replacement fire suppression capabilities that truly serve DoD needs.

This study, reported here and in Grosshandler, *et al.*, (1994), should serve as a cornerstone for the new program. There is a high degree of consistency between results from real-scale fire suppression tests conducted at the Wright Laboratory and those results presented in these reports. This will enable the methods developed here to be used with confidence on future candidate suppressants. Similarly, the methods developed for characterizing new agents, their compatibility with materials, and their delivery toward a fire should also have broad application.

Finally, it is also our hope that the rigor of these two reports will serve as a model for future reports in this field. In a search that is likely to find its successes among many blind alleys, it is important that the methods used and the data obtained be thoroughly documented as guidance for successive research efforts.

☆ U.S. GOVERNMENT PRINTING OFFICE: 1995 – 400 - 020